SINGLE-DOMAIN ANTIBODIES: BIOLOGY, ENGINEERING AND EMERGING APPLICATIONS

EDITED BY: Kevin A. Henry and C. Roger MacKenzie

PUBLISHED IN: Frontiers in Immunology

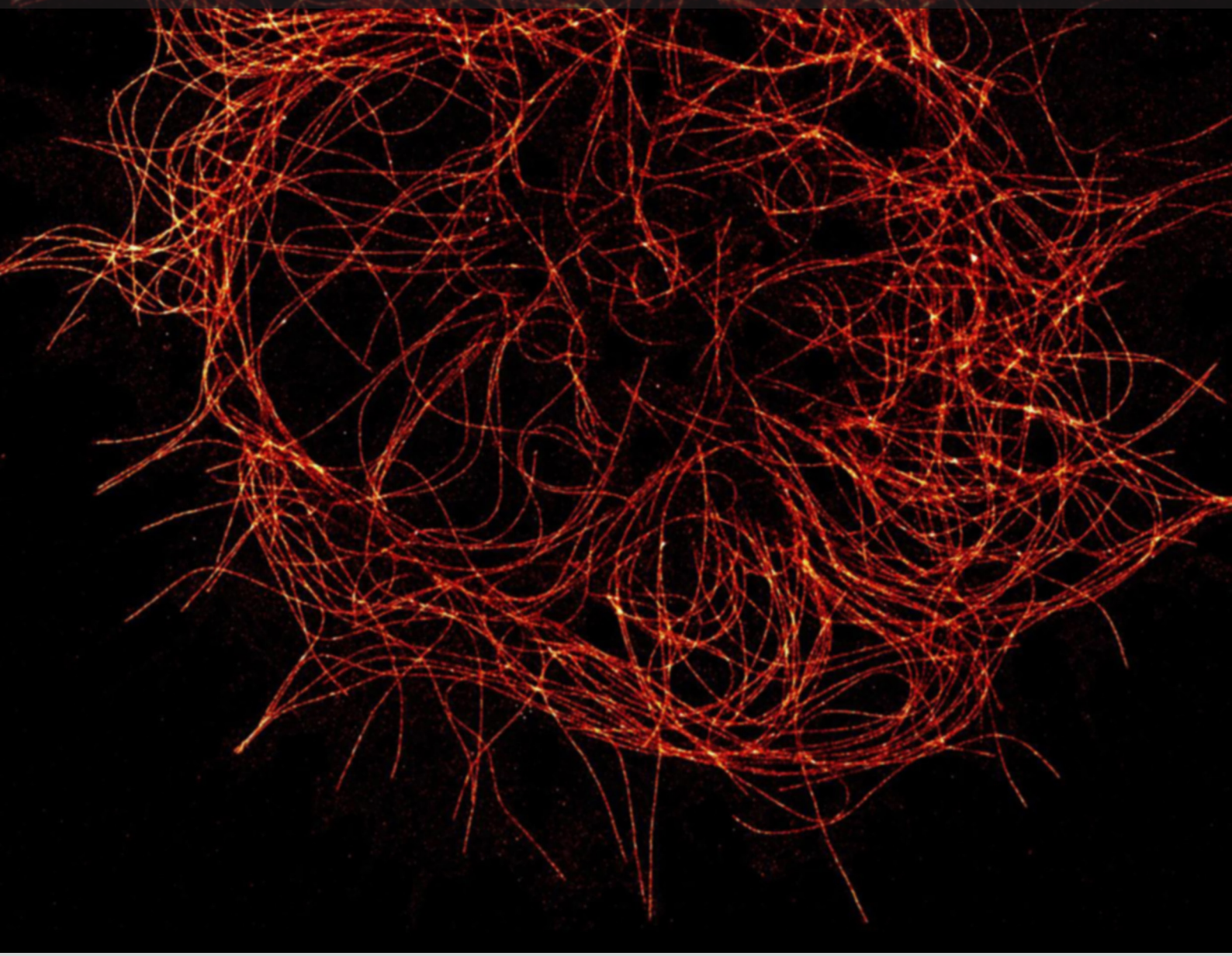

frontiers Research Topics

ISSN 1664-8714
ISBN 978-2-88945-432-7
DOI 10.3389/978-2-88945-432-7

About Frontiers

Frontiers is more than just an open-access publisher of scholarly articles: it is a pioneering approach to the world of academia, radically improving the way scholarly research is managed. The grand vision of Frontiers is a world where all people have an equal opportunity to seek, share and generate knowledge. Frontiers provides immediate and permanent online open access to all its publications, but this alone is not enough to realize our grand goals.

Frontiers Journal Series

The Frontiers Journal Series is a multi-tier and interdisciplinary set of open-access, online journals, promising a paradigm shift from the current review, selection and dissemination processes in academic publishing. All Frontiers journals are driven by researchers for researchers; therefore, they constitute a service to the scholarly community. At the same time, the Frontiers Journal Series operates on a revolutionary invention, the tiered publishing system, initially addressing specific communities of scholars, and gradually climbing up to broader public understanding, thus serving the interests of the lay society, too.

Dedication to quality

Each Frontiers article is a landmark of the highest quality, thanks to genuinely collaborative interactions between authors and review editors, who include some of the world's best academicians. Research must be certified by peers before entering a stream of knowledge that may eventually reach the public - and shape society; therefore, Frontiers only applies the most rigorous and unbiased reviews.
Frontiers revolutionizes research publishing by freely delivering the most outstanding research, evaluated with no bias from both the academic and social point of view.
By applying the most advanced information technologies, Frontiers is catapulting scholarly publishing into a new generation.

What are Frontiers Research Topics?

Frontiers Research Topics are very popular trademarks of the Frontiers Journals Series: they are collections of at least ten articles, all centered on a particular subject. With their unique mix of varied contributions from Original Research to Review Articles, Frontiers Research Topics unify the most influential researchers, the latest key findings and historical advances in a hot research area! Find out more on how to host your own Frontiers Research Topic or contribute to one as an author by contacting the Frontiers Editorial Office: **researchtopics@frontiersin.org**

SINGLE-DOMAIN ANTIBODIES: BIOLOGY, ENGINEERING AND EMERGING APPLICATIONS

Topic Editors:
Kevin A. Henry, National Research Council Canada, Canada
C. Roger MacKenzie, National Research Council Canada, Canada

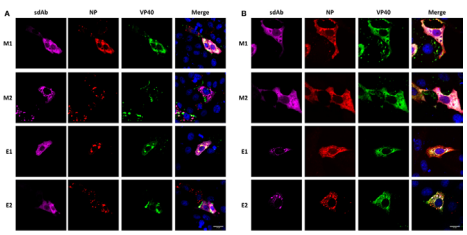

Image: Localization of single-domain antibody (sdAb) monomer or dimer when co-expressed with nucleoprotein (NP) and VP40 and impact on NP-VP40 co-localization. Immunofluorescence microscopy of transiently co-transfected Vero E6 cells producing anti-Marburgvirus (MARV) sdAb monomer (M1) or dimer (M2), or anti-Ebolavirus (EBOV) sdAb monomer (E1) or dimer (E2) with either (A) MARV VP40 and MARV NP genes or (B) EBOV VP40 and NP genes. Reproduced from: Darling TL, Sherwood LJ and Hayhurst A (2017) Intracellular Crosslinking of Filoviral Nucleoproteins with Xintrabodies Restricts Viral Packaging. Front. Immunol. 8:1197 doi: 10.3389/fimmu.2017.01197.

Cover image: Super-resolution microscopy image of a Ptk2 cell stained with AF647-labeled anti-tubulin single-domain antibody. Figure adapted from Mikhaylova et al. (2015) Resolving bundled microtubules using anti-tubulin nanobodies. Nat. Commun. 6:793 doi:10.1038/ncomms8933

Single-domain antibodies (sdAbs) represent the minimal form of an antigen-binding-competent immunoglobulin and have unique properties and applications. SdAbs are naturally produced as the variable domains of the heavy chain-only antibodies of camelid ruminants and cartilaginous fishes, but can also be engineered synthetically from autonomous human or mouse V_H or V_L domains. The scope of this research topic and associated e-book covers current understanding and new developments in (i) the biology, immunology and immunogenetics of sdAbs in camelids and cartilaginous fishes, (ii) strategies for sdAb discovery, (iii) protein engineering approaches to increase the solubility, stability and antigen-binding affinity of sdAbs and (iv) specialized applications of sdAbs in areas such diagnostics, imaging and therapeutics.

Citation: Henry, K. A., MacKenzie, C. R., eds. (2018). Single-Domain Antibodies: Biology, Engineering and Emerging Applications. Lausanne: Frontiers Media. doi: 10.3389/978-2-88945-432-7

Table of Contents

frontiers in Immunology

EDITORIAL
published: 23 January 2018
doi: 10.3389/fimmu.2018.00041

Editorial: Single-Domain Antibodies—Biology, Engineering and Emerging Applications

Kevin A. Henry[1]* *and C. Roger MacKenzie*[1,2]

[1] Human Health Therapeutics Research Centre, National Research Council Canada, Ottawa, ON, Canada, [2] School of Environmental Sciences, University of Guelph, Guelph, ON, Canada

Keywords: single-domain antibody, antibody discovery, antibody engineering, therapeutic antibody, diagnostic antibody

Editorial on the Research Topic

Single-Domain Antibodies—Biology, Engineering and Emerging Applications

Since the discovery of camelid heavy chain-only antibodies (HCAbs) in 1993 (1) and shark immunoglobulin new antigen receptors (IgNARs) in 1995 (2), and the subsequent recognition that the variable domains of these antibodies (V_HHs and $V_{NAR}s$, respectively) function autonomously as single-domain antibodies (sdAbs), sdAbs have found many uses across diverse fields. Early work on naturally-occurring antibodies bearing single variable domains spurred renewed interest in the development of human sdAbs, namely, the light chain variable domains (V_Ls) and the heavy chain variable domains (V_Hs) of human conventional antibodies; the first reported sdAbs were actually V_Hs (3). Synthetic human sdAbs are expected to be less immunogenic than V_HHs or $V_{NAR}s$ but their development is more challenging, requiring steps to ensure the selection of molecules with good biophysical properties and appropriate affinity. There are several advantages offered by sdAbs over conventional antibodies in a wide variety of diagnostic, research, and therapeutic applications, most notably their ease of production in microbial systems, their potential ability to target cryptic epitopes that are inaccessible to larger molecules, and the fact that they can be readily formatted into more complex molecules. This collection brings together 26 reviews and original research articles that together provide extensive coverage of the developments, opportunities, and challenges associated with this unique class of molecules.

OPEN ACCESS

Edited by:
Abdul Qader Abbady, AECS, Syria

Reviewed by:
Serge Muyldermans, Vrije Universiteit Brussel, Belgium

***Correspondence:**
Kevin A. Henry
kevin.henry@nrc-cnrc.gc.ca

Specialty section:
This article was submitted to Vaccines and Molecular Therapeutics, a section of the journal Frontiers in Immunology

Received: *21 December 2017*
Accepted: *08 January 2018*
Published: *23 January 2018*

Citation:
Henry KA and MacKenzie CR (2018) Editorial: Single-Domain Antibodies—Biology, Engineering and Emerging Applications. Front. Immunol. 9:41. doi: 10.3389/fimmu.2018.00041

BIOLOGY OF SINGLE-DOMAIN ANTIBODIES

Although no manuscripts describe the immunobiology of sdAbs themselves, Arbabi-Ghahroudi provides a historical perspective on the discovery and development of camelid sdAbs and highlights how much of the molecular ontogeny of sdAbs still remains poorly understood. Nonetheless, sdAbs have proven to be valuable research tools, especially for studying cellular biology, and two reviews summarize applications of sdAbs in fundamental research. Beghein and Gettemans review and thoroughly assess the current status of sdAbs as research tools in three main areas: (i) the preparation and use of labeled sdAbs in fluorescent microscopy, (ii) the application of sdAbs to the study of protein–protein interactions, and (iii) the use of sAbs as an alternative to RNAi in exploring protein function. They also touch on the usefulness of sdAbs as protein crystallization chaperones in structural biology. Traenkle and Rothbauer briefly review recent development of sdAbs for advanced cellular imaging ("chromobodies") with a focus on (i) live-cell imaging to visualize the dynamics of cytoskeletal proteins and nuclear components and (ii) the advantages and challenges of using sdAbs in super-resolution microscopy. The ability of sdAbs to be expressed in mammalian cell cytosol

and to tolerate fusion with a variety of tags are pivotal in these applications.

DISCOVERY, ENGINEERING, AND CHARACTERIZATION OF SINGLE-DOMAIN ANTIBODIES

One methods article, one original research article and one technology report deal with new approaches to camelid sdAb discovery. Historically, most sdAbs have been isolated by selection from *in vitro* display libraries, yielding binders with desired properties to a target antigen. Deschaght et al. applied a next-generation DNA sequencing (NGS) approach to the identification of antigen-specific sdAbs from a phage-displayed V_HH library constructed from the lymphocytes of an immunized llama. NGS analysis of sdAb-displaying phage enriched after a single round of panning against RON receptor tyrosine kinase correctly identified 35 known binders as well as a large diversity of functional sdAbs that were missed by conventional screening of the same library. Hussack et al. describe the application of an anti-bovine serum albumin (BSA) V_HH with unique properties ("ABTAG") to the medium-throughput affinity screening of sdAbs by surface plasmon resonance. The authors found that sdAb–ABTAG dimers bound to a BSA surface could be completely dissociated using low pH, over multiple cycles, without loss of surface activity, and exploited this to recover rare ultra-high-affinity V_HHs against CEACAM6 that were missed by panning of a phage-displayed V_HH library. Eden et al. describe protocols they have developed for DNA immunization of camelids and identification of sdAbs against membrane proteins; historically, this has been an arduous and unreliable process in large outbred animal species.

One original research article and one technology report describe new approaches to the isolation of human sdAbs. Henry et al. designed a set of novel phage-displayed sdAb libraries, constructed by synthetic randomization of rare fully human autonomous V_H and V_L domains, and provide a molecular explanation for the variable success rates in obtaining antigen-specific binders from such libraries: in the absence of solubilizing framework mutations akin to those of camelid V_HHs, fully human sdAbs rely heavily on their CDR sequences both for stability and solubility as well as for binding, imposing fundamental limitations on the sequences of these molecules. One potential workaround is to increase throughput, and Drabek et al. describe an automatable high-throughput technology for isolating fully human, soluble, high-affinity antigen-specific HCAbs. Building upon a previous generation of transgenic mice bearing hybrid llama-human *igh* loci (llama V_HH genes; human D, J, and C genes), the authors have constructed a new transgenic mouse line (4HVH) whose *igh* locus contains germline human V_H, D, and J genes as well as human C genes lacking the C_H1 exon. HEK293T cells in microtiter plates are transfected with DNA encoding HCAbs derived from bone marrow and spleen plasma cells of immunized mice and positive clones identified by ELISA. The method thus relies on the apparatus of the murine immune system to rearrange, select, and affinity mature human V_H domains with good biophysical properties.

One original research paper and one review deal with engineering sdAbs for higher affinity and improved stability, respectively. Tiller et al. describe a novel approach to sdAb affinity maturation involving (i) identification of CDR residues amenable to randomization by computational and experimental alanine scanning mutagenesis, (ii) conservative randomization of permissive positions with a mixture of the wild-type residue and frequent, naturally occurring residues, and (iii) screening of the resulting libraries by yeast display to identify sdAbs bearing combinations of mutations conferring ≥5-fold affinity gains. Careful analysis of each variant revealed that CDR sequence deviation involves complex tradeoffs between sdAb affinity, specificity, and stability. Goldman et al. give a good overview of the literature on engineering sdAbs for improved stability, including (i) strategies to increase the stability of camelid and shark sdAbs (e.g., through framework mutation or introduction of non-canonical disulfide bonds) and (ii) analytical techniques for assessing sdAb stability.

SINGLE-DOMAIN ANTIBODIES AS DIAGNOSTICS

Because of their generally high stability and low cost of production in microbial systems, sdAbs have been viewed as potentially superior alternatives to conventional antibodies in diagnostic applications. One review and two original research articles focus on diagnostic applications of sdAbs. Gonzalez-Sapienza et al. summarize the pros and cons of sdAbs in analytical and diagnostic applications and review recent developments that highlight the potential of sdAbs in immunodetection technologies. Stijlemans et al. review the use of sdAbs as reagents for the diagnosis and treatment of African trypanosomiasis (AT). Current diagnostic procedures for AT are inadequate, and there is no effective vaccine; chemotherapy is the only treatment but involves high drug toxicity and increasing drug resistance. Anti-AT sdAbs have shown promise for the detection of several parasite antigens as well as for targeted drug delivery, and may even exert Fc-independent trypanolytic activity. Harmsen et al. report on their latest efforts to isolate V_HHs for use in quality control of foot-and-mouth disease vaccines. Only intact inactivated viral particles are efficacious vaccine antigens but intact virus can dissociate to yield ineffective capsid degradation products; reagents specific for intact virus and broadly cross-reactive with multiple viral strains are therefore needed.

SINGLE-DOMAIN ANTIBODIES AS THERAPEUTICS

Two reviews and one perspective article on various aspects of tumor imaging and tumor targeting highlight the intense interest in the development of sdAbs for cancer therapy. Xenaki et al. provide a cell biologist's perspective on the factors (primarily relating to molecular size and binding properties) that govern intratumoral uptake and distribution of antibodies and antibody fragments. Hu et al. review recent progress in developing sdAbs as targeting modules for drug delivery systems, including (i) toxins, enzymes, and cytokines; (ii) liposomes, extracellular vesicles, micelles, microbubbles, and nanoparticles; and (iii) viral vectors. They also discuss emerging technologies for intracellular delivery of sdAbs and sdAbs as tools for molecular imaging. Arezumand

et al. review the development of anti-angiogenic sdAbs for diagnosis and treatment of cancer.

In the development of therapeutic antibodies, an advantage of sdAbs is the relative ease of reformatting them into more complex and efficacious molecules. Nosenko et al. offer a brief perspective on their efforts to develop bispecific TNF inhibitors using sdAbs: one arm of these molecules binds and neutralizes TNF-α, while the second arm targets the effects of the antibody to specific populations of macrophages and monocytes. Two original research articles from Ablynx illustrate the potential of linking two or more sdAbs using polypeptide linkers. Beirnaert et al. elucidated the crystal structures of three V_HHs in complex with TNF. The structures revealed the molecular basis of the very high neutralization potency of a heterodimeric construct in which two of the V_HHs recognizing distinct epitopes are linked by a nine residue linker: the biparatopic V_HH:V_HH heterodimer engages both arms in an intramolecular fashion on a single TNF molecule and blocks two of three receptor-binding sites, but only in one of the two possible V_HH orientations. Similarly, Desmyter et al. developed high-affinity V_HHs against IL23, and, based on the crystal structures of three V_HHs in complex with IL23, rationally designed multivalent sdAb dimers with high IL23 neutralization activity using molecular linkers of appropriate length. A biparatopic sdAb-based heterotrimer in which two anti-IL23 V_HHs flanked an anti-human serum albumin (HSA) V_HH (for serum half-life extension) was a more potent neutralizer than any single anti-IL23 V_HH fused to the same albumin binder.

Three original research articles from Elasmogen demonstrate the modularity and therapeutic utility of shark V_{NAR}s. Kovaleva et al. report that anti-ICOSL V_{NAR}s selected from an immune nurse shark phage display library and reformatted as Fc-fusions markedly reduced inflammation in a mouse model of inflammatory eye disease, uveitis, when administered systemically. The observation that V_{NAR}s, but not IgGs and V_{NAR}–Fcs, could penetrate the cornea when applied topically at high concentration raises the hope that these V_{NAR}s (in multivalent formats lacking Fc) might be useful for topical treatment of uveitis. Extending the results of Beirnaert et al. using llama V_HHs, Ubah et al. isolated immune shark V_{NAR}s against TNF and reformatted them, first as V_{NAR}:V_{NAR} homo- and heterodimers and then as tetravalent biparatopic V_{NAR}–Fcs. Even in the absence of structural information, the authors were able to achieve a ~50,000-fold improvement in the neutralizing potency of the V_{NAR} monomer through molecular reformatting. Steven et al. optimized two previously humanized versions of an anti-HSA V_{NAR} domain which had less desirable biophysical properties than the parental V_{NAR}. After random mutagenesis of the two humanized domains and a phage display selection process, mutants with acceptable biophysical properties were obtained without compromising affinity or species cross-reactivity and extended serum half-life in a rat PK model. When fused in tandem with other humanized V_{NAR} moieties, the optimized anti-HSA V_{NAR} (BA11) should be useful for clinical studies.

Finally, Tian et al. from Helix BioPharma describe the optimized construction of an immunoconjugate in which an anti-VEGFR2 V_HH is linked to urease. The sdAb targets the immunoconjugate to tumor vasculature, where urease enzymatically converts endogenous urea to ammonia resulting in both direct and indirect antitumor effects. A similar conjugate targeting a non-small-cell lung cancer antigen is currently in clinical trials (http://www.helixbiopharma.com/).

ANTIVIRAL SINGLE-DOMAIN ANTIBODIES

One review and two original research articles describe applications of sdAbs directed against viruses in basic research, diagnostics, and biodefense. Wu et al. review the current state of knowledge on sdAb targeting and neutralization of human-tropic viruses and illustrate the potential of sdAbs to probe different sets of epitopes on viral glycoproteins compared to conventional antibodies. Darling et al. investigated the ability of tandem sdAb dimers directed against repetitive epitopes of filoviral nucleoproteins ("Xintrabodies" or cross-linking intrabodies) to cross-link capsid proteins and inhibit viral replication. Minimal amounts of Xintrabody ablated nucleoprotein incorporation into viral particles despite the presence of large amounts of nucleoprotein in the cytoplasm. In a companion manuscript, Garza et al. present the crystal structures of three of the sdAbs in complex with the nucleoprotein of Marburg virus, an agent causing viral hemorrhagic fever and a bioterror threat. The sdAbs bind to a cryptic epitope, a three-helix structure at the nucleoprotein C-terminus that has been conserved over 50 years of virus evolution. Engagement with these sdAbs gave the first crystal structure of the nucleoprotein C-terminus and identified an epitope that should be useful for diagnostic purposes and, possibly, intrabody-based countermeasures.

FINAL THOUGHTS

Single-domain antibodies, once considered immunological oddities of minor academic interest, have become critical tools in fundamental research as well as in the design of biologic drugs. Regulatory approval of the first sdAb-based drug (anti-vWF caplacizumab) is expected shortly, possibly in 2018, and may substantially alter perceptions and attitudes toward these molecules in the medical and scientific communities.

The editors would like to thank all contributors for the many excellent submissions to this Research Topic, as well as the reviewers and the *Frontiers in Immunology* editorial office.

AUTHOR CONTRIBUTIONS

KAH and CRM wrote the manuscript and approved it for publication.

ACKNOWLEDGMENTS

We thank all contributors for the many excellent submissions to this Research Topic. We gratefully acknowledge the reviewers who generously gave their time to help improve the manuscripts, as well as the *Frontiers in Immunology* editorial office for logistical support.

FUNDING

This work was supported by funding from the National Research Council Canada.

REFERENCES

1. Hamers-Casterman C, Atarhouch T, Muyldermans S, Robinson G, Hamers C, Songa EB, et al. Naturally occurring antibodies devoid of light chains. *Nature* (1993) 363:446–8. doi:10.1038/363446a0
2. Greenberg AS, Avila D, Hughes M, Hughes A, McKinney EC, Flajnik MF. A new antigen receptor gene family that undergoes rearrangement and extensive somatic diversification in sharks. *Nature* (1995) 374:168–73. doi:10.1038/374168a0
3. Ward ES, Gussow D, Griffiths AD, Jones PT, Winter G. Binding activities of a repertoire of single immunoglobulin variable domains secreted from *Escherichia coli*. *Nature* (1989) 341:544–6. doi:10.1038/341544a0

Conflict of Interest Statement: The authors declare that the research was conducted in the absence of any commercial or financial relationships that could be construed as a potential conflict of interest.

frontiers in Immunology

PERSPECTIVE
published: 20 November 2017
doi: 10.3389/fimmu.2017.01589

Camelid Single-Domain Antibodies: Historical Perspective and Future Outlook

Mehdi Arbabi-Ghahroudi[1,2]*

[1] Human Health Therapeutics Research Centre, National Research Council Canada, Ottawa, ON, Canada, [2] Department of Biology, Carleton University, Ottawa, ON, Canada

Tremendous effort has been expended over the past two and a half decades to understand many aspects of camelid heavy chain antibodies, from their biology, evolution, and immunogenetics to their potential applications in various fields of research and medicine. In this article, I present a historical perspective on the development of camelid single-domain antibodies (sdAbs or V_HHs, also widely known as nanobodies) since their discovery and discuss the advantages and disadvantages of these unique molecules in various areas of research, industry, and medicine. Commercialization of camelid sdAbs exploded in 2001 with a flurry of patents issued to the Vrije Universiteit Brussel (VUB) and later taken on by the Vlaams Interuniversitair Instituut voor Biotechnologie (VIB) and, after 2002, the VIB-founded spin-off company, Ablynx. While entrepreneurial spirit has certainly catalyzed the exploration of nanobodies as marketable products, IP restrictions may be partially responsible for the relatively long time span between the discovery of these biomolecules and their entry into the pharmaceutical market. It is now anticipated that the first V_HH-based antibody drug, Caplacizumab, a bivalent anti-vWF antibody for treating rare blood clotting disorders, may be approved and commercialized in 2018 or shortly thereafter. This elusive first approval, along with the expiry of key patents, may substantially alter the scientific and biomedical landscape surrounding camelid sdAbs and pave the way for their emergence as mainstream biotherapeutics.

Keywords: camelid single-domain antibody, heavy chain antibody, V_HH, nanobody, antibody engineering, therapeutic antibody

OPEN ACCESS

Edited by:
Marc H. V. Van Regenmortel, Centre national de la recherche scientifique (CNRS), France

Reviewed by:
Serge Muyldermans, Vrije Universiteit Brussel, Belgium
Etienne Weiss, Ecole Supérieure de Biotechnologie de Strasbourg, France

***Correspondence:**
Mehdi Arbabi-Ghahroudi
mehdi.arbabighahroudi@nrc-cnrc.gc.ca

This is NRC publication number: 53362.

Specialty section:
This article was submitted to Vaccines and Molecular Therapeutics, a section of the journal Frontiers in Immunology

Received: *29 September 2017*
Accepted: *03 November 2017*
Published: *20 November 2017*

Citation:
Arbabi-Ghahroudi M (2017) Camelid Single-Domain Antibodies: Historical Perspective and Future Outlook. Front. Immunol. 8:1589. doi: 10.3389/fimmu.2017.01589

INTRODUCTION

The canonical view of antibodies as molecules composed of two heavy chains and two light chains was forever changed one day in 1989 following analysis of total and fractionated immunoglobulin G (IgG) molecules in the serum of a dromedary camel in the laboratory of Professor Raymond Hamers at the Vrije Universiteit Brussel (VUB). The serendipitous discovery of antibodies lacking a light chain [heavy chain-only antibodies (HCAbs)] occurred as part of a student-run project aimed at developing a serodiagnostic test for trypanosome infection in camels and water buffalos. The preliminary data showed that besides conventional IgG1 (MW ~150 kDa), two other immunoglobulin fractions (thereafter called IgG2 and IgG3; MW ~90 kDa) were present which contributed up to 75% of all serum IgGs (1–3). Comparative studies on the sera of new world camelids (*Lama glama* and *Lama pacos*) subsequently confirmed the presence of HCAbs, albeit at concentrations between

30 and 50% (1, 4–8). Following these exciting findings, it became essential to analyze the antigen-binding properties of these IgG fractions since the presence of truncated forms of heavy chain antibodies with no light chains, classically described as "heavy chain disease," had been reported in human patients (9, 10). No functional activity was reported for the pathogenic heavy chain antibodies in these patients, as these proteins were shown to bear extensive internal deletions in the variable (VH) and the first constant region (CH1) domains. By contrast, antibodies from camelids exposed to *Trypanosoma evansi* demonstrated strong binding activity in the IgG2 and IgG3 heavy chain-only fractions as shown by radio-immunoprecipitation and blotting experiments (1).

In two subsequent reports, phage-display technology and high-resolution crystallography were utilized to (a) build a phage-display library from the lymphocytes of immunized camels and isolate monomeric antigen-specific V_HH domains in the absence of the constant regions (11) and (b) solve crystal structures of an unliganded V_HH (12) and a V_HH:lysozyme complex, reported simultaneously by the VUB team and a Dutch–French research group (13). The term V_HH was originally introduced by the VUB team in 1994 to indicate a VH domain derived from camelid heavy chain antibodies. The feasibility of isolating stable and soluble V_HH domains with nanomolar affinities against lysozyme and tetanus toxoid showed very early on the promise of these molecules as high-affinity binding moieties. Crystallography studies revealed additional salient features of an anti-lysozyme V_HH, including deep penetration of its long third complementarity-determining region (CDR3) into the active site of the enzyme; this feature had rarely been seen with conventional antibodies and required a fundamental deviation from known human canonical CDR1 structure (13). Further evidence of the unique antigen recognition behavior of V_HH domains (including enzyme inhibition) was published over the next several years (11, 14, 15), suggesting that V_HHs might probe different sets of epitopes on proteins compared with conventional antibodies. Key proof of concept for producing bivalent/bispecific V_HH modalities *via* genetic fusion (using camelid short and long hinge sequences) of anti-lyzozyme and/or anti-tetanus toxin V_HHs was also established very early on (14).

MOLECULAR ONTOGENY OF CAMELID HCAbs

Molecular biology techniques were subsequently applied to decipher the DNA sequences of HCAbs. The sequencing results showed that nature had designed HCAbs as an additional arm of the immune systems of camelid ungulates over the course of their evolutionary history. The consensus of these studies suggested camelid HCAbs possessed: (a) no CH1 domain, and therefore, a direct connection of the rearranged V_HH exon to the hinge region; (b) one of two types of long (IgG2) and short (IgG3) hinge isotypes; (c) specific conserved amino acid substitutions in framework region 2 (FR2), mainly at VH positions that make contact with the VL in classical antibodies, including Kabat positions 37, 44, 45, and 47; and (d) potentially different CDR3 amino acid composition and a broader length distribution for CDR3 compared to the heavy chains of conventional antibodies (1, 16, 17).

Later genomic studies shed light on the origin of HCAbs in dromedary camels and alpacas. It is now established that HCAbs are produced from the same *igh* locus as conventional antibodies but with distinct sets of genes for the generation of HCAbs. It is estimated that alpaca and dromedary genomes contain ~17 and ~40 V_HH genes, respectively, with an identical organization of the genes that produce conventional antibodies (18, 19). The CH1 exon is present in the genomic DNA of HCAbs but a point mutation (G to A) at the 5′ end of the CH1-hinge intron disrupts the consensus splicing site (GT) and causes omission of this region during splicing (3, 18, 20–22). A complete picture of camelid germline V gene repertoires of heavy and light chains and the classification of VH and V_HH genes is still missing. Published genomic and cDNA data have so far shown that camelid V_HH genes are highly homologous to the human VH3 family of clan III with the exception of several key amino acid substitutions in FR2, namely, Val37 → Phe/Tyr, Gly44 → Glu, Leu45 → Arg, and Trp47 → Gly (Kabat numbering), and are encoded by a distinct subset of germline V genes. Preliminary investigations of published llama V_HH sequences classified them into four subfamilies by sequence similarity, and many of the earliest-described V_HH features such as long CDR3s, additional disulfide bridges, and particular canonical structures of CDR1–3 were shown to be subfamily specific (17, 23). Subsequent studies in alpaca identified at least three V gene subgroups of the alpaca *igh* locus: IGHV1, IGHV2, and IGHV3 which are equivalent to the human IGHV families within clan I (VH families 2, 4, 6), II (VH families 1, 5, 7), and III (VH family 3), respectively, based on sequence homology. The alpaca V_HH genes clustered into six subsets by sequence similarity, but all are homologous to human IGHV3 genes (18). Furthermore, recent investigations have demonstrated the presence of genes belonging to IGHV families 1, 3, and 4 (human clan I and III) in llama and alpaca, and in addition, uncovered new camelid V genes highly homologous to the human IGHV5 and IGHV7 families (human clan II); however, no genes similar to human families 2 or 6 (within human clan I) were found (24). Interestingly, a novel promiscuous class of V genes in camelids was identified that is closely related to the human VH4 family (clan I). These VH4 homologs contribute largely to the classical antibody repertoire and lack the hallmark solubilizing V_HH residues in FR2. Nevertheless, antigen-specific VH4-family fragments with V_HH-like stability and solubility were isolated from an immune llama library (25). In the absence of a complete set of camelid germline VH and V_HH genes, most immunogenetic studies have relied on comparisons with human germline genes.

The consensus of immunogenetic studies of camelid HCAbs is that repertoire diversification of these molecules may involve (a) a large number of unique V_HH gene segments recombining with DH and JH minigenes, possibly with additional non-templated nucleotide insertions leading to longer CDR3 loops; (b) somatic hypermutation, potentially of extended CDR1 regions compared with conventional antibodies; (c) acquisition of non-canonical cysteine residues in the CDRs and FR2; and

(d) involvement of FR2 residues in antigen binding and in structuring the CDR3 loop (3, 22, 26, 27). In agreement with immunogenetic analyses, several structural studies have suggested that due to the loss of VL domains, V_HH paratopes have acquired a higher structural complexity by involving more residues in antigen binding compared to classical VHs (27). As for the evolutionary origin of HCAbs, it is difficult to draw solid conclusions but several hypotheses have been proposed. A common theme among most of these has been the need for generating or expanding a new antigen-binding repertoire in *Camelidae* to address certain antigenic challenges, e.g., cryptic epitopes of commonly encountered pathogens. Phylogenetic analyses have confirmed that HCAbs diverged from conventional antibodies as a result of recent adaptive changes (22, 27–29).

HISTORY OF THE DEVELOPMENT OF CAMELID SINGLE-DOMAIN ANTIBODIES (sdAbs) AS THERAPEUTICS

Prior to the discovery of HCAbs, a single report describing the concept of sdAbs was published by Sally Ward and colleagues in 1989 (30), when they showed that VH domains from an immunized mouse, in the absence of a VL domain, could bind specifically to lysozyme and keyhole limpet hemocyanin. However, poor VH domain stability and solubility, as well as weak antigen-binding affinity compared to its fragment variable region counterpart (Fv) or to the parent antibody, were major impediments to any commercial applications (**Figure 1**).

From a historical perspective, development of camelid V_HHs as drugs has gone through three major phases. The first 10 years (1993–2003) can be classified as the exploratory phase, which coincided with the founding of Ablynx in December 2001 as a spin-off company from the Vlaams Interuniversitair Instituut voor Biotechnologie. The main developments in the first decade included: (i) the first description of V_HHs (1); (ii) sequence analyses of V_HHs with identification of V_HH germline gene segments and classification of V_HH gene subfamilies (16, 20, 23); (iii) adaptation of phage-display technology to V_HHs (11) and isolation of antigen-specific V_HHs, including several enzyme inhibitors (12, 15); (iv) solving the crystal structure of several V_HH:antigen complexes (13, 31–34); (v) development of methods for expression of V_HHs in bacteria and yeast systems and for biophysical characterization of V_HHs (35, 36); and (vi) the use of V_HHs as reagents in immunoaffinity purification and immuno-perfusion (37).

During the second phase of development (2003–2013), V_HHs began to receive more attention and publications in this area grew dramatically, surpassing 1,000 by 2013 [Ref. (38) and personal investigation on Web of Science]. Interestingly, a large and diverse group of countries and institutions (close to 50) were responsible for research on camelid V_HHs during this time, mainly for the purpose of exploring their potential applications in research, biotechnology, and medicine (38). The major hallmark of this decade was the start of preclinical and clinical studies of several nanobodies by Ablynx and others as therapeutics and imaging reagents (39, 40), including V_HHs against (i) blood glycoprotein vWF to control platelet aggregation and clot formation; (ii) viral infection (RSV); (iii) venom toxins; (iv) IL6-R for treatment of rheumatoid arthritis; and (v) the use of radiolabeled nanobodies for Her2+ tumor imaging. There were major technological advancements made in the expression of V_HHs in heterologous systems and in creating an array of bi- and multivalent V_HHs with superior efficacy during this decade.

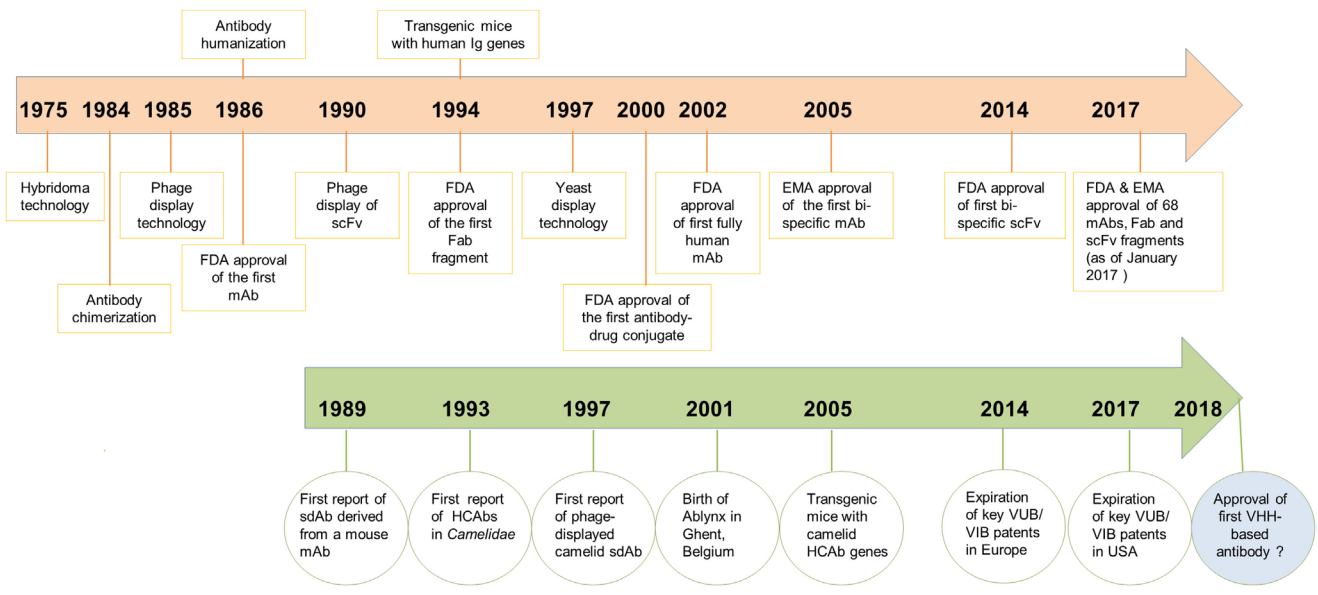

FIGURE 1 | Chronological timeline of major scientific developments in the field of antibody engineering since the discovery of monoclonal antibodies (mAbs) in 1975 leading to the regulatory approval of mAbs, antigen-binding fragments (Fabs) and scFvs as therapeutics. Developments for mAbs are shown in orange and developments of V_HHs/heavy chain-only antibodies (HCAbs) in green. Regulatory approval of the first V_HH-based antibody drug is expected in 2018.

Now in the third phase of development (2014–present), publications continue to grow and more V_HHs have entered into clinical trials or advanced closer to the market. The main patent claims on camelid antibody fragments expired in the summer of 2014 in Europe and in the summer of 2017 in America. Ablynx has expanded its collaborations with large biophama players, such as Merck, Boehringer Ingelheim, Sanofi, and so on, with more than 20 preclinical and clinical programs. It is expected that the first V_HH-based drug (Caplacizumab; bivalent anti-vWF nanobody for treating rare blood clotting disorders) will reach the market sometime in 2018 (www.ablynx.com). Meanwhile, IP limitations on the composition of matter of V_HHs are diminishing and more biotechnology companies (39) are showing interest in commercialization of these domain antibodies as therapeutics, diagnostics, and research reagents (**Figure 1**).

CAMELID sdAbs: PROS, CONS, AND APPLICATIONS

Immunization of *Camelidae* against targets of interest leads to the *in vivo* maturation of HCAb and conventional antibody repertoires. Construction of phage-display libraries is performed by cloning of amplified V_HH repertoires with minimal modification, thus presenting an authentic picture of *in vivo*-matured heavy chain repertoire diversity. By contrast, in both scFv libraries (requiring the artificial joining of VH and VL domains by a synthetic linker) and antigen-binding fragment (Fab) libraries derived from conventional antibody repertoires, natural VH–VL pairings are usually lost. The potential for direct cloning of V_HH repertoires from immunized camelids, the smaller library sizes required to capture the immune V_HH repertoire, the stability of the libraries, the feasibility of displaying V_HHs on a phage or alternative display formats, and the ease of sub-cloning and expression of antigen-specific V_HHs are among the major technical advantages of the camelid V_HH platform over conventional antibody platforms.

Key characteristics of V_HHs include their high affinity and specificity (equivalent to conventional antibodies), high thermostability, good solubility and strictly monomeric behavior, small size (2.5 nm in diameter and about 4 nm in length; ~15 kDa), relatively low production cost, ease of genetic engineering, format flexibility or modularity, low immunogenicity, and a higher penetration rate into tissues (3, 41–44). The short half-life of V_HHs in blood circulation is well suited to certain applications such as tumor imaging or delivery of toxin or radioisotopes to diseased tissues where rapid clearance is required. However, the pharmacokinetic behavior of V_HHs can also be improved by extending their half-lives using different formatting options, including PEGylation or fusion to serum albumin or an anti-serum albumin moiety (43, 45, 46). The immunogenicity of V_HHs domains can also be minimized by humanization (47–49). As with all antibodies of non-human species origin (and even fully human antibodies), immunogenicity and toxicity must be investigated empirically for humanized V_HHs. A complete picture of the immunogenicity of non-humanized and humanized camelid V_HHs is lacking due to insufficient data, but anti-drug immune responses may have been a major reason for the clinical failure of a humanized tetravalent Nanobody®targeting the DR5 receptor (50). As of 2016, V_HHs have been isolated against more than 120 therapeutically important targets relevant to oncology, *in vivo* imaging, hematology, infectious diseases, neurological, and inflammatory disorders, with some in advanced stages of clinical trials (39).

One of the unique characteristics of V_HHs is their ability to target antigenic epitopes at locations which are difficult to access by large molecules such as conventional monoclonal antibodies (mAbs). Examples include intracellular targets (51, 52) or epitopes concealed from mAbs in protein structures (53), G protein-coupled receptors (54, 55), and ion channels (3). V_HHs are ideally suited for such applications due to their small size, target specificity, and long CDR3 loops, bypassing many drawbacks related to small-molecule synthetic drugs such as fine specificity and off-target toxicity (56). As "intrabodies," V_HHs are also ideally suited for cytosolic expression due to their ability to fold in the reducing intracellular environment. This feature likely reflects the single disulfide linkage present in the V_HH domain, as compared to the multi-domain structure and multiple disulfide linkages of conventional antibodies, and may not be completely general to all V_HHs but appears to be quite common; intracellular expression of V_HHs has been widely and productively exploited for *in vivo* cellular imaging (5, 57) as well as to inhibit the function of viral proteins (58, 59). There have been several excellent reviews covering V_HH applications in different areas of basic and applied research and a detailed description of each application is beyond the scope of this article (3, 39, 41, 43, 57, 60–65).

V_HHs are also well suited in the generation of bi- and multi-specific antibodies. In the field of antibody therapeutics, it is now widely accepted that monotherapy of cancer and other diseases may not result in effective outcomes, in particular due to the problem of acquired resistance (66, 67). Bispecific antibodies provide a possible solution in which they could bind simultaneously to a tumor-associated antigen and another activating molecule, e.g., CD3 on T cells, leading to tumor killing/lysis through lymphocyte recruitment, or alternatively, could target two or more tumor epitopes (bi-paratopic) or antigens simultaneously. Bispecific V_HHs may be uniquely positioned for these applications given their simple design and small size relative to other antibody fragments, which may result in better solid tumor penetration rates, homogeneous production at high yield in microbial systems, and ease of fusion to a heterodimerization motif, therefore bypassing issues related to some linker peptides such as aggregation and immunogenicity (45, 66, 68, 69). Interestingly, all of the V_HH-based therapeutic candidates in clinical trials are composed of bivalent, trivalent, or higher valency formats (39). It has been shown that some V_HHs, when properly selected, are able to transmigrate through human brain endothelial cell layers spontaneously and, possibly through a receptor-mediated process (70–72); bispecific molecules incorporating these V_HHs can, thus, deliver attached cargo (e.g., therapeutics) into the brain in rodents (73).

Despite the many advantages of V_HHs, there are several drawbacks to be considered as well. The fact that the antigen-binding

paratope of camelid HCAbs has been restricted to a single domain of about 110 amino acids will automatically put more weight on each and every residue in the V_HH domain. The extended CDR1, longer CDR3, involvement of FR2 in antigen binding and shaping the CDR3 loop, the role of the "CDR4" (residues 76–80) loop in antigen binding, and extensive somatic hypermutation are some of the evolutionary mechanisms adapted to compensate repertoire diversity due to the lack of a VL domain (3). Therefore, there may be limitations on the extent of manipulation and engineering that can be tolerated by antigen-specific V_HHs. For example, complete humanization of camelid V_HHs involving the mutation of residues outside the antigen-binding loops often drastically compromises antigen-binding affinity, V_HH stability, and the expression yield (unpublished data). A survey of the literature clearly demonstrates that almost all V_HHs isolated to date have originated from direct camelid immunization, or from large naïve camelid libraries, although recently, successful isolation of V_HHs from synthetic or semi-synthetic libraries against a number of protein antigens has also been reported (74–77). All available pieces of evidence support the notion that the V_HH domain is a highly complex molecule and that each amino acid (depending on its position) may have direct and indirect effects on the molecule's stability and structural integrity, as well as on antigen-binding affinity and specificity.

Another limitation of V_HHs is their low propensity to bind small molecules, likely due to their dominant convex surface topology as compared to the flat or concave topologies found on conventional antibody fragments (e.g., scFv, Fab). In a number of llama immunization trials, we and others have been able to generate strong conventional immune responses, but rather weak HCAb responses, against several haptens and carbohydrate antigens (unpublished data). However, repeated immunization of camelids with small molecules conjugated or fused to larger proteins has led to the successful isolation of V_HHs against caffeine (78), red dye (79), and linear peptides (80, 81) with affinities ranging from micromolar to low nanomolar. The biophysicochemical properties of V_HHs suggest that they would be well suited to many immunodiagnostic platforms for detecting small molecules and environmental chemicals; however, isolation of high-affinity V_HHs suitable for such applications seems to be a difficult task, although not impossible (3, 64, 65, 78, 82, 83). Immunization of large animals and heterogeneity in immune responses among individual outbred animals is another consideration which is important when alternative immunization techniques such as DNA immunization are applied. DNA immunization has had limited success in camelid and other large animals and reproducibility is often a major issue to be tackled (84–87). To overcome this limitation, transgenic mice bearing either a rearranged dromedary γ2a chain or hybrid llama/human antibody loci have been generated that produce a form of dromedary or human heavy chain antibodies (88–90).

CAMELID sdAbs VERSUS mAbs

The first therapeutic mAb, Orthoclone OKT3, a murine IgG2a for the prevention of kidney transplant rejection, hit the market little more than a decade after the discovery of hydridoma technology in 1975 (91–94). Currently, mAbs constitute about half of marketed biological products and, as of January 2017, 68 mAbs have been approved by the Food and Drug Administration (FDA) in the USA and/or by the European Medicine Agency (EMA) in Europe. The projected global sales of mAbs will be close to $100 billion in 2017 (44, 95). The lack of restrictive IP on the original technology is considered by many as a driving force that allowed researchers to develop effective research tools and diagnostic mAb-based reagents without limitation. The introduction of antibody fragments, such as Fab and scFv (the "second generation" of antibodies), combined with the power of phage-display technology in the late 1990s, opened new horizons in the world of antibodies and empowered researchers with the ability to clone the entire immunoglobulin repertoire of mammalian immune B cells and to isolate specific antibody fragments virtually against any target (96–98). This technology led to the development of the first FDA-approved fully human mAb, Humira, which was obtained from a phage-displayed human antibody library 12 years after the initial paper by McCafferty and co-workers on the construction of phage-displayed human antibody libraries (99–101). Further developments in antibody engineering have so far resulted in three FDA-approved therapeutic Fabs (95).

Overwhelming evidence in the literature suggests that camelid V_HHs, as the so-called "third generation" of antibodies, have many added features that supersede those of conventional mAbs and antibody fragments (Fab and scFv). Although V_HHs have already been commercialized for non-medical applications (63, 102), the research and medical communities eagerly await the first V_HH-based therapeutic to gain approval. If we consider the 9- to 13-year time span between the discovery of the key technology enabling conventional mAbs (hybridoma technology) and the FDA-approval of a mAb or an antibody fragment, a longer time has been required for the development of the first V_HH-based therapeutic. It is unclear if technical challenges, regulatory hurdles, or the need to define a unique niche/indication for V_HHs, have been involved in the prolonged delay of the first V_HH-based therapeutic. It is obvious that issues related to downstream processing, stability, immunogenicity, toxicity, safety, and potency of a V_HH-based therapeutic product will be doubly scrutinized by FDA and EMA since it would represent the first product of its kind to enter the market. The fact that the first potential Ablynx product is an engineered bivalent anti-vWF nanobody and is produced in a microbial system may have raised additional red flags for the approving regulatory bodies.

CONCLUDING REMARKS

Over a quarter century has passed since the first observation by Hamers and colleagues of camelid HCAbs. This finding was a significant milestone in the field of antibody engineering and opened many new opportunities and applications. It was also instrumental in reviving the concept of sdAbs, which had been originally suggested by Ward et al. a few years earlier. The unique and extraordinary features of HCAbs and their antigen-binding

domains (V_HHs) have with no doubt attracted many researchers and commercial entities to the field of antibody engineering. V_HHs are now closer than ever to approval as pharmaceutical drugs to fight a wide range of diseases, including cancer, inflammation, hematology, and respiratory diseases, with five V_HH-based drugs in various stages of clinical development. V_HHs have also been shown to be effective as therapeutics against infectious disease, particularly in viral therapy, as well as robust reagents in the field of diagnostic and imaging applications. While the commercial applications of V_HHs have been slowed by IP limitations, it is probable that demand, as well as extensive research on these antibody domains, will ultimately supersede these limitations and bring many more of these molecules into use as biopharmaceutical reagents within the next decade.

AUTHOR CONTRIBUTIONS

MA-G conceived and wrote the manuscript.

ACKNOWLEDGMENTS

The author gratefully acknowledges Greg Hussack, Roger MacKenzie, Kevin Henry, and Kristin Kemmerich for reading and providing comments on the text.

FUNDING

This work was supported by funding from the National Research Council Canada.

REFERENCES

1. Hamers-Casterman C, Atarhouch T, Muyldermans S, Robinson G, Hamers C, Songa EB, et al. Naturally occurring antibodies devoid of light chains. *Nature* (1993) 363:446–8. doi:10.1038/363446a0
2. Wernery U. Camelid immunoglobulins and their importance for the newborn – a review. *J Vet Med B Infect Dis Vet Public Health* (2001) 48:561–8. doi:10.1111/j.1439-0450.2001.00478.x
3. Muyldermans S. Nanobodies: natural single-domain antibodies. *Annu Rev Biochem* (2013) 82:775–97. doi:10.1146/annurev-biochem-063011-092449
4. van der Linden R, de Geus B, Stok W, Bos W, van Wassenaar D, Verrips T, et al. Induction of immune responses and molecular cloning of the heavy chain antibody repertoire of *Lama glama*. *J Immunol Methods* (2000) 240:185–95. doi:10.1016/S0022-1759(00)00188-5
5. Rothbauer U, Zolghadr K, Tillib S, Nowak D, Schermelleh L, Gahl A, et al. Targeting and tracing antigens in live cells with fluorescent nanobodies. *Nat Methods* (2006) 3:887–9. doi:10.1038/nmeth953
6. Maass DR, Sepulveda J, Pernthaner A, Shoemaker CB. Alpaca (*Lama pacos*) as a convenient source of recombinant camelid heavy chain antibodies (V_HHs). *J Immunol Methods* (2007) 324:13–25. doi:10.1016/j.jim.2007.04.008
7. De Simone EA, Saccodossi N, Ferrari A, Leoni J. Development of ELISAs for the measurement of IgM and IgG subclasses in sera from llamas (*Lama glama*) and assessment of the humoral immune response against different antigens. *Vet Immunol Immunopathol* (2008) 126:64–73. doi:10.1016/j.vetimm.2008.06.015
8. Blanc MR, Anouassi A, Ahmed Abed M, Tsikis G, Canepa S, Labas V, et al. A one-step exclusion-binding procedure for the purification of functional heavy-chain and mammalian-type gamma-globulins from camelid sera. *Biotechnol Appl Biochem* (2009) 54:207–12. doi:10.1042/BA20090208
9. Franklin EC, Lowenstein J, Bigelow B, Meltzer M. Heavy chain disease – a new disorder of serum gamma-globulins: report of the first case. *Am J Med* (1964) 37:332–50. doi:10.1016/0002-9343(64)90191-3
10. Alexander A, Steinmetz M, Barritault D, Frangione B, Franklin EC, Hood L, et al. gamma heavy chain disease in man: cDNA sequence supports partial gene deletion model. *Proc Natl Acad Sci U S A* (1982) 79:3260–4. doi:10.1073/pnas.79.10.3260
11. Arbabi Ghahroudi M, Desmyter A, Wyns L, Hamers R, Muyldermans S. Selection and identification of single domain antibody fragments from camel heavy-chain antibodies. *FEBS Lett* (1997) 414:521–6. doi:10.1016/S0014-5793(97)01062-4
12. Spinelli S, Frenken L, Bourgeois D, de Ron L, Bos W, Verrips T, et al. The crystal structure of a llama heavy chain variable domain. *Nat Struct Biol* (1996) 3:752–7. doi:10.1038/nsb0996-752
13. Desmyter A, Transue TR, Ghahroudi MA, Thi MH, Poortmans F, Hamers R, et al. Crystal structure of a camel single-domain VH antibody fragment in complex with lysozyme. *Nat Struct Biol* (1996) 3:803–11. doi:10.1038/nsb0996-803
14. Arbabi Ghahroudi M. *Generation and Characterization of Phage-Displayed Camel Single-Domain Antibodies [Ph.D. Dissertation]*. Brussels (Belgium): Vrije Universiteit Brussel (VUB) (1996).
15. Lauwereys M, Arbabi Ghahroudi M, Desmyter A, Kinne J, Holzer W, De Genst E, et al. Potent enzyme inhibitors derived from dromedary heavy-chain antibodies. *EMBO J* (1998) 17:3512–20. doi:10.1093/emboj/17.13.3512
16. Muyldermans S, Atarhouch T, Saldanha J, Barbosa JA, Hamers R. Sequence and structure of VH domain from naturally occurring camel heavy chain immunoglobulins lacking light chains. *Protein Eng* (1994) 7:1129–35. doi:10.1093/protein/7.9.1129
17. Vu KB, Ghahroudi MA, Wyns L, Muyldermans S. Comparison of llama VH sequences from conventional and heavy chain antibodies. *Mol Immunol* (1997) 34:1121–31. doi:10.1016/S0161-5890(97)00146-6
18. Achour I, Cavelier P, Tichit M, Bouchier C, Lafaye P, Rougeon F. Tetrameric and homodimeric camelid IgGs originate from the same IgH locus. *J Immunol* (2008) 181:2001–9. doi:10.4049/jimmunol.181.3.2001
19. Nguyen VK, Hamers R, Wyns L, Muyldermans S. Camel heavy-chain antibodies: diverse germline V_HH and specific mechanisms enlarge the antigen-binding repertoire. *EMBO J* (2000) 19:921–30. doi:10.1093/emboj/19.5.921
20. Nguyen VK, Muyldermans S, Hamers R. The specific variable domain of camel heavy-chain antibodies is encoded in the germline. *J Mol Biol* (1998) 275:413–8. doi:10.1006/jmbi.1997.1477
21. De Genst E, Saerens D, Muyldermans S, Conrath K. Antibody repertoire development in camelids. *Dev Comp Immunol* (2006) 30:187–98. doi:10.1016/j.dci.2005.06.010
22. Conrath KE, Wernery U, Muyldermans S, Nguyen VK. Emergence and evolution of functional heavy-chain antibodies in *Camelidae*. *Dev Comp Immunol* (2003) 27:87–103. doi:10.1016/S0145-305X(02)00071-X
23. Harmsen MM, Ruuls RC, Nijman IJ, Niewold TA, Frenken LG, de Geus B. Llama heavy-chain V regions consist of at least four distinct subfamilies revealing novel sequence features. *Mol Immunol* (2000) 37:579–90. doi:10.1016/S0161-5890(00)00081-X
24. Klarenbeek A, El Mazouari K, Desmyter A, Blanchetot C, Hultberg A, de Jonge N, et al. Camelid Ig V genes reveal significant human homology not seen in therapeutic target genes, providing for a powerful therapeutic antibody platform. *MAbs* (2015) 7:693–706. doi:10.1080/19420862.2015.1046648
25. Deschacht N, De Groeve K, Vincke C, Raes G, De Baetselier P, Muyldermans S. A novel promiscuous class of camelid single-domain antibody contributes to the antigen-binding repertoire. *J Immunol* (2010) 184:5696–704. doi:10.4049/jimmunol.0903722
26. Muyldermans S. Single domain camel antibodies: current status. *J Biotechnol* (2001) 74:277–302.
27. Nguyen VK, Su C, Muyldermans S, van der Loo W. Heavy-chain antibodies in *Camelidae*; a case of evolutionary innovation. *Immunogenetics* (2002) 54:39–47. doi:10.1007/s00251-002-0433-0
28. Daley LP, Gagliardo LF, Duffy MS, Smith MC, Appleton JA. Application of monoclonal antibodies in functional and comparative investigations

of heavy-chain immunoglobulins in new world camelids. *Clin Diagn Lab Immunol* (2005) 12:380–6.
29. Flajnik MF, Deschacht N, Muyldermans S. A case of convergence: why did a simple alternative to canonical antibodies arise in sharks and camels? *PLoS Biol* (2011) 9:e1001120. doi:10.1371/journal.pbio.1001120
30. Ward ES, Gussow D, Griffiths AD, Jones PT, Winter G. Binding activities of a repertoire of single immunoglobulin variable domains secreted from *Escherichia coli*. *Nature* (1989) 341:544–6. doi:10.1038/341544a0
31. Spinelli S, Desmyter A, Frenken L, Verrips T, Tegoni M, Cambillau C. Domain swapping of a llama V_HH domain builds a crystal-wide beta-sheet structure. *FEBS Lett* (2004) 564:35–40. doi:10.1016/S0014-5793(04)00304-7
32. Decanniere K, Desmyter A, Lauwereys M, Ghahroudi MA, Muyldermans S, Wyns L. A single-domain antibody fragment in complex with RNase A: non-canonical loop structures and nanomolar affinity using two CDR loops. *Structure* (1999) 7:361–70. doi:10.1016/S0969-2126(99)80049-5
33. Desmyter A, Spinelli S, Payan F, Lauwereys M, Wyns L, Muyldermans S, et al. Three camelid V_HH domains in complex with porcine pancreatic α-amylase: inhibition and versatility of binding topology. *J Biol Chem* (2002) 277:23645–50. doi:10.1074/jbc.M202327200
34. Desmyter A, Decanniere K, Muyldermans S, Wyns L. Antigen specificity and high affinity binding provided by one single loop of a camel single-domain antibody. *J Biol Chem* (2001) 276:26285–90. doi:10.1074/jbc.M102107200
35. Perez JM, Renisio JG, Prompers JJ, van Platerink CJ, Cambillau C, Darbon H, et al. Thermal unfolding of a llama antibody fragment: a two-state reversible process. *Biochemistry* (2001) 40:74–83. doi:10.1021/bi0009082
36. Dumoulin M, Conrath K, Van Meirhaeghe A, Meersman F, Heremans K, Frenken LG, et al. Single-domain antibody fragments with high conformational stability. *Protein Sci* (2002) 11:500–15. doi:10.1110/ps.34602
37. Verheesen P, ten Haaft MR, Lindner N, Verrips CT, de Haard JJ. Beneficial properties of single-domain antibody fragments for application in immunoaffinity purification and immuno-perfusion chromatography. *Biochim Biophys Acta* (2003) 1624:21–8. doi:10.1016/j.bbagen.2003.09.006
38. Eyer L, Hruska K. Single-domain antibody fragments derived from heavy-chain antibodies: a review. *Vet Med* (2012) 9:439–513.
39. Steeland S, Vandenbroucke RE, Libert C. Nanobodies as therapeutics: big opportunities for small antibodies. *Drug Discov Today* (2016) 21:1076–113. doi:10.1016/j.drudis.2016.04.003
40. D'Huyvetter M, Aerts A, Xavier C, Vaneycken I, Devoogdt N, Gijs M, et al. Development of ^{177}Lu-nanobodies for radioimmunotherapy of HER2-positive breast cancer: evaluation of different bifunctional chelators. *Contrast Media Mol Imaging* (2012) 7:254–64. doi:10.1002/cmmi.491
41. Wesolowski J, Alzogaray V, Reyelt J, Unger M, Juarez K, Urrutia M, et al. Single domain antibodies: promising experimental and therapeutic tools in infection and immunity. *Med Microbiol Immunol* (2009) 198:157–74. doi:10.1007/s00430-009-0116-7
42. Saerens D, Ghassabeh GH, Muyldermans S. Single-domain antibodies as building blocks for novel therapeutics. *Curr Opin Pharmacol* (2008) 8:600–8. doi:10.1016/j.coph.2008.07.006
43. Chakravarty R, Goel S, Cai W. Nanobody: the "magic bullet" for molecular imaging? *Theranostics* (2014) 4:386–98. doi:10.7150/thno.8006
44. Fernandes CFC, Pereira SDS, Luiz MB, Zuliani JP, Furtado GP, Stabeli RG. Camelid single-domain antibodies as an alternative to overcome challenges related to the prevention, detection, and control of neglected tropical diseases. *Front Immunol* (2017) 8:653. doi:10.3389/fimmu.2017.00653
45. Holt LJ, Herring C, Jespers LS, Woolven BP, Tomlinson IM. Domain antibodies: proteins for therapy. *Trends Biotechnol* (2003) 21:484–90. doi:10.1016/j.tibtech.2003.08.007
46. Harmsen MM, van Solt CB, Fijten HP, van Keulen L, Rosalia RA, Weerdmeester K, et al. Passive immunization of guinea pigs with llama single-domain antibody fragments against foot-and-mouth disease. *Vet Microbiol* (2007) 120:193–206. doi:10.1016/j.vetmic.2006.10.029
47. Vaneycken I, D'Huyvetter M, Hernot S, De Vos J, Xavier C, Devoogdt N, et al. Immuno-imaging using nanobodies. *Curr Opin Biotechnol* (2011) 22:877–81. doi:10.1016/j.copbio.2011.06.009
48. Hassanzadeh-Ghassabeh G, Devoogdt N, De Pauw P, Vincke C, Muyldermans S. Nanobodies and their potential applications. *Nanomedicine (Lond)* (2013) 8:1013–26. doi:10.2217/nnm.13.86
49. Vincke C, Loris R, Saerens D, Martinez-Rodriguez S, Muyldermans S, Conrath K. General strategy to humanize a camelid single-domain antibody and identification of a universal humanized nanobody scaffold. *J Biol Chem* (2009) 284:3273–84. doi:10.1074/jbc.M806889200
50. Papadopoulos KP, Isaacs R, Bilic S, Kentsch K, Huet HA, Hofmann M, et al. Unexpected hepatotoxicity in a phase I study of TAS266, a novel tetravalent agonistic Nanobody(R) targeting the DR5 receptor. *Cancer Chemother Pharmacol* (2015) 75:887–95. doi:10.1007/s00280-015-2712-0
51. McGonigal K, Tanha J, Palazov E, Li S, Gueorguieva-Owens D, Pandey S. Isolation and functional characterization of single domain antibody modulators of caspase-3 and apoptosis. *Appl Biochem Biotechnol* (2009) 157:226–36. doi:10.1007/s12010-008-8266-4
52. Staus DP, Wingler LM, Strachan RT, Rasmussen SG, Pardon E, Ahn S, et al. Regulation of β2-adrenergic receptor function by conformationally selective single-domain intrabodies. *Mol Pharmacol* (2014) 85:472–81. doi:10.1124/mol.113.089516
53. Stijlemans B, Conrath K, Cortez-Retamozo V, Van Xong H, Wyns L, Senter P, et al. Efficient targeting of conserved cryptic epitopes of infectious agents by single domain antibodies: African trypanosomes as paradigm. *J Biol Chem* (2004) 279:1256–61. doi:10.1074/jbc.M307341200
54. Bradley ME, Dombrecht B, Manini J, Willis J, Vlerick D, De Taeye S, et al. Potent and efficacious inhibition of CXCR2 signaling by biparatopic nanobodies combining two distinct modes of action. *Mol Pharmacol* (2015) 87:251–62. doi:10.1124/mol.114.094821
55. Manglik A, Kobilka BK, Steyaert J. Nanobodies to study G protein-coupled receptor structure and function. *Annu Rev Pharmacol Toxicol* (2017) 57:19–37. doi:10.1146/annurev-pharmtox-010716-104710
56. Baker M. Upping the ante on antibodies. *Nat Biotechnol* (2005) 23:1065–72. doi:10.1038/nbt0905-1065
57. Beghein E, Gettemans J. Nanobody technology: a versatile toolkit for microscopic imaging, protein-protein interaction analysis, and protein function exploration. *Front Immunol* (2017) 8:771. doi:10.3389/fimmu.2017.00771
58. Rossey I, Gilman MS, Kabeche SC, Sedeyn K, Wrapp D, Kanekiyo M, et al. Potent single-domain antibodies that arrest respiratory syncytial virus fusion protein in its prefusion state. *Nat Commun* (2017) 8:14158. doi:10.1038/ncomms14158
59. Darling TL, Sherwood LJ, Hayhurst A. Intracellular crosslinking of filoviral nucleoproteins with Xintrabodies restricts viral packaging. *Front Immunol* (2017) 8:1197. doi:10.3389/fimmu.2017.01197
60. Holliger P, Hudson PJ. Engineered antibody fragments and the rise of single domains. *Nat Biotechnol* (2005) 23:1126–36. doi:10.1038/nbt1142
61. Vanlandschoot P, Stortelers C, Beirnaert E, Ibanez LI, Schepens B, Depla E, et al. Nanobodies(R): new ammunition to battle viruses. *Antiviral Res* (2011) 92:389–407. doi:10.1016/j.antiviral.2011.09.002
62. Unciti-Broceta JD, Del Castillo T, Soriano M, Magez S, Garcia-Salcedo JA. Novel therapy based on camelid nanobodies. *Ther Deliv* (2013) 4:1321–36. doi:10.4155/tde.13.87
63. De Meyer T, Muyldermans S, Depicker A. Nanobody-based products as research and diagnostic tools. *Trends Biotechnol* (2014) 32:263–70. doi:10.1016/j.tibtech.2014.03.001
64. Helma J, Cardoso MC, Muyldermans S, Leonhardt H. Nanobodies and recombinant binders in cell biology. *J Cell Biol* (2015) 209:633–44. doi:10.1083/jcb.201409074
65. Bever CS, Dong JX, Vasylieva N, Barnych B, Cui Y, Xu ZL, et al. V_HH antibodies: emerging reagents for the analysis of environmental chemicals. *Anal Bioanal Chem* (2016) 408:5985–6002. doi:10.1007/s00216-016-9585-x
66. Li J, Zhu Z. Research and development of next generation of antibody-based therapeutics. *Acta Pharmacol Sin* (2010) 31:1198–207. doi:10.1038/aps.2010.120
67. Mazor Y, Sachsenmeier KF, Yang C, Hansen A, Filderman J, Mulgrew K, et al. Enhanced tumor-targeting selectivity by modulating bispecific antibody binding affinity and format valence. *Sci Rep* (2017) 7:40098. doi:10.1038/srep40098
68. Holliger P, Winter G. Engineering bispecific antibodies. *Curr Opin Biotechnol* (1993) 4:446–9. doi:10.1016/0958-1669(93)90010-T
69. Rozan C, Cornillon A, Petiard C, Chartier M, Behar G, Boix C, et al. Single-domain antibody-based and linker-free bispecific antibodies targeting FcγRIII induce potent antitumor activity without recruiting regulatory T cells. *Mol Cancer Ther* (2013) 12:1481–91. doi:10.1158/1535-7163.MCT-12-1012

70. Muruganandam A, Tanha J, Narang S, Stanimirovic D. Selection of phage-displayed llama single-domain antibodies that transmigrate across human blood-brain barrier endothelium. *FASEB J* (2002) 16:240–2.
71. Abulrob A, Sprong H, Van Bergen en Henegouwen P, Stanimirovic D. The blood-brain barrier transmigrating single domain antibody: mechanisms of transport and antigenic epitopes in human brain endothelial cells. *J Neurochem* (2005) 95:1201–14. doi:10.1111/j.1471-4159.2005.03463.x
72. Li T, Bourgeois JP, Celli S, Glacial F, Le Sourd AM, Mecheri S, et al. Cell-penetrating anti-GFAP V_HH and corresponding fluorescent fusion protein V_HH-GFP spontaneously cross the blood-brain barrier and specifically recognize astrocytes: application to brain imaging. *FASEB J* (2012) 26:3969–79. doi:10.1096/fj.11-201384
73. Webster CI, Caram-Salas N, Haqqani AS, Thom G, Brown L, Rennie K, et al. Brain penetration, target engagement, and disposition of the blood-brain barrier-crossing bispecific antibody antagonist of metabotropic glutamate receptor type 1. *FASEB J* (2016) 30:1927–40. doi:10.1096/fj.201500078
74. Moutel S, Bery N, Bernard V, Keller L, Lemesre E, de Marco A, et al. NaLi-H1: a universal synthetic library of humanized nanobodies providing highly functional antibodies and intrabodies. *Elife* (2016) 5:e16228. doi:10.7554/eLife.16228
75. Monegal A, Ami D, Martinelli C, Huang H, Aliprandi M, Capasso P, et al. Immunological applications of single-domain llama recombinant antibodies isolated from a naive library. *Protein Eng Des Sel* (2009) 22:273–80. doi:10.1093/protein/gzp002
76. Goldman ER, Anderson GP, Liu JL, Delehanty JB, Sherwood LJ, Osborn LE, et al. Facile generation of heat-stable antiviral and antitoxin single domain antibodies from a semisynthetic llama library. *Anal Chem* (2006) 78:8245–55. doi:10.1021/ac0610053
77. Yan J, Li G, Hu Y, Ou W, Wan Y. Construction of a synthetic phage-displayed nanobody library with CDR3 regions randomized by trinucleotide cassettes for diagnostic applications. *J Transl Med* (2014) 12:343. doi:10.1186/s12967-014-0343-6
78. Ladenson RC, Crimmins DL, Landt Y, Ladenson JH. Isolation and characterization of a thermally stable recombinant anti-caffeine heavy-chain antibody fragment. *Anal Chem* (2006) 78:4501–8. doi:10.1021/ac058044j
79. Spinelli S, Frenken LG, Hermans P, Verrips T, Brown K, Tegoni M, et al. Camelid heavy-chain variable domains provide efficient combining sites to haptens. *Biochemistry* (2000) 39:1217–22. doi:10.1021/bi991830w
80. Smolarek D, Hattab C, Hassanzadeh-Ghassabeh G, Cochet S, Gutierrez C, de Brevern AG, et al. A recombinant dromedary antibody fragment (V_HH or nanobody) directed against human Duffy antigen receptor for chemokines. *Cell Mol Life Sci* (2010) 67:3371–87. doi:10.1007/s00018-010-0387-6
81. Traenkle B, Emele F, Anton R, Poetz O, Haeussler RS, Maier J, et al. Monitoring interactions and dynamics of endogenous β-catenin with intracellular nanobodies in living cells. *Mol Cell Proteomics* (2015) 14:707–23. doi:10.1074/mcp.M114.044016
82. van der Linden RH, Frenken LG, de Geus B, Harmsen MM, Ruuls RC, Stok W, et al. Comparison of physical chemical properties of llama V_HH antibody fragments and mouse monoclonal antibodies. *Biochim Biophys Acta* (1999) 1431:37–46. doi:10.1016/S0167-4838(99)00030-8
83. Doyle PJ, Arbabi-Ghahroudi M, Gaudette N, Furzer G, Savard ME, Gleddie S, et al. Cloning, expression, and characterization of a single-domain antibody fragment with affinity for 15-acetyl-deoxynivalenol. *Mol Immunol* (2008) 45:3703–13. doi:10.1016/j.molimm.2008.06.005
84. Maussang D, Mujic-Delic A, Descamps FJ, Stortelers C, Vanlandschoot P, Stigter-van Walsum M, et al. Llama-derived single variable domains (nanobodies) directed against chemokine receptor CXCR7 reduce head and neck cancer cell growth in vivo. *J Biol Chem* (2013) 288:29562–72. doi:10.1074/jbc.M113.498436
85. McCoy LE, Rutten L, Frampton D, Anderson I, Granger L, Bashford-Rogers R, et al. Molecular evolution of broadly neutralizing llama antibodies to the CD4-binding site of HIV-1. *PLoS Pathog* (2014) 10:e1004552. doi:10.1371/journal.ppat.1004552
86. Peyrassol X, Laeremans T, Gouwy M, Lahura V, Debulpaep M, Van Damme J, et al. Development by genetic immunization of monovalent antibodies (nanobodies) behaving as antagonists of the human ChemR23 receptor. *J Immunol* (2016) 196:2893–901. doi:10.4049/jimmunol.1500888
87. Liu S, Wang S, Lu S. DNA immunization as a technology platform for monoclonal antibody induction. *Emerg Microbes Infect* (2016) 5:e33. doi:10.1038/emi.2016.27
88. Nguyen VK, Zou X, Lauwereys M, Brys L, Bruggemann M, Muyldermans S. Heavy-chain only antibodies derived from dromedary are secreted and displayed by mouse B cells. *Immunology* (2003) 109:93–101. doi:10.1046/j.1365-2567.2003.01633.x
89. Zou X, Smith JA, Nguyen VK, Ren L, Luyten K, Muyldermans S, et al. Expression of a dromedary heavy chain-only antibody and B cell development in the mouse. *J Immunol* (2005) 175:3769–79. doi:10.4049/jimmunol.175.6.3769
90. Janssens R, Dekker S, Hendriks RW, Panayotou G, van Remoortere A, San JK, et al. Generation of heavy-chain-only antibodies in mice. *Proc Natl Acad Sci U S A* (2006) 103:15130–5. doi:10.1073/pnas.0601108103
91. Kohler G, Milstein C. Continuous cultures of fused cells secreting antibody of predefined specificity. *Nature* (1975) 256:495–7. doi:10.1038/256495a0
92. Prentice HG, Blacklock HA, Janossy G, Bradstock KF, Skeggs D, Goldstein G, et al. Use of anti-T-cell monoclonal antibody OKT3 to prevent acute graft-versus-host disease in allogeneic bone-marrow transplantation for acute leukaemia. *Lancet* (1982) 1:700–3. doi:10.1016/S0140-6736(82)92619-8
93. Cosimi AB, Colvin RB, Burton RC, Rubin RH, Goldstein G, Kung PC, et al. Use of monoclonal antibodies to T-cell subsets for immunologic monitoring and treatment in recipients of renal allografts. *N Engl J Med* (1981) 305:308–14. doi:10.1056/NEJM198108063050603
94. Beck A, Wurch T, Bailly C, Corvaia N. Strategies and challenges for the next generation of therapeutic antibodies. *Nat Rev Immunol* (2010) 10:345–52. doi:10.1038/nri2747
95. Ecker DM, Jones SD, Levine HL. The therapeutic monoclonal antibody market. *MAbs* (2015) 7:9–14. doi:10.4161/19420862.2015.989042
96. Winter G, Griffiths AD, Hawkins RE, Hoogenboom HR. Making antibodies by phage display technology. *Annu Rev Immunol* (1994) 12:433–55. doi:10.1146/annurev.iy.12.040194.002245
97. Hoogenboom HR. Selecting and screening recombinant antibody libraries. *Nat Biotechnol* (2005) 23:1105–16. doi:10.1038/nbt1126
98. Nelson AL, Reichert JM. Development trends for therapeutic antibody fragments. *Nat Biotechnol* (2009) 27:331–7. doi:10.1038/nbt0409-331
99. McCafferty J, Griffiths AD, Winter G, Chiswell DJ. Phage antibodies: filamentous phage displaying antibody variable domains. *Nature* (1990) 348:552–4. doi:10.1038/348552a0
100. Jespers LS, Roberts A, Mahler SM, Winter G, Hoogenboom HR. Guiding the selection of human antibodies from phage display repertoires to a single epitope of an antigen. *Biotechnology (N Y)* (1994) 12:899–903.
101. Kempeni J. Preliminary results of early clinical trials with the fully human anti-TNF-α monoclonal antibody D2E7. *Ann Rheum Dis* (1999) 58 (Suppl 1):I70–2. doi:10.1136/ard.58.2008.i70
102. Wang Y, Fan Z, Shao L, Kong X, Hou X, Tian D, et al. Nanobody-derived nanobiotechnology tool kits for diverse biomedical and biotechnology applications. *Int J Nanomedicine* (2016) 11:3287–303. doi:10.2147/IJN.S107194

Conflict of Interest Statement: The author declares that the research was conducted in the absence of any commercial or financial relationships that could be construed as a potential conflict of interest.

frontiers in Immunology

REVIEW
published: 04 July 2017
doi: 10.3389/fimmu.2017.00771

Nanobody Technology: A Versatile Toolkit for Microscopic Imaging, Protein–Protein Interaction Analysis, and Protein Function Exploration

*Els Beghein and Jan Gettemans**

Nanobody Laboratory, Department of Biochemistry, Faculty of Medicine and Health Sciences, Ghent University, Ghent, Belgium

Over the last two decades, nanobodies or single-domain antibodies have found their way in research, diagnostics, and therapy. These antigen-binding fragments, derived from Camelid heavy chain only antibodies, possess remarkable characteristics that favor their use over conventional antibodies or fragments thereof, in selected areas of research. In this review, we assess the current status of nanobodies as research tools in diverse aspects of fundamental research. We discuss the use of nanobodies as detection reagents in fluorescence microscopy and focus on recent advances in super-resolution microscopy. Second, application of nanobody technology in investigating protein–protein interactions is reviewed, with emphasis on possible uses in mass spectrometry. Finally, we discuss the potential value of nanobodies in studying protein function, and we focus on their recently reported application in targeted protein degradation. Throughout the review, we highlight state-of-the-art engineering strategies that could expand nanobody versatility and we suggest future applications of the technology in the selected areas of fundamental research.

Keywords: nanobody, VHH, single-domain antibody, engineering, super-resolution microscopy, protein–protein interactions, targeted protein degradation, fundamental research

OPEN ACCESS

Edited by:
Kevin A. Henry, National Research Council Canada (NRC-CNRC), Canada

Reviewed by:
Christian Cambillau, Aix-Marseille University, France
Greg Hussack, National Research Council Canada (NRC-CNRC), Canada

***Correspondence:**
Jan Gettemans
jan.gettemans@ugent.be

Specialty section:
This article was submitted to Vaccines and Molecular Therapeutics, a section of the journal Frontiers in Immunology

Received: *28 April 2017*
Accepted: *16 June 2017*
Published: *04 July 2017*

Citation:
Beghein E and Gettemans J (2017) Nanobody Technology: A Versatile Toolkit for Microscopic Imaging, Protein–Protein Interaction Analysis, and Protein Function Exploration. Front. Immunol. 8:771. doi: 10.3389/fimmu.2017.00771

INTRODUCTION

Since the discovery of heavy chain only antibodies (HcAbs) in 1993 by the Hamers-Casterman's group (1), the use of their antigen binding fragments or nanobodies in research, diagnostics, and therapy has evolved at an incredible pace. HcAbs are unique IgGs that are found in sera of *Camelidae*. These antibodies are devoid of the light chain and lack the first constant domain. Consequently, the antigen-binding fragment of HcAbs is solely composed of a single variable domain, referred to as VHH (variable domain of the heavy chain of HcAbs), single-domain antibody or nanobody, which is only ~15 kDa in size. The variable domains of conventional IgGs and HcAbs comprise three complementarity-determining regions (CDRs) that constitute the paratope of the antibody (**Figure 1**). As nanobodies lack the variable domain of the light chain, they only contain three instead of six CDRs. These CDRs are organized in three loops, separated by more conserved framework regions (FRs) and cluster at the N-terminal side of the nanobody. In order to provide an adequate antigen-interacting surface of 600–800 Å^2, nanobodies have longer CDR1 and CDR3 loops than VHs (variable domain of the heavy chain) of conventional antibodies, resulting in similar binding affinities. In dromedary nanobodies, these long loops

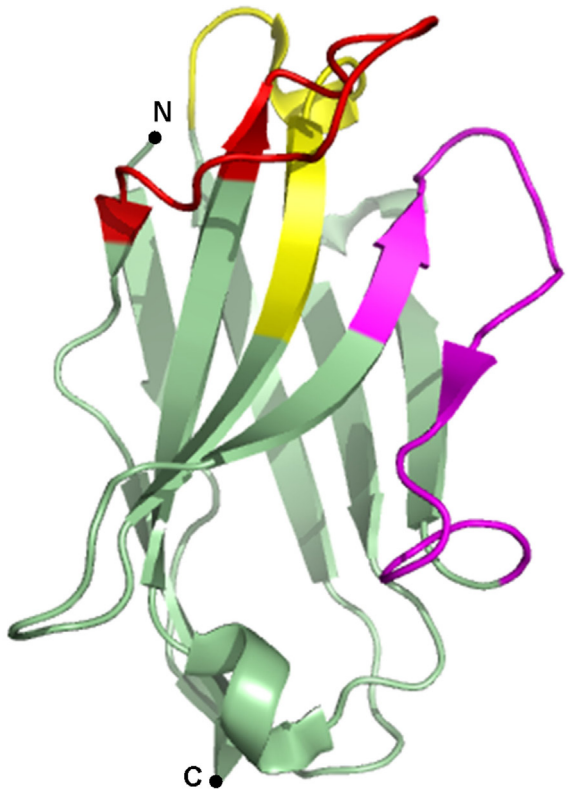

FIGURE 1 | Crystal structure of a gelsolin nanobody. A nanobody is typically composed of three complementarity-determining regions (CDRs), alternated with four framework regions (FRs). CDR1 is depicted in yellow, CDR2 in magenta, CDR3 in red, and the FRs are depicted in green. Image of PDB ID 2X1O (5) created with PyMOL.

are often connected by a disulfide bond that restricts their flexibility and consequently, favors antigen binding. Normally, FR2 region of VHs contains highly conserved hydrophobic amino acids participating in the interaction with the VL (variable domain of the light chain). As this region is water-exposed in nanobodies, the hydrophobic amino acids are substituted by hydrophilic residues, which reduce the likelihood for aggregation. This explains the high solubility of nanobodies (2–4).

Nanobodies are thus endowed with favorable characteristics in terms of size, solubility, and affinity. Furthermore, nanobodies can easily be produced recombinantly in bacteria, yeast, plants, and mammalian cell lines (3, 4). When expressed in eukaryotic cells as intrabodies, nanobodies accurately bind and trace their target as they normally do not appear to suffer from the reducing intracellular environment. Nanobodies can easily be equipped with a customized tag (e.g., fluorescence, affinity, epitope tag, etc.) without losing their affinity or stability (6–9). Moreover, nanobodies feature a convex paratope and can, therefore, but also due to their small size, bind hidden epitopes in small cavities (e.g., active site of enzymes) (10, 11). They mainly bind conformational epitopes (7, 10, 12), but nanobodies recognizing linear epitopes have also been reported (5, 13, 14). These unique biochemical and biophysical properties of nanobodies purportedly render them superior to conventional antibodies or antibody fragments, and make them ideally suited for a myriad of biotechnological applications.

Despite the aforementioned benefits of the nanobody technology, still some drawbacks need to be overcome. First of all, unmodified nanobodies are not able to traverse the cell membrane. Using nanobodies in research thus requires transfection or transduction in cells, or requires the use of transgenic animals. However, several research groups are looking into this issue. Possible solutions are coupling the nanobodies to a cell-penetrating peptide (penetratin) (15) or exploiting the *Escherichia coli* type III protein-secretion system (T3SS) (16, 17). Second, although quite exceptional, nanobodies can lose their functionality when expressed intracellularly (7). A third and perhaps major stumbling block, is the fact that nanobody production (animal housing, immunization, library construction, and phage panning) is equivalent to monoclonal antibody production, CRISPS/Cas9 mouse knockouts, and hence relatively expensive.

In this review, we assess the current status of nanobodies as research tools in diverse facets of fundamental research (microscopy, protein–protein interactions and protein function). Moreover, we focus on the adaptability of nanobodies, or how engineering can expand their versatility, and we discuss future opportunities given the current know-how. As the use of nanobodies in diagnostics and therapy does not fall within the scope of this paper, we refer the reader to some excellent recent reviews (18, 19).

NANOBODIES USED AS RESEARCH TOOL IN MICROSCOPY

Primary Detection Reagents in Fluorescence Microscopy

Several studies confirmed the usefulness of nanobodies as equivalent detection surrogates for antibodies in immunocytochemistry (**Table 1**). de Bruin and coworkers generated and characterized anti-Vγ9 and anti-Vδ2-T cell receptor-directed nanobodies that could successfully be used as primary detection reagents for Vγ9Vδ2-T cells in immunocytochemistry (20). Bound nanobody was detected using a secondary anti-nanobody antibody, followed by a tertiary Alexa Fluor 488-conjugated antibody (20). To shorten staining procedure, Jullien and colleagues mixed their HA-tagged histon H2A-H2B nanobody (chromatibody) with an anti-HA antibody for primary staining (9). Using a tertiary fluorescently labeled antibody, chromatin-specific staining was observed in human HCT116 cells and even in organisms evolutionarily distant from mammals (9). Peyrassol and colleagues developed His-tagged ChemR23 G-protein-coupled receptor (GPCR) nanobodies and tested their binding specificity by immunostaining on fixed CHO cells (21). Visualization was performed by using a fluorescently labeled anti-His secondary antibody, hence avoiding the use of a tertiary antibody (21).

Equipping nanobodies with organic fluorescent dye bypasses the use of a secondary and/or tertiary fluorescently labeled antibody and thus makes the staining procedure cheaper and less elaborate. Braun and colleagues characterized an anti-β-catenin

TABLE 1 | Overview of the different nanobody-based applications in microscopy.

	Application	Strategy	Specifics	Reference
Microscopy	Primary detection reagents in fluorescence microscopy	Indirect immunocytochemistry		(9, 20, 21)
		Direct immunocytochemistry		(8, 13)
	Primary detection reagents in super-resolution microscopy	Anti-GFP and anti-RFP nanobodies	*N*-hydroxysuccinimide *(NHS)* ester-labeling	(22–25)
		Nanobodies targeting endogenous protein	*N*-hydroxysuccinimide *(NHS)* ester-labeling	(26)
			Cysteine-maleimide-labeling	(27, 28)
			Sortase A-labeling	(29)
			Furan-labeling	(30)
	Intracellular nanobodies as microscopic tracers			(6–9, 31–33)

Each application corresponds to the different sections in the main text and the strategies match the different paragraphs therein, which are whether or not further specified.

nanobody, referred to as BC2-VHH, which recognizes a linear epitope of only 12 amino acids with low nanomolar affinity (13). Coupling this nanobody to the organic dyes Alexa Fluor 488 or ATTO 647 by means of *N*-hydroxysuccinimide ester-labeling (see Primary Detection Reagents in Super-Resolution Microscopy) endows it with the capability to visualize BC2-tagged fusion proteins directly (13). Accordingly, Maier and colleagues provided their vimentin nanobodies with a fluorescent ATTO 488 tag (8). Binding specificity was examined in different cell lines (8). Of note, the mentioned VB6 vimentin nanobody is not a genuine nanobody, but a variable domain derived from a conventional antibody.

Primary Detection Reagents in Super-Resolution Microscopy

Diffraction of light limits the resolution of conventional fluorescence microscopy to about 200–300 nm in the lateral and 500–700 nm in the axial direction, leaving many subcellular structures too small to be observed in detail. Several variants on fluorescence microscopy, such as confocal or multiphoton microscopy, only enhance resolution moderately. Groundbreaking progress was made in the 1990s, when a number of super-resolution techniques arose that achieve resolutions far beyond the limit of diffraction, for instance, STED (stimulated emission depletion), STORM (stochastic optical reconstruction microscopy), or PALM (photoactivated localization microscopy) (34, 35). Theoretically, the resolution of these techniques can reach molecular scale. In practice however, resolution is limited by a combination of intrinsic optical properties and sample specific factors. An example of the latter is the size of the fluorescent labels, which become significant at high resolution (35). Using indirect immunochemistry for protein detection, the primary and secondary antibody increases the apparent size of the visualized structure or introduces a localization bias of 10–20 nm (22, 36, 37). Reducing the distance between the antigen and fluorescent label (linkage error) can be achieved by directly coupling an organic dye molecule to a peptide sequence, which is genetically fused to the protein of interest (23, 38, 39). For instance, coupling proteins to a 15 amino acid acceptor peptide tag, allows enzymatic biotinylation and consequent visualization of the protein with fluorophore-labeled monomeric streptavidin (23). Nevertheless, in some experiments, genetic engineering or overexpression is not appropriate (e.g., in case of human samples, peptide interfering with protein interactions or due to lack of time). In these cases, large linkage error can be tackled by direct immunofluorescence, using fluorescently labeled conventional antibodies (40).

Recently, the use of labeled nanobodies as nanoscale detection tools has emerged (**Table 1**), since nanobodies are significantly smaller than antibodies. Several publications describe the use of anti-GFP and anti-RFP nanobodies for super-resolution microscopy. These nanobodies target genetically encoded fluorescent fusion proteins and are equipped with a strong organic dye, usually coupled to the nanobody by means of *N*-hydroxysuccinimide ester-labeling (see later in this section) (22–24). The first use of this technology was reported by Ries and coworkers (22). They labeled individual microtubules in fixed Ptk2 cells stably expressing tubulin-YFP. The acquired resolution of 26.9 ± 3.7 nm is compatible with a microtubule diameter of 25 nm and is considerably smaller than what was achieved with indirect immunochemistry using conventional antibodies ($\pm$45 nm). Moreover, these nanobodies showed also to be valuable tools for high resolution live imaging and dual-color microscopy (22). Accordingly, Chamma and coworkers used GFP nanobodies to live-label synaptogenic adhesion protein neurexin-1β and to image transsynaptic contacts in neurons in a dual-color setup (23). GFP and RFP nanobodies can also be used to study nuclear pore complex (NPC) and caveolae ultrastructure in detail. Unlike indirect antibody immunochemistry, nanobody staining resulted in a far better approximation of the actual dimensions of both structures (24, 25).

Using GFP or RFP nanobodies as detection tool has some advantages. First, high-affinity GFP and RFP nanobodies are commercially available (41), which makes it possible to visualize virtually every protein; even those for which no specific targeting moiety is available. Moreover, it allows comparable and quantitative labeling between different proteins. This method can also be used to image GFP-tagged proteins from GFP-fusion libraries in high throughput (22). Nevertheless, experiments sometimes require visualization of endogenous protein or overexpression of fusion protein is not appropriate (see above). In these cases,

endogenous target-specific nanobodies can be used. Excluding the GFP/RFP-tag for detection practically minimizes linkage error to the length of a nanobody, which is 2–4 nm.

In fact, every nanobody compatible with immunostaining can be used for super-resolution microscopy. Different labeling techniques have been reported. *N*-hydroxysuccinimide (NHS) ester-labeling **1** of primary amines **2** (R-NH_2) is the most widespread labeling strategy (**Figure 2**). NHS ester derivatives of various fluorescent probes are commercially available. The carbonyl carbon of the NHS ester reacts with primary amines in the nanobody, thereby releasing NHS **3** and crosslinking the nanobody with the organic dye **4**. Accordingly, Mikhaylova and coworkers conjugated their anti-β-tubulin nanobodies with Alexa Fluor 647 (26). Applying these nanobodies in super-resolution microscopy, they succeeded in resolving individual microtubules, both *in vitro* and in fixed cells. Furthermore, for densely packed microtubules with a 25-nm lattice-to-lattice spacing, the resolving power of the nanobodies was 2.5-fold and 10-fold higher than primary and primary–secondary antibody labelings, respectively (26).

NHS ester-labeling can, however, abolish or reduce antigen-recognition of the nanobody if the paratope contains primary amines that become labeled. Equipping the nanobodies with a C-terminal oligo-lysine stretch might divert NHS-labeling from intrinsic nanobody lysine residues (24). However, modification of multiple lysines can create hydrophobic patches that increase unspecific binding and thus background staining (27). Several research groups, therefore, attempt to develop a generic site-specific conjugation method. These techniques make it possible to control where and how many labels will be added, resulting in a homogeneous nanobody population.

Massa and coworkers labeled anti-HER2 nanobody using the cysteine-maleimide strategy (28) (**Figure 2**). They introduced a unique place for conjugation by equipping the nanobody with a C-terminal cysteine **5**, spaced by a rigid 14 amino acid linker from the nanobody sequence. This linker presumably prevents the added cysteine from interfering with correct folding of the dromedary nanobody interloop disulfide bond. When adding a bifunctional maleimide-label **6**, the maleimide double bond reacts with the cysteine thiol group, generating a stable

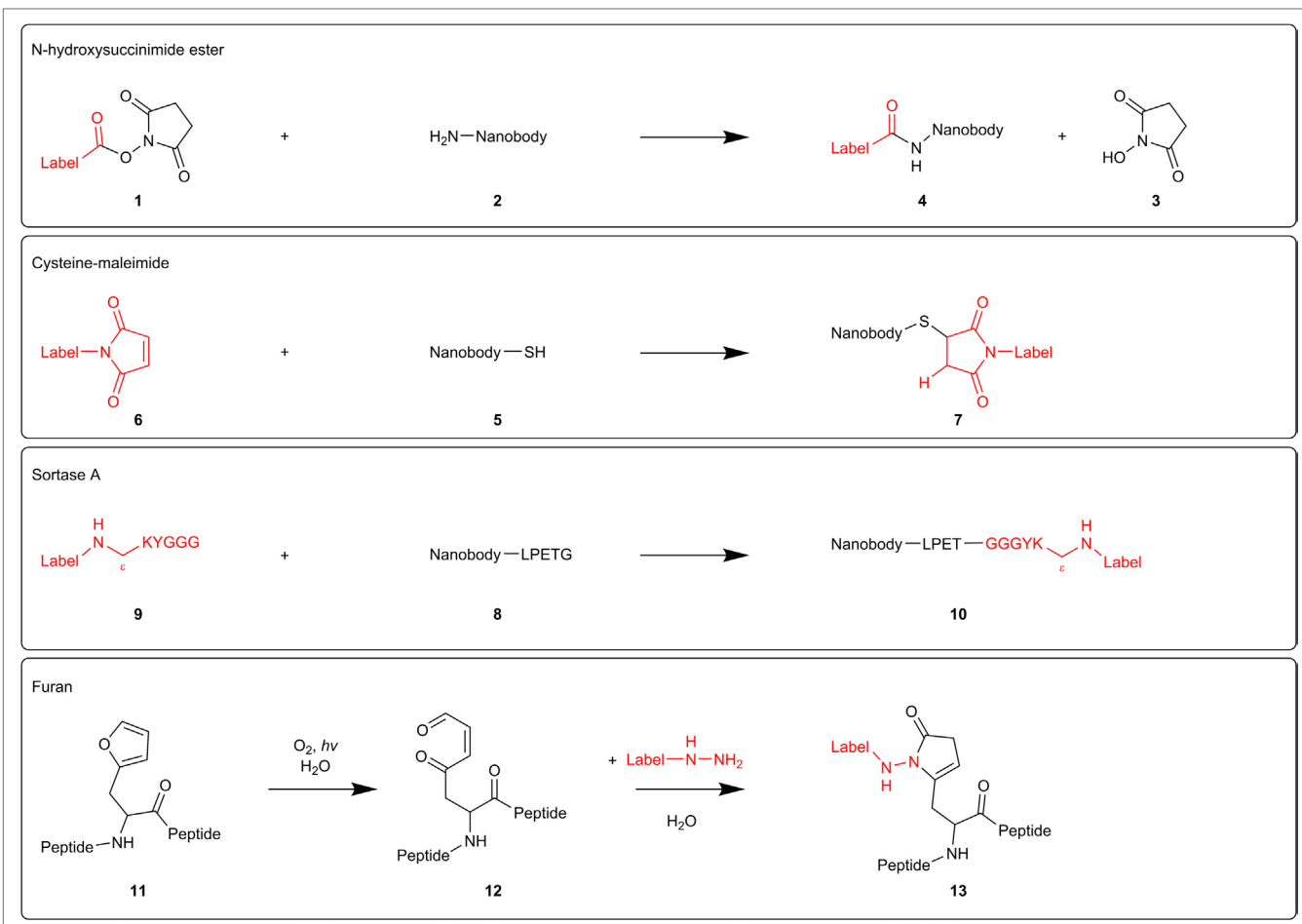

FIGURE 2 | Mechanisms of different nanobody-labeling strategies for super-resolution microscopy. *N*-hydroxysuccinimide ester-labeling **1** (top) randomly labels primary amines **2** in the nanobody. The other techniques mentioned (cysteine-maleimide, Sortase A, and furan technology) site-specifically label introduced tags (respectively, cysteine **5**, sortag or LPETG **8**, and furylalanine **11**).

carbon-sulfur bond **7**. However, this derivatization strategy resulted in a severe reduction in production yields and triggered extensive dimerization of the nanobodies at the introduced C-terminal cysteine, necessitating an additional reduction step. In order to safeguard intradomain disulfide bonds, the reducing agent needs to be titrated carefully (28). Pleiner and coworkers used the cysteine-maleimide labeling in order to visualize individual NPC proteins or nucleoporins (27). They mutated one or more solvent-exposed small residues (framework glycine, serine, or alanine) to cysteines or introduced an N or C-terminal cysteine in GFP nanobody and several nucleoporin nanobodies. These cysteines were subsequently crosslinked with maleimide-Alexa Fluor 647/488. The conjugation reaction was performed at 0°C in order to protect the intradomain cysteines. In confocal laser scanning microscopy, all nanobodies produced a bright punctuate nuclear rim staining against a very low background, even when there was only one dye molecule per nanobody. Strikingly, cysteine-maleimide-labeled nanobodies performed far better than their NHS ester-labeled counterparts in terms of specificity. The nucleoporin nanobodies also performed excellent in super-resolution microscopy, providing very detailed views of individual NPC proteins (27).

Recently, two novel derivatization techniques were reported that hold great promise for future nanobody-labeling with organic dyes. First, researchers exploited a transpeptidase Sortase A (SrtA) derived from *Staphylococcus aureus* to label an anti-HER2 nanobody with the fluorescent dye Cy5 (**Figure 2**). Therefore, nanobodies were provided with a C-terminal SrtA recognition motif or sortag (LPETG) **8**, and Cy5 was coupled to the pentapeptide GGGYK *via* the side chain ε-amine of the lysine residue **9**. SrtA catalyzes the formation of a new peptide bond between the threonine of the sortag and the glycine of the pentapeptide, hence generating a stable bond between nanobody and fluorescent probe **10**. The labeled HER2 nanobody performed excellent in fluorescence reflectance imaging of HER2-positive tumors in mice (29).

The furan crosslinking technology comprises a second potential derivatization approach (**Figure 2**). Albeit not shown for nanobodies yet, researches already successfully labeled thymosin β4 peptides with different fluorescent dyes using this technique. Briefly, a furylalanine building block **11** was incorporated into thymosin β4 peptide. Photooxygenation of the furan moiety results in the formation of a 4-oxo-enal moiety **12**. Subsequent addition of a NH_2NH-coupled label, transforms the furan-containing peptides into pyrrolidinone-based fluorescent probes **13** (30). As super-resolution microscopy techniques can be exploited to their full potential by using nanobodies as detection tool, more site-specific conjugation methods will undoubtedly emerge in the near future.

Intracellular Nanobodies As Microscopic Tracers

Target visualization can also be achieved by intracellular expression of fluorescently labeled nanobodies (chromobodies) or nanobodies equipped with an epitope tag that allows antibody detection (**Table 1**). These intrabodies typically do not interfere with protein function and allow visualization of the endogenous target. Overexpression of (fluorescent) fusion protein is thus no longer needed, which frequently induces artificial changes in cell behavior (8, 9, 31) or results in a false representation of protein dynamics (26). Our lab generated a nanobody against survivin, a protein that exerts key roles during mitosis (7). The survivin nanobody was equipped with a V5-tag, enabeling immunocytochemical detection using an anti-V5 antibody. The nanobody accurately tracks its target during different phases of mitosis and moreover, it detects different surviving subpopulations that are indiscernible for certain commercially antibodies (7). Similarly, intracellular expression of EGFP-tagged nuclear transport factor 2 (NTF2) nanobodies uncovered a new location of NTF2 at the centrosome (6). Maier and colleagues on the other hand, expressed a set of EGFP-labeled vimentin chromobodies in HeLa cells and compared their localization pattern to a canonical anti-vimentin antibody staining (8). As such, they could identify in an early screen which nanobodies are genuine vimentin binders (8). Accordingly, Van Overbeke and coworkers validated binding specificity of endoplasmic reticulum-directed gelsolin nanobodies by immunocytochemistry (32). Colocalization between plasma gelsolin and the V5-tagged nanobodies confirmed proper nanobody binding (32). Fluorescent nanobodies are also excellent research tools for live imaging in cells and whole organisms. The aforementioned vimentin nanobodies were further utilized to monitor endogenous vimentin localization and dynamics in A549 lung cancer cells. In this cell-based chromobody model, it was possible to monitor dynamic changes of vimentin in real-time upon RNAi treatment or induction with TGF-β (8). Recently, similar high resolution spatiotemporal antigen tracking was reported using histon H2A-H2B (9), β-catenin (31), F-actin, and PCNA (33) nanobodies.

NANOBODIES USED AS RESEARCH TOOL TO IDENTIFY PROTEIN–PROTEIN INTERACTIONS

GFP-Targeting Nanobodies

Several studies report the use of a GFP-targeting nanobody to study protein–protein interactions (**Figure 3**; **Table 2**). Herce and colleagues presented the fluorescent-three-hybrid (F3H) strategy as an alternative to the well-known yeast two-hybrid (Y2H) technique (42). They coupled GFP nanobody with a delocalization tag that redirects GFP-tagged bait protein and eventually mCherry-tagged prey toward a well-defined subcellular location. (Co-) localization of bait and prey can be visualized using fluorescence microscopy. Moreover, real-time imaging allows monitoring of the inhibition kinetics of interactions induced by drugs. The F3H approach was validated for delocalization to various subcellular compartments (Lac operator DNA sequence, chromocenters, nuclear lamina, and centrioles), for different cell types and species (baby hamster kidney, mouse myoblast C2C12, and human cervical carcinoma HeLa), emphasizing on the flexibility of the technique. F3H does not require specialized equipment (42). Moreover, this technique overcomes several important drawbacks of Y2H associated with the reporter system or the use of yeast as

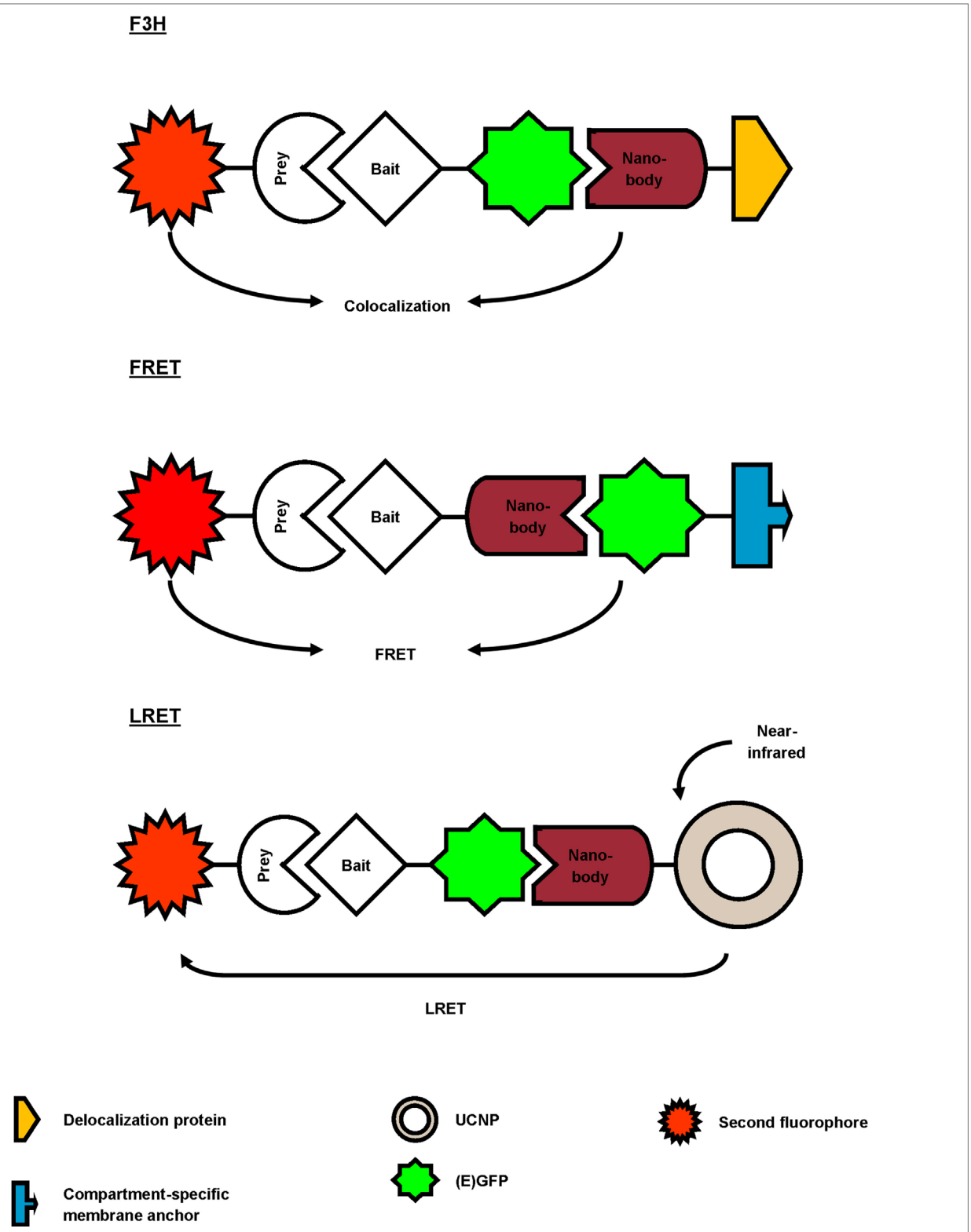

FIGURE 3 | Overview of different reported approaches to investigate protein–protein interactions using a GFP-targeting nanobody. In the fluorescent-three-hybrid (F3H) strategy (top), the GFP nanobody delocalizes GFP-tagged bait toward a defined subcellular location. The nanobody can also be fused with bait protein and as such, relocalize bait toward GFP-tagged membrane protein (middle). Finally, the GFP nanobody can be used to deliver upconversion nanoparticles (UCNPs) toward GFP-tagged bait (bottom). Binding between GFP-bait and labeled prey is then validated by colocalization, Förster or lanthanide-based resonance energy transfer (FRET or LRET, respectively).

TABLE 2 | Overview of the different nanobody-based applications to identify protein–protein interactions.

	Application	Strategy	Specifics	Reference
Identify protein–protein interactions	GFP-targeting nanobodies	Fluorescent-three-hybrid		(42)
		Förster resonance energy transfer		(44)
		Lanthanide-based resonance energy transfer		(45)
	Nanobodies in mass spectrometry	Affinity-purification mass spectrometry *(AP-MS)*	Classical *AP-MS*	(27, 46)
			Footprinting	(6)
			Virotrap	(47)
			BioID proximity-labeling	(48)
		Organellar proteomics		(7)
		Hydrogen/deuterium exchange		(49–52)

Each application corresponds to the different sections in the main text and the strategies match the different paragraphs therein, which are whether or not further specified.

host (42, 43). To circumvent overexpression of fluorescent fusion proteins (bait and prey), one can use a nanobody that targets and delocalizes endogenous protein toward predetermined organelles. Potential interactors colocalize with the target protein, which can be visualized by post-fixation labeling (6). This approach does, however, not allow studying interaction or disruption kinetics.

Künzl and coworkers studied vacuolar sorting in plants using a GFP nanobody sensor (44). Soluble proteins are sorted to the vacuole for degradation. Sorting relies on the activity of vacuolar sorting receptors (VSRs) that bind proteins by means of a luminal binding domain (LBD). However, not much was known about the exact locations (endoplasmic reticulum, Golgi, trans-Golgi network/early endosome or multivesicular late endosomes) at which VSRs bind or release their ligands. In order to investigate this, universal and compartment-specific VSR sensors were generated and expressed in tobacco mesophyll protoplasts. A full-functional VSR sensor consists of a LBD (bait)-equipped GFP nanobody and a GFP-tagged membrane marker protein. The latter fluorescently decorates the membrane of a specific compartment, depending on the chosen marker (e.g., GFP-calnexin for visualization of endoplasmic reticulum). A RFP-coupled model ligand (prey), containing a vacuolar sorting motif, was used to study compartment-specific interactions between LBD (bait) and ligand (prey). Upon coexpression and binding of the three constructs, the excited-state energy from GFP (membrane marker) is transferred to RFP (ligand), thereby reducing the fluorescence lifetime of GFP. This phenomenon, also called Förster resonance energy transfer (FRET), can be detected using fluorescence lifetime imaging and makes it possible to discern true binding from interaction-independent colocalization. FRET ceases at the cellular compartment when LBD (bait) releases its ligand (prey). As such, a novel pathway of vacuolar protein sorting in plants was postulated (44).

GFP nanobody has also been exploited as targeting moiety for upconversion nanoparticles (UCNPs) in lanthanide-based resonance energy transfer (LRET) imaging. In simple terms, lanthanide-doped UCNPs are able to convert two or more near-infrared photons into one UV/Vis photon. In its turn, this photon can sensitize a neighboring acceptor fluorophore. The UCNPs were functionalized with anti-GFP nanobody to target a bait EGFP-fusion protein. On the other hand, prey protein was fused to an acceptor fluorophore. Sensitized fluorescence upon LRET from the UCNPs can only be detected when bait and prey interact (in)directly. As proof-of-concept, the indirect interaction between mitochondrial outer membrane (MOM) proteins Tom20 and Tom7 was successfully visualized using UCNP LRET (45).

In the latter three studies, a high-affinity GFP nanobody was used to study protein–protein interactions in living cells, albeit combined with different techniques (F3H, FRET, or LRET). The nanobody was utilized as delocalization tool, thereby enriching bait and eventually prey at defined subcellular locations (F3H, FRET) (42, 44), or was used to target a reporter toward bait protein (LRET) (45). As such, the GFP nanobody emerges as a highly adaptable research tool to study protein–protein interactions.

Nanobodies in Mass Spectrometry (MS) and Perspectives

Nanobodies are valuable tools for MS applications (**Table 2**). Recently, nanobodies have been used as an alternative for antibodies in classical affinity-purification mass spectrometry (AP-MS) to study protein complexes (27, 46). Their small size minimizes background binding and reduces the amount of tryptic peptides released from the affinity resin during on-bead digestion (53). Hypothetically, background binding in AP-MS can be further tackled by nanobody footprinting. In brief, by using nanobodies that target different epitopes in the same protein, true interaction partners may be displaced. This leaves a footprint; hence the name nanobody footprinting (6). Proteins that are shared among different nanobody-based APs either represent false positives or genuine binders that interact with the antigen at an epitope that is not recognized by the nanobodies. False positives can, in their turn, be significantly eliminated by using an appropriate control nanobody (e.g., GFP nanobody) for AP. This finally results in a (shorter) list of *bona fide* interaction partners. Combining this strategy with Virotrap, a lysis-free protein interaction analysis method, could improve the study of protein complexes, as lysis-sensitive protein complexes are preserved. Virotrap implies trapping a bait protein, together with its putative interaction partners, inside protective virus-like particles (VLPs) that bud from cells. Following antibody-based enrichment and lysis of the VLPs, protein complexes can be analyzed by Western blot

or MS. Packing of bait in VLPs is achieved by expression of p55 HIV-1 GAG-bait fusion protein (e.g., expression of GAG-HRAS to detect the HRAS–RAF1 interaction) (47). Similarly, nanobody could be fused to a GAG protein and capture its target (and target interactors) in VLPs, thus avoiding overexpression of bait protein. Lysis-sensitive protein interactions can also be detected by using the BioID proximity-labeling strategy. This technique implies coupling bait to BirA*, a promiscuous biotin ligase that covalently attaches a biotin molecule to exposed lysine residues in proximate and interacting prey. All biotinylated prey is subsequently collected by means of streptavidin-AP and analyzed with MS. Consequently, the technique allows detection of weak and transient protein interactions that could be missed when using classical AP-MS (48). Combining BioID with nanobody footprinting could provide more details on the epitopes of the protein interactome.

In contrast to mitochondria and endoplasmic reticulum, peroxisomes are endowed with the ability to import oligomeric protein complexes (54–59). Combining this unique feature with the nanobody-delocalizing strategy opens up new perspectives for studying protein complexes using MS. Essentially, nanobodies can be equipped with a SKL peroxisomal targeting sequence that shuttles the nanobody and its target to the peroxisomal matrix (7). Target interaction partners could subsequently be identified using organellar proteomics. This technique implicates a subcellular fractionation step of the organelle of interest (e.g., peroxisomes), thus eliminating contaminating cytoplasmic proteins. Hence, sample complexity is compatible with the sensitivity of current mass spectrometers, allowing identification of low-abundance proteins (60). Moreover, as peroxisomal protein catalogs are available (61, 62), it is possible to discriminate true interaction partners from intrinsic peroxisomal protein. Of note, combining nanobody-induced delocalization with organellar proteomics has not been reported yet, implicating that one could encounter unexpected difficulties. The peroxisomal import machinery could possibly face difficulties in transporting large protein complexes, although successful import of 240 kDa tetrameric catalase has already been reported (54). Moreover, in order to obtain significant MS data, peroxisomes need to be isolated with high purity and adequate yields. Seeing that mammalian peroxisomes contribute to only 1–5% of the cell volume, this technique will probably require a substantial amount of cell material. Nevertheless, strategies to isolate pure and high yield peroxisomal fractions for organellar proteomics have been published (61).

As will be discussed in the next section, the nanobody-binding epitope could be used to identify "weak" spots in proteins, which offers opportunities for small molecule development. Hydrogen/deuterium exchange MS (HDX-MS) allows fast epitope characterization with small amounts of sample and has already frequently been used to characterize antibody epitopes (49–52). In brief, backbone amide hydrogens of the target protein are exchanged with deuterium. This process is subsequently repeated for the antibody-target protein complex. Antibody binding limits the accessibility of certain backbone hydrogens for deuterium exchange or alters the exchange rates. Consequently, the resulting MS fractionation patterns differ and allow delineation of the antibody epitope (49). We believe that this strategy could also successfully be exploited for nanobody epitope identification, although this has not been published yet.

NANOBODIES USED AS RESEARCH TOOL TO EXPLORE PROTEIN FUNCTION

Intracellular Nanobodies Interfering with Protein Function

Nanobodies represent a class of high-affinity inhibitors that, unlike RNAi, target proteins directly. They can be expressed in cells (intrabodies) with the purpose of knocking out (one or more) protein function(s), causing measurable effects (**Table 3**). The ultimate goal is to obtain better insight into otherwise poorly understood protein functions and signaling pathways. Moreover, this may represent a stepping stone toward rational drug development. For example, nanobodies were generated against β-catenin, a multi-functional protein, which has roles in cell–cell adhesion and transcriptional activation of Wnt responsive genes (31, 63). Mutations affecting the β-catenin/Wnt signaling pathway play a role in many diseases, including cancer. Newnham and coworkers developed a nanobody that specifically interfered with the transcriptional activating activity of β-catenin (63). This nanobody can enable further unraveling of the still intricate β-catenin/Wnt pathway. Analysis of the nanobody epitope could

TABLE 3 | Overview of the different nanobody-based applications to explore protein function.

	Application	Strategy	Specifics	Reference
Explore protein function	Intracellular nanobodies interfering with protein function			(21, 31, 63–68, 70)
	Customize existing nanobodies by engineering	Delocalization		(7, 64)
		Converting non-invasive to invasive nanobodies		(9)
		Targeted protein degradation	*DeGradFP*	(72)
			Protein interference *(Protein-i)*	(73)
			Affinity-directed protein missile	(74)
	Nanobodies in X-ray crystallography			(69, 71, 75–77)

Each application corresponds to the different sections in the main text and the strategies match the different paragraphs therein, which are whether or not further specified.

offer opportunities for development of small molecule inhibitors (63). Our lab obtained thoroughly characterized nanobodies against actin binding proteins cortactin, fascin, and L-plastin (64–67). We demonstrated their effects on actin bundling or branched actin polymerization, as well as their functional effects on podosome or invadopodia formation and dynamics, both specialized actin-rich membrane protrusions involved in (tumor) cell migration and invasion. In this way, we could sort out the precise contribution of specific protein domains in podosome or invadopodium formation and function (64–67). Our group also thoroughly characterized nanobodies against the DNA-binding domain of p53. We presented a nanobody that interferes with the transcriptional abilities of p53, while maintaining the functional architecture of p53 and even permitting p53 DNA-binding (68). Unlike other research tools, this nanobody allows targeting single functions of p53 with high precision (68). Nanobodies can also serve as elegant tools for the study and regulation of GPCR function. Different sets of nanobodies were developed against the model GPCR β_2-adrenergic receptor (β_2AR) (69–71). These nanobodies stabilize specific inactive or active conformations of the β_2AR and thus are conformationally sensitive. All nanobodies recognize intracellular allosteric epitopes and can be expressed as intrabodies, without losing their preference for a distinctive GPCR conformation (70). Inhibitory nanobodies can, however, also be exploited extracellularly. The aforementioned ChemR23 nanobodies uniquely recognize ChemR23 GPCR and antagonize chemerin-induced receptor activation. As chemerin also binds other GPCRs, the nanobodies can be used to discriminate ChemR23-specific signaling from other chemerin-induced pathways (21).

Customize Existing Nanobodies by Engineering

Existing (inhibitory and non-inhibitory) nanobodies can be engineered to expand their usefulness as a tool for investigating protein function (**Table 3**). Equipping nanobodies with an appropriate delocalization tag induces relocalization of the antigen–nanobody complex toward predetermined organelles and consequently, displaces the protein from where it is needed (7, 64). This can induce a loss-of-function, rather than a direct functional knockout. Correlating these findings with the use of untagged inhibitory nanobodies strengthens which protein functions are (not) important in particular pathways. For instance, we compared the effects of a fascin nanobody that disrupts fascin-mediated F-actin bundling on matrix metalloproteinase 9 (MMP-9) secretion, with its MOM-tagged counterpart (64). The latter nanobody is provided with a MOM delocalization tag and thus delocalizes endogenous fascin toward the outer mitochondrial membrane. Unlike untagged fascin nanobody, the MOM-fascin nanobody significantly reduced MMP-9 secretion, emphasizing a role for fascin in MMP-9 secretion independent of its actin-bundling activity (64).

Non-invasive intrabodies can also be engineered in such way that they can interfere with normal cell biology. As such, Jullien and colleagues transformed their H2A-H2B histon chromatibody into an invasive tool by coupling the nanobody to an E3 ubiquitin ligase (9). Expression of the fusion protein modifies the ubiquitin epigenetic landscape and dramatically distorts DNA double-strand break signaling and repair (9).

Our understanding of protein function has improved considerably by technologies that manipulate protein levels, such as RNAi or Morpholino antisense oligonucleotides. However, as these methods operate upstream of the protein level, they depend on the turnover rate of their target, thus resulting in limited depletion of long-lived proteins. Moreover, they frequently generate off-target effects (78, 79). To address these problems, systems directly acting on the protein level have been developed (80–82) and this is where also nanobodies can play a role.

Different research groups exploit the universal ubiquitin proteasome pathway in combination with high-affinity GFP nanobody for targeted protein degradation (72–74). To this end, they replaced the substrate recognition domain of cullin-RING E3 ubiquitin ligase (CRL) complexes with GFP nanobody (72, 73), or coupled a GFP nanobody to the recognition domain (74) (**Figure 4**). The CRL complexes are composed of a central cullin scaffold that interacts with an E2-recruiting RING protein *via* its C-terminal domain, and with a substrate adaptor protein *via* its N-terminus. The substrate adaptor protein mediates substrate specificity and recognizes its target directly (e.g., SPOP) or indirectly (e.g., SKP1 or Elongin B/C), the latter necessitating an additional adaptor protein (e.g., an F-box protein or VHL) for target binding. The CRL complexes ubiquitylate proteins and as such, mark them for degradation by the proteasome (83). In the deGradFP protocol, a GFP nanobody replaces the substrate recognition domain of an F-box protein, which in its turn recruits GFP-tagged proteins to the SKP1-cullin1 E3 ligase machinery (72). Conversely, the Protein interference (Protein-i) technique implies substituting the substrate recognition domain of adaptor SPOP with GFP nanobody. The GFP nanobody-SPOP fusion in its turn mediates GFP-fusion protein toward the cullin3 E3 ligase complex (73). Finally, the affinity-directed protein missile (AdPROM) approach fuses GFP nanobody with the C-terminal end of the VHL adaptor protein. This fusion protein mediates the association of GFP-tagged proteins with the Elongin B/C-cullin2 E3 complex for degradation. All techniques resulted in specific, fast ubiquitination and consequent proteasome-dependent degradation of GFP-fusion proteins in mammalian cells (72–74), *Drosophila* (72) and *Danio rerio* embryos (73). Compared to traditional RNAi, Protein-i even depleted proteins more rapidly and effectively. However, the Protein-i technique is currently limited to nuclear proteins, as the SPOP protein contains a nuclear localization signal (73). The deGradFP and AdPROM technologies can, however, be used for depletion of cytoplasmic proteins (72, 74). In summary, all three techniques hijack the same conserved pathway for targeted GFP-fusion protein degradation, but differ in range of action (nuclear and/or cytoplasmic) and GFP nanobody fusion (substitution of or fused with the substrate recognition domain). In theory, these techniques can be used for targeted degradation of virtually any (endogenous) protein, when replacing the GFP nanobody with a nanobody of choice.

Tang and coworkers developed a conditional system in which the stability of a nanobody depends upon the expression of its

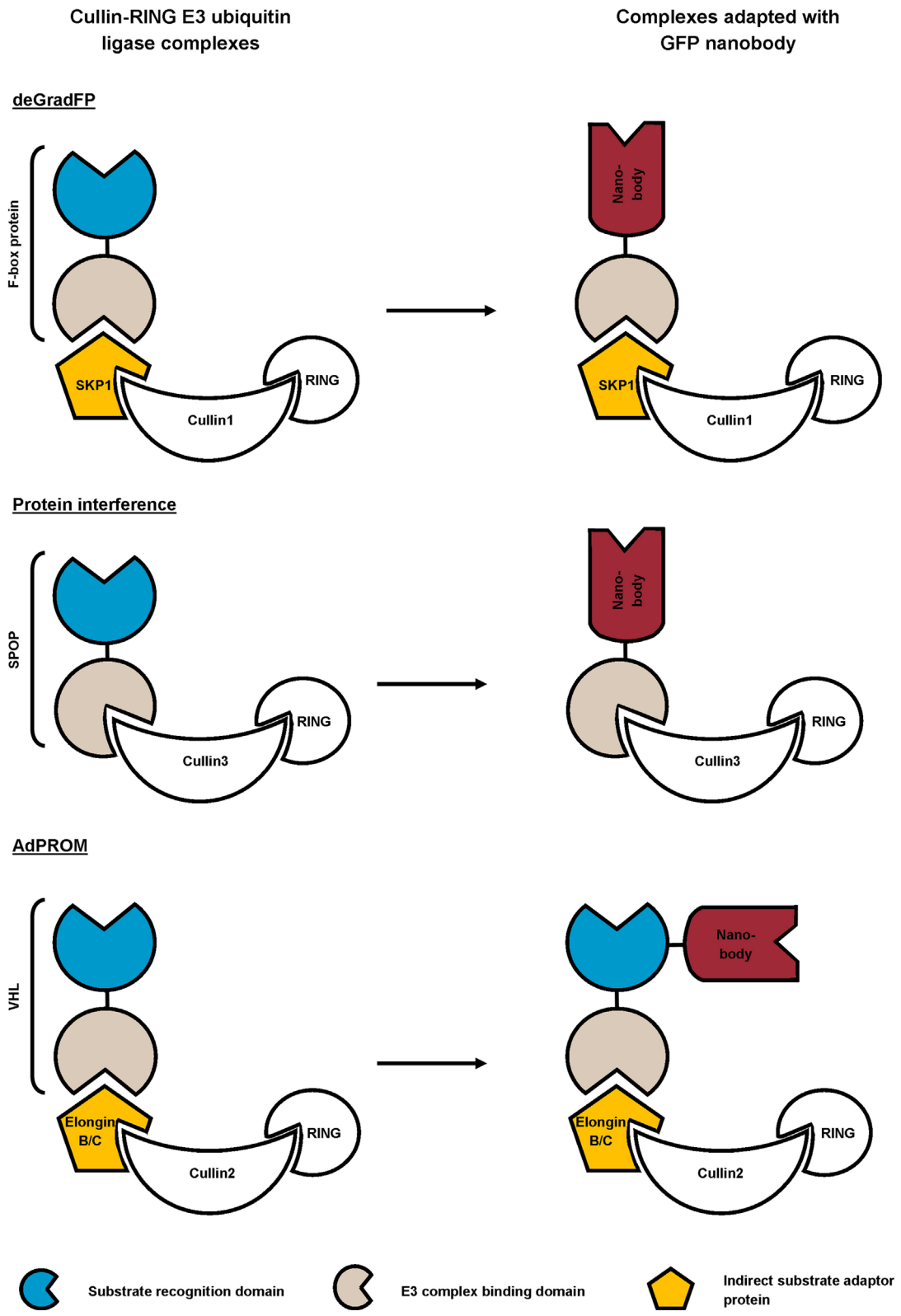

FIGURE 4 | Schematic representation of reported strategies that combine the ubiquitin proteasome pathway with GFP nanobody for targeted degradation of GFP-fusion protein. In the deGradFP and Protein interference approach, the substrate recognition domain of the cullin-RING E3 ubiquitin ligase (CRL) complex is replaced by a high-affinity GFP nanobody. The affinity-directed protein missile (AdPROM) technique on the other hand, implies fusing the GFP nanobody with the substrate recognition domain of the complex.

target (84). Therefore, they introduced destabilizing mutations in the nanobody FR, which could be transferred across different nanobodies (e.g., GFP, HIV-1 capsid protein CA, *Escherichia coli* dehydrofolate reductase nanobody, etc.) and even across nanobodies from different camelid species. Presence of the cognate antigen confers nanobody stability, whereas antigen absence results in proteasomal degradation of the nanobody and its associated tags. As such, it is possible to endow antigen-expressing subsets of cells with particular features. Tang and colleagues for instance exclusively labeled ACH-2 HIV-1 positive T-cells for flow cytometry (84). Therefore, they utilized destabilized chromobodies recognizing the HIV-1 capsid protein CA. Lack of CA expression in uninfected cells causes degradation of the destabilized chromobodies, consequently resulting in disappearance of fluorescence. Coupling a destabilized nanobody to Cas9 even allowed genome editing selectively in antigen-expressing cells using CRISPR/Cas (84). In theory, this technique can be combined with the aforementioned inhibitory nanobodies or with the deGradFP/Protein-i/AdPROM methods to interfere with protein function or target proteins for proteasomal degradation respectively, exclusively in cells expressing specific intracellular epitopes.

Nanobodies in X-Ray Crystallography

Nanobodies also feature as a molecular lens in x-ray crystallography and thus can reveal molecular mechanisms or identify functionally important regions in a protein (**Table 3**). For instance, the crystal structure of a nanobody in complex with the serine protease urokinase-type plasminogen activator revealed valuable information on the mechanism by which peptide segments may act as strong protease inhibitors. The nanobody inserts its CDR3 loop into the active site of the protease in a substrate-like manner and becomes slowly cleaved. However, a rigid intra-loop interaction network which interconnects the putative scissile bond P1–P1′, holds the leaving group in place and favors reformation of the peptide bond over cleavage. The reaction reaches a cleavage-resynthesis equilibrium, thus rendering the nanobody into a strong inhibitor. Conversely, mutating specific amino acids in the CDR3 loop converts the nanobody to a strong substrate. These findings demonstrate the importance of the conformational rigidity of active-site binding peptide segments, when exploited as new protease inhibitors (75). On the other hand, Rudolph and colleagues reported the X-ray crystal structure of five nanobodies in complex with ricin toxin's enzymatic subunit (RTA) (76, 77). The nanobodies all showed different ricin-neutralizing potencies (76, 77, 85). They identified RTA neutralizing hotspots which may prove useful in subunit vaccine development, seeing the low efficiency of current vaccination strategies (76, 77). Finally, when bound to their target, nanobodies can stabilize specific protein conformation and thus serve as chaperones in crystallography. The aforementioned β_2AR nanobodies, binding different conformations of the GPCR, showed to be excellent chaperones in X-ray crystallography (69, 71) and NMR structural research (86), revealing the full allosteric potential of the β_2AR.

CONCLUSION AND PERSPECTIVES

We have provided a brief overview of the various opportunities nanobodies offer in fundamental research, generally subdivided into the categories microscopy, protein–protein interactions, and protein function and we focused on how state-of-the-art engineering techniques can expand their versatility. Nanobodies feature small, stabe (intracellularly), and soluble high-affinity targeting moieties that can easily be produced. Moreover, it is possible to engineer nanobodies in such a way that they display a desired function or set of functions (e.g., fluorescence, delocalization, degradation, etc.), without interfering with its binding characteristics. Hence, they are highly adaptable. These favorable characteristics stimulated their use as research tools in diverse aspects of fundamental research. Undoubtedly, in future years, new applications will continue to surface.

AUTHOR CONTRIBUTIONS

EB and JG wrote the manuscript. All authors reviewed the manuscript.

FUNDING

This research was supported by grants from Research Foundation Flanders (Fonds Wetenschappelijk Onderzoek (FWO) Vlaanderen), Ghent University (BOF13/GOA/010), and Interuniversity Attraction Poles Programme of the Belgian State, Federal Office for Scientific, Technical and Cultural Affairs (IUAP P7/13). EB is supported by a BOF fellowship from Ghent University.

REFERENCES

1. Hamers-Casterman C, Atarhouch T, Muyldermans S, Robinson G, Hamers C, Songa EB, et al. Naturally occurring antibodies devoid of light chains. *Nature* (1993) 363(6428):446–8. doi:10.1038/363446a0
2. Muyldermans S. Nanobodies: natural single-domain antibodies. In: Kornberg RD, editor. *Annual Review of Biochemistry*. (Vol. 82), Palo Alto: Annual Reviews (2013). p. 775–97.
3. Ghahroudi MA, Desmyter A, Wyns L, Hamers R, Muyldermans S. Selection and identification of single domain antibody fragments from camel heavy-chain antibodies. *FEBS Lett* (1997) 414(3):521–6. doi:10.1016/s0014-5793(97)01062-4
4. Muyldermans S. Single domain camel antibodies: current status. *J Biotechnol* (2001) 74(4):277–302. doi:10.1016/S1389-0352(01)00021-6
5. Van den Abbeele A, De Clercq S, De Ganck A, De Corte V, Van Loo B, Soror SH, et al. A llama-derived gelsolin single-domain antibody blocks gelsolin-G-actin interaction. *Cell Mol Life Sci* (2010) 67(9):1519–35. doi:10.1007/s00018-010-0266-1
6. Van Audenhove I, Van Impe K, Ruano-Gallego D, De Clercq S, De Muynck K, Vanloo B, et al. Mapping cytoskeletal protein function in cells by means of nanobodies. *Cytoskeleton (Hoboken)* (2013) 70(10):604–22. doi:10.1002/cm.21122
7. Beghein E, Van Audenhove I, Zwaenepoel O, Verhelle A, De Ganck A, Gettemans J. A new survivin tracer tracks, delocalizes and captures endogenous

survivin at different subcellular locations and in distinct organelles. *Sci Rep* (2016) 6:31177. doi:10.1038/srep31177
8. Maier J, Traenkle B, Rothbauer U. Real-time analysis of epithelial-mesenchmal transition using fluorescent single-domain antibodies. *Sci Rep* (2015) 5:13402. doi:10.1038/srep13402
9. Jullien D, Vignard J, Fedor Y, Bery N, Olichon A, Crozatier M, et al. Chromatibody, a novel non-invasive molecular tool to explore and manipulate chromatin in living cells. *J Cell Sci* (2016) 129(13):2673–83. doi:10.1242/jcs.183103
10. De Genst E, Silence K, Decanniere K, Conrath K, Loris R, Kinne R, et al. Molecular basis for the preferential cleft recognition by dromedary heavy-chain antibodies. *Proc Natl Acad Sci U S A* (2006) 103(12):4586–91. doi:10.1073/pnas.0505379103
11. Desmyter A, Transue TR, Ghahroudi MA, Thi MH, Poortmans F, Hamers R, et al. Crystal structure of a camel single-domain V-H antibody fragment in complex with lysozyme. *Nat Struct Biol* (1996) 3(9):803–11. doi:10.1038/nsb0996-803
12. Delanote V, Vanloo B, Catillon M, Friederich E, Vandekerckhove J, Gettemans J. An alpaca single-domain antibody blocks filopodia formation by obstructing L-plastin-mediated F-actin bundling. *FASEB J* (2010) 24(1): 105–18. doi:10.1096/fj.09-134304
13. Braun MB, Traenkle B, Koch PA, Emele F, Weiss F, Poetz O, et al. Peptides in headlock – a novel high-affinity and versatile peptide-binding nanobody for proteomics and microscopy. *Sci Rep* (2016) 6:19211. doi:10.1038/srep19211
14. De Genst EJ, Guilliams T, Wellens J, O'Day EM, Waudby CA, Meehan S, et al. Structure and properties of a complex of alpha-synuclein and a single-domain camelid antibody. *J Mol Biol* (2010) 402(2):326–43. doi:10.1016/j.jmb.2010.07.001
15. Thueng-in K, Thanongsaksrikul J, Srimanote P, Bangphoomi K, Poungpair O, Maneewatch S, et al. Cell penetrable humanized-VH/VHH that inhibit RNA dependent RNA polymerase (NS5B) of HCV. *PLoS One* (2012) 7(11):e49254. doi:10.1371/journal.pone.0049254
16. Van Impe K, Bethuyne J, Cool S, Impens F, Ruano-Gallego D, De Wever O, et al. A nanobody targeting the F-actin capping protein CapG restrains breast cancer metastasis. *Breast Cancer Res* (2013) 15(6):R116. doi:10.1186/bcr3585
17. Blanco-Toribio A, Muyldermans S, Frankel G, Fernandez LA. Direct injection of functional single-domain antibodies from *E. coli* into human cells. *PLoS One* (2010) 5(12):e15227. doi:10.1371/journal.pone.0015227
18. Van Audenhove I, Gettemans J. Nanobodies as versatile tools to understand, diagnose, visualize and treat cancer. *EBioMedicine* (2016) 8:40–8. doi:10.1016/j.ebiom.2016.04.028
19. Steeland S, Vandenbroucke RE, Libert C. Nanobodies as therapeutics: big opportunities for small antibodies. *Drug Discov Today* (2016) 21(7):1076–113. doi:10.1016/j.drudis.2016.04.003
20. de Bruin RC, Lougheed SM, van der Kruk L, Stam AG, Hooijberg E, Roovers RC, et al. Highly specific and potently activating V gamma 9V delta 2-T cell specific nanobodies for diagnostic and therapeutic applications. *Clin Immunol* (2016) 169:128–38. doi:10.1016/j.clim.2016.06.012
21. Peyrassol X, Laeremans T, Gouwy M, Lahura V, Debulpaep M, Van Damme J, et al. Development by genetic immunization of monovalent antibodies (nanobodies) behaving as antagonists of the human ChemR23 receptor. *J Immunol* (2016) 196(6):2893–901. doi:10.4049/jimmunol.1500888
22. Ries J, Kaplan C, Platonova E, Eghlidi H, Ewers H. A simple, versatile method for GFP-based super-resolution microscopy via nanobodies. *Nat Methods* (2012) 9(6):582–4. doi:10.1038/nmeth.1991
23. Chamma I, Letellier M, Butler C, Tessier B, Lim KH, Gauthereau I, et al. Mapping the dynamics and nanoscale organization of synaptic adhesion proteins using monomeric streptavidin. *Nat Commun* (2016) 7:10773. doi:10.1038/ncomms10773
24. Platonova E, Winterflood CM, Junemann A, Albrecht D, Faix J, Ewers H. Single-molecule microscopy of molecules tagged with GFP or RFP derivatives in mammalian cells using nanobody binders. *Methods* (2015) 88:89–97. doi:10.1016/j.ymeth.2015.06.018
25. Szymborska A, de Marco A, Daigle N, Cordes VC, Briggs JA, Ellenberg J. Nuclear pore scaffold structure analyzed by super-resolution microscopy and particle averaging. *Science* (2013) 341(6146):655–8. doi:10.1126/science.1240672
26. Mikhaylova M, Cloin BM, Finan K, van den Berg R, Teeuw J, Kijanka MM, et al. Resolving bundled microtubules using anti-tubulin nanobodies. *Nat Commun* (2015) 6:7933. doi:10.1038/ncomms8933
27. Pleiner T, Bates M, Trakhanov S, Lee CT, Schliep JE, Chug H, et al. Nanobodies: site-specific labeling for super-resolution imaging, rapid epitope-mapping and native protein complex isolation. *Elife* (2015) 4:e11349. doi:10.7554/eLife.11349
28. Massa S, Xavier C, De Vos J, Caveliers V, Lahoutte T, Muyldermans S, et al. Site-specific labeling of cysteine-tagged camelid single-domain antibody-fragments for use in molecular imaging. *Bioconjug Chem* (2014) 25(5):979–88. doi:10.1021/bc500111t
29. Massa S, Vikani N, Betti C, Ballet S, Vanderhaegen S, Steyaert J, et al. Sortase A-mediated site-specific labeling of camelid single-domain antibody-fragments: a versatile strategy for multiple molecular imaging modalities. *Contrast Media Mol Imaging* (2016) 11(5):328–39. doi:10.1002/cmmi.1696
30. Antonatou E, Hoogewijs K, Kalaitzakis D, Baudot A, Vassilikogiannakis G, Madder A. Singlet oxygen-induced furan oxidation for site-specific and chemoselective peptide ligation. *Chemistry* (2016) 22(25):8457–61. doi:10.1002/chem.201601113
31. Traenkle B, Emele F, Anton R, Poetz O, Haeussler RS, Maier J, et al. Monitoring interactions and dynamics of endogenous beta-catenin with intracellular nanobodies in living cells. *Mol Cell Proteomics* (2015) 14(3):707–23. doi:10.1074/mcp.M114.044016
32. Van Overbeke W, Verhelle A, Everaert I, Zwaenepoel O, Vandekerckhove J, Cuvelier C, et al. Chaperone nanobodies protect gelsolin against MT1-MMP degradation and alleviate amyloid burden in the gelsolin amyloidosis mouse model. *Mol Ther* (2014) 22(10):1768–78. doi:10.1038/mt.2014.132
33. Panza P, Maier J, Schmees C, Rothbauer U, Sollner C. Live imaging of endogenous protein dynamics in zebrafish using chromobodies. *Development* (2015) 142(10):1879–84. doi:10.1242/dev.118943
34. Huang B, Babcock H, Zhuang XW. Breaking the diffraction barrier: super-resolution imaging of cells. *Cell* (2010) 143(7):1047–58. doi:10.1016/j.cell.2010.12.002
35. Huang B, Bates M, Zhuang X. Super-resolution fluorescence microscopy. *Annu Rev Biochem* (2009) 78:993–1016. doi:10.1146/annurev.biochem.77.061906.092014
36. Deschout H, Zanacchi FC, Mlodzianoski M, Diaspro A, Bewersdorf J, Hess ST, et al. Precisely and accurately localizing single emitters in fluorescence microscopy. *Nat Methods* (2014) 11(3):253–66. doi:10.1038/nmeth.2843
37. Bates M, Huang B, Dempsey GT, Zhuang X. Multicolor super-resolution imaging with photo-switchable fluorescent probes. *Science* (2007) 317(5845): 1749–53. doi:10.1126/science.1146598
38. Guignet EG, Hovius R, Vogel H. Reversible site-selective labeling of membrane proteins in live cells. *Nat Biotechnol* (2004) 22(4):440–4. doi:10.1038/nbt954
39. Popp MW, Antos JM, Grotenbreg GM, Spooner E, Ploegh HL. Sortagging: a versatile method for protein labeling. *Nat Chem Biol* (2007) 3(11):707–8. doi:10.1038/nchembio.2007.31
40. Huang B, Wang W, Bates M, Zhuang X. Three-dimensional super-resolution imaging by stochastic optical reconstruction microscopy. *Science* (2008) 319(5864):810–3. doi:10.1126/science.1153529
41. Rothbauer U, Zolghadr K, Tillib S, Nowak D, Schermelleh L, Gahl A, et al. Targeting and tracing antigens in live cells with fluorescent nanobodies. *Nat Methods* (2006) 3(11):887–9. doi:10.1038/nmeth953
42. Herce HD, Deng W, Helma J, Leonhardt H, Cardoso MC. Visualization and targeted disruption of protein interactions in living cells. *Nat Commun* (2013) 4:2660. doi:10.1038/ncomms3660
43. Van Criekinge W, Beyaert R. Yeast two-hybrid: state of the art. *Biol Proced Online* (1999) 2:1–38. doi:10.1251/bpo16
44. Künzl F, Fruholz S, Fassler F, Li BB, Pimpl P. Receptor-mediated sorting of soluble vacuolar proteins ends at the trans-Golgi network/early endosome. *Nat Plants* (2016) 2(4):16017. doi:10.1038/nplants.2016.17
45. Drees C, Raj AN, Kurre R, Busch KB, Haase M, Piehler J. Engineered upconversion nanoparticles for resolving protein interactions inside living cells. *Angew Chem Int Ed Engl* (2016) 55(38):11668–72. doi:10.1002/anie.201603028

46. Shi Y, Pellarin R, Fridy PC, Fernandez-Martinez J, Thompson MK, Li YY, et al. A strategy for dissecting the architectures of native macromolecular assemblies. *Nat Methods* (2015) 12(12):1135–8. doi:10.1038/nmeth.3617
47. Eyckerman S, Titeca K, Van Quickelberghe E, Cloots E, Verhee A, Samyn N, et al. Trapping mammalian protein complexes in viral particles. *Nat Commun* (2016) 7:11416. doi:10.1038/ncomms11416
48. Roux KJ, Kim DI, Raida M, Burke B. A promiscuous biotin ligase fusion protein identifies proximal and interacting proteins in mammalian cells. *J Cell Biol* (2012) 196(6):801–10. doi:10.1083/jcb.201112098
49. Lee JJ, Park YS, Lee KJ. Hydrogen-deuterium exchange mass spectrometry for determining protein structural changes in drug discovery. *Arch Pharm Res* (2015) 38(10):1737–45. doi:10.1007/s12272-015-0584-9
50. Malito E, Faleri A, Lo Surdo P, Veggi D, Maruggi G, Grassi E, et al. Defining a protective epitope on factor H binding protein, a key meningococcal virulence factor and vaccine antigen. *Proc Natl Acad Sci U S A* (2013) 110(9):3304–9. doi:10.1073/pnas.1222845110
51. Yan YT, Wei H, Fu Y, Jusuf S, Zeng M, Ludwig R, et al. Isomerization and oxidation in the complementarity-determining regions of a monoclonal antibody: a study of the modification-structure-function correlations by hydrogen-deuterium exchange mass spectrometry. *Anal Chem* (2016) 88(4): 2041–50. doi:10.1021/acs.analchem.5b02800
52. Jensen PF, Larraillet V, Schlothauer T, Kettenberger H, Hilger M, Rand KD. Investigating the interaction between the neonatal Fc receptor and monoclonal antibody variants by hydrogen/deuterium exchange mass spectrometry. *Mol Cell Proteomics* (2015) 14(1):148–61. doi:10.1074/mcp.M114.042044
53. Smits AH, Vermeulen M. Characterizing protein-protein interactions using mass spectrometry: challenges and opportunities. *Trends Biotechnol* (2016) 34(10):825–34. doi:10.1016/j.tibtech.2016.02.014
54. Otera H, Fujiki Y. Pex5p imports folded tetrameric catalase by interaction with Pex13p. *Traffic* (2012) 13(10):1364–77. doi:10.1111/j.1600-0854.2012.01391.x
55. McNew JA, Goodman JM. An oligomeric protein is imported into peroxisomes in-vivo. *J Cell Biol* (1994) 127(5):1245–57. doi:10.1083/jcb.127.5.1245
56. Glover JR, Andrews DW, Rachubinski RA. *Saccharomyces cerevisiae* peroxisomal thiolase is imported as a dimer. *Proc Natl Acad Sci U S A* (1994) 91(22):10541–5. doi:10.1073/pnas.91.22.10541
57. Yang XD, Purdue PE, Lazarow PB. Eci1p uses a PTS1 to enter peroxisomes: either its own or that of a partner, Dci1p. *Eur J Cell Biol* (2001) 80(2):126–38. doi:10.1078/0171-9335-00144
58. Islinger M, Li KW, Seitz J, Volkl A, Luers GH. Hitchhiking of Cu/Zn superoxide dismutase to peroxisomes – evidence for a natural piggyback import mechanism in mammals. *Traffic* (2009) 10(11):1711–21. doi:10.1111/j.1600-0854.2009.00966.x
59. Freitas MO, Francisco T, Rodrigues TA, Lismont C, Domingues P, Pinto MP, et al. The peroxisomal protein import machinery displays a preference for monomeric substrates. *Open Biol* (2015) 5(4):140236. doi:10.1098/rsob.140236
60. Yates JR, Gilchrist A, Howell KE, Bergeron JJ. Proteomics of organelles and large cellular structures. *Nat Rev Mol Cell Biol* (2005) 6(9):702–14. doi:10.1038/nrm1711
61. Wiese S, Gronemeyer T, Ofman R, Kunze M, Grou CP, Almeida JA, et al. Proteomics characterization of mouse kidney peroxisomes by tandem mass spectrometry and protein correlation profiling. *Mol Cell Proteomics* (2007) 6(12):2045–57. doi:10.1074/mcp.M700169-MCP200
62. Kikuchi M, Hatano N, Yokota S, Shimozawa N, Imanaka T, Taniguchi H. Proteomic analysis of rat liver peroxisome – presence of peroxisome-specific isozyme of Lon protease. *J Biol Chem* (2004) 279(1):421–8. doi:10.1074/jbc.M305623200
63. Newnham LE, Wright MJ, Holdsworth G, Kostarelos K, Robinson MK, Rabbitts TH, et al. Functional inhibition of β-catenin-mediated Wnt signaling by intracellular VHH antibodies. *MAbs* (2015) 7(1):180–91. doi:10.4161/19420862.2015.989023
64. Van Audenhove I, Boucherie C, Pieters L, Zwaenepoel O, Vanloo B, Martens E, et al. Stratifying fascin and cortactin function in invadopodium formation using inhibitory nanobodies and targeted subcellular delocalization. *FASEB J* (2014) 28(4):1805–18. doi:10.1096/fj.13-242537
65. Van Audenhove I, Debeuf N, Boucherie C, Gettemans J. Fascin actin bundling controls podosome turnover and disassembly while cortactin is involved in podosome assembly by its SH3 domain in THP-1 macrophages and dendritic cells. *Biochim Biophys Acta* (2015) 1853(5):940–52. doi:10.1016/j.bbamcr.2015.01.003
66. Van Audenhove I, Denert M, Boucherie C, Pieters L, Cornelissen M, Gettemans J. Fascin rigidity and L-plastin flexibility cooperate in cancer cell invadopodia and filopodia. *J Biol Chem* (2016) 291(17):9148–60. doi:10.1074/jbc.M115.706937
67. Bertier L, Boucherie C, Zwaenepoel O, Vanloo B, Van Troys M, Van Audenhove I, et al. Inhibitory cortactin nanobodies delineate the role of NTA- and SH3-domain-specific functions during invadopodium formation and cancer cell invasion. *FASEB J* (2017) 31(6):2460–76. doi:10.1096/fj.201600810RR
68. Bethuyne J, De Gieter S, Zwaenepoel O, Garcia-Pino A, Durinck K, Verhelle A, et al. A nanobody modulates the p53 transcriptional program without perturbing its functional architecture. *Nucleic Acids Res* (2014) 42(20):12928–38. doi:10.1093/nar/gku962
69. Rasmussen SG, Choi HJ, Fung JJ, Pardon E, Casarosa P, Chae PS, et al. Structure of a nanobody-stabilized active state of the β(2) adrenoceptor. *Nature* (2011) 469(7329):175–80. doi:10.1038/nature09648
70. Staus DP, Wingler LM, Strachan RT, Rasmussen SGF, Pardon E, Ahn S, et al. Regulation of β(2)-adrenergic receptor function by conformationally selective single-domain intrabodies. *Mol Pharmacol* (2014) 85(3):472–81. doi:10.1124/mol.113.089516
71. Staus DP, Strachan RT, Manglik A, Pani B, Kahsai AW, Kim TH, et al. Allosteric nanobodies reveal the dynamic range and diverse mechanisms of G-protein-coupled receptor activation. *Nature* (2016) 535(7612):448–52. doi:10.1038/nature18636
72. Caussinus E, Kanca O, Affolter M. Fluorescent fusion protein knockout mediated by anti-GFP nanobody. *Nat Struct Mol Biol* (2012) 19(1):117–21. doi:10.1038/nsmb.2180
73. Shin YJ, Park SK, Jung YJ, Kim YN, Kim KS, Park OK, et al. Nanobody-targeted E3-ubiquitin ligase complex degrades nuclear proteins. *Sci Rep* (2015) 5:14269. doi:10.1038/srep14269
74. Fulcher LJ, Macartney T, Bozatzi P, Hornberger A, Rojas-Fernandez A, Sapkota GP. An affinity-directed protein missile system for targeted proteolysis. *Open Biol* (2016) 6(10). doi:10.1098/rsob.160255
75. Kromann-Hansen T, Oldenburg E, Yung KW, Ghassabeh GH, Muyldermans S, Declerck PJ, et al. A camelid-derived antibody fragment targeting the active site of a serine protease balances between inhibitor and substrate behavior. *J Biol Chem* (2016) 291(29):15156–68. doi:10.1074/jbc.M116.732503
76. Rudolph MJ, Vance DJ, Cassidy MS, Rong YH, Shoemaker CB, Mantis NJ. Structural analysis of nested neutralizing and non-neutralizing B cell epitopes on ricin toxin's enzymatic subunit. *Proteins* (2016) 84(8):1162–72. doi:10.1002/prot.25062
77. Rudolph MJ, Vance DJ, Cassidy MS, Rong YH, Mantis NJ. Structural analysis of single domain antibodies bound to a second neutralizing hot spot on ricin toxin's enzymatic subunit. *J Biol Chem* (2017) 292(3):872–83. doi:10.1074/jbc.M116.758102
78. Jackson AL, Linsley PS. Recognizing and avoiding siRNA off-target effects for target identification and therapeutic application. *Nat Rev Drug Discov* (2010) 9(1):57–67. doi:10.1038/nrd3010
79. Kok FO, Shin M, Ni CW, Gupta A, Grosse AS, van Impel A, et al. Reverse genetic screening reveals poor correlation between morpholino-induced and mutant phenotypes in zebrafish. *Dev Cell* (2015) 32(1):97–108. doi:10.1016/j.devcel.2014.11.018
80. Renicke C, Schuster D, Usherenko S, Essen LO, Taxis C. A LOV2 domain-based optogenetic tool to control protein degradation and cellular function. *Chem Biol* (2013) 20(4):619–26. doi:10.1016/j.chembiol.2013.03.005
81. Holland AJ, Fachinetti D, Han JS, Cleveland DW. Inducible, reversible system for the rapid and complete degradation of proteins in mammalian cells. *Proc Natl Acad Sci U S A* (2012) 109(49):E3350–7. doi:10.1073/pnas.1216880109
82. Harder B, Schomburg A, Pflanz R, Kustner KM, Gerlach N, Schuh R. TEV protease-mediated cleavage in *Drosophila* as a tool to analyze protein functions in living organisms. *Biotechniques* (2008) 44(6):765–72. doi:10.2144/000112884

83. Errington WJ, Khan MQ, Bueler SA, Rubinstein JL, Chakrabartty A, Prive GG. Adaptor protein self-assembly drives the control of a cullin-RING ubiquitin ligase. *Structure* (2012) 20(7):1141–53. doi:10.1016/j.str.2012.04.009
84. Tang JC, Drokhlyansky E, Etemad B, Rudolph S, Guo B, Wang S, et al. Detection and manipulation of live antigen-expressing cells using conditionally stable nanobodies. *Elife* (2016) 5. doi:10.7554/eLife.15312
85. Vance DJ, Tremblay JM, Mantis NJ, Shoemaker CB. Stepwise engineering of heterodimeric single domain camelid VHH antibodies that passively protect mice from ricin toxin. *J Biol Chem* (2013) 288(51):36538–47. doi:10.1074/jbc.M113.519207
86. Isogai S, Deupi X, Opitz C, Heydenreich FM, Tsai CJ, Rueckner FB, et al. Backbone NMR reveals allosteric signal transduction networks in the β(1)-adrenergic receptor. *Nature* (2016) 530(7589):237–41. doi:10.1038/nature16577

Conflict of Interest Statement: The authors declare that the research was conducted in the absence of any commercial or financial relationships that could be construed as a potential conflict of interest.

The reviewer, GH, and handling editor declared their shared affiliation, and the handling editor states that the process nevertheless met the standards of a fair and objective review.

frontiers in Immunology

MINI REVIEW
published: 24 August 2017
doi: 10.3389/fimmu.2017.01030

Under the Microscope: Single-Domain Antibodies for Live-Cell Imaging and Super-Resolution Microscopy

*Bjoern Traenkle[1] and Ulrich Rothbauer[1,2]**

[1] Pharmaceutical Biotechnology, Eberhard Karls University Tuebingen, Tuebingen, Germany, [2] Natural and Medical Sciences Institute at the University of Tuebingen, Reutlingen, Germany

Single-domain antibodies (sdAbs) have substantially expanded the possibilities of advanced cellular imaging such as live-cell or super-resolution microscopy to visualize cellular antigens and their dynamics. In addition to their unique properties including small size, high stability, and solubility in many environments, sdAbs can be efficiently functionalized according to the needs of the respective imaging approach. Genetically encoded intrabodies fused to fluorescent proteins (chromobodies) have become versatile tools to study dynamics of endogenous proteins in living cells. Additionally, sdAbs conjugated to organic dyes were shown to label cellular structures with high density and minimal fluorophore displacement making them highly attractive probes for super-resolution microscopy. Here, we review recent advances of the chromobody technology to visualize localization and dynamics of cellular targets and the application of chromobody-based cell models for compound screening. Acknowledging the emerging importance of super-resolution microscopy in cell biology, we further discuss advantages and challenges of sdAbs for this technology.

Keywords: nanobodies, intrabodies, chromobodies, cytoskeleton, live-cell imaging, high-content imaging, super-resolution microscopy

OPEN ACCESS

Edited by:
Kevin A. Henry, National Research Council Canada, Canada

Reviewed by:
Etienne Weiss, Ecole Supérieure de Biotechnologie de Strasbourg, France
Paul Van Bergen En Henegouwen, Utrecht University, Netherlands

***Correspondence:**
Ulrich Rothbauer
ulrich.rothbauer@uni-tuebingen.de

Specialty section:
This article was submitted to Vaccines and Molecular Therapeutics, a section of the journal Frontiers in Immunology

Received: *19 June 2017*
Accepted: *09 August 2017*
Published: *24 August 2017*

Citation:
Traenkle B and Rothbauer U (2017) Under the Microscope: Single-Domain Antibodies for Live-Cell Imaging and Super-Resolution Microscopy. Front. Immunol. 8:1030. doi: 10.3389/fimmu.2017.01030

Reflecting the importance of cellular imaging, microscopic technologies ranging from wide-field to super-resolution microscopy are applied in nearly every cell-biological laboratory. Along with recent developments such as high-content live-cell imaging or super-resolution microscopy, there is a concomitant need for advanced labeling strategies to visualize cellular components in physiologically meaningful states. Here, we review recent progress in the development of camelid-derived single-domain antibodies (sdAbs) for live-cell imaging and super-resolution microscopy.

sdAbs FOR LIVE-CELL IMAGING

Antigen staining with conventional antibodies is still the most popular approach to image native cellular antigens, but due to chemical fixation of the cells it is not suitable to monitor dynamic processes. For visualization in living cells, proteins can be fused either to self-labeling enzymes (SNAP-, Halo-, or CLIP-tag) or fluorescent proteins (FP) (1–5). However, addition of such large protein tags (~20–25 kDa) to the N- or the C-terminus may affect the expression level, activity, and localization, and for some targets, it was shown that expression of the corresponding fusion protein affects cellular morphology or function (6–8). To avoid genetic modification, intracellularly

functional binding molecules (intrabodies) have been developed to visualize endogenous targets. While some intrabodies are based on non-antibody scaffolds like peptides, monobodies, or designed ankyrin repeat proteins (9–12), most intrabodies are derived from immunoglobulins (IgGs) comprising a variable heavy (VH) and variable light domain, artificially linked to form a single-chain variable fragment (scFv) (13–15). Due to their compact structure, small size, high stability, and solubility, sdAb fragments (V_HHs, nanobodies) from camelids (16) provide beneficial properties for intracellular applications (11, 17). However, only nanobodies which retain a binding-compatible conformation in the absence of the conserved disulfide bond connecting frameworks 1 and 3 are functionally expressed in live cells, as disulfide bridges are not formed in the reducing environment of the cytoplasm. Such binders have to be selected experimentally, whereas nanobodies comprising additional disulfide bonds, e.g., to stabilize complementarity-determining regions forming the paratope can be excluded *a priori* based on their DNA sequence. Nowadays, numerous protocols and synthetic libraries are available which facilitate the selection of intracellular nanobodies (18–24). For visualization of endogenous antigens, nanobodies were genetically fused to fluorescent proteins and introduced as DNA-encoded expression constructs in living cells. Reflecting their chimeric structure these constructs were termed "chromobodies" (25) (**Figures 1A,B**).

In an initial study, a red fluorescent chromobody directed against GFP was generated. Fluorescence co-localization analysis of living cells expressing the GFP-chromobody in combination with different GFP-labeled marker proteins (components of the cytoskeleton, nuclear lamina, or chromatin) revealed a high overlap of the fluorescence intensities of antigen and chromobody. Besides functional expression in the cytoplasm, the GFP chromobody was shown to enter the nucleus, where it traces dynamic changes of cellular antigens (e.g., H2B-GFP) throughout different stages of the cell cycle (25). Since its first description, the GFP-chromobody has been widely used for multiple functional and imaging applications ranging from targeted relocalization (26–28), induced proteasomal degradation (29, 30), to high-throughput translocation assays (31) of GFP-tagged proteins. While the GFP-chromobody became a unique tool to study GFP-tagged proteins in many facets, numerous chromobodies directed against native proteins have been generated during the last decade.

CHROMOBODIES TO VISUALIZE THE CYTOSKELETON

Chromobodies that visualize, but do not disturb the cytoskeleton network, are highly desirable for live-cell imaging as many of the cytoskeletal proteins become only partially integrated into native structures when administered as FP fusions (7, 32–34). To date, numerous chromobodies targeting proteins involved in the formation of the nuclear lamina, actin, and intermediate filaments have been described. A lamin-chromobody was identified and stably introduced in human cell lines (**Figure 1C**) (35). Fluorescent recovery after photobleaching (FRAP) analysis showed that the lamin-chromobody binds very transiently, which does not interfere with the functional redistribution of the nuclear lamina (25). Live-cell imaging of the chromobody signal

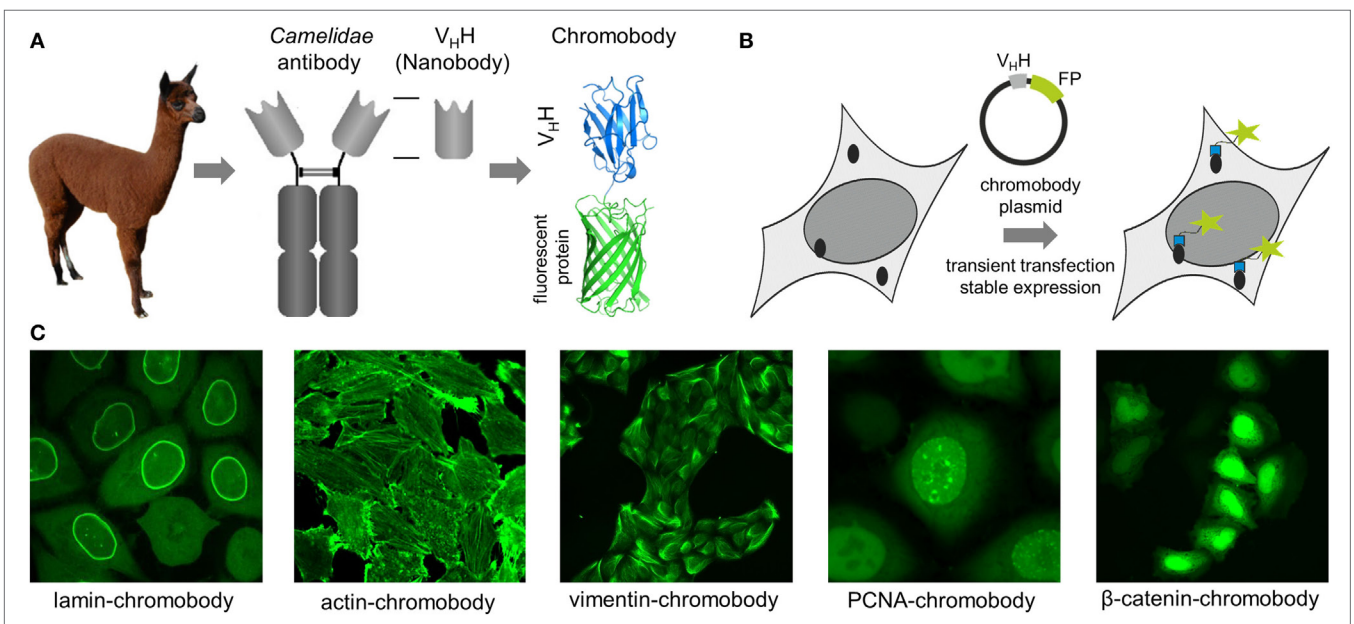

FIGURE 1 | **(A)** Schematic representation of a chromobody derived from a single-domain antibody of *Camelidae*. **(B)** Illustration of intracellular antigen binding of chromobodies followed by introduction and expression of DNA-encoded chromobody expression constructs. **(C)** Representative images of endogenous cellular structures visualized by recently developed chromobodies directed against lamin A, ACTB, vimentin, proliferating cellular antigen (PCNA), and β-catenin in living cells.

revealed the typical nuclear rim structure and monitors its disintegration during mitosis or upon compound-mediated induction of apoptosis (36). For *in vivo* labeling of the actin cytoskeleton, an actin-chromobody with a similar highly transient binding mode was generated (**Figure 1C**) (37). Originally selected against mammalian ACTB, it also recognizes F-actin in parasites, zebrafish, or plant cells (37–40). Not disturbing actin dynamics by steric hindrances or stabilizing effects, the actin-chromobody provides distinct benefits over other labeling approaches such as lifeact-GFP (10) or SiR-Act (41). Thus, the actin-chromobody was used to track the movement of Golgi bodies along actin filaments in tobacco leaf cells. Compared to lifeact-GFP, a more complex movement pattern of the organelles was detectable, indicating that the transiently binding chromobody has only a minor effect on actin dynamics in those plant cells (40). In a recently published report, Periz et al., used the actin-chromobody to visualize actin for the first time in *Toxoplasma gondii*. Previous attempts with other labeling approaches have failed due to the fast turnover of F-actin in those parasites. Since the actin-chromobody preferentially labels filamentous actin the dynamics of the extensive actin network that connects parasites within the parasitophorous vacuole becomes visible and the exchange of vesicles between individual parasites could be monitored (38). In another approach the actin-chromobody was directed to the nucleus of mammalian cells. Following the chromobody signal in stably expressing NIH3T3 cells a fast formation of actin fibers within the nucleus in response to cellular treatment with soluble fibronectin was observed by time-lapse imaging (42). Moreover, the generation of an actin-chromobody expressing zebrafish established the first application of chromobodies in a vertebrate. Embryos ubiquitously expressed the actin-chromobody were raised to adulthood demonstrating that this intrabody does not interfere with normal animal development. Live imaging of whole zebrafish at various developmental stages revealed distribution and dynamics of actin in different cell types including embryonic muscle fibers, migrating primordial cells, epidermal cells, macrophages, or xanthophores and provides novel insights into processes such as wound healing or neuronal development (37).

Addressing another cytoskeletal target, we recently have generated a vimentin-specific chromobody (VB6-chromobody) to label major intermediate filaments *in vivo* (**Figure 1C**) (43). In addition to its role as an essential component of the cytoskeletal network, vimentin is a biomarker of epithelial–mesenchymal transition (EMT), a highly dynamic process involved in the initiation of metastasis and cancer progression. Thus, a lung cancer cell model stably expressing the VB6-chromobody was established and dynamic changes of endogenous vimentin were monitored. Upon treatment with TGF-β as an inductor of EMT, the chromobody signal revealed the incremental formation of vimentin fibers over time, starting from the nucleus toward the cellular periphery while upon RNAi-mediated vimentin depletion we observed an increasingly diffusible distribution of the chromobody in live cells. Based on these findings, we established a phenotypic readout for high-throughput live-cell imaging and quantified dose- and time-dependent effects of vimentin-modulating compounds as novel potential inhibitors of EMT (43, 44). In summary, to date, numerous cytoskeleton-specific chromobodies are available. They provide a promising approach for labeling these components in living cells and can be implemented in phenotypic screening approaches using 2D- or 3D-chromobody cell models (36, 44) or whole organism (37). However, no intracellularly functional tubulin-chromobody was reported so far, which would ideally complement this set of cytoskeletal probes.

CHROMOBODIES VISUALIZING NUCLEAR COMPONENTS

Chromobodies directed against nuclear factors have also found their way into live-cell imaging. Visualizing the dynamic appearance of distinct nuclear foci, formed by the native proliferating cell nuclear antigen (PCNA), a PCNA chromobody allows a detailed time-lapse analysis of S phase progression and quantitative live imaging of endogenous DNA replication in human cells (**Figure 1C**) (45). The potential of the PCNA chromobody to monitor the cell cycle using real-time high-throughput imaging was recently combined with an enzymatic determination of dead cell protease activity in corresponding cell culture supernatants. By this cell cycle modulators derived from a compound library which show low cellular toxicity were identified (46). In a similar setting, a PARP1 chromobody was used to visualize recruitment of endogenous PARP1 to DNA-damaged sites. The possibility to trace the characteristic relocalization of PARP1 from nucleoli to nucleoplasm following the chromobody signal constitutes a novel cell-based screening for rRNA transcription inhibitors or DNA-damaging agents using a translocation-specific, real-time imaging approach (47). Addressing the heterodimer formed by H2A–H2B histones, a chromobody (chromatibody) was developed for chromatin labeling of a wide variety of cell lines ranging from yeast to human. Although this chromobody shows a high affinity, its expression does not affect normal cell cycle progression. Moreover, similar to the actin-chromobody, introduction of the H2A–H2B chromobody in a transgenic *Drosophila* model has no influence on normal development underlining the functionality of chromobodies for non-invasive imaging of native targets in whole organisms (48).

All previously described chromobodies address structurally defined antigens (fibers, spots, etc.). A more challenging approach is to probe soluble cellular components. Recently, a chromobody specific for the Wnt signaling component β-catenin in its hypophosphorylated state was developed and stably introduced into HeLa cells. This chromobody cell line was used to monitor cytoplasmic accumulation and nuclear translocation of endogenous β-catenin in response to compound treatment (**Figure 1C**). This study additionally describes a previously unappreciated dependency of the chromobody level on the amount of its antigen and demonstrates that the chromobody signal can be utilized to trace quantitative changes of cellular β-catenin levels in real time (49).

Finally, a conformation-specific chromobody which visualizes GPCR trafficking from the plasma membrane to endosomes should be highlighted. Starting from a nanobody selectively recognizing the activated β2-adrenoceptor (β2-AR) (50), Irannejad et al. generated a GFP fusion of this binder (Nb80-GFP). Upon activation of β2-AR with isoprenaline, this chromobody was rapidly recruited from a diffuse fraction to the plasma membrane.

Continued time-lapse imaging showed a displacement of the chromobody when β-arrestin binds to internalized β2-AR and relocalization of the chromobody signal to β2-AR-containing endocytic vesicles further revealed a restoration of target binding once endosomes became uncoated (51). This study impressively demonstrates the potential of chromobody-based probes to visualize dynamic conformational changes of signaling proteins with high spatiotemporal resolution in living cells.

The aforementioned examples provide a rather short overview of recent advances of the chromobody technology. For the sake of brevity, many other chromobodies and applications thereof, e.g., to visualize viral morphogenesis (52), actin-binding proteins (19) or to manipulate native targets and structures (53, 54) in living cells are only mentioned briefly here.

Like for any other molecular probe applied for live-cell imaging, influence of chromobody expression has to be carefully evaluated. Especially, impact on antigen mobility or displacement of natural interaction partners has to be considered. This can be addressed, e.g., by selecting transiently binding chromobodies, detectable by FRAP analysis (23, 25, 37, 43), or chromobodies addressing inert epitopes, which can further be analyzed by intracellular immune-precipitations to monitor interactors co-precipitating with the antigen (49). Stable chromobody cell lines further requires detailed evaluation of, e.g. morphology, proliferation, and signaling pathways the target is involved in (43). To date, most chromobodies visualizes proteins present in considerable amounts in the cell. Introduced as genetically-encoded constructs their expression is only partially adjustable and signal of bound chromobodies is affected by the diffuse signal derived from non-bound ones. Gross et al. recently described an elegant approach to adjust the level of an intrabody by fusing it to a DNA-binding KRAB domain which induces a dynamic feedback mechanism transcriptionally repressing the generation of non-target-bound intrabody (9). Another option is to generate destabilized chromobodies. By adding a destruction motif such as PEST domains (55) or introducing distinct point mutations in the framework regions (56), the cellular turnover of chromobodies can be increased. Since we and others have observed that chromobodies are stabilized upon antigen binding (49, 56), such modifications might be suitable to improve the detection of low abundant components within living cells.

In summary, chromobodies are versatile probes to monitor expression and dynamics of endogenous proteins *in vivo*. Their ability to visualize antigens without affecting their function makes them ideally suited for real-time imaging of cellular processes and redistribution assays. To combine *in cellulo* imaging with functional studies, chromobodies which interfere with distinct protein functions or interactions can be selected. Such intrabodies would offer new perspectives for target identification, validation, and visualization in living cells.

sdAbs FOR SUPER-RESOLUTION IMAGING

With structured illumination microscopy (SIM) (57), stimulated emission depletion microscopy (STED) (58) and single-molecule localization techniques such as photoactivation localization microscopy (59) or stochastic optical reconstruction microscopy (STORM) (60), highly advanced methods are now available to image biological samples at resolutions below the diffraction limit of light (61, 62). In parallel, novel labeling strategies and improved affinity probes for SRM are developed (63–65). However, to date SRM-compatible fluorophores are most commonly delivered by expression of (photoactivatable) FPs or indirect labeling using secondary antibodies conjugated to organic dyes. Antibodies as relatively large molecules (150 kDa, 10–15 nm) can interfere with the achievable resolution as they displace the fluorophore from the target and introduce a so-called "linkage error" (66). Obviously, the 10 times smaller nanobodies (15 kDa, 2–4 nm) are predestined to overcome these issues as they have better access to intracellular antigens and can be easily conjugated to fluorophores either by chemical coupling or enzymatic labeling (67). Despite their clear advantages for the field, nanobodies are still at an early stage as novel labeling probes for super-resolution microscopy.

The first nanobody applied for super-resolution was the GFP nanobody in SIM studies (68). SIM requires very photostable labeling and GFP fusions often suffer from massive photobleaching during extended image acquisition. Upon binding to the high-affinity GFP nanobody (25) coupled to green fluorescent organic dye fluorescent intensities of individual GFP fusions can now be "boosted," to restore and increase the signal in the green channel. Combining SIM with ATTO488-conjugated GFP nanobodies, Guizetti et al. regain fluorescence of GFP-labeled components of endosomal sorting complex required for transport-III and obtained insights in the organization of the intracellular cortical constriction zone at the nanoscale (68). For single-molecule localization microscopy (SMLM), Ries et al chemically coupled the GFP and RFP nanobody developed by ChromoTek to AlexaFluor 647 (AF647) and AlexaFluor 700. They stated that nanobody-mediated targeting of organic dyes to FP fusions combines molecular specificity of genetic tagging with high photon yield of organic dyes and minimal linkage error. By staining of tubulin-YFP in Ptk2 cells with the GFP nanobody, they achieved a high-density labeling of microtubules with a full width half maximum of ~30 nm for individual filaments, which is in accordance with the reported microtubule diameter of ~25 nm. Additionally, they showed that the small GFP nanobody is able to penetrate the permeabilized cell wall of intact yeast cells without generating spheroblasts. Thus, they were able to perform STORM imaging of multiple endogenous GFP fusions derived from a haploid genomic library of *S. cerevisiae* (69).

Due to its applicability for nanoscopy of widely available GFP fusions, the GFP nanobody becomes a very popular tool for SMLM. Recently, the GFP nanobody was used to explore the structural background of information transmission in the nervous system. For localization microscopy of nanoclusters in the pre- and postsynaptic neurons the endogenous postsynaptic scaffolding protein PSD-95 was replaced by a GFP-tagged knockdown rescue variant of PSD-95 and labeled with the GFP nanobody conjugated at a 1:1 ratio with ATTO647. This provided a detailed insight in distributions of proteins mediating vesicle

priming in the presynaptic active zone in relation to postsynaptic membranes marked by PSD-95 (70).

While GFP- or RFP nanobodies are highly suitable for SRM of FP fusions in fixed and also live-cells when coupled to quantum dots (71), this strategy relies on the correct expression of FP fusions and does not cope with problems arising from overexpression, mislocalization or dysfunction (6, 8). Thus, nanobodies directed against smaller and inert peptide tags could be advantageous. With the BC2 nanobody, we recently reported the first peptide-binding nanobody which is suitable for cellular imaging (72). Upon chemical conjugation to organic dyes we visualized BC2-tagged proteins in various cellular compartments including the cytoplasm or the nucleus using wide-field or confocal microscopy (72). Further adaption of the BC2 nanobody to generate a SRM-compatible labeling probe is currently under development in our group.

To avoid any interferences derived from the addition of protein- or peptide tags, nanobodies targeting native proteins would be ideally suited for SRM. Considering that only a very few scientific groups or companies are currently developing nanobodies for SRM, only three examples of target-specific nanobodies can be mentioned here. Pleiner et al. have generated a set of nanobodies addressing various components of the nuclear pore complex (NPCs) of *Xenopus laevis*. For stoichiometric dye conjugation, they exchanged individual amino residues within the framework regions with single cysteines and performed maleimide coupling of AF647. They stated, that in comparison to NHS-mediated labeling, the site-specific conjugation leads to a better signal-to-noise

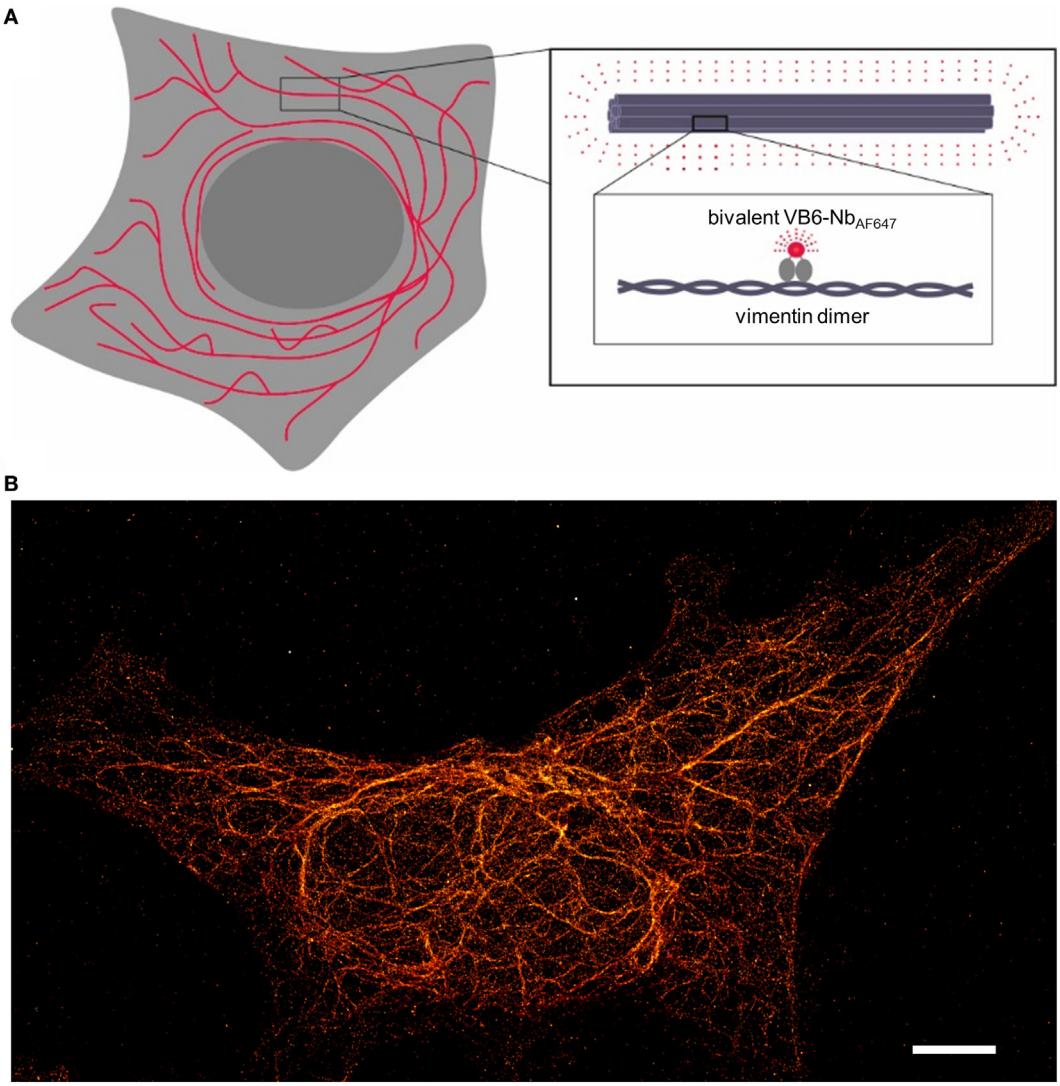

FIGURE 2 | Illustration of the nanobody-based labeling strategy for stochastic optical reconstruction microscopy (STORM) of the native vimentin network. **(A)** Schematical depiction of the bivalent VB6 (bivVB6)-Nb-labeled vimentin network. The boxed regions outline the organization of individual vimentin molecules into larger fibers and highlight the detection of dimeric vimentin with the fluorescently labeled bivalent VB6-Nb (bivVB6-Nb$_{AF647}$). **(B)** Representative STORM image of a HeLa cell, stained with the bivVB6-Nb$_{AF647}$. Scale bar, 5 µm.

ratio as it decreases unspecific background derived from dysfunctional or hydrolyzed NHS-coupled nanobodies. The AF647-conjugated nanobodies were successfully applied for STORM imaging of nuclear pore components including Nup93, Nup98, and Nup153. A detailed insight in the organization of these nuclear pore forming proteins can be deduced from the obtained images (73). In another example, two nanobodies against endogenous β-tubulin have been generated. STORM imaging with the newly identified anti-tubulin nanobodies in comparison to a primary anti-tubulin antibody either directly labeled or detected by a secondary antibody revealed significant differences in resolving bundled microtubules in various cell lines. While individual microtubules were resolvable with both nanobodies, none of the antibody-mediated labeling approaches led to a successful resolution of bundled microtubules. On quantitative level, the diameter of densely labeled microtubules was determined with ~40 nm for the anti-tubulin nanobodies and ~54 to ~62 nm for the directly conjugated primary anti-tubulin antibody or the primary/secondary antibody approach, respectively. From those findings, the authors concluded that conventional antibody labeling displaces the fluorophore on average ~12.5 nm from the microtubule whereas nanobody labeling reduces this distance to less than 2.5 nm (74).

Given the fact that our recently developed bivalent VB6 (bivVB6) nanobody also detects native vimentin structures when it is applied as a dye-conjugated labeling probe (43), we further evaluated this bivalent nanobody format for SRM. Thus, we performed site-directed conjugation of VB6-Nb with AF647. STORM images impressively show a high resolution of the vimentin network in mammalian cells indicating that the bivVB6-Nb nanobody is also suitable for SRM (**Figure 2**, own work).

In summary, nanobodies in combination with site-specific and quantitative fluorescent labeling will be crucial for SRM aiming at detailed structural analysis or determination of absolute protein copy numbers. Although only a limited number of nanobodies are available for SRM, the presented examples excelled in SRM and well-defined cellular structures such as the vimentin network, NPCs, or microtubules labeled with nanobodies have now become benchmarks for many new advancements of SRM. In contrast to conventional poly- or monoclonal antibodies, nanobodies are reliably producible in high yields with a standard quality. Thus, it is conceivable that they will help to avoid current uncertainties regarding antigen labeling and facilitate the reproducibility of results between laboratories and publications. In combination with other approaches developed to deliver bright organic dyes to defined cellular structures such as point accumulation for imaging in nanoscale topography (75), bicyclic peptides (76), or aptamers (77), nanobodies perfectly complement the portfolio of new and reliable labeling probes for super-resolution imaging.

AUTHOR CONTRIBUTIONS

UR and BT have jointly written the manuscript and prepared the figures.

ACKNOWLEDGMENTS

The authors would like to thank Bettina Keller, Philipp Kaiser, and Julia Maier for critical reading the manuscript and helpful discussion. Especially, we thank Ulrike Endesfelder and David Virant for STORM images of vimentin network. The authors acknowledge support by Deutsche Forschungsgemeinschaft and Open Access Publishing Fund of University of Tuebingen and gratefully acknowledge the Ministry of Science, Research and Arts of Baden-Württemberg (V.1.4.-H3-1403-74) for financial support.

REFERENCES

1. Keppler A, Gendreizig S, Gronemeyer T, Pick H, Vogel H, Johnsson K. A general method for the covalent labeling of fusion proteins with small molecules in vivo. *Nat Biotechnol* (2003) 21(1):86–9. doi:10.1038/nbt765
2. Gautier A, Juillerat A, Heinis C, Correa IR Jr, Kindermann M, Beaufils F, et al. An engineered protein tag for multiprotein labeling in living cells. *Chem Biol* (2008) 15(2):128–36. doi:10.1016/j.chembiol.2008.01.007
3. Los GV, Encell LP, McDougall MG, Hartzell DD, Karassina N, Zimprich C, et al. HaloTag: a novel protein labeling technology for cell imaging and protein analysis. *ACS Chem Biol* (2008) 3(6):373–82. doi:10.1021/cb800025k
4. Giepmans BN, Adams SR, Ellisman MH, Tsien RY. The fluorescent toolbox for assessing protein location and function. *Science* (2006) 312(5771):217–24. doi:10.1126/science.1124618
5. Tsien RY. The green fluorescent protein. *Annu Rev Biochem* (1998) 67:509–44. doi:10.1146/annurev.biochem.67.1.509
6. Snapp EL. Fluorescent proteins: a cell biologist's user guide. *Trends Cell Biol* (2009) 19(11):649–55. doi:10.1016/j.tcb.2009.08.002
7. Hosein RE, Williams SA, Haye K, Gavin RH. Expression of GFP-actin leads to failure of nuclear elongation and cytokinesis in *Tetrahymena thermophila*. *J Eukaryot Microbiol* (2003) 50(6):403–8. doi:10.1111/j.1550-7408.2003.tb00261.x
8. Stadler C, Rexhepaj E, Singan VR, Murphy RF, Pepperkok R, Uhlén M, et al. Immunofluorescence and fluorescent-protein tagging show high correlation for protein localization in mammalian cells. *Nat Methods* (2013) 10(4):315–23. doi:10.1038/nmeth.2377
9. Gross GG, Junge JA, Mora RJ, Kwon HB, Olson CA, Takahashi TT, et al. Recombinant probes for visualizing endogenous synaptic proteins in living neurons. *Neuron* (2013) 78(6):971–85. doi:10.1016/j.neuron.2013.04.017
10. Riedl J, Crevenna AH, Kessenbrock K, Yu JH, Neukirchen D, Bista M, et al. Lifeact: a versatile marker to visualize F-actin. *Nat Methods* (2008) 5(7):605–7. doi:10.1038/nmeth.1220
11. Kaiser PD, Maier J, Traenkle B, Emele F, Rothbauer U. Recent progress in generating intracellular functional antibody fragments to target and trace cellular components in living cells. *Biochim Biophys Acta* (2014) 1844(11):1933–42. doi:10.1016/j.bbapap.2014.04.019
12. Plückthun A. Designed ankyrin repeat proteins (DARPins): binding proteins for research, diagnostics, and therapy. *Annu Rev Pharmacol Toxicol* (2015) 55:489–511. doi:10.1146/annurev-pharmtox-010611-134654
13. Biocca S, Neuberger MS, Cattaneo A. Expression and targeting of intracellular antibodies in mammalian cells. *EMBO J* (1990) 9(1):101–8.
14. Nizak C, Martin-Lluesma S, Moutel S, Roux A, Kreis TE, Goud B, et al. Recombinant antibodies against subcellular fractions used to track endogenous Golgi protein dynamics in vivo. *Traffic* (2003) 4(11):739–53. doi:10.1034/j.1600-0854.2003.00132.x
15. Freund G, Desplancq D, Stoessel A, Weinsanto R, Sibler AP, Robin G, et al. Generation of an intrabody-based reagent suitable for imaging endogenous proliferating cell nuclear antigen in living cancer cells. *J Mol Recognit* (2014) 27(9):549–58. doi:10.1002/jmr.2378
16. Hamers-Casterman C, Atarhouch T, Muyldermans S, Robinson G, Hamers C, Songa EB, et al. Naturally occurring antibodies devoid of light chains. *Nature* (1993) 363(6428):446–8. doi:10.1038/363446a0

17. Helma J, Cardoso MC, Muyldermans S, Leonhardt H. Nanobodies and recombinant binders in cell biology. *J Cell Biol* (2015) 209(5):633–44. doi:10.1083/jcb.201409074
18. Jobling SA, Jarman C, Teh M-M, Holmberg N, Blake C, Verhoeyen ME. Immunomodulation of enzyme function in plants by single-domain antibody fragments. *Nat Biotechnol* (2003) 21(1):77–80. doi:10.1038/nbt772
19. Van Audenhove I, Van Impe K, Ruano-Gallego D, De Clercq S, De Muynck K, Vanloo B, et al. Mapping cytoskeletal protein function in cells by means of nanobodies. *Cytoskeleton (Hoboken)* (2013) 70(10):604–22. doi:10.1002/cm.21122
20. Zolghadr K, Mortusewicz O, Rothbauer U, Kleinhans R, Goehler H, Wanker EE, et al. A fluorescent two-hybrid assay for direct visualization of protein interactions in living cells. *Mol Cell Proteomics* (2008) 7(11):2279–87. doi:10.1074/mcp.M700548-MCP200
21. Zolghadr K, Rothbauer U, Leonhardt H. The fluorescent two-hybrid (F2H) assay for direct analysis of protein-protein interactions in living cells. *Methods Mol Biol* (2012) 812:275–82. doi:10.1007/978-1-61779-455-1_16
22. Pellis M, Muyldermans S, Vincke C. Bacterial two hybrid: a versatile one-step intracellular selection method. *Methods Mol Biol* (2012) 911:135–50. doi:10.1007/978-1-61779-968-6_9
23. Pellis M, Pardon E, Zolghadr K, Rothbauer U, Vincke C, Kinne J, et al. A bacterial-two-hybrid selection system for one-step isolation of intracellularly functional nanobodies. *Arch Biochem Biophys* (2012) 526(2):114–23. doi:10.1016/j.abb.2012.04.023
24. Moutel S, Bery N, Bernard V, Keller L, Lemesre E, de Marco A, et al. NaLi-H1: a universal synthetic library of humanized nanobodies providing highly functional antibodies and intrabodies. *Elife* (2016) 5:e16228. doi:10.7554/eLife.16228
25. Rothbauer U, Zolghadr K, Tillib S, Nowak D, Schermelleh L, Gahl A, et al. Targeting and tracing antigens in live cells with fluorescent nanobodies. *Nat Methods* (2006) 3(11):887–9. doi:10.1038/nmeth953
26. Rothbauer U, Zolghadr K, Muyldermans S, Schepers A, Cardoso MC, Leonhardt H. A versatile nanotrap for biochemical and functional studies with fluorescent fusion proteins. *Mol Cell Proteomics* (2008) 7(2):282–9. doi:10.1074/mcp.M700342-MCP200
27. Schornack S, Fuchs R, Huitema E, Rothbauer U, Lipka V, Kamoun S. Protein mislocalization in plant cells using a GFP-binding chromobody. *Plant J* (2009) 60(4):744–54. doi:10.1111/j.1365-313X.2009.03982.x
28. Berry LK, Ólafsson G, Ledesma-Fernandez E, Thorpe PH. Synthetic protein interactions reveal a functional map of the cell. *Elife* (2016) 5:e13053. doi:10.7554/eLife.13053
29. Caussinus E, Kanca O, Affolter M. Fluorescent fusion protein knockout mediated by anti-GFP nanobody. *Nat Struct Mol Biol* (2012) 19(1):117–21. doi:10.1038/nsmb.2180
30. Shin YJ, Park SK, Jung YJ, Kim YN, Kim KS, Park OK, et al. Nanobody-targeted E3-ubiquitin ligase complex degrades nuclear proteins. *Sci Rep* (2015) 5:14269. doi:10.1038/srep14269
31. Kirchhofer A, Helma J, Schmidthals K, Frauer C, Cui S, Karcher A, et al. Modulation of protein properties in living cells using nanobodies. *Nat Struct Mol Biol* (2010) 17(1):133–8. doi:10.1038/nsmb.1727
32. Mendez MG, Kojima S, Goldman RD. Vimentin induces changes in cell shape, motility, and adhesion during the epithelial to mesenchymal transition. *FASEB J* (2010) 24(6):1838–51. doi:10.1096/fj.09-151639
33. Lemieux MG, Janzen D, Hwang R, Roldan J, Jarchum I, Knecht DA. Visualization of the actin cytoskeleton: different F-actin-binding probes tell different stories. *Cytoskeleton (Hoboken)* (2014) 71(3):157–69. doi:10.1002/cm.21160
34. Belin BJ, Goins LM, Mullins RD. Comparative analysis of tools for live cell imaging of actin network architecture. *Bioarchitecture* (2014) 4(6):189–202. doi:10.1080/19490992.2014.1047714
35. Schmidthals K, Helma J, Zolghadr K, Rothbauer U, Leonhardt H. Novel antibody derivatives for proteome and high-content analysis. *Anal Bioanal Chem* (2010) 397(8):3203–8. doi:10.1007/s00216-010-3657-0
36. Zolghadr K, Gregor J, Leonhardt H, Rothbauer U. Case study on live cell apoptosis-assay using lamin-chromobody cell-lines for high-content analysis. *Methods Mol Biol* (2012) 911:569–75. doi:10.1007/978-1-61779-968-6_36
37. Panza P, Maier J, Schmees C, Rothbauer U, Sollner C. Live imaging of endogenous protein dynamics in zebrafish using chromobodies. *Development* (2015) 142(10):1879–84. doi:10.1242/dev.118943
38. Periz J, Whitelaw J, Harding C, Gras S, Minina MIDR, Latorre-Barragan F, et al. *Toxoplasma gondii* F-actin forms an extensive filamentous network required for material exchange and parasite maturation. *Elife* (2017) 6:e24119. doi:10.7554/eLife.24119
39. Melak M, Plessner M, Grosse R. Actin visualization at a glance. *J Cell Sci* (2017) 130(3):525–30. doi:10.1242/jcs.189068
40. Rocchetti A, Hawes C, Kriechbaumer V. Fluorescent labelling of the actin cytoskeleton in plants using a cameloid antibody. *Plant Methods* (2014) 10:12. doi:10.1186/1746-4811-10-12
41. Lukinavicius G, Reymond L, D'Este E, Masharina A, Gottfert F, Ta H, et al. Fluorogenic probes for live-cell imaging of the cytoskeleton. *Nat Methods* (2014) 11(7):731–3. doi:10.1038/nmeth.2972
42. Plessner M, Melak M, Chinchilla P, Baarlink C, Grosse R. Nuclear F-actin formation and reorganization upon cell spreading. *J Biol Chem* (2015) 290(18):11209–16. doi:10.1074/jbc.M114.627166
43. Maier J, Traenkle B, Rothbauer U. Real-time analysis of epithelial-mesenchymal transition using fluorescent single-domain antibodies. *Sci Rep* (2015) 5:13402. doi:10.1038/srep13402
44. Maier J, Traenkle B, Rothbauer U. Visualizing epithelial-mesenchymal transition using the chromobody technology. *Cancer Res* (2016) 76(19):5592–6. doi:10.1158/0008-5472.CAN-15-3419
45. Burgess A, Lorca T, Castro A. Quantitative live imaging of endogenous DNA replication in mammalian cells. *PLoS One* (2012) 7(9):e45726. doi:10.1371/journal.pone.0045726
46. Schorpp K, Rothenaigner I, Maier J, Traenkle B, Rothbauer U, Hadian K. A multiplexed high-content screening approach using the chromobody technology to identify cell cycle modulators in living cells. *J Biomol Screen* (2016) 21(9):965–77. doi:10.1177/1087057116641935
47. Buchfellner A, Yurlova L, Nuske S, Scholz AM, Bogner J, Ruf B, et al. A new nanobody-based biosensor to study endogenous PARP1 in vitro and in live human cells. *PLoS One* (2016) 11(3):e0151041. doi:10.1371/journal.pone.0151041
48. Jullien D, Vignard J, Fedor Y, Bery N, Olichon A, Crozatier M, et al. Chromatibody, a novel non-invasive molecular tool to explore and manipulate chromatin in living cells. *J Cell Sci* (2016) 129(13):2673–83. doi:10.1242/jcs.183103
49. Traenkle B, Emele F, Anton R, Poetz O, Haeussler RS, Maier J, et al. Monitoring interactions and dynamics of endogenous beta-catenin with intracellular nanobodies in living cells. *Mol Cell Proteomics* (2015) 14(3):707–23. doi:10.1074/mcp.M114.044016
50. Rasmussen SG, DeVree BT, Zou Y, Kruse AC, Chung KY, Kobilka TS, et al. Crystal structure of the [bgr] 2 adrenergic receptor-Gs protein complex. *Nature* (2011) 477(7366):549–55. doi:10.1038/nature10361
51. Irannejad R, Tomshine JC, Tomshine JR, Chevalier M, Mahoney JP, Steyaert J, et al. Conformational biosensors reveal GPCR signalling from endosomes. *Nature* (2013) 495(7442):534–8. doi:10.1038/nature12000
52. Helma J, Schmidthals K, Lux V, Nüske S, Scholz AM, Kräusslich H-G, et al. Direct and dynamic detection of HIV-1 in living cells. *PLoS One* (2012) 7(11):e50026. doi:10.1371/journal.pone.0050026
53. Van Audenhove I, Gettemans J. Use of nanobodies to localize endogenous cytoskeletal proteins and to determine their contribution to cancer cell invasion by using an ECM degradation assay. *Methods Mol Biol* (2016) 1365:225–41. doi:10.1007/978-1-4939-3124-8_12
54. Beghein E, Van Audenhove I, Zwaenepoel O, Verhelle A, De Ganck A, Gettemans J. A new survivin tracer tracks, delocalizes and captures endogenous survivin at different subcellular locations and in distinct organelles. *Sci Rep* (2016) 6:31177. doi:10.1038/srep31177
55. Sibler AP, Courtête J, Muller CD, Zeder-Lutz G, Weiss E. Extended half-life upon binding of destabilized intrabodies allows specific detection of antigen in mammalian cells. *FEBS J* (2005) 272(11):2878–91. doi:10.1111/j.1742-4658.2005.04709.x
56. Tang JC, Drokhlyansky E, Etemad B, Rudolph S, Guo B, Wang S, et al. Detection and manipulation of live antigen-expressing cells using conditionally stable nanobodies. *Elife* (2016) 5:e15312. doi:10.7554/eLife.15312
57. Gustafsson MG. Surpassing the lateral resolution limit by a factor of two using structured illumination microscopy. *J Microsc* (2000) 198(Pt 2):82–7. doi:10.1046/j.1365-2818.2000.00710.x

58. Hell SW, Wichmann J. Breaking the diffraction resolution limit by stimulated emission: stimulated-emission-depletion fluorescence microscopy. *Opt Lett* (1994) 19(11):780–2. doi:10.1364/OL.19.000780
59. Betzig E, Patterson GH, Sougrat R, Lindwasser OW, Olenych S, Bonifacino JS, et al. Imaging intracellular fluorescent proteins at nanometer resolution. *Science* (2006) 313(5793):1642–5. doi:10.1126/science.1127344
60. Rust MJ, Bates M, Zhuang X. Sub-diffraction-limit imaging by stochastic optical reconstruction microscopy (STORM). *Nat Methods* (2006) 3(10):793–6. doi:10.1038/nmeth929
61. Lippincott-Schwartz J, Manley S. Putting super-resolution fluorescence microscopy to work. *Nat Methods* (2009) 6(1):21–3. doi:10.1038/nmeth.f.233
62. Schermelleh L, Heintzmann R, Leonhardt H. A guide to super-resolution fluorescence microscopy. *J Cell Biol* (2010) 190(2):165–75. doi:10.1083/jcb.201002018
63. Schnitzbauer J, Strauss MT, Schlichthaerle T, Schueder F, Jungmann R. Super-resolution microscopy with DNA-PAINT. *Nat Protoc* (2017) 12(6):1198. doi:10.1038/nprot.2017.024
64. Chamma I, Rossier O, Giannone G, Thoumine O, Sainlos M. Optimized labeling of membrane proteins for applications to super-resolution imaging in confined cellular environments using monomeric streptavidin. *Nat Protoc* (2017) 12(4):748. doi:10.1038/nprot.2017.010
65. de Castro MAG, Höbartner C, Opazo F. Aptamers provide superior stainings of cellular receptors studied under super-resolution microscopy. *PLoS One* (2017) 12(2):e0173050. doi:10.1371/journal.pone.0173050
66. Wouterlood FG. *Cellular Imaging Techniques for Neuroscience and Beyond*. Amsterdam: Academic Press (2012).
67. Massa S, Vikani N, Betti C, Ballet S, Vanderhaegen S, Steyaert J, et al. Sortase A-mediated site-specific labeling of camelid single-domain antibody-fragments: a versatile strategy for multiple molecular imaging modalities. *Contrast Media Mol Imaging* (2016) 11(5):328–39. doi:10.1002/cmmi.1696
68. Guizetti J, Schermelleh L, Mäntler J, Maar S, Poser I, Leonhardt H, et al. Cortical constriction during abscission involves helices of ESCRT-III-dependent filaments. *Science* (2011) 331(6024):1616–20. doi:10.1126/science.1201847
69. Ries J, Kaplan C, Platonova E, Eghlidi H, Ewers H. A simple, versatile method for GFP-based super-resolution microscopy via nanobodies. *Nat Methods* (2012) 9(6):582–4. doi:10.1038/nmeth.1991
70. Tang A-H, Chen H, Li TP, Metzbower SR, MacGillavry HD, Blanpied TA. A trans-synaptic nanocolumn aligns neurotransmitter release to receptors. *Nature* (2016) 536:210–4. doi:10.1038/nature19058
71. Wang Y, Cai E, Rosenkranz T, Ge P, Teng KW, Lim SJ, et al. Small quantum dots conjugated to nanobodies as immunofluorescence probes for nanometric microscopy. *Bioconjug Chem* (2014) 25(12):2205–11. doi:10.1021/bc5004179
72. Braun MB, Traenkle B, Koch PA, Emele F, Weiss F, Poetz O, et al. Peptides in headlock – a novel high-affinity and versatile peptide-binding nanobody for proteomics and microscopy. *Sci Rep* (2016) 6:19211. doi:10.1038/srep19211
73. Pleiner T, Bates M, Trakhanov S, Lee C-T, Schliep JE, Chug H, et al. Nanobodies: site-specific labeling for super-resolution imaging, rapid epitope-mapping and native protein complex isolation. *Elife* (2015) 4:e11349. doi:10.7554/eLife.11349
74. Mikhaylova M, Cloin BM, Finan K, Van Den Berg R, Teeuw J, Kijanka MM, et al. Resolving bundled microtubules using anti-tubulin nanobodies. *Nat Commun* (2015) 6:7933. doi:10.1038/ncomms8933
75. Sharonov A, Hochstrasser RM. Wide-field subdiffraction imaging by accumulated binding of diffusing probes. *Proc Natl Acad Sci U S A* (2006) 103(50):18911–6. doi:10.1073/pnas.0609643104
76. Heinis C, Rutherford T, Freund S, Winter G. Phage-encoded combinatorial chemical libraries based on bicyclic peptides. *Nat Chem Biol* (2009) 5(7):502–7. doi:10.1038/nchembio.184
77. Opazo F, Levy M, Byrom M, Schafer C, Geisler C, Groemer TW, et al. Aptamers as potential tools for super-resolution microscopy. *Nat Methods* (2012) 9(10):938–9. doi:10.1038/nmeth.2179

Conflict of Interest Statement: UR is shareholder of ChromoTek GmbH. BT declares that the research was conducted in the absence of any commercial or financial relationships that could be construed as a potential conflict of interest.

frontiers in Immunology

METHODS
published: 10 April 2017
doi: 10.3389/fimmu.2017.00420

Large Diversity of Functional Nanobodies from a Camelid Immune Library Revealed by an Alternative Analysis of Next-Generation Sequencing Data

*Pieter Deschaght‡, Ana Paula Vintém‡, Marc Logghe, Miguel Conde, David Felix†, Rob Mensink†, Juliana Gonçalves†, Jorn Audiens, Yanik Bruynooghe, Rita Figueiredo†, Diana Ramos†, Robbe Tanghe, Daniela Teixeira†, Liesbeth Van de Ven†, Catelijne Stortelers and Bruno Dombrecht**

Ablynx N.V., Ghent, Belgium

OPEN ACCESS

Edited by:
Colin Roger MacKenzie, National Research Council Canada, Canada

Reviewed by:
Daniel Zabetakis, United States Naval Research Laboratory, USA
Bryan Briney, Scripps Research Institute, USA
Xin Ge, University of California Riverside, USA

***Correspondence:**
Bruno Dombrecht
bruno.dombrecht@ablynx.com

†Present address:
David Felix, Merus N.V., Utrecht, Netherlands;
Rob Mensink, GenCore Facility, Institute for Research and Innovation in Health, University of Porto, Porto, Portugal;
Juliana Gonçalves, Fair Journey Biologics, Porto, Portugal;
Rita Figueiredo, Immunocore Ltd., Abingdon, UK;
Diana Ramos, Fair Journey Biologics, Porto, Portugal;
Daniela Teixeira, Fair Journey Biologics, Porto, Portugal;
Liesbeth Van de Ven, Argen-X N.V., Ghent, Belgium

‡These authors have contributed equally to this work.*

Specialty section:
This article was submitted to Vaccines and Molecular Therapeutics, a section of the journal Frontiers in Immunology

Received: 22 December 2016
Accepted: 24 March 2017
Published: 10 April 2017

Next-generation sequencing (NGS) has been applied successfully to the field of therapeutic antibody discovery, often outperforming conventional screening campaigns which tend to identify only the more abundant selective antibody sequences. We used NGS to mine the functional nanobody repertoire from a phage-displayed camelid immune library directed to the recepteur d'origine nantais (RON) receptor kinase. Challenges to this application of NGS include accurate removal of read errors, correct identification of related sequences, and establishing meaningful inclusion criteria for sequences-of-interest. To this end, a sequence identity threshold was defined to separate unrelated full-length sequence clusters by exploring a large diverse set of publicly available nanobody sequences. When combined with majority-rule consensus building, applying this elegant clustering approach to the NGS data set revealed a wealth of >5,000-enriched candidate RON binders. The huge binding potential predicted by the NGS approach was explored through a set of randomly selected candidates: 90% were confirmed as RON binders, 50% of which functionally blocked RON in an ERK phosphorylation assay. Additional validation came from the correct prediction of all 35 RON binding nanobodies which were identified by a conventional screening campaign of the same immune library. More detailed characterization of a subset of RON binders revealed excellent functional potencies and a promising epitope diversity. In summary, our approach exposes the functional diversity and quality of the outbred camelid heavy chain-only immune response and confirms the power of NGS to identify large numbers of promising nanobodies.

Keywords: next-generation sequencing, clustering, nanobodies, recepteur d'origine nantais signaling, phage display, sequence homology, amino acid, immune repertoire diversity

INTRODUCTION

Nanobodies are antibody-derived therapeutic proteins based on immunoglobulin single variable domains (1) derived from the variable domains (VHH) of heavy chain-only antibodies that naturally occur in camelids (2). Conventionally, nanobodies with desired functional properties are selected from immune, naïve, or synthetic libraries *via* phage display on the antigen-of-interest (3). More

recently, nanobody libraries have been explored by ribosomal, bacterial, or yeast surface display and by bacterial or yeast two-hybrid selections (4–10). At the end of this selection process, enriched clones are screened *in vitro* after which hit candidates are identified by means of Sanger sequencing. Although this procedure has a proven track record, the conventional screening approach is often limited to throughputs of several hundreds of clones and thus likely represents only a fraction of the functional potential present in the libraries.

Next-generation sequencing (NGS) technologies have significantly contributed to our knowledge of antibody repertoire diversity in different species or diseases (11–13). More so, NGS can be a powerful tool in the discovery process of antibody-based therapeutics. The large number of sequencing reads obtained by NGS not only enables unparalleled library quality control but can be applied to more completely assess the binding potential of antibody and nanobody repertoires (14–21). During the library selection process on the antigen-of-interest, the selective binders are enriched over the background of non-selective clones. A sequence-based frequency analysis then enables the identification of candidate binders which are enriched on the antigen-of-interest in comparison to a negative control condition.

Recepteur d'origine nantais (RON) is a receptor tyrosine kinase member of the MET proto-oncogene family (22, 23). RON dimerization on the cell-surface is required for activation after conformational changes induced by the ligand macrophage-stimulating protein (MSP). Overexpression and splicing variants of RON are implicated in many processes related to cancer initiation, progression, and malignant conversion. Constitutive receptor activation triggers downstream signaling cascades critical for tumorigenesis, including RAS–MAPK and PI-3K–AKT pathways (24).

We used NGS to mine a camelid's nanobody selective immune response to human RON (hRON) in comparison to a conventional screening campaign exploring the same immune library for hRON-specific nanobodies. To this end, samples from phage display selections on hRON were sequenced by Illumina MiSeq (2×250 bp) which allows for a full coverage of the nanobody encoding sequences. A sequence identity-based clustering approach combined with majority-rule consensus building was utilized, which was developed using publicly available nanobody sequence data. This approach elegantly addressed known issues of PCR and sequencing errors as well as sequence diversity reduction and revealed a wealth of candidate hRON-binding nanobodies. Validation of the method came from the confirmation of all leads which were identified by the conventional screening campaign. In addition, many more functional leads were identified.

MATERIALS AND METHODS

Proteins, Antibodies, and Cell Lines

Recombinant extracellular domain of human RON (rhRON), and the ligand MSP were purchased from R&D Systems (MN, USA). Anti-FLAG antibodies and extravidin peroxidase were purchased from Sigma-Aldrich (MO, USA), goat anti-mouse antibody PE or APC conjugated from Jackson Immuno Research (PA, USA), and anti-M13 monoclonal HRP Conjugate from GE Healthcare. HEK293T (DSMZ, Germany) and llama navel cord fibroblast (Llana) (Ablynx, Belgium) cell lines were transiently transfected using FuGENE HD (Promega, WI, USA) transfection reagent with full-length hRON DNA cloned into pcDNA3.1. The human breast cancer cell line T-47D endogenously expressing RON was obtained from ATCC (VA, USA).

Immunizations, Library Construction, and Phage Display Selections

Recepteur d'origine nantais-targeting nanobodies were generated through immunization of a llama with rhRON, essentially as described elsewhere (3). Briefly, a llama was immunized first with 100 μg of protein followed by three times 50 μg, after which blood samples were taken. Phage display libraries derived from peripheral blood mononuclear cells (PBMCs) were prepared and used as previously described (3). The VHH fragments were cloned into a M13 phagemid vector containing the $FLAG_3$ and His_6 tags. The resulting library size was 4.8×10^8 with 91% of insert. The library was rescued by infecting exponentially growing *Escherichia coli* TG1 [(F′ *traD36 proAB lacIqZ* Δ*M15*) *supE thi-1* Δ*(lac-proAB)* Δ*(mcrB-hsdSM)5(rK− mK−)*] cells followed by superinfection with VCSM13 helper phage, resulting in 4.4×10^{13} cfu/ml. For the NGS samples, the RON and the negative control outputs, with sizes of respectively, 8×10^6 and 9×10^5 cfu, were derived from one round of selection on HEK293T cells expressing hRON and on HEK293T cells, respectively. For the conventional screening campaign, phage display selections were performed on HEK239T or Llana cells expressing hRON and on rhRON protein either directly immobilized on plate or captured *via* biotin by streptavidin-coated magnetic beads (Dynabeads, Invitrogen). The phage outputs were rescued as described above for the library. For screening purposes, *E. coli* TG1 cells were infected with the resulting phage outputs and individual colonies were grown in 96-deep-well plates. The expression of monoclonal nanobodies was induced by addition of IPTG and the crude periplasmic extracts containing the nanobodies were prepared by freeze-thawing of the bacterial pellets overnight in PBS followed by centrifugation to remove cell debris.

Cloning and Production of Nanobodies

Synthetic DNA fragments (Integrated DNA Technologies, Belgium) encoding nanobodies from the NGS campaign and nanobody genes derived from the conventional screening approach were cloned into an expression vector in frame with an N-terminal OmpA signal peptide and C-terminal $FLAG_3$ and His_6 tags. Production and purification were in essence performed as described before (3).

NGS Sample Preparation and Sequencing

Polyclonal plasmid DNA preparations from *E. coli* cultures infected with two different phage samples (RON and negative control) were used as PCR template. The first PCR was performed with primers FR1 (5′-GAGGTGCAGCTGGTGGAGTCT-3′, encoding EVQLVES) and FR4 (5′-TGAGGAGACGGTGACCWGGGT-3′, encoding T(L/Q)VTVSS). For each sample, 48 parallel PCR

reactions were run with KAPA HiFi DNA polymerase (Kapa Biosystems) using the following protocol: 3 min at 95°C; 20 cycles of 20 s at 98°C, 25 s at 55°C, 10 s at 72°C; once 5 min at 72°C. After PCR all samples were subjected to sample clean-up (PureLink PCR Purification Kit, Life Technologies). In a second PCR, these DNA amplicons were flanked by barcoded i7 TruSeq adapters as prescribed (Illumina). The samples were sequenced on a MiSeq system using the Illumina v2 2 × 250 bp chemistry kit.

NGS Data Processing

In a first step, the reads were sorted by barcode, followed by barcode and Illumina TruSeq adapter clipping with bcl2fastq 1.8.4 (Illumina). Forward and reverse reads were combined using open source software FLASH 1.2.4 (25) available from https://ccb.jhu.edu/software/FLASH/ (minimal overlap: 10 bases, maximum mismatch rate: 25%). After PCR primer sequence detection, the reads were turned into the forward (FR1 primer) to reverse (FR4 primer) orientation and reads with average Phred scores <38 or lengths <150 bp were discarded. After translation with the freely available BioPhyton package[1] in frame +1, starting at the 5′-end of the FR1 PCR primer, peptides ending in frame with the FR4 primer sequence were considered valid, thus excluding reads with frameshifts and/or premature stop codons.

Downloading Nanobody Sequences

Publicly available nanobody sequences were downloaded from the NCBI Protein database[2] (accessed 15 March 2016) using "*(camelidae[Organism]) AND ((VHH) OR (Nanobody) OR (single domain)) AND immunoglobulin*" as query. Nine hundred forty-five matches were obtained and aligned. After visual inspection of this alignment, obvious non-nanobody and truncated or partial sequences were manually removed, leaving 888 sequences for clustering (Table S1 in Supplementary Material).

Nanobody Clustering and Alignment

Before clustering, the residues corresponding to IMGT V-DOMAIN positions 1–7 and 122–128, the first and last seven residues of FR1 and FR4, respectively (26), were trimmed from the nanobody peptide sequences. This was done in order to remove undesirable sequence variation introduced by the PCR primers used in the preparation of the NGS samples or coming from partial FR1 and/or FR4 regions in publicly available nanobody sequences. The trimmed peptide sequences were clustered with CD-HIT version 4.6.1 (27, 28). A detailed user manual as well as a web server of this freely available and widely used clustering software package can be found at http://weizhongli-lab.org/cd-hit/. The program was run in the slow/accurate mode ($-g = 1$), no length differences were allowed (length difference cutoff $-s = 1$), and different identity cutoffs (sequence identity threshold $-c = 0.70, 0.75, 0.80, 0.85, 0.90, 0.95$, and 1.00) were evaluated.

Alignments were generated with CLC Main Workbench version 7.6.4 (Qiagen).

[1] http://biopython.org/.

[2] http://www.ncbi.nlm.nih.gov/protein/.

Binding ELISA

rhRON (1 µg/ml) was immobilized directly on 384-well microtiter plates. Free-binding sites were blocked by 4% Marvel in PBS. Next, 5 µl of crude periplasmic extracts in 50 µl 2% Marvel PBST were added. Nanobody binding was revealed using a mouse-anti-FLAG HRP-conjugated antibody. The OD_{450nm} values of each clone were divided by those of a negative control nanobody and considered positive if the resulting ratio was ≥2.

Epitope Binning

Biotinylated rhRON (1 nM) was captured by NeutrAvidin immobilized on 96-well microtiter plates (2 µg/ml) and blocked by 1% casein in PBS. Next, 1 µl of purified monoclonal phage (10^{11} cfu/ml) displaying nanobody in 100 µl, 0.1% casein PBST were added in the presence and absence of crude periplasmic extract containing nanobodies at 1/10 dilutions. Phage binding was detected *via* anti-M13 HRP-conjugated antibody. Competition for binding to an overlapping epitope was revealed by the drop in signal of phage binding in the presence of the nanobody in the crude periplasmic extract.

Off-rate Determination

Off-rates were determined by surface plasmon resonance of crude periplasmic extracts on a ProteOn instrument (Biorad, CA, USA). rhRON was immobilized to GLC sensor chips surface and nanobody binding was assessed using 1/10 diluted periplasmic extracts. Each nanobody was injected for 2 min at a flow rate of 45 µl/min to allow binding to chip-bound antigen. Next, binding buffer without nanobody was injected at the same flow rate to allow spontaneous dissociation of bound nanobody. Regeneration was done with 10 mM glycine HCl, pH2.5. From the sensorgrams obtained for the different nanobodies k_{off} values were calculated. Data processing and analysis were done with the ProteOn Manager Software, Version 2.1.1.18 applying the Langmuir kinetic model.

Inhibition of MSP-Induced ERK Phosphorylation

Functional blockade of RON kinase activation by nanobodies was assessed by inhibition of ligand-induced MAPK activation in T-47D breast cancer cells. For screening purposes, the AlphaLISA SureFire Ultra phospho-ERK 1/2 (Thr202/Tyr204) kit was used (PerkinElmer, MA, USA). T-47D cells (2.0×10^4/well in 0.1 ml) were seeded in 96-wells plates in culture medium, incubated for 24 h after which the medium was replaced by serum-free medium to synchronize the cells overnight. Cells were pre-incubated with nanobodies present in crude periplasmic extract (1/25 dilution) for 1 h, after which the RON receptor was stimulated by addition of 3.5 nM of MSP for 15 min at 37°C. The cells were resuspended in 60 µl of lysis buffer after removal of the medium. The amount of phosphorylated ERK versus total ERK was determined following the recommendations from the provider. Inhibition % was calculated using non-stimulated cells and crude periplasmic extract of irrelevant control nanobody as references. For IC_{50} determination, serum-starved T-47D cells (3.5×10^4 cells/well) were incubated with serial dilutions of

purified nanobodies (duplicates, starting at 0.6 μM) and stimulated with 1 nM of MSP for 30 min at 37°C. Quantification of the cellular the pErk levels was done using the HTRF phospho-ERK (Thr202/Tyr204) Assay (Cisbio, France).

Cell Binding Assays

To screen for binding to cell-expressed RON, 1/10 diluted crude periplasmic extracts were incubated with HEK293T-hRON and HEK293T cells (5×10^4 cells/well) in FACS buffer (PBS supplemented with 10% fetal bovine serum and 0.05% sodium azide). Nanobody binding was detected using mouse anti-FLAG antibodies followed by goat anti-mouse APC conjugate. Mean fluorescence intensity values of each clone on the HEK293T-hRON cells were divided by those of the background signal, normalized to the same ratio on HEK293T cells. Clones were considered positive with a ratio ≥2. To determine EC_{50} values, a dilution series of purified nanobodies starting at 500 nM in duplicates was added to T-47D cells (1×10^5/well). The detection was carried out as described above.

Ligand Competition ELISA

A competition ELISA was used to determine blockade of the binding of the MSP ligand to rhRON. rhRON (1 μg/ml) was immobilized directly on 96-well microtiter plates. Free-binding sites were blocked using 4% Marvel in PBS for 1 h at room temperature. Next, a dilution series of purified nanobodies starting at 1 μM (in duplicate) was added simultaneously with 2 nM in-house biotinylated MSP in 100 μl 2% Marvel PBST. MSP binding was detected *via* extravidin peroxidase.

Calculations

The sequence counts per cluster in the RON sample were multiplied with a factor of 1.21 ($3.4 \times 10^6/2.8 \times 10^6$) to normalize for the difference in total counts with the negative control sample (**Table 1**). The enrichment factor of a cluster was calculated as follows: number of sequences (normalized counts) in the RON sample belonging to that cluster divided by the number of sequences (counts) in the negative control sample belonging to the same cluster. For clusters present in the RON sample but not in the negative control sample, the counts in the latter were changed from 0 to 1 in order to calculate the enrichment factor.

Confidence intervals of proportions, EC_{50}, and IC_{50} values were calculated with GraphPad Prism 6 (GraphPad Software).

TABLE 1 | Summary of next-generation sequencing raw data and initial processing output.

	Negative control	Recepteur d'origine nantais
Selection output size (cfu)	9×10^5	8×10^6
Raw reads (counts)	1.0×10^7	7.5×10^6
Joined reads (counts)	4.9×10^6	3.6×10^6
Joinable fraction (%)	94	96
Full-length nanobody sequences (counts)	3.4×10^6	2.8×10^6
Unique sequences (counts)	1.8×10^5	1.1×10^6
Fraction unique sequences (%)	53	39
Unique sequences/selection output size (%)	200	14

RESULTS

Next-generation sequencing was used to mine the functional nanobody repertoire from a camelid immune library. The experiments below describe the NGS-based approach to identify RON-selective nanobodies from an immune library in comparison with a conventional screening campaign (**Figure 1**).

NGS: Raw Data Processing

A nanobody phage library was constructed from the PBMCs obtained from a llama immunized with rhRON. The phages were subjected for one selection round to HEK293T cells overexpressing hRON or to the parental HEK293T cells acting as negative control. The nanobody sequences were PCR-amplified from the resulting outputs, introducing a different DNA barcode to each sample (negative control and RON). A total of 1.75×10^7 raw reads were obtained (MiSeq Kit v2, 2×250 bp). After barcode deconvolution and clipping, 95% of the forward reads could be joined to their corresponding reverse reads. Translation of the joined DNA reads excluded 23–30% of the reads for further analysis caused by the introduction of frameshifts and/or premature stop codons. These clean-up steps yielded around 3×10^6 full-length nanobody sequences per sample (**Table 1**). A difference between the samples was observed with respect to sequence diversity: the negative control sample contained relatively more unique sequences, compared to the RON sample (**Table 1**). Consistent with published data (14, 15), this suggests that the selection process enriched for RON binders, resulting in a

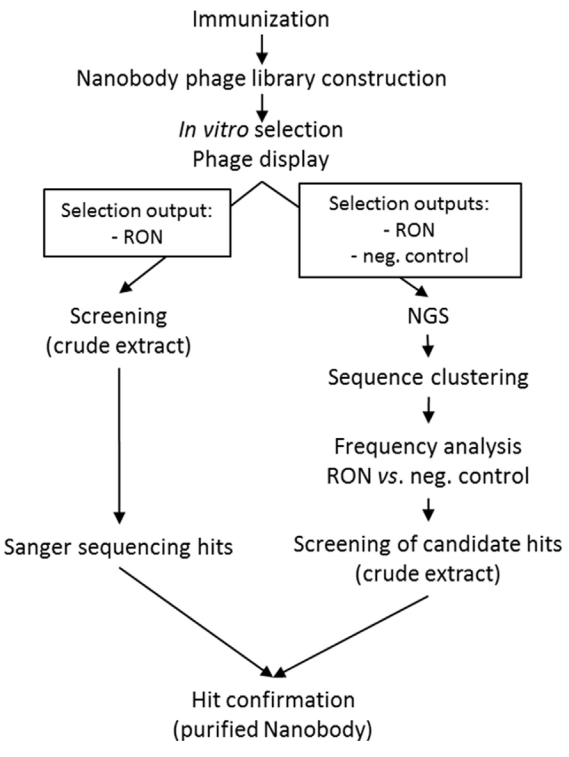

FIGURE 1 | Schematic overview of the work flows for the next-generation sequencing and conventional screening campaigns.

reduction of overall sequence diversity. The selection output sizes (**Table 1**) represent the maximum possible sequence diversity of the sequenced samples. Strong amplification of identical binders by the phage display process explains the 14% ratio of unique sequences over selection output size in the RON sample (**Table 1**). The observation that the negative control sample appears to have twofold (200% ratio) more unique sequences than theoretically possible, can be explained as follows. First, it is reasonable to assume a twofold error on the quantification of the selection output size, which was done by titrating out a phage-infected *E. coli* culture, followed by a count of colony forming units (cfu). Secondly, the different downstream PCR amplification steps and the actual MiSeq sequencing will have introduced errors resulting in an increased diversity.

NGS: Nanobody Sequence Clustering and Frequency Analysis

The large number of unique sequences, $>1 \times 10^6$ per sample (**Table 1**), prompted us to first explore a meaningful reduction of the sequence diversity, before performing an enrichment analysis to identify candidate hRON binders. More so, it is well known that errors introduced by the different PCR and sequencing steps significantly hamper the correct analysis of antibody repertoire sequence diversity, especially for true rare clones (11). Different methodologies have been explored to address error reduction, including CDR-based clustering or clonotyping, frequency-based consensus building, and replicate sequencing. Clustering of related sequences (clonal grouping and B-cell lineage trees) has been used extensively in the field of antibody repertoire sequencing to meaningfully reduce sequence diversity (12, 13). However, the main challenge here is to define a sequence identity threshold that allows for the correct clustering of (clonally) related sequences.

To this purpose, it was decided to explore sequence diversity and relatedness in a large set of publicly available nanobody sequences. Nanobody sequences were downloaded, curated (see Materials and Methods) and the 888 sequences thus obtained were further reduced to a non-redundant set of 629 unique nanobodies. Sequence clustering was done using CD-HIT (27, 28), a freely available program to efficiently handle extremely large datasets. Briefly, the algorithm sorts input sequences from long to short and processes them sequentially. The first sequence is classified as the first cluster representative, after which each of the remaining sequences is compared to the representative sequences found before it and classified as redundant or representative based on similarity. The public dataset was clustered at sequence identity thresholds ranging from 0.7 (70% identity) to 1.0 (100% identity) with no length differences being allowed. For each of the resulting clusters, we checked whether its members were related nanobodies or not. The term related as used here, refers to either targeting the same antigen, originating from the same publication, or sharing a database submission origin (date and authors). Lowering sequence identity thresholds lead to a continuous increase in cluster size (number of sequences per cluster), in number of clusters containing unrelated nanobody sequences, and in number of unrelated nanobody sequences per cluster (**Figure 2**; Table S1 in Supplementary Material). To illustrate this trend better, sequence alignments were generated (Figure S1 in Supplementary Material) with the members of a few representative clusters, identified by capital letters in **Figure 2**. The sequences captured by clusters A, B, and C, respectively, target the same antigen and thus are deemed related. On the other hand, most of the sequences captured by clusters D, E, and F target different antigens and thus are qualified as unrelated. Based on these findings, it was decided to apply an identity threshold of 0.9 for the further analysis of the NGS data set.

Similar to the observation with the clusters of unique (100% identical) sequences (**Table 1**), the negative control sample had more clusters with a sequence identity threshold of 0.9 than the RON sample (**Table 2**). The threefold reduction in number of clusters in the RON sample compared to the negative control sample indicates a decrease in sequence diversity driven by the positive selection pressure. Clusters were subdivided in three groups, based on size: orphan clusters have one single member, medium clusters contain 2–10 members, and large clusters contain >10 members. After selection on the antigen, a reduction in number of orphan and medium clusters was observed also here, while the number of large clusters increased (**Table 2**), suggestive of positive selection pressure for clusters of hRON-binding sequences. Accordingly, the fraction of sequences present in large clusters and the mean cluster sizes increased after the selection on hRON (**Table 2**).

Besides cluster size, also the enrichment factor (ratio of sequence counts per cluster in RON sample over negative control sample) can be considered as a meaningful parameter to select candidate RON-specific nanobodies. To add more statistical robustness to our analysis, only clusters with a size $\geq$10 and an enrichment factor $\geq$10 were considered. These inclusion criteria resulted in a >50-fold reduction in the number of clusters from 2.7×10^5 to 5,173 (**Table 2**; **Figure 3**). The resulting large panel of 5,173 clusters with a sequence identity threshold of 0.9—all different candidate hRON binders—has enrichment factors of up to 3,000 and cluster sizes of up to 2.7×10^5 counts (**Figure 3**).

Binding and Functional Characterization of RON Nanobodies

In the conventional screening campaign, the same immune phage library was selected for up to two rounds on cells overexpressing hRON and/or on rhRON. Crude periplasmic extracts of enriched single clones were evaluated for binding by ELISA and FACS, followed by Sanger sequencing of the hits (Table S2 in Supplementary Material; blue squares in **Figure 4A**). Sequence analysis revealed that all 35 nanobodies derived from the conventional screening were correctly identified by the NGS approach (blue squares in **Figure 3**) with enrichment factors ranging from 13 to 1,364 and cluster sizes ranging from as low as 16 to as high as 2.7×10^5 counts (Table S2 in Supplementary Material). The conventional screening approach tended to identify the most abundant sequences: 17 out of 22 clusters (77%) with a cluster size $>1.0 \times 10^4$ counts were also found *via* the conventional screening. However, small clusters with relatively small enrichment factors were also identified by the conventional approach (see blue squares in bottom left quadrant of **Figure 3**). The fact that all 35 conventionally identified nanobodies were captured by the 5,173 NGS clusters validates our frequency-based CD-HIT clustering NGS approach

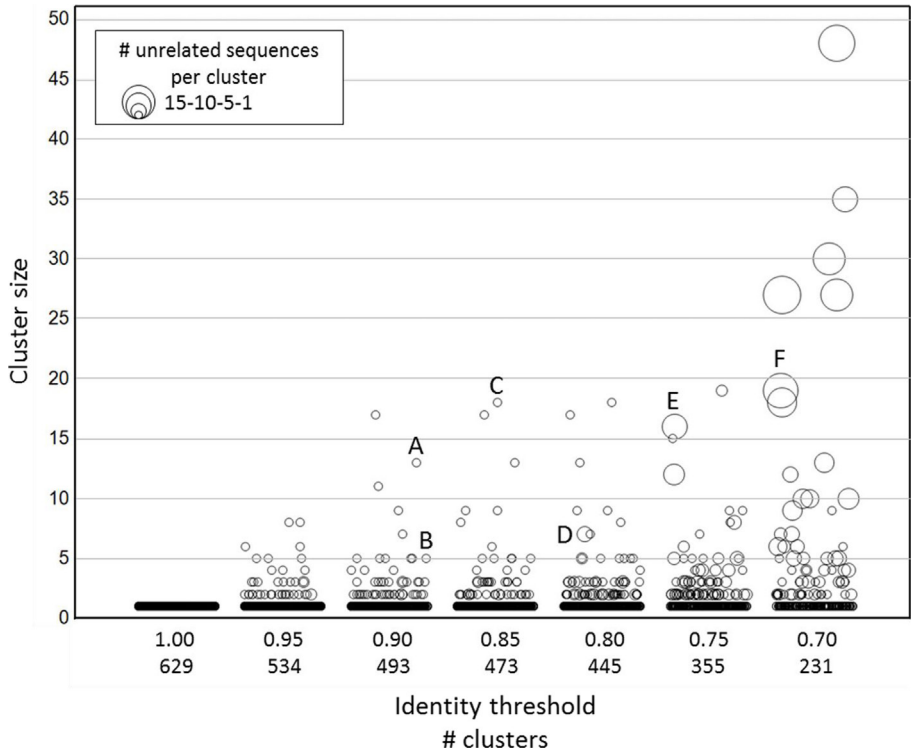

FIGURE 2 | Clustering of publicly available nanobody sequences. On the *x*-axis, the different CD-HIT clustering exercises at various sequence identity thresholds are shown, including the number of clusters at a given threshold. The *y*-axis (cluster size) displays the sequence counts per cluster. The symbol size indicates the number of unrelated nanobody sequences. The identities of the sequences in each cluster are given in Table S1 in Supplementary Material. The alignments of the sequences captured in clusters identified by a capital letter are shown in Figure S1 in Supplementary Material.

TABLE 2 | Summary of next-generation sequencing CD-HIT 0.9 clusters.

	Negative control	Recepteur d'origine nantais
All clusters (count)	8.1×10^5	2.7×10^5
Mean cluster size (# sequences)	4	11
Orphan clusters (1 member) (count)	6.5×10^5	1.9×10^5
Fraction of total sequences (%)	19	7
Medium clusters ($1 < n \leq 10$ members) (count)	1.3×10^5	6.5×10^4
Fraction of total sequences (%)	14	8
Mean cluster size (# sequences)	3.8	3.4
Large clusters ($n > 10$ members) (count)	3.1×10^4	1.2×10^4
Fraction of total sequences (%)	67	86
Mean cluster size (# sequences)	75	208

as an efficient method to identify binders. At the same time, it emphasizes the huge binding potential of the immune library that is left untapped by the conventional approach, which in this particular case means that the RON library could theoretically contain >100 times more binders.

To explore the untapped binding potential predicted by the NGS analysis, 28 additional clusters were randomly selected for evaluation in hRON-binding ELISA and FACS. The selected clusters represent a range of enrichment factors from 13 to 406 and cluster sizes from 309 to 1.4×10^4 counts (Table S2 in Supplementary Material; green triangles in **Figure 3**). The majority-rule

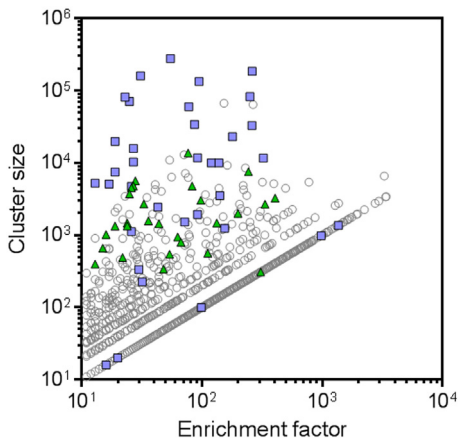

FIGURE 3 | Next-generation sequencing (NGS) frequency analysis identifies 5,173 candidate human RON binders. All symbols represent CD-HIT clusters (0.9 sequence identity threshold) with cluster sizes [sequence counts in the recepteur d'origine nantais (RON) sample] ≥10 and enrichment factors (ratio of sequence counts per cluster in RON sample over negative control sample) ≥10. Blue squares represent the clusters that were also identified by the conventional screening campaign. Green triangles represent the NGS clusters that were selected for further screening. Clusters for which no sequence counts were observed in the negative control sample were attributed a sequence count of one, in order to be able to calculate and plot enrichment factors for these clusters.

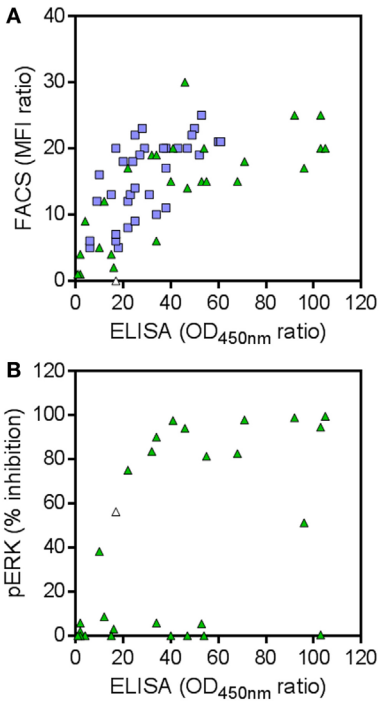

FIGURE 4 | **(A)** Binding to human RON (hRON) of candidate binders. Shown are the selective binding ratios of ELISA and FACS experiments. **(B)** Inhibition of ligand-induced ERK phosphorylation by candidate binders. Shown are the % inhibition of ERK phosphorylation and the selective binding ratios of the ELISA experiment. Green triangles represent 28 randomly selected candidate hRON-binding nanobodies, predicted by the next-generation sequencing (NGS) analysis. Blue squares represent 35 hRON-binding nanobodies, predicted by the NGS analysis and identified in the conventional screening campaign. The white triangle represents nanobody NGS00009 which was not analyzed in the FACS experiment (see Table S2 in Supplementary Material) and as such was given a selective binding ratio of 0, but scored positive in the ELISA and pERK assays.

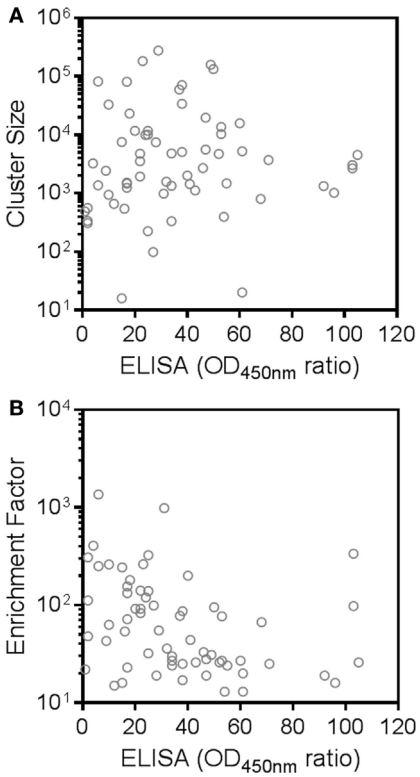

FIGURE 5 | **Absence of correlation between next-generation sequencing cluster size or enrichment factor and binding strength to recepteur d'origine nantais (RON)**. Shown are selective binding ratios from the ELISA experiment of each candidate human RON-binding nanobody and the **(A)** size (sequence counts in the RON sample) or **(B)** enrichment factor (ratio of sequence counts per cluster in RON sample over negative control sample) of the corresponding clusters.

consensus, derived from the alignment of all the sequences that make up a given cluster, was then used as the sequence representative of that cluster. In this manner, the sequence information of the most abundantly present (enriched) sequences in a given cluster is efficiently captured while at the same time PCR and read errors are filtered out (11). The consensus sequences were reverse translated, ordered as synthetic DNA, and cloned into an *E. coli* expression vector. Crude periplasmic extracts of each clone were used to assess binding to hRON in ELISA and FACS. Of these randomly selected NGS nanobodies, 25/28 (89%, with 95% confidence interval of 72–98%) bind to hRON with comparable binding levels to the clones also identified by the conventional campaign (Table S2 in Supplementary Material; compare green triangles to blue squares in **Figure 4A**). Moreover, 14/25 (56%, with 95% confidence interval of 35–76%) of the randomly selected binders show functional blockade in the MSP-induced ERK phosphorylation assay (**Figure 4B**).

An interesting observation is that there is no clear correlation between the binding strength of a given cluster—as measured by its ELISA ratio to rhRON—and its size or enrichment factor (**Figure 5**). In other words, it is probably ill-advised to overly focus on cluster size or enrichment factor as sole inclusion criteria for candidate binders. Good binders can be found in any quadrant of **Figure 3**. Extrapolating from the data of the 28 randomly selected clusters, we speculate that around 90% of the >5,000 remaining unexplored clusters could constitute RON binders, of which more than half could interfere with RON function.

Twelve hRON-binding nanobodies identified by both the NGS and conventional approaches were further characterized as purified protein. Binding affinities were assessed on T-47D cells endogenously expressing RON, indicating EC_{50} values ranging from >1 μM to 50 pM, and with off-rates ranging from 7×10^{-3} to 3×10^{-4} s^{-1} (**Table 3**). More so, all nanobodies completely inhibited MSP-induced ERK phosphorylation in T-47D cells with IC_{50} values ranging from 300 to 5 nM (**Table 3**; **Figure 6**). Nine out of twelve fully block the binding of the MSP ligand to hRON, three others are competing only poorly—if at all—with MSP binding in the tested concentration range (**Table 3**; **Figure 6**). Competition experiments revealed that the nanobodies could be assigned to four non-overlapping epitope bins. Two of the nanobodies share a competing footprint with two epitope bins. Together these data indicate that functionally inhibiting anti-hRON nanobodies are present in the immune repertoire with good potencies and epitope diversity.

TABLE 3 | Overview characterization of selected anti-human RON nanobodies.

ID	k_{off} (s^{-1})	EC_{50} (M) binding	IC_{50} (M) inhibition of MSP binding[a]	IC_{50} (M) inhibition of ERK phosphorylation[a]	Epitope bin
8A09	6.2×10^{-4}	9.3×10^{-11}	1.6×10^{-8} (98%)	4.9×10^{-9} (100%)	A
8F09	6.4×10^{-4}	2.0×10^{-10}	1.2×10^{-8} (98%)	5.2×10^{-9} (99%)	A
11F05	4.6×10^{-4}	5.3×10^{-11}	9.7×10^{-9} (98%)	6.0×10^{-9} (100%)	A
8A12	2.8×10^{-3}	1.2×10^{-10}	7.0×10^{-9} (96%)	1.3×10^{-8} (100%)	C–D
8D12	5.1×10^{-4}	6.1×10^{-11}	1.1×10^{-8} (98%)	1.5×10^{-8} (100%)	A
8C09	2.3×10^{-3}	1.7×10^{-7}	4.7×10^{-8} (90%)	3.3×10^{-8} (100%)	A
8G11	9.7×10^{-4}	3.4×10^{-8}	2.4×10^{-7} (92%)	8.2×10^{-8} (98%)	B
5C06	3.7×10^{-3}	2.0×10^{-7}	2.2×10^{-8} (98%)	1.2×10^{-7} (98%)	A
2C06	6.9×10^{-3}	$>1.0 \times 10^{-6}$	2.5×10^{-7} (90%)	3.0×10^{-7} (92%)	A
5G04	2.9×10^{-4}	3.3×10^{-10}	n.a. (92%)	4.9×10^{-9} (100%)	C–D
2D07	5.0×10^{-3}	5.0×10^{-9}	n.a. (30%)	1.8×10^{-8} (100%)	D
2B09	1.8×10^{-3}	1.3×10^{-9}	n.a. (67%)	9.6×10^{-8} (96%)	C

[a]*Efficacy or maximum inhibition is shown between parentheses.*

n.a.: IC_{50} values could not be determined due to incomplete dose–responses in the range of concentrations tested. The reported inhibition corresponds to the % inhibition observed at 1 μM of 2D07 and 2 μM of 5G04 and 2B09.

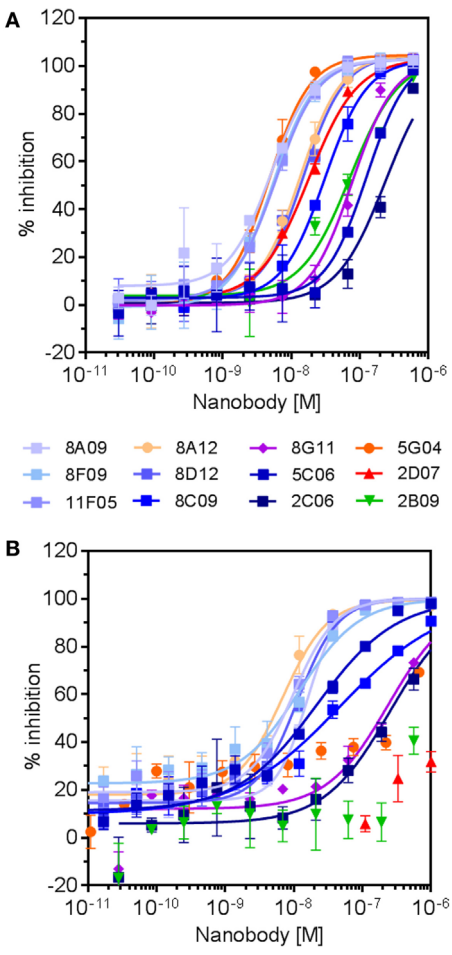

FIGURE 6 | Dose–response curves of selected anti-human RON (hRON) nanobodies inhibiting ligand-induced ERK phosphorylation (A) and binding of ligand to hRON (B). Symbol colors relate to the different epitope bins to which the nanobodies belong (**Table 3**): bin A (shades of blue), bin B (purple), bin C (green), bin D (red), and bin C–D (shades of orange).

Sequence Diversity of RON Nanobodies

Sequence analysis of the 28 randomly selected nanobodies and the 35 nanobodies identified by both conventional and NGS campaigns revealed an extensive functional sequence diversity (**Figure 7**). This is best illustrated by the observation that most nanobodies have very different CDR sequences. Together, these results confirm that our NGS-based approach is able to correctly predict large numbers of unrelated functional nanobody sequences targeting the same antigen and illustrate the functional diversity and quality of the outbred camelid's heavy chain-only immune response.

DISCUSSION

A classic difficulty in the field of antibody repertoire sequencing is the clustering of clonally related sequences derived from the same progenitor during B cell maturation (12, 13). While NGS analysis for antibody-derived binders such as scFvs and Fabs often is limited to the CDR3 region, the short length of nanobodies brings the advantage to obtain high quality full-length coverage by pairing of forward and reverse reads obtained with Illumina 2 × 250 bp chemistry, as demonstrated before (17–21). As a consequence, the downstream data analysis can reliably make use of all the FR and CDR sequence information. Without experimental data to support relatedness of antibody sequences at the phenotypic level, selecting a sequence identity threshold for clustering is relatively arbitrary. Here, we applied an inverse approach to the problem: rather than defining relatedness, we sought to define unrelatedness. Using a large set of publicly available nanobody sequences, we explored a range of sequence identity thresholds. The diverse nature of this data set makes it a highly representative source to sample unrelatedness. Clustering of unrelated nanobody sequences became apparent at sequence identity thresholds of 80% and lower. We selected a threshold of 90% to cluster the NGS dataset and subsequently obtained a high degree of experimental validation for these clusters. Other sequence identity thresholds could of course be explored,

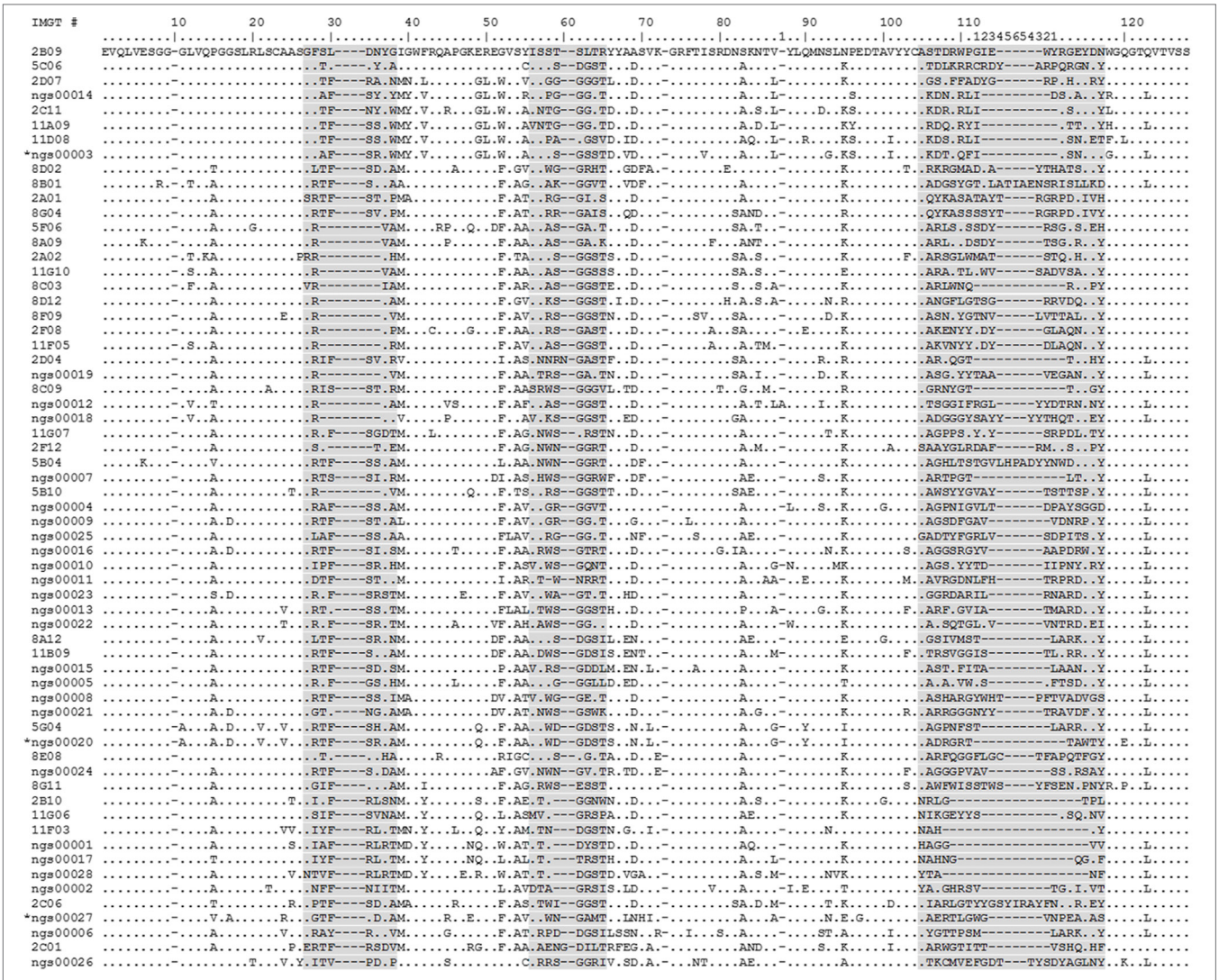

FIGURE 7 | **Alignment of human RON (hRON) nanobodies (see also Table S2 in Supplementary Material)**. The 28 randomly selected candidate hRON-binding nanobodies are identified by the acronym "NGS" followed by a five digit number. The three sequences marked by an asterisk (NGS00003, NGS00020, and NGS00027) are the non-binding sequences from the randomly selected panel of 28. The 35 nanobodies discovered in the conventional screening campaign and predicted by the next-generation sequencing (NGS) analysis are identified by a one or two digit number, followed by a letter, followed by a two digit number. Numbering of alignment positions was done according to the IMGT V-DOMAIN system (26). CDR regions are highlighted in gray. Dots represent residues identical to the top sequence. Dashes represent gaps introduced by the alignment.

involving a tradeoff between the number of candidate clusters and their relative correctness. An increased stringency results in a larger number of clusters containing fewer unrelated sequences, whereas a lower stringency results in fewer clusters to choose from, with a higher proportion of unrelated sequences. The concept of using the diversity of publicly available data to establish meaningful sequence identity thresholds for clustering of related sequences is applicable to other types of antibody-derived binding domains and simple binding scaffolds.

The major challenge was the choice of inclusion criteria to representatively sample such a large diversity of candidate binders. One way to reduce the number of candidate binders is to apply more stringent cutoff values to cluster size and enrichment factor. However, this creates a bias toward the more abundant binders which are also identified by the conventional screening approach, as shown here. More so, we did not observe a clear correlation between the binding properties of a given cluster and its size or enrichment factor. In other words, good binders can be found among the more abundant and enriched clusters as well as among the less frequent clusters. Alternatively, lowering the sequence identity threshold for clustering would result in a lower number of clusters to sample from. However, as discussed above, this would increase the likelihood of clustering unrelated sequences, resulting in a higher proportion of erratic majority-rule consensuses as representatives. By random sampling representatively across a wide range of cluster sizes and enrichment factors, we achieved

around 90% success rate in identifying anti-hRON nanobodies with binding characteristics and functional blockade comparable to those of the conventional screening campaign. Roughly half of these binders functionally inhibited hRON signaling. As such, it appears reasonable to assume that a large fraction of the >5,000 other enriched sequences qualify as nanobodies functionally blocking hRON.

The abovementioned high success rate also validates the combination of clustering related sequences and majority-rule consensus building as a very effective method to deal with PCR-induced and NGS read errors.

An alternative approach could be envisaged, leaving out the negative control sample, whereby sequencing and data analysis costs would be halved. When applying cluster size >10 as the inclusion criterion, this would increase the number of clusters-of-interest in the RON sample from 5,173 to 1.2×10^4 (**Table 2**). Although a large fraction of these clusters can be expected to be enriched and functional, it is reasonable to assume that a fair number of these would be enriched by the phage display selections for the wrong reasons (display efficiency, stickiness, off-target binding). As a result, the fraction of false positives would be higher in comparison to an NGS approach including a proper negative control phage display sample. Hence, the upstream sequencing and analysis cost savings could be offset by an increase in downstream gene synthesis and screening costs.

Twelve of the hRON-binding nanobodies that were further characterized cover four different non-overlapping epitopes. Most of them inhibit MSP ligand binding to hRON and all fully block downstream ERK phosphorylation. This limited sample represents an interesting mix of ligand-dependent and -independent modes-of-action for the blocking of RON signaling. Many examples document the ability of the outbred camelid's immune response to generate nanobodies against challenging targets including ion channels (29–31), GPCRs (32, 33), small molecules and toxins (34, 35), viruses (34, 36) and enzymes (2). To our knowledge, this is the first example to illustrate the potential extent of an outbred camelid's functional immune response in terms of sequence diversity.

In conclusion, an NGS-based discovery approach combining full-length sequence clustering and the use of majority-rule consensuses as representatives reveals a highly diverse landscape of selective, functional nanobodies.

ETHICS STATEMENT

This study was carried out in accordance to EU animal welfare legislation and after approval of the local ethics committee "Ethical Committee Ablynx Camelid Facility LA1400575."

AUTHOR CONTRIBUTIONS

DF, RM, JC, JA, YB, RF, DR, RT, DT, and LV performed experiments. AV, PD, MC, CS, and BD conceived and designed experiments and analyzed data. ML, PD, and BD designed and build the bioinformatics pipeline. PD, AV, CS, and BD wrote the manuscript. All authors read and critically reviewed the manuscript.

ACKNOWLEDGMENTS

The authors want to thank Samuel Arvidsson and Berthold Fartmann at LGC Genomics for their handling of the Illumina MiSeq samples and raw data processing.

FUNDING

This work was supported by Ablynx N.V.

SUPPLEMENTARY MATERIAL

The Supplementary Material for this article can be found online at http://journal.frontiersin.org/article/10.3389/fimmu.2017.00420/full#supplementary-material.

REFERENCES

1. Steeland S, Vandenbroucke RE, Libert C. Nanobodies as therapeutics: big opportunities for small antibodies. *Drug Discov Today* (2016) 21:1076–113. doi:10.1016/j.drudis.2016.04.003
2. Muyldermans S. Nanobodies: natural single-domain antibodies. *Annu Rev Biochem* (2013) 82:775–97. doi:10.1146/annurev-biochem-063011-092449
3. Pardon E, Laeremans T, Triest S, Rasmussen SGF, Wohlkönig A, Ruf A, et al. A general protocol for the generation of nanobodies for structural biology. *Nat Protoc* (2014) 9:674–93. doi:10.1038/nprot.2014.039
4. Bencurova E, Pulzova L, Flachbartova Z, Bhide M. A rapid and simple pipeline for synthesis of mRNA-ribosome-V(H)H complexes used in single-domain antibody ribosome display. *Mol Biosyst* (2015) 11:1515–24. doi:10.1039/c5mb00026b
5. Fleetwood F, Devoogdt N, Pellis M, Wernery U, Muyldermans S, Ståhl S, et al. Surface display of a single-domain antibody library on Gram-positive bacteria. *Cell Mol Life Sci* (2013) 70:1081–93. doi:10.1007/s00018-012-1179-y
6. Koide A, Koide S. Affinity maturation of single-domain antibodies by yeast surface display. *Methods Mol Biol* (2012) 911:431–43. doi:10.1007/978-1-61779-968-6_26
7. De Schutter K, Callewaert N. Pichia surface display: a tool for screening single domain antibodies. *Methods Mol Biol* (2012) 911:125–34. doi:10.1007/978-1-61779-968-6_8
8. Ryckaert S, Pardon E, Steyaert J, Callewaert N. Isolation of antigen-binding camelid heavy chain antibody fragments (nanobodies) from an immune library displayed on the surface of *Pichia pastoris*. *J Biotechnol* (2010) 145:93–8. doi:10.1016/j.jbiotec.2009.10.010
9. Pellis M, Muyldermans S, Vincke C. Bacterial two hybrid: a versatile one-step intracellular selection method. *Methods Mol Biol* (2012) 911:135–50. doi:10.1007/978-1-61779-968-6_9
10. Gao X, Hu X, Tong L, Liu D, Chang X, Wang H, et al. Construction of a camelid VHH yeast two-hybrid library and the selection of VHH against haemagglutinin-neuraminidase protein of the Newcastle disease virus. *BMC Vet Res* (2016) 12:39. doi:10.1186/s12917-016-0664-1
11. Glanville J, D'Angelo S, Khan TA, Reddy ST, Naranjo L, Ferrara F, et al. Deep sequencing in library selection projects: what insight does it bring? *Curr Opin Struct Biol* (2015) 33:146–60. doi:10.1016/j.sbi.2015.09.001
12. Hoehn KB, Fowler A, Lunter G, Pybus OG. The diversity and molecular evolution of B-cell receptors during infection. *Mol Biol Evol* (2016) 33:1147–57. doi:10.1093/molbev/msw015
13. Yaari G, Kleinstein SH. Practical guidelines for B-cell receptor repertoire sequencing analysis. *Genome Med* (2015) 7:121. doi:10.1186/s13073-015-0243-2
14. Ravn U, Gueneau F, Baerlocher L, Osteras M, Desmurs M, Malinge P, et al. By-passing in vitro screening – next generation sequencing technologies

applied to antibody display and in silico candidate selection. *Nucleic Acids Res* (2010) 38:e193. doi:10.1093/nar/gkq789
15. Ravn U, Didelot G, Venet S, Ng K-T, Gueneau F, Rousseau F, et al. Deep sequencing of phage display libraries to support antibody discovery. *Methods* (2013) 60:99–110. doi:10.1016/j.ymeth.2013.03.001
16. Naso MF, Lu J, Panavas T. Deep sequencing approaches to antibody discovery. *Curr Drug Discov Technol* (2014) 11:85–95. doi:10.2174/1570163811310 6660040
17. Fridy PC, Li Y, Keegan S, Thompson MK, Nudelman I, Scheid JF, et al. A robust pipeline for rapid production of versatile nanobody repertoires. *Nat Methods* (2014) 11:1253–60. doi:10.1038/nmeth.3170
18. Henry KA, Tanha J, Hussack G. Identification of cross-reactive single-domain antibodies against serum albumin using next-generation DNA sequencing. *Protein Eng Des Sel* (2015) 28:379–83. doi:10.1093/protein/gzv039
19. Miyazaki N, Kiyose N, Akazawa Y, Takashima M, Hagihara Y, Inoue N, et al. Isolation and characterization of antigen-specific alpaca (*Lama pacos*) VHH antibodies by biopanning followed by high-throughput sequencing. *J Biochem* (2015) 158:205–15. doi:10.1093/jb/mvv038
20. Henry KA, Hussack G, Collins C, Zwaagstra JC, Tanha J, MacKenzie CR. Isolation of TGF-β-neutralizing single-domain antibodies of predetermined epitope specificity using next-generation DNA sequencing. *Protein Eng Des Sel* (2016) 29:439–43. doi:10.1093/protein/gzw043
21. Turner KB, Naciri J, Liu JL, Anderson GP, Goldman ER, Zabetakis D. Next-generation sequencing of a single domain antibody repertoire reveals quality of phage display selected candidates. *PLoS One* (2016) 11:e0149393. doi:10.1371/journal.pone.0149393
22. Ronsin C, Muscatelli F, Mattei MG, Breathnach R. A novel putative receptor protein tyrosine kinase of the met family. *Oncogene* (1993) 8:1195–202.
23. Gaudino G, Follenzi A, Naldini L, Collesi C, Santoro M, Gallo KA, et al. RON is a heterodimeric tyrosine kinase receptor activated by the HGF homologue MSP. *EMBO J* (1994) 13:3524–32.
24. Wang M-H, Zhang R, Zhou Y-Q, Yao H-P. Pathogenesis of RON receptor tyrosine kinase in cancer cells: activation mechanism, functional crosstalk, and signaling addiction. *J Biomed Res* (2013) 27:345–56. doi:10.7555/JBR.27.20130038
25. Magoč T, Salzberg SL. FLASH: fast length adjustment of short reads to improve genome assemblies. *Bioinformatics* (2011) 27:2957–63. doi:10.1093/bioinformatics/btr507
26. Lefranc M-P, Pommié C, Ruiz M, Giudicelli V, Foulquier E, Truong L, et al. IMGT unique numbering for immunoglobulin and T cell receptor variable domains and Ig superfamily V-like domains. *Dev Comp Immunol* (2003) 27:55–77. doi:10.1016/S0145-305X(02)00039-3
27. Li W, Godzik A. Cd-hit: a fast program for clustering and comparing large sets of protein or nucleotide sequences. *Bioinformatics* (2006) 22:1658–9. doi:10.1093/bioinformatics/btl158
28. Fu L, Niu B, Zhu Z, Wu S, Li W. CD-HIT: accelerated for clustering the next-generation sequencing data. *Bioinformatics* (2012) 28:3150–2. doi:10.1093/bioinformatics/bts565
29. Wei G, Meng W, Guo H, Pan W, Liu J, Peng T, et al. Potent neutralization of influenza A virus by a single-domain antibody blocking M2 ion channel protein. *PLoS One* (2011) 6:e28309. doi:10.1371/journal.pone.0028309
30. Hassiki R, Labro AJ, Benlasfar Z, Vincke C, Somia M, El Ayeb M, et al. Dromedary immune response and specific Kv2.1 antibody generation using a specific immunization approach. *Int J Biol Macromol* (2016) 93:167–71. doi:10.1016/j.ijbiomac.2016.06.031
31. Danquah W, Meyer-Schwesinger C, Rissiek B, Pinto C, Serracant-Prat A, Amadi M, et al. Nanobodies that block gating of the P2X7 ion channel ameliorate inflammation. *Sci Transl Med* (2016) 8:366ra162. doi:10.1126/scitranslmed.aaf8463
32. Mujić-Delić A, de Wit RH, Verkaar F, Smit MJ. GPCR-targeting nanobodies: attractive research tools, diagnostics, and therapeutics. *Trends Pharmacol Sci* (2014) 35:247–55. doi:10.1016/j.tips.2014.03.003
33. Cromie KD, Van Heeke G, Boutton C. Nanobodies and their use in GPCR drug discovery. *Curr Top Med Chem* (2015) 15:2543–57. doi:10.2174/1568026615666150701113549
34. Wesolowski J, Alzogaray V, Reyelt J, Unger M, Juarez K, Urrutia M, et al. Single domain antibodies: promising experimental and therapeutic tools in infection and immunity. *Med Microbiol Immunol* (2009) 198:157–74. doi:10.1007/s00430-009-0116-7
35. Bever CS, Dong J-X, Vasylieva N, Barnych B, Cui Y, Xu Z-L, et al. VHH antibodies: emerging reagents for the analysis of environmental chemicals. *Anal Bioanal Chem* (2016) 408:5985–6002. doi:10.1007/s00216-016-9585-x
36. Vanlandschoot P, Stortelers C, Beirnaert E, Ibañez LI, Schepens B, Depla E, et al. Nanobodies®: new ammunition to battle viruses. *Antiviral Res* (2011) 92:389–407. doi:10.1016/j.antiviral.2011.09.002

Conflict of Interest Statement: All authors are or have been employees of Ablynx N.V.

Citation: Deschaght P, Vintém AP, Logghe M, Conde M, Felix D, Mensink R, Gonçalves J, Audiens J, Bruynooghe Y, Figueiredo R, Ramos D, Tanghe R, Teixeira D, Van de Ven L, Stortelers C and Dombrecht B (2017) Large Diversity of Functional Nanobodies from a Camelid Immune Library Revealed by an Alternative Analysis of Next-Generation Sequencing Data. Front. Immunol. 8:420. doi: 10.3389/fimmu.2017.00420

frontiers in Immunology

ORIGINAL RESEARCH
published: 30 October 2017
doi: 10.3389/fimmu.2017.01406

A Novel Affinity Tag, ABTAG, and Its Application to the Affinity Screening of Single-Domain Antibodies Selected by Phage Display

Greg Hussack[1], Toya Nath Baral[1†], Jason Baardsnes[2], Henk van Faassen[1], Shalini Raphael[1], Kevin A. Henry[1], Jianbing Zhang[1*†] and C. Roger MacKenzie[1]*

[1] Human Health Therapeutics Research Centre, National Research Council Canada, Ottawa, ON, Canada, [2] Human Health Therapeutics Research Centre, National Research Council Canada, Montréal, QC, Canada

OPEN ACCESS

Edited by:
Abdul Qader Abbady, Atomic Energy Commission of Syria, Syria

Reviewed by:
Serge Muyldermans, Vrije Universiteit Brussel, Belgium
Daniel Olive, Institut national de la santé et de la recherche médicale, France

***Correspondence:**
Greg Hussack
greg.hussack@nrc-cnrc.gc.ca;
Jianbing Zhang
jianbing.oliver@outlook.com

†Present address:
Toya Nath Baral, Merck and Company Inc., Palo Alto, CA, United States;
Jianbing Zhang, Xiangxue Pharma, Guangzhou, China

Specialty section:
This article was submitted to Vaccines and Molecular Therapeutics, a section of the journal Frontiers in Immunology

Received: *23 August 2017*
Accepted: *11 October 2017*
Published: *30 October 2017*

Citation:
Hussack G, Baral TN, Baardsnes J, van Faassen H, Raphael S, Henry KA, Zhang J and MacKenzie CR (2017) A Novel Affinity Tag, ABTAG, and Its Application to the Affinity Screening of Single-Domain Antibodies Selected by Phage Display. Front. Immunol. 8:1406. doi: 10.3389/fimmu.2017.01406

ABTAG is a camelid single-domain antibody (sdAb) that binds to bovine serum albumin (BSA) with low picomolar affinity. In surface plasmon resonance (SPR) analyses using BSA surfaces, bound ABTAG can be completely dissociated from the BSA surfaces at low pH, over multiple cycles, without any reduction in the capacity of the BSA surfaces to bind ABTAG. A moderate throughput, SPR-based, antibody screening assay exploiting the unique features of ABTAG is described. Anti-carcinoembryonic antigen-related cell adhesion molecule 6 (CEACAM6) sdAbs were isolated from a phage-displayed sdAb library derived from the heavy chain antibody repertoire of a llama immunized with CEACAM6. Following one or two rounds of panning, enriched clones were expressed as ABTAG fusions in microtiter plate cultures. The sdAb-ABTAG fusions from culture supernatants were captured on BSA surfaces and CEACAM6 antigen was then bound to the captured molecules. The SPR screening method gives a read-out of relative expression levels of the fusion proteins and kinetic and affinity constants for CEACAM6 binding by the captured molecules. The library was also panned and screened by conventional methods and positive clones were subcloned and expressed for SPR analysis. Compared to conventional panning and screening, the SPR-based ABTAG method yielded a considerably higher diversity of binders, some with affinities that were three orders of magnitude higher affinity than those identified by conventional panning.

Keywords: antibody discovery, phage display, surface plasmon resonance, single-domain antibody, nanobody, V_HH, carcinoembryonic antigen-related cell adhesion molecule 6

INTRODUCTION

Over the past 25 years, *in vitro* display technologies, most notably phage and yeast display, have increasingly become the methods of choice for the isolation and affinity maturation of monoclonal antibody fragments. This is especially the case in instances where antibodies with particular properties are required (1, 2), as *in vitro* display technologies allow for the selection process to be biased toward desired outcomes (3). To take full advantage of the power of these technologies it is preferable to screen relatively large numbers of clones after one or two selection cycles to increase the odds of identifying clones with the desired properties. There is ongoing interest, therefore, in the

development of more effective and rapid methods for screening antibodies for expression level and for target antigen specificity and affinity.

The classical protocol for isolating antibody fragments against a given target by phage display technology generally includes immunizing an animal, measuring the immune response, constructing a phage-displayed antibody fragment library and performing three to five rounds of panning to enrich for clones that bind to the target. This generally gives a manageable number of clones for subsequent expression, purification and characterization. The antibody fragments can be fragments antigen-binding (Fabs) (4), single-chain variable fragments (scFvs) (4), or single-domain antibodies (sdAbs). sdAbs can be the variable domains (V_HHs) of camelid heavy chain antibodies (5, 6), the variable domains ($V_{NAR}s$) of shark immunoglobulin new antigen receptors (7), the variable heavy domains (V_Hs) of conventional antibodies (8, 9), or the variable light domains (V_Ls) of conventional antibodies (10). After panning, phage ELISA is performed on randomly picked clones to identify the leads. Leads are typically expressed and purified for affinity measurements and functional characterization. This is a relatively slow, costly and laborious process that generally yields no more than a dozen binders, and often fewer.

In this study, we compare different approaches to the isolation sdAbs against carcinoembryonic antigen-related cell adhesion molecule 6 (CEACAM6) from a phage-displayed immune llama V_HH library. We have used a classical panning protocol followed by subcloning, expression and purification of sdAbs for surface plasmon resonance (SPR) analyses. We also describe a screening method in which anti-CEACAM6 sdAbs are fused to an anti-bovine serum albumin (anti-BSA) sdAb characterized by extremely tight, but readily reversible, binding to BSA. The sdAb, initially termed BSA12, has a K_D of 4 pM and a k_d of 9×10^{-6} s^{-1}, equivalent to an sdAb:BSA half-life of approximately 21 h, yet it can be completely dissociated from BSA surfaces with a 3 s pulse of 100 mM HCl (11, 12). In the SPR-based screening method described here (**Figure 1A**), panning-enriched sdAb clones are expressed in fusion with the sdAb BSA12 and captured on BSA surfaces for CEACAM6 binding measurements. For applications such as this, we have given the anti-BSA sdAb BSA12 a new designation, ABTAG, with "AB" alluding to the fact that it is an antibody fragment or, alternatively, that it is an albumin-binding "TAG." With this new methodology, we isolated several extremely high-affinity anti-CEACAM6 sdAbs that were missed by classical panning and screening of the same phage-displayed library. The ABTAG technology should have general utility in the isolation of antibody fragments from phage display libraries—i.e., it could be applied to V_L, V_H, V_{NAR}, scFv, and Fab libraries. ABTAG technology has previously been used to screen sdAbs specific to human Fc (fragment crystallizable) region (13).

MATERIALS AND METHODS

Immunization and Serology

A llama (*Lama glama*) was immunized five times (days 1, 21, 35, 49, and 63) subcutaneously with approximately 100 μg of recombinant CEACAM6 [N- and A-domains, residues 35–232; (14)] per injection, kindly provided by Helix BioPharma (Aurora, ON, Canada), with Complete Freund's Adjuvant on day 1 and Incomplete Freund's Adjuvant on the remaining days. On days 1, 22, 36, 49, 64, and 71 blood (50 mL) was collected, from which sera and peripheral blood lymphocytes were isolated (15). This study was carried out in accordance with Animal Use Protocols approved by the National Research Council Canada Animal Care Committee.

Microtiter plates were coated with 10 μg/mL of CEACAM6 overnight at 4°C in 15 mM Na_2CO_3, pH 9.6, followed by blocking with 2% fat-free dry milk (BioRad Laboratories, Mississauga, ON, Canada) in PBS. Serially diluted serum was then added to the wells. Detection of llama IgGs was performed with goat anti-llama IgG (Bethyl Laboratories, Montgomery, TX, USA) and a horseradish peroxidase anti-goat IgG conjugate (Cedarlane Laboratories, Burlington, ON, Canada). Finally, peroxidase substrate (KPL, Gaithersburg, MD) was added followed by 1 M H_3PO_4 after 15 min. The absorbance at 450 nm was then measured.

Phage-Displayed Library Construction

RNA was extracted from peripheral blood lymphocytes obtained from blood drawn on day 71 by using a QIAamp RNA Blood Mini Kit (Qiagen Inc., Mississauga, ON, Canada). cDNA was synthesized by using a first-strand cDNA synthesis kit (GE Healthcare, Mississauga, ON, Canada). Sense primers MJ1, MJ2, and MJ3 and antisense primers CH2 and CH2b3 (15) were used to amplify V_HH and V_H-C_H1 encoding regions (600 and 900 bp, respectively). These two fragments were separated by agarose gel electrophoresis and the V_HH band was purified from the gel. Nested PCR, using primers MJ7 and MJ8 (15), was performed to amplify all V_HHs. The final PCR fragments were ligated into the phagemid vector pMED1 (16) using *Sfi*I restriction sites. The ligated vector was used to transform electrocompetent *Escherichia coli* TG1 cells.

Selection of sdAbs by Conventional Panning

The V_HH repertoire was expressed on phage surfaces after rescuing with M13K07 helper phage. Three rounds of phage display panning were conducted (**Figure 1B**) as described (17). Briefly, specific V_HHs against CEACAM6 were enriched by *in vitro* selection on microtiter plates coated with antigen (10 μg/mL). Phage particles eluted with 100 mM triethylamine, pH 11, were immediately neutralized with 1 M Tris–HCl, pH 7.4, and used to infect exponentially growing TG1 cells. To assess the enrichment of phage particles carrying antigen-specific V_HHs, serial dilutions of the phage eluted from antigen coated *vs* non-coated control wells were used to infect exponentially growing TG1 cells. Individual colonies randomly picked after all three rounds of panning were tested for binding to CEACAM6 by phage ELISA according to standard procedures (17). Unique clones identified by DNA sequencing were subcloned in pSJF2H, expressed, and purified, as described previously (15), for SPR analysis.

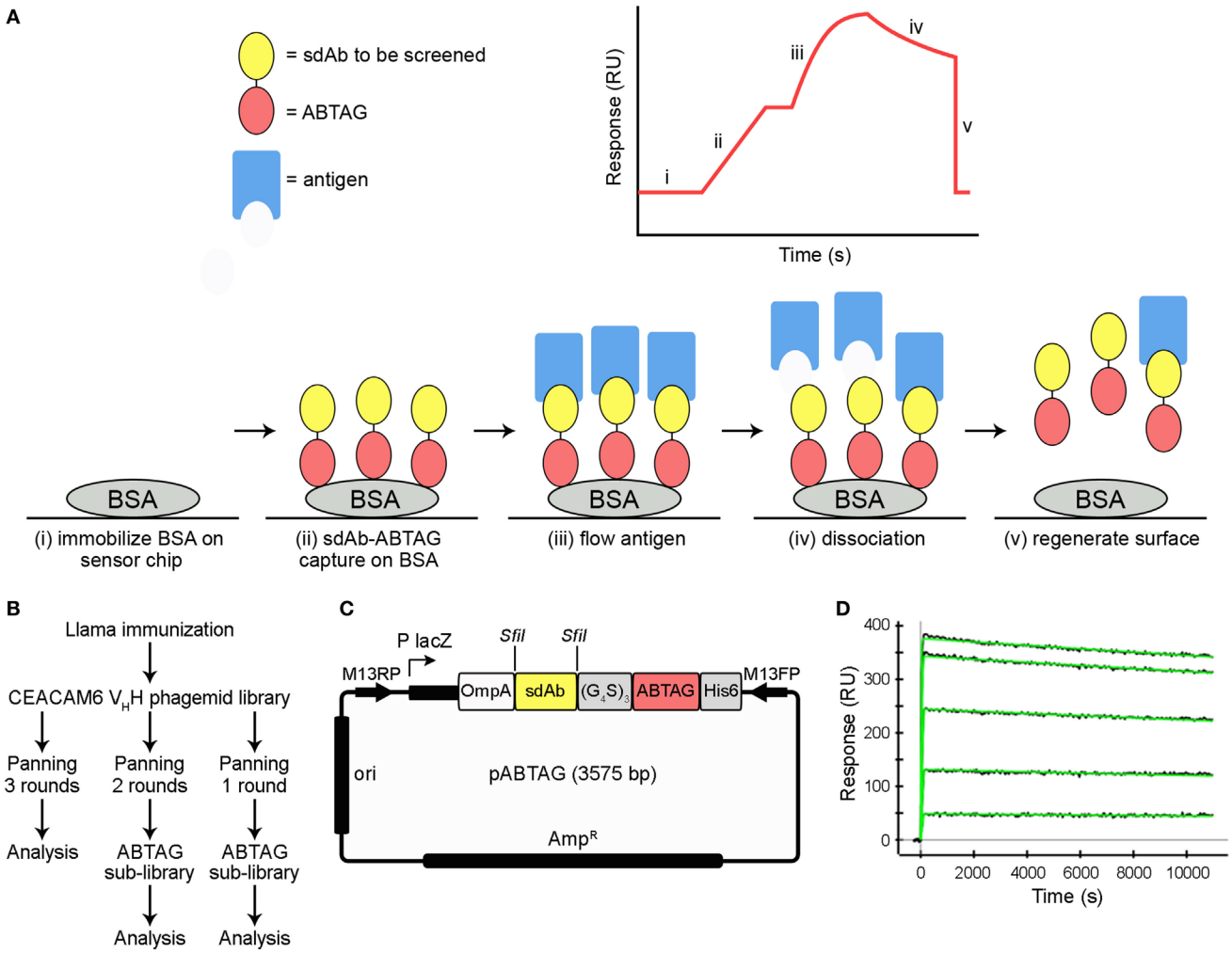

FIGURE 1 | Summary of ABTAG technology and single-domain antibody (sdAb) isolation. Schematic diagram of the ABTAG/surface plasmon resonance (SPR)-based screening method for the evaluation of enriched sdAb clones from phage display panning **(A)**. While anti-CEACAM6 sdAb clones obtained after three rounds of panning were screened by phage ELISA, pools of phage clones enriched after either one or two rounds of phage display library panning were directly subcloned into pABTAG (3,575 bp, representative sdAb of average length), creating two sublibraries, for expression as sdAb-ABTAG fusions by capture on BSA surfaces **(B,C)**. A representative sensorgram demonstrates sdAb-ABTAG fusion proteins are stably retained by BSA surfaces because of an extremely slow dissociation rate **(D)**. BSA, bovine serum albumin; RU, resonance unit.

Subcloning Phage-Displayed sdAbs for sdAb-ABTAG Expression

Phage ELISA was performed with 20–50 monoclonal phage eluted from rounds 1 and 2 to estimate the percentage of phage clones binding to antigen. Eluted phage pools were then used for the construction of two sublibraries, one from round 1 eluted phage and a second from round 2 eluted phage, in which enriched clones were fused to ABTAG in a vector designed for this purpose (**Figures 1B,C**). Briefly, DNA encoding the V_HHs was amplified from eluted phage pools with the introduction of *Sfi*I restriction sites at both ends of the fragments. The PCR fragments were then ligated into the ABTAG fusion vector. Individual clones were inoculated into LB medium supplemented with 100 µg/mL ampicillin in 96-well microtiter plates and grown at 37°C overnight with shaking. Supernatants were collected after centrifugation of the cell cultures for ELISA and SPR.

SPR Analysis of sdAb-ABTAG Binding Affinity to BSA

For ProteOn (BioRad Laboratories Canada Inc., Mississauga, ON, Canada) analysis of sdAb-ABTAG affinity for BSA, covalently immobilized BSA surfaces were prepared using NHS/*N*-ethyl-*N*′-(3-diethylaminopropyl) carbodiimide hydrochloride (EDC) coupling. Immobilization reagents, *N*-sulfohydroxysuccinimide (sNHS), EDC, and ethanolamine were from the ProteOn Amine Coupling Kit (BioRad Laboratories Canada Inc.). The BSA capture surface was created by immobilizing 6.0 µg/mL Fraction V BSA (EMD Chemicals Inc., Gibbstown, NJ, USA) diluted in 10 mM

sodium acetate buffer, pH 4.5, onto a GLM chip activated by a 1:10 dilution of sNHS/EDC that was injected for 300 s at 30 µL/min in the vertical direction as recommended by the manufacturer. Approximately 1,700 resonance units (RUs) of a 2.5 µg/mL BSA solution in 10 mM sodium acetate, pH 4.5, were then immobilized in the vertical direction in order to generate blank control spots in the horizontal direction for referencing. Surfaces were quenched with a 300 s injection of 1 M ethanolamine at 30 µL/min. For affinity determination, a 200 nM threefold dilution series of an sdAb-ABTAG fusion protein clone with buffer blank was injected in triplicate over the BSA surface. Each injection was carried out at 50 µL/min for 120 s with a 3 h dissociation. All experiments were carried out at 25°C and in running buffer consisting of 10 mM HEPES, pH 7.4, containing 150 mM NaCl, 0.05% Tween 20, and 3 mM EDTA. Data from the three independent sensorgrams were double referenced to the control spots and independently fitted to a 1:1 interaction model after determining that the binding was not mass-transport limited.

Screening of CEACAM6 Binding to sdAb-ABTAG Fusions by Dissociation Rate Constants

The binding of CEACAM6 to sdAb-ABTAG fusions captured on immobilized BSA was determined by SPR using a Biacore 3000 (GE Healthcare). Approximately 8,000 RUs of BSA (Sigma-Aldrich Canada, Oakville, ON, Canada) were immobilized on all four flow cells (Fcs) of CM5 sensor chip (GE Healthcare). Immobilizations were carried out at a protein concentration of 50 µg/mL in 10 mM acetate buffer, pH 4.5, using an amine coupling kit (GE Healthcare). Forty microliters of the *E. coli* culture supernatants of 48 randomly picked clones from the round 2 sublibrary, containing the anti-CEACAM6 sdAb-ABTAG fusions, were added to a 96-well microtiter plate and covered with self-adhesive foil (GE Healthcare). Sixty microliters of running buffer (10 mM HEPES, pH 7.4, containing 150 mM NaCl, 3 mM EDTA, and 0.01% surfactant P20) were added to each well to dilute the culture supernatants, followed by mixing. As the Biacore 3000 has four Fcs, three fusions were simultaneously analyzed to increase screening throughput—the fourth Fc served as an ABTAG reference surface. ABTAG and the fusions were captured on the BSA surfaces by sequentially injecting 40 µL of three different diluted culture supernatants over Fcs 2, 3, and 4 at a flow rate of 5 µL/min. For some clones over 4,000 RUs of the sdAb-ABTAG fusions were captured in this manner. For the reference surface, 20 µL of 80 nM ABTAG were injected over Fc 1, followed by injection of a 60 µL buffer blank. Next, 1 µM of CEACAM6 was injected over all four Fcs at a flow rate of 20 µL/min and the dissociations were monitored for 3 min followed by surface regeneration with a 15 s injection of 10 mM glycine/HCl, pH 2.0. In all instances, analyses were carried out at 25°C in running buffer. The reference subtracted data were aligned and a corresponding buffer blank was subtracted from each sensorgram. The dissociation phase was normalized with the highest response in each sensorgram set at 100% and no response set at 0% for all data sets to rank binders by their dissociation rate. This qualitative analysis allowed for easy visual identification of binders with fast, medium and slow dissociation rates, which generally correlate with low, medium, and high affinities. Off-rates were determined using the BIAevaluation v4.1.1 Software (GE Healthcare). DNA sequencing of CEACAM6 binding sdAb-ABTAG clones was then performed as described previously (15).

Screening of CEACAM6 Binding to sdAb-ABTAG Fusions by Full Kinetic Analysis

Full kinetic data for CEACAM6 binding to captured sdAb-ABTAG fusions were obtained by single-cycle kinetics (SCK) using a Biacore T200 (GE Healthcare). The same 48 clones (round 2 sublibrary) that were screened by off-rate analysis above were analyzed in this manner. Fresh microtiter plate cultures were grown as described above. Cultures were harvested and periplasmic extracts prepared as described (15). Approximately 9,500 RUs of BSA (Sigma-Aldrich Canada) were immobilized on all four Fcs of CM5 Series S sensor chips (GE Healthcare). Immobilizations were carried out at a protein concentration of 50 µg/mL in 10 mM acetate buffer, pH 4.5, using an amine coupling kit (GE Healthcare). Fifty microliter of the periplasmic extracts of the 48 clones and 100 µL of running buffer (10 mM HEPES, pH 7.4, 150 mM NaCl, 3 mM EDTA, 0.05% surfactant P20) were added to a 96-well microtiter plate. ABTAG (80 nM) was captured on Fc 1 at a flow rate of 5 µL/min for 4 min, as a reference, and the diluted periplasmic extracts of three clones were captured on Fcs 2, 3, and 4 at a flow rate of 5 µL/min for 8 min per cycle. CEACAM6 was injected over all four Fcs at concentrations of 0.1, 1, 10, 100, and 1,000 nM at a flow rate of 5 µL/min for 3 min at 25°C in running buffer. Dissociations were monitored for 5 min followed by surface regeneration with 10 mM glycine/HCl, pH 2.0, at a flow rate of 10 µL/min for 60 s. Buffer-blank cycles preceded each antigen injection cycle. Data were analyzed using Biacore T200 Evaluation Software v3.0 (GE Healthcare).

Moderate-throughput sdAb screening with affinity and kinetic determination was also carried out using the BioRad ProteOn SPR instrument (BioRad Laboratories Canada Inc.). Microtiter plate cultures of 576 randomly picked clones from the round 1 sublibrary were centrifuged and the supernatants analyzed for binding to CEACAM6 by ELISA. ELISA-positive clones were sequenced (15) and subjected to ProteOn screening. Approximately 1,200 RUs of BSA were immobilized, as described above, except for immobilizing the BSA in the horizontal direction to create horizontal referencing spots with a BSA surface. The screening procedure occurred in two steps with a ligand capture in the vertical direction followed by an analyte injection in the horizontal direction. One buffer injection for 30 s at flow 100 µL/min in the ligand direction was used to stabilize the baseline after switching from the previous analyte injection. For each ligand capture, five individual *E. coli* culture supernatants each containing an sdAb-ABTAG fusion were diluted 1:25 in running buffer containing 1 mg/mL carboxymethyldextran sodium salt (Sigma-Aldrich Canada) to reduce non-specific protein interactions with the GLM chip surface and injected for 240 s at a flow rate of 25 µL/min. This resulted in five individual ligand samples on the GLM-BSA surface with up to approximately 200 RUs of fusion protein being captured for the highest expressing clones.

The first ligand channel was left empty for use as a blank control surface. This was immediately followed by two buffer injections to stabilize the baseline in the analyte direction, each for 30 s at a flow rate of 100 µL/min, and then the CEACAM6 analyte injection. Five CEACAM6 concentrations (50, 16.7, 5.6, 1.85, and 0.62 nM) and buffer were simultaneously injected in individual analyte channels at 50 µL/min for 120 s with a 600 s dissociation, resulting in a set of binding sensorgrams with a buffer reference for each of the five captured sdAb-ABTAG fusions. The BSA surfaces with bound sdAbs were regenerated by an 18 s pulse of 0.85% phosphoric acid at a flow rate of 100 µL/min. Sensorgrams were aligned and double-referenced using the buffer blank injection and the resulting sensorgrams were analyzed using ProteOn Manager software v2.1.1. Kinetic parameters were determined by fitting the referenced sensorgrams to a 1:1 interaction model using local R_{max}, and affinity constants (K_D, nM) were derived from the resulting rate constants [k_d (s^{-1})/k_a (M^{-1} s^{-1})].

SPR Analysis of CEACAM6 Binding to Covalently Immobilized sdAbs and sdAb-ABTAG Fusions

Purified sdAbs identified by conventional panning and the highest affinity binders identified *via* ABTAG screening after one and two rounds of panning were subjected to standard SPR analysis. Following purification by immobilized-metal affinity chromatography (18), sdAbs and sdAb-ABTAG fusions were further purified by size exclusion chromatography (SEC) using Superdex S75 and Superdex S200 Increase columns (GE Healthcare), respectively. CEACAM6 was subjected to Superdex S75 chromatography to remove possible aggregates.

sdAbs from conventional panning and from ABTAG round 2 screening were immobilized on CM5 sensor chips (GE Healthcare) at 50 µg/mL in 10 mM acetate buffer, pH 4. Multiple cycle kinetics were performed on a Biacore 3000 (GE Healthcare) in 10 mM HEPES, pH 7.4, containing 150 mM NaCl, 3 mM EDTA, and 0.005% P20 by flowing appropriate concentrations of CEACAM6 at a flow rate of 40 µL/min. Purified sdAb-ABTAG fusions from ABTAG round 1 screening were immobilized on CM5 sensor chips (GE Healthcare) at concentrations of 12–25 µg/mL in 10 mM acetate buffer, pH 3.5. Single cycle kinetics (SCK) were performed on a Biacore 3000 (GE Healthcare) in 10 mM HEPES, pH 7.4, containing 150 mM NaCl, 3 mM EDTA, and 0.005% P20 by flowing appropriate concentrations of CEACAM6 at a flow rate of 25 µL/min. Data were analyzed using BIAevaluation v4.1.1 Software (GE Healthcare).

Next-Generation DNA Sequencing (NGS)

The phage-displayed immune llama V_HH library was interrogated using an Illumina MiSeq instrument as previously described (1, 2). Briefly, replicative form DNA was purified from phagemid-bearing *E. coli* TG1 cells using a QIAprep® spin miniprep kit (Qiagen Inc.). Amplicons for NGS were prepared using PelB- and FR4-specific barcoded primers using ~25 ng of phagemid DNA as template and purified by gel extraction followed by solid-phase reversible immobilization using Agencourt® AMPure® XP beads (Beckman-Coulter, Pasadena, CA, USA). The data were quality filtered using the FAST-X toolkit with a stringency of Q30 over 95% of the read.

RESULTS

Selection of CEACAM6-Specific Binders by Conventional Panning

Immunization of a llama with recombinant CEACAM6 resulted in strong immune response against the immunogen as indicated by ELISA comparing the preimmune and postimmunization sera collected on day 71 from the animal (Figure S1 in Supplementary Material).

A phage-displayed V_HH library with a functional size of 2.9×10^7 clones was constructed from the lymphocytes of the immunized llama and used to select CEACAM6-binding sdAbs. After three rounds of panning, randomly picked clones were tested by phage ELISA to identify clones displaying CEACAM6-specific sdAbs. DNA sequencing revealed that the positive clones were comprised of five different sequences. The unique clones were named 1B6, 1F6, 2A7, 2F8, and 2G9. After subcloning in an expression vector, all five sdAbs were expressed in *E. coli* periplasms and purified. ELISA showed that all five sdAbs bound to CEACAM6 (data not shown). The actual affinities of these sdAbs were determined to be in the 2–10 nM range by SPR (**Table 1**; Figure S2A in Supplementary Material).

sdAb-ABTAG Binding to Immobilized BSA

The affinity of ABTAG for BSA, as a fusion with an anti-CEACAM6 sdAb, was determined to be 21 pM with a dissociation rate constant, k_d, of $9.1 \pm 0.7 \times 10^{-6}$ s^{-1} (**Figure 1D**). These values are essentially identical to those previously reported for ABTAG (11). As the dissociation rate is extremely slow, it was determined over a long, 10,000 s, dissociation phase.

Dissociation Rate and Expression Screening of sdAb-ABTAG Fusion Proteins

Eluted phage from the second round of panning were amplified by PCR and cloned into the ABTAG fusion vector (**Figures 1B,C**). The size of this sublibrary was 1.4×10^7 independent transformants. Individual clones from this sublibrary were grown in microtiter plates and the culture supernatants were used to rank the dissociation rate constants by SPR analysis. A total of 17 cycles were performed to generate the binding data for 48 clones; two duplicates and a buffer injection were included (Table S1 in Supplementary Material). Surface regeneration between cycles was exceedingly efficient with identical amounts of ABTAG being captured on the reference Fc over the 17 cycles (**Figure 2**). Of the 48 clones, 19 were excluded from off-rate screening and sequence determination: (i) six because the sdAb-ABTAG capture levels were less than 100 RUs, (ii) 11 because there was insignificant antigen binding to the captured fusion proteins and (iii) two because of low sdAb-ABTAG capture levels and poor 1:1 fitting of antigen binding data. As shown in **Figure 3** and Table S1 in Supplementary Material the clones exhibited a wide range of off-rates (k_ds), namely, from 1.48×10^{-4} to 1.67×10^{-12} s^{-1}. As the clones were randomly picked, they were not all unique,

TABLE 1 | Kinetic and affinity data for purified sdAbs binding CEACAM6.

sdAb	Source	RUs immobilized	k_a (M^{-1} s^{-1})	k_d (s^{-1})	K_D (nM)
1B6	Conventional panning	1,004	3.48×10^5	8.73×10^{-4}	2.5
1F6	Conventional panning	257[a]	3.68×10^{6}[b]	8.90×10^{-3}[b]	2.4[b]
2A7	Conventional panning	900	7.78×10^5	8.34×10^{-3}	10.7
2F8	Conventional panning	n.d.	n.d.	n.d.	n.d.
2G9	Conventional panning	1,125	7.46×10^5	5.27×10^{-3}	7.1
2-03	2 rounds + ABTAG	2,221	1.43×10^6	1.17×10^{-3}	0.8
2-15	2 rounds + ABTAG	1,530	6.01×10^5	3.00×10^{-4}	0.5
2-35	2 rounds + ABTAG	2,477	1.37×10^6	1.02×10^{-3}	0.7
1-04	1 round + ABTAG	2,157	2.45×10^6	2.58×10^{-4}	0.105
1-07	1 round + ABTAG	1,012	3.78×10^6	1.73×10^{-4}	0.046
1-09	1 round + ABTAG	1,875	1.94×10^6	7.76×10^{-6}[c]	0.004
1-19	1 round + ABTAG	1,388	2.69×10^6	6.24×10^{-4}	0.232

n.d., not determined.

[a]*RUs of sdAb-ABTAG captured on BSA surface.*

[b]*Determined using full kinetic ProteOn screen.*

[c]*Approximate k_d (2 h dissociation of ~4% and at instrument limit of detection).*

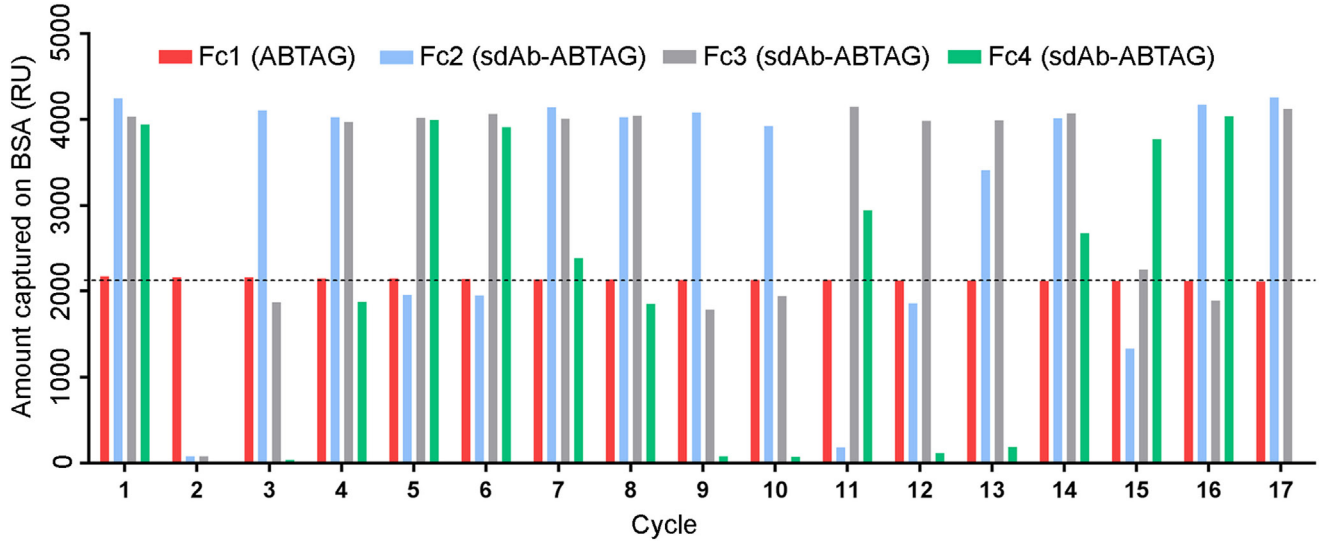

FIGURE 2 | Multiple cycles of ABTAG and single-domain antibody (sdAb)-ABTAG fusion proteins capture on bovine serum albumin (BSA) surfaces for CEACAM6 binding. Capture levels of ABTAG and sdAb-ABTAG fusions over 17 cycles on a Biacore 3000 instrument. The dashed line represents the mean ABTAG capture level on flow cell (Fc) 1. Fc2: flow cell 2; Fc3: flow cell 3; Fc4: flow cell 4.

accounting for the nearly identical dissociation profiles of some of the clones. As the screening measurements were performed at a single CEACAM6 concentration, it was impossible to calculate accurate on-rates and, consequently, accurate K_D values. Of 29 sequenced clones, one of the clones isolated by conventional panning, 2A7, was the most frequent, accounting for 9 of the 29 clones. Another clone isolated by conventional panning, 2G9, occurred twice. The remaining three sdAbs identified by the conventional approach (1F6, 2F8, and 1B6) were not found by the off-rate screening method. Three clones with the slowest off-rates (2-03 = 6.87×10^{-4} s^{-1}; 2-15 = 1.48×10^{-4} s^{-1}; 2-35 = 8.56×10^{-4} s^{-1}) were subcloned into the pSJF2H expression vector and the sdAbs were purified for full kinetic analysis over a range of antigen concentrations. These three unique sdAbs exhibited affinities below 1 nM (0.5–0.8 nM), up to 10 times stronger than the affinities of the binders selected by conventional panning (**Table 1**; Figure S2B in Supplementary Material).

The ABTAG/sdAb-ABTAG capture step, prior to antigen flow and dissociation rate ranking, gave expression level data for the 48 clones. The total RUs captured for the various clones were a good measure of relative expression levels (Table S1 and Figure S3 in Supplementary Material). It was possible to quantify the concentrations of sdAb-ABTAG fusions in the culture supernatants. A plot of fusion protein concentration *vs* initial fusion protein binding rate was generated from the linear, mass transport-limited, portions of the sensorgrams (Figure S3 in Supplementary Material). This plot was used to derive fusion protein concentrations in culture supernatants. Approximately half of the clones

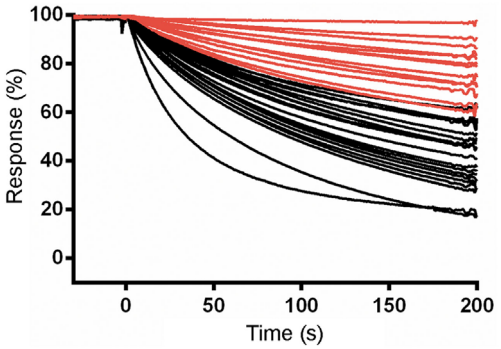

FIGURE 3 | Surface plasmon resonance (SPR) characterization of anti-CEACAM6 single-domain antibodies (sdAbs) obtained by off-rate screening of the round 2 sublibrary. Normalized dissociation phases of SPR sensorgrams of CEACAM6 binding to captured sdAb-ABTAG fusions derived from Biacore 3000 experiments. Red lines represent the sdAb-ABTAG clones with the slowest off-rates.

expressed protein in the 100–600 nM range in microtiter plate cultures (Table S1 in Supplementary Material).

Full Kinetic and Affinity Screening of sdAb-ABTAG Fusion Proteins

A limitation of the dissociation rate screening with the Biacore 3000 instrument is that single antigen concentrations are utilized for screening and clones must be expressed as pure sdAbs to generate full kinetic information. In view of this, we explored two approaches for obtaining full kinetic data using microtiter plate cultures containing sdAb-ABTAG fusions.

In the first approach SCK experiments were performed in which increasing concentrations of CEACAM6 were flowed over captured sdAb-ABTAG fusions using a Biacore T200 instrument. Microtiter plate periplasmic extracts from the 48 clones from round 2 subjected to off-rate screening were screened by SCK to determine k_a, k_d, and K_D (Table S2 in Supplementary Material). A wide range of CEACAM6 concentrations (0.1–1,000 nM) was flowed over the captured clones in order to obtain approximate K_Ds for clones with wide-ranging affinities as the off-rate screening of the 48 clones gave k_ds covering two orders of magnitude (Table S1 in Supplementary Material). As expected, the concentration range was not ideal for individual clones but in most instances two or three of the concentrations gave acceptable responses (**Figure 4A**). Fitting the sensorgrams to a 1:1 interaction model gave a surprisingly good approximation of the rate constants and K_Ds (**Figure 4B**; Table S2 in Supplementary Material), as indicated by the rate constants and affinities of some of the clones determined by more rigorous analyses (**Table 1**). The median K_D for these analyzed clones was 7.98 nM (**Figure 4B**).

In the second approach, five different CEACAM6 concentrations were flowed over five or six captured sdAb-ABTAG fusions in a single injection cycle using a BioRad ProteOn, which has a 6 by 6 grid of microfluidic channels. To take full advantage of these higher throughput approaches, we made a second, more diverse, sublibrary by cloning phage-displayed sdAbs eluted from round 1 panning into the ABTAG-fusion protein expression vector. Of the 576 randomly picked clones from the round 1 sublibrary, 52 were positive for antigen binding by ELISA (data not shown). Microtiter plate culture supernatants containing sdAb-ABTAG fusions from the 52 positive ELISA clones were screened using a ProteOn to determine sdAb-ABTAG capture levels and, by fitting the sensorgram data to a 1:1 interaction model, rate constants, K_Ds and observed R_{max}s (Table S3 in Supplementary Material). No antigen binding was observed for several of the clones—low capture levels and low affinities may account for this observation. Three of the five clones identified by conventional panning (2A7, 2G9, and 1F6) were found in this screen. Eleven of the 52 clones were 2G9, three or four were 2A7, and one was 1F6. Of the remaining 36 clones, 32 were unique; four clones were found twice. The sensorgram data were generally of high quality, fitting well to a 1:1 interaction model (**Figure 5A**). The method gave excellent K_D approximations (**Figure 5B**), as evidenced by the values obtained for clones that were subjected to a more stringent SPR analysis, i.e., the sdAbs that were analyzed by binding antigen to immobilized sdAbs (**Table 1**). The median K_D for these analyzed clones was 0.99 nM (**Figure 5B**). Values are not given for clones with capture levels of less than 100 RUs. Several of the clones had higher affinities, attributable to slower off-rates, than those of clones from the round 2 library. While the very slow ABTAG k_d results in stable capture of sdAb-ABTAG fusions, direct binding assays in which the ABTAG fusions are covalently linked to the surface and antigen is flowed are preferable in instances where the sdAb k_d is very slow. While the off-rates determined by the capture method were derived using double referencing (reference cell and zero-concentration subtraction), accurate determination of very slow off-rates can be challenging, even in the best of circumstances. The four round 1 library clones showing the highest affinities by ProteOn screening were expressed and purified as sdAb-ABTAG fusions for direct binding assays (**Table 1**; Figure S2C in Supplementary Material). Monomeric CEACAM6 peaks from SEC (Figure S2D in Supplementary Material) were used for analysis. The affinities of these four clones, which ranged from 4 to 232 pM (**Table 1**), were all higher than the affinities of the top round 2 clones (**Figure 6**; Table S2 in Supplementary Material) with clone 1-09 exhibiting an exceedingly slow off-rate (**Table 1**). The 1-09 sdAb-ABTAG surface required stringent regeneration conditions (Figure S2C in Supplementary Material).

Next-Generation DNA Sequencing

To better understand why some of the highest-affinity sdAbs against CEACAM6 were not recovered through conventional panning of the phage-displayed V_HH library, we interrogated the library to moderate depth (approximately 2.5×10^5 quality-filtered sequences) using amplicon sequencing on an Illumina MiSeq instrument (**Table 2**). Both the medium-affinity sdAbs recovered *via* conventional panning as well as the extremely high-affinity ones recovered only *via* ABTAG screening were observed in the library at roughly similar frequencies. As panning progressed, the frequencies of all CEACAM6-specific sdAbs increased, indicating that all of the sdAb-phages bound plate-adsorbed CEACAM6 and were eluted from it under high pH. However, several medium-affinity sdAbs (in particular 2A7 and

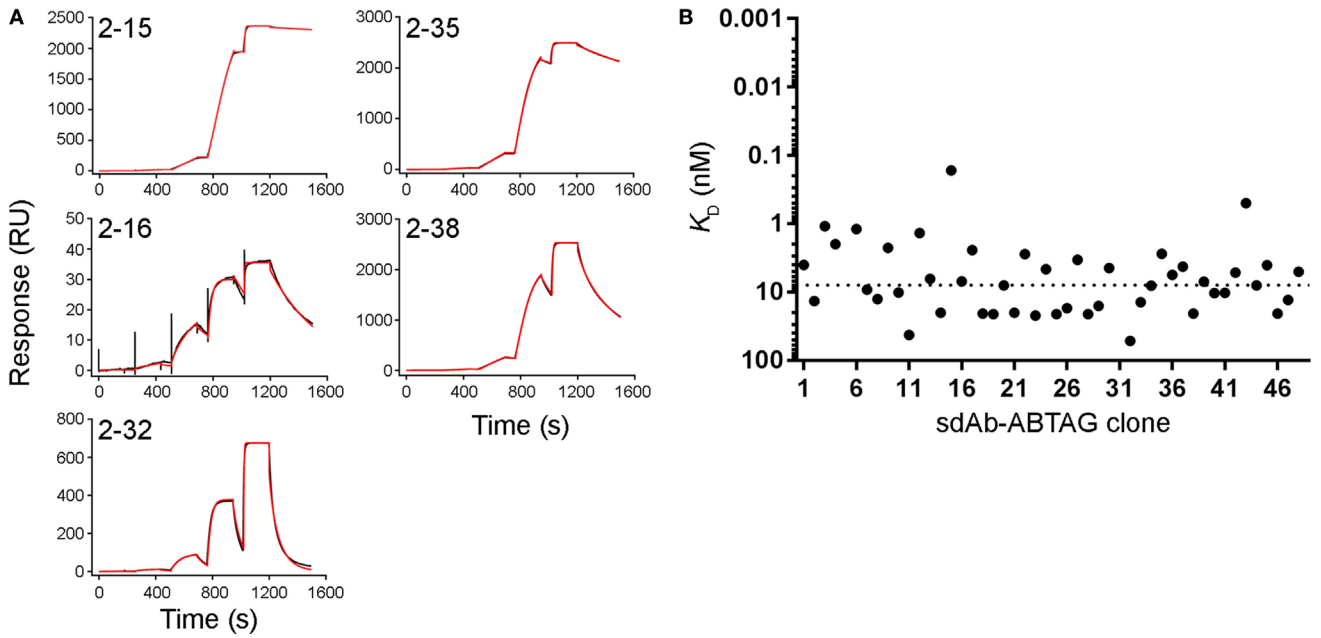

FIGURE 4 | Full kinetic screening of anti-CEACAM6 single-domain antibodies (sdAbs) by single cycle kinetics analysis of the round 2 sdAb-ABTAG sublibrary. Fitting of representative sensorgrams to a 1:1 interaction model **(A)**. Black lines represent raw data; red lines represent 1:1 fits. K_Ds derived from Biacore T200 sensorgrams of the binding of five concentrations of CEACAM6 (0.1–1,000 nM) to captured sdAb-ABTAG fusions **(B)**. The dashed line represents the median K_D = 7.98 nM.

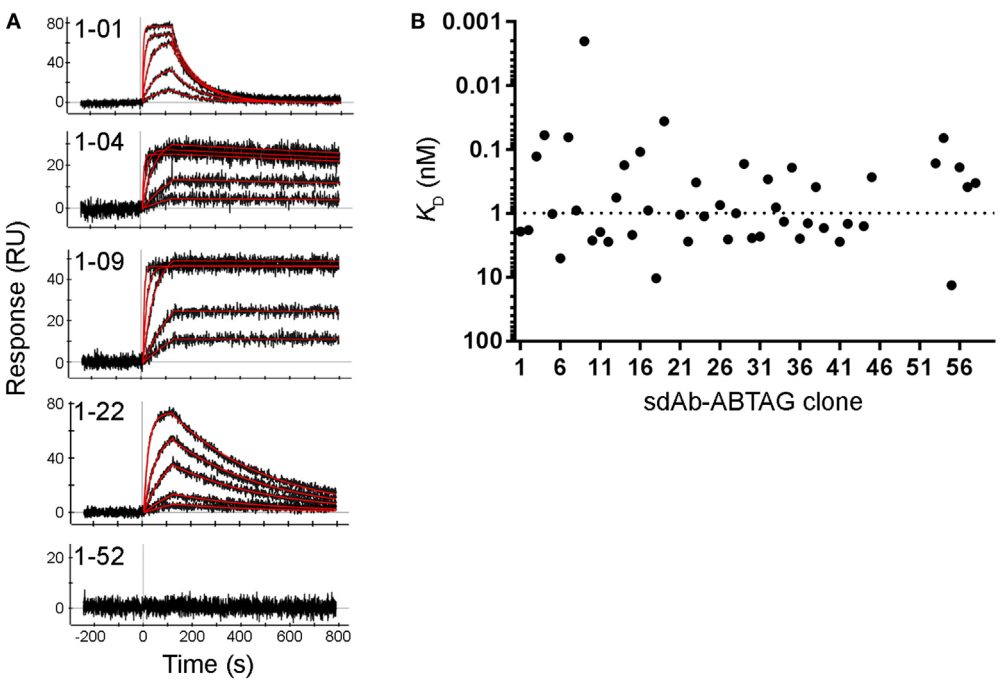

FIGURE 5 | Full kinetic screening of anti-CEACAM6 single-domain antibodies (sdAbs) by multiple cycle kinetics analysis of the round 1 sublibrary. Fitting of representative sensorgrams to a 1:1 interaction model **(A)**. Black lines represent raw data; red lines represent 1:1 fits. K_Ds derived from ProteOn sensorgrams of the binding of five concentrations of CEACAM6 (0.62–50 nM) to captured sdAb-ABTAG fusions **(B)**. The dashed line represents the median K_D = 0.99 nM.

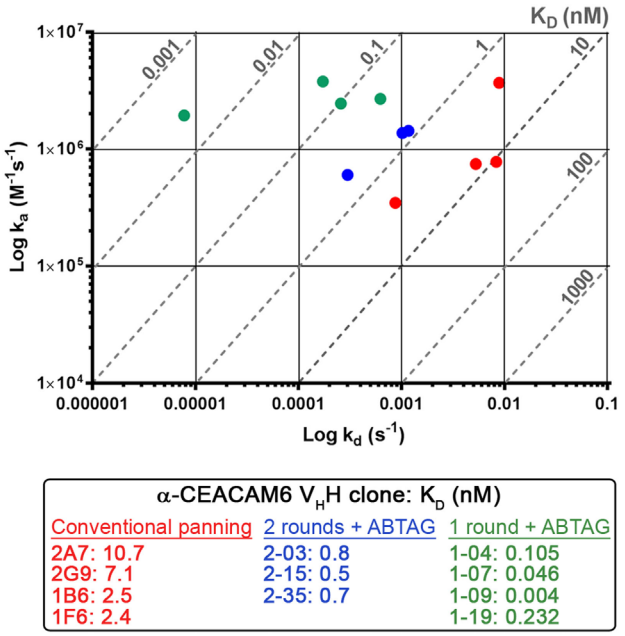

FIGURE 6 | Iso-affinity plots of the highest affinity single-domain antibodies (sdAb) clones obtained using conventional panning or sdAb-ABTAG screening. Reported K_Ds were obtained from purified sdAbs or sdAb-ABTAG fusions immobilized on sensor chips and subsequent binding of various concentrations of CEACAM6.

2G9) rapidly outcompeted the higher-affinity sdAbs, becoming enriched 50–100-fold in the first round of panning and making up the majority of CEACAM6-specific sdAbs by round 2. Thus, utilizing a high-throughput screening technology was necessary in this case to recover the most desirable antibody specificities.

DISCUSSION

The present study has shown that ABTAG can be a useful addition to the toolbox for antibody discovery by *in vitro* display methods. Compared to conventional phage display approaches to antibody isolation, ABTAG technology yielded a much higher number of unique sequences while simultaneously giving detailed antigen binding information. With the rapid rise in antibody drugs in recent years, the number of different applications for this class of biologics is ever increasing. Along with each application is also a desirable set of kinetic parameters and functional properties (19). For instance, naked inhibitory mAbs targeting a surface receptor would preferentially have tight-binding with slow off-rates. Conversely, tumor-imaging molecules, or those carrying a toxic payload, require shorter half-lives and faster off-rates. Selection of antibodies based on kinetics using a full kinetics screening method, such as the ProteOn methods described here, is an obvious advantage, and affords a moderate throughput of up to 200 clones per day, extrapolating from the time required to screen the 52 round 1 clones described here, with generation of high quality kinetic and affinity data. Maximizing the number of clones available for functional screening is also clearly a key aspect of the search for antibodies with desired functionalities such as cross-species reactivity and binding to specific epitopes, for example, epitopes that deliver activation, inhibitory, internalization or no biological activity. The ABTAG technology supports the growing trend away from largely blind selection of limited numbers of binders as evidenced, for example, by the use of next generation sequencing to more effectively capture the full diversity of the immune response and bypass B-cell or antibody library screening (1, 20).

TABLE 2 | Frequencies of anti-CEACAM6 sdAbs in the phage-displayed immune V_HH library and after each of two panning rounds.

sdAb	Source	K_D (nM)	Library (%)[a]	Round 1 (%)	Round 2 (%)
1B6	Conventional panning	2.5	0.01	n.f.[b] (2.2)[c]	n.f.[b]
1F6	Conventional panning	2.4	0.07	0.17[b] (2.2)[c]	n.f.[b] (4.2)[c]
2A7	Conventional panning	10.7	0.04	0.7[b] (2.2)[c]	18.9[b] (41.7)[c]
2F8	Conventional panning	n.d.	0.01	n.f.[b] (2.2)[c]	n.f.[b] (4.2)[c]
2G9	Conventional panning	7.1	0.02	1.9[b]	4.2[b] (29.2)[c]
2-03	2 rounds + ABTAG	0.8	0.01	n.f.[b]	4.2[b]
2-15	2 rounds + ABTAG	0.5	0.005	n.f.[b]	2.1[b]
2-35	2 rounds + ABTAG	0.7	0.01	n.f.[b]	2.1[b]
1-04	1 round + ABTAG	0.105	0.03	0.17[b]	n.f.[b]
1-07	1 round + ABTAG	0.046	0.03	0.17[b]	n.f.[b]
1-09	1 round + ABTAG	0.004	0.005	0.17[b]	n.f.[b]
1-19	1 round + ABTAG	0.232	0.005	0.17[b]	n.f.[b]

n.d., not determined; n.f., not found.
[a]Determined using next-generation DNA sequencing.
[b]Determined using Sanger sequencing of ABTAG sublibrary clones.
[c]Determined using Sanger sequencing of phage-displayed library clones obtained through conventional panning.

Other affinity tags are available for use in purification and in screening technologies such as SPR; however, none of these tags are ideal. The use of streptavidin requires chemical or enzymatic biotinylation of the proteins being screened; SPR screening of biotinylated proteins is not always straightforward and rapid. His-tagged proteins can be captured on Ni^{2+}-surfaces but the capture is not always stable enough for the analysis of high affinity interactions; assays require steps for Ni^{2+} activation and regeneration which slows screening throughput and Ni^{2+}-chelation surfaces are relatively expensive. His-tagged proteins can be captured by anti-His-tag antibodies but commercial sources of these antibodies can be costly and the antibodies can have variable binding affinity depending on the presentation of the His-tag in the context of the protein. Monoclonal antibodies can be captured on anti-Fc surfaces but the use of Fcs as fusion tags generates homodimeric fusion proteins which are undesirable for some assays. The ABTAG capture system described here is in many ways ideal: (i) the capture molecule (BSA) is readily available, inexpensive and stable on SPR surfaces, (ii) there is no indication that ABTAG negatively impacts the expression or activity of the molecules being screened, (iii) the BSA-ABTAG interaction is of very high affinity due to a very slow off-rate, and (iv) the BSA-ABTAG interaction can be completely reversed without any damage to the BSA surface.

Single-domain antibody-ABTAG screening identified 53 anti-CEACAM6 sdAbs that were not found by a conventional phage display panning approach. The five sdAbs identified by

conventional panning grouped into three families—the 2A7/2G9 family, the 1F6/2F8 family, and 1B6. Of the 32 round 2 sublibrary sdAbs, 23 belonged to the 2A7/2G9 family (12 were 2A7 or 2G9) and two belonged to the 1F6/2F8 family. The remaining seven were characterized by longer CDR3s, up to 24 residues; one of these clones was 2-15, which was the round 2 clone with the highest affinity and slowest off-rate (**Table 1**). Of the 52 round 1 sublibrary sdAbs, 20 belonged to the 2A7/2G9 family (11 were 2G9 and three or four were 2A7—there was some sequence ambiguity) and one belonged to the 1F6/2F8 family. The remaining 31 were characterized by CDR3 lengths of 6–25 residues. The CDR3 lengths of clones 1-04, 1-07, 1-09, and 1-19 were 12, 11, 16, and 12 residues, respectively. Clones 1-04, 1-07, 1-09, and 1-19 had off-rates in the 6.24×10^{-4} to 7.76×10^{-6} s^{-1} range (**Table 1**; **Figure 2**) and required stringent surface regeneration conditions (Figure S2C in Supplementary Material). It is unclear why the group of high-affinity, long-CDR3 sdAbs was less efficiently enriched by panning than the 2A7/2G9 family of medium-affinity, short-CDR3 sdAbs given that no obvious bias in their starting frequencies was observed in the library. We speculate that this observation may relate to the very slow off-rates of the former group of sdAbs which may translate into less efficient elution of these sdAb-phages by high pH; however, a stochastic element to the panning process cannot be ruled out. Clearly, as has been the experience of many groups, phage display selection is ineffective in discriminating antibodies based on affinity and probably depends instead on other factors (e.g., starting frequency; fast off-rates; pH-sensitive binding; growth advantages in *E. coli*). The capture levels (Response; RUs) of the 2A7/2G9 moderate-affinity family and the rarer set of high-affinity clones (1-04, 1-07, 1-09, and 1-19) were very similar (Table S3 in Supplementary Material), suggesting, at least at the protein level, there were no significant differences in the expression of these sdAbs in *E. coli* supernatants. Capture levels (Response; RUs) were clearly shown to correlate with sdAb-ABTAG concentrations (Figure S3 and Table S1 in Supplementary Material). However, it is unknown whether the display efficiency of these sdAbs on the surface of phage is comparable to their soluble expression.

Another benefit of the screening method described here is that both *E. coli* culture supernatants and periplasmic extracts of microtiter plate cultures can be used for ABTAG SPR-based screening. Culture supernatants were used directly for off-rate screening and periplasmic extracts were used for SCK screening of the 48 round 2 clones. Similar capture levels were observed for individual clones with both sdAb-ABTAG sources.

The screening of up to 10^4 clones in a week by the approach described here is realistic, provided that antigen cost is not prohibitive. This represents very good sampling of the phage clones eluted after a single round of panning, typically 10^5–10^6. Of the methods described here, the ProteOn method has the highest throughput, followed by the off-rate screening method and the SCK method, although the throughput potential of the latter two methods is not that different. Analysis of about 30 clones a day is possible with the SCK method. The ProteOn instrument used here has recently been discontinued and will be supported only until 2020. However, as newer higher throughput instruments become available, ABTAG screening throughput equaling or exceeding that achieved here with the ProteOn should not be an issue (21).

Beyond its usefulness in screening sdAb libraries, ABTAG has been applied to other antibody and protein engineering projects (JZ, unpublished data). Both scFv and Fab libraries, including humanization and affinity maturation libraries, can be screened in a manner similar to that described here for sdAbs. In addition to screening for affinity, ABTAG technology can be applied to screening for protein stability, an unmet need in the field of protein engineering. When pure to very pure proteins are needed ABTAG can be used as a purification tag for BSA-affinity matrix purification. When the efficacy of a protein needs to be evaluated *in vivo*, the protein-ABTAG can be mixed with BSA to overcome the limitation of short serum half-life of the protein. Finally, screening libraries constructed from other proteins, receptors, ligands or enzymes, for which binding partners are available, could also be exploited with ABTAG. In summary, ABTAG technology provides a powerful and versatile tool for antibody discovery and protein engineering applications.

ETHICS STATEMENT

This study was carried out in accordance with Animal Use Protocols approved by the National Research Council Canada Animal Care Committee.

AUTHOR CONTRIBUTIONS

GH and CRM conceived experiments and planned and wrote the manuscript. GH supervised the Biacore analyses and created the figures. TB constructed the libraries, conducted the panning and coordinated the off-rate and ProteOn screening of the round 1 and round 2 library clones. JB devised and conducted the ProteOn analyses. HvF conducted the off-rate screening and SPR characterization of the purified sdAbs and sdAb-ABTAG fusions. SR conducted the SCK screening of the round 2 clones. KH performed and analyzed NGS experiments. JZ devised the application of ABTAG to the screening of antibody libraries.

ACKNOWLEDGMENTS

We thank Yanal Murad and Shenghua Li for help with the round 1 and round 2 library screening. We thank Shannon Ryan for sdAb-ABTAG expression and purification.

FUNDING

This work was supported by the National Research Council Canada.

SUPPLEMENTARY MATERIAL

The Supplementary Material for this article can be found online at http://www.frontiersin.org/article/10.3389/fimmu.2017.01406/full#supplementary-material.

REFERENCES

1. Henry KA, Tanha J, Hussack G. Identification of cross-reactive single-domain antibodies against serum albumin using next-generation DNA sequencing. *Protein Eng Des Sel* (2015) 28:379–83. doi:10.1093/protein/gzv039
2. Henry KA, Hussack G, Collins C, Zwaagstra JC, Tanha J, MacKenzie CR. Isolation of TGF-β-neutralizing antibodies of predetermined epitope specificity using next-generation DNA sequencing. *Protein Eng Des Sel* (2016) 29:439–43. doi:10.1093/protein/gzw043
3. Bradbury ARM, Sidhu S, Dübel S, McCafferty J. Beyond natural antibodies: the power if *in vitro* display technologies. *Nat Biotechnol* (2011) 29:245–54. doi:10.1038/nbt.1791
4. Nelson AL, Reichert JM. Development trends for therapeutic antibody fragments. *Nat Biotechnol* (2009) 27:331–7. doi:10.1038/nbt0409-331
5. Hamers-Casterman C, Atarhouch T, Muyldermans S, Robinson G, Hamers C, Songa EB, et al. Naturally-occurring antibodies devoid of light chains. *Nature* (1993) 363:446–8. doi:10.1038/363446a0
6. Arbabi Ghahroudi M, Desmyter A, Wyns L, Hamers R, Muyldermans S. Selection and identification of single domain antibodies from camelid heavy-chain antibodies. *FEBS Lett* (1997) 414:521–6. doi:10.1016/S0014-5793(97)01062-4
7. Kovaleva M, Ferguson L, Steven J, Porter A, Barelle C. Shark variable new antigen receptor biologics – a novel technology platform for therapeutic drug development. *Expert Opin Biol Ther* (2014) 14:1527–39. doi:10.1517/14712598.2014.937701
8. To R, Hirama T, Arbabi-Ghahroudi M, MacKenzie R, Wang P, Xu P, et al. Isolation of monomeric V_Hs by a phage selection. *J Biol Chem* (2005) 280:41395–403. doi:10.1074/jbc.M509900200
9. Kim DY, Kandalaft H, Ding W, Ryan S, van Faassen H, Hirama T, et al. Disulfide linkage engineering for improving biophysical properties of V_H domains. *Protein Eng Des Sel* (2012) 25:581–9. doi:10.1093/protein/gzs055
10. Hussack G, Keklikian A, Alsughayyir J, Hanifi-Moghaddam P, Arbabi-Ghahroudi M, van Faassen H, et al. A V_L single-domain antibody library shows a high-propensity to yield non-aggregating binders. *Protein Eng Des Sel* (2012) 25:313–8. doi:10.1093/protein/gzs014
11. Li S, Zheng W, KuoLee R, Hirama T, Henry M, Makvandi-Nejad S, et al. Pentabody-mediated antigen delivery induces antigen-specific mucosal immune response. *Mol Immunol* (2009) 46:1718–26. doi:10.1016/j.molimm.2009.02.007
12. Zhang J, Chen W, MacKenzie R, Arbabi M, Li S. *BSA-Specific Antibodies*. United States Patent No. 9,327,022 B2 (2016).
13. Zhang J, Hirama T. *Screening of Protein Candidates*. United States Patent No. 9,476,887 B2. (2016)
14. Blumenthal RD, Hansen HJ, Goldenberg DM. Inhibition of adhesion, invasion, and metastasis by antibodies targeting CEACAM6 (NCA-90) and CEACAM5 (carcinoembryonic antigen). *Cancer Res* (2005) 65:8809–17. doi:10.1158/0008-5472.CAN-05-0420
15. Hussack G, Arbabi-Ghahroudi M, van Faassen H, Songer JG, Ng KK-S, MacKenzie R, et al. Neutralization of *Clostridium difficile* toxin A with single-domain antibodies targeting the cell receptor binding domain. *J Biol Chem* (2011) 286:8961–76. doi:10.1074/jbc.M110.198754
16. Arbabi-Ghahroudi M, MacKenzie CR, Tanha J. Selection of non-aggregating V_H binders from synthetic V_H phage-display libraries. *Methods Mol Biol* (2009) 525:187–216. doi:10.1007/978-1-59745-554-1_10
17. Arbabi-Ghahroudi M, Tanha J, MacKenzie R. Isolation of monoclonal antibodies from phage display libraries. *Methods Mol Biol* (2009) 502:341–64. doi:10.1007/978-1-60327-565-1_20
18. Hussack G, Luo Y, Veldhuis L, Hall JC, Tanha J, MacKenzie R. Multivalent anchoring and oriented display of single-domain antibodies on cellulose. *Sensors* (2009) 9:5351–67. doi:10.3390/s90705351
19. Carter P. Introduction to current and future protein therapeutics: a protein engineering perspective. *Exp Cell Res* (2011) 317:1261–9. doi:10.1016/j.yexcr.2011.02.013
20. Reddy ST, Ge X, Miklos AE, Hughes RA, Kang SH, Hoi KH, et al. Monoclonal antibodies isolated without screening by analyzing the variable-gene repertoire of plasma cells. *Nat Biotechnol* (2010) 28:965–9. doi:10.1038/nbt.1673
21. Kamat V, Rafique A. Exploring sensitivity & throughput of a parallel flow SPRi biosensor for characterization of antibody-antigen interaction. *Anal Biochem* (2017) 525:8–22. doi:10.1016/j.ab.2017.02.007

Conflict of Interest Statement: CM and JZ are inventors on US patent 9,327,022 B2. JZ is an inventor on US patent 9,476,887 B2. All other authors declare that the research was conducted in the absence of any commercial or financial relationships that could be construed as a potential conflict of interest.

frontiers in Immunology

TECHNOLOGY REPORT
published: 23 January 2018
doi: 10.3389/fimmu.2017.01989

A cDNA Immunization Strategy to Generate Nanobodies against Membrane Proteins in Native Conformation

*Thomas Eden, Stephan Menzel, Janusz Wesolowski, Philine Bergmann, Marion Nissen, Gudrun Dubberke, Fabienne Seyfried, Birte Albrecht, Friedrich Haag and Friedrich Koch-Nolte**

Institute of Immunology, University Medical Center Hamburg-Eppendorf, Hamburg, Germany

OPEN ACCESS

Edited by:
Kevin A. Henry, National Research Council Canada (NRC-CNRC), Canada

Reviewed by:
Ingrid Langer, Université libre de Bruxelles, Belgium
Serge Muyldermans, Vrije Universiteit Brussel, Belgium
Greg Hussack, National Research Council Canada (NRC-CNRC), Canada

***Correspondence:**
Friedrich Koch-Nolte
nolte@uke.de

Specialty section:
This article was submitted to Vaccines and Molecular Therapeutics, a section of the journal Frontiers in Immunology

Received: *16 October 2017*
Accepted: *21 December 2017*
Published: *23 January 2018*

Citation:
Eden T, Menzel S, Wesolowski J, Bergmann P, Nissen M, Dubberke G, Seyfried F, Albrecht B, Haag F and Koch-Nolte F (2018) A cDNA Immunization Strategy to Generate Nanobodies against Membrane Proteins in Native Conformation. Front. Immunol. 8:1989. doi: 10.3389/fimmu.2017.01989

Nanobodies (Nbs) are soluble, versatile, single-domain binding modules derived from the VHH variable domain of heavy-chain antibodies naturally occurring in camelids. Nbs hold huge promise as novel therapeutic biologics. Membrane proteins are among the most interesting targets for therapeutic Nbs because they are accessible to systemically injected biologics. In order to be effective, therapeutic Nbs must recognize their target membrane protein in native conformation. However, raising Nbs against membrane proteins in native conformation can pose a formidable challenge since membrane proteins typically contain one or more hydrophobic transmembrane regions and, therefore, are difficult to purify in native conformation. Here, we describe a highly efficient genetic immunization strategy that circumvents these difficulties by driving expression of the target membrane protein in native conformation by cells of the immunized camelid. The strategy encompasses ballistic transfection of skin cells with cDNA expression plasmids encoding one or more orthologs of the membrane protein of interest and, optionally, other costimulatory proteins. The plasmid is coated onto 1 μm gold particles that are then injected into the shaved and depilated skin of the camelid. A gene gun delivers a helium pulse that accelerates the DNA-coated particles to a velocity sufficient to penetrate through multiple layers of cells in the skin. This results in the exposure of the extracellular domains of the membrane protein on the cell surface of transfected cells. Repeated immunization drives somatic hypermutation and affinity maturation of target-specific heavy-chain antibodies. The VHH/Nb coding region is PCR-amplified from B cells obtained from peripheral blood or a lymph node biopsy. Specific Nbs are selected by phage display or by screening of Nb-based heavy-chain antibodies expressed as secretory proteins in transfected HEK cells. Using this strategy, we have successfully generated agonistic and antagonistic Nbs against several cell surface ecto-enzymes and ligand-gated ion channels.

Keywords: nanobody, heavy-chain antibody, antibody engineering, cDNA immunization, genetic immunization, membrane proteins

INTRODUCTION

Nanobodies (Nbs), single-domain antibodies derived from camelid heavy-chain antibodies, are 10-fold smaller than conventional antibodies (**Figure 1**) and exhibit a number of advantageous features (1–4). In Nbs, the core of the antigen recognition site, i.e., the CDR3 loop, is often much longer than that of conventional antibodies. Consequently, Nbs can bind epitopes that are inaccessible to conventional antibodies, e.g., cryptic functional epitopes such as the active site of an enzyme, the ligand-binding site of an ion channel, or the virus-binding site of a cell surface receptor (5). The single-domain format of Nbs greatly facilitates the construction of multi-specific and multivalent biologics by genetically linking Nbs in a linear fashion. Genetic fusion can endow Nbs with additional effector functions, e.g., cytotoxicity, extended *in vivo* half-life, or translocation through the blood–brain barrier (6–9). Moreover, as chaperones in protein crystallography, Nbs can greatly aid structure function analyses (10, 11). *In vivo*, monomeric Nbs penetrate tissues better than conventional antibodies. Importantly, the *in vivo* half-life of Nbs can easily be adjusted, e.g., by genetic fusion to an albumin-specific Nb (6). To date more than 1,000 patients and healthy subjects have received Nbs in clinical studies without any obvious off-target side effects or the induction of neutralizing antibodies. Caplacizumab is the first Nb for therapy expected to receive approval for the clinic in 2018 (12).

Membrane proteins are particularly interesting Nb targets in research, diagnosis, and therapy (2, 3, 13–15). The extracellular domain(s) of a membrane protein often contain(s) several epitopes accessible to Nbs. Nbs targeting such epitopes can be converted into effective tools for structural studies and for visualizing and tracing membrane proteins on living cells, e.g., by high resolution microscopy (16, 17). Nbs can be used also to mark cells for sorting by flow cytometry or magnetic beads. Antagonistic or agonistic Nbs can be used to modulate the function of the membrane protein and/or the cell expressing the membrane protein. In case of cancer cells, opsonization with Nb-based heavy-chain antibodies can aid anti-tumor responses. Moreover, Nbs can be used to deliver imaging agents, cytotoxic compounds, and immune cells to tumor cells expressing the target membrane protein *in vivo*.

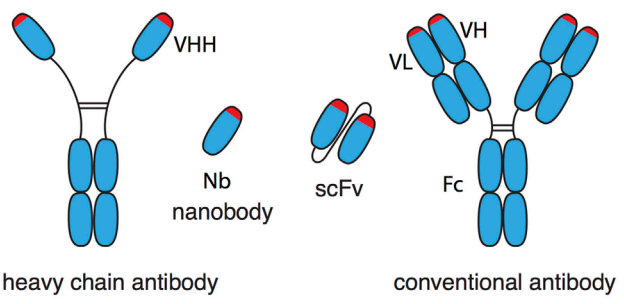

FIGURE 1 | Schematic comparison of nanobodies (Nbs) from heavy-chain antibodies and single-chain variable fragments (scFv) from conventional antibodies. Nbs correspond to the variable domain (VHH) of heavy-chain antibodies. Nbs generally show much better solubility and stability than the corresponding pair of variable domains (VH, VL) of conventional antibodies, even when the latter are connected by a synthetic peptide linker into a scFv.

For such experimental and therapeutic applications, it is important that the Nb recognizes its target membrane protein in native conformation. However, raising Nbs against a membrane protein of interest in native conformation can be challenging. Antibodies induced by synthetic peptides usually work well in Western Blot analyses, where the membrane protein is denatured. Anti-peptide antibodies, however, usually fail to recognize the natively folded protein on the cell surface of living cells. Genetic fusion of peptides to a multimerization domain has been shown to enhance the chance of inducing Nbs against native proteins (12). Purification of membrane proteins for immunization is often hampered by the necessity to use detergents and the tendency of membrane proteins to aggregate upon removal of the detergent (16). Numerous strategies have been employed successfully to overcome these hurdles, including immunization with transfected cells overexpressing the membrane protein of interest and incorporation of the purified membrane protein into liposomes or into the outer membrane of an enveloped virus (14, 18). Notwithstanding, other proteins present in such preparations can interfere with the immune response against the membrane protein of interest.

Genetic or cDNA immunization poses an attractive alternative (19). This strategy aims to transfect cells of the host animal with a mammalian expression vector, akin to transfection of HEK cells in cell culture. The goal of the cDNA immunization strategy is to drive faithful expression and posttranslational modification of the membrane protein of interest on the plasma membrane of skin and immune cells of the immunized animal. Here, we describe a cDNA immunization strategy that has allowed us to generate Nbs and Nb-based heavy-chain antibodies against membrane proteins from immunized llamas (8, 20–22). Moreover, we discuss some of the pitfalls and options for adapting this strategy to other membrane proteins.

MEMBRANE PROTEINS AS TARGETS FOR Nbs

Membrane proteins are interesting targets for therapeutic Nbs because membrane proteins are accessible to systemically injected biologics. For example, Nbs directed against membrane proteins on immune cells may provide an effective means to enhance or dampen immune responses (20–23). Furthermore, Nbs directed against membrane proteins specifically expressed by cancer cells represent potential diagnostics and therapeutics (1, 8, 24–30).

When using cDNA immunization as a strategy to generate Nbs, it is important to consider the molecular architecture of the membrane protein of interest (**Figure 2**). Often, the extracellular domain is composed of a single well-defined protein domain: the checkpoint inhibitor CTLA-4 contains a single immunoglobulin domain, the ecto-enzymes CD38 and ARTC2 a single, well-defined catalytic domain (**Figure 2A**). Other proteins can carry two or more distinct extracellular protein domains, such as integrins or MHC proteins (**Figure 2B**). Membrane proteins with such large extracellular domains often offer many independent

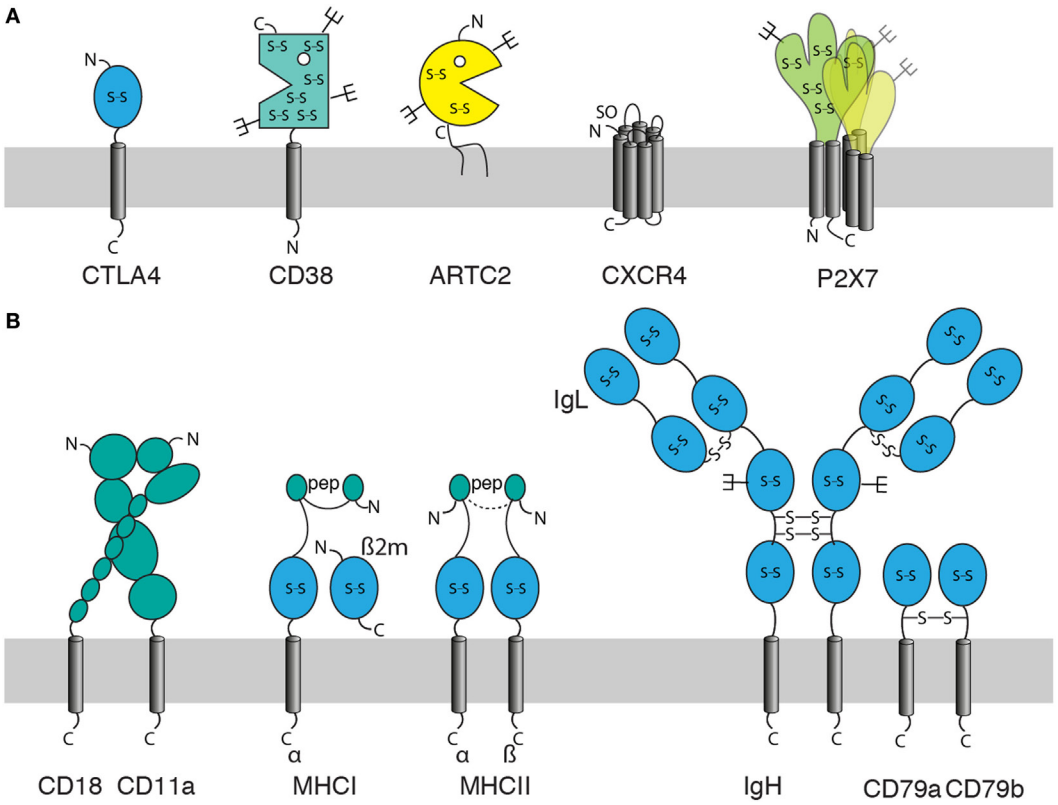

FIGURE 2 | Features of membrane proteins to consider for generation of nanobodies (Nbs) by the cDNA immunization strategy. When using cDNA immunization as a strategy to induce a Nb response against a membrane protein, it is important to consider: the size and structure of its extracellular domain(s), the location of its N- and C-termini (out, in), posttranslational modifications [glycosylation, sulfation], and whether the protein can be expressed alone or in association with partner proteins only. Posttranslational modifications include glycosylation (forks), disulfide bridges (S-S), sulfation (SO), and loading with peptide (pep). **(A)** Examples of monomeric and homo-multimeric membrane proteins: GPI-anchored proteins such as ARTC2 consist of an extracellular domain covalently linked *via* the C-terminal amino acid to a membrane glycolipid. Single span membrane proteins possess extracellular and intracellular domains (or chains of linked domains). The extracellular domain is N-terminal in type I membrane proteins such as CTLA-4 and C-terminal in type II membrane proteins such as CD38. Most double-spanning (and tetra-spanning) membrane proteins have cytosolic N- and C-termini. Some double-spanning proteins such as P2X7 exist as homomultimers. Seven transmembrane proteins [G-protein-coupled receptors (GPCRs)] such as CXCR4 have an N-out C-in orientation and typically exist as monomers or dimers. **(B)** Effective expression of multimeric membrane proteins on the cell surface may require co-expression of one or more partners. These can be other transmembrane, secretory, or cytosolic proteins. Integrins such as LFA-1 (CD11a/CD18) are efficiently expressed on the cell surface only as a pair of non-covalently linked type I membrane proteins. MHC class I molecules are composed of a type I membrane protein, a non-covalently associated secretory protein (β2m) and a peptide docked in the peptide binding groove, MHC class II molecules are composed of two non-covalently linked type I proteins and a docked peptide. Many receptor complexes are assembled from three or more proteins, some of which may be linked by interchain disulfide bonds, as in the B cell receptor (BCR) complex where disulfide bridges link the two heavy chains (type I), each heavy chain to a light chain (secretory protein), and the two accessory type I proteins CD79a and CD79b.

accessible epitopes for different Nbs. However, some membrane proteins, including many G-protein-coupled receptors (GPCRs) and voltage gated ion channels contain only very small extracellular domains encompassing only a handful of amino acid residues. Some of these membrane proteins may not offer sufficient space on the extracellular leaflet of the plasma membrane for even a single Nb.

When the membrane protein of interest is a monomer or homomultimer with a large ecto-domain (**Figure 2A**), cDNA immunization generally is rather straightforward since the protein does not require other proteins for stable expression on the cell surface in native conformation. However, many membrane proteins stably associate with one or more other proteins (**Figure 2B**). Stable heterodimers, for example, are formed by the alpha and beta chains of integrins and the alpha and beta chains of MHC molecules in association with a non-covalently bound peptide. Other membrane proteins such as the B cell receptor (BCR) complex are assembled into multimeric receptor complexes.

For membrane proteins that form heterodimeric or multimeric complexes with other membrane proteins, the cDNA immunization strategy may need to be adjusted. One option is to take the chance that the membrane protein of interest pairs with the orthologous partner protein(s) of the immunized host. For ubiquitously expressed proteins and for proteins expressed by skin cells or Langerhans cells, this may work. However, this is highly risky since the interphase surfaces of the pairing proteins might not be conserved. A better option is to immunize with a mixture of expression constructs encoding all members of the

protein complex. This would require co-transfection and co-expression in individual cells. While this is highly efficient with a combination of two vectors, it may be less efficient with multiple vectors.

In addition to the molecular architecture of the membrane protein of interest, it is important to analyze the conservation of its amino acid sequence to the orthologous protein of the camelid since structural conservation can restrict the antibody response to particular epitopes. In extreme cases, i.e., for a highly conserved protein, it may even be impossible to raise antibodies in camelids. However, since camelids are outbred animals, a dromedary, bactrian camel, llama or alpaca might have a sufficiently diverse ortholog and/or a set of suitable MHC alleles, so that an antibody response can be induced. The immune response of a healthy animal usually ensures that antibodies induced by immunization recognize only those epitopes of the target protein that are different from its own species ortholog, thereby preventing auto-antibody responses. We, therefore, routinely perform an amino acid sequence alignment of the membrane protein of interest and its orthologs from human, mouse and llama (**Figure 3**). With the aid of such an alignment, it is often possible to predict whether known or potential posttranslational protein modifications, including glycosylation, SO, and disulfide bond formation, are conserved (**Figure 3**). If the 3D-structure of one or more species orthologs is known, the alignment may even permit the prediction of possible Nb binding epitopes. The sequence alignment also points out residues that are conserved in mouse and human but not in the camelid. These are potential targets for a cross-reactive antibody. However, it is impossible to predict whether such cross-reactive antibodies will actually be obtained.

In the case of CD38 only one of four N-linked glycosylation sites in the ecto-domain of human CD38 is conserved also in the alpaca homolog. Moreover the ecto-domains of human and alpaca CD38 differ in more than 50 amino acid residues. In the case of CXCR4, the extracellular loops of the human and alpaca orthologs differ by ~20 amino acid substitutions. Based on the degree of sequence conservation, it is more likely to obtain a heavy-chain antibody response in alpacas against CD38 than against CXCR4. Case studies in the literature indicate that antibody responses

FIGURE 3 | Amino acid sequence alignments of CD38 and CXCR4 from human, mouse, and alpaca. Amino acid sequence alignments of the CD38 and CXCR4 species orthologs from human, mouse and alpaca (hs, *homo sapiens*; mm, *mus musculus*; vp, *vicuna pacos*). Symbols below the alignments indicate identical amino acid residues (*), conserved substitutions (. and:), and non-conserved substitutions (blank spaces). Cytosolic amino acid residues are indicated in blue, transmembrane residues in red, and extracellular residues in black. Potential asparagine-linked glycosylation sites and potential tyrosine-linked sulfation (SO) sites are highlighted in cyan. Cysteines engaged in intrachain disulfide bonding are highlighted in yellow. In order to access the sequence of the camelid ortholog, we perform a protein BLAST search (https://blast.ncbi.nlm.nih.gov) using the human protein sequence as input and selecting "Non-redundant protein sequences (nr)" as database and "Camelidae (taxid:9835)" as organism from the respective pull down menus.

can be induced even for antigens that differ only in one or a few amino acid substitutions. In cases of high sequence conservation, tolerance may be overcome by co-immunizing with protein that can deliver foreign peptides to MHCI and MHCII molecules (see below, section on mechanism of antibody induction).

CLONING AND VALIDATION OF THE cDNA EXPRESSION VECTOR ENCODING THE MEMBRANE PROTEIN OF INTEREST

The cDNA expression vectors used for genetic immunization are classical vectors used also for transfection of HEK cells or CHO cells, such as pCMV-Sport6 or pCDNA3 (Invitrogen). The sequences of these vectors are publicly available in the online repository of addgene (https://www.addgene.org/vector-database). **Figure 4** summarizes the essential and some optional features of a suitable cDNA expression vector. Essential components include the open reading frame (ORF) encoding the membrane protein of interest, a strong ubiquitous promoter, and a bacterial antibiotic resistance gene. Optional features include a mammalian antibiotic resistance gene, epitope tags, and an intron. A strong ubiquitous promoter ensures transcription of the membrane protein's open reading frame in cells of the immunized camelid. The promoter commonly is derived from a mammalian virus such as cytomegalovirus. A bacterial antibiotic resistance gene such as β lactamase (ampR) and an origin of replication (pUC_Ori) are required for plasmid propagation in *E. coli*. Since the ampR gene is under control of a bacterial promoter, it is not expressed by mammalian cells and, thus, not relevant for the *in vivo* immune response.

Many available expression vectors contain a second antibiotic resistance gene under control of a eukaryotic promoter, e.g., neomycin phosphotransferase II (neoR) mediating resistance to neomycin under control of the SV40 viral promoter (**Figure 4A**). This resistance marker provides the option of selecting stable transfectants in cell culture. Since this gene is under control of a eukaryotic promoter, it will be expressed by the transfected skin cells of the immunized camelid. Expression of the antibiotic resistance marker may actually enhance an adaptive immune response, since neomycin phosphotransferase can serve as a source of peptides for presentation by MHCI molecules and thereby amplify cytotoxic T cell responses. T cell-mediated cytolysis of transfected cells can facilitate uptake of vesicles containing the membrane protein by antigen-specific B cells (see Mechanism of Antibody Induction by Genetic Immunization).

In order to verify that the expression vector effectively drives the production of the target protein on the plasma membrane, it may be useful to genetically fuse a fluorescent protein (e.g., GFP) and/or a peptide tag (e.g., a FLAG-tag) to the protein of interest (**Figure 4B**). The fused GFP can also enhance the antibody response by providing foreign MHC-binding peptides as helper epitopes (see **Figure 6**). For this, it is important to consider the availability and localization of the N- and C-termini of the membrane protein. Many membrane proteins contain a cleaved N-terminal signal sequence and—in the case of GPI-anchored proteins—a C-terminal signal sequence as well. A fluorescent protein provides a means to verify expression of the fusion protein at the plasma membrane of transfected cells—GFP usually works best when attached to a cytosolic terminus. Similarly, an extracellular epitope-tag provides a means to verify cell surface expression of the membrane protein in transfected cells using a fluorochrome-conjugated tag-specific antibody

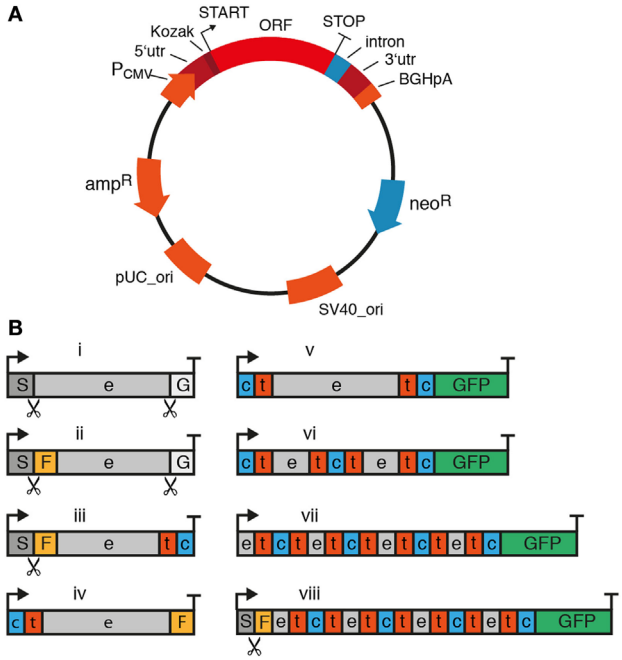

FIGURE 4 | Essential and optional features of mammalian expression vectors for cDNA immunization of camelids. When using cDNA immunization as a strategy to induce a nanobody (Nb) response, it is important to consider components of the plasmid and the cDNA expression cassette. **(A)** Essential components of the plasmid are indicated in red and optional components in blue. The ampicillin resistance (ampR) and bacterial origin of replication (pUC_ori) are required for plasmid propagation in *E. coli*. The expression cassette for the membrane protein of interest contains the entire open reading frame (ORF) preceded by a strong viral promoter (e.g., the cytomegalovirus promoter, P_{CMV}), a 5′ untranslated region (5′utr) and a Kozak sequence upstream of the start codon (arrow). The ORF is followed downstream of the stop codon by a 3′ untranslated region (3′utr) and a polyadenylation signal (e.g., of the bovine growth hormone, BGHpA). A mammalian antibiotic resistance gene (e.g., neomycin phosphotransferase, neoR) can be used for selecting stably transfected cells in culture. During cDNA immunization, this protein can help drive the immune response by providing peptides presented by MHC molecules. An intron can be placed anywhere between the start codon and the poly-adenylation signal to promote transcription and RNA processing. **(B)** In its simplest format (i), the expression cassette contains the full length open reading frame from start codon (arrow) to stop codon (T). A fused tag (e.g., Flag-tag, F) or fluorescent protein [e.g., green fluorescent protein (GFP)] can provide a means to verify expression of the protein at the plasma membrane. For fusion to a tag or protein, it is important to consider the availability and localization of the N- and C-termini of the membrane protein. Many membrane proteins contain a cleaved signal sequence (S) at the N-terminus, i.e., type I membrane proteins (iii) and some G-protein-coupled receptors (GPCRs) (viii). GPI-anchored proteins (i, ii) additionally contain a C-terminal signal sequence (G). The cleavage sites for these signal sequences are indicated by scissors. GFP usually works best when attached to a cytosolic terminus (v–viii).
e: extracellular, t: transmembrane, c: cytosolic.

in microscopy or flow cytometry. For GPI-anchored proteins, only the N-terminus is available for fusion since the C-terminus is covalently attached to a glycolipid. In this case—as with most type I membrane proteins that contain a cleavable signal sequence—the epitope-tag needs to be placed behind the signal sequence since this is proteolytically removed during translation in the ER.

COATING OF PLASMIDS TO GOLD PARTICLES AND BALLISTIC cDNA IMMUNIZATION

Ballistic transfection of skin cells with plasmid-coated gold particles is a very efficient technique to transfect skin cells including epithelial cells (EC), endothelial cells, and professional antigen-presenting cells (APC; e.g., Langerhans cells) (19, 31, 32). Other techniques for cDNA transfection have been used successfully (33–35). Even the simple injection of plasmid DNA in saline can lead to transfection, albeit usually with lower efficiencies (36). High pressure or electric pulses can be used to enhance transfection efficiencies (34, 35, 37, 38).

DNA immunization of larger animals has been problematic, possibly owing to the tougher texture of the skin. Our strategy to overcome this issue includes careful thorough shaving of the lower neck, followed by treatment with a commercial depilation cream, and use of gene gun-mediated ballistic immunization at a high pressure setting. In our experience, this approach is a highly efficient and reproducible technique to induce a heavy-chain antibody response in camelids (20–22). For ballistic cDNA immunization of camelids, we essentially follow the protocol of the provider of the Helios gene gun (BioRad). In brief, freshly purified plasmid DNA is precipitated onto spermidine-coated 1 µm gold particles using $CaCl_2$. 50 µg ultrapure plasmid DNA coated onto 25 mg of gold particles provides sufficient material for 48 shots (4 rounds of immunization). The precipitate is washed and resuspended in absolute ethanol containing polyvinylpyrrolidone. The DNA-coated gold particles are dried onto the inner wall of a long plastic tubing with a gentle flow of nitrogen gas under gentle rotation of the tubing. The tubing with the dried gold particles is cut into 48 cartridges, 12 of which are loaded into the cartridge holder of a gene gun. The gene gun is connected to a helium flask *via* a pressure gauge set at 600 psi. The nozzle of the gene gun is placed approximately 1 cm above the shaved skin of the camelid. Pulling the trigger releases a helium pulse that accelerates the DNA-coated gold particles to a velocity sufficient to penetrate through multiple layers of cells in the skin and to penetrate the plasma membrane of cells in the trajectory. The skin at the site of injection is prepared for immunization by shaving and by depilation using a mild depilation cream. For camelids, the skin of the lower neck and that of the upper hind leg are suitable injection sites. Since the camelid skin is tougher than that of rabbits or rodents, we use a higher pressure setting for camelids (600 psi) than for rodents and rabbits (400 psi). We typically use 12 cartridges per immunization (1 µg plasmid DNA 0.5 mg gold particles per shot). Boost immunizations are performed every 2–6 weeks (**Figure 5**). Longer intervals may improve the antibody response by providing more time for affinity maturation but come at increased costs for animal housing.

Swelling of the draining lymph node and serum titers of specific antibodies can both be used as criteria for a successful immune response. Following ballistic DNA immunization, these responses typically are lower than with adjuvant-assisted protein or cell immunization, presumably owing to the additional time required for transcription, translation and posttranslational modifications and the longer lasting antigen exposure due to extended production of the antigen by long-living cells. In order to induce a shorter and stronger response, we typically perform a final boost with protein or cells. Specific Nbs can be selected with cDNA immunization alone and even in cases without detectable lymph node swelling and/or serum titers. After clonal expansion, antigen-specific B cells are thought to migrate in distinct short waves *via* the blood to the bone marrow. The timing of lymphocyte sampling from blood, therefore, is based on educated guessing and typically lies in the range of 4–14 days after boost immunization. It is, therefore, prudent to take multiple samples. The optimal timing for sampling lymphocytes *via* a lymph node biopsy presumably corresponds to the time of maximal swelling. In principle, it should also be possible to harvest bone marrow, but we are not aware that anyone has performed this yet on camelids. For all practical purposes, it is easiest to obtain blood samples—100 ml samples can readily be harvested from the jugular vein of a llama, alpaca or dromedary. If the draining lymph node responds by swelling, the optimal time window for harvesting of

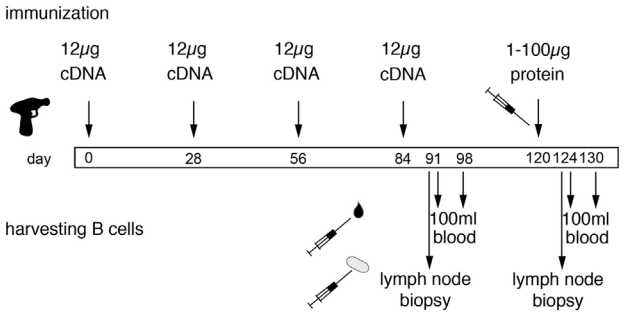

FIGURE 5 | Schematic diagram of the genetic immunization strategy to generate nanobodies (Nbs) against membrane proteins. The scheme illustrates time points for immunization and harvesting of blood cells in order to obtain Nbs directed against membrane proteins in native conformation. Each cDNA immunization comprises 12 shots, each with 1 µg plasmid DNA coated onto 1 mg of gold particles (see **Figure 4**). Boost immunizations are spaced 3–4 weeks apart. A final protein boost is performed with the purified ecto-domain, cells transfected with the membrane protein of interest, or protein immunoprecipitated from transfected cells with bead-conjugated antibodies. B cells are harvested from a sample of blood and/or a lymph node biopsy 7 days after the last cDNA boost and 4 days after the last protein boost, i.e., at the peak of lymph node swelling. A second sample of blood is drawn 6–7 days thereafter. i.e., at the estimated peak of migration of expanded B cells from the lymph node to the bone marrow. We have selected antigen-specific Nbs from libraries constructed from lymphocytes obtained both before and after the protein boost. In case of similar Nbs obtained from both samplings, it can be inferred that the respective clone was induced by DNA immunization—and that this clone was probably reactivated by the final protein boost.

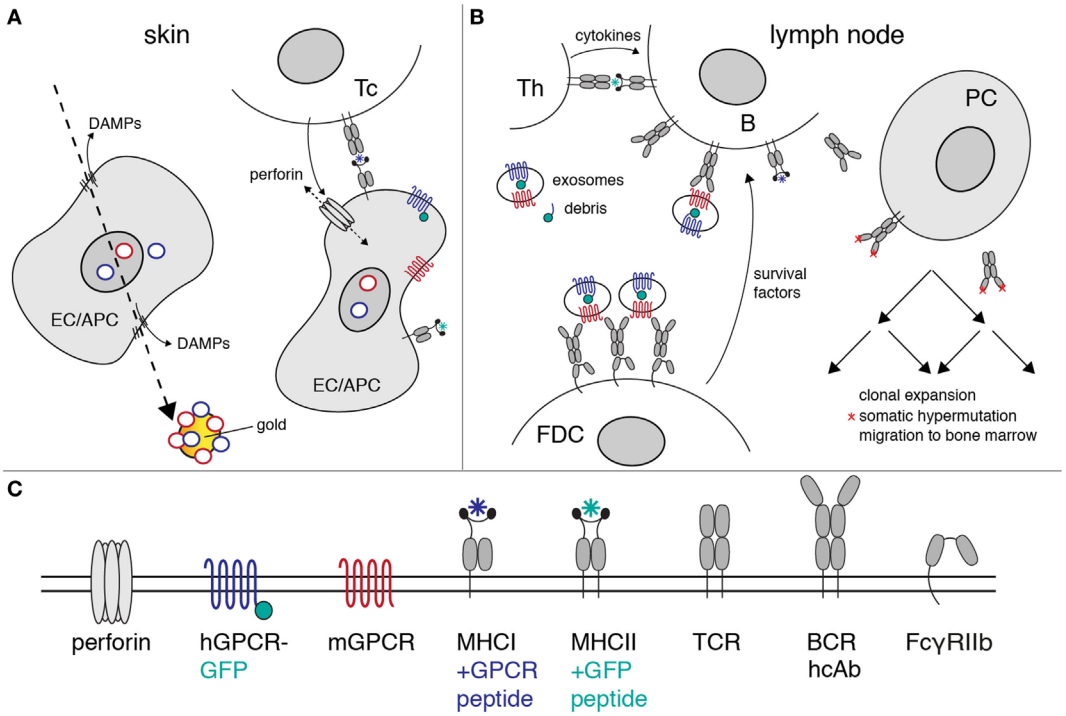

FIGURE 6 | Proposed mechanism of heavy-chain antibody induction by genetic immunization. The figure illustrates the likely mechanism of heavy-chain antibody induction by genetic immunization of a camelid. **(A)** Ballistic injection of gold particles coated with cDNA expression vectors (rings) transfects some epithelial cells (EC) and antigen-presenting cells (APC) in the skin. Injury of the plasma membrane by the penetrating gold particles results in the release of danger-associated molecular patterns (DAMPs). Here, gold particles carry a cocktail of expression vectors encoding a mouse G-protein-coupled receptor (GPCR) (red) and its human homolog (blue) as a fusion protein to green fluorescent protein (green). Transcription and translation results in cell surface expression of native mouse and human GPCRs. Peptides derived from these proteins are presented by MHC-I molecules on the cell surface. A cytotoxic T cell (Tc) with a matching T cell receptor (TCR) is induced to secrete perforins. Insertion of perforins into the plasma membrane of the EC/APC results in lysis of the target cell. **(B)** Exosomes and cellular debris released during cell lysis are transported to the draining lymph nodes. B cells with a matching heavy-chain B cell receptor (BCR) endocytose the immunogen-containing exosomes and debris. Peptides derived from endocytosed proteins are presented on the B cell surface by MHC-II molecules. A helper T cell (Th) with a matching TCR releases growth-promoting cytokines. Follicular dendritic cells (FDCs) bind immune complexes *via* the low-affinity Fc receptor (FcγRIIb). FDCs present complexes of antibodies and immunogen to B cells expressing matching heavy-chain antibodies. Th cytokines and survival factors provided by FDC induce: (i) clonal expansion of B cells expressing specific heavy-chain antibodies, (ii) somatic hypermutation of amino acids in the heavy-chain antibodies (red asterisks), (iii) selection of B cells expressing higher affinity antibodies, and (iv) differentiation of specific B cells into antibody-secreting plasma cells (PC). The latter emigrate from the lymph node and migrate *via* the vascular system to the bone marrow, where some of these cells settle in long-lasting niches. **(C)** Explanation of the logos used in the diagrams to depict cell surface proteins.

blood cells corresponds to a few days following the day of maximum lymph node swelling. DNA immunization often induces a slower and more extended response than adjuvant-assisted immunizations with protein or with cells. This likely reflects the additional time required for transcription and translation of the target protein and possibly also the time required for cytolysis of transfected cells by cytotoxic T cells and transport of membrane protein containing vesicles to the draining lymph node. We usually harvest blood 4–14 days after the last boost immunizations. Blood lymphocytes are purified by density gradient centrifugation, RNA is extracted and transcribed into cDNA using standard techniques. Optionally, plasma cells can be enriched by cell sorting prior to RNA extraction, e.g., using secondary antibodies against cell surface IgG or, by panning on cells expressing the membrane protein of interest. The Nb-coding region is then PCR amplified using appropriate primer pairs (see **Figure 6**). The PCR amplified VHH repertoire is then subjected to next-generation sequencing and cloning into pro- and or eukaryotic expression vectors (see Cloning of the VHH Repertoire and Identification of Specific Binders).

Using this approach we have generated functional Nbs against two ecto-enzymes and a ligand-gated ion channel (20–22). In case of murine ARTC2, three of four Nb families obtained from a single llama blocked the enzymatic activity of ARTC2 (20). A fourth Nb recognizes a distinct epitope and does not affect the enzyme activity. In case of human CD38 only three of 22 Nbs selected from four immunized llamas inhibited enzyme activity (22). Two Nbs that recognize a distinct epitope enhanced enzymatic activity. The other Nbs show little, if any effect on enzyme activity. In case of human P2X7 one of three Nbs isolated from two immunized llamas blocked channel function (21). In case of mouse P2X7 three of 19 Nbs blocked and two Nbs potentiated ATP-induced gating of P2X7. For CD38, we immunized two llamas with a mixture of expression constructs for human and mouse CD38 and two llamas with the purified ecto-domain of CD38 (22). For P2X7, we immunized two llamas with a mixture

of expression constructs for human and mouse P2X7, and two llamas with P2X7-transfected cells (21). We obtained specific Nbs from each immunized animal. From these examples, we could not detect any consistent fundamental differences in the properties of Nbs obtained from cDNA vs. protein/cell immunized animals. We conclude that it is also possible to generate Nbs by protein ecto-domain immunization in case of single span proteins with a soluble extracellular domain, such as CD38. P2X7 and CXCR4 are examples of membrane proteins that cannot be produced as soluble ecto-domains. In such cases, immunization with transfected cells can be a useful alternative strategy to cDNA immunization.

MECHANISM OF ANTIBODY INDUCTION BY GENETIC IMMUNIZATION

Many of the events governing activation, proliferation, and maturation of B cells expressing a complementary antibody to the membrane protein of interest expressed by host cells after cDNA immunization are well understood (39–45). **Figure 6** provides a schematic overview of the proposed mechanisms of antibody induction by cDNA immunization of camelids. The cDNA is transcribed into mRNA, the mRNA is translated into protein, and the protein is modified posttranslationally by the machinery of the transfected host cell (**Figure 6A**). A fraction of the expressed protein is degraded by proteasomes into peptides that are translocated into the lumen of the ER, where fitting peptides are loaded onto MHCI proteins. Bound peptides are presented by MHCI molecules on the surface of transfected cells, rendering the cells susceptible to attack by cytotoxic T cells (46). APC expressing the membrane protein and cellular debris including exosomes from the lysed cells are transported to the draining lymph nodes where they can be bound and endocytosed specifically by B cells expressing a complementary cell surface B cell receptor (BCR; **Figure 6B**). Following uptake and endosomal processing of the membrane protein by B cells, fitting peptides are presented by MHCII molecules on the cell surface of the B cell, rendering the cell responsive for help by CD4+ helper T cells (Th). Immune complexes containing target-exposing exosomes and antigen-specific antibodies are bound and displayed by follicular dendritic cells (FDCs). Binding of B cells to Th and FDCs triggers clonal expansion of the antigen-specific B cells in germinal centers. Clonal expansion is accompanied by somatic hypermutation of the genetic region encoding the variable domains. B cells expressing a cell surface immunoglobulin with higher affinity to the membrane protein displayed by FDCs expand preferentially, while B cells expressing a non or weakly binding surface immunoglobulin die by apoptosis. This Darwinian selection procedure results in the successive expansion of B cells with better fitting BCRs.

COCKTAIL cDNA IMMUNIZATIONS

It is entirely feasible and in many cases even advantageous to perform cDNA immunizations with a mixture of two or more cDNA expression vectors. We routinely immunize camelids with vectors encoding the mouse and human orthologs of the membrane protein of interest. This often "kills three flies with one clap," i.e., yielding Nbs specific for (i) the mouse ortholog, (ii) the human ortholog, and (iii) sometimes even Nbs cross-reactive with both the mouse and human orthologs. It is important to understand that camelids usually express the camelid ortholog of the cell surface protein of interest. The immune system typically recognizes only those portions of the target protein that are distinct from the endogenous protein. Antibodies induced by immunization with a human protein typically recognize the human protein but not the ortholog of the immunized camelid (e.g., llama, alpaca or dromedary). In other words, the antibody response usually is "blind" to conserved epitopes.

Cocktail immunization also provides the opportunity to augment an antibody response by providing helper epitopes (see **Figure 6**). Indeed, it is possible to induce a specific antibody response even if the target protein differs from the endogenous ortholog by only a single amino acid substitution, as exemplified by the classic Thy1 (CD90) alloantigens (47). Inbred strains of mice express either Thy1.1 or Thy1.2. Immunization of a Thy1.1+ mouse with cells expressing Thy1.2 induces a potent Thy1.2-specific antibody response, but only if the cells used for immunization co-express other disparate alloantigens that provide helper determinants (48). As explained in the previous section, antibody responses are driven by antigen-specific Th. This T cell help depends on both a peptide that can be presented by the particular MHCII molecules expressed by the immunized animal and a corresponding specific TCR that has escaped thymic selection. In order to obtain T cell help, the B cell needs to display MHCII-bound peptides on the cell surface. The MHCII presented peptides need not be derived from the membrane protein itself. They can also be derived from proteins encoded by a co-delivered cDNA expression vector during cocktail immunization, provided that the co-delivered protein is taken up and processed by the B cell displaying a specific antibody directed against the membrane protein of interest. In other words, suitable peptides must be delivered to the B cell together with the membrane protein of interest. It is unlikely that naive B cells endocytose intact EC or Langerhans cells. More likely, B cells bind and endocytose membrane-bound vesicles derived from these cells. If one or more distinct membrane proteins are contained in such vesicles, they can serve as a source for MHCII bound peptides.

Similarly, peptides binding to MHCI molecules typically drive cytotoxic T cell responses against the cells transfected with the cDNA expression construct during immunization (49, 50). Such a cytotoxic T cell response may indirectly support an antibody response by enhancing the release of vesicles containing the membrane protein from transfected cells, which can then be transported to the draining lymph nodes, thereby increasing the chances for encounter with and uptake by an antigen-specific B cell. As in case of MHCII-binding peptides, MHCI-binding peptides presented to cytotoxic T cells need not be derived from the target membrane protein of interest. With cDNA cocktail immunizations such peptides can be provided by a co-transfected protein, e.g., an antibiotic resistance marker under control of a mammalian promoter. Mixtures of cDNA expression vectors against two different membrane proteins of interest may therefore

increase the chances of providing suitable peptides for activation of helper and cytotoxic T cells.

CLONING OF THE VHH REPERTOIRE AND IDENTIFICATION OF SPECIFIC BINDERS

Figure 7 schematically outlines the procedure for cloning and sequencing of specific Nbs from immunized camelids. RNA extracted from blood lymphocytes (**Figure 7A**) is transcribed into cDNA and the Nb-coding region is then PCR amplified using appropriate primer pairs (**Figure 7B**). The-PCR-amplified VHH repertoire is then subjected to next-generation sequencing (**Figure 7C**) and cloning into pro- and or eukaryotic expression vectors (**Figures 7D,E**, respectively).

The fact that camelid heavy-chain antibodies recognize their target antigen *via* a single immunoglobulin domain provides a huge technical advantage for cloning of specific binders in comparison to conventional antibodies that recognize their target antigen via a pair of variable domains derived from two distinct protein chains. Cloning of the binding module from heavy-chain antibodies does not face the pairing problem of conventional antibodies. In other words, the VHH-domain can be PCR amplified and cloned directly into a mammalian expression vector so as to fuse the Nb to the hinge and Fc domains of a conventional mouse, human, or rabbit antibody (**Figure 7E**). It is then feasible to express such Nb-based heavy-chain antibodies in transiently transfected HEK cells, e.g., in a 96-well format and to screen the supernatants for production of specific binders. A second important advantage over conventional antibodies is that the entire ~350 bp coding sequence of each Nb is readily determined by a single sequence run. It can, thus, easily be determined whether identified binders are derived from the same or from distinct Nb families.

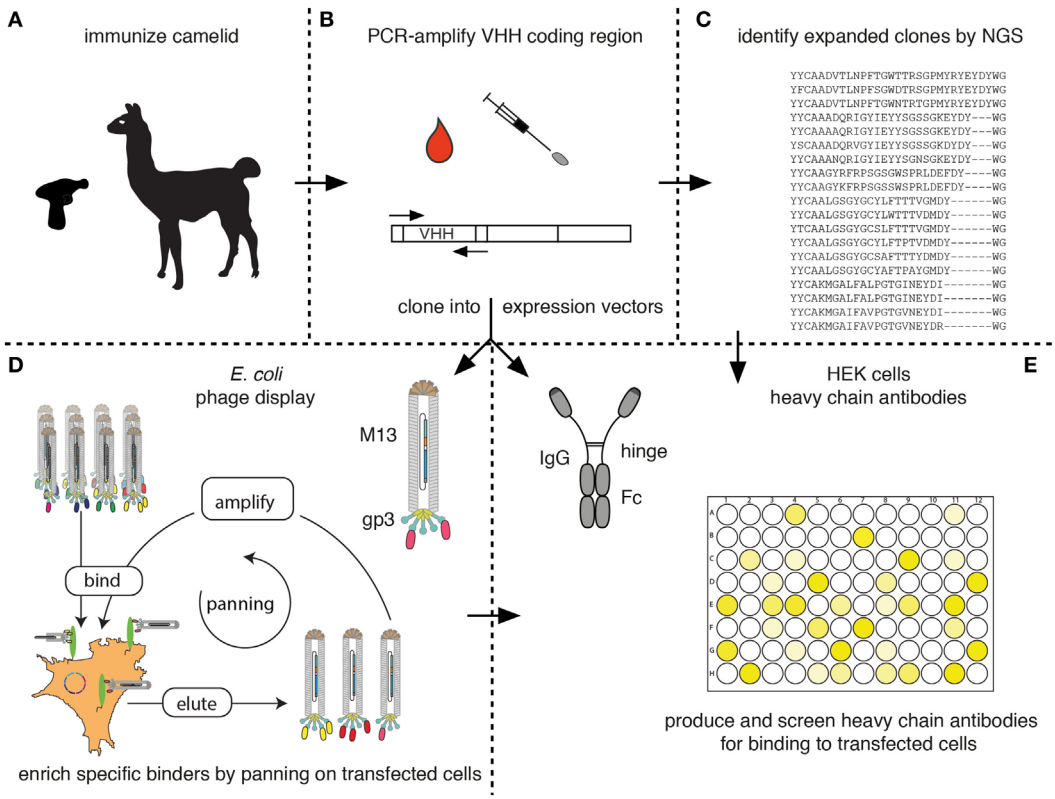

FIGURE 7 | Schematic diagram for the identification of membrane protein-specific nanobodies (Nbs). This figure schematically illustrates the discovery path for membrane-protein-specific Nbs following cDNA immunization. **(A)** Camelids are immunized as described in **Figure 5**. **(B)** RNA is prepared from lymphocytes obtained from blood or a lymph node biopsy and transcribed into cDNA. The Nb (VHH) coding region is PCR amplified. **(C)** An aliquot of the PCR product is subjected to next-generation sequencing. The results permit identification of expanded clones and reveal the extent of somatic hypermutation in such clones. **(D,E)** A second aliquot of the PCR product is cloned into a bacterial **(D)** and/or mammalian **(E)** expression vector. **(D)** During cloning into the bacterial vector, the Nb is genetically fused to the gp3 capsid protein of the M13 phage. Antigen-specific clones can then be enriched from the phage display library by panning on cells transfected with the membrane protein of interest. Bound phage are eluted and panning can be repeated, e.g., on another cell type transfected with the protein of interest. Panning can be performed in the presence of available antibodies or Nbs in order to select for Nbs binding to a distinct epitope. **(E)** During cloning into the mammalian vector, the Nb is genetically fused to the hinge and Fc domains of a conventional rabbit, mouse, or human IgG. Individual clones are transfected into HEK cells. Heavy-chain antibodies secreted into the HEK cell supernatant are then screened for binding to cells transfected with the membrane protein of interest by ELISA or immunofluorescence microscopy using appropriate enzyme- or fluorochrome-conjugated secondary antibodies.

Next-generation sequencing of the PCR-amplified VHH repertoire (**Figure 7C**) provides information about expanded clones and about the degree of somatic hypermutation in expanded clones (12, 51, 52). If the samples are prepared from an appropriate source, e.g., a lymph node biopsy at the peak of B-cell clonal expansion or a sample of blood at the peak of migration of expanded clones from the lymph node to the bone marrow, most of the expanded clones are detected by NGS contain specific binders against the target protein of interest. Therefore, the results of next-generation sequencing can be used as a guide to specifically clone and express members of the expanded clones by simply ordering the coding sequence for each Nb as a synthetic DNA fragment and cloning this into a suitable mammalian heavy-chain antibody expression vector (**Figures 7C–E**).

A library of phage displayed Nbs can be used to select specific binders by panning of the library on immobilized antigen (**Figure 7D**). For membrane proteins, selection can be performed on cells transiently or permanently transfected with the protein of interest. In order to avoid selection of Nbs binding to irrelevant target proteins displayed on the surface of the cells used for selection, additional rounds of selection can be performed while changing the cell background. This can be achieved by using distinct cell types transfected with the same membrane protein of interest, e.g., human HEK cells in the first round and hamster CHO cells in the second round. Moreover, negative selections can be performed to remove phage binding to other cell surface proteins, using cells not expressing the protein of interest, e.g., untransfected HEK or CHO cells.

A convenient strategy for identifying binders using CHO cells transiently transfected with the same plasmid that was used for immunization is illustrated in **Figure 8**. We typically co-transfect CHO cells with expression vectors encoding the membrane protein of interest and a green fluorescent protein (GFP) fused to a nuclear localization signal (**Figure 8**). 24–48 h after transfection, the 10–20% of co-transfected cells are distinguished from untransfected cells by their green fluorescent nucleus. Nb-based rabbit IgG heavy-chain antibodies that bind specifically to co-transfected cells can readily be identified using a fluorochrome-conjugated anti-rabbit IgG secondary antibody.

ASSESSING THE SPECIFICITY, AFFINITY, AND RELATIVE BINDING EPITOPES OF TARGET-SPECIFIC Nbs

The immunofluorescence assay described in **Figure 8** also provides a convenient means to assess the specificity of the selected Nbs, i.e., by comparing the reactivity of the Nbs with CHO cells transfected with related membrane proteins. This provides information on the cross reactivity of the selected Nbs with orthologs of the membrane protein of interest from other species (e.g., human, mouse, rat) or with paralogs of the same species. The same assay can also be used to assess the relative affinity of the selected Nbs, i.e., by performing titration analyses.

Similarly, cross-blocking assays can provide information about the relative binding epitopes of different Nbs directed against the same membrane protein. To this end, cells are incubated sequentially with a large excess of one Nb before addition of the second Nb. The two Nbs must be distinguishable, e.g., *via* linkage to a moiety that permits independent detection of at least the second Nb. There are several options to achieve this, e.g., conjugation of the purified Nb-based heavy-chain antibody to biotin or a fluorochrome. Alternatively, the Nbs can be fused to two different IgG isotypes, e.g., rabbit IgG and human IgG1 allowing detection by isotype-specific secondary antibodies. The same procedure can be used to asses whether the selected Nbs bind to distinct or overlapping epitopes with commercially available monoclonal antibodies against the same target.

GENETIC IMMUNIZATION TO RAISE Nbs AGAINST SECRETORY AND INTRACELLULAR PROTEINS

The strategy described here for raising Nbs against membrane proteins in native conformation can, in principle, be adapted also for raising Nbs against secretory or intracellular proteins in native conformation. Most secretory proteins can readily be produced as recombinant proteins and can thus also be used directly for classic adjuvant-assisted protein immunizations. For panning

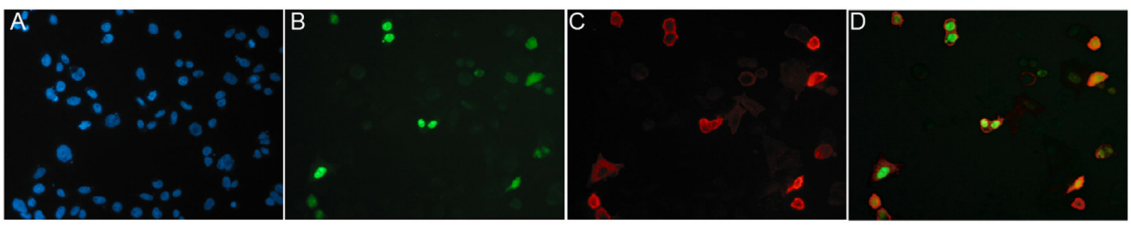

FIGURE 8 | Identification of specific binders using CHO cells transiently co-transfected with expression vectors for the membrane protein of interest and nuclear GFP. CHO cells were transiently co-transfected with expression vectors for GFP fused to a nuclear localization sequence and the cDNA expression vector used for immunization, in this case encoding the homotrimeric ligand-gated P2X7 ion channel. Cells plated onto 96-well plates were analyzed 24 h after transfection by immunofluorescence microscopy. Green nuclei clearly distinguish transfected CHO cells from untransfectd CHO cells (blue nuclei stained with the DNA-binding dye Hoechst 33342). Cells were screened for cell surface binding of specific antibodies and bound antibodies were detected with a phycoerythrin (PE)-conjugated secondary antibody. **(A)** Hoechst dye, **(B)** GFP, **(C)** PE, and **(D)** merged images. Reprinted from Cellular Immunology 236, Sahil Adriouch, Gudrun Dubberke, Philip Diessenbacher, François Rassendren, Michel Seman, Friedrich Haag, Friedrich Koch-Nolte, Probing the expression and function of the P2X7 purinoceptor with antibodies raised by genetic immunization, 72–77, ©2005, with permission from Elsevier.

of phage libraries on secretory proteins, the target protein can be coated onto the walls of a standard 96-well ELISA plate or—after biotinylation—be captured on streptavidin-coated beads. Screening for specific binding can conveniently be performed on transiently transfected cells. In this case, signals can be enhanced by treatment of cells with Brefeldin A for 4–6 h prior to analysis in order to trap secretory proteins in the ER and/or Golgi apparatus. Moreover, cells need to be fixed and permeabilized in order for Nbs or Nb-based heavy-chain antibodies to access the Golgi and ER compartments.

cDNA immunization can effectively induce specific antibody responses also against intracellular proteins, e.g., GFP or neomycin phosphotransferase (our own unpublished observations), even though these intracellular proteins are not directly accessible to the BCR on the B cell plasma membrane. Presumably, cytolysis mediated by specific cytotoxic T cells results in the release of intracellular proteins and their transport to the B cell compartment in draining lymph nodes *via* the lymphatics. We have found that antibody responses against intracellular proteins can be enhanced by forced expression of the entire proteins or distinct domains thereof on the cell surface. To this end, the open reading frame for the entire intracellular protein or for a structurally independent subdomain of the protein is genetically fused upstream to an ORF encoding a signal peptide and downstream to an ORF encoding a GPI-anchor signal sequence. In many cases, this results in forced display of the protein or protein domain on the cell surface. However, not all intracellular proteins or protein domains fold properly in the oxidative environment of the ER. Moreover, if the protein (domain) contains an internal glycosylation site (e.g., N X S/T), it can be aberrantly glycosylated in the ER. Furthermore, unpaired cysteine residues can engage in disulfide bond formation in the ER. These problems can often be circumvented by site-directed mutagenesis, e.g., by conservative substitutions such as asn to gln, or cys to ser. It may be convenient to attach an epitope tag—e.g., a FLAG tag to the N-terminus of the protein (domain), so that successful cell surface expression can be monitored by flow cytometry or immunofluorescence microscopy with a tag-specific antibody. If successful, immunization and selection of Nbs then follow the procedures described above for membrane proteins.

ADVANTAGES AND LIMITATIONS OF BALLISTIC cDNA IMMUNIZATION

Key advantages of the cDNA immunization approach are the high purity of the immunogen and the presentation of the target protein in its native conformation. Moreover, this approach offers the opportunity to co-immunize with other proteins of interest, e.g., target ortholog(s) of other species, a foreign protein(s) as a source of MHC-binding peptides, and inflammation-promoting cytokines. A limitation of cDNA immunization vs. adjuvant-assisted protein or cellular immunizations is the prolonged induction of the immune response resulting from the time required for transcription, translation, and posttranslational modifications. Moreover, lymph node swelling and serum titer typically are lower with cDNA than with protein immunizations. Consequently, it is more difficult to judge the optimal timing of lymphocyte sampling. Another limitation is the high cost of the gene gun. A recent report describes the successful selection of ChemR23-specific Nbs (a GPCR) upon immunization of llamas with the dermojet (AKRA DERMOJET), a needle-less injection device (34). Nbs elicited by cDNA immunization do not differ in terms of affinity, specificity, or other fundamental properties from Nbs elicited by alternative approaches, such as liposomes or virus-like particles bearing membrane proteins.

CONCLUSION AND PERSPECTIVES

Nanobodies and Nb-based heavy-chain antibodies have already proved valuable experimental tools in infection, immunity, oncology, and numerous other settings. The first Nb expected to be licensed for clinical applications next year (caplacizumab) is directed against a soluble protein (von Willebrand factor). This will likely pave the way for a wave of new Nb-based reagents to enter the clinic. Membrane proteins expressed by immune cells and tumor cells in particular represent potential therapeutic Nb targets in immunology and oncology. Conventional immunization strategies with purified protein and/or transfected cells are hampered by the poor solubility of many membrane proteins outside of a lipid environment and by the multitude of other antigens in transfected cells. The cDNA immunization strategy described here provides a powerful tool for the development of Nbs directed against membrane proteins.

AUTHOR CONTRIBUTIONS

FH and FK-N conceived the project. All authors established experimental procedures. TE, SM, JW, and FK-N wrote the manuscript. All authors reviewed and approved the manuscript.

ACKNOWLEDGMENTS

We thank Bianca Morgenrot and Sarah Hewald, UKE central animal facility, for excellent technical help with llama immunizations.

FUNDING

This study was supported by grants No. 310/4, No. 310/5, No. 310/6, No. 310/7, No. 310/8, and SFB1192-B5 from the Deutsche Forschungsgemeinschaft to FH and FK-N.

REFERENCES

1. Revets H, De Baetselier P, Muyldermans S. Nanobodies as novel agents for cancer therapy. *Expert Opin Biol Ther* (2005) 5(1):111–24. doi:10.1517/14712598.5.1.111
2. Wesolowski J, Alzogaray V, Reyelt J, Unger M, Juarez K, Urrutia M, et al. Single domain antibodies: promising experimental and therapeutic tools in infection and immunity. *Med Microbiol Immunol* (2009) 198(3):157–74. doi:10.1007/s00430-009-0116-7
3. Muyldermans S. Nanobodies: natural single-domain antibodies. *Annu Rev Biochem* (2013) 82:775–97. doi:10.1146/annurev-biochem-063011-092449
4. Baral TN, MacKenzie R, Arbabi Ghahroudi M. Single-domain antibodies and their utility. *Curr Protoc Immunol* (2013) 103:Unit 2.17. doi:10.1002/0471142735.im0217s103
5. De Genst E, Silence K, Decanniere K, Conrath K, Loris R, Kinne J, et al. Molecular basis for the preferential cleft recognition by dromedary heavy-chain antibodies. *Proc Natl Acad Sci U S A* (2006) 103(12):4586–91. doi:10.1073/pnas.0505379103
6. Tijink BM, Laeremans T, Budde M, Stigter-van Walsum M, Dreier T, de Haard HJ, et al. Improved tumor targeting of anti-epidermal growth factor receptor nanobodies through albumin binding: taking advantage of modular nanobody technology. *Mol Cancer Ther* (2008) 7(8):2288–97. doi:10.1158/1535-7163.MCT-07-2384
7. Farrington GK, Caram-Salas N, Haqqani AS, Brunette E, Eldredge J, Pepinsky B, et al. A novel platform for engineering blood-brain barrier-crossing bispecific biologics. *FASEB J* (2014) 28(11):4764–78. doi:10.1096/fj.14-253369
8. Li T, Qi S, Unger M, Hou YN, Deng QW, Liu J, et al. Immuno-targeting the multifunctional CD38 using nanobody. *Sci Rep* (2016) 6:27055. doi:10.1038/srep27055
9. Herce HD, Schumacher D, Schneider AFL, Ludwig AK, Mann FA, Fillies M, et al. Cell-permeable nanobodies for targeted immunolabelling and antigen manipulation in living cells. *Nat Chem* (2017) 9(8):762–71. doi:10.1038/nchem.2811
10. Steyaert J, Kobilka BK. Nanobody stabilization of G protein-coupled receptor conformational states. *Curr Opin Struct Biol* (2011) 21(4):567–72. doi:10.1016/j.sbi.2011.06.011
11. Staus DP, Strachan RT, Manglik A, Pani B, Kahsai AW, Kim TH, et al. Allosteric nanobodies reveal the dynamic range and diverse mechanisms of G-protein-coupled receptor activation. *Nature* (2016) 535(7612):448–52. doi:10.1038/nature18636
12. Peyvandi F, Scully M, Kremer Hovinga JA, Cataland S, Knobl P, Wu H, et al. Caplacizumab for Acquired Thrombotic Thrombocytopenic Purpura. *N Engl J Med* (2016) 374(6):511–22. doi:10.1056/NEJMoa1505533
13. Hassanzadeh-Ghassabeh G, Devoogdt N, De Pauw P, Vincke C, Muyldermans S. Nanobodies and their potential applications. *Nanomedicine (Lond)* (2013) 8(6):1013–26. doi:10.2217/nnm.13.86
14. Veugelen S, Dewilde M, De Strooper B, Chavez-Gutierrez L. Screening and characterization strategies for nanobodies targeting membrane proteins. *Methods Enzymol* (2017) 584:59–97. doi:10.1016/bs.mie.2016.10.029
15. Steeland S, Vandenbroucke RE, Libert C. Nanobodies as therapeutics: big opportunities for small antibodies. *Drug Discov Today* (2016) 21(7):1076–113. doi:10.1016/j.drudis.2016.04.003
16. Pardon E, Laeremans T, Triest S, Rasmussen SG, Wohlkonig A, Ruf A, et al. A general protocol for the generation of Nanobodies for structural biology. *Nat Protoc* (2014) 9(3):674–93. doi:10.1038/nprot.2014.039
17. Beghein E, Gettemans J. Nanobody technology: a versatile toolkit for microscopic imaging, protein-protein interaction analysis, and protein function exploration. *Front Immunol* (2017) 8:771. doi:10.3389/fimmu.2017.00771
18. Verheesen P, Laeremans T. Selection by phage display of single domain antibodies specific to antigens in their native conformation. *Methods Mol Biol* (2012) 911:81–104. doi:10.1007/978-1-61779-968-6_6
19. Tang DC, DeVit M, Johnston SA. Genetic immunization is a simple method for eliciting an immune response. *Nature* (1992) 356(6365):152–54. doi:10.1038/356152a0
20. Koch-Nolte F, Reyelt J, Schossow B, Schwarz N, Scheuplein F, Rothenburg S, et al. Single domain antibodies from llama effectively and specifically block T cell ecto-ADP-ribosyltransferase ART2.2 in vivo. *FASEB J* (2007) 21(13):3490–8. doi:10.1096/fj.07-8661com
21. Danquah W, Meyer-Schwesinger C, Rissiek B, Pinto C, Serracant-Prat A, Amadi M, et al. Nanobodies that block gating of the P2X7 ion channel ameliorate inflammation. *Sci Transl Med* (2016) 8(366):366ra162. doi:10.1126/scitranslmed.aaf8463
22. Fumey F, Koenigsdorf J, Kunick V, Menzel S, Schütze K, Unger M, et al. Nanobodies effectively modulate the enzymatic activity of CD38 and allow specific imaging of CD38+ tumors in mouse models in vivo. *Sci Rep* (2017) 7:14289. doi:10.1038/s41598-017-14112-6
23. Jahnichen S, Blanchetot C, Maussang D, Gonzalez-Pajuelo M, Chow KY, Bosch L, et al. CXCR4 nanobodies (VHH-based single variable domains) potently inhibit chemotaxis and HIV-1 replication and mobilize stem cells. *Proc Natl Acad Sci U S A* (2010) 107(47):20565–70. doi:10.1073/pnas.1012865107
24. Altintas I, Kok RJ, Schiffelers RM. Targeting epidermal growth factor receptor in tumors: from conventional monoclonal antibodies via heavy chain-only antibodies to nanobodies. *Eur J Pharm Sci* (2012) 45(4):399–407. doi:10.1016/j.ejps.2011.10.015
25. De Vos J, Devoogdt N, Lahoutte T, Muyldermans S. Camelid single-domain antibody-fragment engineering for (pre)clinical in vivo molecular imaging applications: adjusting the bullet to its target. *Expert Opin Biol Ther* (2013) 13(8):1149–60. doi:10.1517/14712598.2013.800478
26. Maussang D, Mujic-Delic A, Descamps FJ, Stortelers C, Vanlandschoot P, Stigter-van Walsum M, et al. Llama-derived single variable domains (nanobodies) directed against chemokine receptor CXCR7 reduce head and neck cancer cell growth in vivo. *J Biol Chem* (2013) 288(41):29562–72. doi:10.1074/jbc.M113.498436
27. Oliveira S, Heukers R, Sornkom J, Kok RJ, van Bergen En Henegouwen PM. Targeting tumors with nanobodies for cancer imaging and therapy. *J Control Release* (2013) 172(3):607–17. doi:10.1016/j.jconrel.2013.08.298
28. D'Huyvetter M, Xavier C, Caveliers V, Lahoutte T, Muyldermans S, Devoogdt N. Radiolabeled nanobodies as theranostic tools in targeted radionuclide therapy of cancer. *Expert Opin Drug Deliv* (2014) 11(12):1939–54. doi:10.1517/17425247.2014.941803
29. Chakravarty R, Goel S, Cai W. Nanobody: the "magic bullet" for molecular imaging? *Theranostics* (2014) 4(4):386–98. doi:10.7150/thno.8006
30. Kijanka M, Dorresteijn B, Oliveira S, van Bergen en Henegouwen PM. Nanobody-based cancer therapy of solid tumors. *Nanomedicine (Lond)* (2015) 10(1):161–74. doi:10.2217/nnm.14.178
31. Vahlsing HL, Yankauckas MA, Sawdey M, Gromkowski SH, Manthorpe M. Immunization with plasmid DNA using a pneumatic gun. *J Immunol Methods* (1994) 175(1):11–22. doi:10.1016/0022-1759(94)90327-1
32. Pertmer TM, Eisenbraun MD, McCabe D, Prayaga SK, Fuller DH, Haynes JR. Gene gun-based nucleic acid immunization: elicitation of humoral and cytotoxic T lymphocyte responses following epidermal delivery of nanogram quantities of DNA. *Vaccine* (1995) 13(15):1427–30. doi:10.1016/0264-410X(95)00069-D
33. Bradley ME, Dombrecht B, Manini J, Willis J, Vlerick D, De Taeye S, et al. Potent and efficacious inhibition of CXCR2 signaling by biparatopic nanobodies combining two distinct modes of action. *Mol Pharmacol* (2015) 87(2):251–62. doi:10.1124/mol.114.094821
34. Peyrassol X, Laeremans T, Gouwy M, Lahura V, Debulpaep M, Van Damme J, et al. Development by genetic immunization of monovalent antibodies (nanobodies) behaving as antagonists of the human ChemR23 receptor. *J Immunol* (2016) 196(6):2893–901. doi:10.4049/jimmunol.1500888
35. van der Woning B, De Boeck G, Blanchetot C, Bobkov V, Klarenbeek A, Saunders M, et al. DNA immunization combined with scFv phage display identifies antagonistic GCGR specific antibodies and reveals new epitopes on the small extracellular loops. *MAbs* (2016) 8(6):1126–35. doi:10.1080/19420862.2016.1189050
36. Wolff JA, Malone RW, Williams P, Chong W, Acsadi G, Jani A, et al. Direct gene transfer into mouse muscle in vivo. *Science* (1990) 247(4949 Pt 1):1465–8. doi:10.1126/science.1690918
37. van Drunen Littel-van den Hurk S, Luxembourg A, Ellefsen B, Wilson D, Ubach A, Hannaman D, et al. Electroporation-based DNA transfer enhances gene expression and immune responses to DNA vaccines in cattle. *Vaccine* (2008) 26(43):5503–9. doi:10.1016/j.vaccine.2008.07.093
38. Hutnick NA, Myles DJ, Ferraro B, Lucke C, Lin F, Yan J, et al. Intradermal DNA vaccination enhanced by low-current electroporation improves antigen expression and induces robust cellular and humoral immune responses. *Hum Gene Ther* (2012) 23(9):943–50. doi:10.1089/hum.2012.055

39. Barry MA, Johnston SA. Biological features of genetic immunization. *Vaccine* (1997) 15(8):788–91. doi:10.1016/S0264-410X(96)00265-4
40. Boyle JS, Brady JL, Lew AM. Enhanced responses to a DNA vaccine encoding a fusion antigen that is directed to sites of immune induction. *Nature* (1998) 392(6674):408–11. doi:10.1038/32932
41. Kowalczyk DW, Ertl HC. Immune responses to DNA vaccines. *Cell Mol Life Sci* (1999) 55(5):751–70. doi:10.1007/s000180050330
42. Donnelly JJ, Liu MA, Ulmer JB. Antigen presentation and DNA vaccines. *Am J Respir Crit Care Med* (2000) 162(4 Pt 2):S190–3. doi:10.1164/ajrccm.162.supplement_3.15tac10
43. Williams JA. Improving DNA vaccine performance through vector design. *Curr Gene Ther* (2014) 14(3):170–89. doi:10.2174/1566523214031408191225 38
44. Weber CS, Hainz K, Deressa T, Strandt H, Florindo Pinheiro D, Mittermair R, et al. Immune reactions against gene gun vaccines are differentially modulated by distinct dendritic cell subsets in the skin. *PLoS One* (2015) 10(6):e0128722. doi:10.1371/journal.pone.0128722
45. Li L, Petrovsky N. Molecular mechanisms for enhanced DNA vaccine immunogenicity. *Expert Rev Vaccines* (2016) 15(3):313–29. doi:10.1586/14760584.2016.1124762
46. Trimble C, Lin CT, Hung CF, Pai S, Juang J, He L, et al. Comparison of the CD8+ T cell responses and antitumor effects generated by DNA vaccine administered through gene gun, biojector, and syringe. *Vaccine* (2003) 21(25–26):4036–42. doi:10.1016/S0264-410X(03)00275-5
47. Williams AF, Gagnon J. Neuronal cell Thy-1 glycoprotein: homology with immunoglobulin. *Science* (1982) 216(4547):696–703. doi:10.1126/science.6177036
48. Lake P, Douglas TC. Recognition and genetic control of helper determinants for cell surface antigen Thy-1. *Nature* (1978) 275(5677):220–2. doi:10.1038/275220a0
49. Ulmer JB, Otten GR. Priming of CTL responses by DNA vaccines: direct transfection of antigen presenting cells versus cross-priming. *Dev Biol (Basel)* (2000) 104:9–14.
50. Sbai H, Schneider J, Hill AV, Whalen RG. Role of transfection in the priming of cytotoxic T-cells by DNA-mediated immunization. *Vaccine* (2002) 20(25–26):3137–47. doi:10.1016/S0264-410X(02)00251-7
51. Turner KB, Naciri J, Liu JL, Anderson GP, Goldman ER, Zabetakis D. Next-generation sequencing of a single domain antibody repertoire reveals quality of phage display selected candidates. *PLoS One* (2016) 11(2):e0149393. doi:10.1371/journal.pone.0149393
52. Deschaght P, Vintem AP, Logghe M, Conde M, Felix D, Mensink R, et al. Large diversity of functional nanobodies from a camelid immune library revealed by an alternative analysis of next-generation sequencing data. *Front Immunol* (2017) 8:420. doi:10.3389/fimmu.2017.00420

Conflict of Interest Statement: FH and FK-N receive a share of antibody sales *via* MediGate GmbH, a wholly owned subsidiary of the University Medical Center Hamburg-Eppendorf. TE, SM, JW, and FK-N are co-inventors on patent applications on nanobody transgenic mice and/or CD38- or P2X7-specific nanobodies.

The reviewer GH and handling editor declared their shared affiliation.

frontiers in Immunology

ORIGINAL RESEARCH
published: 12 December 2017
doi: 10.3389/fimmu.2017.01759

Stability-Diversity Tradeoffs Impose Fundamental Constraints on Selection of Synthetic Human V_H/V_L Single-Domain Antibodies from *In Vitro* Display Libraries

*Kevin A. Henry[1], Dae Young Kim[1], Hiba Kandalaft[1], Michael J. Lowden[1], Qingling Yang[1], Joseph D. Schrag[2], Greg Hussack[1], C. Roger MacKenzie[1,3] and Jamshid Tanha[1,3,4]**

[1] Human Health Therapeutics Research Centre, National Research Council Canada, Ottawa, ON, Canada, [2] Human Health Therapeutics Research Centre, National Research Council Canada, Montréal, QC, Canada, [3] School of Environmental Sciences, University of Guelph, Guelph, ON, Canada, [4] Department of Biochemistry, Microbiology and Immunology, University of Ottawa, Ottawa, ON, Canada

OPEN ACCESS

Edited by:
Abdul Qader Abbady, Atomic Energy Commission of Syria, Syria

Reviewed by:
Serge Muyldermans, Vrije Universiteit Brussel, Belgium
Oscar R. Burrone, International Centre for Genetic Engineering and Biotechnology, Italy

***Correspondence:**
Jamshid Tanha
jamshid.tanha@nrc-cnrc.gc.ca

This is NRC-HHT publication number: 53364.

Specialty section:
This article was submitted to Vaccines and Molecular Therapeutics, a section of the journal Frontiers in Immunology

Received: 30 September 2017
Accepted: 27 November 2017
Published: 12 December 2017

Citation:
Henry KA, Kim DY, Kandalaft H, Lowden MJ, Yang Q, Schrag JD, Hussack G, MacKenzie CR and Tanha J (2017) Stability-Diversity Tradeoffs Impose Fundamental Constraints on Selection of Synthetic Human V_H/V_L Single-Domain Antibodies from In Vitro Display Libraries. Front. Immunol. 8:1759. doi: 10.3389/fimmu.2017.01759

Human autonomous V_H/V_L single-domain antibodies (sdAbs) are attractive therapeutic molecules, but often suffer from suboptimal stability, solubility and affinity for cognate antigens. Most commonly, human sdAbs have been isolated from *in vitro* display libraries constructed *via* synthetic randomization of rearranged V_H/V_L domains. Here, we describe the design and characterization of three novel human V_H/V_L sdAb libraries through a process of: (i) exhaustive biophysical characterization of 20 potential V_H/V_L sdAb library scaffolds, including assessment of expression yield, aggregation resistance, thermostability and tolerance to complementarity-determining region (CDR) substitutions; (ii) *in vitro* randomization of the CDRs of three V_H/V_L sdAb scaffolds, with tailored amino acid representation designed to promote solubility and expressibility; and (iii) systematic benchmarking of the three V_H/V_L libraries by panning against five model antigens. We isolated ≥1 antigen-specific human sdAb against four of five targets (13 V_Hs and 7 V_Ls in total); these were predominantly monomeric, had antigen-binding affinities ranging from 5 nM to 12 μM (average: 2–3 μM), but had highly variable expression yields (range: 0.1–19 mg/L). Despite our efforts to identify the most stable V_H/V_L scaffolds, selection of antigen-specific binders from these libraries was unpredictable (overall success rate for all library-target screens: ~53%) with a high attrition rate of sdAbs exhibiting false positive binding by ELISA. By analyzing V_H/V_L sdAb library sequence composition following selection for monomeric antibody expression (binding to protein A/L followed by amplification in bacterial cells), we found that some V_H/V_L sdAbs had marked growth advantages over others, and that the amino acid composition of the CDRs of this set of sdAbs was dramatically restricted (bias toward Asp and His and away from aromatic and hydrophobic residues). Thus, CDR sequence clearly dramatically impacts the stability of human autonomous V_H/V_L immunoglobulin domain folds, and sequence-stability tradeoffs must be taken into account during the design of such libraries.

Keywords: single-domain antibody, synthetic antibody, human V_H/V_L, phage display, protein engineering

INTRODUCTION

The concept of an autonomous single immunoglobulin variable domain (single-domain antibodies or sdAbs) as the smallest representation of an antigen-binding-competent antibody was first described by Ward et al. in the mouse (1). With the discovery of naturally occurring heavy chain-only antibodies in *Camelidae* (2) and in cartilaginous sharks (3) several years later (the single variable domains of which can recognize antigen autonomously), it became clear that sdAbs represented not only a theoretical possibility but a viable immunological solution to the problem of antigen recognition. Although the human humoral immune system produces only conventional antibodies with paired heavy and light chains and not sdAbs, the question of whether human sdAbs (autonomous variable heavy- or light-chain domains, V_Hs or V_Ls) could be isolated and/or molecularly engineered *in vitro* was brought to light.

The identification, engineering and biophysical characterization of a handful of non-antigen-specific human V_H/V_L sdAbs has been extensively reported and discussed (4). The first efforts to produce human V_H/V_L sdAbs with novel antigen-binding specificities used "camelized" scaffolds that incorporated the solubilizing framework region (FR) substitutions found in camelid sdAbs (5–9). Although this approach yielded antigen-specific sdAbs with excellent solubility and biophysical properties, it relied on undesirable sequence deviation from the human IGHV germline. Later, rare fully human rearranged V_H and V_L variable domains were discovered that were autonomously stable and monomeric and large phage display libraries were constructed by randomizing their complementarity-determining regions (CDRs), although it was clear from the mid-2000s that certain CDR sequences (potentially low in hydrophobic content and rich in negative charge) were better compatible with solubility and stability of these molecules (9–11). There are now many examples of fully human antibodies (primarily V_Hs) isolated from such libraries against a variety of targets, including α-amylase (12), β-galactosidase (13, 14), *Candida albicans* MP65 and SAP-2 (15), carbonic anhydrase (12), CD154 (16), CD28 (17), CD40 (18, 19), CD40L (20), *Clostridium difficile* toxin B (21), EGFR (22), glypican-2 (23), glypican-3 (24), human serum albumin (HSA) (25–27), lysozyme (28–30), maltose-binding protein (31), MDM4 (32), mesothelin (33), TNF-α (34), TNFR1 (35), and VEGF (22). These fully human V_H/V_L sdAbs exhibit a variety of antigen-binding modes and functional activities and several have entered clinical development, where they have been generally well-tolerated albeit unexpectedly immunogenic (36, 37).

Here, we report the design, construction and characterization of three novel phage-displayed, synthetically randomized human V_H/V_L sdAb libraries. We attempted to circumvent the unfavorable biophysical properties of many human V_H/V_L sdAbs by (i) selecting ultra-stable V_H/V_L sdAbs tolerant to CDR modification as library scaffolds, (ii) maximizing randomized sequence diversity in CDRs using trinucleotide mutagenesis, and (iii) spiking the library with negatively charged residues to encourage solubility. Similarly to the experiences of others, we were able to isolate monomeric, high-affinity V_H/V_L sdAbs from the libraries against some antigens but not against others. The stochastic process of selecting binders from human V_H/V_L sdAb libraries is likely a consequence of fundamental tradeoffs between CDR sequence and human V_H/V_L sdAb stability and aggregation resistance.

MATERIALS AND METHODS

Identification of Human Autonomous V_H/V_L sdAb Scaffolds

The human autonomous V_H and V_L sdAb scaffolds used in this study (**Table 1**; Figure S1 in Supplementary Material) were

TABLE 1 | Properties of human V_H and V_L single-domain antibody scaffolds used in this study.

Type	Scaffold[a]	Disulfide linkages[b]	Germline rearrangement	CDR3 length (aa)	T_m (°C)	Monomer (%)	Reference
V_L	VL383	23–104	IGKV3-20–IGKJ2	9	57.3	>95	(39)
	$VL383_{SS}$	23–104, 54–78	IGKV3-20–IGKJ2	9	73.7	85.3	
	VL382	23–104	IGKV3-20–IGKJ1	9	70.1	>95	(39)
	$VL382_{SS}$	23–104, 54–78	IGKV3-20–IGKJ1	9	83.3	>95	
	VL335	23–104	IGKV3-20–IGKJ1	9	61.7	>95	(39)
	$VL335_{SS}$	23–104, 54–78	IGKV3-20–IGKJ1	9	79.0	>95	(39)
	VL330	23–104	IGKV1-39–IGKJ2	9	62.8	>95	(39)
	$VL330_{SS}$	23–104, 54–78	IGKV1-39–IGKJ2	9	83.7	>95	
	VL325	23–104	IGKV3-11–IGKJ4	9	68.5	>95	(39)
	$VL325_{SS}$	23–104, 54–78	IGKV3-11–IGKJ4	9	82.5	>95	(39)
V_H	VH420	23–104	IGHV3-15–IGHJ4	10	57.8	>95	(38)
	$VH420_{SS}$	23–104, 54–78	IGHV3-15–IGHJ4	10	67.3	>95	
	VH428	23–104	IGHV3-49–IGHJ4	14	62.3	>95	(38)
	$VH428_{SS}$	23–104, 54–78	IGHV3-49–IGHJ4	14	73.1	>95	
	VH429	23–104	IGHV3-23–IGHJ4	12	58.5	>95	(38)
	$VH429_{SS}$	23–104, 54–78	IGHV3-23–IGHJ4	12	71.8	>95	
	VHB82	23–104	IGHV3-23–IGHJ6	6	57.9	>95	(38)
	$VHB82_{SS}$	23–104, 54–78	IGHV3-23–IGHJ6	6	72.9	80.8	
	VHM81	23–104	IGHV3-23–IGHJ3	14	66.9	>95	(38)
	$VHM81_{SS}$	23–104, 54–78	IGHV3-23–IGHJ3	14	76.8	>95	

[a]*Full-length amino acid sequences are listed in Figure S1 in Supplementary Material.*
[b]*IMGT numbering.*

isolated as previously described by To et al. (38) and Kim et al. (39). Disulfide-stabilized versions of each V_H/V_L sdAb (bearing an intradomain disulfide linkage formed between Cys residues at IMGT positions 54 and 78) were produced by overlap extension PCR as described in Kim et al. (40).

CDR Shuffling

All three CDRs of each V_H/V_L scaffold were simultaneously exchanged for those listed in **Table 2** (20 V_H/V_L scaffolds × 12 CDR sets = 240 CDR-shuffled variants). DNA constructs encoding the CDR-shuffled variants were synthesized commercially (GeneArt/Life Technologies, Regensberg, Germany) and subcloned into the pSJF2H bacterial expression vector (12).

Design and Construction of Synthetic Human V_H/V_L sdAb Phage Display Libraries

Three phage-displayed sdAb libraries were constructed by *in vitro* randomization of the sdAb scaffolds VH428, $VHB82_{SS}$ and $VL383_{SS}$. Briefly, nondegenerate oligonucleotides spanning each sdAb were chemically synthesized using the phosphoramidite method (GeneArt/Life Technologies) and purified by HPLC. CDRs were randomized *via* incorporation of defined mixtures of trinucleotide phosphoramidite building blocks (41) during oligonucleotide synthesis. Oligonucleotides were assembled without amplification by Klenow fragment extension, gel purified using a GeneJET™ gel extraction kit (Thermo-Fisher, Waltham, MA, USA) according to the manufacturer's instructions, and resuspended in a total volume of 1 mL TE buffer (10 mM Tris-HCl, 1 mM EDTA, pH 8.0). Non-amplified library DNA was quantified by real-time PCR using Fast SYBR™ Green master mix (Thermo-Fisher), and a StepOnePlus™ real-time PCR system (Thermo-Fisher), then approximately 232–1,069 ng (4.3×10^{11} to 1.5×10^{12} molecules) of DNA was PCR-amplified with Phusion® high-fidelity DNA polymerase (Thermo-Fisher) using M13F and M13R primers (sequences in Table S1 in Supplementary Material), gel purified using a GeneJET™ gel extraction kit, then digested and ligated between the *Nco*I and *Not*I sites of the phagemid vector pMED1 (42). *Escherichia coli* TG1 cells were transformed with the ligation products by electroporation, yielding final library sizes between 1.0×10^{10} and 2.3×10^{10} independent transformants, ≥95% of which carried V_H/V_L sdAb inserts as shown by colony PCR.

Antibodies, Proteins and Reagents

Recombinant human CEACAM6 (residues 145–232) and mouse GITR (residues 20–153) ectodomains were produced by transient transfection of HEK293-6E cells as previously described (43). HSA was from Sigma-Aldrich (St. Louis, MO, USA; Cat. No. A9511).

TABLE 2 | Amino acid sequences of complementarity-determining region (CDR) sets introduced into human V_H/V_L single-domain antibody (sdAb) scaffolds for biophysical stability assessment.

V_L CDR set	CDR-L1[a]	CDR-L2[b]	CDR-L3[c]	CDR-L3 length (aa)
1	RASQSVLVHLA	GDSYRAD	QQTFYPST	8
2	RASQSVISNLA	GDSFRAF	QQVAHPTT	8
3	RASQSVTDTLLA	GISHRAD	QQLVHPFT	8
4	RASQSVVHNLA	GLSTRAH	QQFDHPYT	8
5	RASQSVSSNLA	GASLRAT	QQYLIPPAT	9
6	RASQSVAPSLLA	GTSTRAP	QQPTLFPTT	9
7	RASQSVNLPYLA	GVSTRAY	QQIAVTPYT	9
8	RASQSVDYNLA	DISFRAN	QQSLSPPAT	9
9	RASQSVNITSLA	GTSTRAD	QQTNTHHPVT	10
10	RASQSVSSYLA	GLSLRAV	QQTDSFFPFT	10
11	RASQSVPIVLA	GHSLRAD	QQLAFFDPFT	10
12	RASQSVYLNLA	GVSVRAD	QQILLFYPHT	10
V_H CDR set	**CDR-H1[d]**	**CDR-H2[e]**	**CDR-H3[f]**	**CDR-H3 length (aa)**
1	SNAWMS	RITSKTDGGTTD	DQANAFDI	8
2	DGYAMH	VTNNGGSTS	QSITGPTGAFDI	12
3	SSYAMS	AISGGGDHTY	EGMVRGVSSAPFDY	14
4	ISESMT	AISSSGGSTY	KKIDGARYDY	10
5	NTLSMG	AVSRSGGSTY	AATKSNTTAYRLSFDY	16
6	SMYRMG	VITRNGSSTY	TSGSSYLDAAHVYDY	15
7	SMDPMA	AGSSTGRTTY	APYGANWYRDEYAY	14
8	SRYPVA	VISSTGTSTY	NSQRTRLQDPNEYDY	15
9	SNRNMG	GISWGGGSTR	EFGHNIATSSDEYDY	15
10	NFYAMS	GVSRDGLTTL	VITGVWNKVDVNSRSYHY	18
11	SPTAMG	HITWSRGTTR	STFLRILPEESAYTY	15
12	DNYAMA	TIDWGDGGAR	ARQSRVNLDVARYDY	15

[a]*IMGT positions 24–40 in the acceptor sdAb were replaced with the indicated sequence.*
[b]*IMGT positions 56–69 in the acceptor sdAb were replaced with the indicated sequence.*
[c]*IMGT positions 105–117 in the acceptor sdAb were replaced with the indicated sequence.*
[d]*IMGT positions 35–40 in the acceptor sdAb were replaced with the indicated sequence.*
[e]*IMGT positions 55–66 in the acceptor sdAb were replaced with the indicated sequence.*
[f]*IMGT positions 105–117 in the acceptor sdAb were replaced with the indicated sequence.*

Recombinant human CTLA4 ectodomain (residues 1–162) was from Sino Biological (Beijing, China; Cat. No. 11159-H08H). *E. coli* 0157:H7 intimin (residues 658–934) fused C-terminally to maltose-binding protein (MBP-intimin) was from GenScript (Piscataway, NJ, USA). Horseradish peroxidase-conjugated antibodies used in ELISA (mouse anti-M13, Cat. No. 27942101; mouse anti-c-Myc, Cat. No. 11814150001; rabbit anti-6 × His, Cat. No. A190-114P) were from GE Healthcare (Piscataway, NJ, USA), Bethyl Laboratories (Montgomery, TX, USA) and Roche Diagnostics (Basel, Switzerland), respectively. M13K07 helper phage was from New England BioLabs (Ipswich, MA, USA) and M13K07ΔpIII hyper phage was from Progen Biotechnik (Heidelberg, Germany).

Isolation of Antigen-Specific Human V_H/V_L sdAbs by Panning

Phage particles displaying monovalent V_H/V_L sdAbs were prepared by rescue of the three synthetic human V_H/V_L sdAb phagemid libraries with M13K07 helper phage as previously described (42). Briefly, 2 × YT broth (4 L) containing 1% (w/v) glucose and 100 μg/mL ampicillin was inoculated with 1 mL phagemid-bearing *E. coli* TG1 cells (7.3×10^{10} to 1.6×10^{11}) and grown at 37°C with 250 rpm shaking to an OD_{600} of 0.5. Phagemid-bearing cells were superinfected with M13K07 helper phage at a multiplicity of infection of 20:1 at 37°C for 30 min with no shaking, then pelleted and resuspended in 6 L of 2 × YT broth containing 100 μg/mL ampicillin and 50 μg/mL kanamycin. The next day, phage particles were purified from bacterial supernatants using two rounds of polyethylene glycol precipitation; neither heat treatment nor filtration steps were used to remove residual bacterial cells. For panning, 5 μg of each protein in 35 μL phosphate-buffered saline (PBS), pH 7.4, was adsorbed overnight at 4°C in wells of NUNC MaxiSorp™ 96-well microtiter plates (Thermo-Fisher). The next day, wells were blocked with 200 μL PBS containing either 2% (w/v) bovine serum albumin (BSA) or 2% (w/v) skim milk for 1 h at 37°C, then rinsed 3 × with PBS. Approximately 5×10^{11} infective library phage particles (5×10^{12} virions) were added to wells in 100 μL of PBS containing 1% BSA or skim milk and 0.1% (v/v) Tween-20 for 2 h at room temperature. The blocking protein (BSA and skim milk) was switched in alternate rounds of panning, except for panning on HSA in which only skim milk was used. Wells were washed 5 × with PBS containing 0.1% Tween-20, 2 × with PBS and then bound phage were eluted for 10 min with 50 μL of 100 mM triethylamine, neutralized with 50 μL 1 M Tris-HCl, pH 7.5, and used to reinfect exponentially growing *E. coli* TG1 cells. The cultures were superinfected with M13K07 helper phage. The next day, amplified phage were purified by polyethylene glycol precipitation from 10 mL overnight cultures and used in subsequent panning rounds. After four or five rounds of selection, antigen-specific V_H- or V_L-displaying phage clones were identified by their binding in polyclonal and monoclonal phage ELISA as previously described (42).

Selection for Monomeric and Expressible Human V_H/V_L sdAbs by Panning

Phage particles displaying monovalent V_H/V_L sdAbs were prepared by rescue of phagemid libraries with M13K07 helper phage as described above. Phage particles displaying multivalent V_H/V_L sdAbs on all copies of pIII were prepared as described above, except that: (i) smaller volumes (100 mL) of 2 × YT broth were inoculated with 1 mL phagemid-bearing *E. coli* TG1 cells, (ii) phagemid libraries were rescued with M13K07ΔpIII hyper phage at a multiplicity of infection of 10:1, and (iii) the final overnight culture volume was 150 mL of 2 × YT broth.

For panning, 5 μg of either protein A (for the $VHB82_{SS}$ library; Thermo-Fisher) or protein L (for the $VL383_{SS}$ library; Thermo-Fisher) in 50 μL PBS, pH 7.4, was adsorbed overnight at 4°C in wells of NUNC MaxiSorp™ 96-well microtiter plates. The next day, wells were blocked with 300 μL PBS containing either 2% BSA or skim milk for 1 h at 37°C, then rinsed 1 × with PBS. Approximately 10^{11} infective library phage particles (10^{12} virions) were added to wells in 100 μL of PBS containing 1% skim milk and 0.1% Tween-20 for 2 h at room temperature. Wells were washed 5 × with PBS containing 0.1% Tween-20, 2 × with PBS and then bound phage were eluted for 10 min with 50 μL of 100 mM triethylamine, neutralized with 50 μL 1 M Tris-HCl, pH 7.5, and used to reinfect exponentially growing *E. coli* TG1 cells. The cultures were superinfected with either M13K07 helper phage or M13K07ΔpIII hyper phage. The next day, amplified phage were purified by polyethylene glycol precipitation from 10 mL overnight cultures and used in subsequent panning rounds. After three rounds of selection, pools of sdAb-phage (either phage bound by and eluted from protein A/L, or phage amplified from overnight cultures) were interrogated using next-generation DNA sequencing (NGS) as described below.

Soluble V_H/V_L Protein Expression

Monomeric V_H/V_L sdAbs bearing C-terminal 6 × His and c-Myc tags were expressed from overnight cultures of *E. coli* TG1 cells grown in 250 mL to 1 L of 2 × YT broth under IPTG (isopropyl β-D-1-thiogalactopyranoside) induction, then extracted from periplasmic space by osmotic sucrose shock and purified by immobilized metal affinity chromatography as previously described (42). For small-scale expression screening, 5 mL overnight cultures were grown as above, lysed using FastBreak™ reagent (Promega, Madison, WI, USA) and sdAbs purified using PureProteome™ nickel magnetic beads (EMD Millipore, Billerica, MA, USA). Expression yields from 5 mL cultures were determined using the Bradford protein assay (Bio-Rad, Hercules, CA, USA) as per manufacturer's instructions with a V_HH sdAb of known concentration as the protein standard. Titration ELISAs using soluble V_H/V_L sdAbs were performed as previously described (42, 44, 45), using either anti-6 × His or anti-c-Myc secondary antibodies to detect binding.

Size Exclusion Chromatography (SEC) and SEC with Multiangle Light Scattering (MALS)

Size exclusion chromatography analyses of monomeric V_H/V_L sdAbs were conducted using a Superdex™ 75 GL column (GE Healthcare) connected to an ÄKTA FPLC protein purification system (GE Healthcare) as previously described (42). UPLC-SEC-MALS analyses of V_H/V_L sdAbs were conducted essentially

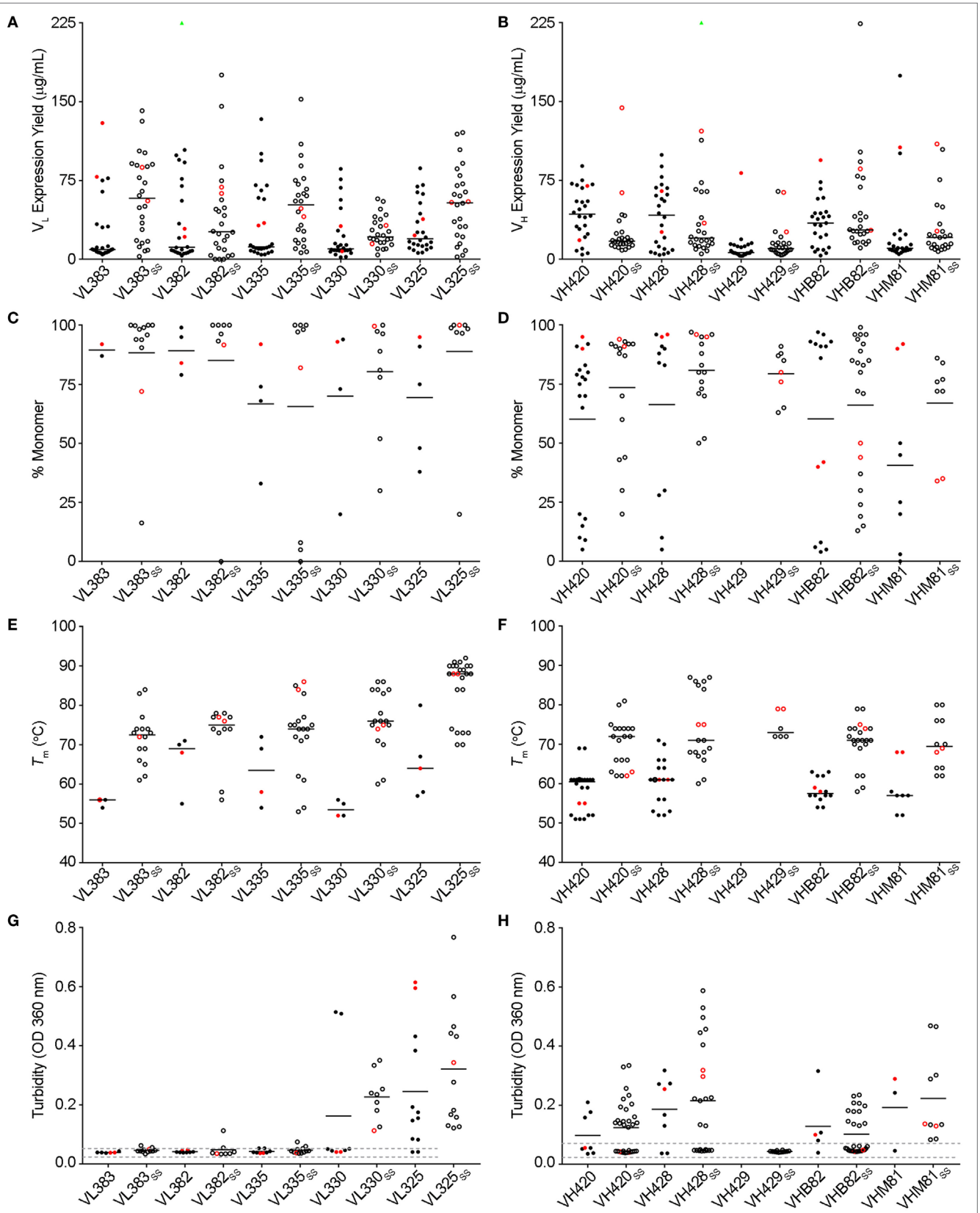

FIGURE 1 | Continued

FIGURE 1 | Continued
Biophysical stability assessment of complementarity-determining region (CDR)-shuffled human V_H/V_L single-domain antibody (sdAb) variants. **(A,B)** Expression yields of CDR-shuffled V_L **(A)** and V_H **(B)** sdAbs from 5 mL overnight cultures, as determined by Bradford assay. Two outliers (VL382 + CDR set 9, expression yield 467.7 μg/mL and $VH428_{SS}$ + CDR set 2, 356.4 μg/mL) are indicated by green triangles. **(C,D)** Aggregation tendencies of CDR-shuffled V_L **(C)** and V_H **(D)** sdAbs, as determined by SEC-MALS. **(E,F)** Melting temperatures (T_ms) of CDR-shuffled V_L **(E)** and V_H **(F)** sdAbs, as determined by thermal shift assay. **(G,H)** Turbidity upon thermal denaturation of CDR-shuffled V_L **(G)** and V_H **(H)** sdAbs, as measured by spectrophotometry at 360 nm wavelength. Dashed lines represent the range of turbidity measurements for unheated V_H/V_L sdAbs. The aggregation tendencies, T_ms and turbidities of CDR-shuffled variants of VH429 were not characterized due to inadequate expression yields. Horizontal lines represent mean **(C,D,G,H)** or median **(A,B,E,F)** values and wild-type V_H/V_L sdAbs with unmodified CDRs are shown in red. Open and solid circles represent V_H/V_L sdAbs with, or without, a stabilizing exogenous disulfide linkage. The number of data points in each panel reflects whether the experiment was conducted in singlicate **(C,E)** or duplicate **(A,B,D,F–H)** and for panels **(C–H)**, whether the CDR-shuffled variant expressed sufficiently for analysis.

as previously described (39) using an Acquity BEH-125 column (Waters, Milford, MA) connected to an Acquity UPLC H-Class Bio system (Waters) with miniDAWN™ MALS detector and Optilab® UT-rEX™ refractometer (Wyatt Technology, Santa Barbara, CA, USA). V_H/V_L sdAbs (10–20 μg) were injected at 30°C in a mobile phase consisting of calcium- and magnesium-free DPBS (GE Healthcare) at a flow rate of 0.4 mL/min. Weighted average molecular mass (M_{MALS}) was calculated using a protein concentration determined using A_{280} from the PDA detector with extinction coefficients calculated from amino acid sequences. Data were processed using ASTRA 6.1 software (Wyatt).

Surface Plasmon Resonance (SPR)

All monomeric human V_H/V_L sdAbs were SEC-purified and buffer-exchanged into HBS-EP buffer (10 mM HEPES, 150 mM NaCl, 3 mM EDTA, 0.005% (v/v) surfactant P20, pH 7.4) prior to SPR analyses. All SPR analyses were performed on a Biacore™ 3000 instrument (GE Healthcare) at a temperature of 25°C. Briefly, proteins (CEACAM6, 370 resonance units (RUs); HSA, 1614 RUs; GITR, 796 RUs; MBP-intimin, 1536 RUs) were immobilized *via* amine coupling on research-grade CM5 sensor chips (GE Healthcare) in 10 mM acetate buffer, pH 4.0, according to the manufacturer's instructions. V_H/V_L sdAbs were injected at concentrations ranging from 1 nM to 10 μM, at flow rates of 20–50 μL/min and with contact time between 120 s and 300 s, then allowed to dissociate for 7–10 min. All surfaces were regenerated using 10 mM glycine, pH 1.5. Ethanolamine-blocked flow cells served as reference surfaces. The data were fitted to a 1:1 interaction model and binding affinities (K_Ds) and/or kinetic parameters were determined either by steady-state analysis or by multicycle kinetic analysis using BIAevaluation 4.1 software (GE Healthcare).

Surface plasmon resonance analyses of two V_L sdAbs (VL_{SS}-2 and VL_{SS}-5) against MBP-intimin were conducted as described above, except that 234 RUs of MBP-intimin were immobilized on a research-grade C1 sensor chip (GE Healthcare) *via* amine coupling in 10 mM acetate buffer, pH 4.5, according to the manufacturer's instructions. These two V_L sdAbs were injected in HBS-EP buffer containing either 150 or 500 mM NaCl with an extended contact time (600 s).

Protein Turbidity Assays

V_H/V_L sdAb samples (0.2 mL) in 1.5 mL microcentrifuge tubes were heated to 85°C in a heating block for 10 min, then allowed to cool to room temperature for 30 min. Absorbance at 360 nm was measured pre- and post-heat treatment in a quartz NanoQuant Plate™ (Tecan, Männedorf, Switzerland) using an Infinite® M200 PRO microplate reader (Tecan). V_H/V_L sdAb concentrations were adjusted to 0.25 mg/mL in PBS prior to analysis.

Thermal Shift Assays

V_H/V_L sdAb samples (45 μL) in 96-well thin-wall optical plates (Bio-Rad) were mixed with 5 μL SYPRO® Orange (diluted 1:100 from 5,000 × stock; Life Technologies, Carlsbad, CA, USA) and sealed with optical quality sealing tape (Bio-Rad). Using an iQ™ 5 real-time PCR system (Bio-Rad), a temperature ramp of 1°C/min was applied and thermal unfolding was monitored by measuring fluorescence at 0.5°C intervals as previously described (46, 47). The wavelengths for excitation and emission were 490 and 575 nm, respectively. Melting temperatures (T_ms) were calculated as the temperature at which the maximum rate of change in fluorescent signal ($d(RFU)/dt$) was achieved. V_H/V_L sdAb concentrations were adjusted to 1 mg/mL in PBS prior to analysis.

Circular Dichroism

T_ms were also determined by circular dichroism as previously described (39, 40). Ellipticity of V_H/V_L sdAbs (100 μg/mL) was measured at wavelengths between 205 and 210 nm in 100 mM sodium phosphate buffer, pH 7.4. Ellipticity measurements were normalized to a percentage scale and then T_ms were determined by plotting percent folded versus temperature and fitting the data to a Boltzmann distribution.

Next-Generation DNA Sequencing

V_H/V_L sdAb libraries were interrogated using an Illumina MiSeq instrument as described previously (44, 45, 48). Amplicons for NGS were prepared using FR1- and FR4-specific barcoded primers (sequences in Table S1 in Supplementary Material) using as template either phagemid DNA (~10 ng) or phage virions (~10^6 particles).

Statistical Analyses

Descriptive statistics (mean, median) were used to describe datasets as described in figure legends. No inferential statistical tests were used.

RESULTS

Antigen-specific human autonomous V_H/V_L sdAbs do not exist in nature, and are most commonly isolated from synthetically randomized *in vitro* display libraries. These molecules are notoriously unstable and aggregation prone (4), which probably negatively

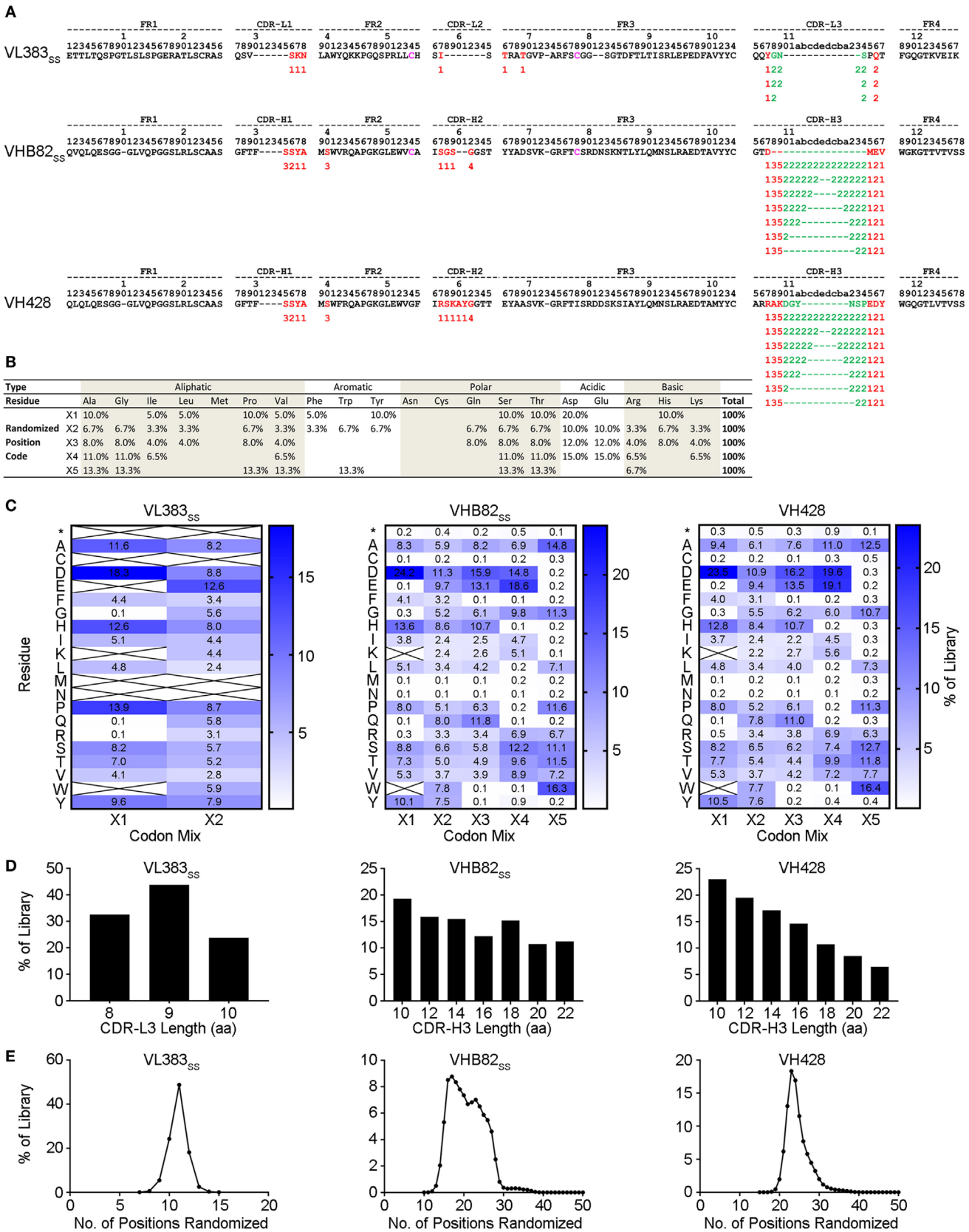

FIGURE 2 | Continued

FIGURE 2 | Continued
Design and construction of the $VL383_{SS}$, VH428, and $VHB82_{SS}$ synthetic human V_H/V_L single-domain antibody (sdAb) libraries. **(A)** Design of the human V_H/V_L sdAb libraries. The parental V_H/V_L sdAb sequence is shown at top with IMGT numbering. Intradomain disulfide linkage-forming cysteine residues at positions 54 and 78 are shown in magenta. Randomization positions are highlighted in either red (no length polymorphism) or green (length polymorphism). Arabic numerals indicate the codon mixture (X1, X2, X3, X4, or X5) incorporated at each randomization position. **(B)** Expected amino acid frequencies at V_H/V_L sdAb library randomization positions. **(C)** Observed amino acid frequencies at V_H/V_L sdAb library randomization positions, measured from phagemid DNA isolated from *Escherichia coli* TG1 cells. Crossed-out cells indicate a frequency of <0.1%. **(D)** CDR3 length distributions of the V_H/V_L sdAb libraries. **(E)** Degree of randomized sequence diversity (Levenshtein distance, or number of amino acid changes with respect to the parental scaffold) in the V_H/V_L sdAb libraries. Analyses shown in **(C–E)** are representative of 7.7×10^4 to 7.9×10^5 sequences per library.

TABLE 3 | Attrition rates of human V_H/V_L single-domain antibodies (sdAbs) through isolation and characterization.

Library	Target	No. of binding sdAbs		
		Phage ELISA	Soluble ELISA	SPR
$VL383_{SS}$	CEACAM6	1	1	1
	CTLA4	4	0	
	GITR	0		
	HSA	2	0	
	MBP-intimin[a]	3, 5	2, 4	2, 4
		15 (100%)	7 (47%)	7 (47%)
VH428	CEACAM6	3	3	3
	CTLA4	3	0	
	GITR	4	0	
	HSA	2	0	
	MBP-intimin	4	2	2
		16 (100%)	5 (31%)	5 (31%)
$VHB82_{SS}$	CEACAM6	5	5	5
	CTLA4	9	0	
	GITR	5	1	1
	HSA	6	3	1
	MBP-intimin	3	2	1
		28 (100%)	11 (39%)	8 (29%)
Total		59 (100%)	23 (39%)	20 (34%)

[a]*Double entries reflect two independent isolation attempts.*

impacts the selection of antigen-specific binders from synthetic V_H/V_L sdAb libraries. In an effort to mitigate these factors, we attempted to identify ultra-stable V_H/V_L sdAb scaffolds upon which we could construct highly diverse, stability-enhanced phage-displayed V_H/V_L sdAb libraries designed to yield soluble and thermostable antigen-specific human sdAbs.

Biophysical Stability Assessment of Wild-Type Human V_H/V_L sdAb Scaffolds

The T_ms and aggregation tendencies of 22 potential V_H sdAb scaffolds and 18 potential V_L sdAb scaffolds were determined by circular dichroism and SEC (Tables S2 and S3 in Supplementary Material). Five V_H and five V_L sdAb scaffolds as well as their disulfide-stabilized equivalents (**Table 1**) were selected as the most promising candidates for library construction based on: (i) primarily monomeric folding, (ii) high thermostability with reversible thermal unfolding, and (iii) reasonable expression yields (>1 mg/L) from overnight *E. coli* TG1 cultures. As reported previously (39, 40), incorporation of a disulfide linkage spanning IMGT positions 54–78 increased the T_m of each scaffold by ~5–20°C but also had unpredictable effects on expression yields.

Tolerance of Human V_H/V_L sdAb Scaffolds to CDR Modification

As a preliminary investigation into which of the 20 V_H/V_L sdAb scaffolds might best tolerate library randomization, we grafted 12 sets of exogenous CDRs (**Table 2**) into each scaffold and assessed the resulting molecules' expression level (Bradford assay), aggregation tendency (SEC-MALS), T_m (thermal shift assay), and ability to refold after thermal denaturation (turbidity assay). For V_L sdAb scaffolds, the 12 sets of exogenous CDRs were derived from non-antigen-specific human V_L sdAbs isolated from previously constructed libraries with expression yields ≥10 mg/L and for V_H sdAb scaffolds, the 12 sets of exogenous CDRs were selected from either human V_H sdAbs of unknown antigen specificity isolated from previously constructed libraries or camelid V_HH sdAbs with expression yields ≥3 mg/L.

The V_L sdAb scaffolds yielding the best-expressing CDR-shuffled variants were $VL383_{SS}$, $VL325_{SS}$ and $VL335_{SS}$ (**Figure 1A**). CDR-shuffled variants of $VL383_{SS}$ and $VL325_{SS}$ were primarily monomeric by SEC-MALS, while CDR-shuffled variants of $VL335_{SS}$ showed some tendency to aggregate (**Figure 1C**). All three of these V_L sdAb scaffolds, especially $VL325_{SS}$, yielded CDR-shuffled variants with high T_ms (**Figure 1E**); however, many CDR-shuffled variants of $VL325_{SS}$ showed significant turbidity upon heat denaturation (**Figure 1G**), reflecting their inability to refold as soluble monomers. The V_H sdAb scaffolds yielding the best-expressing CDR-shuffled variants were VH420, VH428, VHB82, $VHB82_{SS}$, and $VHM81_{SS}$ (**Figure 1B**). CDR-shuffled variants of all five of these V_H sdAb scaffolds were similarly monomeric (**Figure 1D**) but as expected, the two disulfide-stabilized sdAb scaffolds ($VHB82_{SS}$ and $VHM81_{SS}$) yielded CDR-shuffled variants with higher T_ms (**Figure 1F**). Similar proportions of the CDR-shuffled variants of all five V_H sdAb scaffolds showed minor turbidity upon heat denaturation (**Figure 1H**). On the basis of these data, we selected one V_L sdAb scaffold ($VL383_{SS}$) and two V_H sdAb scaffolds (VH428 and $VHB82_{SS}$) for library construction, reflecting a balance of their tolerance to CDR modification as well as their differing CDR3 lengths and germline gene rearrangements.

Design and Construction of Phage-Displayed Human V_H/V_L sdAb Libraries

Three synthetic sdAb libraries ($VL383_{SS}$, VH428, and $VHB82_{SS}$) were constructed by limited *in vitro* randomization of the CDRs of these V_H/V_L sdAb scaffolds and cloning of the resulting DNA

into the pMED1 phagemid vector (**Figures 2A,B**). CDR3 length was varied in each library (**Figures 2A,D**; $VL383_{SS}$ library: 8, 9, or 10 residues; VH428 and $VHB82_{SS}$ libraries: 10, 12, 14, 16, 18, 20, or 22 residues) while CDR1 and CDR2 lengths were constant. The major technical advances of these over our previously described phage-displayed synthetic human V_H/V_L sdAb libraries (12, 21, 31) were (i) trinucleotide mutagenesis allowed for incorporation of defined mixtures of amino acids at each randomization position, based on alignments of human and llama antibodies with additional bias toward solubility-promoting residues (Asp, Glu) and against undesirable residues (Asn, Cys, and Met) and stop codons (**Figures 2B,C**; Figure S2 in Supplementary Material) and (ii) near-complete randomization of all three CDRs of each V_H/V_L sdAb scaffold resulted in much higher sequence diversity for the vast majority of library molecules (**Figure 2E**). All three V_H/V_L sdAb libraries were transformed into *E. coli* TG1 cells, yielding final library sizes ($1.0–2.3 \times 10^{10}$ independent transformants) that, as expected, vastly under-sampled theoretical library diversity ($VL383_{SS}$: 2.9×10^{13} unique sequences; $VHB82_{SS}$: 2.3×10^{33} unique sequences; VH428: 2.3×10^{35} unique sequences). At this stage, prior to helper phage rescue, no major clonality biases or deviations from library design were observed (data not shown).

Isolation and Characterization of Antigen-Specific Human V_H/V_L sdAbs

All three V_H/V_L sdAb libraries were rescued with M13K07 helper phage and panned for four or five rounds against five model antigens (CEACAM6, CTLA4, GITR, HSA, and MBP-intimin). All library pannings were performed in duplicate by two independent operators at the same time and using the same materials, except for panning against MBP-intimin, in which

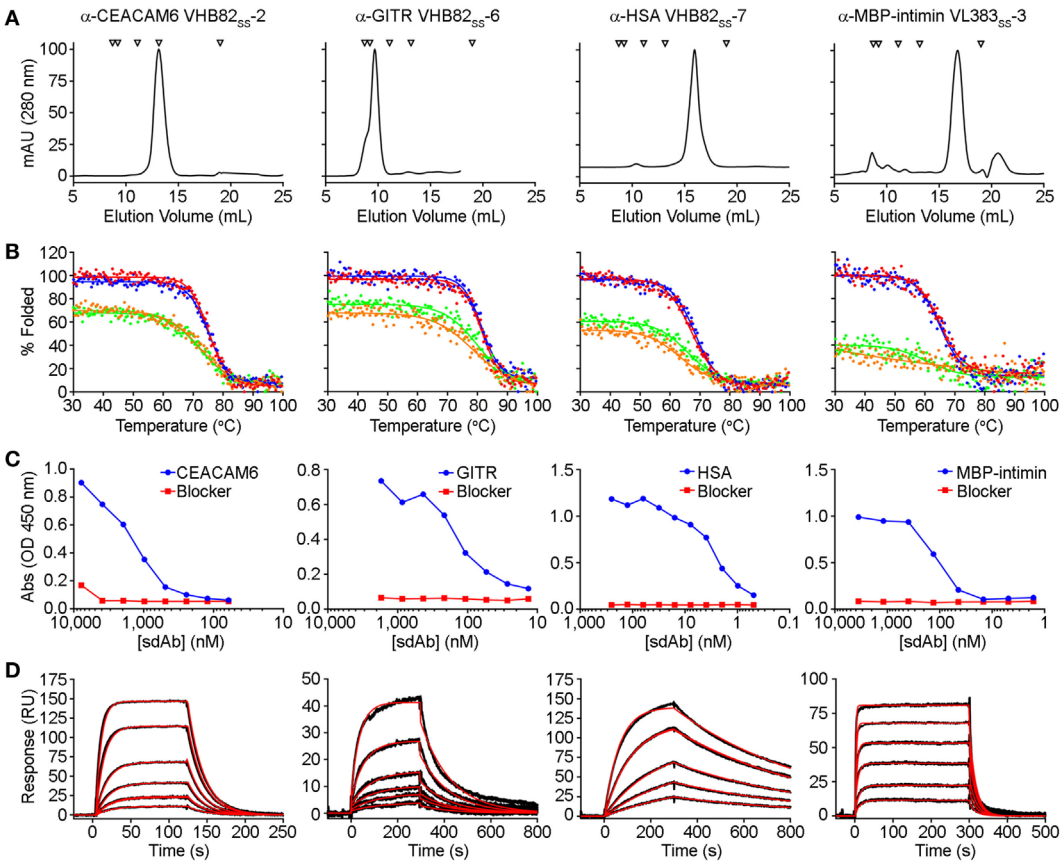

FIGURE 3 | Properties of selected antigen-specific single-domain antibodies (sdAbs) isolated from the $VL383_{SS}$, VH428, and $VHB82_{SS}$ synthetic human V_H/V_L sdAb libraries. The single highest affinity sdAb against each target is shown, except for MBP-intimin, where VL_{SS}-3 is shown instead of VL_{SS}-4 or VL_{SS}-5 because of better fit to a 1:1 binding model. **(A)** Size exclusion chromatography (SEC) profiles of representative antigen-specific human V_H/V_L sdAbs. Arrows show molecular mass standards, from left to right: thyroglobulin (670 kDa), gamma globulin (158 kDa), ovalbumin (44 kDa), myoglobin (17 kDa), and vitamin B12 (1.35 kDa). **(B)** Thermal unfolding of representative antigen-specific V_H/V_L sdAbs as determined by circular dichroism. Replicate unfolding curves are shown in red and blue; the sdAbs were then cooled to room temperature and remelted (shown in orange and green). **(C)** Titration ELISA of representative antigen-specific V_H/V_L sdAbs. Horseradish peroxidase mouse anti-c-Myc secondary antibody (clone 9E10, diluted 1:3,000) was used for detection. **(D)** Binding of antigen-specific V_H/V_L sdAbs to cognate antigen by SPR. Each antigen was immobilized on a CM5 sensor chip using amine coupling, then the indicated V_H or V_L sdAb was flowed over the surface at concentrations ranging from 25 to 1,000 nM (α-CEACAM6 $VHB82_{SS}$-2), 25 to 500 nM (α-GITR $VHB82_{SS}$-6), 2.5 to 50 nM (α-HSA $VHB82_{SS}$-7), or 62.5 to 2,500 nM (α-MBP-intimin $VL383_{SS}$-3). Black lines show data and red lines show fits.

TABLE 4 | Properties of antigen-specific single-domain antibodies (sdAbs) isolated from the phage-displayed synthetic human V_H/V_L libraries.

Target	V_H/V_L sdAb	Expression yield (mg/L)	Monomer (%)	T_m (°C)	K_D (nM)
CEACAM6	$VL383_{SS}$-1	18.4	>95	76.9	454[a]
	VH428-1	3.4	>95	57.6	2,180[a]
	VH428-2	3.6	>95	61.5	1,230[b]
	VH428-3	1.9	>95	52.9	290[b]
	$VHB82_{SS}$-1	6.4	>95	81.4	638[b]
	$VHB82_{SS}$-2	18.8	>95	75.1	245[b]
	$VHB82_{SS}$-3	5.4	>95	72.5	2,730[a]
	$VHB82_{SS}$-4	3.2	80.0	68.3	1,070[a]
	$VHB82_{SS}$-5	2.4	>95	71.9	2,200[a]
GITR	$VHB82_{SS}$-6	7.2	0[e]	81.4	196[b]
HSA	$VHB82_{SS}$-7	8.0	>95	67.7	5[b]
MBP-intimin	$VL383_{SS}$-2	2.0	>95	69.6	905[b,c]
	$VL383_{SS}$-3	0.2	83.4	65.1	395[b]
	$VL383_{SS}$-4	1.2	88.7	65.3	227[b]
	$VL383_{SS}$-5	3.7	94.6	74.2	252[b,c]
	$VL383_{SS}$-6	9.9	>95	76.6	7,470[a]
	$VL383_{SS}$-7	8.0	>95	76.7	11,500[a,d]
	VH428-4	0.1	>95	58.9	2,590[b]
	VH428-5	0.1	>95	n.d.	4,430[a]
	$VHB82_{SS}$-8	8.0	72.5	69.3	5,230[a]

[a]*Determined using steady-state analysis at 25°C.*
[b]*Determined using multicycle kinetic analysis and fitting to a 1:1 binding model at 25°C.*
[c]*Antigen was immobilized on a C1 sensor chip, evidence of complex binding.*
[d]*K_D is an estimate only due to lack of curvature in the steady-state plot.*
[e]*Size exclusion chromatography elution volume suggests $VHB82_{SS}$-6 is a strict dimer.*
n.d., not determined.

panning was done in triplicate. High attrition rates of V_H/V_L sdAbs showing false positive binding either as sdAb-phage or as soluble sdAb proteins ($VL383_{SS}$: 53% attrition; VH428: 69% attrition; VHB82ss: 71% attrition; **Table 3**) resulted in a final yield of 20 unique antigen-specific V_H/V_L sdAbs against four targets. Of the 15 library-target screens we conducted, eight (53%) yielded at least one antigen-specific V_H/V_L sdAb (four screens yielded one sdAb, two screens yielded two sdAbs, one screen yielded three sdAbs, and two screens yielded five sdAbs). Most of the recovered sdAbs were monomeric (**Figure 3A**; **Table 4**; Figure S3 in Supplementary Material), thermostable (**Figure 3B**; **Table 4**), and had affinities for antigen ranging from 5 nM to ~12 μM (**Figures 3C,D**; **Table 4**). One notable exception was the α-GITR V_H sdAb $VHB82_{SS}$-6, whose elution volume by SEC suggested it existed in solution as a strict dimer (**Figure 3A**). Stable homodimerization has previously been reported for several human V_H sdAbs and was critical for antigen binding (49–52); this phenomenon is distinct from the general tendency of some V_H domains to forms soluble aggregates. Antigen-specific V_H/V_L sdAbs isolated from all three libraries had aggregation tendencies and thermostabilities reflective of the parental V_H/V_L sdAb scaffold from which they were derived, but generally poorer expression yields (**Figure 4A**). Reproducibility in the selection of specific sdAb sequences from the libraries was modest, with only 45% (9/20) of antigen-specific V_H/V_L sdAbs recovered by both operators (**Figure 4B**) and no apparent connection between antigen-binding affinity and consistency of isolation.

Evaluation of Stability-Sequence Diversity Tradeoffs in Human V_H/V_L sdAb Libraries

To better understand potential constraints on the CDR sequences of monomeric and stable human V_H/V_L sdAbs, we examined the effects of stability selection (three rounds of protein A or L selection followed by amplification of the eluted phage overnight in *E. coli* TG1 cells; **Figure 5**) on randomized sequence diversity of two V_H/V_L sdAb libraries ($VL383_{SS}$ and $VHB82_{SS}$). We performed this experiment in duplicate using either phage particles displaying monovalent sdAb (rescued with M13K07 helper phage; simultaneous expression of pIII from helper phage and pIII-sdAb from phagemid) or phage particles displaying multivalent sdAb (rescued with M13K07ΔpIII hyper phage; only pIII-sdAb expressed from phagemid). Out-of-frame and/or stop-codon-encoding V_H/V_L sdAb clones were rare in both libraries ("Library Cells"), but rose substantially in frequency upon phage rescue ("Library Phage") and upon amplification in *E. coli* ("Amplification in *E. coli*"), suggesting a growth advantage for non-sdAb expressing cells over sdAb-expressing ones (**Figures 5A,B**); this phenomenon was mitigated somewhat using hyper phage rescue. After three rounds of protein A/L selection and overnight amplification in *E. coli* with helper phage rescue, there were clear clonal biases observed in the resulting populations of sdAb-phage (**Figures 5C,D**). Using an arbitrary frequency cutoff (0.00006% for $VL383_{SS}$ and 0.00004% for $VHB82_{SS}$; sdAbs at frequencies greater than these cutoffs were not present in any other dataset) to identify unique sdAb sequences enriched by stability selection, we found that different sdAb clones were selected in the two replicate pannings, although both sets of sdAbs were heavily biased toward the parental V_H/V_L sdAb scaffold's CDR3 length (9 residues for the $VL383_{SS}$ library and 10 residues for the $VHB82_{SS}$ library, which is the shortest CDR3 length possible in the library design and the nearest to the $VHB82_{SS}$ scaffold's CDR3 length of 6 residues; Figure S4 in Supplementary Material). However, stability selection reproducibly yielded V_H/V_L sdAbs with biased CDR amino acid composition (**Figures 5E,F**; Figures S5 and S6 in Supplementary Material). In order of magnitude, stability biases in the $VL383_{SS}$ library favored Asp, His, Pro, Ser and Thr and disfavored aromatic (Phe, Trp, Tyr) and hydrophobic (Ile, Leu, Val) residues. Similarly, stability biases in the $VHB82_{SS}$ library favored Asp, His, Pro, and Gln and disfavored aromatic (Phe, Trp, Tyr) and hydrophobic (Ile, Leu, Val) residues. These biases were especially acute at the C-terminus of CDR1 and N-terminus of CDR2, both of which flank FR2. Identical molecular signatures were observed to a lesser degree in the pools of all sdAb-phage (irrespective of frequency or mono- vs. multivalent display format) subjected to three rounds of stability selection (Figures S7 and S8 in Supplementary Material) as well as in the pools of sdAb-phage after phage rescue and eluted from protein A/L (data not shown), suggesting a common ontogeny.

DISCUSSION

The starting point for this investigation was the observation that several of our previously described synthetic human V_H/V_L sdAb libraries performed unpredictably (12, 21, 31), yielding monomeric antigen-specific binders against some targets but

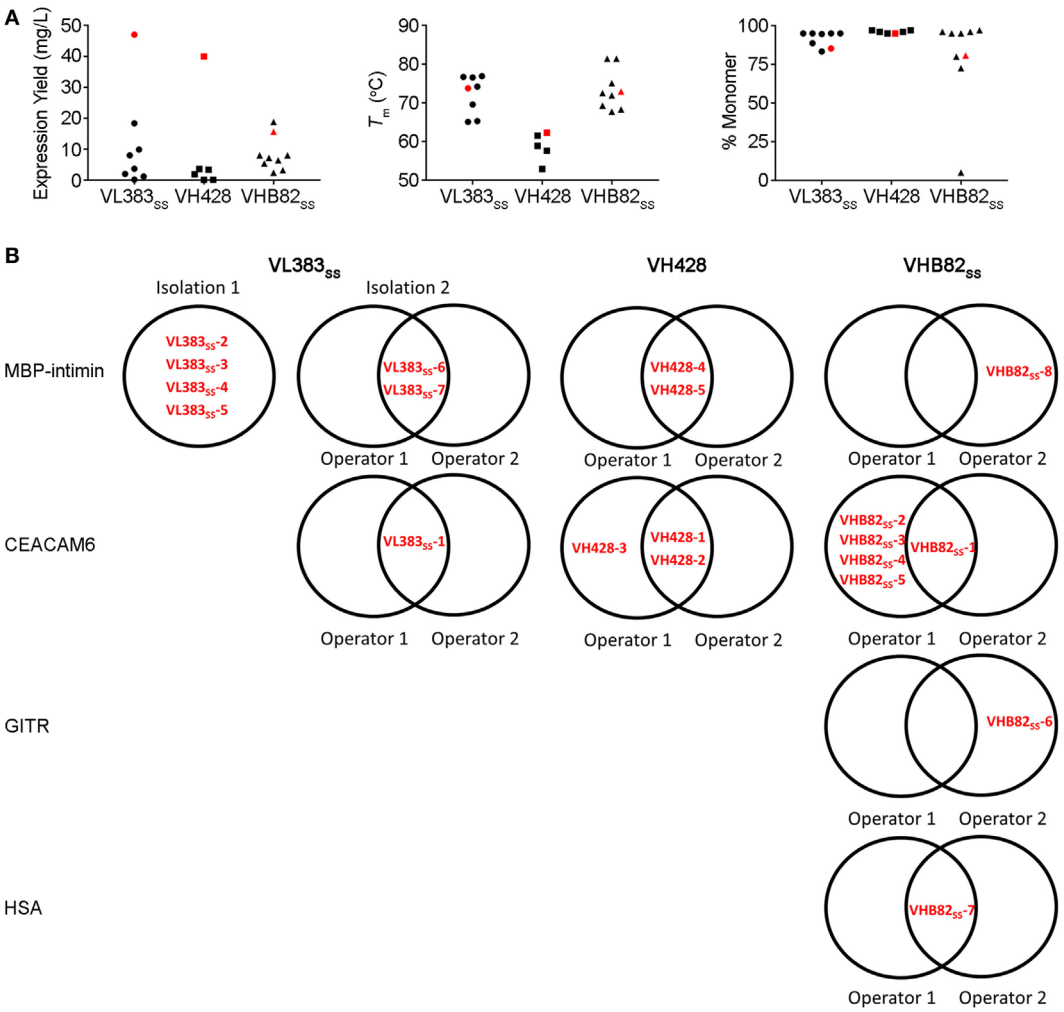

FIGURE 4 | Properties of all antigen-specific single-domain antibodies (sdAbs) isolated from the $VL383_{SS}$, VH428 and $VHB82_{SS}$ synthetic human V_H/V_L sdAb libraries. **(A)** Expression yields (as measured by spectrophotometry at 280 nm), T_ms (as determined by circular dichroism), and aggregation tendencies (as determined by size exclusion chromatography) of antigen-specific V_H/V_L sdAbs isolated from the libraries in comparison to the parental scaffold from which they were derived (shown in red). **(B)** Interoperator reproducibility in isolating individual V_H/V_L sdAb sequences.

not others. Thus, we tested the hypothesis that these issues might be solved by: (i) building libraries on ultrastable V_H/V_L sdAb scaffolds that maintain their biophysical properties upon CDR modification and (ii) randomizing the CDRs of the V_H/V_L sdAb libraries more extensively using trinucleotide mutagenesis. A few general lessons became apparent during the course of these experiments. First, although V_H/V_L sdAb scaffolds clearly vary in their tolerance to CDR modification, no "perfect" scaffold exists (i.e., some CDR-shuffled variants of every scaffold showed poor biophysical properties). Second, the trinucleotide mutagenesis approach used here was dramatically more effective at incorporating randomized sequence diversity in V_H/V_L sdAb CDRs compared to the Kunkel mutagenesis (21, 31) and splicing by overlap extension PCR mutagenesis approaches using degenerate oligonucleotides (12) that we have used previously. Third, as we showed previously (31), incorporating a stabilizing exogenous disulfide linkage spanning IMGT positions 54–78 into V_H/V_L sdAb libraries is clearly compatible with selection of antigen-specific binders, as 15/20 of the binders shown here bear this linkage. Finally, it is clearly possible, at least under some circumstance, to select monomeric, high-affinity binders from synthetic human V_H/V_L sdAbs libraries, as evidenced by the α-HSA VH_{SS}-7 sdAb (K_D: 5 nM) reported here.

However, the more general issues afflicting synthetic human V_H/V_L sdAb libraries (high attrition rates due to false positive binding, possibly caused by sdAb aggregation; inconsistency of isolation; variable expression yield and aggregation of isolated sdAbs) were not completely solved by using more stable V_H/V_L scaffolds or building more diverse and non-degenerate libraries. The additional randomized sequence diversity we achieved by the use of trinucleotide mutagenesis is almost certainly negligible when compared to the theoretical size of the libraries, and massive undersampling may account at least in part for inconsistent isolation of sdAbs. Other potential solutions to the problem

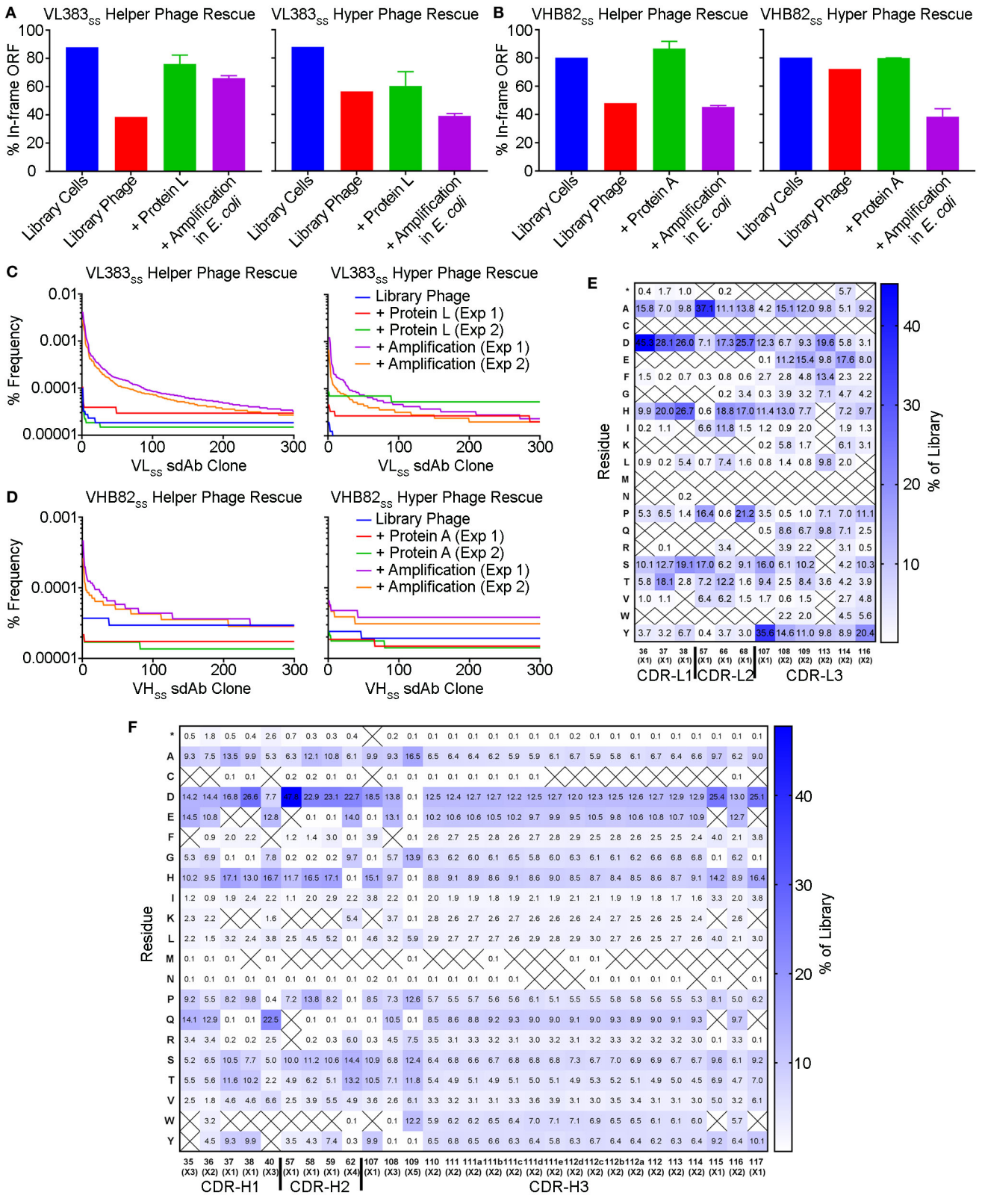

FIGURE 5 | Continued

FIGURE 5 | Continued
Impact of stability selection on human V_H/V_L single-domain antibody (sdAb) library sequence diversity. After transformation of *Escherichia coli* TG1 cells with phagemid DNA, phage were rescued by superinfection of overnight cultures with M13K07 helper phage or M13K07ΔpIII hyper phage. The purified sdAb-displaying phage were bound and eluted from protein A ($VHB82_{SS}$ library) or protein L ($VL383_{SS}$ library), then amplified by reinfection of *E. coli* TG1 cells. Three rounds of panning were performed, and V_H/V_L sdAb sequences were interrogated by NGS at the stage of rescued phage, phage eluted after a single round of protein A/L selection, and phage amplified after the final round of panning. **(A,B)** Proportion of functional sdAb sequences (in-frame ORF, no stop codons) observed in V_L **(A)** and V_H **(B)** library phage and panning outputs. **(C,D)** Clonality of V_L **(C)** and V_H **(D)** library phage and panning outputs. **(E,F)** Complementarity-determining region (CDR) amino acid composition of enriched V_L **(E)** and V_H **(F)** sdAb clones after three rounds of stability selection. Crossed-out cells indicate a frequency of <0.1%. Analyses in **(A–F)** are representative of 7.7×10^4 to 7.9×10^5 sequences per sample.

of undersampling include increasing throughput (53), use of V_H/V_L sdAb-transgenic mice (54, 55) and use of *in vitro* VDJ recombination systems (56). Nonetheless, modest inter-operator reproducibility in isolating the same binders clearly demonstrates that antigen-specific human V_H/V_L sdAbs are not always isolated even when they were present in the library. We currently have no understanding of the factors influencing the number of V_H/V_L sdAb binders isolated, their affinities or biophysical properties, nor if these depend on the library, the target antigen quality or composition, or the panning methodology. One possibility, for example, is that the numbers of input library sdAb-phage used here, the target antigen surface size and density, and/or the numbers of eluted phage amplified from each round of selection were inadequate to consistently recover very rare sdAb specificities that may be present in the libraries. These factors could be investigated empirically in future studies.

It is virtually certain that some of the challenges of human synthetic V_H/V_L sdAbs relate to fundamental tradeoffs between stability and sequence diversity. There is no necessary reason why rare autonomous rearranged human V_H/V_L sdAbs should be compatible with any CDR sequence; rather, it should be expected that these molecules rely chiefly on particular CDR sequences for their solubility and stability, given that human V_H and V_L domains have evolved to be paired with one another, occluding a hydrophobic surface between the two domains. We expect that such challenges are much less of a problem for protein domains that naturally exist as soluble monomers such as camelid and shark sdAbs and non-antibody scaffolds (e.g., FN3 and SH3 domains). Some camelid V_HHs rely on CDR residues for solubility as well (57), albeit likely to a lesser extent due to the presence of solubility-enhancing FR2 residues. One obvious explanation for the previously described bias toward negatively charged residues resulting in acidic overall pIs of V_H/V_L sdAbs (4, 12), especially in CDR1 and CDR2 (10, 11), is that this may enhance solubility and aggregation resistance. The role of charge and negative charge in particular in solubilizing V_H/V_L sdAbs with hydrophobic CDRs has been previously demonstrated (58, 59), and appears to be highly position and scaffold dependent (4). Bias in favor of His residues is less easy to explain, although its imidazole side chain may also have stabilizing and solubilizing effects near physiological pH (60). Notably, "camelized" human V_H sdAbs and human V_H/V_L sdAbs selected *in vitro* to bear solubility-promoting FR substitutions (9, 61), may not be subject to the same stability-sequence diversity tradeoffs. We caution that although the growth advantages conferred by V_H/V_L sdAbs with the most stable and soluble CDR sequences were most apparent using helper phage rescue of phagemid libraries, forcing pIII-sdAb expression using hyper phage rescue or by using phage (not phagemid) or yeast display systems would not be expected to circumvent the issue of bias; instead, it might be expected to result in immediate loss of a large population of V_H/V_L sdAbs with poorly stable and soluble CDR sequences.

In conclusion, we have described three novel synthetic human V_H/V_L sdAb libraries as well as antigen-specific binders against a variety of target antigens selected from these libraries. Future work will seek to better understand the constraints imposed on human V_H/V_L sdAbs by stability-sequence diversity tradeoffs, and whether it is possible to circumvent them by *in vitro* engineering of human autonomous immunoglobulin variable domain folds. One possibility would be to identify and fix a minimal set of stability-enhancing CDR residues in human V_H/V_L sdAb libraries, which might allow for more effective randomization of the remaining CDR positions. However, doing so without significant divergence from human germline IGHV sequences, increasing the risk of immunogenicity, may be very challenging.

AUTHOR CONTRIBUTIONS

DK, HK, and JT isolated and characterized human V_H/V_L sdAb scaffolds and conducted CDR-shuffling experiments and designed the libraries. JS conducted SEC-MALS experiments. ML, HK, and KH isolated and characterized antigen-specific sdAbs. ML and KH conceived and carried out stability selections and next-generation DNA sequencing analyses. QY, GH, and CRM designed, carried out, and analyzed surface plasmon resonance experiments. KH and GH made the figures and KH wrote the manuscript. All authors read and approved the final manuscript.

ACKNOWLEDGMENTS

We gratefully acknowledge the excellent technical help of Camille Hebert-Martineau, Sonia Leclerc, Hongtao Qi, Ken Chan, Shannon Ryan, and Julie Champagne.

FUNDING

This work was supported by funding from the National Research Council Canada.

SUPPLEMENTARY MATERIAL

The Supplementary Material for this article can be found online at http://www.frontiersin.org/articles/10.3389/fimmu.2017.01759/full#supplementary-material.

REFERENCES

1. Ward ES, Gussow D, Griffiths AD, Jones PT, Winter G. Binding activities of a repertoire of single immunoglobulin variable domains secreted from *Escherichia coli*. *Nature* (1989) 341:544–6. doi:10.1038/341544a0
2. Hamers-Casterman C, Atarhouch T, Muyldermans S, Robinson G, Hamers C, Songa EB, et al. Naturally occurring antibodies devoid of light chains. *Nature* (1993) 363:446–8. doi:10.1038/363446a0
3. Greenberg AS, Avila D, Hughes M, Hughes A, McKinney EC, Flajnik MF. A new antigen receptor gene family that undergoes rearrangement and extensive somatic diversification in sharks. *Nature* (1995) 374:168–73. doi:10.1038/374168a0
4. Kim DY, Hussack G, Kandalaft H, Tanha J. Mutational approaches to improve the biophysical properties of human single-domain antibodies. *Biochim Biophys Acta* (2014) 1844:1983–2001. doi:10.1016/j.bbapap.2014.07.008
5. Tanha J, Nguyen TD, Ng A, Ryan S, Ni F, MacKenzie R. Improving solubility and refolding efficiency of human V_Hs by a novel mutational approach. *Protein Eng Des Sel* (2006) 19:503–9. doi:10.1093/protein/gzl037
6. Tanha J, Xu P, Chen Z, Ni F, Kaplan H, Narang SA, et al. Optimal design features of camelized human single-domain antibody libraries. *J Biol Chem* (2001) 276:24774–80. doi:10.1074/jbc.M100770200
7. Davies J, Riechmann L. Single antibody domains as small recognition units: design and *in vitro* antigen selection of camelized, human V_H domains with improved protein stability. *Protein Eng* (1996) 9:531–7. doi:10.1093/protein/9.6.531
8. Davies J, Riechmann L. Antibody V_H domains as small recognition units. *Biotechnology (N Y)* (1995) 13:475–9. doi:10.1038/nbt0595-475
9. Ma X, Barthelemy PA, Rouge L, Wiesmann C, Sidhu SS. Design of synthetic autonomous V_H domain libraries and structural analysis of a V_H domain bound to vascular endothelial growth factor. *J Mol Biol* (2013) 425:2247–59. doi:10.1016/j.jmb.2013.03.020
10. Dudgeon K, Famm K, Christ D. Sequence determinants of protein aggregation in human V_H domains. *Protein Eng Des Sel* (2009) 22:217–20. doi:10.1093/protein/gzn059
11. Dudgeon K, Rouet R, Kokmeijer I, Schofield P, Stolp J, Langley D, et al. General strategy for the generation of human antibody variable domains with increased aggregation resistance. *Proc Natl Acad Sci U S A* (2012) 109:10879–84. doi:10.1073/pnas.1202866109
12. Arbabi-Ghahroudi M, To R, Gaudette N, Hirama T, Ding W, MacKenzie R, et al. Aggregation-resistant V_Hs selected by *in vitro* evolution tend to have disulfide-bonded loops and acidic isoelectric points. *Protein Eng Des Sel* (2009) 22:59–66. doi:10.1093/protein/gzn071
13. Christ D, Famm K, Winter G. Repertoires of aggregation-resistant human antibody domains. *Protein Eng Des Sel* (2007) 20:413–6. doi:10.1093/protein/gzm037
14. Christ D, Famm K, Winter G. Tapping diversity lost in transformations – *in vitro* amplification of ligation reactions. *Nucleic Acids Res* (2006) 34:e108. doi:10.1093/nar/gkl605
15. De Bernardis F, Liu H, O'Mahony R, La Valle R, Bartollino S, Sandini S, et al. Human domain antibodies against virulence traits of *Candida albicans* inhibit fungus adherence to vaginal epithelium and protect against experimental vaginal candidiasis. *J Infect Dis* (2007) 195:149–57. doi:10.1086/509891
16. Pinelli DF, Wagener ME, Liu D, Yamniuk A, Tamura J, Grant S, et al. An anti-CD154 domain antibody prolongs graft survival and induces Foxp3(+) iTreg in the absence and presence of CTLA-4 Ig. *Am J Transplant* (2013) 13:3021–30. doi:10.1111/ajt.12417
17. Suchard SJ, Davis PM, Kansal S, Stetsko DK, Brosius R, Tamura J, et al. A monovalent anti-human CD28 domain antibody antagonist: preclinical efficacy and safety. *J Immunol* (2013) 191:4599–610. doi:10.4049/jimmunol.1300470
18. Yamniuk AP, Suri A, Krystek SR, Tamura J, Ramamurthy V, Kuhn R, et al. Functional antagonism of human CD40 achieved by targeting a unique species-specific epitope. *J Mol Biol* (2016) 428:2860–79. doi:10.1016/j.jmb.2016.05.014
19. Walker A, Chung CW, Neu M, Burman M, Batuwangala T, Jones G, et al. Novel interaction mechanism of a domain antibody-based inhibitor of human vascular endothelial growth factor with greater potency than ranibizumab and bevacizumab and improved capacity over aflibercept. *J Biol Chem* (2016) 291:5500–11. doi:10.1074/jbc.M115.691162
20. Xie JH, Yamniuk AP, Borowski V, Kuhn R, Susulic V, Rex-Rabe S, et al. Engineering of a novel anti-CD40L domain antibody for treatment of autoimmune diseases. *J Immunol* (2014) 192:4083–92. doi:10.4049/jimmunol.1303239
21. Hussack G, Keklikian A, Alsughayyir J, Hanifi-Moghaddam P, Arbabi-Ghahroudi M, van Faassen H, et al. A V_L single-domain antibody library shows a high-propensity to yield non-aggregating binders. *Protein Eng Des Sel* (2012) 25:313–8. doi:10.1093/protein/gzs014
22. Zhang H, Yun S, Batuwangala TD, Steward M, Holmes SD, Pan L, et al. A dual-targeting antibody against EGFR-VEGF for lung and head and neck cancer treatment. *Int J Cancer* (2012) 131:956–69. doi:10.1002/ijc.26427
23. Li N, Fu H, Hewitt SM, Dimitrov DS, Ho M. Therapeutically targeting glypican-2 via single-domain antibody-based chimeric antigen receptors and immunotoxins in neuroblastoma. *Proc Natl Acad Sci U S A* (2017) 114:E6623–31. doi:10.1073/pnas.1706055114
24. Feng M, Gao W, Wang R, Chen W, Man YG, Figg WD, et al. Therapeutically targeting glypican-3 via a conformation-specific single-domain antibody in hepatocellular carcinoma. *Proc Natl Acad Sci U S A* (2013) 110:E1083–91. doi:10.1073/pnas.1217868110
25. Jespers L, Schon O, Famm K, Winter G. Aggregation-resistant domain antibodies selected on phage by heat denaturation. *Nat Biotechnol* (2004) 22:1161–5. doi:10.1038/nbt1000
26. Walker A, Dunlevy G, Rycroft D, Topley P, Holt LJ, Herbert T, et al. Anti-serum albumin domain antibodies in the development of highly potent, efficacious and long-acting interferon. *Protein Eng Des Sel* (2010) 23:271–8. doi:10.1093/protein/gzp091
27. Holt LJ, Basran A, Jones K, Chorlton J, Jespers LS, Brewis ND, et al. Anti-serum albumin domain antibodies for extending the half-lives of short lived drugs. *Protein Eng Des Sel* (2008) 21:283–8. doi:10.1093/protein/gzm067
28. Rouet R, Dudgeon K, Christie M, Langley D, Christ D. Fully human V_H single domains that rival the stability and cleft recognition of camelid antibodies. *J Biol Chem* (2015) 290:11905–17. doi:10.1074/jbc.M114.614842
29. Mandrup OA, Friis NA, Lykkemark S, Just J, Kristensen P. A novel heavy domain antibody library with functionally optimized complementarity determining regions. *PLoS One* (2013) 8:e76834. doi:10.1371/journal.pone.0076834
30. Jespers L, Schon O, James LC, Veprintsev D, Winter G. Crystal structure of HEL4, a soluble, refoldable human V_H single domain with a germ-line scaffold. *J Mol Biol* (2004) 337:893–903. doi:10.1016/j.jmb.2004.02.013
31. Henry KA, Kandalaft H, Lowden MJ, Rossotti MA, van Faassen H, Hussack G, et al. A disulfide-stabilized human V_L single-domain antibody library is a source of soluble and highly thermostable binders. *Mol Immunol* (2017) 90:190–6. doi:10.1016/j.molimm.2017.07.006
32. Yu GW, Vaysburd M, Allen MD, Settanni G, Fersht AR. Structure of human MDM4 N-terminal domain bound to a single-domain antibody. *J Mol Biol* (2009) 385:1578–89. doi:10.1016/j.jmb.2008.11.043
33. Tang Z, Feng M, Gao W, Phung Y, Chen W, Chaudhary A, et al. A human single-domain antibody elicits potent antitumor activity by targeting an epitope in mesothelin close to the cancer cell surface. *Mol Cancer Ther* (2013) 12:416–26. doi:10.1158/1535-7163.MCT-12-0731
34. Gay RD, Clarke AW, Elgundi Z, Domagala T, Simpson RJ, Le NB, et al. Anti-TNF-α domain antibody construct CEP-37247: full antibody functionality at half the size. *MAbs* (2010) 2:625–38. doi:10.4161/mabs.2.6.13493
35. Bertok S, Wilson MR, Morley PJ, de Wildt R, Bayliffe A, Takata M. Selective inhibition of intra-alveolar p55 TNF receptor attenuates ventilator-induced lung injury. *Thorax* (2012) 67:244–51. doi:10.1136/thoraxjnl-2011-200590
36. Holland MC, Wurthner JU, Morley PJ, Birchler MA, Lambert J, Albayaty M, et al. Autoantibodies to variable heavy (V_H) chain Ig sequences in humans impact the safety and clinical pharmacology of a V_H domain antibody antagonist of TNF-α receptor 1. *J Clin Immunol* (2013) 33:1192–203. doi:10.1007/s10875-013-9915-0
37. Cordy JC, Morley PJ, Wright TJ, Birchler MA, Lewis AP, Emmins R, et al. Specificity of human anti-variable heavy (V_H) chain autoantibodies and impact on the design and clinical testing of a V_H domain antibody antagonist of tumour necrosis factor-α receptor 1. *Clin Exp Immunol* (2015) 182:139–48. doi:10.1111/cei.12680

38. To R, Hirama T, Arbabi-Ghahroudi M, MacKenzie R, Wang P, Xu P, et al. Isolation of monomeric human V_Hs by a phage selection. *J Biol Chem* (2005) 280:41395–403. doi:10.1074/jbc.M509900200
39. Kim DY, To R, Kandalaft H, Ding W, van Faassen H, Luo Y, et al. Antibody light chain variable domains and their biophysically improved versions for human immunotherapy. *MAbs* (2014) 6:219–35. doi:10.4161/mabs.26844
40. Kim DY, Kandalaft H, Ding W, Ryan S, van Faassen H, Hirama T, et al. Disulfide linkage engineering for improving biophysical properties of human V_H domains. *Protein Eng Des Sel* (2012) 25:581–9. doi:10.1093/protein/gzs055
41. Virnekas B, Ge L, Pluckthun A, Schneider KC, Wellnhofer G, Moroney SE. Trinucleotide phosphoramidites: ideal reagents for the synthesis of mixed oligonucleotides for random mutagenesis. *Nucleic Acids Res* (1994) 22:5600–7. doi:10.1093/nar/22.25.5600
42. Baral TN, MacKenzie R, Arbabi Ghahroudi M. Single-domain antibodies and their utility. *Curr Protoc Immunol* (2013) 103:Unit 2.17. doi:10.1002/0471142735.im0217s103
43. Dorion-Thibaudeau J, St-Laurent G, Raymond C, De Crescenzo G, Durocher Y. Biotinylation of the Fcγ receptor ectodomains by mammalian cell co-transfection: application to the development of a surface plasmon resonance-based assay. *J Mol Recognit* (2016) 29:60–9. doi:10.1002/jmr.2495
44. Henry KA, Hussack G, Collins C, Zwaagstra JC, Tanha J, MacKenzie CR. Isolation of TGF-β-neutralizing single-domain antibodies of predetermined epitope specificity using next-generation DNA sequencing. *Protein Eng Des Sel* (2016) 29:439–43. doi:10.1093/protein/gzw043
45. Henry KA, Tanha J, Hussack G. Identification of cross-reactive single-domain antibodies against serum albumin using next-generation DNA sequencing. *Protein Eng Des Sel* (2015) 28:379–83. doi:10.1093/protein/gzv039
46. Lo MC, Aulabaugh A, Jin G, Cowling R, Bard J, Malamas M, et al. Evaluation of fluorescence-based thermal shift assays for hit identification in drug discovery. *Anal Biochem* (2004) 332:153–9. doi:10.1016/j.ab.2004.04.031
47. Ericsson UB, Hallberg BM, Detitta GT, Dekker N, Nordlund P. Thermofluor-based high-throughput stability optimization of proteins for structural studies. *Anal Biochem* (2006) 357:289–98. doi:10.1016/j.ab.2006.07.027
48. Henry KA, Sulea T, van Faassen H, Hussack G, Purisima EO, MacKenzie CR, et al. A rational engineering strategy for designing protein A-binding camelid single-domain antibodies. *PLoS One* (2016) 11:e0163113. doi:10.1371/journal.pone.0163113
49. Baral TN, Chao SY, Li S, Tanha J, Arbabi-Ghahroudi M, Zhang J, et al. Crystal structure of a human single domain antibody dimer formed through V_H-V_H non-covalent interactions. *PLoS One* (2012) 7:e30149. doi:10.1371/journal.pone.0030149
50. Sepulveda J, Jin H, Sblattero D, Bradbury A, Burrone OR. Binders based on dimerised immunoglobulin V_H domains. *J Mol Biol* (2003) 333:355–65. doi:10.1016/j.jmb.2003.08.033
51. Jin H, Sepulveda J, Burrone OR. Selection and characterisation of binders based on homodimerisation of immunoglobulin V_H domains. *FEBS Lett* (2003) 554:323–9. doi:10.1016/S0014-5793(03)01182-7
52. Jin H, Sepulveda J, Burrone OR. Specific recognition of a dsDNA sequence motif by an immunoglobulin V_H homodimer. *Protein Sci* (2004) 13:3222–9. doi:10.1110/ps.04921704
53. Wu Y, Batyuk A, Honegger A, Brandl F, Mittl PRE, Plückthun A. Rigidly connected multispecific artificial binders with adjustable geometries. *Sci Rep* (2017) 7:11217. doi:10.1038/s41598-017-11472-x
54. Drabek D, Janssens R, de Boer E, Rademaker R, Kloess J, Skehel J, et al. Expression cloning and production of human heavy-chain-only antibodies from murine transgenic plasma cells. *Front Immunol* (2016) 7:619. doi:10.3389/fimmu.2016.00619
55. Brüggemann M, Zou X, Inventors; Crescendo Biologics Ltd., Assignee. *Mouse λ Light Chain Locus.* United States patent US 9439405 B2 (2016).
56. Gallo M, Kang JS, Pigott CR, Inventors; Innovative Targeting Solutions, Inc., Assignee. *Sequence Diversity Generation in Immunoglobulins.* United States patent US 8012714 B2 (2011).
57. Conrath K, Vincke C, Stijlemans B, Schymkowitz J, Decanniere K, Wyns L, et al. Antigen binding and solubility effects upon the veneering of a camel V_HH in framework-2 to mimic a V_H. *J Mol Biol* (2005) 350:112–25. doi:10.1016/j.jmb.2005.04.050
58. Perchiacca JM, Ladiwala AR, Bhattacharya M, Tessier PM. Aggregation-resistant domain antibodies engineered with charged mutations near the edges of the complementarity-determining regions. *Protein Eng Des Sel* (2012) 25:591–601. doi:10.1093/protein/gzs042
59. Perchiacca JM, Lee CC, Tessier PM. Optimal charged mutations in the complementarity-determining regions that prevent domain antibody aggregation are dependent on the antibody scaffold. *Protein Eng Des Sel* (2014) 27:29–39. doi:10.1093/protein/gzt058
60. Chan P, Warwicker J. Evidence for the adaptation of protein pH-dependence to subcellular pH. *BMC Biol* (2009) 7:69. doi:10.1186/1741-7007-7-69
61. Barthelemy PA, Raab H, Appleton BA, Bond CJ, Wu P, Wiesmann C, et al. Comprehensive analysis of the factors contributing to the stability and solubility of autonomous human VH domains. *J Biol Chem* (2008) 283:3639–54. doi:10.1074/jbc.M708536200

Conflict of Interest Statement: JT and DK are inventors of US patents 8293233B2 and 9371371B2 as well as other patents and patent applications governing human V_H/V_L sdAb scaffolds.

frontiers in Immunology

TECHNOLOGY REPORT
published: 19 December 2016
doi: 10.3389/fimmu.2016.00619

Expression Cloning and Production of Human Heavy-Chain-Only Antibodies from Murine Transgenic Plasma Cells

Dubravka Drabek[1], Rick Janssens[1], Ernie de Boer[1], Rik Rademaker[2], Johannes Kloess[3], John Skehel[3] and Frank Grosveld[1,2]*

[1] Department of Cell Biology, Erasmus MC, Rotterdam, Netherlands, [2] Harbour Antibodies BV, Rotterdam, Netherlands, [3] WHO Influenza Centre, Frances Crick Institute, London, UK

OPEN ACCESS

Edited by:
Kevin A. Henry,
National Research Council Canada, Canada

Reviewed by:
Johan Nilvebrant,
Royal Institute of Technology, Sweden
Dae Young Kim,
Osong Medical Innovation Foundation, South Korea
Andrew Hayhurst,
Texas Biomedical Research Institute, USA

***Correspondence:**
Dubravka Drabek
d.drabek@erasmusmc.nl

Specialty section:
This article was submitted to Vaccines and Molecular Therapeutics, a section of the journal Frontiers in Immunology

Received: 28 September 2016
Accepted: 06 December 2016
Published: 19 December 2016

Citation:
Drabek D, Janssens R, de Boer E, Rademaker R, Kloess J, Skehel J and Grosveld F (2016) Expression Cloning and Production of Human Heavy-Chain-Only Antibodies from Murine Transgenic Plasma Cells. Front. Immunol. 7:619. doi: 10.3389/fimmu.2016.00619

Several technologies have been developed to isolate human antibodies against different target antigens as a source of potential therapeutics, including hybridoma technology, phage and yeast display systems. For conventional antibodies, this involves either random pairing of VH and variable light (VL) domains in combinatorial display libraries or isolation of cognate pairs of VH and VL domains from human B cells or from transgenic mice carrying human immunoglobulin loci followed by single-cell sorting, single-cell RT-PCR, and bulk cloning of isolated natural VH–VL pairs. Heavy-chain-only antibodies (HCAbs) that naturally occur in camelids require only heavy immunoglobulin chain cloning. Here, we present an automatable novel, high-throughput technology for rapid direct cloning and production of fully human HCAbs from sorted population of transgenic mouse plasma cells carrying a human HCAb locus. Utility of the technique is demonstrated by isolation of diverse sets of sequence unique, soluble, high-affinity influenza A strain X-31 hemagglutinin-specific HCAbs.

Keywords: plasma cells, transgenic mice, human VH, HCAb, HEK cell library

INTRODUCTION

Camelidae produce not only conventional antibodies, composed of two heavy and two light chains (H2L2), but also antibodies composed of heavy chains only. Although in the conventional antibodies both chains contribute to the antigen binding site, the antigen binding site of camelid heavy-chain-only antibodies (HCAbs) is formed by single heavy chain variable domain (VHH) (1, 2). We have previously generated transgenic mice containing hybrid llama-human antibody loci with two llama variable VHH regions and human D, J, and C_μ and/or C_γ constant regions. Such loci rearrange productively and rescue B cell development efficiently (3).

Heavy-chain-only antibodies are expressed at high levels in camelids (4) and in transgenic mice (3, 5), provided that the CH1 domain is deleted from the constant regions. HCAb production does not require an IgM stage for effective pre-B cell signaling, and antigen-specific heavy-chain-only IgGs are produced upon immunization (3). Camelid VHH segments are soluble and this is attributed to the presence of a germ line-encoded tetrad of specific hydrophilic amino acid substitutions at the hydrophobic interface of the conventional VH domain that normally interacts with a variable light

chain domain (VL) (6) and a CDR3 loop that folds over the VHH, covering the side of the domain that normally interacts with a VL domain (7).

In contrast, human VH domains usually aggregate and are less stable due to exposure of the hydrophobic amino acids at the former interface (8) and the loss of contacts between the V regions, respectively. This limits their applicability [see Rosenberg (9) and Fahrner et al. (10)]. However, extensive engineering and selection (7, 8) mainly by increasing the hydrophilicity of the VH domain (8) and by replacing exposed hydrophobic residues in the CDR3 region (7) will increase the solubility of the VH domain. These methods have the disadvantage that they require extensive work and that amino acid changes particularly in the CDR3 region could reduce or change the specificity and affinity of antigen binding.

We hypothesized that the mouse would be much more effective at such engineering *in vivo* through the natural process of selection. We, therefore, introduced a fully human HCAb locus into mice to generate fully human HCAbs of different classes or fragments thereof in response to antigen challenge for use as therapeutic agents in man. To this end, we replaced the llama VHH domains with human VH domains in the transgenic construct used by Janssens et al. (3), generated a number of transgenic lines, and derived a number of HCAb against different antigens by hybridoma and phage display technology. Both the hybridoma and phage display technologies have a number of disadvantages, are quite laborious, and in addition phage display needs additional full-format HCAb recloning in eukaryotic systems.

It has been known that long-term production of Abs is maintained by a combination of short-lived and long-lived plasma cells (PCs), usually defined functionally as Ab-secreting cells (ASC). Although short-lived ASC die within 3–5 days, Ab levels can be maintained by continuous proliferation and differentiation of memory B cells (MBC) into short-lived ASC upon continuous reactivation (11, 12), such as persistent antigen exposure. Alternatively, long-term production of Ab is maintained by long-lived ASC, which migrate to survival niches within the bone marrow (13, 14) and spleen (15). Thus, we used CD138$^+$ CD45R B220$^{low/-}$ CD19$^{low/-}$ antibody-secreting PCs (16), bone marrow, and spleen of immunized mice containing a human HCAb locus (4HVH) as the enriched RNA source for the production of an expression library.

Here, we describe an automatable alternative method for rapid cloning and identification of antigen-specific HCAbs from immunized transgenic mice (4HVH) carrying a fully human heavy chain locus by cloning the VDJ region of the HCAb cDNA directly into a mammalian expression vector and identifying the human embryonic kidney 293 T (HEK293T) clones secreting antigen-specific HCAb (See **Figure 1**).

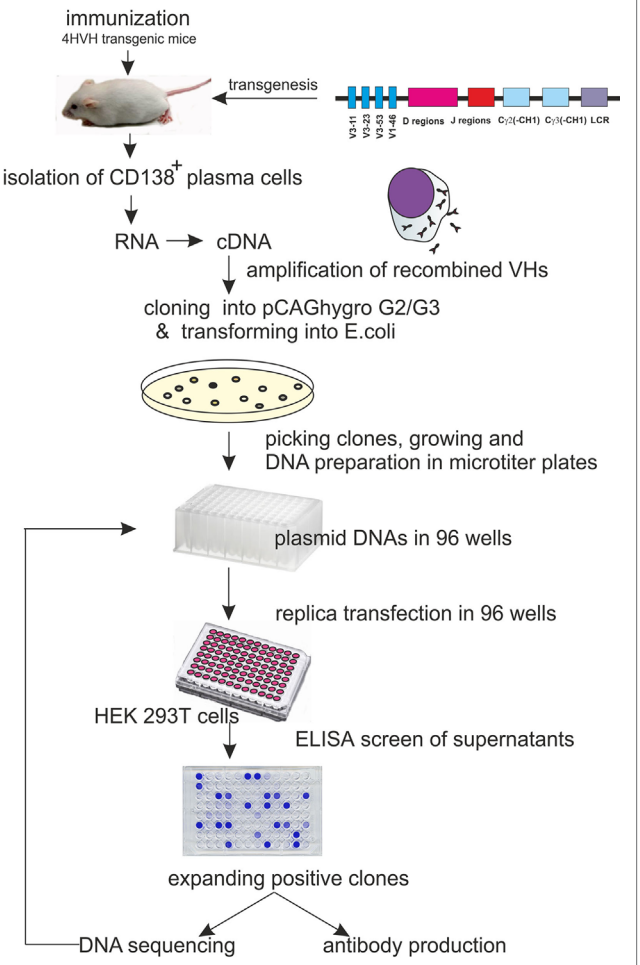

FIGURE 1 | Schematic representation of the procedure leading to heavy-chain-only antibody (HCAb) production with human HCAb locus construct used for transgenesis. It carries 4VH regions, all of the human D and J regions and the Cγ2 and Cγ3 regions lacking the CH1 domain.

METHODS

Immunization

4HVH transgenic mice and control wild-type (WT) mice were immunized according to the protocol approved by the Dutch Experimental animal committee DEC Nr EUR 1944. Briefly, mice were injected i.p. five times at 2-week intervals with the influenza virus X-31 hemagglutinin (HA), prepared as described by Ruigrok et al. (17), and dissolved in phosphate-buffered saline (PBS) at pH 7.4 using Stimune adjuvant (Prionics, Switzerland) according to the formulation provided by the supplier. The last injection was without the adjuvant. Four days after the last injection, 4HVH mice were sacrificed and PCs isolated.

PC Isolation and Library Construction

A single-cell suspension was prepared from spleens and femurs in 0.5% BSA, 2 mM EDTA in PBS. Cells were counted (Burke chamber), and magnetic cell sorting of CD138$^+$ cells was performed using mouse CD138$^+$ plasma isolation kit (Miltenyi Biotec GmbH, Germany) according to the manufacturer's instructions. Basically, this consists of two steps: first a depletion of non-PCs by indirect magnetic labeling of CD49b and CD45R

cells with a non-PC depletion cocktail and anti-biotin microBeads followed by magnetic separation using LD columns (Miltenyi Biotec GmbH, Germany), and the next step is a positive selection of PCs by direct labeling with CD138 MicroBeads followed by magnetic separation on a MS column (Miltenyi Biotec GmbH, Germany). PCs eluted from the column were spun down and the pellet resuspended in 400 µl of Ultraspec™ RNA reagent (Biotecx laboratories, Inc., Houston, TX, USA). Total RNA was made according to the manufacturer's instructions. The RNA was dissolved in 20 µl of dH_2O and 3 µg was used in a 20 µl reaction volume for a first strand cDNA synthesis using SuperScript™ II RT (Invitrogen by Fisher Scientific, USA) according to the instructions using oligo dT priming with oligo (dT) 12-18 primer (Invitrogen by Life Technologies, USA). The transgenic mice contain four different VHs (1-46, 3-11, 3-53, and 3-23), and hence three different leader-specific primers were designed for the 5′-end. All of them contained a *Pvu*II site that is unique in the final expression vectors (pCAG hygro G2 and pCAG hygro G3 containing leader sequence from VH3-23). The following 5′-primers were used:

lib-3-23/53-S: 5′-GTGTCCAGTGTGAGGTGCAGCTG-3′,
lib-3-11-S: 5′-GTGTCCAGTGTCAGGTGCAGCTG-3′, and
lib-1-46-S: 5′-GTGCTCACTCCCAGGTGCAGCTG.

For the 3′-end, we used primer HINGEIgG2rv [previously used and described for phage display library (3)] and HINGEIgG3rv: 5′-AATTGTGTGAGCGGCCGCACCAAGTGGGGTTTT GAGCTC.

An additional 3′-end primer was used: lib-IgG2/3-CH3-AS: 5′-CTGACCTGGTTCTTGGTCATCTCCTC.

This primer from the CH3 constant region is common for both G2 and G3. However, in combination with any of the 5′-primers, it amplifies only IgG2. To make sure that all of the VHs were represented in the library, each of the 5′-end primers was used separately in combination with each of the 3′-end primers, and the products were mixed in an equimolar ratio later. PCR was performed with high-fidelity DNA polymerase Phusion™ (New England Biolabs, Inc., USA) using cycling conditions recommended by the manufacturer for the three-step protocol with an annealing temperature of 68°C and 35 cycles in total. PCR products for IgG2 were cut either with *Pvu*II/*Bst*EII or *Pvu*II/*Bsr*GI (unique site in the constant region) if the amplified fragment originated from using the combination with the Lib-IgG2/3-CH3 primer and cloned into *Pvu*II/*Bst*EII or *Pvu*II/*Bsr*GI cut and phosphatase-treated pCAGhygro G2 vector.

PCR products for IgG3 were digested with *Pvu*II/*Bst*EII or *Pvu*II/*Sac*I and cloned into *Pvu*II/*Bst*EII cut and phosphatase-treated pCAGhygro G2 or *Pvu*II/*Sac*I cut and phosphatase-treated pCAGhygro G3 vector.

pCAGhygro G2 and pCAG hygro G3 are depicted in **Figure 2**. In short, the vector contains an ampicillin resistance gene for bacteria selection and a hygromycin resistance for the eukaryotic cell selection. The HCAb expression is driven by ubiquitous CMV enhancer and chicken beta actin promoter. The human VH 3-23 leader is responsible for secretion of the antibody. Constant regions have a deleted CH1 exon.

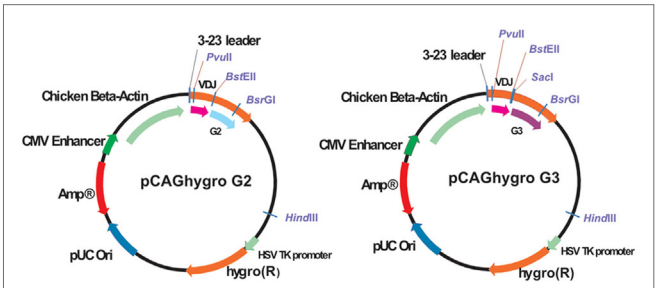

FIGURE 2 | Schematic representation of the pCAGhygro G2 and the pCAGhygro G3 eukaryotic expression vectors used to generate the HEK293T cell libraries.

Transformation, Plasmid Preparation, and Transfection into HEK 293T Cells

All ligations were done overnight at 16°C in 10 µl total volume using 120 ng of vector alone (control) or in combination with 30 ng of insert using T4DNA ligase (Promega, Madison, WI, USA). Ligations were diluted 5× (40 µl of dH_2O into 10 µl ligation), and 1 µl was used to transform 20 µl of electrocompetent MegaX DH10B™ T1® cells (Invitrogen by Life Technologies, Grand Island, NY, USA) according to the instructions provided by the manufacturer.

Plating was done on 2XTY/Amp agar plates, and 960 individual colonies were picked into 1.5 ml of 2XTY/Amp medium in 96-well format. A total of 960 DNA plasmid preparations were done using NucleoSpin R96 flash (Macherey-Nagel, Germany) designed for rapid manual and automated 96-well DNA preparation of high- and low-copy plasmid and Bac DNA from *Escherichia coli*. Each DNA was dissolved in 50 µl sterile dH_2O. A total of 200 ng of DNA (estimated to be in10 µl of DNA preparations based on random sample concentration measurements) was used for transfection into HEK 293T cells. The HEK 293T cells were plated into 96-well plates and transfected using Lipofectamine™ 2000 (Invitrogen, Carlsbad, CA, USA) according to the manufacturer's instructions for 96-well format. The following day, medium was removed and replaced with DMEM medium (Lonza, Belgium) supplemented with hygromycin (Roche, Diagnostics GmbH, Germany) at a concentration of 200 µg/ml, non-essential amino acids (NEAA, Lonza, Belgium), and 10% fetal calf serum (FCS). On day 4 posttransfection, 100 µl of medium was taken from each well for an antigen-specific enzyme-linked immunosorbent assay (ELISA) and replaced with a fresh medium.

ELISA Assay

Enzyme-linked immunosorbent assay plates were coated overnight at 4°C with 5 µg/ml of antigen in PBS or PBS only. Blocking was done for 1 h at room temperature (RT) with 1% milk 1% BSA/PBS (W/V). This was done to exclude possible "sticky" binders to plastic or non-specific binders to BSA/milk. Washing steps included 3× PBS/0.05% Tween-20 and 3× PBS. A total of 50 µl of transgenic mouse serum were diluted in PBS (for initial testing of immunized animals), or supernatants from HEK 293T

cells were mixed with 50 µl of 2% milk 2% BSA/PBS (W/V) and incubated for 1 h at RT. After washing, the antigen-specific serum/supernatants were detected by incubation with goat antihuman IgG Fc coupled to horse radish peroxidase (HRP; Jackson Immuno Research Laboratories, Inc., USA) diluted 1:5,000 for 1 h at RT, followed by washing steps and incubation with peroxidase substrate BM Blue POD (Roche Diagnostics GmbH, Germany). The reaction was stopped with 1M H_2SO_4, and the absorption was measured at 450 nm (against reference wavelength 690 nm).

For the initial testing of immunized WT and 4HVH transgenic mice sera for the presence of antigen-specific mouse antibodies, polyclonal goat antimouse immunoglobulins, HRP (Dako, Denmark) diluted 1:2,000 was used.

Sequencing

Sequencing of the positive DNA clones was done using primer CAG seq2-s 5′-GCTGGTTATTGTGCTGTCTCATC-3′.

Initial Affinity Measurement Screen and Full Kinetics

Medium was collected from HEK 293T cells, stably transfected with an HCAb expression vector and grown to confluence. To screen for the clones that expressed the highest affinity HCAb for HA, 200 µl of HEK 293T cell medium from each clone was transferred to a single well of a black 96-well microtiter plate (Greiner Bio-One, Germany). The binding of the HCAbs to influenza HA was studied using the Octet QK (ForteBio, USA). Anti-human IgG-coated tips (ForteBio, USA) were incubated with PBS/0.05% Tween-20 (120 s) to establish baseline signals. To allow the capturing of HCAbs, the tips were then transferred to 200 µl HEK 293T medium containing HCAbs (600 s), HEK 293T medium without HCAbs and PBS/0.05% Tween-20 as a reference. Subsequently, the tips were transferred to 200 µl PBS/0.05% Tween-20 (480 s) to establish the binding levels after the dissociation of non-specific interactions. Next, the loaded tips were transferred to 200 µl 512 nM bromelain-released HA (BHA; 600 s) to allow HA binding to the captured anti-HA HCAbs and to 200 µl PBS/0.05% Tween-20 (1,200 s) to determine the dissociation rate of the HA from the HCAb.

The reference binding signal was subtracted from the binding curves, and the binding data were fitted to a 1:1 binding model using Octet 4.0 software. The HCAb clones that showed binding in initial affinity screen were selected for further analysis.

Full kinetics experiments were performed with purified HCAbs dialyzed against PBS. Anti-human IgG(Fc) sensors were dipped for 180 s in PBS/0.05% Tween 20. HCAb (10 µg/ml) was used for the loading step (300 s, 900 rpm), followed by 180 s in PBS/0.05% Tween 20. The association step with HA ligand in a concentration range from 0 to 512 nM was performed (600 s at 900 rpm), followed by dissociation step of 1,200 s in PBS/005% Tween 20 at 900 rpm. All steps were done in 200 µl volume. The buffer only well (PBS/0.05% Tween 20) was used as a reference well. The reference binding signal was subtracted from the binding curves, and the binding data were fitted to a1:1 binding model using Octet 7.1 software.

Production and Purification of Anti-HA HCAbs

Positive clones were further expanded in medium containing 10% FCS. Alternatively, plasmid DNA was linearized with *Hin*dIII, stably transfected into HEK293T cells, and individual clones picked for the purpose of selecting the best expressors.

For production purposes, clones were grown in 15 cm Petri dishes in 25 ml of OPTI-MEM® (1×) + GlutaMAX™ (Gibco by Life technologies, CA, USA) medium. Medium was collected and replaced twice per week. Collected medium was spun down at 1,000 rpm (Eppendorf centrifuge 5810R) for 5 min to remove cell debris, and HCAbs were purified on Protein A agarose Fast Flow 50% (V/V; Sigma, USA). A total of 100 µl of Protein A beads were incubated with 50 ml of medium overnight at 4°C on a rotating wheel. After spinning at 1,000 rpm for 5 min, beads were washed in PBS/0.01% Tween-20 and loaded onto homemade columns (insulin syringe with cotton wool), washed 3× with PBS/0.01% Tween-20, 3× with PBS, and eluted with 3M potassium thiocyanate (KSCN). Eluted HCAbs were dialyzed for 5–6 h using Spectra/Por dialysis membrane MWCO 10000 (Spectrum Laboratories Inc., USA) against 1,000× volume excess of PBS at 4°C. The procedure was repeated three times.

Production and Purification of VH Domains in *E. coli*

VH domains from HCAbs were cloned without a tag into pET SUMO vector (Champion pET SUMO Expression system, Invitrogen, CA, USA). Production of fusion protein, cleavage, and removal of SUMO and SUMO protease were done according to the manufacturer's instruction with recommended reagents.

VH domains in fusion with SUMO were purified from inclusion bodies starting with 200 ml BL21 transfected cells after 4 h of induction (1 mM IPTG). Cells were harvested, pellet frozen overnight, and lysed in 20 ml lysis buffer (50 mM KPO_4, pH 7.8; 400 mM NaCl; 10 mM KCl; 10% glycerol; and 0.5% Triton X-100). After sonication 20 × 20 s ampl 12 and spinning for 15 min at 4,000 rpm at 4°C, pellet was taken in 1 ml PBS with addition of 10 µl benzonase for 30 min at RT. After washing in washing buffer (100 mM Tris pH 7.5; 5 mM EDTA; 2 M urea; and 2% Triton X-100), sample was spun for 15 min at 4,000 rpm, washed 2× in 10 ml of 100 mM Tris pH 7.5 and 5 mM EDTA. Pellet was taken into 8 M urea; 10 mM Tris pH 7.5; and 2 mM DTT, rotated for 2 h at RT, spun for 30 min, 15,000 rpm at 4°C, and the supernatant was used in refolding. Base refolding buffer 2 from Pierce refolding kit was used (440 mM 1-arginine; 55 mM Tris pH 8.2; 21 mM NaCl; and 0.88 mM KCl). Protein was diluted to 1 mg/ml; in 8 M urea, 10 mM Tris pH 7.5; and 2 mM DTT. To fold 0.5 mg of protein, we used 9 ml base refolding buffer, 100 µl 0.1 M EDTA, 6.75 mg GSH (reduced glutathione), 2.65 mg of GSSG (oxidized glutathione), and H_2O up to 9.5 ml. Protein was added in 50 µl aliquots, well mixed, and left on ice for at least 1 min after each addition. After overnight incubation at 4°C, sample was dialyzed against PBS buffer.

Solubility Test and FPLC

A total of 500 μg of each HCAbs was concentrated to an end point of 30 μl volume using Centriprep-10 K centrifugal filter device (Merck Millipore Ltd., Ireland) as suggested by the manufacturer. Concentrated samples were diluted 10× in 8M guanidine hydrochloride (Gdn-HCl) and the OD at 280 nm measured on a NanoDrop 2000 spectrophotometer (Thermo Scientific, Ireland). The same procedure was used for selected VHs expressed in *E. coli*.

A total of 2 μg of purified and PBS-dialyzed HCAb in 50 μl of PBS was run on a Superdex 200 (3.2/30) column (GE HealthCare Life Sciences, USA) on the FPLC Smart system from Pharmacia. Samples were run in PBS. Bio-Rad's gel filtration standard as a mixture of molecular weight markers ranging from 1,350 to 670,000 Da was used as a control. The same procedure was done with selected VHs expressed in *E. coli* run on a Superdex 75 (3.2/30) column (GE HealthCare Life Sciences, USA).

Virus Reduction Assay

The microtiter plaque reduction assay, as described by Matrosovich et al. (18), was performed using MDCK-SIAT1 cells. Twofold dilutions of the HCAbs were incubated on cell monolayers prior to addition of virus. The neutralization titer is determined as the reciprocal of the dilution of HCAbs, which corresponds to 50% reduction in plaque formation, compared to the virus control.

Hemagglutination Inhibition (HI) Assay

Hemagglutination inhibition assays were performed according to standard methods, Kendall et al. (19), using 0.75% and 1.0% of Turkey and guinea pig red blood cell suspensions, respectively. Four HA units and twofold dilutions of HCAbs were used in these assays. HI titers are reciprocals of the highest dilution of HCAbs, which inhibited hemagglutination.

RESULTS

4HVH transgenic mouse lines contain four non-mutated human germ line heavy variable regions (VH3-11, VH3-23, VH3-53, and VH1-46) followed by all human D and J regions, the $C_\gamma 2$ and $C_\gamma 3$ constant regions, each with a deleted CH1 exon and the human immunoglobulin 3′LCR (**Figure 1**). All transgenic mouse lines rearranged the human HCAb locus and rescued B cell development in a mouse Cμ knockout background (20). They express HCAb dimers in the serum of the correct size (75–90 kDa). These mice were immunized and used as a source of antigen-specific antibodies in developing the method of cloning HCAbs directly into mammalian cells.

Immunization of Transgenic Mice Leads to Successful Production of Antigen-Specific HCAbs

A total of 20 or 50 μg of influenza X-31 HA protein, prepared as described by Ruigrok et al. (17), per mouse was injected intraperitoneally in 2 weeks intervals into eight of 4HVH transgenic mice (two transgenic lines, 4HVH-B and 4HVH-C, originating from different founders, having different integration site of the transgene) and two WT mice as a control, using Stimune as an adjuvant. After the third injection, mice were bled, and an ELISA assay was performed on serum, using HA protein-coated plates (5 μg/ml) and anti-human IgG-HRP or anti-mouse IgG-HRP for the detection of HA-specific antibodies. In seven out of eight transgenic mice and two out of two WT mice, HA-specific antibodies were detected (Figure S1 in Supplementary Material). The higher amount of antigen did not lead to a better response, thus we concluded that 20 μg is sufficient for successful immunization. Seven transgenic ELISA positive mice were immunized three or more times with 20 μg of HA.

HEK 293T HCAbs Library Construction and Subsequent Screening Result in a Diverse Repertoire of Antigen-Specific Soluble Antibodies

Four days after the last injection without adjuvant, mice were sacrificed, and CD 138$^+$ PCs were isolated from bone marrow and spleen. Total RNA was isolated, and cDNA was synthesized (depicted schematically in **Figure 1**). Human VDJ domains were amplified using a set of three different 5′-end primers specific for the leader sequences in the transgenic mouse construct in combination with two different 3′-end primers specific for either the human IgG2 or IgG3 hinge (3). Due to the high sequence similarity, the same 5′-end primer was used for amplification of both VH3-23 and VH3-53. All 5′-primers were designed to contain a *Pvu*II restriction site. A *Pvu*II site appears usually at the beginning of the DNA encoding VH regions (third to fourth codons at the amino acid level) and rarely occurs anywhere else in human VHs. Amplified PCR products were cut either with *Pvu*II/*Sac*I or with *Pvu*II/*Bst*EII restriction enzymes. The *Sac*I site is a unique site at the beginning of the IgG3 hinge, while the *Bst*EII site in frame 4 is unique in most of the VHs and is commonly used for constructing phage libraries (21, 22).

The VDJ fragments were cloned into bacteria using either pCAGhygro G2 or pCAGhygro G3 expression vectors, containing the ubiquitously expressed chicken β-actin promoter, the leader sequence from human VH3-23, and the constant region of human IgG2 or IgG3 (**Figure 2**). The ligated cDNA was transfected into electrocompetent *E. coli* cells, totaling 1 part out of almost 700,000 of the available RNA in the mice (PCs were isolated from half of the total number of cells, 1/4 of total RNA was made into cDNA, 1/30 of the gel purified PCR amplified cDNA was used in the ligations; 1/50 of the ligation was transformed, 1/32 of the transformed bacteria was plated, and 0.57 of total colonies counted were picked from those plates). A total of 960 colonies were picked from both the G2 and G3 library into 96-well plates filled with 2XTY medium. The resulting recombinant bacteria were grown overnight, and plasmid DNA was prepared in the same 96-well format. In parallel, HEK 293T cells were also grown in a 96-well format and transfected with the plasmid DNA maintaining the same 96-well format. A 96-well HA-specific ELISA

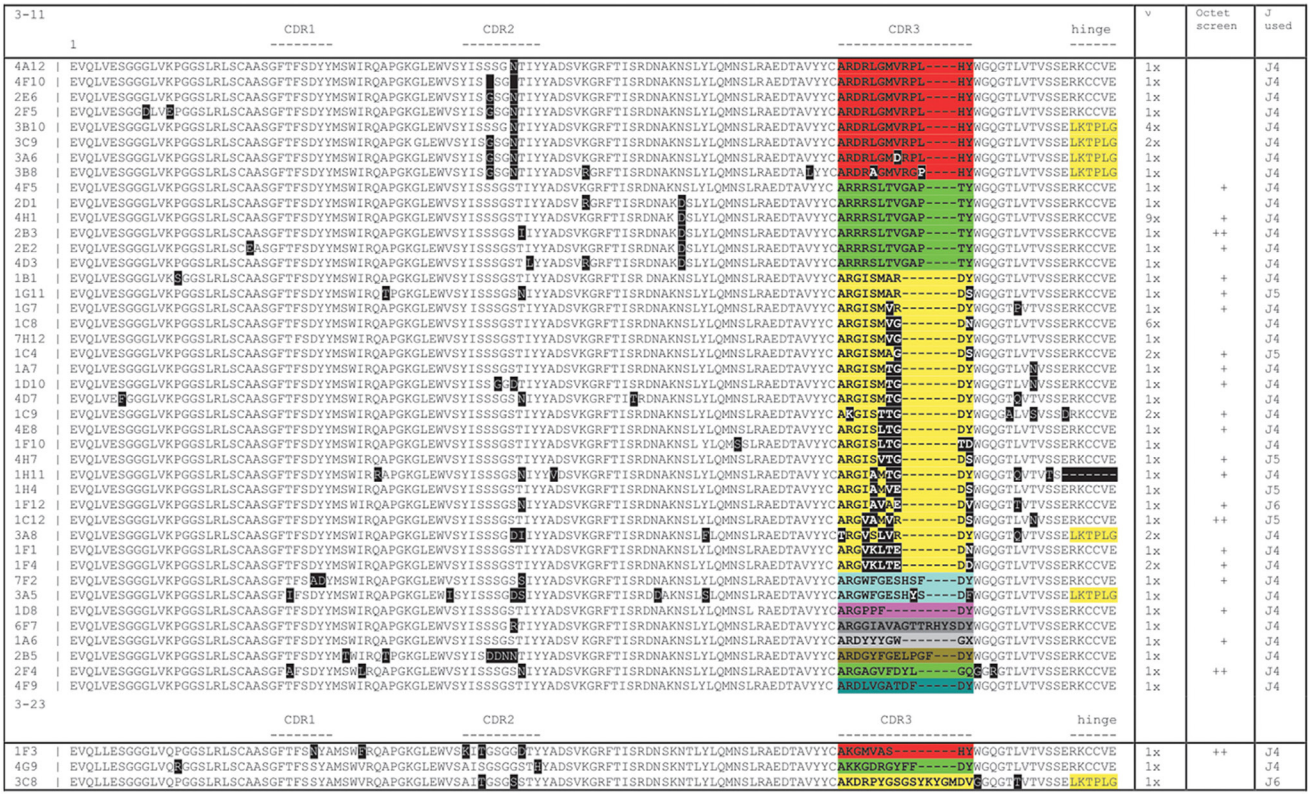

FIGURE 3 | Sequence analysis of hemagglutinin X-31 ELISA positive clones showing a broad range of diversity based on somatic mutations (black boxes) and CDR3 loops (blocks of different colors). The columns on the right show the number of times a particular sequence was found, whether it tested positively on Octet and which J region was used. Yellow shading at the carboxy-terminal end of the sequence shows an IgG3 sequence (LKTPLG), the others are IgG2 (RKCCVE).

screen was performed with supernatants from each well 4 days after transfection. This yielded 66 positive supernatants/clones. The corresponding cDNAs were sequenced (**Figure 3**), which showed that two out of the four available variable segments were used preferentially (VH3-11 and VH3-23); the VDJ domains contained somatic hypermutations; J4 was predominantly used but J5 and J6 were also found; both IgG2 and IgG3 antibodies were present, confirming that class switching occurred in the transgenic mouse. Most prevalent are IgG2 HCAbs, and it is not surprising taking into account that the IgG2 constant region is the most proximal in the transgenic construct and thus the first to recombine. Out of 66 sequences, 45 were unique and these account for 33 different DJ regions. Based on the different CDR3 regions, the HCAbs were classified into 13 distinct groups represented in different colors (**Figure 3**). Positive clones were cultured further, and supernatants were collected for affinity screening, using the same HA antigen preparation. Twenty four clones showed significant binding. A selected number of clones (based on sequence diversity and affinity) were produced in serum free medium. The antibodies with low affinities were not tested at all in a functional assay (see below). Four groups represented by 7F2 (**Figure 3**, blue), 2F4 (green), 1F3 (red), and 3A8 (yellow) were left. Of these, 1F3 and 2F4 appear to bind the same epitope(s), while 3A8 and 7F2 appear to bind a different but overlapping epitope(s).

Characterization of Anti-HA Antibodies

Heavy-chain-only antibodies from medium were purified on protein A, eluted in 3M KSCN, and dialyzed against PBS. The average yield was estimated to be 2–4 μg/ml of medium. On SDS-PAGE gel, HCAbs are of expected size for a monomer (~40–45 kDa) under reducing and of a dimer (~80–90 kDa) under non-reducing conditions (**Figure 4A**). Size differences originate from different sizes and compositions of VH regions and different sizes (longer hinge) of IgG3 HCAbs, accounting for >5 kDa difference per monomer in comparison to IgG2 HCAbs. The profiles on size chromatography (smart columns) showed a single peak of the expected size; the peaks of the IgG3 HCAbs, 3A11, and 3B10 were of higher molecular weight than IgG2 HCAbs (**Figure 4B**). Solubility in PBS was tested with 500 μg of each HCAb by concentrating it to ~30 μl of final volume. The selected HCAb differed with concentrations up to 15.4 μg/μl for 1F1, the equivalent of 30 mg/ml of a normal H2L2 antibody (**Figure 4C**). Further concentration of the very soluble antibodies was not tested. Two of the VHDJ segments (3A8 and 2F4) were also expressed in bacteria and shown to be soluble in at least 5 mg/ml, which is

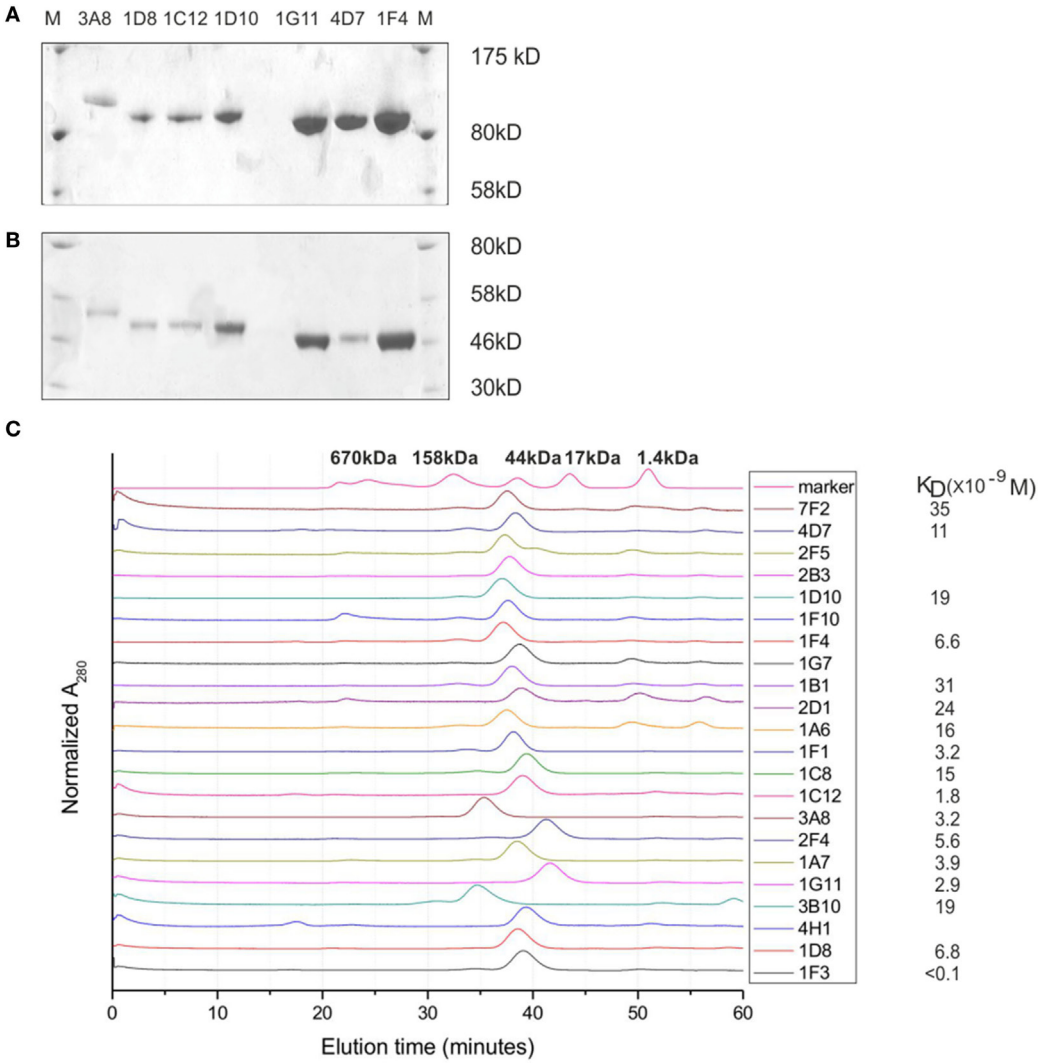

FIGURE 4 | **Characterization of heavy-chain-only antibodies (HCAbs)**. **(A,B)** An example of SDS-PAGE gels run under non-reducing conditions **(A)** and reducing conditions **(B)** shows that HCAbs form dimers. **(C)** HPLC SMART profiles show a single peak for each antibody, the solubility and affinity measurements for selected HCAb clones. Note that 3A8 and 3B10 are IgG3 HCAbs and are of higher molecular weight due to a longer hinge region.

also equivalent to 30 mg/ml of a normal H2L2 antibody (Figure S2 in Supplementary Material). Binding affinities of the HCAb were determined on an Octet instrument with purified antibodies. A BHA preparation (23) that lacks a transmembrane anchor was used to prevent rosette formation and aggregation of antigen. The majority of KD values (9 of 17) for HCAbs were in the 10^{-9} molar range, 7 were in the 10^{-8} molar range, while the KD value for the highest affinity 1F3 HCAb was better than 10^{-10}. HCAbs 1G7, 1G11, 2F4, 1F4, 1C12, 4H1, and 3A11 react on Western blots under both non-reducing and reducing conditions recognizing denatured BHA monomer and the BHA1 chain, respectively. 7F2 reacts with BHA only under non-reducing conditions, while 1F3 preferentially recognizes BHA1 under reducing conditions (data not shown).

Anti-HA HCAbs Function in Virus Neutralization and HI

The HA HCAbs were first evaluated for their ability to neutralize X.31 (H3N2) influenza virus in a plaque reduction assay. Neutralization is reported as the reciprocal of the highest dilution of the antibodies corresponding to 50% plaque reduction compared to the virus control. A total of 18 of the antibodies tested show visible inhibition, and 50% reduction is observed for four HCAb, 1F3 > 2F4 > 3A8 > 4H1 = 7F2 (**Table 1**). A modified neutralization experiment was also performed, where antibodies were incubated for 30 min with the virus prior to addition to MDCK-SIAT1 cells. This led to an increased neutralizing effect especially in the case of 2F4 and 1F3 antibodies [2F4 neutralizing at ≥1.4 μg/ml (18nM) and 1F3 at ≥0.9 μg/ml (11.7nM)]. Ferret

TABLE 1 | Neutralization analysis of heavy-chain-only antibodies (HCAbs) against X-31 influenza virus.

	NI	I	NI	I	NI	I	NI	I	NI	NI	NI
HCAbs	2F4	2F4	1F3	1F3	3A8	3A8	4H1	4H1	7F2	HC19	X31
Concentration (mg/ml)	0.85	0.9	1.2	1.2	0.48	0.55	1.6	0.8	0.4	NK	NK
X31(50% reduction)	32	640	>256	>1,280	16	20	2	2	2	6,400	2,560
X31 (any visible reduction)	64	>1,280	>256	>1,280	64	160	2	8	64	>12,800	>5,120

The numbers show best neutralizing capacity for 1F3 HCAb at ≥0.9 μg/ml (~11nM), followed by 2F4 at 1.4 μg/ml (~18nM).
NI, not preincubated with the virus; I, preincubated with the virus; NK, not known; neutralization titer, reciprocal of the 50% plaque reduction.

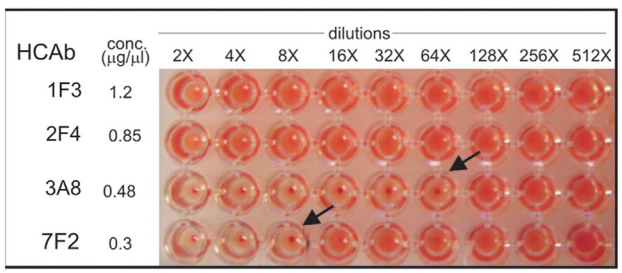

FIGURE 5 | Hemagglutination inhibition assay performed on Turkey red blood cells. 3A8 and 7F2 HCAbs inhibit at a concentration of 0.0075 mg/ml (84 nM) and 0.0375 mg/ml (483 nM), respectively.

anti X-31 serum and HC19, an anti-X31 HA mouse monoclonal antibody, were used as positive controls. 3A8 and 7F2 HCAbs also showed an HI performed with Turkey red blood cells (**Figure 5**) and with guinea pig blood (data not shown), suggesting that 3A8 and 7F2 neutralize infectivity by obstructing the binding of virus to the host cell.

DISCUSSION

Here, we describe a very efficient method for obtaining fully human, antigen-specific, soluble, high-affinity HCAbs, which can easily be automated. Our approach is based on capturing the antibody repertoire of antibody-secreting PCs from both bone marrow and spleen of immunized transgenic mice. Recently, other laboratories have used mouse spleen PCs (24), mouse bone marrow PCs (25), human peripheral blood PCs (26, 27), or human MBC from patient recovered from infection (28) to obtain antigen-specific monoclonal antibodies. Basically, those methods utilize single-cell sorting, single-cell RT-PCR, and natural VH–VL pairing (27, 28). Screening methods have been developed to improve efficiency and enable detection of antigen-specific secreting cells before a single-cell RT-PCR step, such as enzyme-linked immunospot (29), immunospot array assay on chip or microengraving (30). Recently, a method was described (24) omitting a screening step, utilizing massive DNA sequencing and bioinformatics tools to analyze the VL and VH gene repertoires and to find several abundant VH and VL sequences that are paired based on their relative frequencies with 78% efficiency and a method that combines the next-generation sequencing and protein mass spectroscopy to obtain antigen-specific antibody repertoires (31). DeKosky and colleagues developed a low-cost, single-cell, emulsion-based technology for sequencing of antibody VH–VL repertoires with even better pairing precision of >97% (32).

The 4HVH transgenic mice produce human HCAb, without light chains, thus there is no pairing or the necessity for single-cell RT-PCR. The major concern was the solubility of human VH domains, that are not soluble *per se*, but as our results show, antigen-specific HCAbs selected through our screen show high solubility both as a full-length HCAbs and as VH fragments only, thus, the method allows easy isolation of soluble VH regions and the construction of multivalent soluble VH complexes.

The soluble human VH domains obtained from transgenic mice presented here do not possess the hallmark amino acid changes present in VHHs of camelid HCAbs (at positions 44, 45, and 47), which reduce the hydrophobicity of the former light chain interface. They remain as germ line VH being G, L, and W, respectively. As for replacing the V 37 of VH by more hydrophilic F or Y in VHHs, 1 out of 66 VH domains have mutated at this position to F 37, one to L 37. All V3-11-derived HCAbs have I-37 as in the germ line. We have analyzed many sequences from different immunizations with different antigens, beyond the restricted list of anti HA HCAbs shown in **Figure 3**. We have seen FR2 substitutions, which are not found in antibodies that comprise heavy and light chain. We found an increased net hydrophobicity within CDR1 and an increased number of charged amino acids present in CDR3, amino acid substitutions within the framework β-pleated sheet leading to increased net hydrophobicity within FR1, and increased number of charged amino acids present in FR3, all of which could lead to solubility of autonomous soluble VH domains obtained from transgenic mice (33).

This experiment was done in 4HVH transgenic mice bred into our own Cμ MT heavy chain knockout background. It was previously reported that Cμ MT knockout mice can produce low levels of IgG antibodies after prolonged time (34). In such a case, mouse light chains might theoretically attach to the human VHs and affect their solubility, which could cause a problem in using hybridoma fusions. If the reason for increased solubility is light chain attachment, the solubility will be hampered by cloning the heavy chain only (VH) in expression vectors. Once produced, such antibodies would have aggregation problems, which we do not see using HEK 293T libraries. Knocking out the loci completely would avoid the problem.

The choice of VHs in the transgenic construct was based on the VH usage in a human population. It is also known that soluble llama VHHs mostly resemble family three of human VHs (6). The fact that in this particular experiment most of the obtained

antibodies originated from VH3-11, a few fromVH3-23, while none from V3-53 and VH1-47 could be explained by antigen-related specific usage. A new class of influenza-neutralizing antibodies that target a conserved site in the HA stem, most of them being VH 1-69, have been described, but this VH is not present in our transgenic mouse (35). In other experiments, the other VH regions are also used (data not shown). The soluble human VH domains obtained from transgenic mice presented here do not possess hallmark amino acid changes present in VHHs of camelid HCAbs (at positions 44, 45 and 47), which function to reduce hydrophobicity of the former light chain interface. They remain as in germ line VH situation being G, L, and W, respectively.

The four human VHs obtained from transgenic mice were cloned into human IgG2 and IgG3 vectors to reproduce characteristics of antibodies circulating in transgenic mouse. For most therapeutic purposes, human IgG1 and IgG4 antibodies are preferred, due to their effector functions. Once obtained, selected VHs could be cloned and expressed as human IgG1 or IgG4 in appropriate vectors.

We are improving our transgenic mouse platform by increasing the numbers of germ line VHs in the construct, thus increasing the repertoire. The human constant regions in the new generation of transgenic mice have been replaced by the mouse constant region/s reported to be better suited to the mouse machinery (36), while direct cloning might be performed into human IgG vectors of choice.

The pilot experiment performed with 960 plasmid DNAs from the bacterial library and an estimated 7% vector contamination (plasmids without the cDNA insert) gave 66 ELISA-positive clones, 45 of these being unique. If we take into account that the mice carry only 4VH regions, that only a tiny fraction of the available material was used, and that 83% of retrieved antibody sequences were represented only once in the sample tested, a very high efficiency of obtaining many more high-affinity antibodies in an industrial scale automated/robotized process at low cost can be predicted.

ETHICS STATEMENT

The animal study described was approved by the Animal ethical comity [**D**ieren**e**xperimenten**c**ommissie (DEC)] under the immunization protocol EUR 1944.

AUTHOR CONTRIBUTIONS

DD, FG, and JS contributed to the design of the experiments. DD, EB, RJ, RR, JK, and JS contributed to acquisition and analysis of data. DD, FG, and JS contributed to interpretation of data and writing of the manuscript.

ACKNOWLEDGMENTS

The authors thank Tao Chen for helpful discussions and Rose Gonzalves for help with HI assay. The modified Madin Darby canine kidney, MDCK-SIAT1, cells were kindly provided by Dr. M. Matrosovich, Marburg.

FUNDING

This work was supported by the "Foundation Incubator ErasmusMC" and "Harbour Antibodies B.V."

SUPPLEMENTARY MATERIAL

The Supplementary Material for this article can be found online at http://journal.frontiersin.org/article/10.3389/fimmu.2016.00619/full#supplementary-material.

REFERENCES

1. Hamers-Casterman C, Atarhouch T, Muyldermans S, Robinson G, Hamers C, Songa EB, et al. Naturally occurring antibodies devoid of light chains. *Nature* (1993) 363:446–8. doi:10.1038/363446a0
2. Muyldermans S, Lauwereys M. Unique single-domain antigen binding fragments derived from naturally occurring camel heavy-chain antibodies. *J Mol Recognit* (1999) 12:131–40. doi:10.1002/(SICI)1099-1352(199903/04)12:2<131::AID-JMR454>3.3.CO;2-D
3. Janssens R, Dekker S, Hendriks RW, Panayotou G, van Remoortere A, San JK, et al. Generation of heavy-chain-only antibodies in mice. *Proc Natl Acad Sci U S A* (2006) 103:15130–5. doi:10.1073/pnas.0601108103
4. Nguyen VK, Hamers R, Wyns L, Muyldermans S. Loss of splice consensus signal is responsible for the removal of the entire C(H)1 domain of the functional camel IGG2A heavy-chain antibodies. *Mol Immunol* (1999) 36:515–24. doi:10.1016/S0161-5890(99)00067-X
5. Zou X, Smith JA, Nguyen VK, Ren L, Luyten K, Muyldermans S, et al. Expression of a dromedary heavy chain-only antibody and B cell development in the mouse. *J Immunol* (2005) 175:3769–79. doi:10.4049/jimmunol.175.6.3769
6. Nguyen VK, Muyldermans S, Hamers R. The specific variable domain of camel heavy-chain antibodies is encoded in the germline. *J Mol Biol* (1998) 275:413–8. doi:10.1006/jmbi.1997.1477
7. Desmyter A, Decanniere K, Muyldermans S, Wyns L. Antigen specificity and high affinity binding provided by one single loop of a camel single-domain antibody. *J Biol Chem* (2001) 276:26285–90. doi:10.1074/jbc.M102107200
8. Davies J, Riechmann L. 'Camelising' human antibody fragments: NMR studies on VH domains. *FEBS Lett* (1994) 339:285–90. doi:10.1016/0014-5793(94)80432-X
9. Rosenberg AS. Effects of protein aggregates: an immunologic perspective. *AAPS J* (2006) 8:E501–7. doi:10.1208/aapsj080359
10. Fahrner RL, Knudsen HL, Basey CD, Galan W, Feuerhelm D, Vanderlaan M, et al. Industrial purification of pharmaceutical antibodies: development, operation, and validation of chromatography processes. *Biotechnol Genet Eng Rev* (2001) 18:301–27. doi:10.1080/02648725.2001.10648017
11. Gatto D, Martin SW, Bessa J, Pellicioli E, Saudan P, Hinton HJ, et al. Regulation of memory antibody levels: the role of persisting antigen versus plasma cell life span. *J Immunol* (2007) 178:67–76. doi:10.4049/jimmunol.178.1.67
12. Zinkernagel RM, Hengartner H. Protective 'immunity' by pre-existent neutralizing antibody titers and preactivated T cells but not by so-called 'immunological memory'. *Immunol Rev* (2006) 211:310–9. doi:10.1111/j.0105-2896.2006.00402.x
13. Benner R, Hijmans W, Haaijman JJ. The bone marrow: the major source of serum immunoglobulins, but still a neglected site of antibody formation. *Clin Exp Immunol* (1981) 46:1–8.
14. Manz RA, Thiel A, Radbruch A. Lifetime of plasma cells in the bone marrow. *Nature* (1997) 388:133–4. doi:10.1038/40540
15. Radbruch A, Muehlinghaus G, Luger EO, Inamine A, Smith KG, Dörner T, et al. Competence and competition: the challenge of becoming a long-lived plasma cell. *Nat Rev Immunol* (2006) 6:741–50. doi:10.1038/nri1886
16. Wehrli N, Legler DF, Finke D, Toellner KM, Loetscher P, Baggiolini M, et al. Changing responsiveness to chemokines allows medullary plasmablasts to

leave lymph nodes. *Eur J Immunol* (2001) 31:609–16. doi:10.1002/1521-4141(200102)31:2<609::AID-IMMU609>3.0.CO;2-9
17. Ruigrok RW, Wrigley NG, Calder LJ, Cusack S, Wharton SA, Brown EB, et al. Electron microscopy of the low pH structure of influenza virus haemagglutinin. *EMBO J* (1986) 5:41–9.
18. Matrosovich M, Matrosovich T, Carr J, Roberts NA, Klenk HD. Overexpression of the alpha-2,6-sialyltransferase in MDCK cells increases influenza virus sensitivity to neuraminidase inhibitors. *J Virol* (2003) 77:8418–25. doi:10.1128/JVI.77.15.8418-8425.2003
19. Kendall LV, Steffen EK, Riley LK. Hemagglutination inhibition (HAI) assay. *Contemp Top Lab Anim Sci* (1999) 38:54.
20. Kitamura D, Roes J, Kuhn R, Rajewsky K. A B cell-deficient mouse by targeted disruption of the membrane exon of the immunoglobulin mu chain gene. *Nature* (1991) 350:423–6. doi:10.1038/350423a0
21. Koh WW, Steffensen S, Gonzalez-Pajuelo M, Hoorelbeke B, Gorlani A, Szynol A, et al. Generation of a family-specific phage library of llama single chain antibody fragments that neutralize HIV-1. *J Biol Chem* (2010) 285:19116–24. doi:10.1074/jbc.M110.116699
22. de Haard HJ, van Neer N, Reurs A, Hufton SE, Roovers RC, Henderikx P, et al. A large non-immunized human Fab fragment phage library that permits rapid isolation and kinetic analysis of high affinity antibodies. *J Biol Chem* (1999) 274:18218–30. doi:10.1074/jbc.274.26.18218
23. Ha Y, Stevens DJ, Skehel JJ, Wiley DC. H5 avian and H9 swine influenza virus haemagglutinin structures: possible origin of influenza subtypes. *EMBO J* (2002) 21:865–75. doi:10.1093/emboj/21.5.865
24. Jin A, Ozawa T, Tajiri K, Obata T, Kondo S, Kinoshita K, et al. A rapid and efficient single-cell manipulation method for screening antigen-specific antibody-secreting cells from human peripheral blood. *Nat Med* (2009) 15:1088–92. doi:10.1038/nm.1966
25. Reddy ST, Ge X, Miklos AE, Hughes RA, Kang SH, Hoi KH, et al. Monoclonal antibodies isolated without screening by analyzing the variable-gene repertoire of plasma cells. *Nat Biotechnol* (2010) 28:965–9. doi:10.1038/nbt.1673
26. Wrammert J, Smith K, Miller J, Langley WA, Kokko K, Larsen C, et al. Rapid cloning of high-affinity human monoclonal antibodies against influenza virus. *Nature* (2008) 453:667–71. doi:10.1038/nature06890
27. Meijer PJ, Andersen PS, Haahr Hansen M, Steinaa L, Jensen A, Lantto J, et al. Isolation of human antibody repertoires with preservation of the natural heavy and light chain pairing. *J Mol Biol* (2006) 358:764–72. doi:10.1016/j.jmb.2006.02.040
28. Traggiai E, Becker S, Subbarao K, Kolesnikova L, Uematsu Y, Gismondo MR, et al. An efficient method to make human monoclonal antibodies from memory B cells: potent neutralization of SARS coronavirus. *Nat Med* (2004) 10:871–5. doi:10.1038/nm1080
29. Czerkinsky CC, Nilsson LA, Nygren H, Ouchterlony O, Tarkowski A. A solid-phase enzyme-linked immunospot (ELISPOT) assay for enumeration of specific antibody-secreting cells. *J Immunol Methods* (1983) 65:109–21. doi:10.1016/0022-1759(83)90308-3
30. Love JC, Ronan JL, Grotenbreg GM, van der Veen AG, Ploegh HL. A microengraving method for rapid selection of single cells producing antigen-specific antibodies. *Nat Biotechnol* (2006) 24:703–7. doi:10.1038/nbt1210
31. Cheung WC, Beausoleil SA, Zhang X, Sato S, Schieferl SM, Wieler JS, et al. A proteomics approach for the identification and cloning of monoclonal antibodies from serum. *Nat Biotechnol* (2012) 30:447–52. doi:10.1038/nbt.2167
32. DeKosky BJ, Kojima T, Rodin A, Charab W, Ippolito GC, Ellington AD, et al. In-depth determination and analysis of the human paired heavy-and light chain antibody repertoire. *Nat Med* (2015) 21:86–91. doi:10.1038/nm.3743
33. Grosveld F, Janssens RW, Drabek D, Chen T, De Boer E, Craig R. *Soluble "Heavy-Chain Only" Antibodies*. (2010). EP 20100711069.
34. Hasan M, Polic B, Bralic M, Janjic S, Rajevsky K. Incomplete block of B cell development and immunoglobulin production in mice carrying the muMT mutation in BALB/c backround. *Eur J Immunol* (2002) 32:3463–71. doi:10.1002/1521-4141(200212)32:12<3463::AID-IMMU3463>3.0.CO;2-B
35. Pappas L, Foglierini M, Piccoli L, Kallewaard NL, Turrini F, Silacci C, et al. Rapid development of broadly influenza neutralizing antibodies trough redundant mutation. *Nature* (2014) 516:418–22. doi:10.1038/nature13764
36. Lee EC, Liang Q, Ali H, Bayliss L, Beasley A, Bloomfield-Gerdes T, et al. Complete humanization of the mouse immunoglobulin loci enables efficient therapeutic antibody discovery. *Nat Biotech* (2014) 32:356–63. doi:10.1038/nbt.2825

Conflict of Interest Statement: The authors declare that the research was conducted in the absence of any commercial or financial relationships that could be construed as a potential conflict of interest.

frontiers in Immunology

ORIGINAL RESEARCH
published: 04 September 2017
doi: 10.3389/fimmu.2017.00986

Facile Affinity Maturation of Antibody Variable Domains Using Natural Diversity Mutagenesis

*Kathryn E. Tiller[1], Ratul Chowdhury[2], Tong Li[2†], Seth D. Ludwig[1], Sabyasachi Sen[1], Costas D. Maranas[2] and Peter M. Tessier[1]**

[1] Isermann Department of Chemical and Biological Engineering, Center for Biotechnology and Interdisciplinary Studies, Rensselaer Polytechnic Institute, Troy, NY, United States, [2] Department of Chemical Engineering, The Pennsylvania State University, University Park, PA, United States

OPEN ACCESS

Edited by:
Kevin A. Henry,
National Research Council Canada, Canada

Reviewed by:
Jennifer Maynard,
University of Texas at Austin, United States
Xin Ge,
University of California, Riverside, United States
Yongku Cho,
University of Connecticut, United States

***Correspondence:**
Peter M. Tessier
ptessier@umich.edu

†Present address:
Tong Li,
BASF Corporation, San Diego, CA, United States

Specialty section:
This article was submitted to Vaccines and Molecular Therapeutics, a section of the journal Frontiers in Immunology

Received: 07 June 2017
Accepted: 02 August 2017
Published: 04 September 2017

Citation:
Tiller KE, Chowdhury R, Li T, Ludwig SD, Sen S, Maranas CD and Tessier PM (2017) Facile Affinity Maturation of Antibody Variable Domains Using Natural Diversity Mutagenesis. Front. Immunol. 8:986. doi: 10.3389/fimmu.2017.00986

The identification of mutations that enhance antibody affinity while maintaining high antibody specificity and stability is a time-consuming and laborious process. Here, we report an efficient methodology for systematically and rapidly enhancing the affinity of antibody variable domains while maximizing specificity and stability using novel synthetic antibody libraries. Our approach first uses computational and experimental alanine scanning mutagenesis to identify sites in the complementarity-determining regions (CDRs) that are permissive to mutagenesis while maintaining antigen binding. Next, we mutagenize the most permissive CDR positions using degenerate codons to encode wild-type residues and a small number of the most frequently occurring residues at each CDR position based on natural antibody diversity. This mutagenesis approach results in antibody libraries with variants that have a wide range of numbers of CDR mutations, including antibody domains with single mutations and others with tens of mutations. Finally, we sort the modest size libraries (~10 million variants) displayed on the surface of yeast to identify CDR mutations with the greatest increases in affinity. Importantly, we find that single-domain (V_HH) antibodies specific for the α-synuclein protein (whose aggregation is associated with Parkinson's disease) with the greatest gains in affinity (>5-fold) have several (four to six) CDR mutations. This finding highlights the importance of sampling combinations of CDR mutations during the first step of affinity maturation to maximize the efficiency of the process. Interestingly, we find that some natural diversity mutations simultaneously enhance all three key antibody properties (affinity, specificity, and stability) while other mutations enhance some of these properties (e.g., increased specificity) and display trade-offs in others (e.g., reduced affinity and/or stability). Computational modeling reveals that improvements in affinity are generally not due to direct interactions involving CDR mutations but rather due to indirect effects that enhance existing interactions and/or promote new interactions between the antigen and wild-type CDR residues. We expect that natural diversity mutagenesis will be useful for efficient affinity maturation of a wide range of antibody fragments and full-length antibodies.

Keywords: complementarity-determining region, stability, specificity, library, directed evolution, yeast surface display, protein design

INTRODUCTION

The widespread interest in using antibodies in diagnostic and therapeutic applications has led to considerable efforts in developing methods for optimizing their properties (1–6). Methods for improving antibody affinity are particularly important because lead antibodies identified using *in vivo* (immunization) and *in vitro* (e.g., phage display) methods typically do not have high enough affinity for therapeutic applications. Moreover, improvements in antibody affinity are generally expected to enhance the performance of diagnostic antibodies due to improved specificity at reduced antibody concentrations. Methods such as phage, yeast surface and ribosome display are commonly used for *in vitro* affinity maturation because of their many attractive properties (7–13). These properties include the ability to precisely control antigen presentation, conformation, and concentration as well as the ability to perform negative selections against various types of non-antigens to eliminate non-specific variants (14–17). These display methods have been used to achieve large enhancements in affinity for a wide variety of antibody fragments and full-length antibodies (9, 18–23).

Nevertheless, there are several outstanding challenges related to *in vitro* affinity maturation that need to be addressed. First, while it is possible to use saturation mutagenesis to evaluate every possible single mutation in antibody complementarity-determining regions (CDRs), single mutations typically do not result in large gains in affinity (1, 3, 24). Therefore, it is often necessary to generate sub-libraries to identify combinations of single mutations that result in large increases in affinity, which is a slow and laborious process. Second, it is not possible to test all combinations of single and multiple mutations in the CDRs of antibodies in a single library due to intractably large library sizes. For example, a library size of $>10^{39}$ would be required to sample all possible combinations of single and multiple mutations at ~30 residues in the CDRs of typical variable domains. This means that only an extremely small subset of the possible single and multiple mutations can be tested using display methods, which is largely dictated by transformation efficiencies [$\sim10^{9}$–10^{10} for phage (25, 26) and $\sim10^{7}$–10^{8} for yeast (9, 27) using conventional transformation methods]. Therefore, it is important to develop smart library design methods that sample a relatively small number of residues at each CDR position that are most likely to generate antibodies with significant gains in affinity (28–41).

A third common challenge related to antibody affinity maturation is the identification of affinity-enhancing mutations that lead to reductions in antibody specificity (42–44). Highly interactive residues—such as arginine and aromatic residues—can be readily enriched in the CDRs during affinity maturation, which is concerning because they have increased risk for promoting non-specific interactions (43–47). While negative selections are useful for removing some non-specific variants, it is critical to use libraries with the highest possible fraction of specific variants to maximize the likelihood of isolating antibodies with not only increased affinity but also with high specificity. A related problem is that affinity-enhancing CDR mutations can lead to reductions in stability (48–51). Antibody affinity/stability trade-offs appear to be due to structural changes in the CDRs and frameworks that are necessary to increase affinity, and additional compensatory mutations are needed in some cases to maintain thermodynamic stability (48, 49, 51). Therefore, it is important to generate antibody libraries with the highest possible fraction of stable antibodies to minimize the frequency of isolating destabilized antibodies that require additional mutagenesis to restore stability.

To evaluate potential solutions to these challenges, we have sought to identify mutations that increase the affinity of a camelid single-domain antibody specific for the C-terminus of α-synuclein (52) (**Figure 1**). This variable (V_HH) domain—originally referred to as NbSyn2 and herein referred to as N2—was previously isolated from an immune library. We selected this antibody domain for further optimization because its crystal structure is available in complex with antigen at high resolution (**Figure 1**), it is relatively simple to display on the surface of yeast for *in vitro* selections relative to more complex multidomain (scFv) and/or multichain (Fab or IgG) antibodies, it has intermediate affinity (K_D of 58 ± 9 nM) that can be further increased, and it has relatively high stability (apparent melting temperature of 68 ± 0.3°C). We posit that efficient affinity maturation of antibody variable domains such as N2 can be accomplished in three steps: (i) identification of the most permissive sites in the CDRs that can be mutated without large (negative) impacts on affinity using

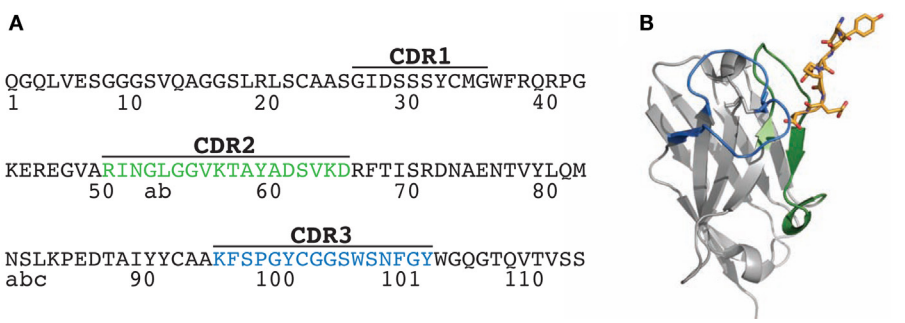

FIGURE 1 | Sequence and structure of the N2 V_HH antibody. **(A)** Amino acid sequence of wild-type N2 V_HH antibody (originally referred to as NbSyn2). The framework and complementarity-determining region (CDR) sequences are defined according to Kabat. **(B)** Structure of N2 in complex with its antigen, a C-terminal α-synuclein peptide (residues 132-GYQDYEPEA-140; PDB 2X6M). Two of the key N2 CDRs involved in antigen binding are highlighted in green (CDR2) and blue (CDR3), while the antigen (α-synuclein peptide) is highlighted in yellow stick form.

alanine scanning mutagenesis; (ii) sampling of a small number of mutations at each permissive CDR site that correspond to either the wild-type residue or residues most commonly observed in natural antibodies at each CDR site; and (iii) screening of all possible combinations of single and multiple natural diversity antibody mutations in a single library. Here, we test this methodology by identifying the most permissive CDR sites in N2 and use these findings to generate a single library that is based on natural antibody diversity and includes both single and multiple (up to 14) CDR mutations. We demonstrate how this library design approach can be used along with yeast surface display to identify stable and specific variable domains with increased affinity.

RESULTS

Alanine Scanning Mutagenesis Reveals Permissive CDR Sites

Toward our goal of developing systematic and robust affinity maturation methods, we first sought to identify permissive sites in the CDRs of N2 that weakly impact antibody affinity using both computational and experimental methods. Two of the CDRs (CDR2 and CDR3) are involved in mediating antigen binding (**Figure 1**). Our computational alanine scanning analysis of these CDRs identified two residues in CDR2 (N52 and K56) and two residues in CDR3 (Y100 and W100e) that are sensitive to mutation (Table S1 in Supplementary Material). We tested these observations using experimental alanine scanning mutagenesis at 18 sites in CDR2 and CDR3. Three sites in these CDRs (R50, P98, and C100a) were excluded from this analysis because they were either shown previously to be involved in mediating antigen binding (52) or suspected to be important for antibody structure and stability.

The alanine mutants were expressed in bacteria and purified using metal-affinity chromatography (purification yields of 0.7–2.6 mg/L). SDS-PAGE analysis revealed high purities (Figure S1 in Supplementary Material). The relative binding of each mutant was evaluated using fluorescence polarization at three V_HH concentrations (44, 133, and 400 nM; **Figure 2**; Figure S2 in Supplementary Material). Consistent trends were observed at each V_HH concentration. Eleven of the 18 mutants retained >50% of the wild-type binding activity, including three in CDR2 (L52b, G53, and V55) and eight in CDR3 (F96, S97, G99, G100b, G100c, S100d, S100f, and N100g). The other seven mutants that displayed greater reductions in binding included five CDR2 mutants (I51, N52, G52a, G54, and K56) and two CDR3 mutants (Y100 and W100e), which were not subjected to further mutagenesis. Four of the disruptive mutations (N52 and K56 in CDR2 and Y100 and W100e in CDR3) were identified in our computational alanine scanning mutagenesis (Table S1 in Supplementary Material). These and other previous results (39, 53, 54) highlight the value of alanine scanning mutagenesis to identify permissive CDR sites that can be mutated during antibody affinity maturation.

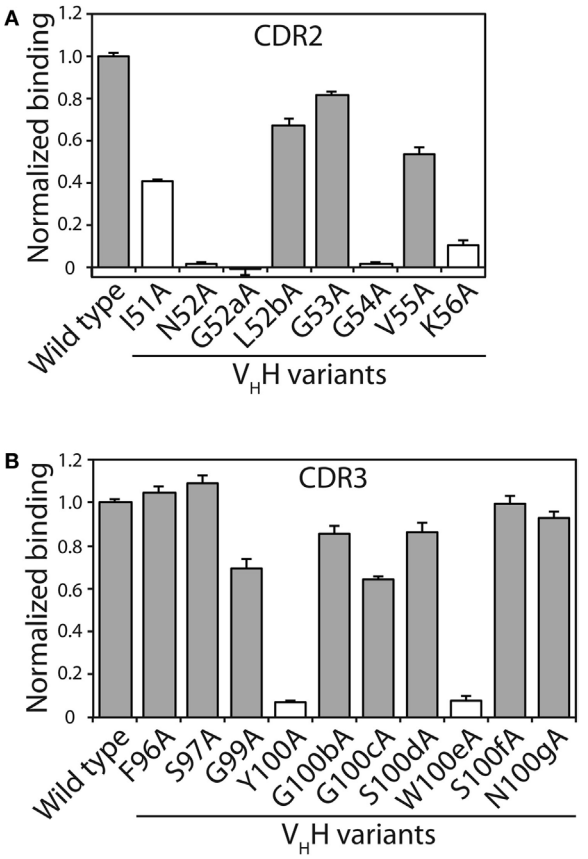

FIGURE 2 | Identification of V_HH complementarity-determining region (CDR) residues involved in antigen binding *via* alanine scanning mutagenesis. The relative antigen binding of the V_HH variants (400 nM) with single alanine substitution mutations in **(A)** CDR2 and **(B)** CDR3 was evaluated using fluorescence polarization (2 nM TAMRA-labeled α-synuclein peptide). Raw polarization signals were background subtracted (background signals were obtained using samples with only TAMRA α-synuclein peptide), and normalized signals are reported (signal for mutant divided by that for wild type). Error bars represent the SD for three independent experiments. The V_HH sequence is defined using Kabat numbering. Alanine mutants that have modest impacts on antigen binding (mutant binding is at least 50% of wild-type binding) are highlighted in gray fill, while those mutants with larger negative impacts on antigen binding are indicated in white fill.

Design of Antibody Libraries Using Natural Diversity Mutagenesis

We next sought to design a single antibody library with mutations in N2 at permissive sites in CDR2 and CDR3. We aimed to accomplish multiple objectives in our library design. First, we limited the library size to ~10^7 variants to enable 10-fold oversampling of the library using yeast surface display given that our typical yeast transformation efficiencies are ~10^8 transformants. Second, we aimed to generate a single library with all possible combinations of wild-type residues as well as single and multiple mutations at the 11 permissive sites in CDR2 and CDR3 as well as at three additional sites not tested during alanine mutagenesis (A49, A94, and K95). This limits the number of possible mutations at each CDR site to typically one to two mutations in addition to the wild-type residue. Third, we sought to sample mutations that most closely correspond to those observed in the CDRs of natural antibodies

in a site-specific manner. To accomplish this, we used the AbYsis database to identify the most common amino acids in camelid V_HH and human V_H domains at each site in CDR2 and CDR3 (55). We used an average site-specific amino acid frequency for camelid and human domains at each CDR site given that there are many more sequences for human domains than for camelid domains. Fourth, we aimed to use inexpensive primer synthesis methods to generate the libraries encoded by standard degenerate codons. Therefore, we sought to identify degenerate codons at each CDR site that encoded the wild-type residue and ~1–5 additional residues that maximize the coverage (sum of individual site-specific amino acid frequencies) of the combined camelid and human natural diversity at each site (**Figure 3**).

Based on these four key objectives, we designed the library shown in **Figure 3** and generated it using the process outlined in Figure S3 in Supplementary Material. The library contains 9.4×10^6 unique variants and includes wild-type residues at each position as well as all possible combinations of single and multiple mutations at 14 sites in CDR2 and CDR3. We sequenced several (22) members of the initial library, and the results are summarized in **Figure 4** and Figure S4 in Supplementary Material. All variants were found to be unique and contained mutations according to the proposed library design.

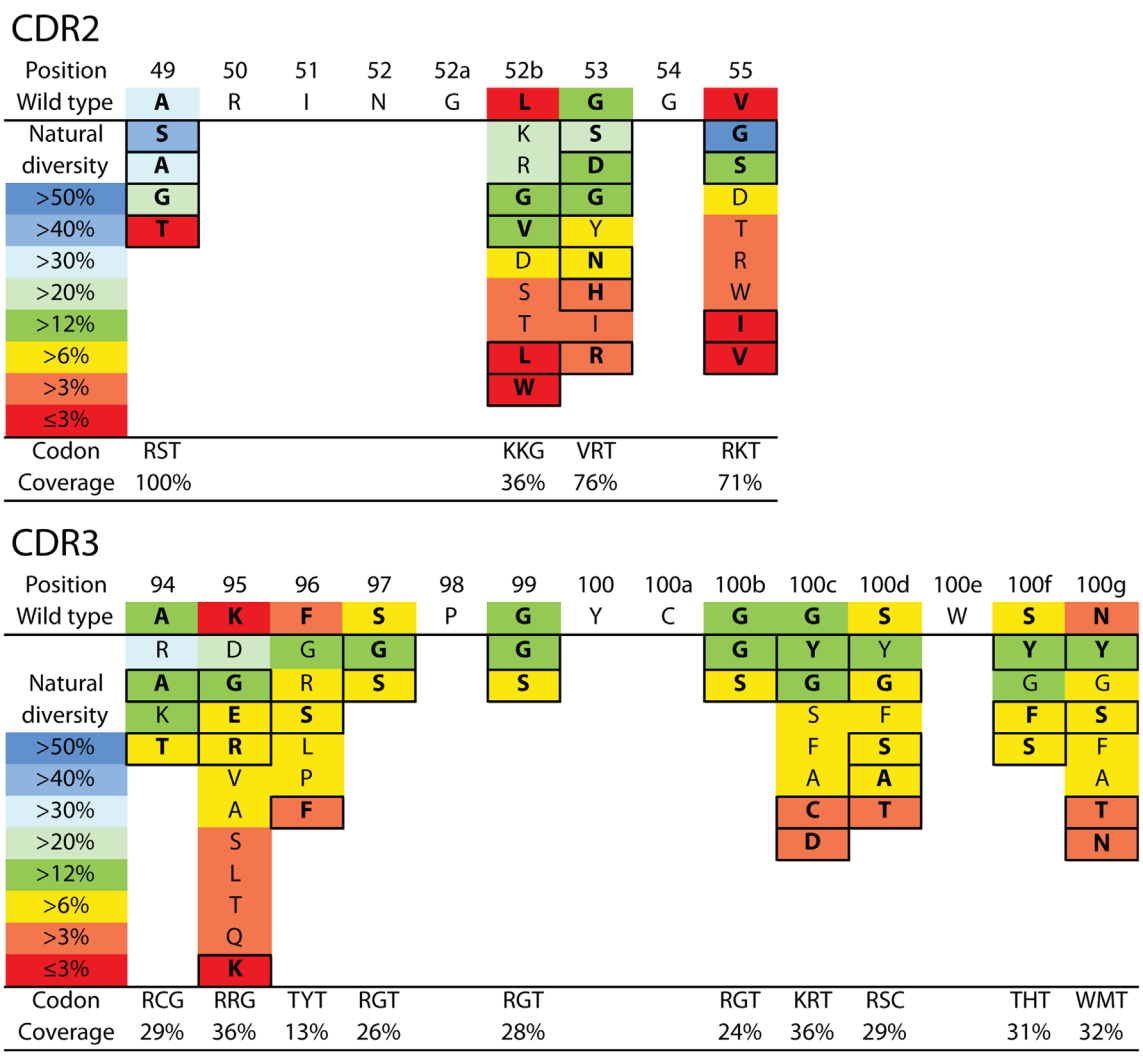

FIGURE 3 | V_HH library design for N2 affinity maturation using natural diversity mutagenesis. A single V_HH library was designed that involved mutating four sites in CDR2 (top) and 10 sites in CDR3 (bottom). The CDR sites selected for mutagenesis were identified primarily using alanine scanning mutagenesis (11 CDR sites). Each mutated CDR site involved sampling the wild-type residue and one to five of the most common natural diversity mutations. Degenerate codons were selected at each CDR site that maximized the natural diversity coverage and minimized the total number of mutations. It was not possible to sample the wild-type residue and the most common natural diversity mutations at each CDR site due to the limitations of degenerate codons. The resulting library (9.4×10^6 variants) theoretically encodes all possible combinations of single and multiple CDR mutations (up to 14 mutations per V_HH). The reported CDR site-specific natural diversity statistics are averaged values for human (V_H) and camelid (V_HH) variable domains, as reported in the abYsis database (55). Boxed amino acids correspond to the selected natural diversity mutations.

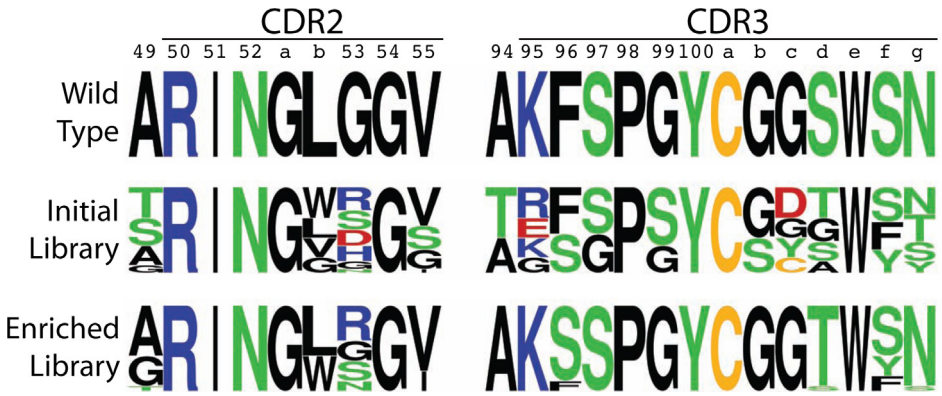

FIGURE 4 | Amino acid logo summary of initial and enriched V_HH libraries relative to the wild-type N2 V_HH. The logo plots for the mutated portions of CDR2 and CDR3 were generated from sequencing results for 22 (initial library) and 17 (enriched library) V_HH variants. The CDR sequences are defined using Kabat numbering, and the logos were generated using a web application (http://weblogo.berkeley.edu).

Sequence Analysis of V_HH Libraries after Sorting for Enhanced Antigen Binding

The library of antibody variable domains was displayed on the surface of *S. cerevisiae* and screened for variants with increased affinity for the α-synuclein peptide. The sorting process involved five rounds of selection *via* magnetic-activated cell sorting (MACS) with progressively reduced concentrations of α-synuclein peptide (starting at 50 nM peptide and ending at 5 nM) and one additional round of selection *via* fluorescence-activated cell sorting (FACS) (20 nM peptide). The sorting process was continued until the antigen binding of the library was increased by at least fivefold relative to wild type, as judged by flow cytometry. Selections were performed in a buffer (PBS) that contained both BSA (1 mg/mL) and milk (1% w/v). We have found previously that antibody selections in complex environments (e.g., buffers supplemented with milk) lead to identification of antibodies with improved specificity (56).

The enriched V_HH library was sequenced after sorts 5 and 6, and 17 unique variants were identified and further analyzed (based on sequencing 23 clones) with 1–6 mutations in CDR2 and CDR3. Sequence logos in **Figure 4** summarize the general enrichment of amino acids in the CDRs, while the amino acid enrichment ratios are given in Figure S5 in Supplementary Material and the CDR sequences are given in Figure S6 in Supplementary Material. Most of the sites in CDR2 and CDR3 (11 out of 14) displayed either intermediate or strong preference for the wild-type residue (**Figure 4**). However, three sites (53 in CDR2, 96 and 100d in CDR3) either displayed similar preference for mutations as the wild-type residue (Arg, Gly, Ser, and Asn at position 53) or strong preference for a specific mutated residue (Ser at position 96 and Thr at position 100d). It is also notable that the four positions that were varied in CDR2 did not display strong preference for any single amino acid, while almost every residue in CDR3 (9 out of 10) displayed strong preference for a single residue. This result is unexpected based on alanine scanning mutagenesis, as the identified sites in CDR3 appeared to be as permissive (or even more permissive) to mutagenesis than those identified in CDR2.

Identification of Affinity-Matured Variable Domains with High Stability and Specificity

To evaluate the effectiveness of the affinity maturation process, we next expressed and purified the unique V_HH variants that were identified in the enriched library. The variable domains expressed at levels (purification yields of 0.1–2.0 mg/L) that were generally similar to wild type (1.0 mg/L), and also displayed purities similar to wild type (Figure S7 in Supplementary Material). We first used fluorescence polarization to evaluate the affinities of the variable domains for the α-synuclein peptide (**Figure 5A**). The equilibrium dissociation constant for the wild-type N2 variable domain (K_D of 57.6 ± 9.0 nM) was approximately threefold lower than the previously reported value (K_D of 190 ± 30 nM) that was measured by isothermal calorimetry (52).

We chose to characterize two V_HH domains in more detail (N2.12 and N2.17). Both variable domains displayed improved affinity (K_D of 7.6 ± 0.4 nM for N2.12 and 13.2 ± 4.8 nM for N2.17 relative to 57.6 ± 9.0 nM for wild type; **Figure 5A**). Interestingly, the improved affinity of the N2.12 variant came at the cost of reduced stability (apparent T_m of 59.7 ± 0.3°C relative to 67.8 ± 0.3°C for wild type; **Figure 5B**). By contrast, the N2.17 variant displayed similar stability as wild type (66.9 ± 0.1°C for N2.17 relative to 67.8 ± 0.3°C for wild type; **Figure 5B**). This finding demonstrates that our affinity maturation method can be used to identify antibody variable domains such as N2.17 with increased affinity without significant reduction in stability despite the common observation of affinity/stability trade-offs (such as those observed for N2.12) during affinity maturation (51, 58).

We also evaluated the specificity of the N2.12 and N2.17 V_HH domains to evaluate if gains in affinity were offset by reductions

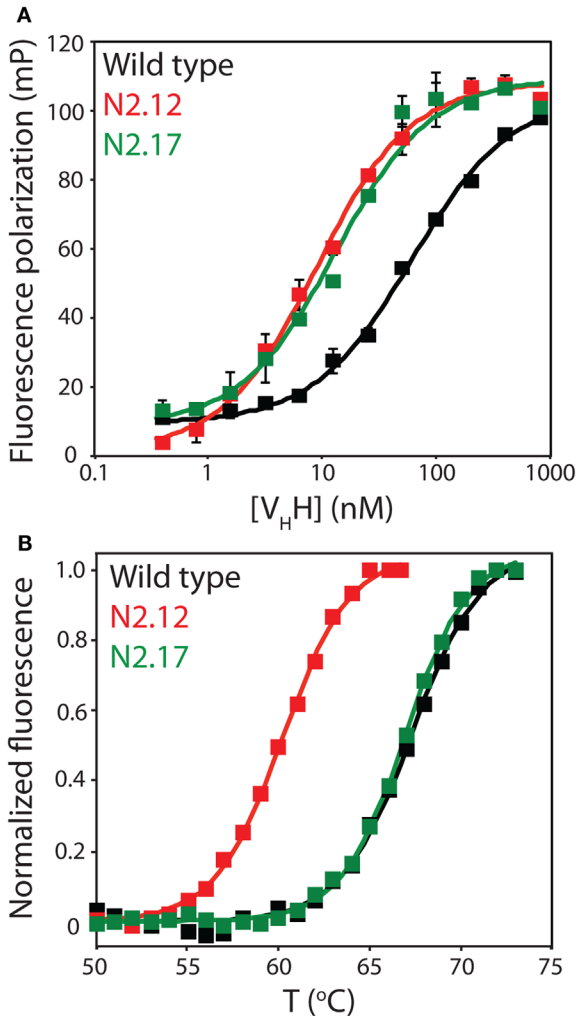

FIGURE 5 | Evaluation of the affinity and stability of select V_HH mutants that were enriched after library sorting for improved antigen binding. **(A)** Fluorescence polarization analysis of V_HH binding to labeled antigen (2 nM TAMRA-labeled α-synuclein peptide). The analysis was performed in a PBS buffer supplemented with BSA (0.001%) and Tween 20 (0.001%). Three independent experiments were performed, and representative binding curves are shown for wild type (black), N2.12 (red), and N2.17 (green). Each point shown is the average of two repeats and the error bars are SD. Data were fit with a binding model that accounted for the fact that the V_HH antibodies were not in excess of the antigen at some of the V_HH concentrations (57). **(B)** Extrinsic fluorescence analysis of apparent V_HH unfolding as a function of temperature. The fluorescence data were obtained using an extrinsic dye (Protein Thermal Shift dye, Life Technologies). Three independent experiments were performed, and representative melting curves are shown for wild type (black), N2.12 (red), and N2.17 (green). The data were background subtracted using background signals obtained without antibody. Next, the fluorescence data were subtracted by the relatively low signal at 50°C, and divided by the maximum fluorescence signal (after the maximum signal was subtracted by the signal at 50°C). Finally, the pre- and post-transition regions of the normalized fluorescence data were flattened using linear fits.

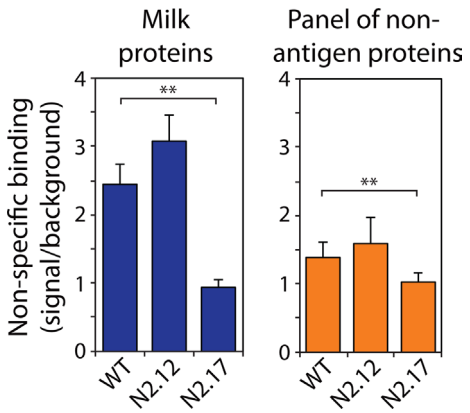

FIGURE 6 | Analysis of non-specific binding for wild-type and affinity-matured V_HH domains. Non-specific binding of V_HH variants was evaluated using well plates coated with milk proteins (left) and a panel of six non-antigen proteins (right). The non-specific binding analysis was performed at an antibody concentration of 1,000 nM. The reported non-specific binding values are the signals for antibody binding to well plates coated with milk proteins or other non-antigen proteins divided by the background signal without primary antibody (V_HH). The reported binding values (right) are the averages for six non-antigen proteins (ovalbumin, BSA, KLH, ribonuclease A, avidin, and lysozyme). The values are averages of three independent experiments, and the error bars are SD. A two-tailed Student's *t*-test was used to determine statistical significance [*p*-values < 0.01 (**)].

in specificity (**Figure 6**; Figure S8 in Supplementary Material). A simple test of non-specific interactions is to evaluate the propensities of antibodies to interact with well plates coated with different types of non-antigen proteins (milk proteins and a panel of six non-antigen proteins in **Figure 6** and Figure S8 in Supplemental Material) at relatively high antibody concentrations (~1 μM). Interestingly, the N2.17 variant displays significantly lower non-specific interactions than wild type (*p*-values of 0.003 for milk proteins and 0.009 for six non-antigen proteins), while the N2.12 variant displays similar non-specific binding as wild type (*p*-values of 0.129 for milk proteins and 0.342 for non-antigen proteins). These results demonstrate that the affinity-matured V_HH domains display similar or improved specificity relative to wild type.

We next analyzed the affinity and stability of the other 15 unique V_HH variants that were isolated during the sorting process (**Figure 7**; Figures S9 and S10 in Supplementary Material). All but one of the variable domains (N2.5) displayed a statistically significant increase in affinity relative to wild type (*p*-values <0.01; **Figure 7A**). This suggests that our library design and selection strategies enable robust identification of variable domains with improved affinity. Interestingly, variants with the greatest improvements in affinity (at least threefold) contained at least three mutations and up to six mutations. This highlights the inherent limitations of attempting to identify variable domains with large increases in affinity using single mutations.

The stability analysis of these variable domains also revealed interesting behaviors (**Figure 7B**). Most notably, the apparent stability of the V_HH domains is much more variable than the affinity measurements. About one-third of variable domains (6 of 17) display similar stabilities as wild type (apparent melting temperature within 1°C of wild type). The variable domains with the largest reductions in apparent melting temperature (>7°C;

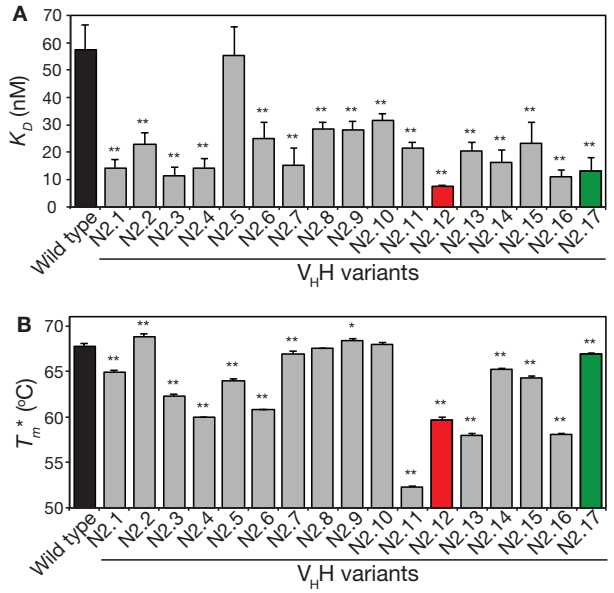

FIGURE 7 | Analysis of affinity and stability for the panel of V_HH mutants that were isolated after library sorting for improved antigen binding. **(A)** Equilibrium dissociation constant (K_D) values were measured using fluorescence polarization. **(B)** Apparent melting temperatures (T_m*) were measured using extrinsic fluorescence measurements as a function of temperature. In **(A,B)**, the measurements were performed as described in **Figure 5**, the values are averages for three independent experiments, and the error bars are SD. A two-tailed Student's *t*-test was used to determine statistical significance [*p*-values < 0.05 (*) or 0.01 (**)].

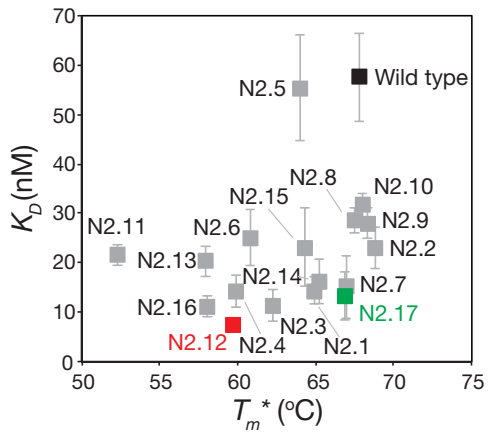

FIGURE 8 | Comparison of the affinities and stabilities of the affinity-matured V_HH variants. The equilibrium dissociation constants (K_D) and apparent melting temperatures (T_m*) are from **Figure 7**. The values are averages of three independent experiments, and the error bars are SD (horizontal error bars for stability are smaller than the size of the data points).

N2.4, N2.11, N2.12, N2.13, and N2.16) had the highest number of mutations (5–6 mutations). A direct comparison of affinity versus stability for the V_HH domains reveals a wide range of affinity/stability trade-offs (**Figure 8**).

Origins of Affinity/Stability and Affinity/Specificity Trade-offs for Affinity-Matured V_HH Domains

To better understand the origins of the strong and weak trade-offs between affinity and both stability and specificity for the selected V_HH domains, we performed reversion mutational analysis for two of the variable domains (N2.12 and N2.17) to evaluate the impact of the acquired mutations on affinity, stability, and specificity. Six single reversion mutants were created for N2.12, while four single reversion mutations were created for N2.17. The purities of the reversion mutants were similar to wild type (Figure S11 in Supplementary Material).

The affinity and stability measurements are summarized in **Figure 9** and Figures S12 and S13 in Supplementary Material. In **Figure 9**, the affinity is reported as the equilibrium association constant (K_A). Reversion mutations that reduced affinity and/or stability—which signifies that the original mutations increased affinity and/or stability—correspond to reduced K_A or apparent melting temperature (T_m*) values. For the highest affinity variant identified in our studies (N2.12), one mutation (G49) is highly destabilizing and reversion to the wild-type residue (A49) results in a large increase in stability (T_m* increases by 7.4°C; *p*-value of 2×10^{-5}; **Figure 9A**) without a significant change in affinity (*p*-value of 0.67; **Figure 9A**). Surprisingly, this reversion mutant is the most desirable affinity-matured V_HH domain that we obtained, as the large affinity enhancement (>7-fold) is achieved without compromising stability (*p*-value of 0.099 for comparison to wild type). This reversion mutational analysis also reveals that the affinity enhancement of N2.12 is largely due to four mutations (W52b, R53, S96, and T100d). The S96 mutation is particularly interesting because it contributes positively both to affinity and stability, as judged by the fact that the reversion mutation (F96) reduces both properties (*p*-values <0.03). By contrast, the R53 mutation increases affinity (*p*-value of 0.004) at the cost of stability (*p*-value of 0.001), and the W52b and T100d mutations increase affinity (*p*-values <0.005) without significantly impacting stability (*p*-values >0.1).

Reversion mutational analysis of the more stable V_HH domain (N2.17) revealed key differences relative to the less stable N2.12 variant (**Figure 9B**). None of the four reversion mutations in N2.17 resulted in changes in apparent melting temperature >2°C. The most destabilizing N2.17 mutation was F100f, and the reversion mutation S100f increased stability to levels modestly higher than the wild-type N2 domain without a significant change in affinity relative to N2.17 (*p*-value of 0.74). The three key affinity mutations (W52b, S96, and T100d)—which were also observed in the less stable N2.12 domain—had little impact on stability (<1°C). These findings highlight that the affinity/stability trade-offs observed in our enriched library can be addressed either by screening a sufficient number of V_HH variants or by performing reversion mutational analysis to identify destabilizing mutations that are not required for affinity.

The specificity of the reversion mutants was analyzed by evaluating their relative propensity to interact with milk proteins (**Figure 10**). A decrease in the normalized specificity

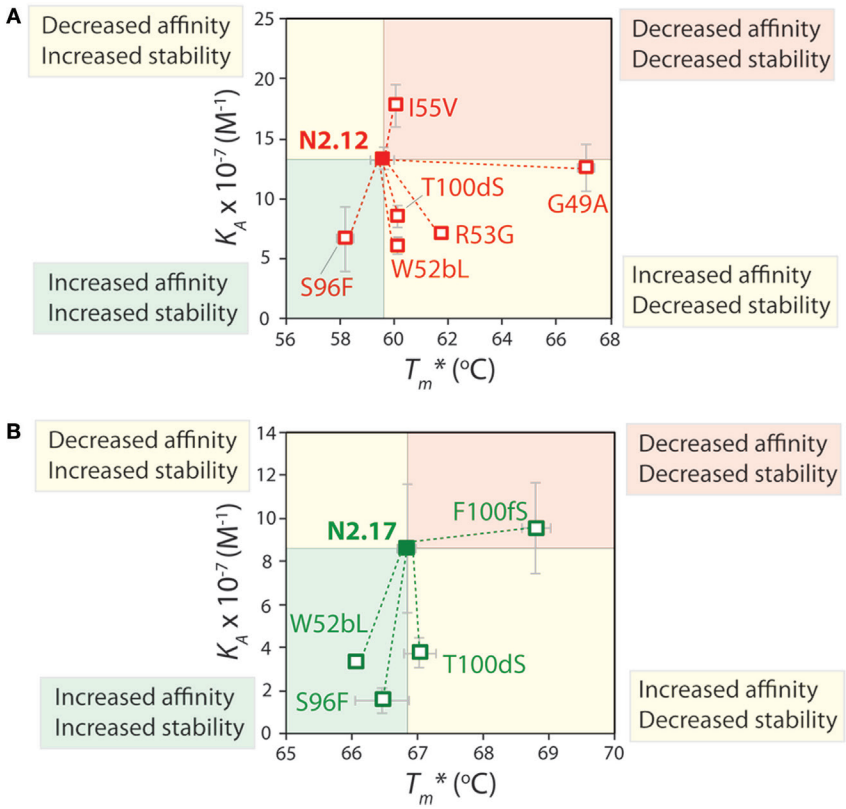

FIGURE 9 | Mutational analysis of the contributions of specific V_HH mutations to affinity and stability. Single reversion mutations were generated for two affinity-matured V_HH variants [**(A)** N2.12 and **(B)** N2.17] to determine the contribution of each acquired mutation to affinity and stability. Values of the equilibrium association constant (K_A) were measured using fluorescence polarization, and values of the apparent melting temperature (T_m*) were measured using extrinsic fluorescence measurements as a function of temperature. Reductions in either affinity or stability due to reversion mutations indicate that the original mutations acquired during affinity maturation contribute positively to either property. The values of K_A and T_m* are averages from three independent experiments and the error bars are SD.

of a reversion mutant indicates that the original mutation has a positive impact on antibody specificity. The N2.12 variable domain—which possesses similar specificity as the wild-type N2 domain—acquired five mutations that decreased specificity (p-values <0.01; **Figure 10A**). However, N2.12 also acquired a single mutation (W52b) that increased specificity (p-value of 9.4×10^{-6}; **Figure 10A**) and which appears to offset the negative effects of the other five mutations. Interestingly, the improved specificity of N2.17 relative to wild type appears to be due to three mutations that enhance specificity (W52b, S96, and F100f; p-values $<1.1 \times 10^{-5}$; **Figure 10B**). This analysis highlights that affinity-enhancing mutations can contribute both positively and negatively to antibody specificity, and that significant improvements in specificity can be due to the cumulative effects of multiple mutations.

Computational Analysis of Natural Diversity Mutations That Enhance Affinity

To gain further understanding about how the selected mutations increased V_HH affinity, we performed computational modeling of two of the mutant variable domains (N2.12 and N2.17). This was accomplished by introducing the corresponding mutations into the crystal structure of the wild-type N2 domain in complex with the α-synuclein peptide (PDB: 2X6M) and relaxing the structures *via* CHARMM force field energy minimization (59). The highest affinity domain we identified after library sorting (N2.12) contains six mutations that are located near but generally not in direct contact with the antigen (**Figure 11A**). The one exception is I55 in CDR2 (V55 in wild type), which forms a direct contact with E137 in the α-synuclein peptide *via* an interaction between the backbone amide in the antibody (I55) and carboxylate oxygen in the antigen (E137). However, this does not appear to explain the increased affinity of N2.12 because the mutation increases the interaction distance (2.6 Å) relative to wild type (1.7 Å). Instead, the increase in affinity for N2.12 appears to be due to indirect effects that involve enhancement of existing interactions as well as introduction of new interactions that involve wild-type CDR residues (**Figure 11B**). This includes an enhanced salt bridge between K56 (side chain nitrogen) in CDR2 and E139 (carboxylate oxygen) in the antigen. Moreover, a new electrostatic interaction is introduced between T57 (backbone carbonyl oxygen) in CDR2 and A140 (backbone amide nitrogen) in the antigen. The latter interaction appears to be mediated by a water bridge in both the crystal structure and energy minimized (relaxed) structure of the wild-type antibody-antigen complex (data not shown).

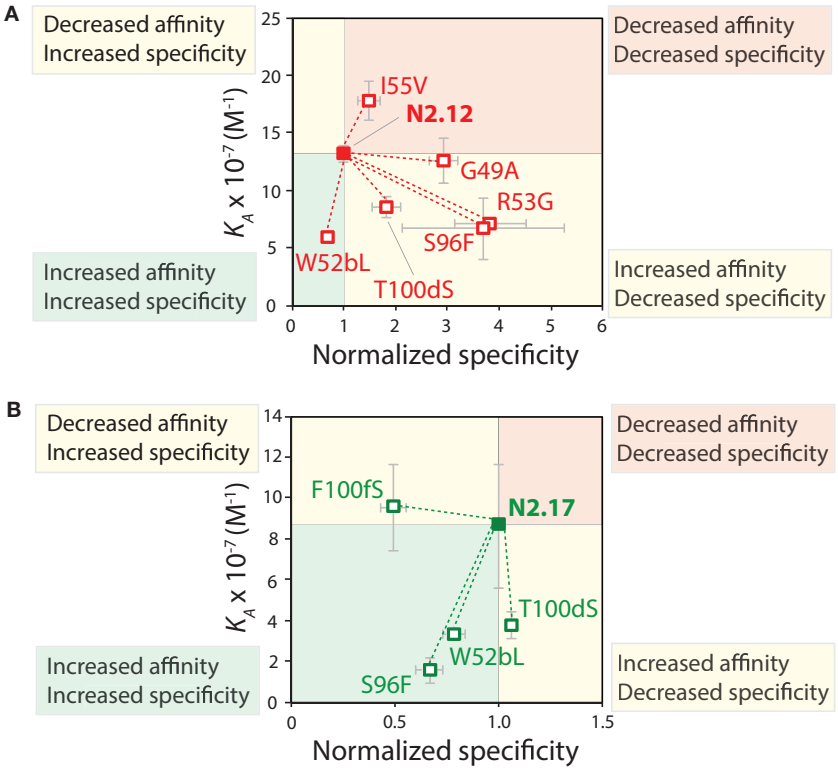

FIGURE 10 | Mutational analysis of the contributions of specific V_HH mutations to affinity and specificity. Single reversion mutations were generated for two affinity-matured V_HH variants [**(A)** N2.12 and **(B)** N2.17] to determine the contribution of each acquired mutation to affinity and specificity. Values of the equilibrium association constant (K_A) were measured as described in **Figure 9**. Normalized specificity was measured as the binding of the parent antibody to milk-blocked wells divided by that for the reversion mutant (parent/reversion mutant). Reductions in affinity or specificity for the reversion mutants indicates that the original mutations acquired during affinity maturation contribute positively to either property. The values of K_A are averages from three independent experiments, and values for normalized specificity are averages of six replicates obtained from three independent experiments. The error bars are SD.

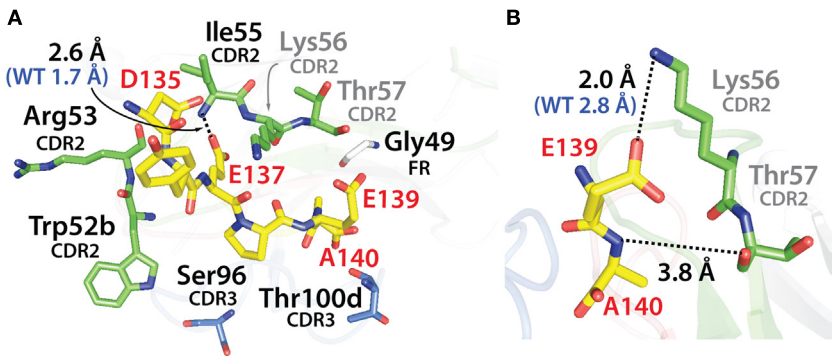

FIGURE 11 | Analysis of the contributions of the acquired mutations in the N2.12 V_HH antibody to enhanced affinity using computational models of the antibody–antigen complex. **(A)** Model of the N2.12 V_HH in complex with the α-synuclein peptide. The six acquired CDR mutations are highlighted in black text, the wild-type residues are shown in gray, the nitrogen atoms are shown in blue, and the oxygen atoms are shown in red. Only one of the CDR mutations (Ile55) makes direct contact with the antigen, and the distance of this interaction is increased relative to wild type. **(B)** New or enhanced interactions between the N2.12 V_HH and the α-synuclein peptide. Direct electrostatic interactions are shown with black dotted lines, and the distances are indicated in black for N2.12 relative to the original distances for wild type in blue (if there was a wild-type interaction). V_HH residues are numbered according to Kabat.

Similar findings were obtained by examining the modeled structure of the more stable N2.17 variant in complex with the α-synuclein peptide (**Figure 12A**). None of the four mutations make direct contact with the antigen. Instead, the gains in V_HH affinity appear to be due to indirect effects involving wild-type CDR residues (**Figure 12B**), as observed for N2.12 (**Figure 11B**).

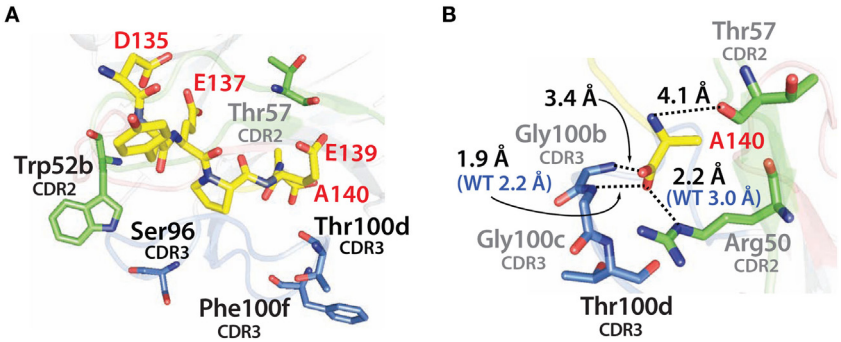

FIGURE 12 | Analysis of the contributions of the acquired mutations in the N2.17 V_HH antibody to enhanced affinity using computational models of the antibody–antigen complex. **(A)** Model of the N2.17 V_HH in complex with the α-synuclein peptide. The four acquired CDR mutations are highlighted in black text. No CDR mutations make direct contact with the antigen. **(B)** New or enhanced interactions between the N2.17 V_HH and the α-synuclein peptide. The labeling is the same as in **Figure 11**.

We observe enhanced hydrophobic packing between G100b, G100c, and T100d in CDR3 with A140 in the antigen (**Figure 12B**). In addition, there are new direct electrostatic interactions between T57 (CDR2) and A140 (antigen) as well as G100b (CDR3) and A140 (antigen). Finally, two electrostatic interactions are enhanced, namely R50 (CDR2) with A140 (antigen) and G100c (CDR3) with A140 (antigen). This enhancement is due to A140 in the α-synuclein peptide moving deeper into the binding pocket of the V_HH domain, which is mediated by structural rearrangement of the CDRs. These results are consistent with the general understanding that affinity maturation of antibodies involves subtle changes to the antigen-binding site and beneficial mutations often mediate their effects indirectly *via* structural changes that optimize interactions involving wild-type CDR residues (60–63).

DISCUSSION

This work identifies several key factors that impact the efficiency and robustness of antibody affinity maturation. First, we find that multiple mutations (>4) are necessary to achieve large (>5-fold) gains in affinity for the N2 V_HH antibody. While there are obvious exceptions to our findings (1, 3, 5), they are generally consistent with previous findings that many single affinity-enhancing mutations cause relatively modest increases in affinity (24, 64–66). It is possible to identify and combine several single mutations that enhance affinity, but the collective effects of multiple mutations on antibody affinity are complex and often not additive (58, 62, 67, 68). Moreover, generating all possible combinations of single antibody mutations is a time-consuming process that involves multiple rounds of expression and affinity evaluation. It is also notable that the need for several mutations to achieve large increases in antibody affinity is likely at least part of the reason that it is particularly challenging to use computational methods for antibody affinity maturation (3, 24, 58, 67, 69). Accurate prediction of subtle structural changes caused by combinations of CDR mutations is notoriously difficult. Our natural diversity mutagenesis approach is attractive because it enables sampling of all possible combinations of single and multiple CDR mutations (~1–5 mutations per CDR site across 14 sites in this work) for rapid identification of antibody variants with large increases in affinity using a single antibody library.

There are multiple considerations related to our natural diversity mutagenesis approach that deserve further consideration. First, the primary problem during affinity maturation is obtaining mutations that increase affinity but reduce specificity. Our use of natural antibody diversity to guide library design—which has been reported previously in related ways by others (28–41, 70)—avoids overrepresentation of highly interactive residues that are likely to promote non-specific interactions. Many previous studies (including those from our own lab) have used NNN or NNK degenerate codons in antibody CDRs to identify affinity-enhancing mutations (58, 71–73). One of the limitations of this approach is that the frequency of sampling each amino acid is based on its corresponding codon frequency. In our experience, this is especially problematic for highly interactive residues such as arginine that have a large number of codons (up to six depending on the specific degenerate codon). By contrast, our library design infrequently sampled highly interactive residues, such as arginine (2 out of 14 CDR sites), tryptophan (1 out of 14 CDR sites), and phenylalanine (2 out of 14 CDR sites). In fact, one of the key affinity mutations in both N2.12 and N2.17 was F96S, which removed an aromatic residue and increased the hydrophilicity of CDR3.

It is also notable that our mutational approach was useful for identifying beneficial mutations in the highly variable CDR3 in addition to the less variable CDR2. Two of the key affinity mutations in both N2.12 and N2.17—F96S and S100dT—were in CDR3. The most common residues at many sites in CDR3 occur at relatively low frequency (13–21% for positions 95–100 g). Therefore, it was not obvious that sampling such a small number of natural diversity mutations (1–3 mutations per site for nine sites in CDR3) in such a highly diverse CDR would be sufficient to identify affinity-enhancing mutations. For example, the natural occurrence of the wild-type residue (Phe) at position 96 in CDR3 is 4% (combined human and camelid diversity), and we sampled only one mutation (Ser) at this site that is also relatively uncommon (9%) despite being more common than most other residues

at this CDR3 site. Likewise, we sampled three mutations at position 100d in CDR3 (Gly, Ala, and Thr) that were all relatively uncommon (5–11%). Nevertheless, we identified a beneficial mutation (Thr) that occurs relatively infrequently (5%) at this site in CDR3. These results suggest that natural diversity mutations in CDR3—especially for affinity maturation—may be particularly useful for libraries aimed at isolating combinations of mutations that result in large increases in affinity without over enrichment in highly interactive residues that are likely to also mediate non-specific interactions.

Despite the strengths of our natural diversity mutagenesis approach, one obvious weakness is related to the use of inexpensive primer synthesis methods that rely on standard degenerate codons to generate libraries. This results in the limitation that some combinations of wild-type CDR residues and the most common natural diversity mutations are (i) not possible, (ii) require too many additional mutations to justify including them, and/or (iii) require inclusion of undesirable codons (e.g., those encoding cysteine or stop codons). While we allowed a cysteine mutation at one position (100c) to maximize natural diversity coverage, it is undesirable to include too many cysteine mutations due to complications associated with unpaired cysteines.

An example of the limitations of using degenerate codons to generate antibody libraries is related to position 52b in CDR2. The wild-type residue at position 52b is Leu, and the two most common residues at this position are Lys (29% based on combined camelid and human natural diversity) and Arg (22%). However, this requires sampling a minimum of six codons, which corresponds to a minimum of five residues and overrepresentation of arginine (two codons) to achieve natural diversity coverage of 56% (an average of ~9% per codon). Therefore, we sampled Gly, Val, and Trp in addition to the wild-type residue (Leu) at position 52b using four codons to achieve natural diversity coverage of 36% and similar average diversity per codon (9%). Likewise, the wild-type residue at position 96 in CDR3 is Phe. In order to sample Phe and the most common residue (Gly), this requires sampling a minimum of four codons that include Val (5%) and Cys (1.5%). Sampling these four residues would result in natural diversity coverage of 23% (an average of ~6% per codon). Instead, we sampled Ser in addition to Phe using two codons to achieve natural diversity coverage of 13% (an average of ~6% per codon). This approach allowed us to sample a similar amount of natural diversity per codon and eliminated the use of an undesirable codon (Cys). These examples highlight the limitations of using standard degenerate codons to achieve the highest possible coverage of natural diversity mutations. This limitation could be readily solved using more expensive trinucleotide synthesis methods.

Our results also demonstrate that affinity/stability trade-offs are common during antibody affinity maturation. We and others have previously found that CDR mutations that increase antibody affinity can be destabilizing (48, 49, 51). Indeed, several examples of natural antibodies have been reported that demonstrate how affinity-enhancing mutations can be destabilizing (48, 49). This destabilization is likely due to strain on the antibody framework that results from modifying the structure and chemistry of the antigen-binding site for increased affinity. Encouragingly, about one-third of our affinity-matured antibodies displayed little reduction in stability (<1°C) and we identified one of the highest affinity variants with similar stability as wild type after additional mutational analysis (N2.12 with A49; T_m^* of 67.1 ± 0.3°C relative to 67.8 ± 0.3°C for wild type). Nevertheless, the fact that the highest affinity variants identified after library sorting were some of the most destabilized ones (e.g., N2.12 and N2.16) highlights the challenge of affinity/stability trade-offs during affinity maturation. One promising approach is to combine natural diversity mutations in the CDRs with those that naturally occur in the frameworks (74) to co-select for both affinity and stability mutations. We are currently in the process of evaluating this strategy to further improve the affinity maturation process for a wide range of single- and multidomain antibodies to isolate variants that possess high stability in addition to high affinity.

Another notable aspect of our findings relates to the impact of affinity-enhancing mutations on antibody specificity. Specificity is arguably the most difficult antibody property to maintain or enhance during affinity maturation (42–44). This is likely due to the natural tendency to accumulate highly interactive (solvent exposed) amino acids in antibody CDRs during affinity maturation that improve antigen binding but also promote non-specific interactions and reduced specificity. Indeed, we observed trade-offs between affinity and specificity for the N2.12 variant, as three of the four key affinity-enhancing mutations (R53, S96, and T100d) reduced specificity (**Figure 10A**). Interestingly, the N2.17 variant displayed reduced affinity/specificity trade-offs, as two (W52b and S96) of the three affinity-enhancing mutations also increased specificity (**Figure 10B**). The latter results are particularly notable because these same mutations (W52b and S96) also increased the stability of N2.17. It is also notable that the impacts of mutations on affinity and specificity were context dependent, as some mutations (e.g., S96) that increased affinity displayed opposite impacts on specificity (reduced specificity for N2.12 and increased specificity for N2.17). Despite these complexities, it will be important in the future to better define how CDR sequence and structure impacts antibody specificity because antibody specificity appears to be a key factor in differentiating approved antibody therapeutics from those in clinical trials (75).

CONCLUSION

Our systematic approach for using natural antibody diversity to design libraries with combinations of single and multiple mutations with limited diversity at each CDR site is effective for increasing the affinity of a camelid V_HH domain while maintaining or enhancing stability and specificity. These encouraging results will need to be evaluated for other types of single- and multidomain antibodies to evaluate their generality. It will also be important to develop computational methods to improve library design by optimizing natural diversity coverage while minimizing the number of mutations. This is relatively straightforward to perform at any given CDR site but it is more challenging to globally optimize with increasing numbers of CDR sites. Nevertheless, efforts in optimizing antibody library design are key to avoid oversampling abnormal CDR sequences that are unlikely to lead to high antibody stability and specificity in addition to high affinity. We expect that methods such as the ones we have demonstrated in this work will

be useful for rapidly and systematically optimizing antibodies for a wide range of diagnostic and therapeutic applications.

EXPERIMENTAL METHODS

Cloning and Library Construction

The wild-type N2 gene was created using PCR-based gene synthesis (76). The amino acid sequence of the N2 V_HH domain (**Figure 1**) was obtained from the PDB (2X6M). A hexahistidine tag was added to the C-terminus of the V_HH domain for purification. The gene was flanked with N-terminal *HindIII* and C-terminal *XhoI* restriction sites. The digested PCR product was then ligated into a bacterial expression vector (pET-17b, Novagen) that contained an N-terminal pelB sequence for periplasmic secretion. Single point mutations of N2 were generated *via* site-directed mutagenesis using *PfuUltra* II (600850, Agilent Technologies).

The N2 natural diversity library was created using overlap extension PCR to introduce mutations in portions of CDR2 and CDR3 (Figure S3 in Supplementary Material). Mutagenesis was performed using degenerate codons at 14 sites in CDR2 and CDR3 (**Figure 3**). The first step in library generation was to perform three PCRs. These included amplification of DNA fragments encoding the N-terminus of V_HH domain to framework 2, CDR2 to framework 3, and CDR3 to the C-terminus of V_HH domain. The DNA fragments overlapped each other by ~20 bases, which enabled the three DNA fragments to be combined in a final amplification step using terminal primers. The terminal primers contained flanking *NheI* and *SalI* restriction sites as well as 45 bases of homology on each end with the yeast display plasmid (pCTCON2).

The N2 natural diversity library genes were ligated into the yeast display plasmid and transformed into *S. cerevisiae* (EBY100) *via* homologous recombination. This process was performed as described previously (9) with minor modifications to increase transformation efficiency. These modifications include using more yeast cells (500 mL of EBY100 was grown to OD_{600} of 1.2) for a single library transformation, more DNA (nine preparations of 4 μg PCR product and 1 μg digested vector), and electroporation at higher voltage (2,500 V). After the yeast cells were allowed to recover, the yeast library was grown in SDCAA (500 mL of 20 g/L dextrose, 6.7 g/L yeast nitrogen base, 5 g/L casamino acids, 14.7 g/L sodium citrate, and 4.3 g/L citric acid) for 48 h, and aliquotted for storage at −80°C. The library transformation resulted in 2×10^8 transformants. To assess the quality of the library, a small amount of the yeast library culture (1 mL) was miniprepped (Zymoprep II yeast miniprep kit, Zymo Research) and transformed into electroporation-competent bacterial cells (XL1-Blue, 200228, Agilent Technologies). Several (22) plasmids from the initial library were isolated and sequenced, and all were found to be unique.

Yeast Surface Display and Library Screening

The yeast cultures were first grown at 30°C with agitation in SDCAA to an OD value of 1–2. To induce the expression of Aga2-V_HH fusion proteins, the medium was switched to SGCAA (20 g/L galactose, 6.7 g/L yeast nitrogen base, 5 g/L casamino acids, 8.56 g/L $NaH_2PO_4 \cdot H_2O$, and 6.76 g/L $Na_2HPO_4 \cdot 2H_2O$) and grown for 16 h at 30°C with agitation. The yeast medium was supplemented with ampicillin (100 μg/mL; BP1760-25, Thermo Fisher Scientific), kanamycin (100 μg/mL; BP906-5, Thermo Fisher Scientific), and penicillin-streptomycin (diluted to 1×; 15140122, Thermo Fisher Scientific).

The natural diversity library was sorted *via* five rounds of MACS and one round of FACS. For each sort, yeast were washed twice with PBS containing BSA (1 mg/mL; PBS-B) and resuspended in a solution containing the biotinylated α-synuclein peptide (biotin-GYQDYEPEA) and PBS-B supplemented with 1% milk (non-fat dry milk, PBS-BM). For the FACS sort, 1,000× diluted anti-c-myc chicken IgY antibody (A-21281, Life Technologies) was added to this mixture to detect V_HH display. The yeast and α-synuclein peptide solution was mixed end-over-end at room temperature for 2–3 h. Next, the cells were washed once with PBS-B and sorted for antigen binding.

For MACS sorts, yeast cells were resuspended in PBS-B (5 mL) and mixed with Streptavidin MicroBeads (100 μL; 130-048-102, Miltenyi Biotec). After incubation on ice (10 min), the yeast cells were pelleted and resuspended in PBS-B and passed through a MACS separation column (130-042-401, Miltenyi Biotec). The column was connected to a MidiMACS separator magnet (130-042-302, Miltenyi Biotec) that was attached to a MACS MultiStand (130-042-303, Miltenyi Biotec). Next, the bound yeast cells were eluted by removing the column from the magnetic stand and flowing SDCAA (7 mL) through the column. The collected cells were then grown overnight in SDCAA (30°C) with agitation and subjected to additional rounds of sorting. For the FACS sort, yeast cells were resuspended in PBS-B (200 μL) with 100-fold diluted secondary reagents (Alexa Fluor 488-conjugated goat anti-chicken IgG, A-11039 and Alexa Fluor 647-conjugated streptavidin, S-32357; Life Technologies), and allowed to incubate on ice (5 min). The cells were washed once, analyzed, and sorted *via* flow cytometry (FACSAria, BD Biosciences). The enriched yeast cultures after sorts 5 and 6 were miniprepped and subcloned into a bacterial expression vector (pET-17b). Several (~10) plasmids from each sort were isolated and sequenced.

Bacterial Expression and Purification

V_HH domains were expressed in bacteria [BL21(DE3)pLysS, 200132, Agilent Technologies] using auto-induction media (200 mL) supplemented with ampicillin (100 μg/mL) and chloramphenicol (35 μg/mL) (77). After 48 h of growth at 30°C, the cultures were pelleted and the supernatants were incubated overnight (4°C, 80 rpm) with 3 mL of Ni-NTA beads (30230, Qiagen). The beads were then washed with PBS (150 mL), eluted at pH 3 (PBS), and neutralized to pH 7.4. The protein samples were centrifuged at 21,000 × *g* (5 min) and filtered (0.22 μm filter, SLGV013SL, Millipore). Next, the V_HH domains were refolded *via* buffer exchange (Zeba spin desalting columns, 89893, Thermo Fisher Scientific) into 6 M GuHCl (pH 7.4). The antibody domains were allowed to equilibrate overnight (4°C) before being buffer exchanged into PBS (pH 7.4). Finally, the V_HH domains were concentrated (3 kDa spin filters; UFC800324, EMD Millipore) and filtered again (0.22 μm filters). The concentrations of the

V_HH domains were measured *via* UV absorbance measurements at 280 nm. The extinction coefficients of the V_HH domains were 27,180–32,680 $M^{-1}cm^{-1}$, which were calculated based on their amino acid sequences. The purity of the V_HH domains was evaluated using SDS-PAGE analysis (WG1203BOX, Life Technologies), and the gels were stained using Coomassie dye (24615, Thermo Fisher Scientific).

Antibody Affinity Analysis

The affinities of the N2 V_HH and variants thereof were measured using fluorescence polarization. The V_HH domains were prepared at a range of concentrations (0.8 nM–1.6 μM) and mixed (75 μL) with the α-synuclein peptide labeled with a tetramethylrhodamine (TAMRA) fluorophore (4 nM, 75 μL; Genemed Synthesis Inc.). The antibody–antigen mixtures were prepared in 96 well flat bottom black polystyrene plates (7605, ThermoFisher Scientific). The binding buffer was PBS supplemented with BSA [0.001% (w/v)] and Tween 20 [0.001% (v/v)]. Background wells were prepared that contained the same concentration of TAMRA-labeled α-synuclein peptide without antibody. The antibody–antigen mixtures were allowed to equilibrate at room temperature for 3 h. Fluorescence polarization was then measured (Infinite M1000 PRO, Tecan) at an excitation wavelength of 530 nm (5 nm bandwidth) and an emission wavelength of 582 nm (10 nm bandwidth).

The fluorescence polarization raw signals were background subtracted and two replicates were averaged for each antibody concentration. The average data were then fit to determine the K_D value using a four-parameter model that accounts for the fact that the antibody is not in excess of antigen at some of the evaluated antibody concentrations:

$$FP = FP_{min} + FP_{max}\frac{\left([Ab]+[Ag]+K_D\right)-\sqrt{\left([Ab]+[Ag]+K_D\right)^2-4[Ab][Ag]}}{2[Ag]}$$

where FP is the measured fluorescence polarization value, FP_{min} is the minimum fluorescence polarization value, FP_{max} is the maximum fluorescence polarization value, [Ab] is the total V_HH concentration, [Ag] is the total antigen concentration, and K_D is the equilibrium dissociation constant. The equation was fit using the Microsoft Excel solver tool to minimize differences—namely the sum of squared differences—between the data and the model. At least three independent experiments were performed for each V_HH antibody.

Antibody Stability Analysis

The apparent stabilities of the V_HH domains were determined using measurements of extrinsic fluorescence (Protein Thermal Shift dye, 4461146, Life Technologies) as a function of temperature. Protein Thermal Shift buffer (5 μL), V_HH domains (12.5 μL of 0.08 μg/μL V_HH), and Protein Thermal Shift dye (2.5 μL of 8× solution) were mixed in opaque 96-well PCR plates and sealed with foil (04729692001, Roche). The background samples were prepared with water (12.5 μL) instead of V_HH domains. Thermal melts were performed using a LightCycler 480 real-time PCR instrument (Roche). The fluorescence (Ex: 558 nm, Em: 610 nm) was measured as the plate was heated from 37 to 95°C. Many (>60) acquisitions were collected per 1°C, and the heating rate was ~0.6°C/min.

The apparent melting temperatures of the V_HH domains were determined by analyzing the first derivative of the fluorescence with respect to temperature. This involved fitting a second-order polynomial to the major peak and solving for the temperature at which the maximum occurred (or the minimum if the negative derivative is used). The reported melt curves were background subtracted using background signals obtained without antibody. Next, the fluorescence data were subtracted by the relatively low signal at 50°C and divided by the maximum fluorescence signal (after the maximum signal was subtracted by the signal at 50°C). Finally, the pre- and post-transition regions of the normalized fluorescence data were flattened using linear fits (58).

Antibody Specificity Analysis

The specificities of the V_HH domains were evaluated using two methods. The first method evaluated the propensity of the purified antibodies to bind to well plates coated with milk proteins. Transparent 384 well plates (MaxiSorp, 464718, ThermoFisher Scientific) were coated with milk [100 μL of 10% (w/v) milk in PBS with 0.1% (v/v) Tween 20; PBST] for 8 h and then washed with PBS. The V_HH domains were diluted to 1,000 nM in PBST, added to the well plates and allowed to incubate overnight at room temperature. The well plates were then washed with PBS and secondary reagents were added to detect bound antibodies. The second method evaluated the propensity of the purified antibodies to bind to six immobilized non-antigens [ovalbumin (A5503, Sigma), BSA (BP9706, Fisher Bioreagents), KLH (H8283, Sigma), ribonuclease A (R6513, Sigma), avidin (A9275, Sigma), and lysozyme (L6876, Sigma)]. Non-antigen proteins were diluted in PBS (75 μL, 0.2 mg/mL) and immobilized in separate wells at 37°C for 1 h in 384 well plates. The wells were subsequently washed with PBST. Variable domains (1,000 nM, 25 μL) in PBS with 1 g/L BSA and 0.1% (v/v) Tween 20 were added to the well plates and allowed to incubate at room temperature for 2 h.

Detection of bound V_HH was performed similarly for both specificity tests. Secondary antibody (25 μL of 1,000× diluted anti-6X His tag antibody; ab18184, Abcam) in PBST was added, allowed to incubate for 1 h, and then washed with PBS. Next, the well plates were incubated with diluted horseradish peroxidase-conjugated goat anti-mouse IgG (25 μL of 1,000× dilution; 32430, Thermo Fisher Scientific) in PBST for 1 h and then were washed with PBS. The bound antibody was detected by adding substrate (25 μL of 1-Step Ultra TMB-ELISA, 34028, Thermo Fisher Scientific), quenching after 20–40 min (25 μL of 2 M H_2SO_4) and measuring the absorbance values at 450 nm (Tecan Safire^2 plate reader). Normalized binding signals were calculated as signal divided by background, and the background values were absorbance measurements without primary (V_HH) antibody.

Computational Modeling

The V_HH-antigen crystal structure (PDB: 2X6M) was energy minimized using the CHARMM force field and the adopted basis Newton–Raphson routine (78). We applied the Newton–Raphson

algorithm to a subspace of the coordinate vectors that were sampled by the displacement coordinates (during each iteration) with the objective of minimizing the energy of the complex. This enabled the rate of change of the gradient vectors to be computed and coupled with a subsequent eigenvector analysis to avoid saddle points (metastable energy states). At every Newton–Raphson iteration, the residual gradient vector was calculated and a steepest descent step was added to the Newton–Raphson step. This was done to incorporate a new direction into the basis set to avoid metastable states and find the shortest trajectory toward the atomic coordinates corresponding to the minimum potential energy of the complex.

Computational alanine scanning mutagenesis was performed in a similar manner as described previously (79). Python scripts were written for a new OptMAVEn module to compute the difference between binding energies of the N2 single alanine mutants (which were energy-minimized) and wild-type N2 (2X6M). Binding energy calculations were performed using the conformation-dependent binding energy function as used in the Robetta full-chain protein structure prediction server (80, 81).

Structural models of two affinity-matured V_HH variants (N2.12 and N2.17) in complex with antigen were also generated. These structures were simulated alongside the energy-minimized wild-type complex. We created the N2.12 and N2.17 variants using the Mutator program of IPRO suite of programs (82). This approach uses the residue positions and mutations as input, and it performs backbone perturbation, rotamer repacking and energy minimization. A mixed-integer linear programming optimization step was performed to systematically identify the optimal rotamer combination of the new residues at the mutation sites and residues within 4.5 Å (83). This was done to prevent energetically unfavorable steric clashes upon mutation. We performed ensemble structure refinements to establish favorable Lennard-Jones interactions in addition to eliminate severe steric repulsions. The N2.12 and N2.17 variants were visualized in complex with antigen using PyMOL (version 1.8, Schrödinger). Shell scripts were written to identify direct and indirect polar contacts between the antigen (α-synuclein residues DYEPEA) and V_HH variants. Only contacts within 5 Å were analyzed.

AUTHOR CONTRIBUTIONS

KT, PT, RC, TL, and CM designed the research; KT and SS performed experiments; RC and TL performed computational analysis; SL performed bioinformatics analysis; and KT, RC, CM, and PT wrote the paper.

ACKNOWLEDGMENTS

We thank Dane Wittrup for providing the pCTCON2 yeast display vector, EBY100 yeast strain and for their helpful discussions; and Eric Shusta, David Colby, Jennifer Cochran, Eric Boder, and Ben Hackel for their helpful advise in performing yeast surface display. We thank Catherine Royer for the use of the Infinite M1000 PRO plate reader. We also thank members of the Tessier lab for their helpful suggestions. This work was supported by the National Institutes of Health (R01GM104130 to PT), National Science Foundation (CBET 1159943 and 1605266 to PT, Graduate Research Fellowship to KT), and Rensselaer Polytechnic Institute (the Richard Baruch M.D. Chair to PT).

SUPPLEMENTARY MATERIAL

The Supplementary Material for this article can be found online at http://journal.frontiersin.org/article/10.3389/fimmu.2017.00986/full#supplementary-material.

REFERENCES

1. Tiller KE, Tessier PM. Advances in antibody design. *Annu Rev Biomed Eng* (2015) 17:191–216. doi:10.1146/annurev-bioeng-071114-040733
2. Zolot RS, Basu S, Million RP. Antibody-drug conjugates. *Nat Rev Drug Discov* (2013) 12:259–60. doi:10.1038/nrd3980
3. Kuroda D, Shirai H, Jacobson MP, Nakamura H. Computer-aided antibody design. *Protein Eng Des Sel* (2012) 25:507–21. doi:10.1093/protein/gzs024
4. Desjarlais JR, Lazar GA. Modulation of antibody effector function. *Exp Cell Res* (2011) 317:1278–85. doi:10.1016/j.yexcr.2011.03.018
5. Maynard J, Georgiou G. Antibody engineering. *Annu Rev Biomed Eng* (2000) 2:339–76. doi:10.1146/annurev.bioeng.2.1.339
6. Perchiacca JM, Tessier PM. Engineering aggregation-resistant antibodies. *Annu Rev Chem Biomol Eng* (2012) 3:263–86. doi:10.1146/annurev-chembioeng-062011-081052
7. McCafferty J, Griffiths AD, Winter G, Chiswell DJ. Phage antibodies: filamentous phage displaying antibody variable domains. *Nature* (1990) 348:552–4. doi:10.1038/348552a0
8. Sidhu SS. Phage display in pharmaceutical biotechnology. *Curr Opin Biotechnol* (2000) 11:610–6. doi:10.1016/S0958-1669(00)00152-X
9. Chao G, Lau WL, Hackel BJ, Sazinsky SL, Lippow SM, Wittrup KD. Isolating and engineering human antibodies using yeast surface display. *Nat Protoc* (2006) 1:755–68. doi:10.1038/nprot.2006.94
10. Boder ET, Wittrup KD. Yeast surface display for screening combinatorial polypeptide libraries. *Nat Biotechnol* (1997) 15:553–7. doi:10.1038/nbt0697-553
11. Irving RA, Coia G, Roberts A, Nuttall SD, Hudson PJ. Ribosome display and affinity maturation: from antibodies to single V-domains and steps towards cancer therapeutics. *J Immunol Methods* (2001) 248:31–45. doi:10.1016/S0022-1759(00)00341-0
12. Hanes J, Jermutus L, Weber-Bornhauser S, Bosshard HR, Pluckthun A. Ribosome display efficiently selects and evolves high-affinity antibodies in vitro from immune libraries. *Proc Natl Acad Sci U S A* (1998) 95:14130–5. doi:10.1073/pnas.95.24.14130
13. Hanes J, Schaffitzel C, Knappik A, Pluckthun A. Picomolar affinity antibodies from a fully synthetic naive library selected and evolved by ribosome display. *Nat Biotechnol* (2000) 18:1287–92. doi:10.1038/82407
14. Ackerman M, Levary D, Tobon G, Hackel B, Orcutt KD, Wittrup KD. Highly avid magnetic bead capture: an efficient selection method for de novo protein engineering utilizing yeast surface display. *Biotechnol Prog* (2009) 25:774–83. doi:10.1002/btpr.174
15. Xu Y, Roach W, Sun T, Jain T, Prinz B, Yu TY, et al. Addressing polyspecificity of antibodies selected from an in vitro yeast presentation system: a FACS-based, high-throughput selection and analytical tool. *Protein Eng Des Sel* (2013) 26:663–70. doi:10.1093/protein/gzt047
16. Mann JK, Park S. Epitope-specific binder design by yeast surface display. *Methods Mol Biol* (2015) 1319:143–54. doi:10.1007/978-1-4939-2748-7_7
17. Sheehan J, Marasco WA. Phage and yeast display. *Microbiol Spectr* (2015) 3:AID–0028–2014. doi:10.1128/microbiolspec.AID-0028-2014
18. Zhao A, Tohidkia MR, Siegel DL, Coukos G, Omidi Y. Phage antibody display libraries: a powerful antibody discovery platform for immunotherapy. *Crit Rev Biotechnol* (2016) 36:276–89. doi:10.3109/07388551.2014.958978

19. Kretzschmar T, von Ruden T. Antibody discovery: phage display. *Curr Opin Biotechnol* (2002) 13:598–602. doi:10.1016/S0958-1669(02)00380-4
20. Dufner P, Jermutus L, Minter RR. Harnessing phage and ribosome display for antibody optimisation. *Trends Biotechnol* (2006) 24:523–9. doi:10.1016/j.tibtech.2006.09.004
21. Groves MA, Osbourn JK. Applications of ribosome display to antibody drug discovery. *Expert Opin Biol Ther* (2005) 5:125–35. doi:10.1517/14712598.5.1.125
22. Pepper LR, Cho YK, Boder ET, Shusta EV. A decade of yeast surface display technology: where are we now? *Comb Chem High Throughput Screen* (2008) 11:127–34. doi:10.2174/138620708783744516
23. Rhiel L, Krah S, Gunther R, Becker S, Kolmar H, Hock B. REAL-select: full-length antibody display and library screening by surface capture on yeast cells. *PLoS One* (2014) 9:e114887. doi:10.1371/journal.pone.0114887
24. Lippow SM, Wittrup KD, Tidor B. Computational design of antibody-affinity improvement beyond in vivo maturation. *Nat Biotechnol* (2007) 25:1171–6. doi:10.1038/nbt1336
25. Sidhu SS, Lowman HB, Cunningham BC, Wells JA. Phage display for selection of novel binding peptides. *Methods Enzymol* (2000) 328:333–63. doi:10.1016/S0076-6879(00)28406-1
26. Winter G, Griffiths AD, Hawkins RE, Hoogenboom HR. Making antibodies by phage display technology. *Annu Rev Immunol* (1994) 12:433–55. doi:10.1146/annurev.iy.12.040194.002245
27. Rakestraw JA, Baskaran AR, Wittrup KD. A flow cytometric assay for screening improved heterologous protein secretion in yeast. *Biotechnol Prog* (2006) 22:1200–8. doi:10.1021/bp0600233
28. Lee CV, Liang WC, Dennis MS, Eigenbrot C, Sidhu SS, Fuh G. High-affinity human antibodies from phage-displayed synthetic Fab libraries with a single framework scaffold. *J Mol Biol* (2004) 340:1073–93. doi:10.1016/j.jmb.2004.05.051
29. Fellouse FA, Esaki K, Birtalan S, Raptis D, Cancasci VJ, Koide A, et al. High-throughput generation of synthetic antibodies from highly functional minimalist phage-displayed libraries. *J Mol Biol* (2007) 373:924–40. doi:10.1016/j.jmb.2007.08.005
30. Birtalan S, Fisher RD, Sidhu SS. The functional capacity of the natural amino acids for molecular recognition. *Mol Biosyst* (2010) 6:1186–94. doi:10.1039/b927393j
31. Birtalan S, Zhang Y, Fellouse FA, Shao L, Schaefer G, Sidhu SS. The intrinsic contributions of tyrosine, serine, glycine and arginine to the affinity and specificity of antibodies. *J Mol Biol* (2008) 377:1518–28. doi:10.1016/j.jmb.2008.01.093
32. Baek DS, Kim YS. Construction of a large synthetic human Fab antibody library on yeast cell surface by optimized yeast mating. *J Microbiol Biotechnol* (2014) 24:408–20. doi:10.4014/jmb.1401.01002
33. Nelson B, Sidhu SS. Synthetic antibody libraries. *Methods Mol Biol* (2012) 899:27–41. doi:10.1007/978-1-61779-921-1_2
34. Fellouse FA, Li B, Compaan DM, Peden AA, Hymowitz SG, Sidhu SS. Molecular recognition by a binary code. *J Mol Biol* (2005) 348:1153–62. doi:10.1016/j.jmb.2005.03.041
35. Knappik A, Ge L, Honegger A, Pack P, Fischer M, Wellnhofer G, et al. Fully synthetic human combinatorial antibody libraries (HuCAL) based on modular consensus frameworks and CDRs randomized with trinucleotides. *J Mol Biol* (2000) 296:57–86. doi:10.1006/jmbi.1999.3444
36. Fellouse FA, Wiesmann C, Sidhu SS. Synthetic antibodies from a four-amino-acid code: a dominant role for tyrosine in antigen recognition. *Proc Natl Acad Sci U S A* (2004) 101:12467–72. doi:10.1073/pnas.0401786101
37. Rajan S, Sidhu SS. Simplified synthetic antibody libraries. *Methods Enzymol* (2012) 502:3–23. doi:10.1016/B978-0-12-416039-2.00001-X
38. Chen G, Sidhu SS. Design and generation of synthetic antibody libraries for phage display. *Methods Mol Biol* (2014) 1131:113–31. doi:10.1007/978-1-62703-992-5_8
39. Robin G, Sato Y, Desplancq D, Rochel N, Weiss E, Martineau P. Restricted diversity of antigen binding residues of antibodies revealed by computational alanine scanning of 227 antibody-antigen complexes. *J Mol Biol* (2014) 426:3729–43. doi:10.1016/j.jmb.2014.08.013
40. Shim H. Synthetic approach to the generation of antibody diversity. *BMB Rep* (2015) 48:489–94. doi:10.5483/BMBRep.2015.48.9.120
41. Zhai W, Glanville J, Fuhrmann M, Mei L, Ni I, Sundar PD, et al. Synthetic antibodies designed on natural sequence landscapes. *J Mol Biol* (2011) 412:55–71. doi:10.1016/j.jmb.2011.07.018
42. Kehoe JW, Whitaker B, Bethea D, Lacy ER, Boakye K, Santulli-Marotto S, et al. Isolation and optimization for affinity and biophysical characteristics of anti-CCL17 antibodies from the VH1-69 germline gene. *Protein Eng Des Sel* (2014) 27:199–206. doi:10.1093/protein/gzu012
43. Dobson CL, Devine PW, Phillips JJ, Higazi DR, Lloyd C, Popovic B, et al. Engineering the surface properties of a human monoclonal antibody prevents self-association and rapid clearance in vivo. *Sci Rep* (2016) 6:38644. doi:10.1038/srep38644
44. Wu SJ, Luo J, O'Neil KT, Kang J, Lacy ER, Canziani G, et al. Structure-based engineering of a monoclonal antibody for improved solubility. *Protein Eng Des Sel* (2010) 23:643–51. doi:10.1093/protein/gzq037
45. Bethea D, Wu SJ, Luo J, Hyun L, Lacy ER, Teplyakov A, et al. Mechanisms of self-association of a human monoclonal antibody CNTO607. *Protein Eng Des Sel* (2012) 25:531–7. doi:10.1093/protein/gzs047
46. Perchiacca JM, Ladiwala AR, Bhattacharya M, Tessier PM. Aggregation-resistant domain antibodies engineered with charged mutations near the edges of the complementarity-determining regions. *Protein Eng Des Sel* (2012) 25:591–601. doi:10.1093/protein/gzs042
47. Perchiacca JM, Lee CC, Tessier PM. Optimal charged mutations in the complementarity-determining regions that prevent domain antibody aggregation are dependent on the antibody scaffold. *Protein Eng Des Sel* (2014) 27:29–39. doi:10.1093/protein/gzt058
48. Sun SB, Sen S, Kim NJ, Magliery TJ, Schultz PG, Wang F. Mutational analysis of 48G7 reveals that somatic hypermutation affects both antibody stability and binding affinity. *J Am Chem Soc* (2013) 135:9980–3. doi:10.1021/ja402927u
49. Wang F, Sen S, Zhang Y, Ahmad I, Zhu X, Wilson IA, et al. Somatic hypermutation maintains antibody thermodynamic stability during affinity maturation. *Proc Natl Acad Sci U S A* (2013) 110:4261–6. doi:10.1073/pnas.1301810110
50. Dimitrov JD, Kaveri SV, Lacroix-Desmazes S. Thermodynamic stability contributes to immunoglobulin specificity. *Trends Biochem Sci* (2014) 39:221–6. doi:10.1016/j.tibs.2014.02.010
51. Julian MC, Li L, Garde S, Wilen R, Tessier PM. Efficient affinity maturation of antibody variable domains requires co-selection of compensatory mutations to maintain thermodynamic stability. *Sci Rep* (2017) 7:45259. doi:10.1038/srep45259
52. De Genst EJ, Guilliams T, Wellens J, O'Day EM, Waudby CA, Meehan S, et al. Structure and properties of a complex of alpha-synuclein and a single-domain camelid antibody. *J Mol Biol* (2010) 402:326–43. doi:10.1016/j.jmb.2010.07.001
53. Kawa S, Onda M, Ho M, Kreitman RJ, Bera TK, Pastan I. The improvement of an anti-CD22 immunotoxin: conversion to single-chain and disulfide stabilized form and affinity maturation by alanine scan. *MAbs* (2011) 3:479–86. doi:10.4161/mabs.3.5.17228
54. Chi SW, Maeng CY, Kim SJ, Oh MS, Ryu CJ, Kim SJ, et al. Broadly neutralizing anti-hepatitis B virus antibody reveals a complementarity determining region H3 lid-opening mechanism. *Proc Natl Acad Sci U S A* (2007) 104:9230–5. doi:10.1073/pnas.0701279104
55. Swindells MB, Porter CT, Couch M, Hurst J, Abhinandan KR, Nielsen JH, et al. abYsis: integrated antibody sequence and structure-management, analysis, and prediction. *J Mol Biol* (2017) 429:356–64. doi:10.1016/j.jmb.2016.08.019
56. Tiller KE, Li L, Kumar S, Julian MC, Garde S, Tessier PM. Arginine mutations in antibody complementarity-determining regions display context-dependent affinity/specificity trade-offs. *J Biol Chem*. (2017). doi:10.1074/jbc.M117.783837
57. Swillens S. Interpretation of binding curves obtained with high receptor concentrations: practical aid for computer analysis. *Mol Pharmacol* (1995) 47:1197–203.
58. Julian MC, Lee CC, Tiller KE, Rabia LA, Day EK, Schick AJ III, et al. Co-evolution of affinity and stability of grafted amyloid-motif domain antibodies. *Protein Eng Des Sel* (2015) 28:339–50. doi:10.1093/protein/gzv050
59. Brooks BR, Brooks CL III, Mackerell AD Jr, Nilsson L, Petrella RJ, Roux B, et al. CHARMM: the biomolecular simulation program. *J Comput Chem* (2009) 30:1545–614. doi:10.1002/jcc.21287
60. Zahnd C, Spinelli S, Luginbuhl B, Amstutz P, Cambillau C, Pluckthun A. Directed in vitro evolution and crystallographic analysis of a peptide-binding single chain antibody fragment (scFv) with low picomolar affinity. *J Biol Chem* (2004) 279:18870–7. doi:10.1074/jbc.M309169200
61. Cauerhff A, Goldbaum FA, Braden BC. Structural mechanism for affinity maturation of an anti-lysozyme antibody. *Proc Natl Acad Sci U S A* (2004) 101:3539–44. doi:10.1073/pnas.0400060101

62. Midelfort KS, Wittrup KD. Context-dependent mutations predominate in an engineered high-affinity single chain antibody fragment. *Protein Sci* (2006) 15:324–34. doi:10.1110/ps.051842406
63. Boder ET, Midelfort KS, Wittrup KD. Directed evolution of antibody fragments with monovalent femtomolar antigen-binding affinity. *Proc Natl Acad Sci U S A* (2000) 97:10701–5. doi:10.1073/pnas.170297297
64. Marvin JS, Lowman HB. Redesigning an antibody fragment for faster association with its antigen. *Biochemistry* (2003) 42:7077–83. doi:10.1021/bi026947q
65. Wells JA. Additivity of mutational effects in proteins. *Biochemistry* (1990) 29:8509–17. doi:10.1021/bi00489a001
66. Daugherty PS, Chen G, Iverson BL, Georgiou G. Quantitative analysis of the effect of the mutation frequency on the affinity maturation of single chain Fv antibodies. *Proc Natl Acad Sci U S A* (2000) 97:2029–34. doi:10.1073/pnas.030527597
67. Clark LA, Boriack-Sjodin PA, Eldredge J, Fitch C, Friedman B, Hanf KJ, et al. Affinity enhancement of an in vivo matured therapeutic antibody using structure-based computational design. *Protein Sci* (2006) 15:949–60. doi:10.1110/ps.052030506
68. Mateu MG, Andreu D, Carreno C, Roig X, Cairo JJ, Camarero JA, et al. Non-additive effects of multiple amino acid substitutions on antigen-antibody recognition. *Eur J Immunol* (1992) 22:1385–9. doi:10.1002/eji.1830220609
69. Kiyoshi M, Caaveiro JM, Miura E, Nagatoishi S, Nakakido M, Soga S, et al. Affinity improvement of a therapeutic antibody by structure-based computational design: generation of electrostatic interactions in the transition state stabilizes the antibody-antigen complex. *PLoS One* (2014) 9:e87099. doi:10.1371/journal.pone.0087099
70. Soderlind E, Strandberg L, Jirholt P, Kobayashi N, Alexeiva V, Aberg AM, et al. Recombining germline-derived CDR sequences for creating diverse single-framework antibody libraries. *Nat Biotechnol* (2000) 18:852–6. doi:10.1038/78458
71. Miersch S, Sidhu SS. Synthetic antibodies: concepts, potential and practical considerations. *Methods* (2012) 57:486–98. doi:10.1016/j.ymeth.2012.06.012
72. Sidhu SS, Li B, Chen Y, Fellouse FA, Eigenbrot C, Fuh G. Phage-displayed antibody libraries of synthetic heavy chain complementarity determining regions. *J Mol Biol* (2004) 338:299–310. doi:10.1016/j.jmb.2004.02.050
73. Li B, Russell SJ, Compaan DM, Totpal K, Marsters SA, Ashkenazi A, et al. Activation of the proapoptotic death receptor DR5 by oligomeric peptide and antibody agonists. *J Mol Biol* (2006) 361:522–36. doi:10.1016/j.jmb.2006.06.042
74. Lombana TN, Dillon M, Bevers J III, Spiess C. Optimizing antibody expression by using the naturally occurring framework diversity in a live bacterial antibody display system. *Sci Rep* (2015) 5:17488. doi:10.1038/srep17488
75. Jain T, Sun T, Durand S, Hall A, Houston NR, Nett JH, et al. Biophysical properties of the clinical-stage antibody landscape. *Proc Natl Acad Sci U S A* (2017) 114:944–9. doi:10.1073/pnas.1616408114
76. Hoover DM, Lubkowski J. DNAWorks: an automated method for designing oligonucleotides for PCR-based gene synthesis. *Nucleic Acids Res* (2002) 30:e43. doi:10.1093/nar/30.10.e43
77. Studier FW. Protein production by auto-induction in high density shaking cultures. *Protein Expr Purif* (2005) 41:207–34. doi:10.1016/j.pep.2005.01.016
78. Brooks BR, Bruccoleri RE, Olafson BD, States DJ, Swaminathan S, Karplus M. CHARMM: a program for macromolecular energy, minimization, and dynamics calculations. *J Comput Chem* (1983) 4:187–217. doi:10.1002/jcc.540040211
79. Kortemme T, Baker D. A simple physical model for binding energy hot spots in protein-protein complexes. *Proc Natl Acad Sci U S A* (2002) 99:14116–21. doi:10.1073/pnas.202485799
80. Kim DE, Chivian D, Baker D. Protein structure prediction and analysis using the Robetta server. *Nucleic Acids Res* (2004) 32:W526–31. doi:10.1093/nar/gkh468
81. Kortemme T, Kim DE, Baker D. Computational alanine scanning of protein-protein interfaces. *Sci STKE* (2004) 2004:l2. doi:10.1126/stke.2192004pl2
82. Pantazes RJ, Grisewood MJ, Li T, Gifford NP, Maranas CD. The iterative protein redesign and optimization (IPRO) suite of programs. *J Comput Chem* (2015) 36:251–63. doi:10.1002/jcc.23796
83. Dunbrack RL Jr, Cohen FE. Bayesian statistical analysis of protein side-chain rotamer preferences. *Protein Sci* (1997) 6:1661–81. doi:10.1002/pro.5560060807

Conflict of Interest Statement: PT has received consulting fees and/or honorariums for presentations of this and/or related research findings at MedImmune, Eli Lilly, Bristol-Myers Squibb, Janssen, Merck, Genentech, Amgen, Pfizer, Adimab, Abbvie, Abbott, DuPont, Schrödinger, and Novo Nordisk. All other authors declare that the research was conducted in the absence of any commercial or financial relationships that could be construed as a potential conflict of interest.

frontiers in Immunology

REVIEW
published: 25 July 2017
doi: 10.3389/fimmu.2017.00865

Enhancing Stability of Camelid and Shark Single Domain Antibodies: An Overview

Ellen R. Goldman, Jinny L. Liu, Dan Zabetakis and George P. Anderson*

Center for BioMolecular Science and Engineering, US Naval Research Laboratory, Washington, DC, United States

Single domain antibodies (sdAbs) are gaining a reputation as superior recognition elements as they combine the advantages of the specificity and affinity found in conventional antibodies with high stability and solubility. Melting temperatures (T_ms) of sdAbs cover a wide range from below 50 to over 80°C. Many sdAbs have been engineered to increase their T_m, making them stable until exposed to extreme temperatures. SdAbs derived from the variable heavy chains of camelid and shark heavy chain-only antibodies are termed VHH and VNAR, respectively, and generally exhibit some ability to refold and bind antigen after heat denaturation. This ability to refold varies from 0 to 100% and is a property dependent on both intrinsic factors of the sdAb and extrinsic conditions such as the sample buffer ionic strength, pH, and sdAb concentration. SdAbs have also been engineered to increase their solubility and refolding ability, which enable them to function even after exposure to temperatures that exceed their melting point. In addition, efforts to improve their stability at extreme pH and in the presence of chemical denaturants or proteases have been undertaken. Multiple routes have been employed to engineer sdAbs with these enhanced stabilities. The methods utilized to achieve these goals include grafting complementarity-determining regions onto stable frameworks, introduction of non-canonical disulfide bonds, random mutagenesis combined with stringent selection, point mutations such as inclusion of negative charges, and genetic fusions. Increases of up to 20°C have been realized, pushing the T_m of some sdAbs to over 90°C. Herein, we present an overview of the work done to stabilize sdAbs derived from camelids and sharks. Utilizing these various strategies sdAbs have been stabilized without significantly compromising their affinity, thereby providing superior reagents for detection, diagnostic, and therapeutic applications.

Keywords: single domain antibody, camelid, shark, protein engineering, stability, melting temperature, refolding

OPEN ACCESS

Edited by:
Kevin A. Henry,
National Research Council Canada, Canada

Reviewed by:
Jamshid Tanha,
National Research Council Canada, Canada
Wei Li,
Frederick National Laboratory for Cancer Research (NIH), United States

****Correspondence:***
Ellen R. Goldman
ellen.goldman@nrl.navy.mil

Specialty section:
This article was submitted to Vaccines and Molecular Therapeutics, a section of the journal Frontiers in Immunology

Received: *29 April 2017*
Accepted: *07 July 2017*
Published: *25 July 2017*

Citation:
Goldman ER, Liu JL, Zabetakis D and Anderson GP (2017) Enhancing Stability of Camelid and Shark Single Domain Antibodies: An Overview. Front. Immunol. 8:865. doi: 10.3389/fimmu.2017.00865

INTRODUCTION

Single domain antibodies (sdAbs) are recombinant autonomous variable domains with antigen-binding functionality. The first reported sdAbs were variable heavy domains (VH) derived from IgGs (1). In this pioneering work, several mouse-derived VHs with specificity for lysozyme were shown to have affinities in the 19–27 nM range; however, they were described as "relatively sticky." The idea of a single domain, antibody-derived binding unit, however, was appealing as it offered potential advantages over large intact antibodies and even over Fv fragments containing paired VH and variable light (VL) domains.

In the early 1990s, the first report on the discovery of heavy chain-only antibodies (hcAbs) in camelids was published (2). These unique antibodies were heavy chain dimers, completely lacking light chains. They also lacked the first IgG constant domain, CH1. Consequently, their antigen-binding regions consist of one single VH domain termed VHH. It was observed that in VHHs, several framework region (FR) positions located in the area that would have formed the interface with the VL in conventional tetrameric IgGs were altered relative to the VH consensus sequence, which resulted in a more hydrophilic surface overall. In general, however, the VHH is closely related to the VH domain of conventional IgG. As early as 1994, it was observed that a human VH showed a decrease in aggregation when it was "camelized" by substituting three key FR residues in its former interface with those found in VHHs at equivalent positions (3). In 1995, a report detailed hcAbs derived from shark (IgNARs) whose variable domains, termed VNARs, are more closely related to T-cell receptors than IgG (4).

Production of the first VHHs was described in 1997, and these were demonstrated to function after extensive heating at 37°C (5). Likewise VNARs, described a few years after VHHs, showed an ability to bind antigen after heat challenge (6, 7). This work was key in showing that sdAbs have the potential to provide recognition reagents that combine the specificity and affinity of natural antibodies with high stability and solubility. Because of their stability and solubility, sdAbs including VHHs and VNARs as well as VHs and VLs engineered from conventional antibody variable domains, are being exploited for a number of applications ranging from therapeutics and detection to biotechnology (8–12).

The melting temperatures (T_ms) of sdAbs, which cover a wide range from below 50 to over 80°C, are used as a measure of sdAb stability. However, sdAb stability is also defined by their ability to function after heating. Unlike conventional antibodies and recombinant-binding elements derived from paired VH and VL domains which generally lose their binding ability upon heat denaturation due to irreversible aggregation (13), the binding ability of many sdAbs is restored after heating due to their ability to refold. Refolding can be influenced by variables such as the ionic strength and pH of the sample buffer as well as sdAb concentration. Time and temperature in the unfolded state can also impact the ability of sdAbs to refold, as extended time can allow for a slow aggregation process to accumulate, and temperatures near the transition point often appear more damaging as the temperature is low enough to allow interactions to occur but still too high to allow the sdAb to proceed toward its native conformation. Extended heat exposure can also cause chemical alterations that can prevent proper refolding. For example, chemical modification of Asn was found to be detrimental to the ability of an sdAb to refold (14); disulfide shuffling can also negatively impact the refolding process (15). With so many dynamic issues to resolve to achieve successful refolding, it is not surprising that often the preferred solution for sdAb stabilization is to engineer an increased T_m to prevent denaturation from occurring in the first place.

Recombinant DNA technology enables the manipulation of sdAb genes to increase sdAb T_ms and refolding abilities. Protein engineering has also been utilized to improve sdAb stability against chemical denaturants, extreme pH, and proteases. Mutational approaches to improve the biophysical properties of sdAbs derived from conventional human variable chains (VH and VL) have been detailed in recent reviews (16–18). Herein, we focus on engineering-enhanced stability into sdAbs derived from camelids and sharks (VHHs and VNARs, respectively). A number of reviews detail the properties of sdAbs and their use in biotechnology and therapeutic applications (8, 11, 19–21); however, none has focused on the growing body of work that utilizes protein engineering to improve the stability of VHHs and VNARs. We cover a number of methods that have been successfully employed to increase sdAb stability including grafting complementarity-determining regions (CDRs) onto stable frameworks, introduction of non-canonical disulfide bonds, random mutagenesis combined with stringent selection, point mutations, and genetic fusions (**Table 1**). Through these strategies, stabilized sdAbs have been developed that retain their binding ability under extreme conditions, thereby providing superior reagents for a myriad of biotechnology, detection, diagnostic, and therapeutic applications.

ANALYTICAL TECHNIQUES FOR STUDYING sdAb STABILITY

There are a number of techniques that researchers have utilized to evaluate the biophysical characteristics of sdAbs. Methods

TABLE 1 | Strategies to stabilize VHHs and VNARs.

Strategy	Benefits	Drawbacks
Complementarity-determining region grafting	Can increase stability and expression in *E. coli* (up to 10°C increase in T_m reported)	– Unavailability of a universal stable framework – Affinity may be compromised
Addition of non-canonical disulfide bond	– Reliable approach to increase T_ms (T_m increases of ~4–20°C have been reported). – Increased stability at extreme pH and in the presence of denaturants – Imparts increased protease resistance	– Affinity may be compromised – May lead to decreased expression in *E. coli*
Random mutagenesis/ Stringent selection	Employed to pull out binding single domain antibodies (sdAbs) with improved T_ms and protease stability from sdAb display libraries	Needs to be done separately for each sdAb/target
Point mutations	– Improved refolding ability – Increased function after heating – Increased T_m (T_m increases of ~3–9°C have been reported)	– Need to tailor to each sdAb sequence (might not be universal) – Some mutations that improve refolding ability may decrease T_m
Fusions	– Universal construct that does not have to be engineered for each sdAb sequence – Improved refolding ability (in the absence of canonical disulfide bond has been reported)	– May lead to decrease in T_m – May lead to decrease in expression yield in *E. coli*

for determining stability can be broken broadly into those that measure a physical parameter and those that assess the ability of an sdAb to bind antigen after heating. While circular dichroism, differential scanning calorimetry, and the protein thermal shift method all measure T_m, each approach interrogates a very different biophysical property. Nonetheless, they all track fairly close together, typically within ±3°C. In this section, we will discuss the methods utilized to measure T_m as well as delve into other critical parameters to ascertain for a stabilized sdAb such as solubility and retention of activity. Several methods used to measure T_m can also be adapted to measure the stability of sdAbs in the presence of chemical denaturants (22). Examples of data from several of the methods to assess stability, which is discussed subsequently, are shown in **Figure 1**.

Circular Dichroism

Circular dichroism (CD) is one of the most commonly utilized methods to track protein unfolding as the far UV CD reflects a protein's secondary structure (23). This technique is used to assess both the T_m and refolding ability of sdAbs. CD, which measures the differential absorption of left-handed and right-handed circularly polarized light can monitor the folding status of a protein. As CD is typically performed at relatively low protein concentrations (<0.1 mg/mL), sdAbs can typically be observed to refold as the sample is cooled. For many sdAbs, it is possible to repeat this process many times generating successive unfolding and refolding curves for the same sample. However, not every sdAb isolated is observed to refold in these experiments. In these cases, it would appear that those sdAbs had a greater propensity to aggregate when in the unfolded state. It is this propensity to aggregate that limits the ability of most multidomain proteins, such as scFvs, to refold following thermal denaturation. In our experience, we have found the unfolding and refolding transition of sdAbs to be a rapid process that occurs at virtually the same temperature (24).

Differential Scanning Calorimetry

Differential scanning calorimetry (DSC) is also a popular method for measuring the melting temperatures of proteins (25). DSC measures the amount of energy required to raise the temperature of protein sample to the same extent as a buffer control. The additional energy consumed as a protein unfolds marks the T_m transition. As the amount of energy consumed to unfold a single molecule is very small, DSC requires large amounts of protein to generate a robust signal, ideally 3–5 mg. Another drawback of DSC is that at least partly due to the high concentration of protein required to make the measurement, refolding is not often observed. However, unlike CD, DSC can be performed in various buffers, it can also be useful in determining the T_m of sdAbs with

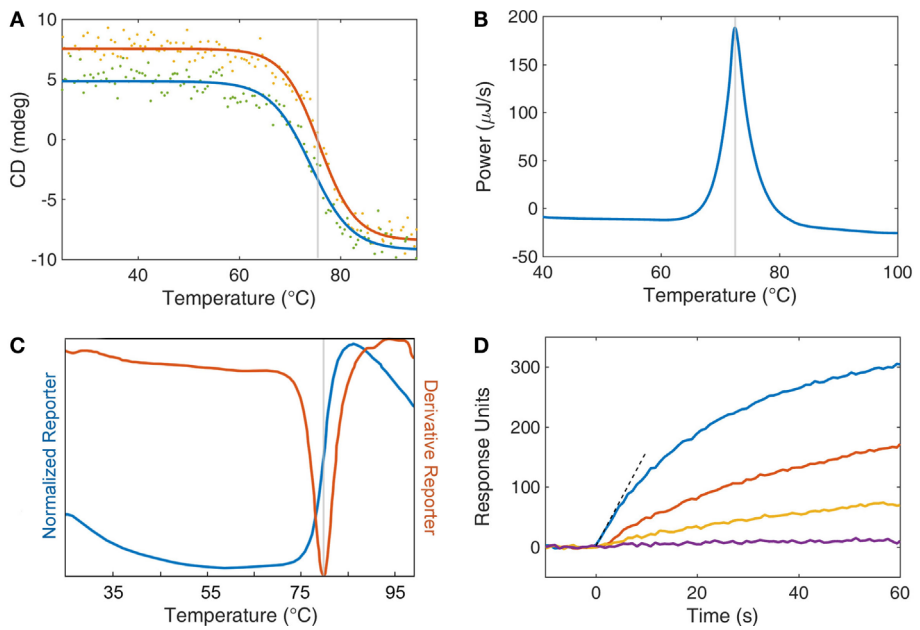

FIGURE 1 | Analytical techniques for studying single domain antibody stability. **(A)** Circular dichroism (CD) is displayed as a function of temperature for both heating (red) and cooling (blue). The inflection point of the heating curve is reported as the T_m of the protein (gray line). Refolding after thermal denaturation is determined by the recovery of CD signal upon cooling. **(B)** Differential scanning calorimetry compares the thermodynamics of a protein sample with a buffer reference while undergoing heating. Protein unfolding is an enthalpic process and so an energy input is required to retain equilibrium with a buffer control. This energy input is recorded (blue) and the peak is reported (gray) as the T_m. **(C)** A thermal dye-based assay can be employed whereby a fluorescent dye's quantum yield is enhanced by the interaction of the dye with hydrophobic amino acids upon denaturation of the protein. Fluorescent data are collected as both a direct measurement (normalized reporter, blue curve) and the first derivative of the fluorescence (red curve). The T_m of the protein (gray line) is taken as the peak of the derivative reporter. **(D)** Surface plasmon resonance is used as an activity assay to assess the retention of function after heat treatment. Individual protein samples are subjected to increasing levels of thermal stress (blue, red, orange, and purple) and then returned to room temperature. The antibodies are then exposed to an antigen-coated surface, and the response to binding is recorded as response units (also called resonance units). The initial rate (dashed line) is a measure of function and may be compared with a control sample to determine loss or retention of function.

T_ms above 90°C, as well as corroborate values obtained through other methods.

Protein Thermal Shift Assay

Protein thermal shift assay, also referred to as a fluorescent dye-based melting assay or dye melt assay, monitors the extrinsic fluorescence of an organic fluorophore, such as Sypro orange, added to the protein solution prior to heating. This method is an attractive approach, due to both the small amount of protein required (5–10 μg) and the ability to test multiple samples simultaneously, as the measurement is performed using a real time PCR instrument (26, 27). Here, the fluorescence intensity of the Sypro orange dye increases rapidly as the protein unfolds and the dye can associate with the hydrophobic amino acids normally inaccessible in the protein's core. Typically, the negative of the first derivative of the fluorescence intensity versus temperature is plotted with the dip in the plot representing the T_m. The main limitation of this method is that unlike CD one cannot evaluate refolding.

Intrinsic Fluorescence

Intrinsic fluorescence can also be monitored during the heating process, as the quantum yield of the buried hydrophobic residues, tryptophan and to a less extent tyrosine, will change upon loss of the proteins secondary structure (28). Some CD instruments are equipped to simultaneously measure intrinsic fluorescence. In one study examining the T_m of an sdAb by these two methods, it appeared that changes in intrinsic fluorescence were not tightly aligned with loss in secondary structure, suggesting that monitoring intrinsic fluorescence should be considered only as a secondary method (29).

Activity Assays

While the methods described previously directly measure the temperature at which the protein loses its secondary structure, it is not uncommon for direct binding activity measurements to be performed to monitor the stability of the sdAb following exposure to temperature extremes or harsh conditions. Measuring activity of sdAbs after exposure to harsh conditions is of utmost importance as in some cases CD has shown ~80–90% refolding while the percentage of binding activity after heating was found to be closer to 50% (22). While activity is certainly the gold standard by which any antibody must be measured, certain precautions are necessary to assure that one does not use an excess amount of antibody so as to accurately measure the true percentage of activity remaining.

A number of binding assays can be adapted to measure the ability of sdAbs to function after exposure to elevated temperature. Traditionally, this was assessed by ELISA or similar binding assays (5, 7, 30). Regardless of the assay format, it is important to utilize a sub-saturating concentration of sdAb in order that measured binding is responsive to loss in activity. A pitfall particularly for high affinity antibodies is that depending on the amount of sdAb used in the binding measurements, the assay may not accurately reflect the amount of activity after heat exposure. Ideally, a range of dilutions of the heated sdAb should be assessed.

We have routinely measured the initial binding rate of the sdAb to its target analyte by measuring the signal increase during the first few seconds by surface plasmon resonance. Measuring the initial on-rate has the advantage that one does not require a standard curve and thus is a simple, sensitive, and direct measure of binding activity (31).

The majority of functional characterizations are performed on soluble sdAbs that act as reporters in assays. However, the activity of immobilized sdAbs can also be assessed, for example, by incubating sdAbs immobilized on nitrocellulose at elevated temperatures (32).

Other Important Parameters

For development of reagents intended for therapeutic applications, other parameters are also of importance, such as proteolytic stability, solubility, and producibility. While it has been observed that proteolytic stability and thermal stability seem to have a positive correlation, the same cannot be said for the other parameters. It has been observed that solubility is enhanced as the net charge on the sdAb is increased, thus increasing intermolecular repulsion, however, the final formulation would also need to take into consideration the role that additives may play in maintaining good solubility. Methods for assessing these other parameters have been reviewed in the context of conventional antibodies (33).

STABILIZING VHHs

It has been over two decades since the first description of VHHs, and there is now a large body of literature describing VHHs that recognize a wide variety of targets, their properties, engineering, and use in applications from biosensors, to therapeutics, and chaperones for crystallization. Although many VHHs are inherently stable and able to refold, several studies have been geared toward understanding the mechanism of VHH stability and increasing their stability. An overview of several key strategies that have been successfully used to increase VHH stability are given in the following sections and summarized in **Table 1**.

We have used the IMGT numbering scheme of V domains (34). The antigen receptor numbering and receptor classification tool was used for numbering the amino acid sequences of the VHH (35).

Complementarity Determining Region Grafting

Given the structure of sdAbs, where four FRs are interspersed with three well-defined CDRs, it is a natural approach in antibody engineering to construct hybrid swaps of CDRs and FRs (**Figure 2**). CDR grafting involves substituting the binding loops that comprise the CDRs of one V domain onto the FR of a different V domain. Taking a lead from the extensive use of CDR grafting to produce humanized murine antibodies, Saerens et al. (36) sought a universal VHH framework that had a set of beneficial defined properties. Their candidate, the cAbBCII10 VHH, featured good expression levels and stability and could be produced in *Escherichia coli* within the reducing environment of

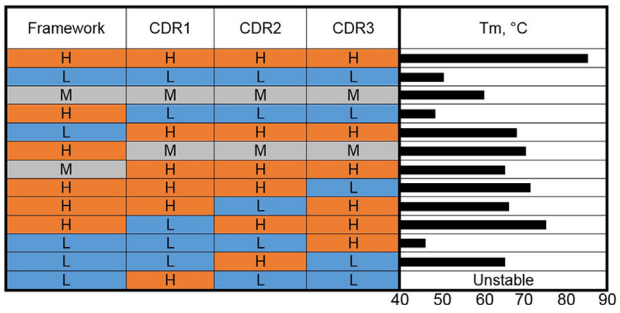

FIGURE 2 | Complementarity-determining region (CDR) grafting and thermal stability. VHHs of high (H), medium (M), and low (L) thermal stability (color coded as red, gray, and blue) were used as the basis for construction of genetic hybrids. The framework regions (as a unit) and the individual CDRs were mixed in various combinations. The T_ms of the resulting hybrids are shown as a bar graph on the right side.

the cytoplasm or without its conserved canonical disulfide bond. This VHH was found to function well as a scaffold, retaining the function of grafted CDRs from a donor VHH. The cAbBCII10 VHH was derived from a dromedary and is a member of the dromedary subfamily 2. CDR grafts of subfamily 2 dromedary VHHs onto the cAbBCII10 FR all retained binding and showed increased stability and production at least equivalent to the donor VHH. However, while cAbBCII10 showed promise as a universal scaffold for one large subfamily of dromedary VHHs, it was not ideal for a different subfamily of dromedary VHHs or a llama-derived VHH. This work suggests that it may not be possible to identify one universal VHH scaffold for increased stability but that there is benefit in exploring CDR grafting for improving sdAb properties.

This work of Saerens et al. (36) was extended to humanization of cAbBCII10 for use in the development of human therapeutics (37). A humanized version of the VHH showed a slightly lower T_m than the wild type (74.3 versus 77.5°C). The humanized version, however, showed only ~8% refolding after heat denaturation. Grafting of CDRs from a dromedary subfamily 2 VHH with a T_m of 79.7°C and over 90% refolding ability onto the humanized cAbBCII10 scaffold resulted in a VHH that melted at 82.1°C and refolded at 68%, indicating that the CDRs contribute to the stability and refolding ability of VHH either by forming more or less favorable interactions with backbone residues or intra-/inter-CDR interactions.

We carried out a molecular dissection of llama-derived VHHs of high, low, and moderate stability in an effort to reveal the features most responsible for VHH stability (38) (**Figure 2**). The high stability VHH was specific for Staphylococcal enterotoxin B (SEB), while the other two VHH utilized in these experiments bound ricin. In a first set of experiments, the three CDRs and the FRs of VHHs that melt at 85, 60, and 50°C were exchanged, examining clones resulting from the high melting VHH CDRs on the moderate and low melting FRs and the CDRs from the low and moderate VHHs on the high melting FR. The resultant clones were examined in terms of T_m and binding kinetics. In each case, grafting the three CDRs from the high melting VHH resulted in VHHs with higher T_ms than those of the FR donors but lower than the CDR donor. Grafting the three CDRs from the medium melting VHH onto the stable FR led to a VHH that showed an increase in T_m over the CDR donor of 10°C and maintained sub nM affinity (0.46 nM for the graft versus 0.16 nM for the original). The graft variant also showed greater stability than the CDR donor at pH 4.5 (39). Interestingly, grafting the three CDRs from the low melting VHH onto the FR from the high melting clone resulted in a VHH with a low melting point (38). This is another example that while CDR grafting can be an excellent tool to increase the stability of sdAbs, no universal framework has been defined. It also shows how both the CDR and FR sequence contribute to VHH stability.

To further dissect the situation, CDRs from VHHs that melt at 85 and 50°C were mixed-and-matched (38). The results of grafting individual CDRs show that CDR2 was the major contributor to stability in the high T_m VHH. Grafting only CDR2 from the high melting VHH onto the low melting VHH produced a clone that bound SEB, the target of the high melting VHH, and had a T_m of 65°C. This work corroborates that both the FR and CDR can be important for stability and that in at least some instances affinity and stability are linked and cannot be freely engineered.

Introduction of Non-Canonical Disulfide Bonds

The stability of the sdAb has been found to be highly dependent upon the formation of its highly conserved disulfide bond. When VHHs are produced in the *E. coli* cytoplasm, which has a relatively reducing environment, the resultant VHHs are found to have a much lower T_m than the same VHHs produced in the oxidizing environment of the *E. coli* periplasm (40–42). This difference in stability is attributable to the failure of the conserved disulfide bond to form. Thus, nature has shown a simple and direct method for engineering sdAbs with enhanced stability; namely, the addition of a second disulfide bond. Indeed, engineering of an additional disulfide bond into VHHs is a well-known approach for enhancing their thermal stability (41, 43–47).

Although this technique had been applied to many proteins, it was Hagihara et al. (41) who first showed that it was possible to stabilize VHHs by inserting an extra disulfide bond by changing the highly conserved buried residues Ala54 and Ile78 [IMGT numbering scheme (34)] both to Cys (41). This new disulfide bond adds an additional constraint between two of the β-sheet strands of the sdAb's secondary structure, resulting in a stabilized tertiary structure, with a T_m increase of ~10°C over the wild-type sdAb.

Shortly after, Saerens et al. (45) evaluated a VHH that naturally had an extra pair of Cys at the same positions (54/78), leading to a disulfide bond linking FR2 and FR3 (45). They found that the addition of this extra disulfide bond to three additional VHHs resulted in a 4–18°C increase in T_m, however one of the VHHs showed a ~43-fold loss in binding activity. They also examined another location for insertion of an additional disulfide bond that linked FR2 to FR3 by introducing Cys at positions 39 and 87. This location was selected for its distance in the crystal structure of β-strands from opposing β-sheets and with side chains oriented

suitably for disulfide bond formation. Testing three different VHHs that included nearly all the possible permutations of these three disulfide bonds, including none at all, they deduced that the native highly conserved disulfide bond was the most favorable, with addition of a second disulfide bond adding further stability but with possible negative impacts on affinity that were not easily predictable.

In work of a similar nature, we examined four locations for the insertion of a second disulfide bond in a llama VHH that already had an impressive T_m of ~84°C (46) (**Figure 3**). In addition to the disulfide bond between a pair of Cys introduced at positions 54 and 78, analogous to the one added by previous groups, cysteine residues were engineered at positions 38 and 110 (to promote disulfide bond formation between CDRs 1 and 3), at 55 and 111B (for a disulfide bond linking CDRs 2 and 3), and at 3 and 117 (for formation of a disulfide bond between FR1 and CDR3). In all cases, the added disulfide bond led to an increase in T_m, with the largest ($T_m > 90$°C) afforded by the disulfide bond between Cys 54 and Cys 78. In this case, none of the added disulfide bonds had a significant detrimental effect on affinity.

In addition to elevating T_m, introduction of a disulfide bond linking FR2 and FR3 has been shown to increase protease resistance and stability at acidic pH and in the presence of chemical denaturants (47, 48). For example, engineering a disulfide bond at positions 54 and 78 was shown to increase the T_m of a VHH by ~17°C when measured at a pH of 5.5 and in the presence of 3 M urea (47). A separate study showed that the same disulfide bond addition generated VHHs that had increased T_m at both neutral pH and pH 2. These VHHs were also more resistant to pepsin, and additionally, four out of six VHHs showed improved resistance to chymotrypsin (48).

Addition of non-canonical disulfide bonds has proven a robust way to stabilize VHHs. The increases in T_m resulting from an added disulfide bond tend to be between 4 and 20°C (44, 47–49). One limitation is that addition of an extra disulfide bond as well as even the presence of the canonical disulfide bond has been seen to decrease the stability of the sdAb when exposed to temperatures above its T_m, presumably due to disulfide shuffling or other deleterious chemical reactions that prevent refolding (15). An additional limitation is that in some cases affinity can be negatively affected by disulfide bond introduction, nonetheless, many such stabilized clones retain excellent binding ability. Also problematic is that the expression of VHHs in *E. coli* can suffer upon disulfide bond introduction due to improper disulfide bond formation during the folding process. In this case however, we have ascertained that the addition of helper plasmids that produce disulfide isomerases can serve to mitigate this limitation (49, 50).

Random Mutagenesis and Stringent Selection

To obtain sdAbs stable enough to perform in harsh environments, stringent selection of sdAb libraries can be employed to enrich sdAbs with desired properties such as protease, heat, or chemical stability. This can be done starting with immune libraries, naive libraries, or alternatively starting with sdAbs that bind target but do not possess the desired stability. When starting with binding sdAbs, sequence diversity is often introduced through random mutagenesis/DNA shuffling into sdAb repertoires to better guarantee the inclusion of strong binders toward desired targets.

Traditional panning methodology, based solely on binding as the selective pressure is likely to lead to the isolation of binding

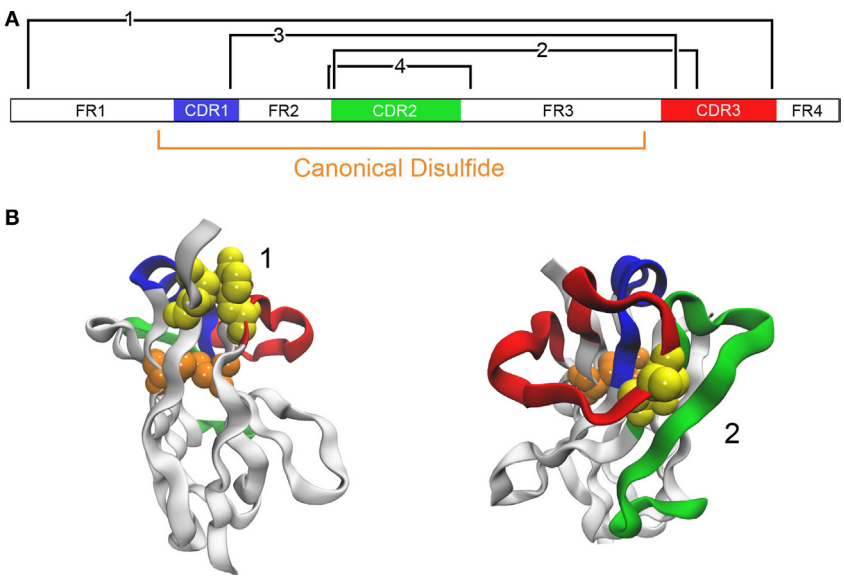

FIGURE 3 | Addition of disulfide bonds to stabilize an antibody. **(A)** The domain structure of a VHH A3 is schematically shown (46). The canonical disulfide bond is formed between Cys located at positions 23 and 104. Locations where it is predicted that disulfide bonds may be introduced are shown in black (Cys introduced at positions 3 and 117 for bond 1, 55 and 111B for bond 2, 38 and 110 for bond 3, and 54 and 78 for bond 4). **(B)** Examples of two candidates are shown with the same color coding. The native residues that are to be mutated to cysteine are shown as a yellow space-filling model. The model uses A3 with PDB code 4TYU.

sdAbs; however, it does not guarantee isolation of sdAbs with the desired stability characteristics. This is due to the fact that the CDRs mainly determine the specificity and affinity to target, however, the stability against chemical denaturants, heat, protease and extremes of pH mostly relies on the conserved FR sequences in the variable domains. Small sequence variation in FRs that do not have a significant effect on target binding under mild, physiological conditions can lead to dramatic differences in binding under harsh, stringent conditions. In one study researchers selected VHH sequences binding to *Malassezia furfur*, a fungus responsible for the formation of dandruff, under stringent selection for chemical denaturation stability. This study showed that charges and stable structures due to FR sequences facilitated the stability of VHHs and maintained binding to the fungal targets in shampoo and chemical denaturants (51). The sequence analysis, crystal structure conformation, and point mutation analysis showed that a positively charged residue at position 44, (Arg44/Lys44), located in a well conserved 38–45 loop within FR2 is essential for VHH binding to the fungus in shampoo at high pH, and increasing concentrations of denaturants, guanidine-HCl and urea (51). The stability is likely due to the fact that the positively charged residue at position 44 enhances the electrostatic interaction with the negatively charged molecules present in the medium.

The physicochemical attributes desired for orally administered therapeutic sdAbs are stability in low pH and resistance to various gastrointestinal proteases. Random mutagenesis using error-prone PCR to further vary the binder sequence and the subsequent panning under protease pressure were performed to select protease-resistant VHHs that inhibit *Campylobacter jejuni* (52). The proteolytically stable VHHs consisting of two unique residues, Q3 and V5, from their parental binder sequences are resistant to the digestion by trypsin and chymotrypsin, but not pepsin. To further enhance the resistance to all three proteases, an additional non-canonical disulfide bond was introduced by adding two Cys at positions 54 and 78 as described in the Section "Introduction of Non-Canonical Disulfide Bonds" (48). The resulting mutants have almost 100% resistance to pepsin and chymotrypsin and 50% resistance to trypsin with parental wild-type affinity (52). The Cys54/Cys78 disulfide bond also increased the T_m at acidic pH, which positively correlates with pepsin resistance.

Sequence variation can also be generated through shuffling DNA fragments derived from multiple starting binders. It was shown that without stringent selection, DNA shuffling improved *in vitro* proteolytic stability of the parental anti-*E. coli* F4 fimbriae VHH to 100% resistance to trypsin and chymotrypsin, and 21% resistance to pepsin and also exhibited a 10-fold increase in affinity (53). The most stable and strongest VHH binder had unique G11 and L24 amino acids within the FR1 compared to the wild-type sequences, however, there was no confirmation of the altering effects of these mutations on the proteolytic stability. To further improve the pepsin resistance of the proteolytically stable VHHs, stringent stability selection conditions could be employed.

Although, VHHs already exhibit intrinsically high conformational stability under heat, chemical, and pressure denaturation (22), their physicochemical stability can still be further enhanced using random mutagenesis in conjunction with stringent selection for thermal stability. Our group used a highly thermostable SEB-binding VHH with a T_m of 84°C as a template to construct a random mutagenesis library and conducted panning under high temperature and high concentration of guanidine-HCl. We found that a clone with two mutated residues, T29I and S77I, further increased the T_m up to 90°C without compromising the binding affinity to SEB toxin (54) (**Figure 4**). Like the abovementioned

FIGURE 4 | Introduction of point mutations for thermal stabilization. Three case studies in stabilization are illustrated. The original protein sequence is given with color-coding of the complementarity-determining regions. Mutated amino acids are indicated below each sequence.

studies with stringent selection, we have also seen that a few amino acid changes within FRs can have significant effects on the physicochemical properties of VHHs.

Point Mutations

Stability can be engineered into sdAbs by the addition of point mutations (**Figure 4**). Successful strategies have included the restoration of consensus sequences, substitution of amino acids prone to chemical modification, and changes to the isoelectric points of VHHs.

Although there is variation in the composition of the FR of VHHs, some positions are nearly universally conserved. When binding VHHs are isolated with deviations in these positions, merely restoring the conserved sequence can result in an increase in T_m. For example, ~90% of VHHs contain a Trp at position 118 (20, 55). However, we isolated a ricin-binding VHH that contained an Arg at position 118. Changing Arg to Trp resulted in a 6°C increase in T_m without compromising the VHH's affinity (31).

In work examining the mechanism of heat-induced irreversible denaturation of VHHs, researchers assessed the contribution of chemical modification to denaturation by mutating Asn residues in a VHH (14). Three changes were made, one in CDR2 and two in FR regions. In each case the Asn was changed to either Ser or Thr. Although one of the mutations was within a CDR, binding ability was not compromised by the change. Both the wild-type and mutant were subject to continuous heating at 90°C for various times as well as cycling between 90 and 20°C and in each case it was the total time at 90°C that was found to be the critical factor in determining irreversible denaturation. The mutant showed both a small increase in T_m (~3°C) along with increased functionality on heating to 90°C.

Lowering the isoelectric point is a strategy that has been used to engineer stability and ability to refold after heat denaturation into VHs (56, 57). Introducing mutations that increase the negative charge of VHHs can also improve refolding ability. Three llama-derived VHHs that regained 40–70% of their secondary structure based on CD measurements were subjected to mutagenesis to lower their isoelectric points. In each case, two or three changes were engineered either within FRs or CDRs. In two of the three VHHs, the mutations included changing the neutral wild-type amino acid to Glu or Asp; in the third VHH, two mutations introduced negative charges while the third eliminated a positive charge by mutating a Lys. All three resultant mutants showed marked improvement, being able to refold greater than 95% following heat denaturation (31). The mutations that were used to decrease the charge of these VHHs were located throughout the VHH sequence; in one case the mutations resulted in 5°C decrease in the T_m and in other cases the T_ms were essentially unchanged.

For VHH variants that fail to refold, increasing their net negative charge such that they experience increased charge repulsion in the unfolded state appears to be sufficient to recover the bulk of the refolding ability of the VHHs. In the case of a VHH that lost the ability to refold on addition of a non-canonical disulfide bond, we found that incorporation of three negative charges within FR1 restored refolding ability and also led to a ~3.5-fold increase in protein expression in *E. coli* without sacrificing affinity or T_m (58).

Further, we showed that changes within FR1 (Q5V; A6E) of a VHH that lowered the isoelectric point and introduced a sequence observed in several high-T_m anti-toxin VHH led to a ~7°C increase in the T_m (58). These changes, incorporated along with other mutations, have also led to increases in T_m or improved protein expression in *E. coli* in several other VHHs (59). Recently, we demonstrated that a set of changes within FR1 (1E or D, 3Q, 5 V, 6E) of 4 VHHs consistently gave increases in T_m of 5–9°C, indicating that this might be a general method to increase T_m of VHHs (60). Independently, two of these changes (1E and 5 V) were identified as stabilizing in a study that examined a large repertoire of sdAb sequences (61).

Fusion Proteins

One advantage of VHHs is that their ease of expression in many systems facilitates the development of a wide variety of fusion constructs. The vast majority of these constructs have been designed to enhance the utility of VHHs or add additional functionality. For example, their fusion to antiserum albumin sdAbs can extend their serum half-life (62). Fusions to Fc domains or anti-Fc receptor sdAbs can endow them with effector function (63, 64). Fusions with alkaline phosphatase enhances affinity as it homodimerizes and at the same time facilitates the colorimetric detection of targets (65, 66). Fusions with biotin-binding molecules, such as streptavidin or rhizavidin, also form VHH multimers, and allow for the oriented immobilization onto biotinylated surfaces (67, 68). VHH pentamers have also been described, again to take advantage of the binding avidity of multimeric interactions (69).

Comparatively few VHH fusion constructs have been developed with the goal of enhancing stability. In one instance, we utilized the maltose-binding protein (MBP) isolated from the thermophile *Pyrococcus furiosus* to form a VHH-PfuMBP fusion (40). The primary purpose of this fusion was to facilitate production of a VHH in the *E. coli* cytoplasm at higher levels than achievable from the periplasm. A thermostable version of MPB was chosen primarily in order to avoid decreasing the stability of the construct. When produced in the cytoplasm, VHHs often do not form the canonical disulfide bond and hence have lower T_m than versions of the same VHH produced in the periplasm with an intact disulfide bond. When we measured the T_m of the VHH portion of the VHH-PfuMBP fusion it was observed to unfold at 68°C which corresponded to the VHH with an intact disulfide bond despite being folded in the cytoplasm. Cytoplasmic production of the unfused VHH showed a lower T_m (46°C), suggesting that the fusion to MBP enabled the VHH to form its disulfide bond.

In other work, we looked at the effect of adding an α-synuclein tail to the C-terminus of a VHH as a general method for introducing negative charge to increase VHH stability (70). Addition of the negatively charged tail decreased aggregation, increased the ability of several VHHs to bind antigen after heating above their T_m, and restored refolding ability in VHHs that lacked the canonical disulfide bond due to either cytoplasmic expression or mutation of the Cys residues that form the disulfide bond. Impressively, a mutant which lacked the canonical disulfide bond and showed no ability to refold after heat denaturation, was able to regain almost 100% of its secondary structure after heating

when expressed with the α-synuclein tail (70). Additionally, we observed that one of the cytoplasmically expressed VHHs with the α-synuclein tail melted at the low temperature associated with lack of the canonical disulfide bond formation, and refolded at the higher temperature observed with an intact canonical disulfide bond. Subsequent heating cycles led to unfolding and refolding both at the higher temperature leading to speculation that the disulfide bond may have formed while the VHH was denatured.

STABILIZING VNARs

There is much less literature focusing on shark VNARs compared to camelid VHHs. Several recent publications examine stability of VNARs. One detailed the stability of VNARs at extreme pH, in the presence of proteases, and on exposure to elevated temperatures for prolonged periods in liquid, lyophilized, and immobilized formats (32). In another study, the T_ms and refolding ability of VNARs from spiny and smooth dogfish sharks were examined (71).

The first demonstration of engineering stability into a shark VNAR combined strategies of CDR grafting and consensus sequence mutagenesis that had been shown to be effective in raising the stability of VHHs (72). The starting point for this work was a VNAR specific for the nucleoprotein of Ebola virus (73) with a low T_m (53°C) and a recovery of ~75% of its structure following a single heat denaturation cycle. Two initial graft variants were constructed using a previously identified stable shark VNAR framework. A graft of all 3 CDRs displayed excellent affinity with a low T_m, while a clone where only CDRs 1 and 3 were grafted had poor affinity but a 15°C higher T_m. These two graft variants only had three amino acid differences within CDR2. The CDR2 of shark VNAR (also called HV2) is truncated compared to VHH CDR2. To elucidate which of the amino acids were responsible for the affinity and stability, three double- and three single-point mutants were constructed that covered all the variations between the two graft variants. It was found that a single amino acid change resulted in a 10°C higher T_m over the original VNAR while maintaining sub-nM affinity equivalent to the original VNAR.

VNARs are gaining popularity as alternatives to VHHs. Protein engineering has been used to increase the affinity of VNARs and there have been efforts to humanize and to improve their pharmacokinetic properties (74–77). It is likely that the other strategies that have been applied to stabilize VHHs and VHs will be tested for their ability to stabilized VNARs as well.

CONCLUDING REMARKS

The availability of stable recognition elements is almost always desirable. Inherently, VHHs and VNARs are generally more robust than conventional recombinant antibody binding domains. However, while these sdAbs are often heat resistant, they are not heatproof. Protein engineering has been applied to VHHs and VNARs to improve their properties. Variants have been produced that are endowed with higher T_ms, greater ability to refold after denaturation, ability to function after heat exposure, and increased tolerance to the presence of chemical denaturants, proteases, and extreme pHs.

We have provided an overview of several methods that have been used successfully to enhance the stability of VHHs and VNARs. Each method, summarized in **Table 1**, has been used successfully to improve stability, but the extent of improvement varies and needs to be determined empirically. Each method has its benefits and liabilities; the addition of a non-canonical disulfide bond always guarantees at least a few degrees increase in T_m but can compromise affinity, specificity and/or protein expression in *E. coli*. The strategies for improving sdAb stability can be combined for better results. For example, negatively charged amino acids have been introduced into constructs that also contained an added non-canonical disulfide bond to provide additional increase in T_m (59). In another instance, non-canonical disulfide bonds were used along with stringent stability selection to develop sdAbs resistant to multiple proteases (52).

Greater understanding of the mechanism of sdAb stability can potentially lead to more general and predictable methods to increase sdAb robustness. These advances will further increase the utility of sdAbs in medical, industrial and biotechnological applications.

AUTHOR CONTRIBUTIONS

EG, JL, DZ, and GA outlined, drafted, and revised the manuscript.

FUNDING

Our work was supported by NRL base funding and the Defense Threat Reduction Agency, Joint Science and Technology Office and DTRA J9 Chemical and Biological Technologies Department project number HDTRA1518114.

REFERENCES

1. Ward ES, Gussow D, Griffiths AD, Jones PT, Winter G. Binding activities of a repertoire of single immunoglobulin variable domains secreted from *Escherichia coli*. *Nature* (1989) 341:544–6. doi:10.1038/341544a0
2. Hamers-Casterman C, Atarhouch T, Muyldermans S, Robinson G, Hamers C, Songa EB, et al. Naturally occurring antibodies devoid of light chains. *Nature* (1993) 363:446–8. doi:10.1038/363446a0
3. Davies J, Riechmann L. 'Camelising' human antibody fragments: NMR studies on VH domains. *FEBS Lett* (1994) 339:285–90. doi:10.1016/0014-5793(94)80432-X
4. Greenberg AS, Avila D, Hughes M, Hughes A, Mckinney EC, Flajnik MF. A new antigen receptor gene family that undergoes rearrangement and extensive somatic diversification in sharks. *Nature* (1995) 374:168–73. doi:10.1038/374168a0
5. Arbabi Ghahroudi M, Desmyter A, Wyns L, Hamers R, Muyldermans S. Selection and identification of single domain antibody fragments from camel heavy-chain antibodies. *FEBS Lett* (1997) 414:521–6. doi:10.1016/S0014-5793(97)01062-4
6. Nuttall SD, Krishnan UV, Doughty L, Nathanielsz A, Ally N, Pike RN, et al. A naturally occurring NAR variable domain binds the Kgp protease from *Porphyromonas gingivalis*. *FEBS Lett* (2002) 516:80–6. doi:10.1016/S0014-5793(02)02506-1
7. Dooley H, Flajnik MF, Porter AJ. Selection and characterization of naturally occurring single-domain (IgNAR) antibody fragments from immunized sharks by phage display. *Mol Immunol* (2003) 40:25–33. doi:10.1016/S0161-5890(03)00084-1
8. de Marco A. Biotechnological applications of recombinant single-domain antibody fragments. *Microb Cell Fact* (2011) 10:44. doi:10.1186/1475-2859-10-44

9. Muyldermans S, Baral TN, Retarnozzo VC, De Baetselier P, De Genst E, Kinne J, et al. Camelid immunoglobulins and nanobody technology. *Vet Immunol Immunopathol* (2009) 128:178–83. doi:10.1016/j.vetimm.2008.10.299
10. Eyer L, Hruska K. Single-domain antibody fragments derived from heavy-chain antibodies: a review. *Vet Med* (2012) 57:439–513.
11. Wesolowski J, Alzogaray V, Reyelt J, Unger M, Juarez K, Urrutia M, et al. Single domain antibodies: promising experimental and therapeutic tools in infection and immunity. *Med Microbiol Immunol* (2009) 198:157–74. doi:10.1007/s00430-009-0116-7
12. Barelle C, Porter A. VNARs: an ancient and unique repertoire of molecules that deliver small, soluble, stable and high affinity binders of proteins. *Antibodies* (2015) 4:240. doi:10.3390/antib4030240
13. Vermeer AWP, Norde W. The thermal stability of immunoglobulin: unfolding and aggregation of a multi-domain protein. *Biophys J* (2000) 78:394–404. doi:10.1016/S0006-3495(00)76602-1
14. Akazawa-Ogawa Y, Takashima M, Lee YH, Ikegami T, Goto Y, Uegaki K, et al. Heat-induced irreversible denaturation of the camelid single domain VHH antibody is governed by chemical modifications. *J Biol Chem* (2014) 289:15666–79. doi:10.1074/jbc.M113.534222
15. Akazawa-Ogawa Y, Uegaki K, Hagihara Y. The role of intra-domain disulfide bonds in heat-induced irreversible denaturation of camelid single domain VHH antibodies. *J Biochem* (2016) 159:111–21. doi:10.1093/jb/mvv082
16. Kim DY, Hussack G, Kandalaft H, Tanha J. Mutational approaches to improve the biophysical properties of human single-domain antibodies. *Biochim Biophys Acta* (2014) 1844:1983–2001. doi:10.1016/j.bbapap.2014.07.008
17. Rouet R, Lowe D, Christ D. Stability engineering of the human antibody repertoire. *FEBS Lett* (2014) 588:269–77. doi:10.1016/j.febslet.2013.11.029
18. Nilvebrant J, Tessier PM, Sidhu SS. Engineered autonomous human variable domains. *Curr Pharm Des* (2016) 22:6527–37. doi:10.2174/1381612822666160921143011
19. Muyldermans S. Nanobodies: natural single-domain antibodies. In: Roger K, editor. *Annual Review of Biochemistry*. (Vol. 82), Palo Alto, CA: Annual Reviews (2013). p. 775–97.
20. Harmsen MM, De Haard HJ. Properties, production, and applications of camelid single-domain antibody fragments. *Appl Microbiol Biotechnol* (2007) 77:13–22. doi:10.1007/s00253-007-1142-2
21. Alzogaray V, Danquah W, Aguirre A, Urrutia M, Berguer P, Vescovi EG, et al. Single-domain llama antibodies as specific intracellular inhibitors of SpvB, the actin ADP-ribosylating toxin of *Salmonella typhimurium*. *FASEB J* (2011) 25:526–34. doi:10.1096/fj.10-162958
22. Dumoulin M, Conrath K, Van Meirhaeghe A, Meersman F, Heremans K, Frenken LGJ, et al. Single-domain antibody fragments with high conformational stability. *Protein Sci* (2002) 11:500–15. doi:10.1110/ps.34602
23. Micsonai A, Wien F, Kernya L, Lee YH, Goto Y, Refregiers M, et al. Accurate secondary structure prediction and fold recognition for circular dichroism spectroscopy. *Proc Natl Acad Sci U S A* (2015) 112:E3095–103. doi:10.1073/pnas.1500851112
24. Anderson G, Bernstein R, Swain M, Zabetakis D, Goldman E. Binding kinetics of antiricin single domain antibodies and improved detection using a B chain specific binder. *Anal Chem* (2010) 82:7202–7. doi:10.1021/ac100961x
25. Johnson CM. Differential scanning calorimetry as a tool for protein folding and stability. *Arch Biochem Biophys* (2013) 531:100–9. doi:10.1016/j.abb.2012.09.008
26. Lavinder JJ, Hari SB, Sullivan BJ, Magliery TJ. High-throughput thermal scanning: a general, rapid dye-binding thermal shift screen for protein engineering. *J Am Chem Soc* (2009) 131:3794–5. doi:10.1021/ja8049063
27. McConnell AD, Spasojevich V, Macomber JL, Krapf IP, Chen A, Sheffer JC, et al. An integrated approach to extreme thermostabilization and affinity maturation of an antibody. *Protein Eng Des Sel* (2013) 26:151–64. doi:10.1093/protein/gzs090
28. Royer CA. Probing protein folding and conformational transitions with fluorescence. *Chem Rev* (2006) 106:1769–84. doi:10.1021/cr0404390
29. Graef RR, Anderson GP, Doyle KA, Zabetakis D, Sutton FN, Liu JL, et al. Isolation of a highly thermal stable lama single domain antibody specific for staphylococcus aureus enterotoxin B. *BMC Biotechnol* (2011) 11:86. doi:10.1186/1472-6750-11-86
30. Goldman ER, Anderson GP, Liu JL, Delehanty JB, Sherwood LJ, Osborn LE, et al. Facile generation of heat-stable antiviral and antitoxin single domain antibodies from a semisynthetic llama library. *Anal Chem* (2006) 78:8245–55. doi:10.1021/ac0610053
31. Turner KB, Liu JL, Zabetakis D, Lee AB, Anderson GP, Goldman ER. Improving the biophysical properties of anti-ricin single-domain antibodies. *Biotechnol Rep (Amst)* (2015) 6:27–35. doi:10.1016/j.btre.2015.01.001
32. Griffiths K, Dolezal O, Parisi K, Angerosa J, Dogovski C, Barraclough M, et al. Shark variable new antigen receptor (VNAR) single domain antibody fragments: stability and diagnostic applications. *Antibodies* (2013) 2:66. doi:10.3390/antib2010066
33. Lowe D, Dudgeon K, Rouet R, Schofield P, Jermutus L, Christ D. Aggregation, stability, and formulation of human antibody therapeutics. *Adv Protein Chem Struct Biol* (2011) 84:41–61. doi:10.1016/b978-0-12-386483-3.00004-5
34. Lefranc MP, Pommie C, Ruiz M, Giudicelli V, Foulquier E, Truong L, et al. IMGT unique numbering for immunoglobulin and T cell receptor variable domains and Ig superfamily V-like domains. *Dev Comp Immunol* (2003) 27:55–77. doi:10.1016/S0145-305X(02)00039-3
35. Dunbar J, Deane CM. ANARCI: antigen receptor numbering and receptor classification. *Bioinformatics* (2016) 32:298–300. doi:10.1093/bioinformatics/btv552
36. Saerens D, Pellis M, Loris R, Pardon E, Dumoulin M, Matagne A, et al. Identification of a universal VHH framework to graft non-canonical antigen-binding loops of camel single-domain antibodies. *J Mol Biol* (2005) 352:597–607. doi:10.1016/j.jmb.2005.07.038
37. Vincke C, Loris R, Saerens D, Martinez-Rodriguez S, Muyldermans S, Conrath K. General strategy to humanize a camelid single-domain antibody and identification of a universal humanized nanobody scaffold. *J Biol Chem* (2009) 284:3273–84. doi:10.1074/jbc.M806889200
38. Zabetakis D, Anderson GP, Bayya N, Goldman ER. Contributions of the complementarity determining regions to the thermal stability of a single-domain antibody. *PLoS One* (2013) 8:e77678. doi:10.1371/journal.pone.0077678
39. Legler PM, Compton JR, Hale ML, Anderson GP, Olson MA, Millard CB, et al. Stability of isolated antibody-antigen complexes as a predictive tool for selecting toxin neutralizing antibodies. *MAbs* (2017) 9:43–57. doi:10.1080/19420862.2016.1236882
40. Walper SA, Battle SR, Audrey Brozozog Lee P, Zabetakis D, Turner KB, Buckley PE, et al. Thermostable single domain antibody-maltose binding protein fusion for *Bacillus anthracis* spore protein BclA detection. *Anal Biochem* (2014) 447:64–73. doi:10.1016/j.ab.2013.10.031
41. Hagihara Y, Mine S, Uegaki K. Stabilization of an immunoglobulin fold domain by an engineered disulfide bond at the buried hydrophobic region. *J Biol Chem* (2007) 282:36489–95. doi:10.1074/jbc.M707078200
42. George J, Compton JR, Leary DH, Olson MA, Legler PM. Structural and mutational analysis of a monomeric and dimeric form of a single domain antibody with implications for protein misfolding. *Proteins* (2014) 82:3101–16. doi:10.1002/prot.24671
43. Arbabi-Ghahroudi M, To R, Gaudette N, Hirama T, Ding W, MacKenzie R, et al. Aggregation-resistant VHs selected by in vitro evolution tend to have disulfide-bonded loops and acidic isoelectric points. *Protein Eng Des Sel* (2009) 22:59–66. doi:10.1093/protein/gzn071
44. Hagihara Y, Saerens D. Engineering disulfide bonds within an antibody. *Biochim Biophys Acta* (2014) 1844:2016–23. doi:10.1016/j.bbapap.2014.07.005
45. Saerens D, Conrath K, Govaert J, Muyldermans S. Disulfide bond introduction for general stabilization of immunoglobulin heavy-chain variable domains. *J Mol Biol* (2008) 377:478–88. doi:10.1016/j.jmb.2008.01.022
46. Zabetakis D, Olson MA, Anderson GP, Legler PM, Goldman ER. Evaluation of disulfide bond position to enhance the thermal stability of a highly stable single domain antibody. *PLoS One* (2014) 9:e115405. doi:10.1371/journal.pone.0115405
47. Chan PH, Pardon E, Menzer L, De Genst E, Kumita JR, Christodoulou J, et al. Engineering a camelid antibody fragment that binds to the active site of human lysozyme and inhibits its conversion into amyloid fibrils. *Biochemistry* (2008) 47:11041–54. doi:10.1021/bi8005797
48. Hussack G, Hirama T, Ding W, MacKenzie R, Tanha J. Engineered single-domain antibodies with high protease resistance and thermal stability. *PLoS One* (2011) 6:e28218. doi:10.1371/journal.pone.0028218
49. Shriver-Lake LC, Goldman ER, Zabetakis D, Anderson GP. Improved production of single domain antibodies with two disulfide bonds by co-expression

of chaperone proteins in the *Escherichia coli* periplasm. *J Immunol Methods* (2017) 443:64–7. doi:10.1016/j.jim.2017.01.007
50. Schlapschy M, Grimm S, Skerra A. A system for concomitant overexpression of four periplasmic folding catalysts to improve secretory protein production in *Escherichia coli*. *Protein Eng Des Sel* (2006) 19:385–90. doi:10.1093/protein/gzl018
51. Dolk E, van Vliet C, Perez JM, Vriend G, Darbon H, Ferrat G, et al. Induced refolding of a temperature denatured llama heavy-chain antibody fragment by its antigen. *Proteins* (2005) 59:555–64. doi:10.1002/prot.20378
52. Hussack G, Riazi A, Ryan S, van Faassen H, MacKenzie R, Tanha J, et al. Protease-resistant single-domain antibodies inhibit *Campylobacter jejuni* motility. *Protein Eng Des Sel* (2014) 27:191–8. doi:10.1093/protein/gzu011
53. Harmsen MM, van Solt CB, van Bemmel AMV, Niewold TA, van Zijderveld FG. Selection and optimization of proteolytically stable llama single-domain antibody fragments for oral immunotherapy. *Appl Microbiol Biotechnol* (2006) 72:544–51. doi:10.1007/s00253-005-0300-7
54. Turner KB, Zabetakis D, Goldman ER, Anderson GP. Enhanced stabilization of a stable single domain antibody for SEB toxin by random mutagenesis and stringent selection. *Protein Eng Des Sel* (2014) 27:89–95. doi:10.1093/protein/gzu001
55. Harmsen MM, Ruuls RC, Nijman IJ, Niewold TA, Frenken LG, de Geus B. Llama heavy-chain V regions consist of at least four distinct subfamilies revealing novel sequence features. *Mol Immunol* (2000) 37:579–90. doi:10.1016/S0161-5890(00)00081-X
56. Perchiacca JM, Lee CC, Tessier PM. Optimal charged mutations in the complementarity-determining regions that prevent domain antibody aggregation are dependent on the antibody scaffold. *Protein Eng Des Sel* (2014) 27:29–39. doi:10.1093/protein/gzt058
57. Perchiacca JM, Ladiwala AR, Bhattacharya M, Tessier PM. Aggregation-resistant domain antibodies engineered with charged mutations near the edges of the complementarity-determining regions. *Protein Eng Des Sel* (2012) 25:591–601. doi:10.1093/protein/gzs042
58. Liu JL, Goldman ER, Zabetakis D, Walper SA, Turner KB, Shriver-Lake LC, et al. Enhanced production of a single domain antibody with an engineered stabilizing extra disulfide bond. *Microb Cell Fact* (2015) 14:158. doi:10.1186/s12934-015-0340-3
59. Anderson GP, Liu JH, Zabetakis D, Liu JL, Goldman ER. Thermal stabilization of anti-α-cobratoxin single domain antibodies. *Toxicon* (2017) 129:68–73. doi:10.1016/j.toxicon.2017.02.008
60. Shriver-Lake LC, Zabetakis D, Goldman ER, Anderson GP. Evaluation of anti-botulinum neurotoxin single domain antibodies with additional optimization for improved production and stability. *Toxicon* (2017) 135:51–8. doi:10.1016/j.toxicon.2017.06.002
61. Kunz P, Flock T, Soler N, Zaiss M, Vincke C, Sterckx Y, et al. Exploiting sequence and stability information for directing nanobody stability engineering. *Biochim Biophys Acta* (2017) 1861(9):2196–205. doi:10.1016/j.bbagen.2017.06.014
62. Roovers RC, Laeremans T, Huang L, De Taeye S, Verkleij AJ, Revets H, et al. Efficient inhibition of EGFR signaling and of tumour growth by antagonistic anti-EFGR nanobodies. *Cancer Immunol Immunother* (2007) 56:303–17. doi:10.1007/s00262-006-0180-4
63. Rozan C, Cornillon A, Petiard C, Chartier M, Behar G, Boix C, et al. Single-domain antibody-based and linker-free bispecific antibodies targeting FcgammaRIII induce potent antitumor activity without recruiting regulatory T cells. *Mol Cancer Ther* (2013) 12:1481–91. doi:10.1158/1535-7163.mct-12-1012
64. Gunaydin G, Yu SZ, Graslund T, Hammarstrom L, Marcotte H. Fusion of the mouse IgG1 Fc domain to the VHH fragment (ARP1) enhances protection in a mouse model of rotavirus. *Sci Rep* (2016) 6:30171. doi:10.1038/srep30171
65. Swain MD, Anderson GP, Serrano-Gonzalez J, Liu JL, Zabetakis D, Goldman ER. Immunodiagnostic reagents using llama single domain antibody-alkaline phosphatase fusion proteins. *Anal Biochem* (2011) 417:188–94. doi:10.1016/j.ab.2011.06.012
66. Sherwood LJ, Osborn LE, Carrion R, Patterson JL, Hayhurst A. Rapid assembly of sensitive antigen-capture assays for Marburg virus, using in vitro selection of llama single-domain antibodies, at biosafety level 4. *J Infect Dis* (2007) 196:S213–9. doi:10.1086/520586
67. Walper SA, Lee PAB, Goldman ER, Anderson GP. Comparison of single domain antibody immobilization strategies evaluated by surface plasmon resonance. *J Immunol Methods* (2013) 388:68–77. doi:10.1016/j.jim.2012.11.014
68. Liu JL, Zabetakis D, Walper SA, Goldman ER, Anderson GP. Bioconjugates of rhizavidin with single domain antibodies as bifunctional immunoreagents. *J Immunol Methods* (2014) 411:37–42. doi:10.1016/j.jim.2014.06.004
69. Zhang JB, Tanha J, Hirama T, Khieu NH, To R, Hong TS, et al. Pentamerization of single-domain antibodies from phage libraries: a novel strategy for the rapid generation of high-avidity antibody reagents. *J Mol Biol* (2004) 335:49–56. doi:10.1016/j.jmb.2003.09.034
70. Goldman ER, Brozozog-Lee PA, Zabetakis D, Turner KB, Walpey SA, Liu JL, et al. Negative tail fusions can improve ruggedness of single domain antibodies. *Protein Expr Purif* (2014) 95:226–32. doi:10.1016/j.pep.2014.01.003
71. Liu JL, Zabetakis D, Brown JC, Anderson GP, Goldman ER. Thermal stability and refolding capability of shark derived single domain antibodies. *Mol Immunol* (2014) 59:194–9. doi:10.1016/j.molimm.2014.02.014
72. Anderson GP, Teichler DD, Zabetakis D, Shriver-Lake LC, Liu JL, Lonsdale SG, et al. Importance of hypervariable region 2 for stability and affinity of a shark single-domain antibody specific for Ebola virus nucleoprotein. *PLoS One* (2016) 11:e0160534. doi:10.1371/journal.pone.0160534
73. Goodchild SA, Dooley H, Schoepp RJ, Flajnik M, Lonsdale SG. Isolation and characterisation of Ebola virus-specific recombinant antibody fragments from murine and shark immune libraries. *Mol Immunol* (2011) 48:2027–37. doi:10.1016/j.molimm.2011.06.437
74. Zielonka S, Empting M, Grzeschik J, Könning D, Barelle CJ, Kolmar H. Structural insights and biomedical potential of IgNAR scaffolds from sharks. *MAbs* (2015) 7:15–25. doi:10.4161/19420862.2015.989032
75. Simmons DP, Abregu FA, Krishnan UV, Proll DF, Streltsov VA, Doughty L, et al. Dimerisation strategies for shark IgNAR single domain antibody fragments. *J Immunol Methods* (2006) 315:171–84. doi:10.1016/j.jim.2006.07.019
76. Kovalenko OV, Olland A, Piche-Nicholas N, Godbole A, King D, Svenson K, et al. Atypical antigen recognition mode of a shark immunoglobulin new antigen receptor (IgNAR) variable domain characterized by humanization and structural analysis. *J Biol Chem* (2013) 288:17408–19. doi:10.1074/jbc.M112.435289
77. Muller MR, Saunders K, Grace C, Jin M, Piche-Nicholas N, Steven J, et al. Improving the pharmacokinetic properties of biologics by fusion to an anti-HSA shark VNAR domain. *MAbs* (2012) 4:673–85. doi:10.4161/mabs.22242

Conflict of Interest Statement: The authors declare that the research was conducted in the absence of any commercial or financial relationships that could be construed as a potential conflict of interest.

The reviewer, JT, and handling Editor declared their shared affiliation, and the handling Editor states that the process nevertheless met the standards of a fair and objective review.

frontiers in Immunology

REVIEW
published: 21 August 2017
doi: 10.3389/fimmu.2017.00977

Single-Domain Antibodies As Versatile Affinity Reagents for Analytical and Diagnostic Applications

Gualberto Gonzalez-Sapienza, Martín A. Rossotti and Sofía Tabares-da Rosa*

Cátedra de Inmunología, Facultad de Química, Instituto de Higiene, UDELAR, Montevideo, Uruguay

With just three CDRs in their variable domains, the antigen-binding site of camelid heavy-chain-only antibodies (HcAbs) has a more limited structural diversity than that of conventional antibodies. Even so, this does not seem to limit their specificity and high affinity as HcAbs against a broad range of structurally diverse antigens have been reported. The recombinant form of their variable domain [nanobody (Nb)] has outstanding properties that make Nbs, not just an alternative option to conventional antibodies, but in many cases, these properties allow them to reach analytical or diagnostic performances that cannot be accomplished with conventional antibodies. These attributes include comprehensive representation of the immune specificity in display libraries, easy adaptation to high-throughput screening, exceptional stability, minimal size, and versatility as affinity building block. Here, we critically reviewed each of these properties and highlight their relevance with regard to recent developments in different fields of immunosensing applications.

Keywords: nanobodies, VHH, immunodetection, phage display, imaging, haptens

OPEN ACCESS

Edited by:
Colin Roger MacKenzie, National Research Council Canada, Canada

Reviewed by:
George P. Anderson, United States Naval Research Laboratory, United States
Carole Henry, University of Chicago, United States

****Correspondence:***
Gualberto Gonzalez-Sapienza
ggonzal@fq.edu.uy

Specialty section:
This article was submitted to Vaccines and Molecular Therapeutics, a section of the journal Frontiers in Immunology

Received: *20 June 2017*
Accepted: *31 July 2017*
Published: *21 August 2017*

Citation:
Gonzalez-Sapienza G, Rossotti MA and Tabares-da Rosa S (2017) Single-Domain Antibodies As Versatile Affinity Reagents for Analytical and Diagnostic Applications. Front. Immunol. 8:977. doi: 10.3389/fimmu.2017.00977

INTRODUCTION

While most analytical methods rely on the separation of the analyte, the exquisite specificity of antibody recognition allows the detection of trace amounts of the target analyte even in highly complex matrices. This principle of immunodetection was first demonstrated in 1959 when Berson and Yalow developed the first radioimmunoassay for human insulin using a guinea pig antiserum (1). A second major milestone occurred in 1975 when Köhler and Milstein developed the hybridoma technology, enabling the production of high quantities of monoclonal antibodies of the desired specificity (2). Interesting, these two Nobel Prize winning achievements were not patented, which contributed highly to the widespread use of antibodies for immunodetection assays. Further progress in molecular biology and the genetics of antibody diversity added new venues for antibody discovery, with higher control on the selection process and new engineering possibilities (3–5). This paved the way for the current bloom of therapeutic applications of antibodies but also provided the technology to create new assays and biosensors based on the use of recombinant antibody fragments that could be easily tagged and produced at low cost by microbial fermentation (6, 7). All this progress has been dominated by the use of conventional hetero tetrameric antibodies, prototypically represented by the IgG molecule and its fragments (**Figure 1**), but more recently, the recombinant binding domain of a special type of antibodies devoid of light chain have emerged as a salient alternative for immunosensing. Here, we first present an overview of the heavy-chain-only antibodies (HcAbs) and then

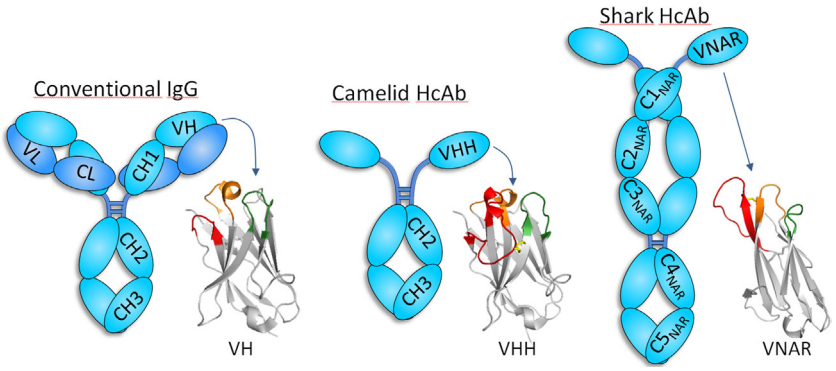

FIGURE 1 | Schematic representation of conventional and heavy-chain-only antibodies (HcAbs). Conventional antibodies, formed by heavy (cyan) and light (blue) chains, are found in all vertebrate, but camelids and cartilaginous fish also have antibodies devoid of light chain, whose antigen-binding site sits exclusively in the heavy chain variable domain. The organization of the heavy chain variable domain of each of these antibodies is shown using three representative structures [PDB IDs: 5WT9 (VH); 5TP3 (VHH); and 2COQ (V-NAR)]. CDR1, CDR2, and CDR3 are depicted in orange, green, and red, respectively, except for V-NAR that lacks CDR2, and the green color is used to denote the HV4 region that sometimes participates in antigen binding. VHHs and V-NARs usually have long CDR3 and non-canonical disulfide bridges (yellow). While the antigen-binding site of conventional antibodies is formed by the combination of the six CDRs of the heavy and light chain, only three and two CDRs are involved in the formation of binding site of camelid and shark HcAb, respectively. Notice that HcAbs do not have the CH1 or an equivalent domain, which forms a strong interaction with the constant domain of the light chain in conventional antibodies.

outline the characteristics that make them to stand out as unique analytical and diagnostic tools.

CAMELIDS AND SHARKS HAVE A SPECIAL TYPE OF ANTIBODIES DEVOID OF LIGHT CHAIN

In 1993 researchers from the Vrije University in Brussel reported the existence of a special type of antibodies in camels that were devoid of light chain (8). These, so-called, HcAbs account for up to 50–80% of the circulating antibodies in camels and were also found to be present in the serum of the South American camelids, though in lower concentration (11–25%) (9, 10). Camelid HcAbs have a typical IgG Fc region with dedicated isotypes (IgG2 and IgG3) but lack the CH1 constant domain and have a distinctive variable domain (VHH) with structural features that increase its solubility (**Figure 1**). Other than camelids, HcAb have not been found in other organisms, with the curious exception of sharks and other cartilaginous fish (Chondrichthyes), the oldest living beings with an adaptive immune system. In addition to heterotetrameric IgM and IgW, these fishes possess the so-called Ig new antigen receptor (IgNAR) (11). IgNARs are formed by two identical heavy chains composed of five constant domains and a dedicated variable domain (V-NAR) (12, 13) (**Figure 1**). In spite of an evolutionary gap of 425 million years, VHHs and V-NARs share some convergent features that differ from those found in conventional variable domains, more notably, changes in conserved amino acids involved in the VH–VL interaction that make them soluble and independently folding domains, non-canonical Cys pairs in CDRs and frameworks (FRs) that increase their stability and diversity, and higher frequency of hypermutation hotspots and longer than average CDR3 that enlarge their recognition repertoire (11, 14, 15). Formed by fewer CDRs, the antigen-binding sites of VHH and V-NAR domains are smaller

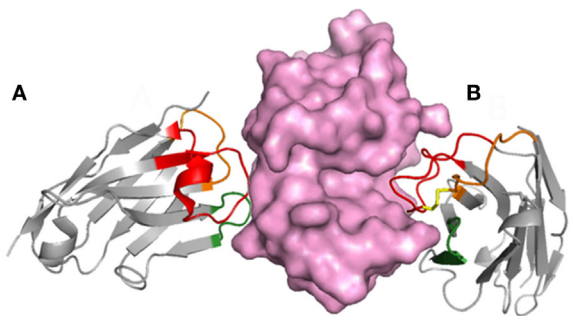

FIGURE 2 | The typically long CDR3 of VHHs provides flexibility to their epitope recognition. The complex of lysozyme (purple) with two VHHs shows that the long CDR3 may contribute to form a flat paratope **(A)** or penetrate in concave epitopes **(B)**; based on PDB structures 1OP9 and 1IR8.

than those of conventional antibodies, particularly in V-NARs that present a deletion of the CDR2 region, and thus are formed by 8 instead of 10 β-strands, making them the smallest (12 kDa) antigen-binding domain (16). The reduced paratope and the frequently extended and flexible CDR3 make VHHs and V-NARs particularly capable of binding concave and hidden epitopes (e.g., enzyme active sites, cryptic viral epitopes, etc.) that are not accessible to conventional antibodies (16–19). With no distinctive effector functions associated to their constant domains (20), this unique epitope binding capability has been suggested as the main force that drove the evolution of HcAb (21, 22). Nevertheless, the reactivity of their antigen-binding site is not limited to hidden targets (**Figure 2**), and HcAbs reacting with a broad range of structurally diverse epitopes have been described, including flat surfaces in macromolecules and small molecules (23–27). Since camelids are easier to handle, produce stronger antibody responses than sharks (28, 29), and the recombinant expression

of the heavy chain variable domain of camelid HcAb is typically higher (30), these antibody fragments are more frequently used and will be the focus of this review.

CAMELID HcAbs BEAR INDEPENDENT FOLDING VARIABLE DOMAINS THAT INCLUDE MOSTLY VHHs BUT ALSO VHs

The solubility and independent folding of the VHH domain is to a great extent the result of the substitution of conserved residues of FR 2 involved in the VH/VL interaction and the shielding created by the bending of CDR3, **Figure 3**. In VHHs, Phe/Tyr42; Glu/Gln49; Arg50; and Phe/Gly/Leu52 frequently substitute for the more hydrophobic residues, Val42; Gly49; Leu50; and Trp52 of conventional VH domains, respectively (31). These hallmark substitutions are encoded by dedicated VHH gene segments that are intermixed with the classical VH gene segments in the IgH loci, sharing the same D and J cluster (32). However, not all the variable domains found in HcAb are VHHs. Up to 10% of HcAbs carry conventional VH variable domains (31). The solubility of these VHs is often sustained by a long CDR3 that compensates for the interactions lost by the absence of the light chain, or by the introduction of a hydrophilic residue that substitutes Trp118, which is essential for the interaction with the light chain. This change is often caused by an Arg codon that arises as a consequence of an unusual D–J recombination (33). The camelid HcAb ontogeny is still unclear, but it has been suggested that after recombination of the heavy chain locus in the pre-B cells stage, the poor interaction of the newly formed VHH or "soluble" VH with the VpreB/λ5 surrogate light chain precludes the release of the IgM heavy chain that is bound through the unfolded CH1 domain to the BiP protein in the endoplasmic reticulum (34). This arrests B cell development, but in camelids it might trigger a class switch to the IgG2 and IgG3 constant genes, which resumes cell development because in these isotypes the CH1 region is lost by defective splicing of the RNA primary transcript and thus, the HcAb BCR can be exported to the cell surface (35, 36). This is supported by the fact that light-chain-deficient ($L^{-/-}$) mice and $L^{-/-}$ chicken spontaneously produce HcAbs, but only after deletion of the CH1 domain due to an imprecise recombination event at the genomic level (37, 38). This mechanism selects for independently folding soluble domains, which has important practical consequences, because they can be expressed as stable recombinant fragments with outstanding biotechnological properties. The terms VHH antibody, single-domain antibody, or nanobody (Nb) are often used to refer to the recombinant form of these fragments, but the former can be confusing because, as we have seen, they sometimes consist of soluble VH fragments. For instance, in different studies we have selected both VHHs and VHs against human soluble epoxy hydrolase and tetanus toxin. In both cases, the recombinant VHs and VHHs had similar affinity (in the nanomolar to subnanomolar range) and showed also similar levels of expression and stability (39, 40). In the following sections, we will highlight the properties of Nbs that make them a salient option for immunosensing applications.

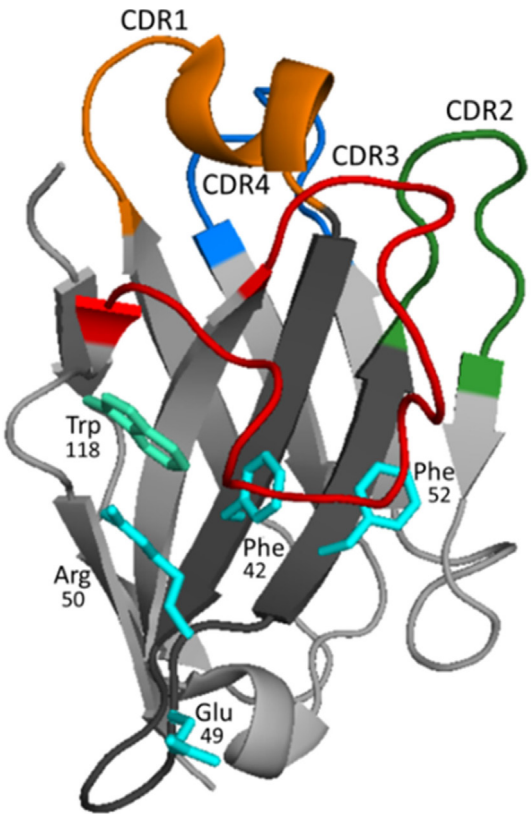

FIGURE 3 | Structure and binding characteristics of the VHH domain. The typical organization of the VHH domain is represented using the structure of a VHH to carbazol (PDB 1U0Q). In framework (FR) 2 (dark gray), the amino acids shown in cyan [in this case Phe42, Glu49, Arg50, and Phe52 (IMGT numbering)] represent the hallmark residues that substitute the critical amino acids of VHs that participate in the interaction with the light chain. CDRs 1, 2, and 3 are colored in orange, green, and red, respectively. The loop of FR 3 shown in blue (also known as CDR4) presents significant variability (higher than in VHs of conventional antibodies) and may also interact with the antigen (41–43). Frequently, the CDR3 is long and bends over FR 2 shielding its hydrophobic residues and helping to mask Trp118 (cyan–green), which is key for the interaction of VH with the VL chain. The structure of the long CDR3s, much more frequently in camels, may be stabilized by non-canonical disulfide bridge, typically formed between Cys residues of CDR1 and CDR3.

Nbs CAN BE EASILY SELECTED FROM DISPLAY LIBRARIES BECAUSE THE IMMUNE SPECIFICITY IS FULLY RECOVERED

Dromedaries, llamas, and alpacas are not the easiest animals to breed, and their immunizations require larger antigen doses than smaller animals; however, the generation of HcAb libraries stands out as a highly convenient option to easily generate specific binders, because the immune specificity is not shuffled during the construction of the library, **Figure 4**. In practical terms, that means that the size of HcAb antibody libraries can be several orders smaller than that of conventional antibody libraries to reach a similar representation of the original immune repertoire. The magnitude of this matter can be inferred from the data

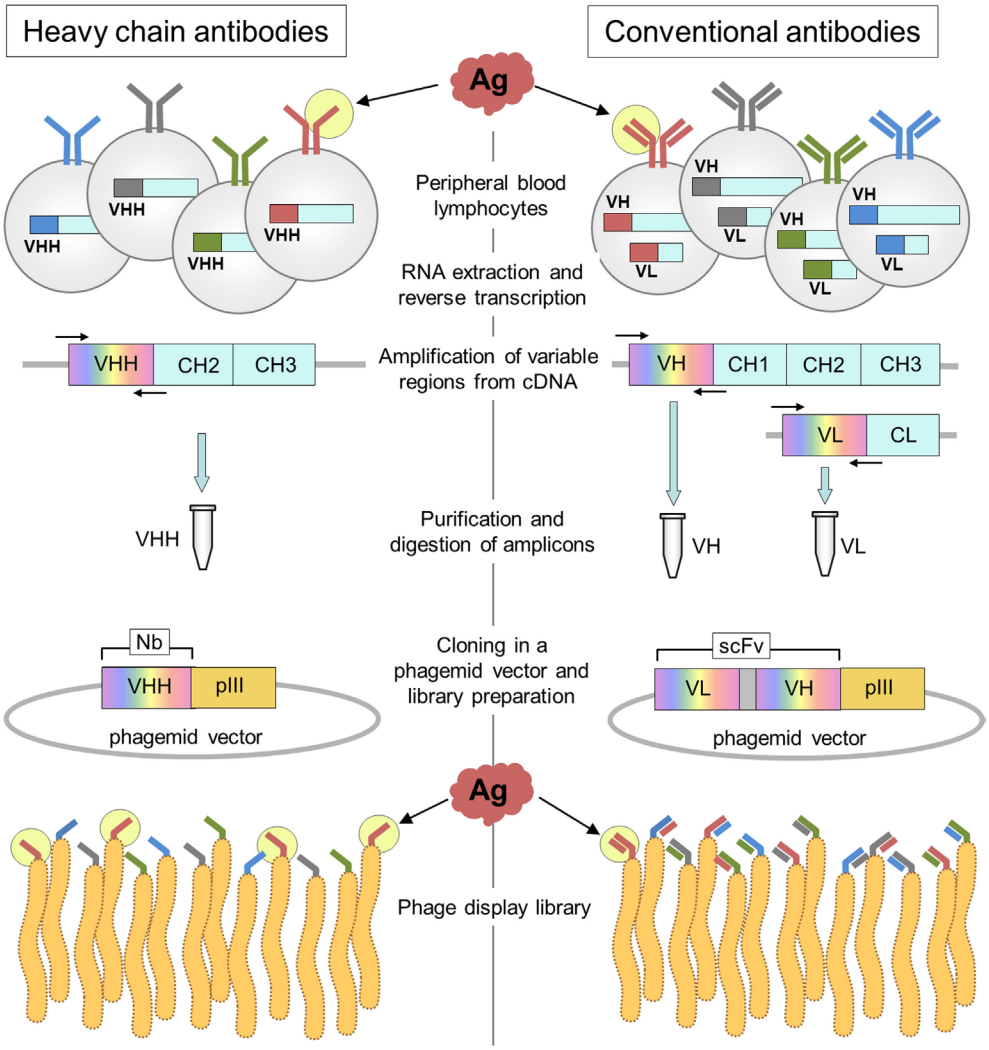

FIGURE 4 | Schematic representation of the construction of heavy-chain-only antibody and conventional antibody libraries. The main steps in the generation of nanobody (Nb) and conventional antibody (scFv) libraries are outlined on the left and right, respectively. The key difference occurs during PCR amplification of the variable gene regions that is done separately for the VH and VL genes. Upon assembly of the VL spacer–VH cassette that encodes the scFv, the VL and VH genes are shuffled, and the original pairing of the light and heavy variable domains occurs only at a very low frequency.

provided by next-generation sequencing (NGS) of VHH libraries. Recently, the specific repertoire of an immune llama VHH library of 4.8×10^8 independent transformants was studied by data mining of NGS data. Using a sequence identity threshold defined by cluster analysis of the publicly available VHH sequences, the authors were able to identify a wealth of up to >5,000 potential antigen-binding sequences, 90% of which were confirmed as actual functional binders (44). However, many of these binders are not necessarily highly represented in the library. The NGS analysis of the cDNA obtained from a llama immunized with staphylococcal enterotoxin B revealed an exceptional VHH diversity, because out of 5.4 million intact sequences, 88% (4.3 million) were present at a single copy number (45). Just in this case, a VHH library of 5×10^6 transformants would provide a good representation of this diversity, while in theory due to the VH/VL shuffling, an scFv library of $(5 \times 10^6)^2 = 2.5 \times 10^{13}$ transformants would be required to have a similar coverage of the original specificity repertoire. In our experience, when the immune antibody titer is >1/2,000, even a modest size VHH library of 10^6 individual transformants will easily yield high-affinity binders after one or two rounds of panning, even if a rare epitope-restricted selection is performed (36). Excellent reviews exist on the preparation of single-domain antibody libraries, for instance, see Pardon et al. (46).

THE SIMPLE NATURE OF Nbs MAKES THEM PARTICULARLY AMENABLE TO HIGH-THROUGHPUT SCREENING

While direct screening of the enriched phages after panning is generally satisfactory for initial selection of binders, the identification of antibodies with the desired diagnostic or analytical

properties requires a more careful screening. This is facilitated by transference *en masse* of the enriched VHHs into a strong expression vector generating different antibody constructs that can be interrogated in a flexible way. A particularly useful modification is the metabolic addition of biotin to the C-terminal peptide tag GLNDIFEAQKIEWHE. In the context of this peptide the side chain of its Lys residue is coupled with biotin by overexpression of the biotin ligase BirA of *Escherichia coli* during the production of the Nb (47). We recently adopted this strategy to develop a method for high-throughput screening of Nbs to cell receptors (48). The *in vivo* biotinylation facilitates the parallel analysis of hundreds of Nb clones by cell cytometry, because there is no need of blocking the interactions of the primary or secondary antibodies in case of cells expressing Fc receptors. The strong biotin–streptavidin binding also allows for stringent conditions during pull-down experiments yielding neat finger printings for mass spectrometry identification. Moreover, by adding or not adding biotin during the expression of the Nbs, each clone can be produced with or without this label, which allows to perform competitive epitope binning of the selected Nbs directly on the cells (48). Once selected, the biotinylated Nbs are ready-to-use reagents for cell cytometry diagnosis or immunohistochemistry (49). The method was also adapted to screen for the best Nb pairs to develop two-site immunoassays. After panning, the biotinylated Nbs are produced in 96-well culture blocks and after biotin separation using 96-well Ni-NTA agarose column plates, the eluted Nbs are used to saturate the binding capacity of avidin-coated wells. In this way, equal amounts of the oriented antibodies are retained in each well that can next be probed with an optimized amount of the labeled antigen to spot the clones producing the highest readouts. Once the best capture antibodies are selected, they can be tested in parallel against the rest of the Nb clones using trace amounts of the antigen in a sandwich format. Using this method, we empirically found a pair of Nbs that performed with a detection limit of 63 pg/mL of human soluble epoxy hydrolase in highly complex matrices (40). The use of biotinylated Nbs for two-site immunoassay also has the advantage of the uniform orientation of the immobilized antibody, which has been show to contribute to enhance the assay sensitivity for the detection of bacterial toxins and influenza virus (50, 51).

Nbs ARE STABLE UNDER CHEMICAL AND PHYSICOCHEMICAL STRINGENT CONDITIONS

Robustness is a desirable property of any antibody, but for some uses, it may be critical. This is the case of analytical applications that are performed under stringent conditions (i.e., high solvent concentration, high temperature, etc.). A striking example is an anti-caffeine llama Nb that allowed determination of the alkaloid in beverages as hot as 70°C (52). Similarly a VHH to a red azo dye was shown to be active in a binding assay at 90°C (53). The thermal stability of Nbs also translates into prolonged shelf lives. For instance, the unaltered storage of microelectrodes intended for point of care detection of ricin increased 7-fold when conventional antibodies were substituted by single-domain antibodies (54). Nbs possess high conformational stability with native-to-unfold free energy transitions between 30 and 60 kJ mol^{-1}, and are generally resistant to thermally induced denaturation with melting temperatures in the 60–80°C range (55, 56). By random mutagenesis and stringent selection, their thermal stability can be further improved as shown by Turner et al. that selected a double mutant of an anti-SEB toxin with a melting point of 90°C that was 6.5°C higher that the parent antibody. However, their distinctive property is the reversibility of the thermal unfolding process that allows some VHHs to regain functionality at room temperature even after 1–2 h at extreme temperatures (57). This unfolding–refolding process occurs through a simple two-state mechanism, without intermediate states that would lead to aggregation (58). However, depending on their sequence, not all VHH are able to return to the native conformation. In some cases, they will tend to aggregate when in the unfolded state due to lack of sufficient charge repulsion. This was evidenced studying the thermal stability of Nbs to ricin, which showed a significant improvement in their refolding properties after the introduction of additional charged residues by mutations or addition of fusion tails (59, 60). Aggregation can also occur due to the chemical modifications caused by heat treatment (e.g., Asn deamidation), which could lead to irreversible denaturation. In these cases, the mutation of Asn residues to Asp has also shown to increase the heat resistance of the Nb (61). Likewise, the removal of the extra disulfide bonds has proved beneficial for the thermal resistance of Nbs, although this modification has a negative impact in their thermodynamic stability (62).

Nanobodies have also been shown to tolerate the presence of organic solvents, which are frequently needed for analyte extraction. High tolerance to solvents avoids dilution of the sample with the corresponding gain in sensitivity. For example, efficient extraction of gliadins for the analysis of gluten-free products requires the use of solvents as well as reducing and denaturing agents that were shown to interfere with the binding of conventional antibodies causing false negative results. Careful selection from a VHH library allowed the development of an Nb-based immunoassay that detected gliadins in the presence of 15% ethanol, 0.5% 2-mercaptoethanol, and 0.5 M guanidine hydrochloride (63). Similarly, He et al. found that two of their anti-aflatoxin B1 Nbs were still reactive in the presence of up to 80% of methanol, 80% acetone, or 20% acetonitrile, which allowed them to develop an immunoassay for aflatoxin B1 that could be used for direct analysis of 70% methanol extracts of the toxin (64). We found similar results with Nbs against the pyrethroid metabolite 3-phenoxybenzoic acid. While the best Nb immunoassay was unaffected by the presence of 50% methanol or 50% DMSO, an equivalent polyclonal antibody assay rapidly lost activity. Interestingly, the addition of methanol even improved the assay sensitivity (65).

WHEN BEING SMALL MATTERS

The small size of Nbs is in itself an advantage in different analytical and diagnostic applications. One of the clearest examples is their use for *in vivo* molecular imaging (66, 67). Conventional monoclonal antibodies conjugated to different probes have been

used for tumor imaging, but their large size (150 kDa) impairs tumor penetration and after administration, they circulate in the blood for several days, requiring long waits and making it difficult to achieve high-contrast images. In addition, their Fc region can cause inappropriate activation of immune effector mechanisms leading to toxic effects. On the other hand, the small size (15 kDa) of Nbs enables a rapid biodistribution and homogeneous tumor labeling, whereas the unbound fraction is rapidly cleared by renal filtration and (68–70). Thus, high-contrast images are generated by single-photon emission computed tomography (SPECT), positron emission tomography (PET), or near-infrared imaging as early as 1 h after administration, which contrasts markedly with the time required for imaging with conventional antibodies. For instance, only 45 min were necessary for SPECT imaging of small xenograft tumors with an anti-epidermal growth factor receptor (EGFR) Nb labeled with ^{99m}Tc, while at least 24 h were necessary to visualize similar tumors with the IgG1 cetuximab labeled with the same radionuclide (71). The short time require for imaging with Nbs enables the use to short-lived radionuclides, such as ^{68}Ga (half-life = 68 min) or ^{18}F (half-life = 109.8 min). An anti-EGFR Nb labeled with ^{68}Ga allowed PET imaging of xenograft tumors after 1 h postinjection (72). This rapid clearance has a significant impact in the reduction of the patient's exposure to radiation. Unfortunately, kidney retention due to non-specific reabsorption in the proximal tubuli is a common problem associated with small radiolabeled agents. However, some studies have shown that modification of the polarity of the Nb C-terminal region and co-infusion with gelofusine and positively charged amino acids can contribute to reduce this effect (73). Nbs have also proven to be advantageous targeting contrast agents for optical molecular imaging, which is more cost-effective than other imaging methods. For example, an Nb to EGFR labeled with the near-infrared fluorophore IRDye800CW produced a clear delineation of tumor xenografts in mice, just 30–120 min after administration, while cetuximab labeled with the same fluorophore reached a less homogeneous distribution in the tumor stroma and required longer time for accumulation and clearance (74). Similarly, a VHH against the epidermal growth factor receptor 2 (HER2) was ~20 times faster and yielded a clearer images than trastuzumab for optical detection of human breast tumor xenografts (75). These imaging techniques have been also applied to monitor inflammatory diseases, such as arteriosclerosis and arthritis and to visualize the antitumor immune response (76–79). The methods used to conjugate the Nbs to the imaging probes will be discussed in the following section.

In biosensor, the interaction of the biological recognition component with the target analyte is converted into an electrical or optical signal, because it changes the physicochemical properties of the sensor surface. As we have seen, the great stability of Nbs adds to a better performance and extend the shelf-life of biosensors (54), but their small size (4 nm × 2.5 nm × 3 nm) also contributes to obtaining higher coating density on the sensor surface, which, together with their oriented immobilization has been shown to improve the biosensors performance (80). Controlled immobilization of Nbs onto biosensor surfaces have been accomplished by C-terminal alkyne function *via* Expressed Protein Ligation (81) (see below) and *in vivo* biotinylated Nbs bound to streptavidin (50). Also, the compact size of Nbs enabled their direct use as templates to synthesis highly derivatized gold nanoparticles that were incorporated into microelectrodes and used to detect the analyte by changes on the tunneling current of the gold-antibody networks. Using Nbs and IgG against cholera toxin β-subunit, the gold nanoparticles, templated and formed with both types of antibodies, showed functional recognition of the toxin. However, while the close packing of the Nb nanoparticles made it possible to detect the very low concentrations of the toxin in the 5–50 pg/mL range, negligible signals were obtained with the IgG particles (82).

The reduced size of Nbs proved to be an asset for the development of homogeneous immunoassays base on Förster resonance energy transfer (FRET). Indeed, the efficiency of FRET is highly dependent on the distance between the donor and acceptor fluorophores and rapidly vanishes when the gap is larger than 10 nm. This is the case of sandwich assays set up with whole IgG molecules; however, using a pair of Nbs to EGFR conjugated to a terbium cryptate (Lumi4-Tb) and quantum dots, it was possible to develop a mix-and measure time-gate FRET assay for this biomarker that detected, after 1 h incubation, diagnostic relevant concentrations of circulating EGFR in biological fluids (83). In another study, surface residues selected based on the crystallographic structure of an Nb against the nuclear pore complex (NPC), were mutated to cysteine and used to conjugate fluorescent dyes close to the antigen-binding site. In this way, they produced imaging reagents that could position fluorophores as close as 1–2 nm of NPC targets, which allowed to obtain super resolution images of the NPC using STORM imaging techniques (84).

The minimal size of Nbs may not always be an advantage. This is the case for the isolation of Nbs against small compounds, which are a huge and relevant group of analytes of toxicological, medical, and environmental analytical interest. While the smaller number of CDRs does not seem to threaten the ability of Nbs to bind macromolecular antigens with high affinity, the lack of a light chain may hamper their ability to bind small molecules (haptens). Indeed, conventional antibodies typically bind haptens at the interface of the VH–VL domains (42), and different studies have consistently found that the camelid immune response against small molecules is dominated by conventional IgG1, with lower titers of the IgG2 and IgG3 monodomain isotypes (57, 85, 86). There is very little information on the way in which Nbs bind small molecules, with only three hapten–VHH structures available, corresponding to the azo dyes Reactive Red 1 (733 Da) and Reactive Red 6 (717 Da), and the chemotherapy agent methotrexate (454 Da) (42, 87, 88). There is a great deal of variation in the combining site (**Figure 5**). Reactive Red 1 accommodates in a lateral fashion in a groove formed between CDRs 2 and 3. Reactive Red 6 binds in a cavity formed by the three CDRs, while the cupper atoms of the hapten interact with two histidines of CDR1. Interestingly, methotrexate is bound in a non-canonical way, being deeply buried in the structure of the Nb in a "tunnel" roofed by CDR1 and closed by residues in a loop of FR3 that the authors identified as CDR4, which participates in direct and critical interactions with the hapten. Indeed, the absence of some residues of this loop causes a loss of up to 1,000-fold in the binding affinity. Surprisingly, the

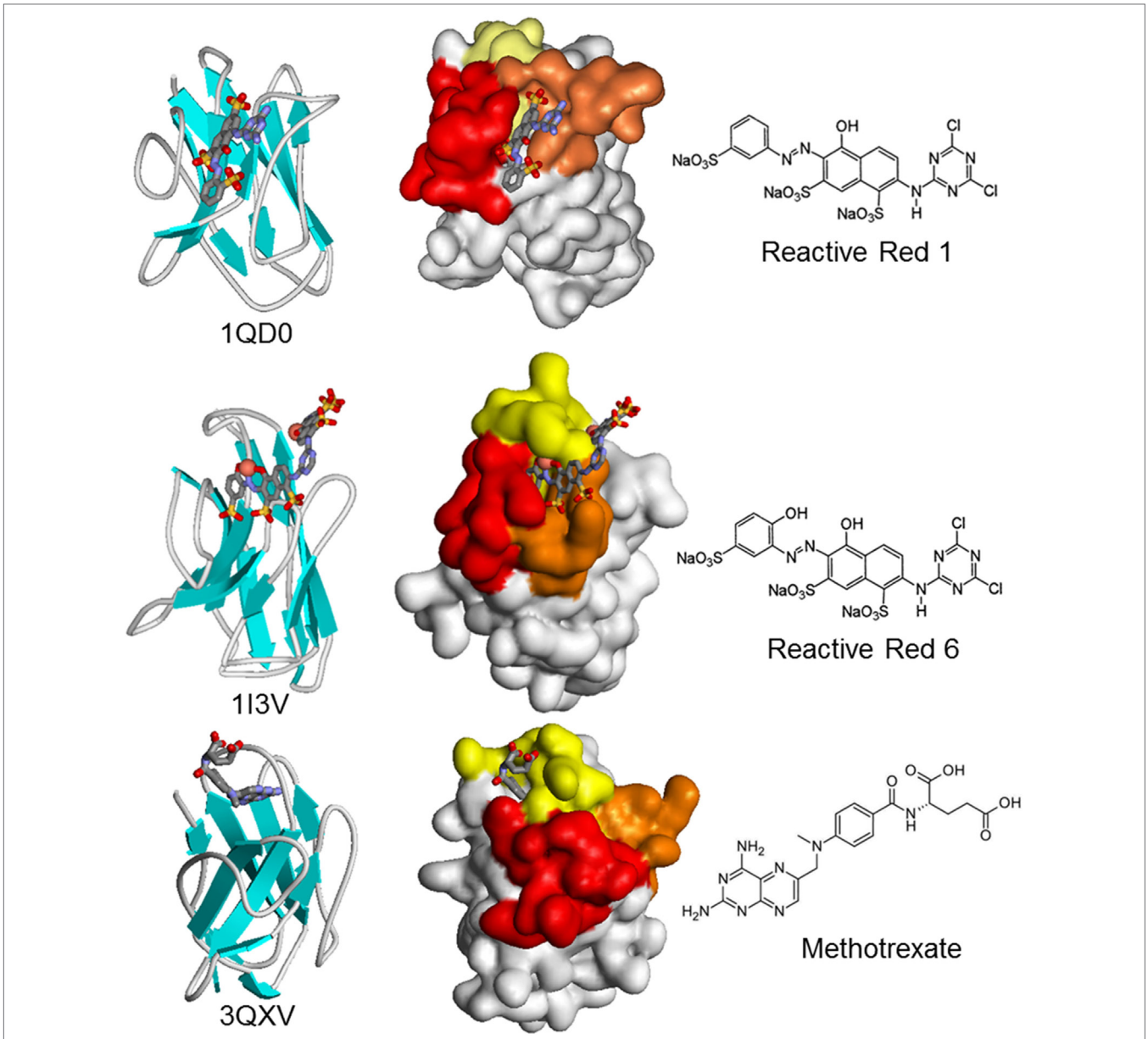

FIGURE 5 | Schematic and surface representation of three VHH structures in complex with haptens (CPK). In the surface representation, CDR1, CDR2, and CDR3 are shown in yellow, orange, and red, respectively. Upon crystallization, two molecules of Reactive Red 6 reacted through the triazine group to form a dimer of the dye.

VHH–hapten complexes present a total change in solvent accessible surface area upon binding that is larger than that observed for conventional antibody–hapten complexes, particularly for methotrexate that buries 895 Å^2 (42).

Despite the unfavorable HcAb immune response against haptens, high-affinity Nbs to a diverse group of small compounds have been generated and used to develop highly sensitive immunoassays (low ng/mL to pg/mL range). Those compounds include the toxins 15-acetyldeoxynivalenol (338 Da), ochratoxin A (404 Da), and aflatoxin B1 (312 Da); the drug methotrexate (454 Da); and the environmental contaminants triclocarban (316 Da), 3-phenoxybenzoic acid (214 Da), tetrabromobisphenol A (543 Da), and brominated diphenyl ether-47 (486 Da), reviewed by Bever et al. (89). In all cases, these Nbs were selected from immune phage display libraries by competitive selection with the free analyte. Recently, using the cyanotoxin microcystin-LR (995 Da) as a model hapten and a high-throughput screening, we compared this way of selection with two additional strategies. We found that selecting for Nbs with the slowest k_{off} for the immobilized hapten allowed us to attain a detection limit of 50 pg/mL, which was 10-fold better that the one obtained using the Nbs isolated by competitive selection (90). While the usefulness of this

approach still needs to be demonstrated for other haptens, alternative methods for the selection of anti-hapten Nbs are needed, because, conversely to what happens with other antigens, failures in the generation of Nbs that recognize small molecules in solution are common (89). The reasons underlining these failures are unknown, but additional structural studies of small analyte–Nb complexes will help to understand this interaction and allow a more rational design of immunizing and selecting haptens.

Nbs AS MULTIPURPOSE AFFINITY BUILDING DOMAINS

For many analytical and diagnostics applications Nbs have been directly used as phage borne antibody fragments. The M13 phage particle, commonly used for phage display, has ~2,700 copies of the pVIII protein providing a large surface for tracer attachment, which translates in higher assay sensitivity that can be up to two orders of magnitude better than that obtained with the soluble Nb (91). Likewise, the phage DNA can be used for ultrasensitive detection of the phage borne antibody using real-time PCR in different immunoassay formats, which also extends the dynamic range of the assay in several orders of magnitude (92, 93). Nevertheless, being the smallest antibody fragments, VHHs are ideal candidates for building chimeric recombinant proteins for analytical and diagnostic applications. Nbs have been produce as recombinant fusion proteins with hyperactive mutated versions of the alkaline phosphatase (AP) of *E. coli* (94). The combination of target binding with signal transduction domains reduces the number of steps in immunoassay applications (95), and due to the spontaneous dimerization of AP the functional affinity of the Nb partner increases significantly, improving the assay sensitivity. Surface plasmon resonance measurement of the interaction of five VHHs to different bacterial toxins showed in all cases that the K_D of the VHH–AP fusion was roughly an order of magnitude lower than that of the parent Nb (96). Nbs have also been produced with good yields as bioconjugates of the biotin binding protein rhizavidin and employed as ready-to-use reagents in sandwich immunoassays (97). In another study, Nbs have been fused to bacterial cellulose-binding domains (CBD) for paper based analytical applications. The pentamerizing subunit of verotoxin B was used as scaffold to produce pentavalent constructs and was sandwiched between an anti-*Staphylococcus aureus* VHH and the CBD. The bispecific pentavalent recombinant construct was anchored to a cellulose filter surface through the interaction of the CBD domains providing high avidity for the detection of the bacteria in a flow-through device (98). In an interesting proof of concept, an Nb to red fluorescent protein was expressed as a fusion protein with the magnetosome protein MamC in the magnetite-synthesizing bacterium *Magnetospirillum gryphiswaldense*. This generated Nb decorated biogenic magnetic bioparticles that were ready to be used *in vitro* to pull-down antigens from complex cell extracts (99). Genetic fusion of VHHs to fluorescent proteins, termed chromobodies, have also been devised for live cell microscopy. In a first demonstration, Rothbauer et al. fused and anti-green fluorescent protein (GFP) VHH with the monomeric fluorescent red protein and showed that the chimeric recombinant Nb could detect and track different cell proteins fused to GFP in different cell compartments (100). Recently, zebrafish lines expressing chromobodies were generated and used to captured full localization dynamics of the endogenous targets in the live animal (101).

Nanobodies have also been conjugated to fluorophores and radionuclides for immunosensing applications using different strategies that allow site-specific derivatization. We have already discussed the *in vivo* biotinylation of Nbs as a versatile strategy that facilitates their high-throughput screening but also their upstream applications. The addition of a cysteine residue at the carboxyl-terminus has also been used to prepared Nb conjugates. The paired cysteine promotes the spontaneous dimerization of the Nb, but this disulfide bridge can be selective reduced using 2-mercaptoethylamine, allowing the conjugation to maleimide probes with preservation of the VHH functionality (102). A particularly powerful approach is the site-specific sortase-mediated ligation. In this approach, the Nb is expressed with a C-terminal sequence corresponding to the recognition motif of the sortase, commonly -LPXTG for *S. aureus* sortase A or -LPXTA for *Streptococcus pyogenes* sortase A. After incubation with the enzyme, the C-terminal residue is cleaved and a thioester Nb-sortase intermediate is formed, which is resolved by a nucleophilic attack of a short poly-glycine sequence of a protein or peptide conjugate (103) (**Figure 6**). This strategy was used to conjugate an anti-HER2 Nb to three different imaging probes, the chelating compounds of ^{111}In and ^{68}Ga for SPECT and PET, respectively, and the fluorescent dye Cy5 for optical molecular imaging. All three conjugates were fully functional and facilitated the attainment of high-contrast images of xenografted tumors after 1 h incubation (104). Sortase has also been used to label Nbs to Mac1 (CD11b/CD18) and class II MHC with ^{18}F and ^{64}Cu for PET studies. Since these markers are highly expressed in myeloid cells, which are recruited to the tumor microenvironment as part of the immune response, these antibodies allowed clear visualization of the tumors with remarkable specificity, in both, xenogeneic and syngeneic mouse models. Since the course of the antitumor immune response would be affected by therapy, the method may provide additional valuable information for the evaluation of the treatment (78). Sortase-mediated reactions were also used for direct attachment of Nbs in a site-specific manner to graphene oxide nanosheets for the rapid analysis of cell populations. To this end, the graphene oxide surface was initially derivatized with diaminopolyethylene glycol, which was reacted with dibenzocyclooctyne-*N*-hydroxysuccinimidyl ester to make it "click chemistry-ready." On the other hand, a sortase-mediated reaction was used to conjugate the Nbs against different leukocyte subpopulations to a Gly_3 peptide equipped with a TAMRA fluorophore and an azide group for the click chemistry reaction. The graphene sheets derivatized with different Nbs were arranged in tandem in a flow chamber, which allowed the characterization of the target cells populations from tiny (30 μL) volumes of blood (105). Intein-mediated protein ligation has also been used to introduce site-specific modifications at the C-terminus of the Nb molecule. Good cytoplasmic expression of an Nb to vascular cell adhesion molecule 1 fused to an intein equipped with a chitin binding domain was obtained in *E. coli* Shuffle T7 cells. The fusion protein was then immobilized onto

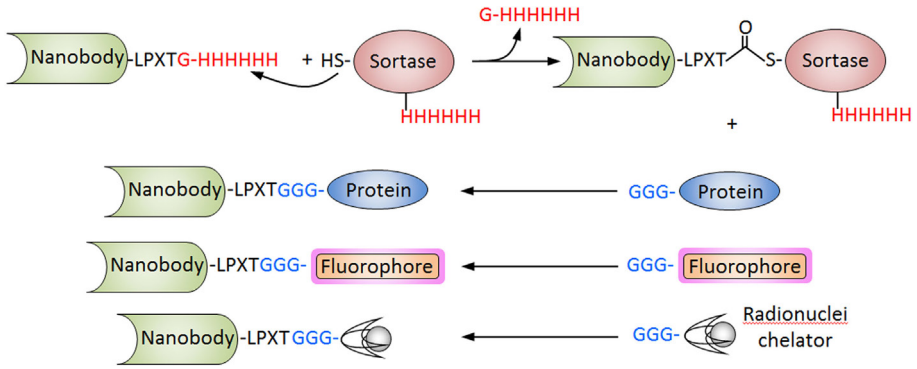

FIGURE 6 | Sortase-mediated conjugation of nanobodies (Nbs). The procedure is schematized for the *Staphylococcus aureus* sortase. The Nb is produced with the C-terminal tag (LPXTG) and is incubated with the recombinant sortase that cleaves the Thr–Gly bond forming an acyl intermediate. The nucleophilic attack of the poly-Gly stretch of the partner protein, fluorophore of chelating compound breaks the thioester forming conjugate. The hexa His tag in the Nb and sortase is used to separate the unreacted Nb and the sortase from the final reaction.

chitin-agarose and self-cleavage was induced by incubation with cysteine-alkyne, releasing the Nb modified with a clickable alkyne function (106). Using this procedure, biosensors for detecting this atherosclerosis biomarker were generated using a click chemistry reaction that enable the oriented immobilization of the modified Nb onto azide-derivatized silicon baffles or surface plasmon resonance chips (81).

CONCLUSION

In the previous sections, we have discussed the distinctive properties of Nbs and recent developments that highlight their enormous potential as immunoreagents. This becomes evident, by the exponential growth in the number of studies reporting their application in innovative immunodetection formats. Nbs have a broad recognition capability and bind their antigens with affinity values that rival those of conventional antibodies. The possibility of comprehensively representing the immune specific repertoire in phage libraries is perhaps the single most outstanding property of the Nb technology. This is particularly needed when not just binding, but epitope specific recognition is required, the case for the differential diagnosis of related pathogens, disease-linked conformation as is determinants, monitoring of chemically similar analytes, etc. In spite of that, some antigens will still require special considerations. As we have seen, new studies will be necessary to improve the rate of success in the preparation of Nbs to small analytes. Similarly, the generation of Nbs against native epitopes on difficult targets, such as cell receptors, may also face some limitations, particularly when recombinant soluble antigens are used. Nbs have a strict conformation-dependent recognition of their epitopes, and the native folding of the antigen can be altered during the preparation of the immunogen, or if direct adsorption onto solid phase is used during panning or screening (46). The existence of dromedary (Dubca ATCC® CRL-2276) and alpaca cell lines (107) that can be used as transfection carriers for immunization, in conjunction with streamlined methods of screening on antigen-expressing cells (48) may offer a solid alternative to overcome these limitations.

The outstanding properties of Nbs will continue to promote innovation, enabling completely novel types of immunodetection developments in research and commercial applications. While the size of the analytical and diagnostic antibody market is only a fraction of the therapeutic antibody business, this is still a multi-billion dollar competitive market. With the recent expiration of the original patents on camelid antibodies and the rapid progress in the technology for their production and selection, we foresee a growing interest of the industry to incorporate Nbs as a new generation of immunoreagents to add a competitive edge to their products, increase robustness, facilitate automation, and produce improved diagnostics.

Finally, Nbs will offer unsurpassed opportunities for standardization. Owing to their simplicity, high yield and straightforward production by bacterial fermentation, once selected and validated for their intended purpose, their ~400 bp DNA sequence will be all that would be required to reproduce their specificity over the years, and in any laboratory in the world. With the continued drop in the cost of synthetic genes, this will also allow the "electronic" exchange of highly standardize binders, avoiding the cost and regulatory inconveniences of shipping hybridomas or limited amounts of protein antibodies. This perfectly fulfills the claims of the scientific community expressed by Bradbury, Plückthun, and 110 cosignatories about the need of advancing toward the use of validated recombinant antibodies that will allow the user community to avoid the frustration and monetary waste caused by the poorly characterized and ill-defined commercial antibodies (108).

AUTHOR CONTRIBUTIONS

GG-S—contributed to the conception, design, writing, and revision of the manuscript. MR and ST—contributed to the writing and revision of the manuscript.

FUNDING

This work was supported with funds provided by grants CSIC 984 UdelaR.

REFERENCES

1. Yalow RS, Berson SA. Assay of plasma insulin in human subjects by immunological methods. *Nature* (1959) 184(Suppl 21):1648–9. doi:10.1038/1841648b0
2. Köhler G, Milstein C. Continuous cultures of fused cells secreting antibody of predefined specificity. *Nature* (1975) 256:495–7. doi:10.1038/256495a0
3. Winter G, Griffiths AD, Hawkins RE, Hoogenboom HR. Making antibodies by phage display technology. *Annu Rev Immunol* (1994) 12:433–55. doi:10.1146/annurev.iy.12.040194.002245
4. Rader C, Barbas CF III. Phage display of combinatorial antibody libraries. *Curr Opin Biotechnol* (1997) 8:503–8. doi:10.1016/S0958-1669(97)80075-4
5. Finlay WJ, Almagro JC. Natural and man-made V-gene repertoires for antibody discovery. *Front Immunol* (2012) 3:342. doi:10.3389/fimmu.2012.00342
6. Teillaud JL. From whole monoclonal antibodies to single domain antibodies: think small. *Methods Mol Biol* (2012) 911:3–13. doi:10.1007/978-1-61779-968-6_1
7. Gupta SK, Shukla P. Microbial platform technology for recombinant antibody fragment production: a review. *Crit Rev Microbiol* (2017) 43:31–42. doi:10.3109/1040841X.2016.1150959
8. Hamers-Casterman C, Atarhouch T, Muyldermans S, Robinson G, Hamers C, Songa EB, et al. Naturally occurring antibodies devoid of light chains. *Nature* (1993) 363:446–8. doi:10.1038/363446a0
9. De Simone EA, Saccodossi N, Ferrari A, Leoni J. Development of ELISAs for the measurement of IgM and IgG subclasses in sera from llamas (*Lama glama*) and assessment of the humoral immune response against different antigens. *Vet Immunol Immunopathol* (2008) 126:64–73. doi:10.1016/j.vetimm.2008.06.015
10. Blanc MR, Anouassi A, Ahmed Abed M, Tsikis G, Canepa S, Labas V, et al. A one-step exclusion-binding procedure for the purification of functional heavy-chain and mammalian-type gamma-globulins from camelid sera. *Biotechnol Appl Biochem* (2009) 54:207–12. doi:10.1042/BA20090208
11. Greenberg AS, Avila D, Hughes M, Hughes A, Mckinney EC, Flajnik MF. A new antigen receptor gene family that undergoes rearrangement and extensive somatic diversification in sharks. *Nature* (1995) 374:168–73. doi:10.1038/374168a0
12. Roux KH, Greenberg AS, Greene L, Strelets L, Avila D, Mckinney EC, et al. Structural analysis of the nurse shark (new) antigen receptor (NAR): molecular convergence of NAR and unusual mammalian immunoglobulins. *Proc Natl Acad Sci U S A* (1998) 95:11804–9. doi:10.1073/pnas.95.20.11804
13. Feige MJ, Grawert MA, Marcinowski M, Hennig J, Behnke J, Auslander D, et al. The structural analysis of shark IgNAR antibodies reveals evolutionary principles of immunoglobulins. *Proc Natl Acad Sci U S A* (2014) 111:8155–60. doi:10.1073/pnas.1321502111
14. Muyldermans S, Atarhouch T, Saldanha J, Barbosa JA, Hamers R. Sequence and structure of VH domain from naturally occurring camel heavy chain immunoglobulins lacking light chains. *Protein Eng* (1994) 7:1129–35. doi:10.1093/protein/7.9.1129
15. Nguyen VK, Hamers R, Wyns L, Muyldermans S. Camel heavy-chain antibodies: diverse germline V(H)H and specific mechanisms enlarge the antigen-binding repertoire. *EMBO J* (2000) 19:921–30. doi:10.1093/emboj/19.5.921
16. Stanfield RL, Dooley H, Flajnik MF, Wilson IA. Crystal structure of a shark single-domain antibody V region in complex with lysozyme. *Science* (2004) 305:1770–3. doi:10.1126/science.1101148
17. Lauwereys M, Arbabi Ghahroudi M, Desmyter A, Kinne J, Holzer W, De Genst E, et al. Potent enzyme inhibitors derived from dromedary heavy-chain antibodies. *EMBO J* (1998) 17:3512–20. doi:10.1093/emboj/17.13.3512
18. Henderson KA, Streltsov VA, Coley AM, Dolezal O, Hudson PJ, Batchelor AH, et al. Structure of an IgNAR-AMA1 complex: targeting a conserved hydrophobic cleft broadens malarial strain recognition. *Structure* (2007) 15:1452–66. doi:10.1016/j.str.2007.09.011
19. Lutje Hulsik D, Liu YY, Strokappe NM, Battella S, El Khattabi M, Mccoy LE, et al. A gp41 MPER-specific llama VHH requires a hydrophobic CDR3 for neutralization but not for antigen recognition. *PLoS Pathog* (2013) 9:e1003202. doi:10.1371/journal.ppat.1003202
20. Daley-Bauer LP, Purdy SR, Smith MC, Gagliardo LF, Davis WC, Appleton JA. Contributions of conventional and heavy-chain IgG to immunity in fetal, neonatal, and adult alpacas. *Clin Vaccine Immunol* (2010) 17:2007–15. doi:10.1128/CVI.00287-10
21. De Genst E, Silence K, Decanniere K, Conrath K, Loris R, Kinne J, et al. Molecular basis for the preferential cleft recognition by dromedary heavy-chain antibodies. *Proc Natl Acad Sci U S A* (2006) 103:4586–91. doi:10.1073/pnas.0505379103
22. Flajnik MF, Deschacht N, Muyldermans S. A case of convergence: why did a simple alternative to canonical antibodies arise in sharks and camels? *PLoS Biol* (2011) 9:e1001120. doi:10.1371/journal.pbio.1001120
23. Decanniere K, Desmyter A, Lauwereys M, Ghahroudi MA, Muyldermans S, Wyns L. A single-domain antibody fragment in complex with RNase A: non-canonical loop structures and nanomolar affinity using two CDR loops. *Structure* (1999) 7:361–70. doi:10.1016/S0969-2126(99)80049-5
24. Dooley H, Flajnik MF, Porter AJ. Selection and characterization of naturally occurring single-domain (IgNAR) antibody fragments from immunized sharks by phage display. *Mol Immunol* (2003) 40:25–33. doi:10.1016/S0161-5890(03)00084-1
25. Dumoulin M, Last AM, Desmyter A, Decanniere K, Canet D, Larsson G, et al. A camelid antibody fragment inhibits the formation of amyloid fibrils by human lysozyme. *Nature* (2003) 424:783–8. doi:10.1038/nature01870
26. Deckers N, Saerens D, Kanobana K, Conrath K, Victor B, Wernery U, et al. Nanobodies, a promising tool for species-specific diagnosis of *Taenia solium* cysticercosis. *Int J Parasitol* (2009) 39:625–33. doi:10.1016/j.ijpara.2008.10.012
27. Al Qaraghuli MM, Ferro VA. Analysis of the binding loops configuration and surface adaptation of different crystallized single-domain antibodies in response to various antigens. *J Mol Recognit* (2017) 30(4):e2592. doi:10.1002/jmr.2592
28. Dooley H, Flajnik MF. Shark immunity bites back: affinity maturation and memory response in the nurse shark, *Ginglymostoma cirratum*. *Eur J Immunol* (2005) 35:936–45. doi:10.1002/eji.200425760
29. Crouch K, Smith LE, Williams R, Cao W, Lee M, Jensen A, et al. Humoral immune response of the small-spotted catshark, *Scyliorhinus canicula*. *Fish Shellfish Immunol* (2013) 34:1158–69. doi:10.1016/j.fsi.2013.01.025
30. Zielonka S, Weber N, Becker S, Doerner A, Christmann A, Christmann C, et al. Shark attack: high affinity binding proteins derived from shark vNAR domains by stepwise in vitro affinity maturation. *J Biotechnol* (2014) 191:236–45. doi:10.1016/j.jbiotec.2014.04.023
31. Harmsen MM, Ruuls RC, Nijman IJ, Niewold TA, Frenken LG, De Geus B. Llama heavy-chain V regions consist of at least four distinct subfamilies revealing novel sequence features. *Mol Immunol* (2000) 37:579–90. doi:10.1016/S0161-5890(00)00081-X
32. Achour I, Cavelier P, Tichit M, Bouchier C, Lafaye P, Rougeon F. Tetrameric and homodimeric camelid IgGs originate from the same IgH locus. *J Immunol* (2008) 181:2001–9. doi:10.4049/jimmunol.181.3.2001
33. Deschacht N, De Groeve K, Vincke C, Raes G, De Baetselier P, Muyldermans S. A novel promiscuous class of camelid single-domain antibody contributes to the antigen-binding repertoire. *J Immunol* (2010) 184:5696–704. doi:10.4049/jimmunol.0903722
34. Lee YK, Brewer JW, Hellman R, Hendershot LM. BiP and immunoglobulin light chain cooperate to control the folding of heavy chain and ensure the fidelity of immunoglobulin assembly. *Mol Biol Cell* (1999) 10:2209–19. doi:10.1091/mbc.10.7.2209
35. Nguyen VK, Hamers R, Wyns L, Muyldermans S. Loss of splice consensus signal is responsible for the removal of the entire C(H)1 domain of the functional camel IGG2A heavy-chain antibodies. *Mol Immunol* (1999) 36:515–24. doi:10.1016/S0161-5890(99)00067-X
36. Muyldermans S. Nanobodies: natural single-domain antibodies. *Annu Rev Biochem* (2013) 82:775–97. doi:10.1146/annurev-biochem-063011-092449
37. Matheson LS, Osborn MJ, Smith JA, Corcos D, Hamon M, Chaouaf R, et al. Light chain-deficient mice produce novel multimeric heavy-chain-only IgA by faulty class switching. *Int Immunol* (2009) 21:957–66. doi:10.1093/intimm/dxp062
38. Schusser B, Collarini EJ, Pedersen D, Yi H, Ching K, Izquierdo S, et al. Expression of heavy chain-only antibodies can support B-cell development in light chain knockout chickens. *Eur J Immunol* (2016) 46:2137–48. doi:10.1002/eji.201546171
39. Rossotti MA, Gonzalez-Techera A, Guarnaschelli J, Yim L, Camacho X, Fernandez M, et al. Increasing the potency of neutralizing single-domain antibodies by functionalization with a CD11b/CD18 binding domain. *mAbs* (2015) 7:820–8. doi:10.1080/19420862.2015.1068491
40. Rossotti MA, Pirez M, Gonzalez-Techera A, Cui Y, Bever CS, Lee KS, et al. Method for sorting and pairwise selection of nanobodies for the development

of highly sensitive sandwich immunoassays. *Anal Chem* (2015) 87:11907–14. doi:10.1021/acs.analchem.5b03561
41. Bond CJ, Wiesmann C, Marsters JC Jr, Sidhu SS. A structure-based database of antibody variable domain diversity. *J Mol Biol* (2005) 348:699–709. doi:10.1016/j.jmb.2005.02.063
42. Fanning SW, Horn JR. An anti-hapten camelid antibody reveals a cryptic binding site with significant energetic contributions from a nonhypervariable loop. *Protein Sci* (2011) 20:1196–207. doi:10.1002/pro.648
43. Kunz P, Flock T, Soler N, Zaiss M, Vincke C, Sterckx Y, et al. Exploiting sequence and stability information for directing nanobody stability engineering. *Biochim Biophys Acta* (2017) 1861:2196–205. doi:10.1016/j.bbagen.2017.06.014
44. Deschaght P, Vintem AP, Logghe M, Conde M, Felix D, Mensink R, et al. Large diversity of functional nanobodies from a camelid immune library revealed by an alternative analysis of next-generation sequencing data. *Front Immunol* (2017) 8:420. doi:10.3389/fimmu.2017.00420
45. Turner KB, Naciri J, Liu JL, Anderson GP, Goldman ER, Zabetakis D. Next-generation sequencing of a single domain antibody repertoire reveals quality of phage display selected candidates. *PLoS One* (2016) 11:e0149393. doi:10.1371/journal.pone.0149393
46. Pardon E, Laeremans T, Triest S, Rasmussen SG, Wohlkonig A, Ruf A, et al. A general protocol for the generation of nanobodies for structural biology. *Nat Protoc* (2014) 9:674–93. doi:10.1038/nprot.2014.039
47. Beckett D, Kovaleva E, Schatz PJ. A minimal peptide substrate in biotin holoenzyme synthetase-catalyzed biotinylation. *Protein Sci* (1999) 8:921–9. doi:10.1110/ps.8.4.921
48. Rossotti M, Tabares S, Alfaya L, Leizagoyen C, Moron G, Gonzalez-Sapienza G. Streamlined method for parallel identification of single domain antibodies to membrane receptors on whole cells. *Biochim Biophys Acta* (2015) 1850: 1397–404. doi:10.1016/j.bbagen.2015.03.009
49. Even-Desrumeaux K, Fourquet P, Secq V, Baty D, Chames P. Single-domain antibodies: a versatile and rich source of binders for breast cancer diagnostic approaches. *Mol Biosyst* (2012) 8:2385–94. doi:10.1039/c2mb25063b
50. Li M, Zhu M, Zhang C, Liu X, Wan Y. Uniform orientation of biotinylated nanobody as an affinity binder for detection of *Bacillus thuringiensis* (Bt) Cry1Ac toxin. *Toxins (Basel)* (2014) 6:3208–22. doi:10.3390/toxins6123208
51. Zhu M, Gong X, Hu Y, Ou W, Wan Y. Streptavidin-biotin-based directional double nanobody sandwich ELISA for clinical rapid and sensitive detection of influenza H5N1. *J Transl Med* (2014) 12:352. doi:10.1186/s12967-014-0352-5
52. Ladenson RC, Crimmins DL, Landt Y, Ladenson JH. Isolation and characterization of a thermally stable recombinant anti-caffeine heavy-chain antibody fragment. *Anal Chem* (2006) 78:4501–8. doi:10.1021/ac058044j
53. van der Linden RH, Frenken LG, De Geus B, Harmsen MM, Ruuls RC, Stok W, et al. Comparison of physical chemical properties of llama VHH antibody fragments and mouse monoclonal antibodies. *Biochim Biophys Acta* (1999) 1431:37–46. doi:10.1016/S0167-4838(99)00030-8
54. Singh A, Pasha SK, Manickam P, Bhansali S. Single-domain antibody based thermally stable electrochemical immunosensor. *Biosens Bioelectron* (2016) 83:162–8. doi:10.1016/j.bios.2016.04.054
55. Dumoulin M, Conrath K, Van Meirhaeghe A, Meersman F, Heremans K, Frenken LG, et al. Single-domain antibody fragments with high conformational stability. *Protein Sci* (2002) 11:500–15. doi:10.1110/ps.34602
56. Ewert S, Cambillau C, Conrath K, Pluckthun A. Biophysical properties of camelid V(HH) domains compared to those of human V(H)3 domains. *Biochemistry* (2002) 41:3628–36. doi:10.1021/bi011239a
57. Tabares-da Rosa S, Rossotti M, Carleiza C, Carrion F, Pritsch O, Ahn KC, et al. Competitive selection from single domain antibody libraries allows isolation of high-affinity antihapten antibodies that are not favored in the llama immune response. *Anal Chem* (2011) 83:7213–20. doi:10.1021/ac201824z
58. Perez JM, Renisio JG, Prompers JJ, Van Platerink CJ, Cambillau C, Darbon H, et al. Thermal unfolding of a llama antibody fragment: a two-state reversible process. *Biochemistry* (2001) 40:74–83. doi:10.1021/bi0009082
59. Goldman ER, Brozozog-Lee PA, Zabetakis D, Turner KB, Walper SA, Liu JL, et al. Negative tail fusions can improve ruggedness of single domain antibodies. *Protein Expr Purif* (2014) 95:226–32. doi:10.1016/j.pep.2014.01.003
60. Turner KB, Alves NJ, Medintz IL, Walper SA. Improving the targeting of therapeutics with single-domain antibodies. *Expert Opin Drug Deliv* (2016) 13:561–70. doi:10.1517/17425247.2016.1133583
61. Akazawa-Ogawa Y, Takashima M, Lee YH, Ikegami T, Goto Y, Uegaki K, et al. Heat-induced irreversible denaturation of the camelid single domain VHH antibody is governed by chemical modifications. *J Biol Chem* (2014) 289:15666–79. doi:10.1074/jbc.M113.534222
62. Akazawa-Ogawa Y, Uegaki K, Hagihara Y. The role of intra-domain disulfide bonds in heat-induced irreversible denaturation of camelid single domain VHH antibodies. *J Biochem* (2016) 159:111–21. doi:10.1093/jb/mvv082
63. Dona V, Urrutia M, Bayardo M, Alzogaray V, Goldbaum FA, Chirdo FG. Single domain antibodies are specially suited for quantitative determination of gliadins under denaturing conditions. *J Agric Food Chem* (2010) 58:918–26. doi:10.1021/jf902973c
64. He T, Wang Y, Li P, Zhang Q, Lei J, Zhang Z, et al. Nanobody-based enzyme immunoassay for aflatoxin in agro-products with high tolerance to cosolvent methanol. *Anal Chem* (2014) 86:8873–80. doi:10.1021/ac502390c
65. Kim HJ, Mccoy MR, Majkova Z, Dechant JE, Gee SJ, Tabares-Da Rosa S, et al. Isolation of alpaca anti-hapten heavy chain single domain antibodies for development of sensitive immunoassay. *Anal Chem* (2012) 84:1165–71. doi:10.1021/ac2030255
66. Vaneycken I, D'huyvetter M, Hernot S, De Vos J, Xavier C, Devoogdt N, et al. Immuno-imaging using nanobodies. *Curr Opin Biotechnol* (2011) 22:877–81. doi:10.1016/j.copbio.2011.06.009
67. Chakravarty R, Goel S, Cai W. Nanobody: the "magic bullet" for molecular imaging? *Theranostics* (2014) 4:386–98. doi:10.7150/thno.8006
68. Revets H, De Baetselier P, Muyldermans S. Nanobodies as novel agents for cancer therapy. *Expert Opin Biol Ther* (2005) 5:111–24. doi:10.1517/14712598.5.1.111
69. Hassanzadeh-Ghassabeh G, Devoogdt N, De Pauw P, Vincke C, Muyldermans S. Nanobodies and their potential applications. *Nanomedicine (Lond)* (2013) 8:1013–26. doi:10.2217/nnm.13.86
70. Hoefman S, Ottevaere I, Baumeister J, Sargentini-Maier M. Pre-clinical intravenous serum pharmacokinetics of albumin binding and non-half-life extended nanobodies®. *Antibodies* (2015) 4:141. doi:10.3390/antib4030141
71. Kruwel T, Nevoltris D, Bode J, Dullin C, Baty D, Chames P, et al. In vivo detection of small tumour lesions by multi-pinhole SPECT applying a (99m) Tc-labelled nanobody targeting the epidermal growth factor receptor. *Sci Rep* (2016) 6:21834. doi:10.1038/srep21834
72. Vosjan MJ, Perk LR, Roovers RC, Visser GW, Stigter-Van Walsum M, Van Bergen En Henegouwen PM, et al. Facile labelling of an anti-epidermal growth factor receptor nanobody with 68Ga via a novel bifunctional desferal chelate for immuno-PET. *Eur J Nucl Med Mol Imaging* (2011) 38:753–63. doi:10.1007/s00259-010-1700-1
73. Chatalic KL, Veldhoven-Zweistra J, Bolkestein M, Hoeben S, Koning GA, Boerman OC, et al. A novel (1)(1)(1)in-labeled anti-prostate-specific membrane antigen nanobody for targeted SPECT/CT imaging of prostate cancer. *J Nucl Med* (2015) 56:1094–9. doi:10.2967/jnumed.115.156729
74. Oliveira S, Van Dongen GA, Stigter-Van Walsum M, Roovers RC, Stam JC, Mali W, et al. Rapid visualization of human tumor xenografts through optical imaging with a near-infrared fluorescent anti-epidermal growth factor receptor nanobody. *Mol Imaging* (2012) 11:33–46.
75. Kijanka M, Warnders FJ, El Khattabi M, Lub-De Hooge M, Van Dam GM, Ntziachristos V, et al. Rapid optical imaging of human breast tumour xenografts using anti-HER2 VHHs site-directly conjugated to IRDye 800CW for image-guided surgery. *Eur J Nucl Med Mol Imaging* (2013) 40:1718–29. doi:10.1007/s00259-013-2471-2
76. Broisat A, Hernot S, Toczek J, De Vos J, Riou LM, Martin S, et al. Nanobodies targeting mouse/human VCAM1 for the nuclear imaging of atherosclerotic lesions. *Circ Res* (2012) 110:927–37. doi:10.1161/CIRCRESAHA.112.265140
77. Zheng F, Put S, Bouwens L, Lahoutte T, Matthys P, Muyldermans S, et al. Molecular imaging with macrophage CRIg-targeting nanobodies for early and preclinical diagnosis in a mouse model of rheumatoid arthritis. *J Nucl Med* (2014) 55:824–9. doi:10.2967/jnumed.113.130617
78. Rashidian M, Keliher EJ, Bilate AM, Duarte JN, Wojtkiewicz GR, Jacobsen JT, et al. Noninvasive imaging of immune responses. *Proc Natl Acad Sci U S A* (2015) 112:6146–51. doi:10.1073/pnas.1502609112
79. Van Elssen CH, Rashidian M, Vrbanac V, Wucherpfennig KW, El Habre Z, Sticht J, et al. Noninvasive imaging of human immune responses in a human xenograft model of graft-versus-host disease. *J Nucl Med* (2017) 58:1003–8. doi:10.2967/jnumed.116.186007

80. Zhou Y, Hu W, Peng B, Liu Y. Biomarker binding on an antibody-functionalized biosensor surface: the influence of surface properties, electric field, and coating density. *J Phys Chem C* (2014) 118:14586–94. doi:10.1021/jp501885p
81. Ta DT, Guedens W, Vranken T, Vanschoenbeek K, Steen Redeker E, Michiels L, et al. Enhanced biosensor platforms for detecting the atherosclerotic biomarker VCAM1 based on bioconjugation with uniformly oriented VCAM1-targeting nanobodies. *Biosensors (Basel)* (2016) 6:E34. doi:10.3390/bios6030034
82. Slocik JM, Kim SN, Auvil T, Goldman ER, Liu J, Naik RR. Single domain antibody templated nanoparticle resistors for sensing. *Biosens Bioelectron* (2010) 25:1908–13. doi:10.1016/j.bios.2010.01.004
83. Wegner KD, Linden S, Jin Z, Jennings TL, El Khoulati R, Van Bergen En Henegouwen PM, et al. Nanobodies and nanocrystals: highly sensitive quantum dot-based homogeneous FRET immunoassay for serum-based EGFR detection. *Small* (2014) 10:734–40. doi:10.1002/smll.201302383
84. Pleiner T, Bates M, Trakhanov S, Lee CT, Schliep JE, Chug H, et al. Nanobodies: site-specific labeling for super-resolution imaging, rapid epitope-mapping and native protein complex isolation. *Elife* (2015) 4:e11349. doi:10.7554/eLife.11349
85. Lange IG, Daxenberger A, Meyer HH. Studies on the antibody response of *Lama glama* – evaluation of the binding capacity of different IgG subtypes in ELISAs for clenbuterol and BSA. *Vet Immunol Immunopathol* (2001) 83:1–9. doi:10.1016/S0165-2427(01)00376-2
86. Anderson GP, Goldman ER. TNT detection using llama antibodies and a two-step competitive fluid array immunoassay. *J Immunol Methods* (2008) 339:47–54. doi:10.1016/j.jim.2008.08.001
87. Spinelli S, Frenken LG, Hermans P, Verrips T, Brown K, Tegoni M, et al. Camelid heavy-chain variable domains provide efficient combining sites to haptens. *Biochemistry* (2000) 39:1217–22. doi:10.1021/bi991830w
88. Spinelli S, Tegoni M, Frenken L, Van Vliet C, Cambillau C. Lateral recognition of a dye hapten by a llama VHH domain. *J Mol Biol* (2001) 311:123–9. doi:10.1006/jmbi.2001.4856
89. Bever CS, Dong JX, Vasylieva N, Barnych B, Cui Y, Xu ZL, et al. VHH antibodies: emerging reagents for the analysis of environmental chemicals. *Anal Bioanal Chem* (2016) 408:5985–6002. doi:10.1007/s00216-016-9585-x
90. Pirez-Schirmer M, Rossotti MA, Badagian N, Leizagoyen C, Brena BM, Gonzalez-Sapienza GG. Comparison of three antihapten VHH selection strategies for the development of highly sensitive immunoassays for microcystins. *Anal Chem* (2017) 89:6800–6. doi:10.1021/acs.analchem.7b01221
91. Goldman ER, Anderson GP, Bernstein RD, Swain MD. Amplification of immunoassays using phage-displayed single domain antibodies. *J Immunol Methods* (2010) 352:182–5. doi:10.1016/j.jim.2009.10.014
92. Lei J, Li P, Zhang Q, Wang Y, Zhang Z, Ding X, et al. Anti-idiotypic nanobody-phage based real-time immuno-PCR for detection of hepatocarcinogen aflatoxin in grains and feedstuffs. *Anal Chem* (2014) 86:10841–6. doi:10.1021/ac5029424
93. Liu Y, Jiang D, Lu X, Wang W, Xu Y, He Q. Phage-mediated immuno-PCR for ultrasensitive detection of Cry1Ac protein based on nanobody. *J Agric Food Chem* (2016) 64:7882–9. doi:10.1021/acs.jafc.6b02978
94. Muller BH, Lamoure C, Le Du MH, Cattolico L, Lajeunesse E, Lemaitre F, et al. Improving *Escherichia coli* alkaline phosphatase efficacy by additional mutations inside and outside the catalytic pocket. *Chembiochem* (2001) 2:517–23. doi:10.1002/1439-7633(20010803)2:7/8<517::AID-CBIC517>3.0.CO;2-H
95. Wang J, Majkova Z, Bever CR, Yang J, Gee SJ, Li J, et al. One-step immunoassay for tetrabromobisphenol a using a camelid single domain antibody-alkaline phosphatase fusion protein. *Anal Chem* (2015) 87:4741–8. doi:10.1021/ac504735p
96. Swain MD, Anderson GP, Serrano-Gonzalez J, Liu JL, Zabetakis D, Goldman ER. Immunodiagnostic reagents using llama single domain antibody-alkaline phosphatase fusion proteins. *Anal Biochem* (2011) 417:188–94. doi:10.1016/j.ab.2011.06.012
97. Liu JL, Zabetakis D, Walper SA, Goldman ER, Anderson GP. Bioconjugates of rhizavidin with single domain antibodies as bifunctional immunoreagents. *J Immunol Methods* (2014) 411:37–42. doi:10.1016/j.jim.2014.06.004
98. Hussack G, Luo Y, Veldhuis L, Hall JC, Tanha J, Mackenzie R. Multivalent anchoring and oriented display of single-domain antibodies on cellulose. *Sensors (Basel)* (2009) 9:5351–67. doi:10.3390/s90705351
99. Pollithy A, Romer T, Lang C, Muller FD, Helma J, Leonhardt H, et al. Magnetosome expression of functional camelid antibody fragments (nanobodies) in *Magnetospirillum gryphiswaldense*. *Appl Environ Microbiol* (2011) 77:6165–71. doi:10.1128/AEM.05282-11
100. Rothbauer U, Zolghadr K, Tillib S, Nowak D, Schermelleh L, Gahl A, et al. Targeting and tracing antigens in live cells with fluorescent nanobodies. *Nat Methods* (2006) 3:887–9. doi:10.1038/nmeth953
101. Panza P, Maier J, Schmees C, Rothbauer U, Sollner C. Live imaging of endogenous protein dynamics in zebrafish using chromobodies. *Development* (2015) 142:1879–84. doi:10.1242/dev.118943
102. Massa S, Xavier C, De Vos J, Caveliers V, Lahoutte T, Muyldermans S, et al. Site-specific labeling of cysteine-tagged camelid single-domain antibody-fragments for use in molecular imaging. *Bioconjug Chem* (2014) 25:979–88. doi:10.1021/bc500111t
103. Theile CS, Witte MD, Blom AE, Kundrat L, Ploegh HL, Guimaraes CP. Site-specific N-terminal labeling of proteins using sortase-mediated reactions. *Nat Protoc* (2013) 8:1800–7. doi:10.1038/nprot.2013.102
104. Massa S, Vikani N, Betti C, Ballet S, Vanderhaegen S, Steyaert J, et al. Sortase A-mediated site-specific labeling of camelid single-domain antibody-fragments: a versatile strategy for multiple molecular imaging modalities. *Contrast Media Mol Imaging* (2016) 11:328–39. doi:10.1002/cmmi.1696
105. Chen GY, Li Z, Theile CS, Bardhan NM, Kumar PV, Duarte JN, et al. Graphene oxide nanosheets modified with single-domain antibodies for rapid and efficient capture of cells. *Chemistry* (2015) 21:17178–83. doi:10.1002/chem.201503057
106. Ta DT, Redeker ES, Billen B, Reekmans G, Sikulu J, Noben JP, et al. An efficient protocol towards site-specifically clickable nanobodies in high yield: cytoplasmic expression in *Escherichia coli* combined with intein-mediated protein ligation. *Protein Eng Des Sel* (2015) 28:351–63. doi:10.1093/protein/gzv032
107. Franceschi V, Jacca S, Sassu EL, Stellari FF, Van Santen VL, Donofrio G. Generation and characterization of the first immortalized alpaca cell line suitable for diagnostic and immunization studies. *PLoS One* (2014) 9:e105643. doi:10.1371/journal.pone.0105643
108. Bradbury A, Pluckthun A. Reproducibility: standardize antibodies used in research. *Nature* (2015) 518:27–9. doi:10.1038/518027a

Conflict of Interest Statement: The authors declare that the research was conducted in the absence of any commercial or financial relationships that could be construed as a potential conflict of interest.

frontiers in Immunology

REVIEW
published: 30 June 2017
doi: 10.3389/fimmu.2017.00724

Nanobodies As Tools to Understand, Diagnose, and Treat African Trypanosomiasis

Benoit Stijlemans[1,2†], Patrick De Baetselier[1,2†], Guy Caljon[3], Jan Van Den Abbeele[4], Jo A. Van Ginderachter[1,2] and Stefan Magez[1,5]*

[1] Laboratory of Cellular and Molecular Immunology, Vrije Universiteit Brussel (VUB), Brussels, Belgium, [2] Myeloid Cell Immunology Lab, VIB-UGent Center for Inflammation Research, Ghent, Belgium, [3] Laboratory of Microbiology, Parasitology and Hygiene (LMPH), University of Antwerp (UA), Antwerp, Belgium, [4] Unit of Veterinary Protozoology, Department of Biomedical Sciences, Institute of Tropical Medicine Antwerp (ITM), Antwerp, Belgium, [5] Laboratory for Biomedical Research, Ghent University Global Campus, Incheon, South Korea

OPEN ACCESS

Edited by:
Colin Roger MacKenzie, National Research Council, Canada

Reviewed by:
Toya Nath Baral, Merck Pharmaceuticals, United States
Raffael Nachbagauer, Icahn School of Medicine at Mount Sinai, United States

***Correspondence:**
Benoit Stijlemans
benoit.stijlemans@vub.be

[†]The first two authors' share coauthorship.

Specialty section:
This article was submitted to Vaccines and Molecular Therapeutics, a section of the journal Frontiers in Immunology

Received: 29 April 2017
Accepted: 08 June 2017
Published: 30 June 2017

Citation:
Stijlemans B, De Baetselier P, Caljon G, Van Den Abbeele J, Van Ginderachter JA and Magez S (2017) Nanobodies As Tools to Understand, Diagnose, and Treat African Trypanosomiasis. Front. Immunol. 8:724. doi: 10.3389/fimmu.2017.00724

African trypanosomes are strictly extracellular protozoan parasites that cause diseases in humans and livestock and significantly affect the economic development of sub-Saharan Africa. Due to an elaborate and efficient (vector)–parasite–host interplay, required to complete their life cycle/transmission, trypanosomes have evolved efficient immune escape mechanisms that manipulate the entire host immune response. So far, not a single field applicable vaccine exists, and chemotherapy is the only strategy available to treat the disease. Current therapies, however, exhibit high drug toxicity and an increased drug resistance is being reported. In addition, diagnosis is often hampered due to the inadequacy of current diagnostic procedures. In the context of tackling the shortcomings of current treatment and diagnostic approaches, nanobodies (Nbs, derived from the heavy chain-only antibodies of camels and llamas) might represent unmet advantages compared to conventional tools. Indeed, the combination of their small size, high stability, high affinity, and specificity for their target and tailorability represents a unique advantage, which is reflected by their broad use in basic and clinical research to date. In this article, we will review and discuss (i) diagnostic and therapeutic applications of Nbs that are being evaluated in the context of African trypanosomiasis, (ii) summarize new strategies that are being developed to optimize their potency for advancing their use, and (iii) document on unexpected properties of Nbs, such as inherent trypanolytic activities, that besides opening new therapeutic avenues, might offer new insight in hidden biological activities of conventional antibodies.

Keywords: nanobody, diagnosis, treatment, African trypanosomes, paratransgenesis

INTRODUCTION

African trypanosomiasis (AT), caused by strictly extracellular unicellular flagellated protozoan parasites belonging to the genus *Trypanosoma*, is a "neglected" disease of medical and veterinary importance that significantly affects the socioeconomic development of sub-Saharan Africa (1–5). Hereby, AT affects mainly remote rural areas with minimal health infrastructure and its distribution coincides mostly with the habitat of the hematophagous insect vector, i.e., the tsetse fly (*Glossina* sp.) (6). In humans, the disease is known as human African trypanosomiasis (HAT) or sleeping sickness,

and is caused by (i) *Trypanosoma brucei gambiense* (Western and central Africa) which is an anthroponotic disease with a minor role for animal reservoirs accounting for 98% of the reported HAT cases, and causing a chronic, gradually progressing disease with limited symptoms, whereby the late meningoencephalitic stage is reached after months/years of infection (7–9), and (ii) *Trypanosoma brucei rhodesiense* (Eastern/southern Africa) which is a zoonotic disease affecting mainly animals (livestock and wildlife), with humans being only occasionally infected, and representing 2% of the reported HAT cases, whereby the infections are more acute and virulent/lethal with a rapid progression (within weeks) to the late meningoencephalitic stage (3, 9–12). Hence, the zoonotic nature of *T. b. rhodesiense* infections makes them more difficult to control compared to *T. b. gambiense* infections (8, 13, 14). Animal African trypanosomiasis (AAT) or Nagana is the second form of AT affecting sub-Saharan Africa, which is mainly caused by *Trypanosoma congolense*, *Trypanosoma vivax*, and to a lesser extent *Trypanosoma brucei brucei*, whereas Surra and Dourine are also forms of AAT caused by *Trypanosoma evansi* and *Trypanosoma equiperdum*, respectively (15–17). Overall, *T. congolense* is a major constraint for livestock production in sub-Saharan Africa, whereby cattle succumb to infection primarily due to parasite-induced anemia or complications resulting from secondary, opportunistic infections (18). In addition, the estimated annual losses associated with AAT are about US$5 billion (1, 19–21), which is mainly due to a combined result of political, sociocultural, environmental, entomological, and livestock management factors (22–24). So far, chemotherapy is the only strategy available to treat the disease, whereby unique organelles of trypanosomes (glycosomes or kinetoplast) that are absent in the mammalian host or trypanosome metabolic pathways that differ from their host counterparts (carbohydrate metabolism, protein and lipid modifications, and programmed cell death) are targeted (25–27). Given that chemotherapy is associated with high drug toxicity, there is an urgent need to optimize trypanocide usage and delivery in order to decrease the risk of toxicity and/or resistance development (28–30). Control of AT is also hampered due to inefficient diagnosis of the infection especially for AAT and *T. b. rhodesiense* HAT where microscopical parasite detection (cheap but with low sensitivity), detection of the parasite's DNA (expensive but with high sensitivity), or anti-parasite antibodies remain the only available tools for diagnosis. Yet, these techniques require specialized equipment and personnel and hence are not suitable for direct use in the field. Only for *T. b. gambiense*, monitoring tools are available for both detection and staging of the disease (4, 31–33). Existing field applicable antibody-based diagnostic tests still suffer from a lack of positive predictive value and cannot differentiate between active or cured infections (32, 34, 35). Direct diagnosis aimed at parasite antigen detection is often hampered by sequestration of parasite antigens by the host's antibodies or by concealing of epitopes from the diagnostic monoclonal antibodies (mAbs) (36). Although immunodiagnostics based on antigen detection would be preferable, they are currently not available for trypanosomiasis in the field (32).

In contrast to conventional antibodies, nanobodies [Nbs or VHHs, i.e., camelid-derived single-domain antibody fragments (~15 kDa) that are selected through phage display technology and panning methodologies] (37, 38) could be used to overcome certain challenges faced by mAb-based tests (see above). Hereby, Nbs exhibit characteristic features such as (i) a nanomolar affinity for their target (39), (ii) a unique epitope recognition spectrum different from conventional antibodies, thereby allowing detection of both free antigens and those bound by host antibodies (40), (iii) high solubility (40), (iv) easy tailorability (multimerization or tagging) for molecular imaging and drug-delivery applications (41–44), and (v) small size that circumvents problems of tissue or blood–brain barrier (BBB) penetrability (44, 45). Due to these unique biochemical and biophysical properties, they are considered as promising next-generation therapeutics with great potential in pharmaceutical and industrial applications (46, 47). Indeed, Nbs are increasingly exploited in protein structure/function studies and in the development of alternative or new medical diagnostic and therapeutic applications (48, 49). Nbs also possess a relatively high thermostability (50, 51) and are consequently attractive for the development of immunodiagnostic tests that could be applicable in hot climatic conditions (i.e., sub-Saharan Africa).

In the next sections, we will give an overview of how the Nb technology can be implemented in the fight against AT both at the level of diagnosis and treatment and finally how acquired knowledge on Nbs in AT might lead to new insights in the function of conventional antibodies in the immune system.

LIFE CYCLE OF AFRICAN TRYPANOSOMES

In order to point out at which stages Nbs might be applicable to fight AT, it is appropriate to overview briefly their life cycle. African trypanosomes exhibit a digenetic life cycle, alternating between the blood/tissues of the mammalian host and alimentary tract of the tsetse fly vector, whereby they exist as procyclic or trypomastigote forms (52), respectively (see **Figure 1**). The lifecycle within the mammalian host is initiated upon the bite of a trypanosome-infected tsetse fly when taking a blood meal (see **Figure 1**). Hereby, metacyclic parasites are inoculated in the host dermis in concert with tsetse saliva components that play a key role in the modulation of the host early immune response and in sculpturing an immune privileged microenvironment for infection initiation (53–55). From the dermal infection site, parasites reach the blood circulation through the lymphatics (55). Subsequently, these metacyclic parasites expressing a heterogeneous metacyclic variable surface glycoprotein (VSG) coat will differentiate into dividing long slender (LS) bloodstream dividing forms (BF), which express a unique VSG coat and are adapted to survive in the glucose-rich and highly oxygenated blood of the mammalian host. Next, these BFs rapidly multiply, giving rise to a first parasitemia peak. At the peak of parasitemia, most likely *via* a quorum sensing mechanism (56, 57), the LS parasites differentiate into non-dividing short stumpy (SS) forms pre-adapted for survival in the tsetse fly vector. Within the tsetse fly vector, these SS forms differentiate within the midgut into procyclic forms (PF) that express a procyclin coat,

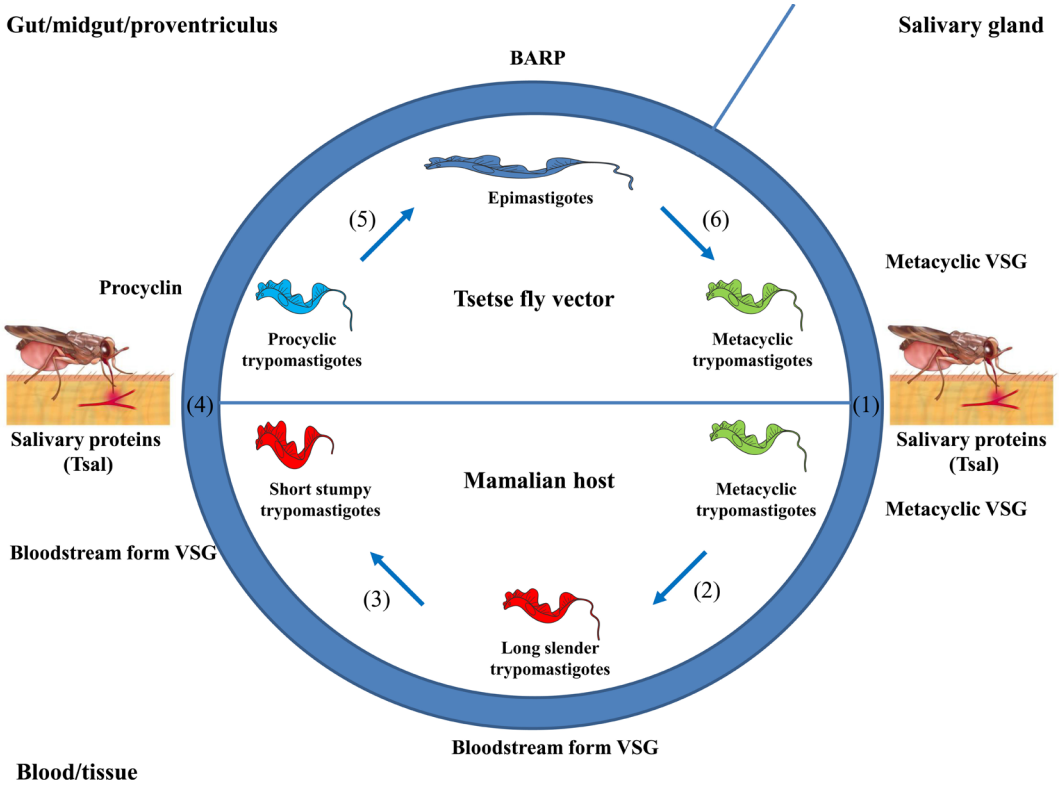

FIGURE 1 | Life cycle of African trypanosomes. (1) Upon the bite of a trypanosome-infected tsetse fly, metacyclic parasites (trypomastigotes) and saliva components (such as Tsal) are inoculated into the mammalian host. (2) The metacyclic parasites [expressing a heterogeneous metacyclic variable surface glycoprotein (VSG)] differentiate into long slender (LS) trypomastigotes (i.e., LS, dividing/proliferating forms, expressing a unique bloodstream form VSG) giving rise to a first peak of parasitemia. (3) At the peak of parasitemia, these LS forms differentiate into non-dividing short stumpy (SS) forms that are pre-adapted to be taken up by the vector. (4) Upon taking a blood meal, these SS forms are ingested and in the midgut these parasites differentiate into procyclic forms (PF), whereby the coat is switched toward procyclin. (5) The PF differentiate into epimastigote forms when migrating to the proventriculus (expressing a bloodstream alanine rich protein coat). (6) Upon migration to the salivary glands, the parasites differentiate into metacyclic forms that are ready to complete their life cycle.

which are adapted to survive in the proline-rich (carbon source) and low-oxygenated environment. Within the tsetse fly, these parasites undergo several differentiation stages in the different parts of the alimentary tract, mouthparts, and salivary glands (58, 59). In order to adapt to the growth conditions imposed by the different environments of their hosts, trypanosomes undergo essential morphological and metabolic changes (52), consisting of fine-tuning their energy metabolism, a dedicated iron and nutrient uptake, organelle reorganization, and biochemical and ultrastructural remodeling (60–65). Hence, tools to interfere with the various stages in the parasite life cycle might be an attractive strategy to combat AT.

Nbs AS VERSATILE TOOLS FOR AT

The control over AT would benefit from more efficient diagnosis and treatment intervention strategies. Hereby, since their serendipitous discovery 30 years ago, Nbs attracted a progressively growing interest from fundamental research on antibody structure and ontogeny to diagnostical and therapeutical applications (66–68). With respect to fundamental research, the Nb technology was found to provide a novel tool in structural biology, whereby they can be used as crystallization-aid, or as a tool to design novel drugs based on co-crystallization of Nbs with their cognate antigen (69, 70). Although such applications in the field of AT are not yet documented, this will most likely become an emerging field of study in the near future. Moreover, given the tremendous efforts to identify novel targets for AT through proteomic approaches (71), the merging of the Nb technology with the current technologies might pave the way to develop additional tools/targets to fight AT. In this section, we will give an overview of the applications of the Nb technology in the field of AT.

Nbs As Tools for Diagnosis

To date, several obstacles hamper an efficient and reliable diagnosis of AT, whereby (i) inefficient antibody-based detection due to interferences caused by the host's antibody response (i.e., antibodies remaining in circulation for long periods of time) impairs discrimination between active and cured infections and (ii) antigen-based trypanosome detection methods that might allow circumventing the problems encountered in the antibody-based detection system are not yet available. In this context, Nbs are emerging as promising tools to overcome the limitations of

antibody-based diagnosis and to improve antigen-based detection of African trypanosomes (see **Figure 2** and **Table 1**). For instance, though the binding interference caused by the host's antibody response upon infection might hamper sensitive detection, this response might also be exploited using the Nb technology. Indeed, Caljon et al. (72) showed that following immunization of an alpaca with the sialome of the savannah tsetse fly vector (*Glossina morsitans morsitans*), Nbs could be generated against an abundant highly immunogenic tsetse salivary gland (Tsal) endonuclease protein and could subsequently be used to monitor tsetse fly bite exposure (73). Monitoring this bite exposure level in a target host population is important as the probability of a trypanosome transmission event to a new host is directly linked to the exposure level of the host to tsetse bites in that area (=risk factor). Indeed, only a very limited number of flies in a natural tsetse population carries the final infective parasite stage, so the more frequent a host is bitten by tsetse the higher the risk is that it will trap a trypanosome infection through the bite of a rarely occurring infected fly in that area. The assay principle relies on the detection of specific

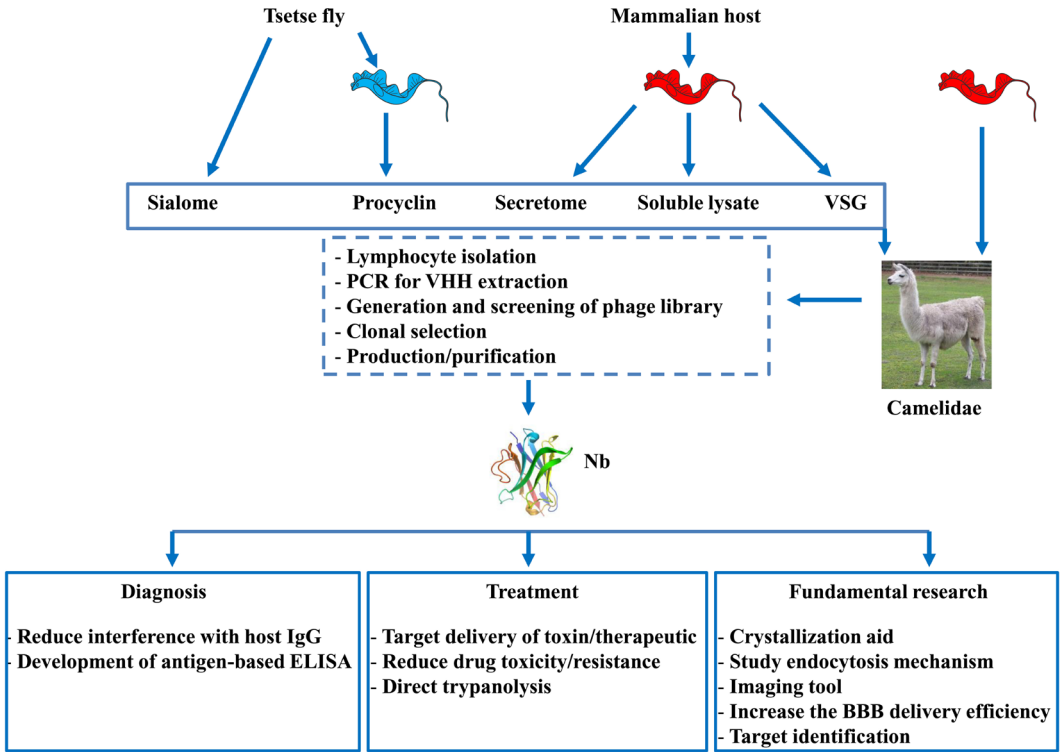

FIGURE 2 | Overview of strategies used to generate nanobodies (Nbs) and their applications. Nbs can be obtained from llama's that are either immunized with factors derived from (i) tsetse flies (i.e., sialome or procyclin coat isolated form procyclic forms) or (ii) purified blood stream parasites originally grown in the mammalian host [i.e., secretome, soluble lysate, or variable surface glycoprotein (VSG)] or (iii) from infected (naturally or experimentally) with trypanosomes. After immunization, lymphocytes are isolated from the blood and *via* the PCR, phage display, and different selection procedures, individual Nbs can be obtained and purified. These Nbs can find application in diagnosis, therapy, or be used for fundamental research aiming at developing novel strategies to fight African trypanosomiasis.

TABLE 1 | Overview of the different targets against which nanobodies (Nbs) have been generated.

Target	Vector	PF	BF	Specificity	Diagnosis	Treatment	Reference
Tsal	+	–	–	Saliva	+	–	(72)
Procyclin	–	+	–	**Tb**	?	?	–
Aldolase	–	–	+	**Tc**	+	?	(78)
Paraflagellar rod protein	–	+	+	**Te**, Tb, Tc, Tv	+	?	(77)
Conserved variable surface glycoprotein (VSG) epitope	–	–	+	**Tb**, (Tc?)	+	+	(81)
Variable VSG epitope	–	–	+	**Tb**, (Tc?)	+	+	(98)
Transferrin receptor	–	?	+	**Tb**, Tc, Te, Tv	?	?	–

In addition, the Nb specificity and applicability (diagnosis/treatment) is mentioned.
PF, procyclic forms; BP, bloodstream form; Tb, Trypanosoma brucei; Tc, Trypanosoma congolense; Te, Trypanosoma evansi; Tv, Trypanosoma vivax.
Trypanosome species in bold refers to the species against which the target was originally generated.
"?" stands for not tested or unknown.

anti-Tsal1 antibodies in an assay that measures the competitive binding onto the immunogenic Tsal1protein of diagnostic Nbs (Tsal1Nb-5 and -11) and host antibodies that are typically induced by bite exposure. This Nb-based competition assay allows specific detection of exposure to a range of important tsetse fly species in the context of sero-epidemiological surveys based on salivary proteins. This could not only allow monitoring/estimating the intensity of the host exposure to tsetse fly bites but also reveal the efficacy of applied and/or ongoing tsetse fly control activities. This approach might be further extended by generating anti-proteome and/or anti-infectome Nb libraries in order to identify diagnostic Nbs (74–76). Indeed, the work by Obishakin et al. (77) showed that upon immunization of a llama with *T. evansi* lysate, Nbs against the paraflagellar rod (PFR) protein of trypanosomes could be generated and used in a solid phase antigen-ELISA to detect this protein in different *T. evansi* strains. Although the assay was not sensitive enough to detect *T. congolense* and *T. vivax* lysates in ELISA, one of the anti-PFR Nbs (Nb392) was found to cross-react with multiple parasite species such as *T. brucei*, *T. congolense*, and *T. vivax* as well as PF. Detection was achieved using fixed and permeabilized parasites and *via* flow cytometry and immunofluorescence microscopy, inferring that this Nb could be used to develop a broad spectrum diagnostic reagent. Moreover, this Nb could also be exploited as a PFR marker and/or as a useful research tool to isolate PFR proteins. More recently, Odongo et al. (78) identified following immunization of a llama with the soluble proteome of bloodstream form (BF) *T. congolense* a Nb (Nb474) recognizing glycosomal aldolase (*Tco*ALD) that could be used in a Nb-based sandwich ELISA to specifically detect active *T. congolense* infections in experimentally and naturally infected cattle. In experimental *T. congolense* infection models, parasitemia and detected antigenemia followed the same trend and the assay was suggested to be suitable as a test of cure. Although no formal detection limit was determined, the Nb474-based test was able to detect *T. congolense* infections in two field collected cattle blood samples that underwent the traditional parasitological diagnosis using the buffy coat technique followed by 18S-PCR-RFLP-based parasite species identification. Furthermore, it was suggested that the robustness of this Nb474-ELISA to specifically monitor *T. congolense* infections in the field might be improved once the structural and biophysical determinants of the specific Nb474–*Tco*ALD interaction can be determined. Of note, also in other parasitic diseases such as malaria, aldolase was reported as a proficient biomarker for the detection of *Plasmodium vivax* (79). In addition, in regions of sub-Saharan Africa where animals are infected with human and animal infective trypanosomes, this selective test for *T. congolense* using aldolase as a biomarker would allow discriminating between the two parasite groups, hence enabling assessment of the potential risk for human infection (80).

Besides recognizing low abundant proteins, Nbs have also been generated against the highly abundant VSG coat of the *T. congolense* parasite, yet due to the system of antigenic variation their diagnostic value is rather limited (unpublished data). However, the work by Stijlemans et al. (81), using the *T. brucei* model parasites, showed that the reduced size of a Nb allows to target conserved, less-immunogenic, cryptic VSG epitopes, that are inaccessible to conventional antibodies. Hereby, the fluorescently labeled anti-VSG Nb-33 was found to be very proficient to detect different isoforms of the *T. brucei* family and to specifically stain trypanosomes in infected blood. This suggests that even Nbs directed against specific conserved regions of the VSG molecule can be used as diagnostic tools.

Collectively, these data suggest that a Nb-based strategy could be a unique approach for diagnosis development and might bring us a step closer toward obtaining an antigen-detection test that can be used for rapid and reliable detection of vector exposure as well as the presence of pathogen infections in reservoir hosts (see **Figure 2** and **Table 1**). In addition, Nbs could also be used for target discovery given that following immunizations with complex protein mixtures and *via* different purification techniques, their cognate antigens with diagnostic potential can be identified.

Nbs As Therapeutic Devices

Nbs As Tools for Drug/Toxin Delivery

Although the currently used chemotherapeutics are proficient in killing trypanosomes, their *in vivo* application suffers from systemic drug toxicity and occurrence of drug resistance (82). Therefore, delivering the chemotherapeutic (or toxin) directly to the parasite could be a more efficient way for treating AT. The possibility of using Nbs as targeting entity was investigated using the Nb-33 as model Nb (**Figure 2**; **Table 1**). With respect to using Nb-33 as a *toxin-delivery system* to African trypanosomes, apolipoprotein L-1 (ApoL-1) was selected as a trypanolytic component. ApoL-1 is a component of normal human serum (NHS) that exerts a direct trypanolytic effect on all AAT species, except resistant forms such as *T. brucei rhodesiense* (83). Indeed, *T. b. rhodesiense* expresses the apoL-I-neutralizing serum resistance-associated (SRA) protein, endowing this parasite with the ability to infect humans and cause HAT (83, 84). Hence, Nb-33, recognizing a conserved/cryptic region within the VSG coat, was coupled to a truncated form of Apo-L1 (i.e., Tr-apoL-1), which is engineered by deleting the SRA-interacting domain. This engineered immunotoxin was shown to function curatively and to alleviate effects on acute and chronic infections in mice infected with both NHS-resistant and sensitive parasites (85, 86). The Nb-33 was also used as a *delivery system for therapeutics* using *T. b. gambiense* parasites as a model. Hereby, nanoparticles loaded with pentamidine [i.e., drug used for treating the early disease stage, before central nervous system involvement (87), as the second-line option to suramin] were coupled to Nb-33. This targeted drug-bullet allowed decreasing the half-inhibitory concentration (IC50) 7-fold compared to free drug *in vitro* and cured all mice at a 10-fold lower dose than the minimal full curative dose of free pentamidine (88–90). Moreover, recently an improved version of this nanocarrier allowed reducing the curative dose 100-fold and circumvented drug resistance that is due to mutations in aquaglyceroporin 2 (i.e., the surface channel protein that mediates pentamidine uptake in *T. brucei*) (29, 91, 92). Overall, targeting the trypanosome surface using Nb-coated drug-loaded nanoparticles can be an elegant way to deliver drugs *via* endocytosis and bypass the usual drug delivery

route altogether. Recently, using the Nb-33, it was shown that Nbs are able to pass the BBB during the late stage of *T. brucei* infection using murine and rat models, which suggests they might be valuable tools to target toxins even at the levels of the BBB. Yet, they were incapable of accumulating in the brain at therapeutically relevant concentrations (93), which is most likely due to the systemic pharmacokinetics of monovalent Nbs (42, 94). Hence, efforts should be undertaken to tailor these Nbs *via* for instance CDR grafting to yield improved brain penetrating properties without losing their beneficial size (95, 96). In addition, to quantitatively study the penetration of Nbs into the CNS *in vivo*, intracerebral microdialysis represents a powerful and sensitive technique. Given that much effort is put into developing new drugs against African trypanosomes, the Nb-based drug/toxin-delivery approach might allow increasing their efficacy, even against drug resistant parasites, and be applicable for many other diseases (97).

Nbs As Direct Trypanolytic Entities by Blocking Endocytosis

By serendipity, besides a drug-targeting potential, Nbs were found to exert direct trypanolytic activities. Indeed, it was shown that some Nbs specific for the variable part of VSG of *T. b. brucei* parasites were able to induce parasite lysis *in vitro*. The lytic process consists of a rapid immobilization of the parasites, followed by massive enlargement of the flagellar pocket and a major blockage of endocytosis (98). Given that endocytosis is essential for trypanosome survival, playing a key role in nutrient uptake and in regulating intracellular ATP-levels as well as in maintaining the mitochondrial membrane potential, it is a prime candidate target for therapeutic interventions (99). Moreover, the endocytosis is confined to the flagellar pocket, which can be considered as the gateway to and from the cell surface that regulates the host–parasite interface as well as significantly contributes toward interactions with therapeutics. Hence, this might be the trypanosomal Achilles' heel and offer perspectives for directed drug delivery focusing on proteins essential in endocytosis (100). Also, targeting specific receptors essential for nutrient uptake could be considered as therapeutic targets. For instance, given that iron is essential for the survival of both the trypanosome and the mammalian host and that their receptor for iron/transferrin uptake differs (i.e., a heterodimer and homodimer, respectively) (101), specific targeting of the parasite transferrin receptor using Nbs might be an opportunity to selectively deprive trypanosomes from this essential nutrient or alternatively be used as drug delivery or diagnostic tool. Also, the fact that low-molecular weight VSG-specific trypanolytic Nbs can impede endocytosis suggests that Nbs can be used as tools to further unravel the fascinating endocytosis mechanism used by trypanosomes. This in turn may offer new opportunities for developing novel trypanosomiasis therapeutics aimed at affecting endocytosis.

One aspect that could compromise the therapeutic applications of Nbs, in for instance HAT patients, is the potential immunogenicity of Nbs, especially in treatments that require repeated injections. Currently, the immunogenicity of Nb-based therapeutic applications is controversial. For instance, a clinical trial study conducted by GSK revealed the occurrence of anti-TNFR1 Nb autoantibodies and in another study with a tetravalent anti-DR5 receptor Nb hepatotoxicity in patients with such pre-existing antibodies has been described (102, 103). By contrast, no anti-HER2 Nb autoantibodies could not be detected in patients who received a non-humanized Nb (104), nor in patients receiving a Nb against von Willebrand factor (105). Also in the murine model, so far, multiple injections of Nbs in different disease settings did not result in immunogenicity, neither at the level of specific antibodies against Nbs nor at the level of cell proliferation and cytokine levels (68, 106–108). Hence, it seems that the occurrence of immunogenicity might depend on the target and disease situation (46). Yet, to reduce/minimize the risk of an immune response within the mammalian host, there are strategies currently implemented, such as humanization of the Nbs, whereby the camelid-specific amino acid sequences are mutated to their human heavy chain variable domain equivalent. In this context, a universal humanized Nb scaffold has been generated that allows grafting the antigen-binding loops from other Nbs, thereby transferring the antigen specificity and affinity (109).

Paratransgenesis As Tool to Deliver Nbs within the Tsetse Fly Vector

The applications of Nbs against AT may be not restricted to the BF of the parasites within the mammalian host, but could be applied/extrapolated to the vector. In this context, the possibility to exploit the tsetse fly bacterial symbiont *Sodalis glossinidius* as a paratransgenic platform organism for the expression and delivery of trypanosome-interfering proteins (i.e., Nbs) within the tsetse fly vector was evaluated. To this end, both the non-lytic Nb-33 and the trypanolytic Nbs were shown to be successfully expressed without affecting *S. glossinidius* fitness/viability (110). Moreover, using the trypanolytic Nb as proof of concept, recombinant *S. glossinidius* could settle in different tsetse fly tissues at high densities. Furthermore, significant levels of functional anti-trypanosome Nbs were released in several tissues including the midgut where important developmental stages of the parasite reside (111). Here, the level of Nb expression was estimated to be in the low nanogram (<10 ng), which was calculated to be sufficient to lyse the expected low number of transforming blood stream trypanosomes (around 10^3 parasites) in the tsetse midgut during the early developmental period after ingestion by the fly (111). Accordingly, this paratransgenic approach using *Sodalis* to deliver Nbs that target the parasite or the trypanosome–tsetse fly cross talk could open new avenues to unravel the molecular determinants of this specific parasite–vector interplay and to ultimately render tsetse flies trypanosome resistant [reviewed by Caljon et al. (112)]. Given that the trypanosome is not exposed to an adaptive immune system in the tsetse vector, this parasite stage is not undergoing antigenic variation with the major surface antigen being encoded by a limited set of procyclin genes. In this context, the potential of Nbs delivered using the *Sodalis* endosymbiont targeting the major developmental stages in the tsetse fly, such as the procyclic trypanosomes that need to overcome the midgut barrier in order to achieve colonization of the tsetse fly vector, is currently being investigated. Stable integration of

Nb expression cassettes in the *Sodalis* genome (e.g., by using recently established procedures) and efficient vertical transfer of the transgenic *Sodalis* have been achieved (113). Important issues, such as the identification of highly potent infection-blocking Nbs and the increased proteolytic stability, are still to be addressed (114). The latter feature will be highly beneficial to maintain potent effector levels in the strong proteolytic digestive environment of the insect midgut. Yet, such strategies could potentially culminate in a drug-targeting strategy to eliminate trypanosomes within the tsetse fly vector. An important achievement in the context of the *Sodalis*-based paratransgenesis is the efficient transfer of genetically modified *Sodalis* from the mother tsetse fly to its offspring through intrauterine nourishment (113). This implies that a large-scale tsetse fly colony can be established of flies harboring a Nb-expressing *Sodalis*. The paratransgenic trypanosome-resistant male flies from these colonies can then be released (after sterilization through irradiation) at a massive scale in the context of the Sterile Insect Technique (SIT). SIT was already successfully used to eradicate the tsetse fly in Zanzibar and is currently an important pillar in the tsetse fly control campaigns in Ethiopia and Senegal (http://www.fao.org/in-action/senegal-celebrates-first-victory-against-tsetse-fly-eradication/en/).

LYTIC Nbs: RELEVANCE *IN VIVO*?

The observation that the antigen-binding domain (i.e., Nb) on itself, in the absence of the Fc part can exert a significant Fc-independent killing of African trypanosomes *in vitro* and *in vivo* is remarkable (98). Moreover, it was found that both the size and affinity were of crucial importance for this trypanolytic activity (98, 115). Indeed, whereas polyclonal antibodies (including heavy-chain antibodies) specific for the VSG of African trypanosomes are completely harmless to trypanosomes in the absence of complement or any other bystander effector (116, 117), polyclonal Fabs or Nbs derived from the serum antibody pools and monoclonal/polyclonal Fabs or Nbs that are deprived of all effector functions (i.e., Fc) could exhibit an intrinsic trypanolytic activity *in vitro* (98). It is surprising that removal of the Fc part from antibodies unveils a novel but deadly situation, because trypanosomes and other extracellular pathogens mostly coped during evolution with intact immunoglobulins and thus developed multiple ways to avoid the destructive action of such large molecules (118, 119). In case of African trypanosomes such escape mechanisms include (i) antigenic variation of the VSGs, (ii) dense packing of VSG molecules on the parasite's coat prohibiting the recognition of conserved and/or physiologically important epitopes by intact antibodies, (iii) clearing of VSG-bound antibodies by endocytosis of the VSG–antibody complex [reviewed in Ref. (120–123)]. In contrast to intact Abs, the small-sized Fabs or Nbs may penetrate the dense VSG coat and trigger new processes or avoid removal of VSG–antibody complexes, which is dictated by the bivalency of Abs (possibly due to cross-linking of the VSGs) and/or antibody size, e.g., whereby the presence of the Fc part leads to steric occlusion (123, 124).

The concept that the Fc part within an antibody is masking the intrinsic destructive capacity of the antigen-binding fragment is intriguing. Consequently, other polyclonal or mAbs may share similar features and harbor hidden activities that remain occluded within intact Abs and might manifest themselves upon generation of monovalent Fabs or Nbs (see **Figure 3**). Evidence for a possible intrinsic anti-pathogen activity of *in vivo* generated Fabs or Nbs within the *bona fide* antibody independent of the Fc part is difficult to provide as there is so far no simple assay to demonstrate such an event. Nevertheless, such mechanisms might exist as Nbs with competitive enzyme-inhibiting activity or Fabs with catalytic activity (termed Abzymes) have been identified (117–120). Under certain conditions, antibodies were documented to exert bactericidal activities in the absence of complement or phagocytes (125). For instance, antibodies catalyze the generation of hydrogen peroxide (H_2O_2) from singlet molecular oxygen and water, thereby producing an additional molecular species with a chemical signature similar to that of ozone (126). Interestingly, this singlet molecular oxygen is only present when the host is under assault, thereby making it an "event-triggered" substrate and consequently suggests that the additional function of an antibody might only be apparent under "inflammatory" conditions (127). In addition, it was shown that high H_2O_2 in concert with transition metal ions ($FeCl_2$) (i.e., factors that are typically produced/released *via* apoptotic neutrophils during inflammation) can generate hydroxyl radicals (*via* a Fenton-like reaction) that induce hinge fragmentation of IgG1 mAb [(128) consisting of (i) a Fab domain and the upper hinge of one of the Fc domains and (ii) another Fab domain linked to the Fc domain (see proposed model in **Figure 3**)]. This indicates that under certain *in vivo* inflammatory conditions hidden biological activities could become unmasked from *bona fide* antibodies. To the best of our knowledge, the observation that an antibody-derived fragment on itself can exert a biological function is a new conceptual insight which might broaden the potentiality of Ab applications in different fields.

CONCLUSION AND FUTURE PERSPECTIVES

Over the years, Nbs have been found to be valuable tools in the field of AT both at the level of diagnosis and treatment. They were shown to have potential to circumvent problems encountered with antibody-based detection systems and in addition allow the development of antigen-based approaches that were so far lacking (32). With the era of proteomics (71), allowing additional biomarkers to be discovered, the application of a Nb-based immunoproteomic approach might allow developing more efficient tools to improve trypanosomiasis control (diagnosis/treatment) in the near future. With respect to treatment against AT, it seems that Nbs are a very proficient tool to deliver drugs/toxins to parasites, thereby reducing the side effects due to drug toxicity and possibly the probability to develop drug resistance. Their small size, low immunogenicity, and tailorability furthermore favor their application in AT with respect to BBB drug delivery, routine/systemic administration, and generation of half-life extended formats. Also for research purposes, their advantages are increasingly appreciated and

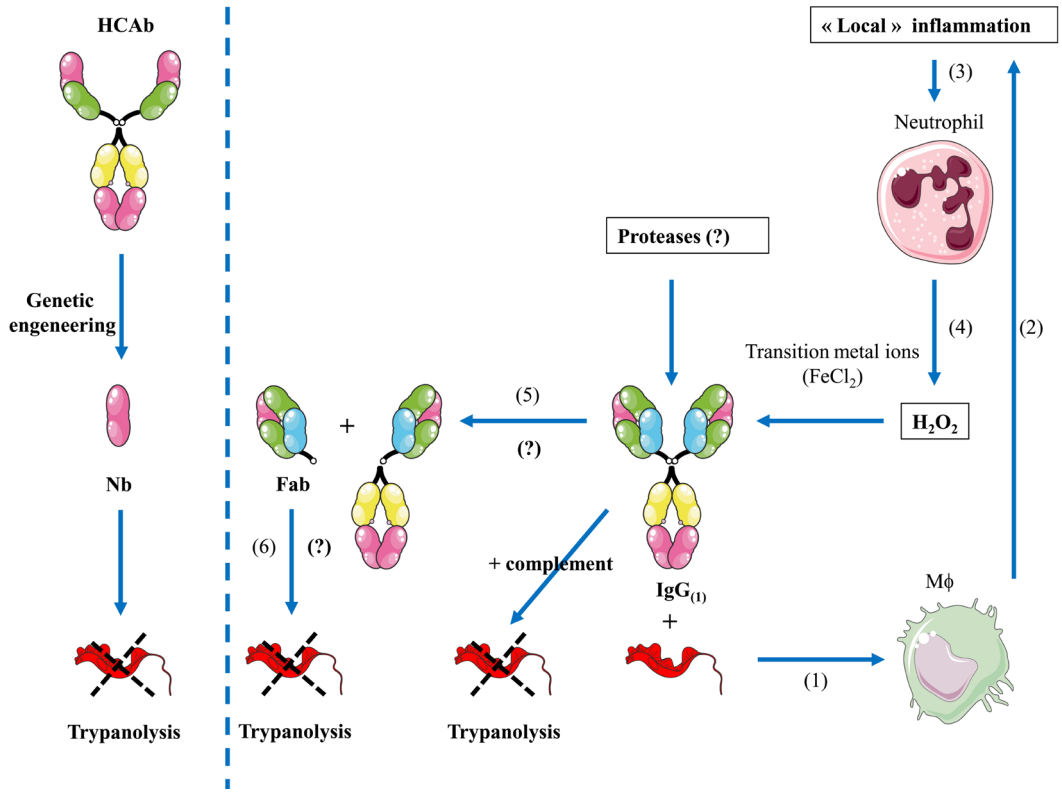

FIGURE 3 | Proposed model of "hidden" functions of antibodies during inflammation. (Left panel) Through genetic engineering, camelid-derived heavy-chain antibodies (HCAbs) can be fragmented to the size of a nanobody that might exert a direct effect on pathogens (i.e., trypanosomes). (Right panel) (1) During infection (i.e., trypanosome infection), parasite-derived factors in concert with host-derived factors trigger macrophage (Mϕ) activation. (2) Hereby, elicited antibodies opsonize parasites and in concert with complement trigger parasite destruction, further leading to release of macrophage activating components and inflammatory responses. (3) The local inflammation may lead to recruitment, activation, and apoptosis of neutrophils. (4) Release of H_2O_2 as well as transitional metal ions and proteases by neutrophils/activated macrophages can fragment intact IgG (1). (5) Next, this will induce hinge fragmentation of IgG1 giving rise to a fragmented antibody into moieties including the Fab domain. (6) This Fab domain might exert a direct lytic effect on trypanosomes.

they will most likely become a useful tool with respect to crystallization and imaging. Finally, the concept that a Nb or a Fab fragment derived from an intact IgG might exert a biological function by itself in the absence of the Fc-bystander warrants further investigation. Moreover, this suggests that intact antibodies harbor hidden functions that only become apparent upon fragmentation into a Fab, a process that might occur under certain conditions, and this might have a broad range of implications and applications in other diseases.

AUTHOR CONTRIBUTIONS

BS, PB, GC, JA, JG, and SM collectively wrote the manuscript.

FUNDING

We acknowledge the financial support of the Interuniversity Attraction Pole Program (PAI-IAP N. P7/41, http://www.belspo.be/belspo/iap/index_en.stm) and grants from the FWO (FWO G015016N and G.0.028.10.N.10) and the Bill and Melinda Gates Foundation grant 641K760. BS is a research fellow supported by the Strategic Research Program (SRP3, VUB): targeting inflammation linked to infectious diseases and cancer (Nanobodies for Health). GC is funded by a research fund of the University of Antwerp (TT-ZAPBOF 33049). The funders had no role in study design, data collection and analysis, decision to publish, or preparation of the manuscript.

REFERENCES

1. Yaro M, Munyard KA, Stear MJ, Groth DM. Combatting African animal trypanosomiasis (AAT) in livestock: the potential role of trypanotolerance. *Vet Parasitol* (2016) 225:43–52. doi:10.1016/j.vetpar.2016.05.003
2. Simarro PP, Cecchi G, Franco JR, Paone M, Diarra A, Ruiz-Postigo JA, et al. Estimating and mapping the population at risk of sleeping sickness. *PLoS Negl Trop Dis* (2012) 6:e1859. doi:10.1371/journal.pntd.0001859
3. Franco JR, Simarro PP, Diarra A, Jannin JG. Epidemiology of human African trypanosomiasis. *Clin Epidemiol* (2014) 6:257–75. doi:10.2147/CLEP.S39728
4. World Health Organization. Control and surveillance of human African trypanosomiasis. *World Health Organ Tech Rep Ser* (2013) (984):1–237.
5. Kennedy PG. Clinical features, diagnosis, and treatment of human African trypanosomiasis (sleeping sickness). *Lancet Neurol* (2013) 12:186–94. doi:10.1016/S1474-4422(12)70296-X

6. Welburn SC, Molyneux DH, Maudlin I. Beyond tsetse – implications for research and control of human African trypanosomiasis epidemics. *Trends Parasitol* (2016) 32:230–41. doi:10.1016/j.pt.2015.11.008
7. MacLean LM, Odiit M, Chisi JE, Kennedy PG, Sternberg JM. Focus-specific clinical profiles in human African trypanosomiasis caused by *Trypanosoma brucei rhodesiense*. *PLoS Negl Trop Dis* (2010) 4:e906. doi:10.1371/journal.pntd.0000906
8. WHO. Control and surveillance of human African trypanosomiasis. *World Health Organ Tech Rep Ser* (2013):1–237. Available from: http://www.ncbi.nlm.nih.gov/pubmed/24552089
9. MacLean L, Reiber H, Kennedy PG, Sternberg JM. Stage progression and neurological symptoms in *Trypanosoma brucei rhodesiense* sleeping sickness: role of the CNS inflammatory response. *PLoS Negl Trop Dis* (2012) 6:e1857. doi:10.1371/journal.pntd.0001857
10. Simarro PP, Diarra A, Ruiz Postigo JA, Franco JR, Jannin JG. The human African trypanosomiasis control and surveillance programme of the World Health Organization 2000-2009: the way forward. *PLoS Negl Trop Dis* (2011) 5:e1007. doi:10.1371/journal.pntd.0001007
11. World Health Organization. *Trypanosomiasis, Human African (Sleeping Sickness)*. (Vol. 259). World Health Organization (2013). Fact Sheet. Available from: http://www.who.int/mediacentre/factsheets/fs259/en/
12. Lejon V, Bentivoglio M, Franco JR. Human African trypanosomiasis. *Handb Clin Neurol* (2013) 114:169–81. doi:10.1016/B978-0-444-53490-3.00011-X
13. Ruiz-Postigo JA, Franco JR, Lado M, Simarro PP. Human African trypanosomiasis in South Sudan: how can we prevent a new epidemic? *PLoS Negl Trop Dis* (2012) 6:e1541. doi:10.1371/journal.pntd.0001541
14. Hasker E, Mpanya A, Makabuza J, Mbo F, Lumbala C, Kumpel J, et al. Treatment outcomes for human African trypanosomiasis in the Democratic Republic of the Congo: analysis of routine program data from the world's largest sleeping sickness control program. *Trop Med Int Heal* (2012) 17:1127–32. doi:10.1111/j.1365-3156.2012.03042.x
15. Claes F, Büscher P, Touratier L, Goddeeris BM. *Trypanosoma equiperdum*: master of disguise or historical mistake? *Trends Parasitol* (2005) 21:316–21. doi:10.1016/j.pt.2005.05.010
16. Desquesnes M, Dargantes A, Lai DH, Lun ZR, Holzmuller P, Jittapalapong S. *Trypanosoma evansi* and surra: a review and perspectives on transmission, epidemiology and control, impact, and zoonotic aspects. *Biomed Res Int* (2013) 2013:321237. doi:10.1155/2013/321237
17. Brun R, Hecker H, Lun ZR. *Trypanosoma evansi* and *T. equiperdum*: distribution, biology, treatment and phylogenetic relationship (a review). *Vet Parasitol* (1998) 79:95–107. doi:10.1016/S0304-4017(98)00146-0
18. Naessens J. Bovine trypanotolerance: a natural ability to prevent severe anaemia and haemophagocytic syndrome? *Int J Parasitol* (2006) 36:521–8. doi:10.1016/j.ijpara.2006.02.012
19. Giordani F, Morrison LJ, Rowan TG, De Koning HP, Barrett MP. The animal trypanosomiases and their chemotherapy: a review. *Parasitology* (2016) 143(14):1862–89. doi:10.1017/S0031182016001268
20. Swallow B. *Impacts of Trypanosomiasis on African Agriculture*. Nairobi, Kenya: Int Livest Res Institute (1999). p. 1–46. Available from: http://www.cabdirect.org/abstracts/20003010139.html
21. Gilbert M, Jenner C, Pender J, Rogers D, Slingenbergh J, Wint W. The programme against African trypanosomiasis information system (PAATIS). In: *The African Trypanosomiasis*. Vol 1 World Class Parasites. p. 11–24. Available from: https://link.springer.com/chapter/10.1007/0-306-46894-8_2?no-access=true
22. Baker N, de Koning HP, Maser P, Horn D. Drug resistance in African trypanosomiasis: the melarsoprol and pentamidine story. *Trends Parasitol* (2013) 29:110–8. doi:10.1016/j.pt.2012.12.005
23. Delespaux V, de Koning HP. Drugs and drug resistance in African trypanosomiasis. *Drug Resist Updat* (2007) 10:30–50. doi:10.1016/j.drup.2007.02.004
24. Bouyer J, Bouyer F, Donadeu M, Rowan T, Napier G. Community- and farmer-based management of animal African trypanosomosis in cattle. *Trends Parasitol* (2013) 29:519–22. doi:10.1016/j.pt.2013.08.003
25. Wenzler T, Schumann Burkard G, Schmidt RS, Mäser P, Bergner A, Roditi I, et al. A new approach to chemotherapy: drug-induced differentiation kills African trypanosomes. *Sci Rep* (2016) 6:22451. doi:10.1038/srep22451
26. Naula C, Burchmore R. A plethora of targets, a paucity of drugs: progress towards the development of novel chemotherapies for human African trypanosomiasis. *Expert Rev Anti Infect Ther* (2003) 1:157–65. doi:10.1586/14787210.1.1.157
27. Haanstra JR, Gerding A, Dolga AM, Sorgdrager FJ, Buist-homan M, Toit F, et al. Targeting pathogen metabolism without collateral damage to the host. *Sci Rep* (2017) 7:40406. doi:10.1038/srep40406
28. Barrett MP, Vincent IM, Burchmore RJ, Kazibwe AJ, Matovu E. Drug resistance in human African trypanosomiasis. *Futur Microbiol* (2011) 6:1037–47. doi:10.2217/fmb.11.88
29. Unciti-Broceta JD, Arias JL, Maceira J, Soriano M, Ortiz-González M, Hernández-Quero J, et al. Specific cell targeting therapy bypasses drug resistance mechanisms in African trypanosomiasis. *PLoS Pathog* (2015) 11:e1004942. doi:10.1371/journal.ppat.1004942
30. Kroubi M, Karembe H, Betbeder D. Drug delivery systems in the treatment of African trypanosomiasis infections. *Expert Opin Drug Deliv* (2011) 8:735–47. doi:10.1517/17425247.2011.574122
31. Kennedy PG. Human African trypanosomiasis-neurological aspects. *J Neurol* (2006) 253:411–6. doi:10.1007/s00415-006-0093-3
32. Bonnet J, Boudot C, Courtioux B. Overview of the diagnostic methods used in the field for human African trypanosomiasis: what could change in the next years? *Biomed Res Int* (2015) 2015:583262. doi:10.1155/2015/583262
33. Jamonneau V, Camara O, Ilboudo H, Peylhard M, Koffi M, Sakande H, et al. Accuracy of individual rapid tests for serodiagnosis of gambiense sleeping sickness in West Africa. *PLoS Negl Trop Dis* (2015) 9(2):e0003480. doi:10.1371/journal.pntd.0003480
34. Rebeski DE, Winger EM, Rogovic B, Robinson MM, Crowther JR, Dwinger RH. Improved methods for the diagnosis of African trypanosomosis. *Mem Inst Oswaldo Cruz* (1999) 94:249–53. doi:10.1590/S0074-02761999000200024
35. Moti Y, Fikru R, Buscher P, Van Den Abbeele J, Duchateau L, Delespaux V. Detection of African animal trypanosomes: the haematocrit centrifugation technique compared to PCR with samples stored on filter paper or in DNA protecting buffer. *Vet Parasitol* (2014) 203:253–8. doi:10.1016/j.vetpar.2014.04.014
36. Lambert PH, Berney M, Kazyumba G. Immune complexes in serum and in cerebrospinal fluid in African trypanosomiasis. *J Clin Invest* (1981) 67:77–85. doi:10.1172/JCI110035
37. Hamers-Casterman C, Atarhouch T, Muyldermans S, Robinson G, Hamers C, Songa EB, et al. Naturally occurring antibodies devoid of light chains. *Nature* (1993) 363:446–8. doi:10.1038/363446a0
38. Dmitriev OY, Lutsenko S, Muyldermans S. Nanobodies as probes for protein dynamics in vitro and in cells. *J Biol Chem* (2016) 291:3767–75. doi:10.1074/jbcR115.679811
39. Skottrup PD, Leonard P, Kaczmarek JZ, Veillard F, Enghild JJ, O'Kennedy R, et al. Diagnostic evaluation of a nanobody with picomolar affinity toward the protease RgpB from *Porphyromonas gingivalis*. *Anal Biochem* (2011) 415:158–67. doi:10.1016/j.ab.2011.04.015
40. De Genst E, Silence K, Decanniere K, Conrath K, Loris R, Kinne J, et al. Molecular basis for the preferential cleft recognition by dromedary heavy-chain antibodies. *Proc Natl Acad Sci U S A* (2006) 103:4586–91. doi:10.1073/pnas.0505379103
41. Oliveira S, Heukers R, Sornkom J, Kok RJ, van Bergen en Henegouwen PMP. Targeting tumors with nanobodies for cancer imaging and therapy. *J Control Release* (2013) 172:607–17. doi:10.1016/j.jconrel.2013.08.298
42. De Groeve K, Deschacht N, De Koninck C, Caveliers V, Lahoutte T, Devoogdt N, et al. Nanobodies as tools for in vivo imaging of specific immune cell types. *J Nucl Med* (2010) 51:782–9. doi:10.2967/jnumed.109.070078
43. De Vos J, Devoogdt N, Lahoutte T, Muyldermans S. Camelid single-domain antibody-fragment engineering for (pre)clinical in vivo molecular imaging applications: adjusting the bullet to its target. *Expert Opin Biol Ther* (2013) 13:1149–60. doi:10.1517/14712598.2013.800478
44. Movahedi K, Schoonooghe S, Laoui D, Houbracken I, Waelput W, Breckpot K, et al. Nanobody-based targeting of the macrophage mannose receptor for effective in vivo imaging of tumor-associated macrophages. *Cancer Res* (2012) 72:4165–77. doi:10.1158/0008-5472.CAN-11-2994
45. Zheng F, Devoogdt N, Sparkes A, Morias Y, Abels C, Stijlemans B, et al. Monitoring liver macrophages using nanobodies targeting Vsig4:

concanavalin A induced acute hepatitis as paradigm. *Immunobiology* (2015) 220:200–9. doi:10.1016/j.imbio.2014.09.018
46. Muyldermans S, Smider VV. Distinct antibody species: structural differences creating therapeutic opportunities. *Curr Opin Immunol* (2016) 40:7–13. doi:10.1016/j.coi.2016.02.003
47. Wesolowski J, Alzogaray V, Reyelt J, Unger M, Juarez K, Urrutia M, et al. Single domain antibodies: promising experimental and therapeutic tools in infection and immunity. *Med Microbiol Immunol* (2009) 198:157–74. doi:10.1007/s00430-009-0116-7
48. Hassanzadeh-Ghassabeh G, Devoogdt N, De Pauw P, Vincke C, Muyldermans S. Nanobodies and their potential applications. *Nanomedicine* (2013) 8:1013–26. doi:10.2217/nnm.13.86
49. Muyldermans S, Baral TN, Retamozzo VC, De Baetselier P, De Genst E, Kinne J, et al. Camelid immunoglobulins and nanobody technology. *Vet Immunol Immunopathol* (2009) 128:178–83. doi:10.1016/j.vetimm.2008.10.299
50. Ewert S, Huber T, Honegger A, Plückthun A. Biophysical properties of human antibody variable domains. *J Mol Biol* (2003) 325:531–53. doi:10.1016/S0022-2836(02)01237-8
51. Wang P, Li G, Yan J, Hu Y, Zhang C, Liu X, et al. Bactrian camel nanobody-based immunoassay for specific and sensitive detection of Cry1Fa toxin. *Toxicon* (2014) 92:186–92. doi:10.1016/j.toxicon.2014.10.024
52. Rodrigues JC, Godinho JL, de Souza W. Biology of human pathogenic trypanosomatids: epidemiology, lifecycle and ultrastructure. *Subcell Biochem* (2014) 74:1–42. doi:10.1007/978-94-007-7305-9
53. Caljon G, Van Den Abbeele J, Stijlemans B, Coosemans M, De Baetselier P, Magez S. Tsetse fly saliva accelerates the onset of *Trypanosoma brucei* infection in a mouse model associated with a reduced host inflammatory response. *Infect Immun* (2006) 74:6324–30. doi:10.1128/IAI.01046-06
54. Van Den Abbeele J, Caljon G, De Ridder K, De Baetselier P, Coosemans M. *Trypanosoma brucei* modifies the tsetse salivary composition, altering the fly feeding behavior that favors parasite transmission. *PLoS Pathog* (2010) 6:e1000926. doi:10.1371/journal.ppat.1000926
55. Caljon G, Van Reet N, De Trez C, Vermeersch M, Pérez-Morga D, Van Den Abbeele J. The dermis as a delivery site of *Trypanosoma brucei* for tsetse flies. *PLoS Pathog* (2016) 12:e1005744. doi:10.1371/journal.ppat.1005744
56. Seed JR, Wenck MA. Role of the long slender to short stumpy transition in the life cycle of the African trypanosomes. *Kinetoplastid Biol Dis* (2003) 2:3. doi:10.1186/1475-9292-2-3
57. Mony BM, MacGregor P, Ivens A, Rojas F, Cowton A, Young J, et al. Genome-wide dissection of the quorum sensing signalling pathway in *Trypanosoma brucei*. *Nature* (2014) 505:681–5. doi:10.1038/nature12864
58. Rotureau B, Van Den Abbeele J. Through the dark continent: African trypanosome development in the tsetse fly. *Front Cell Infect Microbiol* (2013) 3:53. doi:10.3389/fcimb.2013.00053
59. Sharma R, Gluenz E, Peacock L, Gibson W, Gull K, Carrington M. The heart of darkness: growth and form of *Trypanosoma brucei* in the tsetse fly. *Trends Parasitol* (2009) 25:517–24. doi:10.1016/j.pt.2009.08.001
60. Bringaud F, Riviere L, Coustou V. Energy metabolism of trypanosomatids: adaptation to available carbon sources. *Mol Biochem Parasitol* (2006) 149:1–9. doi:10.1016/j.molbiopara.2006.03.017
61. Natesan SK, Peacock L, Matthews K, Gibson W, Field MC. Activation of endocytosis as an adaptation to the mammalian host by trypanosomes. *Eukaryot Cell* (2007) 6:2029–37. doi:10.1128/EC.00213-07
62. Jones NG, Thomas EB, Brown E, Dickens NJ, Hammarton TC, Mottram JC. Regulators of *Trypanosoma brucei* cell cycle progression and differentiation identified using a kinome-wide RNAi screen. *PLoS Pathog* (2014) 10:e1003886. doi:10.1371/journal.ppat.1003886
63. Gruszynski AE, van Deursen FJ, Albareda MC, Best A, Chaudhary K, Cliffe LJ, et al. Regulation of surface coat exchange by differentiating African trypanosomes. *Mol Biochem Parasitol* (2006) 147:211–23. doi:10.1016/j.molbiopara.2006.02.013
64. Matthews KR, Ellis JR, Paterou A. Molecular regulation of the life cycle of African trypanosomes. *Trends Parasitol* (2004) 20:40–7. doi:10.1016/j.pt.2003.10.016
65. Steverding D. Bloodstream forms of *Trypanosoma brucei* require only small amounts of iron for growth. *Parasitol Res* (1998) 84:59–62. doi:10.1007/s004360050357
66. De Meyer T, Muyldermans S, Depicker A. Nanobody-based products as research and diagnostic tools. *Trends Biotechnol* (2014) 32:263–70. doi:10.1016/j.tibtech.2014.03.001
67. Pardon E, Laeremans T, Triest S, Rasmussen SG, Wohlkonig A, Ruf A, et al. A general protocol for the generation of nanobodies for structural biology. *Nat Protoc* (2014) 9:674–93. doi:10.1038/nprot.2014.039
68. Muyldermans S. Nanobodies: natural single-domain antibodies. *Annu Rev Biochem* (2013) 82:775–97. doi:10.1146/annurev-biochem-063011-092449
69. Lam AY, Pardon E, Korotkov KV, Hol WG, Steyaert J. Nanobody-aided structure determination of the EpsI:EpsJ pseudopilin heterodimer from *Vibrio vulnificus*. *J Struct Biol* (2009) 166:8–15. doi:10.1016/j.jsb.2008.11.008
70. Pathare GR, Nagy I, Śledź P, Anderson DJ, Zhou H-J, Pardon E, et al. Crystal structure of the proteasomal deubiquitylation module Rpn8-Rpn11. *Proc Natl Acad Sci U S A* (2014) 111:2984–9. doi:10.1073/pnas.1400546111
71. Holzmuller P, Grebaut P, Semballa S, Gonzatti MI, Geiger A. Proteomics: a new way to improve human African trypanosomiasis diagnosis? *Expert Rev Proteomics* (2013) 10:289–301. doi:10.1586/epr.13.14
72. Caljon G, Hussain S, Vermeiren L, Van Den Abbeele J. Description of a nanobody-based competitive immunoassay to detect tsetse fly exposure. *PLoS Negl Trop Dis* (2015) 9:e0003456. doi:10.1371/journal.pntd.0003456
73. Caljon G, Van Den Abbeele J, Sternberg JM, Coosemans M, De Baetselier P, Magez S. Tsetse fly saliva biases the immune response to Th2 and induces anti-vector antibodies that are a useful tool for exposure assessment. *Int J Parasitol* (2006) 36:1025–35. doi:10.1016/j.ijpara.2006.05.002
74. Saerens D, Stijlemans B, Baral TN, Nguyen Thi GT, Wernery U, Magez S, et al. Parallel selection of multiple anti-infectome nanobodies without access to purified antigens. *J Immunol Methods* (2008) 329:138–50. doi:10.1016/j.jim.2007.10.005
75. Yardehnavi N, Behdani M, Bagheri KP, Mahmoodzadeh A, Khanahmad H, Shahbazzadeh D, et al. A camelid antibody candidate for development of a therapeutic agent against *Hemiscorpius lepturus* envenomation. *FASEB J* (2014) 28:4004–14. doi:10.1096/fj.13-247478
76. Hassanzadeh-Ghassabeh G, Saerens D, Muyldermans S. Generation of anti-infectome/anti-proteome nanobodies. *Methods Mol Biol* (2011) 790:239–59. doi:10.1007/978-1-61779-319-6_19
77. Obishakin E, Stijlemans B, Santi-Rocca J, Vandenberghe I, Devreese B, Muldermans S, et al. Generation of a nanobody targeting the paraflagellar rod protein of trypanosomes. *PLoS One* (2014) 9:e115893. doi:10.1371/journal.pone.0115893
78. Odongo S, Sterckx YG, Stijlemans B, Pillay D, Baltz T, Muyldermans S, et al. An anti-proteome nanobody library approach yields a specific immunoassay for *Trypanosoma congolense* diagnosis targeting glycosomal aldolase. *PLoS Negl Trop Dis* (2016) 10:e0004420. doi:10.1371/journal.pntd.0004420
79. Dzakah EE, Kang K, Ni C, Wang H, Wu P, Tang S, et al. *Plasmodium vivax* aldolase-specific monoclonal antibodies and its application in clinical diagnosis of malaria infections in China. *Malar J* (2013) 12:199. doi:10.1186/1475-2875-12-199
80. Hutchinson OC, Webb H, Picozzi K, Welburn S, Carrington M. Candidate protein selection for diagnostic markers of African trypanosomiasis. *Trends Parasitol* (2004) 20:519–23. doi:10.1016/j.pt.2004.08.007
81. Stijlemans B, Conrath K, Cortez-Retamozo V, Van Xong H, Wyns L, Senter P, et al. Efficient targeting of conserved cryptic epitopes of infectious agents by single domain antibodies. African trypanosomes as paradigm. *J Biol Chem* (2004) 279:1256–61. doi:10.1074/jbc.M307341200
82. Jacobs RT, Nare B, Phillips MA. State of the art in African trypanosome drug discovery. *Curr Top Med Chem* (2011) 11:1255–74. doi:10.2174/156802611795429167
83. Vanhamme L, Paturiaux-Hanocq F, Poelvoorde P, Nolan DP, Lins L, Van Den Abbeele J, et al. Apolipoprotein L-I is the trypanosome lytic factor of human serum. *Nature* (2003) 422:83–7. doi:10.1038/nature01461
84. Lecordier L, Vanhollebeke B, Poelvoorde P, Tebabi P, Paturiaux-Hanocq F, Andris F, et al. C-terminal mutants of apolipoprotein L-I efficiently kill both *Trypanosoma brucei brucei* and *Trypanosoma brucei rhodesiense*. *PLoS Pathog* (2009) 5:e1000685. doi:10.1371/journal.ppat.1000685
85. Baral TN, Magez S, Stijlemans B, Conrath K, Vanhollebeke B, Pays E, et al. Experimental therapy of African trypanosomiasis with a nanobody-

conjugated human trypanolytic factor. *Nat Med* (2006) 12:580–4. doi:10.1038/nm1395
86. Braddock M. Overcoming resistance with designer immunotoxins. *Expert Opin Pharmacother* (2006) 7:1409–12. doi:10.1517/14656566.7.10.1409
87. Barrett MP, Boykin DW, Brun R, Tidwell RR. Human African trypanosomiasis: pharmacological re-engagement with a neglected disease. *Br J Pharmacol* (2007) 152:1155–71. doi:10.1038/sj.bjp.0707354
88. Arias JL, Unciti-Broceta JD, Maceira J, Del Castillo T, Hernández-Quero J, Magez S, et al. Nanobody conjugated PLGA nanoparticles for active targeting of African trypanosomiasis. *J Control Release* (2015) 197:190–8. doi:10.1016/j.jconrel.2014.11.002
89. Garcia-Salcedo JA, Unciti-Broceta JD, Soriano M. Could specific cell targeting overcome resistance associated with current treatments for African trypanosomiasis? *Nanomedicine (Lond)* (2015) 10(24):3515–7. doi:10.2217/nnm.15.167
90. Garcia-Salcedo JA, Unciti-Broceta JD, Valverde-Pozo J, Soriano M. New approaches to overcome transport related drug resistance in trypanosomatid parasites. *Front Pharmacol* (2016) 7:351. doi:10.3389/fphar.2016.00351
91. Baker N, Glover L, Munday JC, Aguinaga Andres D, Barrett MP, de Koning HP, et al. Aquaglyceroporin 2 controls susceptibility to melarsoprol and pentamidine in African trypanosomes. *Proc Natl Acad Sci U S A* (2012) 109:10996–1001. doi:10.1073/pnas.1202885109
92. Song J, Baker N, Rothert M, Henke B, Jeacock L, Horn D, et al. Pentamidine is not a permeant but a nanomolar inhibitor of the *Trypanosoma brucei* aquaglyceroporin-2. *PLoS Pathog* (2016) 12(2):e1005436. doi:10.1371/journal.ppat.1005436
93. Caljon G, Caveliers V, Lahoutte T, Stijlemans B, Ghassabeh GH, Van Den Abbeele J, et al. Using microdialysis to analyse the passage of monovalent nanobodies through the blood-brain barrier. *Br J Pharmacol* (2012) 165:2341–53. doi:10.1111/j.1476-5381.2011.01723.x
94. Iqbal U, Trojahn U, Albaghdadi H, Zhang J, O'Connor-McCourt M, Stanimirovic D, et al. Kinetic analysis of novel mono- and multivalent VHH-fragments and their application for molecular imaging of brain tumours. *Br J Pharmacol* (2010) 160:1016–28. doi:10.1111/j.1476-5381.2010.00742.x
95. Saerens D, Pellis M, Loris R, Pardon E, Dumoulin M, Matagne A, et al. Identification of a universal VHH framework to graft non-canonical antigen-binding loops of camel single-domain antibodies. *J Mol Biol* (2005) 352:597–607. doi:10.1016/j.jmb.2005.07.038
96. Vaneycken I, Govaert J, Vincke C, Caveliers V, Lahoutte T, De Baetselier P, et al. In vitro analysis and in vivo tumor targeting of a humanized, grafted nanobody in mice using pinhole SPECT/micro-CT. *J Nucl Med* (2010) 51:1099–106. doi:10.2967/jnumed.109.069823
97. Zoltner M, Horn D, de Koning HP, Field MC. Exploiting the Achilles' heel of membrane trafficking in trypanosomes. *Curr Opin Microbiol* (2016) 34:97–103. doi:10.1016/j.mib.2016.08.005
98. Stijlemans B, Caljon G, Natesan SK, Saerens D, Conrath K, Pérez-Morga D, et al. High affinity nanobodies against the *Trypanosoma brucei* VSG are potent trypanolytic agents that block endocytosis. *PLoS Pathog* (2011) 7(6):e1002072. doi:10.1371/journal.ppat.1002072
99. Field MC, Carrington M. The trypanosome flagellar pocket. *Nat Rev Microbiol* (2009) 7:775–86. doi:10.1038/nrmicro2221
100. Manna PT, Obado SO, Boehm C, Gadelha C, Sali A, Chait BT, et al. Lineage-specific proteins essential for endocytosis in trypanosomes. *J Cell Sci* (2017) 130(8):1379–92. doi:10.1242/jcs.191478
101. Salmon D, Geuskens M, Hanocq F, Hanocq-Quertier J, Nolan D, Ruben L, et al. A novel heterodimeric transferrin receptor encoded by a pair of VSG expression site-associated genes in *T. brucei*. *Cell* (1994) 78:75–86. doi:10.1016/0092-8674(94)90574-6
102. Holland MC, Wurthner JU, Morley PJ, Birchler MA, Lambert J, Albayaty M, et al. Autoantibodies to variable heavy (VH) chain Ig sequences in humans impact the safety and clinical pharmacology of a VH domain antibody antagonist of TNF-α receptor 1. *J Clin Immunol* (2013) 33:1192–203. doi:10.1007/s10875-013-9915-0
103. Papadopoulos KP, Isaacs R, Bilic S, Kentsch K, Huet HA, Hofmann M, et al. Unexpected hepatotoxicity in a phase I study of TAS266, a novel tetravalent agonistic Nanobody® targeting the DR5 receptor. *Cancer Chemother Pharmacol* (2015) 75:887–95. doi:10.1007/s00280-015-2712-0
104. Keyaerts M, Xavier C, Heemskerk J, Devoogdt N, Everaert H, Ackaert C, et al. Phase I study of 68Ga-HER2-nanobody for PET/CT assessment of HER2 expression in breast carcinoma. *J Nucl Med* (2016) 57:27–33. doi:10.2967/jnumed.115.162024
105. Bartunek J, Barbato E, Heyndrickx G, Vanderheyden M, Wijns W, Holz JB. Novel antiplatelet agents: ALX-0081, a nanobody directed towards von Willebrand factor. *J Cardiovasc Transl Res* (2013) 6:355–63. doi:10.1007/s12265-012-9435-y
106. Steeland S, Vandenbroucke RE, Libert C. Nanobodies as therapeutics: big opportunities for small antibodies. *Drug Discov Today* (2016) 21:1076–113. doi:10.1016/j.drudis.2016.04.003
107. Cortez-Retamozo V, Lauwereys M, Hassanzadeh Gh G, Gobert M, Conrath K, Muyldermans S, et al. Efficient tumor targeting by single-domain antibody fragments of camels. *Int J Cancer* (2002) 98:456–62. doi:10.1002/ijc.10212
108. Coppieters K, Dreier T, Silence K, de Haard H, Lauwereys M, Casteels P, et al. Formatted anti-tumor necrosis factor alpha VHH proteins derived from camelids show superior potency and targeting to inflamed joints in a murine model of collagen-induced arthritis. *Arthritis Rheum* (2006) 54:1856–66. doi:10.1002/art.21827
109. Vincke C, Loris R, Saerens D, Martinez-Rodriguez S, Muyldermans S, Conrath K. General strategy to humanize a camelid single-domain antibody and identification of a universal humanized nanobody scaffold. *J Biol Chem* (2009) 284:3273–84. doi:10.1074/jbc.M806889200
110. De Vooght L, Caljon G, Stijlemans B, De Baetselier P, Coosemans M, Van den Abbeele J. Expression and extracellular release of a functional anti-trypanosome Nanobody® in *Sodalis glossinidius*, a bacterial symbiont of the tsetse fly. *Microb Cell Fact* (2012) 11:23. doi:10.1186/1475-2859-11-23
111. De Vooght L, Caljon G, De Ridder K, Van Den Abbeele J. Delivery of a functional anti-trypanosome nanobody in different tsetse fly tissues via a bacterial symbiont, *Sodalis glossinidius*. *Microb Cell Fact* (2014) 13:156. doi:10.1186/s12934-014-0156-6
112. Caljon G, De Vooght L, Van Den Abbeele J. Options for the delivery of anti-pathogen molecules in arthropod vectors. *J Invertebr Pathol* (2013) 112(Suppl):S75–82. doi:10.1016/j.jip.2012.07.013
113. De Vooght L, Caljon G, Van Hees J, Van Den Abbeele J. Paternal transmission of a secondary symbiont during mating in the viviparous tsetse fly. *Mol Biol Evol* (2015) 32:1977–80. doi:10.1093/molbev/msv077
114. Harmsen MM, Van Solt CB, Van Zijderveld-Van Bemmel AM, Niewold TA, Van Zijderveld FG. Selection and optimization of proteolytically stable llama single-domain antibody fragments for oral immunotherapy. *Appl Microbiol Biotechnol* (2006) 72:544–51. doi:10.1007/s00253-005-0300-7
115. Caljon G, Stijlemans B, Saerens D, van den Abbeele J, Muyldermans S, Magez S, et al. Affinity is an important determinant of the anti-trypanosome activity of nanobodies. *PLoS Negl Trop Dis* (2012) 6:e1902. doi:10.1371/journal.pntd.0001902
116. Dean SD, Matthews KR. Restless gossamers: antibody clearance by hydrodynamic flow forces generated at the surface of motile trypanosome parasites. *Cell Host Microbe* (2007) 2:279–81. doi:10.1016/j.chom.2007.10.006
117. Engstler M, Pfohl T, Herminghaus S, Boshart M, Wiegertjes G, Heddergott N, et al. Hydrodynamic flow-mediated protein sorting on the cell surface of trypanosomes. *Cell* (2007) 131:505–15. doi:10.1016/j.cell.2007.08.046
118. Cnops J, Magez S, De Trez C. Escape mechanisms of African trypanosomes: why trypanosomosis is keeping us awake. *Parasitology* (2015) 142:417–27. doi:10.1017/S0031182014001838
119. Bruschi F, Chiumiento L. Immunomodulation in trichinellosis: does *Trichinella* really escape the host immune system? *Endocr Metab Immune Disord Drug Targets* (2012) 12:4–15. doi:10.2174/187153012799279081
120. Stijlemans B, Caljon G, Van Den Abbeele J, Van Ginderachter JA, Magez S, De Trez C. Immune evasion strategies of *Trypanosoma brucei* within the mammalian host: progression to pathogenicity. *Front Immunol* (2016) 7:233. doi:10.3389/fimmu.2016.00233
121. Schwede A, Macleod OJ, MacGregor P, Carrington M. How does the VSG coat of bloodstream form African trypanosomes interact with external proteins? *PLoS Pathog* (2015) 11:e1005259. doi:10.1371/journal.ppat.1005259
122. Jackson DG, Owen MJ, Voorheis HP. A new method for the rapid purification of both the membrane-bound and released forms of the variant surface

glycoprotein from *Trypanosoma brucei*. *Biochem J* (1985) 230:195–202. doi:10.1042/bj2300195
123. Schwede A, Jones N, Engstler M, Carrington M. The VSG C-terminal domain is inaccessible to antibodies on live trypanosomes. *Mol Biochem Parasitol* (2011) 175:201–4. doi:10.1016/j.molbiopara.2010.11.004
124. Engstler M, Thilo L, Weise F, Grünfelder CG, Schwarz H, Boshart M, et al. Kinetics of endocytosis and recycling of the GPI-anchored variant surface glycoprotein in *Trypanosoma brucei*. *J Cell Sci* (2004) 117:1105–15. doi:10.1242/jcs.00938
125. Wentworth P Jr, McDunn JE, Wentworth AD, Takeuchi C, Nieva J, Jones T, et al. Evidence for antibody-catalyzed ozone formation in bacterial killing and inflammation. *Science* (2002) 298:2195–9. doi:10.1126/science.1077642
126. Wentworth P Jr, Jones LH, Wentworth AD, Zhu X, Larsen NA, Wilson IA, et al. Antibody catalysis of the oxidation of water. *Science* (2001) 293:1806–11. doi:10.1126/science.1062722
127. Wentworth AD, Jones LH, Wentworth P, Janda KD, Lerner RA. Antibodies have the intrinsic capacity to destroy antigens. *Proc Natl Acad Sci U S A* (2000) 97:10930–5. doi:10.1073/pnas.97.20.10930
128. Yan B, Yates Z, Balland A, Kleemann GR. Human IgG1 hinge fragmentation as the result of H_2O_2-mediated radical cleavage. *J Biol Chem* (2009) 284:35390–402. doi:10.1074/jbc.M109.064147

Conflict of Interest Statement: The authors declare that the research was conducted in the absence of any commercial or financial relationships that could be construed as a potential conflict of interest.

frontiers in Immunology

ORIGINAL RESEARCH
published: 17 August 2017
doi: 10.3389/fimmu.2017.00960

Isolation of Single-Domain Antibody Fragments That Preferentially Detect Intact (146S) Particles of Foot-and-Mouth Disease Virus for Use in Vaccine Quality Control

Michiel M. Harmsen[1], Julian Seago[2], Eva Perez[2], Bryan Charleston[2], Phaedra L. Eblé[1] and Aldo Dekker[1]*

[1] Wageningen Bioveterinary Research, Lelystad, Netherlands, [2] The Pirbright Institute, Woking, United Kingdom

OPEN ACCESS

Edited by:
Kevin A. Henry, National Research Council Canada, Canada

Reviewed by:
Ming Yang, Canadian Food Inspection Agency, Canada
Mehdi Arbabi Ghahroudi, National Research Council Canada (NRC-CNRC), Canada

***Correspondence:**
Michiel M. Harmsen
michiel.harmsen@wur.nl

Specialty section:
This article was submitted to Vaccines and Molecular Therapeutics, a section of the journal Frontiers in Immunology

Received: *25 April 2017*
Accepted: *26 July 2017*
Published: *17 August 2017*

Citation:
Harmsen MM, Seago J, Perez E, Charleston B, Eblé PL and Dekker A (2017) Isolation of Single-Domain Antibody Fragments That Preferentially Detect Intact (146S) Particles of Foot-and-Mouth Disease Virus for Use in Vaccine Quality Control. Front. Immunol. 8:960. doi: 10.3389/fimmu.2017.00960

Intact (146S) foot-and-mouth disease virus (FMDVs) can dissociate into specific (12S) viral capsid degradation products. FMD vaccines normally consist of inactivated virions. Vaccine quality is dependent on 146S virus particles rather than 12S particles. We earlier isolated two llama single-domain antibody fragments (VHHs) that specifically recognize 146S particles of FMDV strain O_1 Manisa and shown their potential use in quality control of FMD vaccines during manufacturing. These 146S-specific VHHs were specific for particular O serotype strains and did not bind strains from other FMDV serotypes. Here, we describe the isolation of 146S-specific VHHs against FMDV SAT2 and Asia 1 strains by phage display selection from llama immune libraries. VHHs that bind both 12S and 146S particles were readily isolated but VHHs that bind specifically to 146S particles could only be isolated by phage display selection using prior depletion for 12S particles. We obtained one 146S-specific VHH—M332F—that binds to strain Asia 1 Shamir and several VHHs that preferentially bind 146S particles of SAT2 strain SAU/2/00, from which we selected VHH M379F for further characterization. Both M332F and M379F did not bind FMDV strains from other serotypes. In a sandwich enzyme-linked immunosorbent assay (ELISA) employing unlabeled and biotinylated versions of the same VHH M332F showed high specificity for 146S particles but M379F showed lower 146S-specificity with some cross-reaction with 12S particles. These ELISAs could detect 146S particle concentrations as low as 2.3–4.6 µg/l. They can be used for FMD vaccine quality control and research and development, for example, to identify virion stabilizing excipients.

Keywords: enzyme-linked immunosorbent assay, single-domain antibody, foot-and-mouth disease, virion stability, foot-and-mouth disease virion, vaccine quality control

INTRODUCTION

Foot-and-mouth disease (FMD) is an animal disease that is caused by a picornavirus, FMD virus (FMDV), which encompasses seven serotypes: A, O, C, Asia1, SAT1, SAT2, and SAT3. Infection with any one serotype does not produce significant humoral immunity against other serotypes. In FMD endemic areas vaccination is used as a preventive method (1). Due to differences in serotype prevalence in the field most vaccines are used for serotypes O and A. Further vaccines generally are specific

for Asia1 or SAT2 serotypes. Conventional FMD vaccines (2) are based on chemically inactivated FMDVs that are formulated with an adjuvant. FMD virions consist of an RNA molecule and a capsid composed of 60 copies each of VP1, VP2, VP3, and VP4 proteins (3). Intact virions sediment at 146S in sucrose gradients. Some FMDV strains also produce empty capsids that lack the RNA molecule and sediment at 75S. Mild heating or incubation at pH below 6.5 leads to irreversible dissociation of 146S or 75S particles into stable 12S particles that contain five copies each of VP1, VP2, and VP3. Dissociation into 12S particles results in a strongly reduced immunogenicity (4–7).

Several methods have been developed to measure the concentration of 146S particles of the crude FMDV antigen preparation used for vaccine preparation. This is traditionally measured by sucrose density gradient (SDG) centrifugation (8). Novel methods that are more easy to automate are based on size-exclusion high-performance liquid chromatography (9, 10) or lateral flow immunoassay (11). All these methods have the advantage of being suitable for all FMDV strains, but the disadvantage of low sensitivity, limited sample throughput, and inability to discriminate different vaccine strains in multivalent vaccines. Double antibody sandwich (DAS) enzyme-linked immunosorbent assays (ELISAs) using monoclonal antibodies (mAbs) were also developed for FMDV antigen quantification (7, 12–16). They are more sensitive, but often not specific for intact 146S particles. Only two DAS ELISAs were specific for 146S particles due to use of a mAb showing such specificity. They were suitable for detection of A or O serotype strains (15, 16). We have recently developed two DAS ELISAs using two recombinant llama single-domain antibody fragments (VHHs) that bind specifically to either 146S particles or 12S particles of strain O_1 Manisa (17, 18). In each ELISA, the same VHH was used for coating as well as for detection of captured antigen using biotinylated VHH. The DAS ELISA employing 146S-specific VHH M170 was specific for particular O serotype strains, including strain O_1 Manisa. The DAS ELISA employing 12S-specific VHH M3 could detect FMDV antigen of several A, O, and Asia 1 strains but not SAT2 strain. We were also able to measure 146S particles of A and Asia 1 serotype strains employing the M3 DAS ELISA of heated and untreated samples (17). However, this latter ELISA approach is not suitable for detecting 146S particles in the presence of higher concentrations of 12S particles. An ELISA approach employing a 146S-specific VHH is therefore preferred. We here describe the isolation of two VHHs for specific detection of 146S particles of strains Asia 1 Shamir and SAT2 SAU/2/00.

Many conventional mAbs against FMDV have been isolated in the past. Most of those mAbs bind to both 12S and 146S particles (7, 19–22). However, mAbs that specifically detect 146S particles are rarely isolated (15, 16). VHHs against FMDV have recently been isolated (23, 24) without reporting their particle specificity. M170 is the only 146S-specific VHH that is currently described (17). It was isolated by screening a panel of 24 VHHs against strain O_1 Manisa that were earlier isolated from llama immune libraries (25). It is not surprising that 146S-specific VHHs or mAbs are rare since 12S and 146S particles share many epitopes.

VHHs are normally isolated by phage display selection from immunized llamas or dromedaries (26). One of the advantages of using VHHs for this purpose is the high functional diversity of immune libraries derived from heavy chain antibodies since random shuffling of antibody heavy and light chains does not occur. Phage display VHH immune libraries therefore contain VHHs with many different specificities. The isolation of rare specificities requires dedicated selection procedures. The removal from libraries of clones with unwanted cross-reaction to particular antigens can be accomplished by prior depletion of libraries on these antigens before performing selection of VHHs on the target antigen (27), although such depletion often is inefficient (28, 29). We here describe the selection of VHHs specific for 146S particles by depletion on 12S particles. We focus on VHHs specific for Asia 1 and SAT2 FMDV since 146S-specific VHHs or mAbs are not yet available for these serotypes.

MATERIALS AND METHODS

mAbs, VHHs, and FMDV Antigens

Monoclonal antibody 13A6 was raised against SAT1 Zimbabwe/89 that does not neutralize FMDV *in vitro*, cross-reacts to SAT2 Zimbabwe/86 and binds in a trypsin-sensitive manner in ELISA (30). VHHs were produced in baker's yeast as a fusion to the natural llama heavy-chain antibody long hinge region and a hexahistidine tag using vector pRL188 (25) and purified from culture supernatant using immobilized-metal affinity chromatography as described earlier. VHHs produced in this manner are indicated by the suffix "F." At least 20% of the VHH amount produced in this manner is dimerized through the single cysteine present at the C-terminus of the VHH, immediately preceding the his6 tag. Both such monomeric and dimeric VHHs are useful for functional immobilization of VHHs to polystyrene surfaces by passive adsorption (31). Yeast-produced VHHs were biotinylated at a weight ratio of protein to biotin of 10 using amine-reactive sulfo-*N*-hydroxysuccinimide-LC-biotin (Pierce, Rockford, IL, USA). Buffer was exchanged to PBS and free biotin removed by at least three consecutive 10-fold dilutions and concentration using Amicon Ultra 3-kDa molecular weight cutoff concentration devices (Millipore, Billerica, MA, USA). The VHH2 M3ggsVI4$_{Q6E}$ specific for 12S particles has been previously described (32).

The FMD vaccine strains Asia 1 Shamir/Israel/89, SAT2 SAU/2/00, O_1 Manisa/Turkey/69, O_1 British Field Strain 1860 (BFS)/67, A Turkey/98, and A_{24} Cruzeiro/Brazil/55 were used for antigen production. FMDV antigen originated from the virus production facilities in Lelystad. FMDV was cultured using BHK-21 cells grown in suspension in industrial size bioreactors. FMDV present in the clarified culture was inactivated with 0.01 M binary ethylenimine and concentrated using two consecutive polyethylene glycol-6000 precipitations, resulting in crude antigen. Infectious FMDV was prepared at laboratory scale by growing them on monolayers of BHK-21 cells and harvesting the culture supernatant without further treatment. Work with infectious FMDV was done in a high containment unit at Wageningen Bioveterinary Research using appropriate measures for virus handling and waste disposal to prevent FMDV introduction into the environment. Wageningen Bioveterinary Research is authorized to work with live FMDV according to EU directive 2003/85/EC.

Foot-and-mouth disease virus antigens were fractionated using 10–40% SDGs that were centrifuged for 2.5 h at 10°C and 200,000 × *g*. The gradients were fractionated into 20 0.61 ml aliquots and the absorbance at 254 nm was determined to identify the 146S peak. The 146S concentration in milligrams per liter was then calculated by multiplying the absorbance at 254 nm with 126.7. 12S particles were prepared from 146S preparations by acidification ($12S^A$) or heat treatment for 1 h at 56°C ($12S^H$) as previously described (33).

Llama Immunization and Phage Library Construction

Llama immunizations were performed after ethical review by Wageningen Bioveterinary Research and in accordance with Dutch national guidelines on animal use. The immunization of llama 6058 with crude antigen of FMDV strain Asia 1 Shamir has been described earlier (25). The immunization of llamas 3049 and 3050 with influenza antigens and subsequent phage library construction was earlier described (34). Simultaneously with these influenza antigens llamas 3049 and 3050 were immunized with FMDV 146S particles purified from SDG. For each of the three immunizations llama 3049 received 40 µg Asia 1 Shamir 146S particles and 45 µg A_{24} Cruzeiro 146S particles, whereas llama 3050 received 50 µg SAT2 SAU/2/00 146S particles. Phage display immune libraries in phagemid vector pRL144 (35) of at least 10^7 independent clones were generated as previously described (25, 34).

Phage Display Selection of Antigen Binding VHHs

Phage display selections were performed by two consecutive rounds of biopanning (36) in polystyrene 96-well plates (Greiner, Solingen, Germany, Cat. No. 655092), using 100 µl/well for each incubation. Many variations on the procedure were used (**Table 1**). In general, antigen was immobilized to 96-well plates at three serial 10-fold dilutions and a control without antigen was included. VHHs were normally coated at concentrations of 1, 0.1, and 0.01 mg/l in 0.05 M carbonate/bicarbonate buffer, pH 9.6 (coating buffer), overnight at 4°C. Purified 146S particles (1 mg/l) were separately incubated in PBS buffer containing 1% milk and 0.05% Tween-20 (PBSTM) for 1 h at room temperature (RT). Controls included wells coated with VHH without subsequent incubation with FMDV antigen and uncoated wells incubated with 1 mg/l FMDV antigen. Plates were then incubated with 1×10^9 transducing phage units per well. In initial experiments, phages were preincubated in PBSTM containing 10 mg/l $12S^A$ particles and then added to wells with captured 146S particles to compete for binding to $12S^A$. In later experiments, phages binding to $12S^A$ particles were depleted prior to biopanning by incubation on plates containing immobilized $12S^A$ particles. For this purpose, separate plates were coated with coating buffer containing 1 mg/l $M3ggsVI4_{Q6E}$ or M311F specific for SAT2 SAU/2/00 antigen and subsequently incubated with 5 mg/l $12S^A$ particles of strains Asia 1 Shamir or SAT2 SAU/2/00, respectively. Phages were then incubated on these plates with captured $12S^A$ particles after which the unbound phages were transferred

TABLE 1 | Phage display conditions used to retrieve FMDV binding VHHs.

Llama	Coating		Captured FMDV		Competing FMDV		Depleting FMDV		VHHs selected	No. VHH sequenced	No. Unique VHHs	No. CDR3 groups
	Conc. (mg/l)	Protein	Conc. (mg/l)	FMDV antigen	Conc. (mg/l)	FMDV Antigen	Conc. (mg/l)	FMDV antigen				
6058	1	Streptavidin	0.1	Biotinylated Asia 1 Shamir antigen	–	None	–	None	M98	1	1	1
3050	0.1	mAb13A6	0.5	SAT2 SAU/2/00 146S	10	SAT2 SAU/2/00 $12S^A$	–	None	M311–M317	7	5	4
3050	0.1	M311F	0.5	SAT2 SAU/2/00 146S	–	None	5	SAT2 SAU/2/00 $12S^A$	M371–M381	11	7	3
3049	0.1	M98F	0.5	Asia 1 Shamir 146S	10	Asia 1 Shamir $12S^A$	–	None	M301–M308	8	8	7
3049	0.1	M98F	0.5	Asia 1 Shamir 146S	–	None	5	Asia 1 Shamir $12S^A$	M331–M337	7	7	6
6058												

FMDV, foot-and-mouth disease virus.

to biopanning plates containing captured 146S particles. To ensure binding of most $12S^A$ reactive phages we used 20-fold lower amounts of phage (5×10^7 transducing phage units per well) when employing depletion. Bound phages were finally eluted by incubation with 1 mg/ml trypsin in PBS for 30 min at 37°C and immediately transduced to *Escherichia coli* TG1 [(F′ *traD36 proAB lacIqZ* Δ*M15*) *supE thi-1* Δ*(lac-proAB)* Δ*(mcrB-hsdSM)5(rK⁻ mK⁻)*] cells. In each selection round, we performed a phage ELISA simultaneous with the phage display selection for evaluation of the phage display selection. For this purpose, a duplex plate containing similar concentrations and types of antigen and phage was incubated with a peroxidase-conjugated mAb against M13 phage instead of incubation with trypsin. The amount of bound antigen-specific phage was then measured by phage ELISA.

Production of Soluble VHH in *E. coli*

After the second round of panning phages was transduced to *E. coli* TG1 cells, individual colonies were picked and the VHH genes were induced with 1 mM isopropyl β-D-thiogalactopyranoside. Recombinant VHHs, extracted from the periplasm, were tested for binding to FMDV antigens at 10-fold dilution as described below in Section "Enzyme-Linked Immunosorbent Assays."

Sequence Analysis

Sequence analysis of the VHH encoding region was performed, as previously described (37). The deduced VHH amino acid sequences were aligned according to the IMGT system (38) for alignment, numbering, and complementarity-determining region definition of immunoglobulins. VHHs were classified into subfamilies as earlier defined (37). Potential N-glycosylation sites were defined as Asn-X-Ser/Thr, where X represents any amino acid, except Pro.

Enzyme-Linked Immunosorbent Assays

Three different ELISA procedures were used. We first describe the basic ELISA procedure that was commonly used in these three procedures. ELISAs were performed by coating high-binding polystyrene 96-well plates (Greiner) with 0.1–1 mg/l of unlabeled VHH, VHH2, or mAb in 50 mM carbonate/bicarbonate buffer, pH 9.6 (coating buffer), overnight at 4°C. Coating and subsequent incubations were performed using 100 µl per well. After washing, the coated plates were incubated with FMDV antigens in ELISA-buffer (1% skimmed milk; 0.05% Tween-20; 0.5 M NaCl; 2.7 mM KCl; 2.8 mM KH_2PO_4; 8.1 mM Na_2HPO_4; pH 7.4) or PBSTM for 1 h at RT. The 146S concentration of the FMDV antigens was determined by measuring the absorbance at 254 nm as described above. The concentration of the 12S antigens was derived from the 146S concentration of the sample from which it was prepared assuming complete conversion of 146S into 12S particles. Plates were next incubated with either phage-displayed VHH, *E. coli*-produced VHH, or yeast-produced biotinylated VHH, and subsequently with a suitable specific peroxidase conjugate, using the same buffer as used for incubation with FMDV antigen (ELISA-buffer or PBSTM). The peroxidase conjugate was subsequently detected by staining with 3,3′,5,5′-tetramethylbenzidine. After stopping the reaction by addition of 0.5 M H_2SO_4 (50 µl per well) the absorbance at 450 nm was measured using a Multiskan Ascent spectrophotometer (Thermo Labsystems, Helsinki, Finland).

For phage ELISA plates were preferably coated with low concentrations of VHH (0.1 mg/l) and FMDV antigen (0.5 mg/l) as described in **Table 1**. Many variations on the procedure were used during phage display selection as described above. Bound phage displayed VHH was detected by incubation with peroxidase-conjugated mAb against the M13 p8 coat protein (GE Healthcare, Little Chalfont, UK) in PBSTM.

For ELISA using *E. coli*-produced soluble VHH plates were preferably coated with 1 mg/l VHH and then subsequently incubated with 1 mg/l FMDV antigen in ELISA buffer. Bound FMDV antigens were detected by incubation with 10-fold diluted *E. coli*-produced soluble VHH, which contains a myc-tag, and a peroxidase-conjugated mAb against the c-myc tag (clone 9E10; Roche Applied Science).

For DAS ELISA to measure the FMDV antigen concentration plates were coated with 0.5 mg/l of unlabeled VHH or VHH2. These plates were then incubated with serial 2-fold dilution series of FMDV antigen preparations in ELISA buffer. Normally, standards of untreated FMDV antigen were included in the ELISAs for quantification of 146S particles. However, $12S^A$ preparations of FMDV antigen were used as standards in the ELISA employing M3ggsVI-4_{Q6E}. Standards were serial twofold dilutions of 1 mg/l start concentration. Plates were next incubated with 0.25 mg/l of biotinylated VHH(2). Bound biotinylated VHH(2) was detected with 1 mg/l PO-conjugated streptavidin (Jackson ImmunoResearch Laboratories Inc., West Grove, PA, USA). Absorbance data were evaluated using an Excel® spreadsheet template (Microsoft Corporation, Redmond, WA, USA). A four-parameter logistic curve was fitted to absorbance and FMDV antigen concentrations of standards by non-linear least squares using the Excel® solver tool. The FMDV antigen concentration in unknown samples was then determined by interpolation. For determination of the quality of binding of VHHs to particular FMDV antigens these antigens were titrated in twofold dilution series. The effective antigen concentration required to reach a particular absorbance value was then interpolated after four-parameter logistic curve fitting of absorbance and antigen concentrations.

The limit of detection (LOD) of ELISAs was measured by titrating FMDV antigens in triplicate and interpolating the VHH concentration required to reach the average and three times the SD of nine blank measurements without antigen.

RESULTS

Selection of 146S-Specific VHHs

We earlier immunized llama 6058 with crude antigen of FMDV strains O_1 Manisa, A Turkey, A_{22} Iraq, and Asia 1 Shamir. We isolated many FMDV O_1 Manisa binding VHHs from this llama by phage display employing biotinylated FMDV antigen captured with streptavidin-coated magnetic beads (25). The VHH M98 was similarly selected from llama 6058 using biotinylated FMDV Asia 1 Shamir antigen. Yeast-produced M98F VHH neutralized Asia 1 Shamir FMDV *in vitro*, confirming M98F binds FMDV

virions rather than a host protein present in the crude FMDV antigen used to perform the selection. As further confirmed below M98F was found to bind both 12S and 146S particles. This was not unexpected since 146S-specific VHHs were also rarely retrieved during phage display selection of O_1 Manisa binding VHHs (25).

To improve the selection process of 146S-specific VHHs we purified 146S particles by SDGs. The purified 146S particles were then used for both novel llama immunization and phage display selection of VHHs. One llama (3049) was immunized with FMDV Asia 1 Shamir 146S and another llama (3050) with SAT2 SAU/2/00 146S. As observed with many other proteins (39) FMDV loses much of its antigenicity upon direct passive adsorption to polystyrene (40). We, therefore, used M98F VHH that binds Asia 1 Shamir and mAb 13A6 that binds SAT2 SAU/2/00 to capture purified 146S particles in ELISA. We initially tried to select VHHs that bind specifically to 146S particles by competition during phage display selection with a surplus of $12S^A$ particles. This approach was not successful as all VHHs isolated bound both 146S and $12S^A$ particles when tested as soluble VHH produced from *E. coli* TG1 cells (results not shown). After sequence analysis (**Table 1**), we identified five unique clones (M311-M317) binding SAT2 SAU/2/00 and eight unique clones (M301–M308) binding Asia 1 Shamir 146S. Their cross-reaction with 12S was later confirmed using yeast-produced VHH (**Table 2**). To increase enrichment of 146S-specific VHHs we improved phage display selections in two ways. Since mAb 13A6 preferentially binds $12S^A$ particles (see below), it was replaced by a novel isolated VHH that was highly produced in yeast, M311F, for capture of SAT2 SAU/2/00 146S particles. Furthermore, novel selections were performed using depletion with immobilized $12S^A$ particles instead of competition with soluble $12S^A$ particles. Using these novel selection procedures we retrieved seven unique SAT2 SAU/2/00 binding VHHs comprising three novel CDR3 groups (**Table 1**) that are different from earlier isolated SAT2 SAU/2/00 binding VHHs (**Table 2**) and seven unique Asia 1 Shamir binding VHHs comprising six CDR3 groups (**Table 1**) that are mostly different from earlier isolated VHHs (**Table 2**).

146S Specificity of VHHs

Seventeen VHHs with different CDR3 sequences (**Table 2**) were produced by yeast expression. They all lacked potential *N*-glycosylation sites to prevent compromised antigen binding due to fortuitous *N*-glycosylation. The purified VHHs were biotinylated for use in DAS ELISA in combination with the same unlabeled VHH for coating. To assess the specificity of the biotinylated VHHs for the different FMDV particles we performed DAS-ELISAs with a titration series of untreated antigen, 146S particles and $12S^H$. Similar to earlier methods (17), the FMDV antigen concentration required to reach an absorbance value of 0.4 was calculated for each FMDV antigen. The absorbance value of 0.4 was chosen because for all different ELISAs used it is sufficiently above background absorbance values to be indicative of antigen binding and sufficiently below the maximal absorbance value. The ratio between these antigen concentration values for $12S^H$ and 146S was taken as a measure for particle

TABLE 2 | VHH sequence characteristics and specificity of VHHs for 12S and 146S particles in DAS ELISA using the same VHH for coating and as biotinylated VHH.

VHH or mAb	Llama	CDR3 sequence	VHH subfamily[a]	Antigen concentration (μg/l) to reach absorbance = 0.4			Ratio $12S^H$/146S
				antigen	146S	$12S^H$	
SAT2 SAU/2/00							
M311F	3050	NAITYYTDAPDY	2	2.7	2.2	5.7	2.6
M314F	3050	AADKWLYISGWRHCRPVFGS	3	8.3	20	17	0.85
M315F	3050	YGDIRVRNY	2	5.7	3.6	17	4.7
M317F	3050	AADWRFVEAVAGRAKY	3	27	66	95	1.4
M377F	3050	NALVLSSSWSEGDY	2	0.76	0.58	5.9	10
M379F	3050	NLVNWGYGENY	2	1.8	1.2	34	28
M380F	3050	NYQRPLSNDNY	2	0.70	0.59	8.7	15
mAb 13A6	NA[b]	NA	NA	>1,000[c]	>1,000	164	<0.16
Asia 1 Shamir							
M98F	6058	AAQSPGMSGTYSRSDVYPY	1	4.1	5.5	29.8	5.4
M301F	3049	AATEDYYSGSLGSYYVCPDYYNMDY	3	60	67	>1,000	>15
M303F	3049	AADEPERVYCRDYVRTQYPMDY	3	53	81	>1,000	>12
M304F	3049	AADPPDQDYCSDYDVTVGTELWGS	3	35	42	>1,000	>24
M306F	3049	AADQGAYCSDHGEIGYYGMDY	3	45	62	>1,000	>16
M307F	3049	AAAPEDYYCSDYDGPSEDDYGMDY	3	38	51	>1,000	>20
M308F	3049	AGDQDPAYCSDYWDLNEYDY	3	39	55	>1,000	>18
M332F	3049	AAAWSFRSDYGARLKSAYDF	1	8.4	7.6	433	57
M334F	3049	AADDSGLHGCSDYWILYEYEY	3	245	342	>1,000	>2.9
M336F	6058	AAEESWSTSTYYYTHSYSY	1	>1,000	>1,000	>1,000	ND
M3ggsVI4$_{Q6E}$	NA	NA	NA	51	746	13	0.017

[a]*As defined by reference (37).*

[b]*NA, Not applicable.*

[c]*>1,000 indicates absorbance does not exceed 0.4 at the highest VHH concentration analyzed (1 mg/l).*

DAS, double antibody sandwich; ELISAs, enzyme-linked immunosorbent assays; mAb, monoclonal antibody.

specificity (**Table 2**). A ratio > 1 corresponds to 146S specificity and a ratio < 1 corresponds to 12S specificity.

In the case of SAT2 SAU/2/00 antigen mAb 13A6 shows 12S specificity with a ratio below 0.16, the four VHHs selected by competition with $12S^A$ show no or limited 146S specificity with ratios of 0.85–4.7, whereas the three VHHs selected by depletion with $12S^A$ (M377F, M379F and M380F) show higher 146S specificity with ratios of 10–28 (**Table 2**). M379F exhibited the highest 146S specificity and recognized relatively low antigen and 146S concentrations as compared to other SAT2 SAU/2/00 binding VHHs. Among the Asia 1 Shamir binding VHHs, M332F that was selected by depletion on $12S^A$ particles showed highest 146S specificity with a ratio of 57. Furthermore, M332F recognized lower concentrations of untreated antigen and 146S as compared to most of the other nine VHHs. Only M311F recognized slightly lower antigen concentrations, although with far lower 146S specificity (**Table 2**). In conclusion, M332F exhibited high 146S specificity for strain Asia 1 Shamir, whereas M379F showed some 146S specificity for strain SAT2 SAU/2/00.

We next titrated FMDV antigens and $12S^H$ of strains SAT2 SAU/2/00 and Asia 1 Shamir in triplicate in the $M3ggsVI4_{Q6E}$, M311F, M379F, M98F, and M332F ELISAs using the same VHH as used for detection also for coating. The LOD was calculated for each ELISA (**Table 3**). The M332F ELISA had an LOD of 4.6 μg/l and the M379F ELISA of 2.3 μg/l for antigen. We also titrated the antigens in these latter two ELISAs in the presence of a constant amount of $12S^H$ particles to determine if antigen quantification is affected by the presence of $12S^H$ particles. Asia 1 Shamir antigen quantification in the M332F ELISA was not affected by the presence of 4 mg/l $12S^H$ (**Figure 1B**) but SAT2 SAU/2/00 quantification in the M379F ELISA was affected already by the lowest $12S^H$ concentration analyzed (0.15 mg/l; **Figure 1E**). This is consistent with the earlier observed higher specificity of M332F for 146S particles than M379F.

FMDV Strain Specificity

To further characterize the 17 VHHs, their respective ability to bind to strains of other FMDV serotypes was investigated. As a control we included mAb 13A6 and $M8ggsVI4_{Q6E}$, to demonstrate successful immobilization of the various antigens (**Table 4**). All seven SAT2 SAU/2/00 binding VHHs did not cross-react to strains Asia 1 Shamir, A Turkey, A_{24} Cruzeiro, O_1 BFS, or O_1 Manisa. Similarly, all 10 Asia 1 Shamir binding VHHs did not cross-react to strains SAT2 SAU/2/00, A Turkey, A_{24} Cruzeiro, O_1 BFS, or O_1 Manisa (**Table 4**).

TABLE 3 | LOD of different DAS ELISAs.

FMDV strain	DAS ELISA	LOD (μg/l)	
		Antigen	$12S^H$
SAT2 SAU/2/00	M311F	5.2	12
SAT2 SAU/2/00	M379F	2.3	19
Asia 1 Shamir	M98F	3.8	19
Asia 1 Shamir	M332F	4.6	>2,000[a]
Asia 1 Shamir	$M3ggsVI4_{Q6E}$	17	83

[a]*>2,000 indicates LOD not reached at the highest VHH concentration used (2 mg/l).*
DAS, double antibody sandwich; ELISAs, enzyme-linked immunosorbent assays; LOD, limit of detection.

Binding to 12S, 75S, and 146S Particles in SDGs

Next, we analyzed the specificity of M332F and M379F, as well as the earlier isolated M170F, for different FMDV particles (12S, 75S, and 146S) present in SDG fractions. As controls, we also analyzed each fraction using VHHs that detect both 12S and 146S particles of Asia 1 Shamir, SAT2 SAU/2/00, or O_1 Manisa.

When FMDV Asia 1 Shamir, SAT2 SAU/2/00, or O_1 Manisa purified 146S particles were again separated on SDG a peak was seen in fractions 15–18 that corresponds to 146S particles (**Figures 2A–C**). The absence of further peaks indicated virions had not dissociated into smaller particles during virus handling. The peak in fraction 20 of Asia 1 Shamir FMDV (**Figure 2A**) probably represents aggregated 146S particles. When 146S particles purified from SDG were acidified and again subjected to SDG only fractions 2–5 contained FMDV antigen (**Figures 2D–F**), indicating full conversion into $12S^A$ particles. When crude antigen was separated on SDG some antigenic material was detected in fractions 6–14 by ELISA (**Figures 2G–I**). This could represent 75S particles that sediment between $12S^A$ and 146S particles, although 75S particles would be expected to form a sharper peak. The amount of putative 75S particles as compared to 146S particles is especially high for strain Asia 1 Shamir (**Figure 2G**), somewhat lower but still considerable for strain SAT2 SAU/2/00 (**Figure 2H**) and quite low, but clearly detectable for strain O_1 Manisa (**Figure 2I**). To visualize the low amount of putative 75S particles of strain O_1 Manisa the material in fractions 1–15 was plotted on a scale of 0–0.5 mg/l on the right axis (**Figure 2I**). When crude antigen was acidified prior to SDG fractionation a 12S peak was readily observed for Asia 1 Shamir (**Figure 2J**) and O_1 Manisa (**Figure 2L**), but was less evident for SAT2 SAU/2/00 (**Figure 2K**). This could have been due to a combination of reduced $12S^A$ particle reactivity in the M311F ELISA and the use of untreated antigen that predominantly consisted of 146S particles as a standard. Acidified O_1 Manisa antigen consisted only of 12S particles, indicating full dissociation of 146S and 75S particles into 12S (**Figure 2L**). However, acidified SAT2 SAU/2/00 antigen also contained a broad peak in the fractions corresponding to 75S particles (**Figure 2K**), whereas Asia 1 Shamir antigen contained both a broad peak corresponding to putative 75S particles as well as a 146S peak, although both peaks were considerably lower as compared to untreated antigen (**Figure 2J**). This indicates that, unlike SDG purified 146S particles, 75S and 146S particles present in Asia 1 Shamir crude antigen, and 75S particles present in SAT2 SAU/2/00 antigen are only partially converted into 12S by acidification. Such a difference in acid liability between SDG purified and crude antigen could be due to matrix effects due to different buffer composition, as was also reported earlier (41).

The M170F DAS ELISA detects only O_1 Manisa 146S particles (**Figures 2C,F,I,L**). The M332F DAS ELISA detects both Asia 1 Shamir 146S and the putative 75S particles, although the latter are detected with reduced efficiency as compared to the M98F DAS

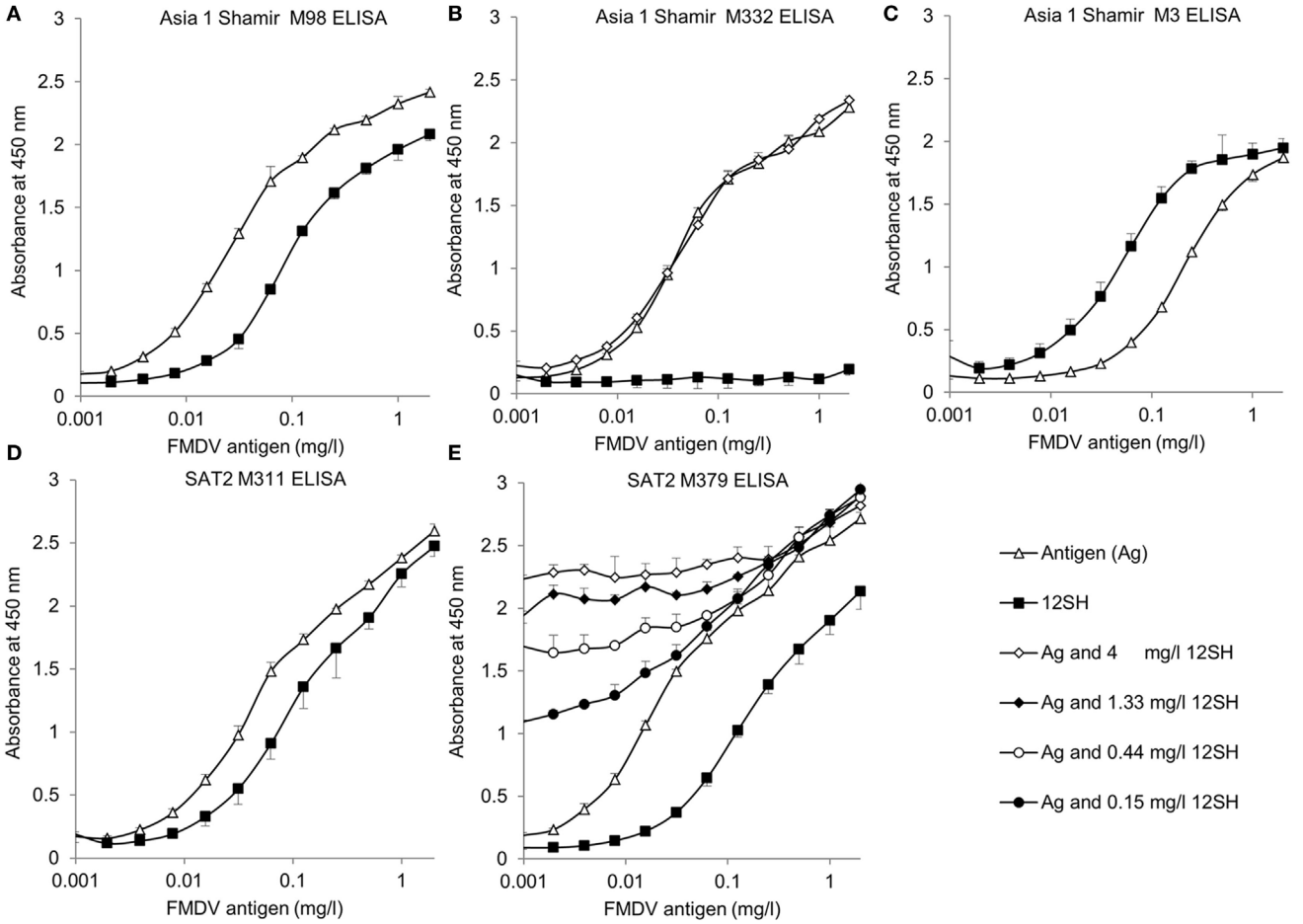

FIGURE 1 | Titration of foot-and-mouth disease virus (FMDV) antigens or $12S^H$ particles derived thereof in double antibody sandwich (DAS) enzyme-linked immunosorbent assays (ELISAs). FMDV strains Asia 1 Shamir **(A–C)** and SAT2 SAU/2/00 **(D,E)** were used. The different DAS ELISAs employed the same VHH for coating in unlabeled form and for detection in biotinylated form. The different VHHs used are indicated above the panels. Antigen or $12S^H$ particles were twofold titrated with a starting concentration of 2 mg/l. The two ELISAs using 146S-specific VHHs **(B,E)** were also titrated with a 2-fold dilution series of antigen to which a constant amount of $12S^H$ particles was added. In the legend the concentration of the constant amount of $12S^H$ particle is indicated. ELISAs were performed in triplicate. Mean and SD are indicated.

ELISA (**Figures 2A,D,G,J**). The M379F DAS ELISA detects both SAT2 SAU/2/00 146S and putative 75S particles with an efficiency that is equal to the M311F DAS ELISA, whereas SAT2 SAU/2/00 $12S^A$ particles are detected with reduced efficiency as compared to the M311F ELISA (**Figures 2B,E,H**). The binding of M379F to $12S^A$ particles, although with reduced efficiency compared to 146S particles, is consistent with the relatively low 146S specificity observed for M379F.

To elucidate the nature of the putative 75S particles we fractionated infectious FMDV on SDG and determined the presence of infectious virus in each fraction by plaque assay. In addition, we determined the concentration of total FMDV antigen present in each fraction by M3 ELISA after acidification. The M3 ELISA facilitates reliable quantification of 12S, 75S, and 146S particles against a 12S standard. This analysis was only done for strains Asia 1 Shamir and O_1 Manisa since strain SAT2 SAU/2/00 is not detected by M3 ELISA (**Figures 3A,B**). Notably, FMDV O_1 Manisa infectious virus contained a considerable putative 75S peak (**Figure 3B**). Infectious virus was only found in fractions 16–19, consistent with the notion that this represents 146S particles and that FMDV antigen in fractions 9–11 represent 75S particles.

DISCUSSION

We aimed to isolate VHHs that specifically bind to FMDV 146S particles of strains SAT2 SAU/2/00 and Asia 1 Shamir. For this purpose, llamas 3049 and 3050 were immunized with SDG purified 146S particles of these strains. We preferentially used a 12S depletion step in phage display selections to enrich for 146S-specific VHHs. In this manner, we isolated three novel SAT2 SAU/2/00 binding VHHs showing reasonable 146S specificity and one novel Asia 1 Shamir binding VHH showing high 146S specificity. However, when using a depletion step there is some risk of detachment of captured 12S particles and carryover of this material into the wells containing 146S

TABLE 4 | Binding of biotinylated VHHs to different FMDV strains.

Biotinylated VHH(2) or mAb	VHH concentration (μg/l) to reach absorbance of 0.4					
	SAT2 SAU/2/00[a]	Asia 1 Shamir[b]	A Turkey[c]	A_{24} Cruzeiro[c]	O_1 BFS[d]	O_1 Manisa[d]
M311F	0.25	>1,000[e]	>1,000	>1,000	>1,000	>1,000
M314F	2.8	>1,000	>1,000	>1,000	>1,000	>1,000
M315F	0.27	>1,000	>1,000	>1,000	>1,000	>1,000
M317F	0.06	>1,000	>1,000	>1,000	>1,000	>1,000
M377F	1.6	>1,000	>1,000	>1,000	>1,000	>1,000
M379F	0.29	>1,000	>1,000	>1,000	>1,000	>1,000
M380F	1.6	>1,000	>1,000	>1,000	>1,000	>1,000
mAb 13A6	39	21	11	12	566	450
M98F	>1,000	2.5	>1,000	>1,000	>1,000	>1,000
M301F	>1,000	0.59	>1,000	>1,000	>1,000	>1,000
M303F	>1,000	0.14	>1,000	>1,000	>1,000	>1,000
M304F	>1,000	0.50	>1,000	>1,000	>1,000	>1,000
M306F	>1,000	1.8	>1,000	>1,000	>1,000	>1,000
M307F	>1,000	0.75	>1,000	>1,000	>1,000	>1,000
M308F	>1,000	0.11	>1,000	>1,000	>1,000	>1,000
M332F	>1,000	5.4	>1,000	>1,000	>1,000	>1,000
M334F	>1,000	2.0	>1,000	>1,000	>1,000	>1,000
M336F	>1,000	213	>1,000	>1,000	>1,000	>1,000
M8ggsVI4$_{Q6E}$	>1,000	284	113	398	66	5.2

[a] *1 mg/l FMDV antigen captured with 1 mg/l M311F.*
[b] *1 mg/l FMDV antigen captured with 1 mg/l M98F.*
[c] *1 mg/l FMDV antigen captured with 1 mg/l M8F.*
[d] *1 mg/l FMDV antigen captured with 1 mg/l M170F.*
[e] *>1,000, absorbance does not exceed 0.4 at the highest VHH concentration used (1 mg/l).*
BFS, British Field Strain 1860; FMDV, foot-and-mouth disease virus; mAb, monoclonal antibody.

particles for panning, resulting in binding to capturing VHH and unwanted enrichment for 12S binding phage clones. Since 12S binding VHHs are generally not serotype specific this can be prevented by using 12S particles from another strain for depletion in combination with a serotype-specific VHH for capturing 146S particles. We currently favor this approach for isolation of 146S-specific VHHs. Selection of VHHs specifically recognizing *Taenia solium* antigen without cross-reacting with other *Taenia* species was earlier described (27). Furthermore, VHHs recognizing a recombinant immunotoxin without binding an undesired deamidated derivative of this immunotoxin were isolated recently (42). Together with our study these are further examples where the high functional diversity of camelid heavy-chain antibody immune libraries in combination with careful phage display selection schemes allows isolation of rare VHHs that can discriminate closely related antigens.

We developed two DAS ELISAs that utilize the same yeast-produced VHH for coating, as well as detection when in a biotinylated form, for quantification of FMDV 146S particles. The ELISA with M379F VHH for quantification of SAT2 SAU/2/00 FMDV required 28-fold higher 12S concentrations than 146S concentrations to reach similar absorbance values. Thus, it shows reasonable specificity for 146S particles. However, it cannot be used for quantification of 146S particles in the presence of high concentrations of 12S particles due to cross-reaction with 12S particles. Since the 12S content of vaccines is generally less than 20% of total FMDV antigen (18), such specificity is sufficient to measure the 146S content of SAT2 vaccines with only an about 1% error. Similar analyses performed with M332F VHH to quantify Asia 1 Shamir exhibited a 51-fold increase in specificity for 146S particles, revealing this VHH could be used for 146S quantification in the presence of high concentrations of 12S particles. Both ELISAs showed an LOD of 2.3–4.6 μg/l 146S. Assuming that the antigen concentration in FMDV vaccines is about 10 mg/l and that extraction of antigens from vaccines for use in VHH-ELISA involves a 10-fold dilution of vaccines (18), such sensitivity is amply sufficient for quantification of FMDV antigens in vaccines as well as stability studies of vaccines, which requires measurement of FMDV antigen concentrations that decrease to even lower levels. However, when needed for other applications the LOD could possibly be further increased by genetic fusion of VHH domains to increase affinity as was earlier demonstrated for an antitumor necrosis factor alpha VHH (43) and many further VHHs. In addition, both ELISAs did not detect strains belonging to other serotypes. The M332F ELISA also does not recognize strain Asia 1 Bahrain (results not shown). Both 146S-specific VHHs bind in a serotype-specific manner, and M332F binding is also strain specific. Such coincidence of strain and serotype specificity and 146S specificity was observed before with the 146S-specific O_1 Manisa binding VHH M170F (25) and two 146S-specific A serotype strain binding mAbs (15, 16). This suggests that the 146S-specific antigenic sites that we now detect on strains of O, SAT2, and Asia 1 serotypes are located on the same region of the FMDV capsid. This notion is consistent with the conservation of three of the four neutralizing antigenic sites between O, A, C, and Asia 1 serotype FMDV strains (44). The 146S-specific antigenic site most likely overlaps with the interface of two 12S pentamers.

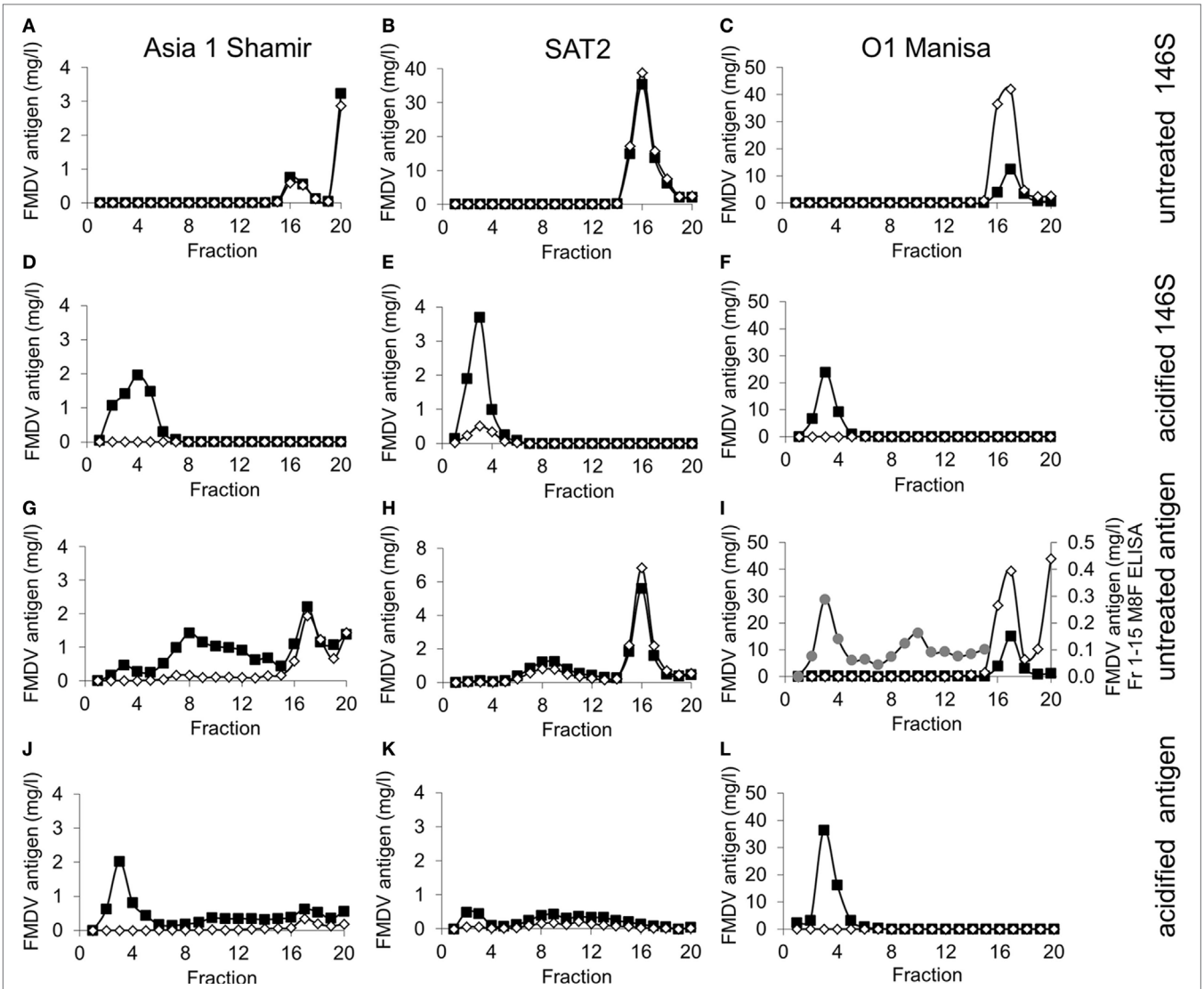

FIGURE 2 | Specificity of double antibody sandwich (DAS) enzyme-linked immunosorbent assays (ELISAs) for inactivated foot-and-mouth disease virus (FMDV) antigen fractionated by sucrose density gradient (SDG). FMDV strains Asia 1 Shamir **(A,D,G,J)**, SAT2 SAU/2/00 **(B,E,H,K)**, and O_1 Manisa **(C,F,I,L)** were used. FMDV 146S particles purified by SDG were again layered on SDG without further treatment **(A–C)** or after prior acidification for conversion into $12S^A$ particles **(D–F)**. Crude FMDV antigen was similarly fractionated on SDG without further treatment **(G–I)** or after prior acidification **(J–L)**. Twenty fractions of each SDG were analyzed by ELISA using either a VHH that is specific for 146S particles (open diamonds) or that binds both 12S and 146S particles (closed squares). The different 146S-specific VHHs used were M332F **(A,D,G,J)**, M379F **(B,E,H,K)**, and M170F **(C,F,I,L)**. The different 12S- and 146S-recognizing VHHs used were M98F **(A,D,G,J)**, M311F **(B,E,H,K)**, and M8F **(C,F,I,L)**. In panel **(I)**, the low amount of FMDV antigen detected in fractions 1–15 by M8 ELISA is visualized by plotting on a different scale (right axis; gray circles). FMDV antigen concentrations in fractions were calculated from titration series in ELISA against a standard of untreated FMDV antigen with known 146S content. Fraction 1 corresponds to top of gradient.

Double antibody sandwich enzyme-linked immunosorbent assay analysis of SDG fractionated inactivated FMDV antigen of strains SAT2 SAU/2/00, Asia 1 Shamir, and O_1 Manisa reveals that some immunoreactive material fractionates between the 12S and 146S peaks (**Figure 2**). This material could represent 75S empty capsids, although the peak is shallower compared to the 12S and 146S peaks, especially for strain Asia 1 Shamir. Consistent with this notion SDG fractionation of infectious Asia 1 Shamir and O_1 Manisa FMDV confirms that this material is not infectious (**Figure 3**). These putative 75S particles derived from inactivated antigen are not recognized by M170F, recognized with reduced efficiency by M332F, and recognized well by M379F (**Figure 2**). Acidification of crude inactivated antigen did not fully convert the putative 75S particles of strains SAT2 SAU/2/00 and Asia 1 Shamir and the 146S particles of strain Asia 1 Shamir into 12S particles. We, therefore, recommend that preparation of a 12S standard for use in the 12S-specific M3 ELISA is preferably done by SDG purification of 146S particles and subsequent heating. The preparation of 12S standards by conversion of 146S present in crude antigen into 12S as done

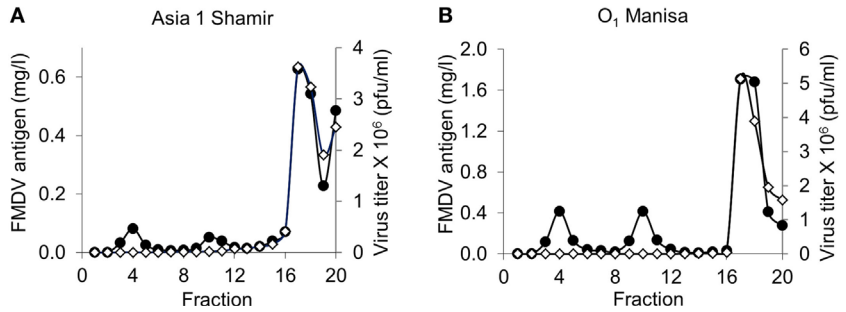

FIGURE 3 | Specificity of double antibody sandwich (DAS) enzyme-linked immunosorbent assays (ELISAs) for infectious foot-and-mouth disease virus (FMDV) particles fractionated by sucrose density gradient (SDG). Infectious virus of FMDV strain Asia 1 Shamir **(A)** or O_1 Manisa **(B)** was fractionated on SDG. Each fraction was analyzed for infectious FMDV titer (open diamonds) or the FMDV antigen concentration (closed circles). FMDV antigen concentration was measured by M3 ELISA on samples that were first acidified for conversion into $12S^A$ particles against a $12S^A$ standard. Fraction 1 corresponds to top of gradient.

earlier by us (17) is inaccurate as it ignores the 12S particles already present in the sample and the 12S particles derived from 75S particles.

The ELISAs developed here for quantification of 146S particles of strains Asia 1 Shamir and SAT2 SAU/2/00 can be used for quality control of FMD vaccines during and after manufacturing. There is a need for such quality control as many locally produced FMD vaccines show poor quality (45, 46). Several other ELISAs have been described recently for this purpose (7, 12–17). There are only three reports of ELISAs specific for 146S particles (15–17). They were only suitable for O and A serotype strains. Our VHH-based ELISAs that detect 146S particles of SAT2 and Asia 1 serotype strains thus complement the currently available 146S-specific ELISAs. The serotype and strain specificity of the VHHs are advantageous for independent quantification of different FMD strains in multivalent vaccines but has the disadvantage that their use is limited to the FMD strains recognized by these VHHs. The ELISAs developed here can also be used for analysis of FMDV stability in oil-adjuvanted vaccines as described earlier for O_1 Manisa FMDV using the M170F ELISA (17, 18). As compared to the recently described thermofluor assay for measuring FMDV stability (47) our ELISAs have the advantage of increased sensitivity but disadvantage of strain specificity.

ETHICS STATEMENT

Llama immunizations were performed after ethical review by Wageningen Bioveterinary Research and in accordance with Dutch national guidelines on animal use.

AUTHOR CONTRIBUTIONS

MH and EP performed experiments. MH, JS, PE, BC, and AD conceived and designed experiments and analyzed data. MH, JS, and AD wrote the manuscript. All the authors read and critically reviewed the manuscript.

ACKNOWLEDGMENTS

The authors want to thank Froukje van Hemert-Kluitenberg at Wageningen Bioveterinary Research for performing many experiments.

REFERENCES

1. Paton DJ, Sumption KJ, Charleston B. Options for control of foot-and-mouth disease: knowledge, capability and policy. *Philos Trans R Soc Lond B Biol Sci* (2009) 364(1530):2657–67. doi:10.1098/rstb.2009.0100
2. Doel TR. Natural and vaccine induced immunity to FMD. *Curr Top Microbiol Immunol* (2005) 288:103–31. doi:10.1007/3-540-27109-0_5
3. Jamal SM, Belsham GJ. Foot-and-mouth disease: past, present and future. *Vet Res* (2013) 44:116. doi:10.1186/1297-9716-44-116
4. Brown F, Crick J. Application of agar-gel diffusion analysis to a study of the antigenic structure of inactivated vaccines prepared from the virus of foot-and-mouth disease. *J Immunol* (1959) 82(5):444–7.
5. Doel TR, Chong WK. Comparative immunogenicity of 146S, 75S and 12S particles of foot-and-mouth disease virus. *Arch Virol* (1982) 73(2):185–91. doi:10.1007/BF01314726
6. Rao MG, Butchaiah G, Sen AK. Antibody response to 146S particle, 12S protein subunit and isolated VP1 polypeptide of foot-and-mouth disease virus type Asia-1. *Vet Microbiol* (1994) 39(1–2):135–43. doi:10.1016/0378-1135(94)90094-9
7. Seki C, Robiolo B, Periolo O, Iglesias M, D'Antuono A, Maradei E, et al. Rapid methodology for antigenic profiling of FMDV field strains and for the control of identity, purity and viral integrity in commercial virus vaccines using monoclonal antibodies. *Vet Microbiol* (2009) 133(3):239–51. doi:10.1016/j.vetmic.2008.07.011
8. Barteling SJ, Meloen RH. A simple method for the quantification of 140S particles of foot-and-mouth disease virus (FMDV). *Arch Gesamte Virusforsch* (1974) 45(4):362–4. doi:10.1007/BF01242879
9. Spitteler MA, Fernandez I, Schabes E, Krimer A, Regulier EG, Guinzburg M, et al. Foot and mouth disease (FMD) virus: quantification of whole virus particles during the vaccine manufacturing process by size exclusion chromatography. *Vaccine* (2011) 29(41):7182–7. doi:10.1016/j.vaccine.2011.05.078
10. Yang Y, Li H, Li Z, Zhang Y, Zhang S, Chen Y, et al. Size-exclusion HPLC provides a simple, rapid, and versatile alternative method for quality control of vaccines by characterizing the assembly of antigens. *Vaccine* (2015) 33(9):1143–50. doi:10.1016/j.vaccine.2015.01.031
11. Yang M, Goolia M, Xu W, Bittner H, Clavijo A. Development of a quick and simple detection methodology for foot-and-mouth disease virus serotypes

O, A and Asia 1 using a generic RapidAssay device. *Virol J* (2013) 10:125. doi:10.1186/1743-422X-10-125
12. Feng X, Ma JW, Sun SQ, Guo HC, Yang YM, Jin Y, et al. Quantitative detection of the foot-and-mouth disease virus serotype O 146S antigen for vaccine production using a double-antibody sandwich ELISA and nonlinear standard curves. *PLoS One* (2016) 11(3):e0149569. doi:10.1371/journal.pone.0149569
13. Ma LN, Zhang J, Chen HT, Zhou JH, Ding YZ, Liu YS. An overview on ELISA techniques for FMD. *Virol J* (2011) 8:419. doi:10.1186/1743-422X-8-419
14. Morioka K, Fukai K, Yoshida K, Yamazoe R, Onozato H, Ohashi S, et al. Foot-and-mouth disease virus antigen detection enzyme-linked immunosorbent assay using multiserotype-reactive monoclonal antibodies. *J Clin Microbiol* (2009) 47(11):3663–8. doi:10.1128/JCM.00695-09
15. Van Maanen C, Terpstra C. Quantification of intact 146S foot-and-mouth disease antigen for vaccine production by a double antibody sandwich ELISA using monoclonal antibodies. *Biologicals* (1990) 18(4):315–9. doi:10.1016/1045-1056(90)90036-Y
16. Yang M, Holland H, Clavijo A. Production of monoclonal antibodies against whole virus particles of foot-and-mouth disease virus serotype O and A and their potential use in quantification of intact virus for vaccine manufacture. *Vaccine* (2008) 26(27–28):3377–82. doi:10.1016/j.vaccine.2008.04.062
17. Harmsen MM, Fijten HP, Westra DF, Coco-Martin JM. Effect of thiomersal on dissociation of intact (146S) foot-and-mouth disease virions into 12S particles as assessed by novel ELISAs specific for either 146S or 12S particles. *Vaccine* (2011) 29(15):2682–90. doi:10.1016/j.vaccine.2011.01.069
18. Harmsen MM, Fijten HPD, Westra DF, Dekker A. Stabilizing effects of excipients on dissociation of intact (146S) foot-and-mouth disease virions into 12S particles during storage as oil-emulsion vaccine. *Vaccine* (2015) 33:2477–84. doi:10.1016/j.vaccine.2015.03.066
19. Butchaiah G, Card JL, Morgan DO. Antigenic relationships of foot-and-mouth disease virus serotype Asia-1 isolates demonstrated by monoclonal antibodies. *Vet Immunol Immunopathol* (1992) 30(2–3):275–92. doi:10.1016/0165-2427(92)90144-F
20. McCullough KC, Butcher R. Monoclonal antibodies against foot-and-mouth disease virus 146S and 12S particles. *Arch Virol* (1982) 74(1):1–9. doi:10.1007/BF01320777
21. Pfaff E, Thiel HJ, Beck E, Strohmaier K, Schaller H. Analysis of neutralizing epitopes on foot-and-mouth disease virus. *J Virol* (1988) 62(6):2033–40.
22. Saiz JC, Gonzalez MJ, Morgan DO, Card JL, Sobrino F, Moore DM. Antigenic comparison of different foot-and-mouth disease virus types using monoclonal antibodies defining multiple neutralizing epitopes on FMDV A5 subtypes. *Virus Res* (1989) 13(1):45–60. doi:10.1016/0168-1702(89)90086-5
23. Wang D, Yang S, Yin S, Shang Y, Du P, Guo J, et al. Characterization of single-domain antibodies against foot and mouth disease virus (FMDV) serotype O from a camelid and imaging of FMDV in baby hamster kidney-21 cells with single-domain antibody-quantum dots probes. *BMC Vet Res* (2015) 11(1):120. doi:10.1186/s12917-015-0437-2
24. Yin S, Yang S, Shang Y, Sun S, Zhou G, Jin Y, et al. Characterization of Asia 1 sdAb from camels bactrianus (*C. bactrianus*) and conjugation with quantum dots for imaging FMDV in BHK-21 cells. *PLoS One* (2013) 8(5):e63500. doi:10.1371/journal.pone.0063500
25. Harmsen MM, Van Solt CB, Fijten HPD, Van Keulen L, Rosalia RA, Weerdmeester K, et al. Passive immunization of guinea-pigs with llama single-domain antibody fragments against foot-and-mouth disease. *Vet Microbiol* (2007) 120(3–4):193–206. doi:10.1016/j.vetmic.2006.10.029
26. Pardon E, Laeremans T, Triest S, Rasmussen SG, Wohlkonig A, Ruf A, et al. A general protocol for the generation of nanobodies for structural biology. *Nat Protoc* (2014) 9(3):674–93. doi:10.1038/nprot.2014.039
27. Deckers N, Saerens D, Kanobana K, Conrath K, Victor B, Wernery U, et al. Nanobodies, a promising tool for species-specific diagnosis of *Taenia solium* cysticercosis. *Int J Parasitol* (2009) 39(5):625–33. doi:10.1016/j.ijpara.2008.10.012
28. Even-Desrumeaux K, Nevoltris D, Lavaut MN, Alim K, Borg JP, Audebert S, et al. Masked selection: a straightforward and flexible approach for the selection of binders against specific epitopes and differentially expressed proteins by phage display. *Mol Cell Proteomics* (2014) 13(2):653–65. doi:10.1074/mcp.O112.025486
29. Hoogenboom HR, de Bruine AP, Hufton SE, Hoet RM, Arends JW, Roovers RC. Antibody phage display technology and its applications. *Immunotechnology* (1998) 4(1):1–20. doi:10.1016/S1380-2933(98)00007-4
30. Freiberg B, Hohlich B, Haas B, Saalmuller A, Pfaff E, Marquardt O. Type-independent detection of foot-and-mouth disease virus by monoclonal antibodies that bind to amino-terminal residues of capsid protein VP2. *J Virol Methods* (2001) 92(2):199–205. doi:10.1016/S0166-0934(00)00287-1
31. Harmsen MM, Fijten HPD. Improved functional immobilization of llama single-domain antibody fragments to polystyrene surfaces using small peptides. *J Immunoassay Immunochem* (2012) 33(3):234–51. doi:10.1080/15321819.2011.634473
32. Harmsen MM, Fijten HPD, Dekker A, Eblé PL. Passive immunization of pigs with bispecific llama single-domain antibody fragments against foot-and-mouth disease and porcine immunoglobulin. *Vet Microbiol* (2008) 132:56–64. doi:10.1016/j.vetmic.2008.04.030
33. Harmsen MM, Jansen J, Westra DF, Coco-Martin JM. Characterization of foot-and-mouth disease virus antigen by surface-enhanced laser desorption ionization-time of flight-mass spectrometry in aqueous and oil-emulsion formulations. *Vaccine* (2010) 28(19):3363–70. doi:10.1016/j.vaccine.2010.02.084
34. Harmsen MM, Blokker JC, Pritz-Verschuren SB, Bartelink W, Van der Burg H, Koch G. Isolation of panels of llama single-domain antibody fragments binding all nine neuraminidase subtypes of influenza A virus. *Antibodies* (2013) 2:168–92. doi:10.3390/antib2020168
35. Harmsen MM, Van Solt CB, Fijten HPD, Van Setten MC. Prolonged *in vivo* residence times of llama single-domain antibody fragments in pigs by binding to porcine immunoglobulins. *Vaccine* (2005) 23(41):4926–34. doi:10.1016/j.vaccine.2005.05.017
36. McCafferty J, Johnson KS. Construction and screening of antibody display libraries. In: Kay BK, Winter J, McCafferty J, editors. *Phage Display of Peptides and Proteins*. San Diego: Academic Press (1996). p. 79–111.
37. Harmsen MM, Ruuls RC, Nijman IJ, Niewold TA, Frenken LGJ, de Geus B. Llama heavy-chain V regions consist of at least four distinct subfamilies revealing novel sequence features. *Mol Immunol* (2000) 37(10):579–90. doi:10.1016/S0161-5890(00)00081-X
38. Lefranc MP, Pommie C, Ruiz M, Giudicelli V, Foulquier E, Truong L, et al. IMGT unique numbering for immunoglobulin and T cell receptor variable domains and Ig superfamily V-like domains. *Dev Comp Immunol* (2003) 27(1):55–77. doi:10.1016/S0145-305X(02)00039-3
39. Butler JE, Ni L, Nessler R, Joshi KS, Suter M, Rosenberg B, et al. The physical and functional behavior of capture antibodies adsorbed on polystyrene. *J Immunol Methods* (1992) 150(1–2):77–90. doi:10.1016/0022-1759(92)90066-3
40. McCullough KC, Crowther JR, Butcher RN. Alteration in antibody reactivity with foot-and-mouth disease virus (FMDV) 146S antigen before and after binding to a solid phase or complexing with specific antibody. *J Immunol Methods* (1985) 82(1):91–100. doi:10.1016/0022-1759(85)90228-5
41. Ellard FM, Drew J, Blakemore WE, Stuart DI, King AM. Evidence for the role of His-142 of protein 1C in the acid-induced disassembly of foot-and-mouth disease virus capsids. *J Gen Virol* (1999) 80(8):1911–8. doi:10.1099/0022-1317-80-8-1911
42. Pabst TM, Wendeler M, Wang X, Bezemer S, Hermans P, Hunter AK. Camelid VHH affinity ligands enable separation of closely related biopharmaceuticals. *Biotechnol J* (2017) 12(2):1600357. doi:10.1002/biot.201600357
43. Coppieters K, Dreier T, Silence K, de Haard H, Lauwereys M, Casteels P, et al. Formatted anti-tumor necrosis factor alpha VHH proteins derived from camelids show superior potency and targeting to inflamed joints in a murine model of collagen-induced arthritis. *Arthritis Rheum* (2006) 54(6):1856–66. doi:10.1002/art.21827
44. Grazioli S, Fallacara F, Brocchi E. Mapping of antigenic sites of foot-and-mouth disease virus serotype Asia 1 and relationships with sites described in other serotypes. *J Gen Virol* (2013) 94(3):559–69. doi:10.1099/vir.0.048249-0
45. Jamal SM, Shah SI, Ali Q, Mehmood A, Afzal M, Afzal M, et al. Proper quality control of formulated foot-and-mouth disease vaccines in countries with prophylactic vaccination is necessary. *Transbound Emerg Dis* (2014) 61(6):483–9. doi:10.1111/tbed.12051
46. Robinson L, Knight-Jones TJ, Charleston B, Rodriguez LL, Gay CG, Sumption KJ, et al. Global foot-and-mouth disease research update and

gap analysis: 3 – vaccines. *Transbound Emerg Dis* (2016) 63(S1):30–41. doi:10.1111/tbed.12518

47. Kotecha A, Zhang F, Juleff N, Jackson T, Perez E, Stuart D, et al. Application of the thermofluor PaSTRy technique for improving foot-and-mouth disease virus vaccine formulation. *J Gen Virol* (2016) 97(7):1557–65. doi:10.1099/jgv.0.000462

Conflict of Interest Statement: The authors declare that the research was conducted in the absence of any commercial or financial relationships that could be construed as a potential conflict of interest.

The reviewer, MG, and handling editor declared their shared affiliation, and the handling editor states that the process nevertheless met the standards of a fair and objective review.

frontiers in Immunology

REVIEW
published: 02 November 2017
doi: 10.3389/fimmu.2017.01442

Nanobody-Based Delivery Systems for Diagnosis and Targeted Tumor Therapy

*Yaozhong Hu[1,2,3], Changxiao Liu[1,3] and Serge Muyldermans[2]**

[1] Department of Pharmaceutical Engineering, School of Chemical Engineering and Technology, Tianjin University, Tianjin, China, [2] Laboratory of Cellular and Molecular Immunology, Vrije Universiteit Brussel, Brussels, Belgium, [3] State Key Laboratory of Drug Delivery Technology and Pharmacokinetics, Tianjin Institute of Pharmaceutical Research, Tianjin, China

The development of innovative targeted therapeutic approaches are expected to surpass the efficacy of current forms of treatments and cause less damage to healthy cells surrounding the tumor site. Since the first development of targeting agents from hybridoma's, monoclonal antibodies (mAbs) have been employed to inhibit tumor growth and proliferation directly or to deliver effector molecules to tumor cells. However, the full potential of such a delivery strategy is hampered by the size of mAbs, which will obstruct the targeted delivery system to access the tumor tissue. By serendipity, a new kind of functional homodimeric antibody format was discovered in camelidae, known as heavy-chain antibodies (HCAbs). The cloning of the variable domain of HCAbs produces an attractive minimal-sized alternative for mAbs, referred to as VHH or nanobodies (Nbs). Apart from their dimensions in the single digit nanometer range, the unique characteristics of Nbs combine a high stability and solubility, low immunogenicity and excellent affinity and specificity against all possible targets including tumor markers. This stimulated the development of tumor-targeted therapeutic strategies. Some autonomous Nbs have been shown to act as antagonistic drugs, but more importantly, the targeting capacity of Nbs has been exploited to create drug delivery systems. Obviously, Nb-based targeted cancer therapy is mainly focused toward extracellular tumor markers, since the membrane barrier prevents antibodies to reach the most promising intracellular tumor markers. Potential strategies, such as lentiviral vectors and bacterial type 3 secretion system, are proposed to deliver target-specific Nbs into tumor cells and to block tumor markers intracellularly. Simultaneously, Nbs have also been employed for *in vivo* molecular imaging to diagnose diseased tissues and to monitor the treatment effects. Here, we review the state of the art and focus on recent developments with Nbs as targeting moieties for drug delivery systems in cancer therapy and cancer imaging.

Keywords: nanobody, targeted cancer therapy, drug delivery, intracellular targeting, type III secretion system, molecular imaging

OPEN ACCESS

Edited by:
Colin Roger MacKenzie, National Research Council Canada (NRC-CNRC), Canada

Reviewed by:
Oscar R. Burrone, International Centre for Genetic Engineering and Biotechnology, Italy
Guy Caljon, University of Antwerp, Belgium

****Correspondence:***
Serge Muyldermans
svmuylde@vub.ac.be

Specialty section:
This article was submitted to Vaccines and Molecular Therapeutics, a section of the journal Frontiers in Immunology

Received: *23 July 2017*
Accepted: *17 October 2017*
Published: *02 November 2017*

Citation:
Hu Y, Liu C and Muyldermans S (2017) Nanobody-Based Delivery Systems for Diagnosis and Targeted Tumor Therapy. Front. Immunol. 8:1442. doi: 10.3389/fimmu.2017.01442

INTRODUCTION

To date, the development of effective strategies for cancer therapy remains a huge challenge. The conventional chemotherapy and radiotherapy appear to have a potent effect to kill tumor cells, but they also eliminate healthy cells. Therefore, massive attention went to the development of more effective curable options by targeted cancer therapy (1). Over the years, antibodies have

been employed, first as antivenom therapeutic and later as a valued research and clinical diagnostic tool. The first injection of monoclonal antibodies (mAbs) into patients dates back some 30 years ago (2, 3). But murine mAbs elicit immunogenicity problems in patients. Nevertheless, mAb-based cancer therapy has obtained remarkable successes, emphasizing the attention to evolve therapeutic treatments into a personalized curable proposal. To date, the Food and Drug Administration has approved over 30 mAbs for clinical application. Among these mAbs, seven blockbusters are combatting tumors, including Rituximab (anti-CD20), Trastuzumab (directed to HER2), Bevacizumab (anti-VEGF), Alemtuzumab (anti-CD52), Cetuximab, Panitumumab, and Matuzumab (all targeting EGFR) (4, 5). These mAbs were selected for their capacity to disturb the normal function of their targets in tumor cells. The intact mAbs, containing a fully functional Fc domain, evoke antibody-dependent cell-mediated cytotoxicity (ADCC). In addition, mAbs showed significant potential for tumor diagnosis through molecular imaging (6, 7). The mAbs have also been engineered to carry various toxic loads to produce immunotoxins, antibody drug conjugates (ADCs), nanomedicines, or nanoparticles (NPs) encapsulating cytotoxic agents, that work as drug delivery systems (8). For example, mAbs have been directly conjugated to cytotoxic drugs [e.g., auristatin, maytansine, calicheamicin, or doxorubicin (DOX)] and several of these ADCs reached the clinical trials (9). Nevertheless, the large size of mAb (MW 150,000; dimensions: 14.2 nm × 8.5 nm × 3.8 nm), which might be further increased after conjugation with NPs, constitutes a manifest drawback. An enlarged size will lead to a suboptimal biodistribution and a limited tumor penetration (10). Considerable efforts have been put into the development of smaller antibody formats (11, 12), such as the naturally derived or recombinant antigen-binding fragment (Fab; ~50 kDa), variable fragment (Fv; ~28 kDa), or single-chain variable fragment (scFv; ~30 kDa) (**Figure 1**) (13).

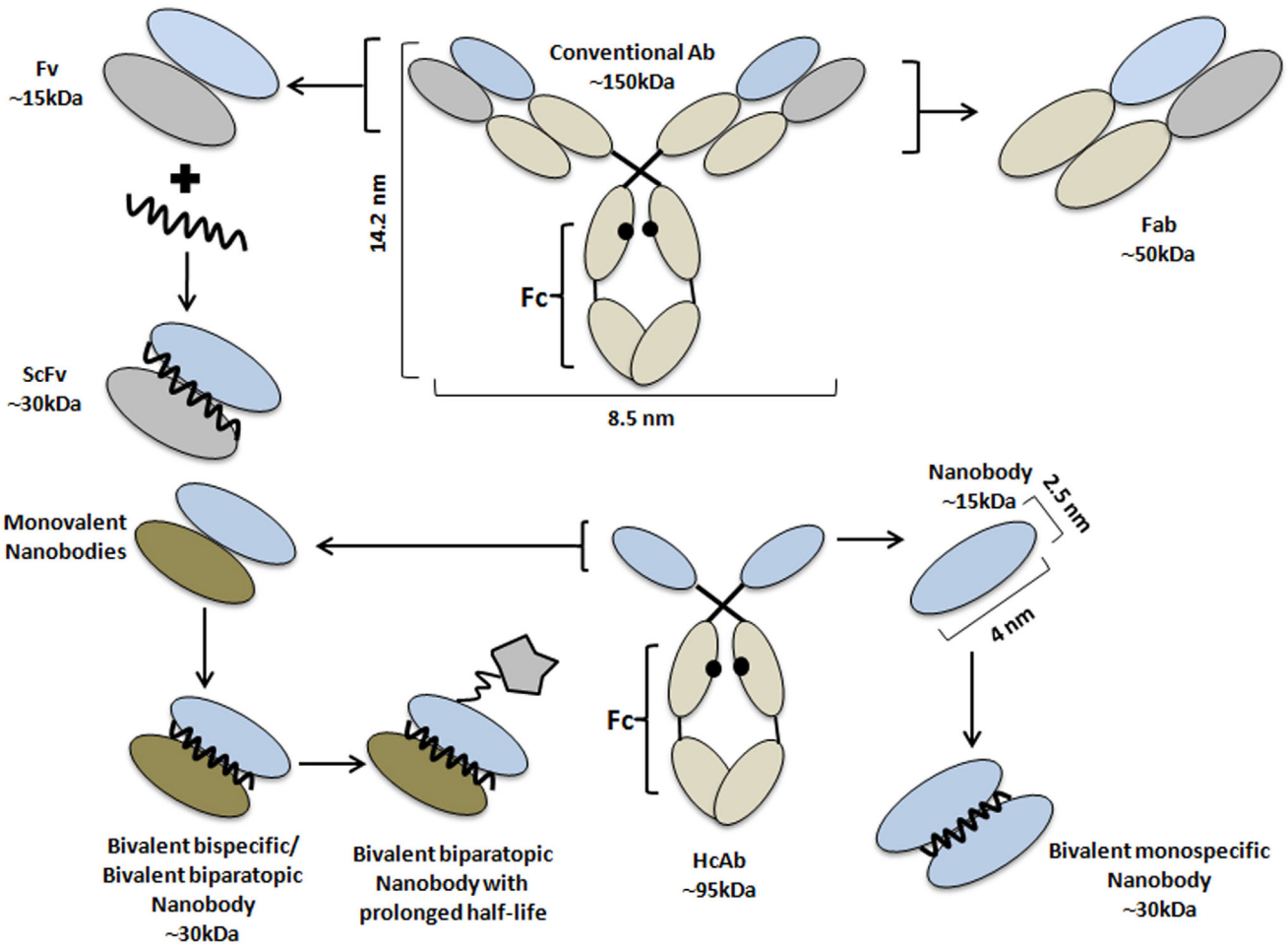

FIGURE 1 | Schematic representation of antibodies and their derivatives from conventional and heavy chain-only antibodies. Schematic structure of a monoclonal antibody (central top part) and its derivatives: Fab (right, top), Fv, and scFv (left, top part); and of a HCAb (central, lower part), together with its antigen-binding fragment, known as VHH or nanobody (Nb) (right, lower part). Besides the monovalent format, Nbs have been engineered into bivalent monospecific constructs (lower part, right). Two different Nbs can be fused into (i) a biparatopic construct where each Nb recognizes a different epitope on the same molecule or (ii) a bispecific construct targeting two independent molecules (lower, left part). The fusion of the Nb-based construct with a large molecule (star-like shaped) or with an Nb with specificity for albumin are standard strategies to prolong the half-life of the construct in the bloodstream. The molecular weight of each Ab format is also given.

To reinstall the bivalency and concomitant avidity effects, the minibody (an engineered antibody fragment made by fusing the scFv binding domain to human CH3) was introduced as a better candidate (14). Important successes were obtained with these size-reduced Abs of which some reached clinical trials, however, detailed immunogenicity studies are underrepresented and research is still ongoing (15–17).

By serendipity, a new type of antibody naturally devoid of light chains and their first constant domain (CH1) in the heavy chain was discovered in the early 90s in camelids (18). These heavy chain-only antibodies (HCAbs) exhibit a similar affinity to their cognate antigen compared to conventional antibodies, despite only one single variable domain (VHH) is involved in antigen recognition (19). It was demonstrated that the autonomous VHH retains its full antigen-binding potential, and it was considered to be the smallest natural intact antigen-binding fragment (20, 21). With a size of below 15 kDa and dimensions in the nanometer range (~2.5 nm in diameter and ~4 nm in height), the VHH molecule was also named nanobody (Nb, **Figure 1**). The immense efforts in the Nb research field underscoring the remarkable prospects of these molecules formed eventually the basis for the foundation of spin-offs such as Ablynx, Chromotek, Agrosavfe, QvQ, Camel-IDS, Hybrigenics, Confo-Therapeutics, and many other companies offering the technology of generating and selecting Nbs (20, 22). The focus of all these companies ranges from service providers to developing therapeutic Nbs, currently tested in clinical trials (23) with ~9 candidates in advanced stage and more than 15 at the discovery and preclinical stage.

In this report, the beneficial characteristics of Nbs will be reviewed and different Nb conjugation systems for tumor targeting and drug delivery will be discussed, as well as strategies to target intracellular tumor markers. The latter will not only facilitate the exploration of new potential therapeutic approaches but also expand our understanding of particular signaling cascades. Finally, the *in vivo* molecular imaging using Nbs will be summarized.

CHARACTERISTICS OF Nbs

The ontogeny and emergence of dedicated genes to produce HCAbs in camelids, including VHH domains generated after gene rearrangement events have been comprehensively covered (22, 24–27).

Nbs Are Easily Selected by Phage Display

The VHH repertoire from peripheral blood cells of the immunized camelid is cloned and phage displayed to retrieve Nbs with highest affinity and specificity for the target (28). The procedure has been adapted to construct large non-immune (naive) or synthetic Nb libraries, from which to select binders. Naive libraries use the VHH repertoire of non-immunized animals. For synthetic libraries, the codons of the antigen-binding loop regions of a robust VHH scaffold are randomized. In all cases, selected Nbs can be produced easily in microorganisms, mammalian cells, or plants (29–32).

The Smaller Size of Nbs Assists in Reaching and Recognizing Unique Epitopes

The Nb holds great promises (33), mainly due to a unique paratope architecture, monomeric, and robust behavior (34–36) and favorable solubility (21). Due to their small size, a rapid extravasation of intravenously administered Nbs and diffusion into tissues is obtained to deliver interesting reagents to the target. Many Nbs possess a long complementarity determining region 3 (CDR3), forming a finger-like structure that penetrates into cavities on the antigen surface (36). For those VHHs that do not have a long CDR3, the prolate shape of the Nb creates a convex paratope that interacts deeply into antigen concave surfaces. Consequently, Nbs are directed against unique antigen epitopes that are low or not antigenic for classical antibodies (37–39).

The Smaller Size of Nbs Is Beneficial for Engineering

The small size and monomeric single-domain nature forms the basis for the flexible engineering of Nbs. Engineering of Nbs facilitates the conjugation of additional proteins, reporter molecules, or drugs. Most methods, employed for the chemical conjugation, depend on presence of lysines. However, the occurrence of multiple lysines (on average 3–4 per Nb) and their random conjugation creates a mixture of conjugates whereby a fraction might have lost its antigen-binding capacity when lysines within the antigen-binding region reacted. The introduction of an extra cysteine at a distant location from the paratope and preferably at the C-terminal end of the domain remediates these issues (40, 41). Alternatively, the C-terminal end of the Nbs have been equipped with short peptide tags, such as the Sortag that undergoes the Sortase A-mediated protein ligation reaction to attach any probe (42, 43).

Inconveniences of Nbs and How to Remediate

The minimal size of an Nb is often considered as an advantage; however, it might also be a handicap. For example, all molecules with a size below 50,000 Da are rapidly cleared from the bloodstream through kidney glomerular filtration. Although a fast blood clearance of Nbs is certainly beneficial for non-invasive *in vivo* imaging (33, 44, 45), for optimal tumor therapy, a longer blood residence time would permit lower injected doses, longer time intervals between two consecutive administrations and still yield a higher load of Nb-based drug at the target. To increase the blood residence time, Tijink et al. (46) generated a tandem fusion of a bivalent Nb against EGFR with an Nb cross-reacting with mouse and human serum albumin (α-EGFR-αEGFR-αAlb, **Figure 1**) (47). Since human serum albumin has a half-life of around 19 days (48), the half-life of the bispecific trivalent α-EGFR-αEGFR-αAlb was prolonged to around 2–3 days in mice. Furthermore, compared to the monovalent Nb, the longer circulation of the trivalent Nb in blood increased its tumor uptake as well. Similar levels of tumor loading were noted with the trivalent Nb and Cetuximab, while a faster and deeper tumor penetration was obtained with the former (47).

For conventional antibodies, it is well established that upon antigen binding, the ADCC and complement-dependent cytotoxicity are triggered by the Fc region (47, 49, 50). These two mechanisms are known to be important in the process of tumor eradication, as they both contribute to activation of cell lysis, and hence apoptosis cascades (47). For this reason, it was proposed to extent Nbs with an Fc region, although the advantages of a small size (extravasation, tumor penetration) will be lost (50).

High Stability of Nbs Admit Their Application under Stringent Conditions

Nanobodies seem to be extraordinarily resistant when exposed to various stress conditions. The Nbs have a long shelf-life and tolerate storage for several months at 4°C, and even longer at −20°C, while maintaining full antigen-binding capacity. Incubating Nbs at 37°C for several weeks seems to be well tolerated as well (28). Although some reports indicate that Nbs might resist temperatures above 90°C (35), this will be more an exception than the rule and Nbs are certainly not always refolding quantitatively upon heat denaturation. Also exposure to elevated pressure does not seem to harm the Nbs. Altogether, most Nbs exhibit a high stability against elevated temperature, high pressure, or chemical denaturants as demonstrated by thermo fluorescence or circular dichroism measurements (34, 51, 52).

Low Immunogenicity of Nbs

The detailed Nb sequence information (21) revealed that VHHs share a high degree of sequence identity with human VHs (of family 3). This feature is considered to contribute to the low immunogenicity, thus allowing prolonged and repeated administrations of Nbs in patients (53). Furthermore, strategies have been developed to humanize Nbs to minimize the possible immune reaction of patients (54, 55). Data from Phase I clinical trials performed by Ablynx (Belgium) also support the notion that Nbs are endowed with low immunogenicity (56, 57).

As it is difficult for Nbs, as well as for other proteins, to migrate across cell membranes, most current investigations had a focus on extracellular targets, such as receptor ligands or transmembrane proteins. However, possible applications of Nbs directed against intracellular tumor markers have been proposed. For example, scFv or Nbs might be transcribed and translated inside the tumor cell. Such intracellular antibodies (known as intrabodies), when folded properly might immediately target the intracellular antigen protein. Groot et al. (58, 59) produced intrabodies against HIF-1α and evaluated its targeting efficacy. Obviously, explorative experiments with Nb-based tools either expressed intracellularly (intrabodies) or introduced *via* viral vectors are underway (60–62).

Nb-CONJUGATED PARTICLES FOR THERAPY AND DIAGNOSIS

From the very beginning, the potential of Nbs as cancer therapeutic agent has been evaluated, whereby the Nb targets the ectodomain or cell surface exposed loops of receptors or biomarkers, aiming at the inactivation of the transcriptional pathways or signaling cascades. In the following section, the therapeutic agents and the different formats of drug delivery systems based on Nbs will be described.

Nbs with an Intrinsic Therapeutic Activity

To date, the most investigated extracellular targets for Nbs include EGFR1 or EGFR2 (HER1 and HER2, respectively), vascular endothelial growth factor receptor-2 (VEGFR2), c-Met and CXCR7, or hepatocyte growth factor (HCG), which all play a crucial role in making a link with the signaling cascades. Binding of Nbs to these tumor markers can potentially block the signaling pathways to halt the growth and proliferation of tumor cells. As such, Nbs against EGFR and c-Met have been evaluated (47, 63). Both Nbs showed potent antagonistic effects *in vitro*, as well as an inhibition of the tumor growth *in vivo* in case of a trivalent biparatopic anti-EGFR Nb 7D12-9G8-Alb (47).

Furthermore, Nbs have been developed to combat different infections and diseases, such as thrombotic thrombocytopenic purpura (64, 65), respiratory syncytial virus (66), and rheumatoid arthritis (67–69). These Nbs reached various stages of preclinical or clinical testings. Some particular Nbs are being developed as allosteric inhibitors that are able to modulate the enzymatic activity of their target protein, such as carbonic anhydrase (CAIX) (70), which plays a significant role for hypoxic tumor cells so that the enzymatic CAIX neutralization with Nbs could reduce malignancy and survival of tumor cells. All these results will expand the research focus and stimulate applications of Nbs for cancer diagnosis and therapy. Theoretically, potent and intrinsic effective Nbs that can completely inhibit tumor growth and lead to cell death should be employed, rather than Nbs that are just inhibiting tumor cell proliferation.

Nb-Toxin Conjugation

However, most Nbs do not exhibit an inherent therapeutic activity, but need to be conjugated with a toxic load or any other effector function. In these applications, the conjugated Nbs are employed for drug delivery, irrespectively whether the conjugate is a single effector domain or a nanocargo containing antitumor drugs (71–73).

The conjugation of Nbs with an enzyme or toxin molecule increases the Nb circulation time in blood due to its enlarged size. Therefore, the constructs become more effective to transfer their load to tumors or diseased tissues. Two strategies can be applied for conjugation, either by chemical conjugation or by gene fusion of the Nb and a toxic protein and cloning in an expression vector (55, 74). For chemical conjugation, the conjugation of the effector moiety to the Nb—mostly to lysine residues—might be heterogeneous as several lysines are present in the Nb and if a Lys in the CDR reacted then the reactant might shield the CDRs from access to antigen, thus resulting in a decrease or loss of antigen recognition by Nbs. In another strategy, a single cysteine—inserted at the C-terminal end of the Nb—allows for a unique site-directed conjugation of a toxic load distant to the paratope so that the disturbance of antigen binding will be minimal (41). Recently, the Sortase A-mediated modification of the C-terminal end of Nbs has been explored to attach chelators and nuclides (42, 43). Anyway, the antigen-binding properties must be confirmed after

conjugation. Hence, it is necessary to ensure the accumulation and retention of specific Nbs at the tumor tissue, rather than normal healthy tissue.

Anti-Carcinoembryonic Nbs with *Enterobacter cloacae* β-Lactamase

In 2004, Cortez-Retamozo et al. (75) introduced the genetic conjugation of anti-carcinoembryonic Nbs to *E. cloacae* β-lactamase, which is an enzyme with excellent catalytic properties for converting a non- or low-toxic prodrug into a potent cytotoxic agent. *In vivo* biodistribution and therapeutic activity of the conjugation was evaluated in nude mice bearing LS174T xenografts. Effective accumulation of the Nb conjugate at the tumor xenograft was noticed and no, or very low, accumulation in kidneys. Regression of the grafted tumor was observed in mice and even complete remission was obtained in this antibody-directed enzyme prodrug therapy model. Although the bacterial origin of β-lactamase will make the immuno-enzyme highly immunogenic and therefore less practical, the study provides the proof of concept to generate highly cytotoxic compounds in the vicinity of the tumor and shows its potential as a promising approach for cancer therapy.

Anti-EGFR Nbs with Tumor Necrosis Factor-Related Apoptosis-Inducing Ligand (TRAIL)

In 2012, a unique conjugation based on anti-EGFR Nbs was introduced for malignant glioblastoma multiforme (GBM). As demonstrated, both neural stem cells (NSCs) and mesenchymal stem cells can migrate toward brain tumors. In this study, bivalent and bispecific Nbs against EGFR were conjugated to TRAIL and packaged into lentivirus (LV) virions to transduce NCS. The secretion of specific Nbs and Nb-TRAIL from engineered NSCs was confirmed and NSCs retained the ability to differentiate. Furthermore, these Nb constructs secreted from NSCs were designed to target GBM tumor tissues, which show an enhanced EGFR expression (76). The therapeutic effect of anti-EGFR Nbs and their variants was evaluated both *in vitro* and in xenografted models. NSC released anti-EGFR Nbs can inhibit EGFR signaling dramatically *in vitro* and reduced the tumor growth in mice bearing GBM. By taking advantage of tropism of the NSCs that could provide on-site delivery of therapeutic Nbs, significant inhibitory effects on GBM were noticed. Direct comparison of the inhibition activity between the bivalent anti-EGFR Nb and the Nb-TRAIL conjugate further revealed that the combined therapeutic approaches were more potent (76). The NSC-delivered Nbs inhibit the proliferation and migration, whereas their conjugation with cytotoxic molecules enhances the therapeutic efficacy, significantly.

Anti-VEGFR2 Nbs with Recombinant *Pseudomonas* Exotoxin A

The conjugation of anti-VEGFR2 Nbs with recombinant *Pseudomonas* exotoxin A (PE38) was proposed to inhibit growth of tumors, highly expressing VEGFR2 (77). PE38 was designed to enter the cell in an endocytic vesicle and to bind to the ADP-ribosylating elongation factor II to kill subsequently tumor cells. As demonstrated by an *in vitro* proliferation assay, this conjugation system could efficiently recognize VEGFR2 expressed on the surface of 293KDR cells and inhibit their proliferation *in vitro* (77). Thus, this anti-VEGFR2–PE38 conjugate act as a potent immuno-cytotoxic effector; however, data of an *in vivo* evaluation have not been reported.

In conclusion, the conjugation of Nbs and toxins combines the advantages of the tumor-specific targeting Nbs and the tumor killing toxins within one molecule. In this case, an effective cell penetration was also achieved, which will help to enhance the therapeutic efficacy *via* this particular effector domain. Several Nb conjugates are in the pipeline for research purposes or clinical evaluation.

Nbs As Targeting Modules for Drug Delivery Systems

Drug delivery systems also involve nano-sized drug carriers or NPs with a diameter below 200 nm. The design of nanoscale vehicles for drug delivery has been one of the most exiting strategies in medicine and pharmaceutical technology. Different drug delivery systems based on NPs have been developed, including inorganic, magnetic, and polymeric NPs (**Figure 2**) (78). These systems can protect drugs against oxido-reduction and enzymatic reactions, increase their bioavailability by reducing the effective dose and they will diminish the potential immunogenicity of the drug. The packaged, administered toxic compounds can avoid damage and negative side effects to normal tissues, solubilize hydrophobic drugs in lipidic bilayers (e.g., liposomes) or hydrophobic cores (micelles). The NPs allow administering larger amounts of drugs in one single dose, and the slow but prolonged drug release will result in a reduced frequency of the administration (79).

The conjugation of drug cargo's to targeting moieties, especially those against receptors that mediate cellular internalization, was introduced to facilitate the transport of drugs or functional agents in target cells and tissues (**Figure 3**) (8, 80, 81). Poly-ethylene glycol (PEG) molecules or surface-charge-shielded NPs have been conjugated on the surface of NPs to extend the circulation in the bloodstream leading to more significant accumulation at tumor sites and reduced liver uptake (82–84). The PEG-ylation of NPs also provides chemical reactive moieties to attach biofunctional molecules for specific cell or organ targeting (85, 86). The damaged vasculature around tumor cells will encourage the enhanced permeability and retention (EPR) effect and enhance the accumulation of NPs in the tumor vasculature (**Figure 3**) (87). After extravasation of NPs into the tumor microenvironment, the interaction between NPs and tumor cells can be enhanced by targeting moieties. Nbs have been employed to serve as targeting molecules, and the delivery systems based on Nbs will be reviewed in the following sections.

Nbs Conjugated to Liposomes

Since the discovery of liposome by Bangham in the 1960s, liposomes have been considered as a valuable drug-carrier system, with a morphology and characteristics very similar to those of cellular membranes (88, 89). Liposomes can be constructed in a broad size range from 100 to 400 nm, which might be useful

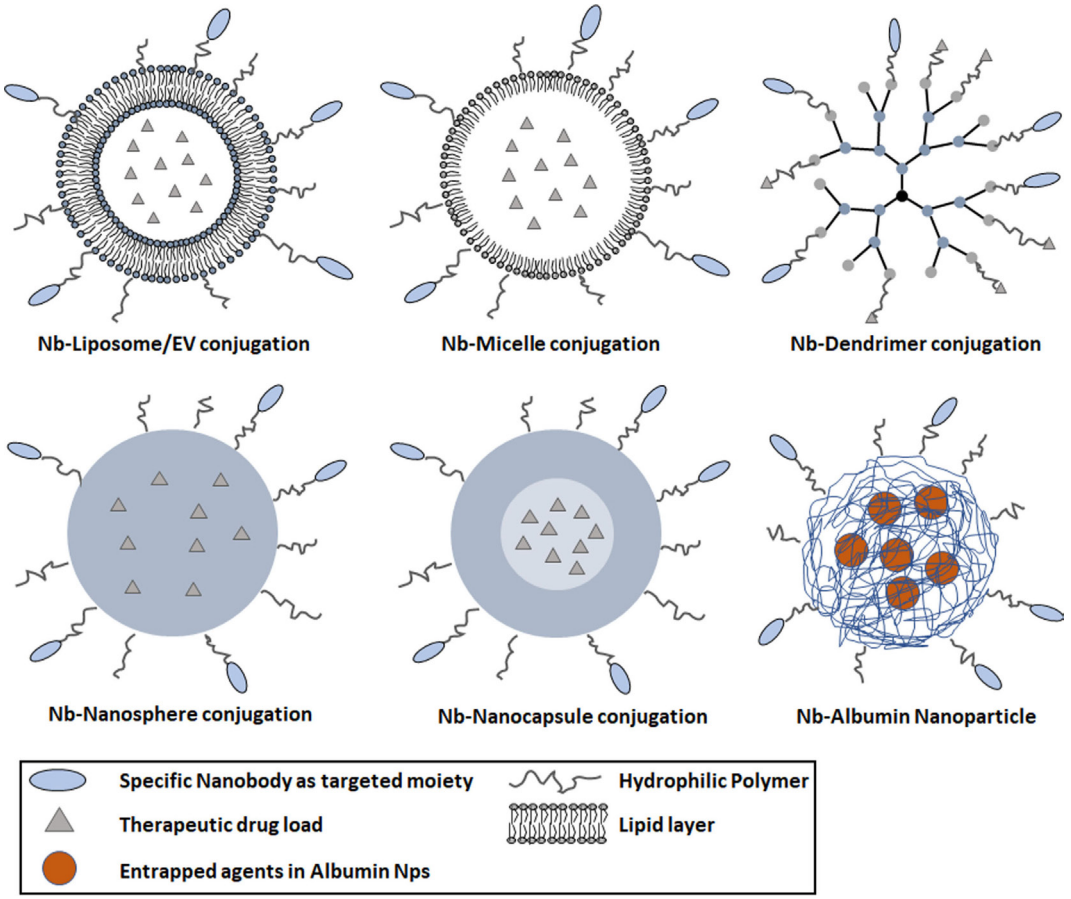

FIGURE 2 | Schematic diagram representing various types of nanoparticles (NPs) decorated with nanobodies (Nbs) for targeted cancer therapy. Commonly used NPs comprise various materials, such as liposomes (100–400 nm), micelles (10–100 nm), dendrimers (3–20 nm), nanospheres (1–100 nm), and nanocapsules (10–1,000 nm). The blue parts of the polymer NP represent the solid hydrophobic polymer matrix with optionally an aqueous core. The nanosphere is composed of a solid polymer matrix, able to encapsulate hydrophobic drugs. The nanocapsule is composed of a spherical polymeric matrix with an aqueous or oily core (light blue part in lower right panel). The poly-ethylene glycol-ylation prolongs the circulation of NPs in the bloodstream; antigen-specific Nbs are conjugated to the surface of NPs for targeting purposes.

in view of the importance of size in tumor targeting. Significant progress was made over the years and several candidates are at the stage of preclinical evaluation or clinical application (90). The external chemical differences of liposomes can facilitate the construction of targeted systems with Nbs or any other protein and will ultimately result in the accumulation of encapsulated liposomes to tumor tissues (89, 91). In conclusion, Nb–liposome systems play a suitable role for a combined therapeutic strategy and have the potential to enhance the antitumor effect.

Anti-EGFR Nbs Conjugated to Empty Liposomes

Oliveira et al. (72) introduced a multivalent Nb–liposome platform without incorporated drugs to target tumors expressing epidermal growth factor receptor (EGFR). Nb EGa1 directed against EGFR was conjugated to the surface of liposomes *via* PEG-ylation. It was shown that the EGa1 C-end modification did not compromise the antigen recognition capacity or change the effective epitope targeting. However, a lower affinity was observed, probably caused by steric hindrance from the attached liposome particles. Nevertheless, a remarkable reduction of more than 90% of cell surface EGFR was observed. Increase of EGa1 on liposomes from 0.4 to 0.8 nmol can even lower the EGFR levels and further enhances the inhibition of tumor growth. The total EGFR protein level in tumors was checked at the end of the study and revealed a remarkable drop in the treated group. Supposedly, the combination of EGa1 to liposomes will retard the clearance from circulation, and the presence of EGa1 ensures specific target interactions, resulting in a measurable increase of accumulated particles in tumor tissues. The poor inhibition of tumor growth *in vivo* is attributed to "blank" liposomes without any drugs incorporated (72).

Anti-EGFR Nbs Conjugated to Liposome with Anti-Insulin-Like Growth Factor 1 Receptor (IGF-1R) Kinase Inhibitor (AG538) Encapsulated

In 2012, an improved version of the EGa1-liposome system was introduced by loading the liposomes with an anti-IGF-1R kinase inhibitor (AG538) (**Figure 2**) (73). IGF-1R plays a crucial role during the progression of particular tumors. It was demonstrated

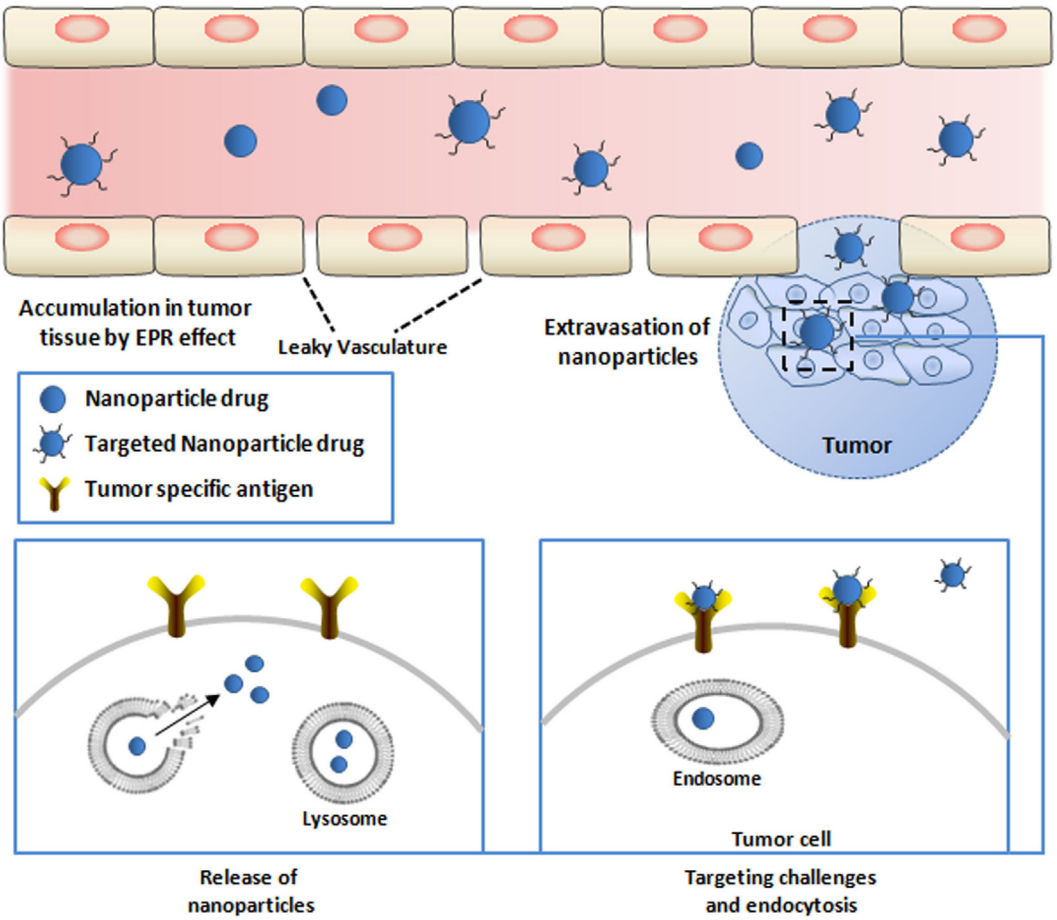

FIGURE 3 | Targeted delivery of therapeutic nanoparticles (NPs) to tumor cells. NPs conjugated with nanobodies (Nbs) against tumor-specific targets are injected into the bloodstream. Circulating NPs need to cross the vascular endothelium of the tumor tissue to infiltrate the tumor site. The endothelium of tumors is poorly formed and allows passage of NPs [causing the enhanced permeation–retention (EPR) effect]. NPs that escape the blood vessel still need to diffuse through the dense extracellular matrix to reach relevant target cells embedded deeply within the tissue. Upon arriving at the surface and attachment with the receptor on the surface of the tumor cells, NPs will be internalized *via* endocytosis (lower right). NPs that are internalized by the cells are conveyed within endosomes, and the release of the active drugs from endosome will exert the antitumor effect (lower left).

that EGFR inhibition will raise the IGF-1R levels in tumors. Hence, a combined therapeutic strategy against EGFR and IGF-1R was chosen as starting point for this targeted system. The 14C human head and neck cancer cell line and the human epidermoid carcinoma cell line A431 were used to evaluate the tumor inhibition efficacy *in vitro*. Compared to empty EGa1-liposome, a stronger growth inhibition is observed from EGa1-AG538-liposome on 14C cells and empty EGa1-liposomes could decrease the total number of cells by about 40%. This percentage can be increased to nearly 80 by exposure to EGa1-liposome (2 mM TL) with a high dose of free AG538 (80–160 μM) (73). However, the EGa1-AG538-liposomes seemed to be a more robust approach as it reached almost the same inhibition efficacy with just 0.25 mM TL, corresponding to 20 μM AG538. The A431 cell line responded similarly as the 14C cell line. These results strongly support the effective delivery of AG538 by this Nb–liposome system. Next, the *in vivo* antitumor efficacy of EGa1-AG538-liposomes was evaluated in a xenograft model of 14C and MB-468. A strong inhibitory response was observed in the group treated with EGa1-AG538-liposomes, confirming the result of the *in vitro* tests (92). Overall, this kind of platform will encourage the study on different combinations of antitumor drug encapsulated systems and specific antibodies.

Anti-EGFR Nbs Conjugated to Extracellular Vesicles (EVs)

Recently, Kooijmans et al. (93) introduced a potent delivery system based on EVs. In this strategy, anti-EGFR Nbs were expressed on the surface of EV fused by glycosylphosphatidylinositol (GPI) anchor signal peptides derived from the decay-accelerating factor. It is demonstrated that the GPI-linked Nbs were successfully displayed and accumulated strongly on the surface of EV. As a result, the targeting efficacy of EVs was dramatically improved *via* their anti-EGFR Nbs, under static conditions. The cancer cell recognition and association was also demonstrated under flow conditions, highlighting the potential of the GPI-anchoring approach and GPI-anchoring drug delivery systems.

Nbs Conjugated to Microbubbles

The development of Nb-microbubble (μB) conjugates as a novel molecular tracer has been reported (94). The biotinylated anti-eGFP (cAbGFP4) and anti-VCAM-1 (cAbVCAM1-5) Nbs were site specifically coupled to lipid μBs containing streptavidin. The specific binding of eGFP to μB-cAbGFP4 was confirmed by fluorescent microscopy, as well as the ability of μB-cAbVCAM1-5 to bind VCAM-1 in fast flow. The application of VCAM-1 conjugated μBs as novel molecular ultrasound contrast agent was demonstrated both *in vitro* and *in vivo* (94). It was further proposed that the encapsulation of specific agents in μBs might be used to control a slow release at the tumor site.

Nb Conjugation to Micelles

A micelle is an aggregate of amphiphilic block molecules dispersed in aqueous solution with the hydrophilic head regions in contact with the surrounding solvent, sequestering the hydrophobic single-tail regions in the micelle center, ranging from 10 to 100 nm based on the composition and concentration. Micelles are commonly used as platform to deliver hydrophobic drugs, which are difficult to carry through the bloodstream. Micelles remain stable upon dilution and assist in the solubility of these hydrophobic drugs. Their nanoscale dimensions permit an efficient accumulation in tumor tissues *via* the EPR effect (95). For an optimal EPR effect, a long circulation time of drugs or particles is necessary, which might be obtained by coating the small drugs with PEG or to attach drugs to the surface of carriers. Thus, according to the last strategy, the coupling of a targeting moiety (e.g., antibody, scFv, or Nb) to the surface of micelles will increase the accumulation of carriers in target tissue and promote uptake of the specific drugs. Coupling of specific Nbs to the micelle surface will generate a targeted drug delivery system promoting the internalization of carried drugs (71).

Anti-EGFR Nbs Conjugated to Micelles

In 2011, a new kind of Nb-micelle drug delivery system was introduced (71). The actively targeted polymeric micelle comprised 80% mPEG-b-p (HPMAm-Lacn) and 20% PDP–PEG-b-p (HPMAm-Lacn) block copolymers. This micelle was decorated with the EGFR antagonist Nb, EGa1, captured to the micellar surface through a disulfide linker (96). The A431 and 14C cell lines and a low endogenous EGFR expressing NIH 3T3 cell line were selected to assess the binding characteristics and uptake of Nb-conjugated micelles. The particles could target effectively to EGFR-positive cells, and no binding was observed to EGFR-negative cells. The results demonstrated that the coupling of EGa1 to the surface of micelles enhanced the recognition of, and uptake by, EGFR-positive target cells.

Anti-EGFR Nbs Conjugated to Micelles with Encapsulated DOX

In a follow-up study, an upgraded version (EGa1-DOX-micelle) of this delivery system with encapsulated DOX was proposed (97). Polymeric micelles without Nbs were developed with covalently entrapped DOX through a pH-sensitive linker (**Figure 2**) (98). Such DOX-micelles showed an increased cytostatic activity against ovarian carcinoma and B16F10 melanoma cells compared to pure DOX. Likewise, in comparison to the free drug, the DOX-micelles exhibited an increased therapeutic efficacy in B16F10 melanoma bearing nude mice. More importantly, mice treated with DOX-micelles showed a prolonged survival compared to the group that received free DOX. The inhibition efficacy to tumor growth dramatically improved by coupling anti-EGFR EGa1 Nbs to the surface of these micelles. EGa1-DOX-micelles were more toxic than the untargeted polymeric micelles for cell lines and xenografted tumors. Early 2010, another biological cargo system was introduced, with EGFR-positive Nbs (EGa1) conjugated to PEG-ylated micelles (98). The subsequent investigation with this delivery system highlighted the importance of the post-insertion strategy, which should target microvesicles to cell lines of interest.

Nbs Conjugated to Polymer NPs

Polymer NPs have attracted the interest and have been exploited in different fields over the past decade. This trend originates from their versatile capacities to meet the demands in various applications and marketing requirements. Several types of NPs, including dendrimers, nanospheres, and nanocapsules, have been exploited for enhanced cancer therapy (99–101).

Dendrimers

Dendrimers are monodisperse, branched structures, with a size ranging from 3 to 20 nm (102). The surface of dendrimers can be functionalized by coupling targeting moieties. Functional agents can be encapsulated in the dendrimer's multifunctional core to facilitate drug delivery. Drug molecules, such as paclitaxel, can also be attached to the exterior of the dendrimer for special purposes. Recently, DOX was conjugated to carboxyl-terminated poly(amidoamine) dendrimers (PAMAM) and assessed against lung metastases for improved pharmacokinetics and biodistribution (103). A dramatic increase in efficacy of DOX treatment was observed, upon pulmonary administration, in a lung metastasis mouse model bearing the B16-F10 melanoma. A decreased tumor weight and increased survival rates of the animals (C57BL/6) were noted. Compared to free DOX, this conjugate was demonstrated to further increase the therapeutic efficacy as indicated by the fewer number of nodules observed in lungs. The results demonstrated that pulmonary administration of DOX conjugated to PAMAM dendrimer is a useful strategy to enhance the therapeutic efficacy and decrease systemic toxicity of DOX. The conjugation of specific Nbs to the surface of dendrimer is expected to further facilitate tumor targeting (**Figure 2**).

Nanospheres

A nanosphere is a delivery vehicle composed of a spherical polymeric matrix ranging from 1 to 100 nm, where the drug can be encapsulated inside the aqueous or oily core from where it is released slowly during the circulation in the bloodstream. The surface of the nanosphere can also be PEG-ylated to increase the half-life and to facilitate the binding of Nbs for targeted therapy (**Figure 2**) (104, 105).

Nanocapsules

Nanocapsules are nanoscale shells of 10–1,000 nm with drugs encapsulated inside their core and separated from the environment by a polymeric membrane (106, 107). Nanocapsules are used in a myriad of fields, including medical applications for drug delivery,

food enhancement, nutraceuticals, and self-healing materials. The most attractive current application is the targeted delivery of agents to particular tissues. Monomer, bivalent, or even trivalent Nbs can be attached to the surface of this delivery system to obtain a specific targeting (**Figure 2**) (108). Although there is no publication yet where such multimeric Nbs are conjugated on nanocapsules, it remains a very attractive material of high potential for future research.

Nbs Conjugated to Albumin NPs

Another type of a highly potent delivery module comprises albumin NPs. Albumin is the most abundant plasma protein in the bloodstream, participating in several important regulations. Moreover, albumin is biocompatible and bio-safe, and albumin NPs as a drug delivery system was proposed by Muller et al. (109). The work inspired several researchers to develop such albumin NPs into a safe drug delivery system (110, 111). In one of these publications, a novel albumin nanoparticle drug carrier system (NANAPs) was loaded with the multi-kinase inhibitor 17864. Furthermore, their anti-EGFR Nb EGa1 was linked *via* maleimide functionalized PEGs and coated to the surface of these NPs to reinforce the target delivery to EGFR-positive 14C squamous head and neck cancer cells (**Figure 2**) (111). PEG-ylated NPs without EGa1 on their surface showed lower targeting and internalization efficacy compared to PEG-NP-EGa1. After binding to the cancer cells, the clathrin-mediated endocytosis leads eventually to the lysosomal degradation of the NPs releasing the multi-kinase inhibitor 17864 inside cells and provoking a notable anti-proliferative effect on tumor cells. The importance of a targeted effect from the EGa1 Nb on NANAPs was demonstrated *in vitro*, whereas the cell proliferation inhibition was not observed by treating cancer cells with non-targeted NPs encapsulated with 17864.

Targeted Therapy with Nb-Decorated Viral Vectors

Gene therapy with the assistance of viral vectors has become a very important technology in basic life sciences and applied medicine. To date, viruses, such as adenovirus, adeno-associated virus (AAV), and herpes simplex virus, are favored for this task (112, 113). LV and AAV are well-established vectors (114, 115), and these viruses can be employed to transfer genes, including those encoding Nbs into the host cells to produce intracellular Nbs (i.e., intrabodies). The LV is the most studied model for gene delivery and immunotherapy. Unfortunately, it remains challenging to deliver the genes of interest within the lentiviral particles after an *in vivo* administration to relevant target cells such as tumor cells or antigen-presenting cells (APCs) (116). The administration of wild-type AAV and LV vectors usually results in virion accumulation in liver and spleen.

Breckpot et al. (116) developed an interesting approach, whereby a modified LV vector was assembled with a binding-defective, but fusion competent, envelope glycoprotein derived from VSV-G decorated with Nb DC2.1 (**Figure 4A**). This Nb targets dendritic cells (DCs) that together with macrophages are imperative for activation of antigen-specific T cells. Such APCs are often targeted in immunotherapeutic strategies for the treatment of cancer and infectious diseases (117, 118). The modified LVs contain genes for tumor-associated antigens (TAAs) (119). Upon transduction of the APC, the TAA will be processed and presented to oncolytic effector cells that will subsequently eradicate cancer cells, both primary and metastasized.

The transducing specificity of Nb DC2.1 displaying LVs was evaluated on both, mouse and human APCs. It was demonstrated that DC2.1 Nb-displaying LVs showed an Nb-dependent and APC-specific transduction on murine cell lines and *in vitro* generated DCs (116). *In vivo* transduction with the DC2.1 Nb-displaying LVs was demonstrated after intranodal injection by bioluminescence imaging, and the transduction results were confirmed by nested PCR (116). Phenotypic characterization of the *in situ* transduced lymph node (LN)-derived DCs demonstrated that the entry of DC2.1 Nb-displaying LVs showed a tendency to accumulate at macrophages, conventional DCs (cDCs), and plasmacytoid DCs. Importantly, myeloid DCs are supposed to mediate immune responses upon LV transduction, and the transduction was enhanced with Nb-displaying LVs.

The use of Nbs on LVs (such as R3_13 LVs) can target specifically to human LN-resident myeloid DCs (120). Later on, an extended study was performed to check the targeting of LVs to cDCs, which are assumed to play a central role in the induction of a TH1-mediated antitumor immune response (117). In this study, the *in vivo* transduction profile and immune stimulatory potential of broad tropism LVs was compared with non-targeting BCII10 Nbs and APC-targeting Nb DC1.8 or DC2.1 displaying LVs. It was demonstrated that the DC1.8-LVs can exclusively transduce cDCs, while also macrophages and pDCs can be transduced with DC2.1-LVs. The transduction of these different cell types opens the potential to stimulate both, the antigen-specific CD8+ and CD4+ T cells (121). Intranodal immunization with ovalbumin encoding LVs induces the proliferation of antigen-specific CD4+ T cells. It has been demonstrated that all targeted LVs were able to stimulate cytotoxic T lymphocytes, and the APC-targeted LVs were as potent in therapy as broad tropism LVs and as such meet their expectations as safer and efficacious LV-based vaccines (117).

INTRACELLULAR TARGETING OF TUMORS WITH Nbs

To date, the majority of the research focuses on extracellular tumor markers, including cytokines, signaling receptors, and extracellular domains of cell surface proteins (122). However, most of the signaling regulation linked to the growth and proliferation of tumor cells occurs intracellularly, and thus intracellular markers should be promising therapeutic targets as well (123). The barrier of the lipid membrane halts the transfer of Nbs to the intracellular compartment, but many researchers try to develop potent delivery strategies to transport intact or at least functional Nbs into cells, and several strategies have been explored for their intracellular transportation. The LVs can be engineered to target to tumor cells *via* decoration with tumor surface marker-specific Nbs, while encoded Nbs within the LVs might produce intracellular Nbs that could associate with intracellular tumor markers to inhibit growth and proliferation (**Figure 4A**).

Alternatively, bacteria have developed sophisticated systems, such as the type III secretion system (T3SS), to translocate

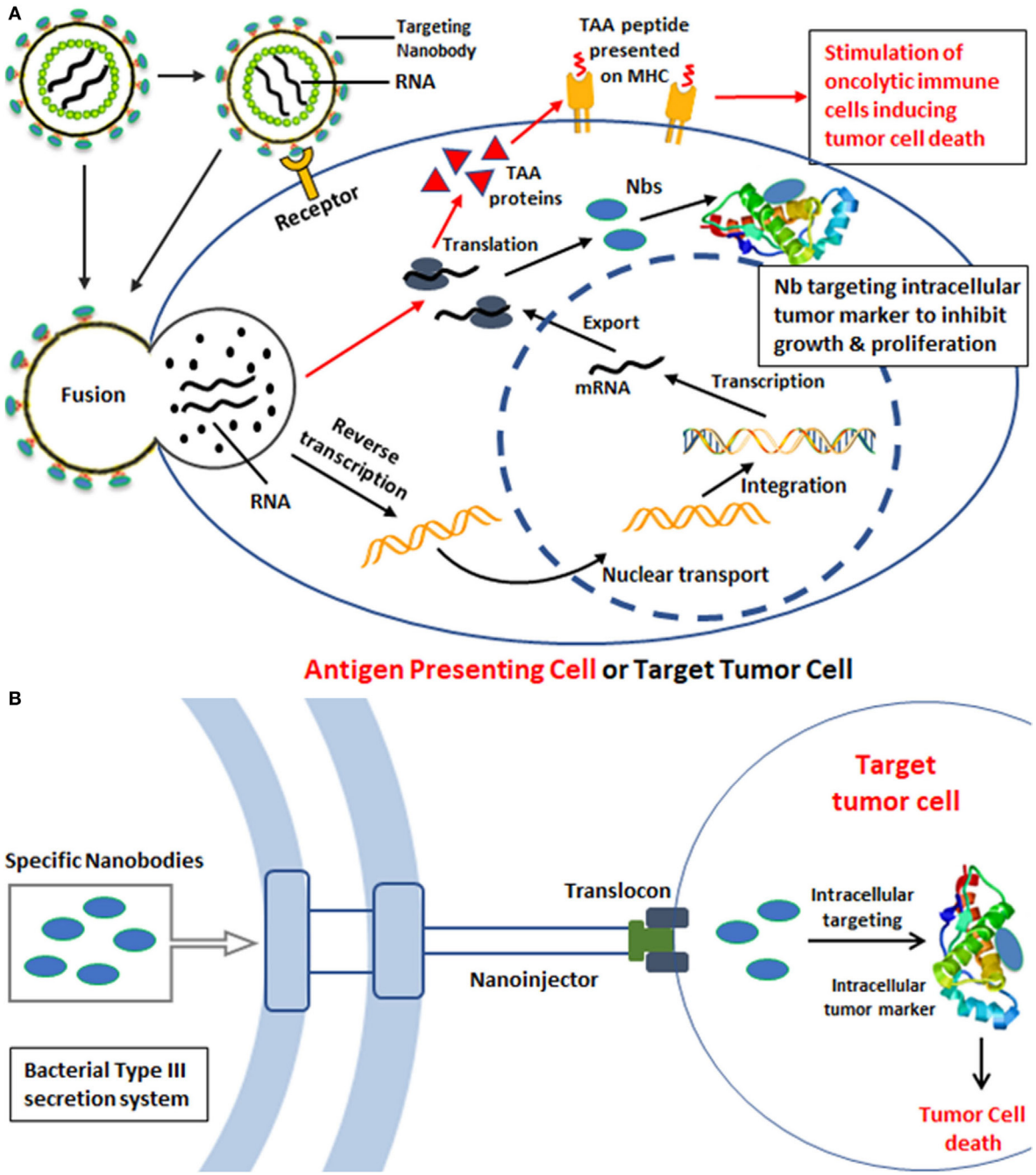

FIGURE 4 | Strategies for intracellular tumor targeting. **(A)** Gene delivery of specific nanoboides (Nbs) against intracellular tumor targets based on lentiviral vectors. The lentivirus displays Nbs directed toward antigen-presenting cells (APCs) such as dendritic cells (DCs). The initial attachment of the virus to the cellular receptor on the surface of APC allows internalization of the viral contents. The viral nucleoprotein core containing the genomic RNA is released into the cytoplasm after entry. Reverse transcription and synthesis of full-length chimeric viral DNA produces an integration-competent nucleoprotein complex that mediates integration of viral DNA into the host cell genome. Integrated chimeric viral DNA serves as a transcription template for the synthesis of tumor-associated antigens that after proteolysis will be presented on MHC to stimulate oncolytic T cells inducing tumor cell death (red arrows). In an alternative approach, the LVs could contain genes encoding Nbs against intracellular tumor markers. The targeting of such LVs to tumor cells could then produce intrabodies (Nbs) that will associate with the intracellular tumor marker to inhibit tumor growth and proliferation (black arrows). **(B)** Transport of specific Nbs into tumor cells *via* bacterial type III secretion system (T3S) for intracellular tumor targeting. Gram-negative bacteria use a specialized secretion apparatus known as the T3S system to inject proteins directly into the eukaryotic cells, such as *Y. enterocolitica* T3S, *S. typhimurium* T3S, and *E. coli* T3S. Bacterial proteins that are delivered by a T3S are injected through the eukaryotic cell membrane *via* a proteinaceous transmembrane channel known as the type III translocon. The schematic components of the T3S nanosyringe are shown and Gram-negative bacteria were engineered to produce antigen-specific Nbs against intracellular tumor markers. The attachment of T3S and tumor cells will facilitate the export of Nb proteins inside tumor cells, such as HeLa cells. These internalized Nbs will block and inhibit the signaling cascades or processes of tumor metastasis, leading to targeted cancer therapy.

exogenous proteins into eukaryotic host cells (124). This needle-like system serves as a sensory probe to detect eukaryotic organisms and to inject bacterial proteins directly in the host cell to prepare these cells and to assist the pathogen to survive and to escape the host immune system.

E. coli Bacteria T3SS

An old observation, that bacteria are homing at the hypoxic environment of solid cancers, inspired researchers to harness bacteria with Nbs that would be translocated *via* the T3SS inside the cancer cells to cause damage (**Figure 4B**). In a first step to explore this strategy, it was demonstrated that the non-invasive *E. coli* bacteria carrying a T3SS could translocate successfully the Nbs into mammalian cells (125). Several constructs of Nb fused to $EspF_{20}$ T3 signal (T3s) were cloned into non-pathogenic *E. coli* cells and shown by western blot to get inside HeLa cells. The immunoprecipitation further demonstrated the intact antigen-binding activity of the injected Nbs (125). Higher levels of injected T3s-Nbs remained inside the HeLa host when they express the cognate antigen. Thus, the non-invasive bacterial T3SS is a promising strategy to deliver Nbs into mammalian cells to target intracellular cell components and signaling pathway molecules.

The *Y. enterocolitica* T3SS

Likewise, Ittig et al. (126) reported a protein delivery system based on the type III secretion of *Y. enterocolitica*. In their research, YopE, a *Y. enterocolitica* effector with Rho GTPase-activating protein activity, was utilized for the expression of protein–YopE fusions in *Y. enterocolitica* and translocation of proteins into mammalian cells. The secretion of multiple proteins was evaluated, including cell-cycle proteins (i.e., Mad2, CDK1, CDKN2A/INK4A, CDKN2B/INK4B, and CDKN2C/INK4C), apoptosis-related proteins(Bad, FADD, caspase-3 [CASP] p17 and p12, zebrafish BID, and zebrafish t-BID), and signaling proteins (TRAF6, TIFA, and the GPCR Gα subunit GNA12). Furthermore, an anti-GFP Nb (VHH GFP4) and a VHH GFP4 fusion construct for targeted protein degradation was also tested (126). The delivery of these functional fusion Nb proteins of different size and structure was demonstrated after infection of HeLa cells. The Nb against GFP was employed to assess the translocation of functional Nbs from *Y. enterocolitica* into HeLa cells. Interestingly, the translocation of YopE1-Nb fusions occurs first in the cytoplasm, whereas translocated YopE1-Nb fusions against GFP were exclusively detected in the nucleus of cells expressing histone 2B-GFP, illustrating the mobility of the fusion inside the cell and its organelles and the interaction between the Nbs and their target antigen (126). The results indicated that YopE fusion are effectively secreted and delivered into eukaryotic cells and that the *Y. enterocolitica*-based delivery is fast, homogenous, and controllable. However, the unspecific targeting of bacteria to normal and tumor cells indicates that further engineering of the bacteria will be required to obtain an exclusive tumor-specific Nb translocation. This might be achieved by anchoring tumor-specific Nbs to the surface of the engineered bacteria.

Clostridium-Directed Antibody Therapy

A non-toxic bacteriolytic strain of *Clostridium* has been engineered for the production of tumor therapeutic proteins (127). This obligatory anaerobic *Clostridium* specifically colonizes hypoxic and necrotic regions present in solid tumors but normally absent in other parts of the body. The efficacy of *Clostridium*-directed tumor therapy (CDAT) has been demonstrated in experimental models as a vehicle for tumor-specific delivery of prodrug converting enzymes (128, 129) and to enhance radiotherapy and chemotherapy (130–132).

Nanobodies targeting HIF-1 were cloned in *Clostridium novyi-NT* and *C. sporogenes* strains. The expression of HIF-specific intrabodies in an oncolytic *C. novyi* strain opened the path for developing a *Clostridium*-directed antibody therapy (133).

MOLECULAR IMAGING WITH Nbs FOR EARLY STAGE DIAGNOSIS OF TUMORS

Early diagnosis is essential to increase chances on a successful treatment of tumors. Recently, Nbs supported by their small size, high stability, and high target specificity and affinity have been engineered into Nb-detective constructs for non-invasive *in vivo* molecular imaging (33). These molecules reach rapidly a maximal contrast between signal in the pathological tissues and that in healthy tissues, which is crucial for optimal *in vivo* molecular imaging. The short half-life of Nbs in the bloodstream due to rapid clearance of excess of non-targeting Nbs *via* kidney and bladder guarantees a high tumor to background ratio at early time points after administering the Nb probe. To date, several imaging techniques have been developed and applied for clinical application, such as positron emission tomography (PET), single photon emission computed tomography (SPECT), computed tomography (CT), magnetic resonance imaging (MRI), optical, ultrasound, and photo-acoustic imaging (134–136). In following sections, radionuclide imaging (by SPECT and PET) will be described as it passed a phase I study (136) and probes based on Nbs developed during the past decade are listed in **Table 1**.

Nbs in Nuclear Imaging

For nuclear imaging, different radionuclides (e.g., ^{99m}Tc, ^{89}Zr, ^{68}Ga, ^{18}F, or ^{64}Cu) are employed for labeling target-specific Nbs. Huang et al. (44) adapted the labeling with ^{99m}Tc-tricarbonyl intermediate [$^{99m}Tc(H_2O)_3(CO)_3$] for an anti-EGFR Nb (8B6) and used this probe for non-invasive imaging with SPECT. A rapid blood clearance (half-life ~1.5 h) of such conjugates was demonstrated and the potential to differentiate tumors with high or low levels of EGFR (44, 142). Likewise, Gainkam et al. (45) performed a similar experiment with two different Nbs using pinhole SPECT and micro-CT. The same group evaluated the relationship between tumor uptake of the EGFR-specific Nb ^{99m}Tc-7C12 and the tumor burden, as well as the possibility to monitor tumor response to erlotinib with this probe (143). A good correlation between tumor uptake of ^{99m}Tc-7C12 with tumor burden was observed. Thus, ^{99m}Tc-7C12 seems to be a promising tool to monitor the therapeutic response and treatment progress in EGFR overexpressing tumors (138).

Besides EGFR, the human epidermal growth factor receptor type 2 (HER2) is also an interesting target for molecular imaging, as one-quarter of all breast cancers is overexpressing HER2 (136).

TABLE 1 | Conjugated systems based on nanobodies (Nbs), employed for imaging of tumors or for drug delivery to cancer cells.

Construct	Cellular target of Nb	Effector domain	Cancer cell lines	Reference
Nb-toxin	Carcinoembryonic antigen	*Enterobacter cloacae* β-lactamase fused to Nb	Mice bearing LS174T xenografts	(75)
	Malignant glioblastoma multiforme	Tumor necrosis factor-related apoptosis-inducing ligand (TRAIL) fused to Nb	U87-mCherry-FLuc cells into the brains of nude mice	(76)
	Vascular endothelial growth factor receptor-2	*Pseudomonas* exotoxin A (PE38) fused to Nb	HEK293, 293KDR cells	(77)
Nb-polymer NP	Epidermal growth factor receptor (EGFR)	Liposome fused to Nb EGa1	14C human head and neck cancer cell line and the human epidermoid carcinoma cell line A431	(72, 73)
		Nb EGa1-liposome encapsulated AG538 anti-insulin-like growth factor 1 receptor kinase inhibitor (AG538)		
		Nb EGa1-extracellular vesicles (EVs) fused to glycosylphosphatidylinositol (GPI) anchor signal peptides derived from decay-accelerating factor	Neuro2A cells, human epidermoid carcinoma cells A431 and HeLa cells	(93)
	EGFR	Nb EGa1-micelles	A431, 14C cell line and low endogenous EGFR expression NIH 3T3 cell lines, ovarian carcinoma and B16F10 melanoma cells	(71, 97, 98)
		Nb EGa1-micelles encapsulated doxorubicin (DOX)		
	EGFR	Nb EGa1-albumin nanoparticles encapsulated multikinase inhibitor 17864	EGFR-positive head and neck squamous cell carcinoma cell line UM-SCC-14C	(111)
		Dendrimers-encapsulated DOX	Mouse melanoma (B16-F10) and Male C57BL/6 mice	(102, 103)
Nb-lentivirus	Dendritic cells (DCs) and macrophages	Nb DC2.1 decorated lentiviral vectors for specific gene delivery specific targeting	HEK 293T, mouse fibroblasts NIH 3T3 cells, mouse leukemic macrophage RAW264.7 cells, mouse T-lymphoma EL4 cells, and mouse B-lymphoma A20 cells	(116, 117, 137)
Molecular imaging	EGFR	^{99m}Tc for single photon emission computed tomography (SPECT) on Nb 8B6	Human epidermoid carcinoma (A431), human prostate carcinoma (DU145)	(44)
		^{99m}Tc for SPECT on Nb 7C12	Human epidermoid carcinoma (A431)	(33, 136, 138, 139)
		^{99m}Tc for SPECT on Nb 7D12		
		^{68}Ga for PET on Nb 7D12		
		IRDye800CW for optical imaging on Nb 7D12		
	Human epidermal growth factor receptor-2 (HER-2)	^{99m}Tc for SPECT on Nb 2Rs15d	Human colon carcinoma (LS174T), human breast cancer (SKBR3), and human ovarian cancer (SKOV3)	(139, 140)
		^{68}Ga for PET on Nb 2Rs15d	Human ovarian cancer (SKOV3)	
		IRDye800CW for optical imaging on Nb 11A4	Human breast cancer (SKBR3)	(55)
	Vascular cell adhesion protein 1 (VCAM1)	^{99m}Tc for SPECT on Nb VCAM1-5	Atherosclerosis (ApoE-deficient mice)	(94, 141)
		Microbubble for ultrasound imaging onto Nbs	Murine adenocarcinoma (MC38)	
Intracellular delivery of specific Nbs	Amylase (Amy) and the green fluorescent protein	Nb Vamy and Vgfp-EspF20 T3 signal (T3s)	HeLa CCL-2, HEK 293T, and Swiss 3T3 fibroblasts	(125, 126)
		Nb against EGFP-YopE based on type III secretion system		
	HIF-1α	Intrabodies produced by *Clostridium novyi*-NT strain	–	(133)

This biomarker is also the target for Trastuzumab. For stratification, it would be preferable to screen breast cancer patients by non-invasive *in vivo* imaging for occurrence of HER2 on their tumors. To this end, multiple Nbs were evaluated to identify a lead Nb (2Rs15d) for imaging of HER2-positive tumors that does not interfere with the binding of the therapeutic Trastuzumab for the same target (140). The accumulation on the tumor tissue was demonstrated by *in vitro*, *ex vivo*, and *in vivo* assays. The *in vivo* assay in mice bearing HER2-expressing tumor xenografts confirmed the high uptake in tumor tissue, with low level of detection at healthy tissues (except for kidneys). Later on, it was shown that the removal of hemaglutinin tag and the His tag on the Nb decreased the kidney retention of the probe drastically (139, 140).

The reduced radio-toxicity at kidneys with "tag-stripped" Nbs allows a switch to targeted radionuclide therapy (TRNT) by changing the label on Nb 2Rs15d to ^{177}Lu (139). Although TRNT has been a promising strategy for tumor killing, the undesirable

pharmacokinetics (prolonged serum retention and poor tumor penetration) of mAb vehicles carrying the radiotoxic load curtailed the application. Therefore, the substitution of mAbs by Nbs having favorable pharmacokinetics and a highly specific target accumulation leads to a low accumulation of label in healthy tissues. Indeed, it has been demonstrated that Nb-based TRNT could target tumors successfully in a xenograft model. This highlights the potential of Nb-based TRNT as a valuable candidate for tumor diagnosis and therapy (144).

Nbs in Optical Imaging

Various methods allow optical molecular imaging where contrast is obtained by fluorescence, bioluminescence, absorption, or reflectance. The most valuable features of optical imaging compared to other imaging techniques include the high safety, high flexibility of the probes, and high sensitivity for the targets (135, 145, 146).

In 2012, a novel platform for optical imaging with Nbs was developed whereby the anti-EGFR Nb 7D12 and Cetuximab were conjugated with the near-infrared (NIR) fluorophore IRDye800CW (33). The 7D12-IR allowed the visualization of tumors as early as 30 min post-injection of the probe, whereas Cetuximab-IR failed to provide a signal at the tumor site above background. Hence, the anti-EGFR Nb conjugated to the NIR fluorophore was demonstrated to possess excellent properties, which will facilitate preclinical or clinical optical imaging applications.

In 2016, Kijanka et al. (147) reported a combination of optical conjugations based on two different Nbs against two different breast tumor markers, for an improved tumor detection: Nb B9 against CAIX, which targets the peri-necrotic regions of tumors, and Nb 11A4 against HER2. This dual-spectral imaging strategy accomplishes successfully the optical molecular imaging of CAIX and HER2-positive DCIS xenografts *in vivo*, under conditions mimicking surgical settings. This strategy is assumed to facilitate a faster detection of tumor markers, and it is highly promising to utilize the dual-spectral imaging strategy for the early diagnosis, treatment program planning, and monitoring the treatment response (147).

Nb Imaging Based on Ultrasound

Ultrasound imaging is widely used for medical applications by collecting sound waves reflected by tissues and organs. Microbubbles (μBs) have been developed as ultrasound contrast agents and can be targeted to tumors by conjugation with specific Nbs. Specific Nbs (μB-cAbVCAM1-5) against the vascular cell adhesion protein 1 (VCAM1) were introduced for μBs targeting (94, 141). The enhancement of ultrasound imaging was observed both *in vitro* and *in vivo*. Although the detection and imaging of this technique has been restricted to the systemic vasculature, it is still worth extending the effort toward other targets (148).

CONCLUSION AND FUTURE PERSPECTIVES

Soon after the initial report on functional heavy chain antibodies in camelidae, Nbs have been introduced in different areas, such as in oncology as antagonists, for the development of Nb-conjugated drug delivery systems, and for molecular imaging. This report contains an overview of drug delivery systems using Nbs, including transport of specific agents to extracellular tumor targets and highly potential intracellular tumor markers. The cellular imaging techniques based on Nbs were also summarized to provide basic knowledge and promising insights from further clinical application. It is well established that antagonists of small size need to exhibit a high affinity and specificity for their cognate target, so that they can associate to the target before being cleared *via* the kidneys. Nbs have demonstrated to fulfill this task. Generally, Nbs seem to be very promising when used as targeting moieties to develop novel drug delivery systems or to generate an intracellular targeting agent (149).

Several different strategies have been developed to broaden the application range of Nbs for diagnosis and cancer therapy: in first instance "naked" Nbs are utilized, in bivalent or bispecific formats to act as antagonists against tumor angiogenesis, metabolism, and metastasis. The small size of Nbs facilitates extravasation and solid tumor penetration. A further development consists in conjugating Nbs with toxins to create a specific drug delivery system. This toxic agent can be conjugated directly to Nbs or can be anchored onto or within NPs, consisting of liposomes, micelles, or polymers. The size and format of these drug delivery systems is crucial and greatly affects its accumulation at the tumor site. Systems that increase the size of the Nb enhances concomitantly its retention in blood circulation and conversely, decreases tumor penetration.

To date, most of the applications just employed Nbs directed against extracellular targets. However, intracellular effectors (e.g., components of signaling cascades) are thought to be excellent therapeutic targets for Nbs as well. In this case, the plasma membrane will block the transport of Nb-based inhibitors into cells, obviously restricting the application. Potential strategies to transfer Nbs inside cells include LVs harnessed with Nbs for cellular targeting or Nbs delivered *via* the bacterial T3 secretion system. Trials with LVs revealed the potential to target different cell types. The simplicity to engineer Nbs permits the recognition of any cell type and subsequent display technology will further enhance the potential of LVs for gene therapy purposes, tumor immunotherapy, and intracellular targeting. Alternatively, protocols to employ T3S have been developed to inject heterologous type III and IV effectors (150, 151), as well as mammalian proteins inside cells. This T3S-based protein delivery strategy could facilitate the transfer of particular antagonist into cells and induce apoptosis (126). It was suggested that transport of Nbs into cells by non-pathogenic bacterial strains equipped with T3S would be a promising technology to target host cells and intracellular signaling pathways.

While *in vivo* molecular imaging with Nbs is mainly relying on SPECT or PET, alternative innovative techniques, such as optical and ultrasound imaging, are being developed (134, 136). Since all imaging technology has its weakness, it is probably best to combine multiple techniques to exploit synergistic advantages and multimodal contrast agents or imaging probes score high on the wish list.

Obviously, Nbs are a versatile tool that will fulfill a central role in various clinically relevant applications.

AUTHOR CONTRIBUTIONS

All authors listed have made a substantial, direct, and intellectual contribution to the work and approved it for publication.

FUNDING

This work was financially supported by IWT SB project Nanocomit 140061.

REFERENCES

1. Baudino TA. Targeted cancer therapy: the next generation of cancer treatment. *Curr Drug Discov Technol* (2015) 12(1):3–20. doi:10.2174/1570163812666150602144310
2. Scott AM, Wolchok JD, Old LJ. Antibody therapy of cancer. *Nat Rev Cancer* (2012) 12(4):278–87. doi:10.1038/nrc3236
3. Bhutani D, Vaishampayan UN. Monoclonal antibodies in oncology therapeutics: present and future indications. *Expert Opin Biol Ther* (2013) 13(2):269–82. doi:10.1517/14712598.2012.758705
4. Elbakri A, Nelson PN, Abu Odeh RO. The state of antibody therapy. *Hum Immunol* (2010) 71(12):1243–50. doi:10.1016/j.humimm.2010.09.007
5. Oldham RK, Dillman RO. Monoclonal antibodies in cancer therapy: 25 years of progress. *J Clin Oncol* (2008) 26(11):1774–7. doi:10.1200/JCO.2007.15.7438
6. Mishani E, Hagooly A. Strategies for molecular imaging of epidermal growth factor receptor tyrosine kinase in cancer. *J Nucl Med* (2009) 50(8):1199–202. doi:10.2967/jnumed.109.062117
7. Zhao H, Cui K, Muschenborn A, Wong ST. Progress of engineered antibody-targeted molecular imaging for solid tumors. *Mol Med Rep* (2008) 1(1):131–4. doi:10.3892/mmr.1.1.131
8. Fay F, Scott CJ. Antibody-targeted nanoparticles for cancer therapy. *Immunotherapy* (2011) 3(3):381–94. doi:10.2217/imt.11.5
9. Alley SC, Okeley NM, Senter PD. Antibody-drug conjugates: targeted drug delivery for cancer. *Curr Opin Chem Biol* (2010) 14(4):529–37. doi:10.1016/j.cbpa.2010.06.170
10. Minchinton AI, Tannock IF. Drug penetration in solid tumours. *Nat Rev Cancer* (2006) 6(8):583–92. doi:10.1038/nrc1893
11. Gong R, Chen W, Dimitrov DS. Expression, purification, and characterization of engineered antibody CH2 and VH domains. *Methods Mol Biol* (2012) 899:85–102. doi:10.1007/978-1-61779-921-1_6
12. Altintas I, Kok RJ, Schiffelers RM. Targeting epidermal growth factor receptor in tumors: from conventional monoclonal antibodies via heavy chain-only antibodies to nanobodies. *Eur J Pharm Sci* (2012) 45(4):399–407. doi:10.1016/j.ejps.2011.10.015
13. Miller KR, Koide A, Leung B, Fitzsimmons J, Yoder B, Yuan H, et al. T cell receptor-like recognition of tumor in vivo by synthetic antibody fragment. *PLoS One* (2012) 7(8):e43746. doi:10.1371/journal.pone.0043746
14. Tramontano A, Bianchi E, Venturini S, Martin F, Pessi A, Sollazzo M. The making of the minibody: an engineered beta-protein for the display of conformationally constrained peptides. *J Mol Recognit* (1994) 7(1):9–24. doi:10.1002/jmr.300070103
15. Orlova A, Tolmachev V, Pehrson R, Lindborg M, Tran T, Sandstrom M, et al. Synthetic affibody molecules: a novel class of affinity ligands for molecular imaging of HER2-expressing malignant tumors. *Cancer Res* (2007) 67(5):2178–86. doi:10.1158/0008-5472.CAN-06-2887
16. Stumpp MT, Binz HK, Amstutz P. DARPins: a new generation of protein therapeutics. *Drug Discov Today* (2008) 13(15–16):695–701. doi:10.1016/j.drudis.2008.04.013
17. Boersma YL, Pluckthun A. DARPins and other repeat protein scaffolds: advances in engineering and applications. *Curr Opin Biotechnol* (2011) 22(6):849–57. doi:10.1016/j.copbio.2011.06.004
18. Hamers-Casterman C, Atarhouch T, Muyldermans S, Robinson G, Hamers C, Songa EB, et al. Naturally occurring antibodies devoid of light chains. *Nature* (1993) 363(6428):446–8. doi:10.1038/363446a0
19. Conrath KE, Wernery U, Muyldermans S, Nguyen VK. Emergence and evolution of functional heavy-chain antibodies in Camelidae. *Dev Comp Immunol* (2003) 27(2):87–103. doi:10.1016/S0145-305X(02)00071-X
20. Kolkman JA, Law DA. Nanobodies – from llamas to therapeutic proteins. *Drug Discov Today Technol* (2010) 7(2):e139–46. doi:10.1016/j.ddtec.2010.03.002
21. Muyldermans S, Atarhouch T, Saldanha J, Barbosa JA, Hamers R. Sequence and structure of VH domain from naturally occurring camel heavy chain immunoglobulins lacking light chains. *Protein Eng* (1994) 7(9):1129–35. doi:10.1093/protein/7.9.1129
22. Muyldermans S. Nanobodies: natural single-domain antibodies. *Annu Rev Biochem* (2013) 82:775–97. doi:10.1146/annurev-biochem-063011-092449
23. Romao E, Morales-Yanez F, Hu Y, Crauwels M, De Pauw P, Hassanzadeh GG, et al. Identification of useful nanobodies by phage display of immune single domain libraries derived from camelid heavy chain antibodies. *Curr Pharm Des* (2016) 22(43):6500–18. doi:10.2174/1381612822666160923114417
24. Nguyen VK, Muyldermans S, Hamers R. The specific variable domain of camel heavy-chain antibodies is encoded in the germline. *J Mol Biol* (1998) 275(3):413–8. doi:10.1006/jmbi.1997.1477
25. Nguyen VK, Hamers R, Wyns L, Muyldermans S. Loss of splice consensus signal is responsible for the removal of the entire C(H)1 domain of the functional camel IGG2A heavy-chain antibodies. *Mol Immunol* (1999) 36(8):515–24. doi:10.1016/S0161-5890(99)00067-X
26. Nguyen VK, Hamers R, Wyns L, Muyldermans S. Camel heavy-chain antibodies: diverse germline V(H)H and specific mechanisms enlarge the antigen-binding repertoire. *EMBO J* (2000) 19(5):921–30. doi:10.1093/emboj/19.5.921
27. Deschacht N, De Groeve K, Vincke C, Raes G, De Baetselier P, Muyldermans S. A novel promiscuous class of camelid single-domain antibody contributes to the antigen-binding repertoire. *J Immunol* (2010) 184(10):5696–704. doi:10.4049/jimmunol.0903722
28. Arbabi-Ghahroudi M, Desmyter A, Wyns L, Hamers R, Muyldermans S. Selection and identification of single domain antibody fragments from camel heavy-chain antibodies. *FEBS Lett* (1997) 414(3):521–6. doi:10.1016/S0014-5793(97)01062-4
29. Arbabi-Ghahroudi M, Tanha J, MacKenzie R. Prokaryotic expression of antibodies. *Cancer Metastasis Rev* (2005) 24(4):501–19. doi:10.1007/s10555-005-6193-1
30. Frenken LG, van der Linden RH, Hermans PW, Bos JW, Ruuls RC, de Geus B, et al. Isolation of antigen specific llama VHH antibody fragments and their high level secretion by *Saccharomyces cerevisiae*. *J Biotechnol* (2000) 78(1):11–21. doi:10.1016/S0168-1656(99)00228-X
31. Frenken LG, Hessing JG, Van den Hondel CA, Verrips CT. Recent advances in the large-scale production of antibody fragments using lower eukaryotic microorganisms. *Res Immunol* (1998) 149(6):589–99. doi:10.1016/S0923-2494(98)80011-4
32. Ismaili A, Jalali-Javaran M, Rasaee MJ, Rahbarizadeh F, Forouzandeh-Moghadam M, Memari HR. Production and characterization of anti-(mucin MUC1) single-domain antibody in tobacco (*Nicotiana tabacum* cultivar Xanthi). *Biotechnol Appl Biochem* (2007) 47(Pt 1):11–9. doi:10.1042/BA20060071
33. Oliveira S, van Dongen GA, Stigter-van Walsum M, Roovers RC, Stam JC, Mali W, et al. Rapid visualization of human tumor xenografts through optical imaging with a near-infrared fluorescent anti-epidermal growth factor receptor nanobody. *Mol Imaging* (2012) 11(1):33–46. doi:10.2310/7290.2011.00025
34. Dumoulin M, Conrath K, Van Meirhaeghe A, Meersman F, Heremans K, Frenken LG, et al. Single-domain antibody fragments with high conformational stability. *Protein Sci* (2002) 11(3):500–15. doi:10.1110/ps.34602
35. van der Linden RH, Frenken LG, de Geus B, Harmsen MM, Ruuls RC, Stok W, et al. Comparison of physical chemical properties of llama VHH antibody fragments and mouse monoclonal antibodies. *Biochim Biophys Acta* (1999) 1431(1):37–46. doi:10.1016/S0167-4838(99)00030-8
36. Desmyter A, Transue TR, Ghahroudi MA, Thi MH, Poortmans F, Hamers R, et al. Crystal structure of a camel single-domain VH antibody fragment in complex with lysozyme. *Nat Struct Biol* (1996) 3(9):803–11. doi:10.1038/nsb0996-803

37. Wesolowski J, Alzogaray V, Reyelt J, Unger M, Juarez K, Urrutia M, et al. Single domain antibodies: promising experimental and therapeutic tools in infection and immunity. *Med Microbiol Immunol* (2009) 198(3):157–74. doi:10.1007/s00430-009-0116-7
38. Schmitz KR, Bagchi A, Roovers RC, van Bergen en Henegouwen PM, Ferguson KM. Structural evaluation of EGFR inhibition mechanisms for nanobodies/VHH domains. *Structure* (2013) 21(7):1214–24. doi:10.1016/j.str.2013.05.008
39. De Genst E, Silence K, Decanniere K, Conrath K, Loris R, Kinne J, et al. Molecular basis for the preferential cleft recognition by dromedary heavy-chain antibodies. *Proc Natl Acad Sci U S A* (2006) 103(12):4586–91. doi:10.1073/pnas.0505379103
40. Behrens CR, Liu B. Methods for site-specific drug conjugation to antibodies. *MAbs* (2014) 6(1):46–53. doi:10.4161/mabs.26632
41. Massa S, Xavier C, De Vos J, Caveliers V, Lahoutte T, Muyldermans S, et al. Site-specific labeling of cysteine-tagged camelid single-domain antibody-fragments for use in molecular imaging. *Bioconjug Chem* (2014) 25(5):979–88. doi:10.1021/bc500111t
42. Massa S, Vikani N, Betti C, Ballet S, Vanderhaegen S, Steyaert J, et al. Sortase A-mediated site-specific labeling of camelid single-domain antibody-fragments: a versatile strategy for multiple molecular imaging modalities. *Contrast Media Mol Imaging* (2016) 11(5):328–39. doi:10.1002/cmmi.1696
43. Wagner K, Kwakkenbos MJ, Claassen YB, Maijoor K, Bohne M, van der Sluijs KF, et al. Bispecific antibody generated with sortase and click chemistry has broad antiinfluenza virus activity. *Proc Natl Acad Sci U S A* (2014) 111(47):16820–5. doi:10.1073/pnas.1408605111
44. Huang L, Gainkam LO, Caveliers V, Vanhove C, Keyaerts M, De Baetselier P, et al. SPECT imaging with 99mTc-labeled EGFR-specific nanobody for in vivo monitoring of EGFR expression. *Mol Imaging Biol* (2008) 10(3):167–75. doi:10.1007/s11307-008-0133-8
45. Gainkam LO, Huang L, Caveliers V, Keyaerts M, Hernot S, Vaneycken I, et al. Comparison of the biodistribution and tumor targeting of two 99mTc-labeled anti-EGFR nanobodies in mice, using pinhole SPECT/micro-CT. *J Nucl Med* (2008) 49(5):788–95. doi:10.2967/jnumed.107.048538
46. Tijink BM, Laeremans T, Budde M, Stigter-van Walsum M, Dreier T, de Haard HJ, et al. Improved tumor targeting of anti-epidermal growth factor receptor nanobodies through albumin binding: taking advantage of modular nanobody technology. *Mol Cancer Ther* (2008) 7(8):2288–97. doi:10.1158/1535-7163.MCT-07-2384
47. Roovers RC, Vosjan MJ, Laeremans T, el Khoulati R, de Bruin RC, Ferguson KM, et al. A biparatopic anti-EGFR nanobody efficiently inhibits solid tumour growth. *Int J Cancer* (2011) 129(8):2013–24. doi:10.1002/ijc.26145
48. Sleep D, Cameron J, Evans LR. Albumin as a versatile platform for drug half-life extension. *Biochim Biophys Acta* (2013) 1830(12):5526–34. doi:10.1016/j.bbagen.2013.04.023
49. Bell A, Wang ZJ, Arbabi-Ghahroudi M, Chang TA, Durocher Y, Trojahn U, et al. Differential tumor-targeting abilities of three single-domain antibody formats. *Cancer Lett* (2010) 289(1):81–90. doi:10.1016/j.canlet.2009.08.003
50. Richard G, Meyers AJ, McLean MD, Arbabi-Ghahroudi M, MacKenzie R, Hall JC. In vivo neutralization of alpha-cobratoxin with high-affinity llama single-domain antibodies (VHHs) and a VHH-Fc antibody. *PLoS One* (2013) 8(7):e69495. doi:10.1371/journal.pone.0069495
51. Dolk E, van Vliet C, Perez JM, Vriend G, Darbon H, Ferrat G, et al. Induced refolding of a temperature denatured llama heavy-chain antibody fragment by its antigen. *Proteins* (2005) 59(3):555–64. doi:10.1002/prot.20378
52. Harmsen MM, De Haard HJ. Properties, production, and applications of camelid single-domain antibody fragments. *Appl Microbiol Biotechnol* (2007) 77(1):13–22. doi:10.1007/s00253-007-1142-2
53. Cortez-Retamozo V, Lauwereys M, Hassanzadeh Gh G, Gobert M, Conrath K, Muyldermans S, et al. Efficient tumor targeting by single-domain antibody fragments of camels. *Int J Cancer* (2002) 98(3):456–62. doi:10.1002/ijc.10212
54. Vincke C, Loris R, Saerens D, Martinez-Rodriguez S, Muyldermans S, Conrath K. General strategy to humanize a camelid single-domain antibody and identification of a universal humanized nanobody scaffold. *J Biol Chem* (2009) 284(5):3273–84. doi:10.1074/jbc.M806889200
55. Kijanka M, Warnders FJ, El Khattabi M, Lub-de Hooge M, van Dam GM, Ntziachristos V, et al. Rapid optical imaging of human breast tumour xenografts using anti-HER2 VHHs site-directly conjugated to IRDye 800CW for image-guided surgery. *Eur J Nucl Med Mol Imaging* (2013) 40(11):1718–29. doi:10.1007/s00259-013-2471-2
56. Steeland S, Vandenbroucke RE, Libert C. Nanobodies as therapeutics: big opportunities for small antibodies. *Drug Discov Today* (2016) 21(7):1076–113. doi:10.1016/j.drudis.2016.04.003
57. Oliveira S, Heukers R, Sornkom J, Kok RJ, van Bergen En Henegouwen PM. Targeting tumors with nanobodies for cancer imaging and therapy. *J Control Release* (2013) 172(3):607–17. doi:10.1016/j.jconrel.2013.08.298
58. Groot AJ, Verheesen P, Westerlaken EJ, Gort EH, van der Groep P, Bovenschen N, et al. Identification by phage display of single-domain antibody fragments specific for the ODD domain in hypoxia-inducible factor 1alpha. *Lab Invest* (2006) 86(4):345–56. doi:10.1038/labinvest.3700395
59. Groot AJ, Gort EH, van der Wall E, van Diest PJ, Vooijs M. Conditional inactivation of HIF-1 using intrabodies. *Cell Oncol* (2008) 30(5):397–409. doi:10.3233/CLO-2008-0442
60. Revets H, De Baetselier P, Muyldermans S. Nanobodies as novel agents for cancer therapy. *Expert Opin Biol Ther* (2005) 5(1):111–24. doi:10.1517/14712598.5.1.111
61. Roovers RC, van Dongen GA, van Bergen en Henegouwen PM. Nanobodies in therapeutic applications. *Curr Opin Mol Ther* (2007) 9(4):327–35. doi:10.2217/nnm.13.86
62. Hemmer C, Djennane S, Ackerer L, Hleibieh K, Marmonier A, Gersch S, et al. Nanobody-mediated resistance to Grapevine fanleaf virus in plants. *Plant Biotechnol J* (2017). doi:10.1111/pbi.12819
63. Roovers RC, Laeremans T, Huang L, De Taeye S, Verkleij AJ, Revets H, et al. Efficient inhibition of EGFR signaling and of tumour growth by antagonistic anti-EFGR nanobodies. *Cancer Immunol Immunother* (2007) 56(3):303–17. doi:10.1007/s00262-006-0180-4
64. Holz JB. The TITAN trial – assessing the efficacy and safety of an anti-von Willebrand factor nanobody in patients with acquired thrombotic thrombocytopenic purpura. *Transfus Apher Sci* (2012) 46(3):343–6. doi:10.1016/j.transci.2012.03.027
65. Callewaert F, Roodt J, Ulrichts H, Stohr T, van Rensburg WJ, Lamprecht S, et al. Evaluation of efficacy and safety of the anti-VWF nanobody ALX-0681 in a preclinical baboon model of acquired thrombotic thrombocytopenic purpura. *Blood* (2012) 120(17):3603–10. doi:10.1182/blood-2012-04-420943
66. Detalle L, Stohr T, Palomo C, Piedra PA, Gilbert BE, Mas V, et al. Generation and characterization of ALX-0171, a potent novel therapeutic nanobody for the treatment of respiratory syncytial virus infection. *Antimicrob Agents Chemother* (2015) 60(1):6–13. doi:10.1128/AAC.01802-15
67. Van Roy M, Ververken C, Beirnaert E, Hoefman S, Kolkman J, Vierboom M, et al. The preclinical pharmacology of the high affinity anti-IL-6R Nanobody(R) ALX-0061 supports its clinical development in rheumatoid arthritis. *Arthritis Res Ther* (2015) 17:135. doi:10.1186/s13075-015-0651-0
68. Zheng F, Put S, Bouwens L, Lahoutte T, Matthys P, Muyldermans S, et al. Molecular imaging with macrophage CRIg-targeting nanobodies for early and preclinical diagnosis in a mouse model of rheumatoid arthritis. *J Nucl Med* (2014) 55(5):824–9. doi:10.2967/jnumed.113.130617
69. Put S, Schoonooghe S, Devoogdt N, Schurgers E, Avau A, Mitera T, et al. SPECT imaging of joint inflammation with nanobodies targeting the macrophage mannose receptor in a mouse model for rheumatoid arthritis. *J Nucl Med* (2013) 54(5):807–14. doi:10.2967/jnumed.112.111781
70. Araste F, Ebrahimizadeh W, Rasooli I, Rajabibazl M, Mousavi Gargari SL. A novel VHH nanobody against the active site (the CA domain) of tumor-associated, carbonic anhydrase isoform IX and its usefulness for cancer diagnosis. *Biotechnol Lett* (2014) 36(1):21–8. doi:10.1007/s10529-013-1340-1
71. Talelli M, Rijcken CJ, Oliveira S, van der Meel R, van Bergen En Henegouwen PM, Lammers T, et al. Nanobody-shell functionalized thermosensitive core-crosslinked polymeric micelles for active drug targeting. *J Control Release* (2011) 151(2):183–92. doi:10.1016/j.jconrel.2011.01.015
72. Oliveira S, Schiffelers RM, van der Veeken J, van der Meel R, Vongpromek R, van Bergen En Henegouwen PM, et al. Downregulation of EGFR by a novel multivalent nanobody-liposome platform. *J Control Release* (2010) 145(2):165–75. doi:10.1016/j.jconrel.2010.03.020
73. van der Meel R, Oliveira S, Altintas I, Haselberg R, van der Veeken J, Roovers RC, et al. Tumor-targeted nanobullets: anti-EGFR nanobody-liposomes loaded

with anti-IGF-1R kinase inhibitor for cancer treatment. *J Control Release* (2012) 159(2):281–9. doi:10.1016/j.jconrel.2011.12.027
74. Sukhanova A, Even-Desrumeaux K, Kisserli A, Tabary T, Reveil B, Millot JM, et al. Oriented conjugates of single-domain antibodies and quantum dots: toward a new generation of ultrasmall diagnostic nanoprobes. *Nanomedicine* (2012) 8(4):516–25. doi:10.1016/j.nano.2011.07.007
75. Cortez-Retamozo V, Backmann N, Senter PD, Wernery U, De Baetselier P, Muyldermans S, et al. Efficient cancer therapy with a nanobody-based conjugate. *Cancer Res* (2004) 64(8):2853–7. doi:10.1158/0008-5472.CAN-03-3935
76. van de Water JA, Bagci-Onder T, Agarwal AS, Wakimoto H, Roovers RC, Zhu Y, et al. Therapeutic stem cells expressing variants of EGFR-specific nanobodies have antitumor effects. *Proc Natl Acad Sci U S A* (2012) 109(41):16642–7. doi:10.1073/pnas.1202832109
77. Behdani M, Zeinali S, Karimipour M, Khanahmad H, Schoonooghe S, Aslemarz A, et al. Development of VEGFR2-specific nanobody *Pseudomonas* exotoxin A conjugated to provide efficient inhibition of tumor cell growth. *N Biotechnol* (2013) 30(2):205–9. doi:10.1016/j.nbt.2012.09.002
78. Zamboni WC, Torchilin V, Patri AK, Hrkach J, Stern S, Lee R, et al. Best practices in cancer nanotechnology: perspective from NCI nanotechnology alliance. *Clin Cancer Res* (2012) 18(12):3229–41. doi:10.1158/1078-0432.CCR-11-2938
79. Lu Y, Liang K, Li X, Fan Z. Responses of cancer cells with wild-type or tyrosine kinase domain-mutated epidermal growth factor receptor (EGFR) to EGFR-targeted therapy are linked to downregulation of hypoxia-inducible factor-1alpha. *Mol Cancer* (2007) 6:63. doi:10.1186/1476-4598-6-63
80. Mamot C, Drummond DC, Noble CO, Kallab V, Guo Z, Hong K, et al. Epidermal growth factor receptor-targeted immunoliposomes significantly enhance the efficacy of multiple anticancer drugs in vivo. *Cancer Res* (2005) 65(24):11631–8. doi:10.1158/0008-5472.CAN-05-1093
81. Mamot C, Ritschard R, Kung W, Park JW, Herrmann R, Rochlitz CF. EGFR-targeted immunoliposomes derived from the monoclonal antibody EMD72000 mediate specific and efficient drug delivery to a variety of colorectal cancer cells. *J Drug Target* (2006) 14(4):215–23. doi:10.1080/10611860600691049
82. Maruyama K. PEG-immunoliposome. *Biosci Rep* (2002) 22(2):251–66. doi:10.1023/A:1020138622686
83. Dickson JL, Shah PS, Binks BP, Johnston KP. Steric stabilization of core-shell nanoparticles in liquid carbon dioxide at the vapor pressure. *Langmuir* (2004) 20(21):9380–7. doi:10.1021/la048564u
84. Jokerst JV, Lobovkina T, Zare RN, Gambhir SS. Nanoparticle PEGylation for imaging and therapy. *Nanomedicine (Lond)* (2011) 6(4):715–28. doi:10.2217/nnm.11.19
85. Suk JS, Xu Q, Kim N, Hanes J, Ensign LM. PEGylation as a strategy for improving nanoparticle-based drug and gene delivery. *Adv Drug Deliv Rev* (2016) 99(Pt A):28–51. doi:10.1016/j.addr.2015.09.012
86. Huang JY, Lu YM, Wang H, Liu J, Liao MH, Hong LJ, et al. The effect of lipid nanoparticle PEGylation on neuroinflammatory response in mouse brain. *Biomaterials* (2013) 34(32):7960–70. doi:10.1016/j.biomaterials.2013.07.009
87. Maeda H. The enhanced permeability and retention (EPR) effect in tumor vasculature: the key role of tumor-selective macromolecular drug targeting. *Adv Enzyme Regul* (2001) 41(1):189–207. doi:10.1016/S0065-2571(00)00013-3
88. Bozzuto G, Molinari A. Liposomes as nanomedical devices. *Int J Nanomedicine* (2015) 10(1):975–99. doi:10.2147/IJN.S68861
89. Muller LK, Landfester K. Natural liposomes and synthetic polymeric structures for biomedical applications. *Biochem Biophys Res Commun* (2015) 468(3):411–8. doi:10.1016/j.bbrc.2015.08.088
90. Debets MF, Leenders WP, Verrijp K, Zonjee M, Meeuwissen SA, Otte-Holler I, et al. Nanobody-functionalized polymersomes for tumor-vessel targeting. *Macromol Biosci* (2013) 13(7):938–45. doi:10.1002/mabi.201300039
91. Neophytou CM, Constantinou AI. Drug delivery innovations for enhancing the anticancer potential of vitamin E isoforms and their derivatives. *Biomed Res Int* (2015) 2015:584862. doi:10.1155/2015/584862
92. van der Meel R, Oliveira S, Altintas I, Heukers R, Pieters EH, van Bergen en Henegouwen PM, et al. Inhibition of tumor growth by targeted anti-EGFR/IGF-1R nanobullets depends on efficient blocking of cell survival pathways. *Mol Pharm* (2013) 10(10):3717–27. doi:10.1021/mp400212v
93. Kooijmans SA, Aleza CG, Roffler SR, van Solinge WW, Vader P, Schiffelers RM. Display of GPI-anchored anti-EGFR nanobodies on extracellular vesicles promotes tumour cell targeting. *J Extracell Vesicles* (2016) 5:31053. doi:10.3402/jev.v5.31053
94. Hernot S, Unnikrishnan S, Du Z, Shevchenko T, Cosyns B, Broisat A, et al. Nanobody-coupled microbubbles as novel molecular tracer. *J Control Release* (2012) 158(2):346–53. doi:10.1016/j.jconrel.2011.12.007
95. Gong J, Chen M, Zheng Y, Wang S, Wang Y. Polymeric micelles drug delivery system in oncology. *J Control Release* (2012) 159(3):312–23. doi:10.1016/j.jconrel.2011.12.012
96. Talelli M, Iman M, Varkouhi AK, Rijcken CJ, Schiffelers RM, Etrych T, et al. Core-crosslinked polymeric micelles with controlled release of covalently entrapped doxorubicin. *Biomaterials* (2010) 31(30):7797–804. doi:10.1016/j.biomaterials.2010.07.005
97. Talelli M, Oliveira S, Rijcken CJ, Pieters EH, Etrych T, Ulbrich K, et al. Intrinsically active nanobody-modified polymeric micelles for tumor-targeted combination therapy. *Biomaterials* (2013) 34(4):1255–60. doi:10.1016/j.biomaterials.2012.09.064
98. Talelli M, Iman M, Rijcken CJ, van Nostrum CF, Hennink WE. Targeted core-crosslinked polymeric micelles with controlled release of covalently entrapped doxorubicin. *J Control Release* (2010) 148(1):e121–2. doi:10.1016/j.jconrel.2010.07.092
99. Rao JP, Geckeler KE. Polymer nanoparticles: preparation techniques and size-control parameters. *Prog Polym Sci* (2011) 36(7):887–913. doi:10.1016/j.progpolymsci.2011.01.001
100. Steichen SD, Caldorera-Moore M, Peppas NA. A review of current nanoparticle and targeting moieties for the delivery of cancer therapeutics. *Eur J Pharm Sci* (2013) 48(3):416–27. doi:10.1016/j.ejps.2012.12.006
101. Cerqueira BB, Lasham A, Shelling AN, Al-Kassas R. Nanoparticle therapeutics: technologies and methods for overcoming cancer. *Eur J Pharm Biopharm* (2015) 97(Pt A):140–51. doi:10.1016/j.ejpb.2015.10.007
102. Hughes GA. Nanostructure-mediated drug delivery. *Nanomedicine* (2005) 1(1):22–30. doi:10.1016/j.nano.2004.11.009
103. Zhong Q, Bielski ER, Rodrigues LS, Brown MR, Reineke JJ, da Rocha SR. Conjugation to poly(amidoamine) dendrimers and pulmonary delivery reduce cardiac accumulation and enhance antitumor activity of doxorubicin in lung metastasis. *Mol Pharm* (2016) 13(7):2363–75. doi:10.1021/acs.molpharmaceut.6b00126
104. Karathanasis E, Ghaghada KB. Crossing the barrier: treatment of brain tumors using nanochain particles. *Wiley Interdiscip Rev Nanomed Nanobiotechnol* (2016) 8(5):678–95. doi:10.1002/wnan.1387
105. Kim SS, Harford JB, Pirollo KF, Chang EH. Effective treatment of glioblastoma requires crossing the blood-brain barrier and targeting tumors including cancer stem cells: the promise of nanomedicine. *Biochem Biophys Res Commun* (2015) 468(3):485–9. doi:10.1016/j.bbrc.2015.06.137
106. Haley B, Frenkel E. Nanoparticles for drug delivery in cancer treatment. *Urol Oncol* (2008) 26(1):57–64. doi:10.1016/j.urolonc.2007.03.015
107. Jeong Y, Kim ST, Jiang Y, Duncan B, Kim CS, Saha K, et al. Nanoparticle-dendrimer hybrid nanocapsules for therapeutic delivery. *Nanomedicine (Lond)* (2016) 11(12):1571–8. doi:10.2217/nnm-2016-0034
108. Spencer DS, Puranik AS, Peppas NA. Intelligent nanoparticles for advanced drug delivery in cancer treatment. *Curr Opin Chem Eng* (2015) 7:84–92. doi:10.1016/j.coche.2014.12.003
109. Muller BG, Leuenberger H, Kissel T. Albumin nanospheres as carriers for passive drug targeting: an optimized manufacturing technique. *Pharm Res* (1996) 13(1):32–7. doi:10.1023/A:1016064930502
110. Elzoghby AO, Samy WM, Elgindy NA. Albumin-based nanoparticles as potential controlled release drug delivery systems. *J Control Release* (2012) 157(2):168–82. doi:10.1016/j.jconrel.2011.07.031
111. Altintas I, Heukers R, van der Meel R, Lacombe M, Amidi M, van Bergen En Henegouwen PM, et al. Nanobody-albumin nanoparticles (NANAPs) for the delivery of a multikinase inhibitor 17864 to EGFR overexpressing tumor cells. *J Control Release* (2013) 165(2):110–8. doi:10.1016/j.jconrel.2012.11.007
112. Waehler R, Russell SJ, Curiel DT. Engineering targeted viral vectors for gene therapy. *Nat Rev Genet* (2007) 8(8):573–87. doi:10.1038/nrg2141
113. Frecha C, Szecsi J, Cosset FL, Verhoeyen E. Strategies for targeting lentiviral vectors. *Curr Gene Ther* (2008) 8(6):449–60. doi:10.2174/156652308786848003
114. Escors D, Breckpot K. Lentiviral vectors in gene therapy: their current status and future potential. *Arch Immunol Ther Exp (Warsz)* (2010) 58(2):107–19. doi:10.1007/s00005-010-0063-4

115. Dropulic B. Lentiviral vectors: their molecular design, safety, and use in laboratory and preclinical research. *Hum Gene Ther* (2011) 22(6):649–57. doi:10.1089/hum.2011.058
116. Goyvaerts C, De Groeve K, Dingemans J, Van Lint S, Robays L, Heirman C, et al. Development of the nanobody display technology to target lentiviral vectors to antigen-presenting cells. *Gene Ther* (2012) 19(12):1133–40. doi:10.1038/gt.2011.206
117. Goyvaerts C, Kurt de G, Van Lint S, Heirman C, Van Ginderachter JA, De Baetselier P, et al. Immunogenicity of targeted lentivectors. *Oncotarget* (2014) 5(3):704–15. doi:10.18632/oncotarget.1680
118. Liechtenstein T, Perez-Janices N, Bricogne C, Lanna A, Dufait I, Goyvaerts C, et al. Immune modulation by genetic modification of dendritic cells with lentiviral vectors. *Virus Res* (2013) 176(1–2):1–15. doi:10.1016/j.virusres.2013.05.007
119. Goyvaerts C, Breckpot K. Pros and cons of antigen-presenting cell targeted tumor vaccines. *J Immunol Res* (2015) 2015:785634. doi:10.1155/2015/785634
120. Goyvaerts C, Dingemans J, De Groeve K, Heirman C, Van Gulck E, Vanham G, et al. Targeting of human antigen-presenting cell subsets. *J Virol* (2013) 87(20):11304–8. doi:10.1128/JVI.01498-13
121. Goyvaerts C, Broos K, Escors D, Heirman C, Raes G, De Baetselier P, et al. The transduction pattern of IL-12-encoding lentiviral vectors shapes the immunological outcome. *Eur J Immunol* (2015) 45(12):3351–61. doi:10.1002/eji.201545559
122. Lo AS, Zhu Q, Marasco WA. Intracellular antibodies (intrabodies) and their therapeutic potential. *Handb Exp Pharmacol* (2008) 181:343–73. doi:10.1007/978-3-540-73259-4_15
123. Kontermann RE. Intrabodies as therapeutic agents. *Methods* (2004) 34(2):163–70. doi:10.1016/j.ymeth.2004.04.002
124. Cornelis GR, Wolf-Watz H. The *Yersinia* Yop virulon: a bacterial system for subverting eukaryotic cells. *Mol Microbiol* (1997) 23(5):861–7. doi:10.1046/j.1365-2958.1997.2731623.x
125. Blanco-Toribio A, Muyldermans S, Frankel G, Fernandez LA. Direct injection of functional single-domain antibodies from *E. coli* into human cells. *PLoS One* (2010) 5(12):e15227. doi:10.1371/journal.pone.0015227
126. Ittig SJ, Schmutz C, Kasper CA, Amstutz M, Schmidt A, Sauteur L, et al. A bacterial type III secretion-based protein delivery tool for broad applications in cell biology. *J Cell Biol* (2015) 211(4):913–31. doi:10.1083/jcb.201502074
127. Van Mellaert L, Barbe S, Anne J. *Clostridium* spores as anti-tumour agents. *Trends Microbiol* (2006) 14(4):190–6. doi:10.1016/j.tim.2006.02.002
128. Liu SC, Minton NP, Giaccia AJ, Brown JM. Anticancer efficacy of systemically delivered anaerobic bacteria as gene therapy vectors targeting tumor hypoxia/necrosis. *Gene Ther* (2002) 9(4):291–6. doi:10.1038/sj.gt.3301659
129. Theys J, Pennington O, Dubois L, Anlezark G, Vaughan T, Mengesha A, et al. Repeated cycles of *Clostridium*-directed enzyme prodrug therapy result in sustained antitumour effects in vivo. *Br J Cancer* (2006) 95(9):1212–9. doi:10.1038/sj.bjc.6603367
130. Dang LH, Bettegowda C, Huso DL, Kinzler KW, Vogelstein B. Combination bacteriolytic therapy for the treatment of experimental tumors. *Proc Natl Acad Sci U S A* (2001) 98(26):15155–60. doi:10.1073/pnas.251543698
131. Bettegowda C, Dang LH, Abrams R, Huso DL, Dillehay L, Cheong I, et al. Overcoming the hypoxic barrier to radiation therapy with anaerobic bacteria. *Proc Natl Acad Sci U S A* (2003) 100(25):15083–8. doi:10.1073/pnas.2036598100
132. Dang LH, Bettegowda C, Agrawal N, Cheong I, Huso D, Frost P, et al. Targeting vascular and avascular compartments of tumors with *C. novyi*-NT and anti-microtubule agents. *Cancer Biol Ther* (2004) 3(3):326–37. doi:10.4161/cbt.3.3.704
133. Groot AJ, Mengesha A, van der Wall E, van Diest PJ, Theys J, Vooijs M. Functional antibodies produced by oncolytic clostridia. *Biochem Biophys Res Commun* (2007) 364(4):985–9. doi:10.1016/j.bbrc.2007.10.126
134. Chakravarty R, Goel S, Cai W. Nanobody: the "magic bullet" for molecular imaging? *Theranostics* (2014) 4(4):386–98. doi:10.7150/thno.8006
135. Hilderbrand SA, Weissleder R. Near-infrared fluorescence: application to in vivo molecular imaging. *Curr Opin Chem Biol* (2010) 14(1):71–9. doi:10.1016/j.cbpa.2009.09.029
136. Capala J, Bouchelouche K. Molecular imaging of HER2-positive breast cancer: a step toward an individualized 'image and treat' strategy. *Curr Opin Oncol* (2010) 22(6):559–66. doi:10.1097/CCO.0b013e32833f8c3a
137. Levy C, Verhoeyen E, Cosset FL. Surface engineering of lentiviral vectors for gene transfer into gene therapy target cells. *Curr Opin Pharmacol* (2015) 24:79–85. doi:10.1016/j.coph.2015.08.003
138. Gainkam LO, Caveliers V, Devoogdt N, Vanhove C, Xavier C, Boerman O, et al. Localization, mechanism and reduction of renal retention of technetium-99m labeled epidermal growth factor receptor-specific nanobody in mice. *Contrast Media Mol Imaging* (2011) 6(2):85–92. doi:10.1002/cmmi.408
139. D'Huyvetter M, Aerts A, Xavier C, Vaneycken I, Devoogdt N, Gijs M, et al. Development of 177Lu-nanobodies for radioimmunotherapy of HER2-positive breast cancer: evaluation of different bifunctional chelators. *Contrast Media Mol Imaging* (2012) 7(2):254–64. doi:10.1002/cmmi.491
140. Vaneycken I, Devoogdt N, Van Gassen N, Vincke C, Xavier C, Wernery U, et al. Preclinical screening of anti-HER2 nanobodies for molecular imaging of breast cancer. *FASEB J* (2011) 25(7):2433–46. doi:10.1096/fj.10-180331
141. Broisat A, Hernot S, Toczek J, De Vos J, Riou LM, Martin S, et al. Nanobodies targeting mouse/human VCAM1 for the nuclear imaging of atherosclerotic lesions. *Circ Res* (2012) 110(7):927–37. doi:10.1161/CIRCRESAHA.112.265140
142. Zarschler K, Prapainop K, Mahon E, Rocks L, Bramini M, Kelly PM, et al. Diagnostic nanoparticle targeting of the EGF-receptor in complex biological conditions using single-domain antibodies. *Nanoscale* (2014) 6(11):6046–56. doi:10.1039/c4nr00595c
143. Gainkam LO, Keyaerts M, Caveliers V, Devoogdt N, Vanhove C, Van Grunsven L, et al. Correlation between epidermal growth factor receptor-specific nanobody uptake and tumor burden: a tool for noninvasive monitoring of tumor response to therapy. *Mol Imaging Biol* (2011) 13(5):940–8. doi:10.1007/s11307-010-0428-4
144. D'Huyvetter M, Vincke C, Xavier C, Aerts A, Impens N, Baatout S, et al. Targeted radionuclide therapy with A 177Lu-labeled anti-HER2 nanobody. *Theranostics* (2014) 4(7):708–20. doi:10.7150/thno.8156
145. Ntziachristos V, Bremer C, Weissleder R. Fluorescence imaging with near-infrared light: new technological advances that enable in vivo molecular imaging. *Eur Radiol* (2003) 13(1):195–208. doi:10.1007/s00330-002-1524-x
146. Solomon M, Liu Y, Berezin MY, Achilefu S. Optical imaging in cancer research: basic principles, tumor detection, and therapeutic monitoring. *Med Princ Pract* (2011) 20(5):397–415. doi:10.1159/000327655
147. Kijanka MM, van Brussel AS, van der Wall E, Mali WP, van Diest PJ, van Bergen En Henegouwen PM, et al. Optical imaging of pre-invasive breast cancer with a combination of VHHs targeting CAIX and HER2 increases contrast and facilitates tumour characterization. *EJNMMI Res* (2016) 6(1):14. doi:10.1186/s13550-016-0166-y
148. Stride E, Saffari N. Microbubble ultrasound contrast agents: a review. *Proc Inst Mech Eng H* (2003) 217(6):429–47. doi:10.1243/09544110360729072
149. Schmidt MM, Wittrup KD. A modeling analysis of the effects of molecular size and binding affinity on tumor targeting. *Mol Cancer Ther* (2009) 8(10):2861–71. doi:10.1158/1535-7163.MCT-09-0195
150. Abby SS, Cury J, Guglielmini J, Neron B, Touchon M, Rocha EP. Identification of protein secretion systems in bacterial genomes. *Sci Rep* (2016) 6:23080. doi:10.1038/srep23080
151. Hachani A, Wood TE, Filloux A. Type VI secretion and anti-host effectors. *Curr Opin Microbiol* (2016) 29:81–93. doi:10.1016/j.mib.2015.11.006

Conflict of Interest Statement: The authors declare that the research was conducted in the absence of any commercial or financial relationships that could be construed as a potential conflict of interest.

frontiers in Immunology

PERSPECTIVE
published: 12 October 2017
doi: 10.3389/fimmu.2017.01287

Antibody or Antibody Fragments: Implications for Molecular Imaging and Targeted Therapy of Solid Tumors

*Katerina T. Xenaki[1], Sabrina Oliveira[1,2] and Paul M. P. van Bergen en Henegouwen[1]**

[1] Division of Cell Biology, Science Faculty, Department of Biology, Utrecht University, Utrecht, Netherlands, [2] Pharmaceutics, Department of Pharmaceutical Sciences, Utrecht Institute of Pharmaceutical Sciences, Utrecht University, Utrecht, Netherlands

The use of antibody-based therapeutics has proven very promising for clinical applications in cancer patients, with multiple examples of antibodies and antibody–drug conjugates successfully applied for the treatment of solid tumors and lymphomas. Given reported recurrence rates, improvements are clearly still necessary. A major factor limiting the efficacy of antibody-targeted cancer therapies may be the incomplete penetration of the antibody or antibody–drug conjugate into the tumor. Incomplete tumor penetration also affects the outcome of molecular imaging, when using such targeting agents. From the injection site until they arrive inside the tumor, targeting molecules are faced with several barriers that impact intratumoral distribution. The primary means of antibody transport inside tumors is based on diffusion. The diffusive penetration inside the tumor is influenced by both antibody properties, such as size and binding affinity, as well as tumor properties, such as microenvironment, vascularization, and targeted antigen availability. Engineering smaller antibody fragments has shown to improve the rate of tumor uptake and intratumoral distribution. However, it is often accompanied by more rapid clearance from the body and in several cases also by inherent destabilization and reduction of the binding affinity of the antibody. In this perspective, we discuss different cancer targeting approaches based on antibodies or their fragments. We carefully consider how their size and binding properties influence their intratumoral uptake and distribution, and how this may affect cancer imaging and therapy of solid tumors.

Keywords: molecular imaging, cancer therapy, antibody, antibody fragments, single-domain antibodies, nanobody

OPEN ACCESS

Edited by:
Kevin A. Henry, National Research Council Canada, Canada

Reviewed by:
Jan Gettemans, Ghent University, Belgium
Peter Timmerman, Pepscan, Netherlands

****Correspondence:***
Paul M. P. van Bergen en Henegouwen
p.vanbergen@uu.nl

Specialty section:
This article was submitted to Vaccines and Molecular Therapeutics, a section of the journal Frontiers in Immunology

Received: *30 June 2017*
Accepted: *25 September 2017*
Published: *12 October 2017*

Citation:
Xenaki KT, Oliveira S and van Bergen en Henegouwen PMP (2017) Antibody or Antibody Fragments: Implications for Molecular Imaging and Targeted Therapy of Solid Tumors. Front. Immunol. 8:1287. doi: 10.3389/fimmu.2017.01287

INTRODUCTION

Selectivity for tumor over healthy tissue is of utmost importance when it comes to successful diagnosis and treatment of cancer. Over the last several decades, great progress has been made in the development of novel targeting molecules. Traditionally, antibodies directed against antigens overexpressed in tumors are the most commonly used targeting molecules. The development of monoclonal antibody (mAb) technology together with biotechnological advances in antibody engineering has established the use of mAbs in the field of cancer (1, 2). Despite their wide success, antibody-based treatment of many solid tumors remains challenging. In most of these cases, poor efficacy is linked

to non-homogeneous distribution of the mAb-based agent inside the tumor. This can subsequently result in an untargeted subpopulation of cancer cells, potentially leading to tumor relapse (3, 4). Both tumor-related factors, such as tumor microenvironment and architecture, as well as antibody characteristics contribute to this heterogeneous targeting (5). The rapidly growing field of antibody engineering has exploited the naturally occurring immunoglobulins to develop different functional antibody fragments. Modifying antibody features such as molecular size, valency, binding affinity, and pharmacokinetics allows for the development of antibody fragments with tailor-made properties for a variety of clinical applications (6, 7). A number of antibody fragments have already entered clinical trials (8) with antigen-binding fragments (Fab, ~50 kDa) and single-chain variable fragments (scFv, ~28 kDa) accounting for most of them. In the last 20–25 years, there has been a growing interest in single-domain antibodies (sdAbs) or nanobodies, the smallest naturally occurring antigen-binding fragment, consisting of the variable domain of the heavy-chain antibodies found in camelids (VHH, ~15 kDa). Their high-binding affinity, ease of production, low immunogenicity, and high stability make them a very attractive alternative to employ for targeting solid tumors. Variation in molecular size and binding properties among antibody fragments is considered to possess a central role in the intratumoral distribution of targeting molecules. In the present perspective, we aim to describe potential implications of molecular size and binding properties on tumor uptake and retention of antibody-based tracers used in molecular imaging or antibody-based therapy of solid tumors.

FROM SITE OF INJECTION TO TUMOR SITE

The most common route of administration of a therapeutic antibody molecule is by intravenous injection. After entering the bloodstream, it can reach tissues throughout the body *via* blood circulation. Antibody molecules can circulate many times before they successfully extravasate at the tumor site (9). There, after they have crossed the vessel wall, they need to distribute through interstitial space and finally reach their target inside the tumor (**Figure 1**). Once in the tumor interstitium, molecules need to diffuse through the extracellular matrix (ECM) to reach their targets on tumor cells, where binding can take place. Their diffusion deeper inside the tumor mass largely depends on their size and antibody–antigen-binding kinetics (clearance modulus) as well as on their endocytic uptake and catabolism inside the tumor cells (Thiele modulus) (10). In addition, systemic clearance of the administered molecules lowers their concentration. Consequently, because this concentration gradient is the driving force for diffusion into the tumor, tumor accumulation is also decreased (4, 11, 12).

MOLECULAR SIZE AND VASCULAR PERMEABILITY

After administration, the targeting antibody/antibody fragments need to cross the vascular wall of the tumor blood vessels, in order to reach the tumor cells. Properties of both the targeting macromolecule (e.g., size, shape, and charge) and the vessel wall

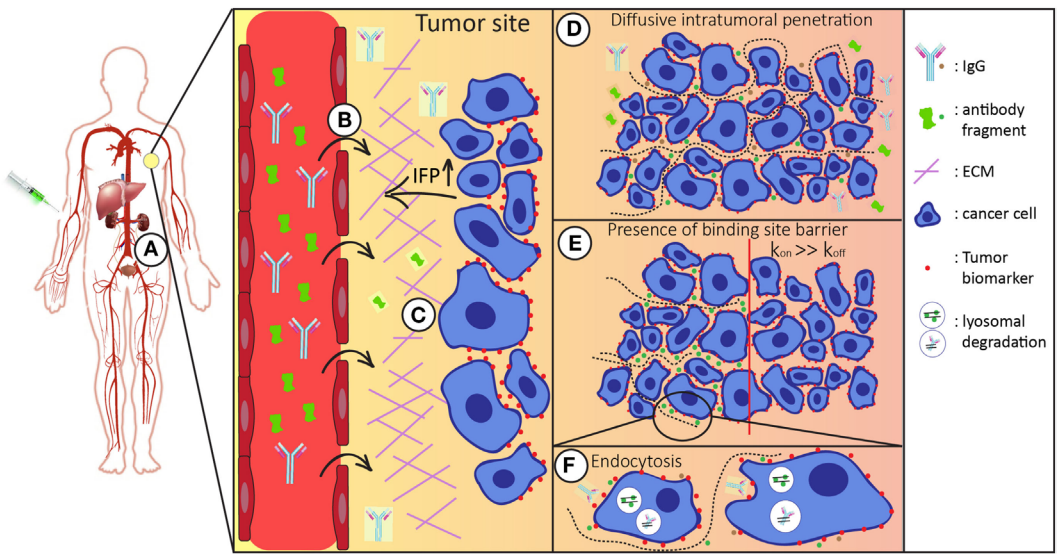

FIGURE 1 | Schematic representation of the route of the antibody/antibody fragment after administration. After intravenous administration the injected antibodies/antibody fragments **(A)** enter the blood stream and circulate throughout the whole body. Both the size and binding properties of the molecule used influences tumor targeting in various ways. **(B)** It is necessary that antibodies/antibody fragments effectively extravasate into the tumor interstitium. In general, the enhanced permeability and retention (EPR) effect favors tumor accumulation of larger molecules. **(C)** In the tumor interstitium, molecules travel through tumor extracellular matrix (ECM) to reach tumor cells. Smaller molecules diffuse faster in the more densely packed ECM. **(D)** For tumor retention, the antibodies/antibody fragments should have sufficient affinity for their target molecule on the surface of the tumor cells. **(E)** Binding site barrier: molecules with high affinities have restricted penetration inside the tumor mass, which is more apparent for larger molecules. **(F)** Upon binding, antibodies are endocytosed and degraded in lysosomes. Cellular catabolism reduces the local concentration, which is the driving force of diffusive transport. Systemic clearance (*via* liver and/or kidneys) reduces the overall concentration of the administered molecules, thereby affecting intratumoral distribution.

(e.g., pore size) can influence vascular permeability [reviewed in Ref. (13)]. Mathematical modeling, using a two-pore model of the capillary wall, clearly showed that there is an inverse correlation between the size of molecules (indicated by the molecular radius) and vascular permeability (14). Experimental data measuring the vascular permeability of molecules with different molecular weights in human colon adenocarcinoma xenografts are in agreement with this prediction (15). Tumor vasculature has significant differences to that of healthy tissues. Hypervascularization and increased vascular permeability, with vessels having abnormal architecture due to the higher cell proliferation rate, as well as wider fenestrations (16) are features that promote tumor accumulation of larger macromolecules. In addition to irregular blood vasculature, there is often a lack of a proper lymphatic network inside tumors. This results in inefficient lymphatic drainage allowing for better retention of macromolecules in tumors (17, 18). This enhanced permeability and retention (EPR) effect is reported to occur in the majority of solid tumors (19). The EPR effect facilitates the accumulation of non-targeted macromolecules larger than ~40 kDa in tumors, giving an advantage to the use of larger molecules. This molecular size dependence of the EPR effect is directly linked to the systemic clearance (discussed in detail below) of the injected probes. Macromolecules larger than 40 kDa manage to circumvent renal excretion resulting in extended circulation time, increasing the chances of extravasation in the tumor interstitium (20, 21). Despite this contribution to the targeting process, the EPR effect, when present, does not guarantee sufficient and specific tumor penetration that is crucial for therapeutic applications.

Besides the improved retention at the tumor, poor lymphatic drainage also increases the interstitial fluid pressure (IFP) (17, 18). As a result, the transport of molecules into the tumor interstitium is largely dependent on diffusion rather than advective transport across the vessel wall (22). Diffusion of larger molecules is much slower, when compared to pressure-based advective transport of molecules. In cases where IFP exceeds the vascular fluid pressure, intravasation back to the blood circulation can even occur. Together, both increased IFP and abnormal tumor vasculature (leading to non-homogeneous distribution of larger molecules within the tumor) counteract the benefits of the EPR effect.

MOLECULAR SIZE AND DIFFUSIVITY

The next barrier that antibodies/antibody fragments face after successful extravasation is the presence of the ECM that surrounds tumor cells. In principle, transport through ECM is based on both advective movement and diffusion, which are collectively termed convection. As a result of the elevated IFP, the pressure gradient in the tumor is considered negligible, and therefore, diffusion along a concentration gradient is the main driving force for the transport of molecules in the intercellular space. The tumor interstitium contains ECM, the composition of which differs between healthy and tumor tissues and also among tumors. The tumor ECM is often characterized by a more densely packed network of highly aligned collagen fibers, which evidently contributes to transport resistance. In both *in vivo* tumors and in multicellular spheroids, the diffusion coefficients of IgGs were lower when collagen concentration was increased (23). Next to collagen concentration, macromolecular hydrodynamic radius is inversely correlated to the diffusion coefficient. Experimental data using IgGs and dextrans of varying sizes (4–70 kDa) show decreased diffusivity when their size is larger (24, 25), which is in agreement with the Stokes–Einstein equation.

Besides the ECM composition, the arrangement of the tumor cells also contributes to geometric tortuosity, which can hinder the diffusion of macromolecules. As can be expected, diffusion rates through intercellular or interfibrillar space is directly related to the size of the diffusing molecules. Larger molecules might be restricted from diffusing within narrower tortuous intercellular paths in the same way that they are through compact collagen bundles (26, 27). Inhibition of the adherens junction protein E-cadherin (and therefore disruption of cell–cell junctions) resulted in improved penetration and cytotoxicity of an immunotoxin used in a 3D cell culture system of tumor cells (28). This is in agreement with the fact that cell density influences the distribution of anticancer agents. It has been shown that in solid tumors, consisting of more loosely packed cells, penetration of anticancer agents was faster, compared to more tightly packed cells (29).

EFFECT OF MOLECULAR SIZE AND BINDING AFFINITY ON DIFFUSION AND TUMOR RETENTION

An essential property of targeting molecules is their specific interaction with a cell-surface molecule on tumor cells which they bind to with high affinity. However, such binding may also contribute to heterogeneity of intratumoral distribution of antibodies. The "binding site barrier" effect, as suggested by Fujimori and colleagues, proposes that higher affinity antibodies might show restricted penetration into the tumor mass, as a result of their binding to surface located receptors (30). As seen also in studies using multicellular tumor spheroids (MTS), antibodies diffuse toward the center of the MTS covering cell layer after cell layer, which can be described as a shrinking core model. At the same time, they are able to bind to the cell surface, hindering further diffusion of unbound antibodies, therefore delaying penetration into the MTS. Diffusion into the MTS only occurs if antibody concentration is not limiting and is sufficient for saturated binding (10); thus, after all antigens have an antibody bound there would still be free molecules available to diffuse toward the center. Otherwise, when the antibody concentration is not sufficient, there will be incomplete coverage of the MTS/tumor. It has been experimentally proven, both *in vivo* and *in vitro*, that improving the affinity of the targeting molecule can result in increased tumor retention. Using anti-HER2 scFvs differing only in their dissociation constants (k_{off}), Adams and colleagues demonstrated that there is a certain affinity threshold that needs to be met in order to achieve sufficient tumor retention. Even though the lower affinity scFv (K_D of 320 nM) showed better tumor retention than the non-binding negative control, it did not manage to achieve the high tumor accumulation levels

obtained with the higher affinity scFvs (K_D of 16 or 1 nM) (31). However, affinity enhancement is restricted to a certain range, as beyond that no further improvement in tumor retention was documented. Mathematical modeling has shown that this affinity threshold is size dependent, with smaller molecules (~10 kDa) requiring higher affinities (0.1–10 nM) in order to reach maximum tumor uptake (14). High-affinity scFvs were at the same time shown to have less homogeneous distribution compared to ones with lower affinity (32). Similar results were obtained with scFvs targeting carcinoembryonic antigen in MTS studies, with lower affinity scFvs showing better homogeneity in their distribution (10), which is in agreement with computational modeling of antibody and antibody fragment distribution (5, 33).

One could speculate that the binding site barrier effect is more apparent when using larger molecules compared to smaller ones, provided they have similarly high affinities. In this case, there are greater chances of having local molecular crowding when using a bigger molecule consequently resulting in delay of diffusion. However, in the case of smaller fragments, one needs to make sure that they demonstrate a sufficiently high affinity (14). Otherwise, it is easier for them to diffuse back into vasculature and eventually be cleared from the system, compromising tumor retention. Other factors that may influence the binding site barrier effect are antibody catabolism by tumor cells and the dissociation kinetics (k_{off}) of the antibodies. In this respect, it can be expected that a bivalent antibody, with reduced dissociation will contribute more significantly to a binding site barrier effect than the monovalent fragments.

THE THIELE MODULUS AND SYSTEMIC CLEARANCE

As mentioned above, the driving force for diffusion of an antibody or antibody fragment through the vasculature and into the interstitial space of a solid tumor is the concentration gradient. This concentration can be compromised both inside the tumor (because of endocytic uptake followed by degradation within tumor cells) as well as outside the tumor (because of systemic elimination of the antibody). Antibody clearance is therefore of great importance for its distribution within the tumor, as lowering the available antibody concentration results in its decreased penetration into tumor tissue (11, 14). Intracellular degradation of the antibody largely depends on the internalization rate of the targeted tumor antigen, provided that this eventually results in the endocytosis of the targeting antibody and degradation in lysosomes. The Thiele modulus (φ^2), describing the ratio between internalization rate and diffusion/binding rates, determines whether the administered antibody successfully targets the whole tumor. Only when diffusion is faster than clearance ($\varphi^2 < 1$) will the moving antibody front successfully reach the core of the tumor.

Unlike endocytic catabolism, systemic clearance of the targeting molecule is dependent on its size or hydrodynamic radius. An increase in the molecular radius leads to a rapid decrease of the plasma clearance (14). In general, globular molecules smaller than ~40 kDa (hydrodynamic radii 2–6 nm) are rapidly removed from the body *via* renal filtration (34, 35). The larger IgG antibodies exhibit longer circulation times, with serum half-life of 2–3 weeks. This is due to their large hydrodynamic volume as well as to their interaction with the FcRn receptor. IgGs bound to the FcRn receptors on endothelial cells are internalized and recycled back to the cell surface (36). This prevents them from lysosomal degradation, prolonging their residence time in the circulation, with IgGs being detected to be present in the body for around 30 days after administration (37). Smaller antibody fragments exhibit shorter plasma half-lives not only because of their smaller size but also because of their inability to bind FcRn. Fab fragments, with a molecular weight of approximately 50 kDa, have been demonstrated to have a half-life of around 28 min (38); smaller scFv fragments, in the range of 30 kDa, have been shown to be cleared even faster, with plasma half-lives of only 10 min. Engineering of multivalent Fvs that results in tracers of larger size has proven to be efficient for the improvement of their half-lives (39, 40). Plasma half-life of a non-relevant radiolabeled nanobody has been calculated to be around 2 h (41), while targeting nanobodies are shown to be completely eliminated from the blood 24 h post-administration, with some levels still present mainly in the kidneys (42, 43). This short half-life of smaller antibody fragments is suggested to be beneficial, when they are used as radiolabeled tracers for imaging, to reduce the exposure of patients to ionizing radiations. Nanobodies have been shown to accumulate rapidly into tumors resulting in high tumor-to-background ratios already obtained 3–5 h postinjection.

When intended for use in therapeutic applications, half-life extension should be considered. Most of the strategies used for half-life extension of antibody fragments exploit the long half-life of serum albumin (36). Fusion to albumin targeting nanobodies (44–46) or even albumin itself (47) has proven to be successful for the half-life extension of nanobodies and scFvs. As an alternative, and with the intention to keep the size of the targeting moiety the smallest possible, fusion to albumin-binding peptides (48) or albumin-binding domains of streptococcal proteins have been used (49, 50).

CONCLUDING REMARKS

Antibodies or larger antibody fragments show sufficient tumor uptake, regardless of their binding affinity for tumor-associated antigens, due to their longer circulation time. Their longer half-life is advantageous for therapeutic applications, as it grants them a better chance to accumulate at the tumor. At the tumor site, a longer half-life allows for a longer time for the therapeutic drug to act on the tumor cells, increasing the therapeutic index. Because of their long half-lives in combination with the EPR effect, tumor accumulation of even non-targeted macromolecular antitumor agents can be achieved. However, this comes with the cost of an uneven intratumoral distribution of such large molecules, which could potentially result in incomplete tumor cell targeting followed by tumor recurrence. Smaller antibody fragments, such as Fabs, scFvs, and nanobodies, have a more rapid tumor accumulation because of their better diffusion into the tumor as a result of their small size and different binding properties (i.e., valency), which reduce the binding site barrier effect.

Similarly, non-natural binding scaffolds, such as DARpins [~14 kDa; reviewed in Ref. (51)], affibodies [~58 aa residues, 6 kDa; reviewed in Ref. (52, 53)], and non-immunoglobulin based peptides [reviewed in Ref. (54)], having even smaller sizes than nanobodies, are being successfully employed as targeting agents. As such, small antibody fragments and scaffolds, with high binding affinities, are ideal to use as imaging tracers. High tumor-to-background ratios are achieved at earlier time points and as a result of their rather quick clearance the radioactive burden of the patient in case of nuclear imaging is reduced.

When small targeting proteins are to be employed as therapeutic agents, modifications in order to improve their half-life and binding affinity are required. Smaller molecules engineered to have a longer half-life would have longer residence time in the patient and likely a more homogeneous distribution throughout the tumor. In addition, antibody fragments allow the relatively easy generation of multivalent or multispecific molecules with different binding kinetics or specificities [reviewed in Ref. (55, 56)]. This can be accomplished by genetic fusion of the respective binding domains interspaced with artificial linkers (40, 45, 57, 58). In conclusion, parameters such as affinity, valency, antigen density, antibody catabolism, and half-life extension should all be considered when choosing the appropriate antibody-based targeting agent to be used. When they have the right properties, smaller fragments can have a considerable advantage over larger ones.

AUTHOR CONTRIBUTIONS

KX prepared the manuscript, and SO and PH edited it.

ACKNOWLEDGMENTS

The authors wish to thank Irati Beltran Hernandez for helpful discussions. KX is supported by a grant from the Netherlands Organisation of Scientific Research (NWO) grant number 731 015.201.

REFERENCES

1. Strebhardt K, Ullrich A. Paul Ehrlich's magic bullet concept: 100 years of progress. *Nat Rev Cancer* (2008) 8:473–80. doi:10.1038/nrc2394
2. Scott AM, Wolchok JD, Old LJ. Antibody therapy of cancer. *Nat Rev Cancer* (2012) 12:278–87. doi:10.1038/nrc3236
3. Jain RK. Delivery of molecular medicine to solid tumors: lessons from in vivo imaging of gene expression and function. *J Control Release* (2001) 74:7–25. doi:10.1016/S0168-3659(01)00306-6
4. Stylianopoulos T, Jain RK. Design considerations for nanotherapeutics in oncology. *Nanomedicine* (2015) 11:1893–907. doi:10.1016/j.nano.2015.07.015
5. Thurber GM, Schmidt MM, Wittrup KD. Antibody tumor penetration: transport opposed by systemic and antigen-mediated clearance. *Adv Drug Deliv Rev* (2008) 60:1421–34. doi:10.1016/j.addr.2008.04.012
6. Jain M, Venkatraman G, Batra SK. Optimization of radioimmunotherapy of solid tumors: biological impediments and their modulation. *Clin Cancer Res* (2007) 13:1374–82. doi:10.1158/1078-0432.CCR-06-2436
7. Holliger P, Hudson PJ. Engineered antibody fragments and the rise of single domains. *Nat Biotechnol* (2005) 23:1126–36. doi:10.1038/nbt1142
8. Nelson AL, Reichert JM. Development trends for therapeutic antibody fragments. *Nat Biotechnol* (2009) 27:331–7. doi:10.1038/nbt0409-331
9. Nichols JW, Bae YH. Odyssey of a cancer nanoparticle: from injection site to site of action. *Nano Today* (2012) 7:606–18. doi:10.1016/j.nantod.2012.10.010
10. Thurber GM, Wittrup KD. Quantitative spatiotemporal analysis of antibody fragment diffusion and endocytic consumption in tumor spheroids. *Cancer Res* (2008) 68:3334–41. doi:10.1158/0008-5472.CAN-07-3018
11. Thurber GM, Schmidt MM, Wittrup KD. Factors determining antibody distribution in tumors. *Trends Pharmacol Sci* (2008) 29:57–61. doi:10.1016/j.tips.2007.11.004
12. Minchinton AI, Tannock IF. Drug penetration in solid tumours. *Nat Rev Cancer* (2006) 6:583–92. doi:10.1038/nrc1893
13. Michel CC, Curry FE. Microvascular permeability. *Physiol Rev* (1999) 79:703–61.
14. Schmidt MM, Wittrup KD. A modeling analysis of the effects of molecular size and binding affinity on tumor targeting. *Mol Cancer Ther* (2009) 8:2861–71. doi:10.1158/1535-7163.MCT-09-0195
15. Yuan F, Dellian M, Fukumura D, Leunig M, Berk DA, Torchilin VP, et al. Vascular permeability in a human tumor xenograft: molecular size dependence and cutoff size. *Cancer Res* (1995) 55:3752–6.
16. Hobbs SK, Monsky WL, Yuan F, Roberts WG, Griffith L, Torchilin VP, et al. Regulation of transport pathways in tumor vessels: role of tumor type and microenvironment. *Proc Natl Acad Sci U S A* (1998) 95:4607–12. doi:10.1073/pnas.95.8.4607
17. Carmeliet P, Jain RK. Principles and mechanisms of vessel normalization for cancer and other angiogenic diseases. *Nat Rev Drug Discov* (2011) 10:417–27. doi:10.1038/nrd3455
18. Heldin C-H, Rubin K, Pietras K, Östman A. High interstitial fluid pressure—an obstacle in cancer therapy. *Nat Rev Cancer* (2004) 4:806–13. doi:10.1038/nrc1456
19. Matsumura Y, Maeda HA. A new concept for macromolecular therapeutics in cancer-chemotherapy – mechanism of tumoritropic accumulation of proteins and the antitumor agent Smancs. *Cancer Res* (1986) 46:6387–92.
20. Nakamura H, Jun F, Maeda H. Development of next-generation macromolecular drugs based on the EPR effect: challenges and pitfalls. *Expert Opin Drug Deliv* (2015) 12:53–64. doi:10.1517/17425247.2014.955011
21. Maeda H. Toward a full understanding of the EPR effect in primary and metastatic tumors as well as issues related to its heterogeneity. *Adv Drug Deliv Rev* (2015) 91:3–6. doi:10.1016/j.addr.2015.01.002
22. Jain RK, Stylianopoulos T. Delivering nanomedicine to solid tumors. *Nat Rev Clin Oncol* (2010) 7:653–64. doi:10.1038/nrclinonc.2010.139
23. de L Davies C, Berk DA, Pluen A, Jain RK. Comparison of IgG diffusion and extracellular matrix composition in rhabdomyosarcomas grown in mice versus in vitro as spheroids reveals the role of host stromal cells. *Br J Cancer* (2002) 86:1639–44. doi:10.1038/sj.bjc.6600270
24. Netti PA, Berk DA, Swartz MA, Grodzinsky AJ, Jain RK. Role of extracellular matrix assembly in interstitial transport in solid tumors. *Cancer Res* (2000) 60:2497–503.
25. Galgoczy R, Pastor I, Colom A, Giménez A, Mas F, Alcaraz J. A spectrophotometer-based diffusivity assay reveals that diffusion hindrance of small molecules in extracellular matrix gels used in 3D cultures is dominated by viscous effects. *Colloids Surf B Biointerfaces* (2014) 120:200–7. doi:10.1016/j.colsurfb.2014.05.017
26. Pluen A, Boucher Y, Ramanujan S, McKee TD, Gohongi T, di Tomaso E, et al. Role of tumor-host interactions in interstitial diffusion of macromolecules: cranial vs. subcutaneous tumors. *Proc Natl Acad Sci U S A* (2001) 98:4628–33. doi:10.1073/pnas.081626898
27. Ramanujan S, Pluen A, McKee TD, Brown EB, Boucher Y, Jain RK. Diffusion and convection in collagen gels: implications for transport in the tumor interstitium. *Biophys J* (2002) 83:1650–60. doi:10.1016/S0006-3495(02)73933-7
28. Xiang X, Phung Y, Feng M, Nagashima K, Zhang J, Courtney Broaddus V, et al. The development and characterization of a human mesothelioma in vitro 3D model to investigate immunotoxin therapy. *PLoS One* (2011) 6:e14640. doi:10.1371/journal.pone.0014640
29. Grantab RH, Tannock IF. Penetration of anticancer drugs through tumour tissue as a function of cellular packing density and interstitial fluid

pressure and its modification by bortezomib. *BMC Cancer* (2012) 12:214. doi:10.1186/1471-2407-12-214
30. Fujimori K, Covell DG, Fletcher JE, Weinstein JN. A modeling analysis of monoclonal antibody percolation through tumors: a binding-site barrier. *J Nucl Med* (1990) 31:1191–8.
31. Adams GP, Schier R, Marshall K, Wolf EJ, Mccall AM, Marks JD, et al. Increased affinity leads to improved selective tumor delivery of single-chain Fv antibodies. *Cancer Res* (1998) 58:485–90.
32. Adams GP, Schier R, McCall AM, Simmons HH, Horak EM, Alpaugh RK, et al. High affinity restricts the localization and tumor penetration of single-chain Fv antibody molecules. *Cancer Res* (2001) 61:4750–5. doi:10.1234/12345678
33. Graff CP, Wittrup KD. Theoretical analysis of antibody targeting of tumor spheroids: importance of dosage for penetration, and affinity for retention. *Cancer Res* (2003) 63:1288–96.
34. Longmire M, Choyke PL, Kobayashi H. Clearance properties of nano-sized particles and molecules as imaging agents: consideration and caveats. *Nanomedicine (Lond)* (2008) 3:703–17. doi:10.2217/17435889.3.5.703. Clearance
35. Choi HS, Liu W, Misra P, Tanaka E, Zimmer JP, Ipe BI, et al. Renal clearance of quantum dots. *Nat Biotechnol* (2007) 25:1165–70. doi:10.1038/nbt1340
36. Kontermann RE. Half-life extended biotherapeutics. *Expert Opin Biol Ther* (2016) 16:903–15. doi:10.1517/14712598.2016.1165661
37. Roopenian DC, Akilesh S. FcRn: the neonatal Fc receptor comes of age. *Nat Rev Immunol* (2007) 7:715–25. doi:10.1038/nri2155
38. Chapman AP, Antoniw P, Spitali M, West S, Stephens S, King DJ. Therapeutic antibody fragments with prolonged in vivo half-lives. *Nat Biotechnol* (1999) 17:780–3. doi:10.1038/11717
39. Adams GP, McCartney JE, Tai MS, Oppermann H, Huston JS, Stafford WF III, et al. Highly specific in vivo tumor targeting by monovalent and divalent forms of 741F8 anti-c-erbB-2 single-chain Fv. *Cancer Res* (1993) 53:4026–34.
40. Goel A, Colcher D, Baranowska-Kortylewiez J, Augustine S, Booth BJM, Pavlinkova G, et al. Genetically engineered tetravalent single-chain Fv of the pancarcinoma monoclonal antibody CC49: improved biodistribution and potential for therapeutic application. *Cancer Res* (2000) 60:6964–71.
41. Tchouate Gainkam LO, Caveliers V, Devoogdt N, Vanhove C, Xavier C, Boerman O, et al. Localization, mechanism and reduction of renal retention of technetium-99m labeled epidermal growth factor receptor-specific nanobody in mice. *Contrast Media Mol Imaging* (2011) 6:85–92. doi:10.1002/cmmi.408
42. Kijanka M, Warnders FJ, El Khattabi M, Lub-De Hooge M, Van Dam GM, Ntziachristos V, et al. Rapid optical imaging of human breast tumour xenografts using anti-HER2 VHHs site-directly conjugated to IRDye 800CW for image-guided surgery. *Eur J Nucl Med Mol Imaging* (2013) 40:1718–29. doi:10.1007/s00259-013-2471-2
43. Oliveira S, Van Dongen GAMS, Stigter-Van Walsum M, Roovers RC, Stam JC, Mali W, et al. Rapid visualization of human tumor xenografts through optical imaging with a near-infrared fluorescent anti-epidermal growth factor receptor nanobody. *Mol Imaging* (2012) 11:33–46. doi:10.2310/7290.2011.00025
44. Tijink BM, Laeremans T, Budde M, Stigter-van Walsum M, Dreier T, de Haard HJ, et al. Improved tumor targeting of anti-epidermal growth factor receptor nanobodies through albumin binding: taking advantage of modular nanobody technology. *Mol Cancer Ther* (2008) 7:2288–97. doi:10.1158/1535-7163.MCT-07-2384
45. Roovers RC, Vosjan MJWD, Laeremans T, El Khoulati R, De Bruin RCG, Ferguson KM, et al. A biparatopic anti-EGFR nanobody efficiently inhibits solid tumour growth. *Int J Cancer* (2011) 129:2013–24. doi:10.1002/ijc.26145
46. Hoefman S, Ottevaere I, Baumeister J, Sargentini-Maier M. Pre-clinical intravenous serum pharmacokinetics of albumin binding and non-half-life extended Nanobodies®. *Antibodies* (2015) 4:141–56. doi:10.3390/antib4030141
47. Andersen JT, Cameron J, Plumridge A, Evans L, Sleep D, Sandlie I. Single-chain variable fragment albumin fusions bind the neonatal Fc receptor (FcRn) in a species-dependent manner: implications for in vivo half-life evaluation of albumin fusion therapeutics. *J Biol Chem* (2013) 288:24277–85. doi:10.1074/jbc.M113.463000
48. Dennis MS, Jin H, Dugger D, Yang R, McFarland L, Ogasawara A, et al. Imaging tumors with an albumin-binding Fab, a novel tumor-targeting agent. *Cancer Res* (2007) 67:254–61. doi:10.1158/0008-5472.CAN-06-2531
49. Hopp J, Hornig N, Zettlitz KA, Schwarz A, Fuß N, Müller D, et al. The effects of affinity and valency of an albumin-binding domain (ABD) on the half-life of a single-chain diabody-ABD fusion protein. *Protein Eng Des Sel* (2010) 23:827–34. doi:10.1093/protein/gzq058
50. Cantante C, Lourenço S, Morais M, Leandro J, Gano L, Silva N, et al. Albumin-binding domain from *Streptococcus zooepidemicus* protein Zag as a novel strategy to improve the half-life of therapeutic proteins. *J Biotechnol* (2017) 253:23–33. doi:10.1016/j.jbiotec.2017.05.017
51. Plückthun A. Designed ankyrin repeat proteins (DARPins): binding proteins for research, diagnostics, and therapy. *Annu Rev Pharmacol Toxicol* (2015) 55:489–511. doi:10.1146/annurev-pharmtox-010611-134654
52. Nord K, Gunneriusson E, Ringdahl J, Ståhl S, Uhlén M, Nygren PA. Binding proteins selected from combinatorial libraries of an alpha-helical bacterial receptor domain. *Nat Biotechnol* (1997) 15:772–7. doi:10.1038/nm0798-822
53. Dong D, Xia G, Li Z, Li Z. Human serum albumin and HER2-binding affibody fusion proteins for targeted delivery of fatty acid-modified molecules and therapy. *Mol Pharm* (2016) 13:3370–80. doi:10.1021/acs.molpharmaceut.6b00265
54. Wang Y, Cheetham AG, Angacian G, Su H, Xie L, Cui H. Peptide–drug conjugates as effective prodrug strategies for targeted delivery. *Adv Drug Deliv Rev* (2017) 11(0–111):112–26. doi:10.1016/j.addr.2016.06.015
55. Spiess C, Zhai Q, Carter PJ. Alternative molecular formats and therapeutic applications for bispecific antibodies. *Mol Immunol* (2015) 67:95–106. doi:10.1016/j.molimm.2015.01.003
56. Lameris R, de Bruin RCG, Schneiders FL, van Bergen en Henegouwen PMP, Verheul HMW, de Gruijl TD, et al. Bispecific antibody platforms for cancer immunotherapy. *Crit Rev Oncol Hematol* (2014) 92:153–65. doi:10.1016/j.critrevonc.2014.08.003
57. Heukers R, Vermeulen JF, Fereidouni F, Bader AN, Voortman J, Roovers RC, et al. Endocytosis of EGFR requires its kinase activity and N-terminal transmembrane dimerization motif. *J Cell Sci* (2013) 126:4900–12. doi:10.1242/jcs.128611
58. Van Driel PBAA, Boonstra MC, Slooter MD, Heukers R, Stammes MA, Snoeks TJA, et al. EGFR targeted nanobody-photosensitizer conjugates for photodynamic therapy in a pre-clinical model of head and neck cancer. *J Control Release* (2016) 229:93–105. doi:10.1016/j.jconrel.2016.03.014

Conflict of Interest Statement: The authors declare that the authors KX and SO have no commercial or financial relationships that could be construed as a potential conflict of interest. PBH is shareholder of QVQ BV, Utrecht, the Netherlands.

frontiers in Immunology

REVIEW
published: 08 December 2017
doi: 10.3389/fimmu.2017.01746

Nanobodies As Novel Agents for Targeting Angiogenesis in Solid Cancers

*Roghaye Arezumand[1], Abbas Alibakhshi[2], Javad Ranjbari[2], Ali Ramazani[3] and Serge Muyldermans[4]**

[1] Department of Biotechnology and Molecular Science, School of Medicine, North Khorasan University of Medical Sciences, Bojnourd, Iran, [2] Department of Biotechnology, School of Advanced Technologies in Medicine, Shahid Beheshti University of Medical Sciences, Tehran, Iran, [3] Cancer Gene Therapy Research Center, Zanjan University of Medical Sciences, Zanjan, Iran, [4] Cellular and Molecular Immunology, Vrije Universiteit Brussel, Brussels, Belgium

Solid cancers are dependent on angiogenesis for sustenance. The FDA approval of Bevacizumab in 2004 inspired many scientists to develop more inhibitors of angiogenesis. Although several monoclonal antibodies (mAbs) are being administered to successfully combat various pathologies, the complexity and large size of mAbs seem to narrow the therapeutic applications. To improve the performance of cancer therapeutics, including those blocking tumor angiogenesis, attractive strategies such as miniaturization of the antibodies have been introduced. Nanobodies (Nbs), small single-domain antigen-binding antibody fragments, are becoming promising therapeutic and diagnostic proteins in oncology due to their favorable unique structural and functional properties. This review focuses on the potential and state of the art of Nbs to inhibit the angiogenic process for therapy and the use of labeled Nbs for non-invasive *in vivo* imaging of the tumors.

Keywords: angiogenesis, nanobody, monoclonal antibody, cancer therapy, vascular endothelial growth factor family

OPEN ACCESS

Edited by:
Colin Roger MacKenzie, National Research Council Canada (NRC-CNRC), Canada

Reviewed by:
Ian Richard Catchpole, GlaxoSmithKline, United Kingdom
Jamshid Tanha, National Research Council Canada (NRC-CNRC), Canada

****Correspondence:***
Serge Muyldermans
serge.muyldermans@vub.be

Specialty section:
This article was submitted to Vaccines and Molecular Therapeutics, a section of the journal Frontiers in Immunology

Received: *03 July 2017*
Accepted: *23 November 2017*
Published: *08 December 2017*

Citation:
Arezumand R, Alibakhshi A, Ranjbari J, Ramazani A and Muyldermans S (2017) Nanobodies As Novel Agents for Targeting Angiogenesis in Solid Cancers. Front. Immunol. 8:1746. doi: 10.3389/fimmu.2017.01746

INTRODUCTION

Chemotherapy, radiotherapy, and surgery are routine methods to eradicate tumor tissues; however, nowadays more efficient and less harmful methods are in sight. Carefully selected monoclonal antibodies (mAbs) have been shown to exert strong suppression of tumor growth. These effects are provoked by different strategies, such as a direct targeting of malignant cells, delivering cytotoxic moieties, modifying the host immune response, and retargeting the cellular immunity toward malignant cells (1, 2). Since proliferating cancer cells induce and form new blood vessels to meet their needs for nutrients, inhibition of blood vessel formation seems to be an attractive option for cancer therapy (3).

During the past decades, administration of mAbs as cancer therapeutics has increased steadily, and currently, approximately 350 mAbs have entered clinical trial programs and over 70 intact antibodies or fragments thereof received approval from FDA or EMEA for clinical applications (4). Although, the mouse hybridoma technique, developed in 1975, pioneered the identification of mAbs of defined specificity, this first generation of mAbs failed to fulfill its promises to produce therapeutics, mainly because the rodent origin of mAbs provoked severe immune responses in humans. Chimeric, humanized, and fully human mAbs were developed to remedy these immunogenicity problems and nearly all currently marketed antibodies belong to one of these types (5). Despite these improvements, the full potential of mAbs remains curtailed due to their large size, necessity to be produced in a multimeric format, high production and purification costs and their poor diffusion within tissues and the solid tumor (6). Intact functional mAbs are complex,

glycosylated proteins with a molecular mass of about 150 kDa. Moreover to be used as therapeutic proteins, they have to be produced and purified in large quantities under GMP conditions. In addition, the vast majority of the administered mAbs usually remains in the bloodstream, and despite having a high specificity for a particular tumor associated antigen, they fail to reach and to associate with their target outside the blood compartment (7).

The miniaturization of mAbs to smaller antigen-binding fragments (**Figure 1**) avoids many of the above shortcomings as these products overcome

i. the necessity of using complex expression systems,
ii. the poor diffusion within the solid tumor, and
iii. the nonspecific Fc-dependent immunologic responses.

In contrast to whole antibodies, microbial expression systems manage to produce functional antigen-binding fragments in high yields. These smaller antigen-binding fragments are produced successfully at an industrial scale in microbial systems (bacteria, yeasts, and fungi), providing access to a faster and larger production of a safer drug at a lower cost. So, antibody fragments including the antigen-binding fragment (Fab ~55 kDa), the single chain variable Fragment (scFv: 26–30 kDa), and single-domain antibody fragments (sdAb ~12–14 kDa) have been expressed from bacteria and yeasts for therapeutic purposes and are indeed being evaluated in clinical trials (8, 9).

The search for smaller antibody fragments eventually led to the development of engineered sdAbs consisting of the variable fragment (about 110 amino acids) of heavy or light chain immunoglobulin polypeptides. These sdAbs from human origin as engineered originally at Domantis (Cambridge, UK, now part of GlaxoSmithKline) may overcome immunogenicity issues and could be administered orally, by inhalation or topically in a gel or cream (10).

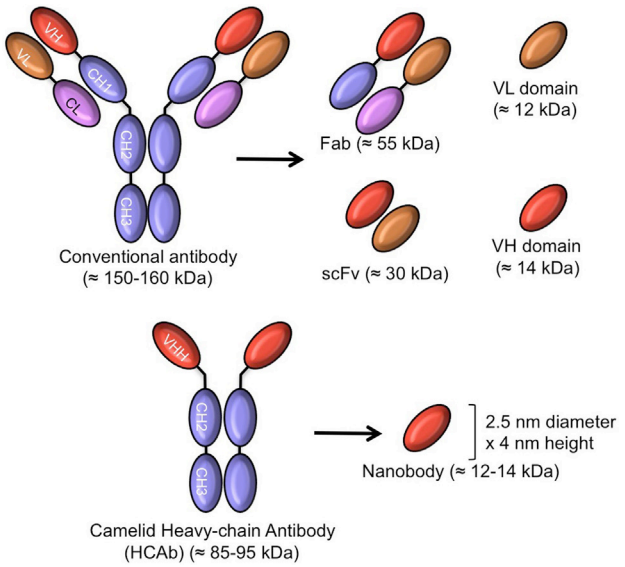

FIGURE 1 | Schematic representation of intact antibody and antibody-derived fragments of conventional and camelid heavy chain-only antibodies (HCAb). The molecular mass of all molecules is given in parentheses.

Remarkably, an alternative to human immunoglobulin to generate sdAbs was proposed from the serendipitous discovery of heavy chain-only antibodies (HCAb) in sera of camelids. These are naturally occurring, functional antibodies, devoid of light chains, and without the first constant domain, the CH1 (11). They recognize the antigen by virtue of the *v*ariable domain of the *h*eavy chain of *h*eavy chain-only antibodies (known as VHH). The recombinant VHH was later on also referred to as nanobody (Nb), because of its dimensions in the low nanometer scale (MW: 12–14 kDa) (12). The amino acid sequence of VHH (as occurring in camelids) is close to sequences of family 3 of human VH and up until now Nbs are not generally immunogenic in patients participating in clinical trial projects (13).

The differences between VH from classical antibodies and VHH from HCAbs in the framework region 2 (FR2) and in the length of the CDRs (complementary determining region) are well established (14). Large hydrophobic amino acids in FR2 of the VH domain that associate with the VL (variable light chain), are substituted in VHHs by smaller and/or more hydrophilic amino acids. These mutations increase the solubility and stability of autonomous VHHs in absence of partner VL domains (14). The hypervariable region that overlaps with CDR1, is extended by four more amino acids toward the N terminal end and this region in a VHH is probably involved directly or indirectly in antigen recognition. Likewise, the CDR3 is on average longer in a VHH than in a VH and part of it can form a protruding loop contacting grooves or concave epitope architectures on the surface of the antigen (15–17). These longer CDR1 and CDR3 loops are regularly connected through an interloop disulfide bond (in camels or dromedaries), which might further contribute favorably to the stability of the domain under stringent conditions such as elevated temperature or pH extremes (18).

Among the main properties of Nbs, we note their

i. small size (1/10 of intact conventional antibody),
ii. high degree of sequence identity with human VH,
iii. high expression in microbial hosts,
iv. high stability and solubility, and
v. high specificity and affinity for their cognate antigen.

Each of these characteristics leads to a number of beneficial outcomes (14) and their robustness even allows gut passage of orally taken Nbs to reduce the morbidity of rotavirus infected animals (19).

The small size and monomeric behavior of Nbs facilitates their gene manipulation (**Table 1**) and assists their penetration into tumor tissues where a prevalent high pressure of the interstitial space prevents the transport of larger molecules (whole antibodies) (16). Although the monomeric Nbs are rapidly cleared from the blood *via* the kidneys (half-life of around 30 min), nonetheless, a high tumor accumulation can be reached (20). The conjugation of Nbs with nuclides or dyes generates tracers for usage in non-invasive, *in vivo* imaging of tumors for diagnosis or to monitor the therapeutic treatment (21). Furthermore, the monovalent Nb can

TABLE 1 | Characteristics of nanobodies (Nbs) (23–25).

Nb	The recombinant form of the variable antigen-binding domain of heavy chain-only antibodies (HCAbs) from camelids
Main sources	HCAbs expressed from peripheral blood lymphocytes of camelids (bactrian camel, dromedary, llama, and vicugna)
Size	2.5 nm diameter, 4 nm height (molecular mass 12–15 kDa)
Structure	A single monomeric, variable immunoglobulin domain
Function	Binds specifically and with high affinity to its cognate antigen
Preferred production technique	Immunization of camelids to raise a HCAbs immune response; cloning of VHH repertoire from peripheral blood lymphocytes; retrieval of antigen-specific Nbs after phage display (or other display methods)
Application areas	Therapeutic applications: selective toxin neutralizing or tumor targeting (e.g., targeted radionuclide therapy); Diagnosis: non-invasive *in vivo* imaging; antigen capturing agent in micro-arrays and biosensors; Research: affinity chromatography, crystallization chaperones, drug discovery, intracellular expression, and target tracing, elimination, modulating, relocation, degradation,….
Biochemical properties	High expression yields in microorganisms; nano- to picomolar affinities; recognition of unique epitopes; generally non-immunogenic; facile gene manipulation
Biophysical properties	Stability usually higher than conventional antibodies; high solubility; rapid blood clearance; fast tissue penetration, short half-life in blood due to renal clearance and absence of Fc/FcR interaction
Disadvantages	Small size may cause problems in parenteral applications; lack of effector function-mediated effects; increased frequency of dosing for systemic applications

be easily manipulated to form bivalent, multivalent, bispecific, or bi-paratopic constructs. The fusion of a Nb to another Nb with specificity to albumin increases its half-life blood retention from less than 30 min to 2–3 days (22).

The natural source of Nbs, in addition to their unique properties have attracted a lot of attention and many research groups are currently developing new Nbs as candidates for therapeutic and diagnostic applications (**Table 1**). Nb ALX0061 and Nb ALX00171 against interleukin 6 receptor and respiratory syncytial virus (RSV) for treatment of rheumatoid arthritis and RSV infection might be on the market soon (8). In addition, several Nb-based therapeutic agents against TNF-α, IL17A (26), VEGF/angiopoietin-2 (Ang-2) (27), CXCR1, CXCR2 (28), vWF (29), RANKL (30) applicable in autoimmune disease, malignant disease, inflammation, hematopoitic disorders, and bone disorder, respectively, are at various stages of clinical trials.

The aforementioned beneficial properties support Nbs as potent agents in targeting a wide variety of disease-related antigens, especially those related to cancer. At present there are many more active projects on the identification and development of new Nbs against cancer specific antigens.

Nb GENERATION TECHNIQUES

Phage Display

Phage display is powerful technique to retrieve binders against various targets from a large and diverse library (31). This technology applied for Nbs after immunizing a camelid turns out to be relatively fast and efficient, certainly since the animal can be immunized simultaneously with multiple antigens and a hyper immunization scheme can be shortened to about 6 weeks. The phage display vectors have been adapted for a straightforward cloning of Nbs amplified by RT-PCR. To improve the transformation efficiency, phagemid vectors, such as pCOM3 and pHEN series have been designed and used in combination with M13K07, R408, or VCSM13 helper phages to produce monovalent displayed Nbs at the tip of the virions (32). The immune Nb libraries are unique as they give access to the intact, affinity-matured, antigen-binding fragments. This means that a relative small library is sufficiently adequate to retrieve potent antigen-binders. Immune or naïve scFv libraries and even synthetic man-made scaffold libraries require much larger libraries to retrieve specific binders of high affinity although synthetic or naïve phage display system have remediated some limitations of hybridoma or immune libraries (e.g., in the case where the target is a weak immunogen) (33). However, the success of retrieving good binders is correlated with the size and diversity of the library. Fresh blood and quality of mRNA and cDNA preparations are very crucial to construct a high quality library and to ensure the identification of potent binders (34).

Other Techniques

Apart from phage display, which remains the first choice because of its robustness, alternative selection techniques for Nbs have also been successfully applied, including ribosome or mRNA display, yeast or bacterial surface display, and even bacterial two-hybrid screenings (35). The multivalent display of Nbs in yeast or bacterial display systems in combination with fluorescent activated cell sorter (FACS) selection allows a rapid identification of the very best Nbs within the library. Conversely, the acellular ribosome and mRNA display techniques clearly avoid the transformation step into an *E. coli* host. In addition, the reverse transcriptase and PCR amplification steps after each round of selection, might introduce minor sequence variations that could contribute to the identification of stronger binders (36).

ANGIOGENESIS IN CANCER

Angiogenesis is the physiologic pathway whereby new blood vessels are formed from existing vessels. These new vessels are induced by various stimulators such as hypoxia, vessel damage, or angiogenesis growth factors that act as environmental triggers (37). This process needs to be controlled under strict conditions and each disturbance in its balance might cause pathologic distress such as tumorigenesis. Tumor angiogenesis is one of the main properties of cancer cells whereby new blood vessels are formed in the vicinity of the tumor so that tumor cells are supplied with the required oxygen and nutrients. Therefore, upregulation of angiogenesis factors stimulates tumor growth and metastasis.

Indeed, some of the angiogenic modulators like members of the vascular endothelial growth factor (VEGF) family and the VEGF receptor (VEGFR) family have a direct role in both the pysiological and the pathological conditions (38) (**Figure 2**).

In the VEGF/VEGFR signaling pathway, the ligands, including VEGF-A, VEGF-B, VEGF-C, VEGF-D, and placental growth factor (PLGF), interact with membrane bound tyrosine kinase receptors VEGFR-1 (FLT-1), VEGFR-2 (FLK-1/KDR), and VEGFR-3 (FLT4) (**Figure 2**). VEGFs also bind to particular co-receptors, including neurophilin NRP-1 and NRP-2. The association of VEGF-A (known as VEGF) to VEGFR-2 has been discovered to be a key mediator of angiogenesis. VEGF-A, which is expressed in many human tumors, triggers a number of intracellular signaling cascades in endothelial cells leading to formation and enhancement of tumor microvasculature (39). A variety of factors like AKT, Raf, P13K, MEK, and ERK may be involved in the molecular mechanism of the intracellular signaling pathways of angiogenesis (40).

Furthermore, several studies revealed that tumor tissues express additional factors, such as cancer-associated antigens, that

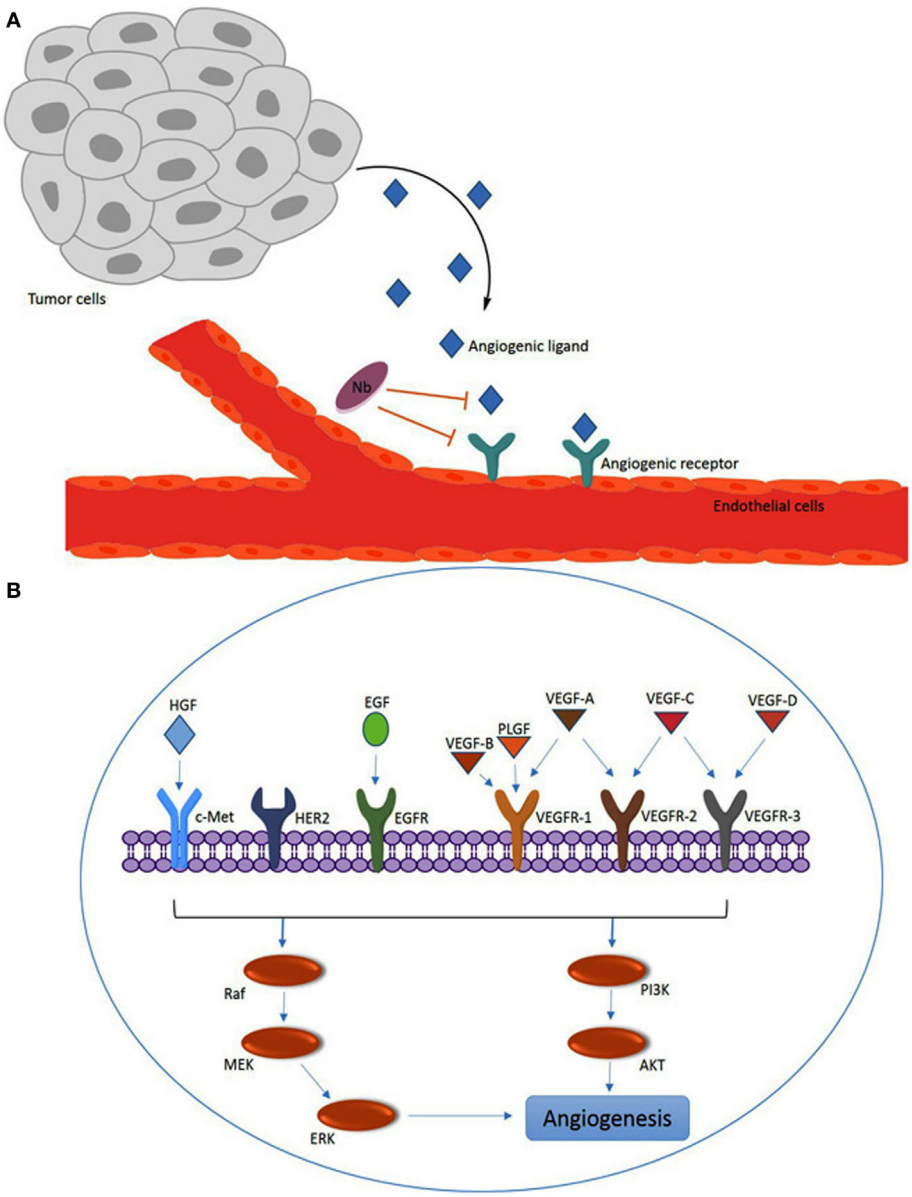

FIGURE 2 | Overview of angiogenesis induced by the vascular endothelial growth factor (VEGF) family members and other angiogenesis factors. **(A)** Angiogenic ligands (e.g., VEGF) are released by tumors and captured by ligand receptors [e.g., VEGF receptor (VEGFR)] on endothelial cells. The nanobodies (Nbs) with specificity for the ligand or the receptor can interfere with for example the VEGF–VEGFR interaction by steric hindrance upon binding to VEGF or VEGFR. **(B)** Overview of major VEGF/VEGFR family members and other angiogenesis factors [c-Met, HER2 and epidermal growth factor receptor (EGFR); and hepatocyte growth factor (HGF) and EGF] that are involved in intracellular signaling *via* the PI3K or Raf pathways to promote angiogenesis.

have indirect effects on angiogenesis. Tyrosine kinase inhibitors or mAbs, targeting these angiogenic factors are currently used in the clinic. Despite their strong inhibitory potential of angiogenesis, they offer only limited success in treating cancer patients due to the defense mechanisms of the tumor to escape and to resist the anti-angiogenesis therapy, for example by overexpressing other angiogenesis factors (41).

In the following sections, we will discuss in detail the Nbs that target the angiogenesis factors.

MAJOR ANGIOGENESIS TARGETS FOR Nbs IN CANCER

Tumor angiogenesis involves a complex network of interactions. It has been demonstrated that some of the transmembrane proteins, such as tyrosine kinase receptors, are one of the best options for Nb targeting. Here, the prevention of ligand association on the tyrosine kinase receptor by Nbs and avoiding the intracellular cascade signaling is the main objective. Some receptors have several extracellular domains [e.g., epidermal growth factor receptor (EGFR), HER2, c-Met] and thus expose multiple potential epitopes for Nb recognition. Possibly, targeting these epitopes might lead to subsequent internalization of the associated molecule inside the cell, which might be an effective route to transport a drug, toxin, nuclide, or any other harmful substance inside cancer cells. Alternatively, Nbs against the ligand of the transmembrane receptor is also a feasible strategy, especially when the signaling pathway is activated by only one ligand. The effectiveness of this approach was exemplified with Nbs against hepatocyte growth factor (HGF) that activate c-Met, but fail to interfere with the EGFR signaling as this receptor is activated by multiple ligands (12).

The high potential of Nbs as magic bullets that can interfere with angiogenesis are expected to bridge easily the gap from bench to clinic. The targeting of angiogenesis with Nbs has been explored to reach various outcomes. For therapeutic objectives, a clear inhibition of tumor growth and metastasis is required, so that Nbs against the receptor or against the ligand can be employed. For diagnosis and monitoring the treatment follow up, the primary target will be the tumor receptor. For these purposes, the Nb itself should likely be manipulated to improve its potential. These modifications include (i) increasing the valency of Nbs *via* designing bifunctional, bispecific, or bi-paratopic constructs and (ii) increasing the half-life of Nbs either by increasing their hydrodynamic volume (e.g., PEGylation) or by hooking on an abundant compound with long half-life (e.g., decorating the therapeutic Nb directly with albumin or tethering a Nb against serum albumin to the therapeutic Nb). Currently, there are several Nbs that reached different clinical stages and most of these are multivalent Nbs, such as Caplacizumab (28), Vobarilizumab (42), ALX0171 (43), Ozoralizumab (44), and ALX0761 (45).

Vascular endothelial growth factor, because of its strong effect on angiogenesis stimulation, is the main target for development of strategies in anti-angiogenesis therapy. Bevacizumab (Avastin, Genentech, San Francisco, CA, USA), a humanized anti-VEGF-A mAb and potent anti-angiogenesis agent has been approved since 2004, along with other chemotherapeutic drugs (46). Apart from tumor therapy, the VEGF antibody and its antibody fragments have been used to combat other angiogenic disorders, such as age-related macular degeneration (AMD). Aflibercept ((Eleya), Regeneron and Sanofi Aventis, Bridgewater, NJ, USA) is a fusion protein consisting of the VEGF-binding regions of the extracellular domains of human VEGFR-1 or VEGFR-2 fused to the Fc regions of human immunoglobulin G1. This hybrid molecule could block VEGF-A, B, and PLGF in wet AMD and diabetic macular edema and is also being investigated for retinal vein occlusion (46).

Vascular endothelial growth factor is also a major target for development of domain antibodies. Recently, a VEGF dual domain antibody has been reported that seems to be more effective than Avastin or Aflibercept (47). Several studies indicated favorable targeting properties for molecules that combine high affinity and a small molecular size (48).

Following another strategy, Ablynx developed a tri-specific humanized Nb for targeting angiogenesis. In their complex, a Nb against VEGF, a second Nb against Ang-2 and a third Nb against serum albumin for half-life extension are combined. The VEGF and Ang-2 are cross talking and the VEGF upregulates expression of Ang-2. The dual targeting Nb (BI1836880) developed by Ablynx and Boehringer Ingelheim inhibits the VEGF and Tie-2 (the Ang-2 receptor) signaling and prevents the proliferation of endothelial cells. In different *in vivo* models, this Nb construct seems to be superior in efficacy in comparison to Avastin (49).

In one of our studies, we could select VEGF-binding Nbs with specificity for VEGF-121, an isoform of VEGF-A. This Nb inhibits proliferation and tube formation of human umbilical vein endothelial cells (HUVEC) (50). Farajpour et al. developed a Nb against VEGF-165, this binder not only blocked interaction of VEGF with its receptor in cell ELISA but could also prevent significantly the proliferation of HUVEC in a dose-dependent manner (51). Ebrahimzadeh et al. also developed a Nb (VA12) against VEGF, which exhibited high affinity (3 nM) and stability along with significant anti-angiogenesis potential in a chorioallantoic membrane (CAM) assay (52). The CAM assay is an *in vivo* angiogenesis model of fertilized chicken eggs, used for studying the neovascularation (38).

The VEGFR-2, type II of transmembrane tyrosine kinase receptor, expressed on endothelial cells and on circulating bone marrow-derived endothelial progenitor cells, is a key receptor in tumorigenesis. The importance of VEGFR-2 signaling in tumor angiogenesis suggests that targeting of this receptor would be a useful therapeutic strategy to inhibit angiogenesis and tumor growth. Ghavamipour et al. developed a set of high-affinity Nbs (K_D down to 0.6 nM) against a conformational epitope corresponding to the VEGF-binding domain of VEGFR-2. To increase the chances to retrieve Nbs with this specificity, a combinatorial screening strategy was applied employing a competition phage ELISA panning (53).

In 2012, Behdani et al. reported the identification of an Nb against VEGFR-2 after phage display and panning on immobilized extra cellular domain of VEGFR-2 (54). VEGFR-2, in contrary to VEGFR-1 is switched on in pathologic conditions such as tumorigenesis. In this study, the Nb could inhibit tube formation of HUVEC cells. The Nb was used to develop pseudo-lentiviral

vectors for potential transductional targeting of tumor vasculature (55). In another study, Ma et al. selected a high quality Nb against VEGFR-2 domain 3 (VEGFR-2 D3) after panning with antigen in solution. The affinity, as measured by surface plasmon resonance (SPR) indicated a moderate K_D of 49 ± 1.8 nM for VEGFR-2 domain 3. Nevertheless, this Nb could inhibit the growth and tube formation of HUVEC cells (56).

Placental growth factor is a member of the VEGFs family. This factor is responsible for physiologic angiogenesis but it is also overexpressed in many cancers. Multiple studies have been reporting the anti-angiogenesis effect of PLGF targeting by applying mAbs (57, 58), gene inactivation methods, and antagonist peptides (59). Studies have shown how this factor and its receptor (VEGFR-1) are upregulated in tumor tissues. The mAb against PLGF had inhibitory effects on growth and metastasis in different tumor tissues. This mAb could enhance the effect of chemotherapy agents (57). Currently, a fully human mAb against PLGF called TB-403 entered clinical trials. The results of a phase I dose-escalation study of this humanized anti-PLGF mAb (TB-403, ThromboGenics/BioInvent) plus Bevacizumab in patients with advanced solid tumors were reported. The toxicity profile of this mAb plus Bevacizumab showed promising results (60). Bevacizumab is the first approved angiogenesis inhibitor which has been used for the treatment of metastatic colorectal cancer by inhibiting VEGF-A, one of the other members of VEGF family (61). Recently, our group reported the successful development of a Nb against PLGF. This Nb inhibited the proliferation, migration, and invasion of endothelial and breast cancer. The results of the CAM assay demonstrated the inhibitory role of the Nb against vascular formation in the chicken CAM (38).

Apparently, Nbs can efficiently block their target antigen in cases where cell killing by Fc mediated effector function is not required. This is probably similar to the activity of Lucentis (Ranibizumab) that also acts in absence of any Fc region (62).

Table 2 gives an overview of studies investigating the effects of Nbs on VEGF, VEGFR, PLGF, HER2/HGF, and EGFR families.

TARGETING OF OTHER POTENTIAL ANGIOGENESIS ACTIVATORS

Leptin

Leptin, encoded by the *obese* gene, plays a critical role in the regulation of body weight. The protein is also known as a potent angiogenic factor involved in tumorigenesis, angiogenesis, and metastasis. Leptin regulates VEGF production in human chondrosarcoma and contributes to tumor-associated angiogenesis (71). The involvement of leptin in cancers such as breast, ovarian, and prostate has been demonstrated and thus the development of mAbs against this target has been initiated. However, it remains uncertain whether anti-leptin antibodies entered the clinic (72). Likewise, McMurphy et al. developed an Nb against the leptin receptor, which causes inhibition of growth of a melanoma tumor in mouse. Local administration of a neutralizing Nb, targeting the leptin receptor, at low doses, and adjacent to the tumor, decreased tumor mass with no effects on body weight or food intake (73).

Endoglin or CD105

CD105 (Endoglin) is one of the tumor-related angiogenesis factors that is upregulated in tumor tissues and neovascularization. This factor activates transforming growth factor beta (TGF-β). Endoglin is a membrane glycoprotein that is a part of the TGF-β receptor complex. Playing a role in tumor angiogenesis, endoglin can be used in diagnosis, prognosis, and therapy (74). The result of phase I of TRC105, a chimeric anti-endoglin (CD105) mAb, in metastatic castration-resistant prostate cancer shows good anti-angiogenic activity and that it is well tolerated (75).

Ahmadvand et al. developed an Nb against CD105, which could inhibit the proliferation of HUVEC cells and tube formation (76, 77).

HGF and c-Met

Hepatocyte growth factor exclusively induces the growth of endothelial cells without replication of vascular smooth muscle cells and acts as a survival factor against endothelial cell death. In tumor tissues, HGF is a key growth factor linked to increasing cancer progression and angiogenesis. The binding of HGF to its receptor (c-Met, belonging to tyrosine kinase receptors) activates the signaling pathway that causes enhancement of angiogenesis in tumor tissues and prevents apoptosis, which all contribute to the outgrowth of tumors (78). Rilotumumab is an intact mAb that binds to HGF and prevents its association with the c-Met receptor. This mAb is currently in clinical phase trials for treatment of different solid tumors (79). Likewise, two Nbs against HGF, referred to as 1E2 and 6E10, were identified and modified for serum half-life extension by fusion with an albumin-binding Nb (Alb8). 1E2-Alb8 and 6E10-Alb8 Nbs binding to HGF inhibits recognition of the c-Met receptor. After labeling with ^{89}Zr, a positron emitter, the biodistribution of Nbs was evaluated in nude mice. The result of these animal studies revealed a tumor growth inhibitory effect of these Nbs in a glioblastoma xenograft model (65).

It is well established that the activation of the c-Met receptor by HGF and its subsequent signaling and angiogenesis activation is involved in many human malignancies (80). Interfering with the signaling by ligand or adding c-Met dimerization blocking antibodies or kinase inhibitors all exert a measurable inhibitory effect on cancer cell progression (81). Onartuzumab, H224G11/ABT700, LY2875358, and ARGX-111 are mAbs against c-Met in clinical trials that are exploiting exactly this therapeutic strategy (82). Slordahl et al. developed an anti c-Met Nb that effectively prevented thymidine incorporation by ANBL-6 MM cells *via* inhibition of an HGF autocrine growth loop and thymidine incorporation into INA-6 MM cells induced by exogenous HGF. Migration and adhesion of INA-6 was completely and specifically abolished by the Nb. Apparently, the Nb also reduces the inhibitory effect of HGF on bone morphogenetic protein-2-induced alkaline phosphatase activity and the mineralization of human mesenchymal stem cells (83). Finally, Heukers et al. developed an Nb delivery system constructed from their anti c-Met Nb decorated albumin nanoparticles (anti-Met-NANAPs). Targeting of c-Met expressing cells could downregulate the HGF receptor protein (84).

TABLE 2 | Examples of published preclinical studies investigating the effect of nanobodies (Nbs) on factors involved in angiogenesis.

Name of selected Nbs	Target	Model or investigated cells	Technique(s) employed	Comments	Results	Reference
Nb22, Nb23, Nb35, and Nb42	Vascular endothelial growth factor (VEGF)	Primary human umbilical vein endothelial cells (HUVECs)	Phage display; cross-reactivity assay; endothelial tube formation assay	Binding affinity from 0.1 to 60 nM; Nbs detect recombinant VEGF-121 and VEGF-165	Inhibition of endothelial cell proliferation or tube formation	(53)
ZFR-5	VEGF	HUVECs	Phage display; whole-cell ELISA experiments; endothelial cell assay	Evaluation of six phage-displayed Nbs from an immune phage library	ZFR-5 blocked interaction of VEGF with its receptor; significant inhibition of proliferation response of HUVECs to VEGF	(50)
V12	VEGF	Chorioallantoic membrane (CAM) of fertilized eggs	Phage display; non-competitive enzyme immunoassay; CAM assay	Twenty-four clones were tested by monoclonal phage ELISA	VA12 Nb showed substantial anti-angiogenesis activity	(51)
3VGR19	VEGF receptor (VEGFR)-2	293KDR and HUVECs	Phage display; fluorescent activated cell sorter (FACS) analysis; endothelial tube formation assay	293KDR cells express high levels of VEGFR-2	Nb recognized antigen on cell surface and inhibited endothelial tube formation	(54)
Nb-C18	Placental growth factor	Chicken CAM model; HUVECs	Phage display; 3D-capillary tube formation assay; transwell migration assay; CAM assay	Twelve clones with strong signals were selected	Nb-C18 significantly inhibited proliferation, migration, and 3D-capillary formation of HUVECs; Nb-C18 inhibits vascular formation	(38)
5F7GGC	HER2	BT474M1 breast carcinoma cells; mice bearing subcutaneous BT474M1 xenografts	Phage display; radio-iodination; binding affinity and internalization assays; paired-label biodistribution		Labeling 5F7GGC with *I-SGMIB targeting HER2 expressing malignancies	(63)
2Rs15d	HER2	CHO cells; LS174T, human $HER2^+$ colon carcinoma; SKBR3, BT474, and MDA-MB-435D, human $HER2^+$ breast cancer; SKOV3, human $HER2^+$ ovarian cancer; xenografts mice model	Phage display; ELISA; binding of Nbs in flow cytometry; surface plasmon resonance; Nb labeling; single-photon-emission computed tomography (SPECT)	2Rs15d selected from a panel of 38 Nbs and labeled for tumor imaging	^{99m}Tc-labeled 2Rs15d has suitable properties as HER2 tracer for *in vivo* non-invasive imaging	(64)
1E2 and 6E10	Hepatocyte growth factor (HGF)	U-87 MG, human glioblastoma; Bx-PC3, human prostate carcinoma; A549, human alveolar basal epithelial cell carcinoma	Phage display; fusion with albumin-binding Nb; phosphorylation assay; proliferation assay; biodistribution study; nude mice model	1E2 and 6E10 selected among a panel of 12 Nbs which showed good binding to HGF	1E2-Alb8 and 6E10-Alb8 are candidate for therapy and PET imaging of HGF-expressing tumors	(65)
Epidermal growth factor receptor (EGFR) Nb	EGFR	A431; NIH 3T3; HeLa	Phage display; functional panning; Production of multivalent anti-EGFR nanobodies; FACS; A431 animal model	Selection of antagonistic Nb fragments by ligand-specific elution	Untagged Nbs were used for *in vivo* treatment of tumors	(66)
7C12 and 7D12	EGFR	Mice bearing subcutaneous A431 ($EGFR^+$) and R1M ($EGFR^-$) xenografts	Nb Labeling; Pinhole SPECT/micro-CT imaging; *ex vivo* analysis		High tumor uptake, low liver uptake, and rapid blood clearance	(67)
8B6	EGFR	A431; human prostate carcinoma cell line DU145; HER14 and NIH3T3; MCF-7	Phage display; ^{99m}Tc labeling; SPECT; FACS		Nb with high specificity and selectivity toward EGFR overexpressing cells	(68)

(*Continued*)

TABLE 2 | Continued

Name of selected Nbs	Target	Model or investigated cells	Technique(s) employed	Comments	Results	Reference
^{99m}Tc-7C12	EGFR	A431; ICR/CD1 mice; A431 animal model; megalin-deficient mice	Nb labeling; *in vitro* and *in vivo* stability assay; ^{99m}Tc-7C12 uptake and biodistribution study		^{99m}Tc-labeled 7C12 Nb accumulates significantly in tumor	(69)
^{99m}Tc-7C12	EGFR	A431 expressing truncated growth factor; male athymic nude mice	Nb Labeling; *in vitro* binding assay and specificity of ^{99m}Tc-7C12; internalization experiment; *in vivo* tumor uptake of ^{99m}Tc-7C12; *in vivo* bioluminescence imaging; Pinhole SPECT/Micro-CT		^{99m}Tc-7C12 is a candidate for the early prediction of, and treatment of cancer-expressing EGFR	(70)

Epidermal Growth Factor Receptor

The EGFR belongs to the HER/ErbB family of receptor tyrosine kinases (85). This family includes HER-1 (EGFR/ErbB-1), HER2 (neu, ErbB-2), HER-3 (ErbB-3), and HER-4 (ErbB-4) (86). Overexpression of EGFR may confer or promote a malignant phenotype and increase the tumor mass (87). One of the processes to enhance tumor angiogenesis consists in the activation of the EGFR pathways (66). Increased levels of EGF and TGF-β can cause activation of VEGF and subsequent tumor angiogenesis (88). On the basis of the pro-angiogenic properties of EGFR, blocking EGFR downregulates VEGF, IL-8, and basic FGF production, interrupts upstream angiogenesis signaling pathways, and is accompanied by a net reduction in microvessel density and metastases (88).

Roovers et al. (89) retrieved the first antagonistic anti-EGFR Nbs for cancer therapy by competitively eluting the EGFR-attached Nbs with EGF. This strategy resulted in the selection of a panel of Nbs that inhibited the recognition of EGF to its receptor without acting as a receptor agonist. The results confirmed that these Nbs inhibited perfectly EGF-induced signaling and EGF-induced cell proliferation *in vitro* and prevented the tumor outgrowth in animal models. Tijink et al. targeted tumors using a bivalent anti-EGFR Nb (αEGFR− αEGFR) that was also fused to a Nb against albumin to improve the biodistribution and circulation time of the construct. To facilitate their quantification, the proteins were radiolabeled with ^{177}Lu. Tumor uptake of ^{177}Lu-αEGFR-αEGFR-αAlb decreased from 5.0 ± 1.4 to 1.1 ± 0.1 %ID/g between 6 and 72 h after injection. Remarkably, this multi-modal construct not only decreased blood clearance but also increased penetration to tumor tissue (22). In 2011, the group of Roovers in continuation of their previous work improved the potential of EGFR Nbs by combining Nbs with specificities similar to both Cetuximab and Matuzumab into a single bi-paratopic molecule (90). This bi-paratopic construct could bind simultaneously to two independent epitopes that overlap with those of Cetuximab and Matuzumab. This Nb (referred to as CONAN-1) could inhibit the cell proliferation that depended on EGF *in vitro* and it could also inhibit the tumor outgrowth with an almost similar potency as the entire Cetuximab mAb and it was more potent than the bivalent, mono-specific Nbs (90). In a recent independent study, Farasat et al. improved the affinity of an EGFR Nb (7D12) by *in silico* tools (91).

Human EGFR 2 (HER2) or ErbB-2 is another member of EGFR family. Uncontrolled expression of HER2 occurs in about 20–30% of breast cancers, 4–6% of non-small cell lung cancers, 20–24% of gastric cancers, and also in colon and ovarian cancers (92). Trastuzumab (Herceptin®, Genentech) is the approved humanized and intact IgG1 mAb, which in combination with Pertuzumab has been used to treat patients with HER2 positive malignancies (93, 94).

Patients with a strong positive result of their biopsy in immunohistochemistry or with the gene amplification assay are expected to benefit from a Trustuzumab therapy. Moreover, with the available HER2 targeting Nbs and fast clearance of excess administered Nb, it became apparent how useful Nbs might be for non-invasive imaging and to screen *in vivo* for HER2$^+$ carcinomas (13). Obviously, if Nbs are shown to be excellent

tumor targeting molecules, then substitution of the nuclide into a more toxic payload will produce a potent compound for targeted radionuclide therapy. Thus, the HER2 targeting Nbs were used for imaging and radiotherapy strategies (95). There are several criteria that dictate the choice for employing radiolabeled nuclides. The radiolabeled prosthetic group should have the least possible toxicity in healthy tissues, high tumor penetration, prolonged residence time at the tumor tissue site and fast clearance of the excess drug from normal tissues, and low retention time in the kidneys and other non-targeted organs. Obviously, the selected nuclide conjugated to the Nb should not change the binding properties to its cognate target (12, 96). According to different studies, a carefully selected anti-HER2 Nb is one of the best candidates to be used as tracer in different imaging strategies such as PET (positron emission topography) or single-photon-emission computed tomography (SPECT) imaging. Vaneycken et al. investigated the performance of about 40 Nbs against HER2 and identified the lead Nb to trace xenografted tumors in mice (64). Their 2Rs15d Nb, which does not compete for HER2 binding with Traztuzumab or Pertuzumab, was selected based on its microbial expression level, SPR-measured affinity, cell targeting in flow cytometry, and radio-ligand binding studies. The use of ^{99m}Tc-labeled 2Rs15d in SPECT imaging quantification and biodistribution analyses demonstrated high tumor uptake in two HER2$^+$ tumor models, fast blood clearance of excess Nb, and low accumulation in non-target organs except kidneys.

Xavier et al. (97) constructed ^{68}GA-NOTA (1,4,7-triazacyclononane-1,4,7-triacetic acid) anti HER2 Nbs for a dosimetry and toxicity assay in interim PET imaging. The biodistribution studies showed fast and specific uptake in HER2 positive tumors, resulting in high-contrast PET/CT images. High-specific contrast imaging and lack of toxicity of ^{68}Ga-NOTA-2Rs15d are ideal properties for human clinical trials with PET tracers. Interestingly, D'Huyvetter et al. observed that the kidney retention of labeled Nb 2Rs15d was reduced significantly upon removal of the haemaglutinin tag and the His tag, in line with the notion that the kidney retention is dominated by the amino acid composition in these C-terminal tags (98).

Recently, Keyaerts et al. reported the results of a phase I study of ^{68}Ga-HER2 Nb in a PET/CT assessment of HER2 expressing breast carcinoma. Their data showed that this Nb has a favorable biodistribution and is safe to use and well tolerated in patients. Acceptable signals in the kidneys, liver, lacrimal glands, and intestines were noted and very low background levels in other organs were observed. Therefore, it seems that this Nb used as a molecular probe might replace histochemical analysis of biopsies in the future (13).

The very low uptake in other organs except the targeted tumor of Nbs in the absence of any tag is considered to be safe for human administration and effective for targeted radionuclide therapy. Indeed, Nb-based targeted radionuclide therapy led to an almost complete blockade of tumor growth in xenograft model. Thus, a very promising strategy was developed by D'Huyvetter et al. (98). They also replaced the ^{99m}Tc with ^{177}Lu on the HER2 Nb using a bifunctional chelator for better *in vivo* behavior and optimized radiolabeling. This adaptation had no effect on the tumor targeting capacity of the Nb in xenografted mice, and *ex vivo* biodistribution studies showed a significant quantity of the therapeutic Nb on tumors expressing medium HER2 levels and low background activity in other tissues except for the kidneys (99).

In an alternative therapeutic approach, Van de Broek et al. (100) conjugated the 2RS15d onto branched gold nanoparticles for photothermal therapy. It is hypothesized that laser irradiation at the site of nanogold accumulation will produce enough heat to destroy tumor cells overexpressing HER2 receptor in contrast to control cells (100). Unfortunately, the biofunctionalized branched gold particles seem to suffer from a serum albumin corona when used *in vivo*. However, this has recently been remediated by preparing the nanoparticles using a different blocking agent to inactivate the reactive groups (101).

Finally, 5F7GGC, originally introduced as an HER2 Nb (89), was radio-iodinated using a conventional method (Iodogen) and IB-Mal-D-GEEEK reagent (102). The radio-iodinated 5F7GGC Nb using the^{131}I-IB-Mal-D-GEEEK indicated better tumor blocking properties both *in vitro* and *in vivo* compared with Nb labeled *via* Iodogen. Moreover, the toxicity of ^{131}I-IB-Mal-D-GEEEK for healthy tissue is lower than that of tumors except in the kidneys where substantially higher radioactivity levels were observed. Radio-iodinated 5F7GGC Nb with the residualizing agent *N*-succinimidyl 4-guanidinomethyl 3-^{125}/^{131}I-iodobenzoate (*I-SGMIB) not only presented a promising new conjugate for targeting HER2-expressing malignancies but also showed improved tumor retention and faster normal-tissue clearance than ^{131}I-IB-Mal-D-GEEEK (63). However, further investigation is needed to demonstrate the potential utility of *I-SGMIB-5F7GGC labeled with ^{124}I, ^{123}I, and ^{131}I for PET and SPECT imaging and for targeted radiotherapy.

Likewise, Jamnani et al. developed oligoclonal Nbs against HER2 receptor by selecting Nbs against the native receptor exposed on the cell surface. These oligoclonal Nbs inhibited growth of breast cancer cells better than each individual Nb (103). Next, genetically engineered T cells were generated expressing chimeric antigen receptors (CAR) comprising five individual HER2 specific Nbs joined to various CD28 and OX40 signaling endodomains. The use of these oligoclonal anti-HER2 Nbs-CAR engineered T cells in an adoptive cell therapy resulted in higher cytokine secretion and enhanced cytotoxicity against HER2$^+$ tumor cells (104).

The application of mAbs in radio-immunotherapy has some severe limitations such as a poor tumor penetration due to their large size and undesirable pharmacokinetics. To date, only two radiolabeled mAbs have been approved for commercial use, ^{90}Y-Ibritumomab (Zevalin, Biogen-Idec Pharmaceuticals) and ^{131}I-Tositumomab (BEXXAR, GlaxoSmithKline), both of which have been used to treat indolent B-cell lymphoma (105, 106).

Table 2 gives an overview of studies investigating the effects of Nbs targeting EGFR and HER2.

Chemokine Receptor Type 7 (CXCR7)

Chemokine receptor type 7 is one of the members of the chemokine receptor family, belonging to the superfamily of G protein-coupled receptors. The overexpression of chemokines

and chemokine receptors in various tumor types and their involvement in cell proliferation, metastasis, and angiogenesis has opened new avenues in targeting the chemokine receptors (107). Maussang et al. reported the development an anti-CXCR7 Nb to reduce head and neck cancer cell growth *in vivo*. Apparently, these Nbs act by inhibiting angiogenesis. The interference with the pathway led to the inhibition of β-arrestin-2 signaling and secretion of angiogenic chemokine ligand 1 (108).

Table 2 gives an overview of studies investigating the effects of Nbs on the major factors known to be involved in the angiogenesis process.

CONCLUSION AND FUTURE PROSPECTS

Although there are a large number of angiogenesis inhibitors, remaining clinical problems, including resistance from the tumor microenvironment, enhanced tumor hypoxia, and reduced delivery of chemotherapeutic agents, have curtailed their full therapeutic potential. Given that mAbs have shown considerable success in tumor-targeted therapies during the past couple of decades, an increasing focus is now going toward remediation of the therapeutic limitations of antibodies, such as those related to their large and complex structure. The introduction of Nbs, a single-domain antigen-binding fragment has demonstrated that they can overcome some drawbacks of intact antibody-based cancer therapeutics and diagnostics. The Nb seems to become a promising therapeutic agent for cancers. Their angiogenesis inhibiting potential can be employed in various ways—as receptor antagonist, by targeting effective epitopes, and by decorating nano-carrier surfaces (17, 109). The small size of Nbs is highly suitable for generating tracers for non-invasive *in vivo* diagnosis of malignant cells. In targeting angiogenesis, Nbs should be equipped with a half-life extension moiety to increase the tumor loading capacity. The recognition of distinct epitopes that is often inaccessible for classical antigen-binding fragments might also broaden their therapeutic applications. Despite the challenges related to the efficacy of Nbs resulting from the lack of natural effector functions as present in the Fc region, the Nb holds promises, both for diagnosis and therapy of cancer.

AUTHOR CONTRIBUTIONS

All authors listed have made a substantial intellectual contribution to write the text and have approved it for publication.

FUNDING

Agentschap voor Innovatie door Wetenschap en Technologie, Belgium. SBO Nanocomit 140061.

REFERENCES

1. Prager G, Poettler M. Angiogenesis in cancer. *Hämostaseologie* (2012) 32(2):105–14. doi:10.5482/ha-1163
2. Weiner GJ. Building better monoclonal antibody-based therapeutics. *Nat Rev Cancer* (2015) 15(6):361–70. doi:10.1038/nrc3930
3. Shojaei F. Anti-angiogenesis therapy in cancer: current challenges and future perspectives. *Cancer Lett* (2012) 320(2):130–7. doi:10.1016/j.canlet.2012.03.008
4. Ecker DM, Jones SD, Levine HL. The therapeutic monoclonal antibody market. *MAbs* (2015) 7(1):9–14. doi:10.4161/19420862.2015.989042
5. Zider A, Drakeman DL. The future of monoclonal antibody technology. *MAbs* (2010) 2(4):361–4. doi:10.4161/mabs.12461
6. Holliger P, Hudson PJ. Engineered antibody fragments and the rise of single domains. *Nat Biotechnol* (2005) 23(9):1126–36. doi:10.1038/nbt1142
7. Chames P, Van Regenmortel M, Weiss E, Baty D. Therapeutic antibodies: successes, limitations and hopes for the future. *Br J Pharmacol* (2009) 157(2):220–33. doi:10.1111/j.1476-5381.2009.00190.x
8. Spadiut O, Capone S, Krainer F, Glieder A, Herwig C. Microbials for the production of monoclonal antibodies and antibody fragments. *Trends Biotechnol* (2014) 32(1):54–60. doi:10.1016/j.tibtech.2013.10.002
9. Scott AM, Wolchok JD, Old LJ. Antibody therapy of cancer. *Nat Rev Cancer* (2012) 12(4):278–87. doi:10.1038/nrc3236
10. Nelson AL. Antibody fragments: hope and hype. *MAbs* (2010) 2(1):77–83. doi:10.4161/mabs.2.1.10786
11. Hamers-Casterman C, Atarhouch T, Muyldermans S, Robinson G, Hamers C, Songa EB, et al. Naturally occurring antibodies devoid of light chains. *Nature* (1993) 363(6428):446–8. doi:10.1038/363446a0
12. Oliveira S, Heukers R, Sornkom J, Kok RJ, van Bergen En Henegouwen PM. Targeting tumors with nanobodies for cancer imaging and therapy. *J Control Release* (2013) 172(3):607–17. doi:10.1016/j.jconrel.2013.08.298
13. Keyaerts M, Xavier C, Heemskerk J, Devoogdt N, Everaert H, Ackaert C, et al. Phase I study of 68Ga-HER2-nanobody for PET/CT assessment of HER2 expression in breast carcinoma. *J Nucl Med* (2016) 57(1):27–33. doi:10.2967/jnumed.115.162024
14. Muyldermans S, Baral TN, Retamozzo VC, De Baetselier P, De Genst E, Kinne J, et al. Camelid immunoglobulins and nanobody technology. *Vet Immunol Immunopathol* (2009) 128(1–3):178–83. doi:10.1016/j.vetimm.2008.10.299
15. Wesolowski J, Alzogaray V, Reyelt J, Unger M, Juarez K, Urrutia M, et al. Single domain antibodies: promising experimental and therapeutic tools in infection and immunity. *Med Microbiol Immunol* (2009) 198(3):157–74. doi:10.1007/s00430-009-0116-7
16. Cortez-Retamozo V, Backmann N, Senter PD, Wernery U, De Baetselier P, Muyldermans S, et al. Efficient cancer therapy with a nanobody-based conjugate. *Cancer Res* (2004) 64(8):2853–7. doi:10.1158/0008-5472.CAN-03-3935
17. Kijanka M, Dorresteijn B, Oliveira S, van Bergen en Henegouwen PM. Nanobody-based cancer therapy of solid tumors. *Nanomedicine (Lond)* (2015) 10(1):161–74. doi:10.2217/nnm.14.178
18. Van der Linden R, Frenken L, De Geus B, Harmsen M, Ruuls R, Stok W, et al. Comparison of physical chemical properties of llama V HH antibody fragments and mouse monoclonal antibodies. *Biochim Biophys Acta* (1999) 1431(1):37–46. doi:10.1016/S0167-4838(99)00030-8
19. Van der Vaart J, Pant N, Wolvers D, Bezemer S, Hermans P, Bellamy K, et al. Reduction in morbidity of rotavirus induced diarrhoea in mice by yeast produced monovalent llama-derived antibody fragments. *Vaccine* (2006) 24(19):4130–7. doi:10.1016/j.vaccine.2006.02.045
20. Revets H, De Baetselier P, Muyldermans S. Nanobodies as novel agents for cancer therapy. *Expert Opin Biol Ther* (2005) 5(1):111–24. doi:10.1517/14712598.5.1.111
21. Chakravarty R, Goel S, Cai W. Nanobody: the "magic bullet" for molecular imaging. *Theranostics* (2014) 4(4):386–98. doi:10.7150/thno.8006
22. Tijink BM, Laeremans T, Budde M, Stigter-van Walsum M, Dreier T, de Haard HJ, et al. Improved tumor targeting of anti-epidermal growth factor receptor nanobodies through albumin binding: taking advantage of modular nanobody technology. *Mol Cancer Ther* (2008) 7(8):2288–97. doi:10.1158/1535-7163.MCT-07-2384
23. Siontorou CG. Nanobodies as novel agents for disease diagnosis and therapy. *Int J Nanomedicine* (2013) 8(1):4215–27. doi:10.2147/IJN.S39428
24. Muyldermans S. Nanobodies: natural single-domain antibodies. *Annu Rev Biochem* (2013) 82:775–97. doi:10.1146/annurev-biochem-063011-092449

25. Hassanzadeh-Ghassabeh G, Devoogdt N, De Pauw P, Vincke C, Muyldermans S. Nanobodies and their potential applications. *Nanomedicine* (2013) 8(6):1013–26. doi:10.2217/nnm.13.86
26. Fan G, Wang Z, Hao M, Li J. Bispecific antibodies and their applications. *J Hematol Oncol* (2015) 8(1):130–43. doi:10.1186/s13045-015-0227-0
27. Könning D, Zielonka S, Grzeschik J, Empting M, Valldorf B, Krah S, et al. Camelid and shark single domain antibodies: structural features and therapeutic potential. *Curr Opin Struct Biol* (2017) 45:10–6. doi:10.1016/j.sbi.2016.10.019
28. Cromie KD, Van Heeke G, Boutton C. Nanobodies and their use in GPCR drug discovery. *Curr Top Med Chem* (2015) 15(24):2543–57. doi:10.2174/1568026615666150701113549
29. Peyvandi F, Callewaert F. Caplacizumab for acquired thrombotic thrombocytopenic purpura. *N Engl J Med* (2016) 374(25):2497–8. doi:10.1056/NEJMoa1505533
30. Spiess C, Zhai Q, Carter PJ. Alternative molecular formats and therapeutic applications for bispecific antibodies. *Mol Immunol* (2015) 67(2 Pt A):95–106. doi:10.1016/j.molimm.2015.01.003
31. Hammers CM, Stanley JR. Antibody phage display: technique and applications. *J Invest Dermatol* (2014) 134(2):e17. doi:10.1038/jid.2013.521
32. Qi H, Lu H, Qiu H-J, Petrenko V, Liu A. Phagemid vectors for phage display: properties, characteristics and construction. *J Mol Biol* (2012) 417(3):129–43. doi:10.1016/j.jmb.2012.01.038
33. Lee CM, Iorno N, Sierro F, Christ D. Selection of human antibody fragments by phage display. *Nat Protoc* (2007) 2(11):3001–8. doi:10.1038/nprot.2007.448
34. Zhao A, Tohidkia MR, Siegel DL, Coukos G, Omidi Y. Phage antibody display libraries: a powerful antibody discovery platform for immunotherapy. *Crit Rev Biotechnol* (2016) 36(2):276–89. doi:10.3109/07388551.2014.958978
35. De Meyer T, Muyldermans S, Depicker A. Nanobody-based products as research and diagnostic tools. *Trends Biotechnol* (2014) 32(5):263–70. doi:10.1016/j.tibtech.2014.03.001
36. Ullman CG, Frigotto L, Cooley RN. In vitro methods for peptide display and their applications. *Brief Funct Genomics* (2011) 10(3):125–34. doi:10.1093/bfgp/elr010
37. Zimna A, Kurpisz M. Hypoxia-inducible factor-1 in physiological and pathophysiological angiogenesis: applications and therapies. *Biomed Res Int* (2015) 2015:549412. doi:10.1155/2015/549412
38. Arezumand R, Mahdian R, Zeinali S, Hassanzadeh-Ghassabeh G, Mansouri K, Khanahmad H, et al. Identification and characterization of a novel nanobody against human placental growth factor to modulate angiogenesis. *Mol Immunol* (2016) 78:183–92. doi:10.1016/j.molimm.2016.09.012
39. McMahon G. VEGF receptor signaling in tumor angiogenesis. *Oncologist* (2000) 5(Suppl 1):3–10. doi:10.1634/theoncologist.5-suppl_1-3
40. Ziyad S, Iruela-Arispe ML. Molecular mechanisms of tumor angiogenesis. *Genes Cancer* (2011) 2(12):1085–96. doi:10.1177/1947601911432334
41. Fischer C, Mazzone M, Jonckx B, Carmeliet P. FLT1 and its ligands VEGFB and PlGF: drug targets for anti-angiogenic therapy? *Nat Rev Cancer* (2008) 8(12):942–56. doi:10.1038/nrc2524
42. Dörner T, Weinblatt M, Van Beneden K, Dombrecht E, De Beuf K, Schoen P, et al. Poster FRI0239: results of a Phase 2B study of vobarilizumab, an anti-Interleukin-6 receptor nanobody, as monotherapy in patients with moderate to severe rheumatoid arthritis. *Ann Rheum Dis* (2017) 76(2):575.
43. Detalle L, Stohr T, Palomo C, Piedra PA, Gilbert BE, Mas V, et al. Generation and characterization of ALX-0171, a potent novel therapeutic nanobody for the treatment of respiratory syncytial virus infection. *Antimicrob Agents Chemother* (2016) 60(1):6–13. doi:10.1128/AAC.01802-15
44. Fleischmann R, Nayiager S, Louw I, Rojkovich B, Fu C, Udata C, et al. A multiple ascending dose/proof of concept study of ATN-103 (ozoralizumab) in rheumatoid arthritis subjects on a background of methotrexate. *Arthritis Rheum* (2011) 63:2630.
45. Dumet C, Pottier J, Gouilleux V, Watier H. New structural formats of therapeutic antibodies for rheumatology. *Joint Bone Spine* (2017) 84(5):385–91. doi:10.1016/j.jbspin.2017.04.007
46. De Falco S. Antiangiogenesis therapy: an update after the first decade. *Korean J Intern Med* (2014) 29(1):1–11. doi:10.3904/kjim.2014.29.1.1
47. Walker A, Chung CW, Neu M, Burman M, Batuwangala T, Jones G, et al. Novel interaction mechanism of a domain antibody-based inhibitor of human vascular endothelial growth factor with greater potency than ranibizumab and bevacizumab and improved capacity over aflibercept. *J Biol Chem* (2016) 291(11):5500–11. doi:10.1074/jbc.M115.691162
48. Zahnd C, Kawe M, Stumpp MT, de Pasquale C, Tamaskovic R, Nagy-Davidescu G, et al. Efficient tumor targeting with high-affinity designed ankyrin repeat proteins: effects of affinity and molecular size. *Cancer Res* (2010) 70(4):1595–605. doi:10.1158/0008-5472.CAN-09-2724
49. Gschwind A, Ott RG, Boucneau J, Buyse M-A, Depla E. *Bispecific Binding Molecules Binding to VEGF and Ang2*. US Patents US 20170247475 A1 (2017).
50. Kazemi-Lomedasht F, Behdani M, Bagheri KP, Habibi-Anbouhi M, Abolhassani M, Arezumand R, et al. Inhibition of angiogenesis in human endothelial cell using VEGF specific nanobody. *Mol Immunol* (2015) 65(1):58–67. doi:10.1016/j.molimm.2015.01.010
51. Farajpour Z, Rahbarizadeh F, Kazemi B, Ahmadvand D. A nanobody directed to a functional epitope on VEGF, as a novel strategy for cancer treatment. *Biochem Biophys Res Commun* (2014) 446(1):132–6. doi:10.1016/j.bbrc.2014.02.069
52. Ebrahimizadeh W, Mousavi Gargari SL, Javidan Z, Rajabibazl M. Production of novel VHH nanobody inhibiting angiogenesis by targeting binding site of VEGF. *Appl Biochem Biotechnol* (2015) 176(7):1985–95. doi:10.1007/s12010-015-1695-y
53. Ghavamipour F, Shahangian SS, Sajedi RH, Arab SS, Mansouri K, Aghamaali MR. Development of a highly-potent anti-angiogenic VEGF8-109 heterodimer by directed blocking of its VEGFR-2 binding site. *FEBS J* (2014) 281(19):4479–94. doi:10.1111/febs.12956
54. Behdani M, Zeinali S, Khanahmad H, Karimipour M, Asadzadeh N, Azadmanesh K, et al. Generation and characterization of a functional nanobody against the vascular endothelial growth factor receptor-2; angiogenesis cell receptor. *Mol Immunol* (2011) 50(1–2):35–41. doi:10.1016/j.molimm.2011.11.013
55. Ahani R, Roohvand F, Cohan RA, Etemadzadeh MH, Mohajel N, Behdani M, et al. Sindbis virus-pseudotyped lentiviral vectors carrying VEGFR2-specific nanobody for potential transductional targeting of tumor vasculature. *Mol Biotechnol* (2016) 58:738–47. doi:10.1007/s12033-016-9973-7
56. Ma L, Gu K, Zhang CH, Chen XT, Jiang Y, Melcher K, et al. Generation and characterization of a human nanobody against VEGFR-2. *Acta Pharmacol Sin* (2016) 37(6):857–64. doi:10.1038/aps.2016.2
57. Fischer C, Jonckx B, Mazzone M, Zacchigna S, Loges S, Pattarini L, et al. Anti-PlGF inhibits growth of VEGF(R)-inhibitor-resistant tumors without affecting healthy vessels. *Cell* (2007) 131(3):463–75. doi:10.1016/j.cell.2007.08.038
58. Bower KE, Lam SN, Oates BD, Del Rosario JR, Corner E, Osothprarop TF, et al. Evolution of potent and stable placental-growth-factor-1-targeting CovX-bodies from phage display peptide discovery. *J Med Chem* (2011) 54(5):1256–65. doi:10.1021/jm101226k
59. Taylor AP, Goldenberg DM. Role of placenta growth factor in malignancy and evidence that an antagonistic PlGF/Flt-1 peptide inhibits the growth and metastasis of human breast cancer xenografts. *Mol Cancer Ther* (2007) 6(2):524–31. doi:10.1158/1535-7163.MCT-06-0461
60. Martinsson-Niskanen T, Riisbro R, Larsson L, Winstedt L, Stenberg Y, Pakola S, et al. Monoclonal antibody TB-403: a first-in-human, phase I, double-blind, dose escalation study directed against placental growth factor in healthy male subjects. *Clin Ther* (2011) 33(9):1142–9. doi:10.1016/j.clinthera.2011.08.007
61. Lassen U, Chinot OL, McBain C, Mau-Sørensen M, Larsen VA, Barrie M, et al. Phase 1 dose-escalation study of the antiplacental growth factor monoclonal antibody RO5323441 combined with bevacizumab in patients with recurrent glioblastoma. *Neuro Oncol* (2015) 17(7):1007–15. doi:10.1093/neuonc/nov019
62. Solomon SD, Lindsley K, Vedula SS, Krzystolik MG, Hawkins BS. Anti-vascular endothelial growth factor for neovascular age-related macular degeneration. *Cochrane Database Syst Rev* (2014) 8:CD005139. doi:10.1002/14651858.CD005139.pub3
63. Pruszynski M, Koumarianou E, Vaidyanathan G, Revets H, Devoogdt N, Lahoutte T, et al. Improved tumor targeting of anti-HER2 nanobody through N-succinimidyl 4-guanidinomethyl-3-iodobenzoate radiolabeling. *J Nucl Med* (2014) 55(4):650–6. doi:10.2967/jnumed.113.127100
64. Vaneycken I, Devoogdt N, Van Gassen N, Vincke C, Xavier C, Wernery U, et al. Preclinical screening of anti-HER2 nanobodies for molecular imaging of breast cancer. *FASEB J* (2011) 25(7):2433–46. doi:10.1096/fj.10-180331

65. Vosjan MJ, Vercammen J, Kolkman JA, Stigter-van Walsum M, Revets H, van Dongen GA. Nanobodies targeting the hepatocyte growth factor: potential new drugs for molecular cancer therapy. *Mol Cancer Ther* (2012) 11(4): 1017–25. doi:10.1158/1535-7163.MCT-11-0891
66. Tabernero J. The role of VEGF and EGFR inhibition: implications for combining anti-VEGF and anti-EGFR agents. *Mol Cancer Res* (2007) 5(3):203–20. doi:10.1158/1541-7786.MCR-06-0404
67. Gainkam LO, Huang L, Caveliers V, Keyaerts M, Hernot S, Vaneycken I, et al. Comparison of the biodistribution and tumor targeting of two 99mTc-labeled anti-EGFR nanobodies in mice, using pinhole SPECT/micro-CT. *J Nucl Med* (2008) 49(5):788–95. doi:10.2967/jnumed.107.048538
68. Huang L, Gainkam LO, Caveliers V, Vanhove C, Keyaerts M, De Baetselier P, et al. SPECT imaging with 99mTc-labeled EGFR-specific nanobody for in vivo monitoring of EGFR expression. *Mol Imaging Biol* (2008) 10(3):167–75. doi:10.1007/s11307-008-0133-8
69. Tchouate Gainkam LO, Caveliers V, Devoogdt N, Vanhove C, Xavier C, Boerman O, et al. Localization, mechanism and reduction of renal retention of technetium-99m labeled epidermal growth factor receptor-specific nanobody in mice. *Contrast Media Mol Imaging* (2011) 6(2):85–92. doi:10.1002/cmmi.408
70. Gainkam LOT, Keyaerts M, Caveliers V, Devoogdt N, Vanhove C, Van Grunsven L, et al. Correlation between epidermal growth factor receptor-specific nanobody uptake and tumor burden: a tool for noninvasive monitoring of tumor response to therapy. *Mol Imaging Biol* (2011) 13(5):940–8. doi:10.1007/s11307-010-0428-4
71. Yang WH, Chen JC, Hsu KH, Lin CY, Wang SW, Wang SJ, et al. Leptin increases VEGF expression and enhances angiogenesis in human chondrosarcoma cells. *Biochim Biophys Acta* (2014) 1840(12):3483–93. doi:10.1016/j.bbagen.2014.09.012
72. Saxena NK, Sharma D. Leptin-signaling pathways as therapeutic targets in cancer. In: Reizes O, Berger N, editors. *Adipocytokines, Energy Balance, and Cancer*. Cham: Springer (2017). p. 67–87.
73. McMurphy T, Xiao R, Magee D, Slater A, Zabeau L, Tavernier J, et al. The anti-tumor activity of a neutralizing nanobody targeting leptin receptor in a mouse model of melanoma. *PLoS One* (2014) 9(2):e89895. doi:10.1371/journal.pone.0089895
74. Nassiri F, Cusimano MD, Scheithauer BW, Rotondo F, Fazio A, Yousef GM, et al. Endoglin (CD105): a review of its role in angiogenesis and tumor diagnosis, progression and therapy. *Anticancer Res* (2011) 31(6):2283–90.
75. Karzai FH, Apolo AB, Cao L, Madan RA, Adelberg DE, Parnes H, et al. A phase I study of TRC105 anti-endoglin (CD105) antibody in metastatic castration-resistant prostate cancer. *BJUInt* (2015) 116(4):546–55. doi:10.1111/bju.12986
76. Ahmadvand D, Rasaee MJ, Rahbarizadeh F, Kontermann RE, Sheikholislami F. Cell selection and characterization of a novel human endothelial cell specific nanobody. *Mol Immunol* (2009) 46(8–9):1814–23. doi:10.1016/j.molimm.2009.01.021
77. Ahmadvand D, Rasaee MJ, Rahbarizadeh F, Mohammadi M. Production and characterization of a high-affinity nanobody against human endoglin. *Hybridoma (Larchmt)* (2008) 27(5):353–60. doi:10.1089/hyb.2008.0014
78. Organ SL, Tsao MS. An overview of the c-MET signaling pathway. *Ther Adv Med Oncol* (2011) 3(1 Suppl):S7–19. doi:10.1177/1758834011422556
79. Oh D-Y, Bang Y-J. Antibodies that inhibit specific cellular pathways in gastric cancer. In: Kerr D, Johnson R, editors. *Immunotherapy for Gastrointestinal Cancer*. Cham: Springer (2017). p. 101–13.
80. Garber K. Bispecific antibodies rise again. *Nat Rev Drug Discov* (2014) 13(11):799. doi:10.1038/nrd4478
81. Gherardi E, Birchmeier W, Birchmeier C, Vande Woude G. Targeting MET in cancer: rationale and progress. *Nat Rev Cancer* (2012) 12(2):89–103. doi:10.1038/nrc3205
82. Prat M, Oltolina F, Basilico C. Monoclonal antibodies against the MET/HGF receptor and its ligand: multitask tools with applications from basic research to therapy. *Biomedicines* (2014) 2(4):359–83. doi:10.3390/biomedicines2040359
83. Slordahl TS, Denayer T, Moen SH, Standal T, Borset M, Ververken C, et al. Anti-c-MET nanobody – a new potential drug in multiple myeloma treatment. *Eur J Haematol* (2013) 91(5):399–410. doi:10.1111/ejh.12185
84. Heukers R, Altintas I, Raghoenath S, De Zan E, Pepermans R, Roovers RC, et al. Targeting hepatocyte growth factor receptor (Met) positive tumor cells using internalizing nanobody-decorated albumin nanoparticles. *Biomaterials* (2014) 35(1):601–10. doi:10.1016/j.biomaterials.2013.10.001
85. Yarden Y, Sliwkowski MX. Untangling the ErbB signalling network. *Nat Rev Mol Cell Biol* (2001) 2(2):127–37. doi:10.1038/35052073
86. Arteaga CL. The epidermal growth factor receptor: from mutant oncogene in nonhuman cancers to therapeutic target in human neoplasia. *J Clin Oncol* (2001) 19(18 Suppl):32S–40S.
87. Laskin JJ, Sandler AB. Epidermal growth factor receptor inhibitors in lung cancer therapy. *Semin Respir Crit Care Med* (2004) 25(Suppl 1):17–27. doi:10.1055/s-2004-829641
88. Ellis LM. Epidermal growth factor receptor in tumor angiogenesis. *Hematol Oncol Clin North Am* (2004) 18(5):1007–21. doi:10.1016/j.hoc.2004.06.002
89. Roovers RC, Laeremans T, Huang L, De Taeye S, Verkleij AJ, Revets H, et al. Efficient inhibition of EGFR signaling and of tumour growth by antagonistic anti-EFGR Nanobodies. *Cancer Immunol Immunother* (2007) 56(3):303–17. doi:10.1007/s00262-006-0180-4
90. Roovers RC, Vosjan MJ, Laeremans T, el Khoulati R, de Bruin RC, Ferguson KM, et al. A biparatopic anti-EGFR nanobody efficiently inhibits solid tumour growth. *Int J Cancer* (2011) 129(8):2013–24. doi:10.1002/ijc.26145
91. Farasat A, Rahbarizadeh F, Hosseinzadeh G, Sajjadi S, Kamali M, Keihan AH. Affinity enhancement of nanobody binding to EGFR: in silico site-directed mutagenesis and molecular dynamics simulation approaches. *J Biomol Struct Dyn* (2016) 35(8):1710–28. doi:10.1080/07391102.2016.1192065
92. Menard S, Casalini P, Campiglio M, Pupa S, Agresti R, Tagliabue E. HER2 overexpression in various tumor types, focussing on its relationship to the development of invasive breast cancer. *Ann Oncol* (2001) 12(Suppl 1):S15–9. doi:10.1093/annonc/12.suppl_1.S15
93. Santin AD, Bellone S, Roman JJ, McKenney JK, Pecorelli S. Trastuzumab treatment in patients with advanced or recurrent endometrial carcinoma overexpressing HER2/neu. *Int J Gynaecol Obstet* (2008) 102(2):128–31. doi:10.1016/j.ijgo.2008.04.008
94. Agus DB, Gordon MS, Taylor C, Natale RB, Karlan B, Mendelson DS, et al. Phase I clinical study of pertuzumab, a novel HER dimerization inhibitor, in patients with advanced cancer. *J Clin Oncol* (2005) 23(11):2534–43. doi:10.1200/JCO.2005.03.184
95. D'Huyvetter M, Xavier C, Caveliers V, Lahoutte T, Muyldermans S, Devoogdt N. Radiolabeled nanobodies as theranostic tools in targeted radionuclide therapy of cancer. *Expert Opin Drug Deliv* (2014) 11(12):1939–54. doi:10.1517/17425247.2014.941803
96. Huhalov A, Chester KA. Engineered single chain antibody fragments for radioimmunotherapy. *Q J Nucl Med Mol Imaging* (2004) 48(4):279–88.
97. Xavier C, Vaneycken I, D'Huyvetter M, Heemskerk J, Keyaerts M, Vincke C, et al. Synthesis, preclinical validation, dosimetry, and toxicity of 68Ga-NOTA-anti-HER2 Nanobodies for iPET imaging of HER2 receptor expression in cancer. *J Nucl Med* (2013) 54(5):776–84. doi:10.2967/jnumed.112.111021
98. D'Huyvetter M, Vincke C, Xavier C, Aerts A, Impens N, Baatout S, et al. Targeted radionuclide therapy with A 177Lu-labeled anti-HER2 nanobody. *Theranostics* (2014) 4(7):708–20. doi:10.7150/thno.8156
99. D'Huyvetter M, Aerts A, Xavier C, Vaneycken I, Devoogdt N, Gijs M, et al. Development of 177Lu-nanobodies for radioimmunotherapy of HER2-positive breast cancer: evaluation of different bifunctional chelators. *Contrast Media Mol Imaging* (2012) 7(2):254–64. doi:10.1002/cmmi.491
100. Van de Broek B, Devoogdt N, D'Hollander A, Gijs HL, Jans K, Lagae L, et al. Specific cell targeting with nanobody conjugated branched gold nanoparticles for photothermal therapy. *ACS Nano* (2011) 5(6):4319–28. doi:10.1021/nn1023363
101. D'Hollander A, Jans H, Velde GV, Verstraete C, Massa S, Devoogdt N, et al. Limiting the protein corona: a successful strategy for in vivo active targeting of anti-HER2 nanobody-functionalized nanostars. *Biomaterials* (2017) 123:15–23. doi:10.1016/j.biomaterials.2017.01.007
102. Pruszynski M, Koumarianou E, Vaidyanathan G, Revets H, Devoogdt N, Lahoutte T, et al. Targeting breast carcinoma with radioiodinated anti-HER2 nanobody. *Nucl Med Biol* (2013) 40(1):52–9. doi:10.1016/j.nucmedbio.2012.08.008
103. Jamnani FR, Rahbarizadeh F, Shokrgozar MA, Ahmadvand D, Mahboudi F, Sharifzadeh Z. Targeting high affinity and epitope-distinct oligoclonal

nanobodies to HER2 over-expressing tumor cells. *Exp Cell Res* (2012) 318(10):1112–24. doi:10.1016/j.yexcr.2012.03.004
104. Jamnani FR, Rahbarizadeh F, Shokrgozar MA, Mahboudi F, Ahmadvand D, Sharifzadeh Z, et al. T cells expressing VHH-directed oligoclonal chimeric HER2 antigen receptors: towards tumor-directed oligoclonal T cell therapy. *Biochim Biophys Acta* (2014) 1840(1):378–86. doi:10.1016/j.bbagen.2013.09.029
105. Jain M, Gupta S, Kaur S, Ponnusamy MP, Batra SK. Emerging trends for radioimmunotherapy in solid tumors. *Cancer Biother Radiopharm* (2013) 28(9):639–50. doi:10.1089/cbr.2013.1523
106. Navarro-Teulon I, Lozza C, Pelegrin A, Vives E, Pouget JP. General overview of radioimmunotherapy of solid tumors. *Immunotherapy* (2013) 5(5):467–87. doi:10.2217/imt.13.34
107. Balkwill FR. The chemokine system and cancer. *J Pathol* (2012) 226(2): 148–57. doi:10.1002/path.3029
108. Maussang D, Mujić-Delić A, Descamps FJ, Stortelers C, Vanlandschoot P, Stigter-van Walsum M, et al. Llama-derived single variable domains (nanobodies) directed against chemokine receptor CXCR7 reduce head and neck cancer cell growth in vivo. *J Biol Chem* (2013) 288(41):29562–72. doi:10.1074/jbc.M113.498436
109. Lin Z, Zhang Q, Luo W. Angiogenesis inhibitors as therapeutic agents in cancer: challenges and future directions. *Eur J Pharmacol* (2016) 793:76–81. doi:10.1016/j.ejphar.2016.10.039

Conflict of Interest Statement: The authors declare that the research was conducted in the absence of any commercial or financial relationships that could be construed as a potential conflict of interest.

The reviewer JT and handling editor declared their shared affiliation.

frontiers in Immunology

PERSPECTIVE
published: 01 September 2017
doi: 10.3389/fimmu.2017.01073

VHH-Based Bispecific Antibodies Targeting Cytokine Production

*Maxim A. Nosenko[1,2], Kamar-Sulu N. Atretkhany[1,2], Vladislav V. Mokhonov[1,3], Grigory A. Efimov[2,4], Andrey A. Kruglov[2,3,5], Sergei V. Tillib[2,6], Marina S. Drutskaya[1,2] and Sergei A. Nedospasov[1,2,3,5]**

[1] Engelhardt Institute of Molecular Biology, Russian Academy of Sciences, Moscow, Russia, [2] Lomonosov Moscow State University, Moscow, Russia, [3] Lobachevsky State University of Nizhny Novgorod, Nizhny Novgorod, Russia, [4] National Research Center for Hematology, Moscow, Russia, [5] German Rheumatism Research Center, Leibniz Institute, Berlin, Germany, [6] Institute of Gene Biology, Russian Academy of Sciences, Moscow, Russia

Proinflammatory cytokines, such as TNF, IL-6, and IL-1, play pathogenic roles in multiple diseases and are attractive targets for biologic drugs. Because proinflammatory cytokines possess non-redundant protective and immunoregulatory functions, their systemic neutralization carries the potential for unwanted side effects. Therefore, next-generation anti-cytokine therapies would seek to selectively neutralize pathogenic cytokine signaling, leaving normal function intact. Fortunately, the biology of proinflammatory cytokines provides several such opportunities. Here, we discuss various applications of bispecific antibodies targeting cytokines with specific focus on selective TNF neutralization targeted directly to the surface of specific populations of monocytes and macrophages. These bispecific antibodies combine an anti-TNF V_HH with V_HHs or scFvs directed against abundant surface molecules on myeloid cells and serve to limit the bioavailability of TNF produced by these cells. Such reagents may become prototypes of a novel class of anti-cytokine biologics.

Keywords: TNF, IL-6, macrophages, single-chain antibodies, V_HH

OPEN ACCESS

Edited by:
Kevin A. Henry, National Research Council Canada, Canada

Reviewed by:
Hans De Haard, Argenx BVBA, Belgium
Luis Alvarez-Vallina, Aarhus University, Denmark

****Correspondence:***
Sergei A. Nedospasov
sergei.nedospasov@gmail.com

Specialty section:
This article was submitted to Vaccines and Molecular Therapeutics, a section of the journal Frontiers in Immunology

Received: *29 April 2017*
Accepted: *17 August 2017*
Published: *01 September 2017*

Citation:
Nosenko MA, Atretkhany KN, Mokhonov VV, Efimov GA, Kruglov AA, Tillib SV, Drutskaya MS and Nedospasov SA (2017) VHH-Based Bispecific Antibodies Targeting Cytokine Production. Front. Immunol. 8:1073. doi: 10.3389/fimmu.2017.01073

Many currently used therapeutic antibodies represent antagonists or inhibitors of signaling cascades that are known to be pathogenic in a particular disease state. Examples include anti-cytokine therapies and immune checkpoint inhibitors, both of which have resulted in major advances in the treatment of autoimmune diseases and cancer. One common problem with many of such inhibitors, when applied systemically, is incomplete discrimination of "pathogenic" signaling from "physiological" signaling, the latter being beneficial for the patient. Therefore, most current therapies have unwanted side effects resulting from collateral damage to beneficial or protective signaling cascades. This problem can be potentially addressed through additional specificity conferred by more sophisticated inhibitory antibodies that target their cognate antigens only in a particular organ or cell lineage.

Therapeutic bispecific antibodies have showed efficacy in both experimental animal models and in clinical trials (1), finding applications in cancer immunotherapy (2) as well as in treatment of autoimmune diseases (3) and hemophilia (4). Examples include: (i) bispecific T-cell engagers (5) that redirect the activity of CD3+ cytotoxic T lymphocytes against CD19+ leukemias and lymphomas (6) and EpCAM+ solid tumors (7); (ii) bispecific NK-cell engagers that redirect the activity of CD16+ natural killer cells against CEA+ solid tumors (8); (iii) bispecific molecules composed of a CD19-binding moiety and an anti-CD47 immune checkpoint inhibitor, allowing for selective CD47 blockade on malignant B cells (9); (iv) bispecific molecules composed of an a β-secretase (BACE-1)-inhibiting moiety and an anti-transferrin receptor "trojan" moiety to facilitate permeation

of the blood–brain barrier (10); and (v) bispecific molecules composed of an anti-HIV gp41 glycoprotein moiety and an anti-CD89 moiety, designed to facilitate virus clearance by blood neutrophils (11). Several designs of bispecific antibodies have been employed, including chemically conjugated monoclonal antibodies, quadroma-produced antibodies, or genetically fused recombinant single-chain Fvs (12). The lattermost molecules lack the Fc region and thus have very short serum half-lives. Recently, an interesting solution to the problem of rapid clearance of these molecules was proposed in the form of RNA delivery (13). Overall, more than a dozen bispecific antibodies have now been evaluated in clinical trials.

Several bispecific antibodies targeting cytokines have been described (14), allowing for dual cytokine blockade (15–18) as well as targeted cytokine neutralization on cytokine-producing cells (19) or at particular anatomical sites, such as inflamed joints (20). One important target in anti-cytokine therapy of autoimmune diseases is TNF, and many systemic anti-TNF biologics are approved for clinical use. There are several experimental reagents that have added a second specificity to an existing anti-TNF moiety. For example, a bispecific antibody directed against TNF and IL-17A was shown to be effective for the treatment of psoriasis (21). A TNF inhibitor with additional specificity to ROS-modified collagen allowed for targeted TNF inhibition in arthritic joints (20). Coppieters et al. (22) reported a highly efficient bispecific antibody that was able to bind TNF as well as an abundant serum protein (albumin), thus resulting in a significant increase of the antibody's half-life *in vivo*. Two different inhibitors of TNFRI signaling, each with a second specificity to serum albumin for half-life extension *in vivo*, are effective in mouse models of Crohn's disease and arthritis (23–25). Other studies have achieved longer half-lives and increased potencies of anti-TNF inhibitors by various types of dimerization or oligomerization (26–28) allowing the demonstration of their biological activity in mouse disease models. Although this was not directly determined, it may be assumed that all of these TNF inhibitors, including bispecifics, neutralized TNF produced by multiple cellular sources in a systemic fashion.

In our studies employing conditional gene targeting, we found that TNF produced by myeloid cells is pathogenic in several experimental mouse disease models (29–32). Assuming that TNF from other immune and non-immune sources may possess beneficial functions (33–35), we wanted to design an approach to pharmacologically limit TNF production only by myeloid cells. To this end, we designed, produced, and evaluated bispecific antibodies that bind TNF with one arm and engage surface molecules abundantly expressed on myeloid cells through another arm. Two such potential surface markers—F4/80 (EMR1, the product of the *Adgre1* gene) and CD11b (Mac-1a, Integrin αM, the product of the *Itgam* gene; expressed by myeloid cells, NK, and some other cells) can be employed.

The discovery of heavy-chain-only antibodies in *Camelidae* (36) led to the development of new technologies based on the ability to generate modular, high affinity binders (V_HHs) specific to almost any protein. One particular aspect that drew our attention was the usefulness of V_HHs in creating bispecific reagents, as two or even three V_HHs can be easily combined in a single polypeptide chain by the methods of genetic engineering (19) and expressed in prokaryotic systems. In order to specifically target TNF produced by myeloid cells, we have initially utilized a single-chain antibody to murine F4/80, which is exclusively expressed on myeloid cells with abundant expression on the surface of all mature macrophages (including microglia), Langerhans cells, and to a lesser degree on blood monocytes (37). We subsequently generated a novel V_HH by immunizing a Bactrian camel with recombinant murine F4/80 and genetically fused it to an anti-hTNF V_HH (19). Because of the specificity of this reagent to human TNF, all subsequent *in vitro* and *in vivo* experiments were performed using human TNF knock-in mice (38). Collectively, for all these bispecific antibodies, a term myeloid cell-specific TNF inhibitor (MYSTI) has been coined. **Figure 1** outlines the design, purification, and experimental protocols for evaluation of these anti-TNF bispecific V_HH-based reagents.

Using flow cytometry, we found that MYSTI (exemplified here by MYSTI-2) binds to the surface of murine macrophages, competes with another anti-F4/80 reagent for this binding (**Figures 2A,B**), and attracts exogenously added human TNF to the surface of macrophages (**Figure 2C**). We then performed experiments to prove that endogenously produced TNF can also be retained on the cell surface. To this end, bone marrow-derived macrophages from humanized TNF knock-in (hTNF KI) mice (38) were incubated with MYSTI-2, or with control TNF-neutralizing antibodies lacking anti-F4/80 targeting module (referred here as systemic TNF inhibitor or STI), then washed and activated with LPS. As shown in **Figure 2D**, the amount of biologically active hTNF released into culture medium is significantly lower in the presence of MYSTI as compared to STI, suggesting that MYSTI indeed retained hTNF on the surface of macrophages and may limit its systemic release *in vivo*.

To get a better insight into the fate of hTNF and of MYSTI after its binding to the surface of macrophage, we utilized confocal microscopy, as outlined in **Figures 1C–F**. As expected, FITC-labeled MYSTI could stain these cells and was detected on the surface of activated macrophages as early as 15 min following incubation and—interestingly—up to 18 h later although in diminished amounts, consistent with our previous results (**Figure 2E**, top row and data not shown). In contrast, STI briefly stained activated macrophages after 15 min of incubation, while upon subsequent washing, such staining rapidly disappeared (**Figure 2E**, bottom row and data not shown). Since we did not detect binding of STI to unstimulated macrophages (data not shown), we hypothesized that such staining is due to recognition of transmembrane TNF (tmTNF) on the surface of activated macrophages. MYSTI was able to bind and retain human TNF produced by macrophages from hTNF KI mice (as indicated by the arrows in **Figure 2E**, top row) and exogenously added human TNF (Figure. 2F). We also detected rapid internalization of MYSTI (**Figure 2F**) starting from approximately 30 min of incubation with macrophages. Both unbound (**Figure 2F**, left) and TNF-bound (**Figure 2F**, right) bispecific antibodies were internalized, suggesting that internalization does not require TNF recognition by MYSTI. Exogenously added TNF, labeled by a secondary PE-conjugated antibody, could be detected on the surface of macrophages for at least 1–2 h (**Figure 2F** and data not shown).

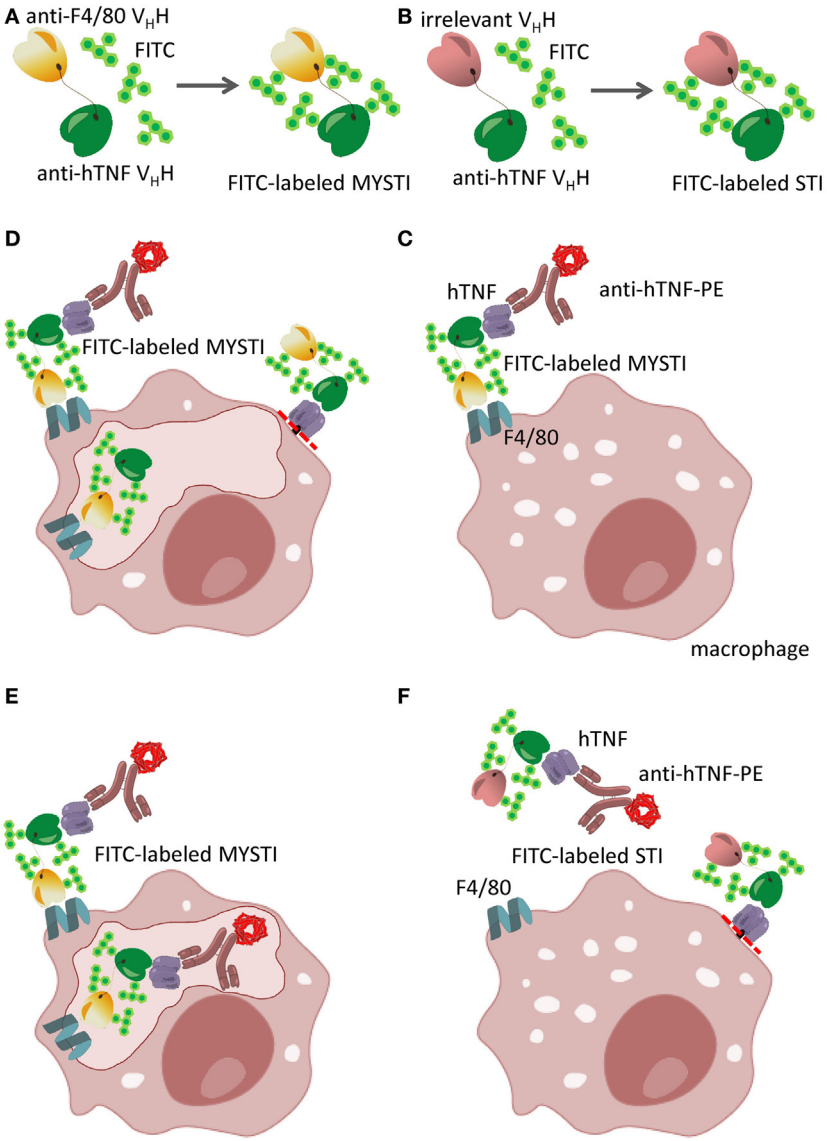

FIGURE 1 | Schematic representation of bispecific anti-cytokine antibodies exemplified by myeloid-specific TNF inhibitors (MYSTI). **(A,B)** Generation of FITC-labeled bispecific antibody composed of anti-hTNF V_HH and anti-F4/80 V_HH (MYSTI, A) and control antibody composed of the same anti-hTNF V_HH and irrelevant V_HH [Systemic TNF Inhibitor, STI, **(B)**]. Briefly, antibodies were expressed and purified as previously described (19) and were subsequently labeled with FITC. Calculated F/P ratio was approximately four FITC molecules per protein molecule. **(C–F)** Schematic representation of MYSTI **(C–E)** and STI **(F)** binding to macrophages analyzed by flow cytometry and confocal microscopy. FITC-labeled MYSTI binds specifically to F4/80 on the surface of macrophages and can bind and retain exogenously added hTNF or hTNF produced by activated cells as detected by anti-hTNF phycoerythrin (PE)-labeled antibody (Miltenyi Biotec). This resulted in surface staining of macrophages both with FITC and PE **(C)**. MYSTI can be quickly internalized by macrophages resulting in intracellular FITC staining only **(D)**, or when hTNF was added exogenously—double staining for both FITC and PE **(E)**. STI did not bind to macrophages, as suggested by the absence of FITC or PE staining **(F)**. Red dotted line indicates the position of tmTNF cleavage by TACE (ADAM17). Adapted from (19).

Based on the encouraging finding that MYSTI, an antibody with two V_HH domains, may be sufficiently long-lived on the surface of cytokine-producing cells, we evaluated these reagents *in vivo*. In LPS/D-Gal lethal toxicity model, pathogenic TNF is known to be produced by myeloid cells (39) and animals become moribund within 6–8 h (19). In this model, administration of MYSTI at 3 mg/kg completely protected mice, while the same dose of the control reagents (such as STI that contained exactly the same TNF-binding and neutralizing V_HH module) failed to do so (19). Moreover, the results suggest that MYSTI retained its protective ability even at 1–1.5 mg/kg dose and modification with FITC did not affect its properties (**Figure 2G** and data not shown), thus allowing us to further investigate its fate *in vivo*. As an additional control, we used Infliximab as a systemic TNF inhibitor control, which also protected mice against LPS/D-Gal-induced hepatotoxicity at the dose of 1.5 mg/kg (data not shown); however, differences in molecular weight and avidity should be taken in account when comparing full-length systemic

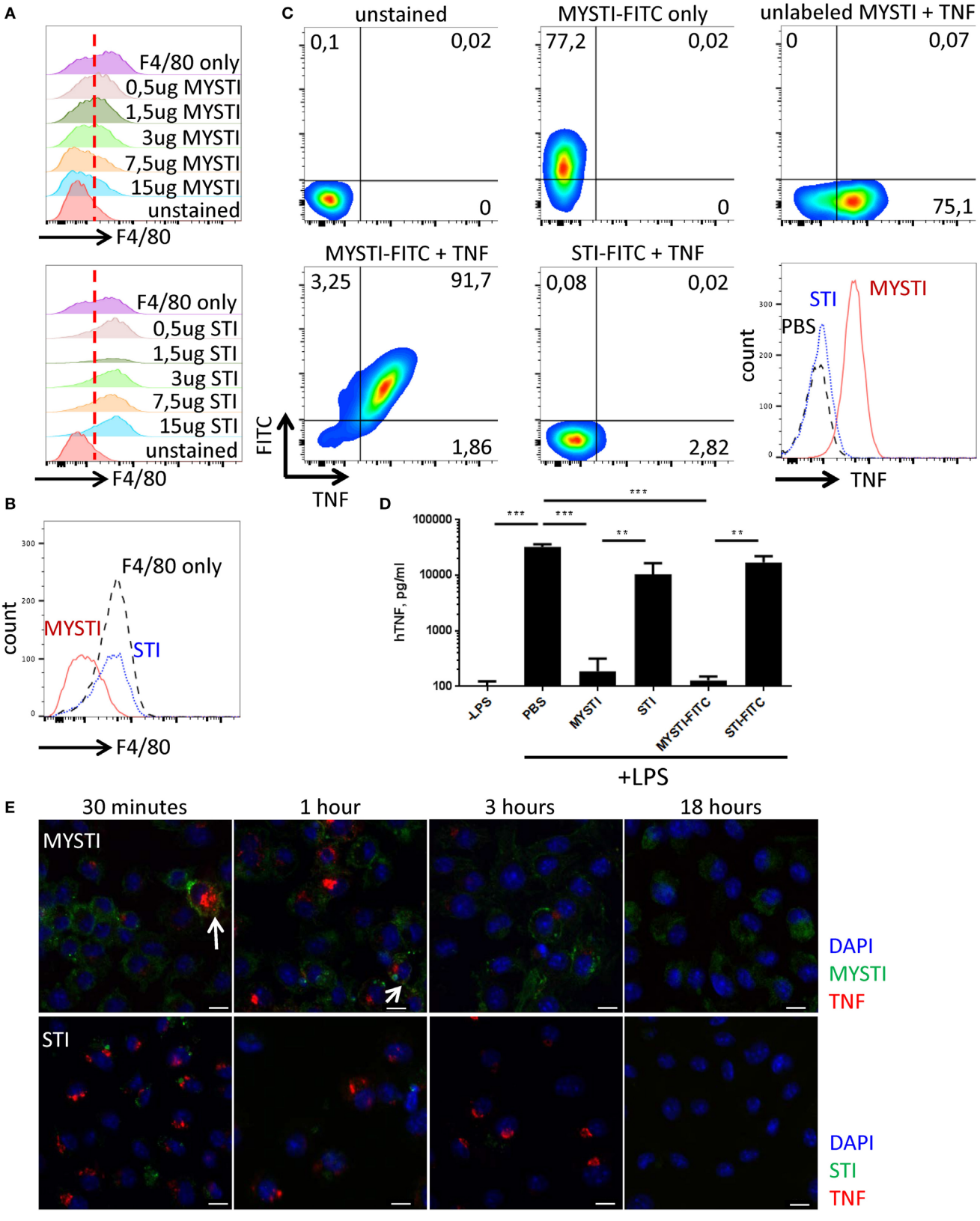

FIGURE 2 | Continued

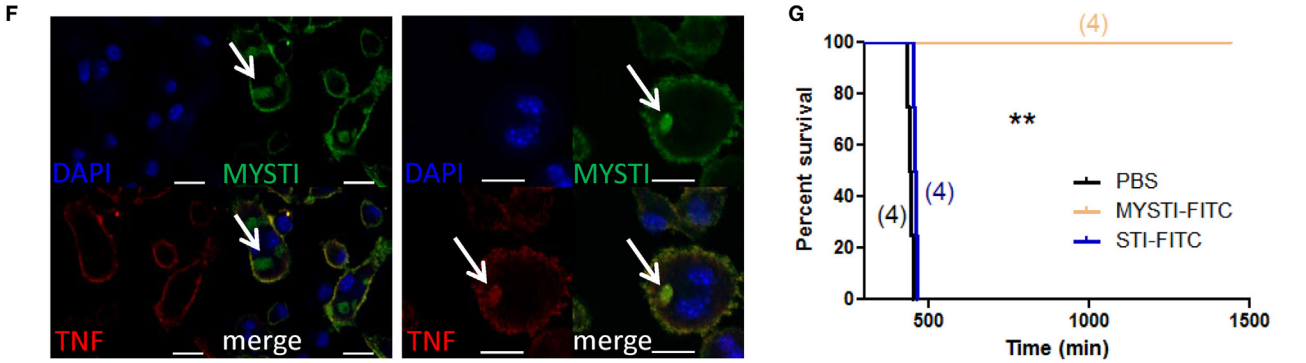

FIGURE 2 | Characterization of MYSTI and STI interaction with macrophages *in vitro* and *in vivo*. **(A)** MYSTI, but not STI, competes with anti-F4/80 antibody for binding sites resulting in reduced staining for F4/80. Staining of macrophages with anti-F4/80 antibody in the presence of indicated concentrations of MYSTI (top panel) or STI (bottom panel). Red dotted line splits $F4/80^-$ and $F4/80^+$ cells on the left and on the right, respectively. Briefly, bone marrow-derived macrophages were simultaneously incubated with anti-F4/80 antibody (clone BM8 that competed for binding to F4/80 with anti F4/80 V_HH, used in MYSTI) and indicated amounts of MYSTI or STI. All cells were gated as $ViabilityDye^-CD11b^+$. **(B)** Staining of macrophages with anti-F4/80 only or in the presence of MYSTI or STI. Data indicate that MYSTI selectively binds to F4/80. **(C)** MYSTI, but not STI, binds to the surface of macrophages and retains exogenously added hTNF. Surface staining of macrophages with MYSTI or STI and hTNF. Top row represents unstained or single stained cells as controls. Bottom row represents staining of macrophages with MYSTI-FITC and hTNF (left), STI-FITC and hTNF (middle), and a summarizing histogram of hTNF staining (right). Briefly, bone marrow-derived macrophages were subsequently incubated with MYSTI or STI followed by recombinant human TNF and with anti-hTNF antibody incubations. All cells were gated as VD^-CD11b^+. **(D)** MYSTI, but not STI, prevents hTNF release into the culture medium by LPS-stimulated macrophages. BMDM from hTNFKI mice were cultured with MYSTI or STI antibodies or PBS, washed once, and stimulated with 100 ng/ml of LPS from *E. coli*. Release of hTNF into culture medium was measured 4 h following induction with LPS using Ready-Set-Go ELISA kit (eBioscience). $^{**}p < 0.01$; $^{***}p < 0.001$ in one-way ANOVA. **(E)** Dynamics of MYSTI and STI staining on LPS-activated macrophages as revealed by confocal microscopy. Briefly, macrophages were activated with 100 ng/ml of LPS for 3 h, followed by incubation with FITC-labeled MYSTI or STI for 15 min, then washed, and fixed at indicated time points. Fixed cells were consequently permeabilized and stained with anti-hTNF Ab labeled with PE. Starting from 30 min of incubation, MYSTI could be detected both on macrophage surface and inside the cells, while weak binding of STI was observed only after 30 min of incubation. Arrows show co-staining of MYSTI and anti-hTNF. Scale bars—10 μm. **(F)** MYSTI is internalized by macrophages. Confocal microscope images of macrophages stained with MYSTI (green), anti-hTNF (red), and counterstained with DAPI (blue). Briefly, cells were consequently incubated with MYSTI-FITC, recombinant hTNF, and anti-hTNF labeled with PE and then fixed. On each of the two images, top left part represents DAPI staining, top right—MYSTI-FITC, bottom left—anti-hTNF-PE, and bottom right—merged picture. Arrows show internalized MYSTI bound (right image) or not bound to hTNF (left image). Scale bars—20 μm. **(G)** FITC-labeled MYSTI retains its ability to protect mice in the model of LPS/D-Gal-induced hepatotoxicity. Briefly, mice were injected i.p. with 1.5 mg/kg, STI, or PBS and after 30 min were injected with lethal dose of LPS/D-Gal.

TNF-inhibitors with MYSTI. Additionally, MYSTI was active in anti-collagen antibody transfer arthritis model (data not shown). Another potential target for the "second specificity" is CD11b for which a V_HH was recently reported (40). However, expression of this molecule is not strictly restricted to myeloid cells (41, 42) and, additionally, F4/80 appears to be expressed at significantly higher levels, as compared to CD11b [according to mass spectrometric database (43)].

CONCLUDING REMARKS AND FUTURE PERSPECTIVES

The remarkable success of anti-cytokine therapy in treating autoimmune and other diseases suggests that bispecific antibodies targeting pro-inflammatory cytokines, such as TNF or IL-6, will be developed and used. V_HH technology has provided attractive antigen-binding modules for such bifunctional antibodies that simplify their engineering, expression, and purification. The central issue here is the nature of the "second specificity." These may include additional anti-cytokine moieties or binding modules directing these reagents to either specific organs or cell types. Our own studies explored the possibility of targeting anti-cytokine antibodies to the surface of specific TNF-producing cell types, as we believe that some cells represent predominantly pathogenic sources of cytokine, at least in a particular disease or disease state. We continue to evaluate the features of selective TNF inhibitors with a focus on their *in vivo* ability to bind and neutralize TNF produced by myeloid cells, but not by other cell types. We aim to expand this concept to other pro-inflammatory cytokines, such as IL-6, using V_HHs generated against human IL-6 (44), although the safety of myeloid-specific IL-6 inhibitors needs to be assessed with regards to IL-6's role in the development of lymphocytes (45). This approach is a pharmacological analog of inducible cell type-restricted gene ablation *in vivo*, with the advantage that the effects of antibodies are reversible and more relevant for preclinical evaluation. Although ongoing studies are mostly performed in animal models, one may expect that some of these V_HH-based multispecific biologics will be eventually approved for human therapy, as has already happened for several such reagents utilizing more conventional antigen-binding modules, such as scFv.

ETHICS STATEMENT

All manipulations with animals were carried out in accordance with recommendations in the Guide for the Care and Use of Laboratory Animals (NRC 2011), the European Convention for the Protection of Vertebrate Animals Used for Experimental and

Other Scientific Purposes, Council of Europe (ETS 123), and "The Guidelines for Manipulations with Experimental Animals" (the decree of the Presidium of the Russian Academy of Sciences of April 02, 1980, no. 12000-496). All animal procedures were approved by Scientific Council of the Engelhardt Institute of Molecular Biology.

AUTHOR CONTRIBUTIONS

MN, K-SA, GE, AK, MD, and SN designed the research and analyzed the data; MN, K-SA, and MD performed the experiments; VM, GE, and ST developed and produced bispecific reagents; all authors contributed to writing the manuscript.

ACKNOWLEDGMENTS

The authors would like to thank Ruslan Zvartsev for help in performing experiments. They would also like to thank both reviewers and editor for helpful comments, critiques, and suggestions.

FUNDING

This study was supported by the Russian Science Foundation grant #14-50-00060. Experiments utilizing flow cytometry using BD FACSCantoII (**Figures 2A–C**) were supported by the Russian Science Foundation grant #14-25-00160.

REFERENCES

1. Kontermann RE, Brinkmann U. Bispecific antibodies. *Drug Discov Today* (2015) 20:838–47. doi:10.1016/j.drudis.2015.02.008
2. Chen S, Li J, Li Q, Wang Z. Bispecific antibodies in cancer immunotherapy. *Hum Vaccin Immunother* (2016) 12:2491–500. doi:10.1080/21645515.2016.1187802
3. Baker KF, Isaacs JD. Novel therapies for immune-mediated inflammatory diseases: what can we learn from their use in rheumatoid arthritis, spondyloarthritis, systemic lupus erythematosus, psoriasis, Crohn's disease and ulcerative colitis? *Ann Rheum Dis* (2017). doi:10.1136/annrheumdis-2017-211555
4. Kitazawa T, Igawa T, Sampei Z, Muto A, Kojima T, Soeda T, et al. A bispecific antibody to factors IXa and X restores factor VIII hemostatic activity in a hemophilia A model. *Nat Med* (2012) 18:1570–4. doi:10.1038/nm.2942
5. Zhang X, Yang Y, Fan D, Xiong D. The development of bispecific antibodies and their applications in tumor immune escape. *Exp Hematol Oncol* (2017) 6:12. doi:10.1186/s40164-017-0072-7
6. Wolach O, Stone RM. Blinatumomab for the treatment of Philadelphia chromosome-negative, precursor B-cell acute lymphoblastic leukemia. *Clin Cancer Res* (2015) 21:4262–9. doi:10.1158/1078-0432.CCR-15-0125
7. Heiss MM, Strohlein MA, Jager M, Kimmig R, Burges A, Schoberth A, et al. Immunotherapy of malignant ascites with trifunctional antibodies. *Int J Cancer* (2005) 117:435–43. doi:10.1002/ijc.21165
8. Li J, Zhou C, Dong B, Zhong H, Chen S, Li Q, et al. Single domain antibody-based bispecific antibody induces potent specific anti-tumor activity. *Cancer Biol Ther* (2016) 17:1231–9. doi:10.1080/15384047.2016.1235659
9. Dheilly E, Moine V, Broyer L, Salgado-Pires S, Johnson Z, Papaioannou A, et al. Selective blockade of the ubiquitous checkpoint receptor CD47 is enabled by dual-targeting bispecific antibodies. *Mol Ther* (2017) 25:523–33. doi:10.1016/j.ymthe.2016.11.006
10. Joy Yu Y, Atwal JK, Zhang Y, Tong RK, Wildsmith KR, Tan C, et al. Therapeutic bispecific antibodies cross the blood-brain barrier in nonhuman primates. *Sci Transl Med* (2014) 6:261ra154. doi:10.1126/scitranslmed.3009835
11. Yu X, Duval M, Gawron M, Posner MR, Cavacini LA. Overcoming the constraints of anti-HIV/CD89 bispecific antibodies that limit viral inhibition. *J Immunol Res* (2016) 2016:9425172. doi:10.1155/2016/9425172
12. Kontermann RE. Dual targeting strategies with bispecific antibodies. *MAbs* (2012) 4:182–97. doi:10.4161/mabs.4.2.19000
13. Stadler CR, Bahr-Mahmud H, Celik L, Hebich B, Roth AS, Roth RP, et al. Elimination of large tumors in mice by mRNA-encoded bispecific antibodies. *Nat Med* (2017) 23(7):815–7. doi:10.1038/nm.4356
14. Drutskaya MS, Efimov GA, Kruglov AA, Nedospasov SA. Can we design a better anti-cytokine therapy? *J Leukoc Biol* (2017). doi:10.1189/jlb.3MA0117-025R
15. Torres T, Romanelli M, Chiricozzi A. A revolutionary therapeutic approach for psoriasis: bispecific biological agents. *Expert Opin Investig Drugs* (2016) 25(7):751–4. doi:10.1080/13543784.2016.1187130
16. Kim Y, Yi H, Jung H, Rim YA, Park N, Kim J, et al. A dual target-directed agent against interleukin-6 receptor and tumor necrosis factor α ameliorates experimental arthritis. *Sci Rep* (2016) 6:20150. doi:10.1038/srep20150
17. Fischer JAA, Hueber AJ, Wilson S, Galm M, Baum W, Kitson C, et al. Combined inhibition of tumor necrosis factor α and interleukin-17 as a therapeutic opportunity in rheumatoid arthritis: development and characterization of a novel bispecific antibody. *Arthritis Rheumatol* (2015) 67:51–62. doi:10.1002/art.38896
18. Qi J, Kan F, Ye X, Guo M, Zhang Y, Ren G, et al. A bispecific antibody against IL-1β and IL-17A is beneficial for experimental rheumatoid arthritis. *Int Immunopharmacol* (2012) 14:770–8. doi:10.1016/j.intimp.2012.10.005
19. Efimov GA, Kruglov AA, Khlopchatnikova ZV, Rozov FN, Mokhonov VV, Rose-John S, et al. Cell-type-restricted anti-cytokine therapy: TNF inhibition from one pathogenic source. *Proc Natl Acad Sci U S A* (2016) 113:3006–11. doi:10.1073/pnas.1520175113
20. Hughes C, Faurholm B, Dell'Accio F, Manzo A, Seed M, Eltawil N, et al. Human single-chain variable fragment that specifically targets arthritic cartilage. *Arthritis Rheum* (2010) 62:1007–16. doi:10.1002/art.27346
21. Silacci M, Lembke W, Woods R, Attinger-Toller I, Baenziger-Tobler N, Batey S, et al. Discovery and characterization of COVA322, a clinical-stage bispecific TNF/IL-17A inhibitor for the treatment of inflammatory diseases. *MAbs* (2016) 8:141–9. doi:10.1080/19420862.2015.1093266
22. Coppieters K, Dreier T, Silence K, De Haard H, Lauwereys M, Casteels P, et al. Formatted anti-tumor necrosis factor α VHH proteins derived from camelids show superior potency and targeting to inflamed joints in a murine model of collagen-induced arthritis. *Arthritis Rheum* (2006) 54:1856–66. doi:10.1002/art.21827
23. Steeland S, Puimège L, Vandenbroucke RE, Van Hauwermeiren F, Haustraete J, Devoogdt N, et al. Generation and characterization of small single domain antibodies inhibiting human tumor necrosis factor receptor 1. *J Biol Chem* (2015) 290:4022–37. doi:10.1074/jbc.M114.617787
24. Schmidt EM, Davies M, Mistry P, Green P, Giddins G, Feldmann M, et al. Selective blockade of tumor necrosis factor receptor I inhibits proinflammatory cytokine and chemokine production in human rheumatoid arthritis synovial membrane cell cultures. *Arthritis Rheum* (2013) 65:2262–73. doi:10.1002/art.38055
25. McCann FE, Perocheau DP, Ruspi G, Blazek K, Davies ML, Feldmann M, et al. Selective tumor necrosis factor receptor I blockade is antiinflammatory and reveals immunoregulatory role of tumor necrosis factor receptor II in collagen-induced arthritis. *Arthritis Rheumatol* (2014) 66:2728–38. doi:10.1002/art.38755
26. Conrad U, Plagmann I, Malchow S, Sack M, Floss DM, Kruglov AA, et al. ELPylated anti-human TNF therapeutic single-domain antibodies for prevention of lethal septic shock. *Plant Biotechnol J* (2011) 9:22–31. doi:10.1111/j.1467-7652.2010.00523.x
27. Plagmann I, Chalaris A, Kruglov AA, Nedospasov S, Rosenstiel P, Rose-John S, et al. Transglutaminase-catalyzed covalent multimerization of camelidae anti-human TNF single domain antibodies improves neutralizing activity. *J Biotechnol* (2009) 142:170–8. doi:10.1016/j.jbiotec.2009.04.002

28. Beirnaert E, Desmyter A, Spinelli S, Lauwereys M, Aarden L, Dreier T, et al. Bivalent Llama single-domain antibody fragments against tumor necrosis factor have picomolar potencies due to intramolecular interactions. *Front Immunol* (2017) 8:867. doi:10.3389/fimmu.2017.00867
29. Awad AS, You H, Gao T, Cooper TK, Nedospasov SA, Vacher J, et al. Macrophage-derived tumor necrosis factor-α mediates diabetic renal injury. *Kidney Int* (2015) 88:722–33. doi:10.1038/ki.2015.162
30. Kruglov A, Tumanov A, Grivennikov SI, Shebzukhov YV, Kuchmiy AA, Efimov GA, et al. Modalities of experimental TNF blockade in vivo: mouse models. In: Wallach D, Kovalenko A, Feldmann M, editors. *Advances in TNF Family Research: Proceedings of the 12th International TNF Conference, 2009*. New York, NY: Springer New York (2011). p. 421–31.
31. Kruglov AA, Lampropoulou V, Fillatreau S, Nedospasov SA. Pathogenic and protective functions of TNF in neuroinflammation are defined by its expression in T lymphocytes and myeloid cells. *J Immunol* (2011) 187:5660–70. doi:10.4049/jimmunol.1100663
32. Atretkhany KSN, Nosenko MA, Gogoleva VS, Zvartsev RV, Qin Z, Nedospasov SA, et al. TNF neutralization results in the delay of transplantable tumor growth and reduced MDSC accumulation. *Front Immunol* (2016) 7:147. doi:10.3389/fimmu.2016.00147
33. Tumanov AV, Grivennikov SI, Kruglov AA, Shebzukhov YV, Koroleva EP, Piao Y, et al. Cellular source and molecular form of TNF specify its distinct functions in organization of secondary lymphoid organs. *Blood* (2010) 116:3456–64. doi:10.1182/blood-2009-10-249177
34. Allie N, Grivennikov SI, Keeton R, Hsu N-J, Bourigault M-L, Court N, et al. Prominent role for T cell-derived tumour necrosis factor for sustained control of *Mycobacterium tuberculosis* infection. *Sci Rep* (2013) 3:1809. doi:10.1038/srep01809
35. Kroetsch JT, Levy AS, Zhang H, Aschar-Sobbi R, Lidington D, Offermanns S, et al. Constitutive smooth muscle tumour necrosis factor regulates microvascular myogenic responsiveness and systemic blood pressure. *Nat Commun* (2017) 8:14805. doi:10.1038/ncomms14805
36. Hamers-Casterman C, Atarhouch T, Muyldermans S, Robinson G, Hammers C, Songa EB, et al. Naturally occurring antibodies devoid of light chains. *Nature* (1993) 363:446–8. doi:10.1038/363446a0
37. Austyn JM, Gordon S. F4/80, a monoclonal antibody directed specifically against the mouse macrophage. *Eur J Immunol* (1981) 11:805–15. doi:10.1002/eji.1830111013
38. Olleros ML, Chavez-Galan L, Segueni N, Bourigault ML, Vesin D, Kruglov AA, et al. Control of mycobacterial infections in mice expressing human tumor necrosis factor (TNF) but not mouse TNF. *Infect Immun* (2015) 83:3612–23. doi:10.1128/IAI.00743-15
39. Grivennikov SI, Tumanov AV, Liepinsh DJ, Kruglov AA, Marakusha BI, Shakhov AN, et al. Distinct and nonredundant in vivo functions of TNF produced by T cells and macrophages/neutrophils: protective and deleterious effects. *Immunity* (2005) 22:93–104. doi:10.1016/j.immuni.2004.11.016
40. Rashidian M, Keliher EJ, Bilate AM, Duarte JN, Wojtkiewicz GR, Jacobsen JT, et al. Noninvasive imaging of immune responses. *Proc Natl Acad Sci U S A* (2015) 112:6146–51. doi:10.1073/pnas.1502609112
41. Kawai K, Tsuno NH, Matsuhashi M, Kitayama J, Osada T, Yamada J, et al. CD11b-mediated migratory property of peripheral blood B cells. *J Allergy Clin Immunol* (2005) 116:192–7. doi:10.1016/j.jaci.2005.03.021
42. Christensen JE, Andreasen SO, Christensen JP, Thomsen AR. CD11b expression as a marker to distinguish between recently activated effector CD8(+) T cells and memory cells. *Int Immunol* (2001) 13:593–600. doi:10.1093/intimm/13.4.593
43. Bausch-Fluck D, Hofmann A, Bock T, Frei AP, Cerciello F, Jacobs A, et al. A mass spectrometric-derived cell surface protein atlas. *PLoS One* (2015) 10:e0121314. doi:10.1371/journal.pone.0121314
44. Tillib SV, Efimov GA, Gubernatorova EO, Goryainova OS, Ivanova TI, Bocharov AA, et al. Preparation and characterization of recombinant single-chain llama antibodies that specifically bind to human interleukin-6. *Russ J Immunol* (2015) 9:400–9.
45. Yang R, Masters AR, Fortner KA, Champagne DP, Yanguas-Casás N, Silberger DJ, et al. IL-6 promotes the differentiation of a subset of naive CD8+ T cells into IL-21–producing B helper CD8+ T cells. *J Exp Med* (2016) 213(11):2281–91. doi:10.1084/jem.20160417

Conflict of Interest Statement: GE, AK, and SN are coauthors of the patent application describing the initial version of MYSTI. Other authors declare no conflict of interest.

frontiers in Immunology

ORIGINAL RESEARCH
published: 31 July 2017
doi: 10.3389/fimmu.2017.00867

Bivalent Llama Single-Domain Antibody Fragments against Tumor Necrosis Factor Have Picomolar Potencies due to Intramolecular Interactions

Els Beirnaert[1†‡], Aline Desmyter[2,3‡], Silvia Spinelli[2,3], Marc Lauwereys[1], Lucien Aarden[4], Torsten Dreier[1†], Remy Loris[5,6], Karen Silence[1†], Caroline Pollet[1], Christian Cambillau[2,3] and Hans de Haard[1†]*

[1] Ablynx NV, Ghent, Belgium, [2] Architecture et Fonction des Macromolécules Biologiques, Aix-Marseille Université, Campus de Luminy, Marseille, France, [3] Architecture et Fonction des Macromolécules Biologiques, Centre National de la Recherche Scientifique (CNRS), Campus de Luminy, Marseille, France, [4] Department of Immunopathology, Sanquin Research, Amsterdam, Netherlands, [5] Structural Biology Brussels, Vrije Universiteit Brussel, Brussels, Belgium, [6] Structural Biology Research Center, VIB, Brussels, Belgium

The activity of tumor necrosis factor (TNF), a cytokine involved in inflammatory pathologies, can be inhibited by antibodies or trap molecules. Herein, llama-derived variable heavy-chain domains of heavy-chain antibody (VHH, also called Nanobodies™) were generated for the engineering of bivalent constructs, which antagonize the binding of TNF to its receptors with picomolar potencies. Three monomeric VHHs (VHH#1, VHH#2, and VHH#3) were characterized in detail and found to bind TNF with sub-nanomolar affinities. The crystal structures of the TNF–VHH complexes demonstrate that VHH#1 and VHH#2 share the same epitope, at the center of the interaction area of TNF with its TNFRs, while VHH#3 binds to a different, but partially overlapping epitope. These structures rationalize our results obtained with bivalent constructs in which two VHHs were coupled *via* linkers of different lengths. Contrary to conventional antibodies, these bivalent Nanobody™ constructs can bind to a single trimeric TNF, thus binding with avidity and blocking two of the three receptor binding sites in the cytokine. The different mode of binding to antigen and the engineering into bivalent constructs supports the design of highly potent VHH-based therapeutic entities.

Keywords: tumor necrosis factor, cytokine, inflammation, nanobody, VHH, intramolecular binding, crystal structure

OPEN ACCESS

Edited by:
Colin Roger MacKenzie, National Research Council, Canada

Reviewed by:
Marina Drutskaya, Engelhardt Institute of Molecular Biology (RAS), Russia
Peter Timmerman, Pepscan Therapeutics B.V., Netherlands

***Correspondence:**
Caroline Pollet
caroline.pollet@ablynx.com

***Present address:**
Els Beirnaert, Vlaams Instituut voor Biotechnologie, Gent, Belgium;
Torsten Dreier, argenx BVBA, Ghent, Belgium;
Karen Silence, argenx BVBA, Ghent, Belgium;
Hans de Haard, argenx BVBA, Ghent, Belgium

‡*These authors have contributed equally to this work.*

Specialty section:
This article was submitted to Vaccines and Molecular Therapeutics, a section of the journal Frontiers in Immunology

Received: *27 April 2017*
Accepted: *07 July 2017*
Published: *31 July 2017*

Citation:
Beirnaert E, Desmyter A, Spinelli S, Lauwereys M, Aarden L, Dreier T, Loris R, Silence K, Pollet C, Cambillau C and de Haard H (2017) Bivalent Llama Single-Domain Antibody Fragments against Tumor Necrosis Factor Have Picomolar Potencies due to Intramolecular Interactions. Front. Immunol. 8:867. doi: 10.3389/fimmu.2017.00867

INTRODUCTION

Tumor necrosis factor (TNF) is a pleiotropic cytokine with beneficial functions in immune regulation and host defense, but deleterious pro-inflammatory and cytotoxic functions during inflammation. TNF is a pro-inflammatory cytokine that represents a critical mediator of the autoimmune process, playing a key role in several inflammatory diseases, including rheumatoid arthritis (RA), ulcerative colitis, and Crohn's disease. Increased understanding of the biological basis of autoimmunity has led to its identification as a major regulator of immune homeostasis, permitting the development of new

TNF antagonists at the forefront of treatments for inflammatory conditions (1). TNF signaling is mediated by binding to two cell-surface receptors: TNF receptor type 1 (TNFR1 or p55), expressed in most tissues, or TNF receptor type 2 (TNFR2 or p75), which is inducible and typically found in cells of the immune system (2). TNFR1 induces pro-inflammatory cascades and apoptosis, while TNFR2 has a role in cell survival, proliferation, and immune regulation (3, 4).

The structure of the related lymphotoxin α (LTα, previously called TNFβ) in complex with TNFR1 has shown that the trimeric cytokine binds three receptor molecules in a symmetrical way (5). The cytokine recruits two or possibly three TNFR1 molecules leading to clustering of the receptors, which results in downstream signaling. TNF has a similar structure as LTα and both compete for binding to the same receptors. Therefore, it was concluded that the structural insights provided by the analysis of the complex of LTα with p55 should also apply for TNF.

Inhibition of the TNF has been achieved by the anti-TNF biologic etanercept, antibodies like infliximab and adalimumab, or with the antibody fragment certolizumab, used to treat autoimmune diseases. However, these therapies have many adverse effects, and a lot of patients do not respond or poorly respond to initial treatment, or lose their response with maintenance therapy due to immunogenicity or other causes (6, 7). An alternative to total TNF blockade is to use a selective TNFR1 inhibitor to target pathogenic TNF signaling in autoimmune disease conditions such as RA. The TNF/TNFR2 pathway and its beneficial immunomodulatory signals and tissue homeostatic functions are thus maintained (8).

While the antibody structure usually comprises a heavy chain combined with a light chain, camelids have antibodies that only consists of a heavy chain (HCAbs) (9). Variable heavy (VH) chain domains of heavy-chain antibody (VHH) or Nanobodies™ are small antigen-binding fragments derived from HCAbs (4). They have advantages over conventional antibodies in that they are small (15 kDa) and robust, with low immunogenicity, a unique binding capability, and high solubility and stability (10). They are encoded by a single gene, requiring no posttranslational modifications and can be produced at high yields in bacteria and yeasts (11).

We generated and isolated Nanobodies™ that were screened for inhibition of the interaction between TNF and the TNFR2. The TNF-specific Nanobodies™ were shown to inhibit the interaction between the cytokine and its receptor in enzyme-linked immunosorbent assay (ELISA). In addition, it is shown that these Nanobodies™ inhibit the TNF-induced necrosis effect in a cell-based assay. These bioassay data suggest that TNF:TNFR1 cascade is also inhibited, which is in accordance with previously published structural analysis of interaction between LTα and TNFR1 (5). Their potency is better than for the commercially available TNF inhibitors, such as etanercept (Enbrel®), adalimumab (Humira®), and infliximab (Remicade®). However, these TNF antagonistic therapeutics act as bivalent molecules, resulting in higher avidity (12). Therefore, bivalent Nanobodies™ with either a short 9 amino acid GlySer linker or a longer 12 and 30 amino acid GlySer linker were constructed and characterized.

The X-ray structures of three complexes of these Nanobodies™ and TNF make it possible to rationalize the impact of linker length on the potency of these TNF binders. This knowledge supports the rational design of the most optimal bivalent Nanobody™ constructs that demonstrate efficacy in the TNF transgenic mouse model of spontaneous arthritis.

MATERIALS AND METHODS

Production and Selection of Nanobodies™ Blocking TNF

The study was approved by the Ethical Committee of the Faculty of Veterinary Medicine, University Ghent, Belgium. Human TNF was produced in house (Ablynx NV, Belgium) as a recombinant protein in *Escherichia coli* using the method described by Marmenout et al. (13). Purification was according to the procedures described by Curnis and Corti (14).

Two llamas were immunized with TNF according to current animal welfare regulations, using the adjuvant Stimune (CEDI Diagnostics, Lelystad, The Netherlands). Two blood samples were collected from each animal as the source of B-cells. Total RNA was isolated according to the procedure described by Chomczynski and Sacchi (15). Random primed complementary DNA was prepared on total RNA, purified and subsequently used as template to amplify the Nanobody™ repertoire. The procedure to amplify and clone the Nanobody™ repertoire was based on a method described in Ref. (16).

For the selection of Nanobodies™ against TNF, a Nunc Maxisorp® 96-well plate was coated with neutravidin and blocked, and biotinylated TNF was added to the wells. Phages were prepared as described by Marks et al. (17) and allowed to bind to the wells for 2 h at room temperature. Phages were removed, and the wells were washed 20 times with phosphate-buffered saline (PBS)/0.1% tween; elution of bound phage was done with 10 μM etanercept (Enbrel®) for 30 min at room temperature, or by denaturation with acid (0.2 M glycine pH 2.5) for 20 min at room temperature. Two rounds of selections were performed.

The ability of the Nanobodies™ to inhibit receptor–ligand interaction was analysed in ELISA. A 96-well Maxisorp plate was coated overnight at 4°C with 2 μg/ml etanercept in PBS. Plates were blocked with 1% casein solution (in PBS) for 2 h at room temperature. Nanobody™ samples were preincubated for 30 min at room temperature with biotinylated TNF (200 pM). The mixtures were added to the plates and incubated for 1 h at room temperature. Biotinylated TNF was detected using Extravidin alkaline phosphatase (Sigma; 1/2,000 diluted) and pNPP (Sigma; 2 mg/ml) as substrate.

Formatting, Expression, and Purification of Nanobodies™

For construction of bivalent anti-TNF Nanobodies™, two separate PCR reactions were used to amplify the N-terminal and the C-terminal Nanobody™ subunits using oligo combinations containing sequences encoding a 9GS [$(Gly)_4Ser(Gly)_3Ser$], 12GS [$(Gly)_3(Ser)]_3$, and 30GS [$(Gly)_4(Ser)]_6$ linker to connect the different Nanobodies™. The N-terminal VHH PCR fragment was

digested with SfiI and BamHI, and the C-terminal VHH PCR fragment was digested with BamHI and BstEII. Ligations and transformations were carried out as described earlier.

For the generation of bispecific Nanobodies™ consisting of two anti-TNF Nanobodies™ combined with one anti-albumin Nanobody™, three PCR reactions were performed for the amplification of the N-terminal, the middle, and the C-terminal Nanobody™ with oligonucleotide primers encoding the 9, 12, or 30 × Gly–Ser linker. The N-terminal VHH encoding PCR fragment was digested with SfiI and BamHI, the middle Nanobody™ fragment was digested with BamHI and BspEI, and the C-terminal VHH PCR fragment was digested with BspEI and BstEII.

Single *E. coli* clones were picked and grown in Luria Broth containing the appropriate antibiotics, and expression was induced with 1 mM isopropyl β-D-1-thiogalactopyranoside. Periplasmic extraction and immobilized metal affinity chromatography purification of the VHH proteins were performed according to Ref. (18). The VHH proteins were further purified by cation exchange and/or gel filtration and dialyzed into PBS.

Affinity Measurements

Binding of Nanobodies™ to TNF was characterized by surface plasmon resonance in a Biacore 3000 instrument (Biacore International AB, Uppsala, Sweden). In brief, TNF was covalently bound to a CM5 sensor chip surface *via* amine coupling until an increase of 250 response units was reached. Remaining reactive groups were inactivated. Nanobody™ binding was assessed, and K_D values were calculated using the instruments software.

Neutralizing Potency Measured in Cell-Based Assay

The TNF sensitive mouse fibroblast cell line L929s was utilized for measuring the anti-TNF activity of the selected Nanobodies™. L929 cells were grown until nearly confluent, plated out in 96-well microtiter plates at 5,000 cells per well, and incubated overnight. Actinomycin D was added to the cells at a final concentration of 1 μg/ml. Serial dilutions of the Nanobodies™ to be tested were mixed with a cytotoxic concentration of TNF (10 pM). After incubation for 30 min at 37°C, this mixture was added to the plated cells and incubated for 24 h at 37°C. Cell viability was determined by using the tetrazolium salt WST-1. Dose–response curves and IC_{50} values (potency) were calculated with GraphPad Prism. The mean potencies for individual Nanobody™ constructs and benchmark anti-TNF biologics were calculated from a number of independent bioassays as well as the SD.

Size Exclusion Chromatography (SEC) of Complexes of TNF with Nanobodies™

Size exclusion chromatography of complexes of TNF with the different formats of VHH using a Superdex 200 HR 10/30 column was carried out according to the procedure described by Santora et al. (19). 20 μg (0.4 nmol) of human TNF in a volume of 100 μl (in PBS) was injected on the column. For analysis of Nanobody™–cytokine complexes, 20 μg (1.3 nmol) of monovalent antibody fragment was mixed with 20 μg (0.4 nmol) of cytokine in 100 μl volume and after 30 min preincubation at room temperature loaded on the column. For the bivalent nanobody construct, 20 μg (0.7 nmol) antibody fragment in 100 μl volume was applied on the column. SEC was performed with the mixture of 20 μg (0.4 nmol) of cytokine and 40 μg (1.3 nmol) of bivalent nanobody in a volume of 100 μl, which was preincubated for 30 min at room temperature. The column has been calibrated one month before the analysis of the bivalent constructs with the Gel Filtration Standards [BioRad, catalog number 151-1901 containing bovine thyroglobulin (MW 670 kD), bovine γ-globulin (158 kD), chicken ovalbumin (44 kD), horse myoglobin (17 kD), and vitamin B12 (1.35 kD)]. This procedure enabled determination of the molecular mass of the complexes and, hence, their stoichiometry.

X-ray Structures Determination

The complex between TNF and VHH#1 was crystallized by mixing 100–300 nl of purified complex (8 mg/ml in HEPES 10 mM pH 7.0) with 100 nl of precipitant solution (20% PEG3000, 0.2 M NaCl, and 0.1 M HEPES at pH 7.5) and equilibrating 100 μl of precipitant solution. A crystal was exposed at beamline ID14-1 (ESRF, Grenoble, France), and a complete dataset was collected at 2.15 Å resolution (**Table 1**). Data were integrated with XDS and scaled using Xscale (20) (**Table 1**). The structure was solved by molecular replacement with Molrep (21) using the TNF trimer from Protein Data Bank (PDB) entry 1TNF and the framework region (FR) of the VHH domain from PDB entry 1HCG as search models. Refinement was carried out with cycles of autoBUSTER (22) alternated with manual rebuilding with Coot (23).

Crystals of the complex between TNF and VHH#2 were obtained by mixing 100–300 nl of purified complex (11 mg/ml in HEPES 10 mM pH 7.0) with 100 nl of precipitant solution (12% PEG4000, 130 mM NaCl, 366 mM $CaCl_2$, 70 mM CAPS pH 9.0, and 30 mM MES pH 8.0) and equilibrating against 100 μl of precipitant solution. Data to 1.9 Å resolution were collected from a single crystal at beamline ID14-1 (ESRF, Grenoble, France) (**Table 1**). Data were integrated with XDS and scaled using XSCALE (20) (**Table 1**). The structure was determined by molecular replacement with Molrep (21) using a single TNF monomer and a single VHH domain stripped from its complementarity determining region (CDR) loops and taken from the TNF–VHH#1 complex as search models. Refinement was performed as described above.

Crystallization of the complex between TNF and VHH#3 was achieved by mixing 100–300 nl of protein (8–10 mg/ml in HEPES 10 mM pH 7.0) with 100 nl of precipitant solution (9% PEG3350, 8% PEG-MME550, 130 mM $NaSO_4$, 70 mM BTP, 30 mM MES, and 3 mM $ZnSO_4$, $7.0 < pH < 8.0$) and equilibrating against 100 μl of precipitant solution. A crystal was exposed at beamline ID14-3 (ESRF, Grenoble, France), and a complete dataset was collected at 2.3 Å resolution (**Table 1**). Data were integrated with XDS and scaled using XSCALE (20). The structure was determined by molecular replacement using the coordinates of the TNF trimer and VHH#1 stripped from its CDR loops as search models. Refinement was performed as described above for the other two TNF complexes.

Protein contacts were analyzed using PISA (24). Figures were prepared with Pymol (Pymol, Schrödinger). Coordinates and structure factors have been deposited at the PDB as entries 5m2i,

TABLE 1 | Data collection and refinement statistics.

Data collection	TNF–VHH#1	TNF–VHH#2	TNF–VHH#3
Protein Data Base	5m2i	5m2j	5m2m
Source	ESRF ID14-1	ESRF ID14-1	ESRF ID14-3
Space group	$P2_12_12_1$	$P6_3$	C2
Cell (Å), angle (°)	a = 110.3, b = 117.4, c = 141.9	$a = b$ = 87.3, c = 62.7	a = 145.4, b = 83.8, c = 150.1, β = 128.8
No. monomers in the AU	6	1	6
Resolution limits (Å)	50–2.15 (2.2–2.15)	50–1.9 (1.95–1.9)	30.0–2.3 (2.42–2.3)
R_{merge}	0.127 (1.11)	0.035 (0.10)	0.09 (0.32)
CC1/2	0.997 (0.72)	0.999 (0.98)	0.999 (0.96)
Unique reflections	100,770 (7,354)	21,089 (1,499)	62,613 (9,101)
Mean [(I)/SD(I)]	8.8 (1.5)	23.5 (11)	11.2 (4.1)
Completeness (%)	99.5 (95.6)	97.9 (94.6)	99.9 (99.9)
Multiplicity	4.15 (4.0)	2.9 (2.7)	4.1 (4.0)
Refinement			
Resolution (Å)	46.5–2.15 (2.21–2.15)	48.3–1.9 (2.0–1.9)	30.0–2.3 (2.36–2.3)
Number of reflections	100,502 (2,376)	21,089 (2,723)	62,613 (4,594)
Number of protein/water atoms	12,521/747	1,966/351	12,810/711
Test set reflections	5,026 (369)	1,045	2,988 (231)
R_{work}/R_{free}	0.208/0.238 (0.234/0.258)	0.16/0.196 (0.16/20.0)	0.211/0.248 (0.212/0.244)
RMSD bonds (Å)/angles (°)	0.008/1.17	0.010/1.11	0.008/1.11
B-Wilson/B-mean (Å)	36.5/44.2	15.6/19.8	35.1/44.5
Ramachandran: preferred/allowed/outliers (%)	96.4/3.1/0.5	97.6/2.4/0	95.8/3.7/0.5

Numbers between brackets refer to the highest resolution bin.

5m2j, and 5m2m for the complexes with VHH#1, VHH#2, and VHH#3, respectively.

Arthritis Treatment in the Tg197 Mouse Model

The transgenic Tg197 model was used to investigate the potency of the different VHH (VHH#1 and VHH#3) antibodies, as described in Keffer et al. (25). Briefly, Tg197 mice carry a human TNF transgene, with its 3′-untranslated region replaced by a sequence from the 3′-untranslated region of the beta-globin gene, thereby allowing deregulated human TNF gene expression. By 4 weeks of age, all human TNF expressing Tg197 mice spontaneously develop a severe bilateral, symmetric, erosive, and disabling polyarthritis similar to RA. Treatment of these arthritic mice with monoclonal antibodies (mAb) against human TNF can prevent development of the disease.

Using this model, 13 groups of 8 mice each were assigned to one of four treatment regimens: PBS treatment, VHH#1-based bivalent molecule, VHH#3-based bivalent molecule, or the biologic etanercept (Enbrel®; a TNFR-Fc fusion protein).

The VHH#3-based bivalent construct consisted of the following, in sequence: a VHH#3 molecule, a 9GS linker, a VHH#3 molecule, a 9GS linker, and finally, an antihuman serum albumin VHH (anti-HSA VHH) at the carboxy-terminus to avoid rapid clearance of the compound from circulation (i.e., a construct of: VHH#3-9GS-VHH#3-9GS-HSA VHH). The VHH#1-based bivalent construct consisted of the following, in sequence: VHH#1, a 9GS linker, the anti-HSA VHH, another 9GS linker, and a VHH#1 molecule (i.e., a construct of: VHH#1-9GS-HSA VHH- 9GS-VHH#1).

Doses of 1, 3, 10, and 30 mg/kg were administered intraperitoneally twice weekly, starting week 3 after birth. The arthritic scoring system (26) was applied based on the macroscopic changes observed in joint morphology on both ankle joints using the following scores: 0 = no arthritis (normal appearance and flexion); 0.5 = onset of arthritis (mild joint swelling); 1 = mild arthritis (joint distortion); 1.5 = as above, but with finger deformation, less strength on flexion; 2 = moderate arthritis (severe swelling, joint deformation, no strength on flexion); 2.5 = as above, but with finger deformation in paws; 3 = heavy arthritis (ankylosis detected on flexion and severely impaired movement).

Arthritic score (AS) was recorded weekly on both ankle joints, and average scores were calculated. Statistical significance was tested using analysis of variance for multiple groups. When significant differences were observed, pairwise testing was performed using Tukey's multiple comparison test. ASs were statistically evaluated at the end of study, i.e., at 10 weeks of age.

RESULTS

Identification and Potency of Antagonistic Anti-TNF VHH

For isolation of Nanobodies™ that act as antagonists of TNF, two llamas were immunized with human TNF, and phage display libraries were generated using RNA derived from peripheral blood lymphocytes. Selection was performed by competitive elution with an excess of Enbrel on biotinylated TNF, captured by immobilized streptavidin (27). The principle of competitive elution is based on saturating all receptor binding sites on the cytokine, thereby preventing rebinding of dissociated phage antibodies, and thus enrichment for antagonistic VHH. A similar approach was used by others for the isolation of human immunodeficiency virus-1 neutralizing VHH (28). Indeed, using this methodology on TNF led to the identification of only "blocking" (antagonistic) Nanobodies™, i.e., VHH#2 and VHH#3 from one llama and VHH#1 from the other llama.

These three Nanobodies™ each represent large families of affinity variants, which contain somatic mutations in the CDR and, to a lesser extent, in the FRs (16, 29). For VHH#3, even (lower affinity) family members exist with a deletion of two amino acids in CDR1, probably as the result of gene conversion during affinity maturation in the llama (30).

Recently, such variants of the anti-TNF VHH have also been identified *via* B-cell display methods [unpublished], which do not suffer from polymerase chain reaction artifacts during library construction. This confirms the occurrence of circulating B cells derived from an ancestor B-cell clone as a consequence of the *in vivo* maturation process.

The VHH encoding gene segments were recloned in an *E. coli* expression vector with or without the carboxy-terminal c-MYC and/or hexa-histidine tags. After expression and purification, VHH were tested in the bioassay for their neutralizing capacity. Murine L929 cells expressing the mouse receptor were used for testing the VHH in combination with the human cytokine. By sensitizing the cells with actinomycin D, picomolar amounts of TNF were sufficient to induce the cytotoxic effect, which was taken as the assay read-out. All three VHHs were found to have low nanomolar potencies in line with the measured affinities for TNF (**Table 2**).

Format Engineering of Nanobodies™

Because of the trimeric nature of TNF, we investigated whether the avid binding of a mAb such as infliximab contributes to its potency. Indeed, a considerable difference in potency was observed when the Fab fragment prepared by proteolytic digestion of infliximab was tested in the bioassay and compared with the intact antibody. The IC_{50} of the monovalent Fab fragment was ~2 nM; compared with that of the bivalent immunoglobulin-G format (IC_{50} ~ 70 pM), the potency of the Fab was approximately 30-fold lower.

VHHs are strictly monomeric proteins and do not show any tendency to aggregate in multimers like single-chain variable fragments (scFv). Bivalent and bispecific formats were constructed by using linkers of variable length to fuse the VHHs. As a linker between the two VHHs, either a stretch of 9GS, 12GS, and 30GS sequence was used. Depending on the VHH and the length of the linker, a dramatic increase in potency was observed.

Binding and Activity Determination

The affinity constants of binding to TNF for each of the three VHHs were determined by Surface Plasmon Resonance. The measured binding constants (K_D) are 540 pM, 130 pM, and 1.5 nM for VHH#1, VHH#2, and VHH#3, respectively. In line with this, the IC_{50} values measured in the bioassay are in a similar range of between 240 pM to 1.5 nM (**Table 2**).

With regard to the bivalent VHHs, potencies increased when compared with the monovalent building blocks (**Table 2**). For the VHH#1-based bivalent constructs, measurements indicate a threefold increase in potency with a short 9GS linker and a greater increase in potency, by a factor of 12, with a longer 30GS linker. For VHH#2-based bivalent constructs, a threefold increase in potency is also observed with the 9GS linker, while a 50-fold increase in potency was measured with a 30GS linker. In contrast, for VHH#3-based bivalent constructs, even a short linker of 9GS allows an increase in potency by a factor of 80, while an increase of 120-fold is observed when using the 12GS linker (potency of 12 pM). However, such a low picomolar potency is not achieved with an Fc fusion, where the VHH is linked directly to the hinge region and to the constant CH2/CH3 domains of human IgG1 (i.e., the human version of the heavy-chain antibody format). The Fc derivative from VHH#3 has a potency of ~100 pM as compared to 1.5 nM for the monovalent VHH#3, showing that avidity-mediated binding does improve its efficacy, but not to the degree of that seen with the bivalent constructs (data not shown).

Increases in potency were also obtained when the two different Nanobodies™ VHH#1 and VHH#3 were linked with the short 9GS linker to create bispecific constructs, either with VHH#1 first or with VHH#3 first (**Table 2**). When VHH#3 is placed first, a 10-fold greater potency is obtained than when VHH#1 is first (**Table 2**). The potency of VHH#3-9GS-VHH#1 is 6 pM and is therefore at least twofold better than the potency of etanercept. Indeed, 10 pM was the amount of TNF used in the bioassay, thus representing the limit of sensitivity. This indicates that the position of the VHH plays an important role in binding, as previously observed (31), and may be determined by the exact epitope to which the respective Nanobodies™ bind.

TABLE 2 | Potency (IC_{50}) and affinity (K_D) of monovalent and bivalent anti-TNF-Nanobody™ constructs.

Nanobody linker	IC_{50} mean (nM)	IC_{50}-SD (nM)	K_D (nM)	Ratio IC_{50}	Minimal linker length[a]	Nr measures
VHH#1	0.242	0.122	0.54	1		21
VHH#1-9GS-VHH#1	0.078	0.047		3.1	20	8
VHH#1-30GS-VHH#1	0.021	0.012		12		16
VHH#2	0.748	0.153	0.13	1		27
VHH#2-9GS-VHH#2	0.236	0.049		3.2	18	4
VHH#2-30GS-VHH#2	0.015	0.005		50		21
VHH#3	1.503	0.84	1.5	1		4
VHH#3-9GS-VHH#3	0.019	–		80	12	1
VHH#3-12GS-VHH#3	0.012	0.007		125		7
VHH#1-9GS-VHH#3	0.059	0.018		1	20	13
VHH#3-9GS-VHH#1	0.006	0.002		10	9	8
Etanercept	0.013	0.006		–		71
Adalimumab	0.127	0.058		–		67
Infliximab	0.144	0.061		–		68

GS, amino acid glycine–serine linker; VHH, variable-domain heavy-chain region. Etanercept (Enbrel®), adalimumab (Humira®), and infliximab (Remicade®). Ratio IC_{50} refers to ratio of IC_{50} of monomeric VHH and bivalent construct.
[a]Minimum possible linker length (number of amino acids) calculated from the 3D structure.

Intramolecular Binding

The molecular masses and hence stoichiometries for the different TNF complexes (monovalent and bivalent VHH constructs) were determined by SEC. The trimeric TNF and the monovalent VHH molecules appear at elution times of 16.71 min (MW of around 50 kDa) and 15.68 min (MW 22.5 kDa), respectively (**Figures 1A,B**). By mixing 0.4 nmol of TNF with 1.3 nmol of VHH#3, a major peak and a smaller peak eluted with retention times of 12.8 and 16.7 min, respectively (**Figure 1C**). The major peak, which according to the elution volume has a molecular weight of around 210 kDa (elutes a bit earlier than the 158 kDa standard), is attributed to a TNF/VHH#3 complex with a 1:3 stoichiometry (three Nanobodies™ on one TNF trimer), and the smaller peak to the VHH#3 molar excess [1.3 nmol − (3 nmol × 0.4 nmol)].

Similar experiments were performed with the bivalent VHH#3 construct containing the 12GS linker. This bivalent VHH#3 construct appears at a retention time of 15.38 min (MW of around 45 kDa; **Figure 1D**). We then mixed 0.4 nmol of TNF with 1.3 nmol bivalent VHH#3. This mixture corresponds to a small molar excess if only one of the two Nanobodies™ binds to TNF [$1.3 - (0.4 \times 3) = 0.1$ nmol], while it corresponds

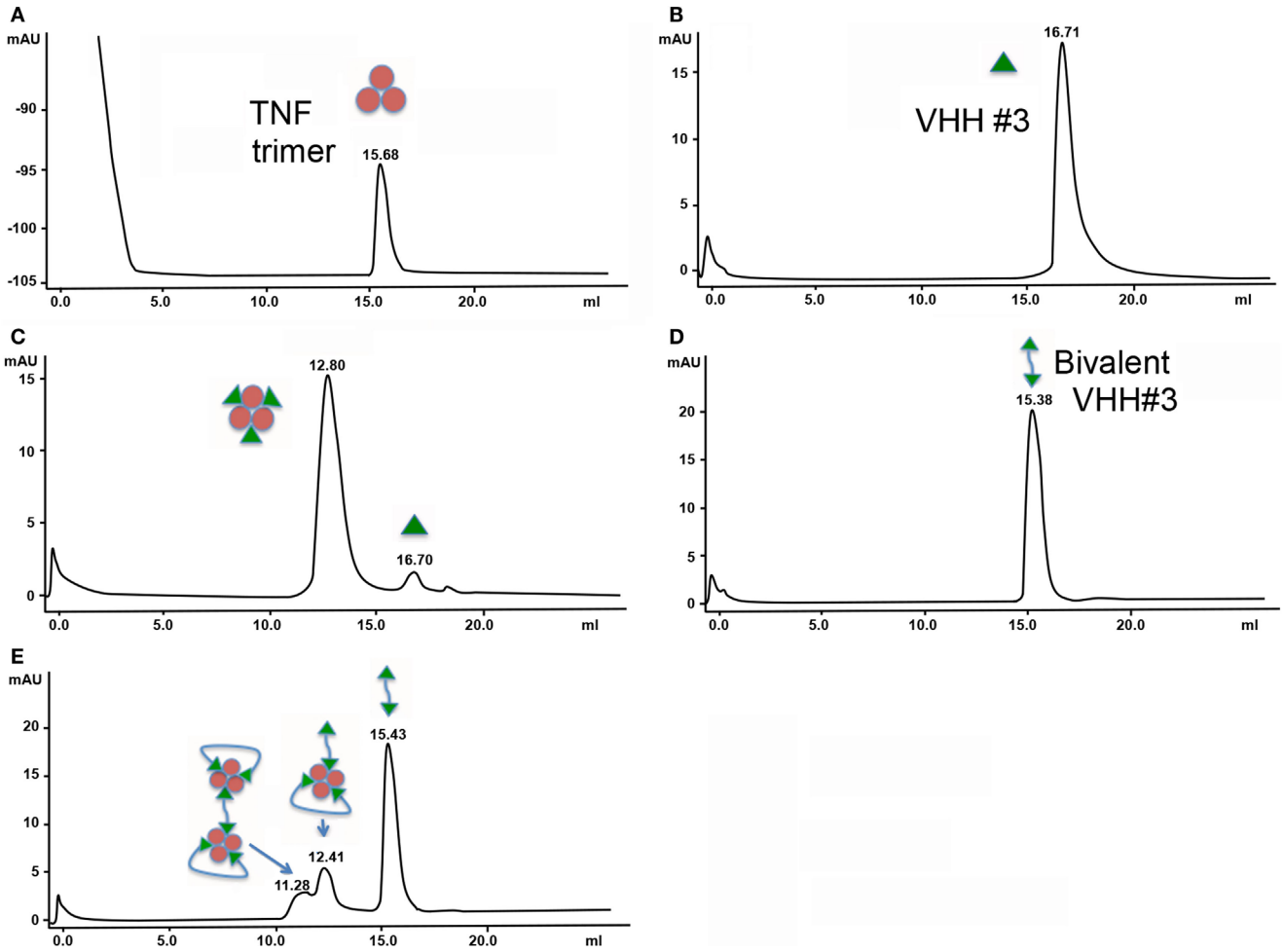

FIGURE 1 | Size exclusion chromatography of complexes of tumor necrosis factor (TNF) with the different formats of VHH. **(A)** 0.4 nmol TNF. **(B)** 1.3 nmol VHH#3. **(C)** 0.4 nmol TNF + 1.3 nmol VHH#3. **(D)** 0.7 nmol bivalent VHH#3 (VHH#3-12GS-VHH#3). **(E)** 0.4 nmol TNF + 1.3 nmol bivalent VHH#3 (VHH#3-12GS-VHH#3).

to a large molar excess if the two Nanobodies™ bind to TNF [1.3 − (0.4 × 2) = 0.5 nmol] as is shown in **Figure 1E**. After injection of this mixture, three peaks were observed: a major peak at 15.43 min, corresponding to the free bivalent VHH#3 (about 0.6 nmol), and two smaller peaks at lower retention times of 12.41 and 11.28 (**Figure 1E**). The amount of free bivalent VHH#3 is above the value of 0.5 nmol calculated above for the situation the two bivalent nanobodies can bind to a single TNF molecule. With regard to the latter peaks, both are at lower retention times compared to the TNF trimer/3× VHH#3 complex, indicating that the complexes are of larger molecular weight. The larger peak of the doublet, at 12.41 min, elutes just a bit earlier than the complex of TNF with three monomeric Nanobodies™ (12.80 min; indicates MW of around 240 kDa) meaning that it must contain more mass than three Nanobody™ subunits. This could implicate that the complex consists of one TNF molecule with two bivalent Nanobody molecules as depicted in **Figure 1E**, in which one bivalent molecule binds to two receptor interaction sites, whereas the other bivalent molecule binds with one arm to a single receptor interaction site. The peak at 11.28 min has an even larger molecular weight; it elutes just after the dimeric thyroglobulin peak of 330 kDa. The difference between the two peaks is around 80 kDa, which could account for one additional TNF and one bivalent VHH molecule. This may account for a complex in which four bivalent VHH molecules bind to two TNF trimers, hence its larger molecular weight.

Structures of the Complexes

To better understand and rationalize the activities of the three Nanobodies™, the crystal structures of the complexes of VHH#1, VHH#2, and VHH#3 with TNF were determined. In agreement with SEC data, each of the three Nanobodies™ associates with the trimeric TNF to form a hetero-hexameric TNF-Nanobody™ complex (**Figure 2**). VHH#1 attaches to the concave surface of the outer β-sheet of TNF and contacts two TNF monomers simultaneously (**Figures 2** and **3**). VHH#1 covers 1,246 Å^2 of the TNF solvent-accessible surface area, of which 902 Å^2 belongs to one TNF monomer and 274 Å^2 to the other monomer (**Table 3**). Its three CDRs interact with TNF, but CDR2 and especially CDR3

are predominant in the interaction, as commonly observed in other Nanobody™ complexes (**Table 3**). VHH#1 is aligned almost parallel to the TNF surface (when comparing the orientations of their β-strands), and its CDR2 lines the TNF surface (**Figures 2** and **3**).

The binding area of VHH#2 coincides almost totally with that of VHH#1 (**Figure 3**; **Table 4**) despite significant differences in CDR lengths and conformations, and a different orientation of both VHH domains relative to the antigen. VHH#2 covers 745 Å^2 of the TNF solvent-accessible surface area, 571 Å^2 on one TNF monomer and 175 Å^2 on the other monomer (**Table 3**). However, the orientation of VHH#2 is more perpendicular to TNF compared to that of VHH#1, which results in a smaller surface area of interaction (**Figures 2** and **3**; **Table 3**). VHH#2 is unusual in

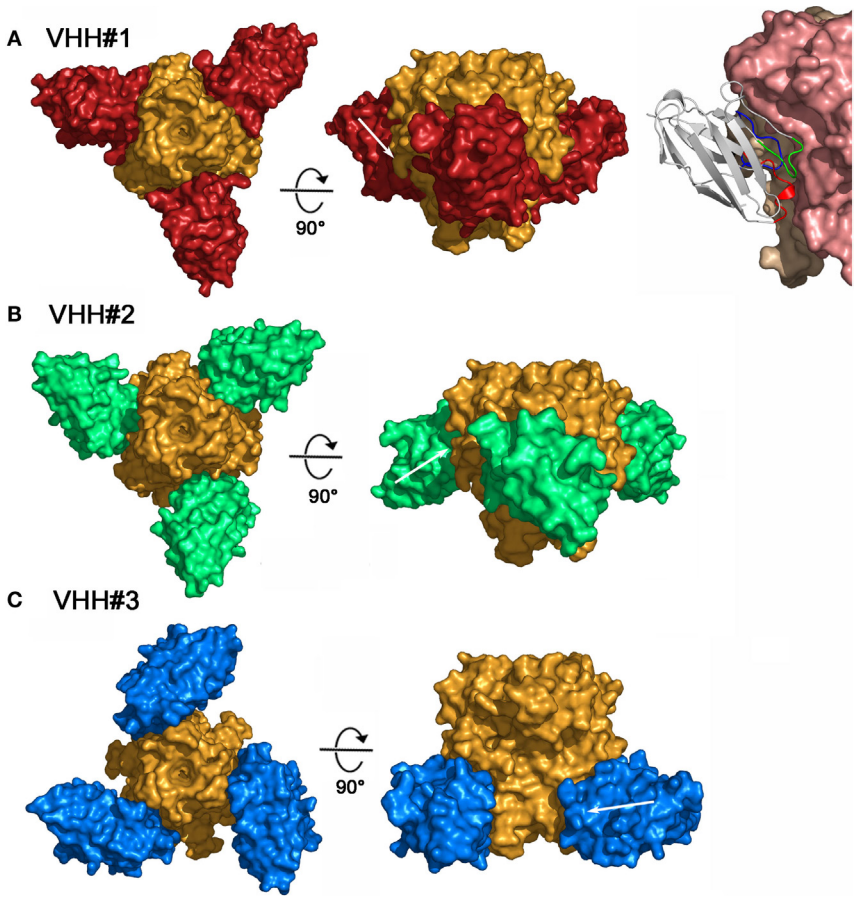

FIGURE 2 | Three-dimensional structures of the three tumor necrosis factor (TNF)–Nanobody™ complexes. **(A)** Complex TNF–VHH#1; TNF and VHH#1 surfaces are colored orange and red, respectively. Shown right: details of the interaction of VHH#1 with TNF; VHH#1 in ribbon representation. **(B)** Complex TNF–VHH#2; TNF and VHH#2 surfaces are colored orange and green, respectively. **(C)** Complex TNF–VHH#3; TNF and VHH#3 surfaces are colored orange and blue, respectively.

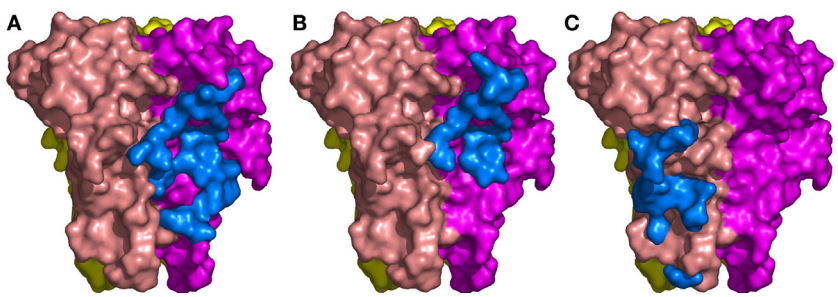

FIGURE 3 | The binding sites of the three Nanobodies™ on tumor necrosis factor (TNF) trimer. **(A)** Complex TNF–VHH#1. **(B)** Complex TNF–VHH#2. **(C)** Complex TNF–VHH#3. TNF-monomer surfaces are colored orange, violet, and yellow. The residues of the Nanobodies™ in interaction with TNF are displayed as blue surfaces.

TABLE 3 | Water accessible surface area (in Å^2) of TNF or VHH covered when complexed.

Part	VHH#1	VHH#2	VHH#3
VHH	1,246	745	736
TNF trimer	1,176	746	749
TNF-monomer 1	902	571	749
TNF-monomer 2	274	175	–
CDR1	236	272	73
CDR2	409	322	314
CDR3	599	131	123

CDR, complementarity determining region; TNF, tumor necrosis factor; VHH, variable-domain heavy-chain region.

TABLE 4 | TNF residues in contact (d < 3.8 Å) with the three VHHs.

TNF	Residues	VHH#1	VHH#2	VHH#3
20	B			
21	B			X
22	B			X
23	B			X
24	B			X
25	B			X
65	B			X
66	B			X
67	B			X
70	B			X
72	B			
73	B			
74	B			
77	B			
79	B			
81	B			
83	B			
83	B			
88	B			
89	B			
90	B			
91	B			
92	B			
97	B			
107	B			
135	B			
136	B			
137	B			
138	B			
139	B			
140	B			
141	B			
115	C			
145	C			
146	C			
147	C			

Shaded boxes represent residues within TNF that are in contact with residues of the indicated Nanobody.
TNF, tumor necrosis factor; VHH, variable-domain heavy-chain region.

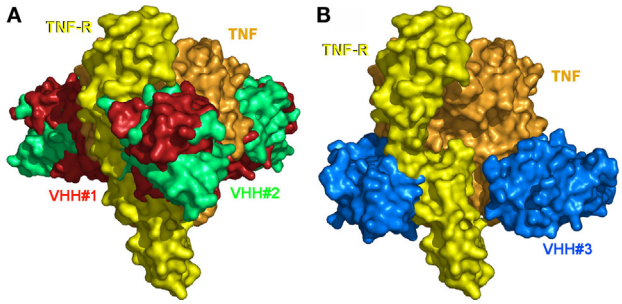

FIGURE 4 | The binding sites of the three Nanobodies™ and of the extracellular domain of the tumor necrosis factor (TNF) receptor p55 (TNFR1) mapped on TNF. **(A)** VHH#1, VHH#2, and TNFR1. **(B)** VHH#3 and TNFR1. The TNF trimer surface is colored orange. The TNFR1 surface of a unique monomer is colored yellow. Surfaces of VHH#1, VHH#2, and VHH#3 are colored red, green, and blue, respectively. Note the superposition of the Nanobodies' surfaces with those of TNFR1.

that most of the contacts with the antigen involve CDRs 1 and 2. CDR3, which normally dominates Nanobody™-antigen interactions, contributes least to the contact surface (**Table 3**). The CDR3 of VHH#2 is among the shortest observed for Nanobodies™ and the FR after the CDR3 sequence deviates from the normal framework-4 structure: the C-terminal β-strand is shortened in order for the CDR3 loop to connect with the previous β-strand.

In contrast, VHH#3 binds to a different epitope that does not overlap with the epitopes of VHH#1 and VHH#2, and that is located toward the thinner end of the trimer, "below" the VHH#1 epitope (**Figures 2** and **3**; **Table 4**). Each VHH#3 molecule contacts only a single TNF monomer and covers 736 Å^2 of accessible surface area of TNF (**Table 3**). Again, all three CDR loops contribute to antigen binding, with CDR2 being dominant and CDR1 showing the smallest contribution despite its relatively long length (**Table 3**).

TNF Receptor Neutralization

The 3D structure of TNF in complex with TNFR is not known. However, given that TNF and LTα bind equally well to TNFR1 (p55) and TNFR2 (p75) and considering the high structural identity between TNF and LTα, a plausible model for the TNF/TNFR1 complex can be obtained by superimposing TNF onto LTα in its complex with the ectodomain of the TNFR1 p55 receptor (PDB entry 1TNR) (5). In this model, each TNFR1 p55 monomer covers about 1,200 Å^2 of one of the three TNF monomers without significant steric clashes.

The structures of the TNF/VHH complexes reported here were superimposed onto that of the TNF/TNFR complex. The binding areas of VHH#1, VHH#2, and VHH#3 overlap in part with that of TNFR (**Figure 4**). VHH#1 and VHH#2 occupy the central area of the receptor binding site, while VHH#3 occupies the "bottom" of the receptor binding area (**Figure 4**). Furthermore, whereas two molecules of VHH#1 or VHH#2 interact with two TNF subunits on either side, only one molecule of VHH#3 interacts with a single TNF subunit (**Figure 3**). However, considering the dramatic steric overlap between TNFR and all three VHH molecules, it is

clear that the three VHH molecules can inhibit the interaction between TNF and TNFR.

Notably, the interaction areas of VHH#1 and VHH#3 are quite distinct, and they can bind simultaneously to TNF at a single receptor binding site, ensuring a possible biparatopic binding. This observation explains why the VHH#1-9GS-VHH#3 bispecific construct yields the highest potency ever observed for any TNF antagonist (6 pM; **Table 2**).

Arthritis Treatment in the Tg197 Mouse Model

Bivalent constructs of VHH#1 and VHH#3, which recognize completely different epitopes on the cytokine, were tested in the Tg197 transgenic human TNF model for polyarthritis, in which mice constitutively produce the human cytokine and develop acute arthritis. VHH#2 was not included in this experiment, because it recognizes a similar epitope in the bulky part of the cytokine as VHH#1 does, but as a monovalent nanobody with a lower affinity and potency than VHH#2. Thirteen groups comprising eight mice each were assigned to one of four treatment regimens: PBS control, VHH#1-based bivalent molecule, VHH#3-based bivalent molecule, or etanercept.

The bivalent constructs consisted of two molecules of VHH#1 or VHH#3, and one molecule of an anti-HSA VHH to avoid rapid clearance of the compound from circulation. For VHH#1 a bispecific construct was generated with the anti-albumin Nanobody™ (human–mouse cross-reactive) in the middle position fused with the 9 amino acid GS linker to both VHH#1 Nanobodies™, thereby bridging a distance of approximately 30 amino acids between the two TNF Nanobodies™, which according to the structural studies should be sufficient for enforcing intramolecular binding to the cytokine. For VHH#2 the albumin binding Nanobody™ was placed in the carboxy-terminal position thereby supporting the use of the smaller 9GS linker for directly connecting the two VHH#2 units that would be required for intramolecular binding. The potencies of the bivalent VHH#1 Nanobody™ (VHH#1-9GS-HSA VHH- 9GS-VHH#1) and the bivalent VHH#3 Nanobody™ (VHH#3-9GS-VHH#3-9GS-HSA VHH) in the cell-based potency assay were 22 and 18 pM, respectively. The potency of etanercept in this assay was 14 pM (data not shown). The amount of TNF used in the bioassay was 10 pM, which therefore represents the limit of sensitivity.

The results of this study show that bivalent Nanobodies™ suppressed the development of arthritis in a dose-dependent fashion. In particular, administration either of bivalent VHH#3 at four different doses (1, 3, 10, or 30 mg/kg) or bivalent VHH#1 at three different doses (3, 10, or 30 mg/kg) had a significant effect ($p < 0.05$) in the amelioration of clinical scores (**Figure 5**) in comparison to the PBS treated group. In contrast, administration of VHH#1 at 1 mg/kg did not show statistically significant differences in clinical scores in comparison to the vehicle treated group ($p > 0.05$). Amelioration of arthritis by treatment of mice with etanercept at 10 or 30 mg/kg was also statistically significant in comparison to PBS treated group, whereas at lower doses (1 or 3 mg/kg) treatments with etanercept were no longer statistically significant. Complete attenuation of disease development was observed mice treated with 30 or 10 mg/kg of bivalent VHH#3, and in animals treated with 10 and 30 mg/kg of bivalent VHH#1. These results show that bivalent VHH#3 is improving clinical scores in all four doses tested ranging from 1 to 30 mg/kg. Bivalent VHH#3 is more potent than bivalent VHH#1 construct or etanercept. Bivalent VHH#1 improves the clinical scores at doses ranging from 3 to 30 mg/kg and is comparable to etanercept in terms of efficacy.

DISCUSSION

The action of TNF can be inhibited by antibodies or trap molecules targeting the cytokine (32). Herein, llama VHH domains were generated for the engineering of bivalent constructs, which antagonize the binding of TNF to its receptor with low picomolar potencies. Three monomeric VHHs, VHH#1, VHH#2, and VHH#3 were identified, which bind TNF with sub-nanomolar affinities. We previously observed that engineering VHH into bivalent constructs improved their potency, as demonstrated for other targets including mouse TNF (33), CXCR4 (34), and viruses (35). Anti-TNF VHH fused to a scFv or another VHH that recognized cell-surface markers of myeloid cells could capture TNF produced by these cells thereby restricting the bioavailability of the cytokine and hence such bispecific constructs were able to prevent the pathogenic effect in an *in vivo* model (36).

VHH#1 and VHH#2 bind to largely the same epitope at the center of the interaction area of TNF with TNFR (**Table 4**). The latter docks into a groove formed by the interface of two TNF monomers in the TNF trimer. Also, the CDR loops of VHH#1 and VHH#2 dock into this groove, although the specifics of the interactions are quite different due to a different orientation of the VHH module relative to the TNF structure. The recognition of clefts and grooves is a quite common feature of Nanobodies™ (37) and is due to the small size of the Nanobody™ relative to a scFv. Indeed, when both Nanobodies™ would be replaced by classical VH domains in the context of a scFv, large steric overlap would be present between the TNF trimer and the variable light (VL) domain, preventing the same mode of binding.

VHH#3 binds to a different epitope, and its recognition site on TNF only marginally overlaps with those of TNFR or VHH#1. There is no overlap between the recognition surfaces of VHH#2 and VHH#3, but steric overlap between the bodies of these two VHHs is still significant and should prevent coincident binding. This explains why VHH#3 was also identified as a blocking antibody.

Bivalent and bispecific Nanobodies™ created as VHH tandems show enhanced affinities and potencies that are dependent of the length of the linker used (**Table 2**). The structures of the three VHH complexes made it possible to rationalize these findings. The shortest distances between the N-terminus of one VHH and the C-terminus of another VHH in the complexes involving VHH#1 and VHH#2 are 69 and 67 Å, respectively. Taking into account the orientations of these termini relative to each other and that a linker needs to avoid steric clashes with the TNF antigen, a minimum linker length of at least 20 amino acids is expected to be required for the VHH#1 bivalent construct, and 18 amino acids for the VHH#2 bivalent construct. This explains

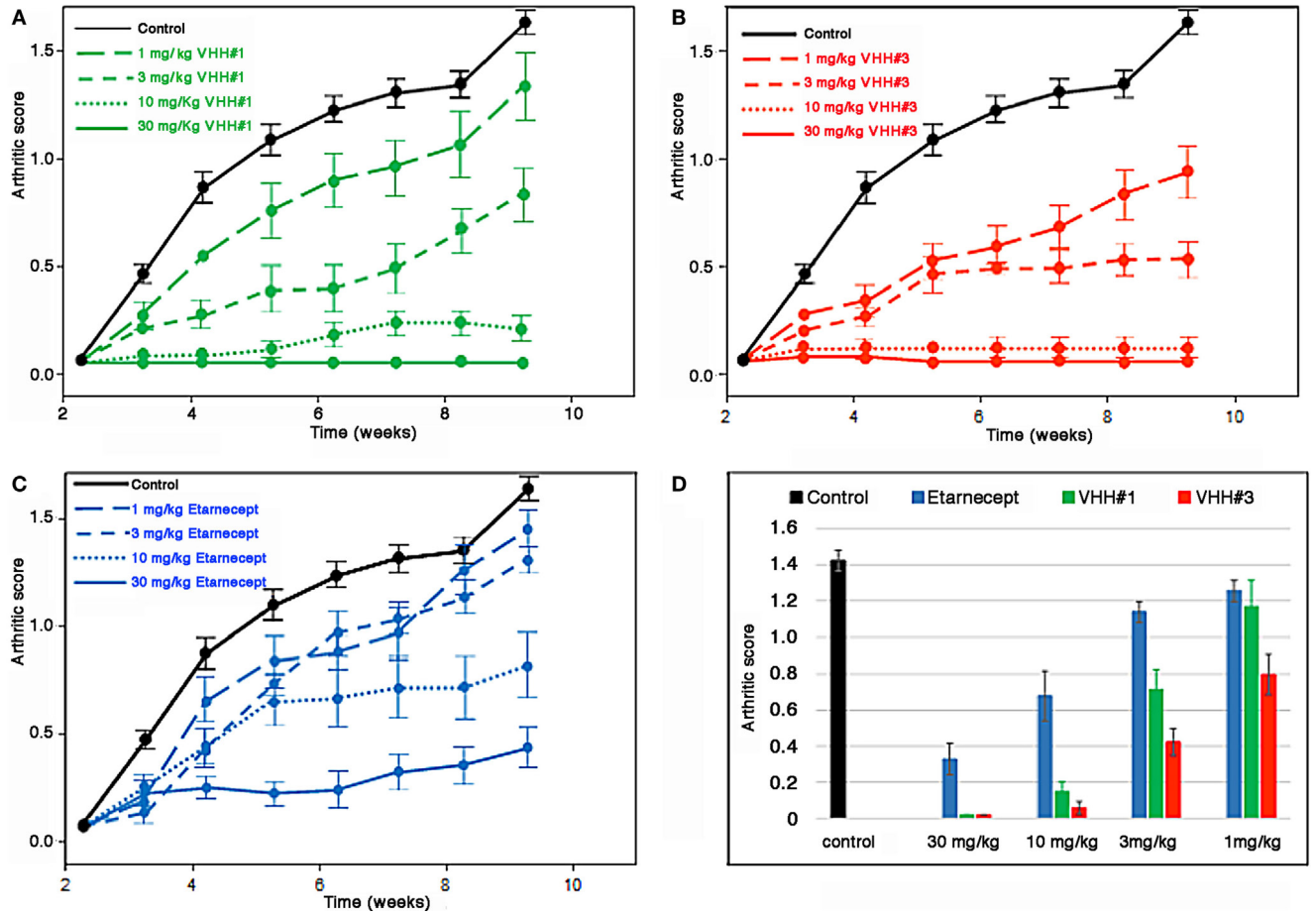

FIGURE 5 | Efficacy of Nanobodies™ in Tg197 mouse model. Human tumor necrosis factor (TNF) transgenic mice were treated at week 3 after birth (one week before arthritic symptoms develop, i.e., in a prophylactic setting) with bivalent anti-TNF/anti-albumin Nanobody™ constructs or etanercept biweekly. Arthritic scores were recorded weekly up to week 10. **(A)** Bivalent VHH#1 (VHH#1-9GS-HSA VHH-9GS-VHH#1) construct versus phosphate-buffered saline (PBS) control. **(B)** Bivalent VHH#3 (VHH#3-9GS-VHH#3-9GS-HSA VHH) construct versus PBS control. **(C)** Etanercept versus PBS control. **(D)** Results for all groups at week 10.

the 12- and 50-fold enhancements in affinity for VHH#1 and VHH#2, respectively, when using the 30 amino acids GlySer linker. Indeed, the observed smaller molecular species using SEC argues for the recognition of two binding sites on the same TNF trimer by these bivalent Nanobody™ constructs.

For the constructs with a short nine amino acids GlySer linker, simultaneous binding of both VHH#1 or VHH#2 modules to the same TNF trimer is not possible. The moderate threefold increase in affinity when employing the short nine amino acids GlySer linker is likely due to a rebinding effect similar to what is observed for galectins binding to asialofetuin (38) or for the recognition of phosporylation sites on Sic1 by Cdc4 (39).

The shortest distance between the N- and C-termini of two VHH#3 molecules bound simultaneously to the TNF trimer is 51 Å, suggesting a minimal required linker length of only 12 amino acids. This is in agreement with 125-fold increase in potency for the bivalent construct with a 12 amino acids linker. Interestingly, the construct with a shorter nine amino acids linker shows an 80-fold increase in potency, indicating that the N- and/or C-terminus of VHH#3 has sufficient conformational flexibility to accommodate such a short linker while still bridging both binding sites.

We determined the three-dimensional structures of the three VHHs in complex with TNF after bispecific constructs had been generated with the two Nanobodies™ VHH#1 and VHH#3 linked *via* a nine amino acid GlySer linker, either with VHH#3 first or with VHH#1 first (**Table 2**). Data show that the combination with VHH#3 at the N-terminal position is superior in potency to the construct with VHH#1 at that position by an order of magnitude (**Table 2**). When superimposing the structures of TNF–VHH#1 and TNF–VHH#3, it becomes clear that only one of the two different combinations of these Nanobodies™ linked to each other with the short linker in a bispecific construct should be able to bind in an intramolecular fashion, since the second leads to steric clashes. The bispecific Nanobody™ VHH#3-9GS-VHH#1 can bind in an intramolecular fashion to the TNF-monomer subunit, whereas the bispecific construct with VHH#1 at the N-terminal position required a linker of at least 20 amino acids in order to achieve intramolecular binding.

Superiority of bivalent over monomeric constructs was recognized many decades ago, when such improvement was termed "avidity" (40). Superiority was due to the localization of the second binder close to the second binding site, which avoided futile random search by diffusion/rotation *via* the increase of local concentration. A bivalent construct containing TNFR1 extracellular domain attached to an Fc domain was found to be more effective than the monovalent isolated extracellular domains (12). Furthermore, superior binding of the TNFR1-Fc inhibitor to TNF than to an anti-TNF mAb was demonstrated (12). In a more recent study it was demonstrated that the TNFR2-Fc fusion product known as etanercept was able to bind in an intramolecular fashion to TNF (41). The authors demonstrated that two discrete, relatively small soluble complexes were formed by the interaction of etanercept to the cytokine, whereas two different anti-TNF mAbs generated extremely large complexes as the result of the avid interaction of both Fab arms to two different TNF molecules, which could be visualized as precipitates in ouchterlony assays.

In contrast, in a cellular system, the mAb infliximab was a superior and more stable inhibitor of membrane-bound TNF than a TNFR-Fc inhibitor, despite comparable avidities (42). This was explained by the ability of the mAb to attach to a higher number of TNF trimers at the cell surface; the TNFR-Fc inhibitor can bind the two sites only *via* the intramolecular interaction with two of the three receptor interaction sites of the cytokine, while the mAb is able to saturate the three sites present on the cell surface, but using the two Fab arms to bind to two different cytokine molecules expressed on the surface of the cell.

Herein, bivalent/bispecific Nanobodies™ imbedding a sufficiently long linker were shown to bind with high avidity to TNF, occupying two of its three sites known to interact with TNFR (**Figures 4A,B**). Contrary to previously reported mAbs (41, 42), the very flexible geometry of the linker and the small size of the Nanobody™ binding site (as compared to a conventional antibody, where the binding site consists of the VH and VL) make it possible for these bivalent constructs to bind the two receptor interaction sites of the cytokine. When saturation occurs, it may be possible to obtain a complex of five bivalent/bispecific Nanobodies™ on two TNF molecules. On the other hand, under non-saturating conditions a single TNF molecule may be bound by two bivalent Nanobody™ constructs, which thereby occupy all three receptor binding sites. With a large excess of cytokine over bivalent Nanobody™ one can speculate that only a single Nanobody™ molecule will bind the TNF trimer, thereby leaving one free receptor binding site; this complex, when interaction with a single receptor molecule will block the cross-linking of this receptor molecule and might therefore function as an antagonist. When the linker is too short, preventing association of the second Nanobody™ module on the same TNF, high order networks of Nanobody™ bivalent/bispecific Nanobody–TNF complexes will form as was observed for anti-TNF mAb, which comes with a lower potency of neutralization (41).

Interestingly, a Tg197 transgenic human TNF mouse model for polyarthritis, confirmed *in vivo* the validity of properly designed Nanobody™ bivalent constructs against arthritis. For this purpose, the TNF Nanobodies™ were combined with the anti-HSA Nanobody™ (which cross-reacts with mouse serum albumin) to achieve appropriate serum half-lives. Bivalent VHH#3 alone or in combination with VHH#1 Nanobody™ in a bispecific construct displayed the best binding to TNF. Their efficacy *in vivo* was found to be comparable to that of the receptor-based inhibitor TNFR-Fc etanercept. Topological considerations indicated that both the 9 amino acid linker of VHH#3-9GS-VHH#3-9GS-HSA and the ~30 amino acid (9GS-HSA-9GS) linker of VHH#1-9GS-HSA-9GS-VHH#1 (taking into account that the albumin-specific Nanobody™ spans a length of approximately 12 amino acids) provide distances compatible with the binding of both VHH#3 and VHH#1 modules to the same TNF molecule. This finding is key to explaining the excellent *in vivo* efficacy of these bivalent Nanobody™ constructs.

ETHICS STATEMENT

This study was carried out in accordance with the recommendations of Ministry of Research, Belgium.

AUTHOR CONTRIBUTIONS

EB: leading program, supervisor research *in vitro* and *in vivo* studies; writing of the manuscript. AD: performing structural studies. SS: crystallized the complexes, collected and integrated the X-ray data. ML: performing experimental work on nanobody production, formatting into multimeric constructs, and purification of complexes for structural studies. LA: bioassay measurements. TD: designing and supervising *in vivo* efficacy studies. CC: solved, refined the structures and wrote the paper. RL: interpretation of structural data and writing of sections on structural studies. KS: involved in experimental work and writing of the manuscript. CP: supervising the research, corresponding author. HH: inventor of and performed the first series of formatting experiments, initiated structural studies, and manuscript writing.

ACKNOWLEDGMENTS

The European Synchrotron Radiation Facility (ESRF) is greatly acknowledged for beam time allocation. The authors would like to thank Eleni Douni and George Kollias [both from the Institute of Immunology of the Biomedical Sciences Research Center in Vari (Greece)] for testing the Nanobodies in the Tg197 model and finally Peter Casteels, Patrick Stanssens, and Frank Landolt (all from Ablynx) for retrieving *in vitro* and *in vivo* data sets.

FUNDING

This work was supported by Ablynx and CNRS.

REFERENCES

1. Blanco P, Palucka AK, Pascual V, Banchereau J. Dendritic cells and cytokines in human inflammatory and autoimmune diseases. *Cytokine Growth Factor Rev* (2008) 19:41–52. doi:10.1016/j.cytogfr.2007.10.004
2. Wajant H, Pfizenmaier K, Scheurich P. Tumor necrosis factor signaling. *Cell Death Differ* (2003) 10:45–65. doi:10.1038/sj.cdd.4401189
3. Faustman D, Davis M. TNF receptor 2 pathway: drug target for autoimmune diseases. *Nat Rev Drug Discov* (2010) 9:482–93. doi:10.1038/nrd3030
4. Steeland S, Puimège L, Vandenbroucke RE, Van Hauwermeiren F, Haustraete J, Devoogdt N, et al. Generation and characterization of small single domain antibodies inhibiting human tumor necrosis factor receptor 1. *J Biol Chem* (2015) 290:4022–37. doi:10.1074/jbc.M114.617787
5. Banner DW, D'Arcy A, Janes W, Gentz R, Schoenfeld HJ, Broger C, et al. Crystal structure of the soluble human 55 kd TNF receptor-human TNF beta complex: implications for TNF receptor activation. *Cell* (1993) 73:431–45. doi:10.1016/0092-8674(93)90132-A
6. Verweij CL. Predicting the future of anti-tumor necrosis factor therapy. *Arthritis Res Ther* (2009) 11:115. doi:10.1186/ar2724
7. Roda G, Jharap B, Neeraj N, Colombel JF. Loss of response to anti-TNFs: definition, epidemiology, and management. *Clin Transl Gastroenterol* (2016) 7(7):e135. doi:10.1038/ctg.2015.63
8. Van Hauwermeiren F, Vandenbroucke RE, Libert C. Treatment of TNF mediated diseases by selective inhibition of soluble TNF or TNFR1. *Cytokine Growth Factor Rev* (2011) 22:311–9. doi:10.1016/j.cytogfr.2011.09.004
9. Hamers-Casterman C, Atarhouch T, Muyldermans S, Robinson G, Hamers C, Songa EB, et al. Naturally occurring antibodies devoid of light chains. *Nature* (1993) 363:446–8. doi:10.1038/363446a0
10. van Doorn P. *The Advantages of Nanobodies and the Prospects These Offer in Cancer Treatment. [Thesis for the Master Molecular and Cellular Life Sciences]* (2013). Universiteit Utrecht (University of Utrecht), Utrecht, Netherlands.
11. Siontorou CG. Nanobodies as novel agents for disease diagnosis and therapy. *Int J Nanomedicine* (2013) 8:4215–27. doi:10.2147/IJN.S39428
12. Peppel K, Crawford D, Beutler B. A tumor necrosis factor (TNF) receptor-IgG heavy chain chimeric protein as a bivalent antagonist of TNF activity. *J Exp Med* (1991) 174:1483–9. doi:10.1084/jem.174.6.1483
13. Marmenout A, Fransen L, Tavernier J, Van der Heyden J, Tizard R, Kawashima E, et al. Molecular cloning and expression of human tumor necrosis factor and comparison with mouse tumor necrosis factor. *Eur J Biochem* (1985) 152:515–22. doi:10.1111/j.1432-1033.1985.tb09226.x
14. Curnis F, Corti A. Production and characterization of recombinant human and murine TNF. *Meth Mol Med* (2004) 98:9–22. doi:10.1385/1-59259-771-8:009
15. Chomczynski P, Sacchi N. Single-step method of RNA isolation by acid guanidinium thiocyanate-phenol-chloroform extraction. *Anal Biochem* (1987) 162:156–9. doi:10.1006/abio.1987.9999
16. de Haard HJ, Bezemer S, Ledeboer AM, Müller WH, Boender PJ, Moineau S, et al. Llama antibodies against a lactococcal protein located at the tip of the phage tail prevent phage infection. *J Bacteriol* (2005) 187:4531–41. doi:10.1128/JB.187.13.4531-4541.2005
17. Marks JD, Hoogenboom HR, Bonnert TP, McCafferty J, Griffiths AD, Winter G. By-passing immunization. Human antibodies from V-gene libraries displayed on phage. *J Mol Biol* (1991) 222:581–97. doi:10.1016/0022-2836(91)90498-U
18. Lauwereys M, Arbabi Ghahroudi M, Desmyter A, Kinne J, Hölzer W, De Genst E, et al. Potent enzyme inhibitors derived from dromedary heavy-chain antibodies. *EMBO J* (1998) 17:3512–20. doi:10.1093/emboj/17.13.3512
19. Santora LC, Kaymakcalan Z, Sakorafas P, Krull IS, Grant K. Characterization of noncovalent complexes of recombinant human monoclonal antibody and antigen using cation exchange, size exclusion chromatography, and BIAcore. *Anal Biochem* (2001) 299:119–29. doi:10.1006/abio.2001.5380
20. Kabsch W. XDS. *Acta Crystallogr D Biol Crystallogr* (2010) 66:125–32. doi:10.1107/S0907444909047337
21. Vagin A, Teplyakov A. Molecular replacement with MOLREP. *Acta Crystallogr D Biol Crystallogr* (2010) 66:22–5. doi:10.1107/S0907444909042589
22. Blanc E, Roversi P, Vonrhein C, Flensburg C, Lea SM, Bricogne G. Refinement of severely incomplete structures with maximum likelihood in BUSTER-TNT. *Acta Crystallogr D Biol Crystallogr* (2004) 60:2210–21. doi:10.1107/S0907444904016427
23. Emsley P, Lohkamp B, Scott WG, Cowtan K. Features and development of Coot. *Acta Crystallogr D Biol Crystallogr* (2010) 66:486–501. doi:10.1107/S0907444910007493
24. Krissinel E, Henrick K. Inference of macromolecular assemblies from crystalline state. *J Mol Biol* (2007) 372:774–97. doi:10.1016/j.jmb.2007.05.022
25. Keffer J, Probert L, Cazlaris H, Georgopoulos S, Kaslaris E, Kioussis D, et al. Transgenic mice expressing human tumour necrosis factor: a predictive genetic model of arthritis. *EMBO J* (1991) 10:4025–31.
26. Thwin MM, Douni E, Aidinis V, Kollias G, Kodama K, Sato K, et al. Effect of phospholipase A2 inhibitory peptide on inflammatory arthritis in a TNF transgenic mouse model: a time-course ultrastructural study. *Arthritis Res Ther* (2004) 6:R282–94. doi:10.1186/ar1456
27. Pavel MA, Lam C, Kashyap P, Salehi-Najafabadi Z, Singh G, Yu Y. Analysis of the cell surface expression of cytokine receptors using the surface protein biotinylation method. *Meth Mol Biol* (2014) 1172:185–92. doi:10.1007/978-1-4939-0928-5_16
28. Forsman A, Beirnaert E, Aasa-Chapman MM, Hoorelbeke B, Hijazi K, Koh W, et al. Llama antibody fragments with cross-subtype human immunodeficiency virus type 1 (HIV-1)-neutralizing properties and high affinity for HIV-1 gp120. *J Virol* (2008) 82:12069–81. doi:10.1128/JVI.01379-08
29. Verheesen P, ten Haaft MR, Lindner N, Verrips CT, de Haard JJ. Beneficial properties of single-domain antibody fragments for application in immunoaffinity purification and immuno-perfusion chromatography. *Biochim Biophys Acta* (2003) 1624:21–8. doi:10.1016/j.bbagen.2003.09.006
30. Conrath KE, Lauwereys M, Galleni M, Matagne A, Frère JM, Kinne J, et al. Beta-lactamase inhibitors derived from single-domain antibody fragments elicited in the camelidae. *Antimicrob Agents Chemother* (2001) 45:2807–12. doi:10.1128/AAC.45.10.2807-2812.2001
31. Conrath KL, Lauwereys M, Wyns L, Muyldermans S. Camel single-domain antibodies as modular building units in bispecific and bivalent antibody constructs. *J Biol Chem* (2001) 276:7346–50. doi:10.1074/jbc.M007734200
32. Kalliolias GD, Ivashkiv LB. TNF biology, pathogenic mechanisms and emerging therapeutic strategies. *Nat Rev Rheumatol* (2016) 12:49–62. doi:10.1038/nrrheum.2015.169
33. Coppieters K, Dreier T, Silence K, de Haard H, Lauwereys M, Casteels P, et al. Formatted anti-tumor necrosis factor alpha VHH proteins derived from camelids show superior potency and targeting to inflamed joints in a murine model of collagen-induced arthritis. *Arthritis Rheum* (2006) 54:1856–66. doi:10.1002/art.21827
34. Jähnichen S, Blanchetot C, Maussang D, Gonzalez-Pajuelo M, Chow KY, Bosch L, et al. CXCR4 nanobodies (VHH-based single variable domains) potently inhibit chemotaxis and HIV-1 replication and mobilize stem cells. *Proc Natl Acad Sci USA* (2010) 107:20565–70. doi:10.1073/pnas.1012865107
35. Hultberg A, Temperton NJ, Rosseels V, Koenders M, Gonzalez-Pajuelo M, Schepens B, et al. Llama-derived single domain antibodies to build multivalent, superpotent and broadened neutralizing anti-viral molecules. *PLoS One* (2011) 6(4):e17665. doi:10.1371/journal.pone.0017665
36. Efimov GA, Kruglov AA, Khlopchatnikova ZV, Rozov FN, Mokhonov VV, Rose-John S, et al. Cell-type-restricted anti-cytokine therapy: TNF inhibition from one pathogenic source. *Proc Natl Acad Sci U S A* (2016) 113:3006–11. doi:10.1073/pnas.1520175113
37. Desmyter A, Spinelli S, Roussel A, Cambillau C. Camelid nanobodies: killing two birds with one stone. *Curr Opin Struct Biol* (2015) 32:1–8. doi:10.1016/j.sbi.2015.01.001
38. Dam TK, Gabius HJ, André S, Kaltner H, Lensch M, Brewer CF. Galectins bind to the multivalent glycoprotein asialofetuin with enhanced affinities and a gradient of decreasing binding constants. *Biochemistry* (2005) 44:12564–71. doi:10.1021/bi051144z
39. Klein P, Pawso NT, Tyers M. Mathematical modeling suggests cooperative interactions between a disordered polyvalent ligand and a single receptor site. *Curr Biol* (2003) 13:1669–78. doi:10.1016/j.cub.2003.09.027
40. Hornick CL, Karuch F. Antibody affinity. 3. The role of multivalance. *Immunochemistry* (1972) 9:325–40. doi:10.1016/0019-2791(72)90096-1
41. Kohno T, Tam LT, Stevens SR, Louie JS. Binding characteristics of tumor necrosis factor receptor-Fc fusion proteins vs anti-tumor necrosis factor mAbs. *J Investig Dermatol Symp Proc* (2007) 12:5–8. doi:10.1038/sj.jidsymp.5650034

42. Scallon B, Cai A, Solowski N, Rosenberg A, Song XY, Shealy D, et al. Binding and functional comparisons of two types of tumor necrosis factor antagonist. *J Pharmacol Exp Ther* (2002) 301:418–26. doi:10.1124/jpet.301.2.418

Conflict of Interest Statement: EB, ML, TD, KS, CP, and HH: Ablynx employee during this research. AD, SS, LA, and CC: research paid in part by contract with Ablynx. RL: no conflict of interest.

frontiers in Immunology

ORIGINAL RESEARCH
published: 21 August 2017
doi: 10.3389/fimmu.2017.00884

Neutralization of Human Interleukin 23 by Multivalent Nanobodies Explained by the Structure of Cytokine–Nanobody Complex

Aline Desmyter[1,2‡], Silvia Spinelli[1,2‡], Carlo Boutton[3], Michael Saunders[3†], Christophe Blachetot[3†], Hans de Haard[3†], Geertrui Denecker[3†], Maarten Van Roy[3], Christian Cambillau[1,2] and Heidi Rommelaere[3]**

[1]Architecture et Fonction des Macromolécules Biologiques (AFMB), UMR 7257, Centre National de la Recherche Scientifique (CNRS), Marseille, France, [2]Architecture et Fonction des Macromolécules Biologiques (AFMB), UMR 7257, Aix-Marseille Université, Marseille, France, [3]Ablynx N.V., Ghent, Belgium

The heterodimeric cytokine interleukin (IL) 23 comprises the IL12-shared p40 subunit and an IL23-specific subunit, p19. Together with IL12 and IL27, IL23 sits at the apex of the regulatory mechanisms shaping adaptive immune responses. IL23, together with IL17, plays an important role in the development of chronic inflammation and autoimmune inflammatory diseases. In this context, we generated monovalent antihuman IL23 variable heavy chain domain of llama heavy chain antibody (V_{HH}) domains (Nanobodies®) with low nanomolar affinity for human interleukin (hIL) 23. The crystal structure of a quaternary complex assembling hIL23 and several nanobodies against p19 and p40 subunits allowed identification of distinct epitopes and enabled rational design of a multivalent IL23-specific blocking nanobody. Taking advantage of the ease of nanobody formatting, multivalent IL23 nanobodies were assembled with properly designed linkers flanking an antihuman serum albumin nanobody, with improved hIL23 neutralization capacity *in vitro* and *in vivo,* as compared to the monovalent nanobodies. These constructs with long exposure time are excellent candidates for further developments targeting Crohn's disease, rheumatoid arthritis, and psoriasis.

Keywords: interleukin 23, nanobody, multivalent binder, crystal structure, anti-inflammatory

OPEN ACCESS

Edited by:
Colin Roger MacKenzie, National Research Council Canada, Canada

Reviewed by:
Harald Kolmar, Technische Universität Darmstadt, Germany
Ellen Goldman, United States Naval Research Laboratory, United States

****Correspondence:***
Christian Cambillau
cambillau@afmb.univ-mrs.fr;
Heidi Rommelaere
Heidi.Rommelaere@ablynx.com

†Present address:
Michael Saunders, Christophe Blachetot and, Hans de Haard, argenx BVBA, Ghent, Belgium; Geertrui Denecker, Center for Medical Genetics Ghent (CMGG), Cancer Research Institute Ghent (CRIG), Medical Research Building (MRB), Ghent, Belgium

‡These authors have contributed equally to this work.

Specialty section:
This article was submitted to Vaccines and Molecular Therapeutics, a section of the journal Frontiers in Immunology

Received: *30 April 2017*
Accepted: *11 July 2017*
Published: *21 August 2017*

Citation:
Desmyter A, Spinelli S, Boutton C, Saunders M, Blachetot C, de Haard H, Denecker G, Van Roy M, Cambillau C and Rommelaere H (2017) Neutralization of Human Interleukin 23 by Multivalent Nanobodies Explained by the Structure of Cytokine–Nanobody Complex. Front. Immunol. 8:884. doi: 10.3389/fimmu.2017.00884

INTRODUCTION

By searching sequence databases for members of the IL6 cytokine family (1), a new protein, designated interleukin (IL) 23p19 was identified. This new protein had no biological activity, but formed in combination with the p40 subunit of IL12 a novel heterodimeric cytokine named IL23. The p40 subunit is shared with IL12, where it forms a heterodimer with another partner p35 (2). The human IL23-specific p19 subunit is a 189 amino acid polypeptide that contains five cysteine residues and no glycosylation sites. The p19 subunit shows an overall sequence identity of ~40% to the p35 subunit of IL12. The identical p40 subunit of both cytokines binds to the receptor (R) IL12Rβ1, the p35 subunit of IL12 binds to the IL12Rβ2 subunit, and the p19 subunit of IL23 binds to the unique IL23R subunit. The IL23 transmembrane receptor belongs to the class I cytokine receptor family, albeit that it lacks

Abbreviations: V_{HH}, variable heavy chain domain of llama heavy chain antibody; CDR, complementarity-determining region; Nb, nanobody; SPR, surface plasmon resonance; K_d, equilibrium dissociation constant; k_{on}, association rate constant; k_{off}, rate constant; rmsd, root mean square deviation; GS linker, glycine–serine linker.

the characteristic membrane-proximal fibronectin type III-like domains. The human IL23 receptor chains are predominantly co-expressed on activated and memory T cells and NK cells, but also at low levels on monocytes, macrophages and dendritic cell (DC) populations. IL23 binds to and signals through the heterodimeric IL12Rβ1/IL23R complex, which is associated with Tyk2 and Jak2, respectively. Upon Jak2-mediated phosphorylation of tyrosine residues located in the intracellular domain of the IL23R subunit, Stat3 molecules are phosphorylated in turn. Phospho-Stat3 proteins homodimerize and translocate into the nucleus, inducing transcription of cytokines such as IL17A, IL17F, IL22, and IFN-γ.

Similar to IL12, IL23 is expressed predominantly by activated DCs and phagocytic cells. IL23 is also produced by antigen-presenting cells and promotes the expansion and survival of a distinct lineage of T cells, Th17 (3). IL17, a proinflammatory cytokine predominantly produced by activated T cells (by Th17 cells), enhances T-cell priming and stimulates fibroblasts, endothelial cells, macrophages, and epithelial cells to produce multiple proinflammatory mediators, including IL1, IL6, TNF-α, NOS2, metalloproteases, and chemokines, resulting in the induction of inflammation (4–6). IL17 expression is increased in patients with a variety of allergic and autoimmune diseases, such as rheumatoid arthritis, multiple sclerosis, inflammatory bowel disease, and asthma, suggesting the contribution of IL17 to the induction and/or development of such diseases. Th17/ThIL17 cells are likely to play critical roles in the development of autoimmunity and allergic reaction, and the IL23/IL17, but not IL12/IFN-γ, axis is critical for the development of autoimmune inflammatory diseases (7).

Our aim was to generate nanobody constructs able to neutralize human interleukin (hIL) 12 and/or hIL23, which could be drug candidates for treatment of Crohn's disease, rheumatoid arthritis, or psoriasis. In this report, we describe the generation and characterization of nanobodies against p40 and the human (h) IL23-specific p19 subunit. Binding and neutralization characteristics of four selected monovalent nanobodies were determined *via* biochemical and *in vitro* cell assays. As nanobodies have proven to be valuable tools for crystallization purposes in academic contexts (8, 9) as well as in biotechnological or biopharmaceutical contexts (10, 11), crystal structures of hIL23 in complex with three of those four nanobodies were generated. The structure of this quaternary complex helped to understand the high binding efficiency and blocking capacity of the nanobodies. As a result, we were able to rationalize the construction of multivalent nanobodies, whereby the two anti-p19 nanobodies were linked to improve potency and hooked up to an antihuman serum albumin (HSA) nanobody to increase the exposure time (12). The multivalent nanobodies displayed significant enhanced *in vitro* potency in neutralizing IL23 and proved to be very effective in an *in vivo* splenocyte assay performed in mice; hence, they are promising drug candidates.

MATERIALS AND METHODS

IL23 Materials

Human interleukin 23 was purchased from R&D Systems Inc. and from eBioscience. hIL12, mouse (m) IL23, hIL23 receptor (R)-fragment crystallizable region (Fc), and IL12Rβ-Fc chimera were purchased from R&D Systems Inc. Cynomolgus monkey (cyno) IL23 was produced at Ablynx, Ghent/Zwijnaarde, Belgium. hIL23 (eBioscience) and hIL12 (R&D Systems Inc.) were biotinylated using Sulfo-NHS-LC-Biotin (Pierce™).

Immunization, Library Construction, and Selection of Nanobodies Directed toward hIL23

Two *Lama glama*s were injected with recombinant hIL23, and two llamas received a cocktail of proteins containing a.o. recombinant hIL23 and hIL12. Each animal received seven doses of intramuscular injected antigen at weekly intervals, as described by Roovers et al. (13, 14). Pre-immune and immune sera were collected at day 0, and after 3 and 6 weeks of immunization. The immune response in each animal was monitored by titration of serum samples on coated hIL12 or hIL23.

RNA was prepared from peripheral blood mononuclear cells (PBMCs) isolated from sera and lymph node biopsies. Library constructions were performed as described previously (13, 14), amplifying the variable heavy (V_H) chain domains of heavy chain antibody (V_{HH}) genes and ligating them into the phagemid vector pAX51 in frame with a C-terminal c-myc and hexa-histidine tag for display on phage.

After superinfection of the *Escherichia coli* TG1 library clones with helper phage, the presence of pAX51 allows for the production of phage particles displaying the individual nanobodies as a fusion protein with the pIII protein. Nanobodies recognizing specifically the p19 subunit of hIL23 were retrieved, allowing phages bind to coated hIL23 (5 or 0.5 nM) on microtiter plates. Phages were counter selected three times by binding to wells coated with 5 μg/ml hIL12 to remove p40-binding phages, and further preincubated with 1 μM hIL12 in solution before adding to the hIL23 coated wells. Phages were specifically eluted with trypsin (in the case of 124C4) or with 5 nM of recombinant IL23R (in the case of 37D5). Nanobodies recognizing specifically the p40 subunit of hIL23 and hIL12 were obtained by trypsin elution of phages bound to coated hIL23 (0.1 nM). Subsequently, exponentially growing *E. coli* TG1 cells were infected with the eluted phages, and individual clones were selected, grown in 96-deep well plates (1 ml volume) and induced by the addition of isopropyl-β-D-thiogalactopyranoside (IPTG) for the production of nanobodies. Since the nanobodies are secreted into the periplasmic space, this fraction was then prepared by freeze-thawing of the bacterial pellet in a phosphate-buffered saline (PBS; 100 μl) solution and centrifugation to remove cell fragments.

ELISA-Binding Screen

1 μg/ml of cytokine (hIL12, hIL23) was immobilized directly on microtiter plates. Free-binding sites were blocked using 4% Marvel in PBS. To this, 5 μl of nanobody containing periplasmic extracts in 100 μl 2% Marvel PBS with Tween 20 were added. Nanobody binding was revealed using a mouse-anti-myc primary antibody, and a horseradish peroxidase-conjugated goat anti-mouse secondary antibody.

AlphaScreen-Based Receptor-Blocking Assay

To determine the capacity of the nanobodies to inhibit the IL23/IL23R or IL12/IL12Rβ1 interaction, a protein-based competition was used. First, periplasmic extracts were screened for the presence of neutralization capacity at 1 dilution (25-fold), and therefore preincubated with 3 nM biotinylated hIL23 or hIL12. Second, the potency of the neutralizing nanobodies was determined by using serial dilutions of purified p19 blocking (p19+) nanobodies (from 250 nM to 1 pM) or of p40 blocking (p40+) nanobodies (from 250 nM to 1 pM) preincubated with 500 pM biotinylated hIL23 and with 3 nM biotinylated hIL12, respectively. To these mixtures, IL23R, respectively IL12Rβ1 acceptor beads (receptors bound *via* an antihuman Fc monoclonal antibody) and the streptavidin-coated donor beads (Perkin Elmer Inc)—were added, and further incubated for 1 h at room temperature. Fluorescence was measured using the EnVision Multilabel Plate Reader (Perkin Elmer Inc.) using an excitation wavelength of 680 nm and an emission wavelength of 520 nm. Decrease in the AlphaScreen signal indicated that binding of biotinylated hIL23 to the IL23R or hIL12 to the IL12Rβ1 is blocked by the nanobody.

Surface Plasmon Resonance (SPR)

Surface plasmon resonance was performed using a Biacore T100 instrument. hIL23 was covalently bound to a CM5 sensor chip surface *via* amine coupling using EDC/NHS for activation and HCl for deactivation. Nanobody binding was assessed using periplasmic extracts diluted 1/10 for off-rate determination, and using purified nanobodies at concentrations ranging from 1 to 300 nM for K_d determination. Each nanobody was injected for 4 min at a flow rate of 45 µl/min to allow binding to chip-bound antigen. Binding buffer without nanobody was then passed over the chip at the same flow rate to allow spontaneous dissociation of bound nanobody. k_{off} values were calculated from sensorgrams obtained for the different nanobodies, and k_{on} and K_d values were calculated from sensorgrams for the purified nanobodies. For binning of nanobodies, hIL23 was captured *via* a p40-binding nanobody, which was immobilized on a chip. After binding of one of the lead nanobodies at 500 nM, RU levels were determined to evaluate whether their levels had increased after the flowing over of the other lead nanobody at 500 nM.

Cloning, Expression, and Purification of Anti-IL23 Nanobodies

Nanobody genes were subcloned into the pAX55 expression vector in frame with a N-terminal *ompA* sequence, and a C-terminal c-myc and hexa-histidine tag (Ablynx; described in WO2008043821). Multivalent nanobody constructs, as outlined in **Table 1** (D), were made in the pAX55 vector. They comprise of one or two anti-p19 nanobody building blocks and one building block corresponding to an anti-HSA nanobody building block (ALB1). The individual building blocks were fused by Gly/Ser linkers: 9GS (GGGGSGGGS) or 15GS (GGGGSGGGGSGGGGS). Non-suppressor *E. coli* TG1 cells (Stratagene Corp.) transformed with the appropriate vector were grown at 37°C in Terrific Broth medium supplemented with 100 µg/ml kanamycin and 0.1% glucose for 3 h until optical density (OD_{600}) reached ~4. Nanobody expression was induced by the addition of 1 mM IPTG, and growth of the cells was continued for 3–4 h at 37°C. The periplasmic fraction was prepared according to the methods of Skerra and Plückthun (15), and His-tagged nanobodies were purified by immobilized metal affinity chromatography on a 1 ml Ni-NTA column.

For crystallization purposes, eluted fractions in 250 mM imidazole were concentrated on an Amicon-Ultra 10 kDa cutoff concentrator prior to being loaded on to a HiLoad 10/30 Superdex75 gel filtration column in Dulbecco's PBS (dPBS; Invitrogen). Protein concentration of the nanobodies was determined by UV spectrometry from the absorbance at 280 nm, using their calculated extinction coefficient. For the nanobodies that had to be tested in the splenocyte assays, lipopolysaccharide (LPS) removal was performed by ion exchange in flow-through mode or by gel filtration in the presence of octylglucosylpyranoside; remaining LPS levels were determined using a limulus amebocyte lysate assay.

IC_{50} Determination in a Mouse Splenocyte Assay

Spleens of five C57BL/6 mice were removed, splenocytes were harvested, and a single cell suspension was prepared. Splenocytes were washed three times in RPMI supplemented with 10% fetal bovine serum, 1% pen/strep, 80 µM β-mercaptoethanol, and 1 mM sodium pyruvate. This medium is further referred to as complete RPMI. The splenocyte suspension was treated with 1× erythrocyte lysis buffer (155 mM NH_4Cl, 10.9 mM $KHCO_3$, 1.3 mM EDTA) to remove all residual erythrocytes. After three wash steps in complete RPMI, the cells were filtered over a 100 µM cell strainer and resuspended in complete RPMI containing 20 ng/ml recombinant mouse interleukin (mIL) 2 (R&D Systems Inc.). Cells were seeded at 400,000 cells/well in 96-well flat bottom plates. Serial dilutions of the nanobodies were preincubated with recombinant hIL23 (eBioscience) in culture medium for 30 min at room temperature and then incubated for a further 5 days with the splenocytes, at a final concentration of 19 pM hIL23. Supernatants were collected, and levels of mIL22 measured using ELISA (mIL22 ELISA construction kit, Antigenix America, NY, USA). All tests were done in triplicate.

Acute *In Vivo* Splenocyte Model

Nanobodies were injected subcutaneously (s.c.) into C57Bl/6 mice ($n = 4$) 24 h before the first of three subsequent intraperitoneal (i.p.) injections of 3 µg hIL23 (at times 0, 7, and 23 h). Test items were administered at a 16-fold, 3.2-fold, or 0.64-fold molar excess to each injection of hIL23. After 31 h, mice were sacrificed and spleens removed. Splenocytes were prepared and mIL22 measured as described above.

hIL12-Dependent Proliferation of PHA Blasts

PHA blasts were derived from cultured PBMC by stimulation with phytohemagglutinin. They were stimulated for 48 h with 300 pg/ml hIL12. The cells were pulsed with 1 µCi/well ^{3}H-thymidine for the last 6 h, and the incorporation of ^{3}H-thymidine was determined by scintillation counting in the presence of serial dilutions of nanobodies over a range of $10–10^{-5}$ µg/ml.

TABLE 1 | Interactions of the various nanobodies constructs with ILs.

(A) Nanobody types identified at screening

	p19 binder = p19−	p19 blocker = p19+	p40 binder = p40−	p40 blocker = p40+
Binding to hIL23	+	+	+	+
Binding to hIL12	−	−	+	+
hIL23/IL23R blocking	−	+	−	−
hIL12/IL12Rβ1 blocking	−	−	−	+

(B) Surface plasmon resonance experiments: k_{on}, k_{off}, and K_d of human p19 and p40 nanobodies binding to hIL23

Nanobody	Specificity	k_{off} hIL23 (s^{-1})	k_{on} hIL23 (M^{-1} s^{-1})	K_d hIL23 (M)
37D5	p19+	1.8×10^{-4}	3.2×10^{5}	0.6×10^{-9}
124C4	p19−	3.3×10^{-4}	1.0×10^{5}	3.3×10^{-9}
22E11	p40+	2.3×10^{-4}	nd	nd
80D10	p40−	9.7×10^{-5}	5.1×10^{4}	0.8×10^{-9}

(C) IC_{50} values of the antihuman p19 and p40 nanobodies in AlphaScreen

Human p19+ nanobody	IC_{50} (pM) hIL23 (confidence range)
37D5	110 (80–170)
Human p40+ nanobody	**IC_{50} (pM) hIL12 (confidence range)**
22E11	1,300 (850–1,950)

(D) Splenocyte assay (performed in triplicate)

(i) Average IC_{50} values of human p19 and p40 nanobodies using 19 pM hIL23 (±10%)

(ii) Comparison of potencies of human p19 formatted, half-life extended nanobodies with 19 pM hIL23 (±10%)

Nanobody ID: P23IL	Specificity	Nanobody construct	IC_{50} (pM)
(i) Monovalent			
37D5	p19 blocker	37D5	19
22E11	P40 blocker	22E11	186
(ii) Multivalent			
0050	p19 blocker	37D5-**9**GS-Alb1	29.8
0051	p19 blocker + p19 binder	37D5-**9**GS-Alb1-**9**GS-124C4	17
0053	p19 blocker + p19 binder	37D5-**9**GS-Alb1-**15**GS-124C4	3.1
0054	p19 binder + p19 blocker	124C4-**15**GS-Alb1-**9**GS-37D5	4.2
0070	p19 binder + p19 blocker	37D5-**15**GS-Alb1-**15**GS-124C4	3.8
0072	p19 binder + p19 blocker	124C4-**15**GS-Alb1-**15**GS-37D5	3.2
0409	P40 blocker + p40 binder	22E11-**9**GS-Alb1-**15**GS-80D10	0.6

h, human; IC_{50}, half maximal inhibitory concentration; IL, interleukin; nd, not determined; R, receptor; hIL, human interleukin. In D(ii), bold numbers emphasize the length of the GS repeats.

hIL23/Nanobody Complex Purification and Characterization

1 mg hIL23 in dPBS pH 7.2 was incubated with a slight molar excess of three different purified nanobodies for 1 h on ice. The resulting complex was separated from free nanobody excess by gel filtration chromatography on a Superdex75 column in 10 mM HEPES pH 7.0, 150 mM NaCl, and then concentrated to 7.6 mg/ml on an Amicon-Ultra filter (cutoff 50 kDa; Millipore). Mass spectrometry was performed on a matrix-assisted laser desorption/ionization time of flight (MALDI-TOF) mass spectrometer (Bruker Autoflex) according to standard procedures.

Crystallization and X-Ray Diffraction

Diffraction-quality crystals of the complex were obtained by sitting-drop vapor diffusion at 277 K after 4–30 days in 16.5% PEG 20 K and 0.1 M MES pH 5.9. Crystals belong to the orthorhombic space group $P2_12_12_1$, with unit cell dimensions: $a = 102.0$ Å, $b = 134.8$ Å, and $c = 138.4$ Å. They contain two complexes per asymmetric unit. Crystals were flash frozen to 100 K using 13% glycerol as the cryoprotectant. Diffraction data were collected under standard cryogenic conditions on beamline ID29, using an ADSC Quantum 4 detector at the ESRF synchrotron (Grenoble, France), processed using MOSFLM (16), and scaled with SCALA (17). The crystal structure of hIL23 in complex with three nanobodies was determined from single-wavelength native diffraction experiments by molecular replacement using PHASER (18). Refinement was performed with BUSTER (19). Figures were constructed using the PyMOL Molecular Graphics System, Version 1.5.0.4 (Schrödinger, LLC). Coordinates were deposited with the Protein Data Bank (PDB) with accession code 4GRW.

RESULTS

Generation and Selection of p19- and p40-Binding Nanobodies

To generate V_H chain domains of Heavy chain antibodies (V_{HH} or Nanobodies®) against the IL23 p19 and p40 subunit, llamas were immunized with recombinant hIL23. Subsequently, phage

nanobody libraries were generated from PBMCs and lymph node biopsies (LNs) collected from these animals. This resulted in four libraries with sizes between 2×10^7 and 4×10^7, and a percentage of insert containing clones ranging from 91 to 100%. After selection, nanobodies present in the periplasmic fractions of isolated clones were screened for their binding specificity to hIL12 versus hIL23 in an ELISA binding assay. Nanobodies binding to p40 were identified and recognized both hIL12 and hIL23, wheras nanobodies binding to p19 specifically recognized hIL23 only.

Periplasmic extracts were then analyzed to determine the ability of the nanobodies herein to inhibit the hIL23-hIL23R or the hIL12-hIL12Rβ1 interaction *via* an Amplified Luminescent Proximity Homogeneous (AlphaScreen) Assay for protein–protein interaction detection. Nanobodies decreasing the signal in this assay inhibit the hIL23/hIL23R (designated p19+) or the hIL12/hIL12Rβ1 interaction (designated p40+).

Different nanobody types were identified in the binding and neutralization screening assays (**Table 1**, A). A selection of p19 binding (p19−), p19 blocking (p19+), p40 binding (p40−), and p40 blocking (p40+) nanobodies were DNA sequenced. Twenty families of anti-p19 nanobody sequences were identified, with 7 families containing p19+ and 13 containing p19− nanobodies; and 24 families of anti-p40 nanobody sequences, with 12 families containing p40+ and 12 containing p40− nanobodies. The off-rates of the unique family members were determined using SPR. The family members with the slowest off-rates on hIL23 or hIL12 were recloned and purified for further characterization.

Affinity Determination of Anti-p19 and Anti-p40 Nanobodies

Binding kinetics of the purified human p19+ nanobody 37D5, the p19− nanobody 124C4, the p40+ nanobody 22E11, and the p40− nanobody 80D10 were determined using SPR. From the sensorgrams obtained, k_{on}, k_{off}, and K_d were calculated where possible (**Table 1**, B). The three compounds were found to display excellent off-rates for hIL23, with nanobody 37D5 having the best affinity (K_d 0.57 nM). Species cross-reactivity profiles of the monovalent nanobodies were also studied using SPR. All four nanobodies bound to cynomolgus monkey (cyno) IL23 with similar off-rates, and only nanobody 124C4 was able to cross-react to mouse (m) IL23. Knowledge of species cross-reactivity is important in light of future animal efficacy and pharmacokinetic/pharmacodynamic studies.

In Vitro Evaluation of the Inhibiting Capacity of Anti-p19 and Anti-p40 Nanobodies

The potency of the nanobodies to inhibit the IL23/IL23R or IL12/IL12Rβ1 interaction was determined either in a protein-based competition assay using AlphaScreen or in cell-based potency assays.

For the AlphaScreen, preincubation of a serial dilution of the p19+ nanobody 37D5 with biotinylated hIL23 reduced fluorescence intensity at 520 nm, demonstrating that this nanobody can effectively inhibit hIL23 binding to IL23R in a dose-dependent manner with a half maximal inhibitory concentration (IC_{50}) of 110 pM. Preincubation of a serial dilution of the p40+ nanobody 22E11 with biotinylated hIL12 also reduced the fluorescence intensity, demonstrating that this nanobody can effectively inhibit hIL12 binding to IL12Rβ1 with an IC_{50} of 1,300 pM (**Table 1**, C).

Inhibition of hIL23-mediated signaling by the nanobodies was investigated using a mouse splenocyte assay. This cell-based potency assay is based on the ability of hIL23 to stimulate mIL22 secretion from mouse spleen cells (20). The p19+ nanobody 37D5 appears to be very potent reaching an average IC50 value of 19 pM when using 19 pM hIL23 for stimulation, whereas the p40+ nanobody 22E11 shows an IC_{50} of 186 pM (**Table 1**, D, i).

Anti-p19 Nanobodies 37D5 and 124C4 Recognize Different Epitopes

As shown above, nanobody 37D5 shows good neutralizing activity toward hIL23. In theory, it would be possible to further improve the hIL23 neutralization by linking nanobody 37D5 to a p19-binding non-blocking nanobody as avid interaction of such a multivalent construct with the cytokine is expected. To do so, both nanobodies need to bind to different epitopes.

An SPR experiment was conducted where hIL23 was captured *via* a p40-binding nanobody (80D10), which was immobilized on a chip. After binding the p19 blocker (nanobody 37D5), it was assessed as to whether a second nanobody could bind simultaneously to hIL23 p19 subunit. The interaction studies show that nanobody 37D5 can bind concurrently with the p19− nanobody 124C4, since RU levels double upon binding of the second nanobody (Figure S1 in Supplementary Material, green trace). For other p19− nanobodies tested, this was not the case (Figure S1 in Supplementary Material, non-green traces). Hence, nanobody 37D5 and nanobody 124C4 could be combined in a multivalent construct and used simultaneously for crystallization in complex with hIL23.

Structure of hIL23 Bound Simultaneously to Nanobodies 37D5, 124C4, and 22E11

The high affinity of the monovalent nanobodies and the existence of different epitopes for the p19+ nanobody 37D5, the p19− nanobody 124C4, and the p40+ nanobody 22E11 encouraged us to crystallize recombinant hIL23 in complex with these three nanobodies. hIL23 was mixed with an excess of the nanobodies, and the complex was purified by gel filtration. Crystals were readily obtained, and the structure was solved by molecular replacement using the hIL23 structure [in complex with the Fab 7G10 (21)] and V_{HH} structures (22, 23) as search models. The crystals contain two complexes in the asymmetric unit and the structure was refined to R/R_{free} values of 18.3%/21.8%, respectively (Table S1 in Supplementary Material).

The overall structure of hIL23 with its three bound nanobodies is depicted in **Figure 1**. hIL23 is formed by two monomers, p19 and p40, linked by a disulfide bridge between Cys 54 (p19) and Cys177 (p40). The monomer p19 is formed by a four antiparallel helix bundle (21, 24, 25). The p40 protein is formed of three domains, each composed of a 7 β-stranded β-sandwich (2, 21, 24, 25). The interaction surface between p19 and p40 is ~900 Å^2 and hence quite large. The p19 monomer inserts its fourth helix between the

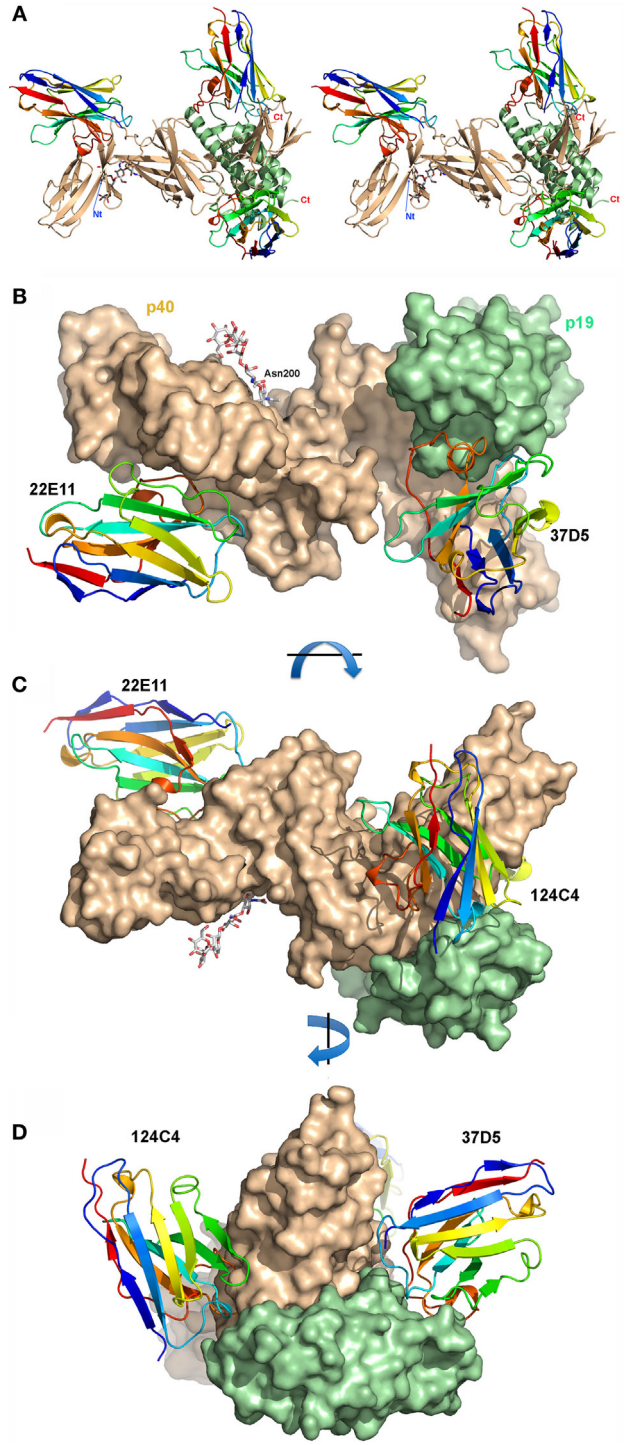

FIGURE 1 | Human interleukin (hIL) 23 in complex with three nanobodies. **(A)** Stereo view of hIL23 in complex with three nanobodies. p40 is shown in brown, p19 green, and the 37D5, 124C4, and 22E11 nanobodies are in rainbow colors. **(B)** Surface representation of hIL23, with the three nanobodies in ribbon representation. The Asn 200 branched sugar is represented by sticks. **(C)** 90° rotation around a horizontal axis [relative to panel **(B)**]. **(D)** 90° rotation around a vertical axis [relative to panel **(C)**].

two first domains of p40. The interface is completed by a p19 loop joining helices H1 and H2. The structure of hIL23 in our complex is close to the structures published previously, with root mean square deviation (rmsd) values of 0.7–1.2 Å, mainly due to slightly different orientations of the three p40 domains. The rmsd values observed between the same domains in different structures are indeed much lower (0.5–0.9 Å). Noteworthy, two saccharidic chains of the complex type are observed at Asn 200 of the two p40 chains, with the five core sugars well defined ($GlcNAc_2$-Man_3) (Figure S2 in Supplementary Material). Superposition of the two independent complexes of the asymmetric unit indicates that the two complexes are quite similar (rmsd < 1.0 Å) for p40, nanobody 124C4, and nanobody 22E11 (Figure S3 in Supplementary Material).

Totally unexpected from the interaction studies in solution, the structure reveals that the p19+ 37D5 nanobody and the p19− nanobody 124C4 interact with both subunits of hIL23, p19 and p40 (**Figures 1** and **2**; Tables S2 and S3 and Figures S4 and S5 in Supplementary Material). As frequently observed with nanobodies (8), nanobody 37D5 and nanobody 124C4 bind to concave surfaces and insert their complementarity-determining regions (CDRs) in the crevices formed at the junction between p19 and p40. In contrast and as expected, the p40+ 22E11 nanobody interacts only with p40 and binds a flat surface of the cytokine's first p40 domain, remote from the two other nanobodies that bind the third p40 domain.

Interaction of the Three Nanobodies with hIL23 and Description of a Novel Neutralizing Epitope

The three nanobodies interact with hIL23 with high affinity, which correlates with very large buried surface areas: ~1,110 Å² for nanobody 37D5, ~830 Å² for nanobody 124C4, and ~780 Å² for nanobody 22E11 (Table S2 in Supplementary Material). Nanobody 37D5 was initially assigned as a p19 binder and has, indeed, a larger surface of interaction with p19 (850 Å²) than with p40 (260 Å²) (Table S2 in Supplementary Material). It binds to the p19 helix bundle with its three CDRs and a few residues from the framework. CDR3, however, exhibits the most extended interaction with seven residues as compared to three residues for CDR1 and CDR2 (Table S3A in Supplementary Material; **Figure 2B**). The interaction with p40 occurs through three residues (Table S3 in Supplementary Material), with Phe 27 inserted deeply between both monomers. The 124C4 nanobody, which was initially assigned as a p19 binder, exhibits a binding pattern opposite to the one of 37D5, with a larger surface of interaction with p40 (625 Å²) than for p19 (200 Å²). Interaction with p40 involves four residues of CDR2 and seven residues of CDR3 (Table S3B in Supplementary Material; **Figure 2C**). Interaction with p19 involves four residues of CDR1 and one residue (Thr97) from CDR3. Finally, nanobody 22E11 interacts exclusively with p40. The interface involves a small number of contacts with CDR1 and CDR2 (two and four residues, respectively) and a large number of contacts (eight residues) from CDR3 (Table S3C in Supplementary Material; **Figure 2D**).

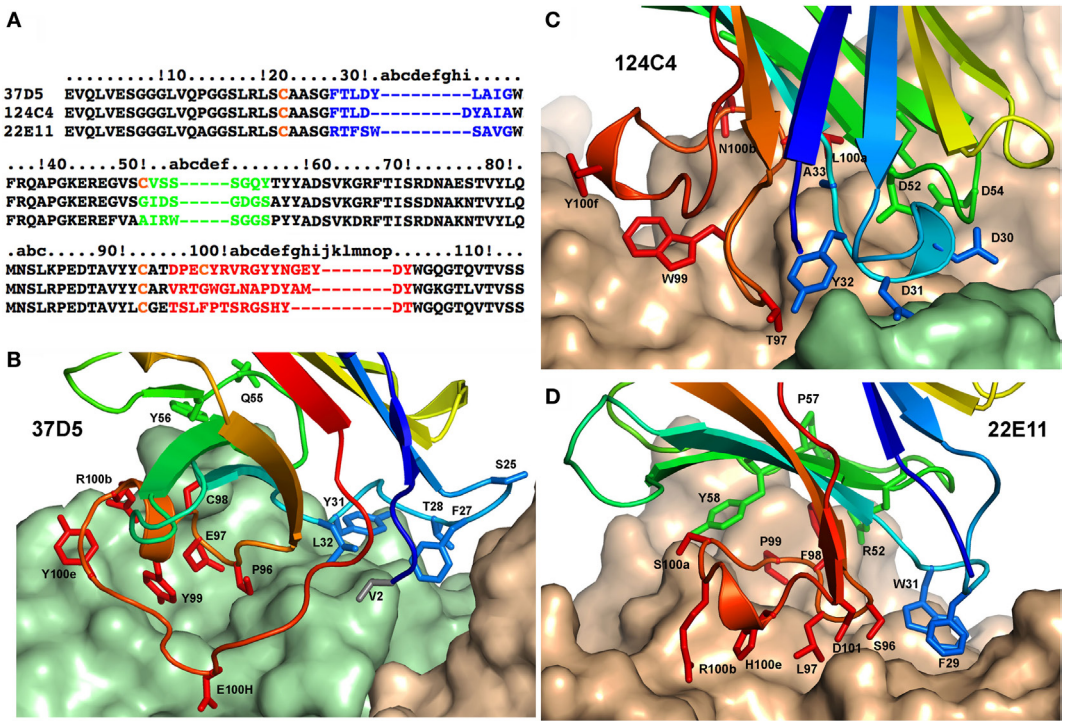

FIGURE 2 | Contacts of human interleukin (hIL) 23 in complex with three nanobodies. **(A)** Sequence alignment of the nanobodies 37D5, 124C4, and 22E11. Complementarity-determining region (CDR) 1 is shown in blue, CDR2 is green, CDR3 is red, and cysteines are shown in orange. **(B)** N-terminal, CDR, and framework 3 residues of nanobody 37D5 that interact with hIL23. **(C)** CDR residues of nanobody 124C4 that interact with hIL23. **(D)** Residues of nanobody 22E11 that interact with p40. In **(B)**–**(D)** p40 is shown in brown, p19 is green, and the 37D5, 124C4, and 22E11 nanobodies are in rainbow colors. CDR1 is shown in green, CDR2 is blue, and CDR3 is red.

Formatting of the Anti-p19 Nanobodies Results in Very Potent hIL23-Neutralizing Molecules

We generated multivalent constructs, whereby we assembled the p19-neutralizing nanobody 37D5 with the non-neutralizing nanobody 124C4. To prolong the half-life of the molecules for use as therapeutic agents in inflammatory diseases, a nanobody that binds serum albumin (Alb1) was included in these constructs. The human-mouse serum albumin cross-reactive nanobody Alb1 was positioned between the two anti-p19 nanobody building blocks (**Figure 3**). The length of the linkers fusing Alb1 to the anti-p19 nanobody building blocks was varied, based on predictions using the crystal structures. In addition, the nanobody order in the constructs was varied, as N- or C-terminal positioning of a certain building block can influence its binding affinity. Next to that, a half-life extended (HLE) version of nanobody 37D5 on its own (37D5-9GS-Alb1, **Table 1**, D, ii) was generated, since nanobody 37D5 is already quite potent in a monovalent format. The potency of the different constructs was determined in the mouse splenocyte assay using hIL23 as described above. The potency of 37D5-9GS-Alb1 is slightly decreased; however, potencies of the trivalent nanobodies are better (**Table 1**, D, ii). When placing nanobody 37D5 at the N-terminal position, the neutralizing potency is

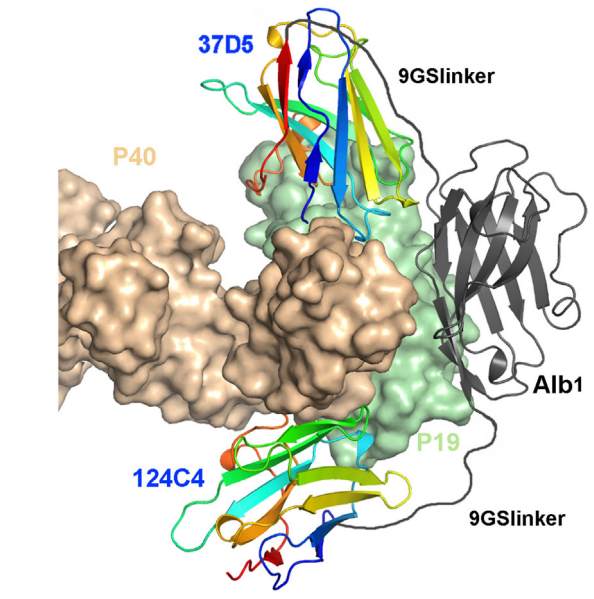

FIGURE 3 | Model of a multivalent construct combining the nanobodies 124C4 and 37D5 with the antihuman serum albumin nanobody Alb1 flanked by two 9GS flexible linkers. This 9GS-Alb1-9GS construct is able to bridge the distance between the C-terminus of 124C4 and the N-terminus of 37D5 when bound to human interleukin 23.

approximately fivefold better with a 9 + 15GS linker compared to a 9 + 9GS linker (**Table 1**, D, ii). When combining 9 + 15GS or 15 + 15GS, the order of the building blocks has little influence on the potency to neutralize hIL23.

HLE Multivalent Anti-p19 Nanobodies Show Improved Efficacy *In Vivo*

An acute *in vivo* mouse splenocyte model assay demonstrated the efficacy of the formatted nanobodies P23IL0050 (37D5-9GS-Alb1) and P23IL0054 (124C4-15GS-Alb1-9GS-37D5). Nanobodies were injected subcutaneously (s.c.) 24 h before the first of three subsequent intraperitoneal (i.p.) injections of 3 µg hIL23 at times 0, 7, and 23 h occurred. Nanobodies were administered at three different doses, at a 16-fold, 3.2-fold, or 0.64-fold molar excess to each injection of hIL23. P23IL0050 and P23IL0054 were capable of neutralizing hIL23 *in vivo,* measured as significant and complete blocking of mIL22 synthesis at the two highest doses tested (**Figure 4**). Administration of the lowest dose of the monovalent nanobody construct P23IL0050 (0.64-fold excess) blocked hIL23-induced mIL22 production only partially, whereas multivalent construct P23IL0054 still shows significant blocking demonstrating the power of combining different anti-p19 nanobodies in one construct (**Figure 4**).

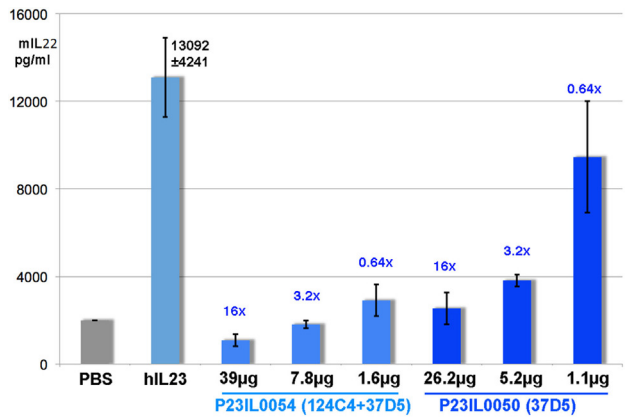

FIGURE 4 | Inhibition of human interleukin (hIL) 23 induced mouse interleukin (mIL) 22 synthesis upon administration of P23IL0050 or P23IL0054. The *y*-axis indicates the average mIL22 synthesis in picograms per milliliter. The *x*-axis depicts the different test groups (two nanobodies, each at three different microgram doses). Numbers in blue positioned above the bars give the molar excess ratio of nanobody administered over the 3 µg hIL23 injected. The number above the hIL23 bar is the mean mIL22 synthesis for the control group receiving hIL23 only (pg/ml ± SD).

DISCUSSION

Structural Analysis of Monovalent Nanobodies

We report here the generation and characterization of high-affinity nanobodies derived from llama heavy chain antibodies raised against hIL23. Two of the nanobodies studied revealed a high efficacy in neutralizing hIL23 in *in vitro* bioassays using mouse splenocytes. The IC_{50} values ranged from ~20 to ~200 pM. To better understand the mode of action of those neutralizing nanobodies, the crystal structure of hIL23 in complex with the nanobodies 37D5 (p19+), 22E11 (p40+), and 124C4 (p19−) was generated. Comparison of our structure of hIL23, with the already known structures, i.e., hIL23 alone [3DUH (24)], hIL23 in complex with the Fab fragment (7G10) of a neutralizing antibody [3D85 (21)], and hIL23 in complex with adnectin [3QWQ (25)], shows that all structures are very similar (**Figure 5**). The rmsd values of p19 are between 1.0 and 1.2 Å, whereas those of p40 range are between 1.0 and 1.9 Å (Table S4 in Supplementary Material).

We compared the binding mode of three p19-neutralizing molecules: nanobody 37D5, Fab 7G10, and adnectin to hIL23 (**Figure 5**; Figure S5 in Supplementary Material). Fab 7G10 binds exclusively to p19, and the surface covered by the V_H and variable light (V_L) chains is convex, as expected from this type of binder. In contrast, both the nanobody 37D5 and adnectin bind

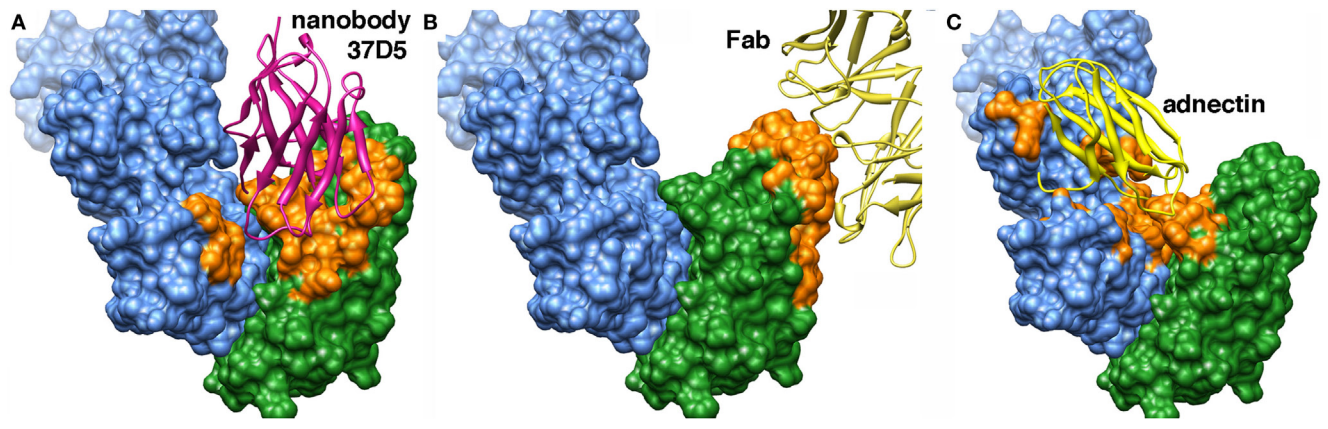

FIGURE 5 | Comparison of three complexes of human interleukin 23 with ligands. The p40 subunit is shown in blue, and p19 is green. The surface of interaction is colored orange. **(A)** Complex with the 37D5 nanobody (shown in pink). **(B)** Complex with the neutralizing Fab 7G10 (partial view; shown in yellow). **(C)** Complex with adnectin (shown in yellow).

concomitantly p19 and p40. They recognize a concave surface, a result often observed for nanobodies (8). When looking at the interaction surface areas [all measured by the same server, PISA (26)], adnectin is by far covering the largest surface area (1,566 Å^2), followed by nanobody 37D5 (870 Å^2), and Fab 7G10 (778 Å^2) (Table S5 in Supplementary Material). As those molecules are neutralizing, and hence competing with IL23R interaction, they probably overlap with the IL23R epitope. To the best of our knowledge, no structure of an IL23-IL23R complex is known to date, but some suggestions on possible IL23R epitopes have been described (21, 24).

To understand the fact that nanobody 124C4 and nanobody 37D5 were initially expected to be solely p19 binders, but bound both p19 and p40, we superimposed our hIL23 structure on that of hIL12 [pdb 1f45 (2)]. IL12 has the p40 subunit in common with IL23 and forms a heterodimer with a p35 subunit, instead of p19 in IL23. There is a good overlap between the two p40 subunits and also the secondary structure elements of p19 overlap well with p35 (backbone rmsd = 1.6 Å). However, since p35 is larger than p19, some exposed regions of p40 in hIL23 are buried in hIL12. Indeed, due to the larger size of p35 versus p19, the binding mode of nanobody 124C4 to IL23 is not compatible with the p35 position and surface in IL12 (Figure S4 in Supplementary Material).

The 22E11 nanobody binds the N-terminal domain of the p40 monomer. Interestingly, its binding area overlaps with that of the Fab of Ustekinumab (Figure S6 in Supplementary Material; PDB: 3HMX) (27, 28). The antibody Ustekinumab targets p40, neutralizes both IL12 and IL23, and is marketed for treatment of psoriasis. Consistent with the overlap in epitopes, the anti-p40 blocking nanobody 22E11 is indeed able to neutralize hIL12 in addition to hIL23, as it could block hIL12-dependent proliferation of PBMCs stimulated with phytohemagglutinin (so called PHA blasts) with an IC_{50} of 95 pM when 4 pM hIL12 was used for stimulation (data not shown). Although the 22E11 nanobody is not as potent as Ustekinumab in neutralizing hIL23, it can be presumed that fusing nanobody 22E11 with an anti-p40 nanobody, recognizing an epitope covering the Ustekinumab p40-binding region not overlapping with 22E11, will significantly improve potency. This hypothesis is supported by a multivalent construct consisting of nanobody 22E11 and a p40 nanobody (nanobody 80D10), recognizing a non-neutralizing epitope. This construct (22E11-9GS-Alb1-15GS-80D10) improves the potency of the monovalent 22E11 by 300-fold (IC_{50} of 0.6 pM in the splenocyte assay, **Table 1**, D, ii).

However, it is preferred to target p19, and hence being specific for IL23, as targeting IL12 could potentially lead to infection-related side effects.

Use of Multivalent Nanobodies to Improve Efficacy

Several multivalent constructs were engineered by flanking Alb1 by a linker on each side, followed by 37D5 or 124C4 on either side, in an attempt to improve the potency/efficacy of the 37D5 nanobody. As control 37D5, fused to the anti-HSA nanobody Alb1, was used. Analysis of the X-ray structure of hIL23 in complex with nanobody 37D5 and nanobody 124C4 was used to predict the peptide linker lengths needed to combine these two nanobodies in a multivalent construct, enabling simultaneous binding of both nanobodies to hIL23. The direct distance between the C-terminus of nanobody 37D5 and the N-terminus of nanobody 124C4 is ~85 Å, indicating that at least a 25GS linker is needed in a bivalent construct. As the Alb1 nanobody was introduced between the anti-p19 nanobodies, it served as part of the linker and was flanked by two 9-mer linkers or a 9- and 15GS linker. Based on protein modeling we concluded that although a (-9GS-Alb1-9GS-) linker might be sufficient to permit binding of both nanobodies, a (-9GS-Alb1-15GS-) provides more flexibility to the construct allowing the Alb1 nanobody to accommodate better with respect to the p19 and p40 units. This flexibility seemed to be important since experimentally, when Alb1 was flanked by a 9- and 15GS linker, the IC_{50} value in the splenocyte assay for hIL23 was significantly better than that obtained with two 9GS linkers. Furthermore, when having 9 + 15GS or 15 + 15GS, the potency became independent of nanobody orientation, with values between 3.2 and 3.8 pM (**Table 1**, D, ii).

In vivo, the multivalent construct P23IL0054 (124C4-15GS-Alb1-9GS-37D5) was more efficient in neutralization of administrated hIL23 to mice (**Figure 4**), than the monovalent p19 blocker 37D5 fused to Alb1, confirming the power of formatting nanobodies. In addition, P23IL0054 is presumably specific for IL23, unless a new heterodimeric cytokine using p19 in conjunction with another subunit emerges.

In conclusion, the multivalent approach designed and reported here has two exquisite beneficial effects. First, formatting leads to avid binding to hIL23, leading to a 10-fold increase in potency, compared to the monovalent p19 blocker. Second and as important, by acting on two different epitopes, chances to retain the specific binding to the heterodimeric hIL23 are increased, avoiding undesired cross-reactivity with other cytokines (known or still unknown) sharing one of its components. The formatting power of the nanobody platform, together with a long *in vivo* residence time and low immunogenicity profile, raises the opportunity for the best of these nanobody constructs to become excellent drug candidates to treat inflammatory diseases.

DATA DEPOSITION

Coordinates were deposited with the Protein Data Bank with accession code 4GRW.

ETHICS STATEMENT

Animal work was conducted according to the guidelines set out in European Economic Community council directive 86/609/EEC, with authorization from the prefecture of Doubs and the Department of Veterinary Services.

AUTHOR CONTRIBUTIONS

HH, MS, HR, and CC designed the experiments. AD, SS, and CC purified, crystallized, and solved the X-ray structures. CB analyzed the X-ray structures and identified molecular interactions. GD, ChB and HR were responsible for nanobody generation and

characterization. All the authors contributed to the analysis of the results and writing of this paper.

ACKNOWLEDGMENTS

The authors would like to acknowledge help from João Viera for phage display selections; Jo Vercammen and Klara Vandriessche for screening; David Vlerick for cellular assays; Koen Van Laer for nanobody cloning and sequencing; Yvonne Mijnsbergen for purifications; and Theo Verrips for discussions. The ESRF synchrotron (Grenoble, France) is gratefully acknowledged for beamtime allocation.

FUNDING

SS and CC were funded in part by Ablynx and by the Centre National de la Recherche Scientifique (France), and Aix-Marseille University (France).

SUPPLEMENTARY MATERIAL

The Supplementary Material for this article can be found online at http://journal.frontiersin.org/article/10.3389/fimmu.2017.00884/full#supplementary-material.

REFERENCES

1. Oppmann B, Lesley R, Blom B, Timans JC, Xu Y, Hunte B, et al. Novel p19 protein engages IL-12p40 to form a cytokine, IL-23, with biological activities similar as well as distinct from IL-12. *Immunity* (2000) 13:715–25. doi:10.1016/S1074-7613(00)00070-4
2. Yoon C, Johnston CJ, Tang J, Stahl M, Tobin JF, Somers WS. Charged residues dominate a unique interlocking topography in the heterodimeric cytokine interleukin-12. *EMBO J* (2000) 19:3530–41. doi:10.1093/emboj/19.14.3530
3. Blauvelt A. New concepts in the pathogenesis and treatment of psoriasis: key roles for IL-23, IL-17A and TGF-b1. *Expert Rev Dermatol* (2007) 2:69–78. doi:10.1586/17469872.2.1.69
4. Fitch E, Harper E, Skorcheva I, Kurtz SE, Blauvelt A. Pathophysiology of psoriasis: recent advances on IL-23 and Th17 cytokines. *Curr Rheumatol Rep* (2007) 9:461–7. doi:10.1007/s11926-007-0075-1
5. Furuzawa-Carballeda J, Vargas-Rojas MI, Cabral AR. Autoimmune inflammation from the Th17 perspective. *Autoimmun Rev* (2007) 6:169–75. doi:10.1016/j.autrev.2006.10.002
6. McGeachy MJ, Cua DJ. Th17 cell differentiation: the long and winding road. *Immunity* (2008) 28:445–53. doi:10.1016/j.immuni.2008.03.001
7. Iwakura Y, Ishigame H. The IL-23/IL-17 axis in inflammation. *J Clin Invest* (2006) 116:1218–22. doi:10.1172/JCI28508
8. Muyldermans S, Cambillau C, Wyns L. Recognition of antigens by single-domain antibody fragments: the superfluous luxury of paired domains. *Trends Biochem Sci* (2001) 26:230–5. doi:10.1016/S0968-0004(01)01790-X
9. Park YJ, Pardon E, Wu M, Steyaert J, Hol WG. Crystal structure of a heterodimer of editosome interaction proteins in complex with two copies of a cross-reacting nanobody. *Nucleic Acids Res* (2012) 40:1828–40. doi:10.1093/nar/gkr867
10. Rasmussen SG, Choi HJ, Fung JJ, Pardon E, Casarosa P, Chae PS, et al. Structure of a nanobody-stabilized active state of the beta(2) adrenoceptor. *Nature* (2011) 469:175–80. doi:10.1038/nature09648
11. Steyaert J, Kobilka BK. Nanobody stabilization of G protein-coupled receptor conformational states. *Curr Opin Struct Biol* (2011) 21:567–72. doi:10.1016/j.sbi.2011.06.011
12. Elsadek B, Kratz F. Impact of albumin on drug delivery – new applications on the horizon. *J Control Release* (2012) 157:4–28. doi:10.1016/j.jconrel.2011.09.069
13. Roovers RC, Laeremans T, Huang L, De Taeye S, Verkleij AJ, Revets H, et al. Efficient inhibition of EGFR signaling and of tumour growth by antagonistic anti-EFGR nanobodies. *Cancer Immunol Immunother* (2007) 56:303–17. doi:10.1007/s00262-006-0180-4
14. Roovers RC, van Dongen GA, van Bergen en Henegouwen PM. Nanobodies in therapeutic applications. *Curr Opin Mol Ther* (2007) 9:327–35.
15. Skerra A, Plückthun A. Assembly of a functional immunoglobulin Fv fragment in *Escherichia coli*. *Science* (1988) 240:1038–41. doi:10.1126/science.3285470
16. Leslie AG. Integration of macromolecular diffraction data. *Acta Crystallogr D Biol Crystallogr* (1999) 55(Pt 10):1696–702. doi:10.1107/S090744499900846X
17. Winn MD, Ballard CC, Cowtan KD, Dodson EJ, Emsley P, Evans PR, et al. Overview of the CCP4 suite and current developments. *Acta Crystallogr D Biol Crystallogr* (2011) 67:235–42. doi:10.1107/S0907444910045749
18. Bunkoczi G, Echols N, McCoy AJ, Oeffner RD, Adams PD, Read RJ. Phaser. MRage: automated molecular replacement. *Acta Crystallogr D Biol Crystallogr* (2013) 69:2276–86. doi:10.1107/S0907444913022750
19. Blanc E, Roversi P, Vonrhein C, Flensburg C, Lea SM, Bricogne G. Refinement of severely incomplete structures with maximum likelihood in BUSTER-TNT. *Acta Crystallogr D Biol Crystallogr* (2004) 60:2210–21. doi:10.1107/S0907444904016427
20. Aggarwal S, Ghilardi N, Xie MH, de Sauvage FJ, Gurney AL. Interleukin-23 promotes a distinct CD4 T cell activation state characterized by the production of interleukin-17. *J Biol Chem* (2003) 278:1910–4. doi:10.1074/jbc.M207577200
21. Beyer BM, Ingram R, Ramanathan L, Reichert P, Le HV, Madison V, et al. Crystal structures of the pro-inflammatory cytokine interleukin-23 and its complex with a high-affinity neutralizing antibody. *J Mol Biol* (2008) 382:942–55. doi:10.1016/j.jmb.2008.08.001
22. Spinelli S, Frenken L, Bourgeois D, de Ron L, Bos W, Verrips T, et al. The crystal structure of a llama heavy chain variable domain. *Nat Struct Biol* (1996) 3:752–7. doi:10.1038/nsb0996-752
23. Spinelli S, Tegoni M, Frenken L, van Vliet C, Cambillau C. Lateral recognition of a dye hapten by a llama VHH domain. *J Mol Biol* (2001) 311:123–9. doi:10.1006/jmbi.2001.4856
24. Lupardus PJ, Garcia KC. The structure of interleukin-23 reveals the molecular basis of p40 subunit sharing with interleukin-12. *J Mol Biol* (2008) 382:931–41. doi:10.1016/j.jmb.2008.07.051
25. Ramamurthy V, Krystek SR Jr, Bush A, Wei A, Emanuel SL, Das Gupta R, et al. Structures of adnectin/protein complexes reveal an expanded binding footprint. *Structure* (2012) 20:259–69. doi:10.1016/j.str.2011.11.016
26. Krissinel E, Henrick K. Inference of macromolecular assemblies from crystalline state. *J Mol Biol* (2007) 372:774–97. doi:10.1016/j.jmb.2007.05.022
27. Gottlieb A, Menter A, Mendelsohn A, Shen YK, Li S, Guzzo C, et al. Ustekinumab, a human interleukin 12/23 monoclonal antibody, for psoriatic arthritis: randomised, double-blind, placebo-controlled, crossover trial. *Lancet* (2009) 373:633–40. doi:10.1016/S0140-6736(09)60140-9
28. Cuchacovich RS, Espinoza LR. Ustekinumab for psoriatic arthritis. *Lancet* (2009) 373:605–6. doi:10.1016/S0140-6736(09)60141-0

Conflict of Interest Statement: This research has been funded by Ablynx, with the exception of research by AD, SS, and CC at the Architecture et Fonction des Macromolécules Biologiques (France), whose work has been funded in part by Ablynx and the Centre National de la Recherche Scientifique (France), and the Aix-Marseille Université (France).

frontiers in Immunology

ORIGINAL RESEARCH
published: 25 September 2017
doi: 10.3389/fimmu.2017.01121

Therapeutic Potential of Shark Anti-ICOSL VNAR Domains is Exemplified in a Murine Model of Autoimmune Non-Infectious Uveitis

Marina Kovaleva[1], Katherine Johnson[2], John Steven[1], Caroline J. Barelle[1] and Andrew Porter[1,3]*

[1] Elasmogen Ltd., Aberdeen, United Kingdom, [2] John Walton Muscular Dystrophy Research Centre, Institute of Genetic Medicine, Newcastle University, Newcastle, United Kingdom, [3] Department of Molecular and Cell Biology, Institute of Medical Sciences, University of Aberdeen, Aberdeen, United Kingdom

Induced costimulatory ligand (ICOSL) plays an important role in the activation of T cells through its interaction with the inducible costimulator, ICOS. Suppression of full T cell activation can be achieved by blocking this interaction and has been shown to be an effective means of ameliorating disease in models of autoimmunity and inflammation. In this study, we demonstrated the ability of a novel class of anti-ICOSL antigen-binding single domains derived from sharks (VNARs) to effectively reduce inflammation in a murine model of non-infectious uveitis. In initial selections, specific VNARs that recognized human ICOSL were isolated from an immunized nurse shark phage display library and lead domains were identified following their performance in a series of antigen selectivity and *in vitro* bioassay screens. High potency in cell-based blocking assays suggested their potential as novel binders suitable for further therapeutic development. To test this hypothesis, surrogate anti-mouse ICOSL VNAR domains were isolated from the same phage display library and the lead VNAR clone selected *via* screening in binding and ICOS/ICOSL blocking experiments. The VNAR domain with the highest potency in cell-based blocking of ICOS/ICOSL interaction was fused to the Fc portion of human IgG1 and was tested *in vivo* in a mouse model of interphotoreceptor retinoid-binding protein-induced uveitis. The anti-mICOSL VNAR Fc, injected systemically, resulted in a marked reduction of inflammation in treated mice when compared with untreated control animals. This approach inhibited disease progression to an equivalent extent to that seen for the positive corticosteroid control, cyclosporin A, reducing both clinical and histopathological scores. These results represent the first demonstration of efficacy of a VNAR binding domain in a relevant clinical model of disease and highlight the potential of VNARs for the treatment of auto-inflammatory conditions.

Keywords: variable domain of shark new antigen receptor, single chain binding domain, shark, autoimmunity, phage display, biologic therapeutics, uveitis

OPEN ACCESS

Edited by:
Colin Roger MacKenzie, National Research Council Canada (NRC-CNRC), Canada

Reviewed by:
Owen Kavanagh, York St John University, United Kingdom
Martin A. Rossotti, National Research Council Canada (NRC-CNRC), Canada

****Correspondence:***
Marina Kovaleva
marina.kovaleva@elasmogen.com

Specialty section:
This article was submitted to Vaccines and Molecular Therapeutics, a section of the journal Frontiers in Immunology

Received: *26 May 2017*
Accepted: *25 August 2017*
Published: *25 September 2017*

Citation:
Kovaleva M, Johnson K, Steven J, Barelle CJ and Porter A (2017) Therapeutic Potential of Shark Anti-ICOSL VNAR Domains is Exemplified in a Murine Model of Autoimmune Non-Infectious Uveitis. Front. Immunol. 8:1121. doi: 10.3389/fimmu.2017.01121

Abbreviations: IgNAR, immunoglobulin like new antigen receptor; VNAR, variable domain of shark new antigen receptor; ICOSL, induced costimulatory ligand; CDR, complementarity determining region; FW, framework; HV, hypervariable region; IRBP, interphotoreceptor retinoid-binding protein; EAU, experimental autoimmune uveitis; APC, antigen-presenting cell.

INTRODUCTION

Inflammatory eye disease, uveitis, is a significant but largely unrecognized cause of visual impairment, characterized by a very rapid and debilitating inflammation of the uvea (the pigmented and vascular structures of the eye) and requires immediate diagnosis and treatment to prevent partial or total and irreversible loss of sight. In the Western world, current incidences vary between 38 and 200 per 100,000 and it is estimated to be 730 per 100,000 in India (1). The proportion of people suffering marked visual loss may be as high as 35% with over 30,000 people in the US annually becoming blind (2, 3). Non-infectious uveitis, which is 70% of the total cases presented, is predominantly an acute manifestation of an underlying chronic autoimmune condition, and T cell activation plays a critical role in its pathogenesis (4).

There is currently no curative therapy and available treatments aim at reducing the inflammation and managing the symptoms. First-line approaches consist of corticosteroids that are often used with anti-metabolites and alkylating agents (5). For the 50% of patients who respond well, corticosteroids are inexpensive, potent and rapidly effective. However, around 30% of patients do not respond to this form of immunomodulation and the rest often suffer significant side effects, including glaucoma and cataracts, which trigger a rapid termination of therapy. Corticosteroid side effects become increasingly common as uveitis episodes recur.

When ocular inflammatory disease cannot be controlled with conventional immunosuppressive drugs (refractory patients), systemically administered adalimumab (Humira) is the most common anti-TNF-α (anti-inflammatory) agent used clinically (6). Humira completed a Phase 3 study in 2015 and reported a significant period of improvement in refractory patients from an average of 3–5.6 months and a reduction in the risk of "vision loss". The product was approved by the FDA in 2016 for posterior uveitis (7–9). While many patients benefited from anti-TNF therapy, a significant number reported serious side effects with prolonged systemic administration considered the most probable cause of the adverse events recorded.

Shark Ig novel antigen receptors (IgNARs) are naturally occurring binding proteins known to play a role in the adaptive immune system of cartilaginous fish (10, 11). While IgNARs perform many of the duties of antibodies they have a different ancestral origin and structural architecture. IgNARs have never had, or lost, a light chain partner and have squeezed an additional binding loop into the single domain format of their two variable binding sites VNARs. An important aspect of their function is the ability to specifically bind with high affinity to target, achieved using four regions of high sequence diversity: complementarity determining region (CDR) 1, hypervariable region (HV) 2, HV4 and CDR3 (12, 13). In some species of shark non-canonical cysteine residues create an additional repertoire of VNAR isotypes that translate into structurally distinct families with diverse paratope topologies capable of binding more cryptic or hidden epitopes (13, 14). The combination of a lack of light chain partner and CDR2 makes VNARs the smallest naturally occurring binding domains in the vertebrate kingdom. This, in addition to their exquisite selectivity for target, inherent solubility and stability, makes them attractive candidates for therapeutic drug and diagnostic development (15–17).

It has been previously demonstrated by Dooley and Flajnik (18) that along with monomeric IgM, sharks can produce an antigen-specific IgNAR response following immunization. Libraries of VNARs from immunized sharks have been constructed and positive clones with high affinity and specificity to different targets like HSA, HEL, TNFα and Ebola virus have been isolated (19). In this work, phage display technology was utilized to isolate VNARs from an immunized shark library, which target and neutralize the induced costimulatory ligand (ICOSL).

ICOSL—also known as B7-related protein (B7RP-1), CD275, and B7 homolog (B7h)—is a cell surface antigen expressed constitutively on antigen-presenting cells (APCs) such as B cells, activated monocytes and dendritic cells, and is the ligand for the B7 family member, inducible costimulator (ICOS; CD278) (20). Initially, it was believed that its action was restricted to activation of T cells but more recently the central role of ICOSL in immune modulation has been expanded to both T cell stimulatory and inhibitory pathways through its interaction with CD28 and CTLA4, respectively (21). The generation of transgenic mice with lineage-restricted ICOSL expression has demonstrated the role of ICOSL–ICOS interaction in stimulating T cell responses, T cell tolerance and T cell-dependent B cell responses (22–24). The role of the ICOS/ICOSL pathway and ICOSL as a possible drug target has been previously validated in murine experimental autoimmune uveoretinitis (25). Here, we describe the isolation and characterization of VNAR domains that bind and neutralize ICOSL in a dose-dependent manner and provide the first evidence of the therapeutic potential of shark VNAR domains in a clinical model of disease. The experimental autoimmune uveitis (EAU) model of choice for this study was an interphotoreceptor retinoid-binding protein (IRBP)-induced uveitis in mice, which is considered to mirror many of the histological and clinical hallmarks of uveitis in humans (26, 27). While this study reports the benefits of systemically delivered VNAR Fc molecules, it is hoped that the progress seen here will become a stepping stone to the site-specific delivery of small, soluble and efficacious VNAR domains directly into the eye, combining the potency of biologics therapy with reduced systemic side effects.

MATERIALS AND METHODS

Shark Immunization

Nurse sharks (*Ginglymostoma cirratum*) were placed in containers filled with artificial sea water containing 0.1% (w/v) tricaine methanesulfonate (MS-222). When the desired level of narcosis was reached, they were removed for immunization or bleeding. Recombinant in-house CHO-expressed mouse and human ICOSL-flag-His (200 μg/shark) emulsified in complete Freund's adjuvant (CFA) were injected using a 20 gauge needle into the lateral fin of the shark. Four weeks later, antigens (200 μg/shark) emulsified in incomplete Freund's adjuvant were similarly administered to the shark. Three immunization boosts (100 μg/shark) were given at 4-week intervals intravenously into the caudal vein as soluble antigen in PBS (sample 0.45 μM sterile filtered). Between

3 and 5 ml of blood samples were collected from the caudal vein into a 30 ml syringe containing 200 µl porcine heparin (1,000 U/ml in PBS) at weeks 0 (pre-immunization bleed), 10, 14, 18 and 22. Blood samples were spun at 1,000 × *g* for 10 min to separate blood cells from plasma. The plasma supernatant fraction was carefully removed into a sterile tube with RNA stabilization buffer and stored at −80°C.

Serum IgNAR Titer ELISA

Immunoplates (Nunc, Thermo Scientific) were coated overnight at 4°C with 1 µg/ml human or murine ICOSL and then blocked with 4% (w/v) milk PBS (MPBS) for 2 h at 37°C. Shark serum was diluted 1:30 and then a 1:3 dilution series set up on each plate and incubated for 1 h at room temperature following incubation for 1 h with anti-nurse shark IgNAR mouse monoclonal antibody GA8 (28) (1:500 in PBST). The plates were incubated for a final time with anti-mouse IgG-HRP (SIGMA) diluted 1:1,000 in PBST. After each step, the ELISA wells were washed three times with 200 µl/well PBST. Plates were developed by adding 100 µl/well TMB substrate (Thermo Scientific) and the reaction stopped with 50 µl/well 1 M H_2SO_4.

Building of a *G. cirratum* VNAR Phage Display Library

Peripheral blood lymphocytes (PBLs) were harvested from the plasma of the bleed with the best IgNAR response (titer) and total RNA isolated using a QIAGEN kit following the manufacturer's instructions. cDNA was synthesized with IgNAR transmembrane- (Tm 5′-TACAAATGTGGTGTACAGCAT-3′) and secretory- (Sec 5′-TAGTACGACCTGAAACATTA AC-3′)-specific primers. Using the NEB Phusion HF PCR Master Mix protocol, VNAR DNA was amplified with framework (FW) nurse shark-specific primer combinations FW1/FW4r1 or FW1/FW4r2:

FW1 5′-GAGGAGGAGGAGAGGCCCAGGCGGCCG CTCGAGTGGACCAAACACCG-3′
FW4r1 5′-GAGGAGGAGGAGGAGGCCCCTGAGGCCG CATTCACAG TCACGACAGTGCCACCTC-3′
FW4r2 5′-GAGGAGGAGGAGGAGGCCCCTGAGGCCGCA TTCACAGTCACGGCAGTGCCATCTC-3′.

Amplicons were cloned into an in-house phage display vector (pEDV1) with in-frame 6xHis-tag and c-myc-tag *via Sfi*I restriction sites. The library was transformed into electrocompetent TG1 cells (Lucigen), and the library size was calculated as described by Müller et al. (29).

VNAR Phage Display Library Screening

To rescue phage to be used in library selections, cultures from library glycerol stocks were grown at 37°C and 250 rpm, in 2xTY, 2% glucose, 100 µg/ml ampicillin to an OD_{600} of 0.5. Cells were superinfected with 10^9 M13K07 helper phage (NEB) and then incubated overnight in 2xTY, 100 µg/ml ampicillin, 50 µg/ml kanamycin at 25°C and 250 rpm. The cultures were PEG-precipitated (20% (w/v) PEG/2.5 M NaCl) twice, and the resulting phage pellets were resuspended in 1 ml PBS. To establish antigen "decorated" bead selections, recombinant ICOSL-flag-His protein was biotinylated with Sulfo-NHS-LC-Biotin as per manufacturer's instructions (21327, Thermo Scientific). Two hundred microliters of magnetic Dynabeads M-280 Streptavidin (11205D, Invitrogen), pre-blocked with 2% (w/v) MPBS, were coated with 50–200 nM biotinylated material by rotating at 20 rpm, at room temperature for 1 h. Library phage was incubated first with Dynabeads for 1 h rotating at room temperature to remove phage specific to the beads and added then to the antigen-coated beads. After 1 h incubation at room temperature at 20 rpm, beads with bound phage were washed 5–10 times with PBST and 5–10 times with PBS, eluted by rotating for 8 min in 400 µl 100 mM TEA and neutralized by the addition of 200 µl 1 M Tris-HCl pH 7.5. *Escherichia coli* TG1 cells (10 ml) were infected with 300 µl of eluted phage for 30 min at 37°C and grown overnight at 37°C on TYE agar plates containing 2% (w/v) glucose and 100 µg/ml ampicillin. Two further rounds of selection were conducted, and outputs were screened for antigen-specific binding by monoclonal phage and periplasmic extract ELISAs against human or mouse ICOSL. Phage binders were detected using HRP-conjugated anti-M13 antibody (27942101, GE Healthcare), and periplasmic protein was detected using HRP-conjugated anti-c-Myc antibody (118 141 50 001, Roche).

Expression and Purification of Monomeric VNAR and VNAR Fc-Fusion Proteins

To express monomeric VNARs, non-amber-suppressor HB2151 *E. coli* cells were used. VNARs were isolated from periplasm by osmotic shock with 50 mM Tris/HCl pH8.0, 1 mM EDTA, 20% sucrose and purified *via* His-tag capture on NiNTA resin. VNARs were eluted with 0.5 M imidazole pH 8.0 followed by dialysis in PBS. Selected positive monomeric VNAR domains were PCR amplified and subcloned into an in-house Fc-fusion mammalian expression vector (pEEE2A), which facilitated Protein A affinity purification of expressed protein post transient expression in a HEK 293 suspension culture. HEK cells at ~10^6 cells/ml in GIBCO FreeStyle 293 media were transiently transfected using Lipofectamine 2000 (Invitrogen) according to the manufacturer's protocol. Twenty four hours post transfection, tryptone (0.5% w/v) in PBS was added to the culture to enhance expression and the cells incubated for 5 days. Cells were pelleted at 1,000 × *g* for 15 min and the supernatants sterile filtered before adding PROSEP A resin (Millipore). After washing with PBS, fractions of purified VNAR Fc were eluted with 0.1 M glycine pH 3.0 (Severn Biotech Ltd.) and neutralized by adding 1 M Tris-HCl pH 8.0. Samples were dialyzed using Slide-A-Lyser dialysis cassettes (Thermo Scientific) in PBS pH 7.4. Expression levels of VNAR Fc-fusion proteins were generally in the range of 50–70 mg per liter using serum-free media. Electrophoresis of purified protein samples was performed on NuPAGE 4–12% Bis-Tris gels using a MES buffer system (Invitrogen) in accordance with the manufacturer's instructions.

Cell-Based Binding

CHO cells expressing human or mouse ICOSL were grown to 90% confluency in DMEM/F12 + 5% FBS media, in 96-well

cell culture plates (Greiner, Bio-One). Anti-human or murine VNARs in DMEM/F12 + 2% FBS were added to the corresponding CHO cells. Following 1 h incubation at 16°C, cells were gently washed three times with DMEM/F12 + 2% FBS and incubated for 40 min at 16°C with anti-His-HRP (SIGMA) diluted 1:1000 in the same media. Cells were washed and developed as described previously.

Cell-Based Ligand–Receptor Blocking Assay

CHO cells expressing human ICOS receptor were grown to 90% confluency. A total of 20 µl at 450 ng/ml of ICOSL-hFc (rhB7-H2/Fc—165-B7, R&D Systems or rmB7-H2/Fc—158-B7, R&D Systems) was preincubated for 1 h with 40 µl of serially diluted anti-ICOSL-VNAR-Fc in DMEM/F12 + 2% FBS and then added to the cells. Following 1 h incubation at 16°C, cells were gently washed three times with DMEM/F12 + 2% FBS and incubated for 40 min at 16°C with goat anti-human Fc-HRP (SIGMA) diluted 1:10,000 in the same media. Cells were washed and developed as described previously. The absorbance was measured at 450 nm wavelength using a microplate reader and data were plotted using Sigma Plot software.

VNAR Binding ELISA

96-well flat bottom Maxisorp Nunc Immuno plates (Thermo Scientific) were coated at 4°C overnight with 1 µg/ml of the antigen of interest: for monomeric VNAR binding—ICOSL-hFc (rhB7-H2/Fc—165-B7, R&D Systems or rmB7-H2/Fc—158-B7, R&D Systems), human ICOSL-IgV, mouse ICOSL-IgV, human ICOSL-IgC, or mouse ICOSL-IgC (all ICOSL-Igs were produced in-house) and for VNAR-Fc binding—human or mouse recombinant ICOSL-flag-His (produced in-house). The plates were washed three times with 200 µl/well PBS before blocking with 200 µl of 4% (w/v) MPBS/well and incubated at 37°C for 1 h. The blocked plates were washed three times with PBS and serial dilutions of VNAR proteins were then added per designated well and the plates incubated at room temperature for 1 h. Plates were washed three times with PBST before 100 µl of 1:1,000 dilution HRP-conjugated anti-His or goat anti-human IgG antibody (for Fc-fused VNAR detection) was added to the plates and incubated for 1 h at room temperature. The plates were washed and developed by adding 100 µl TMB substrate solution and stopped using 1 M H_2SO_4 as previously described. The absorbance was measured at 450 nm wavelength using microplate reader and data were plotted using Sigma Plot software.

Kinetic and Affinity Measurements of VNAR-Fc

The kinetic constants of VNAR-Fc were determined by surface plasmon resonance using Biacore T200 and 2000 biosensors (GE Healthcare). Anti-human IgG1 antibody diluted in 10 mM sodium acetate buffer was immobilized on a CM5 chip, and VNAR-Fcs were captured *via* their Fc region. HuICOSL-flag-His (100 nM) was serially diluted two-fold in HEPES running buffer (HBS EP+, BR-1006-69, GE Healthcare) with 150 mM NaCl, 3 mM EDTA and 0.05% v/v Surfactant P20 pH 7.4, and was injected for 2 min at a flow rate of 60 µl/min. Dissociation phase was monitored for 5 min followed by two 10 µl regeneration pulses using 10 mM glycine pH 1.5, at a flow rate of 100 µl/min. Association and dissociation rates were calculated using the 1:1 global Langmuir binding model fit analysis (Biacore Evaluation Software).

Murine Model of EAU

Adult female C57BL/6 mice were randomly allocated to experimental groups and allowed to acclimatize for 1 week. Treatments were administered according to the schedule below (**Table 1**). Test articles were administered in PBS. On Day 0, animals were administered with an emulsion containing 500 µg of IRBP peptide 1-20 (IRBP p1-20) in CFA supplemented with 2.5 mg/ml *Mycobacterium tuberculosis* H37 Ra by subcutaneous injection. Also on Day 0, animals were administered with 1.5 µg *Bordetella pertussis* toxin by intraperitoneal injection.

From Day 7 until the end of the experiment on Day 28, animals were monitored once per week for clinical signs of uveitis using topical endoscopic fundal imaging (TEFI) (**Table 2**). Animals were also monitored twice weekly for signs of ill-health, weighed and any abnormalities recorded. At termination on Day 28, eyes were removed into tissue fixative for histopathology.

Corneal Penetration

Wild-type mice BALB/C were divided into three groups of two animals each. All procedures were performed on anesthetized animals. Corneal epithelium of the right eye was scratched and 20 µg/3 µl of VNAR, VNAR Fc, or mAb AF158 (R&D) was applied four times topically to the right eye at 5-minute intervals. The eye was then washed with saline solution and 2 µl of anterior fluid sampled. All animal studies were carried out under the Animals (Scientific Procedures) Act 1986 regulations (Home Office UK). For ELISA, 96-well flat bottom Maxisorp Nunc Immuno plates (Thermo Scientific) were coated with 1 µg/ml of rmB7-H2/Fc or mICOSL-flag-His at 4°C overnight. The plates were washed three times with 200 µl/well PBS before blocking with 200 µl of 4% (w/v) MPBS per well and incubated at 37°C for 1 h. The blocked plates were washed three times with PBS, 100 µl of anterior fluid (start dilution 1:50 in PBS, then serial dilutions 1:2) was then added and incubated at room temperature for 1 h. Plates were washed three times with PBST and 100 µl of 1:1,000 dilution HRP-conjugated anti-His (for VNAR detection) or goat anti-human IgG antibody (for Fc-fused VNAR and mAb detection) was added to the plate

TABLE 1 | Schedule of *in vivo* treatments.

Group	Treatment	Dose	Route	Frequency	Disease induction
1	Untreated	n/a			
2	Cyclosporin A	20 mg/kg	PO	SID, Day 1–Day 28	Day 0: IRBP/CFA, SC
3	A5-Fc	10 mg/kg	IP	SID, Day 1–Day 14	Day 0: PTx, IP

n/a, not applicable; PO, oral administration; SC, subcutaneous injection; IP, intraperitoneal injection; SID, once daily; IRBP, interphotoreceptor binding protein; CFA, complete Freund's adjuvant; PTx, pertussis toxin.

TABLE 2 | Clinical score ranking using topical endoscopic fundal imaging.

Clinical score	Optic disk inflammation	Retinal vessels	Retinal tissue infiltration	Structural damage
1	Minimal	1–4 mild cuffings	1–4 small lesions or 1 linear lesion	Retinal lesions or atrophy involving 1/4–3/4 of retinal area
2	Mild	>4 mild cuffings or 1–3 moderate cuffings	5–10 small lesions or 2–3 linear lesions	Panretinal atrophy with multiple small lesions (scars) or ≤3 linear lesions (scars)
3	Moderate	>3 moderate cuffings	>10 small lesions or >3 linear lesions	Panretinal atrophy with >3 linear lesions or confluent lesions (scars)
4	Severe	>1 severe cuffings	Linear lesion confluent	Retinal detachment with folding
5	Not visible (white-out or severe detachment)			

and incubated for 1 h at room temperature. The plates were washed and developed by adding 100 µl TMB substrate solution and stopped using 1 M H_2SO_4 as previously described.

RESULTS

VNAR Library Construction from Immunized Nurse Shark

Two nurse sharks were immunized with both recombinant human and mouse ICOSL. An antigen-specific IgNAR immune response was observed and confirmed after 18 weeks through the analysis of post-immunized sera. The response was exemplified by a gradual increase in titer values from early to late bleeds (data not shown). The VNAR repertoire was amplified from isolated PBLs, cloned into a pEDV1 which contained an in-frame coat protein pIII of the bacteriophage M13 gene and transformed into *E. coli* TG1 cells. The library size was calculated to be 10^8 transformants.

Isolation of Human ICOSL-Specific VNARs

Domains were isolated following three rounds of selection utilizing biotinylated antigen immobilized on streptavidin-coated beads to maximize the chance of delivering potent ICOSL binders (30). huICOSL-specific VNARs were obtained after the first selection round and enriched further after round three with >90% of domains specific for antigen (**Figure 1A**). As blockade of the ICOS–ICOSL interaction was the desired functional outcome of the selection process, a cell-based assay designed to detect domains that can block receptor/ligand binding was introduced into the screen. Positive hits from selections against huICOSL were assessed for their ability to block huICOSL binding to ICOS expressing cells (**Figure 1C**). Signals that decreased by 50% or more were considered positive for receptor–ligand binding inhibition. In total, six unique (based on CDR3 sequence differentiation) anti-human ICOSL VNAR clones were identified. Cell surface antigen-target selectivity was assessed by FACS analysis utilizing CHO cells overexpressing human or murine ICOSL (data not shown) as well as in a binding ELISA format (**Figure 2A**). All domains were found to be strong huICOSL binders but with no species cross-reactivity to the mouse ligand. The affinity of huICOSL binders was in the range 1–9 nM (**Table 3**). ICOSL is a two-domain protein, where receptor binding is mediated solely by the membrane distal IgV domain but requires the membrane proximal IgC domain to maintain the structural integrity of the protein (31). All of the isolated blocking huICOSL VNARs cross-reacted strongly with the ICOSL-IgV domain with weaker or negligible binding to the ICOSL-IgC domain (**Figure 2B**). As the percentage homology between the human and murine IgV region of ICOSL is only 43%, it was not surprising that the screen did not isolate species cross-reactive VNARs that block receptor/ligand interaction.

Isolation of Mouse ICOSL-Specific VNARs

Anti-mouse ICOSL VNAR domains were isolated using the same method as for the anti-human domains and lead clone isolation determined following their performance in *in vitro* (**Figure 1B**) and cell-based binding assays. Four unique binders, all within an EC50 (effective concentration) range from 1.4 to 11.4 nM (**Figure 3A**), were taken forward for further study. Three of these anti-mICOSL clones (A5, A7, and B8) could block ligand/receptor binding in a CHO-cell-based blocking assay, whereas clone F11 lacks this blocking activity and was used here as a non-blocking control (**Figure 3B**). The naïve VNAR domain 2V was also included as an isotype control in ligand/receptor binding assays. This clone originally isolated from the dogfish (*Squalus acanthias*) is part of a sequence database from this species and has no known target, making it an ideal negative control for these and other studies (11).

Specificity of Anti-mICOSL VNARs

Unlike VNARs obtained from the human ICOSL selection campaign, domains isolated from mouse ICOSL selections were species cross-reactive. Three of the four clones recognize both mouse and human ligand in an ELISA with clear binding to IgC domains (**Figures 3C,D**). Interestingly, clone A5, which was the strongest ICOS/ICOSL blocker (**Figure 3B**), bound only to the full length mouse protein, but not to the individual IgV and IgC domains implying that it may recognize an interdomain or linking region between them (**Figure 3C**).

Fc-Reformatting of Anti-mICOSL VNARs

A key aim of this work was to determine the efficacy of VNAR domains in an *in vivo* mouse model. As VNAR domains alone are cleared rapidly from the systemic circulation (11), all VNAR clones were first converted into a fusion format with a human Fc (**Figure 4A**) to facilitate an extension of serum half-life. All VNAR Fcs retained binding to mICOSL with improved, presumably through avidity, EC50s in the range 0.6 to 3 nM

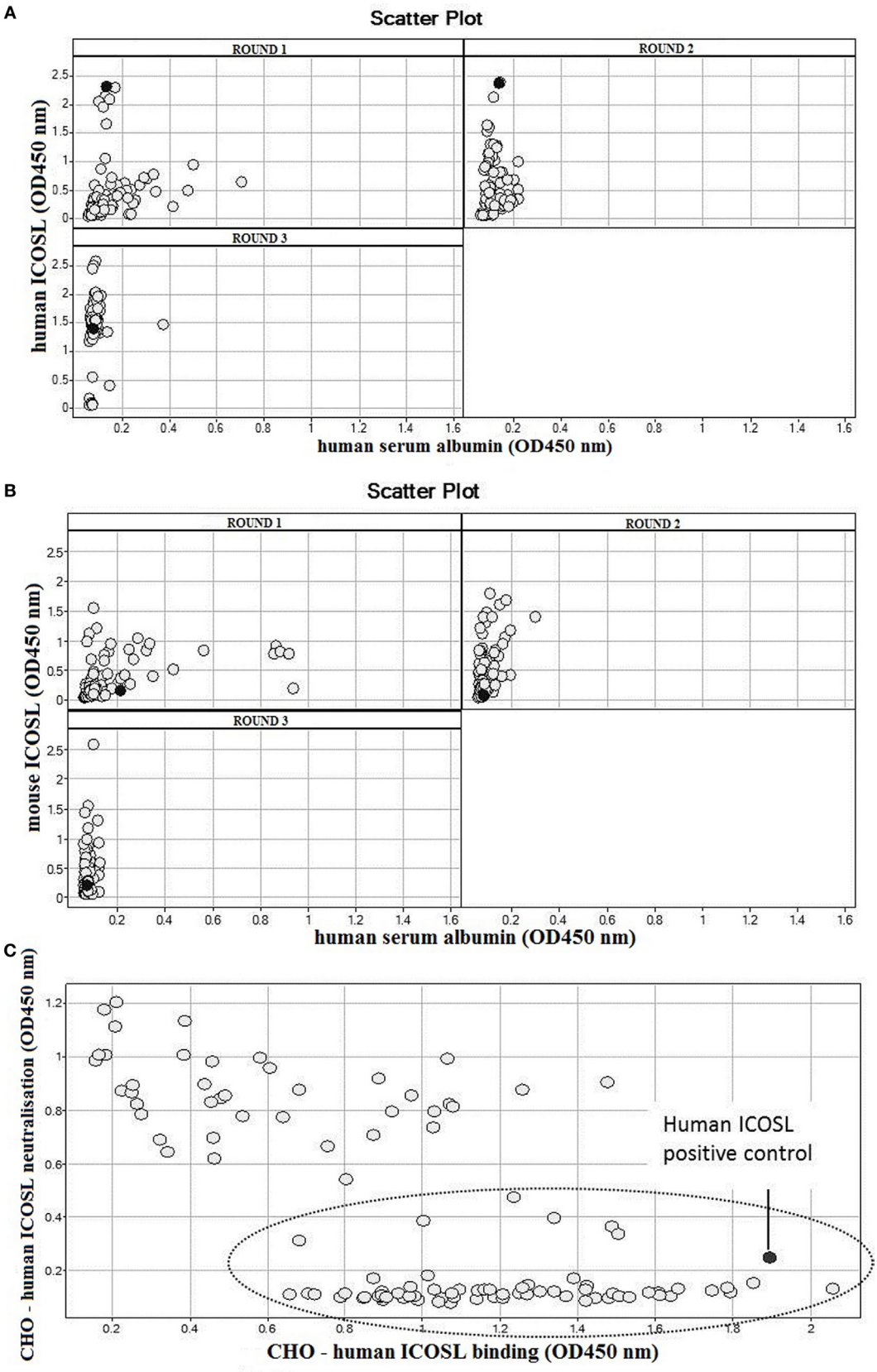

FIGURE 1 | Continued

FIGURE 1 | Continued
Selection of anti-ICOSL VNARs. **(A)** Screening of outputs from a selection campaign with human ICOSL. The scatter plot represents screening data of phage monoclonals from each round of selection for specific binding to huICOSL (*Y* axis) vs non-specific binding to human serum albumin (*X* axis). Each circle denotes a single clone. **(B)** Screening of outputs from a selection campaign with mouse ICOSL. The scatter plot represents screening data of phage monoclonals from each round of selection for specific binding to mICOSL (*Y* axis) vs non-specific binding to human serum albumin (*X* axis). **(C)** Cell-based binding and huICOS-huICOSL blocking assay. Monoclonal VNAR outputs from third round of selection with huICOSL were expressed in periplasm, and periplasmic fractions were tested in cell-based binding and ICOS-ICOSL blocking assays. The *X* axis indicates CHO-huICOSL binding with higher signals corresponding to stronger binders and the *Y* axis identifies clones with decreased signals that are capable of blocking the interaction of ICOSL with CHO-huICOS. The circled area captures all clones which are both strong huICOSL binders and can block ICOS/ICOSL interaction. The human ICOSL positive control is the mouse monoclonal anti-huB7-H2 antibody (MAB165, R&D).

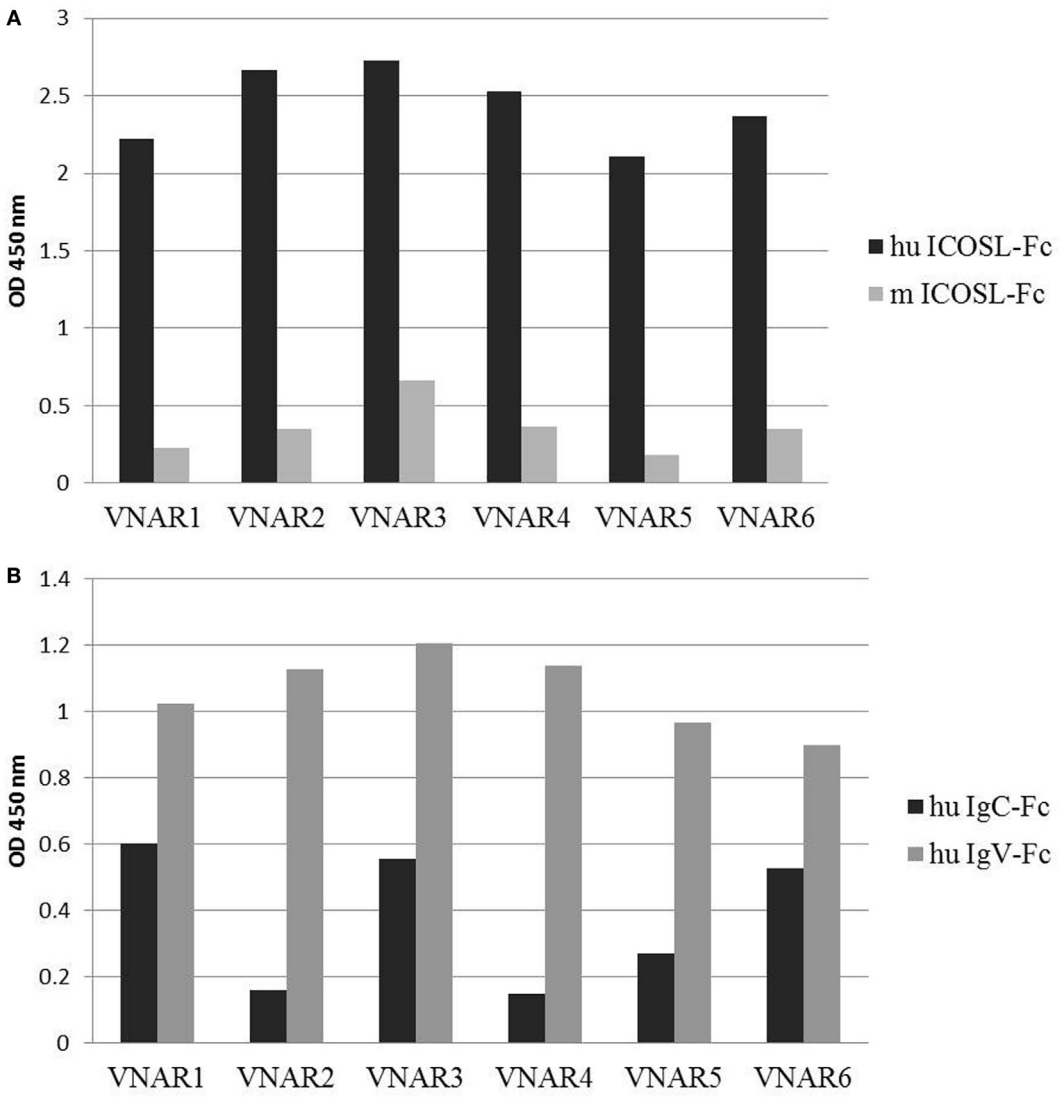

FIGURE 2 | Characterization of anti-huICOSL lead domains binding. **(A)** Lead anti-huICOSL VNAR domains were tested for binding to human and mouse ICOSL in ELISA. **(B)** Binding of lead clones to the IgC and/or IgV domain of the ICOS ligand.

(**Figure 4B**). In cell-based ICOS/ICOSL blocking assays conducted with Fc-reformatted VNAR domains, clone A7, which performed well as a monomeric VNAR, lost this ability after Fc-fusion (**Figure 4C**). The reason for the loss of activity was not investigated further at this time. In summary, A5-Fc and B8-Fc, both blocked receptor/ligand interaction, did not bind human ICOS ligand but did bind mouse and rat protein. F11-Fc did not block ICOS/ICOSL binding, and A7-Fc, which lost its blocking ability after reformatting, bound ligands from all three species (**Figure 4D**).

Evaluation of Anti-mICOSL VNARs in a Murine Model of EAU

The lead domain A5-Fc was assessed in a murine model of EAU by KWS (Bristol, UK). Adult female C57BL/6 mice were randomly allocated to experimental groups and allowed to acclimatize for 1 week. Treatments were administered according to the protocol described in Section "Materials and Methods" from Day 1 to Day 14 or Day 1 to Day 28 for the corticosteroid control (five mice per group) and from Day 1 to Day 14 for the A5-Fc protein (six mice per group). On Day 0, animals were administered with IRBP p1-20 in CFA supplemented with *M. tuberculosis* H37 Ra to induce uveitis. All animals were weighed three times a week and also monitored twice weekly for signs of ill-health and any abnormalities recorded. The disease-induction procedure (subcutaneous administration of IRBP/CFA and intraperitoneal injections of pertussis toxin) caused a mild bodyweight loss on Day 2 and Day 5, as expected for this model. However, from day 7 until the end of the experiment, there was no further treatment-induced bodyweight loss in any of the experimental groups (**Figure 5A**). From day 7 until the end of the experiment, animals were monitored once a week for clinical signs of uveitis using TEFI. A significant increase in TEFI scores was observed on Day 21 when compared with the untreated Day 7 control group. By day 21, both the Cyclosporin A and the anti-mICOSL VNAR domain A5-Fc groups showed a significant reduction in recorded clinical scores and a marked lag in the onset of any disease when compared to the untreated

TABLE 3 | Kinetic parameters and affinity determination of VNAR-Fcs binding to human ICOSL.

VNAR-Fc	ka (1/Ms)	kd (1/s)	KD (M)
VNAR 1	3.11×10^5	9.51×10^{-4}	3.06×10^{-9}
VNAR 2	5.50×10^5	6.69×10^{-4}	1.22×10^{-9}
VNAR 3	5.96×10^5	1.00×10^{-3}	1.68×10^{-9}
VNAR 4	8.73×10^5	3.93×10^{-3}	4.50×10^{-9}
VNAR 5	3.73×10^5	4.15×10^{-3}	1.11×10^{-8}
VNAR 6	3.26×10^5	2.73×10^{-3}	8.39×10^{-9}
Isotype control 2V			Did not bind

Kinetic measurements of anti-huICOSL domains. Kinetic analysis of six anti-huICOSL lead domains is summarized in the table. The interaction between the lead clones and huICOSL was measured by surface plasmon resonance (SPR). An anti-human IgG antibody was immobilized on a Biacore chip and the VNAR clones captured via their Fc region.

ka—association rate constant; kd—dissociation rate constant; KD—binding affinity.

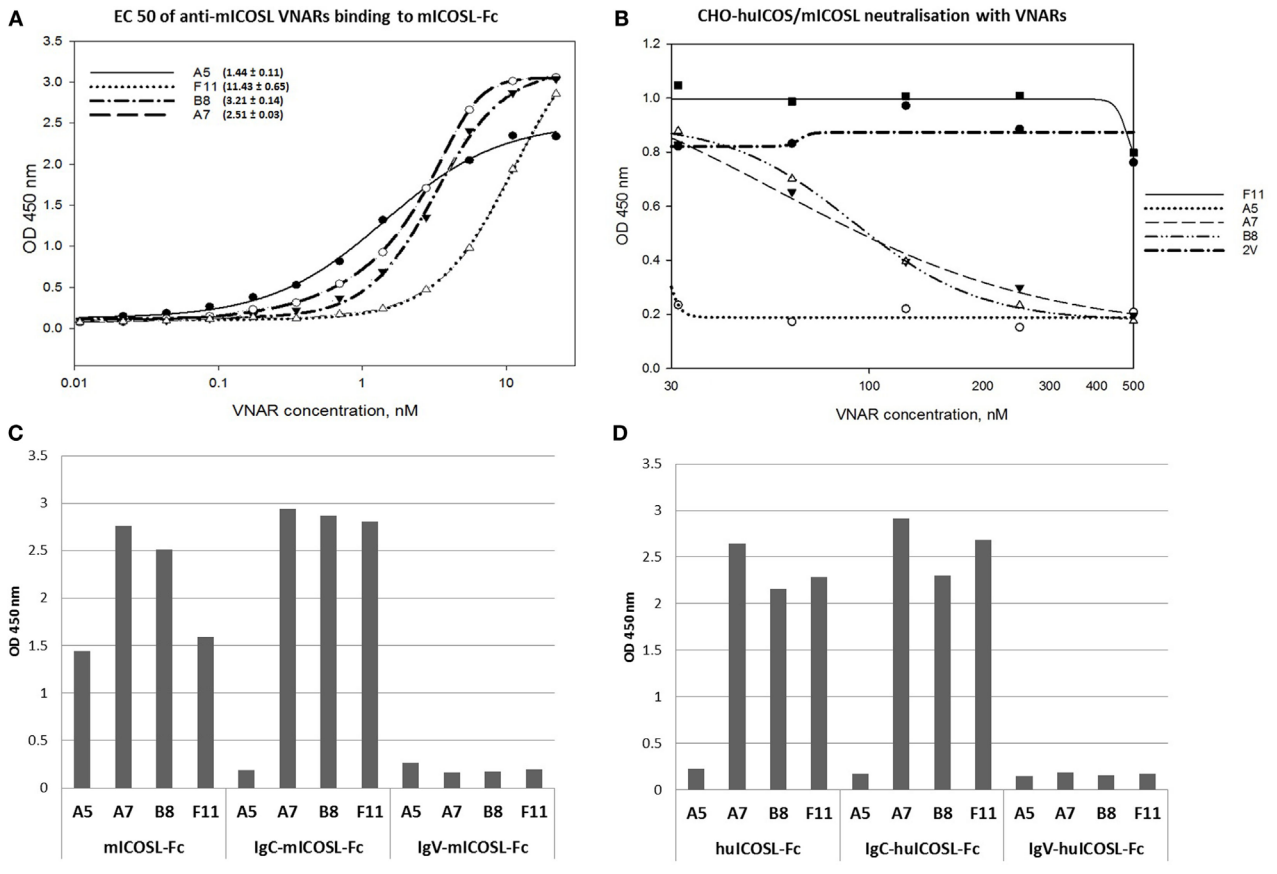

FIGURE 3 | Binding specificity of anti-mICOSL lead domains and blocking of ligand/receptor interaction. **(A)** Binding to mouse ICOSL. Titration curves of four lead anti-mICOSL domains binding to recombinant mouse ICOSL in ELISA and calculated EC50 values. **(B)** Blocking of ligand/receptor binding. Concentration-dependent inhibition of mICOSL-Fc binding to cell surface expressed hICOS by the addition of serial dilutions of anti-mICOSL VNAR domains (from 30 to 500 nM). 2V is the VNAR isotype control used in this experiment. **(C)** Binding to the IgC and IgV domains of the mouse ICOSL. **(D)** Binding to IgC and IgV part of the human ICOSL.

control animals (**Figure 5B**). Histopathology analyses of eyes, removed at the end of the experimental period (Day 28), confirmed that this observed reduction in inflammation translated into differences at the tissue level too (**Figure 5C**). Furthermore, detailed cellular observation clearly showed that animals treated with either Cyclosporin A or with anti-mICOSL VNAR domain A5-Fc presented with mild disease pathology compared to the untreated control. The control animals exhibited extensive cellular inflammation with a high number of neutrophilic cells accumulating in the vitreous, the drainage angle, the anterior chamber, the ciliary body and also in the surrounding blood vessels (**Figure 5D**).

Corneal Penetration of VNAR

The influence of molecular size on the ability of biologics to enter the eye if applied topically was assessed in a scratched corneal mouse model that goes some way to mimicking the situation seen in severe inflammatory eye conditions. It was hoped that the smaller size of the VNAR domains may provide a delivery option for site-specific targeting of ocular disorders. Three formats of increasing molecular weight were tested: VNAR single domains (11 kDa), VNAR Fc (80 kDa) and mAb (150 kDa). All three were applied dropwise onto cornea without an epithelium and anterior fluid was collected after 20 min of treatment. The presence of VNAR was clearly observed in the anterior fluid compared to VNAR-Fc and mAb (**Figure 6**).

DISCUSSION

Uveitis, a major cause of severe visual loss around the world, may be idiopathic or occur as a part of systemic disease such as spondyloarthritis, Vogt–Koyanagi–Harada syndrome, sarcoidosis, autoimmune hepatitis, systemic lupus erythematosus and multiple sclerosis (32). First-line therapy for patients with active uveitis is corticosteroids because of their rapid effect and the flexibility in the choice of their delivery—locally to the eye or systemically. However, long-term corticosteroid treatment is associated with the risk of various adverse events including cataract, glaucoma, diabetes, cushingoid changes, hypercholesterolemia and osteoporosis (33). If a desired response is not achieved with short-term therapy and/or corticosteroids fail to control the inflammation, biological agents may be

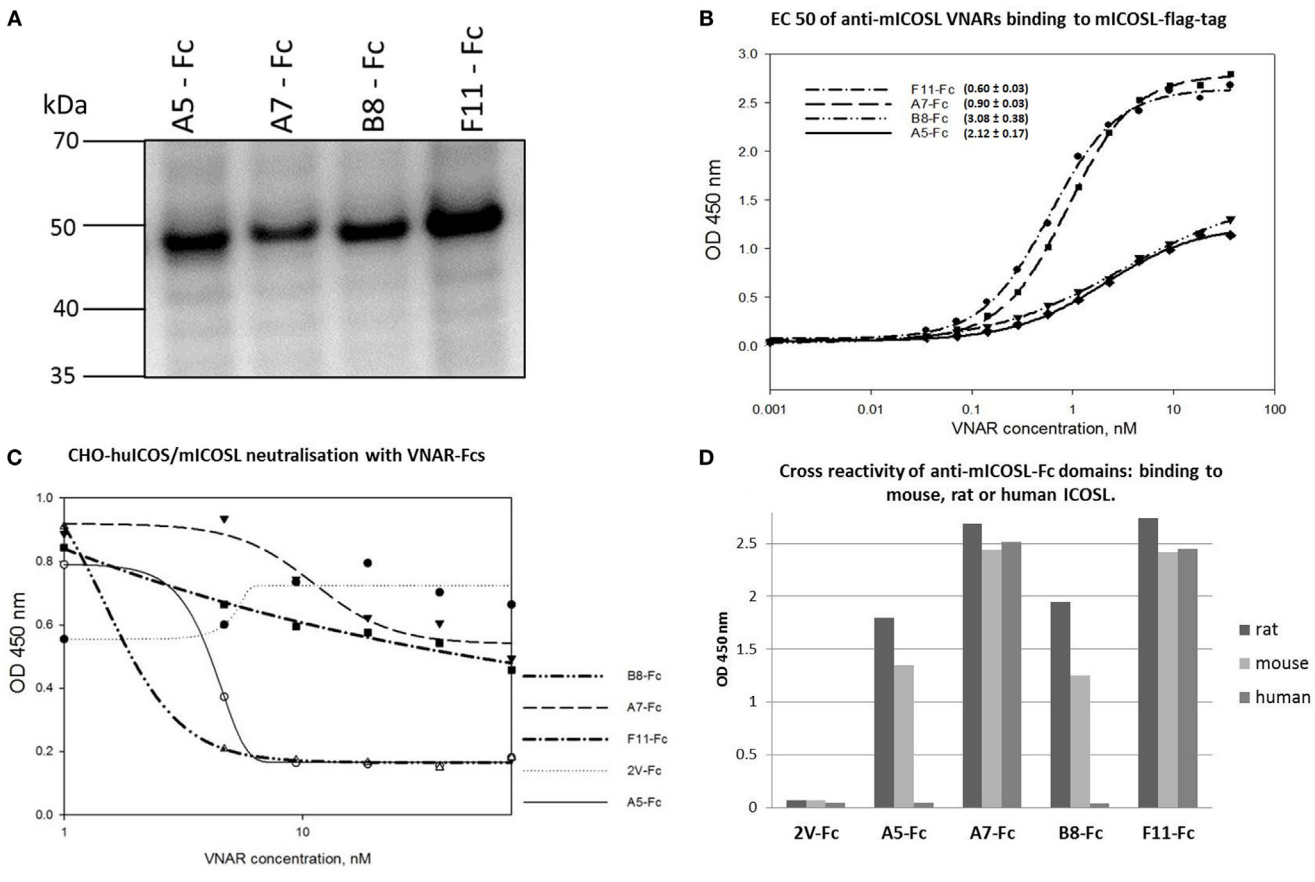

FIGURE 4 | Characterization of anti-mICOSL lead domains after Fc reformatting. **(A)** SDS-PAGE of HEK293 expressed VNAR Fc. **(B)** Binding to mouse ICOSL. Titration curves of anti-mICOSL-Fc domains binding to recombinant mouse ICOSL. **(C)** Blocking of ligand/receptor binding. Concentration-dependent inhibition of recombinant mICOSL-Fc binding to cell surface expressed hICOS by the addition of serial dilutions of anti-mICOSL-Fc domains. 2V-Fc is the isotype control. **(D)** Species cross-reactivity of anti-mICOSL-Fc domains.

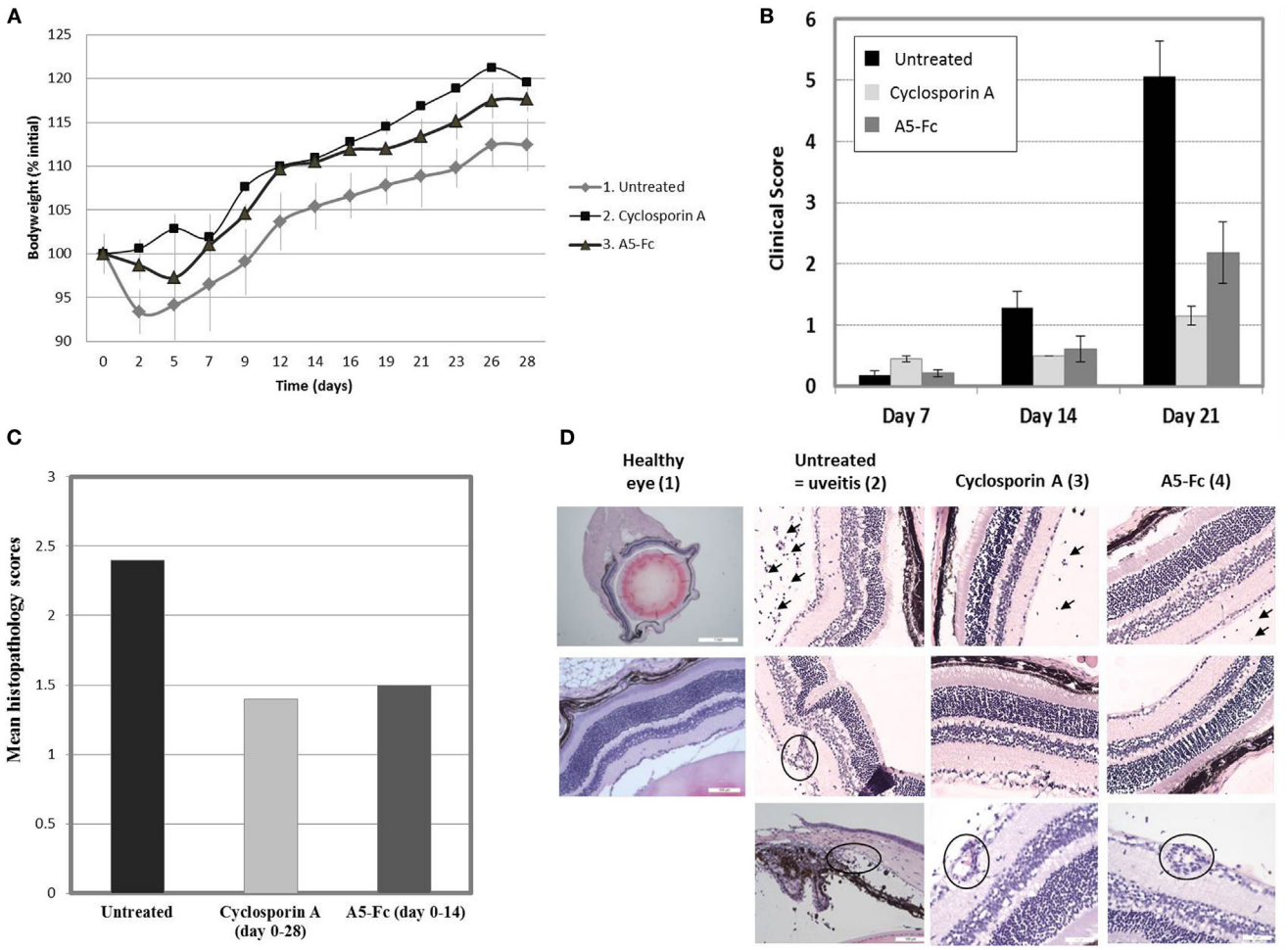

FIGURE 5 | Clinical scores and histopathology sections from the interphotoreceptor retinoid-binding protein-induced uveitis study. **(A)** Bodyweights. All animals were weighed three times a week. Data are presented as mean ± SEM of percentage initial (Day 0) bodyweights. No bodyweight loss was observed. **(B)** Clinical scores. Retinal imaging by topical endoscopic fundal imaging (TEFI) was analyzed by one-way ANOVA followed by Dunn's test for multiple comparisons between experimental days. A significant increase in TEFI scores was observed on Day 21 when compared to Day 7 in the untreated group, as expected for this model of uveitis. Cyclosporin A, administered from Day 1 until the end of the experiment, induced a significant reduction in the clinical scores when compared to the untreated group at Day 21. A5-Fc, administered from Day 1 until Day 14 of the experiment, delivered a comparable result to the Cyclosporin A group treated for 28 days. **(C)** Histopathology scores. Histopathology scores were analyzed by the Kruskal–Wallis test followed by Dunn's post-test for multiple comparisons between experimental groups. The pathological changes observed were consistent with those reported for the model. Greater inflammation was observed in Group 1 (untreated). Cyclosporin A administered from Day 1 until Day 28 and A5-Fc administered from Day 1 until Day 14 caused an equivalent reduction in the histopathology scores. **(D)** Histopathology sections. Dissected eyes were embedded in paraffin wax, sectioned, and stained with hematoxylin and eosin for detailed histopathology analysis at the cellular level. (1) Healthy entire eye glob section and normal retina. (2) Untreated (=uveitis): inflammatory cells in the vitreous (upper panel), a cuff of inflammatory cells surrounding the vessel (middle panel) and neutrophilic inflammation in the drainage angle, anterior chamber, and ciliary body (lower panel). (3) Cyclosporin A treated: mild inflammation of the vitreous (upper and middle panels) and mild vasculitis (lower panel). (4) A5-Fc treated: a low number of inflammatory cells (mild inflammation) in the vitreous (above and middle panels) and mild vasculitis/cuffing (lower panel).

required for the treatment of worsening or refractory disease. Immunomodulatory biologics are powerful drugs that have been used to treat immune-related diseases in a number of different therapeutic areas. They can be designed to dampen down hyperimmune responses and therefore have utility in chronic autoimmune and inflammatory conditions (21). However, it is well known that the prolonged use of powerful systemic biologics can also result in the development of significant off-target side effects and patient complications.

Like the development of many drugs, biologics often rely upon animal models as predictors of clinical efficacy. However, due to the inherent high target specificity of biologics and in some cases low target homology across species, the use of rodent models for preclinical efficacy and safety studies is sometimes precluded. When this situation occurs it is common practice to develop a surrogate or analogous candidate (e.g., for anti-TNF clinical biologics development) that targets the orthologous protein in rat or mouse (34–38). Here, anti-mICOSL VNAR domains could

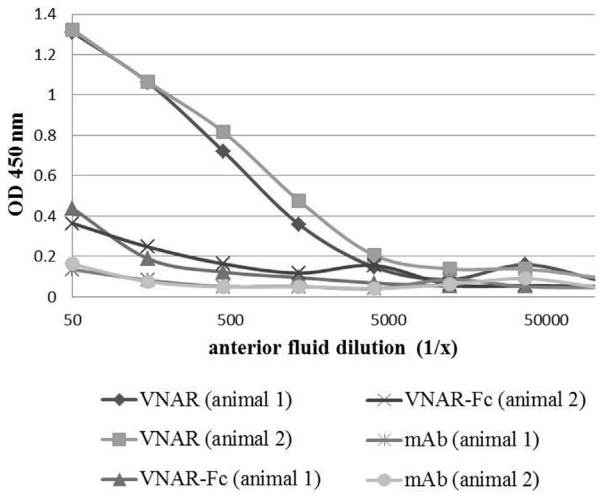

FIGURE 6 | Corneal penetration of VNAR, VNAR Fc, and mAb. A mouse eye with a scratched cornea (to remove epithelium) was treated for 20 min with VNAR (two animals), VNAR-Fc (two animals), or mAb (two animals) by applying drops (4 × 3 µl) directly onto the eye. Anterior fluids were collected and analyzed in ELISA for the presence of VNAR, VNAR Fc, or mAb. VNAR, but not mAb or VNAR-Fc, was detected in anterior fluid of both mice.

be considered surrogates for the use of anti-hICOSL VNARs in patient therapy. In this study, we have isolated anti-mouse and anti-human VNARs from a nurse shark immunized library that can inhibit the receptor/ligand interaction and demonstrated for the first time the efficacy of an anti-mICOSL VNAR domain in a clinically relevant mouse model of EAU. The EAU model is well characterized and widely used as a clinical model of human non-infectious uveitis (39, 40). ICOSL and its importance in antibody-mediated human disease have been verified in a number of preclinical models including RA, SLE and uveitis (22–24, 41–44). The effectiveness of using a mouse mAb to block the interaction between ICOS-ICOSL has also previously been demonstrated in EAU (43).

Shark VNAR domains have been previously isolated against a number of targets from both semisynthetic and immunized sources (10, 11, 19, 45–52). The first demonstration of *in vivo* VNAR activity showed that an anti-HSA VNAR domain isolated from an immunized dogfish could extend the serum half-life of a fused partner VNAR across mouse, rat and monkey pharmacokinetic models (11). In later work, a single anti-TNFα VNAR domain was isolated from an immunized horn shark and showed a modest level of inhibition in a murine model of endotoxic shock (53). Most recently, the isolation of B cell-activating factor-specific VNAR from a synthetic library was shown to function as selective B-cell inhibitors to target B-cell disorders (52). However to date, this uveitis study is the first example of a VNAR domain showing significant *in vivo* efficacy in a recognized clinical model, establishing the potential for the future development of human-specific surrogates as effective treatments of autoimmune disease.

Current advances in ocular drug delivery technologies, suitable for the administration of smaller molecular weight biologics (54–56), provide an encouraging future for the use of VNARs (or their humanized equivalents) in ophthalmology and offer the promise of effective site-specific and systemic side effect-free delivery. At 11 kDa, VNARs are the smallest domains of their type in the animal kingdom and are almost 13 times smaller than an antibody, making the delivery of VNAR to the back of the eye more achievable. We have presented here preliminary evidence that VNAR, if applied topically and at high concentrations, can cross the cornea and be found in the anterior chamber of a mouse eye, whereas an mAb or VNAR-Fc could not. The amounts delivered appeared to reflect the molecular weight of the formats tested with VNAR Fc observed in anterior fluid but at much lower concentrations compared to the single VNAR. It is therefore attractive to speculate that combining the benefits of VNAR domains with a validated inflammatory disease target and new drug delivery technologies could result in the development of a viable drug candidate for ocular disease treatment that could be administered either systemically and/or site-specifically.

ETHICS STATEMENT

This study was carried out in accordance with the recommendations of HMRC under the project license—PPL 7008395. The protocol was approved by the College of Life Sciences and Medicine Ethics Review Board. Work conducted by KWS BioTest (Registered Address: 4 Clifton Road, Clifton, Bristol, BS8 1AG. Registered No. 4980013) was under their ethical guidelines and authorized animal procedures.

AUTHOR CONTRIBUTIONS

CB—leads the science team at Elasmogen and was colead on this program of work alongside AP. Both edited the manuscript. MK—scientific lead on this paper who carried out the majority of the scientific work and wrote the manuscript. KJ—conducted the isolation of the immunized clones and initial characterization and edited the paper. JS—led the expression and purification of the clones.

ACKNOWLEDGMENTS

The authors would like to acknowledge the funding support for this work from Scottish Enterprise and the Biotechnology and Biological Sciences Research Council and would like to extend their thanks to Dr. Lucia Kuffova and Prof. John Forester for their expertise and advice with the ophthalmology studies.

FUNDING

Grateful for support from Biotechnology and Biological Sciences Research Council (BB/K010905/1) and Scottish Enterprise [VNAR_001(2012)].

REFERENCES

1. Durrani OM, Tehrani NN, Marr JE, Moradi P, Stavrou P, Murray PI. Degree, duration, and causes of visual loss in uveitis. *Br J Ophthalmol* (2004) 88:1159–62. doi:10.1136/bjo.2003.037226
2. Bajwa A, Osmanzada D, Osmanzada S, Khan I, Patrie J, Xin W, et al. Epidemiology of uveitis in the mid-Atlantic United States. *Clin Ophthalmol* (2015) 9:889–901. doi:10.2147/OPTH.S80972
3. Gritz DC, Wong IG. Incidence and prevalence of uveitis in Northern California: the Northern California epidemiology of uveitis study. *Ophthalmology* (2004) 111:491–500. doi:10.1016/j.ophtha.2003.06.014
4. Lee RW, Nicholson LB, Sen HN, Chan C, Wei L, Nussenblatt RB, et al. Autoimmune and autoinflammatory mechanisms in uveitis. *Seminars in Immunopathology*. Berlin, Heidelberg: Springer (2014). p. 581–94.
5. Babu K, Mahendradas P. Medical management of uveitis – current trends. *Indian J Ophthalmol* (2013) 61:277–83. doi:10.4103/0301-4738.114099
6. Hoy SM. Adalimumab: a review in non-infectious non-anterior uveitis. *BioDrugs* (2017) 31:135–42. doi:10.1007/s40259-017-0213-x
7. Biester S, Deuter C, Michels H, Haefner R, Kuemmerle-Deschner J, Doycheva D, et al. Adalimumab in the therapy of uveitis in childhood. *Br J Ophthalmol* (2007) 91:319–24. doi:10.1136/bjo.2006.103721
8. Durrani K, Kempen JH, Ying G, Kacmaz RO, Artornsombudh P, Rosenbaum JT, et al. Adalimumab for ocular inflammation. *Ocul Immunol Inflamm* (2016) 25:405–12. doi:10.3109/09273948.2015.1134581
9. Tynjala P, Kotaniemi K, Lindahl P, Latva K, Aalto K, Honkanen V, et al. Adalimumab in juvenile idiopathic arthritis-associated chronic anterior uveitis. *Rheumatology (Oxford)* (2008) 47:339–44. doi:10.1093/rheumatology/kem356
10. Dooley H, Flajnik MF, Porter AJ. Selection and characterization of naturally occurring single-domain (IgNAR) antibody fragments from immunized sharks by phage display. *Mol Immunol* (2003) 40:25–33. doi:10.1016/S0161-5890(03)00084-1
11. Müller MR, Saunders K, Grace C, Jin M, Piche-Nicholas N, Steven J, et al. Improving the pharmacokinetic properties of biologics by fusion to an anti-HSA shark VNAR domain. *MAbs* (2012) 4:673. doi:10.4161/mabs.22242
12. Stanfield RL, Dooley H, Flajnik MF, Wilson IA. Crystal structure of a shark single-domain antibody V region in complex with lysozyme. *Science* (2004) 305:1770–3. doi:10.1126/science.1101148
13. Stanfield RL, Dooley H, Verdino P, Flajnik MF, Wilson IA. Maturation of shark single-domain (IgNAR) antibodies: evidence for induced-fit binding. *J Mol Biol* (2007) 367:358–72. doi:10.1016/j.jmb.2006.12.045
14. Kovalenko OV, Olland A, Piche-Nicholas N, Godbole A, King D, Svenson K, et al. Atypical antigen recognition mode of a shark IgNAR variable domain characterized by humanization and structural analysis. *J Biol Chem* (2013) 288:17408–19. doi:10.1074/jbc.M112.435289
15. Barelle C, Gill DS, Charlton K. Shark novel antigen receptors – the next generation of biologic therapeutics? *Adv Exp Med Biol* (2009) 655:49–62. doi:10.1007/978-1-4419-1132-2_6
16. Griffiths K, Dolezal O, Parisi K, Angerosa J, Dogovski C, Barraclough M, et al. Shark variable new antigen receptor (VNAR) single domain antibody fragments: stability and diagnostic applications. *Antibodies* (2013) 2:66. doi:10.3390/antib2010066
17. Liu JL, Zabetakis D, Brown JC, Anderson GP, Goldman ER. Thermal stability and refolding capability of shark derived single domain antibodies. *Mol Immunol* (2014) 59:194–9. doi:10.1016/j.molimm.2014.02.014
18. Dooley H, Flajnik MF. Shark immunity bites back: affinity maturation and memory response in the nurse shark, Ginglymostoma cirratum. *Eur J Immunol* (2005) 35:936–45.
19. Kovaleva M, Ferguson L, Steven J, Porter A, Barelle C. Shark variable new antigen receptor biologics – a novel technology platform for therapeutic drug development. *Expert Opin Biol Ther* (2014) 14:1527–39. doi:10.1517/14712598.2014.937701
20. Yoshinaga SK, Zhang M, Pistillo J, Horan T, Khare SD, Miner K, et al. Characterization of a new human B7-related protein: B7RP-1 is the ligand to the co-stimulatory protein ICOS. *Int Immunol* (2000) 12:1439–47. doi:10.1093/intimm/12.10.1439
21. Yao S, Zhu Y, Chen L. Advances in targeting cell surface signalling molecules for immune modulation. *Nat Rev Drug Discov* (2013) 12:130–46. doi:10.1038/nrd3877
22. Yoshinaga SK, Whoriskey JS, Khare SD, Sarmiento U, Guo J, Horan T, et al. T-cell co-stimulation through B7RP-1 and ICOS. *Nature* (1999) 402:827–32. doi:10.1038/45582
23. Aicher A, Hayden-Ledbetter M, Brady WA, Pezzutto A, Richter G, Magaletti D, et al. Characterization of human inducible costimulator ligand expression and function. *J Immunol* (2000) 164:4689–96. doi:10.4049/jimmunol.164.9.4689
24. Larimore K, Liang L, Bakkour S, Sha WC. B7h-expressing dendritic cells and plasma B cells mediate distinct outcomes of ICOS costimulation in T cell-dependent antibody responses. *BMC Immunol* (2012) 13:29. doi:10.1186/1471-2172-13-29
25. Sullivan B. Administration of AMG 557, a human anti-B7RP-1 (ICOSL) antibody, leads to the selective inhibition of anti-KLH IgG responses in subjects with SLE: results of a phase I randomized, double-blind, placebo controlled, sequential, rising, multiple dose study. *American College of Rheumatology Annual Scientific Meeting*. San Diego, CA (2013).
26. Agarwal RK, Silver PB, Caspi RR. Rodent Models of Experimental Autoimmune Uveitis. In: Perl A, editor. *Autoimmunity: Methods and Protocols*. Humana Press (2012). p. 443–69.
27. Forrester JV, Klaska IP, Yu T, Kuffova L. Uveitis in mouse and man. *Int Rev Immunol* (2013) 32:76–96. doi:10.3109/08830185.2012.747524
28. Rumfelt L, McKinney E, Taylor E, Flajnik M. The development of primary and secondary lymphoid tissues in the nurse shark *Ginglymostoma cirratum*: B-cell zones precede dendritic cell immigration and T-cell zone formation during ontogeny of the spleen. *Scand J Immunol* (2002) 56:130–48. doi:10.1046/j.1365-3083.2002.01116.x
29. Müller MR, O'Dwyer R, Kovaleva M, Rudkin F, Dooley H, Barelle CJ. Generation and isolation of target-specific single-domain antibodies from shark immune repertoires. In: Chames P, editor. *Antibody Engineering: Methods and Protocols*. 2nd ed. Humana Press (2012). p. 177–94.
30. Chames P, Baty D. Phage display and selections on biotinylated antigens. In: Kotermann R, Dübel S, editors. *Antibody Engineering*. Humana Press (2010). p. 151–64.
31. Chattopadhyay K, Bhatia S, Fiser A, Almo SC, Nathenson SG. Structural basis of inducible costimulator ligand costimulatory function: determination of the cell surface oligomeric state and functional mapping of the receptor binding site of the protein. *J Immunol* (2006) 177:3920–9. doi:10.4049/jimmunol.177.6.3920
32. Barisani-Asenbauer T, Maca SM, Mejdoubi L, Emminger W, Machold K, Auer H. Uveitis – a rare disease often associated with systemic diseases and infections-a systematic review of 2619 patients. *Orphanet J Rare Dis* (2012) 7:57. doi:10.1186/1750-1172-7-57
33. Jabs DA, Rosenbaum JT, Foster CS, Holland GN, Jaffe GJ, Louie JS, et al. Guidelines for the use of immunosuppressive drugs in patients with ocular inflammatory disorders: recommendations of an expert panel. *Am J Ophthalmol* (2000) 130:492–513. doi:10.1016/S0002-9394(00)00659-0
34. Treacy G. Using an analogous monoclonal antibody to evaluate the reproductive and chronic toxicity potential for a humanized anti-TNFalpha monoclonal antibody. *Hum Exp Toxicol* (2000) 19:226–8. doi:10.1191/096032700678815765
35. Wu B, Joshi A, Ren S, Ng C. The application of mechanism-based PK/PD modeling in pharmacodynamic-based dose selection of muM17, a surrogate monoclonal antibody for efalizumab. *J Pharm Sci* (2006) 95:1258–68. doi:10.1002/jps.20475
36. Uchida J, Hamaguchi Y, Oliver JA, Ravetch JV, Poe JC, Haas KM, et al. The innate mononuclear phagocyte network depletes B lymphocytes through Fc receptor-dependent mechanisms during anti-CD20 antibody immunotherapy. *J Exp Med* (2004) 199:1659–69. doi:10.1084/jem.20040119
37. Garrido G, Sanchez B, Rodriguez HM, Lorenzano P, Alonso D, Fernandez LE. 7A7 MAb: a new tool for the pre-clinical evaluation of EGFR-based therapies. *Hybrid Hybridomics* (2004) 23:168–75. doi:10.1089/1536859041224280
38. Clarke J, Leach W, Pippig S, Joshi A, Wu B, House R, et al. Evaluation of a surrogate antibody for preclinical safety testing of an anti-CD11a monoclonal antibody. *Regul Toxicol Pharmacol* (2004) 40:219–26. doi:10.1016/j.yrtph.2004.06.007
39. Caspi RR. Immune mechanisms in uveitis. *Springer Seminars in Immunopathology*. Berlin, Heidelberg: Springer (1999). p. 113–24.
40. Caspi RR, Silver PB, Luger D, Tang J, Cortes LM, Pennesi G, et al. Mouse models of experimental autoimmune uveitis. *Ophthalmic Res* (2008) 40:169–74. doi:10.1159/000119871

41. Iwai H, Kozono Y, Hirose S, Akiba H, Yagita H, Okumura K, et al. Amelioration of collagen-induced arthritis by blockade of inducible costimulator-B7 homologous protein costimulation. *J Immunol* (2002) 169:4332–9. doi:10.4049/jimmunol.169.8.4332
42. Frey O, Meisel J, Hutloff A, Bonhagen K, Bruns L, Kroczek RA, et al. Inducible costimulator (ICOS) blockade inhibits accumulation of polyfunctional T helper 1/T helper 17 cells and mitigates autoimmune arthritis. *Ann Rheum Dis* (2010) 69:1495–501. doi:10.1136/ard.2009.119164
43. Usui Y, Akiba H, Takeuchi M, Kezuka T, Takeuchi A, Hattori T, et al. The role of the ICOS/B7RP-1 T cell costimulatory pathway in murine experimental autoimmune uveoretinitis. *Eur J Immunol* (2006) 36:3071–81. doi:10.1002/eji.200636138
44. Hu YL, Metz DP, Chung J, Siu G, Zhang M. B7RP-1 blockade ameliorates autoimmunity through regulation of follicular helper T cells. *J Immunol* (2009) 182:1421–8. doi:10.4049/jimmunol.182.3.1421
45. Nuttall SD, Krishnan UV, Doughty L, Nathanielsz A, Ally N, Pike RN, et al. A naturally occurring NAR variable domain binds the Kgp protease from *Porphyromonas gingivalis*. *FEBS Lett* (2002) 516:80–6. doi:10.1016/S0014-5793(02)02506-1
46. Nuttall SD, Krishnan UV, Doughty L, Pearson K, Ryan MT, Hoogenraad NJ, et al. Isolation and characterization of an IgNAR variable domain specific for the human mitochondrial translocase receptor Tom70. *Eur J Biochem* (2003) 270:3543–54. doi:10.1046/j.1432-1033.2003.03737.x
47. Nuttall SD, Humberstone KS, Krishnan UV, Carmichael JA, Doughty L, Hattarki M, et al. Selection and affinity maturation of IgNAR variable domains targeting *Plasmodium falciparum* AMA1. *Proteins* (2004) 55:187–97. doi:10.1002/prot.20005
48. Liu JL, Anderson GP, Goldman ER. Isolation of anti-toxin single domain antibodies from a semi-synthetic spiny dogfish shark display library. *BMC Biotechnol* (2007) 7:78. doi:10.1186/1472-6750-7-78
49. Liu JL, Anderson GP, Delehanty JB, Baumann R, Hayhurst A, Goldman ER. Selection of cholera toxin specific IgNAR single-domain antibodies from a naive shark library. *Mol Immunol* (2007) 44:1775–83. doi:10.1016/j.molimm.2006.07.299
50. Goodchild SA, Dooley H, Schoepp RJ, Flajnik M, Lonsdale SG. Isolation and characterisation of Ebolavirus-specific recombinant antibody fragments from murine and shark immune libraries. *Mol Immunol* (2011) 48:2027–37. doi:10.1016/j.molimm.2011.06.437
51. Walsh R, Nuttall S, Revill P, Colledge D, Cabuang L, Soppe S, et al. Targeting the hepatitis B virus precore antigen with a novel IgNAR single variable domain intrabody. *Virology* (2011) 411:132–41. doi:10.1016/j.virol.2010.12.034
52. Häsler J, Flajnik MF, Williams G, Walsh FS, Rutkowski JL. VNAR single-domain antibodies specific for BAFF inhibit B cell development by molecular mimicry. *Mol Immunol* (2016) 75:28–37. doi:10.1016/j.molimm.2016.05.009
53. Bojalil R, Mata-Gonzalez MT, Sanchez-Munoz F, Yee Y, Argueta I, Bolanos L, et al. Anti-tumor necrosis factor VNAR single domains reduce lethality and regulate underlying inflammatory response in a murine model of endotoxic shock. *BMC Immunol* (2013) 14:17. doi:10.1186/1471-2172-14-17
54. Sikandar M, Sharma P, Visht S. Ocular drug delivery system: an overview. *Int J Pharm Sci Res* (2011) 2(5):1168–75. doi:10.13040/IJPSR.0975-8232.2(5).1168-75
55. Patel A, Cholkar K, Agrahari V, Mitra AK. Ocular drug delivery systems: an overview. *World J Pharmacol* (2013) 2:47–64. doi:10.5497/wjp.v2.i2.47
56. Rupenthal ID. Sector overview: ocular drug delivery technologies: exciting times ahead. *ONdrugDelivery* (2015) 54:7–11. doi:10.1002/adhm.201400504

Conflict of Interest Statement: MK, JS, CB and AP are affiliated with Elasmogen Ltd. All other authors have no competing interests to disclose.

The reviewer MR and handling Editor declared their shared affiliation.

frontiers in Immunology

ORIGINAL RESEARCH
published: 22 December 2017
doi: 10.3389/fimmu.2017.01780

Novel, Anti-hTNF-α Variable New Antigen Receptor Formats with Enhanced Neutralizing Potency and Multifunctionality, Generated for Therapeutic Development

Obinna C. Ubah[1], John Steven[1], Marina Kovaleva[1], Laura Ferguson[1], Charlotte Barelle[1], Andrew J. R. Porter[1,2] and Caroline J. Barelle[1]*

[1] Elasmogen Ltd., Aberdeen, Scotland, [2] Scottish Biologics Facility, Institute of Medical Sciences, University of Aberdeen, Aberdeen, Scotland

The management of chronic inflammatory diseases, such as inflammatory bowel disease, psoriasis, and rheumatoid arthritis has significantly improved over the last decade with the clinical availability of anti-TNF-α biologics. Despite this undoubted treatment success, a combination of acquired resistance together with an increased risk of systemic complications, means that a significant number of patients either fail to find a suitable targeted therapy or frustratingly discover that an approach that did work is no longer efficacious. Here, we report the isolation and characterization of a new class of super-neutralizing anti-TNF-α biologics formats, the building blocks of which were originally derived as variable new antigen receptor (VNAR) domains from an immunized nurse shark. These parental small, stable VNAR monomers recognize and neutralize tumor necrosis factor (TNF)-α, in cell-based assays, at nanomolar concentrations. However, the simple, single-chain molecular architecture of VNARs allows for easy and multiple reformatting options. Through reformatting, we achieved a 50,000-fold enhancement in *in vitro* efficacy with super-neutralizing fusion proteins able to block TNF-α induced cytotoxicity in the 2–5 pM range while retaining other functionality through the addition of fusion proteins known to extend serum half-life *in vivo*. In an *in vitro* intestinal epithelial barrier dysfunction efficacy model, the lead VNAR domains, restored barrier function and prevented paracellular flux with comparable efficacy to adalimumab (Humira®). In addition, all multivalent VNAR constructs restored trans-epithelial electrical resistance (TEER) to approximately 94% of the untreated control. Reformatted VNAR domains should be considered as a new class of biologic agents for the treatment of hTNF-α driven diseases; either used systemically with appropriate half-life extension or alternatively where site-specific delivery of small and stable neutralizers may provide improvements to current therapy options.

Keywords: variable new antigen receptor, tumor necrosis factor-α, phage display, cytokine neutralization, chronic inflammation, shark IgNAR, bi-paratopic/bi-specific binding domain, anti-TNF biologics

Abbreviations: VNAR, variable new antigen receptor; TEER, trans-epithelial electrical resistance; hTNF-α, human tumor necrosis factor-alpha; IBD, inflammatory bowel disease; RA, rheumatoid arthritis; IL, interleukin; IgNAR, immunoglobulin new antigen receptor.

OPEN ACCESS

Edited by:
Kevin A. Henry, National Research Council Canada (NRC-CNRC), Canada

Reviewed by:
Ellen Goldman, United States Naval Research Laboratory, United States
Jasna Rakonjac, Massey University, New Zealand

****Correspondence:***
Obinna C. Ubah
obinna.ubah@elasmogen.com

Specialty section:
This article was submitted to Vaccines and Molecular Therapeutics, a section of the journal Frontiers in Immunology

Received: *03 October 2017*
Accepted: *28 November 2017*
Published: *22 December 2017*

Citation:
Ubah OC, Steven J, Kovaleva M, Ferguson L, Barelle C, Porter AJR and Barelle CJ (2017) Novel, Anti-hTNF-α Variable New Antigen Receptor Formats with Enhanced Neutralizing Potency and Multifunctionality, Generated for Therapeutic Development. Front. Immunol. 8:1780. doi: 10.3389/fimmu.2017.01780

INTRODUCTION

Tumor necrosis factor (TNF) alpha is an important cytokine produced by macrophages and a key component of the host's defenses. TNF is released rapidly following all types of trauma and stimuli; however, excessive or persistent production often results in immunopathology, including autoimmune disease and debilitating inflammation (1, 2). It is now well established clinically that targeted neutralization of human (h)TNF-α, or blockade of the receptor mediated signaling pathway, can result in disease control and/or remission (3, 4) with a number of approved antibody-based biologics targeting either TNF-α, or their corresponding receptors in the clinic (3, 5–7). In fact, anti-TNF-α biologic approaches have, for a number of years, been the most commercially lucrative area of disease treatment for many pharmaceutical companies with the anti-TNF-α antibody adalimumab (Humira®) selling over $10 B every year since 2014 (2, 8, 9). Despite this success there still remain significant gaps in the available panel of anti-TNF therapies. From the very first use of anti-TNF-α biologics, clinicians have reported patient cases of non-responders or patients that become suddenly recalcitrant to first one and then subsequent anti-TNF-α biologics. Most cases of therapeutic failure are linked to the development of neutralizing anti-drug antibodies (ADA) with molecular structure, posttranslational modifications, route and frequency of administration, and duration of treatment largely associated with the development of ADAs and treatment withdrawal (10, 11). Furthermore, there is a growing body of evidence warning against the long-term exposure to systemic anti-TNF-α therapy. It appears to increase the risk of some patients developing secondary and life-threatening infections and malignancies (12–14). Therefore, there remains a need for new anti-TNF-α modalities and for new anti-TNF-α biologic formats that may avoid or at least, limit these risks. Extending therapy options for the growing number of patients who have exhausted current biologic-based anti-TNF-α control is also another desirable.

At approximately 11 kDa, variable new antigen receptor (VNAR) domains are the smallest naturally occurring independent binding domains in the vertebrate kingdom (15–21). The characteristic protruding paratopes, of VNARs means that they are often referred to as "canyon-binders," pre-disposed to inserting themselves into pockets or grooves in proteins, resulting in an increased selection propensity of potent neutralizers of receptors and/or enzymes (22–24).

Their simple, single-domain architecture makes reformatting of these domains relatively straightforward with VNARs amenable to both *N*- and *C*- terminal molecular fusions without loss of function (21, 25–27). Here, we demonstrate that a range of additional functionalities can be added that go beyond target specificity and include: quadra-valency, bi-valent-bi-specificity, serum half-life extension, or immune system recruitment (or all four together) and that this multifunctionality can be achieved using a single fusion protein of around 50 kDa or less. While "systemic-friendly" formulations can be readily cloned and expressed, we have also shown that smaller, bi-valent, bi-specific, or even bi-paratopic formats of around 25 kDa, can be expressed cost-efficiently and at scale in non-mammalian systems. These highly stable formats (28–30) retain the neutralizing potency of their larger cousins, but are ideally suited to novel site-specific or topical administration thus minimizing the risk of the systemic side-effects often associated with parenteral administration of, for example, anti-TNF-α biologics.

In this particular study, we have isolated two anti-hTNF-α neutralizing VNARs through shark immunization and phage display and reformatted these domains as multifunctional, multivalent constructs. These fusion proteins retained their inherent binding specificity and stability while delivering improved binding affinity and super-neutralizing anti-hTNF-α potency.

MATERIALS AND METHODS

Shark Immunization

Nurse sharks (*Ginglymostoma cirratum*) were immunized with recombinant hTNF-α (200 μg)/shark emulsified in complete Freund's adjuvant as described by Kovaleva et al. (31). Four weeks later, 200 μg hTNF-α/shark emulsified in incomplete Freund's adjuvant was administered. Two immunization boosts at concentrations of 100 μg hTNF-α/shark and a final boost of 50 μg hTNF-α/shark were given at 4-week intervals intravenously into the caudal vein as soluble antigen in phosphate buffered saline (PBS) (sample 0.45 μM sterile filtered). Blood samples were collected at weeks 0 (pre-immunization bleed), 10, 14, and 18. Peripheral blood lymphocytes (PBLs) isolated and total RNA prepared.

Detection of hTNF-α Specific IgNAR in Shark Serum

IgNAR titer in the bleeds was measured using hTNF-α-coated ELISA plate. Detection was carried out using the IgNAR-specific monoclonal antibody (GA8) at a dilution of 1:200 in PBS, pH 7.4; see Müller et al. (26) for a detailed protocol.

Total RNA Isolation from PBLs and Immune Phage Library Construction

Peripheral blood lymphocytes were harvested from the plasma of the bleed with the best IgNAR response (Bleed 5) and total RNA prepared. Total RNA from the harvested PBLs was used at approximately 2 μg/μl as template for cDNA synthesis using Superscript III First strand synthesis supermix (Invitrogen). cDNA was generated with the framework specific primers NARF4For1 (5′-ATA ATC AAG CTT GCG GCC GCA TTC ACA GTC ACG ACA GTG CCA CCT C-3′) and NARF4For2 (5′-ATA ATC AAG CTT GCG GCC GCA TTC ACA GTC ACG GCA GTG CCA TCT C-3′) (16). Following cDNA synthesis, the common framework one specific primer NARF1Rev (5′-ATA ATA AGG AAT TCC ATG GCT CGA GTG GAC CAA ACA CCG-3′) was introduced and IgNAR V (VNAR) region DNA amplified using a 3-step PCR amplification protocol. The resultant PCR product of approximately 400 base pairs was run on 1.5% agarose gel, and VNAR region cut out and purified (QIAquick purification kit, QIAGEN). Purified DNA was digested at the primer-encoded restriction sites (underlined) with the restriction enzymes *NcoI* and *NotI* (NEB), and re-purified. The VNAR restriction-enzyme

digested DNA library was cloned into a pHEN2 phagemid vector (32), and transformed into a suitable *E. coli* strain.

Phage Display Selection and Screening

A single aliquot of library stock equivalent to OD_{600} of 0.1 was added to 2× TY growth media containing 2% glucose (w/v), 100 µg/ml ampicillin, and grown at 37°C to mid-log phase (OD_{600} of 0.4–0.6) prior to infection with M13K07 helper phage (NEB). Library expression was conducted overnight in 2× TY media, 100 µg/ml ampicillin, and 50 µg/ml kanamycin at 30°C. Phage were PEG-precipitated from the culture supernatant and used for bio-panning. The library was panned against biotinylated rhTNF-α captured on streptavidin beads (Dynabeads, Invitrogen). Library phage and Dynabeads M-280 streptavidin were pre-blocked with block solution [3% (w/v) milk, 1% (w/v) BSA in PBS] for 1 h, rotating at room temperature. Biotin-rhTNF-α (400 nM) was added to blocked beads and incubated for 1 h, rotating at room temperature. Phage were deselected by incubating with blocked beads, 1 h rotating at room temperature. Biotin-rhTNF-α decorated beads were incubated with deselected phage for 1 h, rotating at room temperature. Beads were washed 5× PBST and 5× PBS prior to a strict 8-min elution with 400 µl of 100 mM Triethylamine, and neutralized by adding 200 µl of 1 M Tris–HCl pH 7.5. Mid-log phase *E. coli* TG1 cells (10 ml) were infected with 400 µl eluted phage for 30 min, at 37°C. Then, grown overnight at 37°C on TYE agar plates containing 2% glucose (w/v), 100 µg/ml ampicillin. Three further rounds of selection were conducted and stringency was increased in round 3 and 4 by reducing the concentration of biotin-rhTNF-α to 200 nM. Enrichment of antigen binding monoclonal phage was evaluated using hTNF-α-coated ELISA plates.

VNAR Binding ELISA

Ninety-six well flat bottom Maxisorp Nunc Immuo plates (Thermo Scientific) were coated with antigen of interest [1 µg/ml hTNF-α, BSA, human serum albumin (HSA), etc.] for 1 h at 37°C or 4°C overnight. The plates were washed three times with 200 µl/well PBST [PBS with 0.1% (v/v) Tween 20] before blocking with 200 µl of 4% m (w/v) PBS (MPBS) per well and incubated at 37°C for 1 h. The blocked plates were washed three times with PBST, and 100 µl of VNAR protein solution was added per designated well and plates were incubated at room temperature for 1 h. Plates were washed three times with PBST and 100 µl of 1 in 1,000 dilution HRP conjugated anti-c-myc, anti-poly-histidine, or goat anti-human IgG antibody was added to the plates and incubated for 1 h at room temperature. The plates were washed and developed by adding 100 µl tetramethylbenzidine substrate solution and neutralized using 50 µl 1 M H_2SO_4.

Determination of Anti-hTNF-α VNAR Specificity

Binding specificity was determined on ELISA plates coated with either 1 µg/ml biotin-hTNF-α or unbiotinylated hTNF-α, 10 µg/ml HSA, BSA, streptavidin, single stranded DNA, thyroglobulin, or lysozyme. ELISA plates were suitably blocked in 4% (w/v) Milk-PBS, and VNAR protein samples loaded at a top concentration of 1 µg/ml and a two-fold dilution series performed. Binding was detected with an anti-c-myc-HRP conjugated monoclonal antibody.

Construction of Multivalent Bi-Paratopic/Bivalent VNAR Domains

For this purpose, total DNA was isolated from single clones harboring VNAR fragments of interest. Oligonucleotides required for this formatting were designed in-house, and produced by Sigma-Aldrich, UK. VNAR fragments were PCR amplified with corresponding oligonucleotide pair, thereby introducing desired restriction sites and a flexible linker $(Gly_4Ser)_n$. For dimer constructs, two VNAR fragments PCR formatted with unique cloning sites were cloned into pET28b (+) plasmid vector in two steps *via* their unique restriction sites.

For the trimeric construct, a GeneArt Gene Synthesis plasmid containing a custom-made plug-and-play DNA fragment with VNAR BA11 (a humanized anti-HSA) fragment located at base position 436–744 and flanked by both N- and C- terminal $(Gly_4Ser)_4$ flexible linkers, and cloning sites at positions 52–363 (*Xba*I/*Bam*HI) and 817–1125 (*ApaI*/*EcoR*I) for the insertion of anti-TNF VNAR fragments was utilized. Complete anti-TNF VNAR trimeric construct DNA ligated into pET28b(+) *via* *Xba*I and *EcoR*I restriction sites, followed by transformation into electrocompetent SHuffle® T7 Express cells.

Single *E. coli* clones were picked and grown in terrific broth containing the selection antibiotic.

The Quad™ constructs were designed in-house and the gene made by GeneArt Gene Synthesis (Thermo Fisher Scientific) incorporating cloning sites *BssHII* and *EcoRI*. All Quad™ constructs were designed to incorporate a GlySer-rich short linker before linking to the hinge of a wild-type human IgG1. Specific to the Quad-X™, a $(Gly_4Ser)_4$ flexible was incorporated at the end of CH-3 and a VNAR fused to the flexible linker.

Soluble VNAR Protein Expression and Purification

Soluble VNAR protein was expressed in both prokaryotic (*E. coli*) and eukaryotic systems (*P. pastoris*, HEK293, and CHO K1 cells). Expression in *E. coli* HB2151 cells was induced with 1 mM isopropyl β-D-1-thiogalactopyranoside (IPTG), and soluble VNAR protein was extracted from the periplasm (*E. coli* HB2151 cells) (31). All multivalent non-Fc VNAR constructs were expressed as cytoplasmic protein in IPTG-induced *E. coli* SHuffle® T7 Express cells (NEB) using pET28b(+) expression vector. Extraction of cytoplasmic VNAR protein was achieved using the BugBuster™ protein extraction reagent plus Benzonase® (Novagen).

Polyethylenimine-mediated transfection and transient expression in HEK293 host cells was performed using serum-free FreeStyle™ 293 media (Invitrogen) (31, 33–36). The Quad-X™ construct was also efficiently expressed in suspension-adapted CHO K1 cells by Evitria AG, Zurich, Switzerland (www.evitria.com), using an Evitria expression vector system. The cell-seed was grown in eviGrow medium, a chemically defined, animal-component free, serum-free medium. Cells were transfected with

eviFect, Evitria's custom-made, proprietary transfection reagent, and cells grown after transfection in eviMake^2, an animal-component free, serum-free medium.

Heterologous expression of multivalent VNAR constructs in *P. pastoris* was performed by Novoprotein Scientific Inc., USA, essentially as described by Weidner et al. (36).

All VNAR constructs were purified *via* poly-histidine tag using immobilized metal affinity chromatography, while Protein-A affinity chromatography was adopted for the VNAR-Fc purification. VNAR protein eluted from affinity columns was dialyzed against PBS, pH 7.4. Electrophoresis of purified protein samples was performed on NuPAGE 4–12% Bis-Tris gels using a MES buffer system (Invitrogen) in accordance with the manufacturer's instructions. Expression levels ranged from about 10 mg/l (non-Fc-based VNAR constructs) in *E. coli* systems to up to 150 mg/l (Fc-based VNAR constructs) in mammalian systems.

VNAR Affinity Determination

Octet FortéBio® Biolayer interferometry (BLI) was used to determine the equilibrium dissociation constant (K_D). Dip and Read™ streptavidin biosensors loaded with biotinylated hTNF-α and anti-TNF-α VNAR proteins were diluted using a twofold dilution series with top concentration of 100 nM while VNAR negative controls were assayed at top concentrations of 100 nM and 1 µM. Binding association was monitored for 10 min followed by a 5 min dissociation time. The biosensor was regenerated with 2 × 300 s washes in high salt buffer, TBST (10 mM Tris, 140 mM NaCl, 0.01% Tween 20, pH 7.4).

In addition to the Octet affinity data, a single cycle kinetics screen of the VNAR constructs was also conducted using surface plasmon resonance in a BIAcore™ T200 instrument. In summary, hTNF-α was covalently bound to a CM5 sensor chip surface *via* amine coupling until an increase of around 200 response units was reached. Start-up cycles were composed of a 60-s buffer injection at a flow rate of 30 µl/min followed by a 30-s dissociation period. Anti-hTNF-α VNAR cycles consisted of a 120-s sample injection at 30 µl/min, with a 1,200-s dissociation time. A regeneration step of a 60-s injection of 10 mM glycine buffer, pH 2.0 at 30 µl/ml, followed by a 120-s stabilization period was incorporated at the end of each cycle.

pH Stability Assessment

Variable new antigen receptor protein samples were prepared and incubated at a working concentration of 10 µg/ml in a final volume of 50 µl at designated pH value. Incubation pH 3.0 was titrated using 1 M HCl or 0.1 M citric acid against PBS, pH 7.4. VNAR protein samples were incubated at pH 3 for 28 days, at room temperature. Samples withdrawn at stipulated time points were immediately neutralized in 10× PBS, pH 7.4 to a final concentration of 0.5 µg/ml. Neutralized samples were assessed for activity retention using hTNF-α-coated ELISA plates.

In Vitro hTNF-α Neutralization Assay in L929 Cells

The TNF-α sensitive mouse fibrosarcoma cell line (L929 cells) were grown to 90% confluence, seeded onto 96-well flat bottom microtiter cell culture plate at 5,000 cells per well, and incubated for 48 h. Cells were treated with 1 µg/ml actinomycin-D, before adding a 20 min co-incubated 0.3 ng/ml (1× LD_{80} dose) hTNF-α and anti-hTNF-α VNAR proteins (this step of co-incubation is not crucial as TNF-α can be added directed to wells containing cells, anti-TNF-α VNAR and actinomycin-D). Treated cells were incubated for 24 h at 37°C with 5% (v/v) CO_2 and humidity. Cytotoxicity or cell survival was determined by adding tetrazolium salt (WST-1) cell proliferation reagent (Roche), and incubated for a further 24 h. Absorbance was read at 450 nm using a microplate reader.

FITC-Dextran Paracellular Flux across Polarized Monolayer of Caco-2 Cells

Human epithelial colorectal adenocarcinoma cells (Caco-2) were grown to 90% confluence before seeding onto 24 wells, 0.4 µm semi-permeable tissue culture transwell inserts (Corning Inc.) at 5,000 cells per transwell insert in a final volume of 100 µl, with 600 µl complete DMEM without cells was transferred into the outer containing wells. Transwell plates were incubated at 37°C with 5% (v/v) CO_2, and humidity, and spent DMEM + 10% (v/v) FBS replaced every 48 h. Cell proliferation was monitored under a phase contrast microscope (40× magnification objective) until cells attain 100% confluence, usually between 5 and 7 days post-seeding. Cells were grown for a further 21 days allowing differentiation, with spent medium changed every 48 h until differentiation. Designated insert wells were treated with 10 ng/ml hTNF-α, IFN-γ, and LPS with or without anti-hTNF-α VNAR proteins. Treated cells were incubated for 18 h at 37°C with 5% (v/v) CO_2, and humidity. Following incubation for 18 h with cytokines ± anti-TNF-α VNARs, phase contrast images of treated cells were captured followed by the addition of 5 µl of 10 mg/ml fluorescein isothiocyanate-labeled dextran, molecular weight (3–5 kDa) to the apical side (insert wells) of Caco-2 monolayer. Medium from the basolateral side of the transwell chamber was collected at 2 and 24 h after addition of FITC-dextran. Fluorescence intensity was measured using a Synergy HT (BioTek®) microplate reader at 485 nm excitation and 520 nm emission wavelengths (37, 38).

Epithelial Resistance Dysfunction Assay in Polarized Caco-2 Cell Monolayer

The protocol described for FITC-Dextran paracellular flux across polarized monolayer of Caco-2 cells was followed until designated cells were treated with 10 ng/ml hTNF-α, IFN-γ and LPS with or without anti-TNF-α VNAR proteins. Following incubation for 24 h with cytokines ± anti-hTNF-α VNAR domains, trans-epithelial electrical resistance (TEER) was measured in the apical chamber using Millicell® ERS-2 Epithelial (Volt/Ohm) meter and MERSSTX01 electrode (Merck Millipore). Measured resistance values were normalized to the surface area under treatment.

It is important to note that 12-well tissue culture transwell inserts were seeded with 5 × 10^6 cells/well containing 500 µl DMEM with outer well (basolateral side) containing 1.5 ml DMEM. Also during TEER measurement, DMEM volume in the insert wells was increased to 500 µl to allow volt-ohm meter electrodes to fully submerge in the medium without touching the base of the wells (37, 38).

Statistical Analysis

Graph Pad Prism®, version 5.04 was used to perform statistical analysis on experiments with a minimum of three (3) independent repeat experiments with duplicates/experiment. All values shown are means of $n = 3$ experiments ± SEM (unless otherwise stated).

RESULTS

Immunized Phage Library Construction

An antigen-driven IgNAR immune response was determined post immunization by measuring the IgNAR titer in the sera (pre- and post-bleeds, respectively). An increase in hTNF-α specific IgNAR was observed following each successive immunization boost up to and including the final boost. Unlike the antibody titers seen for a mouse or rabbit immunization which could be up to 100,000, the IgNAR titers appears much more slowly than an any antibody response and peaked here after five boosts at around 1,000 (results not shown).

The VNAR repertoire was PCR amplified from isolated PBLs and cloned into a phagemid vector containing an in-frame M13 bacteriophage truncated coat protein pIII gene. Library quality control including PCR amplification of insert frequency and DNA sequencing of the IgNAR V regions of a representative sample (randomly selected 300 clones) was performed. This analysis confirmed that 85% of the library incorporated a VNAR sequence, and that 79% of the library encoded functional inserts, each possessing a unique amino acid sequence in the CDR3 (data not shown). The corrected library size generated was estimated at 8.7×10^8 transformants.

Isolation of Anti-hTNF-α-Specific VNARs

Variable new antigen receptor domains specific for hTNF-α were isolated following four rounds of selection against biotinylated hTNF-α captured on streptavidin beads. Unlike solid-surface immobilized antigen, this approach presents the target in a "solution state" thereby allowing access to the antigen's entire surface, thus maximizing the chance of isolating specific and high-affinity anti-hTNF-α VNAR. Stringency was introduced in the third and fourth rounds of selection by reducing the concentration of antigen by half. As specific binding to hTNF-α was our key anticipated outcome, randomly selected output monoclonal phage from each selection were screened for binding to target antigen and unrelated non-target protein (HSA and streptavidin). A steady increase in antigen binding was observed from pre-selected clones through to round 2 (100% positive), with a drop in the number of monoclonal phage binders after round 3 (75%) and 4 (80%). No binding to unrelated non-target proteins was observed.

Characterization of Anti-hTNF-α VNARs As Monomers

From an original panel of 24 unique (by DNA sequence) anti-hTNF-α binding clones, two VNAR domains D1 and C4 were eventually selected as leads following a series of assays that considered binding affinity, efficacy in cell-based bio-assays and expressibility in *E. coli*. The expression yield of these two monomeric domains ranged from 7 to 14 mg/l in SHuffle® cells. To benchmark the performance of the VNAR leads, a single-domain anti-hTNF-α VHH TNF30 (39, 40) was included as an appropriate positive control. As monomers, VNARs D1 and C4 recorded a binding affinity (K_D) of 47 and 73 nM (**Table 1**), and neutralized hTNF-α-induced cytotoxicity in L929 cells at 30 and 100 nM, respectively (**Table 2**).

Reformatting VNAR Monomers As Multivalent Constructs

To exploit the ease with which VNARs can accommodate molecular reformatting and in an effort to significantly enhance their activity (binding affinity, avidity, and efficacy), VNARs D1 and C4 were fused *via* a flexible GlySer linker to form homo-and hetero-dimers, with a number of possible dimer outcomes (D1–D1, D1–C4, C4–C4, and C4–D1). These dimer constructs were further screened for neutralization efficacy and expressibility in *E. coli*. VNARs D1–C4 and D1–D1 showed significantly improved neutralizing potencies while expression yields remained almost unaffected (**Table 2**; **Figure 1**). In contrast, dimer constructs with VNAR C4 as the N-terminal fusion partner resulted in poor expression yields (less than 1 mg/l) and

TABLE 1 | Binding kinetics of anti-hTNF-α variable new antigen receptor using Octet® RED96 system.

Binding domain	K_{on} ($M^{-1}s^{-1}$)	K_{off} (s^{-1})	K_D (nM)	K_D (nM) BIAcore
D1	*3.6×10^5*	*1.7×10^{-2}*	n/a	*47.5*
C4	*1.1×10^6*	*8.0×10^{-2}*	n/a	*73.5*
TNF30	*8.2×10^4*	*1.4×10^{-3}*	n/a	*16.7*
D1–D1	5.0×10^5	3.2×10^{-4}	0.6	*n/a*
D1–C4	1.8×10^5	1.1×10^{-4}	0.6	*5.0*
D1–BA11–D1	1.9×10^6	2.0×10^{-4}	0.1	*4.0*
D1–BA11–C4	1.8×10^5	4.8×10^{-5}	0.3	*0.6*

For all measurements, streptavidin Dip and Read™ biosensors were used to immobilize biotinylated hTNF-α. All assessed domains were loaded at a top concentration of 100 nM followed by a twofold dilution series. Values obtained from BIAcore binding analysis are shown in italics, and constructs not tested are shown as "not available" (n/a).

TABLE 2 | Neutralization of 0.3 ng/ml (LD_{80}) hTNF-α-induced cytotoxicity in L929 cells.

Binding molecule	ND_{50} (nM) ($\geq n = 3 \pm$ SEM; except where otherwise stated)
D1	30 ± 3.5 ($n = 2 \pm$ SD)
C4	100 ± 0.1 ($n = 2 \pm$ SD)
TNF30	9.2 ± 2.1
D1–Fc	0.9 ± 0.14
C4–Fc	0.52 ± 0.2
D1–D1	7.0 ± 2.4
D1–C4	0.76 ± 0.06
Humira® (adalimumab)	0.03 ± 0.009
D1–BA11–D1	0.38 ± 0.03
D1–BA11–C4	0.02 ± 0.09
D1–Fc–C4 (Quad-X™)	0.002 ± 0.0011
D1–C4–Fc (Quad-Y™)	0.005 ± 0.001 ($n = 2 \pm$ SD)
C4–D1–Fc (Quad-Y™)	0.012 ± 0.002 ($n = 2 \pm$ SD)

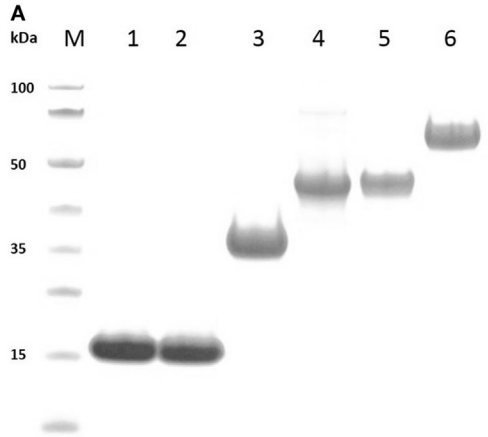

B

SDS PAGE Lane	VNAR construct	Expression Yield/System
1	D1	7 – 10 mg/L (*E. coli*)
2	C4	14 mg/L (*E. coli*)
3	D1-C4	> 100 mg/L (Yeast)
4	D1-BA11-C4	50 mg/L (HEK293)
5	D1-Fc	~ 8 mg/L (HEK293*)
6	D1-Fc-C4 (Quad-X™)	> 150 mg/L (HEK293/CHO)

FIGURE 1 | SDS PAGE and protein expression yield analysis of variable new antigen receptor (VNAR) constructs. **(A)** SDS PAGE and Coomassie blue staining of 5 µg of dithiothreitol-treated VNAR constructs. M, molecular weight marker. **(B)** Protein expression yield in specified expression systems. All expression were conducted in at least 1 l culture volume, except D1–Fc (* refers to a 200-ml culture volume).

minimal efficacy improvement (data not shown). In trivalent formats, where the spacing between the functional anti-TNF-α binding domains was increased further (**Figure 2**) through the inclusion of a well-characterized anti-HSA binding soloMER™ (humanized VNAR) domain BA11 (41), trimers D1–BA11–D1 and D1–BA11–C4 were capable of neutralizing hTNF-α at sub-nanomolar concentrations (**Table 2**).

Affinity Determination

The equilibrium dissociation constant (K_D) for lead VNAR domains was determined on the Octet® RED96 system as described above. As anticipated, the binding affinity of these multivalent domains significantly improved as a result of an enhanced avidity effect. The measured K_D values were in the sub-nanomolar range for the multivalent VNAR constructs, demonstrating a 600-fold improvement in affinity following reformatting of parental domains (**Table 1**).

TNF-α Neutralization in L929 Cell Line

Neutralization of hTNF-α-induced cytotoxicity in L929 cells remains one of the gold-standard *in vitro* efficacy experiments for determining the potency and therapeutic potential of anti-hTNF-α biologics. In this assay, the measured ND_{50} for the unformatted VNAR monomers D1 and C4 was ≈30 and 100 nM, respectively (**Table 2**). The control VHH monomer has an ND_{50} of less than 10 nM in our assay. The ability of the VNAR constructs to neutralize the cytotoxic effect of hTNF-α was significantly improved in the reformatted constructs from monomer to dimer and again to trimer with these trivalent domains showing the most enhanced potencies (**Table 2**). Of particular interest are the D1–C4 and D1–BA11–C4 formats. The D1–C4 had an ND_{50} value 10-fold better than its counterpart homodimer (D1–D1, ND_{50} 7 nM), and D1–BA11–C4 had an ND_{50} value of only 20 pM which is almost 20-fold better than its counterpart D1–BA11–D1 (**Figure 3**; **Table 2**). These consistent and significant improvements seen for the mixed parental dimer clones (with D1 at the N-terminal end of the fusion protein) strongly suggest that D1 and C4 bind unique epitopes on the TNF-α molecule, delivering a bi-paratopic fusion protein of improved neutralizing potency.

Reformatting Parental Domains As VNAR-Fc Constructs

Multivalent VNAR domains in the size range 25–40 kDa (D1–C4 and D1–BA11–C4, respectively) with picomolar neutralizing potency for hTNF-α were expressed successfully in *E. coli*. Although these small domains are well suited to site-specific delivery, they can also be administered systemically because they incorporate BA11, a half-life-extending domain (humanized VNAR), as part of the spacer region of the fusion protein (**Figure 2**). It is also possible to create fusion proteins that are closer to natural antibodies and incorporate an immunoglobulin Fc region. By carrying out these simple molecular fusions both N and C terminally to the human Fc region of an antibody it has been possible to generate the Quad-X™ and Quad-Y™ family of proteins both of around 50 kDa (**Figure 4**). When expressed in a mammalian system these proteins naturally and efficiently assemble as quadra-valent, bi-specific, and bi-paratopic proteins capable of both half-life extension and immune system recruitment. When examined in a "gold-standard" L929 assay the Quad™ family have proved to be super-sensitive neutralizers with 2–5 pM efficacy (**Figure 5B**) and significantly (10×) better than even the leading clinical anti-hTNF-α antibody adalimumab (Humira®). Even the least potent neutralizer amongst the characterized Quad™ constructs (C4–D1–Fc) is twice as potent as Humira® (**Table 2**).

Bivalent D1–Fc and C4–Fc formats show sub-nanomolar efficacies (**Figure 5A**). Interestingly if equimolar dosing of both D1–Fc and C4–Fc are mixed together then a significant enhancement of efficacy is seen over the use of D1–Fc or C4–Fc alone and provides additional evidence that the two parental VNARs are likely binding different epitopes on the hTNF-α molecule (**Figure 5A**).

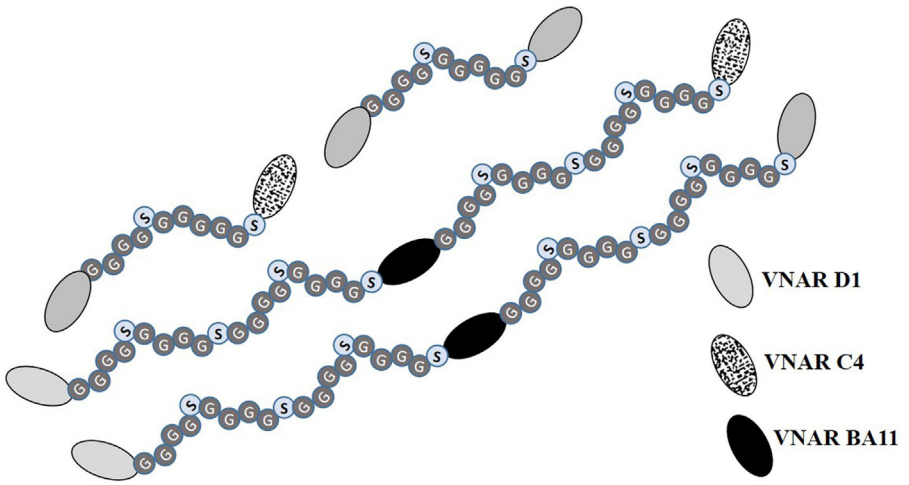

FIGURE 2 | Diagrammatic representation of multivalent anti-hTNF-α variable new antigen receptor (VNAR) constructs. Bivalent constructs contain flexible $(Gly_4Ser)_2$ linkers while their trimeric counterparts in addition to having flexible GlySer linkers incorporate an anti-human serum albumin (HSA) humanized VNAR (soloMER™), called BA11 (26, 41). This additional anti-HSA binder acts as a spacer and a half-life extension tool for prolonged systemic bioavailibity of the trivalent VNAR. The functional binding of BA11 to HSA was not compromised by the presence, in the expressed fusion protein, of the anti-TNF-α binding VNARs (data not shown).

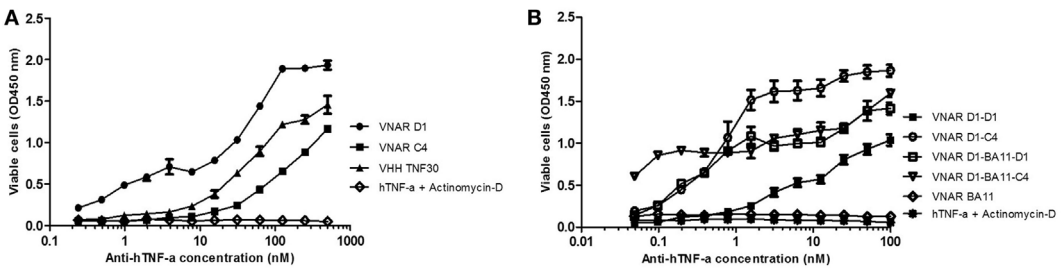

FIGURE 3 | Efficacy assessment in standard L929 cell-based assay. Neutralization of 0.3 ng/ml hTNF-α-induced cytotoxicity in an actinomycin-D primed fibrosarcoma cell line (L929). **(A)** hTNF-α neutralization assay with anti-hTNF-α monomeric constructs at a maximum concentration of 500 nM. Results are the mean ± SD ($n = 2$) with two replicates per experiment. **(B)** Neutralization with multivalent anti-hTNF-α variable new antigen receptor (VNAR) constructs at maximum concentration of 100 nM. Results are the mean ± SEM ($n = 3$) with two replicates per experiment. Results **(B)** were analyzed statistically using a two-way ANOVA with Bonferroni's multiple comparison *post hoc* test. VNAR BA11 was included as a negative control domain in all assays where D1–BA11–D1 and D1–BA11–C4 were tested.

Assessing Efficacy of Anti-hTNF-α VNARs in an *In Vitro* Model of Epithelial Barrier Dysfunction

While the Quad™ family would be suitable for parenteral administration, it is possible that the smaller dimer and trimer proteins may be ideal for topical or localized, site-specific administration avoiding the risk of systemic complications. One such clinical destination may be the lining of the gut to suppress or down-regulate debilitating inflammation in conditions such as inflammatory bowel disease (IBD). While immunogenicity of VNAR domains would not be an important consideration in the intestine, their ability to tolerate and remain functional in this harsh environment would of course be vital if any therapeutic benefit is to be seen. VNARs are known to exhibit exceptional stability in harsh physiological conditions (28–30). Here, we investigated if reformatting of the parental VNAR monomers as multivalent domains impacted on this characteristic stability. In particular these studies focused on low pH 3 stability over extended periods of exposure (3–28 days). All formats tested showed an excellent tolerance to this extreme of pH even after 28 days with the dimer D1–C4 retaining almost full functionality (**Table 3**).

The utility of the VNAR formats was then tested in a series of bio-assays that mimic barrier dysfunction in IBD. Barrier dysfunction can be induced in IFN-γ primed Caco-2 monolayers by hTNF-α and results in disruption of tight junction morphology. Using the method described in Wang et al. (37), epithelial barrier dysfunction was created *in vitro* by treating fully differentiated Caco-2 cells with hTNF-α causing loss in barrier function (measured as leakage of solutes across tight-junctions and a decline in trans-epithelial resistance). The ability of anti-hTNF-α VNAR domains to block this dysfunction was assessed by studying

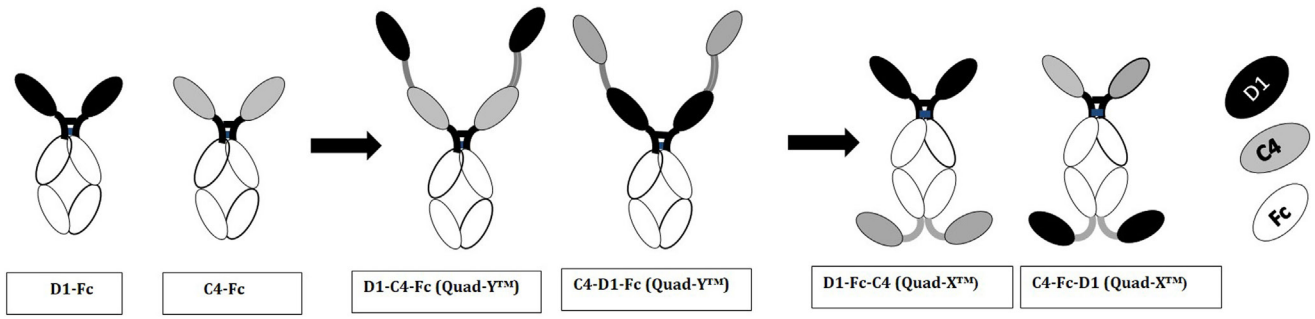

FIGURE 4 | Diagrammatic representation of variable new antigen receptor (VNAR)-Fc constructs. VNAR-Fc constructs of D1 and C4 were generated by direct fusion of VNARs to the hinge of a wild-type human IgG1 Fc. These directly fused VNARs contained a Glycine-rich residue (GGGSGGGGSG) at the end of framework 4 region, and it is this glycine-rich residue that is fused to the hinge. Quad-Y™ constructs are fused to the N-terminal position of the human Fc (as shown in the diagram). The VNARs in a Quad-Y format are linked by a flexible Gly4Ser linker (GGGGSGGGGSGGGGSGGGGS). The Quad-X™ are VNARs fused to both N- and C-terminal ends of the wild-type human IgG1 Fc. The C-terminally fused VNAR is linked to the CH-3 fragment *via* a flexible Gly_4Ser linker (as previously described).

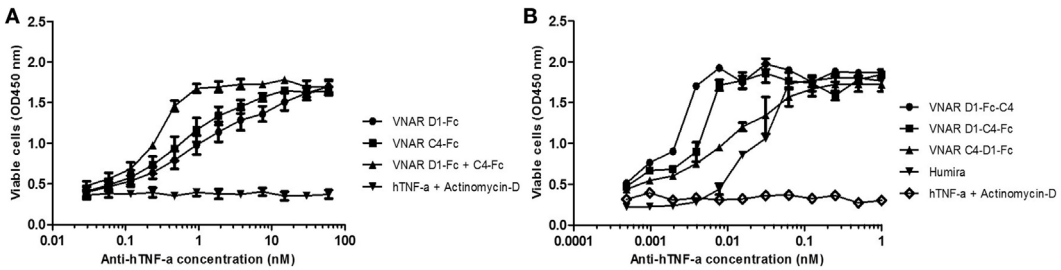

FIGURE 5 | hTNF-α neutralizing capacity of the Fc-based variable new antigen receptor (VNAR) constructs. **(A)** VNAR-Fc constructs demonstrating high neutralization potencies. D1–Fc + C4–Fc denotes equimolar dosing of both constructs. Results shown are the mean ± SEM ($n = 3$) with two replicates per experiment. **(B)** A demonstration of the superior potency of the Quad™ VNAR constructs over Humira® in neutralizing hTNF-α-induced cytotoxicity in L929 cells. Results shown are the mean ± SEM ($n = 4$) with two replicates per experiment (D1–Fc–C4) and mean ± SD ($n = 2$) with two replicates per experiment for the other constructs and Humira®.

TABLE 3 | Binding ELISA of variable new antigen receptor (VNAR) constructs post 28 days incubation at pH 3.

Binding domain	% Retention of binding activity to hTNF-α		
	pH3		
	Day 3	Day 7	Day 28
D1	88 ± 10.2	51 ± 1.3	67 ± 3.4
C4	78.3 ± 3.8	85 ± 0.1	78 ± 3.8
TNF30	90 ± 0.4	78 ± 6.6	80 ± 9.7
D1–D1	91.6 ± 0.3	31.6 ± 1.6	49 ± 0.8
D1–C4	122.8 ± 0.3	106 ± 9.5	81 ± 7.4
D1–BA11–D1	97.9 ± 2.3	106 ± 1.6	77.6 ± 0.7
D1–BA11–C4	72 ± 4.2	60 ± 2.0	73.9 ± 3.8
Anti-HSAmAb	n/a	36.1 ± 0.1	1.6 (Day 21)

VNAR protein samples incubated at pH 3 for 3–28 days were neutralized in phosphate buffered saline, pH 7.4 to a final concentration of 0.5 μg/ml before loading onto a 1 μg/ml hTNF-α and/or human serum albumin (HSA)-coated ELISA plates. Binding activity was measured as percentage residual activity compared to an untreated control at each time point. Results shown are the mean ± SD (n = 1 with multiple replicates per experiment). The control anti-human serum albumin monoclonal is clone HSA-11 produced in mouse (Sigma, A6684).

both the: paracellular flux of large molecular weight hydrophilic molecules such as FITC-dextran and changes in the TEER of the treated Caco-2 cells monolayer. On average the dimer VNAR constructs restored TEER in cytokine treated cells to about 94.4% of the untreated control cells. Interestingly, VNAR D1–C4 restored TEER in cytokine treated cells to about 104.6 ± 5.34% of untreated control and was identical in potency to adalimumab (Humira®) which restored TEER to 103.8 ± 12.1% of untreated control (**Figure 6**).

Variable new antigen receptor monomers restored barrier integrity on average to 63% of untreated, while the VNAR multivalent constructs restored integrity to about 73% of untreated control (**Figure 7**). VNAR D1–C4 and VNAR D1–BA11–C4 restored barrier integrity to about 78 and 84%, respectively, while adalimumab at equimolar dose restored epithelial integrity by 83%. These efficacy data clearly indicate that the VNAR multivalent constructs are comparable in *in vitro* efficacy assays. The barrier leakage can be detected after 2 h of adding FITC-dextran in the unprotected or negative control treated cells (BA11

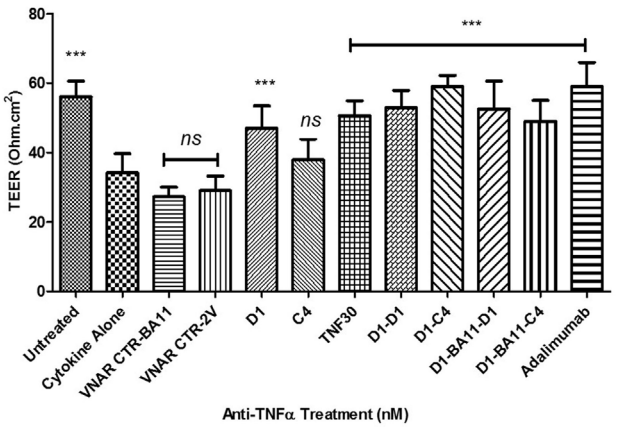

FIGURE 6 | Effect of anti-hTNF-α variable new antigen receptors (VNARs) on trans-epithelial resistance disruption in Caco-2 cell model of cytokine-induced intestinal barrier dysfunction. Monolayer cells were treated with 10 ng/ml hTNF-α and IFN-γ. All VNAR monomers were added at a final concentration of 50 nM while multivalent domains and adalimumab were added at a final concentration of 25 nM. Results shown are the mean ± SD (n = 1 with ≥8 replicates per experiment). Results were statistically analyzed using a one-way ANOVA with Dunnett's *post hoc* test [*** where $P < 0.0001$; not significant (ns) where $P > 0.05$]. VNAR 2V is an isotype control isolated from a naïve library, and has no inherent affinity for any known target antigen (33, 40). VNAR BA11 has been described elsewhere in this paper.

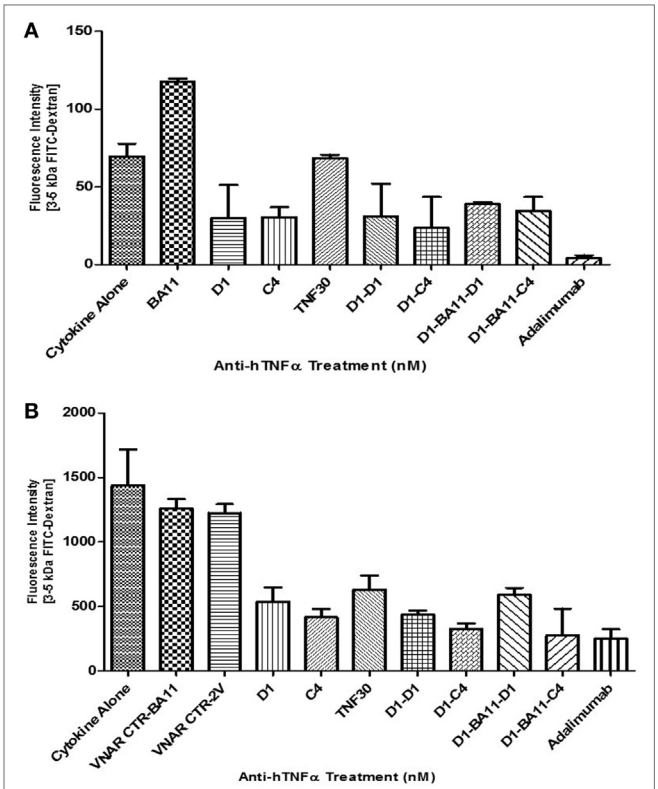

FIGURE 7 | Efficacy of anti-hTNF-α variable new antigen receptors (VNARs) in preventing FITC-dextran paracellular flux in Caco-2 cell model of cytokine induced intestinal barrier dysfunction. All VNAR monomers were added at a final concentration of 50 nM while multivalent domains and adalimumab were added at a final concentration of 25 nM. FITC-Dextran flux was measured by taking media from the basolateral chamber at 2 h **(A)** and 24 h **(B)** post-addition of FITC-Dextran (i.e., 20 and 42 h post cytokine ± anti-TNF-treatment, respectively). Results shown are the mean ± SD (n = 1) with four replicates per experiment, and all treatment groups have been corrected for the fluorescence intensity measured in untreated cells. *y*-Axis on both bar charts are on different scales. VNAR 2V is an isotype control isolated from a naïve library, and has no inherent affinity for any known target antigen (33, 40). VNAR BA11 has been described elsewhere in this paper.

treatment), while protection is evident even at 2 h and sustained over a 24 h period (**Figure 7**).

DISCUSSION

IgNAR V regions (VNAR) have been successfully generated against a range of targets from immunized, naïve and semi-synthetic display VNAR libraries (16, 22, 23, 26, 31, 42–45). The notion that IgNAR are part of the adaptive immune system of sharks has been reported previously (16, 26), and although time consuming, immunization still remains our preferred route for the isolation of high-affinity binders or neutralizers. Shark immunization route can be particularly useful for cross-species conserved proteins as sharks are evolutionarily distant from humans, diverging from a common ancestor approximately 450 million years ago and, therefore, the likelihood of immune tolerance to such a protein antigen is much less likely (15, 20, 46).

In our pre-selected, but immunized VNAR library, 6% of randomly selected clones were specific to hTNF-α. We also observed a post-selection preference for the characteristic CDR3-protruding type II VNARs, suggesting that our anti-hTNF-α VNARs may be accessing recessed epitopes on the hTNF-α molecule.

Here, we demonstrate extensive multivalent reformatting of VNAR fragments, with significant improvement in *in vitro* efficacy (beyond that of clinical antibodies to the same target) and multifunctionality while retaining our unique selling point of "small size" (less than 50 kDa) and flexible expressibility. Using a human antibody Fc region as a spacer in molecular fusions, we have generated for the first time super-potent quadra-valent VNAR-Fc constructs, with two main classes named Quad-X™ and Quad-Y™ after their shape when drawn in a stylized form (**Figure 4**). The significant improvement in binding affinity across the multivalent VNAR constructs (**Table 1**) is likely to be due to avidity effects. A similar stepwise trend was seen in all *in vitro* neutralization experiments, reaching a 50,000-fold efficacy improvement when comparing a single monovalent VNAR to Quad-X™ in the gold-standard L929 neutralization assay.

A number of diseases are associated with alterations in the intestinal barrier and its increased permeability. IBD, Irritable bowel syndrome, celiac disease, as well as extra-intestinal diseases such as type 1 diabetes, acquired immunodeficiency syndrome, multiple sclerosis, and rheumatoid arthritis have all been linked to intestinal barrier defects (47–51). For IBD patients that display increased intestinal paracellular permeability, TNF-α levels become elevated in the intestinal mucosa, serum, and stools of these patients (47), with recent *in vitro* studies further

suggesting that increased TNF-α impairs the intestinal tight junction barrier *via* upregulation of the myosin light-chain kinase protein expression (37, 52). Existing clinically available anti-TNF therapies (e.g., adalimumab, infliximab, and certolizumab) are an effective therapy for these pateints with remission seen for Crohn's disease and other related conditions (53). Despite the relative molecular and valency differences between the different anti-TNF-α biologic drug classes (95–150 kDa), both *in vitro* neutralization studies and clinical retrospective and non-randomized studies have demonstrated comparative efficacy (53–57). However, a common to all approach is a series of well documented systemic complications that include: immunogenicity and resulting ADA, profound issues with patient compliance because of a repeated injection dosing paradigm and serious side-effects associated with prolonged use (risk of life-threatening infections and/or lymphomas) (13, 14, 58). Therefore, the use of smaller molecular weight anti-TNF-α biologics through site-specific delivery may enhance clinical outcomes by reducing the level of systemic exposure to these powerful and pleiotropic biologic drugs (59, 60).

Intra-gastric delivery of an anti-TNF-α VHH constructs using an orally administered engineered *Lactococcus lactis* (*L. lactis*) significantly reduced inflammation in dextran sulfate sodium-induced chronic colitis mice (61). This approach effectively delivers the single-domain VHH to the colon, thereby limiting or circumventing unnecessary exposure of the domain to the very acidic pH of the gastric environment and its associated gastric enzymes. In a preliminary study, VNAR D1–C4 efficiently expressed in *L. lactis* and neutralized hTNF-α in L929 assay with ND_{50} value of 105 pM.

To partially mimic the effects of site-specific delivery, we have utilized an *in vitro* cell-based intestinal epithelial dysfunction model, and have shown that even our monovalent VNAR domains elicit excellent protection against the inflammatory toxicity generated by the presence of human TNF-α. This protection was improved when the VNARs were used in dimer or trimer formats and the level of activity seen was equivalent to that of a clinical antibody control, Humira® (**Figures 6** and **7**). In a pH stability test, designed to mimic the environment of the gut, only the VNAR and VHH domains retained any activity (around 80%) after 7 days exposure (**Table 3**).

It was originally proposed, that unlike the VHH domains (62–64), VNARs might not efficiently form a dimeric fusion molecule, and even where dimerization of VNAR was achieved, the resulting dimeric construct showed a compromised expression level and binding activity thought to be due to steric hindrance or occlusion of the binding site by the incorporated linker (17). It was later shown that VNARs do in fact tolerate both N- and C-terminal molecular fusions to form either a dimer or trimer construct without significant loss of binding characteristics (25). In fact, improvements in binding kinetics, efficacy and pharmacokinetics of domains have been achieved through reformatting parental VNAR and VHH domains as multivalent and/or multi-specific domains (21, 25, 41, 63–66). Increasing the valency of binding domains such as from a monovalent Fab to a bivalent Fab fragment, monovalent scFv to bivalent scFv-Fc, or from a monovalent VHH to a bivalent, or trivalent VHH domain have shown in some cases up to a 500-fold increase in potency and/or affinity for a range of antigens and assays. Enhanced avidity and even additional mechanism of binding fragment-antigen interactions have been shown to be largely responsible for the improved efficacy seen with these multivalent binding domains (64, 65, 67). The improvements we have seen in potency is greater than one would have expected from just avidity (**Tables 1** and **2**) alone with some domains (e.g., D1–BA11–C4, Quad-X™ D1–Fc–C4) showing improvements of over 10,000-fold. As these jumps in potency are always associated with combinations of the D1 and C4 domains (and in that order), we postulate that some of this enhancement in neutralization may be due to bi-paratopic binding, not avidity alone. Further analysis would be required to confirm this hypothesis.

Any increase in valency of the VNAR domains increases the number of possible epitopes that can be assessed on a bioactive hTNF-α trimer, and this capacity has been optimized here using an empirically designed flexible linker (**Figure 2**). Previous studies have shown that multivalent constructs spaced by a short linker can achieve increased functionality by improving their antigen binding through avidity, increased antigen specificity or by cross-linking two hTNF-α trimers (64, 68, 69). We, therefore, hypothesize that the short but flexible 11 amino acid GlySer linker in the dimeric VNAR constructs (D1–C4) allow these domains to interact with two epitopes on one trimeric TNF-α molecules and/or cross-link the interaction of two epitopes on two trimeric TNF-α molecules. Similarly, the trivalent VNAR domains (D1–BA11–C4) were constructed with an increased spatial separation of the anti-TNF-α VNAR domains using two 20 amino acid flexible GlySer linkers and a 103 amino acid VNAR BA11 "spacer," which further enhanced the ability (reach) of these constructs to interact and cross-link bioactive trimeric TNF-α molecules. The VNAR BA11, is a humanized anti-HSA soloMER™ capable of both increasing the spatial separation of the anti-hTNF-α VNAR domains and providing an option for serum half-life extension if used in a systemic, therapeutic setting (25, 41). The logical extension of this approach is our Quad-X™ family of proteins (D1–Fc–C4). Here, we have replaced the BA11 spacer with a human Fc region (half-life extension and immune system recruitment) but have enhanced the neutralizing potency of the fusion protein further by increasing the valency of both D1 and C4 domains through natural and efficient dimerization of the expressed protein. This proved to be the most potent of all the constructs tested delivering complete neutralization at only 2 pM compared to 30 pM by the world's best-selling drug Humira®.

The simple molecular architecture of VNAR domains facilitates flexible reformatting options and the accommodation of additional functionality to deliver a panel of therapeutically useful formats optimized for administration both as systemic and/or site-specific drugs. This flexibility can also be used to enhance drug potency delivering a new class of biologics that can match and even surpass the activity of some of the best studied therapeutic antibodies and deliver this enhanced potency with easily expressed fusion proteins that are two-third the size of a whole antibody.

ETHICS STATEMENT

This study was conducted in accordance with the recommendations of HMRC described in the project license—PPL 60/3799. Work conducted by the Institute of Marine and Environmental Technology (Baltimore, MD, USA) was under their ethical guidelines and authorized animal procedures. Sharks were kept in an extensive state of the art fish-holding facility as part of an environmentally responsible marine core facility that provides excellent experimental capacity for research with marine organisms. It is a completely contained, recirculating operation with large-scale mechanical and biological filtration and life support systems that enable safe and efficient re-use of tank water.

AUTHOR CONTRIBUTIONS

OU: scientific lead on this paper who carried out the majority of the scientific work and wrote the manuscript. JS: assisted in the rational *in-silico* construction and expression of some of the VNAR-Fc constructs. MK and LF: assisted in the library construction and expression of multivalent VNAR proteins. CB: assisted with the VNAR and monoclonal antibody stability assessment. CJB: led the science team at Elasmogen, and co-supervised this project alongside AP. Also both CJB and AP reviewed the manuscript.

ACKNOWLEDGMENTS

The authors wish to acknowledge the funding support for this work from MSD/Scottish Universities Life Sciences Alliance (SULSA), Scottish Enterprise, the Biotechnology and Biological Sciences Research Council (BBSRC), and the University of Aberdeen.

FUNDING

Grateful for support from Biotechnology and Biological Sciences Research Council (BB/K010905/1), Scottish Enterprise [VNAR_001 (2012)], Scottish Universities Life Sciences Alliance/MSD (MSD01_A_Porter-Teismann), and the College of Life Sciences and Medicine, University of Aberdeen (Fee bursary to OU).

REFERENCES

1. Feldmann M, Maini RN. TNF defined as a therapeutic target for rheumatoid arthritis and other autoimmune diseases. *Nat Med* (2003) 9:1245. doi:10.1038/nm939
2. Lai Y, Dong C. Therapeutic antibodies that target inflammatory cytokines in autoimmune diseases. *Int Immunol* (2015) 28:181–8. doi:10.1093/intimm/dxv063
3. Callhoff J, Weiß A, Zink A, Listing J. Impact of biologic therapy on functional status in patients with rheumatoid arthritis – a meta-analysis. *Rheumatology* (2013) 52:2127–35. doi:10.1093/rheumatology/ket266
4. Cohen BL, Sachar DB. Update on anti-tumor necrosis factor agents and other new drugs for inflammatory bowel disease. *BMJ* (2017) 357:j2505. doi:10.1136/bmj.j2505
5. Thalayasingam N, Isaacs JD. Anti-TNF therapy. *Best Pract Res Clin Rheumatol* (2011) 25:549–67. doi:10.1016/j.berh.2011.10.004
6. Llorenç V, Mesquida M, Sainz de la Maza M, Blanco R, Calvo V, Maíz O, et al. Certolizumab pegol, a new anti-TNF-α in the armamentarium against ocular inflammation. *Ocul Immunol Inflamm* (2016) 24:167–72. doi:10.3109/09273948.2014.967779
7. Udalova I, Monaco C, Nanchahal J, Feldmann M. Anti-TNF therapy. *Microbiol Spectr* (2016) 4(4). doi:10.1128/microbiolspec.MCHD-0022-2015
8. Monaco C, Nanchahal J, Taylor P, Feldmann M. Anti-TNF therapy: past, present and future. *Int Immunol* (2014) 27:55–62. doi:10.1093/intimm/dxu102
9. Chaudhari K, Rizvi S, Syed BA. Rheumatoid arthritis: current and future trends. *Nat Rev Drug Discov* (2016) 15:305–6. doi:10.1038/nrd.2016.21
10. Wolbink GJ, Aarden LA, Dijkmans B. Dealing with immunogenicity of biologicals: assessment and clinical relevance. *Curr Opin Rheumatol* (2009) 21:211–5. doi:10.1097/BOR.0b013e328329ed8b
11. Jullien D, Prinz JC, Nestle FO. Immunogenicity of biotherapy used in psoriasis: the science behind the scenes. *J Invest Dermatol* (2015) 135:31–8. doi:10.1038/jid.2014.295
12. Chiang Y, Kuo L, Yen Y, Tang C, Chen H. Infection risk in patients with rheumatoid arthritis treated with etanercept or adalimumab. *Comput Methods Programs Biomed* (2014) 116:319–27. doi:10.1016/j.cmpb.2014.06.008
13. Dulai PS, Thompson KD, Blunt HB, Dubinsky MC, Siegel CA. Risks of serious infection or lymphoma with anti-tumor necrosis factor therapy for pediatric inflammatory bowel disease: a systematic review. *Clin Gastroenterol Hepatol* (2014) 12:1443–51. doi:10.1016/j.cgh.2014.01.021
14. Kalb RE, Fiorentino DF, Lebwohl MG, Toole J, Poulin Y, Cohen AD, et al. Risk of serious infection with biologic and systemic treatment of psoriasis: results from the psoriasis longitudinal assessment and registry (PSOLAR). *JAMA Dermatol* (2015) 151:961–9. doi:10.1001/jamadermatol.2015.0718
15. Greenberg AS, Avila D, Hughes M, Hughes A, McKinney EC, Flajnik MF. A new antigen receptor gene family that undergoes rearrangement and extensive somatic diversification in sharks. *Nature* (1995) 374:168. doi:10.1038/374168a0
16. Dooley H, Flajnik MF, Porter AJ. Selection and characterization of naturally occurring single-domain (IgNAR) antibody fragments from immunized sharks by phage display. *Mol Immunol* (2003) 40:25–33. doi:10.1016/S0161-5890(03)00084-1
17. Simmons DP, Abregu FA, Krishnan UV, Proll DF, Streltsov VA, Doughty L, et al. Dimerisation strategies for shark IgNAR single domain antibody fragments. *J Immunol Methods* (2006) 315:171–84. doi:10.1016/j.jim.2006.07.019
18. Flajnik MF, Deschacht N, Muyldermans S. A case of convergence: why did a simple alternative to canonical antibodies arise in sharks and camels? *PLoS Biol* (2011) 9:e1001120. doi:10.1371/journal.pbio.1001120
19. Streltsov VA, Varghese JN, Masters CL, Nuttall SD. Crystal structure of the amyloid-beta p3 fragment provides a model for oligomer formation in Alzheimer's disease. *J Neurosci* (2011) 31:1419–26. doi:10.1523/JNEUROSCI.4259-10.2011
20. Barelle C, Porter A. VNARs: an ancient and unique repertoire of molecules that deliver small, soluble, stable and high affinity binders of proteins. *Antibodies* (2015) 4:240–58. doi:10.3390/antib4030240
21. Zielonka S, Empting M, Grzeschik J, Könning D, Barelle CJ, Kolmar H. Structural insights and biomedical potential of IgNAR scaffolds from sharks. *MAbs* (2015) 7:15–25. doi:10.4161/19420862.2015.989032
22. Nuttall SD, Krishnan UV, Doughty L, Nathanielsz A, Ally N, Pike RN, et al. A naturally occurring NAR variable domain binds the Kgp protease from *Porphyromonas gingivalis*. *FEBS Lett* (2002) 516:80–6. doi:10.1016/S0014-5793(02)02506-1
23. Nuttall SD, Krishnan UV, Doughty L, Pearson K, Ryan MT, Hoogenraad NJ, et al. Isolation and characterization of an IgNAR variable domain specific for the human mitochondrial translocase receptor Tom70. *FEBS J* (2003) 270:3543–54. doi:10.1046/j.1432-1033.2003.03737.x
24. Stanfield RL, Dooley H, Flajnik MF, Wilson IA. Crystal structure of a shark single-domain antibody V region in complex with lysozyme. *Science* (2004) 305:1770–3. doi:10.1126/science.1101148
25. Muller D, Karle A, Meissburger B, Hofig I, Stork R, Kontermann RE. Improved pharmacokinetics of recombinant bispecific antibody molecules by fusion to human serum albumin. *J Biol Chem* (2007) 282:12650–60. doi:10.1074/jbc.M700820200

26. Müller MR, O'Dwyer R, Kovaleva M, Rudkin F, Dooley H, Barelle CJ. Generation and isolation of target-specific single-domain antibodies from shark immune repertoires. *Methods Mol Biol* (2012) 907:177–94. doi:10.1007/978-1-61779-974-7_9
27. Krah S, Schröter C, Zielonka S, Empting M, Valldorf B, Kolmar H. Single-domain antibodies for biomedical applications. *Immunopharmacol Immunotoxicol* (2016) 38:21–8. doi:10.3109/08923973.2015.1102934
28. Liu JL, Anderson GP, Delehanty JB, Baumann R, Hayhurst A, Goldman ER. Selection of cholera toxin specific IgNAR single-domain antibodies from a naive shark library. *Mol Immunol* (2007) 44:1775–83. doi:10.1016/j.molimm.2006.07.299
29. Griffiths K, Dolezal O, Parisi K, Angerosa J, Dogovski C, Barraclough M, et al. Shark variable new antigen receptor (VNAR) single domain antibody fragments: stability and diagnostic applications. *Antibodies* (2013) 2:66–81. doi:10.3390/antib2010066
30. Liu JL, Zabetakis D, Brown JC, Anderson GP, Goldman ER. Thermal stability and refolding capability of shark derived single domain antibodies. *Mol Immunol* (2014) 59:194–9. doi:10.1016/j.molimm.2014.02.014
31. Kovaleva M, Johnson K, Steven J, Barelle C, Porter A. The therapeutic potential of shark anti-ICOSL VNAR domains is exemplified in a murine model of autoimmune non-infectious uveitis. *Front Immunol* (2017) 8:1121. doi:10.3389/fimmu.2017.01121
32. Hoogenboom HR, Griffiths AD, Johnson KS, Chiswell DJ, Hudson P, Winter G. Multi-subunit proteins on the surface of filamentous phage: methodologies for displaying antibody (Fab) heavy and light chains. *Nucleic Acids Res* (1991) 19:4133–7.
33. Steven J, Muller M, Carvalho M, Ubah O, Kovaleva M, Donohoe G, et al. In vitro maturation of a humanized shark VNAR domain to improve its biophysical properties for facilitating clinical development. *Front Immunol* (2017) 8:1361. doi:10.3389/fimmu.2017.01361
34. Backliwal G, Hildinger M, Hasija V, Wurm FM. High-density transfection with HEK-293 cells allows doubling of transient titers and removes need for a priori DNA complex formation with PEI. *Biotechnol Bioeng* (2008) 99:721–7. doi:10.1002/bit.21596
35. Huh S, Do H, Lim H, Kim D, Choi S, Song H, et al. Optimization of 25kDa linear polyethylenimine for efficient gene delivery. *Biologicals* (2007) 35:165–71. doi:10.1016/j.biologicals.2006.08.004
36. Weidner M, Taupp M, Hallam SJ. Expression of recombinant proteins in the methylotrophic yeast *Pichia pastoris*. *J Vis Exp* (2010) 36:1862. doi:10.3791/1862
37. Wang F, Graham WV, Wang Y, Witkowski ED, Schwarz BT, Turner JR. Interferon-γ and tumor necrosis factor-α synergize to induce intestinal epithelial barrier dysfunction by up-regulating myosin light chain kinase expression. *Am J Pathol* (2005) 166:409–19. doi:10.1016/S0002-9440(10)62264-X
38. Beirnaert EAA. *Nanobodies Against Tumor Necrosis Factor-Alpha*. U.S. Patent No. 8,703,131. Washington, DC: U.S. Patent and Trademark Office (2014).
39. Fernandez JE, Dixon DA, Paulson A. *Formulations of Single Domain Antigen Binding Molecules*. U.S. Patent 9,393,304. Washington, DC: U.S. Patent and Trademark Office (2016).
40. Müller MR, Saunders K, Grace C, Jin M, Piche-Nicholas N, Steven J, et al. Improving the pharmacokinetic properties of biologics by fusion to an anti-HSA shark VNAR domain. *MAbs* (2012) 4:673–85. doi:10.4161/mabs.22242
41. Nuttall SD, Krishnan UV, Hattarki M, De Gori R, Irving RA, Hudson PJ. Isolation of the new antigen receptor from wobbegong sharks, and use as a scaffold for the display of protein loop libraries. *Mol Immunol* (2001) 38:313–26. doi:10.1016/S0161-5890(01)00057-8
42. Camacho-Villegas T, Mata-Gonzalez T, Paniagua-Solis J, Sanchez E, Licea A. Human TNF cytokine neutralization with a vNAR from *Heterodontus francisci* shark: a potential therapeutic use. *MAbs* (2013) 5:80–5. doi:10.4161/mabs.22593
43. Zielonka S, Weber N, Becker S, Doerner A, Christmann A, Christmann C, et al. Shark attack: high affinity binding proteins derived from shark vNAR domains by stepwise in vitro affinity maturation. *J Biotechnol* (2014) 191:236–45. doi:10.1016/j.jbiotec.2014.04.023
44. Ubah OC, Barelle CJ, Buschhaus MJ, Porter AJ. Phage display derived IgNAR V region binding domains for therapeutic development. *Curr Pharm Des* (2016) 22:6519–26. doi:10.2174/1381612822666160907091708
45. Barelle C, Gill DS, Charlton K. Shark novel antigen receptors – the next generation of biologic therapeutics? *Adv Exp Med Biol* (2009) 655:49–62. doi:10.1007/978-1-4419-1132-2_6
46. Lee SH. Intestinal permeability regulation by tight junction: implication on inflammatory bowel diseases. *Intest Res* (2015) 13:11–8. doi:10.5217/ir.2015.13.1.11
47. Zolotarevsky Y, Hecht G, Koutsouris A, Gonzalez DE, Quan C, Tom J, et al. A membrane-permeant peptide that inhibits MLC kinase restores barrier function in in vitro models of intestinal disease. *Gastroenterology* (2002) 123:163–72. doi:10.1053/gast.2002.34235
48. Bischoff SC, Barbara G, Buurman W, Ockhuizen T, Schulzke J, Serino M, et al. Intestinal permeability – a new target for disease prevention and therapy. *BMC Gastroenterol* (2014) 14:189. doi:10.1186/s12876-014-0189-7
49. Fasano A, Not T, Wang W, Uzzau S, Berti I, Tommasini A, et al. Zonulin, a newly discovered modulator of intestinal permeability, and its expression in coeliac disease. *Lancet* (2000) 355:1518–9. doi:10.1016/S0140-6736(00)02169-3
50. Heyman M, Abed J, Lebreton C, Cerf-Bensussan N. Intestinal permeability in coeliac disease: insight into mechanisms and relevance to pathogenesis. *Gut* (2012) 61:1355–64. doi:10.1136/gutjnl-2011-300327
51. Stidham R, Lee T, Higgins P, Deshpande A, Sussman D, Singal A, et al. Systematic review with network meta-analysis: the efficacy of anti-TNF agents for the treatment of Crohn's disease. *Aliment Pharmacol Ther* (2014) 39:1349–62. doi:10.1111/apt.12749
52. Ma TY, Boivin MA, Ye D, Pedram A, Said HM. Mechanism of TNF-{alpha} modulation of Caco-2 intestinal epithelial tight junction barrier: role of myosin light-chain kinase protein expression. *Am J Physiol Gastrointest Liver Physiol* (2005) 288:G422–30. doi:10.1152/ajpgi.00412.2004
53. Kaymakcalan Z, Sakorafas P, Bose S, Scesney S, Xiong L, Hanzatian DK, et al. Comparisons of affinities, avidities, and complement activation of adalimumab, infliximab, and etanercept in binding to soluble and membrane tumor necrosis factor. *Clin Immunol* (2009) 131:308–16. doi:10.1016/j.clim.2009.01.002
54. Kestens C, van Oijen MG, Mulder CL, van Bodegraven AA, Dijkstra G, de Jong D, et al. Adalimumab and infliximab are equally effective for Crohn's disease in patients not previously treated with anti-tumor necrosis factor-α agents. *Clin Gastroenterol Hepatol* (2013) 11:826–31. doi:10.1016/j.cgh.2013.01.012
55. Nesbitt A, Fossati G, Bergin M, Stephens P, Stephens S, Foulkes R, et al. Mechanism of action of certolizumab pegol (CDP870): in vitro comparison with other anti-tumor necrosis factor α agents. *Inflamm Bowel Dis* (2007) 13:1323–32. doi:10.1002/ibd.20225
56. Osterman MT, Haynes K, Delzell E, Zhang J, Bewtra M, Brensinger C, et al. Comparative effectiveness of infliximab and adalimumab for Crohn's disease. *Clin Gastroenterol Hepatol* (2014) 12:811–7.e3. doi:10.1016/j.cgh.2013.06.010
57. Atzeni F, Talotta R, Salaffi F, Cassinotti A, Varisco V, Battellino M, et al. Immunogenicity and autoimmunity during anti-TNF therapy. *Autoimmun Rev* (2013) 12:703–8. doi:10.1016/j.autrev.2012.10.021
58. Miheller P, Kiss LS, Lorinczy K, Lakatos PL. Anti-TNF trough levels and detection of antibodies to anti-TNF in inflammatory bowel disease: are they ready for everyday clinical use? *Expert Opin Biol Ther* (2012) 12:179–92. doi:10.1517/14712598.2012.644271
59. Yadav V, Varum F, Bravo R, Furrer E, Basit AW. Gastrointestinal stability of therapeutic anti-TNF α IgG1 monoclonal antibodies. *Int J Pharm* (2016) 502:181–7. doi:10.1016/j.ijpharm.2016.02.014
60. Vandenbroucke K, De Haard H, Beirnaert E, Dreier T, Lauwereys M, Huyck L, et al. Orally administered *L. lactis* secreting an anti-TNF nanobody demonstrate efficacy in chronic colitis. *Mucosal Immunol* (2010) 3:49–56. doi:10.1038/mi.2009.116
61. Harmsen M, De Haard H. Properties, production, and applications of camelid single-domain antibody fragments. *Appl Microbiol Biotechnol* (2007) 77:13–22. doi:10.1007/s00253-007-1142-2
62. Muyldermans S. Nanobodies: natural single-domain antibodies. *Annu Rev Biochem* (2013) 82:775–97. doi:10.1146/annurev-biochem-063011-092449
63. Beirnaert E, Desmyter A, Spinelli S, Lauwereys M, Aarden L, Dreier T, et al. Bivalent Llama single-domain antibody fragments against tumor necrosis factor have picomolar potencies due to intramolecular interactions. *Front Immunol* (2017) 8:867. doi:10.3389/fimmu.2017.00867

64. Coppieters K, Dreier T, Silence K, Haard HD, Lauwereys M, Casteels P, et al. Formatted anti-tumor necrosis factor α VHH proteins derived from camelids show superior potency and targeting to inflamed joints in a murine model of collagen-induced arthritis. *Arthritis Rheumatol* (2006) 54:1856–66. doi:10.1002/art.21827
65. Kontermann RE, Brinkmann U. Bispecific antibodies. *Drug Discov Today* (2015) 20:838–47. doi:10.1016/j.drudis.2015.02.008
66. Nuñez-Prado N, Compte M, Harwood S, Álvarez-Méndez A, Lykkemark S, Sanz L, et al. The coming of age of engineered multivalent antibodies. *Drug Discov Today* (2015) 20:588–94. doi:10.1016/j.drudis.2015.02.013
67. Els Conrath K, Lauwereys M, Wyns L, Muyldermans S. Camel single-domain antibodies as modular building units in bispecific and bivalent antibody constructs. *J Biol Chem* (2001) 276:7346–50. doi:10.1074/jbc.M007734200
68. Saerens D, Ghassabeh GH, Muyldermans S. Single-domain antibodies as building blocks for novel therapeutics. *Curr Opin Pharmacol* (2008) 8:600–8. doi:10.1016/j.coph.2008.07.006
69. Smith LE, Crouch K, Cao W, Müller MR, Wu L, Steven J, et al. Characterization of the immunoglobulin repertoire of the spiny dogfish (*Squalus acanthias*). *Dev Comp Immunol* (2012) 36:665–79. doi:10.1016/j.dci.2011.10.007

Conflict of Interest Statement: OU, JS, MK, LF, AP, and CJB are affiliated with Elasmogen Limited.

frontiers in Immunology

ORIGINAL RESEARCH
published: 23 October 2017
doi: 10.3389/fimmu.2017.01361

In Vitro Maturation of a Humanized Shark VNAR Domain to Improve Its Biophysical Properties to Facilitate Clinical Development

John Steven[1], Mischa R. Müller[2], Miguel F. Carvalho[3], Obinna C. Ubah[1], Marina Kovaleva[1], Gerard Donohoe[1], Thomas Baddeley[4], Dawn Cornock[4], Kenneth Saunders[5], Andrew J. Porter[1,6] and Caroline Jane Barelle[1]*

[1] Elasmogen Ltd., Aberdeen, United Kingdom, [2] Molecular Partners AG, Zurich, Switzerland, [3] Pfizer, Aberdeen, United Kingdom, [4] Department of Chemistry, University of Aberdeen, Aberdeen, United Kingdom, [5] UCB BioPharma Sprl, Braine-l'Alleud, Belgium, [6] Department of Molecular and Cell Biology, Institute of Medical Sciences, University of Aberdeen, Aberdeen, United Kingdom

OPEN ACCESS

Edited by:
Colin Roger MacKenzie, National Research Council Canada, Canada

Reviewed by:
Serge Muyldermans, Vrije Universiteit Brussel, Belgium
Hans De Haard, argenx BVBA, Belgium
Christian Cambillau, Aix-Marseille University, France

***Correspondence:**
John Steven
john.steven@elasmogen.com

Specialty section:
This article was submitted to Vaccines and Molecular Therapeutics, a section of the journal Frontiers in Immunology

Received: 04 July 2017
Accepted: 04 October 2017
Published: 23 October 2017

Citation:
Steven J, Müller MR, Carvalho MF, Ubah OC, Kovaleva M, Donohoe G, Baddeley T, Cornock D, Saunders K, Porter AJ and Barelle CJ (2017) In Vitro Maturation of a Humanized Shark VNAR Domain to Improve Its Biophysical Properties to Facilitate Clinical Development. Front. Immunol. 8:1361. doi: 10.3389/fimmu.2017.01361

Molecular engineering to increase the percentage identity to common human immunoglobulin sequences of non-human therapeutic antibodies and scaffolds has become standard practice. This strategy is often used to reduce undesirable immunogenic responses, accelerating the clinical development of candidate domains. The first humanized shark variable domain (VNAR) was reported by Kovalenko and colleagues and used the anti-human serum albumin (HSA) domain, clone E06, as a model to construct a number of humanized versions including huE06v1.10. This study extends this work by using huE06v1.10 as a template to isolate domains with improved biophysical properties and reduced antigenicity. Random mutagenesis was conducted on huE06v1.10 followed by refinement of clones through an off-rate ranking-based selection on target antigen. Many of these next-generation binders retained high affinity for target, together with good species cross-reactivity. Lead domains were assessed for any tendency to dimerize, tolerance to N- and C-terminal fusions, affinity, stability, and relative antigenicity in human dendritic cell assays. Functionality of candidate clones was verified *in vivo* through the extension of serum half-life in a typical drug format. From these analyses the domain, BA11, exhibited negligible antigenicity, high stability and high affinity for mouse, rat, and HSA. When these attributes were combined with demonstrable functionality in a rat model of PK, the BA11 clone was established as our clinical candidate.

Keywords: VNAR, soloMER, single chain binding domain, shark, humanization, half-life extension, pharmacokinetics

INTRODUCTION

In recent years, different approaches such as complementarity-determining region (CDR) grafting, framework-homology-based, germline-homology-based re-surfacing, and epitope depletion have been adopted to reduce potential immunogenic responses from non-human therapeutic biologics (1–5). According to Reichert (6), of the 52 antibodies in late stage clinical trials in Europe and the

Abbreviations: IgNAR, immunoglobulin new antigen receptor; VNAR, variable domain of shark new antigen receptor; CDR, complementarity-determining region; FW, framework HV, hypervariable region; PK, pharmacokinetics; HSA, human serum albumin.

US, the majority, 43, are humanized or are fully human exemplifying the success and clinical validation of these processes. Furthermore, the six monoclonal antibodies (mAbs) approved for use in the European Union or the US in 2016, three were humanized, two were fully human, and one was a chimeric IgG1 with a further 10 human or humanized antibodies in review (6). Of those mAbs approved for therapeutic use, three are the blockbuster drugs for oncological indications, Rituximab (Rituxan), Trastuzumab (Herceptin), and Bevacizumab (Avastin), each of which generated in excess of $6 billion in revenues in 2015 (7–9).

The development of next-generation therapeutic biologics has been gaining pace with over 50 products based on both immunoglobulin and non-immunoglobulin scaffolds at varying stages of development (6, 10). Much of this development reflects the drive to overcome the limitations of classical antibodies such as their complex structure, and large size resulting in high cost of manufacture from an economic perspective and limited tissue penetration from a biological perspective (11–14). The focus of this study was the improvement of the biophysical properties of a humanized VNAR, which is the variable binding antigen specific domain derived from the new immunoglobulin antigen receptor or IgNAR (15). As IgNAR forms an integral part of the adaptive immune system of sharks, high-affinity, highly selective IgNARs can be raised through immunization and target-specific VNAR domains selected through classic phage display technology (16–18). Although demonstrating the target-specific attributes of antibodies, VNARs do not originate from an immunoglobulin lineage but are postulated to have evolved from cell surface members of the Ig superfamily such as ICAMs and VCAMs (19–21). Interestingly, their sequence identity is closer to human light chain frameworks than heavy chains. As with other non-human sources of antibodies, this reduced relatedness to human mAbs is the driving force behind developing a humanization strategy for the development of these domains for clinical use. Elasmogen Ltd. has a proven, patented methodology for the humanization of VNAR domains, the endpoint of which are therapeutic clinical candidates known as soloMERs™ (22).

The subject of this work, hE06v1.10, is a humanized version of an anti-HSA clone called E06 that was originally isolated from an immunized dogfish (18, 23). E06 can be fused with many different therapeutic partners including but not limited to, VNAR domains, scFvs, peptides, and proteins to increase their systemic half-life and subsequent therapeutic window (23). With broad utility across multiple indications, the biophysical properties of the final humanized version of E06 were critical to negate any downstream production issues with aggregation or potential immunogenicity. The first steps toward humanization of VNAR domains were conducted by Kovalenko et al. (24) using the anti-hen egg (HEL) domain, 5A7 (16), as a model template. Given the evolutionary distance between VNARs and true IgGs, the foundation of the approach was based primarily on structural similarity to human framework scaffolds. Using this strategy, DPK9 was selected. The underlying methodology used to successfully humanize 5A7 was then transposed onto the anti-human serum albumin (HSA) binding VNAR domain, E06 resulting in the construction of v1.10. A second version of humanized E06, v2.4, was designed based on human Kappa germline framework DPK24.

This work has studied v1.10 and v2.4 in more depth and has revealed a propensity for the v1.10 domains to dimerize and in the case of v2.4 to bind to HSA with lower affinity, questioning their applicability for clinical development. To overcome the unfavorable characteristics of v1.10 and v2.4, these were used as templates for mutagenesis to select better performing humanized versions of these proteins.

MATERIALS AND METHODS

Random Mutagenesis of E06v1.10 and E06v2.4

E06v1.10 and E06v2.4 sequences were cloned into the phage display vector pWRIL-9 and tested as periprep extracts for binding to cognate target and relevant controls. This vector is comparable to pWRIL-1 (25) with the c-Myc tag replaced by an HA tag, and the leader sequence is derived from pelB. Sequences were mutagenized by error-prone PCR to deliver up to 9 substitutions/VNAR sequence using a GeneMorph II random mutagenesis kit (Agilent Technologies, Santa Clara, CA, USA). Libraries were cloned into pWRIL-9 and transformed into TG1 electrocompetent cells (Lucigen, Middleton, WI, USA). Library diversity was analyzed by sequencing over 100 clones from each repertoire.

Selection from Libraries by Phage Display

Libraries were rescued and selected twice using Nunc Maxisorp immunotubes as previously described (26). For the first round of panning, tubes were washed five times with PBS containing 0.1% Tween 20 (PBS-T) and five times with PBS; for pan 2, the number of washes with and without Tween 20 was doubled. Following each round of panning, two 96-well plates of individual colonies were picked with a QPix2 XT (Genetix, San Jose, CA, USA) and grown for periplasmic protein extraction. Binding to HSA (and HEL control) was evaluated by ELISA using 50% of the crude periplasmic protein extract (27). VNARs were detected via their HA tag using a high-affinity mAb HRP conjugate (clone 3F10; Roche, Basel, Switzerland). All samples were processed with a Perkin Elmer MiniTrak robotic liquid handling system (Waltham, MA, USA).

Reformatting to Eukaryotic Expression Vector and Analysis of Output by ELISA

Unique clones showing OD_{450} by periprep ELISA at least 25% higher than the readings obtained from parental huE06v1.10 or v2.4 were selected for batch conversion into the proprietary mammalian expression vector pSMED2. Equal amounts of pWRIL-9 plasmid DNA from clones were pooled, and VNAR sequences were amplified by PCR with primers inserting *Bss*HII and *Eco*RI at the 5′ and 3′ ends, respectively. After cloning and transformation of *Escherichia coli* TG1 electrocompetent cells, a fourfold over-representation of the starting number of clones was grown in 96-deepwell culture plates (Greiner Bio One, Frickenhausen, Germany) and plasmid DNA purified using a QIAprep 96 Turbo BioRobot Kit in a BioRobot 8000 (Qiagen, Hilden, Germany). In a 96-well plate format, each clone was expressed transiently in 200 µL of HEK293 cells previously adjusted to a density of 10^6/mL.

Each 200 µL culture was transfected with 200 ng of plasmid DNA using lipofectamine (Invitrogen, Carlsbad, CA, USA) and grown at 37°C and 8% CO_2 while shaking at 250 rpm to maintain cells in suspension. After 24 h, cultures were supplemented with tryptone to a final concentration of 0.5% and expression continued for 6 days. Post-expression media samples from HEK 293 transfections were tested for binding to HSA and HEL by ELISA. Detection was achieved via an anti-6-His HRP conjugate (ab1187; Abcam, Cambridge, UK).

Off-Rate Selection Screening

Samples of the "best-performing" media from the small scale HEK293 transfections were subject to kinetic analysis using a T200 BIAcore instrument for off-rate ranking (28) (GE Healthcare Life Sciences, Little Chalfont, UK). For off-rate screening samples were diluted 1:5, 0.2 µm-filtered, then filtrates run over a research-grade carboxy-methyl-dextran chip (CM5) onto which HSA was immobilized using standard amine coupling chemistry. The association phase for all samples was 2 min, and the dissociation was monitored for 3 min at a flow rate of 100 µL/min, followed by two 10 µL injections of glycine pH 1.5 at a flow rate of 100 µL/min. All binding experiments were performed at 25°C in HBS/EP buffer. Analysis of the resultant sensorgrams made use of the 1:1 global Langmuir binding model. Those samples showing the slowest dissociation rates were then selected for larger-scale protein production and DNA sequences of VNARs determined.

ELISA Assay and EC50 Determination

Rat, mouse, and HSAs used in ELISA-binding assays were from Sigma-Aldrich. For direct ELISA formats Nunc Maxisorp 96-well plates were coated at 1 µg/mL antigen in PBS and then blocked with 4% non-fat milk in PBS. Purified 6-his-tagged control and humanized VNAR proteins in PBS were diluted 1/3 into wells and double-diluted further across the plate. After incubation for 1 h, plates were washed three times with 0.05% Tween 20 in PBS. The detection of antigen bound VNARs was achieved by incubation with an anti-6-His HRP mAb for 1 h or where appropriate with an anti HA tag mAb HRP conjugate (clone 3F10; Roche) and developed by adding TMB substrate. When fully developed, the reactions were halted by the addition of 1 M H_2SO_4 absorbance measured at 450 nM. Data were processed using SigmaPlot 9.

Affinity Measurements

Affinities of selected clones were determined on a T200 BIAcore surface plasmon resonance instrument essentially as described previously (24). As well as measuring affinity for HSA, the mutated anti-HSA VNARs were also assessed for binding to mouse serum albumin (MSA) and rat serum albumin (RSA). A CM5 chip was prepared in which the first flow cell was used as a reference to correct for bulk refractive index, matrix effects, and non-specific binding. Approximately 300 RU of HSA was immobilized onto flow cell 2, 350 RU of MSA was immobilized onto flow cell 3, and 600 RU of RSA onto flow cell 4. Prior to immobilization, the serum albumins were made up in 10 mM sodium acetate buffer (pH 4.5) and post-coupling the remaining activated groups was blocked with 1.0 M ethanolamine-HCl pH 8.5. For affinity measurements, purified anti-HSA VNAR monomers, dimers, and trimers were diluted to 1.56–100 nM in HBS/EP buffer and injected over the chip as above. Analysis of the resultant sensorgrams was performed using the 1:1 global Langmuir binding model fit analysis (BIAcore Evaluation Software).

Protein Expression and Purification

Expression of VNAR proteins for periprep screening and phage ELISA was carried out as described (29). For small-scale transient expression and off-rate screening, mutated VNAR genes were cloned into pSMED2 vector containing a CMV promoter and a C-terminal 6-His tag. Following off-rate screening plasmid preparations of selected clones were scaled up and used for 1 L PEI-mediated transfection and transient expression in HEK293 host cells (30, 31) using serum free FreeStyle™ 293 media (Invitrogen). Purification of expressed protein was achieved by immobilized metal chelate chromatography using Ni^{2+} charged resin followed by cation exchange chromatography with buffer exchange as appropriate between steps. Final protein samples were buffer exchanged to PBS and stored frozen at −20°C. If required, proteins were then subjected to a final polishing step by preparative size-exclusion chromatography using a Superdex 200 26/60 size-exclusion column equilibrated with PBS. Eluted peaks from this chromatography were pooled, then concentrated using Amicon Ultra filtration units. Protein concentrations were determined by UV spectroscopy. Expression levels of VNAR proteins were generally in the region of 0.5–3 mg/L, and electrophoretic analysis of protein samples was performed on 12% NuPAGE BisTris gels using a MOPS buffer system (Invitrogen). Analytical size-exclusion chromatography was performed using an Agilent 1200 series HPLC system and ZORBAX GF 250 9.4 mm × 250 mm 4 µm column or TSK gel G3000PW 7.5 mm × 30 mm column equilibrated with phosphate-buffered saline at pH 7.4 with instrument set up and run parameters adjusted as required for each run.

Cloning of VNAR Dimeric and Trimeric Constructs

VNAR E06 and lead humanized clones BA11, BB11, and BB10 were selected as the backbone of several dimeric and trimeric fusion protein constructs. Dimers were assembled using a standard PCR overlapping extension techniques joining the albumin binding domain, via a $(GGGGS)_4$GAHS flexible linker to the carboxyl or amino terminal end of a control and naive VNAR domain known as 2V. The trimeric constructs were made by flanking the albumin binding domain with the same naive 2V domain at both terminal ends (23). Constructs were cloned into pSMED2, plasmid preparation scaled up and the resultant DNA used to transiently express protein in HEK 293 cells (30, 31).

Dendritic Cell–T-Cell (DC–T) Assay

A DC–T proliferation assay was used to identify the presence or absence of possible T-cell epitopes within the wild-type E06 and humanized variants 2G, BA11, BB11 and BB10 (performed at ProImmune Ltd., UK using ProImmune's REVEAL® Immunogenicity System DC–T cell assay). For this study, test proteins and controls were incubated with $CD8^+$ T-cell-depleted

peripheral blood mononuclear cells (PBMCs) prepared for 7 days, from a panel of 20 different healthy human donors. Each PBMC sample was HLA-typed and donors were selected (by DRB1 allotyping) to approximately represent MHC class II allele frequency distributions across the global population.

In brief, adherent donor PBMCs were cultured with appropriate growth factors to generate monocyte-derived DCs. DCs were then loaded with either test or control antigen protein or left untreated. Test proteins were loaded at a final concentration of ~0.34 μM (5 μg/mL). Mature antigen-loaded DCs were then co-cultured (at a set ratio) with autologous CFSE-labeled T cells in multi-well plates. Each test condition was set up in octuplet and incubated for 7 days. Positive control antigens used for this assay were Tuberculin purified protein derivative (PPD from *Mycobacterium*) at a final assay concentration of 0.2–0.4 μM (~5 μg/mL) (70–100% of donors are expected to react to this protein as a result of previous vaccination, through a memory immune response). A second control antigen used, keyhole limpet hemocyanin (KLH) is a known potent naive protein immunogen. This was used at ~0.64 μM (0.25 mg/mL) in the assay (up to 70% of donor samples might be expected to react to this protein, driven by a naive immune response). At the end of the incubation period, cell samples were stained with anti-CD4 antibody, then washed and fixed for flow cytometric analysis. Proliferation was determined by measuring a decrease in CFSE intensity.

Pharmacokinetic (PK) Studies

Three groups of four male Sprague Dawley rats received a single intravenous (bolus) administration of 2V-E06-2V, 2V-BA11-2V, or 2V-BB11-2V dosing at 1 mg/kg. Blood samples (0.3 mL) were collected into tubes containing Lithium Heparin as an anticoagulant before dosing and at the following times: 30 min and 4, 12, 24, 48, 84, 96 120, and 144 h. These were placed on ice and plasma collected from each after centrifugation at 3,000 × *g*, at 4°C for 10 min. Prior to analysis plasma samples were stored at −80°C.

LC–MS/MS Methodology for the Bioanalysis of PK Samples

A quantitative LC–MS/MS method had been previously developed to specifically measure concentrations of 2V-E06 in rat plasma (23). In summary, the method utilizes the C-terminal 6x His tag present on these proteins molecules to provide sample enrichment using a magnetic Ni-NTA bead capture step. Following analyte enrichment and tryptic digestion of the sample, targeted LC–MS/MS is used to quantify specific signature peptides in all parts of 2V and the humanized E06 domains. Signature peptides within each partner were identified by *in silico* tryptic digestion. For E06 and humanized variants BA11 and BB11, the signature peptide EQISISGR was selected and AQSLAISTR for 2V. Control signature peptides and a labeled internal standard peptide EQI-[U13C3, 15N-Ser]-ISGRAQS-[U13C6, 15N-Leu]-AISTRHHHHHH were synthesized (by Cambridge Research Biochemicals, Billingham, UK). Assessment of peptides allowed the PK determination of the VNARs (serum half-life) as well as monitoring of $(GGGGS)_4$GAHS linker stability.

Plasma Pull Down and Trypsin Digestion

VNAR 2V-E06-2V protein was diluted into heparinized rat plasma at 30, 20, 10, 5, 3, 1, 0.3, 0.2, and 0.01 μg/mL. A total of 10 μL of each dilution was added to 40 μL of 0.1 M phosphate buffer pH 8 followed by 50 μL of 6 M guanidine hydrochloride containing 1 μg/mL of the heavy isotope labeled internal standard peptide EQI-[U13C3,15N-Ser]-ISGRAQS-[U13C6,15N-Leu]-AISTRHHHHHH. After mixing, these samples were each reduced and alkylated as previously described (23). For the PK sampling time points, 10 μL of plasma was added to 40 μL of 0.1 M phosphate buffer pH 8. The samples were then diluted by the addition of 100 μL 100 mM phosphate, pH 8, 0.1% CHAPS in preparation for sample enrichment. Sample enrichment and magnetic bead processing was performed in 1.5 mL capped tubes and magnetic capture blocks. Twenty-five microliters Ni^{2+}-NTA magnetic beads plus 75 μL 100 mM phosphate, pH 8, 0.1% CHAPS were added to each sample. After mixing, the magnetic beads were trapped by magnetic block and the fluid containing the unbound proteins was removed. The beads were washed three times with 500 μL 100 mM phosphate, pH 8, 0.1% CHAPS with magnetic immobilization of beads between each wash before a final 500 μL wash with 100 mM phosphate, pH 8, 0.1% CHAPS containing 20 mM imidazole. Bound proteins were eluted in 100 μL of 0.5 M Imidazole, 10 mM $CaCl_2$, 50 mM Tris HCl, pH 8. Eluted protein samples were then trypsin digested by addition of 20 μL of proteomics grade trypsin (made up at 20 μg/mL in 10 mM $CaCl_2$, 50 mM Tris HCl, pH 8) followed by incubation at 37°C for 18 h prior to LC–MS/MS analysis.

LC–MS/MS Analysis

The samples were loaded into the auto-sampler module of a Waters Acquity UPLC (chilled at 6°C) and 5 μL of the extracted samples injected onto the LC–MS/MS system. The native and stable-labeled signature peptides were separated on Acquity UPLC BEH C18 1.7 μm 2.1 mm × 50 mm column equilibrated with solvent A water/acetonitrile/formic acid (95/5/0.1) and eluted with a stepped gradient as follows. At a flow rate of 0.5 mL/min, the column was washed with buffer A for 4 min, then from 4 to 8 min buffer was changed by gradient mixing to 20% solvent B + 100% acetonitrile + 0.1% formic acid. From 8 to 8.5 min solvent B increased to 55% then back to 45% solvent B at 9 min and back to 100% solvent A at 10 min in preparation for the next sample injection. Chromatography runs were carried out at ambient temperature, and under these conditions, the retention time for the analytical and reference peptides was 6.11 min for EQISISGR and 6.27 minutes for AQSLAISTR (±0.5 min). The peptide analytes EQISISGR and AQSLAISTR and control internal standard labeled peptides were detected by atmospheric pressure electrospray ionization MS/MS using a Xevo TQS MS/MS detector. The analytical column eluate was delivered into the source operated at an IonSpray voltage of 3,300 eV with settings as follows: cone (V) 25, source offset (V) 45, source temperature 150°C, desolvation temperature (600°C), cone gas flow (L/h) 0, desolvation gas flow (mL/min) 0, collision gas flow (mL/min) 0.15, and nebulizer gas flow (Bar) 7.00.

For the analytes and control labeled internal standard peptides, MRM transitions were 445.2–519.3 for EQISISGR, 473.8–747.4

for AQSLAISTR, 447.2–523.3 for EQISISGR-IS, and 477.3–754.4 for AQSLAISTR-IS. In all experimental runs, a system suitability test was performed by the injection of a 50 µg/mL AQSLAISTR and EQISISGR mixed standard in buffer. The ion chromatograms were quantified by reference to standard curves spiked into fresh control plasma and analyzed over the range 0.01–30 µg/mL and a calibration curve constructed by plotting the peak area ratio of the calibration standards *vs.* the concentration of peptide fragments in a control matrix and determine the linear regression parameters of the curve, using a $1/x^2$ weighting factor. The concentration of peptide fragments in the quality control and test samples were determined by interpolation of the peak area ratios from the calibration curve.

Stability Assay

The stability of VNAR E06 and humanized E06 BA11 was assessed after exposure to extremes of temperature and pH. Samples of E06 and humanized E06 BA11 proteins were prepared at 10 µg/mL working concentration and placed on a 100°C preheated block. Samples were withdrawn from experimental conditions at 0, 5, 10, 20, 30, 40, 50, and 60 min time points and transferred into wells containing appropriate volume of PBS pH 7.4 to obtain a final concentration of 0.5 µg/mL. Boiled samples recovered in PBS were kept on ice for 1 h before assessing VNAR E06 and humanized VNAR BA11 in an has-binding ELISA. In a similar assay the pH stability of VNAR domains was assessed. Samples were prepared and incubated at a working concentration of 10 µg/mL in a final volume of 50 µL at the designated pH value. For acidic conditions, pHs 1.5, 3, and 5.5 protein samples in PBS pH 7.4 were adjusted using 1 M HCl or 0.1 M citric acid and for basic pHs 8.5, 10 and 11 samples in PBS were titrated to required pH value using borax buffer or 1 M NaOH. Samples were incubated at room temperature, and aliquots withdrawn at stipulated time points and neutralized in PBS pH 7.4 to a final concentration of 0.5 µg/mL. Samples were incubated at designated pH values for up to 28 days, and the HSA-binding activity of the treated samples was determined using ELISA.

RESULTS

Affinity Maturation of Humanized VNARs by Random Mutagenesis, Library Screening and Selection

Analysis of E06 clones humanized (hE06) by targeted insertion of residues and sequences from human V Kappa germ lines led to two "parental" molecules (v1.10 and v2.4 **Figure 1A**) with specific but lower binding affinities and undesirable biophysical properties (**Figures 1** and **2** respectively). In order to make improvements to these two humanized variants, two randomly mutated libraries were constructed by error-prone PCR using DNA from these clones as the initial template (v1.10 and v2.4 **Figure 1A**, based on DPK9 and DPK24 human Kappa germline sequences, respectively). To ensure full coverage of the hE06 sequences and to reap any potential benefits of multiple substitutions in the protein sequences, conditions were optimized to deliver a maximum of nine nucleotide mutations per VNAR. Phagemid libraries of ~5×10^7 clones for both hE06v1.10 and v2.4 were constructed

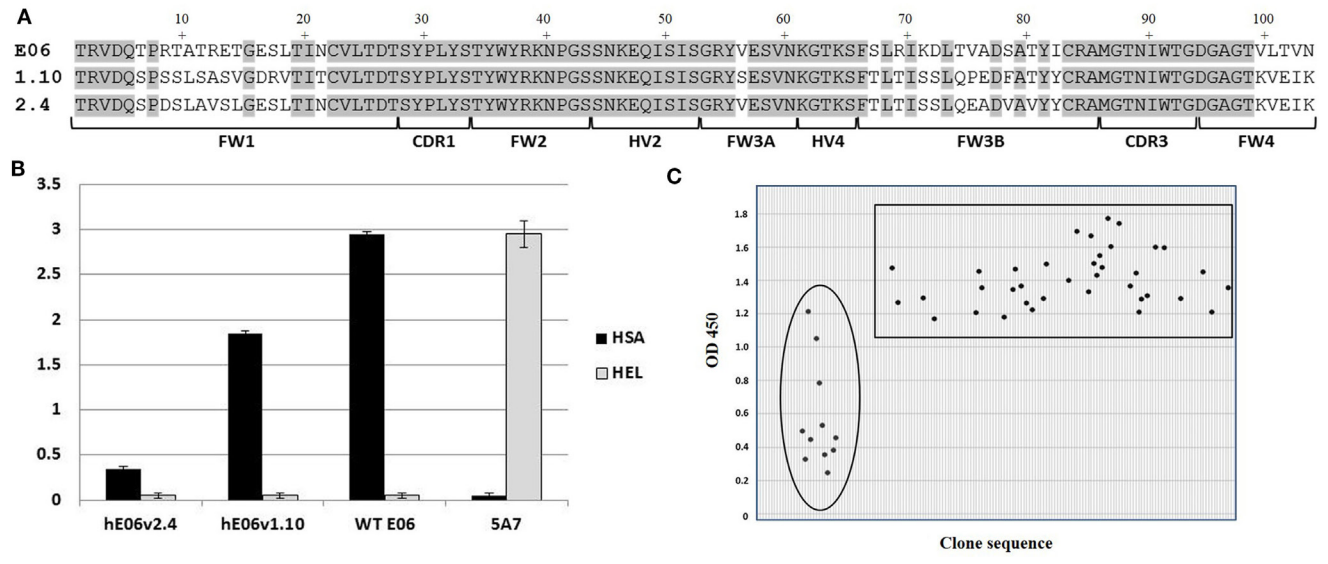

FIGURE 1 | Mutated library design, QC and outputs. **(A)** Amino acid sequence alignment of humanized E06 v1.10 and E06 v2.4 with wild-type E06. FW is framework region; CDR is complementarity-determining region; HV is hypervariable region. **(B)** Phage-binding ELISA to human serum albumin (HSA) and hen egg white lysozyme (HEL)-coated plates. Phage displaying VNAR domains E06, humanized E06 v1.10 and humanized E06 v2.4, and a negative control clone 5A7. Control 5A7 is a hen HEL-binding VNAR. **(C)** Selection of mutated clones based on periprep ELISA binding to HSA. A total of 37 humanized E06v1.10 (boxed) and 12 humanized E06 v2.4 clones (circled) clones were identified for further studies. Criterion for selection was an OD450 (after 5 min development time) of at least 100% of the signal generated by parental humanized E06 v1.10 and E06 v2.4 controls assayed under the same conditions.

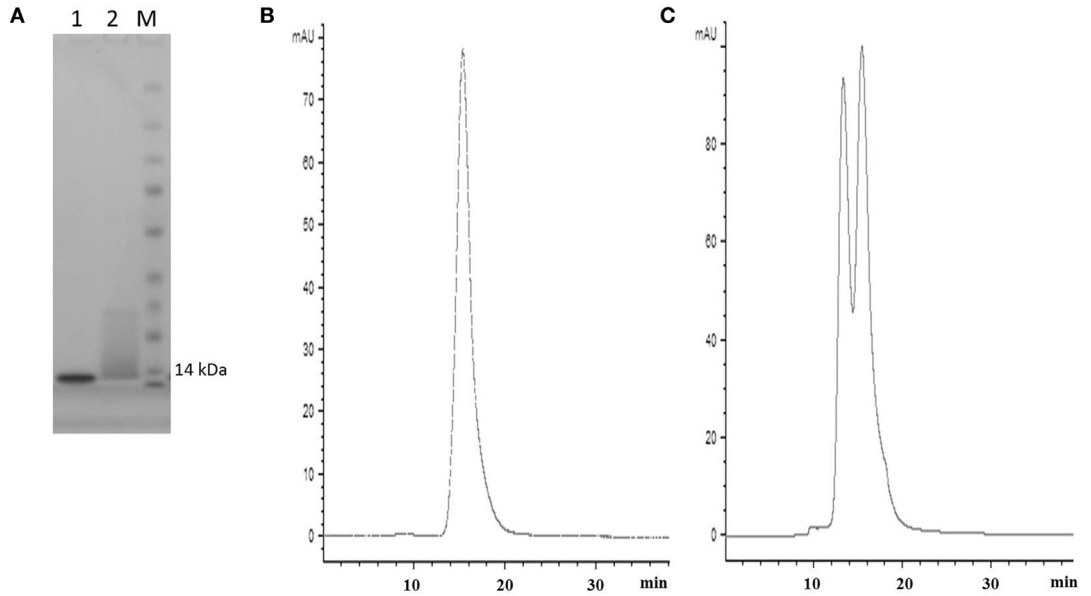

FIGURE 2 | SDS PAGE and SEC profiles of native E06 and humanized E06 v1.10. **(A)** SDS PAGE and Coomassie blue staining of 2 µg of wild-type E06 and E06 humanized v1.10 proteins. Lane 1, E06; Lane 2, E06 v1.10; Lane M, molecular weight markers. **(B)** Analytical SEC chromatogram of wild-type E06 protein. **(C)** Analytical SEC chromatogram of humanized E06 v1.10 protein.

and diversity determined by randomly selecting and sequencing of over 100 individual clones from each library. Results indicated a good coverage of mutations along the full sequence length, with an overall mutation rate of ~90% (90/103 and 94/103 clones had a changed amino acid residue, for hE06v1.10 and v2.4, libraries respectively).

In order to recover molecules with improved binding properties two rounds of phage display selection were performed using HSA as a target. Approximately 200 individual clones were randomly picked from each library and round of panning (total of 800 clones) and tested for binding by ELISA using VNAR protein derived from crude periplasmic extracts. Additional control screening was performed using non target antigens (HEL and blocking agent) to confirm that there was no overall gross VNAR misfolding leading to polyreactivity or non-specific stickiness. An initial examination of the sequences of the enriched clones did not offer up a clear pattern or any obvious positional bias but placed the mutations randomly throughout the parental templates. In addition, parental hE06v1.10 was recovered a total of 53 times from pan 1 and 80 times from pan 2, while hE06v2.4 was observed only once in pan 2 and did not occur in the pan 1 sequences at all. The remaining "new" clones were subjected to further analysis including their expressability and any propensity to form dimers (results not shown). **Figure 1C** shows the isolation of a final panel of mutated clones based on periprep ELISA binding from which 37 humanized E06v1.10 (boxed) and 12 humanized E06v2.4 clones (circled) were selected for further characterization. These 49 clones were transferred to a eukaryotic expression vector and small scale transient expressions performed in HEK 293 cells.

Protein Expression, Assessment, and Characterization

Media samples from HEK 293 expressions were screened for specificity using an HSA-binding ELISA and off-rate ranking was performed on the same samples using a T200 BIAcore surface plasmon resonance instrument. Clones that showed a slow-off rate nearing that of parental E06 and were positive by ELISA, giving signals similar to the parental hE06v1.10 or v2.4 clones, and were selected for further study (**Figure 3A**). The sequences of these selected clones were determined and those from v1.10 and v2.4 derived libraries are shown in **Figures 3B,C,** respectively. The positions of the mutations identified, even in this focused sub-panel of lead clones, were typically one or two amino acid mutations randomly located along the length of the VNAR proteins (**Figures 3B,C**).

Transient expression of these 15 lead clones was scaled up in HEK 293 cells to produce proteins for further study. After scale up and growth in serum free media and post-purification, expression levels of between 3 and 10 mg/L were obtained for the humanized monomeric, dimeric, and trimeric constructs. Purified protein samples were quantified by UV spectroscopy and concentrations determined. For the best expressing clones, together with suitable controls (E06 wild-type, v1.10, AH7, AD4, AG11, BA11, BB11, BB10, and v2.4 derived clones 1H, 2G, 5F, 8C, and 8D), ranking of the purified proteins was determined by ELISA (**Figures 4A,B**) and EC_{50} values calculated using SigmaPlot 9.0 (**Figures 4C,D**). Based on expression levels and EC_{50} values, a final panel four of clones was selected. From the mutated v1.10 library BB10, BA11, and BB11 and from the v2.4 derived library, clone 2G was characterized in more detail.

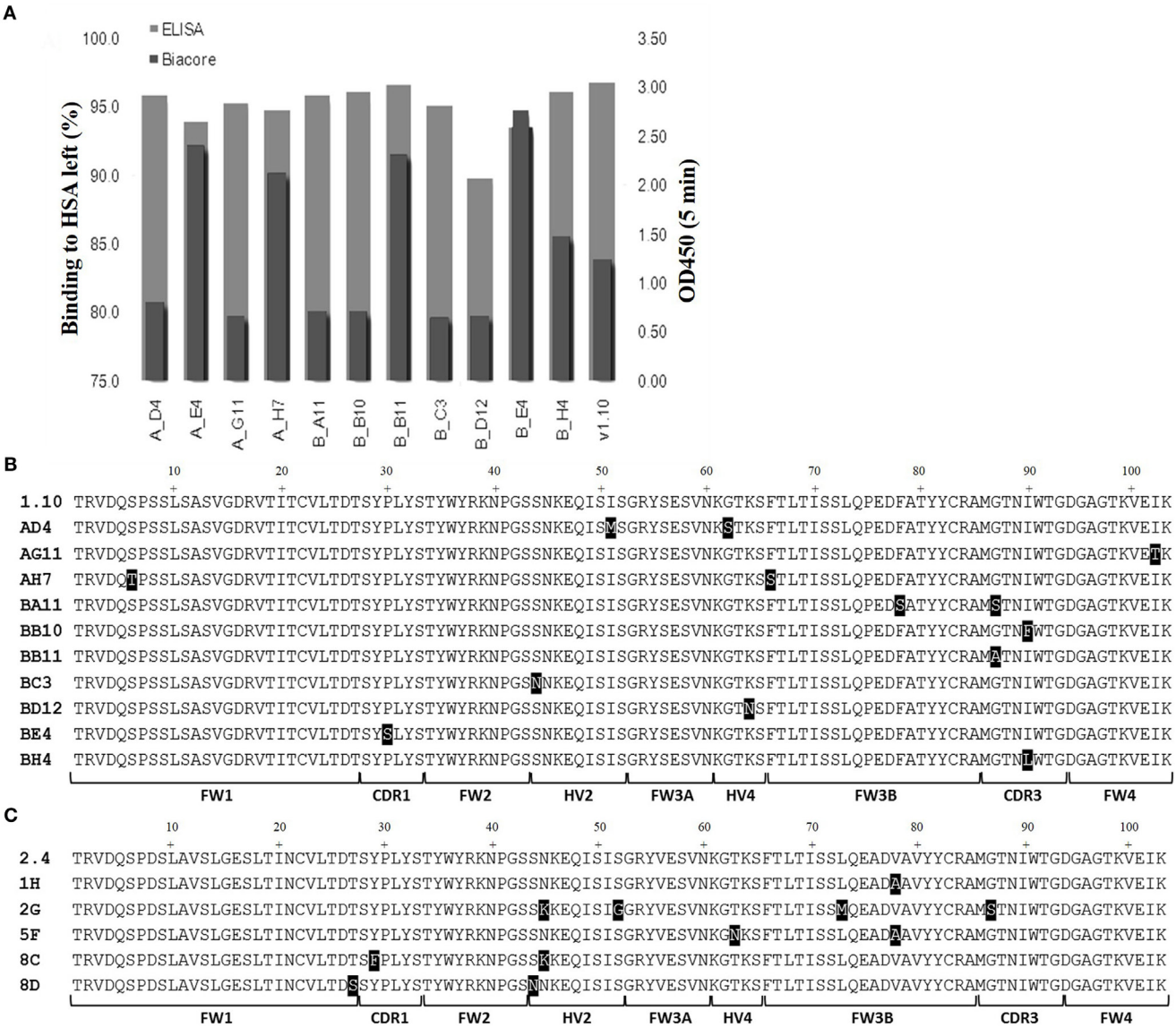

FIGURE 3 | ELISA and off-rate screening analysis of related and humanized mutant. The intensity of binding of media samples from small scale transient expressions in HEK 293 cells were screened and compared by kinetic off-rate analysis, using a T200 BIAcore instrument, and HSA-binding ELISA. **(A)** Selected lead clones derived from v1.10 library (data for v2.4 selection not shown). Off-rate as a percentage of the parental E06 off-rate plotted together with ELISA binding. **(B)** The amino acid sequence of selected clones from the v1.10 mutagenesis library. **(C)** The amino acid sequence of selected clones from v2.4 mutagenesis library. Mutated residues differing from parental sequence are highlighted. See **Figure 1** legend for list of abbreviations.

SDS PAGE and Analytical SEC of Final Four Purified Leads

Post-purification proteins were analyzed by SDS PAGE and analytical SEC. On SDS PAGE, the selected clones ran as a single band (**Figure 5A**), with an expected molecular mass of 14 kDa. Analytical size-exclusion chromatography of the purified monomeric BB10, BA11, BB11, 2G, and E06 control appeared mainly as single peaks showing minimal signs of dimerization (**Figure 5B**) unlike the parental clone v1.10 (**Figure 2C**). The purified BB11 monomer showed a small peak eluting from the column ahead the of the main monomeric protein peak. It is unclear if this is dimerized BB11 protein or low level higher molecular weight contaminating protein. The remaining humanized VNAR monomers eluted as single peaks.

Antigenicity Assessment of E06 and Four Lead Humanized VNAR Clones

Immunogenicity of lead clones was assessed in a T-cell proliferation assay using ProImmune Ltd REVEAL® Immunogenicity System DC–T cell assay. The immunogenicity of each protein was determined by measuring the extent of T cells proliferation and by determining the number of immune-responsive individual

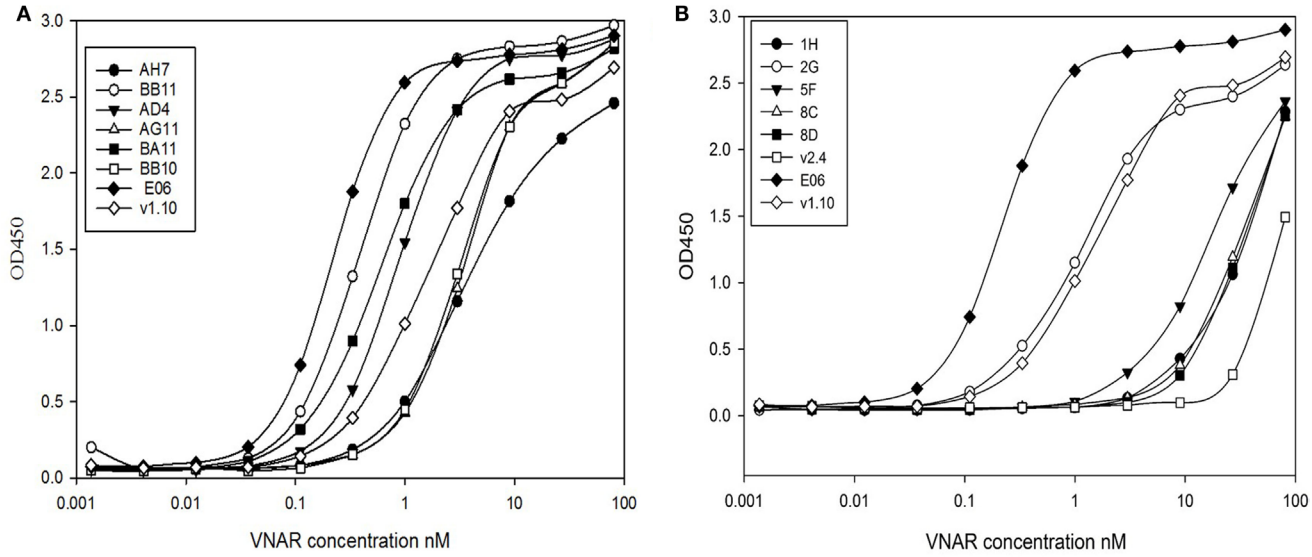

C

CLONE	EC_{50} nM
E06	0.227
v1.10	1.65
AH7	3.76
AD4	0.906
AG11	3.58
BA11	0.615
BB10	3.32
BB11	0.396

D

CLONE	EC_{50} nM
v2.4	171
1H	82
2G	1.255
5F	18
8C	35.6
8D	35

FIGURE 4 | ELISA and EC_{50} determination of lead v1.10 and v2.4 humanized E06 clones. Purified E06 His-tagged VNAR protein and selected lead clones were added to wells of an human serum albumin-coated plate at a concentration of 1 μg/mL and serially diluted threefold across the plate. Four parameter logistic curve, adjustments and EC_{50} calculations were performed with SigmaPlot 9.0. **(A)** Binding curves of selected lead clones derived from mutagenesis of the v1.10 backbone. **(B)** Binding curves of selected lead clones derived from mutagenesis of the v2.4 backbone. **(C)** EC_{50} values of lead v1.10 derived clones. **(D)** EC_{50} values of lead v2.4 derived clones. With the exception of E06 v2.4-2G, clones obtained by mutagenesis of E06 v1.10 performed better with several selected clones showing single digit nanomolar or lower EC_{50} values.

donors treated with test proteins. Stimulation above background was determined using flow cytometric evaluation to count unlabeled, therefore proliferating T cells in each of the eight replicates for each sample. These values were then used to calculate percentage stimulation above background. Thus, the strength and frequency of response to each test sample could be used to calculate a response index (RI) value for each test protein (E06, BB10, BA11, BB11, and 2G) and control antigens (**Figures 6B,C**). Both the wild-type E06 and humanized variants had a very low RI compared to positive controls. Of the four humanized leads, clone 2G had the highest response. Clone BB11 gave a response, which was slightly higher than wild-type E06 with clones BA11 and BB10 having a slightly lower RI. These RI values were considered suitable for further development and similar to those of other therapeutic antibodies currently in the clinic and assayed using an identical protocol. Campath, Avastin, Humira, and Remicade had RI values of 0.26, 0.21, 0.14, and 0.49, respectively, and control RI values of 4 for KLH and 27.5 for PPD.

Based on this antigenicity assessment, clone 2G was not chosen for further study while clones BB10, BA11 BB11, and wild-type E06 were reformatted as dimer or trimer genetic fusions and expressed with a second control VNAR called 2V. Originally isolated from the dogfish *Squalus acanthias*, 2V is part of a sequence database from this species and has no known target, making it an ideal control for these and other studies (23). When reformatted and expressed as amino or carboxyl terminal end dimeric fusion proteins (e.g., 2V-hE06), samples ran as single non-aggregated peaks when analyzed by analytical SEC (**Figure 7A**) with the exception of samples BB11-2V and 2V-BB10 that showed a minor peak eluting before the larger main peak, which may indicate the presence of some dimer in these samples. When the parental clone v1.10 was reformatted as a dimer with 2V, the resultant v1.10-2V protein retained its propensity to run as two peaks (**Figure 7A**). Formatting to produce the trimeric versions, 2V-E06-2V, 2V-BA11-2V, and 2V-BB10-2V also resulted in proteins which after purification

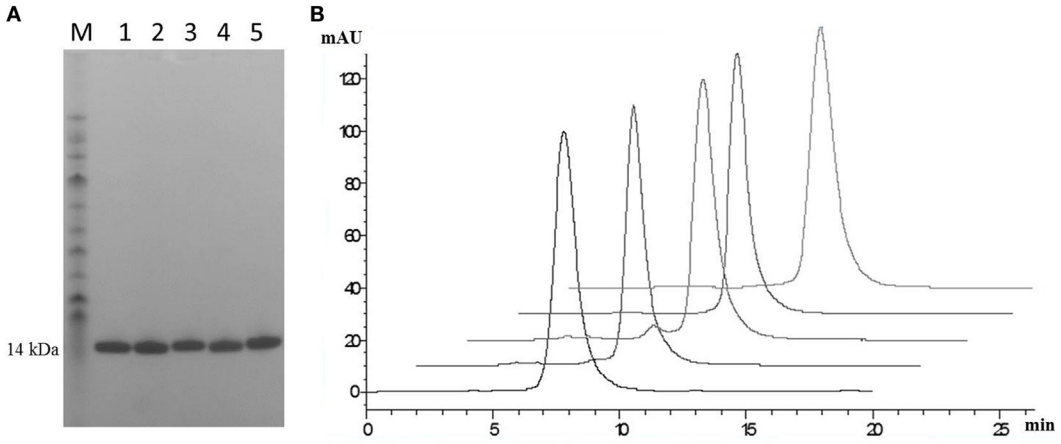

FIGURE 5 | SDS PAGE and analytical SEC analysis of purified lead humanized E06 proteins. **(A)** Samples of purified humanized VNAR protein analyzed by SDS PAGE. Lane M, molecular weight markers; Lane 1, BB10; Lane 2, BA11; Lane 3, BB11; Lane 4, E06 and Lane 5, 2G. **(B)** Analytical SEC profiles of purified lead monomer proteins overlaid and offset to aid comparisons. Profiles are from left to right: BB10, BA11, BB11, E06, and 2G. Data from both analytical techniques confirms that proteins tested appear to be monomeric in nature.

ran predominantly as single peaks (**Figure 7B**) with BB11 containing trimeric construct, 2V-BB11-2V, showing a minor peak which eluted from the SEC column before the main peak. SDS PAGE analysis of monomer BA11, dimers 2V-BA11 and BA11-2V, and trimer 2V-BA11-2V confirmed that all migrated as single bands with significantly improved biophysical properties (**Figure 7C**).

Affinity Measurements

Affinity measurements of purified anti-HSA VNAR and humanized VNAR monomers E06, 2G, BA11, BB11, and BB10 were determined by surface plasmon resonance using a T200 BIAcore instrument. The affinities for HSA, presented as a kinetic distribution plot (6A), were in the range of 0.58–24.9 nM. Affinities for rat and MSAs were in the range of 2.74–130 and 2.01–99 nM, respectively (**Figure 6A**). For all species tested, wild-type E06 had the highest affinity. The loss of binding of clone BB10 to rodent albumin could be attributed to the mutation in CDR3 and was therefore not taken forward as a candidate for further study. The eight dimeric constructs (BB11-2V, 2V-BB11, BB10-2V, 2V-BB10, BA11-2V, 2V-BA11, E06-2V, and 2V-E06) and four trimeric constructs (2V-BB11-2V, 2V-E06-2V, 2V-BA11-2V, and 2V-BB10-2V) bound HSA with high affinity including low picomolar values, 0.08–8.41 nM. In addition, binding and affinities for rat, mouse, and cynomolgus macaque albumins confirmed the utility of BB11 and BA11 as possible candidates for further clinical development (**Figure 8**).

Rat PK Profile and Half-Life Determination of Candidate Clones

A previous PK study, in three animal species, demonstrated the ability of an albumin binding wild-type VNAR domain, E06, to extend the half-life of other proteins when administered as a molecular fusion (23). The present study looked at the ability of the humanized versions of E06, BB11, and BA11 to extend the circulating half-life of fusion proteins. Trimeric fusion proteins, 2V-BB11-2V, 2V-E06-2V, and 2V-BA11-2V, were expressed, purified, and characterized (**Figures 6** and **8**) prior to administration to rats at 1 mg/kg body weight. For this study, the sensitive and quantitative LC–MS techniques developed previously (23) were used to detect the presence of the test trimer VNAR fusion proteins in plasma samples. Circulating half-lives were determined of 11, 15, and 10 h for 2V-E06-2V, 2V-BA11-2V, and 2V-BB11-2V, respectively (**Figure 9**). Peptides derived from the albumin-binding domains E06, BA11, and BB11 as well as the 2V VNAR domain were detected, indicating that the domains remained stably linked for the duration of the study (results not shown).

Stability

The robust nature of VNAR monomeric proteins has been well documented (16, 32, 33). This robustness is characterized by the ability of VNARs to refold and bind cognate antigens after heating to high temperatures, up to 100°C, for extended periods of time. In this study, the ability of the shark VNAR parental protein E06 and candidate humanized variant BA11 were subjected to a challenge at both elevated temperatures and extremes of pH. Incubation at 100°C for 60 min (**Figure 10A**) resulted in both E06 and BA11 proteins retaining a high percentage (~80%) of antigen specific binding activity. When challenged by incubation at extremes of pH for up to 2 weeks, both proteins showed robust stability and retained the capacity to bind HSA after neutralization to pH 7.4 (**Figures 10B,C**). Only prolonged treatment of BA11 at pH 1.5 showed any drop off in antigen binding. Humanization of the E06 VNAR domain appears not to have had any marked detrimental or deleterious effect on the ability of the protein to refold correctly after denaturing challenge.

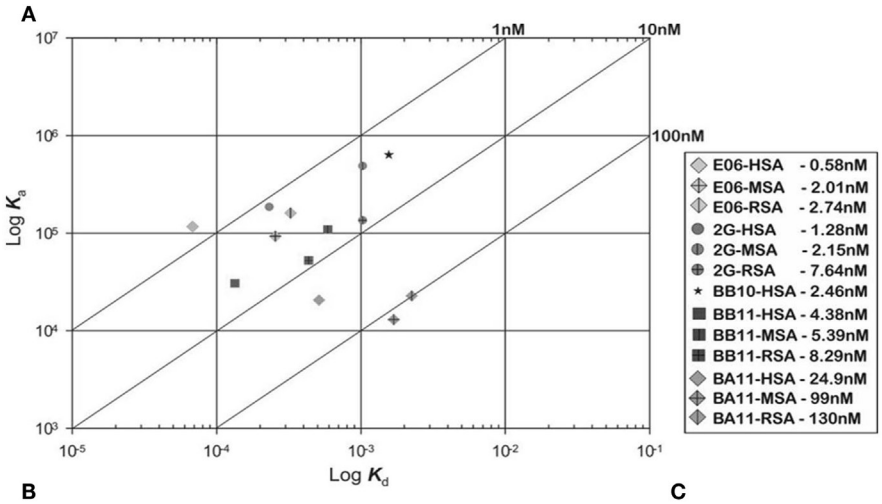

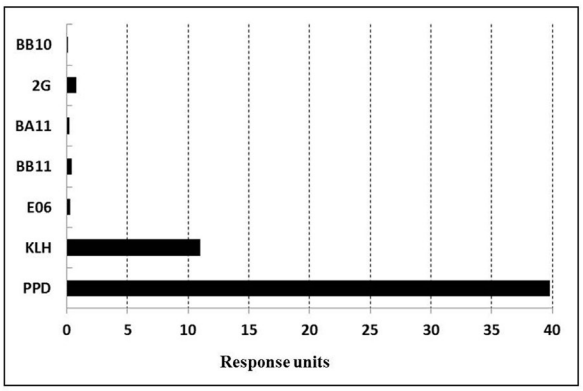

C

Protein	Response Index
PPD POSITIVE CONTROL	36.83
KLH POSITIVE CONTROL	11.018
E06	0.313
BB11	0.375
BA11	0.271
2G	0.767
BB10	0.106

FIGURE 6 | Affinity measurement and antigenicity assessment of lead humanized VNAR albumin binding domains. **(A)** Kinetic distribution plot and BIAcore affinity values for purified monomeric proteins E06, BB10, BA11, BB11 and 2G specific for human serum albumin, rat serum albumin, and mouse serum albumin. Values are the average of at least two experimental runs. **(B)** Proliferative T-cell response used to assess immunogenicity of monomeric E06, BB10, BA11, BB11, and 2G. **(C)** Table of calculated response index values. Positive control antigens used for the assay were (i) Tuberculin purified protein derivative (PPD from *Mycobacterium*) at a final assay concentration of 5 μg/mL (70–100% of donors are expected to react to this protein) and (ii) keyhole limpet hemocyanin, a recognized highly immunogenic protein.

DISCUSSION

The utility of proteins as therapeutic agents is often compromised by their biophysical or biochemical properties which can lead to downstream processing issues including a propensity to precipitate or aggregate during purification and/or subsequent storage. Even if bio-processing is not an issue then a predisposition to elicit an adverse or immune response *in vivo* may also prevent further rapid development (34–36). While *in silico* modeling of VNAR domains predicts a low level of immunogenicity with similar values for those seen for a human Fc region (results not shown), we still embarked on a humanization strategy to accommodate any possible concerns from regulators. Immunogenicity testing of the parental E06 domain (**Figure 6B**) did in fact confirm these original *in silico* predictions. Earlier published efforts to humanize the HSA-binding, VNAR domain, E06 (24) produced a lead clone hE06v1.10, which unfortunately spontaneously dimerized (see **Figure 1**). A further version of humanized E06, based on human germline Kappa sequence DPK24, was also assessed, and although it was monomeric in solution and expressed well in recombinant systems, it unfortunately showed a greatly reduced affinity for target antigen. In an effort to improve these characteristics, both these humanized versions were subjected to a program of random mutagenesis (using error-prone PCR) and functional screening.

A panel of 15 clones (**Figures 3B,C**), demonstrating slow-off rates and strong ELISA binding, were chosen for further study and sequenced. Monomeric proteins for these clones were produced by transient expression in HEK 293 cells and EC_{50} values determined (**Figures 4C,D**). Clones BA11, BB11, BB10, and 2G emerged as the preferred "leads." Only the EC_{50} values of clones generated by mutation of hE06v1.10 were close to the values of the starting HuE06v1.10 and E06 (picomolar range). The 2G clone however saw the greatest improvement in binding to 1.2 nM from a parental hE06v2.4 EC_{50} value of 171 nM (also confirmed by BIAcore). This 2G clone also had the greatest number

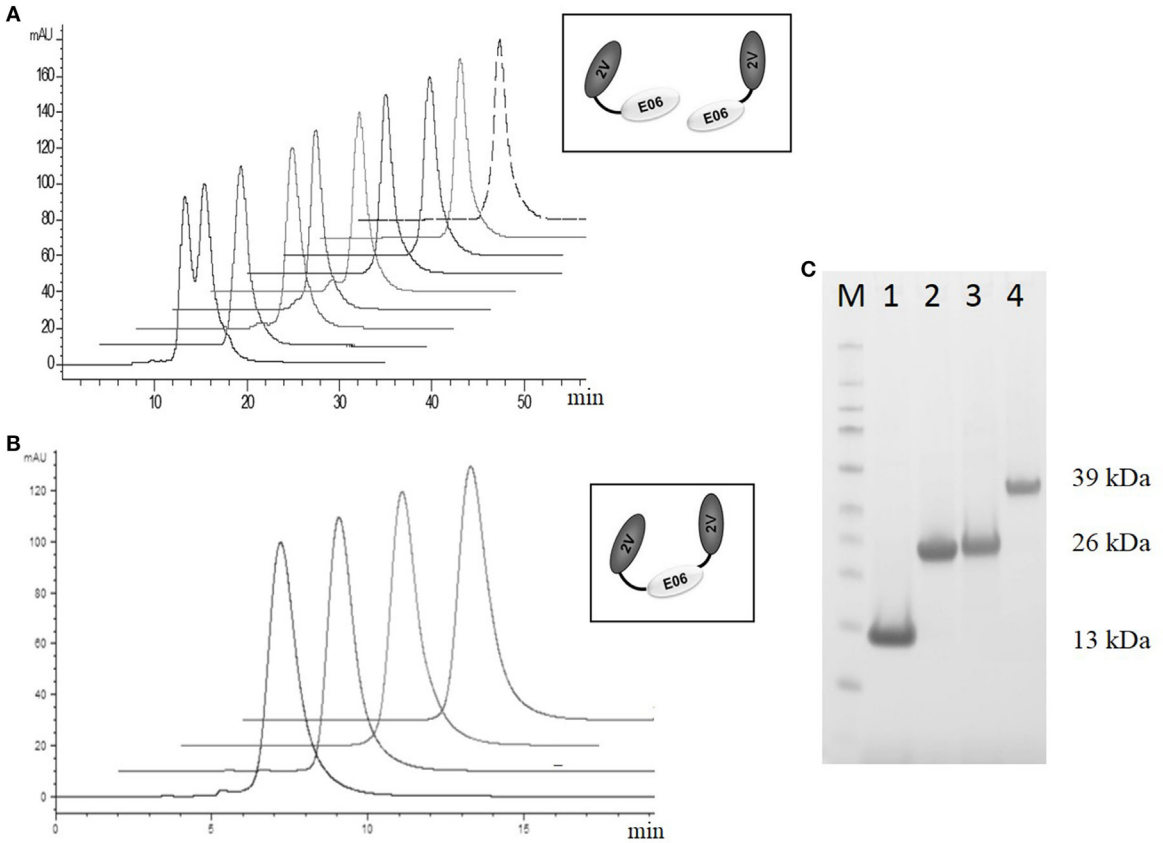

FIGURE 7 | Analytical SEC and SDS PAGE analysis of purified lead humanized proteins reformatted as dimers and trimers. Purification and characterization of fusion proteins **(A)** Analytical SEC chromatograms of dimeric constructs, v1.10-2V, BB11-2V, 2V-BB11, BB10-2V, 2V-BB10, BA11-2V, 2V-BA11, E06-2V, and 2V-E06 overlaid and offset to aid comparisons. Note: The v1.10-2V protein elutes with two distinct peaks demonstrating the dimerization propensity seen originally with the monomeric v1.10 parental clone (**Figure 2C**). **(B)** Analytical SEC analysis of the trimeric constructs 2V-BB11-2V, 2V-E06-2V, 2V-BA11-2V, and 2V-BB10-2V. Chromatograms show trimeric proteins running as a single peak. **(C)** SDS PAGE analysis and Coomassie blue staining of approximately 5 µg of purified lead humanized protein BA11 as monomer and multimers. Lane M, Thermo Scientific Spectra Broad Range Protein Ladder; Lane 1, monomeric BA11; Lane 2, 2V-BA11; Lane 3, BA11-2V; Lane 4, 2V-BA11-2V.

of amino acid changes (4), although it is unclear from this work whether the improvement is the result of a single change or the four changes in concert.

Binding kinetics of the monomeric anti-HSA clones E06, BA11, BB11, BB10, and 2G was measured by surface plasmon resonance. The affinity of E06 was determined as 0.58 nM and that of huE06v1.10 at 6.4 nM (24). The affinities of the candidate humanized and mutated clones all fell within this range. For accelerated clinical development of the humanized clones, it is also important that they have retained the animal species cross-reactivity of E06 with comparable affinities. BA11, BB11, and 2G bound rat and MSAs with affinities between 2 and 130 nM. Interestingly, monomeric BB10 was no longer able to bind rodent albumin. This is due to the substitution of an isoleucine residue at position 90 in CDR3 with a larger hydrophobic phenylalanine residue. This hypothesis is supported by the published crystal structure (24) as isoleucine 90 contributes to hydrophobic intermolecular bonding between huE06 v1.10 and HSA. This lack of species cross-reactivity precluded BB10's use as a candidate clone for future clinical development.

Analysis of a larger number of mutated sequences from both libraries, performed as a part of their quality control, revealed that multiple changes of up to four amino acid positions were observed (data not shown). The four lead clones had a change in CDR3, indeed in clones BB10 and BB11, this was the only region where a change of residue occurs. For BB11, the glycine at position 87 was replaced by an alanine residue. BA11 also has a change at position 87 to a serine and also at position 78 where a phenylalanine is replaced by a serine. Clone 2G, which comes from the v2.4 background, has four mutations from the parental v2.4: asparagine 45 to a lysine, serine 52 to a glycine, leucine 73 to a methionine and a change in CDR3 where glycine 87 is mutated to a serine. The result of these mutations was a recovery of binding affinity but may have also contributed to the increased immunogenicity seen for this clone (**Figure 6**). Interestingly, clones 1H and 5F, from the v2.4 background, both had a substitution at position 88 from a valine to an alanine. Clone 5F also had a mutation at position 63 in HV4 from a threonine to an asparagine. Previous work has noted that although containing no contact residues, the HV4 region of E06 contributed to the binding of albumin by packing

against contact residues of CDR1 (24). This second mutation in the HV4 region of clone 5F may explain the improvement noted in EC_{50} values, which decreased from 82 nM (1H) to 18 nM (5F) and supports the theory that HV4 packs against the CDR1 region, thereby positioning amino acid residues of the CDR1 loop in contact with albumin. The highly selected change of CDR3 residue 87 (BB11, BA11, and 2G) is not an antigen specific contact residue (24), and therefore, retention of binding specificity and affinity is unsurprising. However, it does appear that a change at this position (or close by at position 90 for BB10) has resolved the dimerization bio-processing issue identified as a problem in the parental backbone v1.10 (**Figure 2**). While this phenomenon has been seen previously in antibody CDR regions, where particular motifs contribute to the multimerization of antibody proteins in solution (37, 38), we were surprised that such a small change from a glycine to a serine or even alanine could result in the dramatic improvement in manufacturability of the expressed protein.

Sample	Ligand	ka (M^{-1} s^{-1})	kd (s^{-1})	KD (nM)
2V-E06	HSA	4.54×10^5	4.10×10^{-4}	0.90
E06-2V	HSA	6.89×10^5	5.65×10^{-5}	0.08
2V-E06-2V	HSA	4.46×10^5	2.78×10^{-4}	0.62
	CSA	1.66×10^5	1.26×10^{-4}	0.76
	MSA	1.82×10^6	7.71×10^{-4}	0.42
	RSA	9.84×10^4	7.50×10^{-4}	7.60
2V-BB10	HSA	1.27×10^6	8.53×10^{-3}	6.70
BB10-2V	HSA	9.20×10^5	2.03×10^{-3}	2.20
2V-BB10-2V	HSA	1.72×10^6	3.73×10^{-3}	2.16
	CSA	7.98×10^5	4.39×10^{-3}	5.50
2V-BB11	HSA	5.21×10^5	4.57×10^{-4}	0.88
BB11-2V	HSA	9.07×10^4	1.13×10^{-4}	1.25
2V-BB11-2V	HSA	2.75×10^5	1.19×10^{-3}	4.34
	CSA	7.41×10^5	4.72×10^{-4}	0.64
	MSA	1.09×10^7	4.14×10^{-3}	0.38
	RSA	2.35×10^6	3.50×10^{-3}	1.49
2V-BA11	HSA	7.72×10^5	6.49×10^{-4}	8.41
BA11-2V	HSA	1.63×10^5	4.83×10^{-4}	2.96
2V-BA11-2V	HSA	7.72×10^5	6.49×10^{-4}	8.41
	CSA	1.19×10^4	9.48×10^{-5}	7.95
	MSA	2.88×10^5	1.54×10^{-3}	53.6
	RSA	2.88×10^5	5.40×10^{-4}	18.7

FIGURE 8 | Affinity measurement of monomeric and reformatted dimeric and trimer humanized VNAR lead clones. BIAcore analyses of E06-2V, 2V-E06, 2V-E06-2V, BB10-2V, 2V-BB10, 2V-BB10-2V, BB11-2V, 2V-BB11, 2V-BB11-2V, 2V-BA11, BA11-2V, and 2V-BA11-2V against serum albumin from different species, human serum albumin, cynomolgus serum albumin, mouse serum albumin, and rat serum albumin, using a BIAcore instrument as described in the methods section. Kinetic measurements are summarized as averages from multiple runs.

Human immune response to bio-therapeutic proteins is notoriously difficult to predict and varies from individual to individual. It has been reported that proteins having high homology with human proteins or humanized proteins have reduced immunogenicity (35), but this cannot simply be presumed to be the case. No assay is capable of definitively predicting *in vivo* antigenicity with the only real test being observations from "in human" clinical studies (35). However, *in vitro* testing combined with bench-marking against existing clinical assets can provide a reasonable level of comfort when selecting candidate molecules for costly late stage pre-clinical studies. Humanized E06 VNAR domains BA11, BB11, BB10, and 2G showed very low RI values in a human donor T-cell proliferation assay using ProImmune Ltd. REVEAL® Immunogenicity System DC–T cell assay. Importantly, the RI values were comparable to those obtained when Campath, Avastin, Humira, and Remicade were investigated using the same assay. In fact, when control values are also compared, the humanized VNAR, BB10, had a relative RI slightly below those determined for this panel of well-known clinical agents and chosen lead BA11 has a lower RI than Remicade and is similar to humanized antibodies Campath and Avastin.

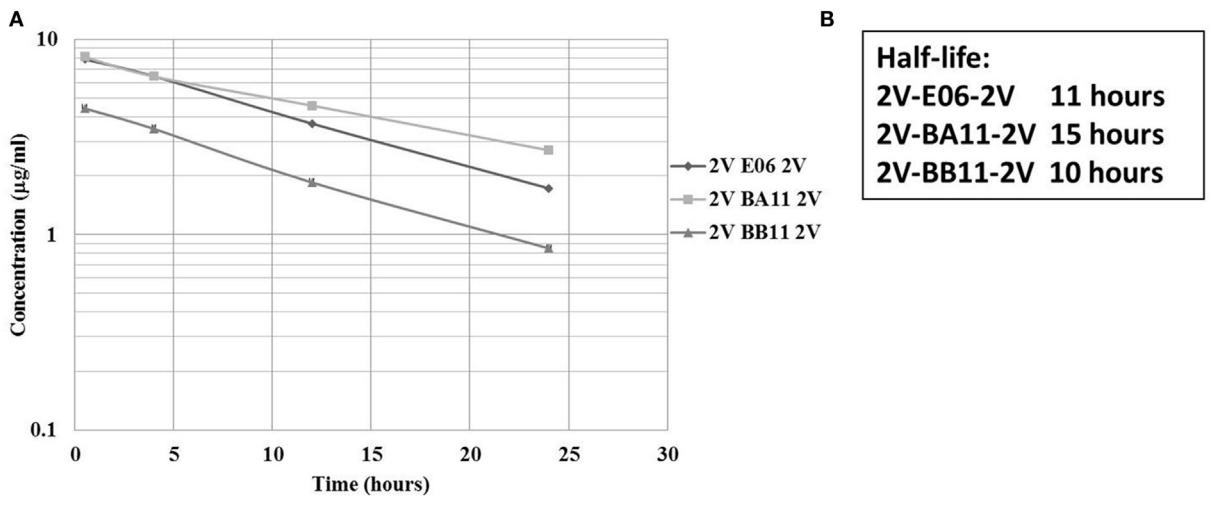

FIGURE 9 | Rat pharmacokinetic (PK) profile and half-life determination of lead trimeric proteins. PK of trimeric VNAR constructs, 2V-BA11-2V, 2V-BB11-2V, and 2V-E06-2V domains delivered into Sprague Dawley rats *via* intravenous administration. **(A)** Graphical representation – mean data from four animals per group. **(B)** Calculated half-lives of administered trimeric proteins. Trimeric protein 2V-BB10-2V was not used in this study due to its loss of binding to rat serum albumin.

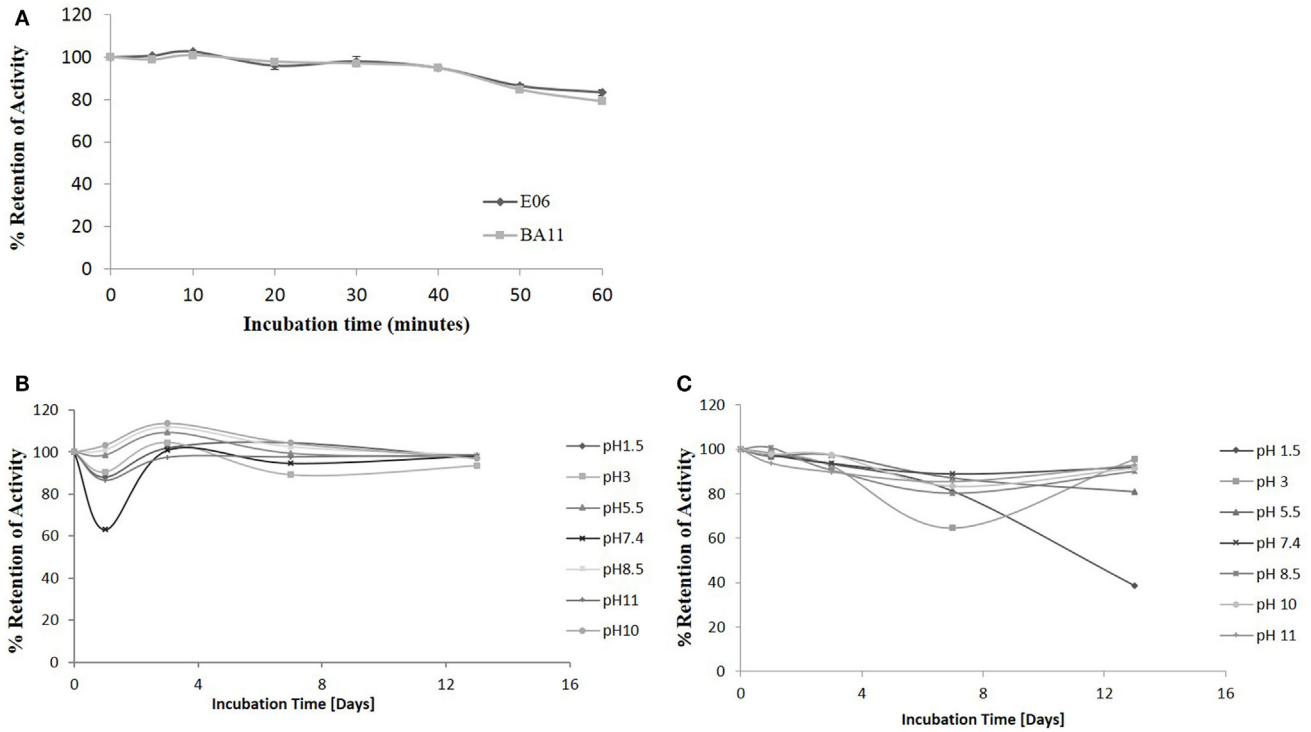

FIGURE 10 | pH and thermo-stability. Stability analysis of the clones "parental" E06 and "candidate" BA11 to thermal and pH denaturation. **(A)** Residual antigen-binding activity was compared to a non-treated time zero control after test proteins were incubated at 100°C for 60 min. The data shown are the average of multiple replicates and a typical data set from 2 repeated experiments. **(B,C)** Residual antigen-binding activity following exposure of test proteins to a range of pH conditions for 14 days shown for E06 **(B)** and BA11 **(C)**.

Based on a combination of affinity, antigenicity, species cross-reactivity, and expressability, BA11 and BB11 (together with E06 and BB10 controls) were reformatted as dimeric and trimeric fusion proteins using a naive control VNAR 2V. By SDS PAGE, these proteins migrated as single bands with predicted molecular masses (**Figure 7C**) and confirmed that the bio-processing and affinity improvements seen for the monomeric humanized mutants was retained when they were assembled in a more relevant therapeutic format (fusions at the carboxyl terminal, amino terminal fusion, or both). Indeed 2V-BA11 protein was concentrated in PBS to therapeutic levels of over 50 mg/mL without precipitation, a favorable property for drug formulation, and retained a single-peak, SEC profile (data not shown).

Albumin half-life in the systemic circulation is prolonged by the FcRn recycling process (39, 40). In an early publication, monomeric and multimeric VNAR constructs containing the wild-type E06 albumin-binding domain showed a very impressive extended half-life equivalent to that of the species-specific (rodent or non-human primates) serum albumin (23). In this study, the functional ability of the humanized albumin-binding domains BA11 and BB11 and the wild-type E06 to extend circulating half-life, formatted as fusion proteins with the 2V VNAR domain (as trimers), was examined in a suitable rodent model. The humanized variants had a half-life (2V-BA11-2V 15 h and 2V-BB11-2V 10 h) equivalent to the parental control (2V-E06-2V 11 h), thereby confirming that the humanized domains remained bound to RSA during the FcRn recycling process.

Based on the accumulated data from affinity, analytical SEC profile, expressability, protein bio-processing quality, immunogenicity, and rodent-half-life studies, BA11 emerged as the clear candidate molecule for further study. To avoid confusion, it is worth noting that recent commercial literature often refers to humanized VNAR as soloMERs™ (22) and BA11 as NDure™.

Single-domain antibodies from shark (16, 32, 33) and camelid (41–43) species have an ability to refold and bind antigen after thermal and chemical denaturation. Here, the candidate clone BA11 was subjected to extreme thermal and pH challenge. Both the monomeric wild-type E06 and candidate clone showed a remarkable ability to bind cognate antigen after temperature or pH induced unfolding, confirming that functional binding and surprisingly functional stability (which had been ignored as part of clone "culling") had been retained through the mutation and selection process.

Naturally occurring protein binding domains with the potential for development as bio-therapeutic drugs are being investigated many research and development laboratories of the pharmaceutical industry. In this article, we have detailed the successful humanization of an albumin binding domain isolated from shark VNAR library. This domain, E06, was humanized in a manner that facilitated the retention of high affinity and

specificity for cognate antigen with low immunogenicity and the hallmark high stability of native VNARs. *In vivo* PK studies have proven this final clinical domain BA11 (NDure™) to have broad utility as an enabling product for increased systemic exposure across multiple therapeutic modalities while retaining the benefit of small size and can be formulated at concentrations concurrent with clinically approved mAbs.

ETHICS STATEMENT

All animal studies were conducted by Charles River (Elpinstone Research Centre, Elphinstone, Tranent EH33 2NE) in accordance with their regulated procedures.

AUTHOR CONTRIBUTIONS

CB is the PI on the project and managed and led the team. AP is the co-PI. JS, MM, MC, OU, MK, and GD are the senior scientists who conducted the work. TB, DC, and KS developed and ran the LC/MS.

ACKNOWLEDGMENTS

The authors would like to acknowledge the funding support for this work from Scottish Enterprise [VNAR_001(2012)] and the Biotechnology and Biological Sciences Research Council (BB/K010905/1).

REFERENCES

1. Padlan EA. A possible procedure for reducing the immunogenicity of antibody variable domains while preserving their ligand-binding properties. *Mol Immunol* (1991) 28:489–98. doi:10.1016/0161-5890(91)90163-E
2. Pelat T, Bedouelle H, Rees AR, Crennell SJ, Lefranc M, Thullier P. Germline humanization of a non-human primate antibody that neutralizes the anthrax toxin, by in vitro and in silico engineering. *J Mol Biol* (2008) 384:1400–7. doi:10.1016/j.jmb.2008.10.033
3. Robert R, Streltsov VA, Newman J, Pearce LA, Wark KL, Dolezal O. Germline humanization of a murine Abeta antibody and crystal structure of the humanized recombinant Fab fragment. *Protein Sci* (2010) 19:299–308. doi:10.1002/pro.312
4. Cheung NV, Guo H, Hu J, Tassev DV, Cheung IY. Humanizing murine IgG3 anti-GD2 antibody m3F8 substantially improves antibody-dependent cell-mediated cytotoxicity while retaining targeting in vivo. *Oncoimmunology* (2012) 1:477–86. doi:10.4161/onci.19864
5. Zhao H, Verma D, Li W, Choi Y, Ndong C, Fiering SN, et al. Depletion of T cell epitopes in lysostaphin mitigates anti-drug antibody response and enhances antibacterial efficacy in vivo. *Chem Biol* (2015) 22:629–39. doi:10.1016/j.chembiol.2015.04.017
6. Reichert JM. Antibodies to watch in 2017. *MAbs* (2016) 9(2):167–81. doi:10.1080/19420862.2016.1269580
7. Demidem A, Lam T, Alas S, Hariharan K, Hanna N, Bonavida B. Chimeric anti-CD20 (IDEC-C2B8) monoclonal antibody sensitizes a B cell lymphoma cell line to cell killing by cytotoxic drugs. *Cancer Biother Radiopharm* (1997) 12:177–86. doi:10.1089/cbr.1997.12.177
8. Goldenberg MM. Trastuzumab, a recombinant DNA-derived humanized monoclonal antibody, a novel agent for the treatment of metastatic breast cancer. *Clin Ther* (1999) 21:309–18. doi:10.1016/S0149-2918(00)88288-0
9. Salgaller ML. Technology evaluation: bevacizumab, Genentech/Roche. *Curr Opin Mol Ther* (2003) 5:657–67.
10. Kovaleva M, Ferguson L, Steven J, Porter A, Barelle C. Shark variable new antigen receptor biologics – a novel technology platform for therapeutic drug development. *Expert Opin Biol Ther* (2014) 14:1527–39. doi:10.1517/14712598.2014.937701
11. Gebauer M, Skerra A. Engineered protein scaffolds as next-generation antibody therapeutics. *Curr Opin Chem Biol* (2009) 13:245–55. doi:10.1016/j.cbpa.2009.04.627
12. Scolnik PA. mAbs: a business perspective. *MAbs* (2009) 1:179–84. doi:10.4161/mabs.1.2.7736
13. Sexton K, Tichauer K, Samkoe KS, Gunn J, Hoopes PJ, Pogue BW. Fluorescent affibody peptide penetration in glioma margin is superior to full antibody. *PLoS One* (2013) 8:e60390. doi:10.1371/journal.pone.0060390
14. Xiang D, Zheng C, Zhou SF, Qiao S, Tran PH, Pu C, et al. Superior performance of Aptamer in tumor penetration over antibody: implication of Aptamer-based theranostics in solid tumors. *Theranostics* (2015) 5:1083–97. doi:10.7150/thno.11711
15. Greenberg AS, Hughes AL, Guo J, Avila D, McKinney EC, Flajnik MF. A novel "chimeric" antibody class in cartilaginous fish: IgM may not be the primordial immunoglobulin. *Eur J Immunol* (1996) 26:1123–9. doi:10.1002/eji.1830260525
16. Dooley H, Flajnik MF, Porter AJ. Selection and characterization of naturally occurring single-domain (IgNAR) antibody fragments from immunized sharks by phage display. *Mol Immunol* (2003) 40:25–33. doi:10.1016/S0161-5890(03)00084-1
17. Goodchild SA, Dooley H, Schoepp RJ, Flajnik M, Lonsdale SG. Isolation and characterisation of Ebolavirus-specific recombinant antibody fragments from murine and shark immune libraries. *Mol Immunol* (2011) 48:2027–37. doi:10.1016/j.molimm.2011.06.437
18. Müller MR, O'Dwyer R, Kovaleva M, Rudkin F, Dooley H, Barelle CJ. Generation and isolation of target-specific single-domain antibodies from shark immune repertoires. *Methods Mol Biol* (2012) 907:177–94. doi:10.1007/978-1-61779-974-7_9
19. Streltsov VA, Varghese JN, Carmichael JA, Irving RA, Hudson PJ, Nuttall SD. Structural evidence for evolution of shark Ig new antigen receptor variable domain antibodies from a cell-surface receptor. *Proc Natl Acad Sci U S A* (2004) 101:12444–9. doi:10.1073/pnas.0403509101
20. Dooley H, Flajnik MF. Shark immunity bites back: affinity maturation and memory response in the nurse shark, *Ginglymostoma cirratum*. *Eur J Immunol* (2005) 35:936–45. doi:10.1002/eji.200425760
21. Dooley H, Flajnik M. Antibody repertoire development in cartilaginous fish. *Dev Comp Immunol* (2006) 30:43–56. doi:10.1016/j.dci.2005.06.022
22. Barelle C, Muller MR, Calabro V, Bikker J, Steven J, Tchistiakova L, et al. *Single Domain Binding Molecule*. U.S.Patent No US20170096475 A1. Washington, DC: U.S. Patent and Trademark Office (2016).
23. Müller MR, Saunders K, Grace C, Jin M, Piche-Nicholas N, Steven J, et al. Improving the pharmacokinetic properties of biologics by fusion to an anti-HSA shark VNAR domain. *MAbs* (2012) 4:673–85. doi:10.4161/mabs.22242
24. Kovalenko OV, Olland A, Piche-Nicholas N, Godbole A, King D, Svenson K, et al. Atypical antigen recognition mode of a shark immunoglobulin new antigen receptor (IgNAR) variable domain characterized by humanization and structural analysis. *J Biol Chem* (2013) 288:17408–19. doi:10.1074/jbc.M112.435289
25. Finlay WJ, Cunningham O, Lambert MA, Darmanin-Sheehan A, Liu X, Fennell BJ, et al. Affinity maturation of a humanized rat antibody for anti-RAGE therapy: comprehensive mutagenesis reveals a high level of mutational plasticity both inside and outside the complementarity-determining regions. *J Mol Biol* (2009) 388:541–58. doi:10.1016/j.jmb.2009.03.019
26. Vaughan TJ, Williams AJ, Pritchard K, Osbourn JK, Pope AR, Earnshaw JC, et al. Human antibodies with sub-nanomolar affinities isolated from a large non-immunized phage display library. *Nat Biotechnol* (1996) 14:309–14. doi:10.1038/nbt0396-309
27. Fennell BJ, Darmanin-Sheehan A, Hufton SE, Calabro V, Wu L, Muller MR, et al. Dissection of the IgNAR V domain: molecular scanning and orthologue database mining define novel IgNAR hallmarks and affinity maturation mechanisms. *J Mol Biol* (2010) 400:155–70. doi:10.1016/j.jmb.2010.04.061

28. Leonard P, Säfsten P, Hearty S, McDonnell B, Finlay W, O'Kennedy R. High throughput ranking of recombinant avian scFv antibody fragments from crude lysates using the Biacore A100. *J Immunol Methods* (2007) 323:172–9. doi:10.1016/j.jim.2007.04.010
29. Cummins E, Luxenberg DP, McAleese F, Widom A, Fennell BJ, Darmanin-Sheehan A, et al. A simple high-throughput purification method for hit identification in protein screening. *J Immunol Methods* (2008) 339:38–46. doi:10.1016/j.jim.2008.07.016
30. Huh S, Do H, Lim H, Kim D, Choi S, Song H, et al. Optimization of 25kDa linear polyethylenimine for efficient gene delivery. *Biologicals* (2007) 35:165–71. doi:10.1016/j.biologicals.2006.08.004
31. Backliwal G, Hildinger M, Hasija V, Wurm FM. High-density transfection with HEK-293 cells allows doubling of transient titers and removes need for a priori DNA complex formation with PEI. *Biotechnol Bioeng* (2008) 99:721–7. doi:10.1002/bit.21596
32. Shao C, Secombes CJ, Porter AJ. Rapid isolation of IgNAR variable single-domain antibody fragments from a shark synthetic library. *Mol Immunol* (2007) 44:656–65. doi:10.1016/j.molimm.2006.01.010
33. Liu JL, Zabetakis D, Brown JC, Anderson GP, Goldman ER. Thermal stability and refolding capability of shark derived single domain antibodies. *Mol Immunol* (2014) 59:194–9. doi:10.1016/j.molimm.2014.02.014
34. Koren E, Smith HW, Shores E, Shankar G, Finco-Kent D, Rup B, et al. Recommendations on risk-based strategies for detection and characterization of antibodies against biotechnology products. *J Immunol Methods* (2008) 333:1–9. doi:10.1016/j.jim.2008.01.001
35. Attarwala H. TGN1412: from discovery to disaster. *J Young Pharm* (2010) 2:332–6. doi:10.4103/0975-1483.66810
36. Chirmule N, Jawa V, Meibohm B. Immunogenicity to therapeutic proteins: impact on PK/PD and efficacy. *AAPS J* (2012) 14:296–302. doi:10.1208/s12248-012-9340-y
37. Dudgeon K, Famm K, Christ D. Sequence determinants of protein aggregation in human VH domains. *Protein Eng Des Sel* (2009) 22:217–20. doi:10.1093/protein/gzn059
38. Wang X, Das TK, Singh SK, Kumar S. Potential aggregation prone regions in biotherapeutics: a survey of commercial monoclonal antibodies. *MAbs* (2009) 1:254–67. doi:10.4161/mabs.1.3.8035
39. Chaudhury C, Brooks CL, Carter DC, Robinson JM, Anderson CL. Albumin binding to FcRn: distinct from the FcRn-IgG interaction. *Biochemistry* (2006) 45:4983–90. doi:10.1021/bi052628y
40. Kim J, Bronson CL, Hayton WL, Radmacher MD, Roopenian DC, Robinson JM, et al. Albumin turnover: FcRn-mediated recycling saves as much albumin from degradation as the liver produces. *Am J Physiol Gastrointest Liver Physiol* (2006) 290:G352–60. doi:10.1152/ajpgi.00286.2005
41. Van der Linden R, Frenken L, De Geus B, Harmsen M, Ruuls R, Stok W, et al. Comparison of physical chemical properties of llama V HH antibody fragments and mouse monoclonal antibodies. *Biochim Biophys Acta* (1999) 1431:37–46. doi:10.1016/S0167-4838(99)00030-8
42. Dumoulin M, Conrath K, Van Meirhaeghe A, Meersman F, Heremans K, Frenken LG, et al. Single-domain antibody fragments with high conformational stability. *Protein Sci* (2002) 11:500–15. doi:10.1110/ps.34602
43. Dolk E, van der Vaart M, Lutje Hulsik D, Vriend G, de Haard H, Spinelli S, et al. Isolation of llama antibody fragments for prevention of dandruff by phage display in shampoo. *Appl Environ Microbiol* (2005) 71:442–50. doi:10.1128/AEM.71.1.442-450.2005

Conflict of Interest Statement: The authors declare that the research was conducted in the absence of any commercial or financial relationships that could be construed as a potential conflict of interest.

frontiers in Immunology

ORIGINAL RESEARCH
published: 21 August 2017
doi: 10.3389/fimmu.2017.00956

Development and Characterization of a Camelid Single Domain Antibody–Urease Conjugate That Targets Vascular Endothelial Growth Factor Receptor 2

*Baomin Tian[1], Wah Yau Wong[1], Marni D. Uger[1], Pawel Wisniewski[2] and Heman Chao[1]**

[1] Helix BioPharma Corp., Toronto, ON, Canada, [2] Helix ImmunoOncology, Warsaw, Poland

Angiogenesis is the process of new blood vessel formation and is essential for a tumor to grow beyond a certain size. Tumors secrete the pro-angiogenic factor vascular endothelial growth factor, which acts upon local endothelial cells by binding to vascular endothelial growth factor receptors (VEGFRs). In this study, we describe the development and characterization of V21-DOS47, an immunoconjugate that targets VEGFR2. V21-DOS47 is composed of a camelid single domain anti-VEGFR2 antibody (V21) and the enzyme urease. The conjugate specifically binds to VEGFR2 and urease converts endogenous urea into ammonia, which is toxic to tumor cells. Previously, we developed a similar antibody–urease conjugate, L-DOS47, which is currently in clinical trials for non-small cell lung cancer. Although V21-DOS47 was designed from parameters learned from the generation of L-DOS47, additional optimization was required to produce V21-DOS47. In this study, we describe the expression and purification of two versions of the V21 antibody: V21H1 and V21H4. Each was conjugated to urease using a different chemical cross-linker. The conjugates were characterized by a panel of analytical techniques, including SDS-PAGE, size exclusion chromatography, Western blotting, and LC-MS^E peptide mapping. Binding characteristics were determined by ELISA and flow cytometry assays. To improve the stability of the conjugates at physiologic pH, the pIs of the V21 antibodies were adjusted by adding several amino acid residues to the C-terminus. For V21H4, a terminal cysteine was also added for use in the conjugation chemistry. The modified V21 antibodies were expressed in the *E. coli* BL21 (DE3) pT7 system. V21H1 was conjugated to urease using the heterobifunctional cross-linker succinimidyl-[(*N*-maleimidopropionamido)-diethyleneglycol] ester ($SM(PEG)_2$), which targets lysine resides in the antibody. V21H4 was conjugated to urease using the homobifunctional cross-linker, 1,8-bis(maleimido)diethylene glycol ($BM(PEG)_2$), which targets the cysteine added to the antibody C-terminus. V21H4-DOS47 was determined to be the superior conjugate as the antibody is easily produced and purified at high levels, and the conjugate can be efficiently generated and purified using methods easily transferrable for cGMP production. In addition, V21H4-DOS47 retains higher binding activity than V21H1-DOS47, as the native lysine residues are unmodified.

Keywords: antibody–drug conjugates, conjugation sites, conjugation ratios, camelid antibodies, urease, vascular endothelial growth factor receptor 2, cancer

OPEN ACCESS

Edited by:
Colin Roger MacKenzie, National Research Council Canada, Canada

Reviewed by:
Peter Timmerman, Pepscan Therapeutics B.V., Netherlands
Patrick Chames, UMR7258 Centre de recherche en cancérologie de Marseille (CRCM), France

****Correspondence:***
Heman Chao
hchao@helixbiopharma.com

Specialty section:
This article was submitted to Vaccines and Molecular Therapeutics, a section of the journal Frontiers in Immunology

Received: *28 April 2017*
Accepted: *26 July 2017*
Published: *21 August 2017*

Citation:
Tian B, Wong WY, Uger MD, Wisniewski P and Chao H (2017) Development and Characterization of a Camelid Single Domain Antibody–Urease Conjugate That Targets Vascular Endothelial Growth Factor Receptor 2. Front. Immunol. 8:956. doi: 10.3389/fimmu.2017.00956

INTRODUCTION

As tumors outgrow local oxygen diffusion gradients, angiogenesis is triggered and new capillaries sprout from pre-existing blood vessels to support tumor cell demands for nutrients and oxygen and spread to distant sites (1, 2). Growth factors secreted by tumor cells mediate the induction of angiogenesis and control the inflammatory infiltrate. Multiple ligand–receptor signaling networks have been associated with tumor angiogenesis. The vascular endothelial growth factor (VEGF)/vascular endothelial growth factor receptor 2 (VEGFR2) ligand–receptor complex is one of the most important signaling pathways identified and extensive research has been done on its roles in vascular functions (3, 4). During cancer-induced angiogenesis, cancer cells secrete VEGF that binds to VEGFR2, triggering a tyrosine kinase signaling cascade *via* the dimerization of VEGFR2. Consequently, the kinase signaling cascade stimulates the production of factors that variously stimulate vessel permeability, proliferation/survival, migration, and finally differentiation of mature blood vessels. Tumor blood vessels are structurally and functionally abnormal and are present at high density. Therefore, targeting tumor vasculature is a rational strategy with great promise and different anti-angiogenic agents targeting the VEGF/VEGFR2 signaling cascade have been developed as cancer therapeutics. Small chemical drugs, such as Sunitinib (SU11248, Sutent, Pfizer), Axitinib, and Sorafenib (BAY43-9006, Nexavar, Bayer) were approved by the FDA as anti-angiogenic agents that directly inhibit the kinase activity of the VEGFR2 intracellular kinase domains (5, 6). Monoclonal antibodies such as bevacizumab (Avastin, Genentech/Roche) and ramucirumab were developed to suppress angiogenesis by binding, respectively, to VEGF and VEGFR2, interrupting VEGFR2 dimerization and consequently inhibiting autophosphorylation (7, 8).

We have developed an antibody–drug conjugate (ADC) approach to suppress angiogenesis. Unlike most of the anti-angiogenic agents that interrupt the kinase signaling cascade by blocking the dimerization of VEGFR2 or by inhibiting kinase activity, our ADC, V21-DOS47, kills VEGFR2-expressing cells by inducing cytotoxic activity at the target cells. Similar to our previous antitumor immunoconjugate, L-DOS47 (9), V21-DOS47 is composed of a camelid single domain antibody and the enzyme urease (derived from jack beans, *Canavalia ensiformis*): the V21 antibody binds to VEGFR2, thus targeting the complex to VEGFR2-expressing cells, whereas the urease enzyme converts endogenous urea into ammonia *in situ* to induce cytotoxicity. Since VEGFR2 is not only expressed in the tumor vasculature but has also been identified on the surface of a variety of tumors (4, 10, 11), V21-DOS47 targets both VEGFR2$^+$ vascular endothelial cells and VEGFR2$^+$ tumor cells. The elevated local concentration of ammonia also neutralizes the acidic environment surrounding the tumor microvasculature, which is otherwise favorable to cancer cell growth (12). As urease is a plant product with no known mammalian homolog, it is likely to be immunogenic, although an auto-immune reaction is not expected. L-DOS47 is currently being tested in clinical trials and results show that anti-urease antibodies are formed, but no known severe immune toxicity is observed. The full impact of urease immunogenicity is still being studied.

One advantage of camelid single domain antibodies is their relatively small size (approximately 15 kDa) compared to conventional immunoglobulins (approximately 150 kDa). This is particularly important when coupling antibodies to urease, as urease is a large protein with a molecular weight of 544 kDa. By using llama single-domain antibodies, multiple antibodies can be coupled to each urease molecule with a relatively minor increase in overall molecular weight. This allows for the generation of a high avidity therapeutic reagent that retains an acceptable biodistribution profile. Other benefits of single domain camelid antibodies (13–15) are that they are easy to clone and express recombinantly (16, 17), they are generally more thermally and chemically stable than conventional IgG (18, 19), and they bind to epitopes that are not recognized by conventional antibodies (20). In addition, they are not particularly immunogenic as human V_H and camelid V_HH domains share approximately 80% sequence identity (21) and renal clearance is high (22).

Antibody–urease conjugates are complex and large proteins: with multiple antibodies per urease, the molecular weight of the conjugate can reach 680 kDa. This provides a challenge to large-scale production. In our previous report, we described conjugation chemistry and separation procedures designed to address these challenges (9). In this study, we evaluated additional antibody production and conjugation chemistry methods to generate a novel antibody–urease conjugate, V21-DOS47.

In order to produce high-affinity antibodies to VEGFR2, a llama was immunized with recombinant VEGFR2 and a V_HH phage display library was generated. The V21 antibody was isolated by panning this library with recombinant VEGFR2. Additional amino acid residues were added to the C-terminus of the V21 antibody in order to fulfill multiple objectives: to optimize the antibody pI, to target antibody expression to bacterial inclusion bodies, and to provide a unique target for cross-linking chemistry. In this report, we describe two versions of the V21 antibody, designated V21H1 and V21H4, and the different methods used to conjugate each antibody to urease. Both antibody–urease conjugates were characterized with a variety of analytical techniques, including size exclusion chromatography (SEC) (to evaluate protein purity), SDS-PAGE (to determine the average number of antibodies conjugated per urease), and ESI mass spectrometry (to identify conjugation sites on both the antibody and urease). The effects of conjugation ratio (CR) were examined, and the binding of the two conjugates with the same CR were compared. Binding to VEGFR2 expressed at the cell surface was confirmed by flow cytometry.

MATERIALS AND METHODS

Purification of High Purity Urease (HPU)

Crude urease (cat #U-80, 236 U/mg) was purchased from BioVectra Inc. (Charlottetown, PE, Canada). Prior to use in conjugation, crude urease was purified to remove jack bean matrix protein contaminants such as canavalin and concanavalin A. One million units of crude urease were dissolved in 430 mL of high

purity (HP) water at room temperature. The solution was brought to pH 5.15 with 10% (v/v) acetic acid and then centrifuged at 9,000 rcf and 4°C for 40 min. The urease-containing supernatant was cooled to 4°C and fractionated by adding chilled ethanol to a final concentration of 25% (v/v) while maintaining the temperature at 0–8°C. The mixture was stirred overnight and then centrifuged at 9,000 rcf and 4°C for 40 min. The pellet was resuspended in 150 mL of acetate–EDTA buffer (10 mM sodium acetate, 1 mM EDTA, 1 mM TCEP, pH 6.5) and then centrifuged at 4°C and 9,000 rcf for 40 min. The supernatant was concentrated to 75 mL using a Minimate TFF system (Masterflex Model 7518-00 with a Minimate TFF capsule, MWCO 100 kDa), diafiltered three times with 200 mL of acetate–EDTA buffer, and then concentrated down to 100 mL. The diafiltered urease solution was collected, and the strained solution in the capsule and tubing connections was expelled from the system with 50 mL acetate–EDTA buffer and added to the collected solution (total volume ~150 mL). The ethanol fractionated urease solution was further purified by anion exchange chromatography using a Bio-Rad Biologic LP system. The urease solution was loaded at a flow rate of 3.5 mL/min onto a 35 mL DEAE column (DEAE Sepharose Fast Flow, GE Healthcare, cat #17-0709-01) which was pre-equilibrated with 150 mL of IEC Buffer A (20 mM imidazole, 1 mM TCEP, pH 6.5). The column was washed with 100 mL of IEC Buffer A, followed by 80 mL of 40% Buffer B (Buffer A with 0.180 M NaCl). The urease was eluted with 100% Buffer B at a flow rate of 3.5 mL/min and fractions with A_{280} >0.1 were pooled. The pooled fractions were concentrated to a target protein concentration of 6–8 mg/mL using a Minimate capsule with a 100 kDa MWCO membrane and then diafiltered against acetate–EDTA buffer (20 mM sodium acetate, 1 mM EDTA, pH 6.5). The HPU was stored at −80°C. The yield from this purification protocol is typically >55% of the starting activity.

Expression of V21H1 and V21H4

Both antibodies were expressed in the *E. coli* BL21 (DE3) pT7 system with kanamycin as the selection antibiotic. Transformation of BL21 (DE3) competent *E. coli* cells (Sigma, B2935-10 × 50 μL) was according to the manufacturer's instructions. One colony from a transformation plate was aseptically inoculated to 200 mL of LB broth (LB media EZ mix, Sigma cat #L76581, 20 g/L) supplemented with 50 mg/L kanamycin. Cultures were incubated at 200 rpm and 37°C. Once the culture reached an OD_{600} greater than 0.6, 50 mL of culture was transferred to four 2 L flasks, each containing 1 L of LB broth with 50 mg/L kanamycin. Flasks were incubated in a shaker incubator at 200 rpm and 37°C. Once the culture reached an OD_{600} of 0.9–1.0, antibody expression was induced by the addition of 1 mM IPTG and overnight incubation at 200 rpm and 37°C. The cells were harvested by centrifugation into aliquots, one per 2 L culture.

Purification of V21H1

The majority of the V21H1 protein was expressed in the *E. coli* cytosolic solution, not in the inclusion bodies. An aliquot of cell pellet was lysed in 100 mL of lysis buffer (50 mM Tris, 25 mM NaCl, pH 6.5) by sonication in an ice-water bath for 10 min (Misonix 3000 sonicator, tip part #4406; each sonicating cycle: sonicating 30 s, cooling 4 min, power 8). The lysate was centrifuged at 9,000 rcf and 4°C for 30 min. In order to remove the most abundant bacterial matrix proteins, the supernatant was mixed with ice-cold ethanol to a final concentration of 10% (v/v) and incubated in an ice-water bath for 30 min, followed by centrifugation at 9,000 rcf and 4°C for 30 min. The supernatant was mixed with ice-cold ethanol to a final concentration of 45% (v/v) and stirred in an ice-water bath for 60 min, followed by centrifugation at 9,000 rcf and 4°C for 30 min. The pellet was resuspended in 200 mL of wash buffer (50 mM acetate, 0.1% Triton X-100, 1 mM DTT, 25 mM NaCl, pH 5.0). After centrifugation at 9,000 rcf and 4°C for 30 min, the pellet was resuspended in 100 mL of SP Buffer A (50 mM acetate, 8 M urea, pH 4.0) supplemented with 2 mM DTT, and filtered through a 0.45-μm filter. The filtered solution was loaded on to a 1 mL SP FF column (GE Healthcare, cat #17-5054-01) with a peristaltic pump at 2 mL/min, and the column was then connected to an ACTA FPLC system (Amersham Bioscience, cat #UPC-920). After washing the column with 10 mL of SP Buffer A at 1 mL/min, the V21H1 antibody was eluted by a gradient of 0–50% SP Buffer B (SP Buffer A with 0.7 M NaCl) over 30 min at a flow rate of 1 mL/min. The OD_{280} of the peak fraction was determined and the concentration was calculated with an extinction coefficient of 1.967 mg/mL. DTT was added to the SP column peak fraction to a final concentration of 1 mM and the pH of the solution was adjusted to 8–8.5 with 2 M Tris-base. The refolding of the antibody was performed by adding the pH adjusted SP peak fraction drop by drop to refolding buffer (100 mM Tris, 10 μM $CuSO_4$, pH 8.8) and continuous stirring at 4°C until the refolding was completed. The refolding process was monitored by intact protein LC-MS. After refolding, the solution was centrifuged at 9,000 rcf and 4°C for 30 min before loading on to a 1 mL QHP column. The column was connected to a FPLC system and washed with 10 mL of Q Buffer A (50 mM HEPES, pH 7.0) at a flow rate of 1 mL/min. The antibody was eluted by a gradient of 0–40% Q Buffer B (Q Buffer A with 0.7 M NaCl) in 40 min at a flow rate of 1 mL/min. The peak fractions from 8 L of cell culture were pooled, concentrated to 2–4 mg/mL, and dialyzed against 20 mM HEPES, pH 7.1 overnight (MWCO 5–8 kDa, volume ratio 1:50) at 4°C. The final V21H1 antibody solution was filtered through a 0.22 μm syringe filter and stored at 4°C.

Purification of V21H4

In contrast to V21H1, the majority of the V21H4 protein was expressed in the *E. coli* inclusion bodies. The cell pellet from each 2 L culture was resuspended in 100 mL of lysis buffer (50 mM Tris, 25 mM NaCl, pH 6.5) and mixed with lysozyme to a final concentration of 0.2 mg/mL. The cell suspension was incubated at room temperature for 30 min, then lysed by sonication in an ice-water bath for 10 min (Misonix 3000 sonicator, tip part #4406; each sonicating cycle: sonicating 30 s, cooling 4 min, power 8). The lysate was centrifuged at 9,000 rcf and 4°C for 30 min. The pellet was washed twice with 400 mL of Pellet Wash Buffer (50 mM Tris, 25 mM NaCl, pH 6.5, 1% Triton X-100, 2 mM DTT) and once with 50 mM of acetic acid containing 2 mM DTT. The pellet was resuspended in 100 mL of SP Buffer A (50 mM acetate, 8 M urea, pH 4.0) supplemented with 2 mM DTT and centrifuged at

9,000 rcf and 4°C for 30 min. The resulting supernatant was filtered through a 0.45-μm filter and loaded on to a 5 mL SP-XL column (GE Healthcare, cat #17-1152-01) at a flow rate of 5 mL/min. After washing the column with 50 mL of SP Buffer A, the protein was eluted by a gradient of 0–50% SP Buffer B (SP Buffer A with 0.7 M NaCl) over 30 min at a flow rate of 5 mL/min. Peak fractions were collected when A_{280} >700 mU. DTT was added to the pooled SP peak fraction to a final concentration of 1.0 mM and the pH was adjusted to pH 8.6–8.7 with saturated Tris-base. Refolding was initiated by mixing the SP peak fraction with refolding buffer (50 mM Tris, 2 M urea, 1.0 mM DTT, pH 8.6–8.7). After stirring at room temperature for 2 h, 1.2 mM cystamine was added to the refolding mixture. Refolding continued at room temperature and was monitored by RP-HPLC [Agilent 1100 system; ZORBAX-C3 column, PN883750-909; Solvent A: 0.025% (v/v) TFA in water; Solvent B: 0.025% TFA in acetonitrile; gradient: 20–60% B over 30 min at a flow rate of 0.25 mL/min. 100 μL of sample was collected at various time points and acidified by immediately adding 1.0 μL of neat formic acid. 30 μL of each sample was injected to the column to record the chromatogram]. The resulting refolding mixture was centrifuged at 9,000 rcf and 4°C for 30 min before loading to a 5 mL QHP column (GE Healthcare, cat #17-1154-01) at a flow rate of 5 mL/min. After washing the column with 50 mL of Q Buffer A (50 mM HEPES, pH 8.7), the protein was eluted by a gradient of 0–70% Q Buffer B (Q Buffer A with 0.7 M NaCl). Peak fractions with A_{280} >700 mU were pooled. The Q peak fractions were pooled, concentrated to 6–10 mg/mL, and buffer exchanged with 10 mM HEPES, pH 7.1. The final V21H4 antibody solution was filtered through a 0.22-μm filter and stored at 4°C.

Conjugation of V21H1 to Urease

10 mg of V21H1 antibody was activated with cross-linker at an antibody to cross-linker molar ratio of 1:2.4 by adding 70.4 μL of $SM(PEG)_2$ (10.0 mg/mL in DMF) stock solution to the V21H1 antibody while vortexing. The reaction solution was incubated at room temperature for 90 min. The reaction was quenched by adding 300 mM of Tris buffer (pH 7.6) to a final concentration of 10 mM and incubating at room temperature for 10 min. The unconjugated, hydrolyzed, and quenched cross-linker was removed with a 20 mL G25 desalting column pre-equilibrated with 50 mM Tris buffer containing 50 mM NaCl and 1 mM EDTA, pH 7.1. After removing the excess cross-linker, the desalting column fraction was pooled and a 100 μL sample was collected for intact protein mass spectrometric analysis and peptide mapping analysis to evaluate the activation sites on the V21H1 antibody. The remaining pooled fraction was chilled in an ice-water bath for 5 min. 20 mg of HPU was thawed and incubated in another ice-water bath for 5 min. The chilled HPU solution was poured into the activated V21H1 antibody solution while stirring. The stirring continued in an ice-water bath for 5 min, and then the reaction solution was moved to a bench at room temperature. After the conjugation reaction solution was incubated at room temperature for 90 min, cysteine solution (200 mM in 300 mM Tris, pH 7–7.5) was added to a final concentration of 5 mM to quench the reaction. The reaction solution was concentrated down to approximately 4 mL by centrifugation in a 15 mL centrifuge filter (MWCO 100 kDa) at 4°C and 2,000 rcf. The resulting concentrated reaction solution was divided into three aliquots before SEC separation. The separation was performed by loading each aliquot of reaction solution to a Superose 6 100/300 GL column (GE) connected to an AKATA FPLC system. The protein was eluted by an isocratic flow at 0.5 mL/min with SEC buffer (50 mM NaCl, 0.2 mM EDTA, pH 7.2) and the major peak fractions of A_{280} >200 mU were pooled. The peak fractions from all three SEC separations were pooled and dialyzed against 1 L of formulation buffer [10 mM histidine, 1% (w/v) sucrose, 0.2 mM EDTA, pH7.0]. The resulting conjugate solution was filtered through a 0.22-μm filter and divided into 0.8 mL aliquots. Aliquots were stored at −80°C.

Conjugation of V21H4 to Urease

20 mg of V21H4 was mixed with TCEP (100 mM in 300 mM Tris buffer, pH 7–7.5) to a final concentration of 1.5 mM and incubated at room temperature for 60 min. The excess TCEP and the resulting cysteamine were removed by a 25 mL G25 desalting column using Tris-EDTA buffer (50 mM Tris, 1 mM EDTA, pH 7.1). The resulting desalting fraction was pooled in a 40 mL beaker and diluted with Tris-EDTA buffer to a total volume of 30 mL. The activation reaction was performed by quickly dispensing 0.420 mL of $BM(PEG)_2$ stock solution (10 mg/mL in DMF) into the V21H4 antibody solution in the beaker while stirring. After incubation at room temperature for 10 min, the reaction solution was transferred to a 200 mL Amicon diafiltration concentrator with a filter membrane (MWCO 5 kD) and mixed with Tris-EDTA buffer up to 100 mL. The excess cross-linker was removed by connecting the diafiltration concentrator to a 70 psi nitrogen source and concentrated down to 20 mL while stirring. After five cycles of dilution and concentration, the diafiltration concentrator was detached from the nitrogen source and a 100 μL sample was collected to determine the antibody activation sites (using intact protein mass spectrometric analysis and peptide mapping analysis). Tris-EDTA buffer was added to the concentrator to dilute the solution up to the 50 mL marker. The concentrator with the activated V21H4 antibody was chilled in an ice-water bath for 10 min while stirring. After completely thawing at 4°C, 80 mg of HPU was incubated in another ice-water bath for 5 min and then poured into the activated V21H4 antibody solution in the concentrator while stirring in its ice-water bath. After stirring in the ice-water bath for 5 min, the concentrator with the reaction solution was moved to a lab bench and incubated at room temperature for 90 min. The conjugation reaction was quenched by adding cysteine (100 mM in 300 mM Tris, pH 7–7.5) to a final concentration of 5 mM. After quenching the reaction at room temperature for 5 min, the reaction solution was transferred to another container and the concentrator was cleaned and re-installed with a new filtration membrane (MWCO 100 kDa). The reaction solution was transferred back to the concentrator and formulation buffer [10 mM histidine, 1% (w/v) sucrose, and 0.2 mM EDTA, pH 7.0] was added to the 160 mL marker. The concentrator was connected to a 10 psi nitrogen source and concentrated down to 20 mL while stirring. After the dilution–concentration cycle was repeated four times, the diafiltration concentrator was detached from the nitrogen source and the V21H4-DOS47 conjugate solution was transferred to a

new container and diluted to 40 mL. The conjugate solution was filtered through a 0.22-μm filter and divided into 0.8 mL aliquots. The aliquots were stored at −80°C.

Size Exclusion Chromatography

A Waters 2695 HPLC system with a 996 PAD was employed with Empower 2 software for data acquisition and processing. Chromatograms were recorded over 210–400 ± 4 nm with the signal at 280 nm extracted for processing. Separation was performed on a Superose 6 100/300 GL column (GE). Proteins were eluted in 10 mM phosphate, 50 mM NaCl, and 0.2 mM EDTA, pH 7.2. Separation was carried out with an isocratic flow at 0.5 mL/min after injection of a certain volume of neat samples. The column temperature was kept at room temperature, while the sample temperature was controlled at 5 ± 2°C.

SDS-PAGE

A Bio-Rad Mini Gel Protein Electrophoresis kit and a Bio-RAD Molecular Imager Gel Doc XR+ with ImageLab software were employed to analyze V21-DOS47 CRs. 10 μg of protein samples were mixed with 60 μL of protein gel loading buffer and the mixture was heated to 70°C for 10 min. Denatured samples were loaded (10 μL/well) to a 4–20% Tris–Glycine gel (Invitrogen, cat #XP04200) and electrophoresis was performed at a constant voltage of 150 V with current <40 mA until the electrophoresis front reached the gel bottom. After washing, staining, and destaining, the gel image was scanned with the Gel Doc XR+ imager for analysis. SDS-PAGE was also used to calculate the average number of antibodies conjugated per urease molecule. This was determined by interrogating the intensities of the five bands in the main cluster [see Ref. (9) for further details]. All CRs reported are average values.

ELISA Assays

A 96-well plate was coated with 100 μL/well of goat anti-human IgG-Fc (Sigma, 5 μg/mL in PBS) at room temperature for 6 h and then blocked with 200 μL/well of 3% BSA/PBS at 2–8°C overnight. After washing 2× with T-TBS (50 mM Tris, 0.15 M NaCl, pH 7.6, containing 0.05% Tween-20), 100 μL/well of VEGFR1/Fc, VEGFR2/Fc, or VEGFR3/Fc [R&D Systems, 0.25 μg/mL in TB-TBS (0.1% BSA/T–TBS)] was added and the plate was incubated at room temperature for 1 h with gentle shaking. After washing 3× with T-TBS, 100 μL/well of antibody–urease conjugate or biotinylated antibody dilutions (in TB-TBS) were added and the plate was incubated at room temperature for 2 h with gentle shaking. For antibody–urease conjugates, plates were washed 3× with T-TBS, 100 μL/well of rabbit anti-urease (1/6,000 or 1/10,000-fold dilution in TB-TBS, Rockland) was added and the plate was incubated at room temperature for 1 h with gentle shaking. For all samples, the plate was washed 3× with T-TBS and 100 μL/well of goat anti-rabbit-AP (1/8,000-fold dilution in TB-TBS, Sigma) was added to detect antibody–urease conjugates or streptavidin–alklaine phosphatase (0.5 μg/mL in TB-TBS, Sigma) was added to detect biotinylated antibodies, and the plate was incubated at room temperature for 1 h with gentle shaking. After washing 3× with T-TBS, 100 μL/well of substrate (4-nitrophenyl phosphate disodium salt hexahydrate, Fluka, 1 mg/mL in diethanolamine substrate buffer, Pierce) was added to each well and incubated at room temperature for 5–15 min with gentle shaking. The absorbance at 405 nm (A_{405}) of each well was acquired by scanning the plates with a UV–Vis spectrophotometer.

Urease Activity Assay

Urease catalyzes the hydrolysis of urea to ammonia. One unit of urease activity is defined as the amount of enzyme that liberates 1 μmol of ammonia per minute at 25°C at pH 7.3. V21H4-DOS47 samples were diluted in sample dilution buffer [0.02 M potassium phosphate containing 1 mM EDTA and 0.1% (w/v) BSA, pH 7.3]. 100 μL of the diluted sample was mixed with 2.00 mL of 0.25 M urea (in phosphate buffer containing 0.3 M sodium phosphate and 0.5 mM EDTA, pH 7.3), and incubated at 25 ± 0.1°C for 5 min, then the reaction was quenched by adding 1.00 mL of 1.0 N HCl. To determine the concentration of ammonium ion produced in the enzyme reaction solution, 100 μL of the quenched reaction solution was mixed with 2.00 mL of phenol solution (0.133 M phenol containing 0.25 mM sodium nitroferricyanide) in a 15 mL testing tube. After 30 s, 2.50 mL of NaOH–NaOCL solution (0.14 N NaOH containing 0.04% sodium hypochlorite) was added to the testing tube, mixed, and incubated at 37°C for 15 min. The absorbance of the solution was determined at 638 nm with the reagent reaction solution (without sample) as the blank. The urease enzyme activity was calculated according to the following equation: $U/mL = D \times (A \times Tc \times Te)/(5 \times E \times Sc \times Se)$ where A = absorbance at 638 nm, Tc = total volume of color reaction (4.60 mL), Te = total volume of enzyme reaction (3.10 mL), E = molar extinction coefficient of indophenol blue per assay condition (20.10 mM^{-1} cm^{-1}), Sc = sample volume for color reaction (0.10 mL), Se = sample volume for enzyme reaction (0.10 mL), and D = dilution time. The protein concentration of each sample was determined with a Sigma total protein kit (cat #TP0200) following the manufacturer's instructions. Urease activity/milligram of conjugate was calculated by dividing the urease activity (units per milliliter) by the amount of protein tested (milligrams per milliliter). Specific urease activity was calculated by dividing the activity/mg conjugate by the proportion of the conjugate's mass which was composed of urease.

Western Blot

V21H4-DOS47 test samples and controls were resolved by SDS-PAGE gel electrophoresis and then transferred to a nitrocellulose membrane using a Bio-Rad blot kit. 1.2 μg of HPU and 4.0 μg of V21H4 as controls and 2.0 μg of V21H4-DOS47 samples were mixed with 60.0 μL of protein gel loading buffer. The resulting sample mixtures were denatured by heating to 60°C for 10 min and 10 μL of each sample was loaded per lane. Duplicate blots were made from gels run in parallel for urease and V21H4 antibody probing. For urease detection, a rabbit anti-urease IgG (Rockland) was used. To detect the V21H4 antibody, a rabbit anti-llama IgG (ImmunoReagents Inc.) was used. A goat anti-rabbit IgG conjugated to AP (Sigma) was used as the secondary visualization antibody. Final development of the Western blots was performed with AP buffer containing NBT/BCIP.

Mass Spectrometry

A Waters Xevo G2 QTOF mass spectrometer and an Acquity UPLC system H class were employed for all mass spectrometry analyses. A lock mass of 785.8426 Da was applied for real time point to point mass calibration. LC-MS data acquisition was controlled by Masslynx V4.1 software.

Intact Protein Mass Spectrometry Analyses

Cross-linker-activated antibody samples were reacted with 5 mM cysteine at room temperature for 30 min, diluted to 0.5–1 mg/mL in water, and acidified by adding neat formic acid to a final concentration of 1% (v/v). A BEH300 C4 (1.7 µm, 2.1 × 50 mm) column was used. The column temperature was set at 60°C and Solvent A (0.025% v/v TFA in water) and Solvent B (0.025% TFA in acetonitrile) were used for UPLC separation. The UPLC was performed with a flow rate of 0.15 mL/min with a gradient from 20 to 60% Solvent B over 30 min. LC-MS TIC (total ion counts) data acquisition was carried out in an *m/z* range of 500–3,500 Da in resolution mode with a scan rate of 0.3/s, capillary voltage 3.0 kV, sample cone voltage 40 V, extraction cone voltage 4.0 kV. Ion source temperature was set at 100°C and desolvation temperature was set at 350°C. Desolvation gas flow rate was 600 L/h. A real time lock mass TIC raw data set (scan/20 s) was acquired with 100 fmol/µL Glu-Fib B at a flow rate of 6.0 µL/min. Mass spectrometric raw data were processed with BiopharmaLynx software (v 1.2) in intact protein mode with a resolution of 10,000. Mass match tolerance was set at 30 ppm, and the protein sequence of each antibody containing one disulfide bond was input as the match protein for protein match searches.

Tryptic Digestion of V21H1-SM(PEG)$_2$-Cys and V21H4-BM(PEG)$_2$-Cys

The cross-linker-activated antibody samples were reacted with 10 mM cysteine at room temperature for 30 min and then diluted to 0.5 mg/mL with 100 mM ammonia hydrogen carbonate. Neat acetonitrile was added to the diluted sample solution to a final concentration of 20% (v/v). Trypsin/Lys-C mix (Promega, cat #V507A) was added at a protein:protease ratio of 20:1 and digested at 37°C for 16–20 h. DTT was added to the digested sample to a final concentration of 10 mM and samples were incubated at 37°C for 30 min to reduce the core disulfide bond. The digestion was stopped by adding neat formic acid to 1% (v/v) before mass spectrometry analysis.

Tryptic Digestion of V21H4-DOS47

100 µg of V21H4-DOS47 was mixed with DTT to a final concentration of 10 mM and neat acetonitrile was added to a final concentration of 20% (v/v). To reduce the disulfide bond and denature the conjugated proteins, the sample mixture was heated at 60°C for 30 min. The denatured protein precipitate was pelleted by centrifugation at 16,000 rcf at room temperature for 5 min. 5.0 µL of 0.20 M iodoacetamide and 100 µL of water were added to the pellet then mixed by vortexing. The suspension was centrifuged at 16,000 rcf at room temperature for 5 min and the supernatant was discarded. The resulting pellet was dissolved in 100 µL of Tris–guanidine buffer (4 M guanidine chloride, 50 mM Tris, 10 mM $CaCl_2$, and 10 mM iodoacetamide, pH 8.0). After this alkylation reaction was performed at room temperature in the dark for 30 min, the reaction was quenched with 5 mM DTT. The resulting solution was diluted four times with Tris buffer (50 mM Tris, 10 mM $CaCl_2$, pH 8.0). Trypsin/Lys-C mix was added to the diluted sample solution at a protein:protease ratio of 25:1. After the digestion was performed at 37°C for 16–20 h, the reaction was stopped by adding neat formic acid at a final concentration of 1% (v/v).

LC-MS^E Peptide Mapping of V21H1-SM(PEG)$_2$-Cys, V21H4-BM(PEG)$_2$-Cys, and V21H4-DOS47 Tryptic Digests

A BEH300 C18 (1.7 µm, 2.1 mm × 150 mm) column was used for UPLC separation. The column temperature was set at 60°C. Solvent A (0.075% v/v formic acid in water) and Solvent B (0.075% formic acid in acetonitrile) were used for peptide elution. UPLC was performed with a flow rate of 0.15 mL/min. A gradient of 0–30% Solvent B in 50 min was used for the separation of the tryptic digests of V21H1-SM(PEG)$_2$-Cys and V21H4-BM(PEG)$_2$-Cys samples. For the tryptic digests of V21H4-DOS47, a gradient of 0–45% Solvent B in 150 min was used. LC-MS^E TIC (total ion counts) data acquisitions were carried out in an *m/z* range of 50–2,000 Da in resolution mode with a scan rate of 0.3/s, capillary voltage 3.0 kV, sample cone voltage 25 V, and extraction cone voltage 4.0 kV. Ion source temperature was set at 100°C and desolvation temperature was set at 350°C. Desolvation gas flow rate was 600 L/h. A real time lock mass TIC raw data set (scan/20 s) was acquired with 100 fmol/µL Glu-Fib B at a flow rate of 3.0 µL/min. With the instrument setup, two interleaved scan functions are applied for data acquisitions. The first scan function acquires MS spectra of intact peptide ions in the sample while applying no energy to the collision cell. The second scan function acquires data over the same mass range; however, the collision energy is ramped from 20 to 60 eV. This scan is equivalent to a non-selective tandem mass spectrometric (MS/MS) scan and allows for the collection of MS^E fragment spectra from the ions in the preceding scan. The high energy collision induced fragmentation randomly cleaves peptide backbone bonds. For each C-N peptide backbone bond cleaved, the amino-terminal ion generated is called the "*b*" ion and the C-terminal ion generated is called the "*y*" ion. In **Tables 1**–**3**, the column entitled "MS/MS *b*/*y* Possible" indicates the theoretical maximum number of *b* and *y* ions that would be produced for each peptide if all peptide bonds in the protein were equally likely to be broken. The column entitled "MS/MS *b*/*y* Found" indicates the actual number of *b* and *y* ions identified for each peptide. The identification of *b*/*y* ions provides unambiguous confirmation of peptide identity. Mass spectrometric raw data were processed with BiopharmaLynx software (v 1.2) in peptide map mode with a resolution of 20,000. A lock mass of 785.8426 Da was applied for real time point to point mass calibration. The low energy MS ion intensity threshold was set at 3,000 counts and the MS^E high energy ion intensity threshold was set at 300 counts. Mass match tolerances were set at 10 ppm for MS and at 20 ppm for MS^E data sets. Peptides with one missed cleavage site were included in mass match searching. V21H1, V21H4, and urease (Uniprot P07374)

TABLE 1 | List of identified peptides and activation sites of V21H1-$(PEG)_2$-Cys.

Tryptic peptide	Activation site	Calculated mass (Da)	MS/MS *b/y* possible	MS/MS *b/y* found	Intensity	Mass match error (ppm)	% of activation
T001		1,985.0364	38	37	28847130	−2.4	
T001*	M_1-SM$(PEG)_2$-Cys	2,416.1726	38	32	5688300	0.2	15.7
T001–002		2,730.3904	54	28	1681792	0.8	
T002		763.3647	14	9	14953790	0.9	
T002–003		2,066.9456	36	2	16053	2.8	
T003		1,321.5913	20	18	87904800	−2.4	
T003–004		180.8562	30	nd	nd	nd	
T004		499.2754	8	7	238539	0.4	
T004–005		784.4191	12	9	1334242	1.1	
T004–005*	K_{44}-SM$(PEG)_2$-Cys	1,215.5553	12	6	369637	0.9	18.4
T005		303.1543	2	0	61996	−3	
T005–006		2,503.1868	42	28	5351105	−1.2	
T006		2,218.043	38	33	20205530	−0.2	
T006–007		2,431.1655	42	10	203405	−3	12.4
T006–007*	K_{66}-SM$(PEG)_2$-Cys	2,862.3018	42	29	2900557	−0.1	
T007		231.1331	2	1	147694	−2.2	
T007–008		835.4664	12	9	1990138	−2.8	
T008		622.3439	8	6	19702980	0	
T008–009		1,050.5458	16	11	747025	0.1	
T009		446.2125	6	5	269841	−1.3	
T009–010		3,129.49	54	nd	nd	nd	
T009–010*	K_{77}-SM$(PEG)_2$-Cys	3,560.6262	54	31	4111249	1.9	3.6
T010		2,701.2881	46	36	108301696	−2.7	
T010		2,701.2881	46	36	108301696	−2.7	
T010*	K_{88}-SM$(PEG)_2$-Cys	3,132.4241	46	23	1836133	−0.8	1.7
T010–011		6,145.7744	108	nd	nd	nd	
T010–011	K_{101}-SM$(PEG)_2$-Cys	6,576.9103	60	nd	nd	nd	
T011		3,462.4971	60	7	105092	1.9	
T011–012		3,590.592	62	43	48704060	0.1	
T011–012*	K_{131}-SM$(PEG)_2$-Cys	4,021.7283	62	12	258662	−1.7	0.5
T012		146.1055	0	nd	nd	nd	
T012	K_{132}-SM$(PEG)_2$-Cys	577.2418	0	nd	nd	nd	

Thick boxes (also shaded blue) around sets of tryptic peptides indicate related groups of peptides used to calculate percentage of activation for each activation site.
nd, not detected.
**indicates the modified version of the peptide.*

protein sequences were, respectively, input into the sequence library for peptide matching/identification. Variable modifiers, including deamidation N, deamidation succinimide N, oxidation M, +K, +Na, and carbamidomethyl C (for alkylated cysteine) were applied for peptide map analysis. SM$(PEG)_2$-Cys (429.1206 Da) was set as a variable modifier to identify the activation sites of V21H1 conjugation, whereas BM$(PEG)_2$-Cys (431.1362 Da) was input as a variable modifier to identify the activation sites of V21H4 conjugation. For the V21H4-DOS47 tryptic digests, GGGEEDDGC-BM$(PEG)_2$ (1,145.3453 Da) was set as a variable modifier to identify the conjugation sites on urease.

Flow Cytometry

293 or 293/KDR cells were detached from flasks using non-enzymatic cell dissociation buffer (Sigma). Cells were centrifuged at 300 × *g* for 5 min and then resuspended in staining buffer at 10^6 cells/mL (PBS with Ca^{2+} and Mg^{2+}, 0.02% NaN_3, 2% FBS). 100 µL of cells was added to wells of a 96-well plate. The plate was centrifuged at 350 × *g* for 4 min, buffer removed, and then cells were resuspended in 50 µL of antibody–urease conjugate or biotinylated antibody (diluted in staining buffer) and then incubated at 2–8°C for 1 h. For cells stained with antibody–urease conjugates, cells were washed 3× with staining buffer and then resuspended in mouse anti-urease (Sigma, cat #U-4879) at 5.8 µg/mL (diluted in staining buffer) and incubated for 30 min at 2–8°C. For all samples, cells were washed 3× with staining buffer and then resuspended in AF488-anti-mouse IgG (Jackson, cat #115-545-164) at 3 µg/mL (diluted in staining buffer) for antibody–urease samples or with PE-SA (Biolegend, cat #405204) at 133 ng/mL (diluted in staining buffer) for biotinylated antibodies. All cells were incubated for 30 min at 2–8°C in the dark, washed 3× with staining buffer, then resuspended in 1% paraformaldehyde (diluted in PBS). The plate was incubated for 15 min at room temperature, covered with tin foil. The plate was then centrifuged as above, paraformaldehyde removed, and the cells were resuspended in staining buffer. The plate was covered in tin foil and stored at 2–8°C until analysis using a Guava flow cytometer and guavaSoft software (Millipore). S/N values are the ratio of V21H4-DOS47 binding to 293/KDR cells vs V21H4-DOS47 binding to 293 cells or the ratio of biotin-V21H4 vs biotin-isotype control antibody (anti-CEACAM6) binding to 293/KDR cells.

TABLE 2 | List of identified peptides and activation sites of V21H4-$(PEG)_2$-Cys.

Tryptic peptide	Activation site	Calculated mass (Da)	MS/MS *b/y* possible	MS/MS *b/y* found	Intensity	Mass match error (ppm)	% of activation
T001		1,985.0364	38	34	25539260	1.2	
T001–002		2,730.3904	54	17	55292	0.6	
T002		763.3647	14	8	7457241	−0.7	
T002*	C_{23}-BM$(PEG)_2$-Cys	1,192.4852	14	5	169047	2.1	2.2
T002–003		2,066.9456	36	nd	nd	nd	
T003		1,321.5913	20	18	29459300	−0.5	
T003–004		1,802.8562	30	nd	nd	nd	
T004		499.2754	8	5	254649	−2.6	
T004–005		784.4191	12	8	1083205	−2.7	
T005		303.1543	2	1	69756	−4	
T005–006		2,503.1868	42	27	4016949	3	
T006		2,218.043	38	35	10074250	−0.4	
T006–007		2,431.1655	42	2	57264	4	
T007		231.1331	2	1	168759	−4.3	
T007–008		835.4664	12	10	1210281	−2.9	
T008–009		1,050.5458	16	6	92188	−2.4	
T009		446.2125	6	5	247926	−0.9	
T009–010		3,129.49	54	nd	nd	nd	
T010		2,701.2881	46	35	62124531	1.3	
T010*	C_{97}-BM$(PEG)_2$-Cys	3,130.4087	46	7	334626	3.3	0.5
T010–011		5,613.6455	98	nd	nd	nd	
T011		2,930.3682	50	37	18549570	−1.4	
T011–012		3,749.6023	68	nd	nd	nd	
T012		837.2446	16	8	150911	−2.1	
T012*	C_{136}-BM$(PEG)_2$-Cys	1,266.3652	16	10	1885506	−0.2	92.6

Thick boxes (also shaded blue) around sets of tryptic peptides indicate related groups of peptides used to calculate percentage of activation for each activation site.
nd, not detected.
**indicates the modified version of the peptide.*

TABLE 3 | ESI LC-MS^E peptide mapping analysis: Identification of urease cysteine residues modified by V21H4-$(PEG)_2$-Cys.

Conjugation sites searched from the urease side

Urease peptide	Conjugation site	Calculated mass (Da)	MS/MS *b/y* Possible	MS/MS *b/y* found	Intensity	Mass match error (ppm)	% of conjugation
1:T010*	UC_{59}-VC_{136}	2,784.2053	28	10	335045	2.6	2.6
1:T026*	UC_{207}-VC_{136}	1,939.6624	12	0	10296	1.9	0.6
1:T063*	UC_{663}-VC_{136}	2,316.7554	18	4	46812	2.9	4.2
1:T081*	UC_{824}-VC_{136}	2,633.1372	26	13	495879	2.1	26.7

Conjugation sites searched from the antibody side

V21H4 C-term peptide	Conjugation site	Calculated mass (Da)	MS/MS *b/y* possible	MS/MS *b/y* found	Intensity	Mass match error (ppm)	% of conjugation
2:T012	na	837.2446	16	2	10403	−3.9	0.4
2:T012*	-UC_{824}	2,633.1472	16	7	1609854	1.2	59.1
2:T012*	-UC_{663}	2,784.2153	16	5	726682	1.6	26.7
2:T012*	-UC_{59}	2,316.7654	16	4	343529	−1.4	12.6
2:T012*	-UC_{207}	1,939.6724	16	0	33038	−3.6	1.2

na, not applicable.
**indicates the modified version of the peptide.*

RESULTS

Production and Purification of V21H1

When generating single domain antibodies for immunoconjugate drugs, HP antibodies must be produced at high yield and with controllable processes, including expression, protein refolding, and purification. Other considerations include the following: the pI of the antibody should be such that the antibody conjugate is stable and soluble at physiologic pH, the properties of the antibody should be suitable for the conjugation chemistry, and the modifications of the antibody residues during conjugation reactions should not compromise the affinity of the antibody binding to its antigen.

The V21 camelid antibody consists of 122 amino acids (ending at S_{122}, **Figure 1A**). Eleven amino acids were added to the C-terminus of the V21 antibody in order to generate V21H1. By

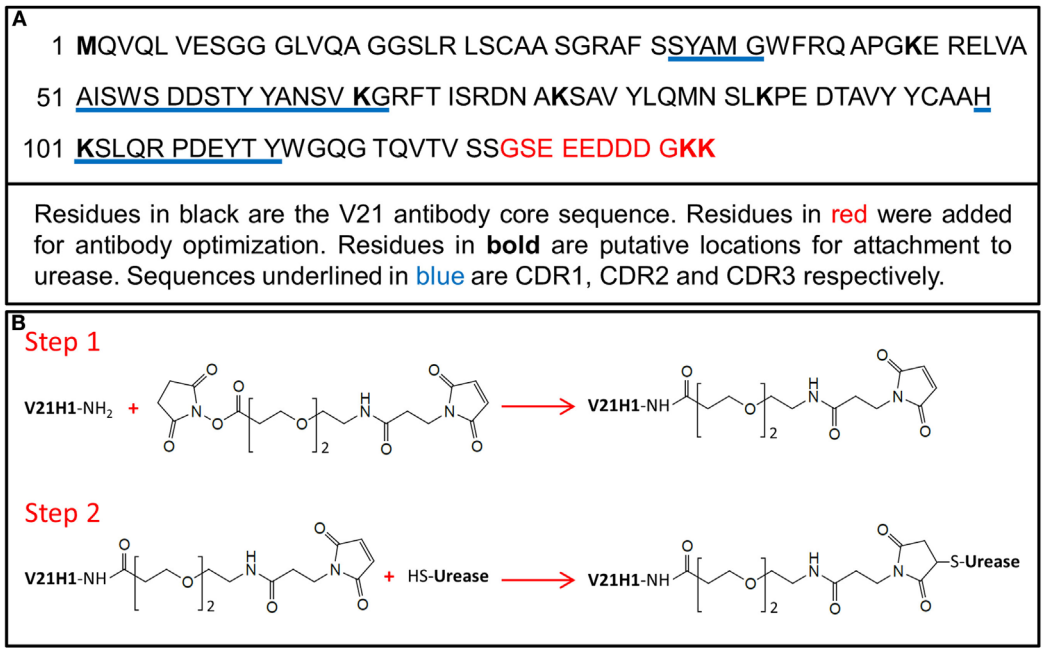

FIGURE 1 | **(A)** Amino acid sequence of the V21H1 antibody. **(B)** Description of conjugation strategy used to conjugate V21H1 to urease to generate V21H1-DOS47. Step 1 is the activation of the antibody using $SM(PEG)_2$. Step 2 conjugates the activated antibody to urease.

adding these amino acids, the pI of the antibody was changed from 8.75 to 5.44, as required for conjugate stability and solubility. The heterobifunctional chemical cross-linker $SM(PEG)_2$ reacts with amine and sulfhydryl groups and was selected for use in conjugating V21H1 to urease (**Figure 1B**). There are five lysine residues in the core V21 sequence, two of which (Lys_{66} and Lys_{101}) are located in the CDR2 and CDR3 sequences, respectively. As these amino acids could be modified by the amine conjugation chemistry utilized by $SM(PEG)_2$, potentially altering antibody activity, two extra lysine residues were added to the antibody C–terminus to minimize this probability.

V21H1 was expressed primarily in the cytosolic solution of BL21(DE3) bacteria, with virtually no expression in inclusion bodies. Therefore, after cell lysis, the antibody was separated from bacterial proteins by ethanol crystallization and cation exchange chromatography. After antibody refolding, the native antibody was further purified by anion exchange chromatography. To confirm that the molecular mass of the purified antibody matched the designed protein sequence, LC-MS intact protein analysis was performed. No impurity proteins were detected from the LC-MS TIC chromatograms and the detected molecular mass of V21H1 matched the theoretical value calculated from its protein sequence within 30 ppm mass match error (data not shown). However, the yield of purified V21H1 was very low (4–6 mg/L of culture) and the purification processes used are not suitable for large-scale cGMP production.

Cross-Linker Activation of V21H1

V21H1 was activated by $SM(PEG)_2$ at pH 7.0 using conditions previously found to be optimal for activation of AFAIKL2 antibody with SIAB in the production of the antibody–urease conjugate L-DOS47. Since the NHS-ester reaction is the same for SIAB and $SM(PEG)_2$ and the LC-MS spectra are similar for AFAIKL2 and V21H1 reaction products (data not shown), these conditions should also be optimal for activation of V21H1 with $SM(PEG)_2$.

Only the NHS-ester group of $SM(PEG)_2$ can react with V21H1. The two cysteine residues in the V21H1 antibody form a disulfide bond and are, thus, unavailable to react with the maleimido end of the cross-linker. The primary amines from the antibody N-terminus and the lysine residues from the protein sequence can all potentially react with the NHS-ester of the cross-linker. The maleimido end of the antibody-carrying cross-linker then reacts with cysteines on the surface of urease molecules. The probability of each amine being activated depends on its accessibility due to its surrounding native structure. To avoid urease dimer and polymers forming in the second reaction step, ideally only one amine per antibody would be activated by the NHS-ester. However, since multiple primary amines are present in each antibody, it is statistically inevitable that some V21H1 antibodies will be activated by more than one cross-linker molecule. The optimal activation condition was selected, which minimizes the percentage of antibodies that are activated by more than one cross-linker while maximizing the total amount of activated antibody. To assess the activation distribution, the $SM(PEG)_2$ activated V21H1 was reacted with excess cysteine and evaluated by intact mass spectrometric analysis. The mass spectrum is shown in **Figure 2**. Approximately 50% of the V21H1 was activated by $SM(PEG)_2$ and of the activated antibody, approximately 30% was activated by two cross-linkers. Thus, only 35% of the V21H1 antibody is optimally activated for cross-linking with urease.

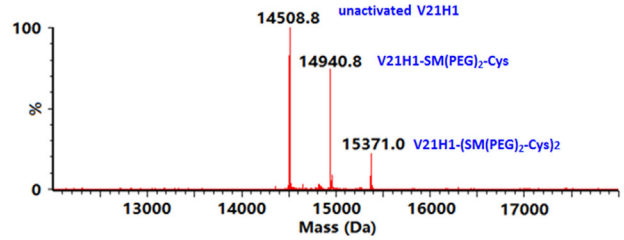

FIGURE 2 | Deconvoluted mass spectrum of the V21H1 antibody after activation by cross-linker and linkage to cysteine showing the distribution of non-activated antibody, antibody activated by one cross-linker, and antibody activated by two cross-linkers.

In order to determine which lysines of V21H1 were targeted by $SM(PEG)_2$, V21H1-$SM(PEG)_2$-Cys was subjected to tryptic digestion followed by LC-MS^E analysis. Trypsin cleaves peptide backbone bonds at the C-terminal side of arginine and lysine residues (unless proline is immediately C-terminal to K or R). If a lysine is activated by $SM(PEG)_2$, the polarity and side-chain structure of the lysine is altered and spatially blocked. Thus, this tryptic site is no longer accessible to the protease. For example, if K_{66} of V21H1 is activated by $SM(PEG)_2$, it is linked to -$SM(PEG)_2$-Cys and is no longer available for tryptic digestion; therefore, a peak with a molecular mass of 2,862.3018 (2,431.1656 + 431.1362) Da should be observed, which represents the -$SM(PEG)_2$-Cys linked lysine-in-middle peptide (ELVAAISWSDDSTYYANSVK_{66}GR)-$SM(PEG)_2$-Cys. In the LC-MS^E peptide mapping analysis, all possible activation sites can be identified by searching all the lysine carrying peptides and the N-terminal peptide with the -$SM(PEG)_2$-Cys (431.1362 Da) as a variable modifier. The detected tryptic peptides along with conjugation sites are listed in **Table 1**.

All tryptic peptides were detected with mass match errors of less than 5 ppm and the amino acid sequence recovery was 100%. Assuming that ESI sensitivity is not affected by the linkage of the modifier, an activation percentage was assessed by comparing the intensity of the cross-linker modified peptide with the sum intensity of all the related peptides. Under the activation conditions used, lysine residue K_{66} in CDR2 was substantially (~25% of the entire activated V21H1 antibody) activated by the cross-linker; however, K_{101} in CDR3 was not modified during cross-linker activation. Surprisingly, the two C-terminal lysine residues that were intentionally added for conjugation chemistry purposes were not modified by the cross-linker.

Production and Purification of V21H4

The antibody V21H4 was designed to improve upon the issues identified during production, purification, and cross-linker activation of V21H1. The amino acid sequence of the V21H4 antibody is shown in **Figure 3A**. As for V21H1, a number of amino acid residues were added to the antibody C-terminus (G_{123}–C_{136}) and the pI of the antibody was adjusted from 8.75 to 5.43. With V21H1, the presence of $SM(PEG)_2$ cross-linker activated K_{66} in the antibody CDR2 region was a concern as this could impair antibody binding affinity. Thus, a cysteine residue (C_{136}) was added to V21H4 for sulfhydryl-to-sulfhydryl cross-linking using a different cross-linker, $BM(PEG)_2$ (**Figure 3B**). The inclusion of a C-terminal cysteine also allowed the antibody to be expressed in bacterial inclusion bodies. As the two core cysteine residues of the V21 antibody form a disulfide bond and are unavailable for chemical conjugation, the additional C-terminal cysteine residue provides a unique activation site for targeted conjugation.

As expected, V21H4 was expressed at high levels in inclusion bodies. After cell lysis, antibody was separated from bacterial matrix proteins by centrifugation. The denatured antibody was purified by cation exchange chromatography to remove nucleic acids and other proteins. The refolding of the V21H4 antibody was performed in an easily controllable manner and was monitored by HPLC (**Figure 3C**).

The refolding process was initiated by mixing the peak fraction of the cation exchange column with refolding buffer. While the folding process was very slow without cystamine, folding was complete in 2 h at room temperature after cystamine was added to a final concentration of 1.2 mM. Anion exchange chromatography was used to isolate the properly folded protein and yields of greater than 80% were generally observed. The typical yield of purified V21H4 is 20–40 mg/L culture, which is considerably higher than that of V21H1. In addition, the method used to produce and purify V21H4 is amenable to scale up and cGMP procedures.

Cross-Linker Activation of V21H4

The C-terminal cysteine of V21H4 is required for conjugation to urease. However, as cystamine was included in the V21H4 refolding buffer, the C-terminal cysteine was modified by forming a disulfide bond with a half cystamine (cysteamine-H). This was confirmed by LC-MS intact protein analysis (**Figure 4A**). Thus, the half cystamine must be removed and the cysteine must subsequently be available for activation by cross-linker. In addition, this removal must occur using a controllable mild reduction under the native conditions to be used for conjugation purposes and it must not reduce the antibody's internal disulfide bond. As shown in **Figure 4B**, after reducing V21H4 with 2 mM TCEP at pH 7.1 for 1 h at room temperature, the detected antibody molecular mass was 14,667.94 Da, suggesting that the protective half cystamine had been removed. In order to confirm that the de-protected cysteine residue was active to the cross-linking reagent, 10 mM iodoacetamide was added to the de-protected V21H4 antibody. After 30 min at room temperature at pH 7.5–8.0, the resulting detected molecular mass was increased to 14,724.83 Da (**Figure 4C**), suggesting a carboxymethyl group (57.05 Da) was alkylated to the cysteine residue. In summary, the C-terminal half cystamine can be removed and the resulting de-protected cysteine is available for chemical conjugation. The alkylated antibody was also digested with trypsin and evaluated by LC-MS^E peptide mapping. The LC-MS^E peptide map (data not shown) covered 100% of the amino acid sequence and the C-terminal cysteine was specifically and effectively alkylated, confirming the specificity of the de-protective reduction reaction and the suitability of the C-terminal cysteine in targeted sulfhydryl cross-linking chemistry.

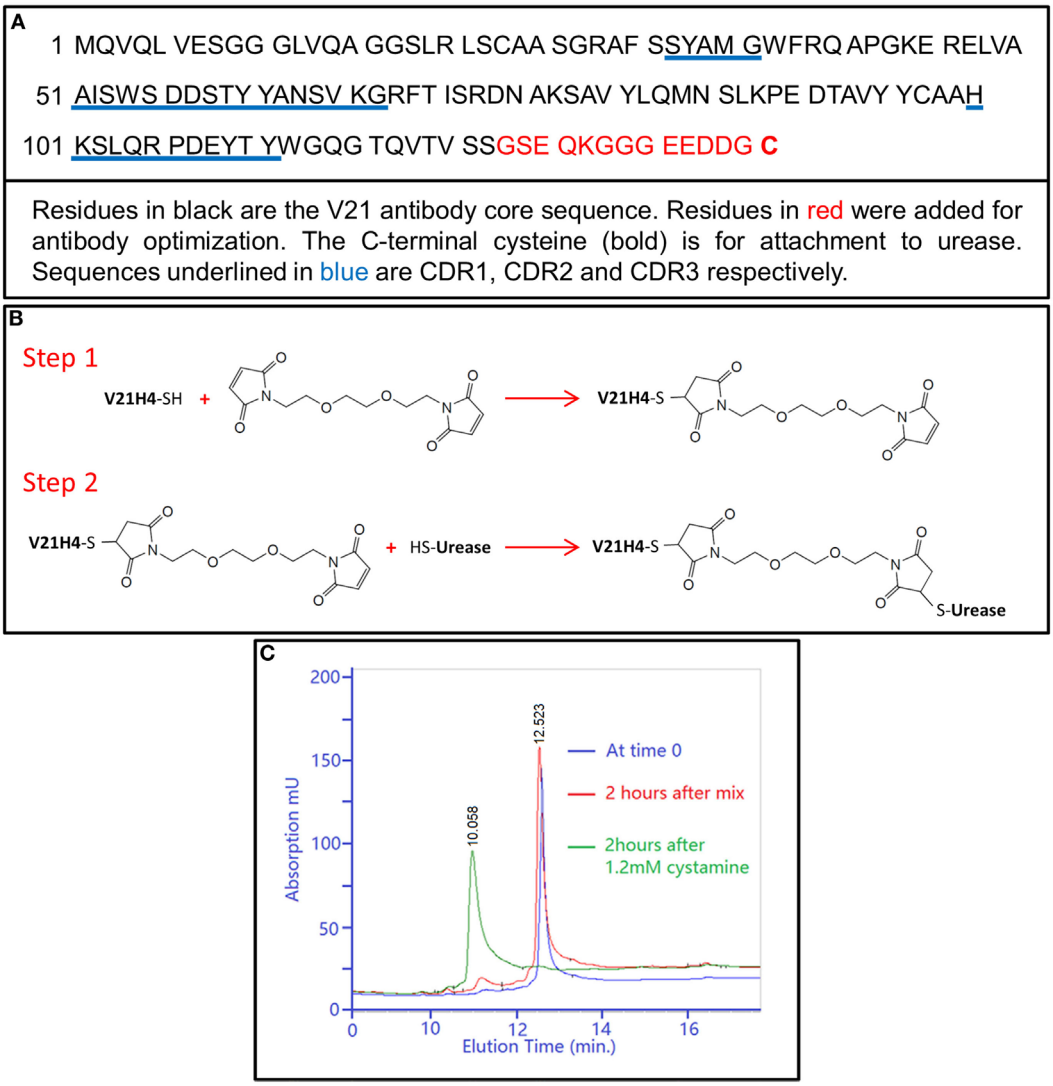

FIGURE 3 | **(A)** Amino acid sequence of the V21H4 antibody. **(B)** Description of conjugation strategy used to conjugate V21H4 to urease to generate V21H4-DOS47. Step 1 is the activation of the antibody using $BM(PEG)_2$. Step 2 conjugates the activated antibody to urease. **(C)** RP-HPLC chromatograms of V21H4 samples at different refolding time points. Blue line: sample at refolding time 0, immediately after the SP pooled fraction was mixed with refolding buffer. Red line: refolding time point 2 h after mixing. Green line: refolding sample 4 h after time 0 and 2 h after addition of 1.2 mM cystamine. Unfolded antibody elutes at 12.513 min and folded antibody elutes at 10.958 min.

The V21H4 antibody was activated by the cross-linker $BM(PEG)_2$. As $BM(PEG)_2$ is a homobifunctional cross-linker, it is possible that both maleimido groups of $BM(PEG)_2$ could react with and link two V21H4 molecules, leading to the generation of antibody dimers that cannot conjugate to urease. The frequency of antibody dimers generated depends upon the molar ratio of the reactants, the native hydrophobicity environment of the cysteine residue and the relative mobility of the molecules in the reaction solution. This reaction was performed with a 10:1 cross-linker to antibody molar ratio. In addition, the molecular weight of the cross-linker is 308.29 Da, which is approximately 50-fold less than the molecular weight of the antibody. To evaluate the activated V21H4 antibody, 100 µL of the activated antibody solution was reacted with excess cysteine and evaluated by intact mass spectrometric analysis (**Figure 4D**). Under the experimental conditions used, more than 99% of the V21H4 was coupled to a single cross-linker, leaving the cross-linker's other maleimido group available for the subsequent reaction to urease.

In order to confirm that the C-terminal cysteine was the sole target of $BM(PEG)_2$, V21H4-$BM(PEG)_2$-Cys was subjected to tryptic digestion followed by LC-MS^E analysis. If the C-terminal cysteine is activated by the cross-linker, a peak with a mass of 1,266.3652 Da representing the cross-linker activated peptide $GGGEEDDGC_{136}$-$BM(PEG)_2$-Cys should be detected. If the core disulfide bond is reduced by TCEP before cross-linker activation, then two peaks—one representing the peptide

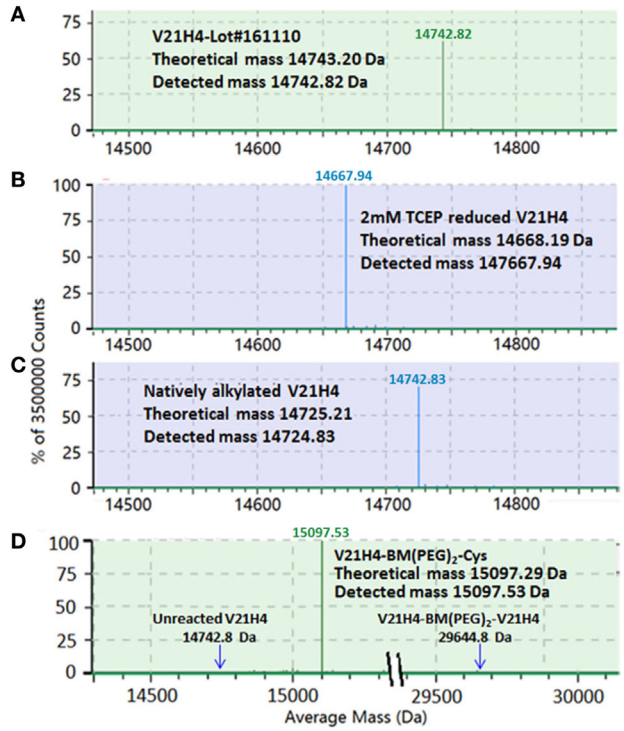

FIGURE 4 | **(A–D)** Screen snapshots of intact protein mass spectra of V21H4 samples from BiopharmaLynx. **(A)** Deconvoluted spectrum of V21H4 showing the attachment of a half cystamine to the C-terminal cysteine by forming a disulfide bond during refolding. **(B)** The deconvoluted spectrum of V21H4 after reduction with 2 mM TCEP showing the detachment of the C-terminal half cystamine. **(C)** The deconvoluted spectrum of the reduced V21H4 after alkylation with iodoacteamide showing the C-terminal cysteine is accessible to a sulfhydryl activation cross-linker. **(D)** Deconvoluted mass spectrum of V21H4 after activation by cross-linker and linkage to cysteine. V21H4 antibody activated by $BM(PEG)_2$ generates a single activated species.

$LSC_{23}AASGR$-$BM(PEG)_2$-Cys (1,192.4852 Da) and the other representing $SAVYLQMNSLKPEDTAVYYC_{97}AAHK$-$BM(PEG)_2$-Cys (3,130.4087 Da) should be identified. The detected tryptic peptides along with the cross-linker activation sites are listed in **Table 2**. All tryptic peptides were detected with mass match errors of less than 5 ppm, and the amino acid sequence recovery was 100%. As expected, more than 90% of the C-terminal cysteine was activated by the cross-linker, and only trace amounts of cross-linker activated core cysteine residues (Cys_{23} and Cys_{97}) were detected. This is a much more desirable scenario than that observed with V21H1 and $SM(PEG)_2$, in which multiple lysines were targeted, including the one in CDR2.

Conjugation of V21H1 and V21H4 to Urease and Initial Characterization

Jack bean urease is a homohexameric enzyme with each subunit approximately 91 kDa. Among the 15 unbound cysteine residues per subunit, five are on the surface of the native structure and are available for linking to single domain antibodies through maleimido cross-linkers (23). Different conjugation chemistries are widely used for protein conjugations. Copper-free click chemistry has been preferentially used in protein labeling and protein–drug conjugations (24) and was a potential option in our conjugations of antibodies to urease. However, either the NHS-ester or maleimido activation step would be needed before performing the click chemistry. Thus, traditional cross-linking chemistries are simpler and are suitable to this particular case.

After V21H1 and V21H4 were cross-linked, they were then conjugated to urease to generate V21H1-DOS47 and V21H4-DOS47, respectively. In both cases, sulfhydryl chemistry was used to conjugate the antibody-linker to urease. SDS-PAGE was performed to evaluate both conjugates (**Figure 5A**). During conjugation, each of the six monomeric urease subunits could potentially be cross-linked with up to five antibody molecules; therefore, under denaturing SDS-PAGE conditions, both V21H1-DOS47 and V21H4-DOS47 would be expected to generate a pattern of six discrete bands ranging from ~90 to 180 kDa. However, it appears that a maximum of four antibodies are conjugated per urease, as only five discrete bands are observed (**Figure 5A**, cluster 1). This suggests that one of the five cysteine residues on the surface of urease has little or no ability to react with maleimide. In addition to the expected five discrete bands, additional clusters of bands are observed for both V21H1-DOS47 and V21H4-DOS47. For V21H1-DOS47, two additional clusters are apparent. Cluster 2 (effective MW from ~200 to 250 kDa) and cluster 3 (effective MW >300 kDa) are likely urease dimers and polymers generated by V21H1 species carrying multiple $SM(PEG)_2$ cross-linkers. While these higher molecular weight species could be composed of multiple native urease molecules, the low levels (less than 5%) of dimer and polymer peaks observed by SEC (**Figure 5B**) suggests that the majority of these species are composed of inter-subunit linkages of a single native urease molecule and not inter-molecular linkages. For V21H4-DOS47, since only the C-terminal cysteine is activated by $BM(PEG)_2$, theoretically only one band cluster should be present. However, as demonstrated in lanes 5 and 6, an additional cluster is observed in the V21H4-DOS47 lanes (MW $\geq$ 150 kDa). The second cluster could be composed of non-covalent dimers that form as the conjugated subunits migrate in the gel. This was confirmed by SDS-PAGE capillary electrophoresis (not shown) in which no dimer clusters were observed. Therefore, V21H4-DOS47 does not contain cross-linked urease dimers or polymers.

SDS-PAGE was also used to determine the antibody:urease conjugation ratio (CR) for each native urease hexamer–antibody conjugate. Band intensities (**Figure 5A**) in cluster 1 depend upon the relative abundance of urease monomers linked to different numbers of antibody molecules. ImageLab software was used to generate histograms corresponding to band intensities and to integrate the peak areas of each histogram. The CR for native urease hexamers was calculated as follows:

$$CR = 6\times\left(PK_1\times 0 + PK_2\times 1 + PK_3\times 2 + PK_4\times 3 + PK_5\times 4\right)/\left(PK_1 + PK_2 + PK_3 + PK_4 + PK_5\right)$$

where PK_i ($i = 1$–5) is the peak area of the urease monomer linked with $i - 1$ antibody molecules.

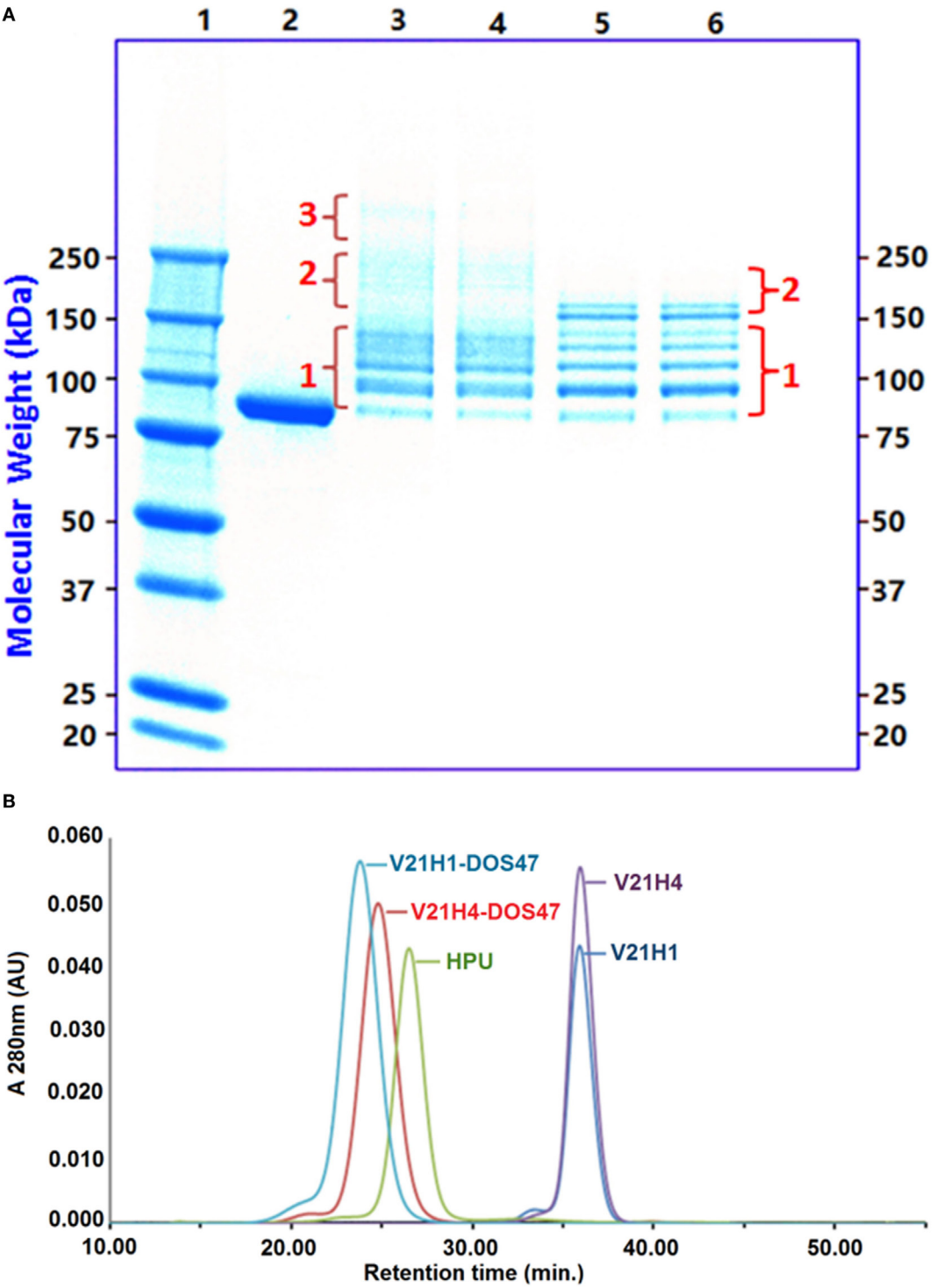

FIGURE 5 | **(A)** SDS-PAGE of V21H1-DOS47 and V21H4-DOS47. Bands labeled in red with 1, 2, or 3 are cluster numbers. Lane 1: molecular weight ladder. Lane 2: high purity urease (HPU). Lanes 3 and 4: V21H1-DOS47. Lanes 5 and 6: V21H4-DOS47. **(B)** Size exclusion chromatograms of V21H1, V21H4, HPU, V21H1-DOS47, and V21H4-DOS47.

Although there is a variable number of antibodies conjugated to each urease monomer, one would predict less variability in the number of antibodies per urease hexamer, as the monomers randomly cluster to form hexamers. This was confirmed by SEC of native V21H4-DOS47 in which the conjugate is observed to migrate as a tight peak (**Figure 5B**). The

V21H4-DOS47 conjugation method reproducibly produced conjugates with 8.7–9.2 antibodies per urease (based on three batches).

The purities and the effective molecular weights of the antibodies, HP urease, and conjugates were assessed by SEC under native conditions (**Figure 5B**). As expected, V21H1 and V21H4 antibodies elute at comparable times (35.9 min). Free HP urease elutes at 26 min. As antibody molecules are linked to urease molecules for both V21H1-DOS47 and V21H4-DOS47, making the conjugates larger than free urease, the conjugates elute earlier than free urease. However, it is interesting that V21H1-DOS47 elutes 1 min before V21H4-DOS47 (22.80 vs 23.80 min). Both conjugates have nearly identical CRs (8.8 antibodies/urease for V21H1-DOS47 and 8.7 antibodies/urease for V21H4-DOS47). The V21H4 antibody has three more amino acids (159.20 Da) than V21H1; however, the theoretically larger V21H4-DOS47 conjugate appears smaller in effective molecular size in SEC than its counterpart V21H1-DOS47. This implies that V21H4-DOS47 is more compact than V21H1-DOS47 under native conditions. The majority of each species is in the monomeric form, with small dimer peaks appearing in front of each monomeric peak. It is notable that the V21H1-DOS47 conjugation procedure requires a SEC step in order to achieve high purity (96%). The SEC step removes urease polymers that are generated by V21H1 antibodies activated by two cross-linkers. However, the SEC step is not necessary to produce V21H4-DOS47, as V21H4 antibodies are activated by one cross-linker only. For V21H4-DOS47, a purity of greater than 97% is typically achieved using only diafiltration to remove unbound V21H4 antibody. As SEC methods are not easily transferred to large-scale GMP processes, it would be technically more difficult and expensive to produce V21H1-DOS47 for clinical use.

Activity of V21H1-DOS47 and V21H4-DOS47

An ELISA assay was performed to evaluate the binding of V21H1-DOS47 (9.2 antibodies/urease), V21H4-DOS47 (8.8 antibodies/urease), and biotin-V21H4 to recombinant VEGFR2/Fc (**Figure 6A**). V21H4-DOS47 (EC_{50} = 44 pM) binds to VEGFR2/Fc with approximately five-fold higher affinity than does V21H1-DOS47 (EC_{50} = 226 pM). As a substantial amount of V21H1 was conjugated to urease *via* the lysine present in CDR2, this is not surprising. V21H4-DOS47 also binds to VEGFR2/Fc with approximately 40-fold higher affinity than does V21H4 antibody alone (EC_{50} = 1.8 nM). This is most likely due to the multivalent nature of the conjugate. As V21H4-DOS47 is the superior conjugate, subsequent characterization was performed for V21H4-DOS47 only.

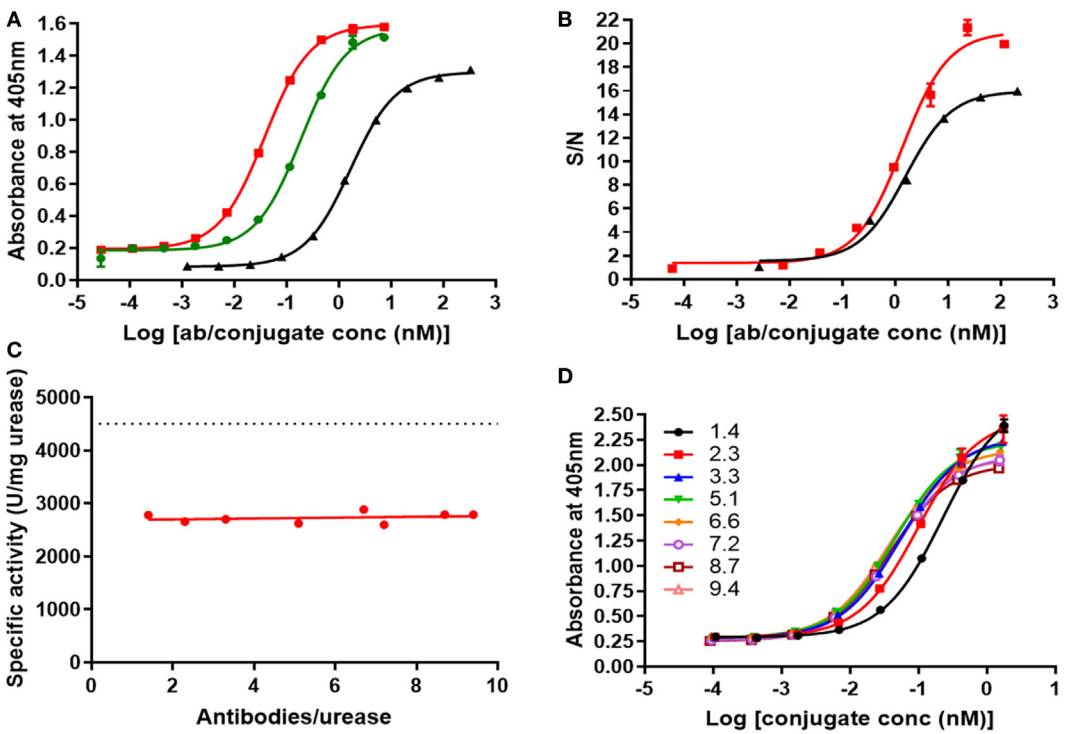

FIGURE 6 | **(A)** ELISA of biotin-V21H4 (black), V21H1-DOS47 (green), and V21H4-DOS47 (red) binding to recombinant VEGFR2. Results shown are representative of two to five experiments performed for each sample and are presented as the means and SE of samples tested in triplicate. **(B)** Binding of biotin-V21H4 (black) and V21H4-DOS47 (red) to VEGFR2 expressed by 293/KDR cells. Binding was quantified by flow cytometry. Results shown are representative of two to three experiments performed for each sample and are presented as the means and SE of samples tested in duplicate. **(C)** Urease enzyme activity of V21H4-DOS47 at different antibody/urease conjugation ratios (CRs). The dotted line represents unconjugated urease activity. **(D)** ELISA of V21H4-DOS47 with different antibody–urease CRs binding to recombinant VEGFR2/Fc. Results shown are representative of two experiments performed for each sample and are presented as the means and SE of samples tested in duplicate.

The ability of V21H4 antibody and V21H4-DOS47 conjugate to bind to cells expressing VEGFR2 (293/KDR) was evaluated by flow cytometry (**Figure 6B**). Biotin-V21H4 (EC_{50} = 1.6 nM) binds to 293/KDR cells with a similar affinity as to recombinant VEGFR2/Fc (EC_{50} = 1.8 nM, **Figure 6A**). This suggests that the VEGFR2 antibody epitope is equally accessible in recombinant VEGFR2/Fc in the ELISA assay and on the cell surface of 293/KDR cells. Interestingly, the binding of V21H4-DOS47 (EC_{50} = 1.2 nM) to the 293/KDR cells is very similar to the binding of biotin-V21H4 antibody to these cells (EC_{50} = 1.6 nM). Although there was an improved affinity observed for V21H4-DOS47 compared to V21H4 antibody in the ELISA assay with VEGFR2/Fc, this was not observed for cell binding. This suggests that the density of VEGFR2 expressed on the surface of 293/KDR cells is lower than in the wells of the ELISA plate.

Several factors contribute to determination of an ideal antibody/urease CR. During the conjugation reaction, the urease molecule is altered by linkage to the V21 antibody; therefore, depending on the CR, urease enzyme activity could be affected. On the other hand, the avidity of the antibody–urease complex increases as more antibodies are coupled to urease. To evaluate the effects of CR on both the urease enzyme activity and on binding activity, V21H4-DOS47 conjugates with different CRs (1.4–9.4 V21H4 per urease) were produced by adjusting the V21H4/HPU molar ratios.

The activity of unmodified urease is approximately 4,500 U/mg. When antibody is conjugated to urease, approximately 40% of the activity is lost (**Figure 6C**). However, the urease enzyme activity is independent of the number of antibodies conjugated, as activity remains consistent at all CRs tested. An ELISA assay using recombinant VEGFR2/Fc was performed to evaluate the binding of conjugates with different numbers of antibodies per urease (**Figure 6D**). When increasing from 1.4 to 2.3 antibodies per urease, the binding of the conjugate to VEGFR2/Fc improves, as indicated by a decrease in EC_{50} values from 226 to 93 pM. Addition of one more antibody (3.3 antibodies/urease) further reduces the EC_{50} to 58 pM. However, addition of subsequent antibodies/urease has a limited benefit: with 9.4 antibodies per urease, the EC_{50} is 31 pM. Thus, there is only a slight improvement in affinity when greater than 3.3 antibodies per urease are present. Thus, a CR of 3.3 antibodies per urease is sufficient for optimal urease activity and conjugate binding.

Additional Characterization of V21H4-DOS47

Dual-panel Western blotting (**Figure 7**) of V21H4-DOS47 was performed to confirm the banding pattern seen by SDS-PAGE. In Western blotting, the dimer and polymer clusters formed in-gel are more prominent than they appeared in SDS-PAGE (**Figure 5A**). When probed with anti-urease antibody, the urease band is visualized at molecular weight ~85 kDa and the bands of urease subunits bound to 1–4 antibodies match with the pattern seen by SDS-PAGE. When probed with an anti-llama antibody, the free urease subunit band is not observed and the antibody–urease conjugate bands are seen in the same pattern as when probed with an anti-urease antibody. The ability of V21H4-DOS47 to be visualized by both the anti-llama and anti-urease antibodies demonstrates the presence of both species in the conjugate.

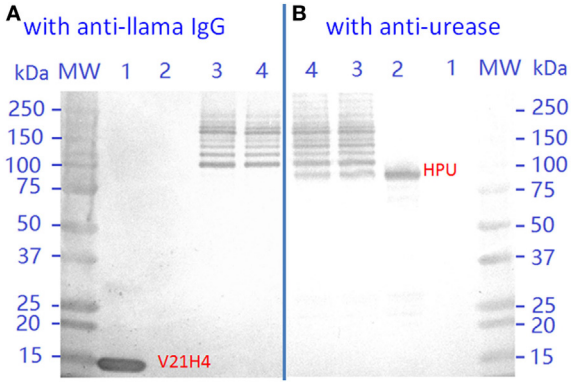

FIGURE 7 | Western blot of V21H4, high purity urease (HPU), and V21H4-DOS47. Blots were probed with **(A)** an anti-llama antibody or **(B)** an anti-urease antibody. Lane MW: molecular weight ladder. Lane 1: V21H4. Lane 2: HPU. Lanes 3 and 4: V21H4-DOS47.

ESI-LC-MS^E peptide mapping analysis was employed to confirm the identities of V21H4 and urease and to identify the conjugation sites of V21H4-DOS47. The LC-MS (TIC) chromatograms of V21H4-DOS47 and HPU are shown in **Figure 8A**. The identified peptides covered 100% of V21H4 and urease protein sequences with mass match errors less than 4 ppm. All identified peptides with greater than three residues were confirmed by elevated energy MS/MS with at least half of the *b*/*y* ions identified. Since only the C-terminal GGGEEDDGC (837.2446 Da) of V21H4 is linked to different cysteine-carrying peptides of urease, the conjugation sites (denoted as UC_x-VC_{136}, where *x* is the amino acid in the urease protein sequence) are those urease peptides modified by GGGEEDDGC-BM$(PEG)_2$ (1,145.3453 Da). To identify those covalent conjugation sites, ESI LC-MS^E raw data of the tryptic digests from V21H4-DOS47 samples were processed by BiopharmaLynx and searched against the urease protein sequence with a variable modifier of 1,145.3453 Da applied to all 15 urease cysteine residues. In order to assess the relative frequency of each conjugation site, the peptide intensities of the conjugated peptides UC_x-VC_{136} were compared with the sum intensities of all the peptides related to UC_x to generate the percentage of conjugation (**Table 3**). Among the 15 cysteine residues of each urease subunit, only 4 were conjugated (consistent with bands observed by SDS-PAGE, **Figure 5A**). The most accessible cysteine is C_{824} (26.7%), followed in order by C_{663} (4.2%), C_{59} (2.6%), and C_{207} (0.6%). No conjugation was detected to cysteine residue C_{592}, which is essential to urease enzyme activity. This is consistent with the observation that urease activity is comparable at all CRs (**Figure 6B**).

Conjugation sites were also identified as V21H4 peptides modified by -UC_x (UC_x + 308.1008 Da). This was done by searching the V21H4 antibody protein sequence against -UC_x as the variable modifier to the C-terminal cysteine of V21H4 (**Table 3**). Among the identified tryptic peptides, 0.4% of them were unmodified (T:012). This trace amount of peptide could be the

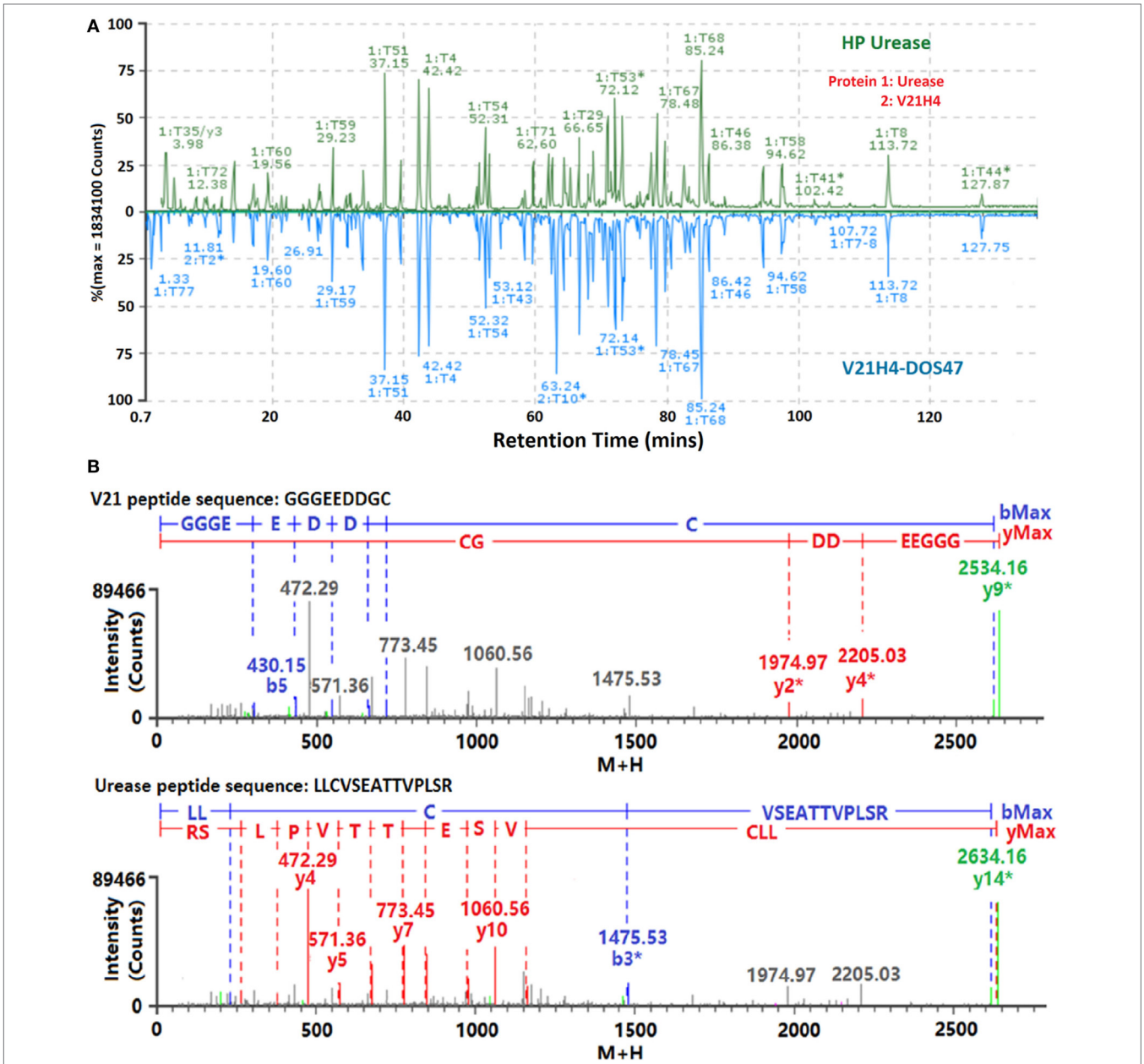

FIGURE 8 | **(A)** Screen snapshots of raw LC-MS (TIC) chromatograms of tryptic digests of HP urease (top) and V21H4-DOS47 (bottom) samples processed by BiopharmaLynx software. **(B)** Screen snapshots of *b*/*y* fragment profiles of conjugation site UC_{824}–VC_{136} mapped as the V21H4 peptide GGGEEDDGC (top) modified by UC_{824}-BM(PEG)$_2$ and as the urease peptide LLCVSEATTVPLS (bottom) modified by VC_{136}-BM(PEG)$_2$.

portion of V21H4 activated by the cross-linker through C_{23} and C_{97} of the core sequence. Alternately, this peptide could be a trace amount of V21H4 attached to the C-terminal half cystamine that was not de-protected in the TCEP reduction step. These results are consistent with those observed with urease peptides modified by -VC_{136}. Most of the V21H4 C-terminal cysteine was conjugated to urease *via* C_{824} (59%), with less conjugation at C_{663} (27%), C_{59} (12%), and C_{207} (1.2%).

The identities of the conjugation sites were confirmed with *b*/*y* ion mapping of urease and V21H4 peptides. Among the 16 possible V21H4 *b*/*y* ions, only a few (4–7) were identified from the three major urease conjugation sites. This could be a result of the ESI ionization property of the GGGEEDDGC residues, which causes a lack of positive charge center in the ionization environment. However, the MS/MS *b*/*y* fragment profiles (**Figure 8B**) can be assessed by looking at both V21H4 and urease proteins. As an example, the conjugated peptide UC_{663}-VC_{133} whose sequence is (LLCVSEATTVPLSR)-linkage-(GGGEEDDGC) and which has a peptide mass of 2,633.1472 was identified with a mass match error of 2.1 ppm by searching it as LLCVSEATTVPLSR, a urease peptide modified with (GGGEEDDGC)-linkage (1,145.3453 Da) from the V21H4 side as the modifier. The same peptide was also

identified with a mass match error of 2.1 ppm by searching it as GGGEEDDGC, a V21H4 C-terminal peptide modified with (LLCVSEATTVPLSR)-linkage (1,795.9026 Da) from the urease side as the modifier. The MS^E collision induced MS/MS spectrum of this conjugated peptide was mapped with 13 *b*/*y* fragment ions from the urease side by searching it as a urease peptide modified with the modifier from the V21H4 side. The same spectrum was also mapped with 7 *b*/*y* ions from the V21H4 side by searching it as a V21H4 peptide with the modifier from the urease side.

Specificity of V21H4-DOS47

An ELISA was performed to evaluate antibody specificity *via* binding of V21H4-DOS47 to VEGFR1, VEGFR2, and VEGFR3 (**Figure 9**). Recombinant Fc fusion proteins of VEGFR1, VEGFR2, and VEGFR3 were captured on 96-well plates coated with goat anti-human IgG/Fc. After incubations with various concentrations of V21H4-DOS47, binding was detected using a rabbit anti-urease antibody, goat anti-rabbit-AP, and substrate. As expected, V21H4-DOS47 binds well to VEGFR2; however, there is minimal, if any, binding to VEGFR1 or VEGFR3. The binding observed to VEGFR1 (shift upwards of the curve) is due to non-specific binding of one of the detection reagents to VEGFR1.

DISCUSSION

Antibody–drug conjugates are emerging as a promising class of anti-cancer drugs. By delivering drugs directly to the target site, non-specific side effects are reduced. We have previously described the production and characterization of L-DOS47, an ADC composed of the enzyme urease and an anti-CEACAM6 antibody (9). L-DOS47 is currently in phase I/II trials for the treatment of non-small cell lung cancer. In this study, we expand our knowledge of this class of drugs with the generation and characterization of V21H4-DOS47, which targets VEGFR2. Although L-DOS47 and V21H4-DOS47 were both generated by conjugating urease to a llama single domain antibody, considerable optimization was required to produce a successful V21H4-DOS47 conjugate. For example, initial V21-DOS47 conjugates generated using the same linker as in L-DOS47, SIAB, were unsuccessful due to poor binding of the conjugate (data not shown). SIAB is a short and rigid linker and it would seem that the orientation of V21 on the surface of the urease was sub-optimal with this linker. Upon switching to the PEG_2 class of linkers, which are relatively long and flexible, binding activity of the conjugate was considerably improved.

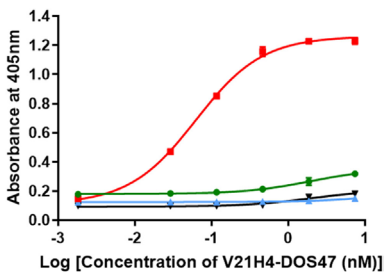

FIGURE 9 | ELISA of V21H4-DOS47 binding to VEGFR1, VEGFR2, and VEGFR3. Green line is VEGFR1. Red line is VEGFR2. Blue line is VEGFR3. Black line is no VEGFR. Results shown are representative of two experiments performed for each sample and are presented as the means and SE of samples tested in triplicates.

In this study, we developed procedures to conjugate and purify the V21-DOS47 immunoconjugate that are suitable for large-scale cGMP production. Single domain camelid antibodies are ideal for use in generating antibody–enzyme conjugates. Their small molecular size allows them to be produced affordably in large amounts. Importantly, they can also be easily modified by adding a short amino acid tag at the C-terminus. The tag serves several purposes, including modification of the antibody pI, promotion of targeted antibody expression, and addition of a specific reaction site. Since the pI of urease is in the 4.8–5.1 range, an antibody–urease conjugate generated with the unmodified core antibody would produce a conjugate with a pI of approximately 7. At this pI, the conjugate is unstable and forms precipitates during and after conjugation. The addition of a short C-terminal peptide tag adjusts the pI of the antibody from 8.75 to 5.43 leading to a conjugate with a pI between 4.8 and 5.5 which is stable during conjugation and purification. The C-terminal tag also improves the yield of antibody production by targeting expression to bacterial inclusion bodies. This allowed antibody purification using only ion exchange chromatography. As the V21 sequence contains two lysine residues in the CDR2 and CDR3 sequences, respectively, lysine-to-sulfhydryl cross-linking chemistry could modify these lysine residues, compromising the binding affinity of the conjugate to its target antigen. For this reason, a C-terminal cysteine residue was included in the C-terminal tag of V21H4 for use in sulfhydryl-to-sulfhydryl cross-linking chemistry. LC-MS^E characterization confirmed the modification of the CDR2 lysine residue by lysine-to-sulfhydryl cross-linking chemistry and an ELISA binding assay confirmed that the affinity of the V21H4-DOS47 produced by sulfhydryl-to-sulfhydryl cross-linking chemistry was approximately five-fold stronger than that of the V21H1-DOS47 conjugate produced by lysine-to-sulfhydryl cross-linking chemistry.

Although the addition of a C-terminal cysteine residue proved extremely useful in the conjugation of V21H4-DOS47, this method cannot be generalized and used for all llama single domain antibodies. The sulfhydryl-to-sulfhydryl chemistry uniquely targets the C-terminal cysteine only because the core cysteine residues are joined in a disulfide bond, and thus unavailable for modification. When working with other llama antibodies, it will be necessary to evaluate the status of any core cysteine residues before determining if this strategy can be used.

Protein refolding can be a slow and unreproducible process. Typically, refolding is performed by dilution or dialysis and the process can take several days. In addition, yield is generally low (25). The introduction of a DTT/cystamine redox couple led to a short and reproducible refolding process that generated high yields of active V21H4 antibody, which is very important for large-scale production.

One benefit of conjugating antibodies to urease is the apparent increased affinity of the conjugate compared to antibody alone. By clustering multiple antibodies per urease, avidity increases as the relative off-rate of the complex is slower than

for free antibody. However, the improvement in antibody avidity must be balanced by the potential detrimental effects of adding antibody to urease, including impairment of urease activity and increased immunogenicity of the conjugate. In addition, high CRs increase production costs and complexity. Each antibody–urease conjugate may have a different ideal CR, as the availability of the target antigen differs and the orientation and activity of the antibody presented on the urease surface changes with different conjugation chemistries. In this study, we observed little improvement in antigen binding at CRs greater than 3.3. This is in contrast to L-DOS47, in which binding increased until eight antibodies were conjugated per urease. The use of a more flexible linker to generate V21H4-DOS47 compared to L-DOS47 may partially explain this difference, as the antibodies may be more accessible to target antigen. However, the difference between the two conjugates is most likely due to the fact that AFAIKL2, the antibody component of L-DOS47, has a much lower affinity for its target antigen than does V21 for VEGFR2 (data not shown). Thus, antibody multimerization has a more pronounced effect for AFAIKL2 than for V21. Future experiments evaluating the cytotoxic activity of V21H4-DOS47 will provide further important information required to determine the optimal CR.

We have extended our knowledge of antibody–urease conjugates by generating two versions of the V21 antibody and conjugating these antibodies to urease using two different linker chemistries. V21H4-DOS47 can be generated in an efficient and controlled manner, using methods that are scalable and amenable to cGMP procedures. We are currently evaluating V21H4-DOS47 as a clinical candidate for cancers that express high levels of VEGFR2.

AUTHOR CONTRIBUTIONS

BT made a substantial contribution to the design of the work; performed, analyzed, and interpreted experiments, and drafted and critically revised the manuscript. WW made a substantial contribution to the design of the work, performed, analyzed and interpreted experiments, and critically revised the manuscript. MU made a substantial contribution to the analysis and interpretation of the work and critically revised the manuscript. PW and HC each made substantial contributions to the conception and design of the work and critically revised the manuscript.

ACKNOWLEDGMENTS

The authors thank the National Research Council of Canada (NRC) for isolation of the original V21 antibody, Iain Wilson and Sharon Molund for sample analysis and technical support, and Kim Gaspar for critical review of the manuscript.

REFERENCES

1. Hanahan D, Folkman J. Patterns and emerging mechanisms of the angiogenic switch during tumorigenesis. *Cell* (1996) 86:353–64. doi:10.1016/S0092-8674(00)80108-7
2. Risau W. Mechanisms of angiogenesis. *Nature* (1997) 386:671–4. doi:10.1038/386671a0
3. Olsson AK, Dimberg A, Kreuger J, Claesson-Welsh L. VEGF receptor signalling – in control of vascular function. *Nat Rev Mol Cell Biol* (2006) 7:359–71. doi:10.1038/nrm1911
4. Guo S, Colbert LS, Fuller M, Zhang Y, Gonzalez-Perez RR. Vascular endothelial growth factor receptor-2 in breast cancer. *Biochim Biophys Acta* (2010) 1806:108–21. doi:10.1016/j.bbcan.2010.04.004
5. Faivre S, Demetri G, Sargent W, Raymond E. Molecular basis for sunitinib efficacy and future clinical development. *Nat Rev Drug Discov* (2007) 6:734–45. doi:10.1038/nrd2380
6. Wilhelm S, Carter C, Lynch M, Lowinger T, Dumas J, Smith RA, et al. Discovery and development of sorafenib: a multikinase inhibitor for treating cancer. *Nat Rev Drug Discov* (2006) 5:835–44. doi:10.1038/nrd2130
7. Ribatti D. From the discovery of vascular endothelial growth factor to the introduction of Avastin in clinical trials – an interview with Napoleone Ferrara. *Int J Dev Biol* (2011) 55:383–8. doi:10.1387/ijdb.103216dr
8. Das M, Wakelee H. Angiogenesis and lung cancer: ramucirumab prolongs survival in 2nd-line metastatic NSCLC. *Transl Lung Cancer Res* (2014) 3:397–9. doi:10.3978/j.issn.2218-6751.2014.09.05
9. Tian B, Wong WY, Hegmann E, Gaspar K, Kumar P, Chao H. Production and characterization of a camelid single domain antibody-urease enzyme conjugate for the treatment of cancer. *Bioconjugate Chem* (2015) 26:1144–55. doi:10.1021/acs.bioconjchem.5b00237
10. Itakura J, Ishiwata T, Shen B, Kornmann M, Korc M. Concomitant over-expression of vascular endothelial growth factor and its receptors in pancreatic cancer. *Int J Cancer* (2000) 85:27–34. doi:10.1002/(SICI)1097-0215(20000101)85:1<27::AID-IJC5>3.0.CO;2-8
11. Tanno S, Ohsaki Y, Nakanishi K, Toyoshima E, Kikuchi K. Human small cell lung cancer cells express functional VEGF receptors, VEGFR-2 and VEGFR-3. *Lung Cancer* (2004) 46:11–9. doi:10.1016/j.lungcan.2004.03.006
12. Wong WY, DeLuca CI, Tian B, Wilson I, Molund S, Warriar N, et al. Urease-induced alkalinization of extracellular pH and its antitumor activity in human breast and lung cancers. *J Exp Ther Oncol* (2005) 5:93–9.
13. De Genst E, Saerens D, Muyldermans S, Conrath K. Antibody repertoire development in camelids. *Dev Comp Immunol* (2006) 30:187–98. doi:10.1016/j.dci.2005.06.010
14. Maass DR, Sepulveda J, Pernthaner A, Shoemaker CB. Alpaca (*Lama pacos*) as a convenient source of recombinant camelid heavy chain antibodies (VHHs). *J Immunol Methods* (2007) 324:13–25. doi:10.1016/j.jim.2007.04.008
15. Harmsen MM, De Haard HJ. Properties, production, and applications of camelid single-domain antibody fragments. *Appl Microbiol Biotechnol* (2007) 77:13–22. doi:10.1007/s00253-007-1142-2
16. Arbabi Ghahroudi M, Desmyter A, Wyns L, Hamers R, Muyldermans S. Selection and identification of single domain antibody fragments from camel heavy-chain antibodies. *FEBS Lett* (1997) 414:521–6. doi:10.1016/S0014-5793(97)01062-4
17. Frenken LG, van der Linden RH, Hermans PW, Bos JW, Ruuls RC, de Geus B, et al. Isolation of antigen specific llama VHH antibody fragments and their high level secretion by *Saccharomyces cerevisiae*. *J Biotechnol* (2000) 78:11–21. doi:10.1016/S0168-1656(99)00228-X
18. van der Linden RH, Frenken LG, de Geus B, Harmsen MM, Ruuls RC, Stok W, et al. Comparison of physical chemical properties of llama VHH antibody fragments and mouse monoclonal antibodies. *Biochim Biophys Acta* (1999) 1431:37–46. doi:10.1016/S0167-4838(99)00030-8
19. Dumoulin M, Conrath K, Van Meirhaeghe A, Meersman F, Heremans K, Frenken LG, et al. Single-domain antibody fragments with high conformational stability. *Protein Sci* (2002) 11:500–15. doi:10.1110/ps.34602
20. Lauwereys M, Arbabi Ghahroudi M, Desmyter A, Kinne J, Hölzer W, De Genst E, et al. Potent enzyme inhibitors derived from dromedary heavy-chain antibodies. *EMBO J* (1998) 17:3512–20. doi:10.1093/emboj/17.13.3512
21. Muyldermans S, Cambillau C, Wyns L. Recognition of antigens by single domain antibody fragments: the superfluous luxury of paired domains. *Trends Biochem Sci* (2001) 26:230–5. doi:10.1016/S0968-0004(01)01790-X
22. Cortez-Retamozo V, Lauwereys M, Hassanzadehgh G, Gobert M, Conrath K, Muyldermans S, et al. Efficient tumor targeting by single-domain antibody fragments of camels. *Int J Cancer* (2002) 98:456–62. doi:10.1002/ijc.10212

23. Takishima K, Suga T, Mamiya G. The structure of jack bean urease. The complete amino acid sequence, limited proteolysis and reactive cysteine residues. *Eur J Biochem* (1988) 175:151–65. doi:10.1111/j.1432-1033.1988.tb14177.x
24. Thirumurugan P, Matosiuk D, Jozwiak K. Click chemistry for drug development and diverse chemical-biology applications. *Chem Rev* (2013) 113:4905–79. doi:10.1021/cr200409f
25. Yamaguchi H, Miyazaki M. Refolding techniques for recovering biologically active recombinant proteins from inclusion bodies. *Biomolecules* (2014) 4:235–51. doi:10.3390/biom4010235

Conflict of Interest Statement: The authors declare the following competing financial interests; BT, WW, MU, and HC are employees of Helix BioPharma Corporation. PW is an employee of Helix ImmunoOncology Sp. z o.o.

frontiers in Immunology

REVIEW
published: 13 December 2017
doi: 10.3389/fimmu.2017.01802

Single-Domain Antibodies As Therapeutics against Human Viral Diseases

*Yanling Wu, Shibo Jiang and Tianlei Ying**

Key Laboratory of Medical Molecular Virology of Ministries of Education and Health, School of Basic Medical Sciences, Fudan University, Shanghai, China

In full-size formats, monoclonal antibodies have been highly successful as therapeutics against cancer and immune diseases. However, their large size leads to inaccessibility of some epitopes and relatively high production costs. As an alternative, single-domain antibodies (sdAbs) offer special advantages compared to full-size antibodies, including smaller size, larger number of accessible epitopes, relatively low production costs and improved robustness. Currently, sdAbs are being developed against a number of viruses, including human immunodeficiency virus-1 (HIV-1), influenza viruses, hepatitis C virus (HCV), respiratory syncytial virus (RSV), and enteric viruses. Although sdAbs are very potent inhibitors of viral infections, no sdAbs have been approved for clinical use against virial infection or any other diseases. In this review, we discuss the current state of research on sdAbs against viruses and their potential as therapeutics against human viral diseases.

Keywords: single-domain antibody, nanobody, viral disease, antiviral therapeutics, human immunodeficiency virus-1

OPEN ACCESS

Edited by:
Colin Roger MacKenzie, National Research Council Canada (NRC-CNRC), Canada

Reviewed by:
Andrew Hayhurst, Texas Biomedical Research Institute, United States
Serge Muyldermans, Vrije Universiteit Brussel, Belgium

***Correspondence:**
Tianlei Ying
tlying@fudan.edu.cn

Specialty section:
This article was submitted to Vaccines and Molecular Therapeutics, a section of the journal Frontiers in Immunology

Received: *01 September 2017*
Accepted: *30 November 2017*
Published: *13 December 2017*

Citation:
Wu Y, Jiang S and Ying T (2017) Single-Domain Antibodies As Therapeutics against Human Viral Diseases. Front. Immunol. 8:1802. doi: 10.3389/fimmu.2017.01802

INTRODUCTION

Antibody-based therapeutics are enjoying significant clinical success, with over 70 such molecules approved by the US FDA and hundreds more in various phases of clinical trials (1). Notably, although antibodies have been proven to be effective against a number of diseases, most FDA-approved monoclonal antibodies (mAbs) are used to treat cancer and immune disorders (1, 2), and only one antiviral humanized mAb, palivizumab, has been approved as a prophylactic to prevent respiratory syncytial virus (RSV) infection in neonates and immunocompromised individuals (3). The development of therapeutic antibodies against viruses has been impeded by high production costs and limited commercial market. Moreover, the relatively large size of antibodies, which results in correspondingly low tissue accessibility and penetration, affects their therapeutic efficacy (4). Therefore, smaller-sized antibodies and engineered variants have become promising alternatives to full-size mAbs (5).

In 1989, researchers reported the isolation of stable mouse antibody VH domains that could bind antigens with relatively high affinity (20 nM), and the term "domain antibodies (dAbs)" was suggested (6). Moreover, in 1993, a unique class of "heavy-chain-only" antibodies (HCAbs) was found in the serum of camels. The variable domains of these HCAbs, referred to as VHHs, nanobodies (a term coined by Ablynx, a biopharmaceutical company) or single-domain antibodies (sdAbs) (7), represent the smallest naturally derived antigen-binding functional fragments (~15 kDa). These sdAbs maintain affinities and antigen-binding specificities comparable to those of full-size mAbs. Importantly, they are easy to engineer and more economical to produce; they also possess other unique and superior properties for a range of therapeutic applications.

Here, we review sdAbs in relation to their possible therapeutic applications against highly aggressive human viral diseases. Potential sdAb-based therapeutics against viruses that are particularly important for public health, such as human immunodeficiency virus-1 (HIV-1), influenza A virus, respiratory syncytial virus (RSV), hepatitis C virus (HCV), and enteric viruses are discussed (**Table 1**). We also provide insight into the current status of the sdAbs, their ongoing development, as well as future challenges toward their successful implementation for therapy of human viral diseases.

TABLE 1 | Update of published sdAbs directed against viruses according to their binding sites [modified from Vanlandschoot et al. (8)].

Binding sites	Reference	Immunogen or panning antigen	Origin	Mechanism	Potency *in vitro*	Breadth	*In vivo*
Extracellular targeting							
HIV CD4-induced binding site (coreceptor binding site)	Chen et al. (9)	HIV-1 Envs	Phage-displayed human VH library	Neutralization	Fusion proteins with CD4 superior to bnAbs	Clade A, B, C, D	–
HIV coreceptor binding site	Matz et al. (10)	Trimeric gp140	Llama	Neutralization	IC_{50}: 0.2–40 μg/ml	Subtypes A, C, G, and CRF01_AE, CRF02_AG	–
HIV CD4-binding site	McCoy et al. (11)	Trimeric HIV-1 gp140	Llama	Neutralization	IC_{50}: 0.03–50 μg/ml	Subtypes A, B, C, D, G and CRF_01 AE, CRF_02AG, AC, ACD, BC, and CD	–
HIV-1 MPER	Gong et al. (12)	Gp41 MPER peptide	CH2 library	Neutralization	–	Clade B, C, D, E	–
HIV-1 MPER	Hulsik et al. (13)	Trimeric gp41	Llama	Neutralization	IC_{50} bivalent: clade A: 2.4–4.6 μg/ml; clade B: 0.2–33.4 μg/ml	Clade A and B	–
RSV F protein	Detalle et al. (14)	Recombinant F protein and inactivated RSV-A	Llama	Neutralization	IC_{50}: subtype A: 0.1 nM; subtype B: 0.24 nM	RSV A and B subtypes	Reducing both nasal and lung RSV titers prophylactically or therapeutically
RSV prefusion F protein	Rossey et al. (15)	Prefusion conformation, DS-Cav1	Llama	Neutralization	IC_{50}: subtype A: 0.038–0.089 nM; subtype B: 0.022–0.032 nM	RSV A and B subtypes	30 μg sdAbs administered intranasally prevent RSV replication in RSV-challenged mice
Influenza M2	Wei et al. (16)	M2 (H3N2)	Synthetic Camel VHH library	Neutralization	Minimal inhibitory concentration at 1.2 μM	H3N2 and H1N1	200 μg antibodies protect 60% mice with H1N1 virus challenge
Influenza HA	Ibanez et al. (17)	Recombinant H5N1-HA	Llama	Neutralization	–	H5N1	Prophylactic or therapeutic treatment to rescue mice against H5N1 challenge
Influenza HA	Tillib et al. (18)	Inactivated H5N2 virus	Camel	Neutralization	Minimal inhibitory concentration at 4.2 nM	H5N2	200 μg protect 100% mice against virus challenge
Influenza HA	Hufton et al. (19)	Recombinant H1-HA	Alpaca	Neutralization	IC_{50}: 3.2–212.2 nM	H1N1	–
Influenza NA	Cardoso et al. (20)	N1rec	Alpaca	Neutralization	IC_{50} of monovalent: 425.2 and 374.9 nM; bivalent: 0.157 and 0.69 nM	Clade 1 and 2 H5N1	60 μg prophylactic treatment protect 100% mice against a lethal challenge with H5N1 and oseltamivir-resistant variant
Influenza NA	Harmsen et al. (21)	Mixtures of purified influenza viruses	Llama	–	–	All N subtypes	–

(*Continued*)

TABLE 1 | Continued

Binding sites	Reference	Immunogen or panning antigen	Origin	Mechanism	Potency *in vitro*	Breadth	*In vivo*
HCV E2	Tarr et al. (22)	E2 glycoprotein	Alpaca	Neutralization and cell-to-cell transmission	IC_{50}: 1–10 μg/ml	Six major genotypes	–
HSV-2 glycoprotein D	Geoghegan et al. (23)	Recombinant gD2	Llama	Killing infected cells by conjugated immunotoxin	IC_{50} of 6.7 nM	HSV-2	–
Rotavirus	van der Vaart et al. (24)	Rhesus-monkey rotavirus serotype G3	Llama	Neutralization	IC_{50}: <1 μg/ml	G3 rotavirus strain	Reduce the morbidity of rotavirus induced diarrhea in mice
Rotavirus VP6	Garaicoechea et al. (25); Vega et al. (26); Maffey et al. (27)	VP6 protein	Llama	Neutralization	IC_{80} of monovalent: 0.2–3.9 μg/ml; bivalent: >3.9 μg/ml	Group A Rotavirus	Monovalent VHH protects and treats against RVA-induced diarrhea in mice and gnotobiotic piglets
Norovirus P domain of VLP	Koromyslova and Hansman (28)	GII.10 VLP	Alpaca	Particle disassembly	–	GII.4, GII.10, and GII.12	–
Poliovirus receptor-binding site	Thys et al. (29); Schotte et al. (30); Strauss et al. (31)	Poliovirus type 1 Sabin strain	Dromedary	Neutralization	IC_{50}: 0.007–0.69 μM; IC_{90}: 0.017–1.77 μM	Poliovirus type I	–
Intracellular targeting							
HIV Vpr	Matz et al. (32)	Synthetic Vpr peptide	Llama	No inhibitory activity	–	–	–
Influenza virus nucleoprotein (NP)	Ashour et al. (33); Hanke et al. (34)	Influenza virus PR8	Alpaca	Block vRNP nuclear import, viral transcription, and replication	–	Common influenza virus strains	–
Influenza virus nucleoprotein (NP)	Schmidt et al. (35)	Inactivated IAV	Alpaca	Block IAV infection	–	Influenza A virus	–
HCV NS5B	Thueng-in et al. (36)	NS5BΔ55 of genotype 3a HCV	Humanized-camel phage library	Inhibition of RdRp catalytic activity	2–4 μg inhibit RdRp activity by 10–69% and 10 μg decrease HCV RNA inside the cells	HCV-JFH1	–
HCV NS3	Phalaphol et al. (37)	rNS3-C	Humanized-camel phage library	Inhibition of helicase activity	–	HCV-JFH1	–
HCV serine protease	Jittavisutthikul et al. (38)	rNS3/4A	Humanized-camel phage library	Inhibition of protease activity	–	HCV-JFH1	–
Ebola and Marburg nucleoprotein (NP)	Sherwood et al. (39, 40); Darling et al. (41)	*Ebolavirus* or MARV-Mus NP	Single-pot semisynthetic llama library	Inhibition of NP packaging	–	Genus specific	–

–, *Not determined.*

OVERVIEW OF ANTIVIRAL sdAbs

Compared to the conventional human antibody VH, a few crucial amino acids are substituted in the framework 2 region (FR2) and complementarity-determining regions (CDRs) of sdAbs. The highly conserved hydrophobic amino acids (Val47, Gly49, Leu50, Trp52) in FR2 region are replaced by hydrophilic amino acids (Phe42, Glu49, Arg50, Gly52) (**Figure 1A**) which are critical to the interaction of V_H-V_L, rendering the overall structure more hydrophilic and contributing to high stability, solubility and resistance to aggregation (42, 43). Moreover, sdAbs possess exceptional resistance to high temperatures and extreme pH (44), which makes them ideal candidates for developing viable treatment strategies against viruses in harsh environments such as the respiratory and gastrointestinal tracts. sdAbs can be easily administered *via* intranasal or oral route, directly to the site of viral infection (25, 45).

Owing to their increased hydrophilicity and single-polypeptide nature, sdAbs can be relatively efficiently produced in bacteria,

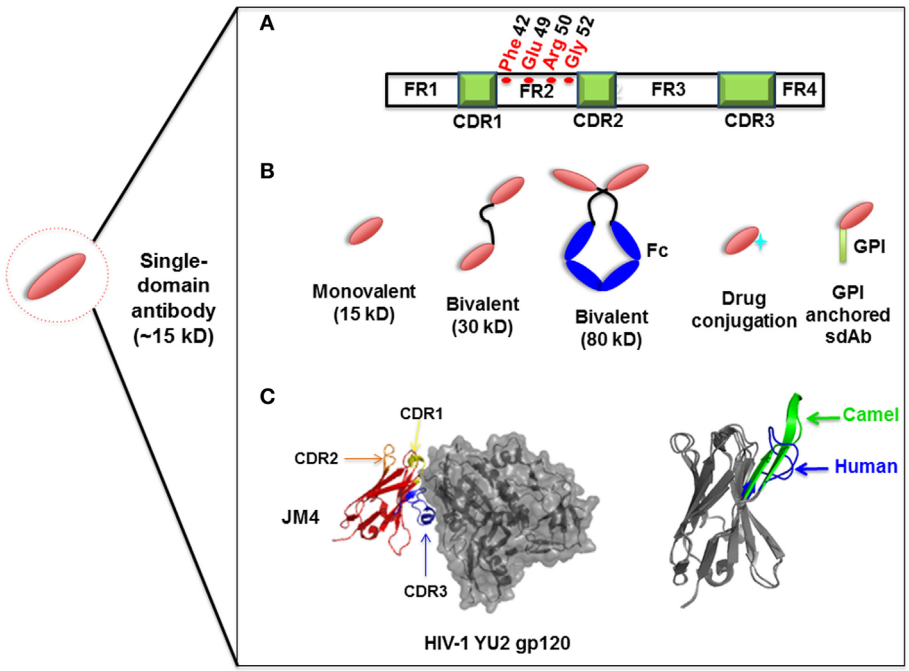

FIGURE 1 | Representation of single-domain antibodies (sdAbs) and their characteristics. **(A)** Representation of camelid sdAb framework (FR) and complementarity-determining (CDR) regions, showing hydrophilic amino acids (Phe42, Glu49, Arg50, Gly52) in the FR2 region compared to conventional human VH (Val42, Gly49, Leu50, Trp52). **(B)** Schematic representation of sdAb-based engineered antibody constructs. **(C)** Neutralizing sdAb JM4 (PDB identifier 4LAJ) in complex with HIV-1 YU2 envelope gp120 glycoprotein, showing CDR1 (yellow), CDR2 (orange), and CDR3 (blue) and comparing CDR3 between human VH domain HEL4 (blue) (PDB identifier 1OHQ) and HIV-1 gp41 MPER-specific llama VHH 2H10 (green) (PDB identifier 4B50).

yeast, mammalian cells or plant cells, enabling large-scale production at reasonable costs. Plant cell expression systems, such as transgenic crops can provide a particularly low-cost option. sdAbs expressed in such crops as rice do not require purification and can be stored at room temperature for a long period without compromising antiviral activity (46), which is beneficial in some areas where cold chains are difficult to maintain.

The small size of sdAbs (~15 kDa) also allows rapid tissue penetration, including the blood–brain barrier (47) and even neurospheres, in comparison to full-size mAbs (48), thus holding promise for therapy of neurotropic virus infections like rabies virus. Rabies virus is a model neurotropic virus, which can cause lethal brain infection in humans. Postexposure treatment with antirabies sdAbs can partly rescue mice from lethal disease and decrease the viral RNA load in the brain. In contrast, treatments with vaccines or human antirabies immune globulins could not meet this test, indicating that antirabies sdAbs can enter the brain and neutralize virus (49, 50). Still, because of their short half-life, sdAbs may not have enough time to cross the endothelial barriers in sufficient amounts to clear out virus, thus limiting the effect of sdAb treatment at the more advanced stages of infection.

Structural analysis of sdAbs in complex with their antigens revealed that some sdAbs display an extended CDR3. The convex conformations formed by the CDR3 of these sdAbs (**Figure 1C**) can target unique and cryptic epitopes and confer unique binding specificities by blocking the concave epitopes of antigens (31, 51).

Single-domain antibodies can be easily engineered as multivalent constructs (**Figure 1B**). A number of studies indicated that multivalent formats are more effective than monovalent sdAbs in virus neutralization. For instance, it was found that a bivalent camelid VHH targeting H5N1 hemagglutinin was at least 60-fold more effective than the monovalent one in controlling virus replication (17, 20). Moreover, conversion of influenza hemagglutinin-specific and cross-neutralizing antibodies into a bivalent format can increase their breadth of subtype cross-reactive neutralization activity (19). ALX-0171, a trimeric RSV-neutralizing VHH that binds to an epitope similar to that of palivizumab, displayed more potent neutralization activity than palivizumab against prototypic RSV subtype A and B strains (14). Moreover, fusion with drugs, such as immunotoxins or cytotoxins, by site-specific conjugation to a C-terminal cysteine not only maintains the binding properties of sdAbs, but also increases their killing power against virus-infected cells (23) (**Figure 2**). Direct fusion to human serum albumin (HSA) (52) and PEGylation (53) can extend the serum half-life of sdAbs. However, such molecules have relatively large size that could lead to decreased inhibitory activity. Another attractive strategy for enhancing antibody pharmacokinetics by fusion to the Fc fragment of an IgG1 (54). Although these strategies increase the size of the antigen binders, the engineered molecules are still expected to target their epitopes more efficiently than full-length antibodies. A previous study reported improved half-life *in vivo* can be achieved by fusing sdAb with a small-sized HSA-binding

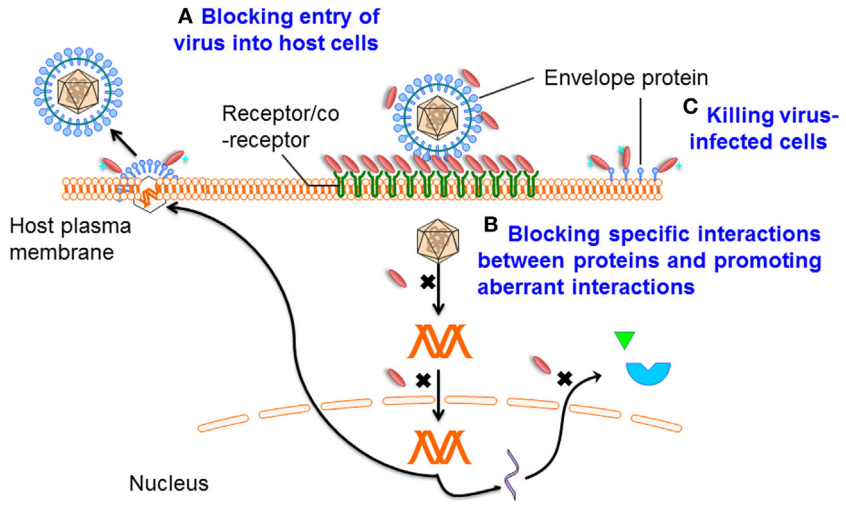

FIGURE 2 | Mechanisms of single-domain antibody (sdAb)-based therapeutics against viruses. Mechanism A: preventing entry of the viral particle into host cells by targeting viral envelope proteins or receptors that mediate cell binding and membrane fusion; mechanism B: blocking specific interactions between virus/virus or virus/host proteins, promoting aberrant interactions, binding in the active sites of enzymes, or through recognition or stabilization of distinct conformations of their targets; and mechanism C: specifically killing virus-infected cells by drug-conjugated or toxin-fused sdAbs.

peptide (15–20 kDa) and the resultant fusion protein showed the same neutralizing activity as that of unconjugated sdAb (9).

Currently, small-molecule drugs are widely available to treat infections caused by HIV-1 (55), HBV (56), HCV (57), as well as influenza viruses (58). For instance, since the discovery of HIV-1, more than 30 compounds have been approved for the treatment of HIV-1 infection (59). These drugs demonstrate that a number of cytosolic proteins could serve as ideal targets for inhibition of viral infections. Although the penetration of sdAbs through the cell membrane remains a problematic issue, many sdAbs have sufficient inherent stability to be functional in antigen-binding, even in the absence of the disulfide bond as occurring in the reducing environment of the cytoplasm. When expressed as intrabodies, they can bind antigens to inhibit viral replication (35, 41). Furthermore, the high binding specificity of sdAbs can only rarely be achieved by small-molecule drugs. Analysis of V-D-J gene rearrangement shows that camelid sdAbs share high similarity (greater than 80%) with the human IGHV3 gene family (44), indicating that the immunogenicity of camelid sdAbs could be low. Data from clinical trials of ALX-0171, an anti-RSV VHH, support this notion (45). These sdAbs can be "humanized" without significant loss of their specific activity (60). Moreover, a high-affinity and high-neutralization sdAb has been isolated from a large human VH-based phage display library (9). Therefore, camelid sdAbs and fully human sdAbs have potential as therapeutics against viral infections.

TARGETS OF ANTIVIRAL sdAbs

Proteins Mediating Entry of Viruses into Host Cells

Infection is conditional on viral entry into host cells. Viral replication can then be initiated. This entry process is initially mediated by one or several viral proteins exposed on the virion surface and receptors or coreceptors on the host cell surface (61, 62). Proteins mediating viral entry are the promising targets for antibody-based antiviral therapy (**Figure 2**). Analysis of virus structure shows that many epitopes on the virion surface are hidden by deep invaginations or canyons and that they are, therefore, barely recognized by the large and typically flat antigen-binding sites of conventional antibodies (15, 63). More importantly, while many protruded epitopes on the viral surface are targeted by conventional antibodies, such epitopes can rapidly change conformation, resulting in the escape of virus from humoral immune responses (64). At the same time, these "hidden" epitopes, typically inaccessible to conventional antibodies, are well conserved across diverse viruses, making them good targets for sdAbs.

sdAbs As Intrabodies Targeting Intracellular Proteins

In the virus life cycle, many proteins encoded by viral genomes play essential roles in replication. Therefore, interfering with the virus life cycle by interrupting the functions of these proteins is another effective strategy (**Figure 2**), as already demonstrated by their successful targeting by small-molecule inhibitors. However, antibodies do not pass the plasma membranes. By gene transfer, intrabodies expressed in the cytoplasm may have broad antiviral therapeutic applications. As a consequence of the reducing environment of the cytoplasm, the formation of disulfide bonds is prevented. For most conventional mAbs, or their fragments, such as Fab and scFv, correct folding and stability generally depend on the formation of intra-domain disulfide bonds. Indeed, it has been shown that antibody fragments expressed in the reducing environment are strongly destabilized (65). In contrast, sdAbs can be functionally expressed in the cytoplasm (35), suggesting that their activities or stabilities are less dependent on the disulfide

bond formation. Furthermore, Darling et al. advanced an alternative approach to generate a dimeric intracellularly expressed sdAb against Filoviruses which targeted highly conserved C-terminal regions of nucleoprotein (NP). This dimeric sdAb can restrict viral packaging and inhibit Marburg and Ebola replication (41). As such, sdAbs represent a rich source of functional intrabodies of potential therapeutic importance.

sdAbs AS POTENTIAL THERAPEUTICS AGAINST VIRUSES

Human Immunodeficiency Virus 1

The HIV-1 Env, a trimeric complex comprised of gp120 and gp41, typically serves as the main target for neutralizing antibodies. HIV-1 entry, the first step of the replication cycle, requires that gp120 engage the host cell surface CD4 and undergo a conformational change to bind either CCR5 or CXCR4, with subsequent fusion of cell and viral membrane mediated by gp41. Recently, a few highly potent and broadly neutralizing antibodies (bnAbs) have been identified from long-term HIV-infected individuals, including, for example, X5 (66), VRC01 (67), PGT121 (68), and 3BNC117 (69). Analysis of their binding models demonstrated that the key epitopes on gp120 for bnAbs are located at the CD4-binding site (CD4bs) and the coreceptor-binding site (CoRbs). The CD4bs is formed as a hydrophobic and recessed pocket (70, 71). This pocket is surrounded by five loop structures, which partially overlay the site and may prevent access to large antibodies (72). CoRbs epitopes are usually inaccessible until gp120 changes its conformation upon CD4 binding. Therefore, these antibodies that specifically bind to exposed epitopes following CD4-gp120 binding are also termed as CD4-induced (CD4i) antibodies, which, however, are also masked by flanking V2 and V3 loops (70). Moreover, the close proximity of viral and cellular membranes leaves only a very narrow space which may not be sufficient to accommodate conventional Ig antibodies (73). The membrane proximal external region (MPER) epitopes on gp41 may also be size-restricted (63). In fact, the transient fusion-intermediate conformation of gp41 (74) is only accessible after the conformational changes induced by receptor/coreceptor binding in Env. It is obvious that these steric constraints require smaller antibody fragments which have smaller paratopes to access these regions. Because of their small size, protruding CDR3 loops, and cleft-recognition properties, sdAbs can reach such inaccessible epitopes and block entry, in many cases more efficiently than the corresponding Fab and scFv fragments and the full-size antibodies.

The first human sdAb, m36, identified from a human antibody variable domain phage-displayed library, targets a highly conserved sterically restricted region on gp120 induced by CD4 binding. The neutralizing activity of m36 is, on average, higher than that of scFv m9 that is a matured derivative of X5 and superior to other known first-generation HIV-1 bnAbs (9). Larger-sized IgG variants of this antibody exhibited a significant reduction in overall neutralization potency compared to m36 (9). To date, m36 is the only reported HIV-1 inhibitor with exceptional potency and broad cross-reactivity based on human dAbs.

Using trimeric gp140 as immunogen in llamas and gp120 for selection, a panel of broadly neutralizing camelid sdAbs (VHHs) were identified that can bind to either CD4bs or CoRbs (10). These camelid sdAbs exhibited potent neutralizing activity against viruses expressing subtype B envelopes, including primary viral isolates resistant to some bnAbs, including 2G12, b12, 2F5, 4E10, PG9, and PG16 (10). One of the sdAbs, JM4, recognized a novel CD4i epitope including elements of both CD4bs and CoRbs (75). JM4 showed greater neutralization efficacy than known human CD4i IgGs as well as their Fab fragments, but IgG2b and IgG3 formats of JM4 showed dramatically enhanced breadth and potency (75). Further, Liu et al. developed GPI-anchored variable regions by genetically linking sdAbs with a glycosylphosphatidylinositol (GPI) attachment signal, which targeted lipid rafts of plasma membrane. Transduction of human $CD4^+$ cell lines and primary CD4 T cells with GPI-VHH JM4 conferred broad and potent neutralization of HIV-1 and efficiently interfered with cell-cell transmission of HIV-1 and HIV-1 envelope-mediated fusion (76). One extremely potent and broad HIV-1-neutralizing sdAb from an immunized llama, J3, targeted the CD4-binding site and neutralized 96% of all strains tested (11). Notably, J3 exhibited high potency in blocking the cell–cell spread of HIV-1 from primary macrophages to CD4 T cells (77).

MPER-specific antibodies are among the broadest cross-reactive HIV-1 neutralizing antibodies (78). However, numerous studies have been performed with purified gp41 proteins and gp41-derived peptides in an attempt to induce such antibodies by immunization, but such attempts have, thus far, met with little success (79, 80). An MPER-specific VHH, 2H10, whose epitope (EQELLELDK) partially overlaps with that of 2F5, was elicited by immunizing llamas with gp41-MPER proteoliposomes (81). 2H10 bound to a linear epitope of gp41 with low nanomolar affinity. Analysis of its crystal structure revealed an extended CDR3 with a solvent-exposed tryptophan (W100) at its tip, which is required for its neutralizing activity (13). Increasing affinity by increasing avidity, as demonstrated for bivalent 2H10, led to the neutralization of various sensitive and resistant strains, including some Tier 2 viruses, with 100-fold higher potency than mAb 2F5. Although bivalent 2H10 lacks the potency and breadth of 2F5, 4E10, or 10E8, optimization of the immunization protocol, such as longer immunization schemes, may produce more extensive somatic mutations and yield antibodies with higher breadth and potency. Interestingly, an IgG1 CH2 domain-based dAb was generated from a phage library. This dAb binds to MPER and can neutralize a limited number of HIV-1 isolates (12). It also binds to FcRn. The term nanoantibody was coined for such CH2-based dAbs because nanoantibodies can mimic some of the functions of full-size antibodies (82).

Previous studies have already found that anti-Nef and anti-Rev intracellular sdAbs could efficiently block most of the activities of these viral proteins (83, 84) to inhibit HIV-1 replication. The HIV-1 viral regulatory protein (Vpr) is involved in regulation of efficient virus replication, and known to induce cell cycle arrest, apoptosis, and the enhancement of HIV-1 transcription in infected cells. Matz et al. isolated a panel of anti-Vpr sdAbs from two libraries of VHHs elicited by two immunized llamas with either a synthetic Vpr peptide or recombinant HIV-1 capsid

protein (32). One of these VHHs was able to bind Vpr in the cytoplasm of eukaryotic cells, leading to its delocalization from the nucleus to the cytoplasm, but had no effect on the activities of Vpr (32). This problem may be solved by fusing sdAb with an SH3 domain, demonstrated by one study from the same research group which found that Neffins, composed of an anti-Nef sdAb and modified SH3 domain, inhibited all key activities of HIV-1 Nef (85).

Influenza A Virus

Influenza viruses are currently classified into A, B, C, and D types on the basis of antigenic differences (86). In particular, highly pathogenic influenza A viruses occasionally cross the species barrier between domesticated birds and humans, such as the H5 and H7 subtypes, leading to seasonal epidemics and, sometimes, worldwide pandemics with high morbidity and mortality owing to severe and fatal acute respiratory diseases (87, 88). In the current decade, zoonotic outbreaks have posed significant threats to public health. However, currently available anti-influenza drugs are limited because of spontaneous virus mutations. Furthermore, such drugs often result in side effects and the emergence of drug-resistant viruses. Influenza A viruses are enveloped viruses antigenically consisting of two major membrane glycoproteins, hemagglutinin (HA), which mediates the binding of influenza virion to host cells and membrane fusion, and neuraminidase (NA), which is critical for the efficient release of newly synthesized influenza viruses by cleaving sialic acids from host cell receptor. While inhibitors specific for either the HA or NA glycoprotein (89, 90) can block virus infection, only HA glycoprotein mediates the virus entry process, making it a potential target for neutralizing antibodies. Several HA-targeting VHHs were isolated from llamas and were found to be specific for the H5N1 strain (17). One of these antibodies potently suppressed influenza A virus replication *in vivo* by intranasal administration. Bivalent antibodies showed 60-fold higher suppression than their monovalent counterparts and protected mice against a lethal challenge with H5N1 (17). In another study, Tillib et al. reported the development of potent camelid HA-specific sdAbs elicited by the immunization of a camel with inactivated avian influenza virus H5N2. The neutralizing activities of the original monovalent antiviral sdAbs are significantly enhanced both *in vitro* and *in vivo* by formatting procedure using the isoleucine zipper domain (ILZ) (18). The expression of ILZ formatted anti-HA sdAb *in vivo* for up to 14 days by an adenoviral vector resulted in prolonged protective effect against influenza virus (91). Decreased NA activities by blocking antibodies helped to protect a mouse model against H5N1 virus challenge (20).

Influenza M2 is a homotetrameric transmembrane protein that functions as a proton channel. M2 is required in several steps of influenza virus infection, including uncoating of the viral ribonucleoprotein core in endosomes, viral assembly and release (92, 93). In contrast to HA and NA, the N-terminal extracellular domain of M2 (M2e) has 24 residues remarkably conserved in all human influenza A strains. As such, neutralizing antibodies against M2e are thought to offer broad protection. Indeed, M2-7A, an sdAb that specifically bound M2, showed broadly cross-reactive neutralization for both amantadine-sensitive and -resistant viruses *in vitro* and protected mice from lethal influenza virus challenge (16).

Given the continued relevance of influenza virus as a serious health threat and its ability to rapidly acquire resistance against drugs or escape from immune responses by antigenic drift, the less variable influenza virus proteins, including virus NP, may prove to be alternative targets for intervention. A panel of sdAbs was generated against NP, a viral protein essential for nuclear trafficking and packaging of the influenza virus genome (33, 34). These sdAbs disrupt virus replication by preventing nuclear import of viral ribonucleoproteins (vRNPs). One such sdAb, termed as αNP-VHH1, exhibited antiviral activity similar to that of Mx protein. Analysis of the crystal structure of this VHH in complex with NP revealed that the binding site overlaps regions associated with viral sensitivity to Mx proteins and is not conserved on the body domain of NP implicated in interactions with host factors (34). Schmidt et al. developed a highly efficient screening approach to identify antiviral sdAbs that confer a phenotype to cells when expressed intracellularly. Anti-NP sdAbs that specifically interact with their respective nucleoproteins protect human cells from lethal Influenza A virus infection by preventing nuclear import of viral vRNPs (35). So far, more than 20 NP-specific sdAbs have been characterized as binding to at least four unique binding sites on NP (33, 35). Continued efforts in this direction might help to map more precisely the contributions of different NP surfaces to the influenza virus life cycle and inspire the development of novel antivirals.

Respiratory Syncytial Virus

Respiratory syncytial virus infection causes serious or even fatal lower respiratory tract infections in infants. It is estimated that about 3.4 million infants are infected by RSV annually and more than 3 million of them develop severe bronchiolitis or pneumonia (94). Currently, neither licensed RSV vaccines nor specific anti-RSV therapeutics are available. RSV has two classes of transmembrane glycoproteins on the viral surface, fusion (F) protein, and attachment (G) protein. Receptor binding is mediated by G protein, followed by fusion of viral and cell membrane and viral entry facilitated by F protein (95). Therefore, both proteins contain epitopes for neutralizing antibodies. The F protein shares high similarity between RSV subgroups A and B (89% amino acid identity) and lower glycosylation compared to G protein, and is thus considered an ideal target for developing anti-RSV agents. The humanized mAb palivizumab (Synagis) binds to RSV F protein and neutralizes RSV by preventing fusion of the viral and host cell membrane (96). Although reducing hospitalizations when administered prophylactically, its high cost and limited efficacy have restricted its use to high-risk infants (97). Recently, an RSV-neutralizing, F protein-specific sdAb, Nb017, was identified from immune libraries of llamas (14). Fusion of three monovalent Nb017s linked by two GS linkers formed a trimeric antibody, ALX-0171, which binds antigenic site II epitope on RSV F, similar to that of palivizumab. ALX-0171 showed exceptional cross-reactive neutralization *in vitro*, much higher than that of palivizumab. Furthermore, ALX-0171, when directly delivered prophylactically or therapeutically to the sites of infection, was shown to be highly effective in reducing RSV replication in both

nasal passage and lung (14). In a phase I/IIa trial, the viral loads in nasal swabs of hospitalized RSV-infected children were reduced by daily treatment for three consecutive days with ALX-0171 delivered by an inhalation device (45). Several studies reported that antibodies specifically binding to prefusion conformation of F protein exhibited more robust neutralizing activity than conformation-independent antibodies (98–100). Two llama-derived, prefusion F-specific sdAbs were identified to have neutralizing activity against RSV A and B subtypes superior to that of mAb palivizumab and motavizumab (15). Crystallization studies revealed that both sdAbs bind to a conserved cavity epitope formed by two F protomers, illustrating that the sdAbs preferentially bind to clefts or cavities. Prophylactic treatments with 30 μg sdAbs administered intranasally prevented RSV replication in RSV-challenged mice (15). Such sdAbs with extraordinarily high RSV-neutralizing activity could be developed as therapeutics for the treatment of RSV infections.

Hepatitis C Virus

Hepatitis C virus infection typically manifests as chronic hepatitis which often progresses to fatal cirrhosis and hepatocellular carcinoma. At present, no effective preventive treatment is available, and currently approved therapeutics are limited by relatively high cost (101). HCV envelope glycoprotein E2 is well conserved across all genotypes and can bind to host cell receptors, including CD81 and scavenger receptor class B type I (SR-BI), making E2 an attractive target for neutralizing antibodies (102). HCV E2-specific neutralizing antibodies have been shown to neutralize genetically diverse HCV isolates and effectively prevent and treat HCV infection in a human liver-chimeric mouse model (103) and chimpanzees (104). More recently, treatment of a neutralizing human mAb targeting HCV E2 significantly delayed viral rebound in patients infected with HCV 1a following liver transplantation (105). From a phage-library displaying an sdAb repertoire of alpaca immunized with HCV E2 glycoprotein, one E2-specific and potent cross-reactive neutralizing sdAb, D03, was identified. D03 recognizes a novel conserved epitope overlapping with that of the CD81 binding site. Structural analysis of D03 revealed a long CDR3 (20 residues) folding over part of the framework. Between the upstream part of CDR2 and CDR3, a disulfide bridge is formed that serves to restrict the flexibility of CDR3, thereby allowing maximal accessibility to the tip region of D03. D03 displayed potently neutralizing activity against a panel of HCV pseudoparticles representing six genotypes by interfering with E2–CD81 interaction, with an IC_{50} ranging between 1 and 10 μg/ml for most isolates. In addition, D03 efficiently inhibited cell-to-cell transmission of HCV, which is resistant to CD81 binding-site bnAbs (22). Although several sdAbs have entered clinical trials, this antibody is the first one that can prevent both cell-free and direct cell-to-cell transmission of a virus, highlighting its potential for the development as a clinically useful entry inhibitor.

A number of anti-NS5B, anti-NS3, and antiprotease sdAbs were identified from a humanized-camel naive VHH phage-display library (36–38). The three proteins are non-structural (NS) proteins, but with different enzymatic activities, and they are involved in HCV replication. By linking of these sdAbs to a cell-penetrating peptide, penetratin, these cell-penetrable sdAbs could suppress the heterologous HCV replication at different degrees, as shown by reduction of both intracellular and released viral RNA copies. Their recognized epitopes are located in the catalytic grooves of the enzymes. Therefore, a cocktail of sdAbs specific to multiple epitopes of HCV highly conserved regions and viral enzymes or enzymatically active proteins may be safe, broadly effective, and relatively mutation-tolerant anti-HCV agents.

Herpes Simplex Virus 2

Herpes simplex virus 2 is one of the most prevalent sexually transmitted viruses (106). HSV-2 infection is often described as a relatively mild and generally not life-threatening disease, but it is still one that significantly contributes to the acquisition of HIV-1 infection (107). Despite decades of intense research dedicated to preventing the sexual transmission of HSV-2, no broadly protective vaccine or therapeutic is available. Glycoprotein D (gD) mainly mediates membrane fusion by the interaction with its receptors, which serves as a key step for successful virus entry (108), as demonstrated by the finding that neutralizing antibodies targeting gD displayed effective protection against HSV infection (109). One gD-specific sdAb, R33, was identified from a VHH immune library obtained after immunizing a llama with HSV-2 gD, but did not show neutralization against HSV-2 virus *in vitro*. Fusion of the cytotoxic domain of *Pseudomonas aeruginosa* exotoxin A (R33ExoA) to R33 did display specific and potent killing of HSV-2-infected cells, with an IC_{50} of 6.7 nM, indicating that R33 can deliver toxins or drugs to HSV-2-infected cells to reduce their nonspecific toxicity to normal cells and diminish side effects (23). This study confirmed that the antiviral activity of sdAbs could be increased by fusing them to toxins to generate immunotoxins.

Enteric Viruses

Up to now, gastroenteritis remains a critical health issue worldwide. Rotaviruses (RVs) and noroviruses (NoVs) are the two primary viral etiologies responsible for nonbacterial diarrhea in adults or children. Although the currently licensed rotavirus vaccines are efficacious in preventing rotavirus infection, no drugs have been approved for norovirus treatment. An anti-rotavirus VHH [termed antirotavirus protein (ARP1)] from a llama immunized with rhesus-monkey group A rotavirus (RVA) strain has been shown to neutralize 11 strains and displayed preventive and therapeutic potency against RVA-induced diarrhea in a neonatal mouse model (24, 46, 110, 111). Interestingly, mitigation of the symptoms was also achieved with freeze-dried ARP1, allowing it to be applied in areas where cold chains are difficult to maintain. Moreover, Pant et al. developed secreted or anchored antirotavirus VHH expressed in *Lactobacillus paracasei* to directly deliver therapeutic agents for the treatment of gastroenteritis (110, 111). Currently, the first clinical trial was performed in infants with RVA-associated diarrhea. This resulted in significant reduction in the frequency of stool output and no side effects after oral ARP1 therapy (112). Another VHH, 3B2, which is specific to the inner capsid protein VP6,

showed more broadly neutralizing capacity against RVA strains at lower doses (25). 3B2 conferred protection against RVA-induced diarrhea not only in neonatal mice (25), but also in gnotobiotic piglets (26), an animal model that has been widely used to study human RVA pathogenesis. Furthermore, postinfection therapeutic treatment with 3B2 or 2KD1 in a neonatal mouse model significantly reduced duration of RVA-induced diarrhea (27).

Human NoVs are single-stranded RNA viruses whose capsid protein is composed of shell (S) and protruding (P) domains linked by a flexible hinge region (113). Because of the inability to cultivate NoVs in cells and continually evolving strains, no vaccines or therapeutics against NoVs are available. The lower region on the P domain contains several highly conserved residues among the genetically distinct genogroup II (GII) noroviruses, which is a dominant epitope recognized by broadly reactive mAbs (114, 115). Nano-85 and Nano-25 were isolated from alpha immunized with GII norovirus virus-like particles. They both bind to the region of P domain that forms occluded sites on the particles, as demonstrated by cryoelectron microscopy structures of sdAbs with viral particle complexes (28). Different from strain-dependent Nano-25, Nano-85 was broadly reactive to several different GII genotypes, including GII.4, GII.10, and GII.12. Furthermore, the binding of Nano-85 to intact particles caused the particles to disassemble *in vitro* (28), but the underlying mechanism needs to be further elucidated.

CONCLUSION AND PERSPECTIVES

In many cases, no vaccines or effective therapeutics are available to combat pathogenic viruses. As an alternative to full-size antibody-based antiviral therapeutics, sdAbs have begun to attract considerable scientific attention. sdAbs are characterized by their unique biophysical and pharmacological features, such as small size, high stability, excellent expression yield in prokaryotic and eukaryotic systems, and low immunogenicity. Antiviral sdAbs with nanomolar neutralization potency could be directly isolated from elicited sdAb repertoires of immunized animals when displayed on the surface of phage, yeast (116) or mammalian cells (35), or from large naive sdAb libraries (9). Moreover, sdAbs serve as excellent molecules for making multivalent constructs. Multimerization of sdAbs can easily increase affinity and potency. Fusion of several sdAbs that recognize different epitopes together might reduce the emergence of resistant virus during treatment. In this respect, sdAbs have an advantage over IgG, as the production of IgG-based bispecific antibodies involves the specific combination of four different polypeptides. Such novel multivalent constructs could be very effective *in vivo*. Finally, as discussed above, future research might focus on exploiting the ability of sdAbs, as intrabodies, to target intracellular proteins.

Despite these advantages, two major issues need to be addressed before sdAbs can be considered for *in vivo* use: their short half-life in circulation and possible immunogenicity. Their relatively short half-life *in vivo* could be improved by various strategies, most of which may, however, lead to increased size and decreased inhibitory activity. For instance, one of the most efficient strategies in extending half-life is to fuse sdAbs with human IgG1 Fc. IgG1 Fc can bind to the neonatal Fc receptor (FcRn) and rescue the fused sdAbs from endosomal degradation, but such fusion will result in greatly increasing the size of sdAbs from ~15 to ~90 kDa. This could be partially addressed by the replacement of wild-type dimeric IgG1 Fc with some novel engineered Fc-based constructs. For example, we previously developed monomeric IgG1 CH3 or CH2–CH3 hybrids which have relatively small size (~15 kDa) and FcRn-binding capability (117–120). Such fusion proteins were easy to produce, stable, and retained the antigen-binding capability of the sdAbs (117, 121).

To reduce the risk of immunogenicity, strategies for the humanization of camelid-derived sdAbs have also become available in recent years. However, these strategies have some limitations, including the loss of heat refoldability upon humanization and the requirement to maintain two camelid residues within the FR2 (60). For biomedical applications, human VH sdAbs would be preferable because of the limited immunogenicity in patients. Although isolated human VH single domains generally display poor stability that causes aggregation, the poor biophysical properties of human VH single domains have recently been improved by the identification and introduction of mutations that allow maximal transfer of the hydrophobic to hydrophilic V_H/V_L interface and do so by direct selection from phage libraries (122, 123). The grafting of CDRs from naive repertoire or immunized individuals into such human sdAb scaffolds could result in the development of fully human sdAbs against various targets. With advancing antibody-related technologies, we can anticipate the development of humanized or fully human sdAbs with minimal immunogenicity as commercially attractive therapeutics to fight viral diseases.

AUTHOR CONTRIBUTIONS

YW, SJ, and TY conceived and wrote the article.

FUNDING

This work was supported by the National Natural Science Foundation of China (31570936, 81630090, and 81561128006) and the 1000 Young Talents Program of China.

REFERENCES

1. Reichert JM. Antibodies to watch in 2017. *mAbs* (2017) 9(2):167–81. doi:10.1080/19420862.2016.1269580
2. Weiner GJ. Building better monoclonal antibody-based therapeutics. *Nat Rev Cancer* (2015) 15(6):361–70. doi:10.1038/nrc3930
3. Scott LJ, Lamb HM. Palivizumab. *Drugs* (1999) 58(2):305–11; discussion 312–3. doi:10.2165/00003495-199958020-00009
4. Samaranayake H, Wirth T, Schenkwein D, Räty JK, Ylä-Herttuala S. Challenges in monoclonal antibody-based therapies. *Ann Med* (2009) 41(5):322–31. doi:10.1080/07853890802698842
5. Holliger P, Hudson PJ. Engineered antibody fragments and the rise of single domains. *Nat Biotech* (2005) 23(9):1126–36. doi:10.1038/nbt1142
6. Ward ES, Gussow D, Griffiths AD, Jones PT, Winter G. Binding activities of a repertoire of single immunoglobulin variable domains secreted from Escherichia coli. *Nature* (1989) 341(6242):544–6. doi:10.1038/341544a0

7. Hamers-Casterman C, Atarhouch T, Muyldermans S. Naturally occurring antibodies devoid of light chains. *Nature* (1993) 363(6428):446–8. doi:10.1038/363446a0
8. Vanlandschoot P, Stortelers C, Beirnaert E, Ibañez LI, Schepens B, Depla E, et al. Nanobodies®: new ammunition to battle viruses. *Antiviral Res* (2011) 92(3):389–407. doi:10.1016/j.antiviral.2011.09.002
9. Chen W, Zhu Z, Feng Y, Dimitrov DS. Human domain antibodies to conserved sterically restricted regions on gp120 as exceptionally potent cross-reactive HIV-1 neutralizers. *Proc Natl Acad Sci U S A* (2008) 105(44):17121–6. doi:10.1073/pnas.0805297105
10. Matz J, Kessler P, Bouchet J, Combes O, Ramos OH, Barin F, et al. Straightforward selection of broadly neutralizing single-domain antibodies targeting the conserved CD4 and coreceptor binding sites of HIV-1 gp120. *J Virol* (2013) 87(2):1137–49. doi:10.1128/JVI.00461-12
11. McCoy LE, Quigley AF, Strokappe NM, Bulmer-Thomas B, Seaman MS, Mortier D, et al. Potent and broad neutralization of HIV-1 by a llama antibody elicited by immunization. *J Exp Med* (2012) 209(6):1091–103. doi:10.1084/jem.20112655
12. Gong R, Wang Y, Ying T, Dimitrov DS. Bispecific engineered antibody domains (nanoantibodies) that interact noncompetitively with an HIV-1 neutralizing epitope and FcRn. *PLoS One* (2012) 7(8):e42288. doi:10.1371/journal.pone.0042288
13. Lutje Hulsik D, Liu YY, Strokappe NM, Battella S, El Khattabi M, McCoy LE, et al. A gp41 MPER-specific llama VHH requires a hydrophobic CDR3 for neutralization but not for antigen recognition. *PLoS Pathog* (2013) 9(3):e1003202. doi:10.1371/journal.ppat.1003202
14. Detalle L, Stohr T, Palomo C, Piedra PA, Gilbert BE, Mas V, et al. Generation and characterization of ALX-0171, a potent novel therapeutic nanobody for the treatment of respiratory syncytial virus infection. *Antimicrob Agents Chemother* (2015) 60(1):6–13. doi:10.1128/AAC.01802-15
15. Rossey I, Gilman MS, Kabeche SC, Sedeyn K, Wrapp D, Kanekiyo M, et al. Potent single-domain antibodies that arrest respiratory syncytial virus fusion protein in its prefusion state. *Nat Commun* (2017) 8:14158. doi:10.1038/ncomms14158
16. Wei G, Meng W, Guo H, Pan W, Liu J, Peng T, et al. Potent neutralization of influenza A virus by a single-domain antibody blocking M2 ion channel protein. *PLoS One* (2011) 6(12):e28309. doi:10.1371/journal.pone.0028309
17. Ibanez LI, De Filette M, Hultberg A, Verrips T, Temperton N, Weiss RA, et al. Nanobodies with in vitro neutralizing activity protect mice against H5N1 influenza virus infection. *J Infect Dis* (2011) 203(8):1063–72. doi:10.1093/infdis/jiq168
18. Tillib SV, Ivanova TI, Vasilev LA, Rutovskaya MV, Saakyan SA, Gribova IY, et al. Formatted single-domain antibodies can protect mice against infection with influenza virus (H5N2). *Antiviral Res* (2013) 97(3):245–54. doi:10.1016/j.antiviral.2012.12.014
19. Hufton SE, Risley P, Ball CR, Major D, Engelhardt OG, Poole S. The breadth of cross sub-type neutralisation activity of a single domain antibody to influenza hemagglutinin can be increased by antibody valency. *PLoS One* (2014) 9(8):e103294. doi:10.1371/journal.pone.0103294
20. Cardoso FM, Ibanez LI, Van den Hoecke S, De Baets S, Smet A, Roose K, et al. Single-domain antibodies targeting neuraminidase protect against an H5N1 influenza virus challenge. *J Virol* (2014) 88(15):8278–96. doi:10.1128/JVI.03178-13
21. Harmsen M, Blokker J, Pritz-Verschuren S, Bartelink W, van der Burg H, Koch G. Isolation of panels of llama single-domain antibody fragments binding all nine neuraminidase subtypes of influenza A virus. *Antibodies* (2013) 2(2):168–92. doi:10.3390/antib2020168
22. Tarr AW, Lafaye P, Meredith L, Damier-Piolle L, Urbanowicz RA, Meola A, et al. An alpaca nanobody inhibits hepatitis C virus entry and cell-to-cell transmission. *Hepatology* (2013) 58(3):932–9. doi:10.1002/hep.26430
23. Geoghegan EM, Zhang H, Desai PJ, Biragyn A, Markham RB. Antiviral activity of a single-domain antibody immunotoxin binding to glycoprotein D of herpes simplex virus 2. *Antimicrob Agents Chemother* (2015) 59(1):527–35. doi:10.1128/AAC.03818-14
24. van der Vaart JM, Pant N, Wolvers D, Bezemer S, Hermans PW, Bellamy K, et al. Reduction in morbidity of rotavirus induced diarrhoea in mice by yeast produced monovalent llama-derived antibody fragments. *Vaccine* (2006) 24(19):4130–7. doi:10.1016/j.vaccine.2006.02.045
25. Garaicoechea L, Olichon A, Marcoppido G, Wigdorovitz A, Mozgovoj M, Saif L, et al. Llama-derived single-chain antibody fragments directed to rotavirus VP6 protein possess broad neutralizing activity in vitro and confer protection against diarrhea in mice. *J Virol* (2008) 82(19):9753–64. doi:10.1128/JVI.00436-08
26. Vega CG, Bok M, Vlasova AN, Chattha KS, Gomez-Sebastian S, Nunez C, et al. Recombinant monovalent llama-derived antibody fragments (VHH) to rotavirus VP6 protect neonatal gnotobiotic piglets against human rotavirus-induced diarrhea. *PLoS Pathog* (2013) 9(5):e1003334. doi:10.1371/journal.ppat.1003334
27. Maffey L, Vega CG, Miño S, Garaicoechea L, Parreño V. Anti-VP6 VHH: an experimental treatment for rotavirus A-associated disease. *PLoS One* (2016) 11(9):e0162351. doi:10.1371/journal.pone.0162351
28. Koromyslova AD, Hansman GS. Nanobody binding to a conserved epitope promotes norovirus particle disassembly. *J Virol* (2015) 89(5):2718–30. doi:10.1128/JVI.03176-14
29. Thys B, Schotte L, Muyldermans S, Wernery U, Hassanzadeh-Ghassabeh G, Rombaut B. In vitro antiviral activity of single domain antibody fragments against poliovirus. *Antiviral Res* (2010) 87(2):257–64. doi:10.1016/j.antiviral.2010.05.012
30. Schotte L, Strauss M, Thys B, Halewyck H, Filman DJ, Bostina M, et al. Mechanism of action and capsid-stabilizing properties of VHHs with an in vitro antipolioviral activity. *J Virol* (2014) 88(8):4403–13. doi:10.1128/JVI.03402-13
31. Strauss M, Schotte L, Thys B, Filman DJ, Hogle JM. Five of five VHHs neutralizing poliovirus bind the receptor-binding site. *J Virol* (2016) 90(7):3496–505. doi:10.1128/JVI.03017-15
32. Matz J, Herate C, Bouchet J, Dusetti N, Gayet O, Baty D, et al. Selection of intracellular single-domain antibodies targeting the HIV-1 Vpr protein by cytoplasmic yeast two-hybrid system. *PLoS One* (2014) 9(12):e113729. doi:10.1371/journal.pone.0113729
33. Ashour J, Schmidt FI, Hanke L, Cragnolini J, Cavallari M, Altenburg A, et al. Intracellular expression of camelid single-domain antibodies specific for influenza virus nucleoprotein uncovers distinct features of its nuclear localization. *J Virol* (2015) 89(5):2792–800. doi:10.1128/JVI.02693-14
34. Hanke L, Knockenhauer KE, Brewer RC, van Diest E, Schmidt FI, Schwartz TU, et al. The antiviral mechanism of an influenza A virus nucleoprotein-specific single-domain antibody fragment. *MBio* (2016) 7(6):e01569-16. doi:10.1128/mBio.01569-16
35. Schmidt FI, Hanke L, Morin B, Brewer R, Brusic V, Whelan SP, et al. Phenotypic lentivirus screens to identify functional single domain antibodies. *Nat Microbiol* (2016) 1(8):16080. doi:10.1038/nmicrobiol.2016.80
36. Thueng-in K, Thanongsaksrikul J, Srimanote P, Bangphoomi K, Poungpair O, Maneewatch S, et al. Cell penetrable humanized-VH/V(H)H that inhibit RNA dependent RNA polymerase (NS5B) of HCV. *PLoS One* (2012) 7(11):e49254. doi:10.1371/journal.pone.0049254
37. Phalaphol A, Thueng-In K, Thanongsaksrikul J, Poungpair O, Bangphoomi K, Sookrung N, et al. Humanized-VH/VHH that inhibit HCV replication by interfering with the virus helicase activity. *J Virol Methods* (2013) 194(1–2):289–99. doi:10.1016/j.jviromet.2013.08.032
38. Jittavisutthikul S, Thanongsaksrikul J, Thueng-In K, Chulanetra M, Srimanote P, Seesuay W, et al. Humanized-VHH transbodies that inhibit HCV protease and replication. *Viruses* (2015) 7(4):2030–56. doi:10.3390/v7042030
39. Sherwood LJ, Osborn LE, Carrion R, Patterson JL, Hayhurst A. Rapid assembly of sensitive antigen-capture assays for Marburg virus, using in vitro selection of llama single-domain antibodies, at biosafety level 4. *J Infect Dis* (2007) 196:S213–9. doi:10.1086/520586
40. Sherwood LJ, Hayhurst A. Ebolavirus nucleoprotein C-termini potently attract single domain antibodies enabling monoclonal affinity reagent sandwich assay (MARSA) formulation. *PLoS One* (2013) 8(4):e61232. doi:10.1371/journal.pone.0061232
41. Darling TL, Sherwood LJ, Hayhurst A. Intracellular crosslinking of filoviral nucleoproteins with xintrabodies restricts viral packaging. *Front Immunol* (2017) 8:1197. doi:10.3389/fimmu.2017.01197
42. Muyldermans S, Atarhouch T, Saldanha J, Barbosa JARG, Hamers R. Sequence and structure of V-H domain from naturally-occurring camel heavy-chain immunoglobulins lacking light-chains. *Protein Eng* (1994) 7(9):1129–35. doi:10.1093/Protein/7.9.1129
43. Vu KB, Ghahroudi MA, Wyns L, Muyldermans S. Comparison of llama V-H sequences from conventional and heavy chain antibodies. *Mol Immunol* (1997) 34(16–17):1121–31. doi:10.1016/S0161-5890(97)00146-6

44. Muyldermans S. Nanobodies: natural single-domain antibodies. *Annu Rev Biochem* (2013) 82:775–97. doi:10.1146/annurev-biochem-063011-092449
45. Van Heeke G, Allosery K, De Brabandere V, De Smedt T, Detalle L, de Fougerolles A. Nanobodies® as inhaled biotherapeutics for lung diseases. *Pharmacol Ther* (2017) 169:47–56. doi:10.1016/j.pharmthera.2016.06.012
46. Tokuhara D, Alvarez B, Mejima M, Hiroiwa T, Takahashi Y, Kurokawa S, et al. Rice-based oral antibody fragment prophylaxis and therapy against rotavirus infection. *J Clin Invest* (2013) 123(9):3829–38. doi:10.1172/JCI70266
47. Rutgers KS, Nabuurs RJA, van den Berg SAA, Schenk GJ, Rotman M, Verrips CT, et al. Transmigration of beta amyloid specific heavy chain antibody fragments across the in vitro blood–brain barrier. *Neuroscience* (2011) 190:37–42. doi:10.1016/j.neuroscience.2011.05.076
48. Rotman M, Welling MM, Bunschoten A, de Backer ME, Rip J, Nabuurs RJA, et al. Enhanced glutathione PEGylated liposomal brain delivery of an anti-amyloid single domain antibody fragment in a mouse model for Alzheimer's disease. *J Control Release* (2015) 203:40–50. doi:10.1016/j.jconrel.2015.02.012
49. Terryn S, Francart A, Lamoral S, Hultberg A, Rommelaere H, Wittelsberger A, et al. Protective effect of different anti-rabies virus VHH constructs against rabies disease in mice. *PLoS One* (2014) 9(10):e109367. doi:10.1371/journal.pone.0109367
50. Terryn S, Francart A, Rommelaere H, Stortelers C, Van Gucht S. Post-exposure treatment with anti-rabies VHH and vaccine significantly improves protection of mice from lethal rabies infection. *PLoS Negl Trop Dis* (2016) 10(8):e0004902. doi:10.1371/journal.pntd.0004902
51. Garza JA, Taylor AB, Sherwood LJ, Hart PJ, Hayhurst A. Unveiling a drift resistant cryptotope within marburgvirus nucleoprotein recognized by llama single-domain antibodies. *Front Immunol* (2017) 8:1234. doi:10.3389/fimmu.2017.01234
52. Muller D, Karle A, Meissburger B, Hofig I, Stork R, Kontermann RE. Improved pharmacokinetics of recombinant bispecific antibody molecules by fusion to human serum albumin. *J Biol Chem* (2007) 282(17):12650–60. doi:10.1074/jbc.M700820200
53. Veronese FM, Mero A. The impact of PEGylation on biological therapies. *BioDrugs* (2008) 22(5):315–29. doi:10.2165/00063030-200822050-00004
54. Bell A, Wang ZJ, Arbabi-Ghahroudi M, Chang TA, Durocher Y, Trojahn U, et al. Differential tumor-targeting abilities of three single-domain antibody formats. *Cancer Lett* (2010) 289(1):81–90. doi:10.1016/j.canlet.2009.08.003
55. Heredia A, Latinovic OS, Barbault F, de Leeuw EP. A novel small-molecule inhibitor of HIV-1 entry. *Drug Des Devel Ther* (2015) 9:5469–78. doi:10.2147/DDDT.S89338
56. Qiu LP, Chen L, Chen KP. Antihepatitis B therapy: a review of current medications and novel small molecule inhibitors. *Fundam Clin Pharmacol* (2014) 28(4):364–81. doi:10.1111/fcp.12053
57. Meanwell NA, Philip S. Portoghese medicinal chemistry lectureship. curing hepatitis C virus infection with direct-acting antiviral agents: the arc of a medicinal chemistry triumph. *J Med Chem* (2016) 59(16):7311–51. doi:10.1021/acs.jmedchem.6b00915
58. Lee KK, Pessi A, Gui L, Santoprete A, Talekar A, Moscona A, et al. Capturing a fusion intermediate of influenza hemagglutinin with a cholesterol-conjugated peptide, a new antiviral strategy for influenza virus. *J Biol Chem* (2011) 286(49):42141–9. doi:10.1074/jbc.M111.254243
59. Flexner C, Saag M. The antiretroviral drug pipeline: prospects and implications for future treatment research. *Curr Opin HIV AIDS* (2013) 8(6):572–8. doi:10.1097/COH.0000000000000011
60. Vincke C, Loris R, Saerens D, Martinez-Rodriguez S, Muyldermans S, Conrath K. General strategy to humanize a camelid single-domain antibody and identification of a universal humanized nanobody scaffold. *J Biol Chem* (2009) 284(5):3273–84. doi:10.1074/jbc.M806889200
61. Plemper RK. Cell entry of enveloped viruses. *Curr Opin Virol* (2011) 1(2):92–100. doi:10.1016/j.coviro.2011.06.002
62. Tan M, Hegde RS, Jiang X. The P domain of norovirus capsid protein forms dimer and binds to histo-blood group antigen receptors. *J Virol* (2004) 78(12):6233–42. doi:10.1128/JVI.78.12.6233-6242.2004
63. Klein JS, Gnanapragasam PN, Galimidi RP, Foglesong CP, West AP Jr, Bjorkman PJ. Examination of the contributions of size and avidity to the neutralization mechanisms of the anti-HIV antibodies b12 and 4E10. *Proc Natl Acad Sci U S A* (2009) 106(18):7385–90. doi:10.1073/pnas.0811427106
64. Ouyang Y, Yin Q, Li W, Li Z, Kong D, Wu Y, et al. Escape from humoral immunity is associated with treatment failure in HIV-1-infected patients receiving long-term antiretroviral therapy. *Sci Rep* (2017) 7(1):6222. doi:10.1038/s41598-017-05594-5
65. Worn A, der Maur AA, Escher D, Honegger A, Barberis A, Pluckthun A. Correlation between in vitro stability and in vivo performance of anti-GCN4 intrabodies as cytoplasmic inhibitors. *J Biol Chem* (2000) 275(4):2795–803. doi:10.1074/Jbc.275.4.2795
66. Xiang SH, Doka N, Choudhary RK, Sodroski J, Robinson JE. Characterization of CD4-induced epitopes on the HIV type 1 gp120 envelope glycoprotein recognized by neutralizing human monoclonal antibodies. *AIDS Res Hum Retroviruses* (2002) 18(16):1207–17. doi:10.1089/08892220260387959
67. Wu X, Yang ZY, Li Y, Hogerkorp CM, Schief WR, Seaman MS, et al. Rational design of envelope identifies broadly neutralizing human monoclonal antibodies to HIV-1. *Science* (2010) 329(5993):856–61. doi:10.1126/science.1187659
68. Walker LM, Huber M, Doores KJ, Falkowska E, Pejchal R, Julien JP, et al. Broad neutralization coverage of HIV by multiple highly potent antibodies. *Nature* (2011) 477(7365):466–70. doi:10.1038/nature10373
69. Scheid JF, Mouquet H, Ueberheide B, Diskin R, Klein F, Oliveira TY, et al. Sequence and structural convergence of broad and potent HIV antibodies that mimic CD4 binding. *Science* (2011) 333(6049):1633–7. doi:10.1126/science.1207227
70. Wyatt R, Kwong PD, Desjardins E, Sweet RW, Robinson J, Hendrickson WA, et al. The antigenic structure of the HIV gp120 envelope glycoprotein. *Nature* (1998) 393(6686):705–11. doi:10.1038/31514
71. Kwong PD, Wyatt R, Robinson J, Sweet RW, Sodroski J, Hendrickson WA. Structure of an HIV gp120 envelope glycoprotein in complex with the CD4 receptor and a neutralizing human antibody. *Nature* (1998) 393(6686):648–59. doi:10.1038/31405
72. Berkower I, Patel C, Ni Y, Virnik K, Xiang Z, Spadaccini A. Targeted deletion in the beta20-beta21 loop of HIV envelope glycoprotein gp120 exposes the CD4 binding site for antibody binding. *Virology* (2008) 377(2):330–8. doi:10.1016/j.virol.2008.03.040
73. Labrijn AF, Poignard P, Raja A, Zwick MB, Delgado K, Franti M, et al. Access of antibody molecules to the conserved coreceptor binding site on glycoprotein gp120 is sterically restricted on primary human immunodeficiency virus type 1. *J Virol* (2003) 77(19):10557–65. doi:10.1128/JVI.77.19.10557-10565.2003
74. Frey G, Peng H, Rits-Volloch S, Morelli M, Cheng Y, Chen B. A fusion-intermediate state of HIV-1 gp41 targeted by broadly neutralizing antibodies. *Proc Natl Acad Sci U S A* (2008) 105(10):3739–44. doi:10.1073/pnas.0800255105
75. Acharya P, Luongo TS, Georgiev IS, Matz J, Schmidt SD, Louder MK, et al. Heavy chain-only IgG2b llama antibody effects near-pan HIV-1 neutralization by recognizing a CD4-induced epitope that includes elements of coreceptor- and CD4-binding sites. *J Virol* (2013) 87(18):10173–81. doi:10.1128/JVI.01332-13
76. Liu L, Wang W, Matz J, Ye C, Bracq L, Delon J, et al. The glycosylphosphatidylinositol-anchored variable region of llama heavy chain-only antibody JM4 efficiently blocks both cell-free and T cell-T cell transmission of human immunodeficiency virus type 1. *J Virol* (2016) 90(23):10642–59. doi:10.1128/JVI.01559-16
77. McCoy LE, Groppelli E, Blanchetot C, de Haard H, Verrips T, Rutten L, et al. Neutralisation of HIV-1 cell-cell spread by human and llama antibodies. *Retrovirology* (2014) 11:83. doi:10.1186/s12977-014-0083-y
78. Huang J, Ofek G, Laub L, Louder MK, Doria-Rose NA, Longo NS, et al. Broad and potent neutralization of HIV-1 by a gp41-specific human antibody. *Nature* (2012) 491(7424):406–12. doi:10.1038/nature11544
79. Qiao ZS, Kim M, Reinhold B, Montefiori D, Wang JH, Reinherz EL. Design, expression, and immunogenicity of a soluble HIV trimeric envelope fragment adopting a prefusion gp41 configuration. *J Biol Chem* (2005) 280(24):23138–46. doi:10.1074/jbc.M414515200
80. Zhou M, Kostoula I, Brill B, Panou E, Sakarellos-Daitsiotis M, Dietrich U. Prime boost vaccination approaches with different conjugates of a new HIV-1 gp41 epitope encompassing the membrane proximal external region induce neutralizing antibodies in mice. *Vaccine* (2012) 30(11):1911–6. doi:10.1016/j.vaccine.2012.01.026
81. Ofek G, Tang M, Sambor A, Katinger H, Mascola JR, Wyatt R, et al. Structure and mechanistic analysis of the anti-human immunodeficiency virus type 1 antibody 2F5 in complex with its gp41 epitope. *J Virol* (2004) 78(19):10724–37. doi:10.1128/JVI.78.19.10724-10737.2004

82. Dimitrov DS. Engineered CH2 domains (nanoantibodies). *MAbs* (2009) 1(1):26–8. doi:10.4161/mabs.1.1.7480
83. Bouchet J, Basmaciogullari SE, Chrobak P, Stolp B, Bouchard N, Fackler OT, et al. Inhibition of the Nef regulatory protein of HIV-1 by a single-domain antibody. *Blood* (2011) 117(13):3559–68. doi:10.1182/blood-2010-07-296749
84. Vercruysse T, Pardon E, Vanstreels E, Steyaert J, Daelemans D. An intrabody based on a llama single-domain antibody targeting the N-terminal alpha-helical multimerization domain of HIV-1 rev prevents viral production. *J Biol Chem* (2010) 285(28):21768–80. doi:10.1074/jbc.M110.112490
85. Bouchet J, Herate C, Guenzel CA, Verollet C, Jarviluoma A, Mazzolini J, et al. Single-domain antibody-SH3 fusions for efficient neutralization of HIV-1 Nef functions. *J Virol* (2012) 86(9):4856–67. doi:10.1128/JVI.06329-11
86. Hause BM, Collin EA, Liu R, Huang B, Sheng Z, Lu W, et al. Characterization of a novel influenza virus in cattle and Swine: proposal for a new genus in the Orthomyxoviridae family. *MBio* (2014) 5(2):e31–14. doi:10.1128/mBio.00031-14
87. Gao R, Cao B, Hu Y, Feng Z, Wang D, Hu W, et al. Human infection with a novel avian-origin influenza A (H7N9) virus. *N Engl J Med* (2013) 368(20):1888–97. doi:10.1056/NEJMoa1304459
88. Tscherne DM, García-Sastre A. Virulence determinants of pandemic influenza viruses. *J Clin Invest* (2011) 121(1):6–13. doi:10.1172/jci44947
89. Basu A, Antanasijevic A, Wang M, Li B, Mills DM, Ames JA, et al. New small molecule entry inhibitors targeting hemagglutinin-mediated influenza a virus fusion. *J Virol* (2014) 88(3):1447–60. doi:10.1128/JVI.01225-13
90. De Clercq E. Antiviral agents active against influenza A viruses. *Nat Rev Drug Discov* (2006) 5(12):1015–25. doi:10.1038/nrd2175
91. Tutykhina IL, Sedova ES, Gribova IY, Ivanova TI, Vasilev LA, Rutovskaya MV, et al. Passive immunization with a recombinant adenovirus expressing an HA (H5)-specific single-domain antibody protects mice from lethal influenza infection. *Antiviral Res* (2013) 97(3):318–28. doi:10.1016/j.antiviral.2012.12.021
92. Pinto LH, Holsinger LJ, Lamb RA. Influenza-virus M2 protein has ion channel activity. *Cell* (1992) 69(3):517–28. doi:10.1016/0092-8674(92)90452-I
93. Palese P, Shaw ML. Orthomyxoviridae: the viruses and their replication. In: Ed Knipe DM, Howley PM, Griffin DE, Lamb RA, Martin MA, Roizman B, et al., editors. *Fields Virology*. Philadelphia, PA: Lippincott Williams & Wilkins (2007) 1647–89.
94. Nair H, Nokes DJ, Gessner BD, Dherani M, Madhi SA, Singleton RJ, et al. Global burden of acute lower respiratory infections due to respiratory syncytial virus in young children: a systematic review and meta-analysis. *Lancet* (2010) 375(9725):1545–55. doi:10.1016/S0140-6736(10)60206-1
95. Battles MB, Langedijk JP, Furmanova-Hollenstein P, Chaiwatpongsakorn S, Costello HM, Kwanten L, et al. Molecular mechanism of respiratory syncytial virus fusion inhibitors. *Nat Chem Biol* (2016) 12(2):87–93. doi:10.1038/nchembio.1982
96. Johnson S, Oliver C, Prince GA, Hemming VG, Pfarr DS, Wang SC, et al. Development of a humanized monoclonal antibody (MEDI-493) with potent in vitro and in vivo activity against respiratory syncytial virus. *J Infect Dis* (1997) 176(5):1215–24. doi:10.1086/514115
97. Group TI-RS. Palivizumab, a humanized respiratory syncytial virus monoclonal antibody, reduces hospitalization from respiratory syncytial virus infection in high-risk infants. *Pediatrics* (1998) 102(3):531–7. doi:10.1542/peds.102.3.531
98. Corti D, Bianchi S, Vanzetta F, Minola A, Perez L, Agatic G, et al. Cross-neutralization of four paramyxoviruses by a human monoclonal antibody. *Nature* (2013) 501(7467):439–43. doi:10.1038/nature12442
99. Zhao M, Zheng ZZ, Chen M, Modjarrad K, Zhang W, Zhan LT, et al. Discovery of a prefusion respiratory syncytial virus F-specific monoclonal antibody that provides greater in vivo protection than the murine precursor of palivizumab. *J Virol* (2017) 91(15):e176–117. doi:10.1128/JVI.00176-17
100. Capella C, Chaiwatpongsakorn S, Gorrell E, Risch ZA, Ye F, Mertz SE, et al. Prefusion F, postfusion F, G antibodies and disease severity in infants and young children with acute respiratory syncytial virus infection. *J Infect Dis* (2017). doi:10.1093/infdis/jix489
101. Gentile I, Maraolo AE, Buonomo AR, Zappulo E, Borgia G. The discovery of sofosbuvir: a revolution for therapy of chronic hepatitis C. *Expert Opin Drug Discov* (2015) 10(12):1363–77. doi:10.1517/17460441.2015.1094051
102. Khan AG, Whidby J, Miller MT, Scarborough H, Zatorski AV, Cygan A, et al. Structure of the core ectodomain of the hepatitis C virus envelope glycoprotein 2. *Nature* (2014) 509(7500):381–4. doi:10.1038/nature13117
103. Law M, Maruyama T, Lewis J, Giang E, Tarr AW, Stamataki Z, et al. Broadly neutralizing antibodies protect against hepatitis C virus quasispecies challenge. *Nat Med* (2008) 14(1):25–7. doi:10.1038/nm1698
104. Morin TJ, Broering TJ, Leav BA, Blair BM, Rowley KJ, Boucher EN, et al. Human monoclonal antibody HCV1 effectively prevents and treats HCV infection in chimpanzees. *PLoS Pathog* (2012) 8(8):e1002895. doi:10.1371/journal.ppat.1002895
105. Chung RT, Gordon FD, Curry MP, Schiano TD, Emre S, Corey K, et al. Human monoclonal antibody MBL-HCV1 delays HCV viral rebound following liver transplantation: a randomized controlled study. *Am J Transplant* (2013) 13(4):1047–54. doi:10.1111/ajt.12083
106. Looker KJ, Gamett GP, Schmid GP. An estimate of the global prevalence and incidence of herpes simplex virus type 2 infection. *Bull World Health Organ* (2008) 86(10):805–12. doi:10.2471/BLT.07.046128
107. Holmberg SD, Stewart JA, Gerber AR, Byers RH, Lee FK, Omalley PM, et al. Prior herpes-simplex virus type-2 infection as a risk factor for HIV infection. *J Am Med Assoc* (1988) 259(7):1048–50. doi:10.1001/Jama.259.7.1048
108. Atanasiu D, Saw WT, Cohen GH, Eisenberg RJ. Cascade of events governing cell-cell fusion induced by herpes simplex virus glycoproteins gD, gH/gL, and gB. *J Virol* (2010) 84(23):12292–9. doi:10.1128/JVI.01700-10
109. Nicola AV, Ponce de Leon M, Xu R, Hou W, Whitbeck JC, Krummenacher C, et al. Monoclonal antibodies to distinct sites on herpes simplex virus (HSV) glycoprotein D block HSV binding to HVEM. *J Virol* (1998) 72(5):3595–601.
110. Pant N, Hultberg A, Zhao Y, Svensson L, Pan-Hammarstrom Q, Johansen K, et al. Lactobacilli expressing variable domain of llama heavy-chain antibody fragments (lactobodies) confer protection against rotavirus-induced diarrhea. *J Infect Dis* (2006) 194(11):1580–8. doi:10.1086/508747
111. Pant N, Marcotte H, Hermans P, Bezemer S, Frenken L, Johansen K, et al. Lactobacilli producing bispecific llama-derived anti-rotavirus proteins in vivo for rotavirus-induced diarrhea. *Future Microbiol* (2011) 6(5):583–93. doi:10.2217/fmb.11.32
112. Sarker SA, Jakel M, Sultana S, Alam NH, Bardhan PK, Chisti MJ, et al. Anti-rotavirus protein reduces stool output in infants with diarrhea: a randomized placebo-controlled trial. *Gastroenterology* (2013) 145(4):740–8.e8. doi:10.1053/j.gastro.2013.06.053
113. Hansman GS, Natori K, Shirato-Horikoshi H, Ogawa S, Oka T, Katayama K, et al. Genetic and antigenic diversity among noroviruses. *J Gen Virol* (2006) 87(Pt 4):909–19. doi:10.1099/vir.0.81532-0
114. Hansman GS, Taylor DW, McLellan JS, Smith TJ, Georgiev I, Tame JR, et al. Structural basis for broad detection of genogroup II noroviruses by a monoclonal antibody that binds to a site occluded in the viral particle. *J Virol* (2012) 86(7):3635–46. doi:10.1128/JVI.06868-11
115. Shiota T, Okame M, Takanashi S, Khamrin P, Takagi M, Satou K, et al. Characterization of a broadly reactive monoclonal antibody against norovirus genogroups I and II: recognition of a novel conformational epitope. *J Virol* (2007) 81(22):12298–306. doi:10.1128/JVI.00891-07
116. Ryckaert S, Pardon E, Steyaert J, Callewaert N. Isolation of antigen-binding camelid heavy chain antibody fragments (nanobodies) from an immune library displayed on the surface of Pichia pastoris. *J Biotechnol* (2010) 145(2):93–8. doi:10.1016/j.jbiotec.2009.10.010
117. Ying T, Chen W, Feng Y, Wang Y, Gong R, Dimitrov DS. Engineered soluble monomeric IgG1 CH3 domain: generation, mechanisms of function, and implications for design of biological therapeutics. *J Biol Chem* (2013) 288(35):25154–64. doi:10.1074/jbc.M113.484154
118. Ying T, Ju TW, Wang Y, Prabakaran P, Dimitrov DS. Interactions of IgG1 CH2 and CH3 domains with FcRn. *Front Immunol* (2014) 5:146. doi:10.3389/fimmu.2014.00146
119. Ying T, Wang Y, Feng Y, Prabakaran P, Gong R, Wang L, et al. Engineered antibody domains with significantly increased transcytosis and half-life in macaques mediated by FcRn. *MAbs* (2015) 7(5):922–30. doi:10.1080/19420862.2015.1067353
120. Ying T, Feng Y, Wang Y, Chen W, Dimitrov DS. Monomeric IgG1 Fc molecules displaying unique Fc receptor interactions that are exploitable to treat inflammation-mediated diseases. *MAbs* (2014) 6(5):1201–10. doi:10.4161/mabs.29835

121. Wang L, Ying T. New directions for half-life extension of protein therapeutics: the rise of antibody Fc domains and fragments. *Curr Pharm Biotechnol* (2016) 17(15):1348–52. doi:10.2174/1389201017666160823144032
122. Jespers L, Schon O, James LC, Veprintsev D, Winter G. Crystal structure of HEL4, a soluble, refoldable human VH single domain with a germ-line scaffold. *J Mol Biol* (2004) 337(4):893–903. doi:10.1016/j.jmb.2004.02.013
123. Dudgeon K, Rouet R, Kokmeijer I, Schofield P, Stolp J, Langley D, et al. General strategy for the generation of human antibody variable domains with increased aggregation resistance. *Proc Natl Acad Sci U S A* (2012) 109(27):10879–84. doi:10.1073/pnas.1202866109

Conflict of Interest Statement: The authors declare that the article content was composed in the absence of any commercial or financial relationships that could be construed as a potential conflict of interest.

frontiers in Immunology

ORIGINAL RESEARCH
published: 27 September 2017
doi: 10.3389/fimmu.2017.01197

Intracellular Crosslinking of Filoviral Nucleoproteins with Xintrabodies Restricts Viral Packaging

*Tamarand Lee Darling[1,2], Laura Jo Sherwood[1] and Andrew Hayhurst[1]**

[1] Department of Virology and Immunology, Texas Biomedical Research Institute, San Antonio, TX, United States, [2] Department of Microbiology, Immunology and Molecular Genetics, The University of Texas Health Science Center at San Antonio, San Antonio, TX, United States

Viruses assemble large macromolecular repeat structures that become part of the infectious particles or virions. Ribonucleocapsids (RNCs) of negative strand RNA viruses are a prime example where repetition of nucleoprotein (NP) along the genome creates a core polymeric helical scaffold that accommodates other nucleocapsid proteins including viral polymerase. The RNCs are transported through the cytosol for packaging into virions through association with viral matrix proteins at cell membranes. We hypothesized that RNC would be ideal targets for crosslinkers engineered to promote aberrant protein–protein interactions, thereby blocking their orderly transport and packaging. Previously, we had generated single-domain antibodies (sdAbs) against Filoviruses that have all targeted highly conserved C-terminal regions of NP known to be repetitively exposed along the length of the RNCs of *Marburgvirus* (MARV) and *Ebolavirus* (EBOV). Our crosslinker design consisted of dimeric sdAb expressed intracellularly, which we call Xintrabodies (X- for crosslinking). Electron microscopy of purified NP polymers incubated with purified sdAb constructs showed NP aggregation occurred in a genus-specific manner with dimeric and not monomeric sdAb. A virus-like particle (VLP) assay was used for initial evaluation where we found that dimeric sdAb inhibited NP incorporation into VP40-based VLPs whereas monomeric sdAb did not. Inhibition of NP packaging was genus specific. Confocal microscopy revealed dimeric sdAb was diffuse when expressed alone but focused on pools of NP when the two were coexpressed, while monomeric sdAb showed ambivalent partition. Infection of stable Vero cell lines expressing dimeric sdAb specific for either MARV or EBOV NP resulted in smaller plaques and reduced progeny of cognate virus relative to wild-type Vero cells. Though the impact was marginal at later time-points, the collective data suggest that viral replication can be reduced by crosslinking intracellular NP using relatively small amounts of dimeric sdAb to restrict NP packaging. The stoichiometry and ease of application of the approach would likely benefit from transitioning away from intracellular expression of crosslinking sdAb to exogenous delivery of antibody. By retuning sdAb specificity, the approach of crosslinking highly conserved regions of assembly critical proteins may well be applicable to inhibiting replication processes of a broad spectrum of viruses.

Keywords: single-domain antibodies, VHH, Marburg, Ebola, nucleoprotein, crosslinker, intrabody, virus-like particle

OPEN ACCESS

Edited by:
Kevin A. Henry, National Research Council, Canada

Reviewed by:
Wanpen Chaicumpa, Mahidol University, Thailand
Serge Muyldermans, Vrije Universiteit Brussel, Belgium

***Correspondence:**
Andrew Hayhurst
ahayhurst@txbiomed.org

Specialty section:
This article was submitted to Vaccines and Molecular Therapeutics, a section of the journal Frontiers in Immunology

Received: *16 May 2017*
Accepted: *11 September 2017*
Published: *27 September 2017*

Citation:
Darling TL, Sherwood LJ and Hayhurst A (2017) Intracellular Crosslinking of Filoviral Nucleoproteins with Xintrabodies Restricts Viral Packaging. Front. Immunol. 8:1197. doi: 10.3389/fimmu.2017.01197

INTRODUCTION

The idea of turning the humoral immune system inside out (1) as a means of intracellular immunization (2) was first demonstrated by Antman and Livingston in 1980 (3) where IgG specific for SV40 T antigens were capable of inhibiting viral DNA synthesis following microinjection into cells permissive for replication. Since that time, many approaches have been tried to deliver antiviral antibodies into the cell cytoplasm in a more efficient manner to transition the approach from experimental to therapeutic. An early validation step in this process is the intracellular expression of antibodies from transfected plasmid DNA that enables the rapid evaluation of the resulting "intrabodies." The process is straightforward and enables screening for desired characteristics such as improved solubility and characterizing inhibitory activities. Rarely IgG genes have been directly employed in this approach for antiviral strategies (4) since they are complex multi-domain ($n = 12$) and multi-chain ($n = 2$) molecules tending to favor secreted environments for productive expression. Instead, smaller antibody fragment genes like Fab (four domains), scFv (two domains), and derivatives have been explored and shown to be functional within the reducing cytosol to varying degrees [for reviews, see Ref. (5, 6)].

Derived from heavy chain only antibodies of camelids, single-domain antibodies (sdAbs or VHH) (7) have also shown promise as intrabodies as they are one domain and one chain, not requiring pairing with a variable light-chain domain to bind antigen. sdAbs are highly soluble and are heat stable, which makes production at physiological temperatures more feasible. sdAbs are also generally not dependent on the formation of their intra-domain disulfide bond for productive expression, making them ideal candidates for expression in the reducing environment of the cytosol. Other small scaffolds have also shown promise as intrabody mimics by combining the simplicity of a single-domain unit that is disulfide bond free with engineered diversity for repertoire selection [e.g., the fibronectin fold (8, 9)].

Although all of these smaller derivatives have favorable production characteristics, they lack the steric bulk that can be advantageous for antiviral activity in occluding the interaction of viral proteins with each other or with host proteins. Since intrabodies are by definition within the cell, they also lack classical effector regions to enhance antiviral activity through classical antibody-dependent cell-mediated cytotoxicity. Unengineered sdAbs also lack the bivalency of IgG and are devoid of antiviral enhancements possible through avidity. Consequently, approaches to employ monovalent intrabodies and antibody mimetics as antivirals have tended to focus on impeding very specific viral functions where the impact of direct binding to target antigen is likely to be large. Examples include a scFv that binds to HPV16 E6 protein and inhibits p53 degradation (10) and a sdAb that inhibits HIV rev multimerization (11).

Selecting the right intrabodies to perform these roles for antiviral development is not trivial and requires identification of appropriate candidates from panels of pre-existing clones that not only express well but also have the desired inhibitory function. Alternatively, intrabody selection campaigns can be introduced to enrich high-expressing clones for screening of inhibitory function (12). More recently, direct selection of clones that allow cell survival after virus challenge with cytotoxic viruses can identify clones with antiviral activity (13).

Here, we advance an alternative approach based on a combination of rational yet simplistic design, basic antibody engineering principles, and a David versus Goliath mindset. We hypothesized that leveraging the steric bulk of macromolecular viral assemblies against one another would convert a normally innocuous monovalent sdAb into one with high-antiviral potency. Therefore, rather than focusing on *inhibiting* specific interactions between virus–virus or virus–cell proteins, we reasoned it should be possible to disrupt viral replication by *promoting* aberrant interactions. We aimed to crosslink cytosolic viral macromolecules using sdAb engineered as tandem dimers. In this manner, we should elicit a large impact on viral replication with a small amount of sdAb, which is ideal for advancing down a therapeutic track where high efficacy is ultimately required. We have christened these sdAb "Xintrabodies" to fuse the abbreviation for crosslinking (X) with the term for intrabody.

We had previously isolated sdAb from our semisynthetic llama library by live panning on *Marburgvirus* (MARV) (14) and *Ebolavirus* (EBOV) (15) at biosafety level four (BSL-4) which bound the C-terminal region of nucleoprotein (NP). All sdAb were capable of forming highly sensitive monoclonal affinity reagent sandwich assays (16) by reacting with detergent-treated virus preparations or recombinant NP suggesting the epitope they bound was displayed polyvalently along the NP polymer as visualized previously by others (17, 18). While our original plan was to employ these sdAbs in developing preclinical diagnostics, we rationalized they might also be promising candidates for exploring our crosslinking approach since the mass of NP polymers would be tens of MDa versus 30 kDa for the sdAb dimers.

A peculiar feature of many viral replication pathways is the formation of virogenic inclusion bodies or virus factories that could lend themselves to being particularly attractive sinks for intrabodies. The high concentration of target antigens and compartmentalization of certain cell processes are thought to drive more efficient genome replication, viral component, and/or even viral particle assembly (depending on the particular virus). Consequently, these sites could be very vulnerable to a crosslinking strategy as opposed to targeting diffusely distributed antigens throughout the cytoplasm. For both MARV and EBOV, the inclusions are highly dynamic sites of replication and contain large numbers of NP polymers (19–21) and several other viral proteins (L, VP24, VP30, and VP35) that together form the ribonucleocapsid (RNC) that encapsidates the RNA genome. These RNC assemblies have been shown to leave the inclusions on a one by one basis for transport through the cytoplasm for assembly at the cell periphery (22, 23). At the membrane, the RNCs interact with matrix protein VP40 to form enveloped infectious virus particles studded with the host cell targeting molecule GP that are then released. We hypothesized that the introduction of Xintrabodies into this model system will crosslink the RNC within the inclusions and impede the migration of NP to the cell periphery and restrict its ability to be packaged (**Figure 1**).

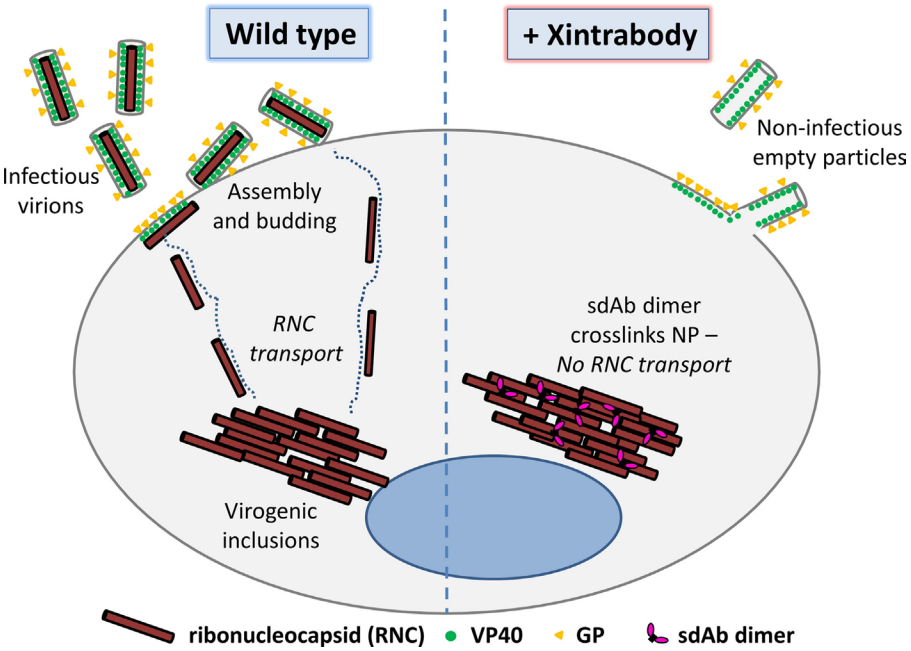

FIGURE 1 | Overall hypothesis of the approach showing that crosslinking a viral structural protein within the cell using a multimeric single-domain antibody (sdAb) will impede viral replication by disrupting the orderly assembly of infectious virus particles (virions). The dimeric sdAb can be introduced into the uninfected target cell or virus-infected cell *via* endogenous gene expression, gene delivery, protein transfection, or protein transduction to mediate the antiviral activity. Here, we focus on utilizing *Marburgvirus* and *Ebolavirus* nucleoprotein (NP) as our model target since we have sdAb to hand that bind polyvalent assemblies. Our working theory is that our sdAb dimers or Xintrabodies are crosslinking NP epitopes among ribonucleocapsids (RNCs) within viral factories and inhibiting their transport to the cell membrane for further assembly into virions. It should be noted that other antigens involved in assembly may be equally effective provided suitable sdAb are available, although targeting antigens that occur in viral factories may be advantageous owing to high local concentrations. The overall approach may be applicable to many other viruses and scaffolding components and leverages relatively small amounts of minute 30 kDa dimeric sdAb crosslinking MDa sized targets to impede productive viral replication.

Herein, we describe our studies on assembling, producing, and evaluating sdAb monomers and dimers *in vitro* and cell culture, comparing and contrasting their impacts on NP crosslinking *in vitro*, NP incorporation into virus-like particles (VLPs), and replication of virus.

RESULTS

Ensuring Tandem sdAbs Were Able to Bind Antigen

Since all of our sdAb were originally selected using g3p phage display with free N-termini we had to ensure that fusions retained binding and ideally showed enhanced activity reflective of avidity when expressed as sdAb–sdAb dimers. We therefore assembled monomers and dimers of anti-MARV sdAb A, B, and C and anti-EBOV sdAb E in our standard dual expression and display vector pecan126 (16) for production of protein in the *Escherichia coli* periplasm. All clones were well expressed as monomers as expected (**Figure 2A**) and as dimers (**Figure 2B**) highlighting the modularity of the single-domain fold for recombinant expression campaigns. To test the binding ability of the sdAb *in vitro*, we generated polymeric MARV and EBOV NP by HEK 293T transient expression and a purification regime that ended with CsCl gradient centrifugation to band the polymers. Both MARV and EBOV proteins are highly pure with the monomeric versions revealed by gel analysis of boiled and reduced samples (**Figure 2C**). Titration of the anti-MARV sdAb on NP revealed that all of the dimeric forms were more effective at binding MARV NP than monomeric sdAb and showed no increase in cross-reactivity with EBOV NP at 1 μM concentrations of antibody (**Figure 2D**). However, the degree of improvement varied between clones with sdAb A and C showing modest 5-fold improvements, while sdAb B was around 500-fold resulting in dimeric sdAb A and B having equivalent binding potency.

Titration of the anti-EBOV sdAb E showed an almost 4-log improvement of the dimer over the monomer (**Figure 2E**), yet we are very guarded in assigning just dimerization as the sole cause of this shift since the background signal on MARV NP was unusually high at 1–0.1 μM antibody concentrations for both monomer and dimer. In our hands, sdAb E performs very well in sandwich-based detection of both viral and recombinant NP and is more conformationally sensitive than other anti-EBOV NP sdAbs (15). Antigens are well known to be unfolded when passively immobilized on plastic surfaces and this may have resulted in sdAb E monomer being a poor performer. We also know that sdAb E monomer can be sparingly soluble at high concentrations while the dimer does not show this problem, which would impact available binding in this form of titration. The combination of solubility and conformational issues may

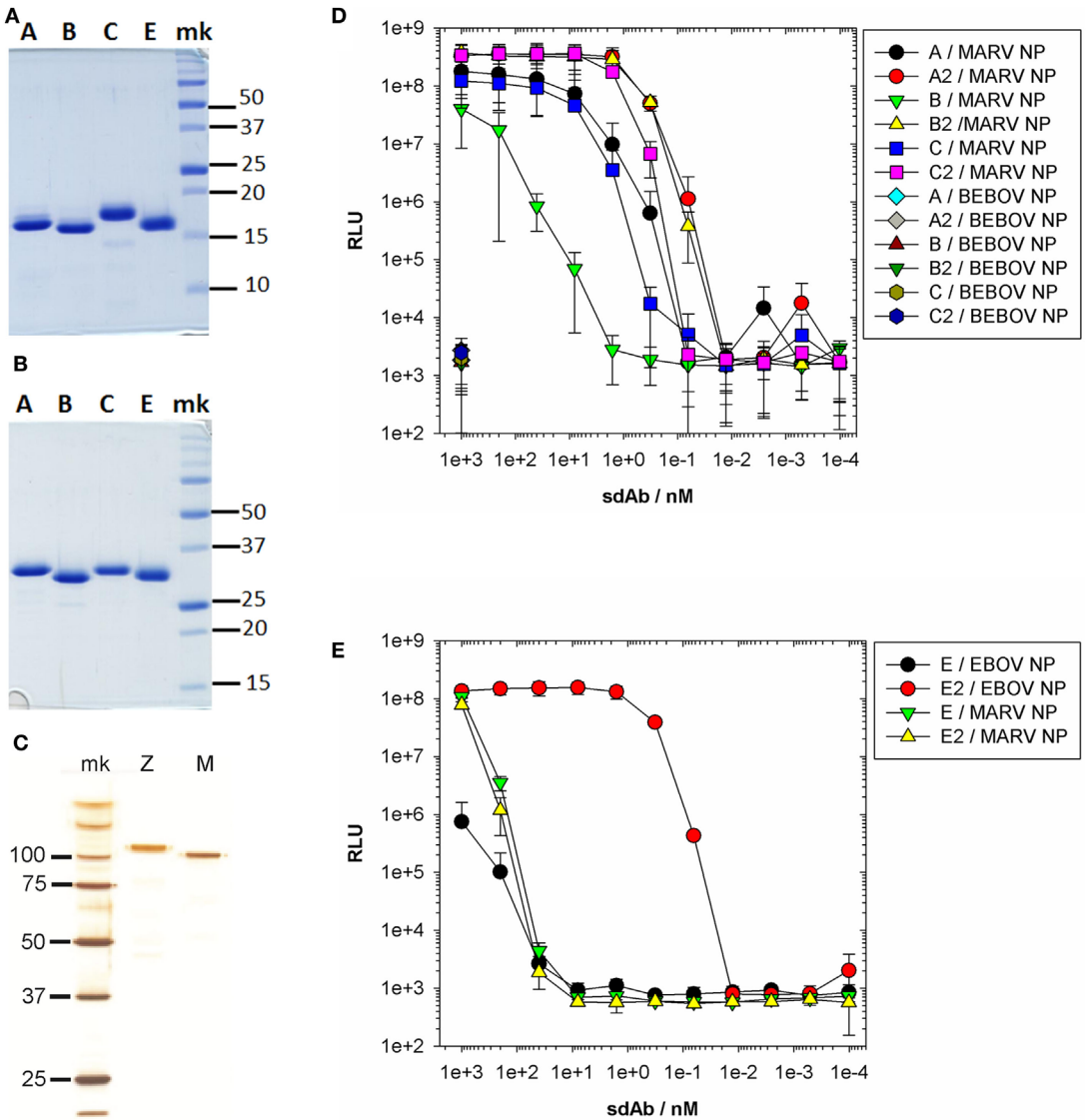

FIGURE 2 | Purification of single-domain antibody (sdAb) proteins and recombinant nucleoprotein (NP) for ELISA characterization. Coomassie stained SDS-PAGE gel showing 5 μg of each sdAb monomer **(A)** and dimer **(B)** purified from *Escherichia coli* periplasm. **(C)** Silver stained SDS-PAGE gel of *Marburgvirus* (MARV) (M) and *Ebolavirus* (EBOV) (Z) NP preparations following large-scale transient transfection and purification through centrifugation steps and banding on CsCl gradients. **(D)** ELISA titration of the anti-MARV sdAb monomers and dimers over MARV NP with the highest concentration also applied to Bundibugyo NP (this was expressed at higher levels than Zaire NP and so was convenient to use for controls yet shares high homology at the C-terminal domain for our studies). **(E)** ELISA titration of anti-EBOV sdAb E monomer and dimer over EBOV NP and MARV NP.

well account for sdAb E dimer performing so much better than monomer.

Identifying Productive Anti-MARV and Anti-EBOV Intrabody Monomers and Dimers

An enhanced mammalian expression vector was assembled to leverage the potent adenovirus tripartite sequence and hybrid intron for high level RNA processing and accumulation as noted by others (24, 25), yet leaving the convenient unidirectional *Sfi*I polylinker intact (**Figure 3A**). Our three primary anti-MARV NP candidate sdAb (A, B, and C), a fourth clone that expressed poorly in *E. coli* (D) and an EBOV NP specific clone (G) were first inserted into the pcDNASfi construct as both llama genes and human codon optimized genes. Plasmids were transfected into human embryonic kidney cells (HEK 293T) for transient expression and subsequent analysis by Western blotting of the whole cell extracts with sdAb detection through the C-terminal C9 tag. We were surprised to see the llama genes appeared to be more productive than the human optimized genes for all clones except sdAb B (**Figure 3B**). Monomeric and dimeric forms of the candidate genes were then assembled in puma1 and we used transient transfection and partial cell fractionation to

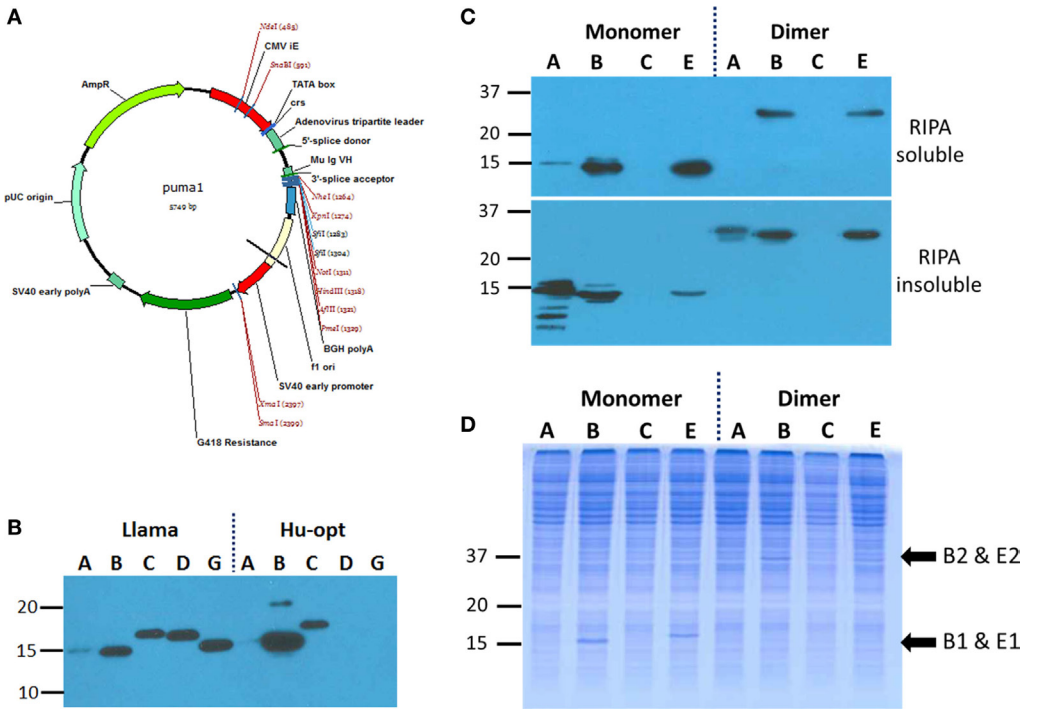

FIGURE 3 | Evaluating expression of various single-domain antibody (sdAb) formats as intrabodies within HEK 293T cells. **(A)** Mammalian expression vector puma1 built for these studies utilizes a human cytomegalovirus immediate early gene enhancer and promoter (CMV IE) and the adenovirus tripartite 5′-non-coding region with a hybrid splice donor acceptor with other components from the pcDNA stable (Invitrogen) including high copy number in both *Escherichia coli* and HEK 293T cells and G418 resistance cassette for stable line generation. **(B)** Anti-C9 Western blot of whole cell lysates of HEK 293T cells transiently transfected with C9 tagged wild-type llama sdAb sequences or human optimized sequences identify those clones with low and high relative expression levels. Cells were harvested 72 h post-transfection. **(C)** Anti-C9 Western blot of HEK 293T soluble (including cytosol) and insoluble (including membranes) fractions following transient expression of llama sdAb as monomeric and dimeric versions. **(D)** Coomassie blue stained SDS-PAGE of the soluble fractions reveal visible bands at the expected places for sdAb B and E monomers and just visible are the corresponding dimers.

determine the relative solubility of the monomers and dimers. Here, we switched from the EBOV-specific clone sdAb G to the highly cross-reactive clone sdAb E since our long-term goal is to develop countermeasures capable of broad reactivity among the Ebola species. Fortunately, both anti-MARV sdAb B and anti-EBOV sdAb E are produced at detectable levels in the soluble fraction as dimers (**Figure 3C**), though the levels appear somewhat reduced compared to monomers, perhaps reflecting the additional complexity required to fold tandem sdAb within the mammalian cytosol. Despite the apparent drop in expression levels, the dimeric forms of sdAb B and sdAb E are still just visible on Coomassie blue staining of the soluble fraction (**Figure 3D**) indicating that at least when expressed alone in the HEK 293T system, these sdAb formats are highly productive. We elected to take these two sdAb clones forward for further study in puma1 and for simplicity refer to them subsequently as M1 (anti-MARV NP sdAb B monomer), M2 (anti-MARV NP sdAb B dimer), E1 (anti-EBOV NP sdAb E monomer), and E2 (anti-EBOV NP sdAb E dimer).

Examining NP Crosslinking Capacity of sdAb Monomers and Dimers *In Vitro*

As we moved toward the intracellular immunofluorescent studies below, we conferred our sdAb and NP constructs with specific tags for visualization and so used these derivatives for *in vitro* crosslinking studies also. The M1, M2, E1, and E2 sdAbs were produced in *E. coli* with the C9 tag through periplasmic expression, IMAC purification, and gel filtration to generate highly pure proteins similar to those produced above (Figure S1A in Supplementary Material). Again, in multiple hands, we noticed similar production levels apparent for monomers and dimers from *E. coli* expressions suggesting tandem dimers are straightforward to produce in this host. Polymeric HA-tagged MARV and HA-tagged EBOV NP proteins were generated using the same optimized scaled up transient HEK 293T expression and purification protocol as above (Figure S1B in Supplementary Material). Different molar ratios of sdAb monomer and dimer proteins were combined with purified HA-NP, equilibrated for 1 h, and then the mixtures analyzed by transmission electron microscopy (**Figure 4**; Figure S2 in Supplementary Material). Here, the purity of the HA-NP preparations can be clearly seen as they form the classical helical filamentous structures seen by others. Only the dimeric forms of each sdAb were able to crosslink their corresponding HA-NP polymers in a genus-specific manner while the monomeric forms had no discernible effect. The crosslinking ability of the dimers extended to 1:1 and 0.1:1 M ratios of sdAb to HA-NP though uncrosslinked helical NP filaments are visible

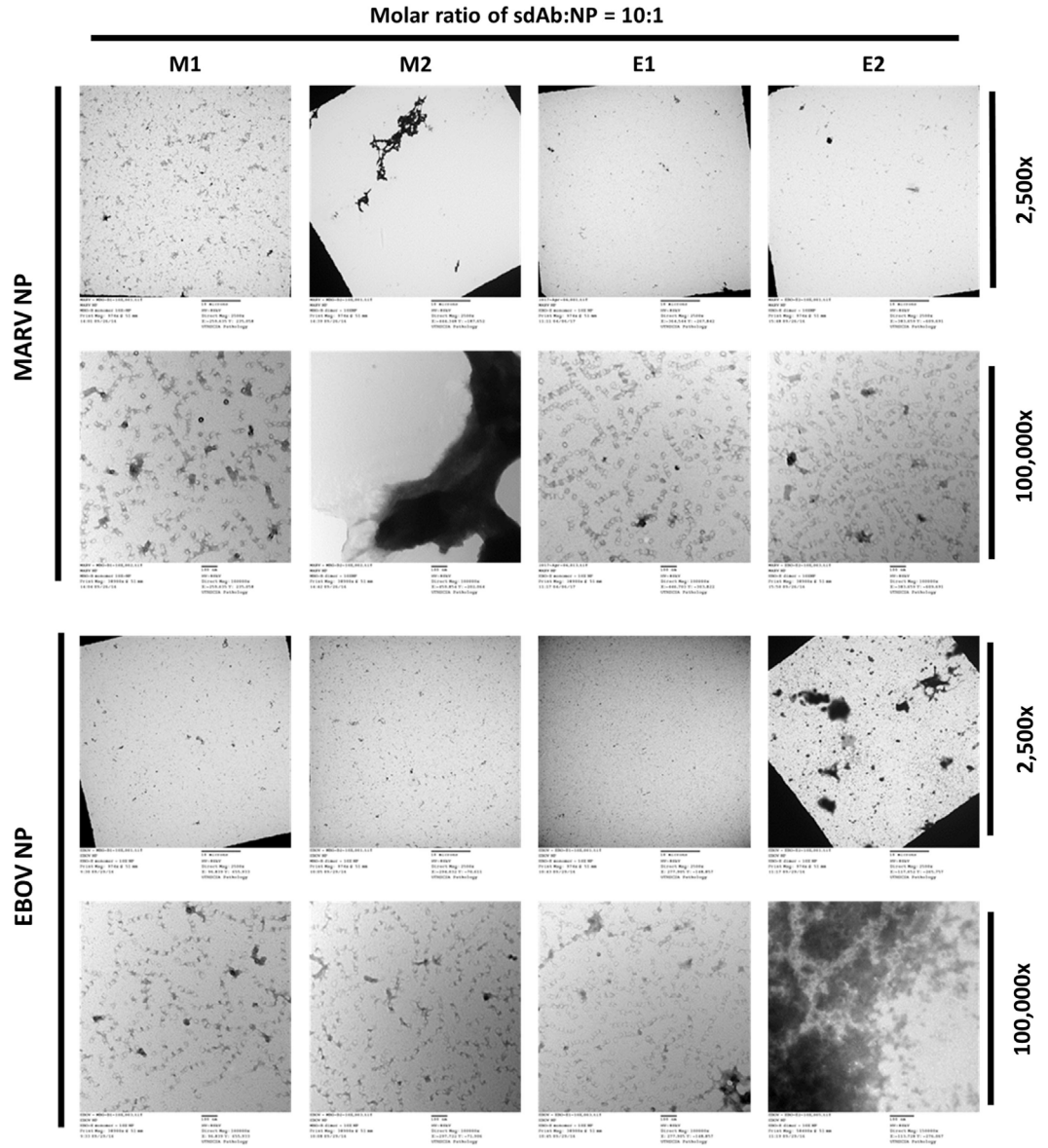

FIGURE 4 | Examining the ability of single-domain antibody (sdAb) monomers and dimers to crosslink nucleoprotein (NP) *in vitro* by electron microscopy. 10:1 M ratios of the anti-*Marburgvirus* (MARV) monomer (M1) or dimer (M2), or anti-*Ebolavirus* (EBOV) monomer (E1) or dimer (E2) were combined with MARV or EBOV NP and equilibrated for 1 h prior to transmission microscopy. In the absence of crosslinking the individual helical filaments of NP, polymers are visible in the 100,000× images for both MARV and EBOV NP.

at lower ratios, suggesting the sdAbs are being out-titrated. At the lower concentrations, the anti-MARV dimer appeared to be better at crosslinking than the anti-EBOV dimer and following quantification, we assessed it to be approximately 10-fold more potent at aggregating HA-NP (**Figure 5**). Crosslinking NP polymers *in vitro* in this manner reassures us that the arbitrarily chosen 20 mer linker between the tandem sdAb B proteins does not restrict binding to two epitopes on a single polymer (intra-NP binding) but allows inter-NP binding. It would be of interest to explore whether alterations in linker length and composition might further improve crosslinking efficacy.

Impact of sdAb Monomers and Dimers on VLP Formation

For both MARV and EBOV, VP40 expression alone is able to form enveloped VLPs (26, 27) and recombinant NP expression alone is enough to drive the formation of cytoplasmic inclusions (28, 29). When NP and VP40 are coexpressed, the result is VLPs made of NP and VP40. VLP composition in terms of ±NP therefore gives us a convenient way of analyzing the impact of Xintrabody expression on NP packaging. Since the particles are non-infectious, the approach is useable at BSL-2 for added convenience. Transient expression of combinations of MARV VP40,

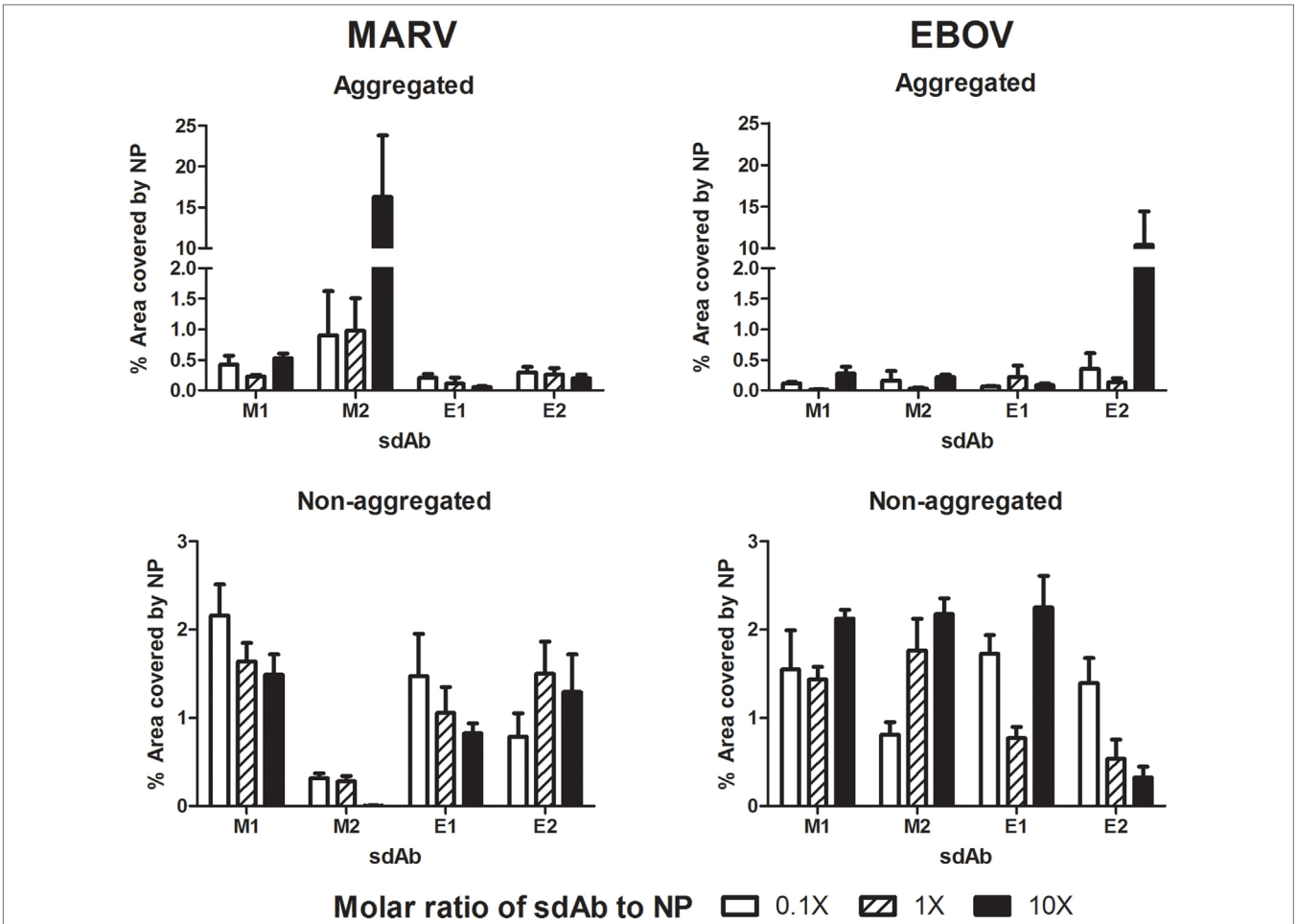

FIGURE 5 | Quantification of the 100,000× images from **Figure 4** using Cell Profiler to reveal the extent of aggregated and non-aggregated nucleoprotein (NP).

HA-NP, and the various sdAb constructs in HEK 293T cells revealed that NP was missing from those VLPs secreted from cells cotransfected with dimeric anti-MARV sdAb (M2) plasmid (**Figure 6A**). Examination of the cell lysates corresponding to these VLP expressions (**Figure 6B**) revealed that HA-NP was well expressed suggesting that the Xintrabody had not blocked NP production but a later step in VLP assembly. Importantly, the levels of sdAb are so low as to be not visible by Coomassie blue staining of SDS-PAGE gels when coexpressed with the viral proteins, yet the dimeric sdAb still has a dramatic inhibitory effect. A similar pattern for EBOV was evident when combinations of EBOV VP40, HA-NP, and the various sdAb were employed (**Figure 6C**) in that dimeric anti-EBOV sdAb (E2) inhibited NP incorporation into particles while other sdAb did not. Again, analysis of whole cell lysates revealed that EBOV HA-NP was being produced within the cells in large amounts suggesting a post-translational block of NP incorporation into VLPs was being elicited by E2 (**Figure 6D**). Figures S3A,B in Supplementary Material show Western blots of the MARV and EBOV cell lysates, respectively, to confirm expression of the sdAb monomers and dimers (since we were unable to visualize these through gel staining) and also confirm expression of NP and VP40.

Impact of sdAb Monomers and Dimers on the Colocalization of VP40 and NP in Vero Cells

While HEK 293T cells are highly transfectable (in our hands >90%) and productive following transfection with SV40 origin containing plasmids they are poor cells for fine-scale microscopy and so here we employed Vero E6 cells which are naturally permissive for both MARV and EBOV replication. By analyzing the transient coexpression of MARV VP40, MARV HA-NP, and the M1, M2, E1 and E2 sdAb *via* immuno-staining the cells, we were able to monitor the impact of intrabody expression on NP and VP40 colocalization, which is normally evident during virion assembly. The M1 monomer shows a mix of cytosolic diffuse presence and localization with HA-NP as expected and does not appear to reduce the overlap of HA-NP with VP40 seen in the merged image (**Figure 7A**). In contrast, the M2 dimer appears to lose the diffuse cytosolic staining pattern, colocalizing at

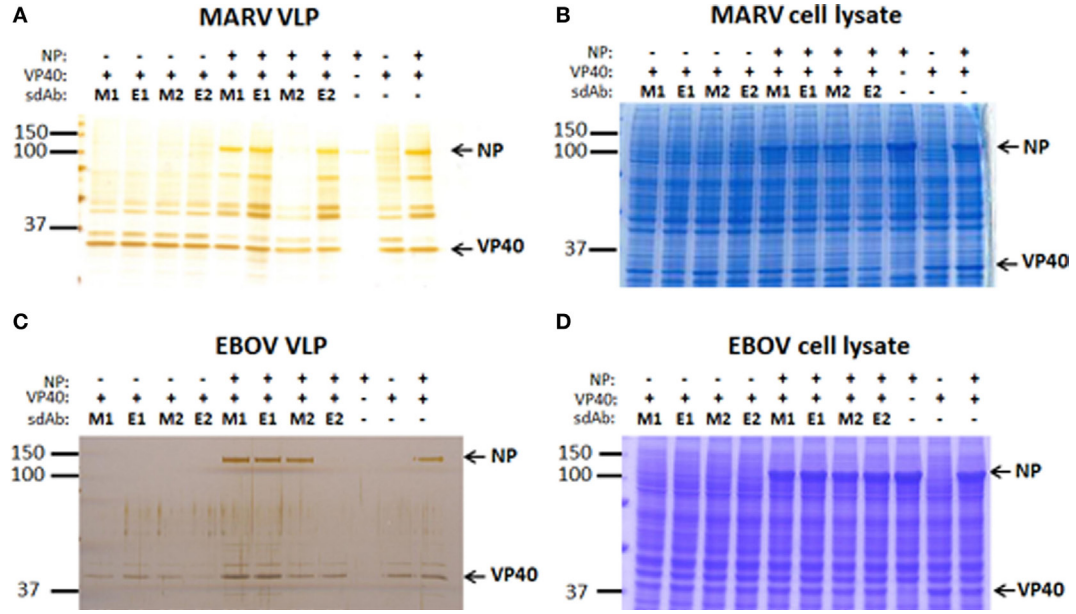

FIGURE 6 | Exploring the impact of coexpressing the anti-*Marburgvirus* (MARV) single-domain antibody (sdAb) monomer (M1) or dimer (M2), or anti-*Ebolavirus* (EBOV) monomer (E1) or dimer (E2) on nucleoprotein (NP) incorporation into VLP. **(A)** Sliver stained SDS-PAGE analysis of crude VLP preparations following coexpression of MARV NP and/or VP40 with the various sdAb monomers and dimers. **(B)** Coomassie stained SDS-PAGE analysis of cell lysates stemming from the VLP production in panel **(A)**. **(C)** Sliver stained SDS-PAGE analysis of crude VLP preparations following coexpression of EBOV NP and/or VP40 with the various sdAb monomers and dimers. **(D)** Coomassie stained SDS-PAGE analysis of cell lysates stemming from the VLP production in panel **(C)**.

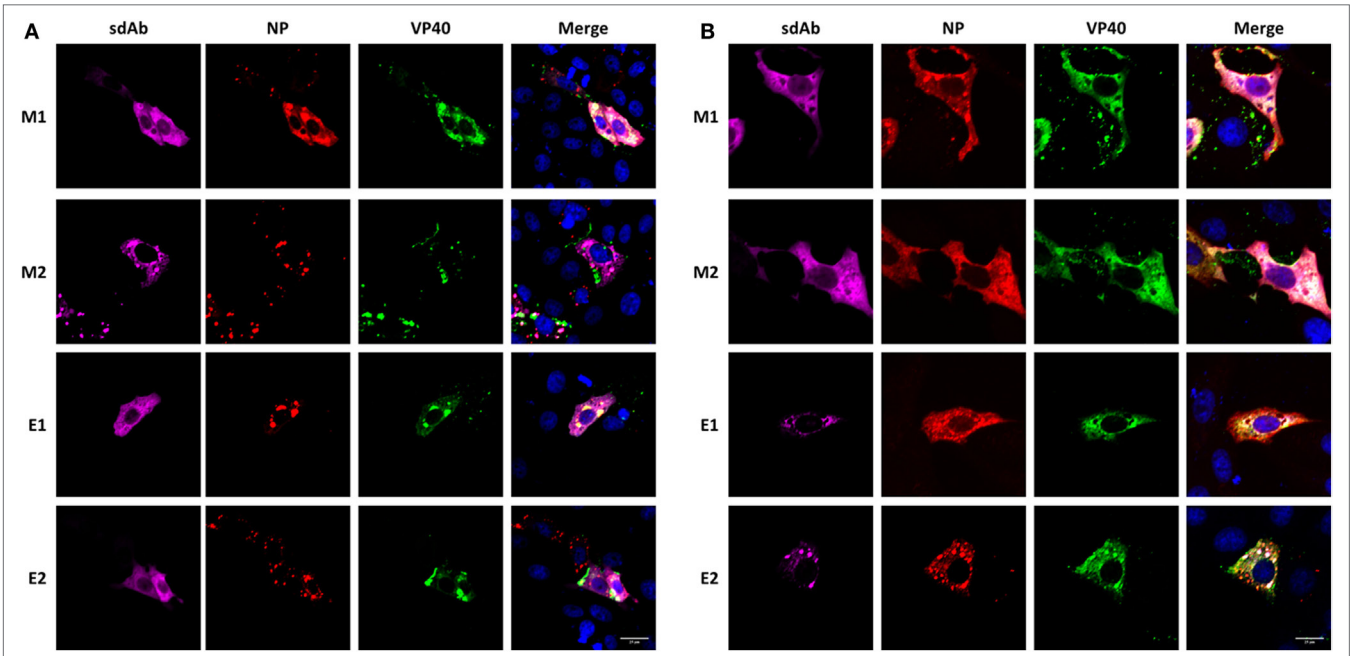

FIGURE 7 | Localization of single-domain antibody (sdAb) monomer or dimer when coexpressed with nucleoprotein (NP) and VP40 and the impact on NP-VP40 colocalization. Immunofluorescence microscopy of transiently cotransfected Vero E6 cells producing anti-*Marburgvirus* (MARV) sdAb monomer (M1) or dimer (M2), or anti-*Ebolavirus* (EBOV) sdAb monomer (E1) or dimer (E2) with either **(A)** MARV VP40 and MARV NP genes or **(B)** EBOV VP40 and NP genes.

HA-NP pools, which are reflective of the virogenic inclusions. HA-NP VP40 colocalization appears to be inhibited and VP40 localization to the membrane appears reduced. As our ELISA data showed the dimeric M2 sdAb may well have better ability to target NP polymers over the monomeric sdAb and may well be enhanced at the NP pooling sites. It is important to note that in the presence of M2 dimer the HA-NP does not appear to be present at high levels in any locations other than focused

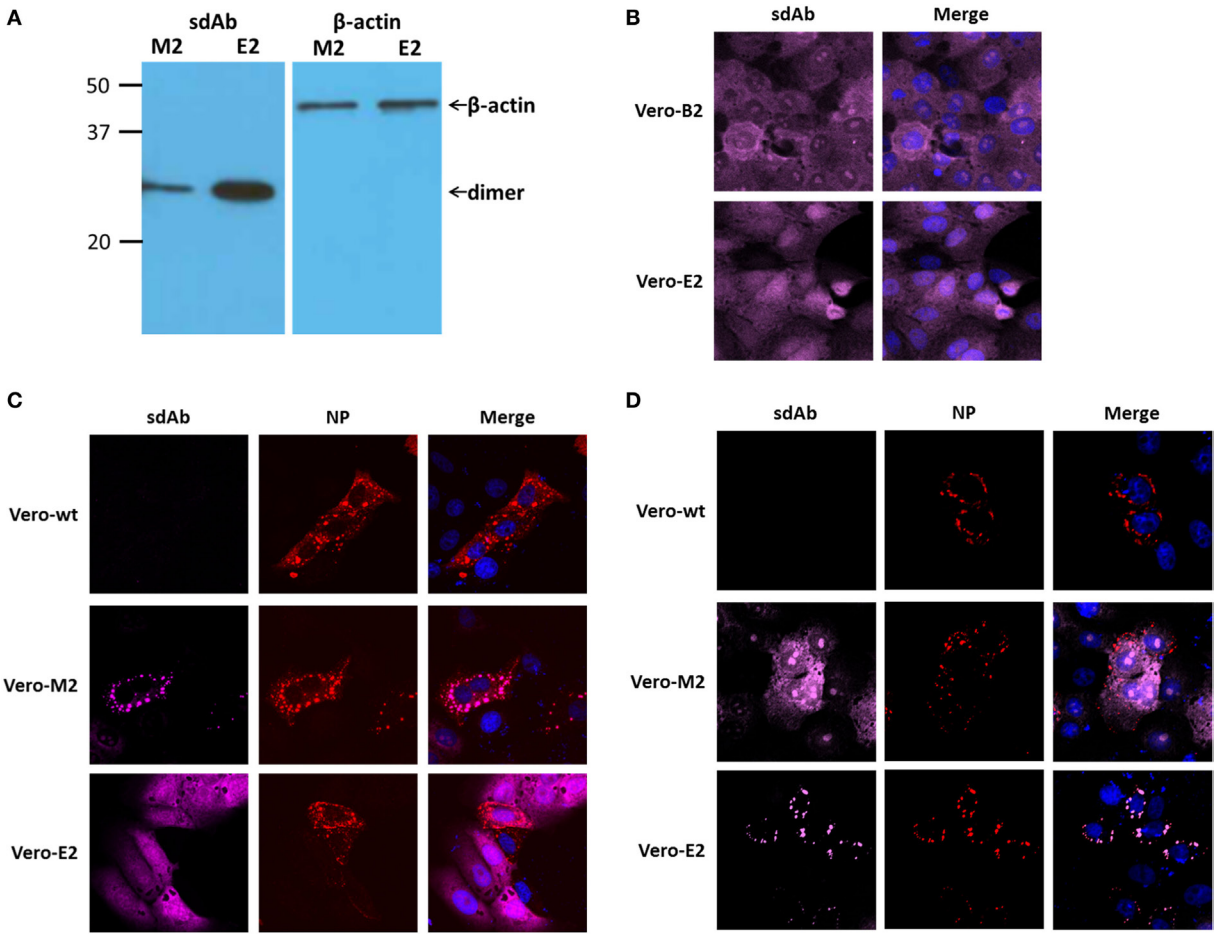

FIGURE 8 | Production and distribution of single-domain antibody (sdAb) dimers within the Vero E6 based stable cell lines. **(A)** Western blot of stable cell lines expressing the anti-*Marburgvirus* (MARV) dimer (Vero-M2) or anti-*Ebolavirus* (EBOV) dimer (Vero-E2) and probing for antibody *via* the C9 tag or for β-actin. **(B)** Staining of parent (Vero-wt) and stable cell lines Vero-M2 and Vero-E2 for the distribution of antibody *via* the C9 tag. **(C)** Transient expression of MARV HA-NP within the parental and transgenic cell lines demonstrates the ability of the anti-MARV dimer but not the anti-EBOV dimer to colocalize with nucleoprotein (NP) puncta. **(D)** Transient expression of EBOV HA-NP within the parental and transgenic cell lines demonstrates the ability of the anti-EBOV dimer but not the anti-MARV dimer to colocalize with NP puncta.

punctate sites suggesting the dimeric sdAb is indeed restricting NP leaving to traffic to the membrane for assembly. The control anti-EBOV E1 and E2 as expected do not appear to colocalize with NP since they are not cross-reactive with MARV, enabling VP40 and NP to colocalize as seen in the merged images. We applied the same methodology to transient transfections of EBOV VP40 and HA-NP and saw the same general trends in that cognate dimer sdAb E2 localized to EBOV HA-NP pools and appeared to restrict colocalization with VP40, whereas the other antibody formats including the monomer sdAb E1 did not (**Figure 7B**).

Impact of sdAb Dimers on MARV and EBOV Replication

The low (in our hands ≤5%) transfection efficiency of Vero E6 cells makes studying the direct impact of transient intrabody expression on viral replication very difficult since only a small number of cells will be producing recombinant protein. We therefore generated G418 selectable stable lines of the anti-MARV M2 (Vero-M2) and anti-EBOV E2 (Vero-E2) sdAb dimers in the puma1 expression vector and chose the cells having the highest levels of expression of products of the desired size by Western blot (**Figure 8A**) and generally diffuse staining when probed for the sdAb dimer C9 tag (**Figure 8B**). We confirmed the ability of each sdAb dimer to colocalize with its cognate NP following transient expression of either MARV HA-NP (**Figure 8C**) or EBOV HA-NP (**Figure 8D**) within parental, Vero-M2 or Vero-E2 cell lines.

We next challenged the cells in a plaque titration with MARV to reveal that the Vero-M2 line is capable of reducing the number of plaques approximately fivefold when compared to control Vero wild-type cells or the Vero-E2 cell line (**Figure 9A**). When a similar experiment was performed with EBOV no difference in the number of plaques was observed between Vero-E2 and the other cell lines (**Figure 9B**),

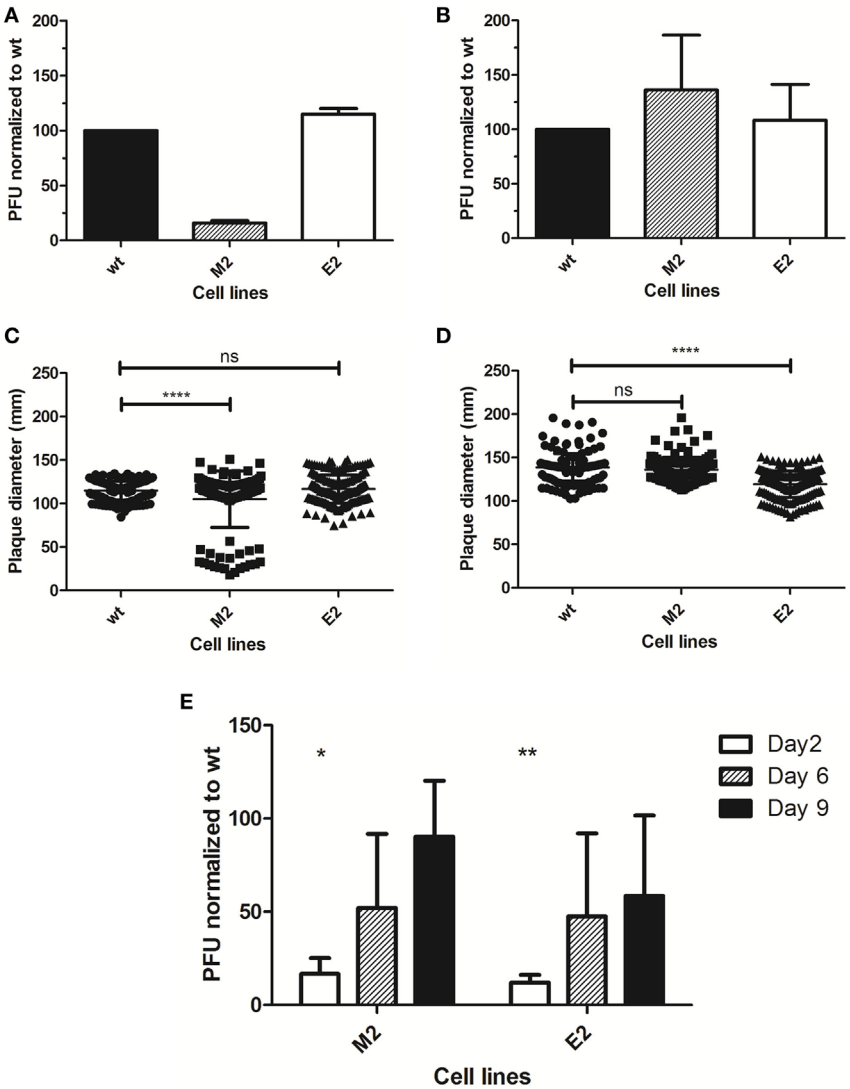

FIGURE 9 | Impact of Xintrabodies on viral replication. *Marburgvirus* (MARV) **(A)** and *Ebolavirus* (EBOV) **(B)** were titrated on wild-type Vero cells (wt) or the stable lines expressing the anti-MARV dimer (M2) or anti-EBOV dimer (E2) and plaque formation under semi-solid overlay allowed to proceed for 10 days. The experiment was performed twice for MARV and three times for EBOV and error bars represent the SD. Diameters of approximately 150 plaques from the titrations were measured using ImageJ measure analysis tool and plotted for MARV **(C)** and EBOV **(D)**. An unpaired, one-tail *t*-test analysis revealed a *p*-value of <0.0001 (****) while ns indicates no significant difference. Bars indicate SD and the mean. **(E)** MARV and EBOV were used to infect wild-type or cognate single-domain antibody dimer stable cell lines in a growth kinetics format with liquid supernatant collections at the times indicated. Plaque titrations of the supernatants were performed on wild-type cells and results are graphed as a percentage of titers resulting from the wild-type time-course. The experiment was performed three times for MARV and twice for EBOV. An unpaired, one-tail *t*-test was conducted using Excel, * indicating a *p*-value <0.05 and ** indicating a *p*-value <0.005.

suggesting that plaque number was not being limited in the semi-solid overlay system. However, analysis of the plaque diameters revealed a significant decrease in the sizes of plaques for MARV in Vero-M2 (**Figure 9C**) and for EBOV in Vero-E2 (**Figure 9D**) compared to the non-cognate and wild-type cell lines. To better study the dynamics of viral replication and the impact of sdAb dimer upon it, we challenged the wild-type and cognate dimer cell lines within a liquid overlay setting. Supernatants were harvested in a time-course and the resulting progeny were titrated on wild-type cells. For both MARV and EBOV, there is a significant reduction in progeny virus early in the time-course but the impact diminishes as the experiment progresses (**Figure 9E**).

The impact of anti-MARV and anti-EBOV sdAb dimers are far from optimal and by no means providing sterilizing immunity, yet combined with all of the previous data are indicating that the Xintrabody approach has potential.

DISCUSSION

Herein, we sought to explore the potential for tandem sdAb dimers to promote aberrant interactions between viral components

within the cytoplasm and focused on viral targets that we hypothesized would have the greatest impact owing to their polyvalent nature. In this manner, we take advantage of small amounts of dimeric sdAbs having a big effect on large amounts of antigen. The approach is admirably suited to targeting viral factories where large amounts of viral antigens can lie in close proximity and become very vulnerable to a crosslinking intrabody or Xintrabody approach. We certainly benefited from a panel of four anti-MARV sdAb clones from which to identify productive intrabodies. In the first place, perhaps tandemization is not ideal where free N-termini are required to take full advantage of bivalency and other N-terminal free oligomerization strategies such as leucine zippers (30) could be useful here. Second, several sdAbs were not especially productive when expressed in the cytosol, yet there are sequence tags available that can rescue poorly soluble clones (31) and can even enhance degradation of target antigens.

Our VLP analyses reveal an ablation of NP incorporation into particles despite large amounts of NP being produced and correspondingly minimal (not visible by Coomassie SDS-PAGE) amounts of Xintrabody indicating the promise of the approach. Microscopic analyses of dimeric sdAb revealed them to be focused on pools of NP and capable of restricting the distribution of NP to the areas where VP40 was localized. Combined with the electron microscopic views of *in vitro* crosslinking of purified NP and sdAb dimer preparations, it is tempting to speculate that in cells we are crosslinking RNC in the virogenic inclusions, yet finer resolution immuno-electron microscopy would be required to confirm this as certain. The stable cell lines expressing the anti-MARV and anti-EBOV Xintrabodies did not show the same dramatic effect as the VLP system but nonetheless resulted in smaller plaques and reduced virus yields when compared to wild-type cells at early timepoints. Yet, when one considers the low levels of constitutively expressed recombinant proteins in cell lines not employing gene amplification or locus control regions, it is quite remarkable that our dimeric sdAbs had any impact at all. Furthermore, it is more than likely that host gene expression patterns are altered upon virus infection to reduce dimer production even further during the course of viral replication one could envisage employing a host cell promoter induced upon infection to drive more Xintrabody expression (32).

Antiviral sdAbs reactive with several viral glycoproteins have been shown to be massively improved in neutralization potency and breadth of reactivity when multimerized and can even protect against disease in animal models [for review, see Ref. (33)]. To the best of our knowledge, leveraging a multimerization routine for intrabodies has not yet been demonstrated and indicates Xintrabodies to be a novel potential therapeutic antibody development route. Though novel for recombinant intrabody technology, the strategy of crosslinking pathogen antigens as a defense mechanism is not new to nature. The immune system encodes natural crosslinkers of viral proteins including the carbohydrate-binding innate defensins, which can crosslink surface glycoproteins to create an inflexible barricade that inhibits entry to cells (34). The innate Mx proteins can be induced cytoplasmically and smother intracellular polymeric target proteins including many viral NPs (35). Adaptive immunity can also generate potent crosslinkers of monomers within the HA trimers of influenza A virus (36) to inhibit viral entry processes. Intra-spike crosslinkers based on IgG-derived Fab have also been further engineered to elevate anti-HIV potency a 100-fold and to reduce the chances of immune evasion (37). Heterologous lectins from algae such as Griffithsin also mediate crosslinking of viral glycoproteins and are being explored as antivirals against HIV (38) and can be enhanced by engineering multimerized forms (39). Perhaps for us the most relevant example of the potency of the crosslinking strategy is the anti-influenza A virus small compound drug nucleozin which exerts both early and late effects through impedance of N (NP) and RNC trafficking with the latter impact restricting packaging also (40, 41).

A common problem with antiviral strategies, including antibodies, small molecules, and even the innate Mx system, is the emergence of resistance within a viral population. Indeed, the anti-influenza VHH isolated recently using antiviral selection was shown to bind an epitope that was poorly conserved and liable to escape rapidly (42). Anti-VSV VHH monomers recently isolated using a similar approach to the anti-influenza A clones were also shown to generate viral escape mutants quite easily, again suggesting a pliable epitope (43). Our sdAbs are known to target highly conserved regions of MARV and EBOV NP lying at the C-terminus which are less likely to mutate to escape sdAb binding. It is tempting to speculate that along the lines of the Bjorkman study that dimerization of the sdAb will further enhance their immune constriction (38).

Although intrabodies are a good starting point to identify and evaluate antiviral sdAb formulations, they likely need transitioning to a protein delivery mechanism for long-term utility approaching the clinic. Here, we note that despite recombinant antibody technology having thrived for over 25 years, examples of success in assembling functional transbodies have been very limited (44). The approach may be fickle owing to incompatibility between compartments required for optimal antibody expression (periplasm) and the highly structured and charged tags required for transduction, e.g., HIV tat domain (45). Once protein is generated, the efficiency of reaching the cytosol may also be low due to endosomal entrapment though newer approaches appear to overcome this impasse using cell surface binding motifs to drive locally higher concentrations favorable for endosomal uptake and release (46). More recently, cyclic arginine rich motifs have shown promise as efficient sdAb delivery motifs (47) though these assemblies required *in vitro* ligation of the motif to the antibody, which may complicate scale-up. Despite these caveats, one group has pioneered monomeric transbodies to several viruses including influenza A (48), HCV (49), and more recently even Ebola (50) which is encouraging us to pursue the transition of Xintrabodies to Xtransbodies.

Multiple lines of evidence suggest that sdAbs have huge potential as therapeutics when delivered as proteins [see Ref. (51) for review] though they must be specifically tailored for their intended purpose. Their small size ensures rapid clearance *via* the kidneys and fast tissue penetration making them superior temporal imaging reagents but for applications requiring longer

half-lives they require fusion to Fc or serum albumin-binding motifs. On the flipside, fast clearance should minimize the likelihood of human anti-llama antibody responses though this still can occur and appears to be on case-by-case basis related to the specific sdAb being used, the doses employed, and the disease under study (52). Since dimeric sdAbs are larger than monomeric sdAb they may have higher half-lives than expected and may well provoke host anti-sdAb antibody responses, though this may be outpaced by Xtransbody uptake. Erring on the side of caution, strategies for the humanization of pre-existing camelid sdAb such as our anti-MARV and anti-EBOV clones using CDR grafting to a universal humanized sdAb scaffold appearing very promising (53).

MATERIALS AND METHODS

General Methods

Recombinant DNA methods were according to established procedures and employed commercially available reagents; Phusion High-Fidelity DNA Polymerase (Thermo Fisher Scientific, Waltham, MA, USA) was used for PCR amplification unless otherwise noted; restriction enzymes and β-agarase (New England BioLabs, Beverly, MA, USA); T4 DNA ligase, CIP and T4 PNK (Roche, Nutley, NJ, USA), GTG low-melting temperature agarose for in agarose cloning (Lonza, Walkersville, MD, USA); oligonucleotides (Integrated DNA Technologies, Coralville, IA, USA); synthetic human codon optimized sdAb and VP40 genes (Genscript, Piscataway, NJ, USA). Assemblies involving cloning and PCR amplification were sequenced through the inserts and junctions to verify the desired construct. Cloning was typically in XL1-Blue unless otherwise stated. Full details of cloning, oligonucleotides, maps, and sequences of resulting constructs are available on request. Parental sdAb genes employed in this work were anti-MARV NP sdAb A, B, C, and D with GenBank accession numbers MF780583, MF780584, MF780585, and MF780586, respectively; anti-EBOV NP sdAb E and G with GenBank accession numbers MF780602 and MF780604, respectively.

Construction of Mammalian Cell Expression Vectors

C9-tagged sdAb A, B, C, D, and G genes were inserted into pcDNASfi as llama versions (GenBank accession numbers; MF871588, MF871589, MF871590, MF871591, and MF871592, respectively) or human codon optimized genes (GenBank accession numbers; MF871583, MF871584, MF871585, MF871586, and MF871587, respectively). pcDNASfi had its three *Nco*I sites deleted by Quick Change mutagenesis to form pcDNASfiNcoI$^-$ with mutations verified by sequencing. Synthetic DNA representing a portion of the hCMV promoter, adenovirus tripartite leader, and hybrid murine splicing region [based on pMT2 (24)] with *Hin*dIII deleted from the intron was mobilized from pUC57 CMV-IVS *via Sna*BI and *Nhe*I to replace the resident 5′-ntr to form puma1. Monomeric and dimeric llama sdAbs with His_6-C9 tags from pecan199 (see below) were mobilized to puma1 (GenBank accession numbers for monomeric sdAb A, B, C, and E are MF871599, MF871601, MF871603, and MF871605, respectively, while dimeric sdAbs are MF871600, MF871602, MF871604, and MF871606 respectively). Previous human codon optimized genes residing in pcDNASfi and encoding Marburg Musoke NP, Ebola Zaire Kikwit, and Bundibugyo NP (15) (GenBank accession numbers MF871598, MF871593, and MF871595, respectively) were subcloned to puma2 (pcDNASfiNcoI$^-$ with the CMV intron A replacing the tripartite leader and murine splicing region) to generate ELISA substrates (see below). The Marburg and Zaire versions were also PCR amplified with a 5′-primer encoding an HA tag and inserted into puma2 to enable production of HA-tagged NP proteins for crosslinking and electron microscopy studies. Human codon optimized versions of Marburg Musoke and Ebola Zaire Kikwit VP40 genes (GenBank accession numbers MF871607 and MF871608, respectively) were also subcloned to puma2.

Construction of Pecan199 *E. coli* Expression Vectors

Pecan73 is our standard tac promoter-driven *pel*B leader based sdAb expression vector (16) designed to secrete proteins to the periplasmic compartment and had a sdAb PCR amplified and re-inserted to replace the C-terminal His_6 sequence with a C-terminal His_6-C9 epitope tag (54) sequence to form pecan199.

Construction of sdAb Dimers

sdAb genes were first mobilized from their original vectors (pecan21) (55) to enable soluble monomeric sdAb protein production of periplasmic hinge-less versions within pecan126 (16). Internal *Nco*I and *Pag*I sites within sdAb C were deleted by splice overlap extension PCR. Dimers were assembled by PCR amplifying the sdAb with an oligonucleotide encoding an *Nco*I site at the 5′-end to match the signal peptidase cleavage region and an oligonucleotide encoding a flexible $(Gly_4Ser)_4$ linker plus *Pag*I site at the 3′-end and re-inserting the amplicon into the cognate monomeric construct. Clones with the correct orientation were identified by restriction mapping with *Nco*I and *Not*I that released the dimer, while clones with the incorrect orientation would only release a monomer (GenBank accession numbers for pecan126 dimers sdAb A, B, C, and E are MF871575, MF871576, MF871577, and MF871578, respectively). SdAb genes were mobilized to pecan199 for expression for electron microscopic crosslinking studies (GenBank accession numbers: sdAb B monomer, MF871579; sdAb B dimer, MF871580; sdAb E monomer, MF871581; sdAb E dimer, MF871582).

E. coli Expression of sdAb Monomers and Dimers

Pecan 126 or 199 sdAb constructs were mobilized to HBV88 or Tuner pRARE, respectively, and grown in 40 ml starter cultures of terrific broth (TB) plus 2% glucose at 30°C overnight with ampicillin (200 μg ml^{-1}) and chloramphenicol (30 μg ml^{-1}) in 250 ml baffled flasks (Bellco, Vineland, NJ, USA). Saturated cultures were transferred to 450 ml of fresh TB without glucose and shaken for 3 h at 25°C in 2,500 ml baffled flasks. Expression was induced by addition of IPTG to 1 mM for 3 h at 25°C, the cells pelleted (typical wet weights of 8–9 g) and osmotically

shocked (56) by resuspension in 14 ml ice-cold 0.75 M sucrose in 100 mM Tris–HCl pH 7.5, addition of 1.4 ml of 1 mg ml^{-1} hen egg lysozyme (Sigma), followed by drop-wise addition of 28 ml of 1 mM EDTA pH 7.5 and swirling on ice for 15 min. A volume of 2.0 ml 0.5 M $MgCl_2$ was added, swirling continued for 15 min, and cells pelleted. The 45-ml supernatant (osmotic shockate) was mixed with 5 ml of 10× IMAC (immobilized metal affinity chromatography buffer—0.2 M Na_2HPO_4, 5 M NaCl, 0.2 M imidazole, 1% Tween-20, pH 7.5), followed by 0.5 ml of High Performance Ni Sepharose (GE Healthcare) and the suspension gently mixed on ice for 1 h. Resin was pelleted at 3,000 rpm for 5 min (Beckman Allegra 6R swing out rotor) and washed twice with 40 ml of 1× IMAC buffer before elution with 2 ml of 500 mM UV grade imidazole in 1× IMAC buffer. Proteins were concentrated in Amicon 10 kDa ultrafiltration devices (Millipore, Billerica, MA, USA) to 200 µl for separation by gel filtration on a Superdex 200 Increase 10/300 GL column (GE Healthcare) operating in PBS. Proteins were quantified by UV adsorption and analyzed by SDS-PAGE and Coomassie blue staining for impurities.

ELISA Titrations of sdAb Monomers and Dimers on NP Antigen

Antigen (NP) in 100 µl of PBS at 1 µg ml^{-1} was used to coat duplicate wells of high binding white ELISA plates overnight at 4°C. Plates were washed three times with PBS and each well probed with 100 µl of the antibody dilutions in PBS 2% non-fat Carnation milk (Nestlé, Vevey, Switzerland) for 1 h static. Probe was removed and plates washed three times with PBS 0.1% Tween-20 and two times with PBS. Anti-His_6 HRP conjugate (Sigma) at 1 in 10,000 in PBS 2% non-fat milk was used to probe the wells for 1 h static. Signals were developed with injection of SuperSignal ELISA Pico Chemiluminescent Substrate (Thermo Fisher Scientific) using a luminometer (Turner BioSystems, Sunnyvale, CA, USA) and data collected with a 2 s integration. Duplicate wells of each dilution were averaged to derive a mean titration, the experiment repeated for an *n* of 2 with the final curves representing the mean of two experiments ± SD.

Cell Lines

Vero E6 and HEK 293T cells were obtained from ATCC (Manassas, VA, USA). All cells were maintained in liquid nitrogen storage when not in use. Cells were maintained in Dulbecco's modified Eagle's medium (DMEM) with 4.5 g l^{-1} glucose, L-glutamine, and sodium pyruvate (Corning cellgro) plus 5% fetal bovine serum (Corning, NY, USA) and penicillin/streptomycin (complete medium) 37°C at 10% CO_2 with humidity.

Small-Scale Transient Recombinant Protein Expression in HEK 293 Cells

HEK 293T cells were seeded at 7.5e+5 cells per well in a 6-well plate in 3 ml of complete medium at 16–18 h prior to transfections. Constructs were transfected using previously established protocols (15, 57). Briefly, 30 µl DNA (approximately 45 ng $µl^{-1}$) and 5 µl of linear polyethylenimine PEI (1 µg $µl^{-1}$ pH 7) were combined and equilibrated for 10–15 min at room temperature in 300 µl serum-free DMEM prior to being carefully added to the cells. For experiments requiring coexpression of NP and VP40, 15 µl of each plasmid was used. For experiments requiring NP, VP40, and sdAb coexpression, 10 µl of each plasmid was used. Total DNA concentration was kept constant with use of an empty vector if required. At 24 h post-transfection, the medium was removed from cells and the monolayer washed with serum-free DMEM and further incubated with 2 ml of serum-free DMEM. At 72 h post-transfection, cells were washed gently with 1 ml warm PBS and then collected in 500 µl of collection buffer; for whole cell lysate collection, equal parts of Tris-buffered saline (TBS) and Laemmli sample buffer with reducing agent were used; for cell fractionation, radioimmunoprecipitation assay buffer (10 mM Tris–HCl pH 7.8, 150 mM NaCl, 1 mM EDTA, 1% NP-40) containing protease inhibitors (Roche Complete) was used. The soluble fraction was separated from the insoluble fraction by microcentrifugation at 15,000 rpm (5415D microcentrifuge, Eppendorf, Hauppauge, NY, USA) for 10 min at 4°C and collection of the supernatant. The pellet representing the insoluble fraction was resuspended in 500 µl of 1:1 TBS/Laemmli sample buffer. For crude VLP analysis, 2 ml of supernatant was collected and clarified in a microcentrifuge at 8,000 rpm for 5 min at room temperature. The supernatant was then overlaid on a 20% sucrose cushion and centrifuged at 38,000 rpm (Beckman SW55 rotor) for 2 h at 4°C. Crude VLPs were resuspended in 100 µl PBS. All samples were stored at −20°C before further processing.

SDS-PAGE and Western Blotting

Samples were combined with an equal volume of Laemmli sample buffer if not already in a 1:1 mix and then heated at 100°C for 5 min. After cooling, samples were electrophoresed on appropriate percentage Laemmli gels. For silver staining, a SilverXpress Silver Staining Kit (Invitrogen) was used. For Coomassie blue staining, standard methods were used. For Western blotting, gels were semi-dry transferred to Immobilon P and the membrane blocked in 2% non-fat dried milk in PBS for 1 h prior to probing with either mouse monoclonal antibody RHO 1D4 (Flintbox, Chicago, IL, USA) specific for the C9 tag or mouse monoclonal antibody GT5512 (GeneTex, Irvine, CA, USA) specific for β-actin. For VP40 probing, mouse monoclonal 6B1 IgG_1 (IBT 0203-016, IBT Bioservices, Rockville, MD, USA) was used for MARV VP40 while mouse monoclonal 3G5 IgG_1 (IBT 0201-016) was used for EBOV VP40. HA-NP was probed for using a mouse IgG_{2a} (sc-7392, Santa Cruz Biotechnology, Inc., Dallas, TX, USA). Following washing three times with PBS 0.1% Tween-20 for 5 min and twice with PBS for 5 min, membranes were probed for 1 h with anti-mouse IgG (H + L) HRP (Thermo Fisher Scientific). Following further washing, the membrane was developed with SuperSignal West Pico Chemiluminescent substrate (Thermo Fisher Scientific) and images captured on CL-XPosure film (Thermo Fisher Scientific).

Generating Vero E6 Cells Constitutively Expressing sdAb Dimers

Cells were seeded in two wells of a 6-well plate at 4e+5 cells per well 18 h prior to transfection. puma1 bearing the dimeric

sdAbs M2 or E2 genes were linearized by *Ahd*I in the ampicillin resistance gene and DNA purified by phenol chloroform extraction and ethanol precipitation. 2.5 μg of DNA and 5 μg of PEI were combined and equilibrated for 15 min at room temperature in 300 μl serum-free DMEM and carefully added to the cells. At 24 h post-transfection, cells were trypsinized, like transfectants pooled and seeded into 10 15 cm diameter dishes. After 3 days, medium was changed and G418 added to 3.2 mg ml^{-1}, which we had determined by titration to be the threshold for Vero E6 cell killing. When colonies were visible by eye they were trypsinized in cloning cylinders (Sigma) adhered to the plate with silicon grease (Beckman) and cells transferred to 24-well plates. Cell lines were analyzed by Western blotting and indirect fluorescence microscopy and one clone expressing dimeric E2 sdAb (Vero-E2) and one clone expressing dimeric M2 sdAb (Vero-M2) with the highest expression levels were used for further experimentation.

Large-scale Transient Expression of NP and HA-NP in HEK 293T Cells

Cells were seeded in 16 10 cm dishes at 5e+6 cells per dish in 20 ml of complete DMEM 16–18 h prior to transfection. Per plate, 105 μl Qiagen miniprep puma2 NP or HA-NP DNA (100 ng μl^{-1}) and 41 μl PEI were combined and equilibrated for 20 min at room temperature in 2.5 ml serum-free DMEM prior to being carefully added to the cells. Cells were collected 48 h post-transfection by trypsinisation in 4 ml trypsin–EDTA solution (Sigma) with two plates worth of cells combined into 50 ml Falcon tubes and topped up to 50 ml with PBS. Cells were pelleted at 1,000 rpm for 5 min (Beckman Allegra 6R swing out rotor) washed once with phosphate buffered saline and repelleted. The cells were lysed in 4 ml of ice-cold hypotonic buffer (20 mM HEPES pH 7.5, 5 mM KCl, 1.5 mM $MgCl_2$, 1 mM DTT, 1 tablet EDTA-free protease inhibitors per 50 ml). DNA was sheared by passing through a 30-G needle several times on ice. Samples were microfuged in 2 ml tubes at 6,000 rpm for 10 min at 4°C and the supernatants transferred to fresh tubes and re-centrifuged at 13,000 rpm for 10 min. Clarified samples were pooled and concentrated in two 15 ml 100 kDa cutoff Amicon centrifugal filters at 3,500 rpm (Beckman Allegra 6R, swing out rotor, room temperature) until the volume was approximately 800 μl. Samples were clarified by microcentrifugation at high speed for 5 min immediately before loading 400 μl atop CsCl gradients (40–25%, 5% steps in TNE—10 mM Tris–HCl pH 7.4, 150 mM NaCl, 1 mM EDTA). Gradients were centrifuged at 25,000 rpm (Beckman SW41Ti) for 18 h at 20°C. The NP or HA-NP bands were collected by side-puncture with an 18-G needle; samples combined, and dialyzed in 10 kDa cutoff Slide-A-Lyzer cassettes (Thermo Fisher Scientific) against PBS at 4°C. Samples were analyzed by SDS-PAGE and silver staining (NP) or Coomassie blue staining (HA-NP) for purity, quantified by micro-BCA assay, and stored at 4°C until needed.

Fluorescence Microscopy

Vero E6 cells were transfected on 8-well micro slides (ibidi, Fitchburg, WI, USA) as above with the following changes: cells were seeded at 1.5e+4 cells/well; 250 ng miniprep DNA and 500 ng PEI were mixed in 30 μl serum-free DMEM and added to cells. As before, total DNA was kept constant with an empty vector used if needed. At 48 h, slides were washed with warm serum-free DMEM twice. Slides were fixed with 10% formalin for 24 h at 4°C. Slides were washed three times with PBS before permeabilizing with 0.1% Triton X-100 (Sigma-Aldrich) in PBS for 10 min. Slides were washed three times with PBS and blocked with 3% BSA in PBS for 1 h. Slides were washed once with PBS and stained with appropriate primary antibody for 1 h in 1.5% BSA in PBS. Cells were washed three times with PBS and then probed with secondary antibodies for 1 h each in 1.5% BSA in PBS, followed by three washes. The primary antibodies used were chicken polyclonal anti-HA tag IgY (ab9111, abcam, Cambridge, MA, USA) at 1:500 for HA-NP detection; mouse monoclonal 6B1 IgG_1 (IBT 0203-016) at 1:500 for MARV VP40 detection; mouse monoclonal 3G5 IgG_1 (IBT 0201-016) at 1:1,000 for EBOV VP40 detection; RHO 1D4 conjugated to Alexa Fluor 647 (antibody labeling kit, Invitrogen) for sdAb detection *via* the C-terminal C9 tag. The secondary antibodies used were donkey anti-mouse IgG labeled with Alexa Fluor 488 (Invitrogen A21202); goat polyclonal anti-chicken IgY labeled with Alexa Fluor 594 (abcam ab150176). Sequential probing of the VP40 antigens was performed before the C9 antibody was applied to minimize anti-mouse secondary cross-reactivity. Slides were placed at 4°C for imaging at a later date and Hoechst stain (Invitrogen H33342) in PBS was added to each well for nuclear staining if required at room temperature for at least 20 min prior to microscopy. Slides were viewed using an Eclipse Ti confocal microscope (Nikon) and NIS Elements Imaging Software. For analysis, 10–20 fields were viewed using a Plan Apo VC 20× DIC N2 objective with a numerical aperture of 0.75 giving 0.62 μm per pixel. For images presented in this manuscript, the same objective was used along with a 5× zoom factor giving 0.12 μm per pixel. Images presented were representative of typical cells and protein distribution. ImageJ within Fiji was used to process *Z*-stack images with average intensity projections to obtain two-dimensional images. For optimal viewing of protein localization, the color balance was adjusted so that the intensity histogram covers only the signal.

Electron Microscopy of HA-NP and sdAb Mixtures

Purified HA-NP (1 μM) was equilibrated with sdAb concentrations of 10, 1, and 0.1 μM binding sites in a final volume of 250 μl for 1 h static. The mixtures were then allowed to passively adhere to grids for 5 min and stained with 20 μl of uranyl acetate for 1–2 min. Images were taken on a JEOL JEM-1230 transmission electron microscope. At least eight representative fields were imaged. For quantitative analysis, Cell Profiler was used on the 100,000× magnified images. To determine the area covered by aggregated NP, objects greater than 12 pixels were accepted. To determine the area covered by helical NP, objects between 2 and 12 pixels were accepted. GraphPad Prism was used to graph results.

Viral Growth Assays

Live virus work was performed within the full-suit BSL-4 laboratory at Texas Biomedical Research Institute, following all local and federal guidelines as part of the Select Agent Program. Marburg Musoke and Ebola Zaire Kikwit were amplified and titrated on Vero E6 cells as described previously (15). Vero E6 wild-type or the constitutive sdAb-expressing cell lines Vero-E2 and Vero-M2 were first used as plaque titrants by seeding 8e+5 cells per well in duplicate 6-well plates in 2 ml of complete medium approximately 18 h prior to infection. Medium was removed and 500 µl of virus in serum-free DMEM added to each duplicate well with serial dilutions (−2 to −6 with one no virus control well per plate). Plates were then incubated at 37°C with humidity and 10% CO_2 with gentle rocking for 1 h. During incubation, aliquots of 1% SeaPlaque GTG agarose were heated to boiling and let cool to 37°C. Eagle's MEM (Lonza) plus 4 mM L-glutamine and 2 mM sodium pyruvate was mixed 1:1 with agarose. Virus was carefully removed with a P1000 pipette and overlayed with 2 ml of the EMEM agarose. The agarose was allowed to solidify for 10 min at room temperature and the plates incubated at 37°C for 10–11 days with humidity and CO_2. The plates and overlays were then fixed in 10% formalin for 24 h and removed from the BSL-4 *via* the chemical dunk tank. Overlays were then removed and cells stained with 1% crystal violet for plaque counting. The experiment was repeated a total of two times for MARV and three times for EBOV. Following scanning of the plates, approximately 150 clearly separated plaques for each cell line were analyzed using ImageJ to record the diameters. An unpaired one-tail *t*-test within Graphpad was used to identify statistical significance.

Marburg Musoke and Ebola Zaire Kikwit growth kinetics were evaluated on Vero E6 wild-type or the constitutive sdAb dimer expressing cell lines Vero-M2 and Vero-E2, respectively, seeded at 8e+5 cells per well in 6-well plates in 2 ml complete medium at approximately 18 h prior to infection. Medium was removed and 500 µl of virus in SF DMEM added per well at a multiplicity of infection of 0.01. Plates were incubated at 37°C with humidity and 10% CO_2 with gentle rocking for 1 h. The virus was carefully removed with a P1000 pipette, cells washed once with 1 ml of complete medium, and incubated at 37°C for 2, 6, or 9 days in 2 ml complete medium. At time of collection, medium from a single well was removed by a P1000 pipette, clarified in a 2 ml Eppendorf tube in a microfuge at 8,000 rpm for 5 min at 4°C. The samples were then transferred to Sarstedt 2 ml screw cap micro tubes (Sarstedt, Nümbrecht, Germany) and immediately stored at −80°C until required. Each time point was titrated on duplicate wells of wild-type Vero E6 cells and the titer averaged. The time-course, collections, and titrations were repeated a total of three times for MARV and twice for EBOV with plaque forming units per milliliter obtained on each stable cell line presented as percentages of those obtained on the wild-type cells ±SD. An unpaired one-tail *t*-test was used to identify statistical significance.

AUTHOR CONTRIBUTIONS

TD, LS, and AH designed experiments, performed the work, and analyzed the data. AH wrote the paper.

ACKNOWLEDGMENTS

We would like to thank Barbara Hunter of UT Health San Antonio for help with electron microscopy.

FUNDING

This work was supported in part by National Institutes of Health grants R21AI105568 and R01AI112851, a Texas Biomedical Research Institute Forum Award, and internal funding.

SUPPLEMENTARY MATERIAL

The Supplementary Material for this article can be found online at http://journal.frontiersin.org/article/10.3389/fimmu.2017.01197/full#supplementary-material.

REFERENCES

1. Marasco WA. Intrabodies: turning the humoral immune system outside in for intracellular immunization. *Gene Ther* (1997) 4:11–5. doi:10.1038/sj.gt.3300346
2. Baltimore D. Gene therapy. Intracellular immunization. *Nature* (1988) 335:395–6. doi:10.1038/335395a0
3. Antman KH, Livingston DM. Intracellular neutralization of SV40 tumor antigens following microinjection of specific antibody. *Cell* (1980) 19:627–35. doi:10.1016/S0092-8674(80)80039-0
4. Fujimoto Y, Ozaki K, Maeda M, Nishijima K, Takakuwa H, Otsuki K, et al. Resistance to influenza A virus infection in transformed cell lines expressing an anti-PB2 monoclonal antibody. *Vet J* (2013) 198:487–93. doi:10.1016/j.tvjl.2013.09.019
5. Kontermann RE. Intrabodies as therapeutic agents. *Methods* (2004) 34:163–70. doi:10.1016/j.ymeth.2004.04.002
6. Lo AS, Zhu Q, Marasco WA. Intracellular antibodies (intrabodies) and their therapeutic potential. *Handb Exp Pharmacol* (2008) 181:343–73. doi:10.1007/978-3-540-73259-4_15
7. Muyldermans S. Nanobodies: natural single-domain antibodies. *Annu Rev Biochem* (2013) 82:775–97. doi:10.1146/annurev-biochem-063011-092449
8. Koide A, Bailey CW, Huang X, Koide S. The fibronectin type III domain as a scaffold for novel binding proteins. *J Mol Biol* (1998) 284:1141–51. doi:10.1006/jmbi.1998.2238
9. Liao HI, Olson CA, Hwang S, Deng H, Wong E, Baric RS, et al. mRNA display design of fibronectin-based intrabodies that detect and inhibit severe acute respiratory syndrome coronavirus nucleocapsid protein. *J Biol Chem* (2009) 284:17512–20. doi:10.1074/jbc.M901547200
10. Griffin H, Elston R, Jackson D, Ansell K, Coleman M, Winter G, et al. Inhibition of papillomavirus protein function in cervical cancer cells by intrabody targeting. *J Mol Biol* (2006) 355:360–78. doi:10.1016/j.jmb.2005.10.077
11. Vercruysse T, Pardon E, Vanstreels E, Steyaert J, Daelemans D. An intrabody based on a llama single-domain antibody targeting the N-terminal alpha-helical multimerization domain of HIV-1 rev prevents viral production. *J Biol Chem* (2010) 285:21768–80. doi:10.1074/jbc.M110.112490
12. Tanaka T, Rabbitts TH. Intrabodies based on intracellular capture frameworks that bind the RAS protein with high affinity and impair oncogenic transformation. *EMBO J* (2003) 22:1025–35. doi:10.1093/emboj/cdg106
13. Schmidt FI, Hanke L, Morin B, Brewer R, Brusic V, Whelan SP, et al. Phenotypic lentivirus screens to identify functional single domain antibodies. *Nat Microbiol* (2016) 1:16080. doi:10.1038/nmicrobiol.2016.80

14. Sherwood LJ, Osborn LE, Carrion R Jr, Patterson JL, Hayhurst A. Rapid assembly of sensitive antigen-capture assays for Marburg virus, using *in vitro* selection of llama single-domain antibodies, at biosafety level 4. *J Infect Dis* (2007) 196(Suppl 2):S213–9. doi:10.1086/520586
15. Sherwood LJ, Hayhurst A. Ebolavirus nucleoprotein C-termini potently attract single domain antibodies enabling monoclonal affinity reagent sandwich assay (MARSA) formulation. *PLoS One* (2013) 8:e61232. doi:10.1371/journal.pone.0061232
16. Sherwood LJ, Hayhurst A. Hapten mediated display and pairing of recombinant antibodies accelerates assay assembly for biothreat countermeasures. *Sci Rep* (2012) 2:807. doi:10.1038/srep00807
17. Bharat TA, Noda T, Riches JD, Kraehling V, Kolesnikova L, Becker S, et al. Structural dissection of Ebola virus and its assembly determinants using cryo-electron tomography. *Proc Natl Acad Sci U S A* (2012) 109:4275–80. doi:10.1073/pnas.1120453109
18. Bharat TA, Riches JD, Kolesnikova L, Welsch S, Krähling V, Davey N, et al. Cryo-electron tomography of Marburg virus particles and their morphogenesis within infected cells. *PLoS Biol* (2011) 9:e1001196. doi:10.1371/journal.pbio.1001196
19. Hoenen T, Shabman R, Groseth A, Herwig A, Weber M, Schudt G, et al. Inclusion bodies are a site of ebolavirus replication. *J Virol* (2012) 86:11779–88. doi:10.1128/JVI.01525-12
20. Nanbo A, Watanabe S, Halfmann P, Kawaoka Y. The spatio-temporal distribution dynamics of Ebola virus proteins and RNA in infected cells. *Sci Rep* (2013) 3:1206. doi:10.1038/srep01206
21. Dolnik O, Stevermann L, Kolesnikova L, Becker S. Marburg virus inclusions: a virus-induced microcompartment and interface to multivesicular bodies and the late endosomal compartment. *Eur J Cell Biol* (2015) 94:323–31. doi:10.1016/j.ejcb.2015.05.006
22. Schudt G, Kolesnikova L, Dolnik O, Sodeik B, Becker S. Live-cell imaging of Marburg virus-infected cells uncovers actin-dependent transport of nucleocapsids over long distances. *Proc Natl Acad Sci U S A* (2013) 110:14402–7. doi:10.1073/pnas.1307681110
23. Schudt G, Dolnik O, Kolesnikova L, Biedenkopf N, Herwig A, Becker S. Transport of Ebolavirus nucleocapsids is dependent on actin polymerization: live-cell imaging analysis of Ebolavirus-infected cells. *J Infect Dis* (2015) 212(Suppl 2):S160–6. doi:10.1093/infdis/jiv083
24. Kaufman RJ, Sharp PA. Amplification and expression of sequences cotransfected with a modular dihydrofolate reductase complementary DNA gene. *J Mol Biol* (1982) 159:601–21. doi:10.1016/0022-2836(82)90103-6
25. Huang MT, Gorman CM. Intervening sequences increase efficiency of RNA 3' processing and accumulation of cytoplasmic RNA. *Nucleic Acids Res* (1990) 18:937–47. doi:10.1093/nar/18.4.937
26. Noda T, Sagara H, Suzuki E, Takada A, Kida H, Kawaoka Y. Ebola virus VP40 drives the formation of virus-like filamentous particles along with GP. *J Virol* (2002) 76:4855–65. doi:10.1128/JVI.76.10.4855-4865.2002
27. Makino A, Yamayoshi S, Shinya K, Noda T, Kawaoka Y. Identification of amino acids in Marburg virus VP40 that are important for virus-like particle budding. *J Infect Dis* (2011) 204(Suppl 3):S871–7. doi:10.1093/infdis/jir309
28. Becker S, Rinne C, Hofsass U, Klenk HD, Muhlberger E. Interactions of Marburg virus nucleocapsid proteins. *Virology* (1998) 249:406–17. doi:10.1006/viro.1998.9328
29. Kolesnikova L, Muhlberger E, Ryabchikova E, Becker S. Ultrastructural organization of recombinant Marburg virus nucleoprotein: comparison with Marburg virus inclusions. *J Virol* (2000) 74:3899–904. doi:10.1128/JVI.74.8.3899-3904.2000
30. Pack P, Pluckthun A. Miniantibodies: use of amphipathic helices to produce functional, flexibly linked dimeric Fv fragments with high avidity in *Escherichia coli*. *Biochemistry* (1992) 31:1579–84. doi:10.1021/bi00121a001
31. Joshi SN, Butler DC, Messer A. Fusion to a highly charged proteasomal retargeting sequence increases soluble cytoplasmic expression and efficacy of diverse anti-synuclein intrabodies. *MAbs* (2012) 4:686–93. doi:10.4161/mabs.21696
32. Cilloniz C, Ebihara H, Ni C, Neumann G, Korth MJ, Kelly SM, et al. Functional genomics reveals the induction of inflammatory response and metalloproteinase gene expression during lethal Ebola virus infection. *J Virol* (2011) 85:9060–8. doi:10.1128/JVI.00659-11
33. Vanlandschoot P, Stortelers C, Beirnaert E, Ibañez L, Schepens B, Depla E, et al. Nanobodies^{R}: new ammunition to battle viruses. *Antiviral Res* (2011) 92:389–407. doi:10.1016/j.antiviral.2011.09.002
34. Leikina E, Delanoe-Ayari H, Melikov K, Cho MS, Chen A, Waring AJ, et al. Carbohydrate-binding molecules inhibit viral fusion and entry by crosslinking membrane glycoproteins. *Nat Immunol* (2005) 6:995–1001. doi:10.1038/ni1248
35. Haller O, Staeheli P, Schwemmle M, Kochs G. Mx GTPases: dynamin-like antiviral machines of innate immunity. *Trends Microbiol* (2015) 23:154–63. doi:10.1016/j.tim.2014.12.003
36. Wu Y, Cho M, Shore D, Song M, Choi J, Jiang T, et al. A potent broad-spectrum protective human monoclonal antibody crosslinking two haemagglutinin monomers of influenza A virus. *Nat Commun* (2015) 6:7708. doi:10.1038/ncomms8708
37. Galimidi RP, Klein JS, Politzer MS, Bai S, Seaman MS, Nussenzweig MC, et al. Intra-spike crosslinking overcomes antibody evasion by HIV-1. *Cell* (2015) 160:433–46. doi:10.1016/j.cell.2015.01.016
38. Lusvarghi S, Bewley CA. Griffithsin: an antiviral lectin with outstanding therapeutic potential. *Viruses* (2016) 8:296. doi:10.3390/v8100296
39. Moulaei T, Alexandre KB, Shenoy SR, Meyerson JR, Krumpe LR, Constantine B, et al. Griffithsin tandemers: flexible and potent lectin inhibitors of the human immunodeficiency virus. *Retrovirology* (2015) 12:6. doi:10.1186/s12977-014-0127-3
40. Kao R, Yang D, Lau L, Tsui W, Hu L, Dai J, et al. Identification of influenza A nucleoprotein as an antiviral target. *Nat Biotechnol* (2010) 28:600–5. doi:10.1038/nbt.1638
41. Amorim MJ, Kao RY, Digard P. Nucleozin targets cytoplasmic trafficking of viral ribonucleoprotein-Rab11 complexes in influenza A virus infection. *J Virol* (2013) 87:4694–703. doi:10.1128/JVI.03123-12
42. Hanke L, Knockenhauer KE, Brewer RC, van Diest E, Schmidt FI, Schwartz TU, et al. The antiviral mechanism of an influenza A virus nucleoprotein-specific single-domain antibody fragment. *MBio* (2016) 7:e01569-16. doi:10.1128/mBio.01569-16
43. Hanke L, Schmidt FI, Knockenhauer KE, Morin B, Whelan SP, Schwartz TU, et al. Vesicular stomatitis virus N protein-specific single-domain antibody fragments inhibit replication. *EMBO Rep* (2017) 18(6):1027–37. doi:10.15252/embr.201643764
44. Marschall AL, Frenzel A, Schirrmann T, Schungel M, Dubel S. Targeting antibodies to the cytoplasm. *MAbs* (2011) 3:3–16. doi:10.4161/mabs.3.1.14110
45. Fawell S, Seery J, Daikh Y, Moore C, Chen LL, Pepinsky B, et al. Tat-mediated delivery of heterologous proteins into cells. *Proc Natl Acad Sci U S A* (1994) 91:664–8. doi:10.1073/pnas.91.2.664
46. Dixon JE, Osman G, Morris GE, Markides H, Rotherham M, Bayoussef Z, et al. Highly efficient delivery of functional cargoes by the synergistic effect of GAG binding motifs and cell-penetrating peptides. *Proc Natl Acad Sci U S A* (2016) 113:E291–9. doi:10.1073/pnas.1518634113
47. Herce HD, Schumacher D, Schneider AFL, Ludwig AK, Mann FA, Fillies M, et al. Cell-permeable nanobodies for targeted immunolabelling and antigen manipulation in living cells. *Nat Chem* (2017) 9:762–71. doi:10.1038/nchem.2811
48. Poungpair O, Pootong A, Maneewatch S, Srimanote P, Tongtawe P, Songserm T, et al. A human single chain transbody specific to matrix protein (M1) interferes with the replication of influenza A virus. *Bioconjug Chem* (2010) 21:1134–41. doi:10.1021/bc900251u
49. Phalaphol A, Thueng-In K, Thanongsaksrikul J, Poungpair O, Bangphoomi K, Sookrung N, et al. Humanized-VH/VHH that inhibit HCV replication by interfering with the virus helicase activity. *J Virol Methods* (2013) 194:289–99. doi:10.1016/j.jviromet.2013.08.032
50. Teimoori S, Seesuay W, Jittavisutthikul S, Chaisri U, Sookrung N, Densumite J, et al. Human transbodies to VP40 inhibit cellular egress of Ebola virus-like particles. *Biochem Biophys Res Commun* (2016) 479:245–52. doi:10.1016/j.bbrc.2016.09.052
51. Steeland S, Vandenbroucke RE, Libert C. Nanobodies as therapeutics: big opportunities for small antibodies. *Drug Discov Today* (2016) 21:1076–113. doi:10.1016/j.drudis.2016.04.003
52. Muyldermans S, Smider VV. Distinct antibody species: structural differences creating therapeutic opportunities. *Curr Opin Immunol* (2016) 40:7–13. doi:10.1016/j.coi.2016.02.003

53. Vincke C, Loris R, Saerens D, Martinez-Rodriguez S, Muyldermans S, Conrath K. General strategy to humanize a camelid single-domain antibody and identification of a universal humanized nanobody scaffold. *J Biol Chem* (2009) 284:3273–84. doi:10.1074/jbc.M806889200
54. Molday LL, Molday RS. 1D4: a versatile epitope tag for the purification and characterization of expressed membrane and soluble proteins. *Methods Mol Biol* (2014) 1177:1–15. doi:10.1007/978-1-4939-1034-2_1
55. Goldman ER, Anderson GP, Liu JL, Delehanty JB, Sherwood LJ, Osborn LE, et al. Facile generation of heat-stable antiviral and antitoxin single domain antibodies from a semisynthetic llama library. *Anal Chem* (2006) 78:8245–55. doi:10.1021/ac0610053
56. Neu HC, Heppel LA. The release of enzymes from *Escherichia coli* by osmotic shock and during the formation of spheroplasts. *J Biol Chem* (1965) 240:3685–92.
57. Nettleship JE, Rahman-Huq N, Owens RJ. The production of glycoproteins by transient expression in mammalian cells. *Methods Mol Biol* (2009) 498:245–63. doi:10.1007/978-1-59745-196-3_16

Conflict of Interest Statement: The authors declare that the research was conducted in the absence of any commercial or financial relationships that could be construed as a potential conflict of interest.

frontiers in Immunology

ORIGINAL RESEARCH
published: 02 October 2017
doi: 10.3389/fimmu.2017.01234

Unveiling a Drift Resistant Cryptotope within *Marburgvirus* Nucleoprotein Recognized by Llama Single-Domain Antibodies

*John Anthony Garza[1†‡], Alexander Bryan Taylor[2‡], Laura Jo Sherwood[1], Peter John Hart[2,3] and Andrew Hayhurst[1]**

[1] Department of Virology and Immunology, Texas Biomedical Research Institute, San Antonio, TX, United States, [2] X-Ray Crystallography Core Laboratory, Department of Biochemistry and Structural Biology, Institutional Research Cores, University of Texas Health Science Center at San Antonio, San Antonio, TX, United States, [3] Department of Veterans Affairs, South Texas Veterans Health Care System, San Antonio, TX, United States

OPEN ACCESS

Edited by:
Colin Roger MacKenzie, National Research Council Canada, Canada

Reviewed by:
Serge Muyldermans, Vrije Universiteit Brussel, Belgium
Wanpen Chaicumpa, Mahidol University, Thailand

***Correspondence:**
Andrew Hayhurst
ahayhurst@txbiomed.org

‡These authors have contributed equally to this work.

†Present address:
John Anthony Garza, Analytical Sciences, Alexion Pharmaceuticals, New Haven, CT, United States

Specialty section:
This article was submitted to Vaccines and Molecular Therapeutics, a section of the journal Frontiers in Immunology

Received: 19 July 2017
Accepted: 19 September 2017
Published: 02 October 2017

Citation:
Garza JA, Taylor AB, Sherwood LJ, Hart PJ and Hayhurst A (2017) Unveiling a Drift Resistant Cryptotope within Marburgvirus Nucleoprotein Recognized by Llama Single-Domain Antibodies. Front. Immunol. 8:1234. doi: 10.3389/fimmu.2017.01234

Marburg virus (MARV) is a highly lethal hemorrhagic fever virus that is increasingly re-emerging in Africa, has been imported to both Europe and the US, and is also a Tier 1 bioterror threat. As a negative sense RNA virus, MARV has error prone replication which can yield progeny capable of evading countermeasures. To evaluate this vulnerability, we sought to determine the epitopes of 4 llama single-domain antibodies (sdAbs or VHH) specific for nucleoprotein (NP), each capable of forming MARV monoclonal affinity reagent sandwich assays. Here, we show that all sdAb bound the C-terminal region of NP, which was produced recombinantly to derive X-ray crystal structures of the three best performing antibody-antigen complexes. The common epitope is a trio of alpha helices that form a novel asymmetric basin-like depression that accommodates each sdAb paratope *via* substantial complementarity-determining region (CDR) restructuring. Shared core contacts were complemented by unique accessory contacts on the sides and overlooks of the basin yielding very different approach routes for each sdAb to bind the antigen. The C-terminal region of MARV NP was unable to be crystallized alone and required engagement with sdAb to form crystals suggesting the antibodies acted as crystallization chaperones. While gross structural homology is apparent between the two most conserved helices of MARV and *Ebolavirus*, the positions and morphologies of the resulting basins were markedly different. Naturally occurring amino acid variations occurring in bat and human *Marburgvirus* strains all mapped to surfaces distant from the predicted sdAb contacts suggesting a vital role for the NP interface in virus replication. As an essential internal structural component potentially interfacing with a partner protein it is likely the C-terminal epitope remains hidden or "cryptic" until virion disruption occurs. Conservation of this epitope over 50 years of *Marburgvirus* evolution should make these sdAb useful foundations for diagnostics and therapeutics resistant to drift.

Keywords: filovirus, sdAb, VHH, nucleoprotein, crystallization chaperone, luciferase, Marburg, Ebola

INTRODUCTION

Marburg virus (MARV) is a single-stranded, negative-sense RNA virus, which first emerged almost half a century ago in Europe to cause transmissible hemorrhagic fever in vaccine production staff handling African green monkey tissues imported from Uganda (1). Reservoiring in Egyptian fruit bats (*Rousettus aegyptiacus*), which are native to large regions of Africa (2), MARV

has re-emerged to spill over into human populations sporadically with increasing severity (3–5). With no approved vaccines or therapeutics available, though several in development (6), diagnosis, quarantine, and contact-tracing have been effective at containing outbreaks so far (5, 7). However, as seen recently in West Africa with the related filovirus *Ebolavirus* (EBOV), outbreaks in highly mobile and populated areas can be difficult to extinguish, especially when combined with limited healthcare infrastructures (8).

Compared to other negative-strand RNA viruses such as influenza A, filoviruses appear relatively stable between different years and geographies, suggesting a high degree of adaptation to the reservoir host(s). However, where extensive human to human transmission has occurred across West Africa, mild viral evolution is apparent for EBOV with mutations improving viral fitness being recently defined (9). Though MARV outbreaks have so far been much smaller, with less extensive human to human transmission sometimes involving multiple separate spillovers, genomic variation has been observed in the largest outbreaks that occurred in Angola and Democratic Republic of Congo (DRC) (4). Nucleotide changes can impact the performance of sequence-based therapeutics (10) and diagnostics assays (11), making it imperative to keep such countermeasures up to date with currently circulating strains (12). Non-synonymous nucleotide changes can also alter the performance of virus protein-based therapeutics (10), especially those targeting the glycoprotein (GP), since it is the target for neutralizing antibodies generated by the host humoral response. Antibodies cloned from human survivors (13) and murine hybridomas (14) can all select escape mutants *in vitro* for MARV GP, which parallels the situation for EBOV as shown *in vitro* (15, 16) and *in vivo* (17), indicating a high degree of epitope plasticity for GP. Though internal viral antigens are not known to be overtly subject to antibody based immune surveillance, they are subject to T-cell surveillance which can cause selection of T-cell epitope variants. Such variations along with enabling compensatory, stabilizing (18), and random mutations can impact sequence (19) and protein-targeted countermeasures.

With these factors in mind, a single monoclonal affinity reagent may at first appear risky as the foundation for long-term viral recognition. However, we postulate that carefully selected non-neutralizing binders to highly conserved motifs of internal antigens should virtually eliminate the chances of antibody reactivity being diminished by natural viral evolution. Previously, we had selected four unique sdAb specific to MARV by panning our semi-synthetic phage display library (20) on virus preparations at BSL-4 (21). Each sdAb recognized nucleoprotein (NP), a critical viral structural protein enveloping the RNA genome as part of the viral ribonucleocapsid (22) and also a vital component of the viral assembly (23) and replication machineries in concert with VP35, polymerase L (24), and VP30 (25). The sdAbs were capable of sensitive and specific recognition of MARV Musoke and Angola strains, plus the closely related Ravn virus (RAVV) in a monoclonal affinity reagent sandwich assay, where a single antibody acts as both captor and tracer against polyvalent antigen (26, 27). Wishing to advance these sdAb further as diagnostic and transbody-based countermeasures, it was imperative that we find out precisely where and how they bind NP, to gauge the likely impact of MARV and RAVV evolution on the sdAb–NP recognition process. To pursue antibodies that are vulnerable to epitope erosion would be foolhardy in the long term, yet to identify antibodies that target completely conserved epitopes would be advantageous.

Here, using mutagenesis and X-ray crystallography, we determine the region of NP recognized by the sdAb and, in so doing, discover a novel tertiary structure of MARV NP. Elucidating this cryptic epitope or "cryptotope" allowed us to predict the likely impact bat and human MARV variation might have upon sdAb interactions, allowed us to compare and contrast local MARV and EBOV NP structures, and speculate on its natural role in viral replication.

RESULTS

Anti-MARV sdAb Bind the NP C-Terminus with nM EC_{50} and Differing Conformational Sensitivities

Predicted amino acid sequences of the four anti-MARV sdAbs (**Figure 1A**) reveal three unique families with sdAb C and D sharing complementarity-determining regions (CDRs) 1 and 3 and all four sdAbs sharing an aromatic residue in the middle of CDR3. Sandwich-based detection of Triton lysed virus employing each purified sdAb as captor and phage displayed sdAb tracer (21) was recapitulated on purified NP (Figures S1A,B in Supplementary Material). The trend shown in **Figure 1B** suggested that other MARV ribonucleoprotein components were unlikely to be involved in sdAb binding in this semi-quantitative polyvalent antigen capture format. In this assay, sdAb D was re-confirmed as the poorest performing clone and was only sparingly studied further since it was also a relatively poor expresser. That sdAb D shares CDRs 1 and 3 with sdAb C yet appears to bind poorly suggest framework region (FR) residues or CDR2 composition might be non-optimal. Prior to any structural work, we mutated the single aromatic residue of CDR3 of sdAb A-C to alanine, and purified mutant proteins (Figure S2A in Supplementary Material) to explore the impact on binding NP since it is known that aromatic R-groups, especially in CDR3 perform critical antigen binding services (28). All three sdAb show diminished antigen binding when amino acid 100 was substituted for alanine (Figure S2B in Supplementary Material). Wild-type sdAb A and C are equivalent binders while sdAb B is a relatively poor performer in this format, where immobilized polyvalent NP captures monomeric sdAb which is then revealed with bivalent anti-His_6 IgG horseradish peroxidase (HRP).

To begin more quantitatively ranking the sdAb, we engineered "glucibodies" which are fusions of sdAb to the N-terminus of *Gaussia* luciferase (gluc) (30). The gluc protein is a sensitive monomeric reporter enzyme and is efficiently secreted to the periplasmic compartment of *E. coli* when fused to other types of recombinant antibody fragments (31) offering a facile route to determine sdAb EC_{50} value for each sdAb. Titration of purified sdAb–gluc fusion proteins (Figures S3A,B in Supplementary

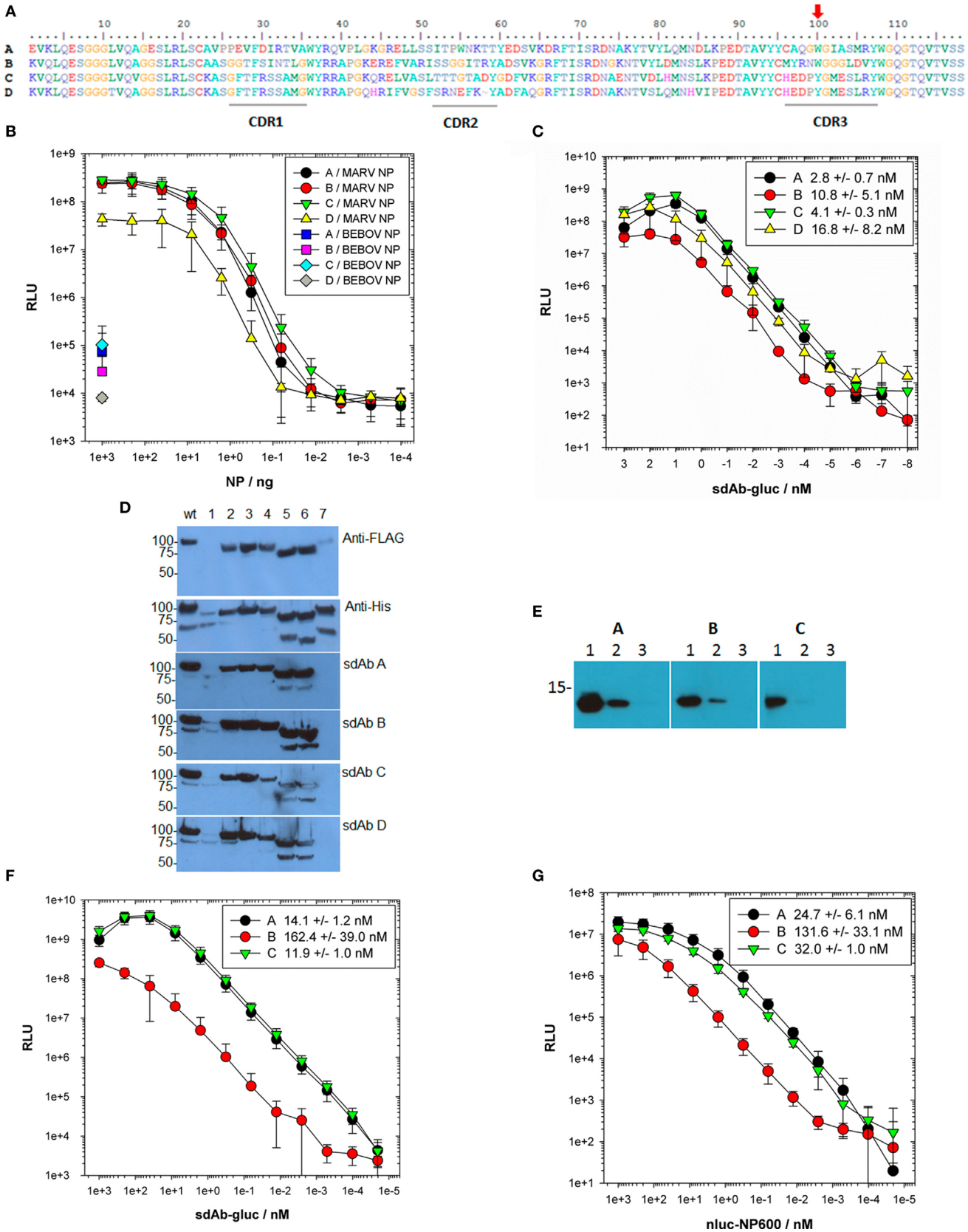

FIGURE 1 | Continued

FIGURE 1 | Continued
Locating the region of nucleoprotein (NP) bound by sdAb and establishing EC_{50} values**. (A)** Predicted amino acid sequences of the 4 anti-Marburg virus (MARV) NP–sdAb made using BioEdit (29) with complementarity-determining regions (CDRs) underlined and the aromatic residue in CDR3 highlighted with a red arrow. **(B)** Purified recombinant MARV or Bundibugyo (BEBOV) NP polymers were titrated over passively immobilized anti-MARV NP–sdAb, and captured NP subsequently detected with a constant amount of each phage displayed sdAb followed by anti-M13–horseradish peroxidase (HRP) conjugate. The experiment was performed three times in duplicate wells and the plots represent the mean values with error bars representing ± SD. **(C)** Fusions of sdAb–gluc were titrated over passively immobilized MARV NP polymer to determine EC_{50} values. Each titration was performed in duplicate wells with a negative control binding curve on BEBOV NP subtracted from each MARV curve. Each experiment was repeated three times and the plots represent the mean values with error bars representing ± SD. The EC_{50} values were determined for each curve and are shown in the legend ± SD. **(D)** Lysates of *E. coli* expressing MARV NP tagged with FLAG at the N-terminus and His_6 at the C-terminus were probed with either anti-FLAG-HRP, anti-His_6-HRP or sdAb–alkaline phosphatase (AP) fusion proteins. Wt represents full-length NP while numbers refer to the deletions of amino acids; 1–100 (1), 101–200 (2), 201–300 (3), 301–400 (4), 401–500 (5), 501–600 (6), and 601–695 (7). **(E)** 1,000 ng (1), 100 ng (2), or 10 ng (3) of purified MARV NP C-terminus was probed with 100 nM of each sdAb–AP fusion protein for equivalent times and developed side-by-side. **(F)** The sdAb–gluc fusions were titrated over passively immobilized mbp-NP600 fusion protein to determine the monovalent EC_{50} values. Each titration was performed in duplicate wells with a negative control mbp only binding curve subtracted from each mbp-NP600 curve. The experiment was repeated three times and the plots represent the mean values with error bars ± SD. The EC_{50} values were determined for each curve and are shown in the legend for each sdAb–gluc fusion protein ± SD. **(G)** The nluc-NP600 fusions were titrated over oriented immobilized sdAb to determine the EC_{50} values in a reversed orientation. Each titration was performed in duplicate wells with a negative control nluc only binding curve subtracted from each nluc-NP600 curve. The experiment was repeated three times and the plots represent the mean values with error bars ± SD. The EC_{50} values were determined for each curve and are shown in the legend for each sdAb ± SD.

Material) over immobilized polyvalent NP defined the EC_{50} values for each antibody in the low nanomolar range (**Figure 1C**) though with no statistical difference (P-value > 0.05).

Deletion mutagenesis of *E. coli* expressed NP followed by probing with bivalent sdAb–alkaline phosphatase (AP) fusion proteins to leverage avidity and precipitating chemiluminescent product, revealed loss of binding for all four sdAb when the last 95 amino acids were absent (**Figure 1D**). Nineteen anti-Ebola virus sdAb previously isolated from the same phage displayed sdAb library using similar selections on four species of EBOV also recognized the NP C-terminal regions and performed as both captor and tracer (27), indicating a particularly attractive epitope for sdAb appears to reside here. The C-termini of both MARV and EBOV NP are known to be repetitively displayed along the ribonucleocapsid (22, 32), explaining why our anti-MARV sdAb perform akin to our anti-Ebola sdAb in sandwich immunoassays, where polyvalent antigen enables one sdAb clone to serve as both captor and tracer.

When the last 95 amino acids of MARV Musoke NP were overexpressed and purified as an N-terminally His-tagged motif (termed NP600) (Figures S4A–C in Supplementary Material), the isolated antigen was able to be recognized by the three bivalent sdAb–AP tested by Western blot, though sdAb C was a relatively poor binder (**Figure 1E** with original blots shown in Figure S5 in Supplementary Material). Since passively immobilized NP600 was also a poor substrate for sdAb C glucibody (data not shown), we immobilized purified fusion proteins (Figures S6A,B in Supplementary Material) of maltose-binding protein (mbp) and NP600 to determine monovalent EC_{50} values for the sdAb as glucibodies (**Figure 1F**). Single-domain antibody B glucibody was significantly different from both sdAb A and C glucibodies (P–value <0.05). To reconfirm these findings using solution phase NP600 antigen, we reversed the assay orientation by immobilizing sdAb *via* a single biotin acceptor peptide (BAP) on a neutravidin coat. The sdAb were probed with purified fusion proteins of NP600 to the C-terminus of nluc (Figures S7A,B in Supplementary Material), another small monomeric luciferase heavily engineered for brightness (33). The nluc protein is highly soluble in the cytosol of *E. coli*, though in our hands is poorly secreted to the periplasm, making it an ideal fusion partner for NP600 which we were also unable to secrete efficiently. Titration of nluc-NP600 fusions over the oriented sdAb revealed EC_{50} values for each antibody on par as before (**Figure 1G**), with sdAb B significantly different from sdAb A but not to sdAb C (P–value <0.05). The monovalent EC_{50} values for the sdAb in both assay formats were higher than when using polyvalent NP antigen as expected, yet the ranking of sdAb A followed by sdAb C and then sdAb B tended to be preserved.

Since linear peptide arrays representing the length of NP600 were unable to identify any reactivity with sdAb C (data not shown) and sdAb C reacted poorly with NP600 on Western blots indicated dependence on a conformational epitope. Classifying epitopes as conformational or non-conformational solely based on Western blotting is ill-advised as immunoblotted antigens can retain sufficient structural information for at least some binding by the sdAb (34). To define the epitope(s) further we chose X-ray crystallography, since it would also yield the structure for the MARV NP C-terminus which has so far proven elusive to tertiary structural assignment (35).

Difficulty Generating Crystals of sdAb–Antigen Complexes Mirrored Reliance on Conformation

Both sdAb A and sdAb B were straightforward to crystallize alone, and in complex with NP600 simply by equilibrating an approximate 1:1 M ratios of the purified sdAb and NP600 proteins overnight before dispensing into crystallization screening experiments. However, sdAb C was highly refractory to crystallization alone and yielded a single polycrystalline cluster from thousands of screening trials. While further attempts to improve this crystal form were unsuccessful, the structure was determined and revealed the C-terminal His_6 tag provided fortuitous packing interactions. We were unable to co-crystallize sdAb C with NP600 by simple equilibration after mixing or following size exclusion chromatography (SEC) of the complex. We, therefore, used a bait prey strategy to allow facile production and purification of large amounts of pre-formed antibody-antigen

complexes. We removed the C-terminal His_6 tag from sdAb C (prey), isolating it from crude osmotic shocks using partially purified His_6-tagged NP600 (bait), and then employed immobilized metal affinity chromatography (IMAC) followed by SEC to purify the complex which yielded occasional, poorly diffracting small crystals. We repeated the strategy using a trimmed version of NP600 that begins at Trp632 (termed NP632), to avoid potentially flexible regions not visible in the sdAb A or B complex structures, resulting in pure sdAb C/NP632 complex (Figure S8 in Supplementary Material). Within the first screen, two wells with small, irregularly shaped, poorly diffracting crystals were discovered that, upon further optimization, yielded crystals that diffracted satisfactorily.

The EC_{50} of sdAb A, B, and C glucibodies for mbp-NP632 were determined to be 15.4 ± 3.9; 189.1 ± 55; 22.3 ± 3.2 nM, respectively, while EC_{50} values of nluc-NP632 for sdAb were 12.8 ± 4.3; 28.5 ± 3.6; 26.6 ± 3.4 nM, respectively (Figures S9A,B in Supplementary Material). In both cases, the sdAb B EC_{50} value was significantly different from those of sdAb A and sdAb C (P-value <0.05). The overall similarity between EC_{50} values determined using NP600 or NP632 suggests the first 31 amino acids of NP600 that are absent in NP632 are not critical for sdAb binding, though sdAb B exhibits variation depending on the assay format. We were unable to generate suitable crystals of NP600 alone, and NP632 proved somewhat insoluble unless produced as a fusion protein. To date, we have also been unable to generate crystals of mbp-NP600 or mbp-NP632, suggesting that our semi-synthetic sdAb had a chaperone effect on the ability of the C-terminal domain to crystallize, as seen previously for a protein refractory to crystallization by itself (36). X-ray diffraction data collection and statistics for the bound and unbound crystal structures for sdAb A–C are shown in **Table 1**.

sdAb Employ Common and Unique Approaches to Engage the MARV NP C-Terminus

All three sdAb–NP complexes are shown in **Figure 2A** revealing the different approach angles used by the antibodies to interact with the MARV NP C-terminal domain with the pivotal CDR3 aromatic side chains shown in stick form. Unique VH and VL domains capable of binding the same epitope through overlapping but non-identical footprints resulting in different approach angles have been revealed to atomic resolution for broadly neutralizing IgG against viral envelope proteins of influenza A (37) and HIV-1 (38). Epitopes that can elicit a wide diversity of antibodies that are now able to be mined through various repertoire selections are dubbed supersites (39). A sdAb's eye view of our more modest NP bijousite is shown in **Figure 2B** in cartoon form where the main chains of the three NP C-termini overlay with one another within 0.4–0.7 Å RMSD for all NP structures in the crystallographic asymmetric units. The last 64 residues of NP visible in the crystal structures primarily consist of three alpha helices associating to form an upper V-like shelf of the two C-terminal most helices (arbitrarily named 1 and 2 counting back from Leu695), with the third descending between them to re-appear after a turn as beta sheet positioned under the C-terminus. Contact mapping analysis using the Weizmann server running part of the SPACE suite (40) identified NP residues potentially involved in binding each sdAb with different combinations of CDRs engaging the three helices (Figure S10 in Supplementary Material). When side chains of all of the potential sdAb contacts are displayed as sticks on the epitope backbone (**Figure 2C**), minor differences are apparent in the disposition of R-groups (e.g., Asn694 and Glu687), though the epitope appears fairly constrained. Electrostatic surface rendering (**Figure 2D**) reveals an asymmetric basin-like depression between helices 1 and 2 with helix 3 forming the basin floor with a hydrophobic core of Leu676, Val691, and Met683 at the closed end, while Leu663, Leu695, and Tyr667 reside at the upper more open end. Single-domain antibodies are well known to target concave active sites of enzymes (41), recessed epitopes of parasite variant surface GPs (42), and canyons of virus particles (43), and it appears that the MARV NP C-terminal basin also constitutes such an attractive cryptotope. The basin overlook also offers potential for alternative modes of interaction with a crescent of negative charges (Glu675, Asp679, Asp682, Glu687, and Asp686) toward the closed end being noteworthy for salt bridge potential.

Figures 3A–C summarize the shape and charge complementarity between NP epitope and sdAb A, B, and C, respectively. Top is the sdAb's eye view of the NP C-terminus as electrostatic surface potential occupied by key hydrophobic paratope residues. The pivotal CDR3 aromatic residue of each sdAb appears nestled toward helix 2 Asp679 and close to Leu676 plus Val691 borne on helix 1 and Met683 on the turn between helices 1 and 2. sdAb A and B dispose Trp100 almost at right angles to each other while sdAb C employs Tyr100. Since Tyr100 of sdAb C is slightly more toward the open end of the basin, this allows Phe29 to engage Asp679, Met683, and Val691 toward the closed end. Secondary hydrophobic areas in the basin formed by Leu663, Tyr667, Leu695, and again Val691 afford suitable accommodation to Ile31, Trp55 of sdAb A, Gly101-103 of sdAb B, and Met102 plus Leu105 of sdAb C.

The electrostatic surface potentials of the undocked sdAb flipped 180° from binding NP (middle of **Figures 3A–C**) give an epitope's eye view of each paratope clearly showing the prominence of the hydrophobic CDR residues that engage the basin. Both sdAb A and C appear to exhibit the classical convex paratope, with relatively large contiguous regions of hydrophobicity, while sdAb B appears less pronounced. Differences in the number and distribution of positively charged paratope residues engaging the negatively charged basin overlook are apparent, and salt bridge and hydrogen bonding potential were revealed by PDBePISA analysis (44). While only Arg106 of sdAb A salt bridges Asp679, sdAb B employs Arg98, Arg50, and Arg58 to engage Glu675 plus Asp679, Asp679, and Asp682, respectively. While sdAb C also shares the Asp679 salt bridge route (with Arg30), this antibody is highly unusual in employing Lys1 of FR1 to engage Asp686 in a second salt bridge. Perhaps this alternative approach to binding may partially compensate for not employing CDR2, a feature only shared with one other sdAb to date (45). Amino acids Glu675, Asp679, and Glu687 are also involved in hydrogen bonding all three sdAb with Asp682 additionally H-bonding sdAb B. Hydrogen bonding potential is

TABLE 1 | Data collection and refinement statistics.

	sdAb A	sdAb A/NP600	sdAb B	sdAb B/NP600	sdAb C	sdAb C/NP632
PDB code	**6APO**	**6APP**	**6APQ**	**4W2O**	**4W2P**	**4W2Q**
Data collection						
X-ray source	Advanced Photon Source 24-ID-E	UTHSCSA X-ray Crystallography Core Laboratory	Advanced Photon Source 24-ID-E	Advanced Light Source 4.2.2	Advanced Photon Source 24-ID-C	UTHSCSA X-ray Crystallography Core Laboratory
Space group	$P2_12_12_1$	$P2_12_12_1$	$P6_522$	$P2_12_12_1$	$P1$	$P2_1$
Cell dimensions						
a, *b*, *c* (Å)	41.6, 49.4, 58.8	41.6, 46.2, 102.8	80.0, 80.0, 89.9	58.0, 108.7, 141.3	33.4, 49.5, 65.4	57.7. 98.5, 68.5
α, β, γ, (°)	90, 90, 90	90, 90, 90	90, 90, 120	90, 90, 90	87.7, 84.8, 79.4	90, 96.2, 90
Wavelength (Å)	0.97917	1.54178	0.97917	0.97626	0.97950	1.54178
Resolution (Å)	41.60–1.17 (1.23–1.17)[a]	46.15–1.75 (1.84–1.75)	69.27–1.90 (2.00–1.90)	58.00–3.20 (3.37–3.20)	48.65–1.77 (1.86–1.77)	46.42–2.70 (2.85–2.70)
R_{sym}	0.067 (0.282)	0.089 (0.640)	0.084 (0.587)	0.189 (0.705)	0.063 (0.390)	0.154 (0.673)
R_{pim}	0.028 (0.198)	0.039 (0.281)	0.043 (0.304)	0.081 (0.297)	0.058 (0.332)	0.092 (0.398)
Mean $I/\sigma I$	17.6 (3.4)	14.1 (2.6)	12.2 (2.5)	10.6 (3.0)	8.6 (2.3)	8.2 (1.9)
Completeness (%)	95.7 (71.3)	99.2 (98.1)	99.9 (100)	100 (100)	91.6 (88.5)	99.0 (98.3)
Redundancy	6.6 (3.2)	6.9 (6.9)	5.5 (5.7)	7.2 (7.4)	2.5 (2.4)	3.7 (3.8)
Wilson value (Å^2)	9.3	19.0	26.9	55.1	16.3	35.8
Refinement						
Resolution (Å)	37.81–1.17	34.34–1.75	69.27–1.90	54.33–3.20	26.77–1.77	41.68–2.70
No. reflections	39,980	20,434	13,899	15,287	36,633	20,587
R_{work}/R_{free}	0.148/0.173	0.171/0.219	0.185/0.216	0.227/0.285	0.165/0.203	0.220/0.274
No. atoms						
Protein	952	1,450	901	5,716	3,745	5,720
Ion	–	–	4 (Na^+, 3 Cl^-)	40 (8 SO_4^{2-})	9 (Na^+, 2 CH_3COO^-)	–
Water	176	321	138	–	379	104
B-factors (Å^2)						
Protein	12.2	19.0	28.3	51.2	19.3	38.9
Ion	–	–	31.2	69.7	17.8	–
Water	28.8	31.0	40.3	–	27.5	28.4
R.m.s deviations						
Bond lengths (Å)	0.007	0.007	0.007	0.003	0.010	0.005
Bond angles (°)	0.967	1.090	1.106	0.557	1.034	0.971
Ramachandran plot						
Favored (%)	98.3	99.4	99.1	94.5	98.7	98.9
Allowed (%)	1.7	0.6	0.9	4.6	1.3	1.1
Outliers (%)	0.0	0.0	0.0	0.8	0.0	0.0

[a]*Highest resolution shell is shown in parentheses.*

also predicted for Asn669 to sdAb A, Ser684 and Ala678 to sdAb B, His690 and Ser672 to sdAb A and C, and finally Tyr667 to sdAb B and C.

The lower panels of **Figures 3A–C** show space-filling representations of all predicted paratope residues giving an indication of the potential breadth of interactions. Here, the different approach angles shown in **Figure 1A** are also reflected in the differential visibility of conserved framework areas. The distribution of paratope residues of sdAb C appears more concentrated than either sdAb A and B, resembling an oval focusing on the basin interior. Together with the absence of additional helix crosslinking mediated by CDR2 and Tyr100 as shown in Figure S10 in Supplementary Material, these deficits may help explain the conformational sensitivity of sdAb C. An additional view of the three sdAb docking is shown in Figure S11 in Supplementary Material. The diverse potential for protein–protein interactions within the MARV C-terminus appears striking, being leveraged by all three sdAb in both unique and overlapping ways, while still preserving the rule of hydrophobic core and hydrophilic surrounds for the complex (46, 47).

Additional PDBePISA analysis of the crystal structures compares the antibody–antigen interfaces according to buried surface area, solvation free energy gain (Δ^iG) from forming the interface, and the *P*-value of Δ^iG which can be described as a value of interface specificity (a lower number <0.5 correlates with higher specificity). The buried surface area values are similar to 686, 653, and 663 Å^2, respectively, for sdAb A, B, and C complexes. The interfaces have values for Δ^iG and the *P*-value of −7.4 kcal/mol

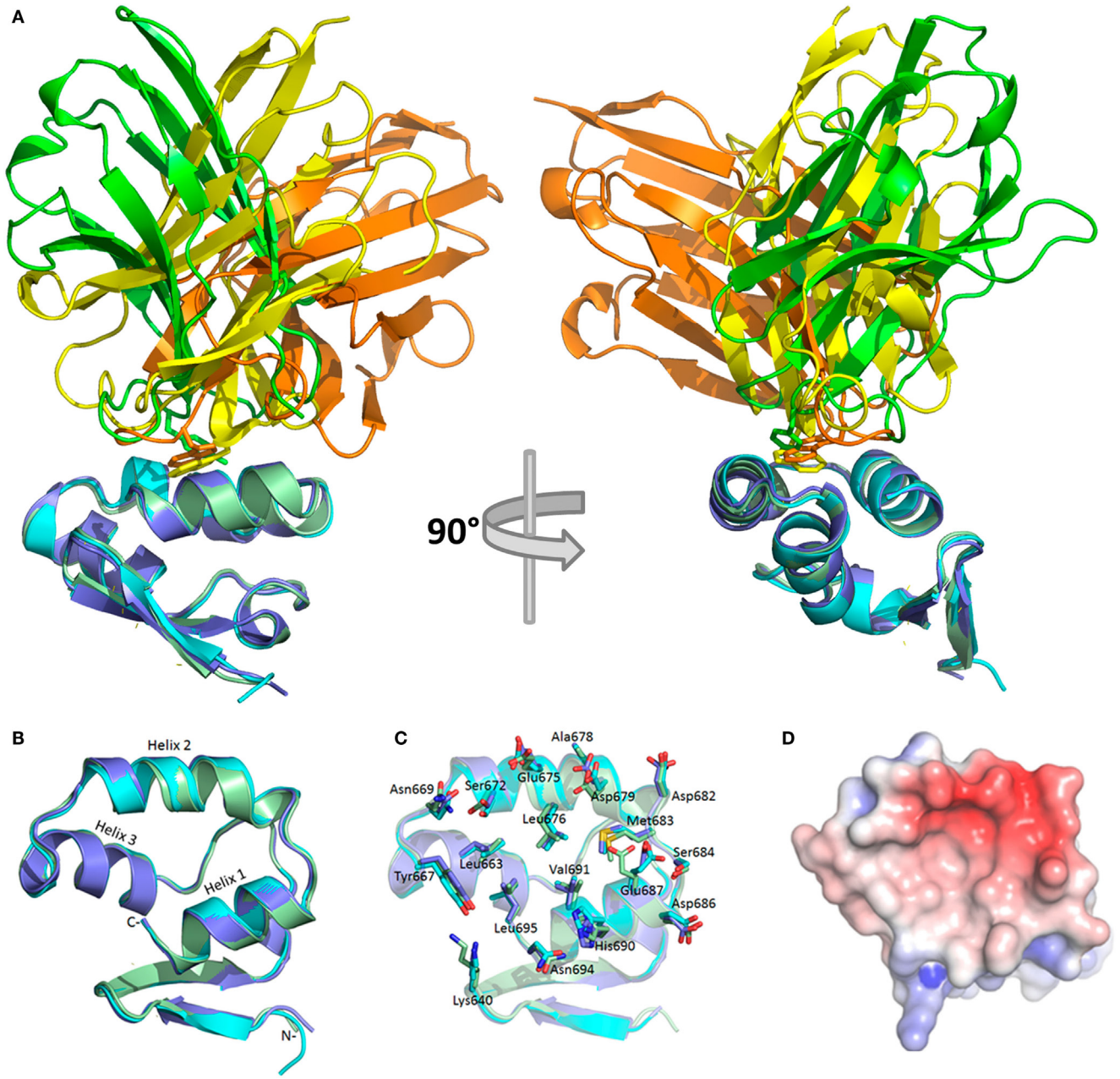

FIGURE 2 | Crystal structures of bound sdAb A, B, and C and the cryptic Marburg virus (MARV) nucleoprotein (NP) C-terminus. **(A)** The three sdAb–NP complexes revealing the different approach angles for sdAb A (yellow), B (orange), and C (green). NP is colored for each sdAb thus; A (purple), B (pale green), C (cyan). NP is oriented to show helices 1 and 2 in the same plane while helix 3 descends at an approximate 45° angle left to right. Residues 600–631 of NP600 and the MetGlyHis$_6$ tag are not visible in the crystal structures. Rotating the structures 90° reveals the end on view from the C-terminus of NP and the grouping of apical CDR3 aromatic residues shown as sticks between helices 1 and 2. **(B)** The sdAbs have been removed and the NP C-terminus rotated from its aspect in **(A)** to give a sdAb's eye view of the epitope and the three major alpha helices with helix 1 (Leu695–Phe685) and helix 2 (Pro681–Pro670) forming a V-like shelf and basin sides, while helix 3 (Tyr667–Pro656) forms the basin floor. From the floor emerges anti-parallel beta-sheet that loops back around under helix 1 *via* Lys640 onward to Trp632. **(C)** NP residues implicated in engaging the sdAb have their side chains shown as sticks and are labeled. Almost all are shared by the three sdAb except Lys640 (not sdAb B), Val671 (not sdAb B or C), Val674 (not sdAb B or C), S684 (not sdAb A). **(D)** Electrostatic surface potential of the NP epitope with scale ranging from −5 (red) to +5 (blue) K_bT/e_c reveals a broad asymmetric hydrophobic basin between helices 1 and 2 with an open aspect toward Tyr667 at the start of helix 3 and a closed aspect toward the descent with an overlook of negative charges in a crescent from Glu675 around to Glu687.

and 0.262, −4.5 kcal/mol and 0.375, and −8.5 kcal/mol and 0.118, respectively, for sdAb A, B, and C complexes. The values calculated for sdAb B and C complexes were averaged over the four complexes in each asymmetric unit, while values for the sdAb A complex were calculated for the single complex in its asymmetric unit.

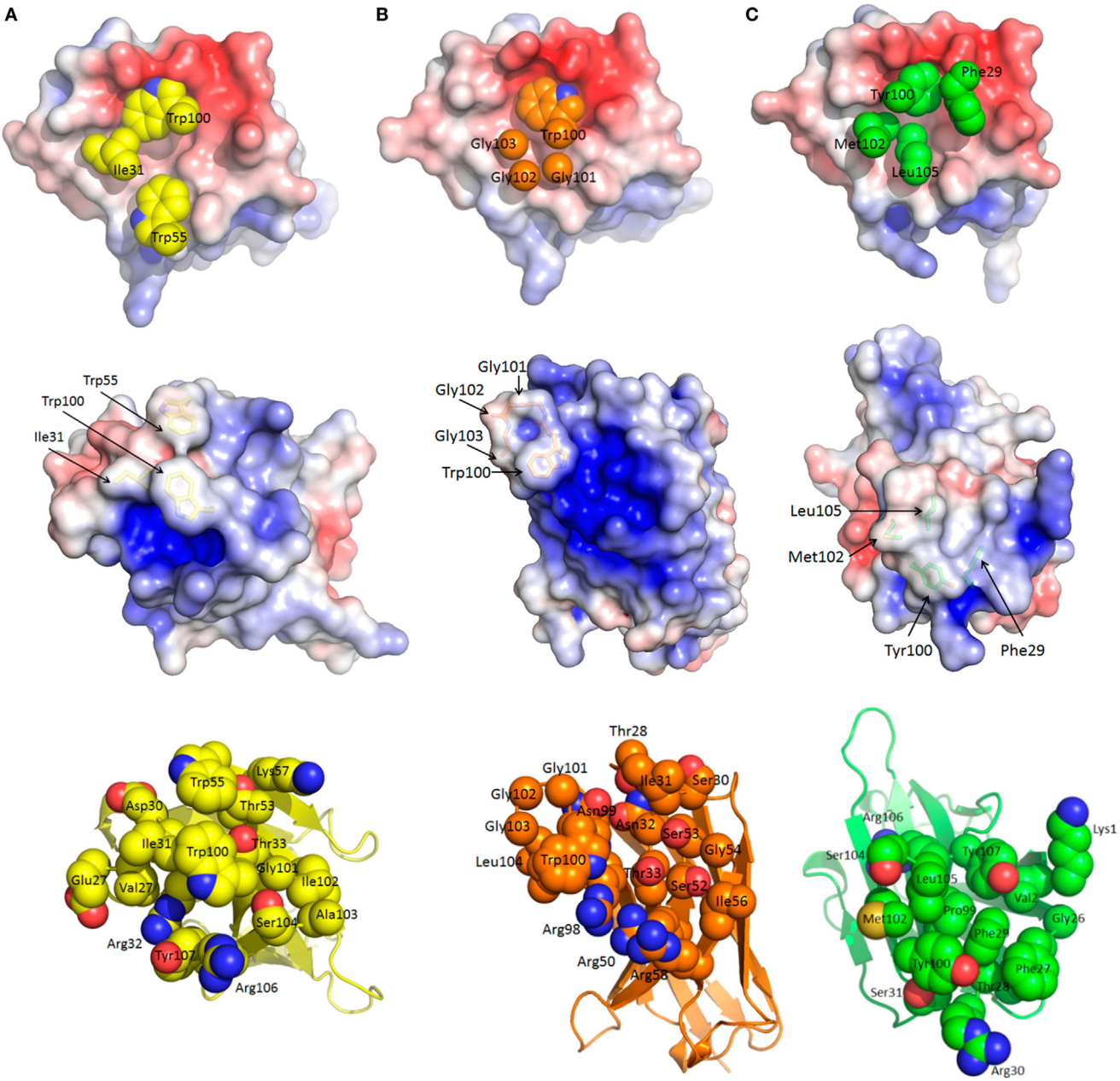

FIGURE 3 | Common and unique features of sdAb–nucleoprotein (NP) engagements. For each sdAb A **(A)**, B **(B)**, and C **(C)**, the epitope is shown first (*top*) with the apical CDR3 aromatic group and other hydrophobic side chains occupying the basin. *Middle* images reveal the sdAb undocked, rotated 180° toward the reader and displayed with electrostatic surface potential [−5 (red) to +5 (blue) K_bT/e_c] to reveal the epitope's eye view of the paratope. The convex hydrophobic networks of the basin filling residues are evident with side chains shown as sticks and annotated. The recessed differential positive charges that engage the negatively charged basin overlook become apparent especially for sdAb B. *Lower* images show the same view of each sdAb as the middle view with each residue predicted to be involved in antigen engagement shown as space-filled representations and labeled. The latter view serves to decode the electrostatic surface and more clearly shows the unique approach angles as the frameworks become more evident to the rear of each sdAb.

Complementarity Requires CDR Restructuring by All Three sdAbs

The shape complementarities (Sc) for the sdAb within the complexes were calculated using the CCP4 suite (48) and are 0.77, 0.52, and 0.67 for A, B, and C, respectively. Bearing in mind, Sc values for several immune antiviral Mab/Fab are in the 0.6–0.8 range (49, 50), the sdAb values are remarkably high for non-immune semi-synthetic sdAb from a single-pot library that have not undergone any affinity maturation. A non-immune antibody is only as good as its antigen and we are left with the sense that serendipity has offered up a remarkably attractive epitope for these sdAb to engage MARV NP. The lower Sc for the lower affinity

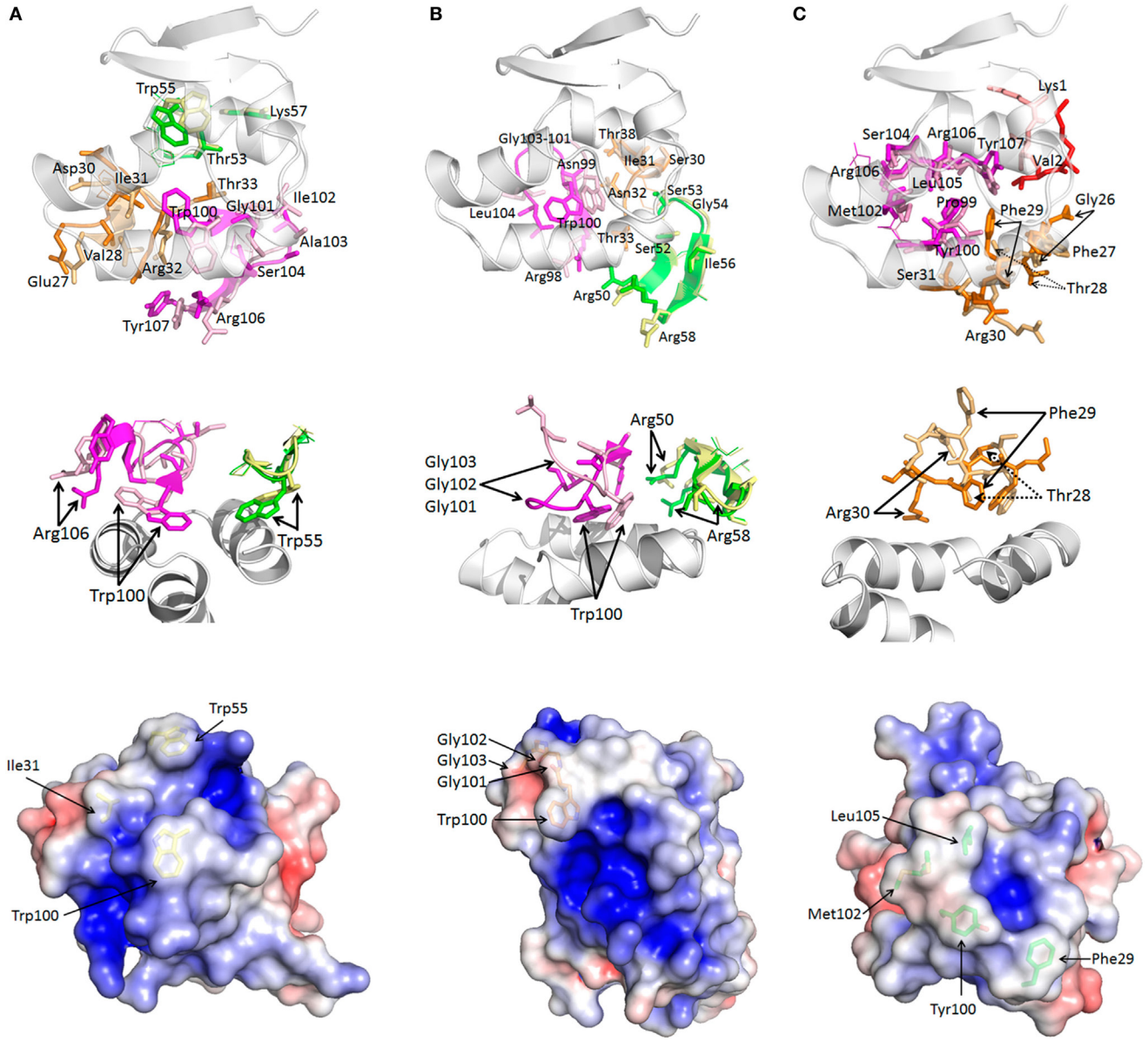

FIGURE 4 | Comparison of bound and unbound sdAb reveals complementarity-determining region (CDR) restructuring. For each sdAb A **(A)**, B **(B)**, and C **(C)** (*top*) looking up from beneath the nucleoprotein (NP) epitope (white) at the bound/unbound CDR1 (orange/beige), CDR2 (green/yellow), CDR3 (magenta/pink), and FR1 (red/salmon for sdAb C) shows CDR loop rearrangements. Residues predicted to engage antigen are displayed in stick form and labeled while those that do not are shown as lines and unlabeled. *Middle* images show each interaction colored as above but aspects have been chosen to more clearly show the primary fits occurring with CDR1 removed for clarity for sdAb A and B, and only CDR1 shown for sdAb C. *Bottom* images present unbound sdAb with electrostatic surfaces and the basin occupying residues shown as sticks. Note that Glu1 and Val2 are not visible in sdAb A while Lys1 is not visible in sdAb C. Two isoforms of Met102 are visible in sdAb C, neither corresponding to the bound disposition. When comparing the unbound sdAb structures to the bound sdAb structures (**Figure 3** middle), the hydrophobic side chains destined to occupy the NP basin appear more diffuse in sdAb A and sdAb C, while sdAb B has equivalent density yet has a more glancing side-on CDR3 disposition.

sdAb B might be in part due to the presence of only one large hydrophobic group in the basin accompanied by three small Gly side chains, while sdAb A and C have two aromatic side chains and bulkier hydrophobic Ile and Leu residues, respectively.

When free and bound sdAb are compared (**Figure 4**), it becomes clear that each antibody still undergoes substantial restructuring as a means to improve antigen recognition (51). sdAb A exhibits a 180° flip for Trp100 and Trp55, with Ile31 also needing adjustment to present a more tightly knit array of hydrophobic side chains evident in the bound electrostatic surface shown in **Figure 3**. sdAb B CDR3 extends and flattens when bound to enable Trp100, Gly101-103, and Ile104 better access to the basin interior. Arg58 and, to a lesser extent, Arg50 at the landing and take-off sites of CDR2 also shift to reach their

salt-bridging partners on the basin overlook. sdAb C is unusual out of the three antibodies in that CDR3 appears to be a reasonable pre-existing fit already, with the majority of fitting occurring in CDR1. Here, the main chain undergoes an S curve reversal (i.e., S to Ƨ) to move Phe29 toward the basin with an ~11 Å maximal repositioning to displace the neighboring Thr28 which shifts by ~6 Å. The final position of Phe29 is almost a supporting role to Tyr100, but it does have modest contacts of its own. Amino acids Arg30 of CDR 1 and Lys1 of FR1 also move to meet their respective salt bridge partners on the overlooks with both having ~9 Å shifts.

Comparison of free and bound forms of a highly unusual human broadly neutralizing Ab, capable of neutralizing all serotypes of influenza A, has recently been shown to exhibit dramatic CDR restructuring (52). The movements enable better accommodation of aromatic and hydrophobic residues within a hydrophobic groove of HA, with a key CDR3 Phe showing a ~5 Å shift. By virtue of having missing electron density in CDR3 of the free form, an anti-HIV gp120 immune llama sdAb capable of cross-clade neutralization may also employ restructuring to fit (53), though the bound form will be required to confirm this. It may well be that the potency of antibody repertoires for cryptic viral antigens not only relies on the total number of unique clones but also on the ability of the CDRs to accommodate such dramatic tertiary changes on transitioning from free and soluble forms to bound and potentially insoluble forms.

Conservation of the sdAb Cryptotope

Alignment of MARV NP amino acid sequences from humans and bats since 1967 derived from the Los Alamos Filovirus database https://www.hfv.lanl.gov (54) revealed positions prone to mutation within the C-terminus summarized in **Figure 5A**. Using Musoke (1980, $n = 1$) as our parental baseline the Leiden (2008, $n = 1$), Popp/Ci67 (1967, $n = 2$), Angola (2005, $n = 8$), Ugandan (2012, $n = 2$), and one Ugandan bat strain (2009, $n = 1$) are all homologous, highlighting conservation across almost 50 years of evolution. One Uganda bat sequence has Val664Ile (2008, $n = 1$). Ozolin (1975, $n = 1$) has Asn654Ser and Ile660Val which also occur together in many human isolates from DRC (1999/2000, $n = 27$) and several Ugandan bat sequences (2007, $n = 2$, 2008, $n = 1$ and 2009, $n = 3$). Within the DRC outbreak, one sequence had Ser658Pro in addition to Asn654Ser and Ile660Val (2000, $n = 1$). Human RAVV sequences from Kenya, DRC, and Uganda differ from Musoke in having Asn654Ser (Kitum Cave 1987, $n = 1$; DRC 1999, $n = 1$; Uganda 2007, $n = 1$) which also occurs in Uganda bat sequences (2007, $n = 2$; 2008, $n = 1$) with one additionally having Glu665Lys (2009, $n = 1$). When residues prone to drifting are mapped on to the C-terminal structure, all reside on helix 3 or just beyond it with their side chains disposed away from the epitope (**Figure 5B**). The relaxed contact mapping analysis (Figure S10 in Supplementary Material) also failed to predict these amino acids as involved in engaging the sdAb. We had previously shown that all four sdAb showed equivalent responses in sandwich capture of Triton-lysed RAVV when compared with Musoke and Angola viruses [Figure 1 of Ref. (21)], showing experimentally that at least Asn654Ser alone did not appear to impact binding. Furthermore, any subtle impacts on affinity due to these mutations are likely to be overcome by avidity effects within the sandwich assay format as indicated by

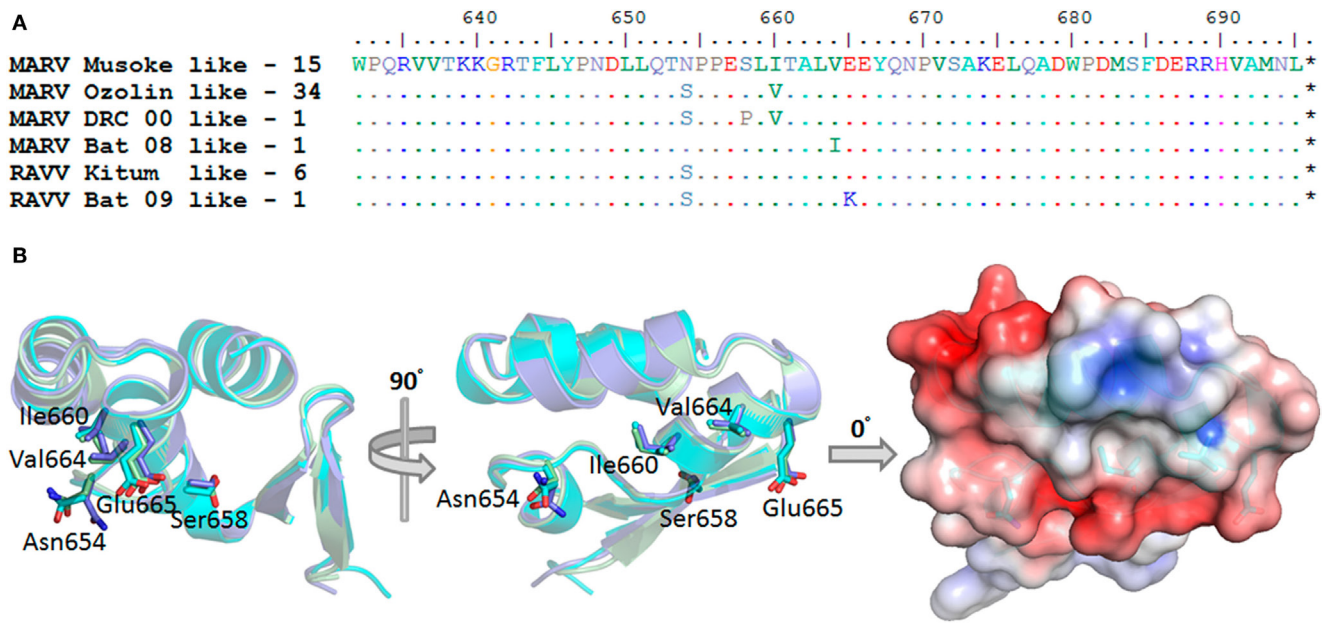

FIGURE 5 | Natural evolution of the Marburg virus (MARV) nucleoprotein (NP) C-terminus is remote from the sdAb epitope. **(A)** Summary of the frequency with which human and bat MARV and Ravn virus (RAVV) NP genes vary within the C-terminal region under study. **(B)** The C-terminal domains and side chains are displayed end or side on as if sdAb were binding the epitope from above as in **Figure 1A**. The amino acids prone to change are identified as sticks and labeled to reveal side chains that do not overlap the sdAb epitope, lying beneath and to one side of the domain. The electrostatic representation of the domain derived from the sdAb C complex is rendered on the right.

our lower EC_{50} values derived from polyvalent versus monovalent binding assays.

The only other known anti-NP MARV antibody we are aware of that has been mapped to the MARV C-terminus is a mouse Mab shown by deletion mutagenesis to require amino acids 643–695 (55). Without structural information, it is difficult to assess exactly where and how this antibody binds, and whether it is likely to be impacted by MARV variation or not. It would be of great interest to compare and contrast the footprints of our sdAb with the conventional IgG, to determine if they share similar approaches to binding the NP C-terminus or not.

Similarities and Differences between the MARV and EBOV C-Termini

That our sdAb epitope appears resistant to natural evolutionary variation suggests a critical function in viral replication such as interfacing with host proteins or other viral proteins. Such protein–protein interfaces are generally more conserved than non-interface surfaces (56) since mutations in one surface may require compensatory mutations in the other and will be less likely to occur. If the interface becomes part of the virion, as would occur if it was between two viral structural proteins, it will only be exposed upon virion dissociation (57). A 3D structural homology search using the Dali server (58) identified the C-terminal structures of Zaire (59), Bundibugyo, and Tai Forest (35) viruses as homologous to our MARV domain *via* the two last alpha helices. Perhaps surprisingly, overlaying the MARV and EBOV (Zaire) structures (**Figure 6A**) reveals that the EBOV motif is not at the C-terminus but 66 residues upstream indicating there is plasticity in where the motif needs to be in order to function. Secondary structure prediction using JPred (60) was unable to identify the preceding residues as prone to alpha helix formation, suggesting that in EBOV the basin may well rely on just the V-shelf helices without a third helix forming the basin floor. Indeed, the EBOV basin is comparatively shallow (**Figure 6B**) and smaller than MARV with a wall of stacked aromatic side chains between the helices occupying potential inter-helix space (**Figure 6C**). The more open end of the EBOV shallow basin appears to be across the axis of one of the helices between Ala664 and Val665 which create a dip rather than a route out over the Tyr667 of MARV (cf. **Figure 2D**). The basin overlooks of EBOV are not highly negatively charged with only Asp663 appearing to share a similar position to the Glu687 of MARV. The differences between MARV and EBOV motifs imply that if they do have similar roles in protein–protein interactions they may use alternative approaches to engage their particular partner protein(s). The differences also explain why our anti-MARV sdAb do not cross-react among the EBOV genus [Figure 1 of Ref. (21)] since the shape and charge complementarities required for sdAb binding are absent.

DISCUSSION

To our knowledge, our study represents the first high-resolution structural study of an antibody binding a filoviral NP. As such, the information can guide us through structure based design to improve the performance of the sdAb by focused *in vitro* evolution or educated mutagenesis. NP is an important biomarker for Marburg hemorrhagic fever, and high-end antibodies to conserved epitopes that may push the limits of detection toward nucleic acid test levels would be a significant step forward for point-of-care tests. The innate thermal stability of the sdAb format may make the resulting assays more suitable for resource poor environments where cold-chains are lacking. A mandate for conservation of the sdAb epitope, to play a vital role in viral

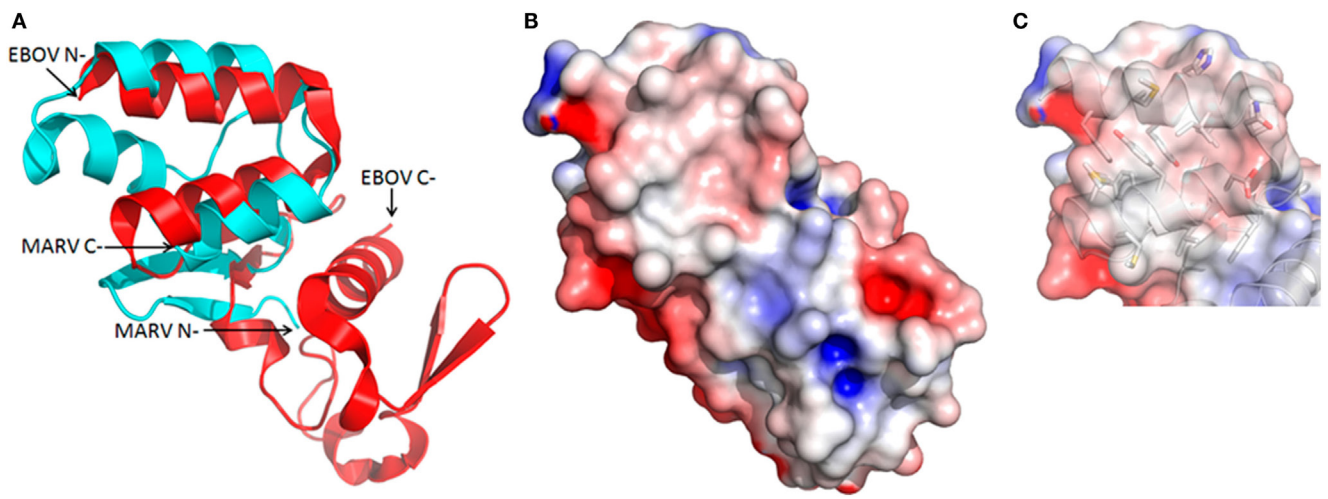

FIGURE 6 | Structural but not positional homology between Marburg virus (MARV) and EBOV nucleoprotein (NP) C-termini. **(A)** Cartoon overlay of the *Ebolavirus* (EBOV) (red) and MARV (cyan) C-termini as deduced from a Dali homology search reveals the two alpha helices forming the upper V-shelf are somewhat conserved. Note that while the V-shelf is at the extreme C-terminus of the MARV NP it is internal to the EBOV NP C-terminus. **(B)** Electrostatic surface potential reveals a much shallower and compact basin for EBOV. **(C)** Reduced basin width in EBOV is primarily due to Phe648 and Tyr652 from one helix stacking with Tyr667 from the other to form a wall-like structure that fills in the cavity as opposed to shorter side chains lining the MARV basin (cf. **Figure 2D**).

replication, bodes well for its long-term utility in enabling sdAb to recognize MARV and RAVV strains yet to emerge.

While crystal structures of constructs bearing amino acids 19–370 (61) and 552–579 (25) of MARV NP have been resolved, the remaining C-terminal region has proved more challenging, existing as a molten globule (35). Herein, by engaging the MARV C-terminal region with sdAb we overcame this roadblock. While two of the sdAb performed well as crystallization chaperones, the third (sdAb C) required much optimization for success, suggesting the approach is still somewhat empirical. However, since we were unable to generate any crystals of NP600, NP632, or the fixed arm maltose binding fusion protein equivalents, trans-sdAb rather than cis-mbp chaperoning appeared essential for success in this case. While we cannot rule out contributions to crystal packing afforded by the hydrophilic surface of the sdAb, it is more likely their role was to reduce conformational heterogeneity (62) of the MARV C-terminus to allow crystals to form. We do not know the precise choreography that occurs when transitioning between free and bound sdAb, only the end-points. It could be that the sdAb architectures were encouraged to form a more focused hydrophobic apical core, around which the basin could form from the molten state and the overlooks could be subsequently crosslinked to "fix" the MARV C-terminus. Alternatively, the molten state may transition through a folded C-terminal structure, which was then selectively extracted by the sdAb over time. Since all of these recombinant fragments are highly productive and relatively small, it should be possible to further explore the contributions of induced fitting and conformational selection using biophysical techniques.

It is tempting to speculate that like EBOV (63), the MARV C-terminus engages VP40 matrix protein for virus particle assembly, resulting in a layer of matrix between the polyvalent NP of the ribonucleocapsid and the viral membrane (22, 32). If we consider portions of the sdAb paratopes as mimics of VP40, much the same as some anti-influenza A virus broadly neutralizing antibodies can mimic portions of the influenza virus A HA receptor (64, 65), the loops revealed in the crystal structure of the MARV VP40 dimer (66) could potentially play this role (**Figure 7A**). The loops appear borne on scaffold-like structures that uncannily resemble CDRs borne on frameworks of antibodies. While one set of loops is visible in MARV VP40, there is missing electron density in the other set (Ser156, Thr157 and Ala71, Tyr72) indicating enough flexibility to undergo restructuring if required. Though it is impossible to draw definitive conclusions based on the structure of the complete MARV VP40 loop that is visible since it is involved in crystal packing, the occurrence of Phe, Thr, Tyr, and Arg residues may indicate involvement in protein–protein interaction since these residues are all highly favored at interfaces (47, 56). The fit between VP40 and NP need not be perfect nor high affinity since the "unusual, flexible Velcro-like" interaction (22) when polyvalent nucleocapsids laterally meet VP40 lattices for assembly at the membrane (67) could capitalize on avidity. The NP C-terminus is regularly displayed on the outer face of the nucleocapsid several thousand times and would be an ideal candidate to be proximal to the loop regions of VP40. Furthermore, during disassembly following virus entry and fusion, a weak interaction between VP40 and NP would be preferable for rapid dissociation to enable the nucleocapsid to be delivered to the cytoplasm efficiently. The high prediction of disorder at the C-terminus of MARV (68) combined with prior observations of the molten globule with three alpha helices present (35) suggests that our current crystal structure may represent the more orderly end of a dynamic molecular switch for virus assembly and disassembly (**Figure 7B**).

MATERIALS AND METHODS

General Cloning

Recombinant DNA methods were according to established procedures and employed commercially available reagents; Phusion High-Fidelity DNA Polymerase (Thermo Fisher, Waltham, MA, USA); restriction enzymes and β-agarase (New England BioLabs, Beverly, MA, USA); T4 DNA ligase, CIP and T4 PNK (Roche,

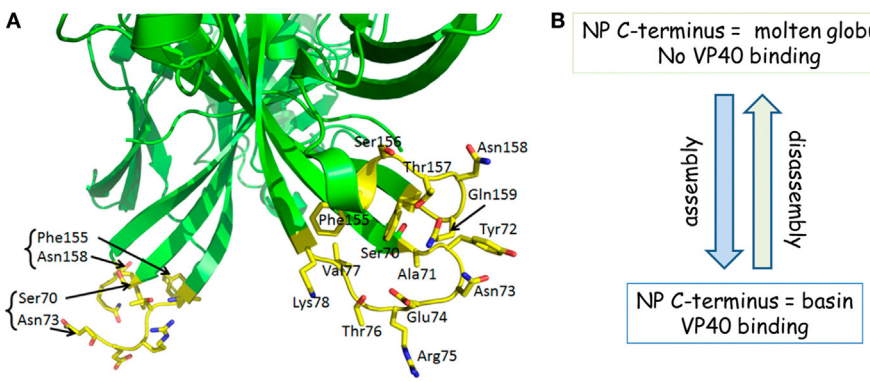

FIGURE 7 | **(A)** Marburg virus (MARV) VP40 appears to have loops that resemble complementarity-determining regions (CDRs). Loops in the region distal to the membrane binding patches (out of view) of the MARV VP40 dimer show a striking similarity to antibody CDRs, stemming from a scaffold crudely resembling frameworks. While one loop is visible in the crystal structure, the other is not which implies a flexibility that might be employed for restructuring. **(B)** A summary of our working hypothesis that the transition from disorder to order and *vice versa* within the nucleoprotein (NP) C-terminus is a molecular switch for virus assembly and disassembly by being able to host or release VP40.

Nutley, NJ, USA); GTG low melting temperature agarose for in gel cloning (Lonza, Walkersville, MD, USA); oligonucleotides (Integrated DNA Technologies, Coralville, IA, USA); cloned synthetic DNA (Genscript, Piscataway, NJ, USA). Assemblies involving cloning and PCR amplification were sequenced through the inserts and junctions to verify the desired construct. Cloning was typically carried out in XL1-Blue cells unless otherwise stated. Parental sdAb genes employed in this work were anti-MARV NP–sdAb A, B, C, and D with GenBank accession numbers MF780583, MF780584, MF780585, and MF780586, respectively. Full details of cloning, oligonucleotides, maps, and sequences of resulting constructs are available on request.

Expression and Purification of sdAb from *E. coli* for ELISA

For the NP sandwich ELISA freshly made soluble anti-MARV NP sdAb A, B, C, and D proteins derived from *lac* promoter and *pel*B signal-based periplasmic secretion vector pecan22 (21) were expressed and purified from 500 mL scale cultures in *E. coli* Tuner + pRARE. Clones were grown in 50 mL starter cultures of terrific broth (TB) plus 2% glucose at 30°C overnight with ampicillin (200 μg mL^{-1}) and chloramphenicol (30 μg mL^{-1}) in 250 mL Bellco baffled flasks. Saturated cultures were transferred to 450 mL of fresh TB without glucose and shaken for 3 h at 25°C in 2,500 mL Bellco baffled flasks. Expression was induced by addition of IPTG to 1 mM for 3 h at 25°C, the cells pelleted (typical wet weights of 8–9 g) and osmotically shocked (69) by resuspension in 14 mL ice-cold 0.75 M sucrose in 100 mM Tris–HCl pH 7.5, addition of 1.4 mL of 1 mg mL^{-1} hen egg lysozyme (Sigma), followed by drop-wise addition of 28 mL of 1 mM EDTA pH 7.5 and swirling on ice for 15 min. 2 mL of 0.5 M $MgCl_2$ was added, swirling continued for 15 min and cells pelleted. The 45 mL supernatant (osmotic shockate) was mixed with 5 mL of 10× IMAC (IMAC buffer—0.2 M Na_2HPO_4, 5 M NaCl, 0.2 M imidazole, 1% Tween-20, pH 7.5), followed by 0.5 mL of High-Performance Ni Sepharose (GE Healthcare) and the suspension gently mixed on ice for 1 h. Resin was pelleted at 3,000 rpm for 5 min (Beckman Allegra 6R swing out rotor) and washed twice with 50 mL of 1× IMAC solution before elution with 2 mL 0.5 M UV-grade imidazole in 1× IMAC buffer, pH 7.4. Proteins were concentrated in Amicon 10 kDa ultrafiltration devices (Millipore, Billerica, MA, USA) to 200 μL for separation by gel filtration on a Superdex 200 10/300 or Increase 10/300 GL column (GE Healthcare, Pittsburgh, PA, USA) operating in PBS. Proteins were quantified by UV adsorption and analyzed by SDS-PAGE and Coomassie blue staining for impurities.

Expression and Purification of Recombinant NP from Human Embryonic Kidney (HEK) 293T Cells

Human embryonic kidney 293T cells (ATCC, Manassas, VA, USA) were grown in Dulbecco's modified Eagle's medium (DMEM) with 4.5 g L^{-1} glucose, L-glutamine, sodium pyruvate (Corning cellgro), 5% fetal bovine serum (Corning, NY, USA), and penicillin/streptomycin (complete medium) at 37°C and 10% CO_2 with humidity. Cells were seeded in sixteen 10 cm diameter dishes at 5e+6 cells per dish in 25 mL of complete medium 16–18 h prior to transfection. The backbone of pcDNASfi (27) was modified by deletion of three internal *Nco*I sites using Quick change mutagenesis (Stratagene) and synthetic DNA encoding a portion of the hCMV promoter and intron A was mobilized from pUC57 CMV-INTA *via Sna*BI and *Nhe*I to replace the resident 5′-ntr to create puma2. Previously described human codon-optimized genes residing in pcDNASfi encoding Marburg Musoke (MARV), Ebola Zaire Kikwit (EBOV), or Ebola Bundibugyo NP were back inserted to puma2 *via Sfi*I. Qiagen miniprep DNA (105 μL at 100 ng μL^{-1}) and 41 μL linear polyethylenimine (1 μg μL^{-1}, pH 7.0) were combined and equilibrated for 20 min at room temperature in 2.5 mL serum-free DMEM prior to being carefully added to the medium. Cells were collected 48 h post transfection by trypsinization in 4 mL trypsin–EDTA solution (Sigma, St. Louis, MO, USA) with 2-plates worth of cells combined into 50 mL Falcon tubes and topped up to 50 mL with phosphate-buffered saline (PBS). Cells were pelleted at 1,000 rpm for 5 min (Beckman Allegra 6R swing out rotor) washed once with PBS and repelleted. The cells were lysed in 4 mL of ice-cold hypotonic buffer consisting of 20 mM HEPES pH 7.5, 5 mM KCl, 1.5 mM $MgCl_2$, 1 mM DTT, 1 tablet of cOmplete™ EDTA-free protease inhibitor cocktail (Roche) per 50 mL. DNA was sheared by passing through a 30-G needle several times on ice. Samples were microfuged in 2 mL tubes at 6,000 rpm for 10 min at 4°C (5415D microcentrifuge, Eppendorf, Hauppauge, NY, USA) and the supernatants transferred to fresh tubes and re-centrifuged at 13,000 rpm for 10 min. Clarified samples were pooled and concentrated in two 15 mL 100 kDa cut-off Amicon centrifugal filters at 3,500 rpm (Beckman Allegra 6R, swing out rotor, room temperature) until the volume was approximately 800 μL. Samples were clarified by microcentrifugation at high speed for 5 min immediately before loading 400 μL on to CsCl gradients (40–25%, 5% steps in TNE—10 mM Tris–HCl pH 7.4, 150 mM NaCl, 1 mM EDTA). Gradients were centrifuged at 25,000 rpm (Beckman SW41Ti) for 18 h at 20°C. The NP bands were collected by side-puncture with an 18-G needle, samples combined and dialyzed in 10 kDa cut-off Slide-A-Lyzer cassettes (ThermoFisher Scientific) against PBS at 4°C. Samples were quantified by micro-BCA assay and analyzed by SDS-PAGE and silver stain. Samples were made to 15% glycerol, aliquoted and flash frozen in liquid nitrogen and stored at −80°C.

NP Sandwich ELISA

sdAbs were used to coat duplicate Costar white high binding ELISA plate wells at 100 μL of 100 nM in PBS overnight at 4°C. Plates were rinsed with PBS and wells blocked with 2% non-fat dried milk (Carnation, MPBS) to brimming for 1 h at room temperature. Purified NP in MPBS was serially diluted over the sdAb and incubated for 5 min shaking. Plates were washed three times with PBS + 0.1% Tween-20 and two times with PBS. Phage displayed versions of the sdAb derived from pecan21 were used from the original stocks that had been stored at −80°C since 2007 and 1 μL used per well in 100 μL of MPBS for 5 min shaking. Plates were washed as before and 100 μL of 1/2,500 dilution of anti-M13KO7–HRP conjugate (GE Healthcare) in MPBS applied to each well and left for 5 min with shaking. Following

washing, signals were developed with SuperSignal ELISA Pico chemiluminescent substrate (Thermo-Fisher) with 2 s integration using a luminometer (Turner Biosystems) and the duplicates averaged. The assay was performed two more times to create a graph representing the average of the three plots with maximum and minimum bars representing the SD. The negative was not a full titration but the maximum concentration of recombinant Bundibugyo NP.

Aromatic Residue Knockout Analysis

Quick change site-directed mutagenesis was employed to mutate the CDR3 aromatic residue of sdAb A, B, and C to Ala and expressed in pecan126 which encodes a BAP sequence downstream of the sdAb (26). Proteins were expressed in HBV88 as for Tuner + pRARE and purified as above. 100 µL of 1 µg mL^{-1} purified MARV or EBOV NP in PBS was used to coat duplicate ELISA plate wells overnight at 4°C. Following rinsing and blocking as above, sdAb proteins in MPBS were titrated over the NP and left for 1 h static. Following washing, 100 µL of 1/10,000 anti-His_6-HRP conjugate (Sigma) in MPBS was applied for 1 h. Following washing, the plates were developed and duplicate wells averaged. The ELISA was repeated once and curves represent the average of the two plots with bars representing SDs.

Gluc-Based EC_{50} Determination

The sequence encoding an *E. coli* codon-optimized Gaussia luciferase (gluc) gene within pUC19 from the NanoLight™ Technology website (Pinetop, AZ, USA) was used as the basis for designing overlapping oligonucleotides encoding the open reading frame plus a His_6 sequence flanked by unique *Nco*I and *Hin*dIII compatible overlaps. Following kinasing, the oligonucleotides were heated and slowly cooled in Taq DNA ligase buffer, enzyme added and ligated to gel purified pecan22 from which a resident sdAb gene had been removed with *Nco*I and *Hin*dIII. A faithful clone was used to confirm active gluc enzyme could be expressed and purified at 500 mL scale as above and then the gene was re-engineered to enable insertion of recombinant antibody fragments. Hingeless sdAb A-D genes from pecan73 were subsequently inserted *via Nco*I and *Not*I to generate the pecan35 sdAb–gluc gene fusions. The resulting glucibodies were expressed and purified as for sdAb above within Tuner + pRARE.

Recombinant NP of either MARV or negative control Bundibugyo Ebola in 100 µL of PBS at 1 µg mL^{-1} were used to coat duplicate wells of ELISA plates at 4°C overnight. Plates were washed three times with PBS and each well blocked to brimming with MPBS for 1 h. Wells were then probed with 100 µL of the gluc control or glucibody dilutions in MPBS for 1 h static. Probe was removed and plates washed three times with PBS containing 0.1% Tween-20 (PBST) and two times with PBS. Signals were developed with injection of coelenterazine (NanoLight™ Technology) in lucky buffer (10 mM Tris, 1 mM EDTA, 500 mM NaCl, pH 7.4) and collected using the luminometer with a 2 s integration. Duplicate wells of each dilution were averaged and the Bundibugyo NP signals subtracted from the MARV NP signals. The titrations were repeated twice with the final plots representing the mean of three experiments and the error bars representing ± SD. The EC_{50} *y*-value was calculated for each curve using the equation $[RLU_{min} + (RLU_{max} - RLU_{min})/2]$. The corresponding *x* values were calculated using one observed point greater and one less than the *y* EC_{50} using the trend function in Excel and the three values averaged and presented ± SD. Statistical significance was determined using a paired two-sample Student's *t*-test with an alpha value of 0.05 within the Excel data analysis toolpak.

The *mal*E gene from XL1-Blue was amplified to encode a modified N-terminus of MetLysIleHis_6 (70) and a C-terminal fixed arm of Ala_3 encoded by a *Not*I restriction site (71) and inserted into pE (see below) *via Nde*I and *Hin*dIII. An oligonucleotide bridge encoding Ala_3GlySer was then inserted between *Not*I and *Hin*dIII sites to create a control maltose-binding protein (mbp) gene, while NP600 and NP632 were amplified and inserted between the *Not*I and *Hin*dIII sites to create the mbp-NP600 and mbp-NP632 fusion protein expression vectors. Proteins were expressed, purified, quantified, and analyzed by SDS-PAGE and then substituted for recombinant NP as immobilized antigen in the glucibody EC_{50} determination above. Signals on the mbp control protein were subtracted from the mbp-NP600 and mbp-NP632 signals and the experiments repeated three times to generate plots representing the means with error bars representing ± SD. Statistical significance was determined using a paired two-sample Student's *t*-test with an alpha value of 0.05 within the Excel data analysis toolpak.

NP Deletion Mutagenesis

Phagemid pecan42, a *tac* promoter-based vector harboring the MARV Musoke NP gene with a C-terminal His_6 tag (21) was first used as a template for introducing an N-terminal FLAG tag by splice-overlap extension (SOE) PCR. Stepwise deletions of 100 amino acids (the C-terminal region was 95 amino acids) from the authentic NP initiation codon were then made using SOE-PCR. Clones were mobilized to Tuner + pRARE and 20 mL expression cultures used to generate lysates from 20 OD units in 2 mL tubes using a Mini-beadbeater 16 (Biospec Products). Lysates (10 µL) were Western blotted to Immobilon P (Millipore) for probing with anti-FLAG M1-HRP conjugate (Sigma), anti-His_6-HRP (Sigma) or the hyperactive AP fusions of each sdAb from pecan16 described previously (21) at 100 nM in MTBS (where Tris–HCl replaces phosphate buffer). Signals were developed with Lumi-Phos WB (Thermo-Fisher) sufficiently for each clone to reveal as much signal as possible without blowout.

Production of NP600 for Crystallization

Phagemid pE is a T7 promoter-based vector assembled from the high copy number backbone of pecan but bearing a T7 cassette assembled from overlapping oligonucleotides to enable high yield of DNA from mini-preps to afford facile sequencing and manipulation and high gene dosage for expression. The perfectly symmetrical *lac* operator (72) ensures tight regulation within expression hosts like BL21 (DE3) despite the high copy number. The MARV Musoke NP C-terminus was amplified from pecan42 MARV NP and inserted into pE such that a MetGlyHis_6GlyGlyGlySer sequence preceded the NP sequence. 50 mL overnight starter cultures with BL21(DE3) + pRARE in TB with 2% glucose, ampicillin at 200 µg mL^{-1} and chloramphenicol at 30 µg mL^{-1} were

grown at 30°C until saturation. Cultures were poured into 450 mL glucose-free TB, grown with vigorous aeration in Bellco baffled flasks for 3 h at 25°C and induced for 3 h with 0.1 mM IPTG. Cultures were centrifuged and the pellets drained of excess media and stored at −80°C until ready for beadbeating. Once thawed, the pellets were resuspended in 40 mL 1× IMAC plus a complete protease inhibitor tablet (Roche) and added to a 50 mL chamber filled halfway with 0.1 mm glass beads. The chamber was topped off with 1× IMAC buffer to remove any air bubbles and the cell/bead mixture was blended on ice within a 4°C fridge for a total of 12 min with 2 min on and 2 min cooling on ice in between. Once contents settled, the cell debris was transferred to a 50 mL conical tube and centrifuged at 3,000 rpm for 15 min at 4°C (Beckman Allegra 6R, swing out). The supernatant was decanted into a new 50 mL tube and centrifuged at 9,500 rpm for 15 min at 4°C (Sorvall RC 6+, F13 FiberLite rotor). The supernatant was filtered through a 32 mm diameter 0.8/0.2 µm filter (Pall) and applied to a 5 mL HisTrapHP column equilibrated in 1× IMAC. Protein was eluted with a 0–500 mM imidazole gradient in 1× IMAC buffer. The fractions were pooled and dialyzed into 20 mM Tris–HCl pH 7.4, 5% glycerol and loaded onto a column (20 mL bed volume) of High-Performance Q-Sepharose resin (GE Healthcare) equilibrated in 20 mM Tris–HCl pH 7.4. The protein was eluted with a 0–500 mM sodium chloride gradient, pooled, and concentrated to 2 mL. The sample was further purified on a Superdex 75 16/60 column in 10 mM Tris pH 7.4, 150 mM NaCl. Protein was quantified by UV adsorption and analyzed by SDS-PAGE to access purity. For crystallography, preparations were diluted to 12 mg mL^{-1}, aliquoted and stored at −80°C.

Western blotting of tenfold dilutions of NP600 employed 100 nM of the sdAb–AP fusions in MTBS with each probed membrane subsequently aligned side-by-side for simultaneous development to ensure accurate comparison across the sdAb clones.

nluc-Based EC_{50} Determination

A pE variant (pENCO1) was first engineered where the ATG start codon was within an *Nco*I site rather than an *Nde*I to allow genes coming from *pel*B leader constructs to be shuttled conveniently over. A synthetic gene encoding nluc based on the Promega website (Madison, WI, USA) with and without the single Cys had been explored for secretion capacity in pecan73 (26) (a *tac* promoter *pel*B leader vector) as a C-terminally His_6-tagged motif and found very lacking. The nluc Cys minus gene was therefore mobilized from the periplasmic to the cytosolic system to create pENCO9 for control protein production. MARV Musoke NP600 and NP632 were separately fused to nluc using SOE-PCR such that the gene fusions sandwiched the His_6 tag between the nluc and NP domains. Proteins were expressed, purified, and quantified as for NP600 except that the dramatic solubility enhancement afforded by the nluc fusions obviated the need for ion exchange. ELISA plates were coated overnight at 4°C with 100 µL of 1 µg mL^{-1} of neutravidin in PBS. Plates were washed three times with PBS and then blocked by filling to brimming with Bioplex buffer (2% bovine serum albumin, 0.05% Tween-20 in PBS) for 1 h. 100 µL of 100 nM sdAb as a BAP fusion purified from pecan126 as described above was applied to the well in Bioplex buffer for 1 h. Wells were washed to brimming three times with PBST and two times with PBS. MPBS was added to the well to brimming for 1 h to further block the sdAb and then dilutions of nluc, nluc-NP600, or nluc-NP632 in MPBS were added to duplicate wells for 1 h. Following washing the same substrate and buffer as used for gluc was added to wells and signals captured as above. The experiment was repeated two more times and curves are the plots of three mean RLU of nluc-NP600 or nluc-NP632 minus the corresponding mean of the nluc alone with error bars representing SD. The EC_{50} values were determined from individual curves as above and statistical significance determined likewise.

Production of sdAb for Crystallization

Genes encoding sdAb A, B, and C were first mobilized to pecan73 using PCR to delete the flexible llama Ig hinges and fuse the His_6 tag closer to FR4. Expressions and harvesting at 500 mL scale were initiated as above and the shockate was made to 100 mM NaCl, 10 mM imidazole, and 5% glucose and frozen at −80°C prior to purification. sdAb was captured using a 5 mL HiTrap sepharose column (GE Healthcare) charged with nickel and equilibrated with TIGS buffer (100 mM Tris–HCl pH 7.4, 100 mM NaCl, 10 mM imidazole, and 5% glycerol). Bound protein was washed with three column volumes of TIGS buffer and eluted with a 10–270 mM imidazole gradient over 18 column volumes, pooled and dialyzed into 50 mM sodium phosphate, pH 7.0 with 5% glycerol. The protein was further purified on a HiLoad 26/600 SP Sepharose column (GE Healthcare). Bound protein was eluted with a 0–500 mM sodium chloride gradient, pooled and concentrated to 1 mL *via* Centricon ultraconcentration. Final purification of the sdAb A and B samples were carried out with a HighLoad 16/60 Superdex 75 prep grade column (GE Healthcare) equilibrated in 10 mM Tris–HCl pH 7.4 while sdAb C required additional 150 mM NaCl to not precipitate. Complexes of sdAb A and B with NP600 were obtained by overnight equilibration of 1:1 mixtures.

Bait Prey Strategy to Generate sdAb C/NP632 Complex

Splice-overlap extension PCR was used to re-amplify the sdAb C gene from pecan73 to delete an internal *Nco*I site and terminate the ORF immediately after FR4 with no His_6 tag. The product was back inserted into pecan73 *via Nco*I and *Hin*dIII to create pecan219 sdAb C. The first 31 amino acids of the pE-NP600 construct were deleted by PCR and back cloning to create pE-NP632 which was used to drive expression of NP632 as for NP600 as above. Culture volumes (2 L) yielding approximately two wet weight pellets of 28 g were bead beated and each partially purified on the 5 mL HiTrap IMAC column and gradient eluted. The peak fractions were combined and applied to the Q-Sepharose column as before and then combined with osmotic shockate derived from 4 × 500 mL pecan219 sdAb C cultures made to 1× TIGS and the mixtures stirred at 4°C overnight. The complex was batch IMAC purified and eluted as for sdAb, and purified on the S75 16/600 column in 10 mM Tris pH 7.5, 150 mM NaCl. The final sample was concentrated to 2 mL, quantified by micro-BCA assay (12.8 mg mL^{-1}) and evaluated for purity by SDS-PAGE.

Crystallization, Structure Determination, and Refinement

Automated screening for crystallization was carried out using the sitting drop vapor-diffusion method with an Art Robbins Instruments Phoenix system in the X-ray Crystallography Core Laboratory at UTHSCSA. Crystals were obtained using the following reagents from commercial crystallization screen kits from Qiagen and Molecular Dimensions: sdAb A (concentrated to 12 mg mL^{-1})—25% polyethylene glycol (PEG) 1000, 0.1 M Tris–HCl pH 8.5 at 22°C; sdAb A/NP600 (12 mg mL^{-1})—15% PEG 6000, 5% glycerol at 22°C; sdAb B (11.3 mg mL^{-1}) 4.0 M sodium chloride, 0.1 M bicine pH 9 at 22°C; sdAb B/NP600 (12 mg mL^{-1})—20% PEG 4000, 0.16 M ammonium sulfate, 20% glycerol, 0.08 M sodium acetate pH 4.6 at 22°C; sdAb C (12 mg mL^{-1})—30% PEG 550 monomethyl ether/PEG 20000, 0.1 M carboxylic acids mix (sodium formate, ammonium acetate, sodium citrate, sodium/potassium tartrate, sodium oxamate), 0.1 M imidazole/MES pH 6.5 at 4°C; sdAb C/NP632 (12.7 mg mL^{-1})—20% PEG 6000, 0.2 M magnesium chloride, 0.1 M 1,2,3-hexanetriol, 0.1 M sodium acetate pH 5 at 4°C. Crystals were transferred to undersized cryoloops and manipulated to wick off excess mother liquor prior to flash-cooling in liquid nitrogen. X-ray diffraction data were acquired using a home source Rigaku MicroMax 007HF X-ray Generator equipped with VariMax HR and HF confocal optics and RAXIS–HTC image plate detectors or national synchrotron facilities. Diffraction data were integrated and scaled using XDS (73). The structure of sdAb A was determined by the molecular replacement method implemented in PHASER (74) using a camel single-domain antibody as the search model [Protein Data Bank (PDB) entry 1YC7 (75)]. All other structures were determined using sdAb A as the search model. Coordinates were refined using PHENIX (76), including simulated annealing with torsion angle dynamics, and alternated with manual rebuilding using COOT (77). Non-crystallographic symmetry restraints were used in the refinement of the sdAb B/NP600 and sdAb C/NP632 complexes. Visualizations of structures employed PyMol (78).

AUTHOR CONTRIBUTIONS

JG, AT, LS, and AH designed experiments, performed the work, and analyzed the data. PH contributed analytic tools. AH wrote the paper.

ACKNOWLEDGMENTS

We thank Lisa Osborn for the NP deletion mutagenesis and probing experiments, and Dr. Jay Nix at ALS Beamline 4.2.2 for acquiring data for the sdAb B/NP600 complex.

FUNDING

This work was supported by National Institutes of Health, National Institute of Allergy and Infectious Diseases R21AI105568 (AH) and R01AI112851 (AH), and in part by the Office of Naval Research/Defense Threat Reduction Agency Basic Research Program N00173-08-1-G003 (AH), The San Antonio Area Foundation (AH), Texas Biomedical Research Institute Forum and Founders Council (AH and JG), and a Cowles Postdoctoral Fellowship (JG). This work is based on research conducted at the Northeastern Collaborative Access Team beamlines, which are funded by the National Institute of General Medical Sciences from the National Institutes of Health (P41 GM103403). The Pilatus 6M detector on 24-ID-C beamline is funded by a NIH-ORIP HEI grant (S10 RR029205). This research used resources of the Advanced Photon Source, a U.S. Department of Energy (DOE) Office of Science User Facility operated for the DOE Office of Science by Argonne National Laboratory under Contract No. DE-AC02-06CH11357. This work is also based on research at Beamline 4.2.2 of the Molecular Biology Consortium at the Advanced Light Source (ALS). ALS is supported by the Director, Office of Science, Office of Basic Energy Sciences, of the DOE under Contract No. DE-AC02-05CH11231. The X-Ray Crystallography Core Laboratory is a part of the Institutional Research Cores supported by the Office of the Vice President for Research and the UT Health Cancer Center (NIH/NCI grant P30 CA054174). PH was funded by the Robert A. Welch Foundation grant AQ-1399.

SUPPLEMENTARY MATERIAL

The Supplementary Material for this article can be found online at http://journal.frontiersin.org/article/10.3389/fimmu.2017.01234/full#supplementary-material.

REFERENCES

1. Slenczka WG. The Marburg virus outbreak of 1967 and subsequent episodes. *Curr Top Microbiol Immunol* (1999) 235:49–75.
2. Towner JS, Amman BR, Sealy TK, Carroll SA, Comer JA, Kemp A, et al. Isolation of genetically diverse Marburg viruses from Egyptian fruit bats. *PLoS Pathog* (2009) 5:e1000536. doi:10.1371/journal.ppat.1000536
3. Bausch DG, Nichol ST, Muyembe-Tamfum JJ, Borchert M, Rollin PE, Sleurs H, et al. Marburg hemorrhagic fever associated with multiple genetic lineages of virus. *N Engl J Med* (2006) 355:909–19. doi:10.1056/NEJMoa051465
4. Towner JS, Khristova ML, Sealy TK, Vincent MJ, Erickson BR, Bawiec DA, et al. Marburgvirus genomics and association with a large hemorrhagic fever outbreak in Angola. *J Virol* (2006) 80:6497–516. doi:10.1128/JVI.00069-06
5. Knust B, Schafer IJ, Wamala J, Nyakarahuka L, Okot C, Shoemaker T, et al. Multidistrict outbreak of Marburg virus disease – Uganda, 2012. *J Infect Dis* (2015) 212(Suppl 2):S119–28. doi:10.1093/infdis/jiv351
6. Mire CE, Geisbert JB, Borisevich V, Fenton KA, Agans KN, Flyak AI, et al. Therapeutic treatment of Marburg and Ravn virus infection in nonhuman primates with a human monoclonal antibody. *Sci Transl Med* (2017) 9:eaai8711. doi:10.1126/scitranslmed.aai8711
7. Grolla A, Jones SM, Fernando L, Strong JE, Ströher U, Möller P, et al. The use of a mobile laboratory unit in support of patient management and epidemiological surveillance during the 2005 Marburg outbreak in Angola. *PLoS Negl Trop Dis* (2011) 5:e1183. doi:10.1371/journal.pntd.0001183
8. Bausch DG, Schwarz L. Outbreak of Ebola virus disease in Guinea: where ecology meets economy. *PLoS Negl Trop Dis* (2014) 8:e3056. doi:10.1371/journal.pntd.0003056
9. Dietzel E, Schudt G, Krahling V, Matrosovich M, Becker S. Functional characterization of adaptive mutations during the West African Ebola virus outbreak. *J Virol* (2017) 91:e01913–16. doi:10.1128/JVI.01913-16
10. Kugelman JR, Sanchez-Lockhart M, Andersen KG, Gire S, Park DJ, Sealfon R, et al. Evaluation of the potential impact of Ebola virus genomic drift on the

efficacy of sequence-based candidate therapeutics. *MBio* (2015) 6:e02227–14. doi:10.1128/mBio.02227-14
11. Gire SK, Goba A, Andersen KG, Sealfon RS, Park DJ, Kanneh L, et al. Genomic surveillance elucidates Ebola virus origin and transmission during the 2014 outbreak. *Science* (2014) 345:1369–72. doi:10.1126/science.1259657
12. Sozhamannan S, Holland MY, Hall AT, Negrón DA, Ivancich M, Koehler JW, et al. Evaluation of signature erosion in Ebola virus due to genomic drift and its impact on the performance of diagnostic assays. *Viruses* (2015) 7:3130–54. doi:10.3390/v7062763
13. Flyak AI, Ilinykh PA, Murin CD, Garron T, Shen X, Fusco ML, et al. Mechanism of human antibody-mediated neutralization of Marburg virus. *Cell* (2015) 160:893–903. doi:10.1016/j.cell.2015.01.031
14. Kajihara M, Nakayama E, Marzi A, Igarashi M, Feldmann H, Takada A. Novel mutations in Marburg virus glycoprotein associated with viral evasion from antibody mediated immune pressure. *J Gen Virol* (2013) 94:876–83. doi:10.1099/vir.0.049114-0
15. Audet J, Wong G, Wang H, Lu G, Gao GF, Kobinger G, et al. Molecular characterization of the monoclonal antibodies composing ZMAb: a protective cocktail against Ebola virus. *Sci Rep* (2014) 4:6881. doi:10.1038/srep06881
16. Davidson E, Bryan C, Fong RH, Barnes T, Pfaff JM, Mabila M, et al. Mechanism of binding to Ebola virus glycoprotein by the ZMapp, ZMAb, and MB-003 cocktail antibodies. *J Virol* (2015) 89:10982–92. doi:10.1128/JVI.01490-15
17. Kugelman JR, Kugelman-Tonos J, Ladner JT, Pettit J, Keeton CM, Nagle ER, et al. Emergence of Ebola virus escape variants in infected non-human primates treated with the MB-003 antibody cocktail. *Cell Rep* (2015) 12:2111–20. doi:10.1016/j.celrep.2015.08.038
18. Gong LI, Suchard MA, Bloom JD. Stability-mediated epistasis constrains the evolution of an influenza protein. *Elife* (2013) 2:e00631. doi:10.7554/eLife.00631
19. Lee HK, Lee CK, Loh TP, Chiang D, Koay ES, Tang JW. Missed diagnosis of influenza B virus due to nucleoprotein sequence mutations, Singapore, April 2011. *Euro Surveill* (2011) 16:19943.
20. Goldman ER, Anderson GP, Liu JL, Delehanty JB, Sherwood LJ, Osborn LE, et al. Facile generation of heat-stable antiviral and antitoxin single domain antibodies from a semisynthetic llama library. *Anal Chem* (2006) 78:8245–55. doi:10.1021/ac0610053
21. Sherwood LJ, Osborn LE, Carrion R Jr, Patterson JL, Hayhurst A. Rapid assembly of sensitive antigen-capture assays for Marburg virus, using *in vitro* selection of llama single-domain antibodies, at biosafety level 4. *J Infect Dis* (2007) 196(Suppl 2):S213–9. doi:10.1086/520586
22. Bharat TA, Riches JD, Kolesnikova L, Welsch S, Krähling V, Davey N, et al. Cryo-electron tomography of Marburg virus particles and their morphogenesis within infected cells. *PLoS Biol* (2011) 9:e1001196. doi:10.1371/journal.pbio.1001196
23. Dolnik O, Stevermann L, Kolesnikova L, Becker S. Marburg virus inclusions: a virus-induced microcompartment and interface to multivesicular bodies and the late endosomal compartment. *Eur J Cell Biol* (2015) 94:323–31. doi:10.1016/j.ejcb.2015.05.006
24. Mühlberger E, Lötfering B, Klenk HD, Becker S. Three of the four nucleocapsid proteins of Marburg virus, NP, VP35, and L, are sufficient to mediate replication and transcription of Marburg virus-specific monocistronic minigenomes. *J Virol* (1998) 72:8756–64.
25. Kirchdoerfer RN, Moyer CL, Abelson DM, Saphire EO. The Ebola virus VP30-NP interaction is a regulator of viral RNA synthesis. *PLoS Pathog* (2016) 12:e1005937. doi:10.1371/journal.ppat.1005937
26. Sherwood LJ, Hayhurst A. Hapten mediated display and pairing of recombinant antibodies accelerates assay assembly for biothreat countermeasures. *Sci Rep* (2012) 2:807. doi:10.1038/srep00807
27. Sherwood LJ, Hayhurst A. Ebolavirus nucleoprotein C-termini potently attract single domain antibodies enabling monoclonal affinity reagent sandwich assay (MARSA) formulation. *PLoS One* (2013) 8:e61232. doi:10.1371/journal.pone.0061232
28. Peng HP, Lee KH, Jian JW, Yang AS. Origins of specificity and affinity in antibody-protein interactions. *Proc Natl Acad Sci U S A* (2014) 111:E2656–65. doi:10.1073/pnas.1401131111
29. Hall TA. BioEdit: a user-friendly biological sequence alignment editor and analysis program for Windows 95/98/NT. *Nucleic Acids Symp Ser* (1999) 41:95–8.
30. Tannous BA, Kim DE, Fernandez JL, Weissleder R, Breakefield XO. Codon-optimized Gaussia luciferase cDNA for mammalian gene expression in culture and *in vivo*. *Mol Ther* (2005) 11:435–43. doi:10.1016/j.ymthe.2004.10.016
31. Venisnik KM, Olafsen T, Gambhir SS, Wu AM. Fusion of Gaussia luciferase to an engineered anti-carcinoembryonic antigen (CEA) antibody for *in vivo* optical imaging. *Mol Imaging Biol* (2007) 9:267–77. doi:10.1007/s11307-007-0101-8
32. Bharat TA, Noda T, Riches JD, Kraehling V, Kolesnikova L, Becker S, et al. Structural dissection of Ebola virus and its assembly determinants using cryo-electron tomography. *Proc Natl Acad Sci U S A* (2012) 109:4275–80. doi:10.1073/pnas.1120453109
33. Hall MP, Unch J, Binkowski BF, Valley MP, Butler BL, Wood MG, et al. Engineered luciferase reporter from a deep sea shrimp utilizing a novel imidazopyrazinone substrate. *ACS Chem Biol* (2012) 7:1848–57. doi:10.1021/cb3002478
34. Zhou YH, Chen Z, Purcell RH, Emerson SU. Positive reactions on Western blots do not necessarily indicate the epitopes on antigens are continuous. *Immunol Cell Biol* (2007) 85:73–8. doi:10.1038/sj.icb.7100004
35. Baker LE, Ellena JF, Handing KB, Derewenda U, Utepbergenov D, Engel DA, et al. Molecular architecture of the nucleoprotein C-terminal domain from the Ebola and Marburg viruses. *Acta Crystallogr D Struct Biol* (2016) 72:49–58. doi:10.1107/S2059798315021439
36. Wu M, Park YJ, Pardon E, Turley S, Hayhurst A, Deng J, et al. Structures of a key interaction protein from the *Trypanosoma brucei* editosome in complex with single domain antibodies. *J Struct Biol* (2011) 174:124–36. doi:10.1016/j.jsb.2010.10.007
37. Friesen RH, Lee PS, Stoop EJ, Hoffman RM, Ekiert DC, Bhabha G, et al. A common solution to group 2 influenza virus neutralization. *Proc Natl Acad Sci U S A* (2014) 111:445–50. doi:10.1073/pnas.1319058110
38. Zhou T, Lynch RM, Chen L, Acharya P, Wu X, Doria-Rose NA, et al. Structural repertoire of HIV-1-neutralizing antibodies targeting the CD4 supersite in 14 donors. *Cell* (2015) 161:1280–92. doi:10.1016/j.cell.2015.05.007
39. Kong L, Lee JH, Doores KJ, Murin CD, Julien JP, McBride R, et al. Supersite of immune vulnerability on the glycosylated face of HIV-1 envelope glycoprotein gp120. *Nat Struct Mol Biol* (2013) 20:796–803. doi:10.1038/nsmb.2594
40. Sobolev V, Eyal E, Gerzon S, Potapov V, Babor M, Prilusky J, et al. SPACE: a suite of tools for protein structure prediction and analysis based on complementarity and environment. *Nucleic Acids Res* (2005) 33:W39–43. doi:10.1093/nar/gki398
41. De Genst E, Silence K, Decanniere K, Conrath K, Loris R, Kinne J, et al. Molecular basis for the preferential cleft recognition by dromedary heavy-chain antibodies. *Proc Natl Acad Sci U S A* (2006) 103:4586–91. doi:10.1073/pnas.0505379103
42. Stijlemans B, Conrath K, Cortez-Retamozo V, Van Xong H, Wyns L, Senter P, et al. Efficient targeting of conserved cryptic epitopes of infectious agents by single domain antibodies. African trypanosomes as paradigm. *J Biol Chem* (2004) 279:1256–61. doi:10.1074/jbc.M307341200
43. Strauss M, Schotte L, Thys B, Filman DJ, Hogle JM. Five of five VHHs neutralizing poliovirus bind the receptor-binding site. *J Virol* (2016) 90:3496–505. doi:10.1128/JVI.03017-15
44. Krissinel E, Henrick K. Inference of macromolecular assemblies from crystalline state. *J Mol Biol* (2007) 372:774–97. doi:10.1016/j.jmb.2007.05.022
45. Koide A, Tereshko V, Uysal S, Margalef K, Kossiakoff AA, Koide S. Exploring the capacity of minimalist protein interfaces: interface energetics and affinity maturation to picomolar KD of a single-domain antibody with a flat paratope. *J Mol Biol* (2007) 373:941–53. doi:10.1016/j.jmb.2007.08.027
46. Clackson T, Wells JA. A hot spot of binding energy in a hormone-receptor interface. *Science* (1995) 267:383–6. doi:10.1126/science.7529940
47. Bogan AA, Thorn KS. Anatomy of hot spots in protein interfaces. *J Mol Biol* (1998) 280:1–9. doi:10.1006/jmbi.1998.1843
48. Winn MD, Ballard CC, Cowtan KD, Dodson EJ, Emsley P, Evans PR, et al. Overview of the CCP4 suite and current developments. *Acta Crystallogr D Biol Crystallogr* (2011) 67:235–42. doi:10.1107/S0907444910045749
49. Epa VC, Colman PM. Shape and electrostatic complementarity at viral antigen-antibody complexes. *Curr Top Microbiol Immunol* (2001) 260:45–53. doi:10.1007/978-3-662-05783-4_3

50. Lawrence MC, Colman PM. Shape complementarity at protein/protein interfaces. *J Mol Biol* (1993) 234:946–50. doi:10.1006/jmbi.1993.1648
51. Rini JM, Schulze-Gahmen U, Wilson IA. Structural evidence for induced fit as a mechanism for antibody-antigen recognition. *Science* (1992) 255:959–65. doi:10.1126/science.1546293
52. Kallewaard NL, Corti D, Collins PJ, Neu U, McAuliffe JM, Benjamin E, et al. Structure and function analysis of an antibody recognizing all influenza A subtypes. *Cell* (2016) 166:596–608. doi:10.1016/j.cell.2016.05.073
53. Hinz A, Lutje Hulsik D, Forsman A, Koh WW, Belrhali H, Gorlani A, et al. Crystal structure of the neutralizing llama V(HH) D7 and its mode of HIV-1 gp120 interaction. *PLoS One* (2010) 5:e10482. doi:10.1371/journal.pone.0010482
54. Yusim K, Yoon H, Foley B, Feng S, Macke J, Dimitrijevic M, et al. Integrated sequence and immunology filovirus database at Los Alamos. *Database (Oxford)* (2016) 2016. doi:10.1093/database/baw047
55. Saijo M, Niikura M, Maeda A, Sata T, Kurata T, Kurane I, et al. Characterization of monoclonal antibodies to Marburg virus nucleoprotein (NP) that can be used for NP-capture enzyme-linked immunosorbent assay. *J Med Virol* (2005) 76:111–8. doi:10.1002/jmv.20332
56. Ma B, Elkayam T, Wolfson H, Nussinov R. Protein-protein interactions: structurally conserved residues distinguish between binding sites and exposed protein surfaces. *Proc Natl Acad Sci U S A* (2003) 100:5772–7. doi:10.1073/pnas.1030237100
57. Van Regenmortel MH. The antigenicity of tobacco mosaic virus. *Philos Trans R Soc Lond B Biol Sci* (1999) 354:559–68. doi:10.1098/rstb.1999.0407
58. Holm L, Laakso LM. Dali server update. *Nucleic Acids Res* (2016) 44:W351–5. doi:10.1093/nar/gkw357
59. Dziubanska PJ, Derewenda U, Ellena JF, Engel DA, Derewenda ZS. The structure of the C-terminal domain of the *Zaire ebolavirus* nucleoprotein. *Acta Crystallogr D Biol Crystallogr* (2014) 70:2420–9. doi:10.1107/S1399004714014710
60. Drozdetskiy A, Cole C, Procter J, Barton GJ. JPred4: a protein secondary structure prediction server. *Nucleic Acids Res* (2015) 43:W389–94. doi:10.1093/nar/gkv332
61. Liu B, Dong S, Li G, Wang W, Liu X, Wang Y, et al. Structural insight into nucleoprotein conformation change chaperoned by VP35 peptide in Marburg virus. *J Virol* (2017) 91:e00825–17. doi:10.1128/JVI.00825-17
62. Koide S. Engineering of recombinant crystallization chaperones. *Curr Opin Struct Biol* (2009) 19:449–57. doi:10.1016/j.sbi.2009.04.008
63. Noda T, Watanabe S, Sagara H, Kawaoka Y. Mapping of the VP40-binding regions of the nucleoprotein of Ebola virus. *J Virol* (2007) 81:3554–62. doi:10.1128/JVI.02183-06
64. Lee PS, Wilson IA. Structural characterization of viral epitopes recognized by broadly cross-reactive antibodies. *Curr Top Microbiol Immunol* (2015) 386:323–41. doi:10.1007/82_2014_413
65. Xu R, Krause JC, McBride R, Paulson JC, Crowe JE Jr, Wilson IA. A recurring motif for antibody recognition of the receptor-binding site of influenza hemagglutinin. *Nat Struct Mol Biol* (2013) 20:363–70. doi:10.1038/nsmb.2500
66. Oda S, Noda T, Wijesinghe KJ, Halfmann P, Bornholdt ZA, Abelson DM, et al. Crystal structure of Marburg virus VP40 reveals a broad, basic patch for matrix assembly and a requirement of the N-terminal domain for immunosuppression. *J Virol* (2015) 90:1839–48. doi:10.1128/JVI.01597-15
67. Welsch S, Kolesnikova L, Krähling V, Riches JD, Becker S, Briggs JA. Electron tomography reveals the steps in filovirus budding. *PLoS Pathog* (2010) 6:e1000875. doi:10.1371/journal.ppat.1000875
68. Cleveland SB, Davies J, McClure MA. A bioinformatics approach to the structure, function, and evolution of the nucleoprotein of the order mononegavirales. *PLoSOne* (2011) 6:e19275. doi:10.1371/annotation/6e05f8a1-c49a-4102-a8c9-188e8dc6290e
69. Neu HC, Heppel LA. The release of enzymes from *Escherichia coli* by osmotic shock and during the formation of spheroplasts. *J Biol Chem* (1965) 240:3685–92.
70. Austin BP, Nallamsetty S, Waugh DS. Hexahistidine-tagged maltose-binding protein as a fusion partner for the production of soluble recombinant proteins in *Escherichia coli*. *Methods Mol Biol* (2009) 498:157–72. doi:10.1007/978-1-59745-196-3_11
71. Center RJ, Kobe B, Wilson KA, Teh T, Howlett GJ, Kemp BE, et al. Crystallization of a trimeric human T cell leukemia virus type 1 gp21 ectodomain fragment as a chimera with maltose-binding protein. *Protein Sci* (1998) 7:1612–9. doi:10.1002/pro.5560070715
72. Sadler JR, Sasmor H, Betz JL. A perfectly symmetric lac operator binds the lac repressor very tightly. *Proc Natl Acad Sci U S A* (1983) 80:6785–9. doi:10.1073/pnas.80.22.6785
73. Kabsch W. XDS. *Acta Crystallogr D Biol Crystallogr* (2010) 66:125–32. doi:10.1107/S0907444909047337
74. McCoy AJ, Grosse-Kunstleve RW, Adams PD, Winn MD, Storoni LC, Read RJ. Phaser crystallographic software. *J Appl Crystallogr* (2007) 40:658–74. doi:10.1107/S0021889807021206
75. Conrath K, Vincke C, Stijlemans B, Schymkowitz J, Decanniere K, Wyns L, et al. Antigen binding and solubility effects upon the veneering of a camel VHH in framework-2 to mimic a VH. *J Mol Biol* (2005) 350:112–25. doi:10.1016/j.jmb.2005.04.050
76. Adams PD, Afonine PV, Bunkóczi G, Chen VB, Davis IW, Echols N, et al. PHENIX: a comprehensive python-based system for macromolecular structure solution. *Acta Crystallogr D Biol Crystallogr* (2010) 66:213–21. doi:10.1107/S0907444909052925
77. Emsley P, Lohkamp B, Scott WG, Cowtan K. Features and development of coot. *Acta Crystallogr D Biol Crystallogr* (2010) 66:486–501. doi:10.1107/S0907444910007493
78. DeLano WL. *The PyMol Molecular Graphics System*. San Carlos, CA: deLano Scientific (2002). Available from: http://www.pymol.org

Conflict of Interest Statement: The authors declare that the research was conducted in the absence of any commercial or financial relationships that could be construed as a potential conflict of interest.

Advantages of publishing in Frontiers

OPEN ACCESS
Articles are free to read, for greatest visibility

COLLABORATIVE PEER-REVIEW
Designed to be rigorous – yet also collaborative, fair and constructive

FAST PUBLICATION
Average 85 days from submission to publication (across all journals)

COPYRIGHT TO AUTHORS
No limit to article distribution and re-use

TRANSPARENT
Editors and reviewers acknowledged by name on published articles

SUPPORT
By our Swiss-based editorial team

IMPACT METRICS
Advanced metrics track your article's impact

GLOBAL SPREAD
5'100'000+ monthly article views and downloads

LOOP RESEARCH NETWORK
Our network increases readership for your article

Frontiers
EPFL Innovation Park, Building I • 1015 Lausanne • Switzerland
Tel +41 21 510 17 00 • Fax +41 21 510 17 01 • info@frontiersin.org
www.frontiersin.org

Find us on